

# LEGIBILITY NOTICE

A major purpose of the Technical Information Center is to provide the broadest dissemination possible of information contained in DOE's Research and Development Reports to business, industry, the academic community, and federal, state and local governments.

Although a small portion of this report is not reproducible, it is being made available to expedite the availability of information on the research discussed herein.

Los Alamos National Laboratory is operated by the University of California for the United States Department of Energy under contract W 7405-ENG-36

LA-UR--89-2920

DE89 016602

TITLE PROCEEDINGS OF THE 10TH MEETING OF THE INTERNATIONAL COLLABORATION ON ADVANCED NEUTRON SOURCES

AUTHOR(S) Dianne K. Hyer, Compiler

SUBMITTED TO ICANS-X Meeting, Los Alamos, NM, October 3-7, 1988  
Published in IOPP Ltd, Bristol, England Vol. 97

**DISCLAIMER**

This report was prepared as an account of work sponsored by an agency of the United States Government. Neither the United States Government nor any agency thereof, nor any of their employees, makes any warranty, express or implied, or assumes any legal liability or responsibility for the accuracy, completeness, or usefulness of any information, apparatus, product, or process disclosed, or represents that its use would not infringe privately owned rights. Reference herein to any specific commercial product, process, or service by trade name, trademark, manufacturer, or otherwise does not necessarily constitute or imply its endorsement, recommendation, or favoring by the United States Government or any agency thereof. The views and opinions of authors expressed herein do not necessarily state or reflect those of the United States Government or any agency thereof.

By acceptance of this article the publisher recognizes that the U.S. Government retains a nonexclusive, royalty-free license to publish or reproduce the published form of this contribution or to allow others to do so for U.S. Government purposes.

The Los Alamos National Laboratory requests that the publisher identify this article as work performed under the auspices of the U.S. Department of Energy.

**Los Alamos** Los Alamos National Laboratory  
Los Alamos, New Mexico 87545

# ICANS X

*Proceedings of the 10th Meeting  
of the  
International Collaboration  
on Advanced Neutron Sources*


**Los Alamos, October 3 - 7, 1988**

**Editor: D. K. Hyer**




## PREFACE

The tenth meeting of the International Collaboration on Advanced Neutron Sources (ICANS) was held at the Los Alamos National Laboratory 3-7 October 1988. The two United States participating ICANS laboratories, Los Alamos and Argonne, co-hosted the meeting with Gary Russell, Los Alamos, serving as chairman. There were 146 participants from ten countries representing 28 institutions. The ICANS conference opened with status reports from the spallation-source laboratories. During the course of the meeting, invited papers were presented in two general interest sessions and in target and instrument parallel sessions. An evening panel discussion on user requirements for spallation sources yielded a variety of opinions while the parallel target and instrument workshop sessions were the framework for even more dynamic discussions. Poster sessions were held throughout the meeting, and an outing gave participants an opportunity to meet informally with their colleagues. Peter Egelstaff's presentation at the final session both summarized the meeting and advanced projections for the future.



These proceedings have been organized by sessions. Contributed papers have been placed in the contents according to subject matter. It was necessary to edit some contributions to the proceedings, either because of the original format or method of submission.



Our deep appreciation is extended to all those who helped make this conference a success—Los Alamos National Laboratory management, conference organizers, presenters, participants, authors, session chairmen, administrative assistants, and other interested parties. Members of the ICANS-X organizing committee were Gary Russell, Roger Pynn, Dick Woods, Dianne Hyer, Jack Carpenter, and Bruce Brown. The LANSCE administrative support staff of Lucille Martinez, Teri Cordova, Paula Geisik, and Jan Kapustinsky assisted participants throughout the meeting. Special thanks go to those typists, paste-up artists, illustrators, and designers who worked on the proceedings: Gail Flower, Andi Kron, Emily Morales, Teri Cordova, and Paula Geisik. We thank all other persons who helped in ways not mentioned and now turn our thoughts with anticipation to the ICANS XI meeting in Japan.

Los Alamos, August 1989

*Dianne K. Hyer*



## ICANS MEETINGS

ICANS I United States, Argonne National Laboratory, *December 12 - 15, 1977*

ICANS II England, Rutherford Laboratory, *July 10 - 14, 1978*

ICANS III United States, Los Alamos Scientific Laboratory,  
*March 19 - 22, 1979*

ICANS IV Japan, KEK National Laboratory for High Energy Physics,  
*October 20 - 24, 1980*

ICANS V West Germany, KFA Jülich, *June 22 - 26, 1981*

ICANS VI United States, Argonne National Laboratory,  
*June 28 - July 2, 1982*

ICANS VII Canada, Chalk River Nuclear Laboratory,  
*September 13 - 16, 1983*

ICANS VIII England, Rutherford-Appleton Laboratory,  
*July 8 - 12, 1985*

ICANS IX Switzerland, Swiss Institute for Nuclear  
Research, *September 22 - 26, 1986*

ICANS X United States, Los Alamos National  
Laboratory and Argonne National Laboratory,  
*October 3 - 7, 1988*

# ***Contents***

*International Collaboration on Advanced Neutron Sources*

## ***Monday, October 3, 1988***

Facility overviews

Invited papers

## ***Tuesday, October 4, 1988***

Invited papers, session I

Invited papers, session II

Instrument workshop, session I

Target-station workshop, session I

Instrument workshop, session II

Target-station workshop, session II

## ***Wednesday, October 5, 1988***

Panel discussion

## ***Thursday, October 6, 1988***

Invited papers

Instrument workshop, session I

Target-station workshop, session I

Instrument workshop, session II

Target-station workshop, session II

## ***Friday, October 7, 1988***

Invited paper

Monday, October 3, 1988

**Facility overviews**

- ISIS        ISIS status report, *J. Finney and D. A. Gray*  
IPNS        Status of the Intense Pulsed Neutron Source, *B. Brown*  
LANSCE    Recent progress at LANSCE, *R. Pynn*  
KENS        Progress at the pulsed-spallation neutron facility KENS,  
              *N. Watanabe*  
SINQ        Status Report of SINQ: a continuous spallation neutron source,  
              *W. E. Fischer*

**Invited papers**

- The ISIS target  
              *A. Carne*  
The Proton Storage Ring: problems and solutions  
              *R. Macek*  
Shielding concerns at a spallation source  
              *G. J. Russell, H. Robinson, G. L. Legate, and R. Woods*

Tuesday, October 4, 1988

**Session I, Invited papers**

Target system materials and engineering problems

*W. E. Fischer*

Cold moderator scattering kernels

*R. MacFarlane*

Cold moderators for spallation sources

*A. T. Lucas and H. Robinson*

The advanced MAPLE reactor concept

*R. F. Lidstone, A. G. Lee, G. E. Gillespie, and H. J. Smith*

Design calculations for the ANS cold source

*R. A. Lillie and R. G. Alsmiller, Jr.*

**Session II, Invited papers**

Opportunities for research program development at LANSCE

*C. D. Bowman*

Introduction to maximum entropy

*D. S. Sivia*

New instruments at IPNS: POSY II and SAD II

*R. K. Crawford, G. P. Felcher, R. Kleb, J. E. Epperson, and*

*P. Thiyagarajan*

The ASPUN project

*R. Kustom*

**Instrument workshop, session I**

Developments in inelastic scattering at ISIS, *A. D. Taylor, Z. A. Bowden,*

*C. J. Carlile, M. E. Hagen, A. C. Hannon, R. S. Holt, J. Mayers,*

*R. Osborn, M. P. Paoli, S. T. Robertson, A. Smith, U. Steigenberger,*

*J. Tomkinson, and W. G. Williams*

Development of a chopper spectrometer at KENS, *M. Arai, M. Kohgi, M. Itoh,*

*H. Iwasa, N. Watanabe, S. Ikeda, and Y. Endoh*

On the kinematics and resolution of spectrometers for neutron

Brillouin scattering, *R. A. Robinson*

Neutron Brillouin scattering in dense nitrogen gas, *P. Egelstaff, G. Kearley,*

*J. B. Suck, and J. P. A. Youden*

The effects of chopper jitter on the time-dependent intensity transmitted by

multiple-slot multiple-disk chopper systems, *J. R. D. Copley*

Application of eV neutron scattering and eV neutron absorption techniques,

*S. Ikeda*

Future perspectives for liquids and amorphous materials diffraction at ISIS,

*A. K. Soper*

Some considerations on TOF-NSE, *S. Ikeda*



Time-of-flight small-angle-neutron-scattering data reduction and analysis at LANSCE with program SMR, *R. P. Hjelm, Jr. and P. A. Seeger*  
A comparison of germanium and copper analyzers for pulsed-source crystal-analyzer spectrometers, *M. Yethiraj and R. A. Robinson, (contributed paper)*  
Recent results with the Los Alamos Constant-Q Spectrometer, *M. Yethiraj and R. A. Robinson, (contributed paper)*  
The new chopper spectrometer at LANSCE, PHAROS, *R. A. Robinson, (contributed paper)*  
Optimal Larmor precession magnets: application to neutron spin echo, *C. M. E. Zeyen, P. C. Rem, R. A. Hartmann, H. H. J. ten Kate and L. J. M. van de Klundert, (contributed paper)*  
Soller collimators for small angle neutron scattering, *R. K. Crawford, J. E. Epperson, and P. Thiyagarajan, (contributed paper)*  
GLAD: the IPNS Glass, Liquid, and Amorphous Materials Diffractometer, *P. K. Crawford, D. L. Price, J. R. Haumann, R. Kleb, D. G. Montague, J. M. Carpenter, S. Susman, and R. J. Dejus, (contributed paper)*  
Workshop summary on inelastic and elastic scattering, *R. K. Crawford, chairman*

#### **Target-station workshop, session I**

Monte Carlo simulation of the LANSCE target/moderator/reflector/shield geometry, *H. G. Hughes, III*  
Experimental determination of neutron beam fluxes at LANSCE from gold foil activation, *J. S. Gilmore, R. A. Robinson, and G. J. Russell*  
The D<sub>2</sub> cold-neutron source for SINQ, *F. Atchison, W. Bucher, A. Höchli, I. Horvath, and L. Nordström*  
LANSCE target system performance, *G. J. Russell, J. S. Gilmore, H. Robinson, G. L. Legate, A. Bridge, R. J. Sanchez, R. J. Brewton, and R. Woods*  
LANSCE steady-state unperturbed thermal neutron fluxes at 100  $\mu$ A, *G. J. Russell, (contributed paper)*  
Scattering cross sections and transport properties of H<sub>2</sub> and D<sub>2</sub> ns obtained from a synthetic model, *J. R. Granada, V. H. Gillette, M. M. Scaffoni and R. E. Mayer (contributed paper)*  
Upgrading of the reactor BER II, *A. Axmann, (contributed paper)*  
New moderator for pulsed-neutron diffraction, *R. E. Mayer, J. R. Granada, V. H. Gillette and J. Dawidowski (contributed paper)*  
Workshop summary on targets and moderators, *W. E. Fischer, chairman*

#### **Instrument workshop, session II**

Detector development at the ISIS facility, *P. L. Davidson, E. M. Mott, N. J. Rhodes, and M. W. Johnson*

New KENS data acquisition system, *M. Arai, M. Furusaka, and S. Satoh*  
Future data acquisition system at ISIS, *W. C. A. Pulford, S. P. H. Quinton,*  
*M. W. Johnson, and J. Norris*  
Workshop summary on data acquisition, *R. Nelson and P. A. Seeger,*  
co-chairmen

**Target-station workshop, session II**

Upgrades to the ISIS moderator configuration, *A. D. Taylor*  
A combined H<sub>2</sub>/CH<sub>4</sub> cold moderator for a short pulse neutron source,  
*A. T. Lucas and K. D. Williamson*  
Efficiency of accelerator-based cold neutron sources, *N. Watanabe*  
Pulsed-neutron production at the Brookhaven 200-MeV linac, *T. E. Ward,*  
*J. Alessi, J. Brennan, P. Grand, R. Lankshear, P. Montemurro,*  
*C. L. Snead, Jr. and N. Tsoupas (contributed paper)*  
Workshop summary on high-power targets and target-assembly  
developments, *A. Carne*, chairman  
LANSCE target-system data collection system, *A. Kernodle*  
Liquid-hydrogen-control-system modifications, *T. Summers*  
Remote handling for an ISIS target change, *T. A. Broome and M. Holding*  
LANSCE target calculations, *D. Grisham and R. D. Brown*  
Workshop summary on target systems, *R. Woods*, chairman

Wednesday, October 5, 1988

**Panel discussion**

User requirements as they impact spallation neutron source design

*C. D. Bowman*

*R. K. Crawford*

*G. Dolling*

*P. Egelstaff*

*F. Mezei*

*A. D. Taylor*

*G. Bauer, moderator*

Thursday, October 6, 1988

**Invited papers**

Advanced spallation sources: scientific opportunities and technical feasibility

*G. Bauer*

The U.S. advanced neutron source

*C. West*

**Instrument workshop, session I**

Progress report on measurement and fitting of pulse shapes of moderators at

IPNS, *R. Bywater, R. E. Williams, and J. M. Carpenter*

Information content of line shapes, *R. Silver, D. Sivia, and R. Pynn*

The performance of maximum entropy methods in spectral deconvolution,

*M. W. Johnson and J. Lister*

Maximum entropy methods in neutron scattering: application to the structure

factor problem in disordered materials, *A. K. Soper*

Optimization of reconstruction algorithms using Monte Carlo simulations,

*K. M. Hanson*

Workshop summary on data treatment and techniques, *M. W. Johnson and*

*R. Silver*, co-chairmen

**Target-station workshop, session I**

Design for a second-generation proton storage ring at LAMPF, *E. Colton*

Some neutronic calculations for KENS-II, *Y. Kiyonagi, M. Arai, and*

*N. Watanabe*

A consideration of cold neutron source for KENS-II, *N. Watanabe*

Calculation of the spallation product distribution in the evaporation process,

*T. Nishida, I. Kanno, Y. Nakahara, and H. Ikeda*

Preliminary optimization experiments of coupled liquid hydrogen moderator for

KENS-II, *N. Watanabe, Y. Kiyonagi, K. Inoue, M. Furusaka, S. Ikeda,*

*M. Arai, and H. Iwasa*

Measured neutron beam line shielding effectiveness of several iron/polyethylene

configurations, *G. L. Legate, M. L. Howe, and R. L. Mundis*

Equivalent spherical-shield-neutron-dose calculations, *G. J. Russell and*

*H. Robinson*

Infinite slab-shield dose calculations, *G. J. Russell*

Workshop summary on computational techniques and shielding, *F. Atchison*

**Instrument workshop, session II**

On the use of acceptance diagrams to calculate the performance of multiple-  
section straight-sided neutron guide systems, *J. R. D. Copley*

Neutron beam handling by inelastic interaction with time-dependent magnetic

fields, *L. Niel, G. Badurek, H. Rauch, J. Summhammer, and*

*H. Weinfurter*

SINQ guide concept, *I. Anderson and F. Atchison*  
Neutron beam compressors for pulse-width reduction, *R. Lechner*  
Summary of the recent conference on thin-film neutron optical devices,  
*C. F. Majkrzak*  
Workshop summary on beam handling, *C. F. Majkrzak*, chairman

**Target-station workshop, session II**  
Neutron spectrum measurement, LANSCE, ER-1, *M. L. Howe and R. L. Mundis*  
The ISIS target halo monitors, *A. Carne*  
Summary of the Los Alamos Spallation Radiation Effects Facility at LAMPF  
(LASREF), *W. Sommer*  
Workshop summary on practical concerns, *T. A. Broome*, chairman

Friday, October 7, 1988  
**Invited paper**  
Summaries and future projections  
*P. A. Egelstaff*

ICANS-X, the tenth meeting of the International Collaboration on Advanced Neutron Sources, was held at the Los Alamos National Laboratory. ICANS was formed in 1977 with four charter-member laboratories: the Los Alamos Scientific Laboratory (U.S.), the Argonne National Laboratory (U.S.), the Rutherford Laboratory (U.K.), and the KEK Laboratory (Japan). The basis for ICANS was the establishment of a forum where information on the development of spallation neutron sources could be freely shared in the form of technical notes, individual conversations, laboratory visits, etc. The general topics of interest at the time were accelerator design, target-station design, and neutron instrument design. In succeeding years additional laboratories joined ICANS, topics of interest broadened, and the meeting format grew from an informal sharing of data at workshop sessions to formal presentations of papers with published proceedings.

The week-long ICANS-X conference was jointly sponsored by the two U. S. member laboratories, Los Alamos and Argonne. In addition to overviews describing the status of the five spallation sources worldwide, plenary speakers covered a variety of topics, including: the complementarity of photons and neutrons, ideas for new experiments on pulsed sources, and the thinking behind advanced-source concepts. An evening panel discussion stimulated dialogue on user requirements as they impact spallation source design. The heart of the conference, however, was still the workshop sessions, where specifics of instrument design and target-station issues were discussed informally.

Indeed, the theme of ICANS-X revolved around the necessary interaction between spectrometer and target-station design and performance and, therefore, the need for feedback that must exist between scientific requirements and source design.

## ISIS status report

*J. L. Finney and D. A. Gray*  
Rutherford-Appleton Laboratory  
Didcot, Oxon, OX11 0QX  
UNITED KINGDOM

**ABSTRACT:** We review the progress on ISIS, the pulsed neutron source at the Rutherford-Appleton Laboratory, since the last ICANS meeting. The machine is now running regularly at 100  $\mu$ A at 750 MeV, and delivering neutrons for an increasing UK and international neutron scattering programme. The current status of the operating and development instruments is summarised, and some examples given of recent science.

### 1. INTRODUCTION

At the last ICANS meeting in September 1986 (Gray 1987) it was reported that ISIS was running at 550 MeV with  $3 \times 10^{12}$  protons per pulse on target at 50 Hz, i.e. a mean current of 24  $\mu$ A.

ISIS is now running at a peak of over 100  $\mu$ A at 750 MeV with a fully scheduled set of neutron spectrometers. It has just completed its most successful cycle ever, achieving record peak currents; records of integrated current per day were broken on three occasions, when figures greater than 2000  $\mu$ A hrs were logged.

This paper gives information on the development of the source, current UK and international usage, and outlines the current state of development of the spectrometers, giving some examples of the science. Detailed reports on ISIS for the two years to March 1988 are given in ISIS 1987 (Rutherford Appleton Laboratory 1987) and ISIS 1988 (Rutherford Appleton Laboratory 1988).

## 2. REVIEW OF OPERATION

The integrated beam current ( $\mu\text{A-hr}$ ) per month since June 1986 is shown in Figure 1. In the calendar year 1986, 22,600  $\mu\text{A-hrs}$  were achieved with 121,000 in 1987 and 129,000  $\mu\text{A-hrs}$  so far in 1988. During the month of August 1988, 37,002  $\mu\text{A-hr}$  were delivered to the target (see Figure 2). The highest average current over one day in August was 84  $\mu\text{A}$  with the peak at just over 100  $\mu\text{A}$ . This maximum average daily current was increased to 86  $\mu\text{A}$  over 24 hours in September. Over the month of August, the average current was 56  $\mu\text{A}$ . There were two two-day shutdowns caused by equipment failure. The run continued until 15 September.

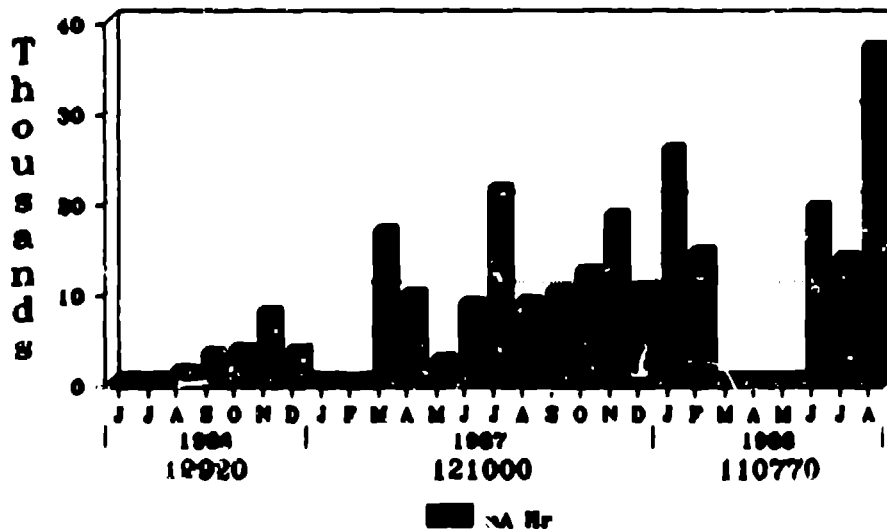


Fig. 1 Integrated ISIS beam current in  $\mu\text{A hrs}$  from June 1986 to date.

During 1987 there were two successful target changes. These are discussed more fully in a paper by A Carne at this meeting. The failure is believed to be caused by swelling of the depleted uranium as a result of repeated thermal shock. After the failure of target number 2, the control system which protects the accelerator and transfer lines against abnormal lost beam pulses was modified and refined. This resulted in the number of temperature shocks to the target being reduced by more than a factor of 10 in a given time. Target number 3 has taken 129,000  $\mu\text{A-hrs}$  and is still mechanically sound. Of the lost time on the facility during 1988, 21% is due to failures in the injector system, 2% in the extraction power supply and 1.3% in the synchrotron RF system.



Experience with running at 100  $\mu\text{A}$  has resulted in a weekly scheduled stop of one 8 hour shift to change the  $\text{P}^-$  ion source and to change the filters in the methane moderator system. This stop accounts in significant part for the 7 day periodicity visible in Figure 2. This arrangement will be reviewed as more experience is gained. The available resources above those required for operation are being used to improve the reliability of operation at 100  $\mu\text{A}$  rather than to increase the operating current.

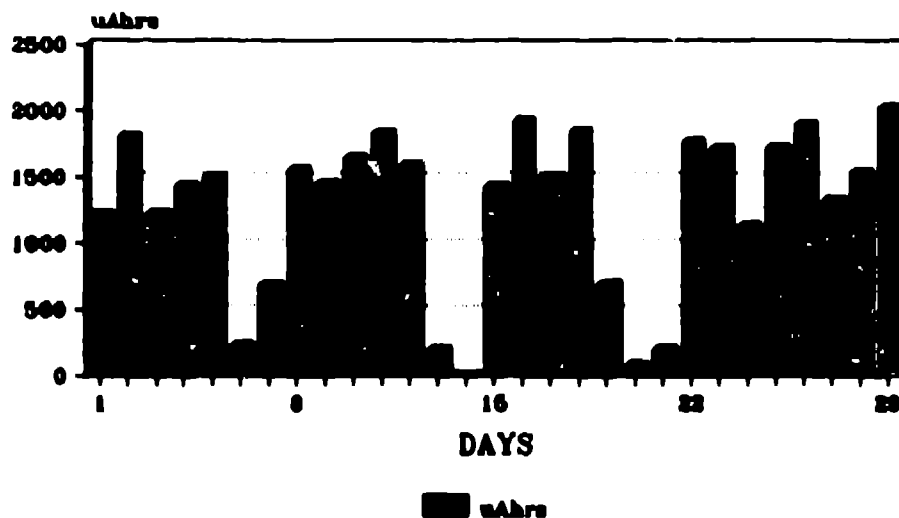


Fig. 2 Integrated beam current in  $\mu\text{A hrs}$  delivered to the target during cycle 4, 1988.

At 100  $\mu\text{A}$  ( $1.25 \times 10^{13}$  protons per pulse), typical beam transfer efficiencies during routine running are :

efficiency	98-99%
Trapping efficiency in synchrotron	86%
Acceleration efficiency	99%
Extraction and transfer to target	99%

The lost beam collector system continues to work well. The system concentrates beam lost at injection at trapping into collectors with suitable materials and which are removable.

Induced activity on synchrotron components leads to radiation levels on contact of 100,000  $\mu\text{Sv/hr}$  at the collectors but of only 250  $\mu\text{Sv/hr}$  in most of the rest of the synchrotron.

It is noticeable that the machine vacuum has not been let up since the shutdown in May.

### 3. BEAM TIME DEMAND AND SCHEDULING

During 1987 and 1988, a total of 1940 days of beam time was allocated for user experiments on between 5 (early 1987) and 10 (current) instruments; with 4310 days requested, this represents an average oversubscription factor (days requested/days available) of 2.2. The distribution between the three allocation rounds is shown in Table 1. Table 2 gives the allocation data by instrument for round 1/88. On the fully scheduled instruments, oversubscription factors range between 1.1 and 3.2.

### 4. INTERNATIONAL PARTICIPATION

In round 1/88, UK users accounted for 64% of the scheduled beam time. Figure 3 shows how the non-UK component was distributed by country. Italy, France, West Germany and Sweden together accounted for 73% of the non-UK time, the remainder being largely taken up by users from the Netherlands, USA, India, Japan and Spain.

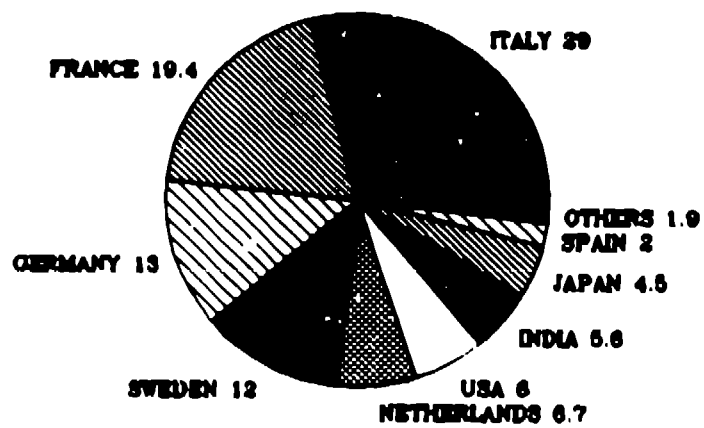
Bilateral use agreements are at an advanced stage of negotiation with Italy, France and Sweden. A four-year agreement with the Netherlands has been signed. Four countries have been or are involved in the construction of neutron instruments, including India (Be filter on the early IRIS spectrometer), Italy (the PRISMA spectrometer), Japan (the multi-angle rotor inelastic instrument MARI). A rotating analyser instrument (ROTAX) will be developed by the University of Würzburg, and a draft agreement relating to this is at the advanced negotiation stage.

TABLE 1

<u>Round</u>	<u>Days Available</u>	<u>Instrument Days Requested</u>	<u>Instrument Days Allocated</u>
1/87	143	965	591
2/87	71	1439	392
1/88	120	1906	957
TOTALS 1987	—	—	—
+ 1988	334	4310	1940

TABLE 2  
ROUND 1/88

<u>Elastic Spectrometers</u>	<u>Days Requested</u>	<u>Days Allocated</u>
HRPD	241	102
LAD	210	103
CRISP	220	100
LOQ	159	100
(POLARIS	91	67)
 <u>Inelastic Spectrometers</u>		
HET	249	95
TFXA	103	92
IRIS	325	100
(eVS	76	104)
	-----	-----
	1674	863
 <u>Muons</u>		
$\mu$ SR	232	94
	-----	-----
	1506	957
	-----	-----



**FOREIGN USE**

Fig. 3 Distribution of non-UK use of ISIS beam time by country for round 1/88.

## 5. SCHEDULED INSTRUMENTS

As indicated in Table 2, nine neutron instruments are now being scheduled, together with the  $\mu$ SR line. Two further instruments are in the commissioning phase (SKD and PRISMA), and three under construction (SANDALS, MARI and ROTAX). KARMEN - the Karlsruhe-Rutherford medium-energy neutrino experiment - has had 1/9 of its detector installed, and is undergoing test. Of the 18 available beam holes around the target station, 13 have been taken up. In addition, a test beam facility has been installed on the methane moderator; its initial use will be for resonance radiography development and detector tests.

Table 3 lists the characteristics of both currently-scheduled and development instruments. The major changes to the various instruments since 1986 are as follows.

### (a) Elastic Instruments

HRPD In 1986 at the time of ICANS-IX, only two of the eight octants of the backscattering bank had been installed. Currently, six are in place, resulting in significant increase in throughput and expansion of the scientific programme. A low angle bank gives access to d-spacings up to about 50Å, and construction of a 90° detector bank for restricted sample environment work (especially pressure) is in hand; a temporary detector module is being used in initial 90° tests.

Although HRPD is classed as a powder diffractometer (which has been used extensively in key high  $T_c$  superconductor experiments), its uniquely high resolution has opened up other exciting areas, through its ability to see fine details in line profiles. Examples include residual stress analysis in engineering components, observing variable oxygen stoichiometry in the warm superconductor  $\text{YBa}_2\text{Cu}_3\text{O}_{6+x}$ , domain structure changes close to phase transitions (e.g. the ferroelastic transition in  $\text{LaNdO}_4$  - see Figure 4), and periodicities in cycloidal magnetic structures (the 760Å repeat in  $\text{BiFeO}_3$  could be seen after only a few seconds exposure time (Figure 5)). Ab initio structure determinations from powders are becoming semi-routine; recent examples include the high temperature  $\alpha$ -phase of malonic acid, and methylamine deuteriodide  $\text{CD}_3\text{ND}_3\text{I}$ . Unit cell parameters can be refined to 5 parts in  $10^6$ , and the instrument is capable of observing inhomogeneities in well-recognised "standards"!

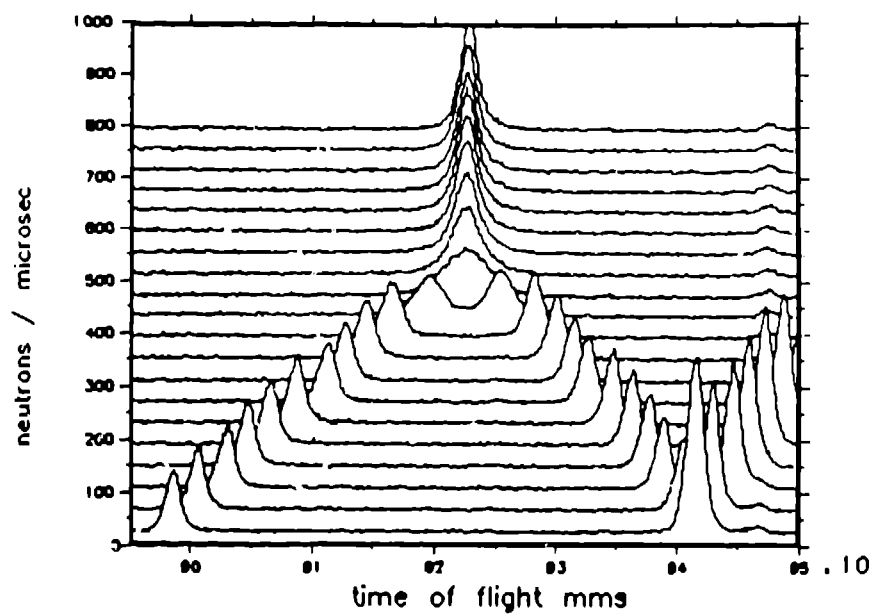


Fig. 4 Scans through the ferroelastic transition of lanthanum niobate at temperature intervals of 10. Not only is the transition well-defined, but detailed peak-shape analysis shows the formation of needle-shaped domains.

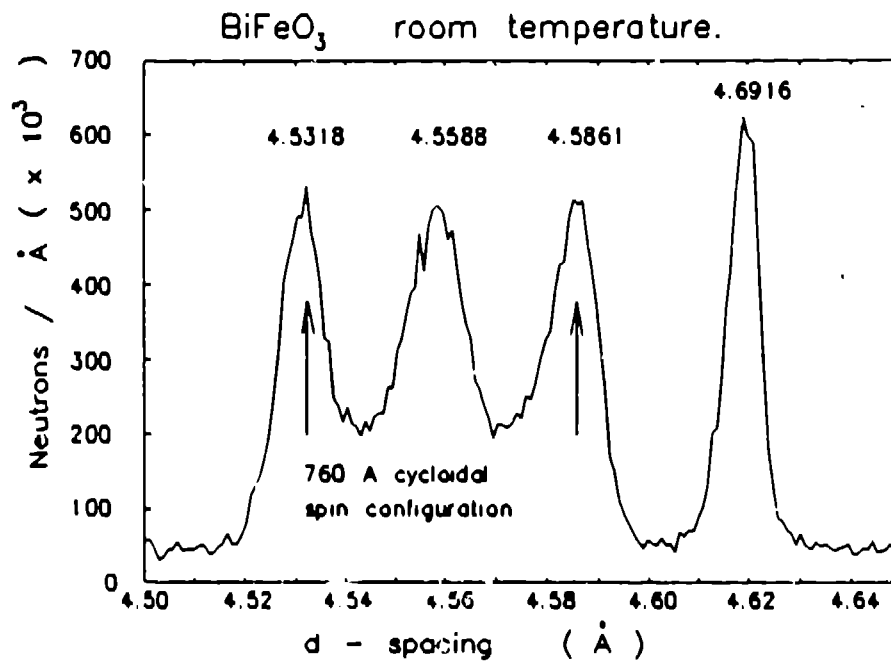


Fig. 5 The 760 Å cycloidal spin configuration splitting in  $\text{BiFeO}_3$ .

TABLE 3

**INSTRUMENTS AT ISIS**

**ELASTIC**

HRPD	High-resolution powder diffractometer	Ab-initio structure determination, large unit cell structure refinement, phase transitions, mixed phases, line broadening, high-pressure studies	$\Delta d/d - 5 \times 10^{-4}$ (backscattering) $\Delta d/d - 0.1$ (low angle bank) guide: $\lambda^* = 0.98\text{\AA}$ minimum wavelength = $0.5\text{\AA}$ .
POLARIS	High intensity powder diffractometer	Magnetic structures, phase transitions, kinetic studies, small samples, high pressure work	$\Delta d/d - 5 \times 10^{-3}$ (backscattering) $\Delta d/d - 8 \times 10^{-3}$ ( $90^\circ$ ) $\Delta d/d - 2.5 \times 10^{-2}$ (forward scattering)
LAD	Liquids and amorphous diffractometer	Structures of liquids and amorphous solids, medium resolution powder diffraction	$0.5 < Q < 100 \text{ (\AA}^{-1}\text{)}$ $\Delta Q/Q = 0.004$ (backscattering)
SANDALS	Small angle diffractometer for amorphous and liquid samples	Static structure factors of fluids, amorphous materials and biological systems	Minimises inelastic corrections: $2\theta_{\text{max}} = 120^\circ$ , $\lambda_{\text{max}} = 6\text{\AA}$ $\Delta Q/Q - 0.01-0.04$ ,
SXD	Single-crystal diffractometer	Single crystal structure determination study of structural phase changes and magnetic order, reciprocal space surveying	$0.2 < Q < 30 \text{ (\AA}^{-1}\text{)}$ 1.2-300K accessible, position sensitive detector.
CRISP	Pulsed source neutron reflectometer for surface studies	Surface structure, interfaces and surface magnetism	Resolution ( $\pm 1\sigma$ ) 2-10 $\mu$ ; Q range 0.01-1.3 $\text{\AA}^{-1}$ using 0.5-6.5 $\text{\AA}$ wavelength neutrons; inclined beam for liquid surfaces.
LOQ	Low-Q diffractometer	Macromolecular, biological and other large scale structures	$0.005 < Q < 0.2 \text{ (\AA}^{-1}\text{)}$ , $\Delta Q/Q - 0.05$

INELASTIC

HET	High-energy transfer spectrometer	Magnetic and vibrational excitations single particle motion in quantum systems	Chopper; incident energy 50-2000 meV $\epsilon$ range 20-1000 meV 1% energy transfer resolution.
MARI	Multi-angle rotor instrument	Dynamic structure factors of liquids and magnetic systems, inelastic excitations in crystalline amorphous and disordered systems, molecular spectroscopy, momentum density	Chopper; incident energy 20-1000 meV $\epsilon$ range 10-500 meV 1% energy transfer resolution $\phi = 3-135^\circ$ .
TFXA	Time-focused crystal analyser	Inelastic scattering from magnetic and vibrational systems, especially molecular spectroscopy of hydrogenous systems	me range 2-1500 meV - 1.5% energy transfer resolution, elastic line width 0.2 meV.
IRIS	High-resolution quasielastic and inelastic spectrometer	Rotational and translational diffusive motion in atomic and molecular systems, quantum tunnelling, crystalline electric field transitions and low lying inelastic modes	Graphite analyser (002) reflection: 15 $\mu$ eV resolution at $E_r = 1.83$ meV $Q^2 = 0.25-1.85 \text{ \AA}^{-2}$ (004) reflection: 50 $\mu$ eV resolution at $E_r = 7.2$ meV $Q^2 = 0.5-3.7 \text{ \AA}^{-2}$
eVS	Electron-volt spectrometer	Momentum density studies in low mass systems	Resonance analysers being developed in the range 1-20 eV
PRISMA	High-symmetry coherent inelastic spectrometer	Phonon and magnon collective excitations in single crystals	16 independent crystal analysers, 3-axis analogue
ROTAX	Rotating analyser crystal spectrometer	Structural and magnetic excitations in single crystals	One rotating Ge analyser, position sensitive detector

HRPD is a very powerful instrument for a wide variety of materials science work. Apart from powder samples, it has potential new uses on single crystals, and tests on its potential in high-resolution inelastic mode are planned.

LAD The original gas detectors in this liquids and amorphous materials diffractometer have been replaced by Li glass scintillator in the 20°, 35°, 58° and 90° positions. The consequent count rate increase of about five has resulted in an expansion of isotope substitution first difference work (e.g. aqueous  $\text{Cu}(\text{NO}_3)_2$  with nitrogen substitution, chromium perchlorate with chromium substitution). Work on the instrument has also expanded to gaseous systems, and an experiment on gaseous deuterium near the critical point having recently been completed. The very high Q capability continues to be capitalised on, a recent experiment on vitreous  $\text{GeO}_2$  showing clear structure in  $S(Q)$  out to  $50 \text{ \AA}^{-1}$ .

POLARIS The direction of polarised neutron work has recently been reassessed at ISIS, with more emphasis being placed on the possible use of polarising mirrors. POLARIS is consequently being reequipped as a medium intensity powder diffractometer, with three detector banks (low angle  $\Delta d/d - 2.5 \times 10^{-2}$ , high angle  $\Delta d/d - 5 \times 10^{-3}$ , and a 90° bank for restricted sample environment work  $\Delta d/d - 8 \times 10^{-3}$ ). The initial complement of detectors was installed within the last week, and commissioning tests are taking place. To give an idea of the kind of data we expect to obtain, Figure 6 shows patterns for an  $\text{Al}_2\text{O}_3$  standard at the 150° and 90° detector positions for a single detector after 24 minutes running on a  $1 \text{ cm}^3$  sample. With all detectors in place, data of this quality will be obtained in around 2 minutes. This gives the potential for up to  $10^5$  simple experiments per year.

CRISP This is a critical reflection spectrometer that has been constructed and commissioned since the last ICANS meeting. Using an incident beam inclined at 1.5° to the horizontal, it probes the density profile of interfaces in the direction normal to the interface. Reflectivities of  $10^{-6}$  are obtained routinely; recently, reflectivities down to  $10^{-7}$  have been achieved, extending CRISP into a region which is crucial for discriminating between competing models of particular interface structures. Figure 7 shows the kind of data obtained from an 1185Å deuterated Langmuir-Blodgett film deposited onto a silicon wafer: the continuous line indicates the theoretical model.



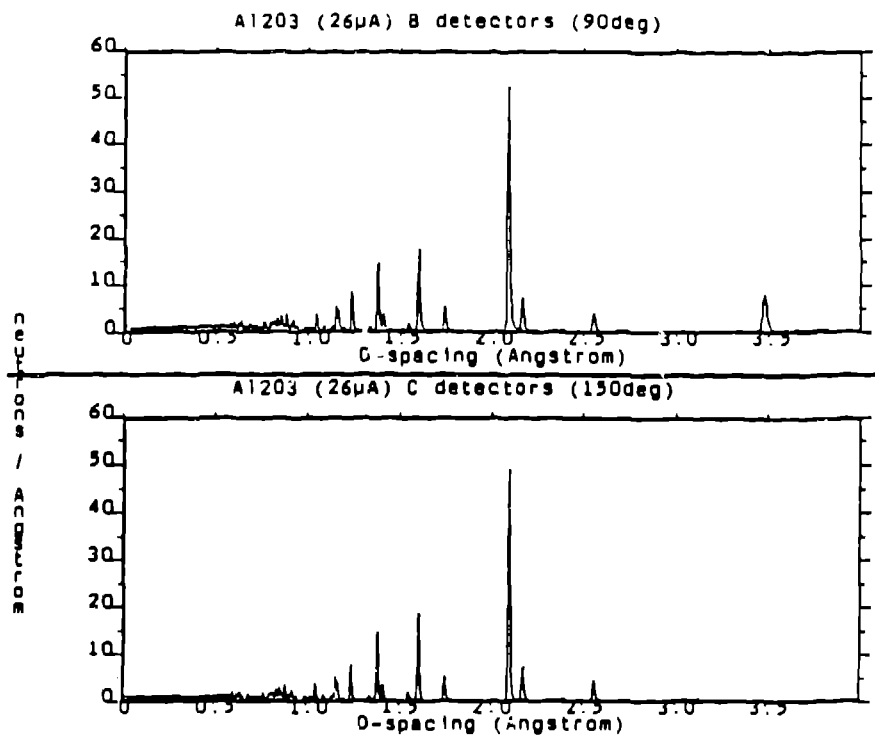


Fig. 6 Test run on POLARIS of a 1 cm<sup>3</sup> Al<sub>2</sub>O<sub>3</sub> standard, showing data obtained at the 90° and 150° detector positions. With all detectors in place, such spectra will be obtainable in about 2 minutes.

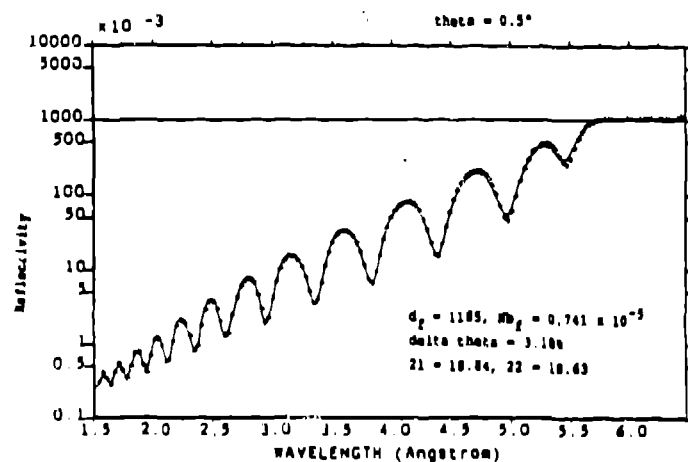


Fig. 7 Reflectivity measurements on an 1185 Å deuterated Langmuir-Blodgett film on silicon; the continuous line indicates the theoretical model (R. M. Richardson).

The versatility of, and demand on, this instrument is illustrated by the very wide ranging nature of its scientific programme in surface chemistry, solid films, and surface magnetism. A high proportion of the demand is from industrial users tackling problems with complex systems. A recent example concerned adsorption at the air solution interface of mixed surfactants, using selective deuteration to determine relative composition and structure.

A resistive wire, one-dimensional multidetector, active area  $200 \times 40 \text{ mm}^2$ , with a positional resolution of  $\sim 0.9 \text{ mm}$  in the long dimension, has recently been successfully tested. This will allow studies to be extended to the diffuse non-specular scattering from interfaces.

LOQ The low-Q diffractometer, designed for investigating macromolecular, biological, and other large scale structures, has been reconfigured. The moderator to sample distance has been reduced from 16 to 11.4m, with a resultant increase in flux, and allowing 25 Hz operation using one chopper. Frame-overlap mirrors remove frame overlap contamination above  $12\text{\AA}$ . A  $\text{BF}_3$  multiwire area detector is installed 4.3m from the sample. A Q range of  $0.005\text{--}0.25 \text{ \AA}^{-1}$  is accessible, allowing size ranges of  $20\text{--}1000\text{\AA}$  to be probed in a single experiment.

The user programme on LOQ - as would be expected of such an instrument - is wide ranging over macromolecule studies, colloid science and materials. Figure 8 shows data from shear-flow-aligned micelles of  $1\%$   $\text{C}_{16}\text{E}_8$  in  $0.5\text{M}$   $\text{Na}_2\text{SO}_4$  at  $30^\circ\text{C}$ , parallel and perpendicular to the long axis of the micellar rods. An example of materials science work is the study of precipitate formation and growth in aluminium-lithium alloys which offer substantial weight savings over existing alloys for engineering structures. These studies showed how small amounts of Cu and Mg modify the precipitate, which is thought to be a significant cause of embrittlement of these alloys with ageing.

SXD Rapid progress has been made on this development instrument over the last few months, largely due to the successful initial testing of a new ZnS position sensitive detector module with  $5 \text{ mm}$  resolution. The low  $\gamma$ -sensitivity of the ZnS scintillator has allowed the detection of very high  $\sin \theta/\lambda$  reflections; this is illustrated in Figure 9 where the (0024) of  $\text{SrF}_2$  ( $d = 0.24\text{\AA}$ ) is clearly observable with the detector at  $90^\circ$ . The comparison with Li glass scintillators is self-explanatory. Other tests have demonstrated the ability of this detector to survey reciprocal space with the examination of one-phonon thermal diffuse scattering in  $\text{SrF}_2$ ; hitherto unseen features in the TDS behaviour have been observed.

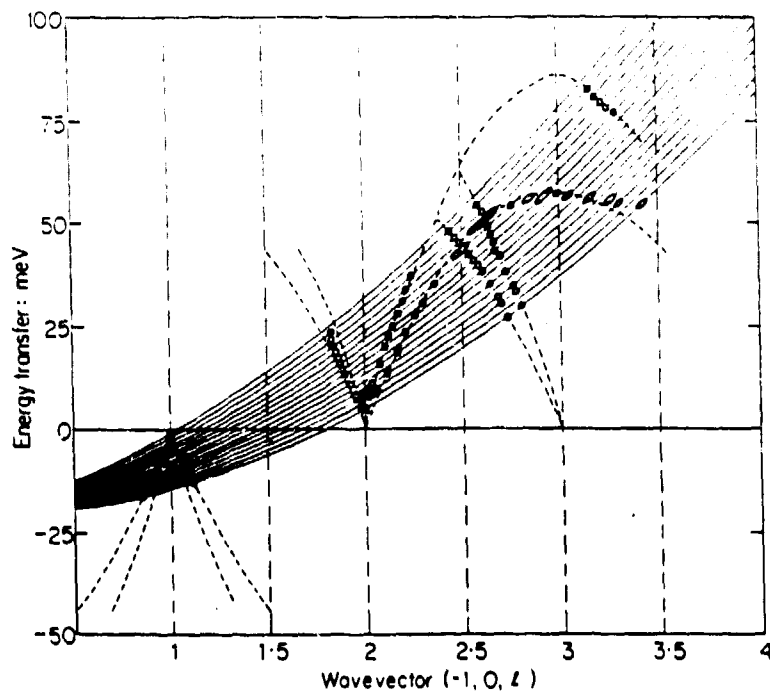


Fig. 8  $Q_{\perp}$ ,  $Q_{\parallel}$  intensity plots for 1%  $C_{13}E_8/0.5$  M  $Na_2SO_4$  at a shear gradient of  $5000 \text{ s}^{-1}$  at a temperature of  $30^\circ\text{C}$  (J. Penfold, P. G. Cummins, and E. J. Staples).

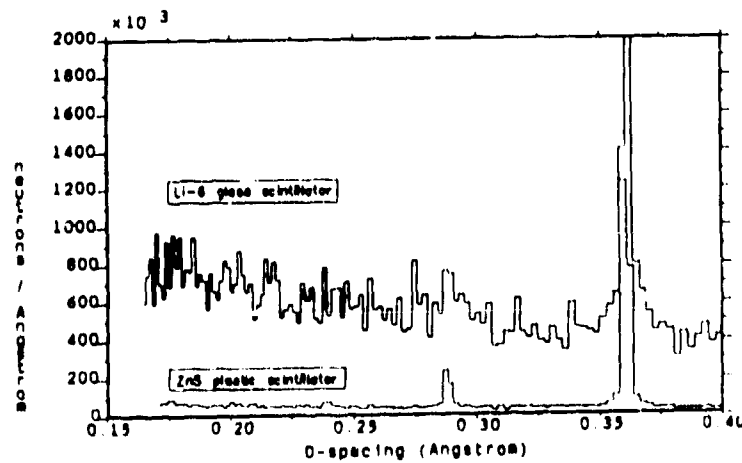


Fig. 9 Test measurements on SXD on a single crystal of  $SrF_2$ , comparing results from the test ZnS detector module with that from Li glass scintillator. The 0024 at a d-spacing of  $0.24 \text{ \AA}$  is just visible in the low-noise ZnS spectrum.

Test work is proceeding on a variety of crystals, including some with large unit cells, to assess the feasibility of high resolution measurements on such crystals. The relatively low cost and ease of manufacture of ZnS modules are expected to result in a  $300 \times 300 \text{ mm}^2$  detector with 3 mm resolution. Once this has been commissioned, regular scheduling of SXD will follow, hopefully in mid 1989.

(b) Inelastic Instruments

As these will be dealt with in more detail in the paper by Andrew Taylor, my comments will be restricted to brief summaries of major modifications and developments.

On HET, the 10-30° 2.5m intermediate angle range detectors have been upgraded with 256  $^3\text{He}$  tubes, and a new chopper slit package has extended the incident energy available down to 50 meV. Two scientific highlights include measurements of the highest-ever observed magnetic excitation ( $^3\text{H}_4 - ^3\text{F}_4$  at 809 meV in Pr metal) and the first successful single crystal experiment on HET of spin waves in cobalt, where measurements were made out to the zone boundary (~ 300 meV). On the time focused crystal analyser spectrometer TFXA, the analyser efficiency has been doubled by using thicker crystals with a more relaxed mosaic spread. The instrument is optimised for the study of vibrational dynamics of hydrogenous samples, recent particularly exciting work including studies of a hydrodesulphuration catalyst ( $\text{MoS}_2$ ). On the high resolution quasielastic and inelastic spectrometer IRIS, resolution has been enhanced with the installation of a pyrolytic graphite analyser.

The development programme on the electron volt spectrometer eVS was fully reassessed during 1988. The resonance detector analyser programme was suspended, and other options are now under consideration. A momentum density user programme has started on eVS, and an intermediate angle bank has been installed.

The study of coherent excitations in single crystals is an area that has been very successfully exploited using triple axis spectrometers on reactor sources. Dispersion curve measurements on ISIS are made using the new PRISMA instrument. This operates in inverted geometry, with the final energy of the scattered neutrons analysed by 16 individually-movable analyser-detector arms.

Under an agreement between SERC and the CNR Frascati, PRISMA was provided by Italy for installation on ISIS. The components arrived at RAL from Italy in mid-1987, and the instrument was installed on ISIS. Within the past few weeks, initial data of impressive quality have been obtained, showing clearly the power of this instrument to measure dispersion curves. Figure 10 shows the sections in  $(E, Q)$  space cut by each of the 16 analysers for a single crystal of Be, while Figure 11 shows the results for one analyser, underlining the excellent signal/background obtained. From such sections, the phonon dispersion curve can be constructed, as on Figure 10, where the known dispersion curve is plotted as dotted lines. These results were obtained in only 600  $\mu\text{A}$  hours, equivalent to about 6-7 hours at current running. In the more complex  $\text{KTaO}_3$ , a good quality dispersion relation was obtained in a single day. The potential of PRISMA for phonon dispersion curve measurements is clear. The instrument will be officially inaugurated at a ceremony on 4 November 1988.

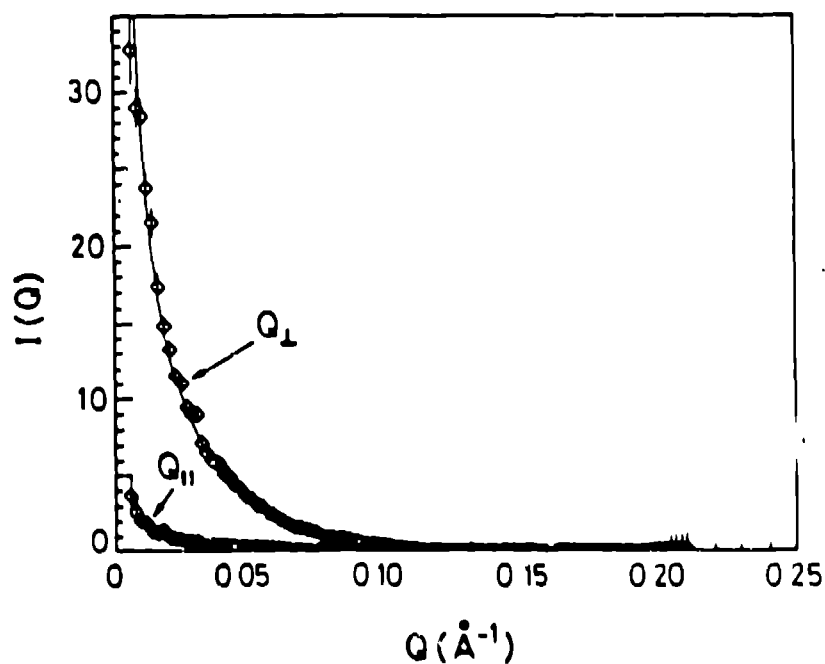


Fig. 10 Dispersion relation measurements on a single crystal of beryllium obtained during early tests of PRISMA. The solid lines are the cuts in  $(E, Q)$  space made by each detector, while the dotted lines denote the known dispersion relation.

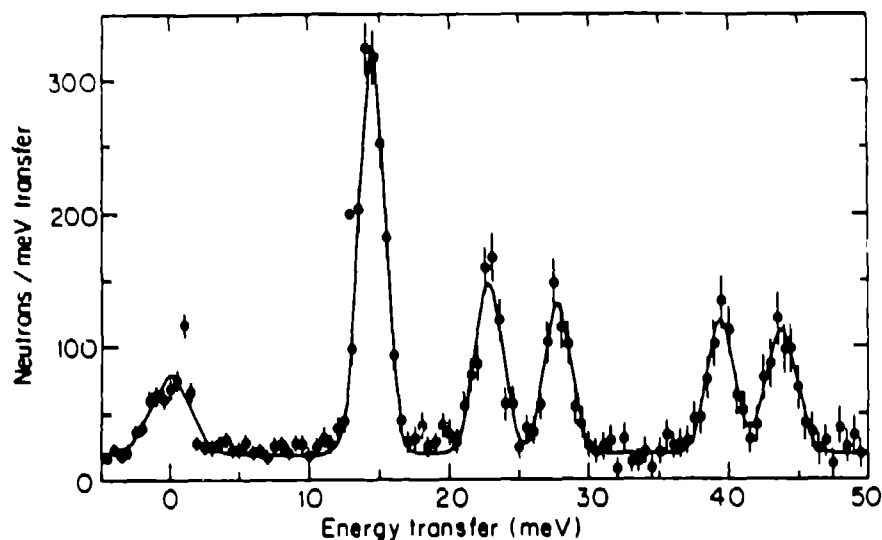


Fig. 11 Measurements taken from one analyser of PRISMA on the same Be crystal as Fig. 10. Figure 10 is constructed from several such scans.

## 6. SUMMARY

ISIS is now running regularly at around 100  $\mu\text{A}$  currents at 750 meV. Nine neutron instruments and the  $\mu\text{SR}$  line are being regularly scheduled, with increasing demand for an increasingly sophisticated user community in the UK, Europe and elsewhere. With this regular running, the capabilities of such a high intensity pulsed source are increasingly resulting in new science in both elastic and inelastic scattering studies. Several further instruments are under development and construction, with the first scheduled experiments on three of these expected during 1989. On the machine side, priority is being given to further improving reliability before the next stage in increasing the current to 120-130  $\mu\text{A}$ .

## REFERENCES

- Gray, D A, 1987, Proc ICANS-IX, 23-29  
 Rutherford Appleton Laboratory, 1987, ISIS Annual Report "ISIS 1987"  
 (RAL-87-050)  
 Rutherford Appleton Laboratory, 1988, ISIS Annual Report "ISIS 1988"  
 (RAL-88-050)

## Status of the Intense Pulsed Neutron Source

*B. S. Brown, J. M. Carpenter, R. K. Crawford, A. V. Rauchs, A. W. Schulke,  
and T. G. Worlton*  
Argonne National Laboratory  
Argonne, Illinois 60439  
USA

### Introduction

In December 1987, the 1000th experiment was performed at IPNS. This is a significant milestone and reflects the great deal of work and progress that have taken place since the first experiments were performed in 1981. Since that time, the average proton current has increased from 4  $\mu\text{A}$  to 14-15  $\mu\text{A}$ . The reliability has averaged 91% since 1981, by far the world's record for pulsed neutron sources. We have gone from room temperature polyethylene to cryogenic methane moderators, from a depleted uranium to a 77% enriched uranium (Booster) target, and from 4 to 11 neutron scattering instruments. Unfortunately, funding has not kept pace in the same ratio, and staff and operating time have been essentially constant over this same time period. For the past 3 years, most of the budget shortfall was covered by a project for the Strategic Defense Initiative (SDI) involving the study of neutral particle beams using our linac with the help of members of our accelerator staff. In addition to SDI funds, we are in the process of pursuing other funding sources such as industry and the National Science Foundation.

IPNS is not unique in having concerns about the level of funding, and the future looks good despite these concerns. This report details the progress made at IPNS during the last two years. Other papers in these proceedings discuss in detail the status of the enriched uranium Booster target, the two instruments that are under construction, GLAD and POSY II, and a proposal for research on an Advanced Pulsed Neutron Source (ASPUN) that has been submitted to the Department of Energy (DOE). Further details on IPNS are available in the IPNS Progress Report 1987-1988, available by writing the IPNS Division Office.

### Operating status of the accelerator system

On September 19, 1987, the accelerator system delivered the two billionth proton pulse to the IPNS neutron target. The total, as of October 1, 1988, has risen to 2,341,622,103 pulses.

The average beam current showed another gratifying increase of 5% since the 1986 ICANS report. A few new techniques were uncovered to help increase the beam current, but most of the gain came from effective utilization of the new equipment installed in 1985 and 1986. Figure 1 is a plot of weekly average proton current on the neutron target since turn-on in 1981; each point represents on average about 148 hours of operation. Although the average beam current has increased since late 1985,

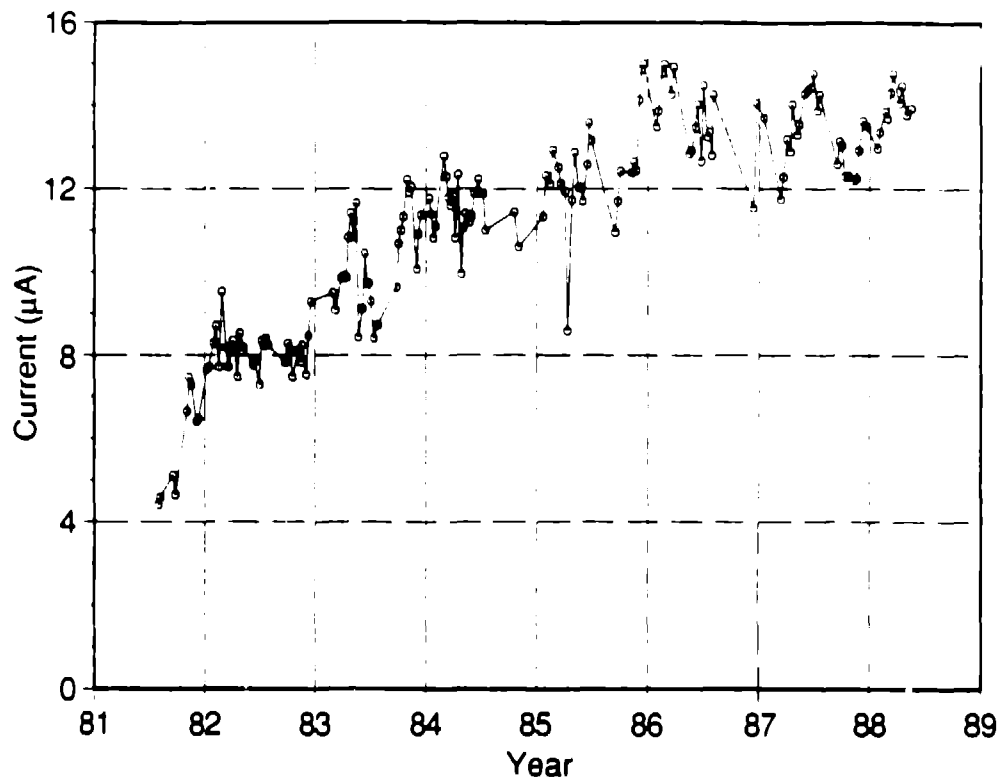


Fig. 1 Average target current of IPNS.

the rate of increase has diminished. Concurrently, the IPNS accelerator group has been involved very heavily with activities outside of IPNS since that time so effort devoted to beam current increase has been minimal.

Two factors should be mentioned in connection with the 5% current increase. The first of these is the use of  $80 \mu\text{g}/\text{cm}^2$  carbon H stripping foils. These foils last a long time (about 40-50 million beam pulses), and eight hours with the old polyparaxylene foils. This feature allows an increase in the long-term, not peak, average current. The second item is substantial improvement in the stability of our extracted beam current sensing toroids. By providing better low inductance image current return paths, we have decreased the dependence of these devices on the spatial properties of the extracted beam pulse. The synchrotron is operated "beam loss limited", and the toroid signals are input data to the "beam loss" computation. Stable, repeatable toroid data allow the synchrotron to be operated very close to the empirically determined "acceptable loss" which, in turn, increases long-term average current on target.

The brightest spot of the IPNS accelerator operation continues to be the operating reliability, that is, the availability to deliver protons as scheduled. Reliability over more than 6200 scheduled hours during the last two years continued to be excellent at



91.9%, despite a spate of serious breakdowns during the first two months after turn-on in August 1986. During the remaining 19 months to June 1988, as-scheduled availability equaled our goal of 94%. Figure 2 is a plot of this availability, averaged weekly. Note the density of points near 100% since late 1987. In fact, during 8 of the last 9 months of operation, availability has exceeded 95%. Even in months when availability is less than is desired, the experiment time is seldom lost, since the IPNS does not run parasitic on another program, but rather is dedicated solely to neutron science and experiments can be rescheduled without the complication of other programs competing for accelerator time.

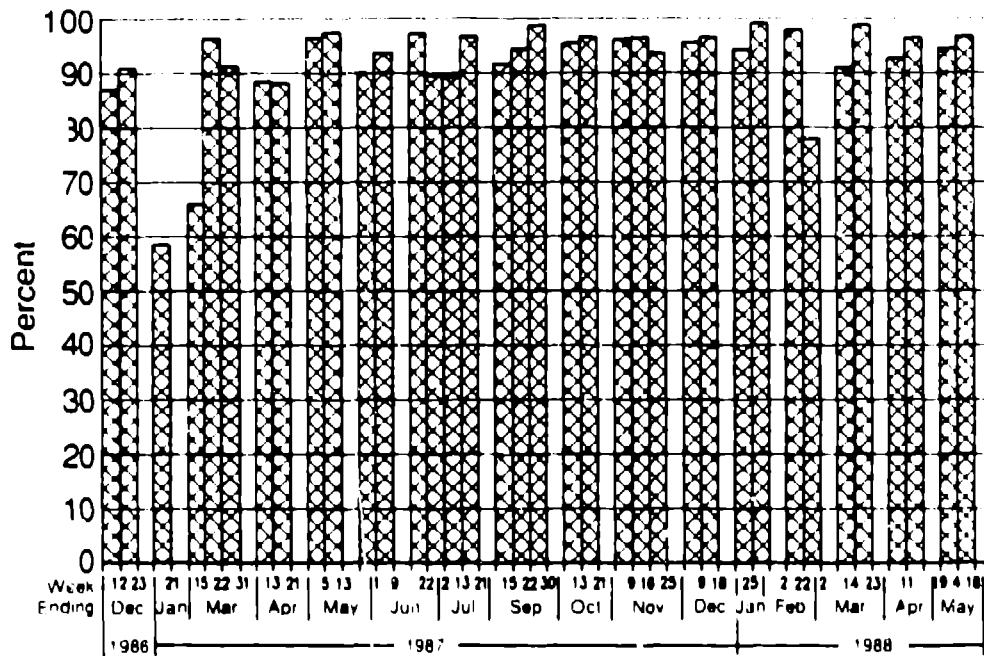


Fig. 2 Reliability of IPNS.

Of very great significance is the success of our beam loss limited operation. Automatic devices as well as operator attitudes help keep proton losses in the accelerator limited to about  $1.5 \mu\text{A}$ . As a result, the residual radiation levels around the synchrotron are no higher, on average, than they were two years ago, and in several of the very high loss regions, residual radiation has actually decreased. Thus, the reparability of the RCS continues to be good! No internal damage to the synchrotron aperture has occurred since the loss limits and protective collimators have been in use.

The most significant equipment upgrade now underway is the installation of 3 new power supplies which drive 7 of the horizontal steering dipole magnets in the 50 MeV  $H^-$  transport line from the linac to the RCS. These magnets provide a  $180^\circ$  bend to the beam, so their field stability is very critical. The old power supplies,

while not particularly prone to breakdown, would often develop periods when their output currents were extremely unstable, making precise injection tuning difficult. The new power supplies will allow more stable injection position control, which should provide the operators with a better opportunity to adjust the injection focusing precisely. Thus, a better match of the linac beam emittance to the synchrotron acceptance can be achieved.

Over the last 4 years, it became increasingly apparent that the beam was clipping the upper portion of the magnet aperture and was causing a good deal of the low energy beam loss in the synchrotron. Our limited diagnostics indicate that, in at least two places, the center of the beam is about 3 mm above the geometric center of the main magnet aperture. This translates into an effective loss of about 5% of the vertical aperture. Computer studies are underway to analyze whether sufficient and appropriately located space is available in the synchrotron lattice to add vertical steering dipole magnets. The hope would be to lower, in as many locations as possible, the vertical orbits.

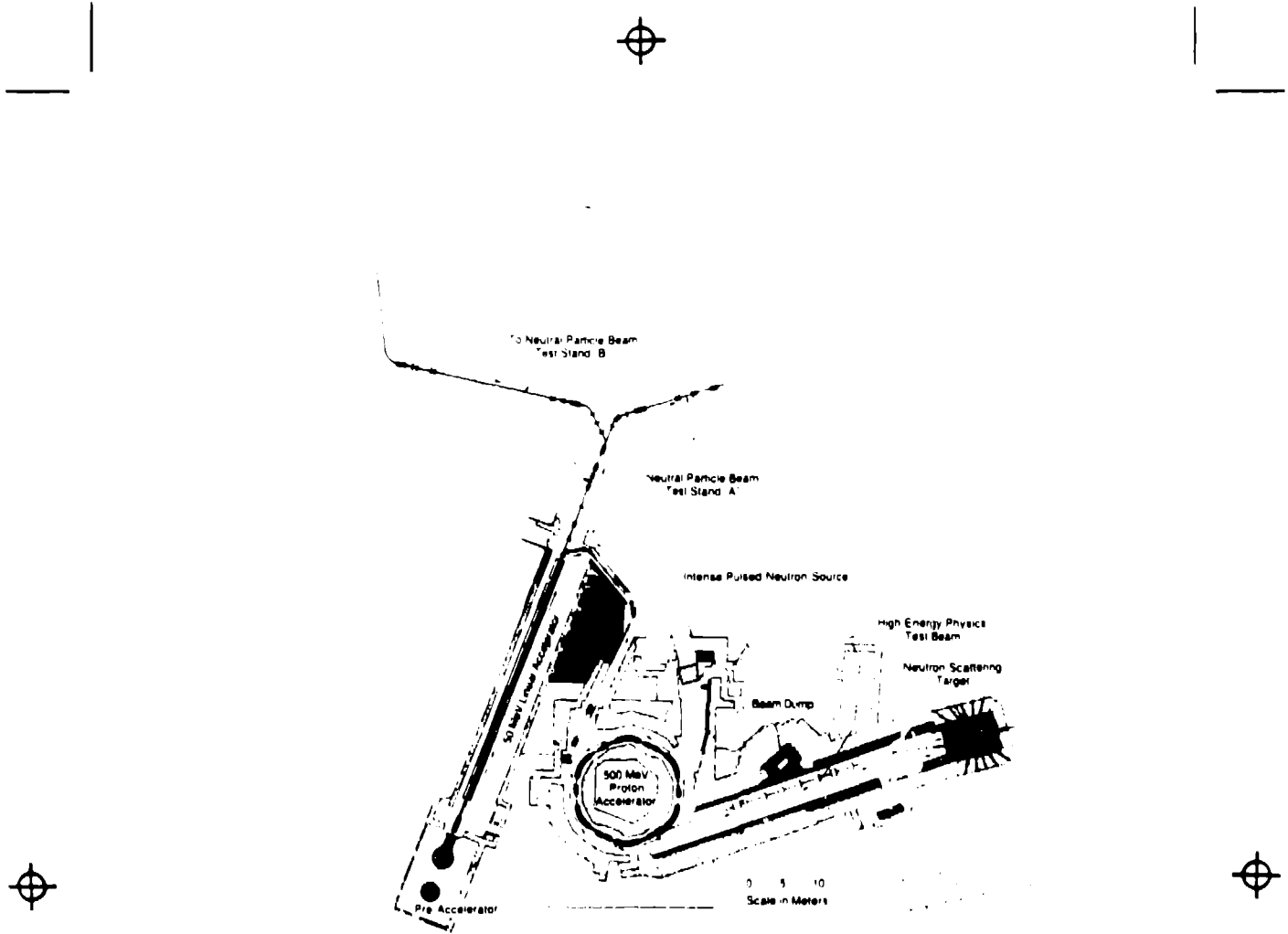
Halo collimators and added vertical steering in the 50 MeV transport line are also being discussed as possible ways to minimize vertical beam losses. In beam loss limited operation, the prevention of a single proton lost should result in nine additional protons on the neutron target.

**Table I** Accelerator operating summary.

	11/81- 7/83	10/83- 2/85	3/85- 7/86	8/86- 6/88
Average beam current ( $\mu\text{A}$ )	8.65	11.90	12.89	13.47
Operating efficiency (%)	89.6	89.3	93.9	91.9
Scheduled operating time (h)	7191	5567	5263	6237
Available operating time (h)	6443	4973	4942	5732
Total pulses on target ( $\times 10^8$ )	6.27	4.91	6.02	6.21
Total $\mu\text{A}$ hours	55,732	59,179	63,702	77,210
Total protons on target ( $\times 10^{21}$ )	1.08	1.22	1.54	1.73
SDI linac operation (h)	0	0	1000	3125

#### Other accelerator activities

The IPNS participation in the Strategic Defense Initiative (SDI) was presented in the previous ICANS report. The participation has continued in the operation of the linac and the first Neutral Particle Beam (NPB) test beam line A. Design and construction of a larger ANL-SDI beam line (B) started in late 1986, and the first test beam was sent down this new line on April 22, 1987. Figure 3 shows the layout of the IPNS accelerator system and the NPB beam lines. The beam optics design was supplied by members of the ANL Engineering Division (ENG), while IPNS personnel supplied much of the hardware design, installation planning and about 90% of the installation labor and initial testing effort. During the past two years, over 35,000 manhours of IPNS accelerator personnel effort was assigned to SDI beam line construction and experiment support.



**Fig. 3 IPNS accelerator system and NPB beam lines.**

In contrast to the SDI line A where almost all of the hardware was surplus, most of the line B apparatus was new. The overall beam line is 70 m long and consists of 7 horizontal steering dipole magnets, 4 vertical steering dipole magnets, 16 quadrupole magnets, power supplies, 4 sets of four-motion collimators, 12 sets of two dimensional segmented Faraday cup diagnostic devices, 5 beam toroids, several vacuum pumps and isolation valves, and a debuncher to reduce beam energy spread. IPNS worked closely with the ANL Engineering and Electronics Divisions to provide computer control and status readout of all these devices.

After a brief shakedown and characterization period on line B, a large team from Los Alamos joined us to install a permanent magnet beam expansion telescope and a considerable amount of sophisticated diagnostic equipment to help judge the performance of the telescope. Its purpose was to achieve a very low divergence beam; the divergence goals were met for the most part. The most active program now underway is the test operation of a new type of beam expansion telescope that was recently installed in SDI line B. It includes trim multipole magnets, which should reduce higher order magnetic aberrations and thus further decrease divergence.

Operation and experiments on SDI line A were interspersed with line B construction and operation. A total of more than 3100 hours of beam time was used on both

beams. Experimental topics included beam neutralization techniques and materials, radiation damage, target composition, and the sensing of neutral beam properties. The non ANL experimenters were assisted by ENG and IPNS personnel.

Future expansion, and even future operation, of the SDI facilities beyond Fall 1988 is, at the present, quite uncertain. A considerable reduction from the past 2 years in our SDI participation is certain. Proposals to utilize the IPNS RCS to accelerate deuterium ions have been made by the ANL-SDI office to military sponsors. A 100 m expansion of line B has also been proposed to obtain a more precise measurement of beam quality. While the military sponsors show some interest in these new activities, there has not yet been a firm financial commitment.

### Instruments

Figure 4 shows the instruments now operating at IPNS, the specifications of which are given in Table 2. Improvements on existing IPNS instruments and ancillary equipment are occurring constantly. Most notable since the last ICANS report is the commissioning of the Low Temperature Chopper Spectrometer (PHOENIX). PHOENIX, in addition to the Polarized Neutron Reflectometer (POSY) and the Quasielastic Neutron Spectrometer (QENS), was built by a Participating Research Team (PRT). In this mode, a significant fraction of the financial and manpower burden is borne by a group of scientists with considerable help from IPNS. These three PRT instruments were added to the user program in 1987 at which time non-PRT members could apply for 25% of the instrument time. The remaining 75% is allocated by the PRT to its members, and manpower is provided by the PRT in a collaborative mode for non-PRT users of the instrument. Neutrons are supplied free of charge to the PRT instruments, and this method of instrument construction and operation (modeled after the synchrotron sources) is an extremely effective way of getting extra instruments and dedicated scientists at the facility.

The instruments for elastic or total scattering consist of two powder diffractometers (SEPD Special Environment Powder Diffractometer, GPPD General Purpose Powder Diffractometer), which have excelled at high resolution and special environment work, coupled with the on-line capability of the Rietveld method and also have proved useful for amorphous systems. As one might expect, these instruments are now used increasingly with furnaces, cryostats, and pressure cells. Over the past 2 years, there has been considerable work on the powder diffractometers on structural and defect studies of the high- $T_c$  superconductors and the determination of residual strains in composite materials. The Single Crystal Diffractometer (SCD) is based on the Laue technique with a two-dimensional (30 x 30 cm) position-sensitive scintillation detector based on the Anger method, designed and built at Argonne, and has investigated crystal structures and a variety of problems involving superstructures, diffuse scattering, and recently, texture determination. The Small Angle Diffractometer (SAD) also includes a two-dimensional position-sensitive detector and is used to investigate metallurgical, polymer, and biological systems. A new detector for the SAD was purchased, which will allow a factor of four increase in total data rate. The broad scientific interest in the SAD and large oversubscription have resulted in the decision to build a second small angle diffractometer, SAD II, dedicated for polymer research.

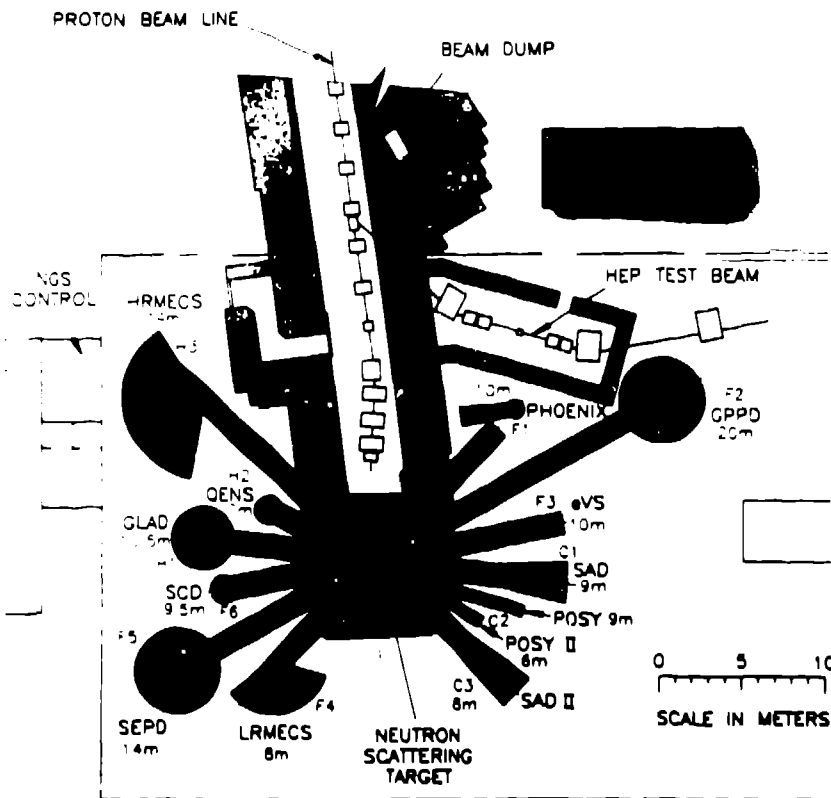


Fig. 4 IPNS neutron scattering instrument layout.

The two chopper spectrometers (LRMECS—Low Resolution Medium Energy Chopper Spectrometer, HRMECS—High Resolution Medium Energy Chopper Spectrometer) have proved exceptionally versatile in a variety of problems involving measurements of  $S(Q,E)$ . Experiments on amorphous materials, electronic transitions, and momentum distributions have all made use of the abundant epithermal spectrum. Based on the very heavy demand for beam time by the groups involved in momentum density— $n(p)$ —measurements in quantum liquids and solids, a new instrument, PHOENIX, was built as a joint construction effort by scientists from Argonne, Harvard University, Penn State University, and University of Illinois Urbana.

The Quasielastic Neutron Scattering Spectrometer performs studies on molecular spectroscopy and diffusion. It takes advantage of good energy resolution ( $70 \mu\text{eV}$ ), coupled with the ability to measure energy changes as a function of momentum transfer.

**Table 2**

IPNS NEUTRON SCATTERING INSTRUMENTS					
Instrument (Instrument Scientist(s))	Beam Line	Range		Resolution	
		Wave Vector* ( $\text{\AA}^{-1}$ )	Energy (eV)	Wave Vector ( $\text{\AA}^{-1}$ )	Energy (eV)
Special Environment Powder Diffractometer (J. Jorgensen/K. Volin)	F5	0.5-50	**	0.35 $\text{\AA}$	**
General Purpose Powder Diffractometer (J. Faber/R. Hitterman)	F2	0.5-100	**	0.25 $\text{\AA}$	**
Single Crystal Diffractometer (A. Schultz)	F6	2-20	**	2 $\text{\AA}$	**
Small Angle Diffractometer (J. Epperson/P. Thiyagarajan)	C1	0.006-0.35	**	0.004	**
Quasielastic Neutron Spectrometer (F. Trouw)	H2	0.42-2.59	0-0.1	0.2	0.02 $E_0$
Low Resolution Medium Energy Chopper Spectrometer (C. Loong)	F4	0.1-30	0-0.6	0.02 $k_0$	0.05 $E_0$
High Resolution Medium Energy Chopper Spectrometer (D. Price)	H3	0.3-9	0-0.4	0.01 $k_0$	0.02 $E_0$
PHOENIX (P. Sokol/K. Herwig)	F1	0.3-30	0.1-0.8	0.01 $k_0$	0.02 $E_0$
Polarized Neutron Reflectometer (G. Felcher)	C2	0.0-0.07	**	0.0003	**

\* Wave Vector,  $k = 4\pi \sin\theta/\lambda$ .  
 \*\* No energy analysis.

INSTRUMENTS NOT YET IN THE USER PROGRAM		
Beam Line	Instrument	Flight Path Length (m)
H1	Glass, Liquid and Amorphous Material Diffractometer (under construction)	10.5
C3	Small Angle Diffractometer II (under development)	8.0
C2	Neutron Reflectometer II	6.0
F3	eV Spectrometer	10.0

The Polarized Neutron Reflectometer has become a state-of-art instrument for obtaining magnetic information in thin films or near the surface of bulk materials. The very interesting basic information is coupled with some very promising applied interest, for example magnetic hysteresis in materials for recording heads. A second reflectometer (POSY II) has been recently constructed. Funded in part (\$150,000) by IBM, this unpolarized version of POSY will be used primarily for studies of interfaces and interdiffusion in polymers, taking advantage of the large scattering

contrast of H and D. The eV Spectrometer (eVS), designed to measure energy transfer to many eV, is temporarily dormant due to difficult background problems.

The Glass, Liquid and Amorphous Material Diffractometer (GLAD) is under construction as a PRT instrument and will be a world class instrument when completed. This new instrument, which will feature high intensity with low-to-moderate resolution and emphasis on low-angle detector banks to simplify inelasticity corrections, is discussed in detail in another paper in these proceedings.

### **Chopper development at IPNS**

A number of chopper-related development projects have been and are underway at IPNS. These include choppers for the reduction of backgrounds due to delayed neutrons, choppers to remove the prompt pulse of high energy neutrons from the beam, a chopper for lower energies, and improved chopper control systems for all of these.

The "delayed-neutron choppers" are lightweight drum choppers that "open" twice per revolution, i.e., they run at 15 Hz rather than the 270 Hz typically used for our other choppers. Two such choppers have been fabricated and installed, one in the GPPD incident beam line at the point where the line exits the biological shield, and a second in a similar position in the SEPD incident beam line. The basic design consists of a 40-cm-diameter, 11.5-cm-high, and 1-cm-thick cylindrical shell of B<sub>4</sub>C powder held in place by epoxy and supported by a thin aluminum shell and aluminum top and bottom plates. The chopper is rotated about the cylindrical axis which is vertical, normal to the incident beam. Each of the chopper shells has a pair of diametrically opposed openings which are designed to allow unimpeded transmission of the entire width of the beam over the time frame of interest to the instruments (nominally the time-of-flight range of 3-30 ns, measured at the detectors). The present design parameters lead to an "open" fraction of the chopper circumference of ~1/3 for the GPPD and ~1/2 for the SEPD. Consequently, these choppers should remove from the beam roughly 2/3 and 1/2, respectively, of the total number of delayed neutrons having energies low enough to permit detection in the <sup>3</sup>He detectors used on the instruments. However, Monte Carlo simulations have shown that the delayed-neutron contribution to the background should be reduced by factors of 10-100 in the long-wavelength part of the spectrum where the delayed-neutron background would otherwise be most serious. These choppers were installed in Summer 1988, so experience with them is currently insufficient to provide quantitative details of their performance.

A prompt-pulse-removal chopper ("t<sub>0</sub> chopper") has been designed and fabricated, and was installed in the PHOENIX incident beam line in Fall 1988. This chopper design is similar to that used in our standard Fermi choppers, except that it contains no slit package, and the opening through the beryllium pieces, which form the body of the chopper, has been widened somewhat to allow transmission of the desired bandwidth at the various different incident energies used on the instrument. The chopper will be phased to be closed totally at the time of the prompt burst of fast neutrons, and so it should remove most of these from the beam. Since these fast neutrons, which can thermalize in the Fermi chopper or in the collimators or shielding, form a major component of the background in chopper instruments, this additional chopper should

lead to significant background reduction in PHOENIX. If this in fact proves to be so, additional choppers will be provided for use on LRMECS and HRMECS as well.

Since a number of users have requested that LRMECS and HRMECS be able to provide lower incident energies, an additional Fermi chopper, optimized for transmission of 10 meV neutrons, has been fabricated and tested. Unfortunately, this chopper also allows significant transmission of higher energy neutrons, and for some experiments, these can produce background in the time frame of interest on the chopper spectrometers. If necessary, these higher energy neutrons can be removed with a filter or by a  $t_0$  chopper, so the 10 meV chopper can be regarded as satisfactory, and it is available now for configuration in those experiments which desire it.

A new chopper control system is being designed to operate the Fermi choppers and the  $t_0$  choppers. This system will implement the same algorithms used in our present chopper controllers, but will be based on readily available PC components to make it more easily programmable and significantly less expensive to reproduce. The lower expense is particularly important since a number of additional controllers will be required to handle the anticipated  $t_0$  choppers (at least three expected in the next 1-2 years) and choppers for GLAD (one or two expected) in addition to the three Fermi choppers that are controlled currently—for LRMECS, HRMECS, and PHOENIX. Development of this new control system is expected to be completed by mid 1989, and additional controllers will be built as needed. A different chopper controller has been developed to drive and control the delayed-neutron choppers, which have much less stringent control requirements. Two of these controllers were placed in operation in Summer 1988, controlling the GPPD and SEPD delayed-neutron choppers.

The floor space devoted to chopper control has been expanded to handle all the new chopper control systems, which are anticipated to be running simultaneously at IPNS. As part of this expansion, considerable care has been devoted to the redesign of the mounting and interconnection of the control systems and monitoring equipment, so chopper control is being turned into a "chopper system command center", optimized for the operation, monitoring, and maintenance of this equipment.

## **Data acquisition**

### **Introduction**

Since the 1986 ICANS-IX Meeting, we have continued to refine and improve the data acquisition system (DAS). Refinements to the existing system include replacement of the encoding electronics for some of the area detectors, development of high-level graphics routines for the GKS graphics system, and installation of cluster software to link our computers. A digital Private Branch Exchange (PBX) telephone system was installed at Argonne last year, permitting us to make significant improvements in access to the IPNS computer systems.

Major changes that have taken place include the conversion of the PDP instrument computer software to run on VAXstations, and the installation of VAXstations as



instrument computers on the Glass, Liquid, and Amorphous Material Diffractometer (GLAD) and the Neutron Reflectometer (POSY II) instruments and as replacements for the PDP computers on two instruments. Replacement of the remaining PDP computers with VAXstations is expected to be done over the next several years. VAXstations are also being used to increase the data analysis capacity at IPNS. An optical disk storage system for virtual on-line storage of large amounts of data is under consideration. Finally, new linear position-sensitive detector (PSD) encoding modules and a new hardware-based FASTDAS histogramming system have been developed for GLAD. (Details of the GLAD PSD encoding and the FASTDAS system are presented elsewhere in these Proceedings).

### **Data encoding modules**

The area PSD, which has been in use on the Small Angle Diffractometer (SAD), uses the rise-time method of position encoding. During the past year, we have purchased two additional detectors which use this same encoding method for SAD II and for POSY II. The two new detectors have come with their own sets of signal-processing electronics, and we have developed a new digitizer module to interface with these electronics to provide digitized position and time of flight information. A similar set of signal-processing electronics and a digitizer module have also been provided to replace the old units in use on SAD, which were becoming unreliable. This compatibility among these three detectors should simplify maintenance of the units.

### **Use of VAXstations**

All of the initial eight IPNS instrument computer systems were based on DEC PDP-11 computers. Several new IPNS instruments need greater on-line computing capabilities and disk storage capacity than is available on the current PDP systems. Furthermore, with the increased data rates expected with the new Booster target, several existing instruments can benefit from the increased computing and storage capacity available on the VAXstations. Finally, the PDP-11 systems are starting to show their age (the oldest have been in continuous operation for more than 8 years) and their failure rate is increasing. For these reasons, we have purchased four DEC VAXstation-II GPX workstations, each with at least 300 Mbytes of disk storage. Our instrument operating software has been converted for use on VAX computers (with some enhancements to take advantage of the VAX capabilities), and we will start using all four of these as instrument computers in Fall 1988. Two of the new systems will be on GLAD and POSY II, and the other two will replace the PDP computers on SAD and the Single Crystal Diffractometer (SCD). The remaining instruments will be converted from PDP-11 to VAXstation-based systems at a rate governed by need and budget.

The four VAXstations procured as instrument computers initially were used very successfully for data analysis. Now that these four are going to be used as instrument computers, a VAXstation 3200 system has been bought for data analysis. The addition of the VAXstations has not only improved the instrument computer situation, but also increased the total computing capacity available for data analysis since the VAXstation instrument computers place significant computing capacity at each instrument. It is expected that in the future more data analysis will be done

directly at the instrument as the data are being collected, rather than on one of the central computers in the system. Our central VAX systems will continue to be used by the VAXstations for data storage and archiving as well as program development and network services.

### **Graphics Improvements**

Until recently, IPNS has used the DISSPLA graphics package from Computer Associates (CA) for most of the graphics programs developed for data analysis. Since DISSPLA is an expensive commercial package, we could only use it on our VAX-11/780, thus preventing us from using all of our computers efficiently. Most of our graphics routines have now been converted to utilize GKS graphics, which is available on all of our computers. This was accomplished by writing a set of high-level graphics tools, called GPLOT, based on the GKS standard. VAX-GKS was the first graphics software package to support the VAXstation, and the use of GKS allowed us to develop device-independent graphics software that could be run on the VAXstation as well as our other graphics devices. The VAXstations produce high resolution color graphics very quickly, which will allow users to interact effectively with data collection and data analysis. This should also pave the way for more interactive modes of data analysis, although in many cases a considerable amount of software modification will be required.

Among other graphics enhancements, we have added a PostScript-compatible laser printer, which provides more flexibility and higher resolution than our other graphics devices.

### **Networking and clustering**

For several years, all of our computers have been linked together by a DECNET/ETHERNET network served by terminal servers, so access to any of these systems and transfer of information among them has become quite straightforward. Two recent developments have expanded these networking capabilities.

During 1987, Argonne installed a digital PBX telephone system which allowed a number of improvements in our computer network. The PBX provides lab-wide network support through the use of bridges to connect divisional ETHERNET segments into one large network. This allows us to access printers and computers in other buildings. The new PBX also allows users in other buildings to have high speed terminal access to our computer facilities.

To simplify access and connection speed among our computer systems, we are joining some of them together in a cluster. This will make it more efficient to store files centrally and still use the VAXstations for data analysis without the necessity of keeping multiple copies of files. Some of the new instruments which have come on-line have strained our computing and data storage capacity severely, and this demand is expected to increase even more with the Booster target; therefore, the cluster is expected to continue expanding.

### **Data archiving/retrieval**

As the amount of on-line disk space increased, it became increasingly difficult to provide file backup. It took typically four high-density tapes to store the data from one disk, and an operator was required to change tapes. We have solved this problem recently by purchasing a helical-scan tape unit which permits us to store the contents of several disks on a single tape cartridge. This has eliminated the need for an operator to change tapes during the backup operation. Because of the cheaper and more compact storage, we will now be able to keep monthly full backup tapes permanently, instead of reusing the tapes after one year.

The installation of the Booster target is expected to result in a large increase in the rate of data collection and the need for data storage facilities. Fortunately, disk technology has kept pace with our need for online storage, and we were able to make a significant increase in our disk storage capacity this past summer. Careful management of data storage will continue to be necessary, however. Some instruments already require frequent archiving of data to tape. The optical disk system under consideration would provide the ability to store this data where it could be accessed quickly with no operator intervention.

### **Booster target**

Since the last Progress Report 1985-1986, in which the design of the Booster target was described in detail, numerous difficulties have had to be overcome in the process of fabricating the Booster target. In the end, we have succeeded—all the required disks and spares have been completed, and insertion and testing are underway. Throughout, we enjoyed the helpful cooperation of our colleagues at the Oak Ridge Y-12 facility where the disk processing was carried out as well as many groups at Argonne. Details of Booster target fabrication and performance are given in another paper in these proceedings.

### **Moderators**

Moderators are also covered in a subsequent paper. Based on operating difficulties with solid methane and the lack of experience with booster operation, startup in the fall of 1988 will include liquid hydrogen ( $T > 14$  K) in the C moderator, that which is viewed by SAD, POSY and POSY II. This will result in a loss of long wavelength neutrons, which should be more than offset in most wavelength regimes by the enhanced flux from the Booster target. The moderator design will permit a return to solid methane in C after we have gained sufficient operating experience on the Booster target.

### **Examples of some recent scientific results**

To illustrate the performance of some of the IPNS scattering instruments, some recent experimental results are discussed. A study was undertaken to investigate the motion of molecules in the pores of molecular sieve zeolites which are used as catalysts in shape-selection hydrocarbon transformation reactions. Figure 5 shows the pore or channel structure in ZSM-5 through which molecules can diffuse. A molecular dynamics calculation followed the rate of diffusion in the various

directions, b clearly being the easiest direction. Figure 6 shows the near-elastic energy region measured for the catalytic material with (symbols connected by a line) and without (solid line) methane. The additional broad component when the methane is present is the quasielastic scattering due to translational and rotational diffusion. The widths of the data yield a translational diffusion constant of  $2.4 \times 10^5 \text{ cm}^2\text{-sec}^{-1}$  at a momentum transfer of  $1 \text{ \AA}^{-1}$ , which is in very good agreement with the simulations and previous NMR results.

The large difference in scattering by hydrogen and deuterium was used to study the interface separating two different molecular weight polymers. Figure 7 shows results from POSY which was used to study the reflectivity of a bilayer of deuterated and normal polystyrene (PS) on silica glass. The oscillations (dots) are due to interference of the reflections from the front and back face of the upper deuterated PS layer. After a short anneal ( $140^\circ\text{C}$  for 5 minutes) the much lighter, deuterated PS has diffused and the change of the period of the oscillations (squares) was used to generate the change in profile shown in Figure 8. These results were our first measurements showing the power of neutron reflectivity for studying polymer diffusion and resulted in the decision to build POSY II.

These are only two examples of recent results and many more examples are detailed in the IPNS Progress Report 1987-1988, published in October, 1988.

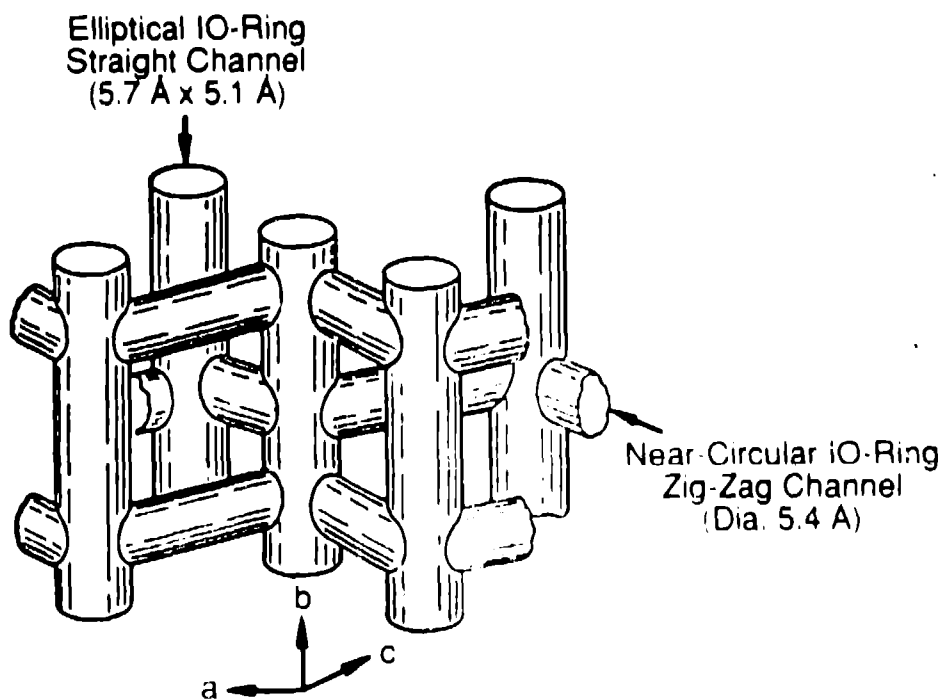
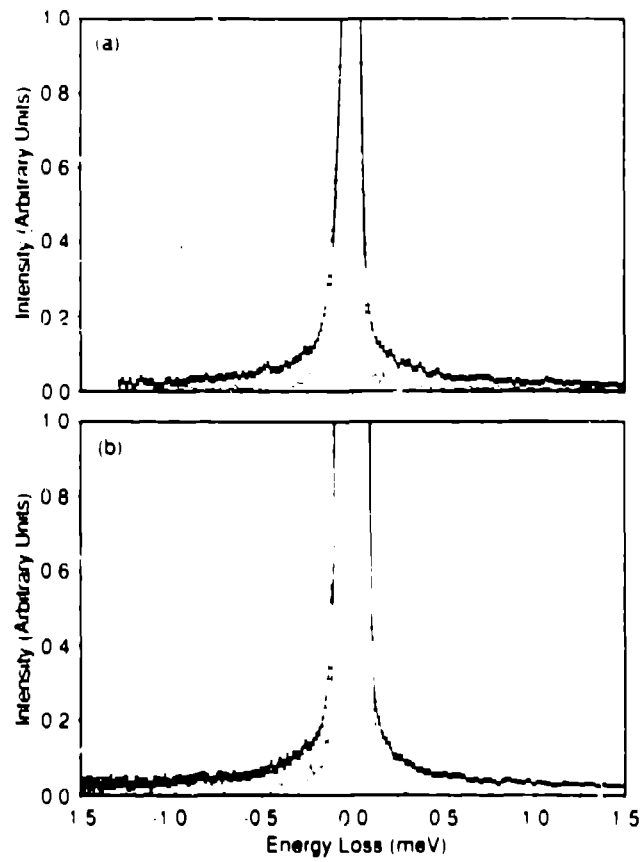


Fig. 5 Diagram of the channel structure of ZSM-5 zeolite.



**Fig. 6** Quasielastic scattering from silicate (solid line) and silicate plus methane (symbols connected by line) measured on (a) QENS at 300 K and (b) IN6 (ILL) at 80 K.

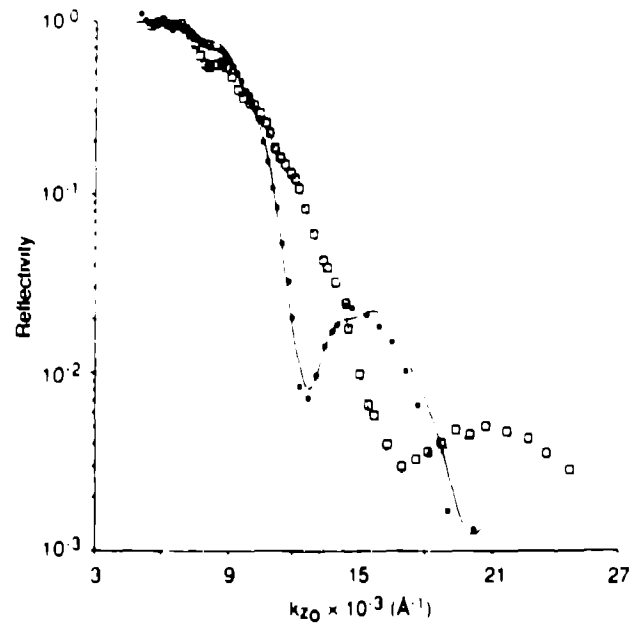


Fig. 7 The reflectivity of a bilayer of d-PS/PS on silica glass as deposited (dots) and after a short anneal (squares).

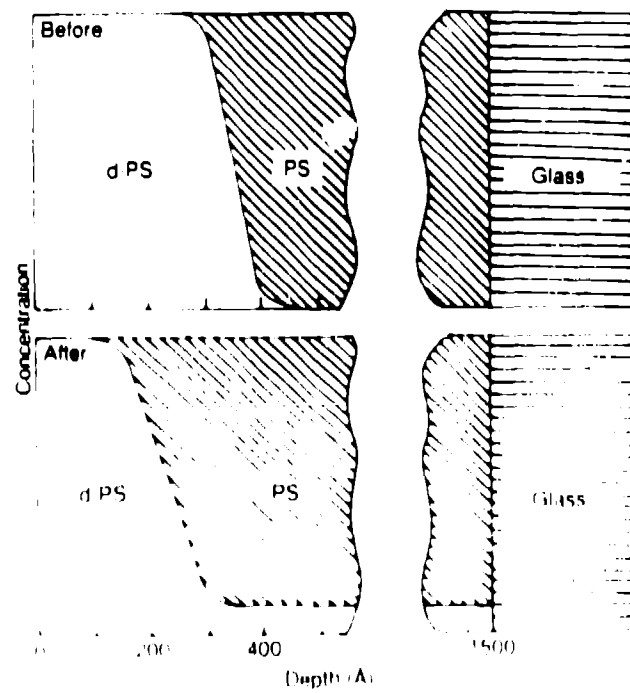


Fig. 8 The concentration profile obtained from the data of Fig. 7

### User program

The operating statistics shown in Table 3 clearly indicate an increase in the number of experiments and scientists at IPNS despite a small decrease in operating time. The increase is due to the proton current increase and the increase in neutron scattering instruments (4 in 1982 vs 11 in 1988).

**Table 3** IPNS user program.

	FY83*	FY84	FY85	FY86	FY87	FY88
Weeks of operation	26	29	21	22	21	18*
No. of experiments performed	110	210	180	212	223	226
Visitors to IPNS for at least one experiment:						
Argonne	41	49	44	52	55	54
Other government labs	9	8	7	11	15	17
Universities	33	45	51	79	78	79
Industry	5	9	7	13	24	17
Foreign	18	39	34	27	24	16
TOTAL	106	150	143	182	196	183

\* FY83 = Fiscal year 1983 = October 1982 through September 1983.

\* 2 weeks to be run early in FY89.

### Recent and planned conferences and workshops

We continue our strong commitment to sponsor conferences and workshops in connection with our efforts to spread the news about neutrons in general, and the capabilities of IPNS in particular. Financial and technical assistance from both the University of Chicago and Argonne's Division of Educational Programs is greatly acknowledged.

#### Conferences and Workshops

December 8-9, 1986

Third IPNS User Meeting

May 12-13, 1987

Design Workshop for an Advanced Chopper Spectrometer at LANSCE

October 26-29, 1987

International Conference on Techniques and Applications of Small Angle Scattering

November 6-7, 1987

Workshop on X-ray and Neutron Scattering from Magnetic Materials

October 3-7, 1988

International Collaboration on Advanced Neutron Sources (ICANS-X), Joint Sponsorship with LANSCE at Los Alamos National Laboratory

**Planned Meetings**

October 24-26, 1988

Workshop on Momentum Distributions

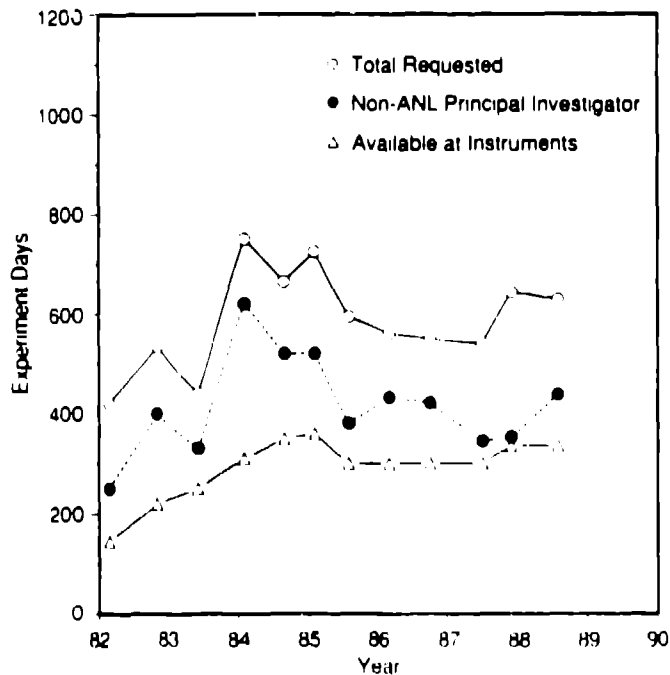
November 14-15, 1988

Fourth IPNS User Meeting

November 16-18, 1988

Short Course on Neutron Powder Diffraction and Rietveld Analysis

Figure 9 shows that the requested beam time under the user program remains high and is dominated by non-Argonne scientists. The large increase in university users is due to the establishment of PRT's and a number of groups consisting of faculty, post-doctoral appointees and graduate students which focus their research at IPNS.





**Fig. 9** Experimental beam time requested under the IPNS User Program.

**Advanced Pulsed Neutron Source (ASPUN)**

The need for more intense neutron sources has been the subject of many meetings and reports. The most thorough workshop took place at Shelter Island, New York, in October 1984. The major findings of the workshop were:

1. The case for a new higher flux neutron source is extremely strong, and such a facility will lead to qualitatively new advances in condensed matter science.





- 
- 
2. To a large extent, the future needs of the scientific community could be met with either a  $5 \times 10^{15} \text{n-cm}^{-2}\text{-s}^{-1}$  steady state source or a  $10^{17} \text{n-cm}^{-2}\text{-s}^{-1}$  peak flux spallation source.

The scientific output and future of pulsed neutron sources have been growing steadily in recent years. It is the goal of the ASPUN project to develop fully the potential of pulsed neutron sources by designing the next generation source. The goal of present generation pulsed sources is in the 100-200  $\mu\text{s}$  range, which would yield a neutron flux that is a factor of 3-6 higher than IPNS when operating with the enriched uranium (Booster) target.

The ASPUN project would increase proton currents by a factor of 20 or more beyond the design goals of presently operating sources. This project would be the  $10^{17} \text{n-cm}^{-2}\text{-s}^{-1}$  peak flux spallation source as recommended by the Shelter Island report. Funds for a design effort to start in fiscal year 1990 have been requested of the Department of Energy. Details of ASPUN are given in another paper in these proceedings.



### Conclusion



The report on DOE neutron sources that was released in December, 1987, and chaired by P. Pincus, praised IPNS for its effectiveness as a user facility and its world leadership role in instrument development. An extended tenure of operation was recommended as well as support for pulsed neutron instrumentation and development of next generation sources. The ever increasing instrument capability, the Booster target and our very active involvement with the scientific user community guarantee a productive scientific future for IPNS.

### Acknowledgments

This work is supported by the U.S. Department of Energy. This manuscript has been authored by a contractor of the U. S. Government under contract No. W-31-109-ENG-38. Accordingly, the U. S. Government retains a nonexclusive, royalty-free license to publish or reproduce the published form of this contribution, or allow others to do so, for U. S. Government purposes.



## Recent progress at LANSCE

*R. Pynn*  
Los Alamos Neutron Scattering Center  
Los Alamos National Laboratory  
Los Alamos, New Mexico 87545  
USA

Since the last ICANS meeting in 1986, a new construction project, funded at the level of \$17.5 million by the U.S. Department of Energy, has been started at the Los Alamos Neutron Scattering Center (LANSCE). This project comprises an experimental hall with an area of 1700 square meters, a support building which includes both laboratories and offices, and four new spectrometers. The experimental hall was occupied in April of this year and we anticipate the use of the support building within six months. Both of these buildings, an artist's impression of which is shown in Fig. 1, are essential for the national user program which is described below.

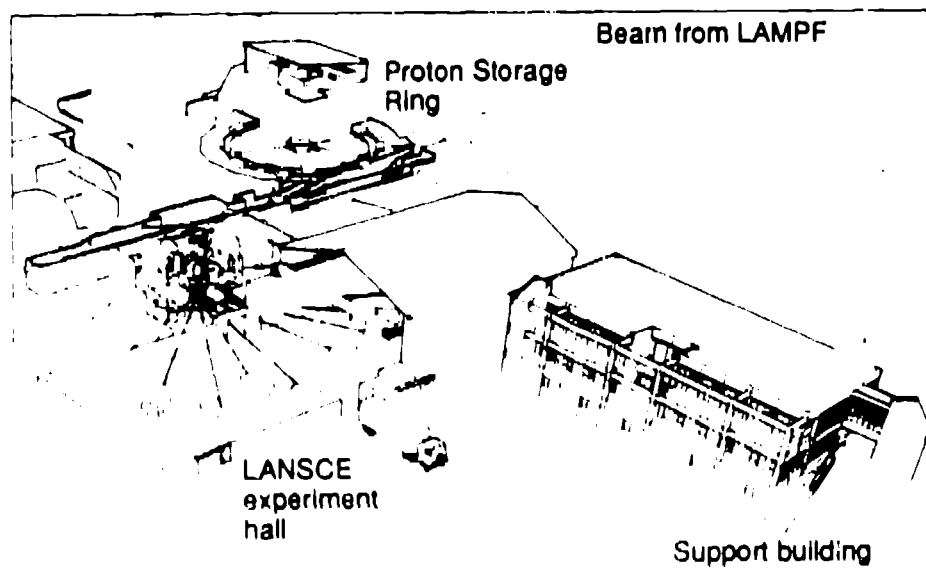
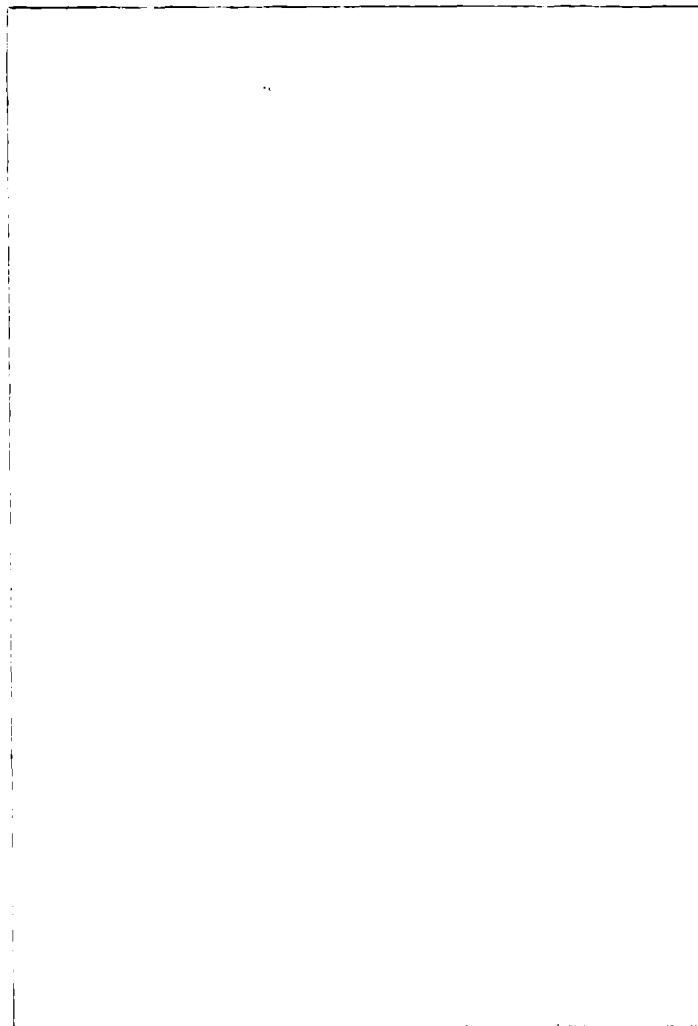


Fig. 1 Artist's impression of the new LANSCE facility.

The four instruments included in the construction project are a medium-resolution powder diffractometer (NPD), a reflectometer for surface studies, a high-resolution chopper spectrometer with a Brillouin scattering option, and a back-scattering

spectrometer. Design workshops for each of these instruments have been held and have involved participation of scientists from both the United States and Europe.

The first incarnation of the NPD (c.f. Fig. 2) was installed in August of this year, in time to benefit from several weeks of beam. Experiments have been performed on a number of samples and the spectrometer has been found to have the predicted resolution (currently the highest for any US powder diffractometer) and low background. In future, new detector banks, comprising linear, position-sensitive detectors, will be added, and the instrument should reach its "final" configuration within two years.



**Fig. 2** The Neutron Powder Diffractometer (NPD) recently installed in the new experimental hall.

During the past two weeks, first measurements have been made with our prototype reflectometer, yielding data such as those shown in Fig. 3. Since no serious effort has yet been made to reduce background on this instrument, the results in the figure are encouraging. The reflectometer has a novel design involving two beams incident on the horizontal plane of the scattering sample at different angles. Although the instrument will be in regular use from 1989 onwards, it will not be included fully in the user program until 1990.

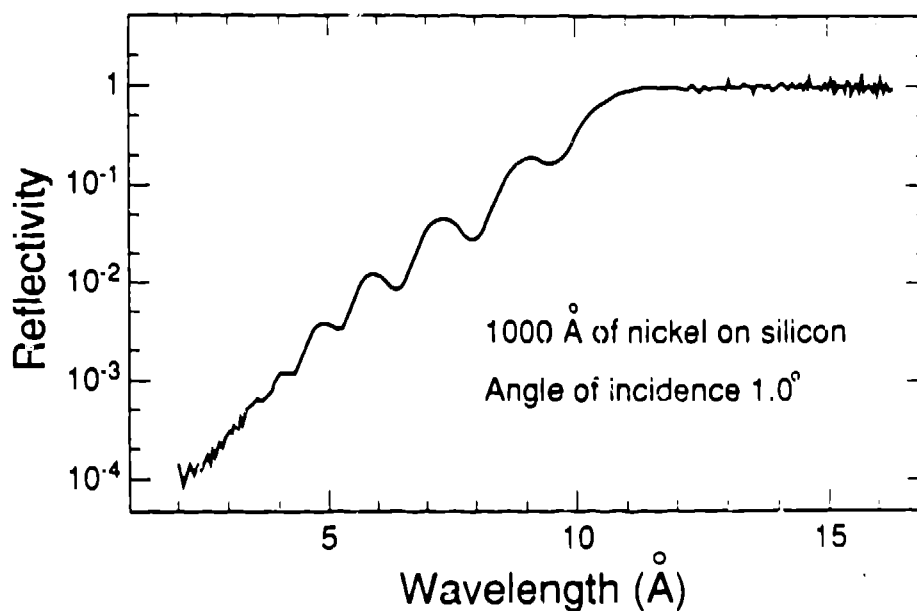


Fig. 3 One of the first reflectivity profiles obtained with the LANSCE reflectometer.

Detailed design is already in progress for the chopper spectrometer and we anticipate the installation of the incident beam line by next year. The first operational part of this instrument will involve the low-angle detectors needed for Brillouin scattering, some of which should be installed by next year. The vacuum tank containing the high-angle detectors is unlikely to be available before 1990, however, and the full complement of detectors will not be implemented until 1991.

The last of the four new instruments, the back-scattering spectrometer, has been designed conceptually but not in detail. This spectrometer will be positioned at the end of a  $^{58}\text{Ni}$ -coated guide viewing the existing liquid-hydrogen moderator. The guide tube will be ordered in the very near future, but a debate concerning the relative merits of straight and curved guides has to be concluded first.

Part of our construction program involves making four additional penetrations in the existing bulk-shield and bringing these beams into the new experimental hall. The penetrations will be made next year, but upgraded and new moderators will not be installed until 1991 or 1992. One of our current exercises is to determine the

locations and identities of the new moderators and the disposition of the spectrometers they will serve. Plans in this area are far from concrete, but it appears likely that we will install at least one liquid-methane moderator. In all probability the existing (or renovated) versions of the single crystal diffractometer (SCD) and the filter-difference spectrometer (FDS) will be moved to the new experimental hall when the upgraded moderators are installed. Options for less conventional moderators, such as mixtures of metal hydride and liquid hydrogen, are also being studied.

This year was the first in which LANSCE ran a formal user program, similar to the widely-copied ILL model, with proposals examined by an External Program Advisory Committee (EPAC). LANSCE shares this committee with the IPNS, and it is our intention to hold joint meetings at which proposals for the two centers are examined at the same time. Operational issues prevented such a joint meeting in 1988, but one is planned for March of next year. A policy for the distribution of LAMPF protons between the LANSCE target and the Weapons Neutron Research facility has been agreed. Essentially this policy results in LANSCE spectrometers being available to external users for non-classified research during about 60% of each 6-month LAMPF run-cycle. Classified measurements may also be performed, and may occupy up to 20% of the available beam time. Such experiments are chosen on the basis of proposals which are examined by an Internal Program Advisory Committee (IPAC). It was gratifying to observe that beam time was over-subscribed by a factor of about two in 1988, with a total of 102 proposals submitted for non-classified research on 5 spectrometers. In addition there were 12 proposals for research of programmatic interest to Los Alamos National Laboratory.

Unfortunately, statistics for beam availability were unimpressive this year. Although the overall beam availability was about 64% during the six weeks of cycle 52 (18th August to 3rd October), cycle 51 (15th June to 22nd July) averaged only 30%. The technical reasons for this poor performance will be discussed in more detail by Bob Macek in a later presentation. To a limited extent the numbers are reduced by our definition of availability. Beam is defined as available only when the proton current exceeds 50% of the planned value (30  $\mu$ A at 15 Hz for most of 1988). Since the potential exists for unacceptable radiation levels to be generated in the neutron scattering halls during PSR tuning, the latter operation has to be carried out at reduced proton current. Tuning accounted for 13% of scheduled time in cycle 51 and 9% during cycle 52.

The peculiarity of our accounting system for beam availability does not really reduce the severity of our problems in this area, however, and an increase of availability is the major short-term priority at LANSCE. I believe that Bob Macek and his group have now identified many of the improvements to existing hardware which will be required to ensure improved reliability. These will be implemented as rapidly as possible as part of the Laboratory plan to ensure that PSR reaches its full potential within the next three years.

In spite of the poor reliability of PSR, we were able to carry out 42 of the 49 experiments approved by EPAC and all 8 of the experiments ratified by IPAC. However, 22 experiments had to be rescheduled and user satisfaction was only achieved by using LANSCE discretionary time. Even so, 33 experiments in support of the LANSCE research program were accomplished during discretionary periods.

Although PSR was originally designed to deliver 100  $\mu\text{A}$  of protons, we have been unable to increase the current beyond about 35  $\mu\text{A}$  without compromising hands-on maintenance. The problem has been traced to the  $\text{H}^0$  injection scheme which, when it was implemented, was seen as a cost-effective attempt to solve a difficult technical problem. Unfortunately, the scheme results in an unprecedented increase in beam emittance before injection and to a non-Gaussian beam profile. Both of these features, which will be discussed in Macek's talk, lead to unacceptable spill for proton currents above about 35  $\mu\text{A}$ . To achieve the 100  $\mu\text{A}$  of which PSR is capable will therefore require a modification of the injection scheme. The management of Los Alamos Laboratory has decided that this task has high priority and that it will be accomplished within the coming three years.

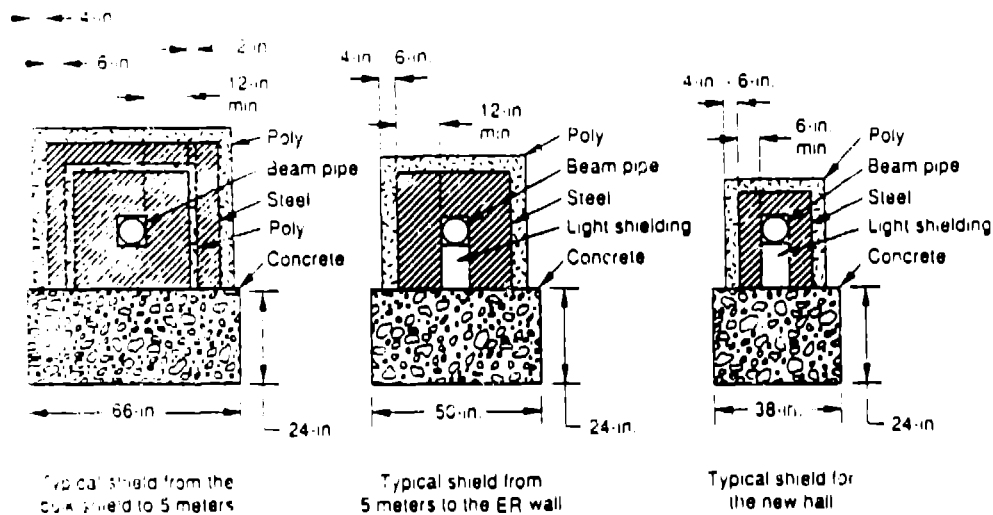
Those of you who visited LANSCE prior to the 1988 run cycles will remember that experimenters had no access to their spectrometers during proton beam delivery. At that time, unforeseen spills of the protons could have caused massive radiation doses close to the neutron spectrometers. Solution of this problem was our first priority in 1988. A triply-redundant system of fail-safe instrumentation has been installed to detect beam spills and unacceptable radiation levels. The system is able to interrupt the proton beam sufficiently rapidly to prevent unreasonable exposure of personnel to radiation fields. However, as mentioned above, it is necessary to diminish the proton current during tuning operations, when beam spill is inherently more likely, in order to avoid trips of the safety instrumentation. To be able to tune without incurring this reduction of current will require the installation of additional shielding around the pipe through which protons pass from PSR to the LANSCE target.

During the past year we have made a concerted effort to understand the shielding requirements for neutron beam lines and spectrometers at a high-current spallation source. On the basis of Monte Carlo calculations which he will describe at this meeting, Gary Russell has been able to generate an algorithm for effective shielding which minimizes the amount of unnecessary material. This cost-effective solution, shown schematically in Fig. 4, has been implemented on NPD and found to work well.

A development at LANSCE that has paid dividends recently is the Generalized Structure Analysis System (GSAS), which is used to treat diffraction data obtained with both powders and single crystals. This software, which was written by Allen Larson and Bob Von Dreele, is currently in use at more than 35 sites in addition to LANSCE. The programs were written with the ability to refine simultaneously multiple, independent data-sets. It has proved particularly useful to combine data obtained with x-rays and neutrons on the same powder sample. The crystallographic structure obtained from the refinement is more accurate than could be obtained with either technique alone and local minima in the least-squares refinement are avoided. Furthermore, the maximum level of structural complexity which can be treated is increased when independent data sets are used. I believe this to be a true example of what is meant by the complementarity of x-rays and neutrons: the simultaneous use of both probes to solve complex structural problems.

A LANSCE initiative which may revolutionize the way in which pulsed-source data are analyzed involves the use of maximum entropy methods. Devinder Sivia, who will talk tomorrow, has already demonstrated the power of this method in the

treatment of data obtained on the FDS. However, I believe that the method may have use beyond the simple implementation of data treatment algorithms. The maximum entropy method provides an impartial assessment of the information content of data. Thus, it may be used to rank the relative effectiveness of different spectrometer resolution functions. In particular, Devinder has shown that resolution functions with one sharp edge are superior to symmetric functions of the same variance. At pulsed spallation sources, where the physics of the neutron moderation usually leads to asymmetric lineshapes, this observation may have far-reaching consequences.



**Fig. 4** Cross section of LANSCE beam line shielding which has been optimized with the help of detailed, neutron-transport codes.

In conclusion, the past year has been one of great change at LANSCE. It has been an exciting time during which new developments have occurred almost daily.

## Progress at the pulsed-spallation neutron facility KENS

*N. Watanabe*  
National Laboratory for High Energy Physics  
Oho 1-1, Tsukuba-shi  
Ibaraki, 305  
JAPAN

### 1. Outline

The world's smallest pulsed-spallation neutron facility KENS is still active and has been successfully operated since the last ICANS with increasing proton-beam intensity. Scientists of the proton accelerator group at KEK have convinced themselves that a beam intensity of  $2 \times 10^{12}$  protons per pulse came within range.

The beam time allocated to neutron-scattering experiments was about 1150 hours per year, which is saturated since 1981. Visiting scientists spent about 3500 man-days at the KENS facility in the last year from about 40 different institutes to perform experiments. Fig. 1 shows the total number of registered users in each fiscal year since FY 1981.

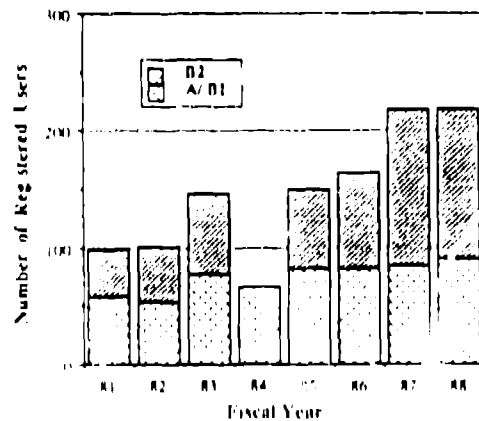


Fig. 1. Number of registered users

Figure 2 shows the number of proposals accepted each year. About 60 proposals including test experiments were accepted each recent year from more than 65 proposals, and about 55 experiments were successfully completed. At KENS we have two categories of proposal. Proposals by large groups responsible for construction, operation, maintenance and improvement of the instruments which they are concerned with are classified in the first category A/B1 and they can use up to 60% of the beam time. On the other hand, proposals by small groups of pure



users are in the second category, B2, and they have to share the remaining 40% beam time in competition. We intend to increase the B2 fraction; for example, in the case of the small angle scattering instrument SAN, more than 60% of the beam time is allocated to B2.

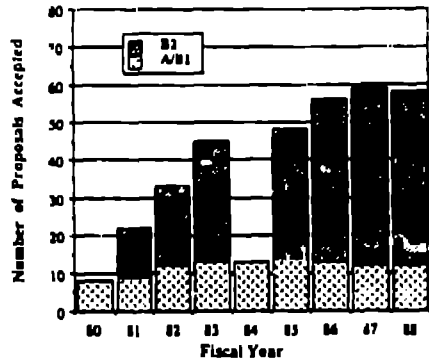


Fig. 2 Number of proposals accepted

Figure 3 shows a beam-time distribution of each instrument used in various research fields in recent years.

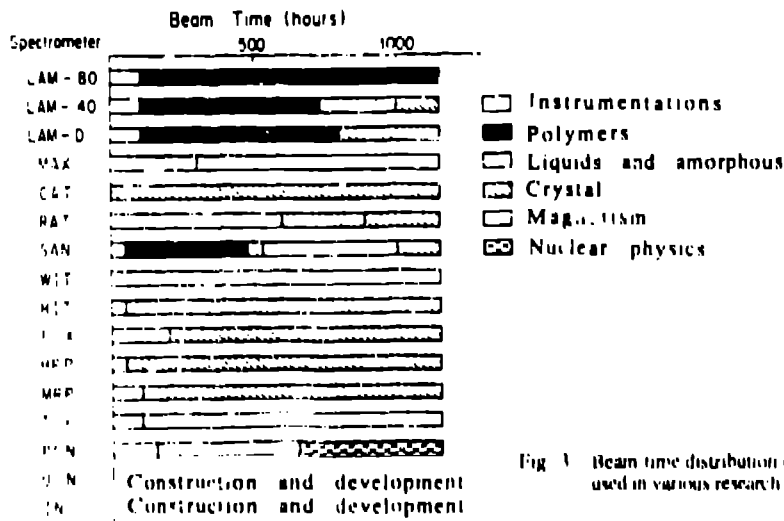


Fig. 3 Beam time distribution of each instrument used in various research fields

The budget for KENS has also been saturated since FY 1985. Table I shows, in round numbers, the budget in FY 1988 after adjustments at KEK. Costs for manpower and for accelerator operation are not included. Laboratory overhead and various costs for radiation safety, electricity, water, air conditioning etc. have been subtracted. KEK supports full expenses for travel and stay of outside visitors.

Table I Budget for KENS in FY 1988 (unit is ¥M)

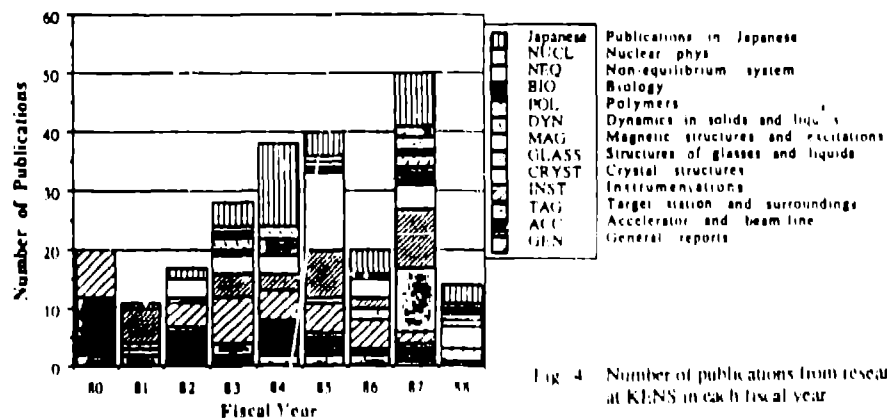
Operation of KENS	facility Beam line	Neutron scattering experiments	
		Experiment	Travel and lodging
85	51	96	16

Table II shows the number of scientists and engineers in the Booster Synchrotron Utilization Facility (BSF).

Table II Number of Scientists and Engineers in BSF

	Scientists	Engineers
Director	1	
Neutron scattering	6	2
Beam-line	3	4

The number of publications for research at KENS are shown in Figs. 4 and 5. The total number of papers published in journals and conference proceedings came to about 250 including reviews, status reports, accelerator/beam-line development for KENS, and publications in Japanese, in addition to neutron scattering results.



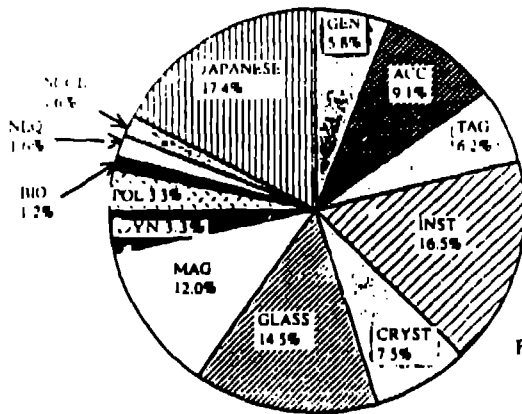


Fig. 5 Proportions of publications in each field

## 2. Target and Moderators

The neutron-production-target system of depleted uranium<sup>1)</sup> has worked quite well with great stability during these years. In Fig. 6 the measured temperature rise at the center of the first target block (the block with the heaviest heat-load) is plotted as a function of proton beam current at a rated coolant-flow (60l/min). The temporal change in the temperature rise is probably due to fluctuations of the proton-beam position on the target. Error bars indicated in the figure represent the maximum and the minimum of the temperature distribution. The temperature rise per  $\mu\text{A}$  was thus determined as  $15.6 \pm 3.2^\circ\text{C}/\mu\text{A}$ . The maximum temperature of the target block is, therefore, estimated to be  $177 \pm 32^\circ\text{C}$  at the designed proton-beam current of  $10 \mu\text{A}$  with a coolant temperature of  $21^\circ\text{C}$ . The estimated temperature is significantly lower than the highest safe value estimated in the safety analysis report.

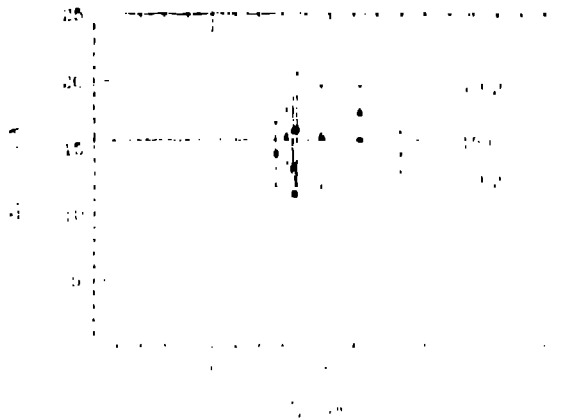


Fig. 6 Measured temperature rise at the center the first Target block

It was recently found that the polyethylene moderator at room temperature suffered from serious radiation damage due to the increased proton-beam-current and the use of the depleted uranium target. We therefore, decided to replace the polyethylene with circulating light water. Full installation of the new moderator system was completed September 1988.

Some improvements were performed on the hardware of the KENS cold neutron source<sup>2</sup>). The vacuum-pump system was improved by replacing the previous diffusion pump with a turbo-molecular pump (RTP-300 RIGAKU, 320//sec). The control system was also improved so that the vacuum can be held in the event of an electric power failure and the pump starts automatically on recovery.

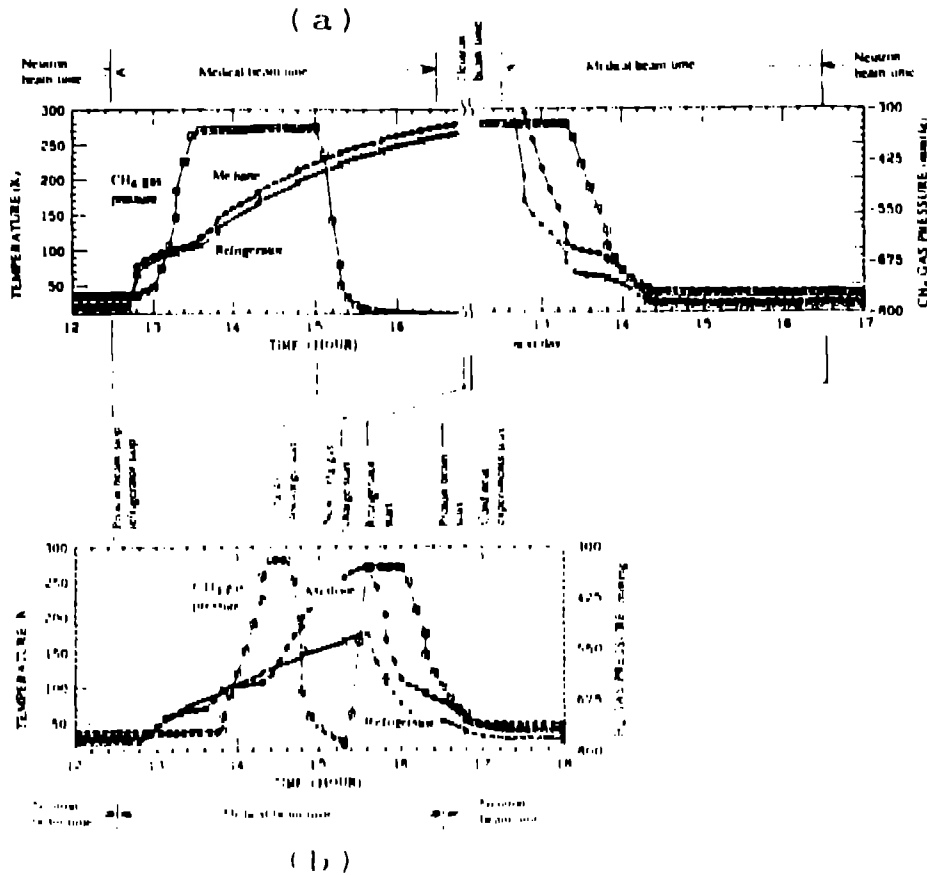


Fig. 7 Operational records on renewing solid methane moderator (standard operation until June 1988 (upper), quick operation (lower))

We, however, have serious problems on the solid methane moderator. We experienced a so-called "burp" three times and the cryogenic moderator chamber suffered from serious damage<sup>2)</sup>. The chamber was replaced by a new one in September 1987. Although the "burp" problem has not been overcome, we can avoid the burp by renewing solid methane before reaching a critical value of integrated protons on the target, which is empirically determined to be about  $6 \times 10^{18}$ . Therefore after the installation of the new chamber we renewed solid methane at the midpoint of the beam cycle before reaching the critical dose. We had to waste almost one day of cold neutron beam-time in each cycle for renewing as shown in Fig. 7(a). In order to minimize the wasteful time, we tried to renew the solid methane as quickly as possible. Every working day of beam-time about 4 hours in the afternoon is allocated to the medical group, Particle Radiation Medical Science Center, university of Tsukuba, for cancer therapy using protons. If we can complete the renewing within the medical beam-time, we have no loss. The result of the first quick renewing is shown in Fig. 7(b). We confirmed that we can restart experiments with the solid methane moderator immediately after the end of the medical beam-time.

Another important problem is cryostat trouble. Since December 1985 we use a new-type cryostat in which the heat exchanger is embedded into the side walls of the moderator container. The performance of the second cryostat of this type, which was installed in September 1987, became poor since April 1988: sometimes the methane temperature went up to 40 K associated with poor vacuum. We found that it was, at least partly, due to a leak of coolant helium to the vacuum space of the cryostat. Even though the second cryostat had no experience of burp, it suffered from damage. It is not clear what is the major mechanism of such damage, but we guess that a welded part between the wall-heat-exchanger and the external piping of coolant-helium cracked by the stress associated with the volume increase of solid methane by radiation. Similar cryostat trouble at IPNS was reported by Carpenter.<sup>3)</sup> They avoided burp by raising the methane temperature periodically, but the life of the cryostat was rather short. September 1988 we replaced the second cryostat by a third one. We, however, have to develop a new type of cryostat in due course.

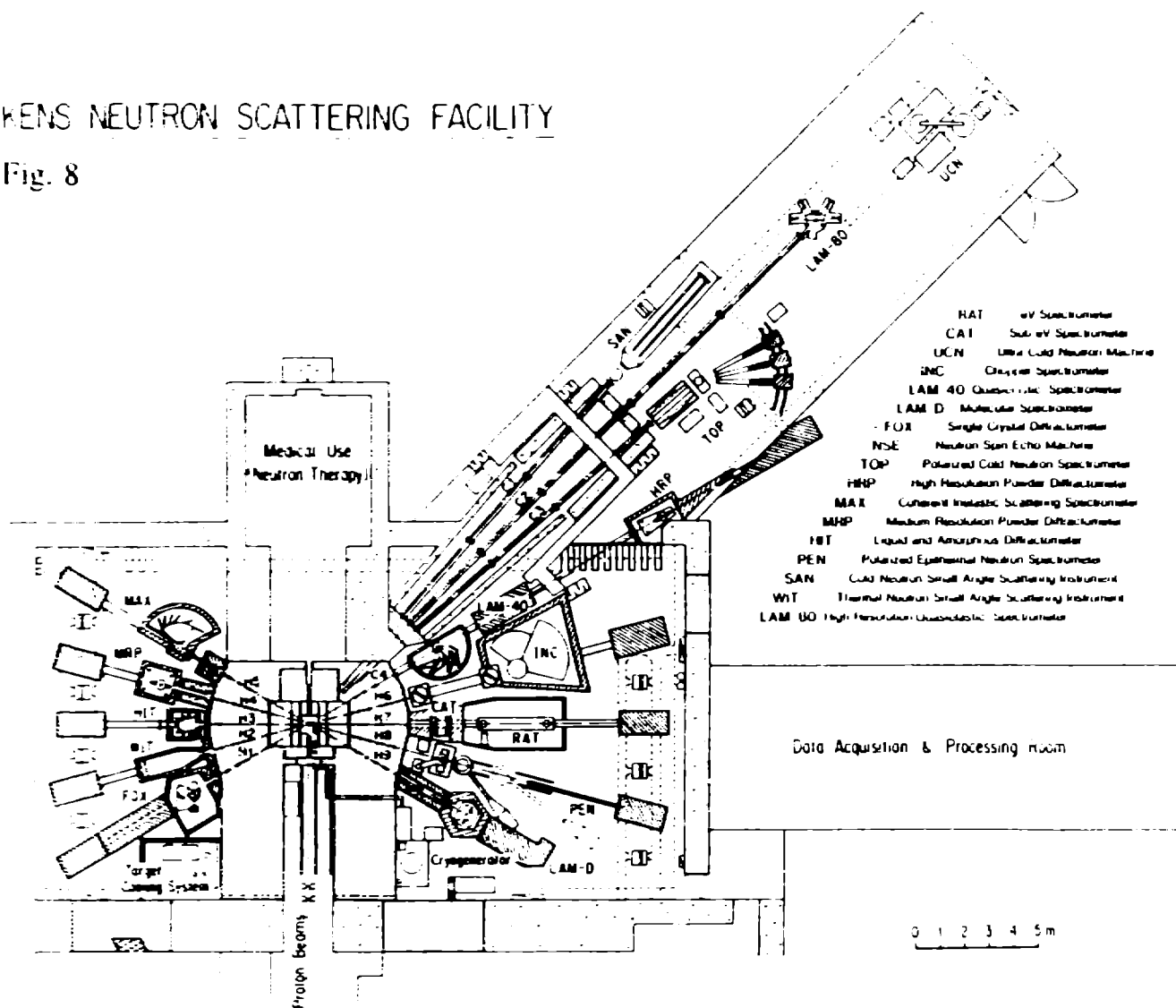
### 3. Development of Neutron Scattering Instruments

In the KENS facility there are sixteen instruments: Fourteen are in operation, a chopper spectrometer INC is under construction and an ultra cold neutron generator test UCN is still under development. Recent layout of these instruments is shown in Fig. 8.

INC was designed for complementary use with a sister instrument MARI which is under construction at ISIS. The mechanical chopper of INC is almost the same as that of MARI. Since INC has shorter flight path lengths than MARI, the

# KENS NEUTRON SCATTERING FACILITY

Fig. 8

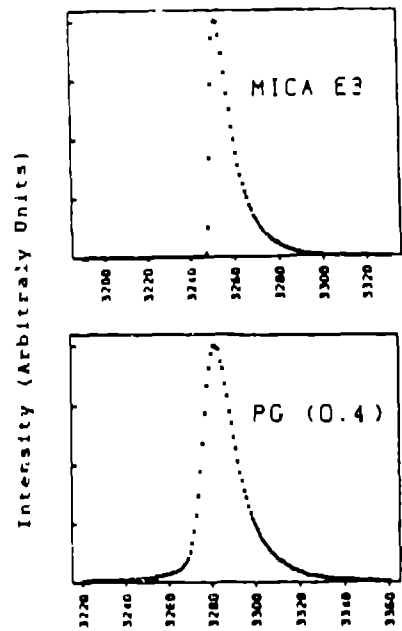


counting rate can be made comparable by relaxing the energy and momentum resolutions slightly. A vacuum scattering chamber and a spectrometer shield were installed in place. Data acquisition electronics and computer are ready. About 170 He-3 detectors will be installed within this year. A fast Fermi chopper was supplied from the Rutherford Appleton Laboratory. The construction of INC will be completed by the end of FY 1988. Details will be presented at a Poster Session by Arai.

The energy resolution of the high-resolution quasielastic spectrometer LAM-80<sup>4)</sup> was improved by use of mica instead of pyrolytic graphite as analyzer crystals<sup>5)</sup>. The energy resolution attained is about 19  $\mu\text{eV}$  with 6.6  $\text{\AA}$  and 8  $\mu\text{eV}$  with 9.9  $\text{\AA}$  neutrons. LAM-80 has an incident flight path about 31 m long which makes a contribution to the energy width  $\Delta E_i = 13 \mu\text{eV}$  for 6 $\text{\AA}$  incident neutrons. Energy resolution of the analyzer crystal has to be matched with  $\Delta E_i$ . Pyrolytic graphite (PG) with any mosaic spread is too bad and perfect crystal of silicon is too good for this. Mica crystal seems to be the best in this energy-resolution range. In Fig. 9, the third order Bragg reflection from a mica crystal (1.83 meV) is compared to the 002 reflection from a PG with mosaic spread of 0.4°. Those are measured with analyzer angle  $\theta_A = 87^\circ$  at the exit of the 31 m long neutron guide (C2) from the solid methane moderator. The peak shape of the mica is superior, especially in the rising side. Note that the faint intensity on the both sides of the peak observed with PG is completely eliminated. Neutron scattering spectra from a vanadium sample on the LAM-80 using the third order reflection of the mica crystal (6.6 $\text{\AA}$  at  $\theta_A = 80^\circ$ ) is also shown in Fig. 9.

The performance of the coherent inelastic scattering spectrometer MAX<sup>6)</sup> was also improved. By use of vertically focused analyzers instead of previous flat ones, the counting efficiency was increased by a factor 1.7 and the signal to background ratio by about 1.5 times as shown in Fig. 10.<sup>7)</sup> Each analyzer mirror consists of 16 pieces of pyrolytic graphite (6mm x 50mm) aligned on a curved holder which is a part of a simple cylinder instead of an ellipsoid. Since the essential feature of MAX is that the curvature of the analyzer varies with  $\theta_A$ , many holders with different curvatures were prepared. Further improvement on analyzers is in the planning stage.

The characteristics of the MAX are most suitable for measurements of spin wave excitations in two-dimensional magnets because simultaneous constant  $\omega$  scans by many analyzer-detector sets become possible. Typical TOF spectrum and measured dispersion relations for a two-dimensional random antiferromagnet  $\text{Rb}_2\text{CoO}_{14}\text{Ni}_{10}\text{Fe}_4$  are shown in Fig. 11 for reference.<sup>8)</sup>



Time-of-flight Channels (16µs/ch)

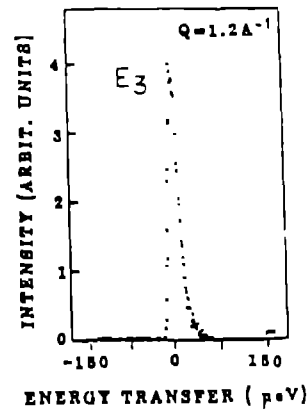


Fig. 9 Comparison of Bragg reflections between mica crystal ( $E_3=1.83$  meV) and PG with mosaic spread of  $0.4^\circ$  (left), and neutron scattering spectrum from vanadium sample on LAM-80 with mica analyzer crystal i.e., resolution function (right)

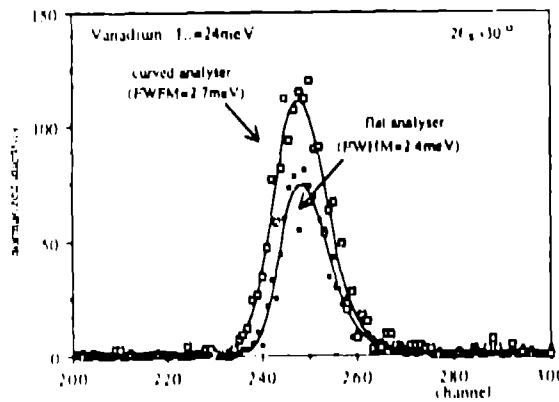


Fig. 10 Comparison of Intensities between curved and flat analyzer



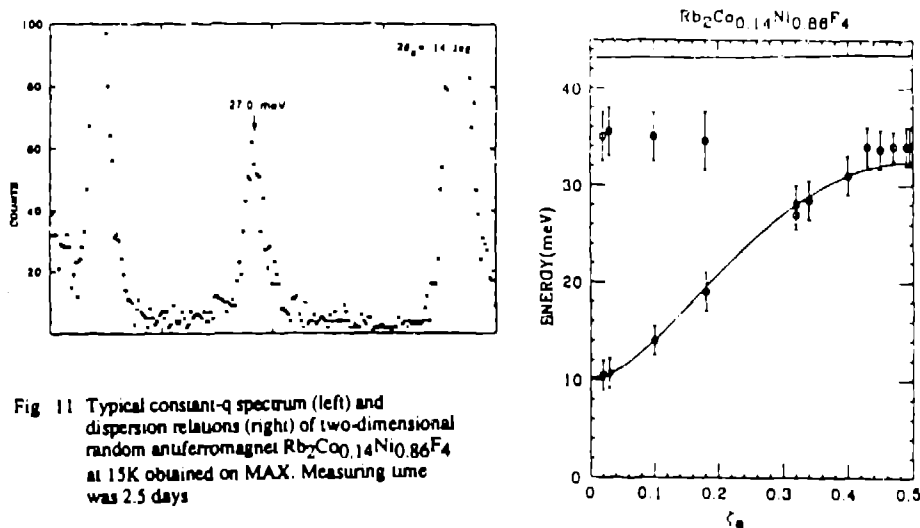


Fig 11 Typical constant-q spectrum (left) and dispersion relations (right) of two-dimensional random antiferromagnet  $Rb_2Co_{0.14}Ni_{0.86}F_4$  at 15K obtained on MAX. Measuring time was 2.5 days

The performance of the polarized epithermal neutron spectrometer PEN was also improved.<sup>9)</sup> A polarized proton filter is used as a neutron polarizer and proton polarization more than 80% was achieved by microwave pumping in a  $^4He$  bath at 0.5K. Epithermal neutron polarization of more than 70% was obtained, with a neutron transmittance about 25%.

The polarized cold neutron spectrometer TOP<sup>10)</sup> has been modified. By the installation of PSD's at small angle region with a newly constructed vacuum chamber, small angle scattering using polarized cold neutrons has become possible.<sup>11)</sup>

The number of backward neutron detectors of the high resolution powder diffractometer HRP<sup>12)</sup> was increased to improve counting efficiency. A new computer program<sup>13)</sup> has been developed for the Rietveld analysis of time-of-flight neutron diffraction data on the HRP. KENS is a low repetition pulsed-neutron-source (20Hz) which makes it easy to enlarge the d-spacing accessible. Powder diffraction in larger d-spacing region becomes possible by adding lower angle counter banks. Results of a test experiment to detect 001 diffraction from  $Ba_2Y(CuZn)_3O_{7.4}$  ( $d=11.626\text{\AA}$ ) and 002 diffraction from  $Tl_2Ba_2Ca_2Cu_3O_{10}$  ( $d=17.8\text{\AA}$ ) are shown in Fig 12 with Rietveld refined profiles. The installation of lower-angle-counter banks is under progress. The data acquisition electronics of the HRP was also upgraded: a new electronic time-focussing hardware was developed at KENS, which can accept neutron signals in much higher rate than the computer focussing.

The medium resolution powder diffractometer MRP is being converted to a multi purpose diffractometer. In addition to the original function as a

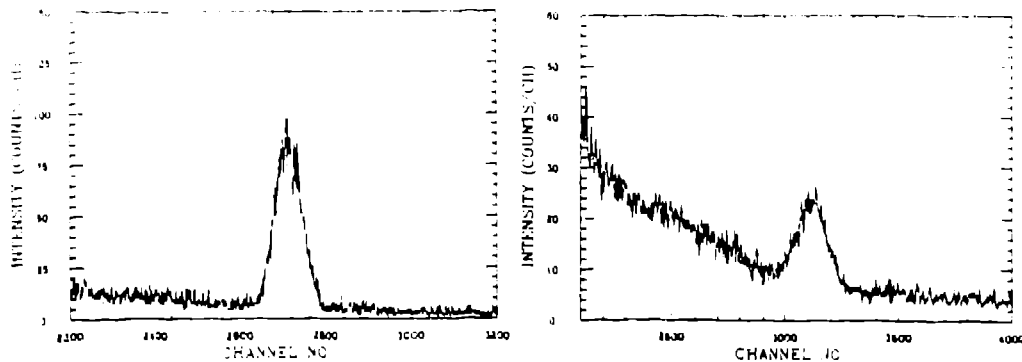


Fig. 12 001 diffraction from  $\text{Ba}_2\text{Y}(\text{CuZn})_3\text{O}_{7-x}$  ( $d=11.626\text{\AA}$ ) (left) and 002 diffraction from  $\text{Tl}_2\text{Ba}_2\text{Ca}_2\text{Cu}_3\text{O}_{10}$  ( $d=17.8\text{\AA}$ ) observed by a low angle test counter on HRP

conventional powder diffractometer, options for single crystal diffraction and epithermal neutron diffraction are built in. For the former option, MRP is equipped with 1D-PSD's and a sample goniometer table which allows the use of a heavy helium cryostat, and for the latter, with a high-efficiency small-angle counter bank to detect epithermal neutrons from neutron-absorbing samples.

The down-scattering crystal spectrometer LAM-D, designed mainly for molecular spectroscopy, was moved from the H-6 beam hole to the H-9 after upgrading. The number of analyzer-detector arms was increased from one to four to realize larger analyzer solid-angle.<sup>14)</sup>

#### 4. Data Acquisition and Processing System

The installation of the KENS new data acquisition and processing system based on the VAX has been completed. A VAX 8350 was chosen as a hub computer and eight VAX station II's were introduced as data acquisition computers with many Macintosh front end computers. The data-acquisition software ICP/GENIE developed at RAL was introduced to our new system by M.W. Johnson (RAL) under UK-Japan collaboration. Details of the new system will be presented at Poster Session by Furusaka.

#### 5. Activities in Neutron Scattering

One of the highlights of the research achieved in these periods was the first successful determination of the crystal structure of a high- $T_c$  superconductor  $\text{Ba}_2\text{YCu}_3\text{O}_{7-x}$ . It is already historical, but highly exciting at that time of the "High- $T_c$  fever". Early March 1987 our colleagues in National Institute for Research in Inorganic Materials, Tsukuba, informed us that they were just successful in preparation of a high quality single phase powder sample of  $\text{Ba}_2\text{YCu}_3\text{O}_{7-x}$ .

Proton accelerators at KEK were already shut-down finishing the scheduled operation in that fiscal year. Director General, professor T. Nishikawa, decided to restart the proton-accelerators and immediately carry out the diffraction experiment on this sample with the high resolution powder diffractometer HRP. The sample was in fact not a single-phase one but a mixture of orthorhombic and tetragonal forms, but fortunately we were successful to determine the crystal structures of both phases simultaneously. It was almost the same time with three other independent experiments performed at IPNS, ISIS and ILL with their high resolution powder diffractometers. In succession, we studied the crystal structure of various 123 compounds  $R\text{Ba}_2\text{Cu}_3\text{O}_{7-\delta}$  (R : Y or lanthanide elements) using the HRP and showed that the variation of the long apical Cu-O bond distance of the  $\text{CuO}_3$  pyramid must have a crucial role in forming Cooper pairs of O-2p holes between  $\text{CuO}_4$  layers. We also studied various nonstoichiometric compounds  $R_{1+x}\text{Ba}_{2-x}\text{Cu}_3\text{O}_{7-\delta}$  and showed that  $[\text{Cu-O}]^+$  concentration controls  $T_c$ .

The crystal and magnetic structures of  $(\text{LaSr})_2\text{CuO}_4$  system were also studied. Powder diffraction on the HRP showed that the space group of  $\text{La}_2\text{CuO}_4$  is  $\text{Cmca}$ . Since the superconductivity is believed to be strongly related to the magnetism of these systems, the magnetic contribution to small angle neutron scattering is being measured using large single crystals on the small angle scattering instrument SAN.

New superconductors of Tl- and Bi-systems were also measured on HRP. Structural parameters of  $\text{La}_{1.9}\text{Ca}_{1.1}\text{Cu}_2\text{O}_x$ , which does not show superconductivity, were also refined. The results will be useful in the examination of theories.

As an interesting application of an eV-spectrometer utilizing a nuclear resonance, a combined method of high Q scattering spectroscopy with resonance absorptior spectroscopy was developed on RAT (resonance detector spectrometer). This method is useful to determine the mean kinetic energies, i.e., effective temperatures of specific elements in multi-component systems such as high  $T_c$  superconductors. Ikeda found that the effective temperature of oxygen atoms is unchanged in various oxides, while that of copper atoms changes significantly; the effective temperature of copper atoms in the  $\text{La}_2\text{CuO}_4$  system is higher than those in metal Cu and CuO, and the  $\text{YBa}_2\text{Cu}_3\text{O}_{7-x}$  system has much higher effective temperature of copper atoms than those mentioned above. A technical aspect of this application will be presented at a Workshop Session by Ikeda.

A parity-nonconserving (PNC) effect in neutron radiative capture was extensively studied using polarized epithermal neutrons from PEN. A new  $\gamma$ -ray annular detector made of  $\text{BaF}_2$  scintillators was constructed and the  $\gamma$ -ray detection efficiency was increased. Simultaneous measurements of capture  $\gamma$  rays and neutron transmission with positive and negative helicity states gave consistent results on the p-wave resonance of  $^{139}\text{La}$  at 0.734 eV.

Kinetics of first order phase transitions has been examined on Al-Li alloys

by use of SAN. Experimental results show a peculiar behavior at very early stages of the phase transition; the exponent  $n$  in the scattering law  $q^{-n}$  changes with time. It is explained by a competition between phase separation process and order-disorder transformations.

In addition to the above topics, many experiments in various fields, for example, precipitation in Nb-Ti multifilamentary superconducting composites, magnetic excitation in the two-dimensional random antiferromagnets  $Rb_2Co_xNi_{1-x}F_4$ , magnetic structure of the reentrant spin glass Fe-Al alloy system, structure and dynamics near the glass transition, dynamics of fractal structure, and so on have been extensively carried out in these periods.

#### 6. Japan-UK Collaboration

This is the third year of the UK-Japan collaboration on neutron scattering. The construction of the chopper spectrometer MARI, which is provided by KEK for installation on ISIS in Rutherford Appleton Laboratory, is going well. A vacuum scattering chamber is ready for installation. A fast Fermi chopper is almost ready. The computer for the data acquisition system and associated electronics are ready as well. The construction of MARI is expected to be completed in FY 1989 on schedule.

The workshop of the collaboration "Neutron Scattering Research with Intense Spallation Neutron Source-Today and Tomorrow" was held at KEK on Oct. 6-7, 1987. About fifty participants attended at the meeting. The proceedings of the meeting has been completed and will be distributed soon.

In FY 1987 a Japanese scientist stayed RAL for a long term and three visited RAL for a short term to perform neutron scattering experiments and collaborate on the construction of MARI.

#### 7. KENS-II

The future program of the pulsed spallation neutron source KENS-II was included in the Japanese Hadron Facility Project as an important part of four major fields. The project was already authorized by the Science Council of Japan, and is now under examination by the government.

Details on the KENS-II project will be presented by Endoh at a succeeding Session. Here I give only very brief comments on some technical aspects. Proton-beam energy is still not fixed: 1 GeV with a 1 GeV proton linac and a storage ring, or 2 GeV (or less) with a 1 GeV linac and a synchrotron. Time-averaged proton-beam current is expected to be 200  $\mu$ A.

We are thinking of adopting a coupled cold moderator, probably a composite moderator of liquid hydrogen with light water at room temperature, in order to obtain higher time-averaged cold neutron flux albeit in longer pulses. One idea of the target moderator-reflector assembly is a combination of a coupled cold

moderator with decoupled moderators at ambient and reduced temperatures. The former could hopefully be located in a large  $D_2O$  tank above the target. The latter would serve short-pulse uses similarly to the present operation of other spallation neutron sources (ICANS laboratories).

We performed some neutronic calculations for the KENS-II with higher proton energies, say 2 GeV. A result will be presented at a Workshop Session.

## References

- 1) N. Watanabe, M. Miwata, S. Ikeda, Y. Masuda, M. Arji and S. Satoh: KENS Report-VI, KEK Progress Report 86-2 (1987) 11
- 2) S. Ikeda, N. Watanabe, S. Satoh, M. Furusaka and K. Inoue: ibid 24
- 3) J. M. Carpenter: private communication
- 4) K. Inoue, Y. Ishikawa, N. Watanabe, K. Kaji, Y. Kiyonagi, H. Iwasa and M. Kohgi: Nucl. Instrum. Methods A238 (1985) 401
- 5) K. Inoue, S. Ikeda, Y. Kiyonagi, K. Shibata, T. Kanaya, H. Iwasa, H. Niizeki, K. Kobayashi and T. Yoshihara: KENS Report-VII. (1988) 17
- 6) K. Tajima, Y. Ishikawa, K. Kanai, C.G. Windsor and S. Tomiyoshi: Nucl. Instrum. Methods 201 (1982) 491
- 7) Y. Todate, H. Ikeda and K. Tajima: KENS Report-VII (1988) 16
- 8) K. Tajima, Y. Todate and H. Ikeda: presented at ICNS '88, to be appeared in Physica B
- 9) Y. Masuda, S. Shimoto, A. Masaike, Y. Ishikawa and M. Kohgi: Nucl. Instrum. Methods A264 (1988) 169
- 10) Y. Endoh, S. Ikeda, S. Mitsuda and H. Fujimoto: Nucl. Instrum. Methods A240 (1985) 115
- 11) S. Itoh and Y. Endoh, KENS Report-VII(1988) 19
- 12) N. Watanabe, H. Asano, H. Iwasa, S. Satoh, H. Murata, K. Karahashi, S. Tomiyoshi, F. Izumi and K. Inoue: Jpn. J. Appl. Phys. 26(1987) 1164
- 13) F. Izumi, H. Asano, H. Murata and N. Watanabe: J. Appl. Cryst. 20 (1987) 411
- 14) K. Inoue, to be published

# Status report of SINQ: A continuous spallation neutron source

*W. E. Fischer*  
Paul Scherrer Institute (PSI)  
CH-5232 Villigen  
SWITZERLAND

## 1 Introductionary Remarks

A most significant development at SIN the past year has been the merging of several research institutes to what is today called the "Paul Scherrer Institute" (PSI). Good old SIN fell prey to this undertaking. The new institute contains the former

Swiss Institute for Nuclear Research (SIN)  
Federal Institute for Reactor Research (EIR)  
Radio Corporation of America Laboratory in Zurich (RCA)

Since, within the new organisation, the research domains "physics of condensed matter" and "material science" are supposed to gain considerable significance, I would like to present this PSI here as an introductory remark.

PSI contains four research departments, namely (Fig. 1)

Nuclear- and Particle Physics  
Biological- and Medical Science  
Physics of Condensed Matter, Material Science  
Energy Research and Engineering Sciences

One of the tasks of the institute is the development and operation of complex research facilities, which are beyond the scope of universities. The relationship between PSI and the federal and cantonal schools are based on the principles of complementarity and close collaboration. International scientific collaboration, in particular through common research- and development programs, is strongly anticipated.

With Fig. 2 we try to demonstrate the significance of the institute's accelerator system (formerly SIN) for the research activities of the various research departments. It shows that this facility is still the backbone (the central hardware unit) for the present and future research program.

A layout of the accelerator and the meson facilities is presented in Fig. 3. The location of the neutron hall, containing SINQ station and the guide hall is at the upper right of the picture.

# PSI

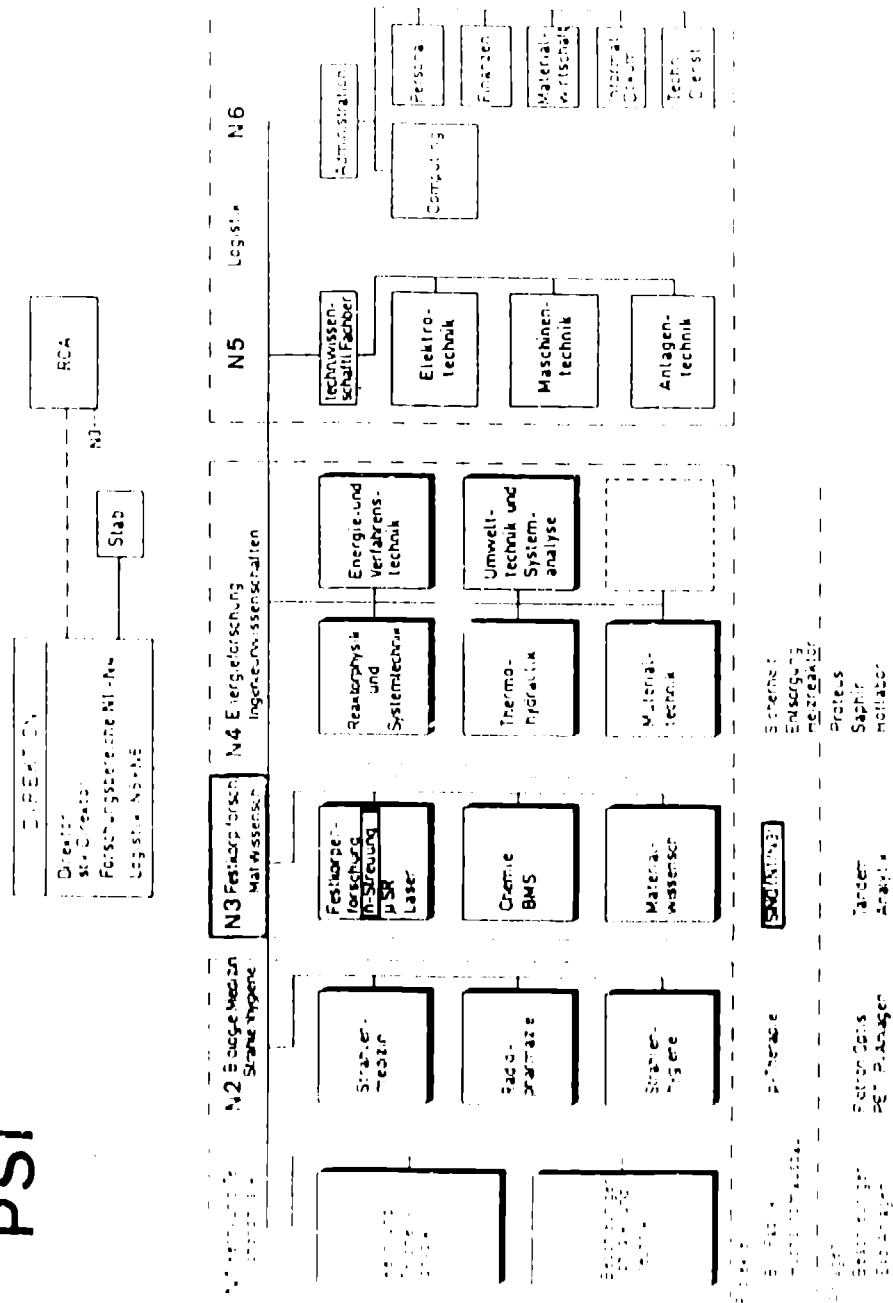


Fig. 1 Organigram of the "Paul Sherrer Institute", PSI.

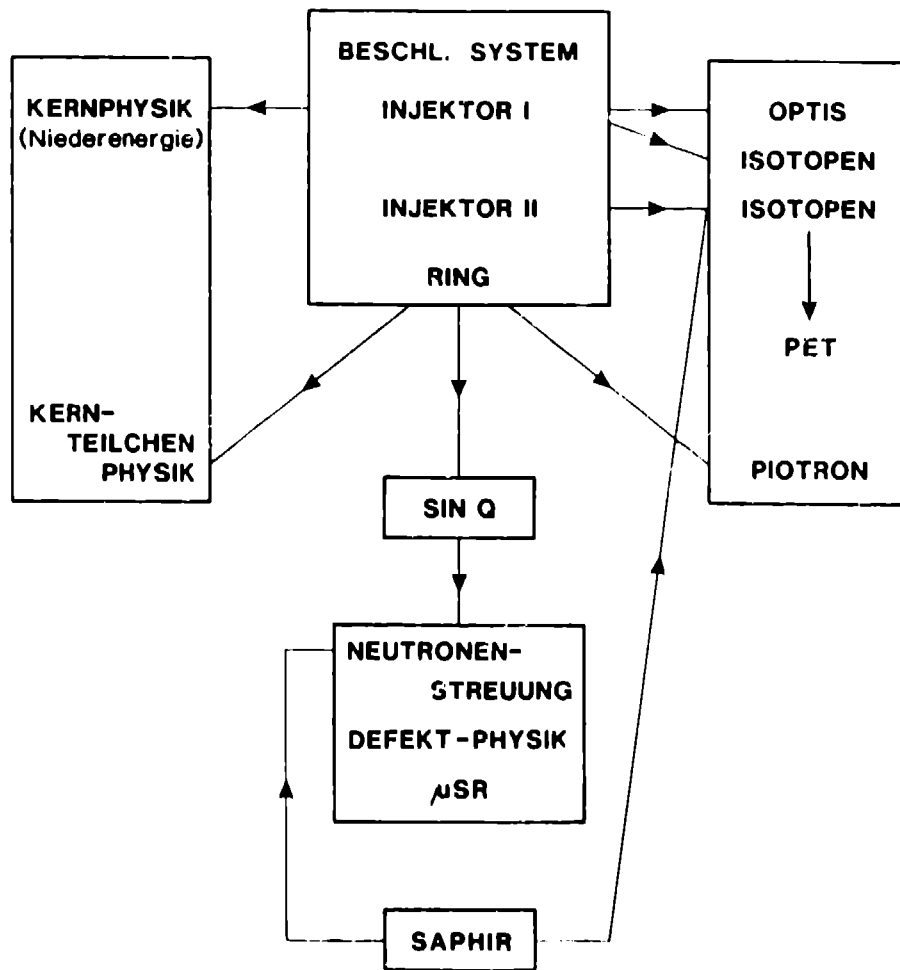


Fig. 2 Research domains at PSI, which make use of the accelerator facility.



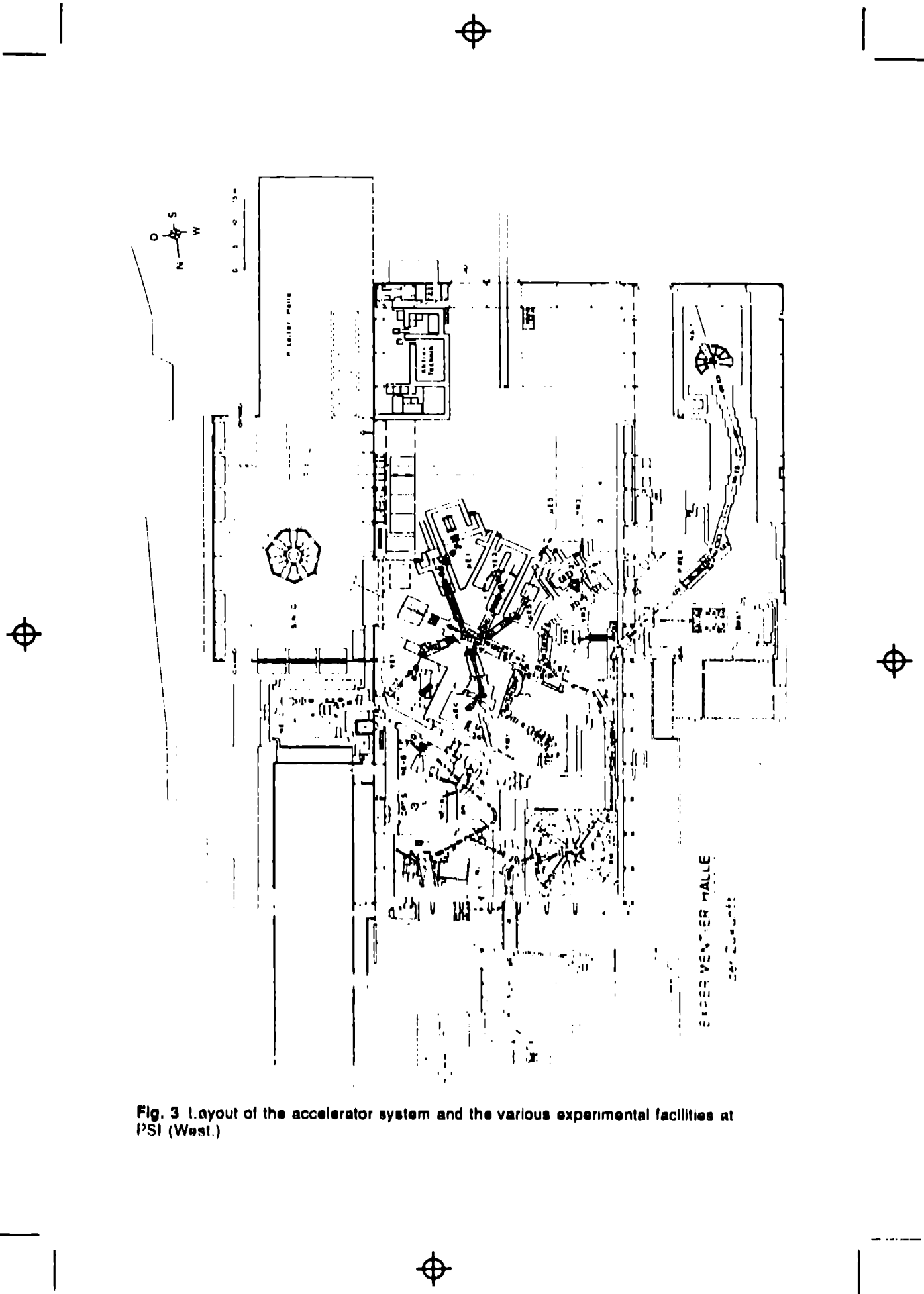


Fig. 3 Layout of the accelerator system and the various experimental facilities at PSI (West.)

The accelerator system delivers today a proton beam of 200 - 250  $\mu\text{A}$  at 590 MeV onto the meson targets. While the accelerator could run currents of 500  $\mu\text{A}$  the operation is restricted today by the second target station which has still to be improved for the higher currents. For currents above 1 mA the rf-system of the ring-cyclotron will be upgraded by doubling the rf-power of the main amplifiers. The time schedule for these tasks is given in Fig. 9.

## 2 The Spallation-Neutrons source

A vertical cut of the central part of SINQ is shown in Fig. 4. Proton beam injection into a molten lead-bismuth target (eutectic mixture) through a solid window is from below. Natural convection of the target material driven by the power deposition of the proton beam is used as cooling mechanism for the target. The heat exchanger is located in the upper part of the slim target cylinder.

The  $\text{D}_2\text{O}$  moderator is in a double walled Al-tank. The gap between the two walls is filled with light water, which acts as a shield for thermal neutrons. They are hence captured mainly in the water and do not contribute anymore via  $(n,\gamma)$ -reactions to the heating of the surrounding iron shield. The heating of this shield is therefore dominated by the energy deposition of high energy neutrons. While the upper shield part and the ring around the moderator tank have still to be actively cooled, the lower part does not need active water cooling under these conditions.

The whole source is surrounded by a contained helium atmosphere. An additional safety barrier is defined by a controlled nitrogen containment. Beam extraction systems - beam tubes and guides - are installed in a similar way, as in a beam tube reactor. Remember that SINQ - due to the absence of macro-timestructure in the beam - is a continuous source.

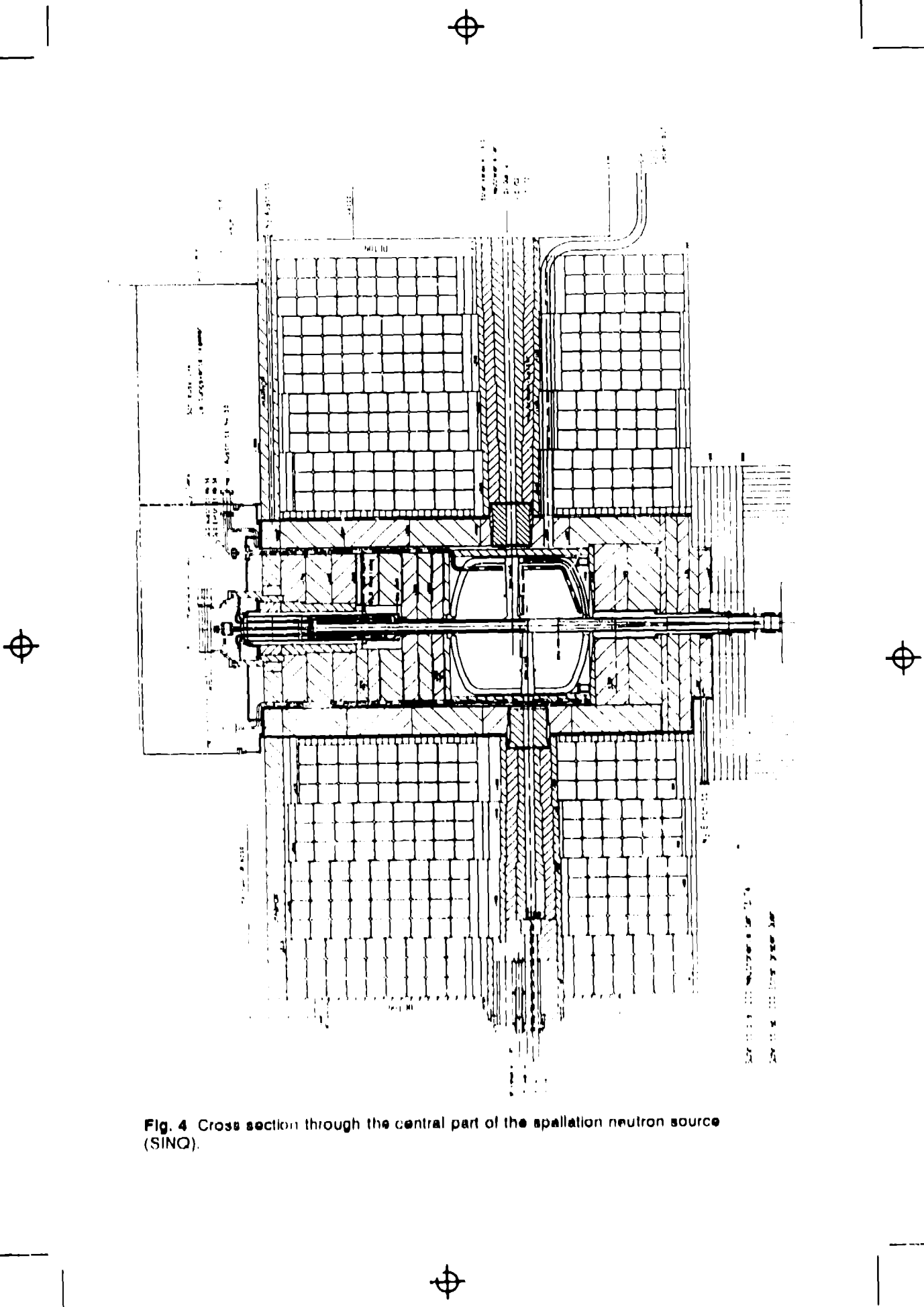
Before entering into the spallation target, the proton beam is forced through a collimator system to prevent - given the emittance - any focus on the target window.

The proton beamline over the distance of 54 m between the second meson target and the spallation target is given in Fig. 5. The halo produced by scattering in the meson target is scrapped off in a four stage collimator system just behind this target. After this clean up a virtually lossless transport of the beam up to the spallation target appears to be possible. Hand-on maintenance of the transport system in the channel ditch is the aim.

The beam envelope in Fig. 5 is of  $4\sigma$  width and in second order.

The layout of the inserted plugs for the neutron extraction channels is shown in Fig. 6. We plan to install two cold sources into this facility - a light hydrogen and a deuterium source. The neutronics and hydraulics of the 20 l deuterium source will be discussed in detail by E. Atchison at this workshop.

SINQ will provide thermal neutrons at four beam tubes viewing the  $\text{D}_2\text{O}$  moderator. Another four beam tubes view the light hydrogen source which appears to provide



**Fig. 4** Cross section through the central part of the spallation neutron source (SINQ).

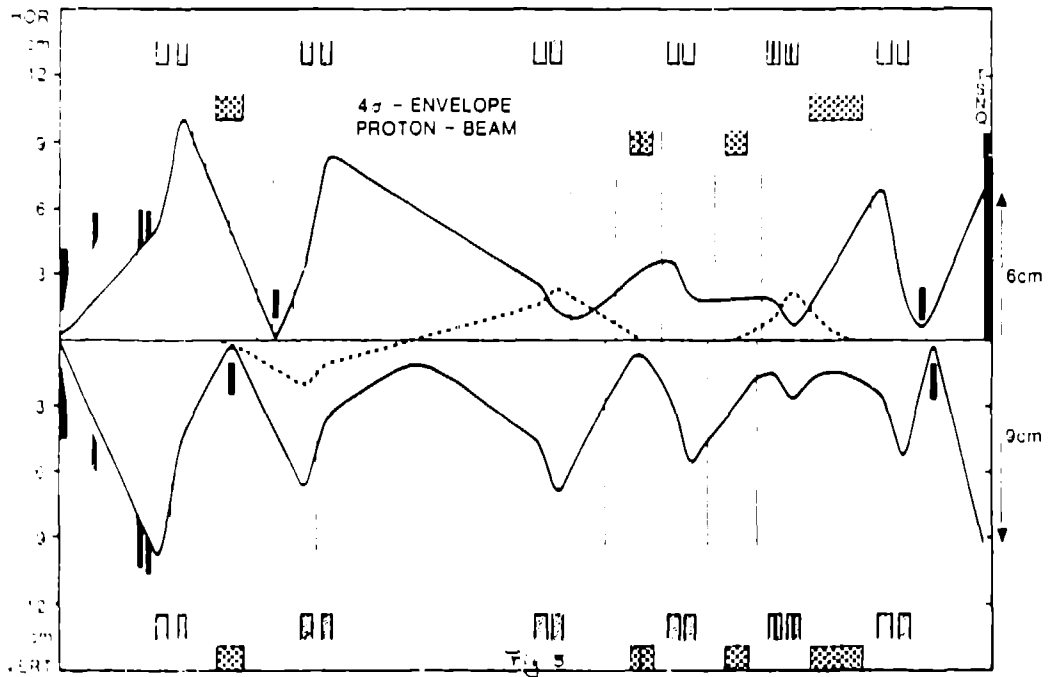
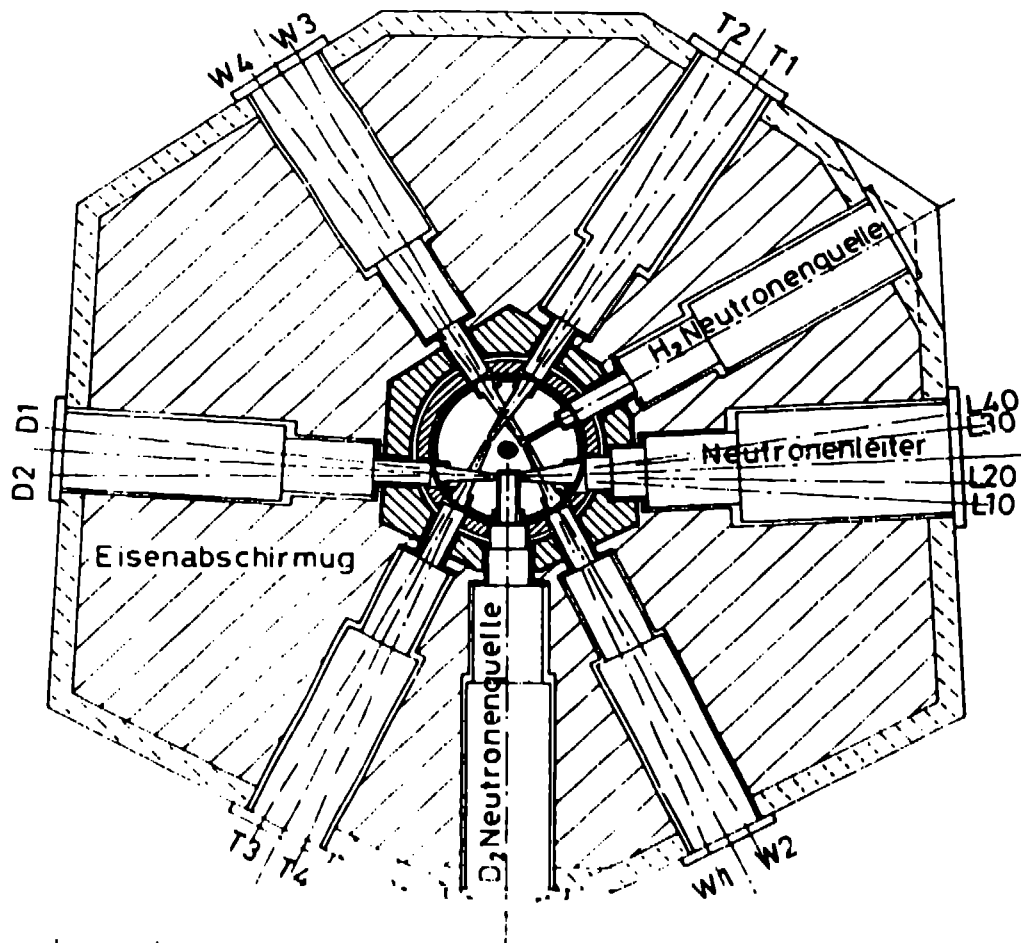


Fig. 5 Envelope ( $4\sigma$ ) of the proton beam injected into the spallation source.



Legende:

(a) Pb-Bi Target

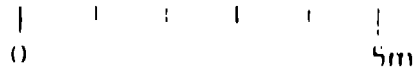


Fig. 6 Layout of the neutron channels.

the highest flux in the wave length region between 2 - 4 Å (Fig. 7). To the D<sub>2</sub>-source we shall attach a beam tube pair and the guide system. This guide system was presented as a poster at this workshop by I. Anderson and F. Atchison.

In view of the favorable performance of pulsed neutron sources for hot and epithermal neutrons we refrained from installing a hot source into our system.

In Fig. 7 we present the expected spectral fluxes for a nominal primary proton current of 1.5 mA. These fluxes are given at the positions of the monochromators for beam tubes and at the exit of neutron guides at possible end-standing instruments. The option to install short supermirror guides in (and at) beam tubes viewing the light hydrogen source has been kept open.

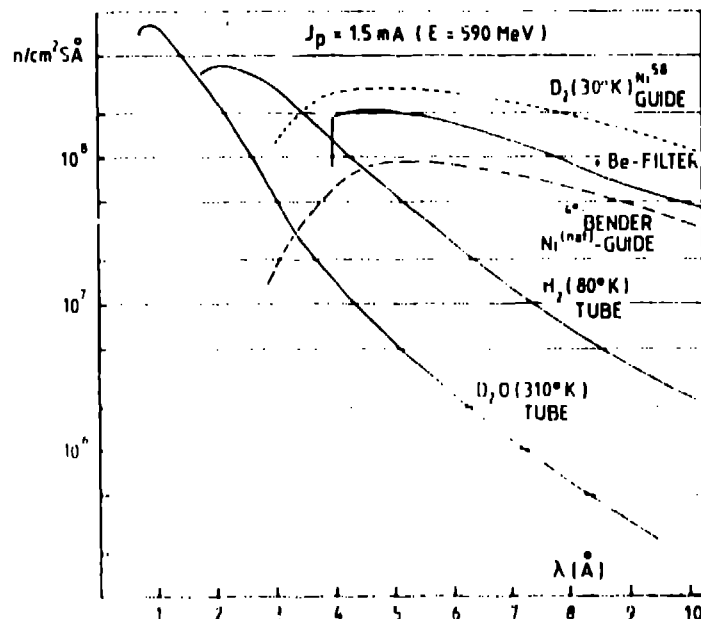


Fig. 7 Spectral fluxes at the position of the monochromators or neutron guide exits.

### 3 Instrumentation

In table I we list the spectrometers planned to be installed at the spallation source. Two priorities are distinguished - the highest priority being given to the instruments at the guide system (3.3 - 5.2, 6.1, 6.3). Instruments already in operation now at the reactor "Saphir" (formerly EIR) planned to be rebuild or possibly transferred have second priority.

Generally speaking the instrumental set corresponds to the experimental installations realized today at a modern beam tube reactor.

Fig. 8 presents the layout of the instruments in the Target Hall and the Neutron Guide Hall.

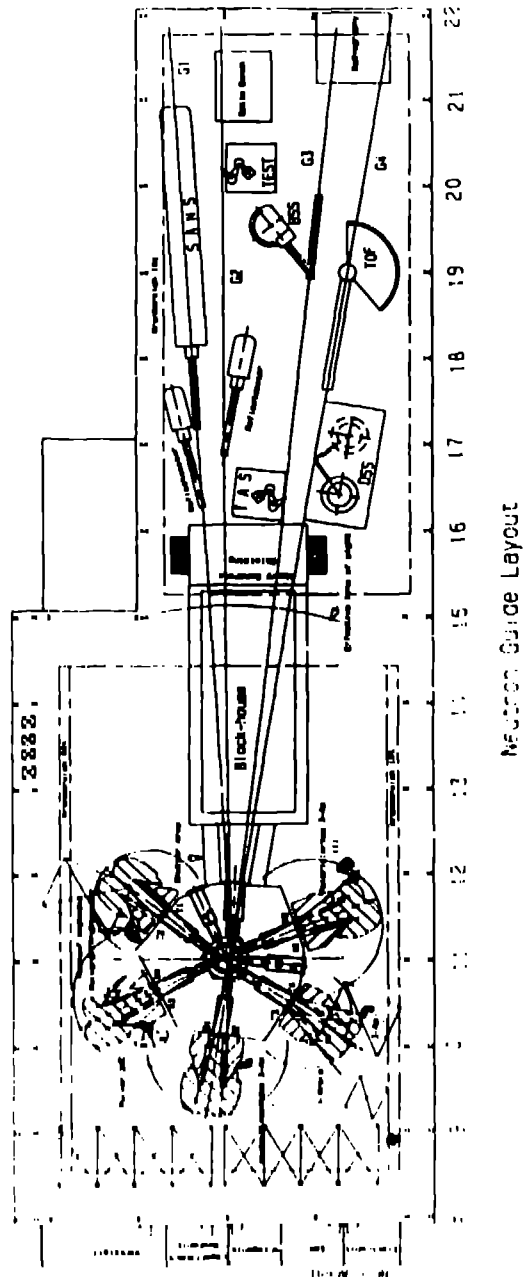


Fig. 8 Layout of the instruments in the target hall and the guide hall.

## 4 Time Schedule

Construction work has been started this summer 1988. We plan to begin with the installation of the actual target station towards the end of 1990. This phase is supposed to last for about  $2\frac{1}{2}$  years - first trial operation to be expected towards the end of 1993.

As can be recognized from Fig. 9 this schedule is strongly coupled with the activities for upgrading the second meson-target station (Target E). A general shutdown lasting at least one year (1990) is foreseen for this task. During the same shutdown preparatory work for the improvement program at the accelerators will be done. The short shutdowns during the years 1991/92 are inserted in order to install - one by one - the rf-amplifiers delivering higher power to the accelerator cavities of the ring-cyclotron. As a consequence a gradual increase of the operational beam current can be achieved.

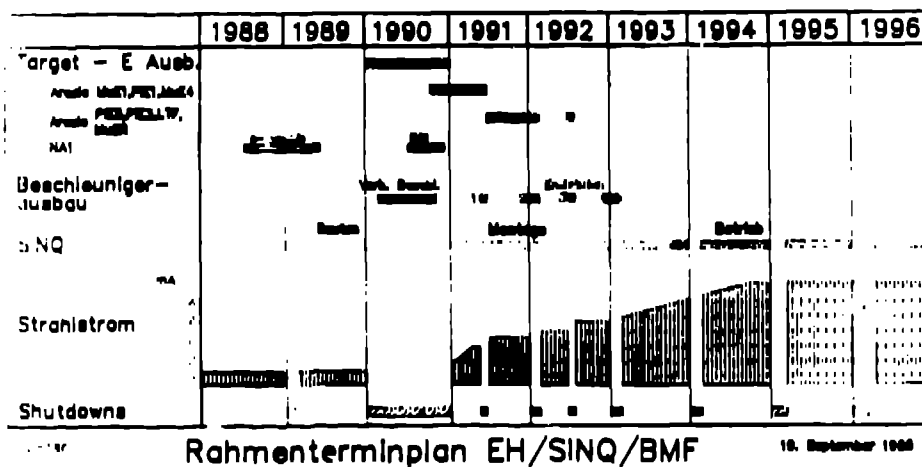


Fig. 9 Time schedule of the major tasks at PSI from 1988-1994.



SINQ-Spektrometerplanung (Stand: 9.1.87)

Nr.	Spektrometertyp	SINQ		Saphir
		1. Priorität	2. Priorität	
1.1	Pulver (höchstauflösend)	○		
1.2	Pulver (Lineardetektor)		○ ← ○	
2.1	4-Kreis (Flächendetektor)	○		
2.2	4-Kreis (grosse Q)		○	
2.3	2-Achsen		○ ← ○	○
3.1	3-Achsen (kleine $\omega$ )	○		
3.2	3-Achsen (grosse $\omega$ )		○	○ ○
3.3	Diffuse Streuung	○ (CHOI)	○	
4.1	3-Achsen (Monochr.-Turbine)	} ○	} ○	
4.2	Rückstreuung			
4.3	Flugzeit			
5.1	Kleinwinkelstreuung	○		
5.2	Reflektometer		○	
6.1	3-Achsen (polarisiert)	○		
6.2	2-Achsen (polarisiert)	○	○ ← ○	
6.3	Neutronenoptik-bank	○ (A01)		

Legende: ( ) Planung ( ) Optio.

## The ISIS target

*A. Carne, T. A. Broome, J. R. Hogston and M. Holding*  
Rutherford-Appleton Laboratory  
Chilton, Nr Didcot, Oxon  
UNITED KINGDOM

### 1. Introduction

The ISIS Target Station and its Target(s) have been described in many reports, including the Proceedings of the previous nine ICANS Conferences. They are, by now we hope, familiar devices to many of the participants at this Conference. Participants will hear elsewhere in this Conference details of other parts of the Target Station, but this presentation discusses the two target failures that have occurred, gives our understanding of the causes and indicates the steps being taken to alleviate the problems.

At the outset of the design we were aware that the target would have a finite lifetime, due to radiation damage effects, exacerbated by mechanical damage due to thermal cycling and fatigue. Estimates of target lifetime at full intensity are about 2 years for radiation damage swelling and about  $10^4$  gross thermal excursions. The latter number is the one which gives uncertainty in defining the life of the target, since it is dependent on the reliability of the accelerator and quality of the proton beam.

The commissioning of an accelerator system and bringing it up to high beam intensities have their own special problems. There must be protection of components against uncontrolled beam loss, which produces thermal damage, prompt radiation and induced activity. Fast beam trips for beam loss protection, or equipment failures, result in quenches from high temperature in the target which get bigger with increasing beam intensity. But the target itself is a difficult device to make, taking about 12 months to manufacture. Further, changing one is a complex and time-consuming task, not without its hazards. There is thus something of a balancing act to bring the accelerator towards specification before the

target fails due to thermal cycling fatigue. In the early days of ISIS beam loss protection was the dominant consideration and the target was regarded somewhat as a sacrificial lamb to the goddess of machine reliability.

During 1987 there were two failures of ISIS targets. The first target had received 92,400  $\mu\text{A-hr}$  of beam, with an unknown number of gross thermal cycles; the second had received 54,000  $\mu\text{A-hr}$  with about 40,000 gross thermal cycles ( $\sim 20,000$  beam trips from all causes). Actual lives were 25 months and 3 months respectively.

## 2. The ISIS Target

A schematic of the ISIS target is shown in Figure 1. The target consists of a 'module' containing 23 disks of depleted uranium of diameter 90 mm and varying thickness (dependent on axial position in the target). The disks are clad in zircaloy-2, 0.25 mm thick, and mounted in square picture frames of stainless steel to form a set of parallel plates separated by cooling channels 1.75 mm wide. The  $\text{D}_2\text{O}$  coolant flows through these channels which are grouped to be fed from 3 main cooling channels via stainless steel manifolds bolted to either side of the module. The module and manifolds are mounted within a stainless steel pressure vessel which has its own independent cooling circuit, the "casing circuit".

The condition of the target is monitored by

- a) Thermocouples located at the centres of alternate uranium disks, numbers 1, 3, 5 ... Response time for these thermocouples, including all effects, is about 0.5 sec.
- b) Monitoring the water flow and pressures of each cooling channel. The information is collected to define the effective width of the cooling gaps,  $g$ , proportional to  $(\text{flow})/(\text{pressure drop})^{0.55}$ .
- c) A Fission Product Monitor which uses a lithium-germanium detector and multichannel analyser to detect and display the gamma spectrum from radionuclides in the  $\text{D}_2\text{O}$  coolant. First indications of spallation and/or fission products can be seen presently in about 10-40 minutes after beam turn off.

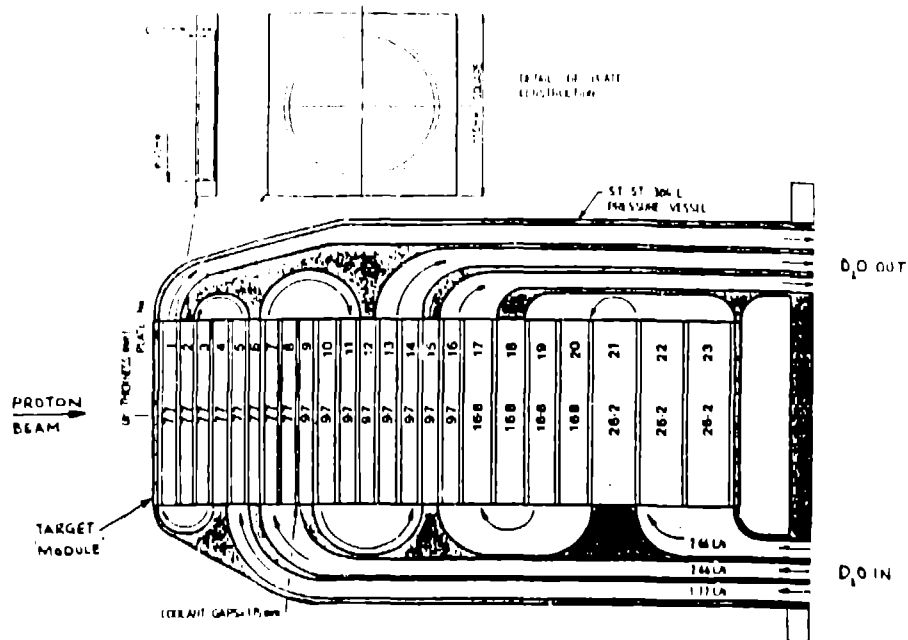


FIG 1. ISIS TARGET SCHEMATIC

The main manifestation of damage to the target, whether due to radiation damage or thermo-mechanical effects, is in swelling of the target uranium. This swelling has the effect of closing the cooling gaps, so reducing the flow and increasing the pressure drop. The reduction of cooling results in increased target plate temperatures. The effects are the first indications of the approaching end of the target life, or a developing serious problem, and in themselves would be sufficient to indicate the need for a target change (regarded as a normal end-of-life target change). This may be confirmed, if after a delay to allow cooldown of general background, fission products are detected in the  $D_2O$  coolant.

Both failed targets displayed the above sequence and for both, fission products were seen in the coolant. The onset to failure was quite rapid in both targets (about 16-24 hours), a point that will be discussed later.

### 1. The Target Failures

#### a) Target Number 1

Target number 1 had been operating since the start up of ISIS in July 1985. There had been no problems, except for a small internal leak between the plate and casing circuits. The beam intensity had been increased over the operating period so that in August 1987 it was at about 60  $\mu\text{A}$ . There was a suspected blockage in the front cooling channel which was cleared (suspect filter bits) and the target was run normally for a further 2 weeks when the flow fell from its normal  $113 \text{ lmin}^{-1}$  to  $93 \text{ lmin}^{-1}$  and the pressure drop increased from 1.85 bar to 2.11 bar (the corresponding gap constant fell from 19.4 to 14.1). These values were outside the limits set for normal operation and the control system reacted, as designed, by warning the operators. The temperatures of plates 1 and 3 rose about  $50^\circ\text{C}$  above the operating level of about  $250^\circ\text{C}$  causing the beam to be tripped off. The beam was restored at reduced level but the water leak developed to an unacceptable level. The decision was taken to change the target when, in addition to the leakage, the gamma spectrum from the plate circuit  $\text{D}_2\text{O}$  showed fission products, indicating a breach of the cladding. The fission products were individually identified by gamma spectroscopy and the gamma spectrum is shown in figure 2. Fission products gases released to the atmosphere due to this target failure and subsequent operations were less than 10 GBq (i.e. less than 0.05% of a reportable release).

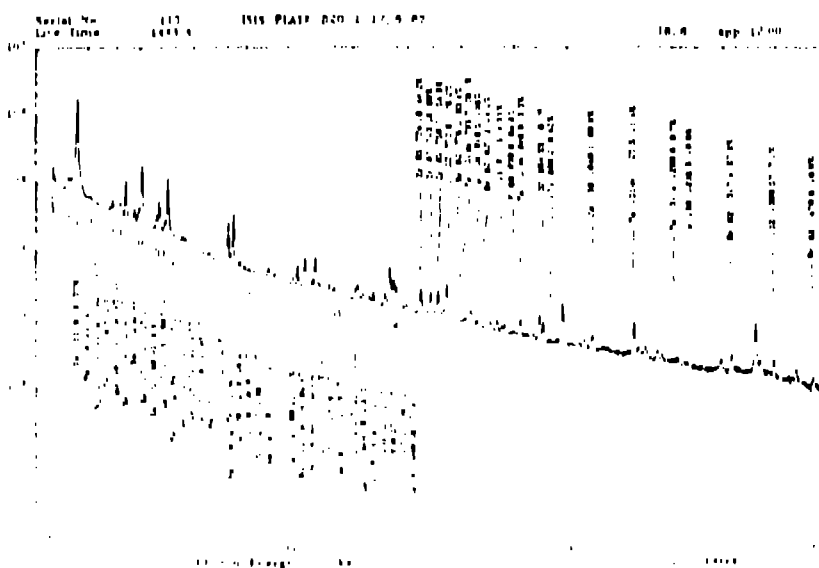


FIG 2 GAMMA SPECTRUM FOR  $\text{D}_2\text{O}$  COOLING, TARGET NO 1

b) Target Number 2

The experience of target number 2 followed closely that of number 1. There was a small inter-circuit leak which did not however worsen. The target operated from early September to early December 1987 with beam at 70 - 80  $\mu$ A. Over a period of about 20 hours the gap constant fell from 18.4 to 16.7. Figure 3 shows the gap constants over the last 90 hours of the target's life, the fall-off for channel 1 can be clearly seen. At this stage the beam was turned off and within 3 hours fission products were seen in the coolant  $D_2O$ . The target had operated for 3 months at high intensity, up to 85  $\mu$ A. Early in this period a beam trip counter was installed which registered 19,400 trips. The trips were followed by instantaneous turn-on to full intensity, inducing similar mechanical stress, to give a total for the whole operational period of about 40,000 gross temperature excursions. Gaseous releases from this target, due mainly to water circuit blowdown prior to target removal, were 46 GBq and contained some fission product gases.

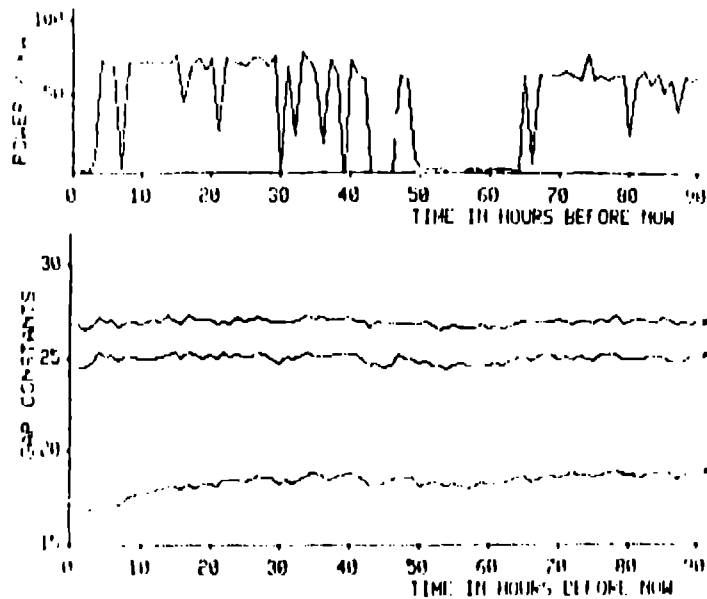


FIG. 3. GAP CONSTANTS OVER LAST 90 HOURS OF LIFE OF TARGET NO 2

In both target failures the target control, monitoring and safety systems worked well and gave clear indications of the problems at an early stage. The experiences have led to some refinements in the monitoring systems, both in terms of beam on target and of display of target parameters.

#### 4. The Target Changes

The work to change the targets was done entirely by remote means in the purpose-built Remote Handling Cell (RHC) which is an integral part of the Target Station. Details of the remote handling operations and the lessons learned are reported elsewhere in this Conference (1) and only a few comments will be made here. Though the RHC was substantially complete, much initial preparation was necessary to equip it with TV cameras and tools before work could start. Special tools for use with the manipulators were prepared and, as far as possible equipment and procedures were tested initially in a dummy run. Both changes were very much learning exercises and some modifications and improvements were made between the first and second change. Of the RH problems encountered, only one might have been related to the proton beam, when the pressure vessel of target number 1 was distorted due possibly to beam misalignment which would give non-uniform heating of the stainless steels in the target. Leakage between the plate and casing cooling circuits could also be explained this way.

Generally the work went very much as planned. All work was done with the guidance of a nominated radiation protection supervisor. After removal both targets were placed in the storage well within the RHC, pending further action. Times for doing the work were

Target 1: Remove and store 5 days. Install new, ready for operation  
10 days

Target 2: Remove and store 2 days. Install new, ready for operation  
17 days

In both cases some preparation time was required. With increasing experience less preparation time would be needed and the overall task might be achieved in 2 weeks.

Dose rate measurements on the targets gave values much as expected from design calculations, i.e. about  $80 \text{ mGy hr}^{-1}$  at 2 m. The general radiation level in the RHC due to other components was about  $200 \text{ mGy hr}^{-1}$ , with  $800 \text{ mGy hr}^{-1}$  on contact with the reflector. The average radiation dose received by the staff on the work was one twelfth of the derived dose based on the ICRP limit for classified workers.

#### 5. Examination of Target 2

Both target failures came sooner than hoped in terms of total current though there was increasing concern at the very large number of beam trips. An examination of a failed target was crucial and Target 2 (which had a better known history) was sent to the Harwell Remote Handling Facility for dismantling and expert examination. Figure 4 shows the inlet side of the target module with the pressure vessel and manifolds removed. The gaps between plates 3, 4 and 5, all part of the first cooling channel, can be seen to be partially blocked. Detailed examination showed that disks 1 through 16 had wrinkling of the zircaloy cladding over a diameter 5 - 7 cm, with the remaining disks appearing undamaged. Wrinkling of the cladding is due to radiation growth of the underlying uranium randomly orientated crystals, and its area reflects the proton beam size (expected to be 7 cm dia at full beam, full emittance). Disks 3, 4 and 5 had localised swelling, with cracks in the cladding. The cracks were both radial and circumferential, and were biaxial due to the underlying localised swelling of the uranium. There were also witness marks due to the ribs, almost all due to pressure from disk number 4. The cracks were black within and outside there were witness rings due to the formation of zirconium hydride due to the loss of cooling with gap closure. By far the most damaged disk was number 4, where figure 5 shows the localised swelling over a diameter of about 3 cm on the front face with several cracks in the cladding. The swelling is clearly offset with respect to the disk centre and was so large as to press into the corresponding faces of plates 3 and 5. The damage was recognised (2) as "entirely commensurate with failure due to thermal cycling growth, probably caused by on/off cycles of the beam, possibly exaggerated by irradiation. There was no evidence of engineering faults in the target".

A zinc sulphide screen was placed in front of disk number 4, to indicate the induced activity in the plate. For comparison purposes, this was repeated with disk number 1, which was relatively undamaged. When the



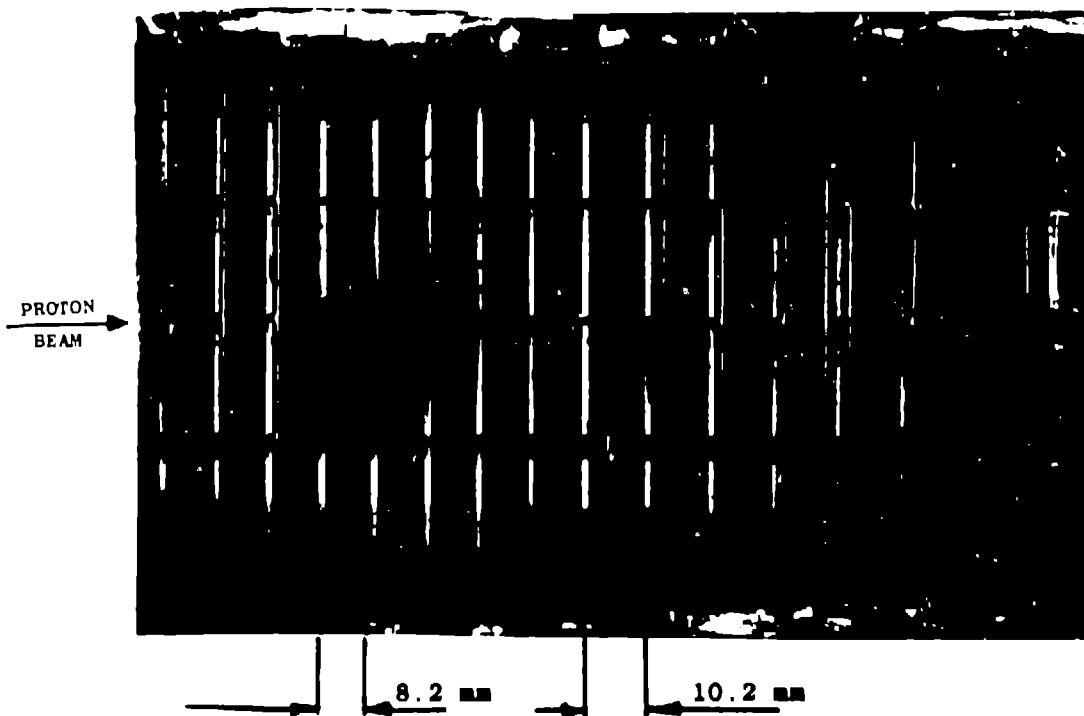


FIG. 4 INLET SIDE OF TARGET MODULE, TARGET NO 2

scintillation trace was overlaid on the photograph of disk number 1, it showed a good fit to the wrinkled area of the disk. A contour plot was also made which showed a "humped" elliptic distribution about 7 cm (v) by 5 cm (h) and reasonably well centred on the disk. On disk number 4, however, this scintillation was again a humped elliptic distribution 7 cm(v) by 5 cm (h) but like the wrinkling, offset to the left horizontally by about 1 cm. The region of severe mechanical damage, about 2 cm diameter was offset to the right by about 1 cm and down by 1 cm to the edge of the scintillation with no enhancement of the scintillation, i.e. this damage, and its induced activity occurred in a time short compared with the total irradiation time. Recalling the reduction of gap constant occurred over a period of the last 16 or so hours of the target we conclude this damage occurred in this same period.

How can this effect be so localized and how can it occur so rapidly? Firstly, the beam intensity at this time was 85  $\mu$ A and the horizontal and vertical emittances were about half the full design value. Due to power supply instabilities in the extracted proton beam line the spot size on

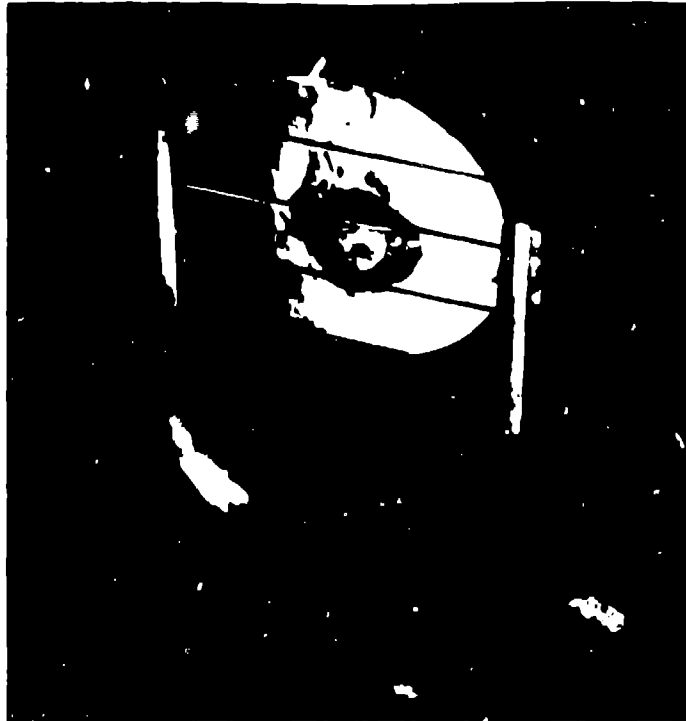


FIG 5. FRONT FACE OF DISK 4 SHOWING LOCALISED SWELLING

target varied both in size and location. Beam transport calculations have shown that such small spot sizes were possible with the result that at these intensities the energy density in the plate could be twice the maximum design value. Secondly, the uranium in the target itself is polycrystalline, of small crystals with random orientation. During a temperature excursion an unrestrained single crystal will not experience mechanical stress. However when the crystals are contiguous some crystals experience compressive, and some tensile, stress during a quench. Plastic elongation is produced in those crystals experiencing tensile stress, which is retained on heating and eventually shared with the other crystals by creep. Successive cycles produce further elongation. The strain of individual crystals increase linearly with the number of cycles but there is no volume change until the voids, defects, etc are filled, when it changes rapidly.

Underlying the above mechanisms, the uranium during operation suffers from irradiation growth. Stress is developed due to the mismatch between the

⊕

movements of adjacent grains which gives rise to plastic deformation. The internal strain introduced by growth at the boundary between two grains will reach the yield strain in a time  $t_m$  dependent on the fissioning rate and, for ISIS at full intensity is about 170 secs. Continuous plastic yielding occurs after this time and the uranium becomes almost devoid of strength at low strain rates. Any external stresses applied in times  $\geq 170$  secs will relax to a low value, but in times  $< 170$  secs will not relax. These times indicate how some of the effects of a quench can be alleviated, by applying external stress at a rate no faster than naturally occurs during burn-up of the uranium.

#### 6. ISIS Operations

As a result of these experiences a number of improvements in the operation of ISIS have been instituted:

- ⊕
- i) With the addition of further diagnostics in the EPB together with auto-align programs the proton beam on target has been improved. Further beam line quadrupole programs are coming into use and a long term program to improve power supply stability is underway.
  - ii) The original halo monitor has been replaced by an 8-sector device, with two sets of 4 thermocouples at 2 different radii. Uniform temperatures are sought and, after warning, the beam is tripped off if the alignment is bad (measured by the difference temperatures of opposite TC's).
  - iii) The Beam Loss Trip System has been modified so that rather than trip the beam due to one faulty pulse in 50, the trip is initiated by comparing the beam loss at several points in the machine over 3 pulses with a pre-set value, or 4 pulses in the case of the injector. This has had the effect of reducing the trip rate by a factor 8.
  - iv) A 'soft start' system is incorporated when, following a beam trip and quench, the beam is brought to operating intensity in 140 - 180 secs. This then avoids the mechanical stress induced by a fast up-cycle by allowing the uranium to plastically yield, so a quench now results in 1 thermal excursion rather than 2. The combination of iii) and iv) gives a factor 16 improvement in trip rate.
- ⊕

v) The gap constant is now determined once per hour and compared with a calculated temperature corrected value (g varies linearly with the bulk D<sub>2</sub>O temperature). Warnings are given when the measured value differs by 0.5 (warning) or 1.0 (beam-off), and the problems are investigated. In this way it is hoped to recognise an impending target failure before the cladding is breached. The subsequent target change can then be made without the complication (and possible hazards) of free fission products. This system will be incorporated into auto-control in due course.

vi) As part of the transfer of control of the Target Station from "local" to the main ISIS control room, improved displays are provided, including a colour display of the 7 front plate temperatures, figure 6, also a longitudinal display of plate temperature. These displays have greatly increased the operator awareness of the health of the target.

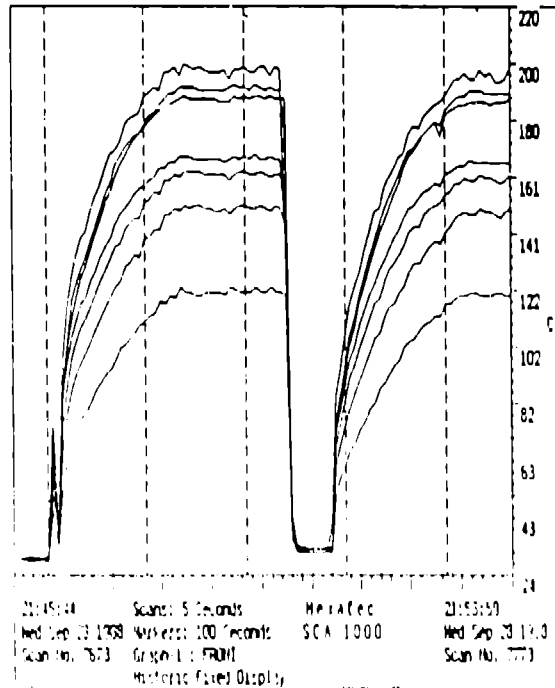


FIG 6 DISPLAY OF FRONT 7 TARGET PLATE TEMPERATURES  
(NOTE QUENCH FOLLOWED BY A 'SOFT START')

At 15 September 1988, the beginning of a scheduled short shut-down period for ISIS, ISIS Target number 3 had received 129,300  $\mu\text{A}\cdot\text{hr}$  and 8900 soft starts (= beam trips). Other parameters appear to be behaving normally. Many isotopes of krypton have been seen in the  $\text{D}_2\text{O}$  coolant but, in the absence of other radionuclides, these are recognised as spallation products of zirconium. Deo Volente ....

#### 7. Acknowledgements

It is a pleasure to record the continued support and efforts of many people on ISIS and the Target Station in particular: David Gray, Brian Boardman, Gordon Grossart, Eddie Fitzharris, Alan Thorne, Ken Roberts, David Perry, Martin Bly, Bob Hall, John Sexton, John Hirst and the late Colin Thomas.

#### 8. References

- 1) T A Broome and M Holding "Remote Handling for an ISIS Target Change" this Conference.
- 2) B Hudson. Private communication to A Carne, May 1988

## **The Proton Storage Ring: problems and solutions**

*R. J. Macek*  
Los Alamos National Laboratory  
Los Alamos, NM 87545  
USA

**ABSTRACT:** The Los Alamos Proton Storage Ring (PSR) now operates with  $35\mu\text{A}$  at 20-Hz pulse repetition rate. Beam availability during 1988 suffered because of a number of problems with hardware reliability and from narrow operating margins for beam spill in the extraction line. A strong effort is underway to improve reliability with an eventual goal of obtaining beam availability in excess of 75%. Beam losses and the resulting component activation have limited operating currents to their present values. In detailed studies of the problem, loss rates were found to be approximately proportional to the circulating current and can be understood by a detailed accounting of emittance growth in the two-step injection process along with Coulomb scattering of the stored beam during multiple traversals of the injection foil. It is now apparent that the key to reducing losses is in reducing the number of foil traversals. A program of upgrades to reduce losses and improve the operating current is being planned.

### **1. Introduction**

The Proton Storage Ring (PSR) at Los Alamos functions as a high-current accumulator or pulse compressor to provide intense pulses of 800-MeV protons for the Los Alamos Neutron Scattering Center (LANSCE) spallation Neutron Source. The neutron scattering community has seen several proposals for similar neutron sources based on compressor rings fed from a proton linac e.g., SNQ from Jülich, one from Moscow, JEP from Japan, and LANSCE II from Los Alamos. To date, only the PSR has been constructed, hence

the experience with PSR should be helpful in assessing this approach to the design of advanced neutron sources.

### 1.1 Layout

The layout of PSR in relationship to other relevant facilities at the LAMPF site is shown schematically but not to scale in Fig. 1. An 800-MeV  $H^-$  beam from the LAMPF linac is kicked into Line D and transported through Line D and the Ring Injection Line to a high-field stripper magnet where it is converted with 100% efficiency to  $H^0$ . The  $H^0$  beam then enters the lattice of the ring through a dipole and is stripped to  $H^+$  beam with  $\sim 92\%$  efficiency in a  $200 \text{ g/cm}^2$  carbon foil. Up to 2800 turns can be injected and accumulated during a single macropulse. Beam is normally extracted in a single turn shortly after the end of injection and transported to the LANSCE neutron-production target in ER-1.

### 1.2 Performance to Date

Performance parameters of general interest are summarized in Table I where the values as of October 1988 are compared with the design goals. The peak current (on the 100 nanosecond time scale) available from LAMPF is 8-10 mA and is limited by the  $H^-$  source. By increasing the pulse length beyond the design value to  $950 \mu\text{S}$  we have accumulated (in test runs) as many as  $3.8 \times 10^{13}$  protons per pulse (ppp) or 70% of the original design goal for this parameter. Unfortunately, we cannot use this peak intensity for routine operation because of "slow" losses during accumulation. In the present operation at 20 Hz, we are limited to an average current of  $35 \mu\text{A}$  by losses of  $\sim 0.5 \text{ A}$  which have caused activation at the maximum acceptable level for hands-on maintenance of ring components. These losses occur primarily in the injection and extraction regions which contain the known limiting apertures. Further information on the design and initial performance are published elsewhere.<sup>1</sup>

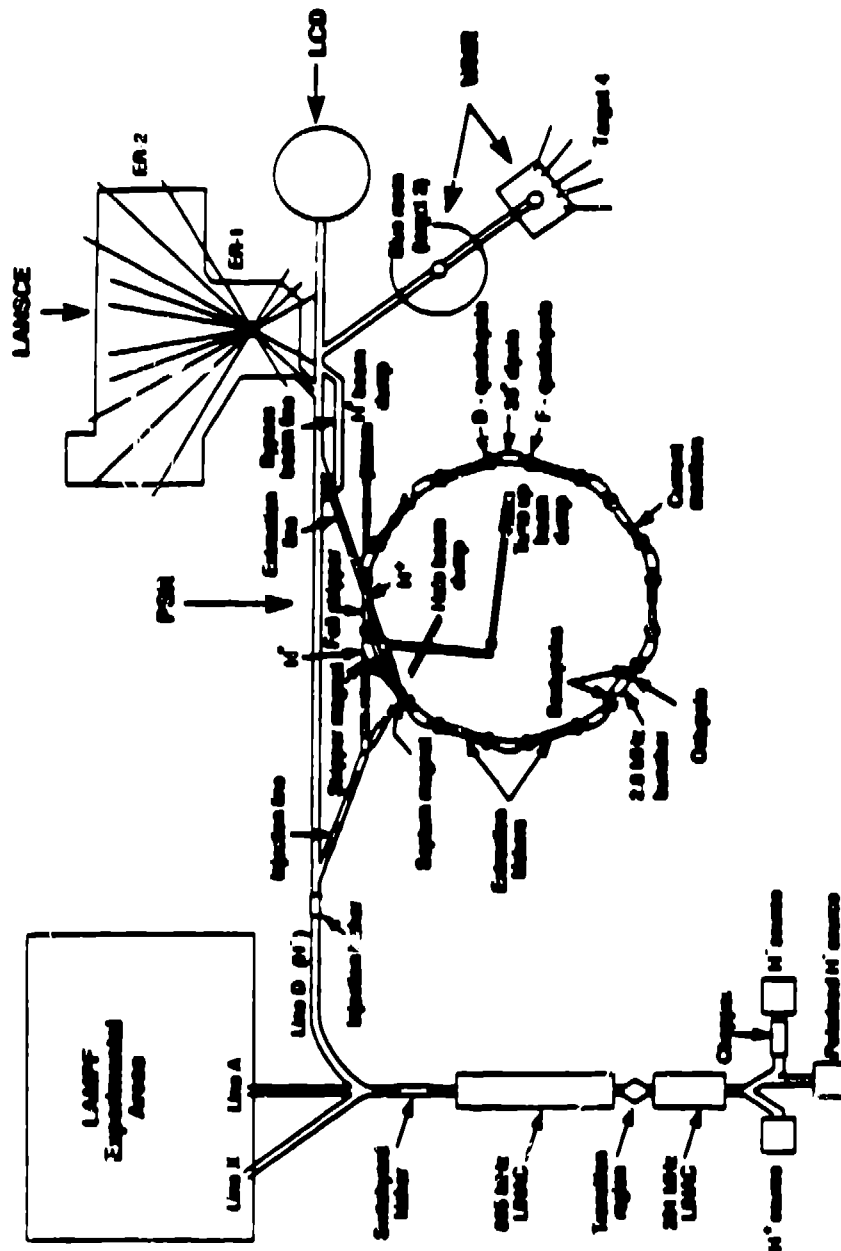


Fig. 1. Schematic layout of PSR at the LAMPF site.



TABLE I. Summary of Performance (to October 1988)

	<b>Design</b>	<b>Achieved</b>	
• Peak Injected Current	15 mA	8-10 mA	
• Injection Pulse Length	750 $\mu$ s	975 $\mu$ s	
• Protons/Pulse	$5.2 \times 10^{13}$	$3.8 \times 10^{13}$	
• Repetition Rate	12 Hz	20 Hz	
• Average Current	100 $\mu$ A	35 $\mu$ A	
• Losses:			
Accumulation	0.1-0.3 $\mu$ A	0.5 $\mu$ A	
	● 100 $\mu$ A	● 35 $\mu$ A	
	[0.1-0.3%]	[1.4%]	
Extraction	<0.1%	0.1-0.3%	
		(● 30 $\mu$ A)	
• Availability	75% ?	62% ave.	1987
		(80% Best Run)	
		30% Avg	Cycle 51
		64% Avg	Cycle 52

## 2. Reliability and Beam Availability

Beam availability was never specified in the original PSR design documents; however, the LANSCE user community has shown a strong preference for a value of 75%, or greater. We define beam availability as the ratio of the time beam was available (at greater than 50% of the scheduled current) for delivery at the LANSCE target to the beam time scheduled for LANSCE research.

### 2.1. Daily Availability in 1988

The operation of PSR during the summer of 1988 (LAMPF Cycles 51 and 52) was the first attempt at sustained running for a formal users program. Beam availability and machine reliability were a great disappointment especially in Cycle 51 when beam availability was about 30%. The details on a daily basis are shown in Fig. 2 where the availability is plotted as a function of time using only the days when beam was scheduled for research at LANSCE. At the 30% level of reliability, the research program at LANSCE suf-

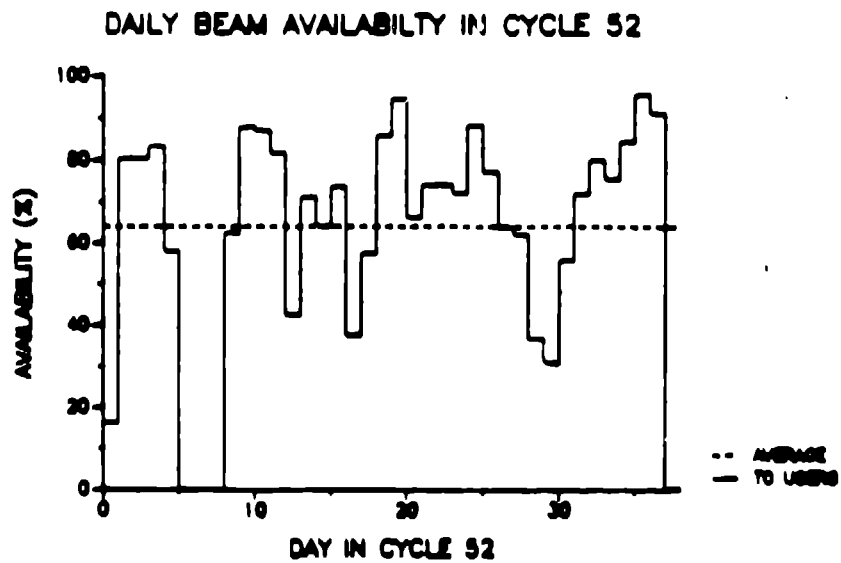
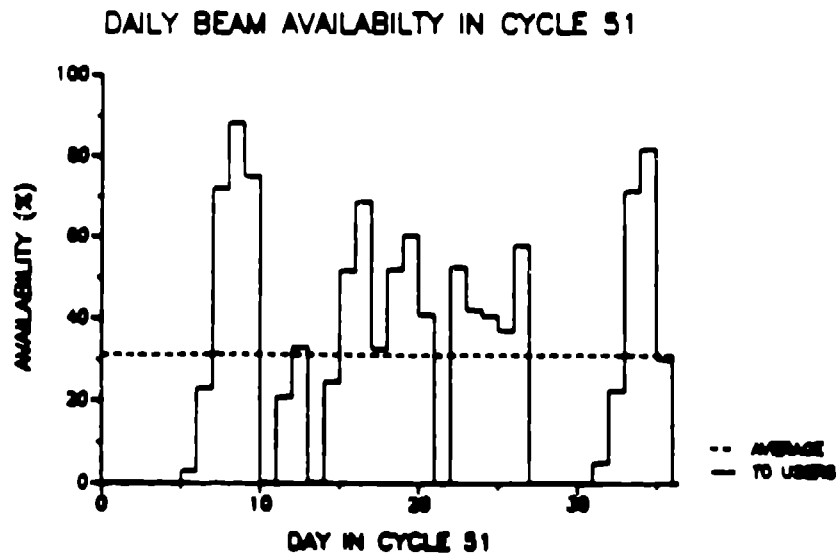


Fig. 2. Daily beam availability in 1988 for LANSCE.

ferred; great frustration and dissatisfaction were evident amongst the user community, and the PSR staff became thoroughly exhausted making numerous expedient repairs to more deep-seated problems.

## **2.2. Subsystems Availability**

Much of the downtime came from the pulsed power systems, as can be seen in Table II, Subsystems Availability. Thermal failures of the water-cooled loads on the switchyard kickers and massive failures of high-voltage vacuum feedthroughs on the stripline kickers of the ring extraction system were the most acute of the numerous problems which developed in 1988. Expedient repairs were designed and implemented in the short time between beam cycles in what is best described as a frantic effort to recover the momentum of the LANSCE research program before the end of the 1988 running period. These repairs and a sustained effort to keep all systems operational resulted in a marked improvement in availability which averaged about 65% in cycle 52.

The LAMPF linac is also a significant source of downtime. It is a mature facility whose availability has been 80 to 85% for many years and is at a level that is satisfactory for the nuclear and particle physics program which funds the operation of LAMPF. Further improvement is an expensive undertaking. The 201-MHz RF system is a major source of downtime for the linac and estimates for improving it are between 5 and 10 million dollars; it is not a cost-effective candidate for improving overall reliability. The problem for the LANSCE facility is that beam availability is the product of the availability of LAMPF and that of PSR and the rest of the beam-delivery system. Therefore, to achieve 75% or greater overall availability, the PSR and other beam-delivery system availability will need to reach 95%. This has been achieved with other circular machines such as the Booster Synchrotron at CERN.

## **2.3. Improvements to Reliability and Operational Efficiency**

The  $H^-$  source has run at 90 to 95% availability and has required two shifts of downtime every two weeks for reconditioning. Efforts are currently underway to reduce the arc-down rate and improve

Table II. Subsystems Availability in 1988

	Cycle 51	Cycle 52	Long Term Goal
• Linac and H <sup>-</sup> Source	75%	82%	85%
• Pulsed Power Systems	68%	94%	95%
• Other Beam Delivery Systems	85%	91%	
Product (Available from PSR)	43%	70%	80%
• Beam On and Current ≥ 50% of Scheduled	76%	92%	97%
• LANSCE Target/Moderator	96%	98%	
• Beam Available to Users at ≥ 50% of Scheduled Current	31%	64%	>75%

source lifetime. A spare source is being fabricated to reduce the amount of downtime needed for periodic reconditioning. Our goal is source availability of 97-98%.

Many other systems contribute to downtime but a complete discussion is beyond the scope of this paper. The pulsed power systems were discussed earlier. Deionized water systems have presented a number of problems including numerous leaks, corrosion of brass fittings, and deposits in certain power supplies. The use of lead-free solder (95% tin, 5% antimony) with its small workable temperature range undoubtedly contributed to the large number of voids found in the solder joints of the larger copper pipes. Improvements underway include redoing all the joints in the 4-inch water line and more instrumentation to monitor water quality.

Another important loss of beam time arose from frequent tuning to reduce spills in the PSR and in the extraction line. In cycle 51 about 25% of the time when beam otherwise was available, operators were tuning at half or less of the scheduled current primarily to eliminate spills which caused tripping of the errant beam protection instrumentation. Margins on beam spill were much tighter in 1988 than before because users were allowed in the experimental area of LANSCE while beam was on. Prior to 1988 users were excluded when the beam was on. Safe access with the beam on

was guaranteed in 1988 by the newly installed fail-safe Personnel Safety System (PSS) whose three levels of fail-safe errant beam detection instrumentation insured that the beam was promptly shut off under any beam spill conditions which would present a hazard to personnel in occupied areas.

There is very little margin for error in transporting the extracted beam to LANSCE. In the region of transport where the floor of the beam tunnel is also the roof of the experimental area, small spills of order 3-5 nanoamperes (0.01% of the beam) can cause radiation levels of about 20 millirem/hour in certain areas of the experimental hall where users must have free access. In this situation, the least deviation from the optimal tune can cause spills of this magnitude.

The addition of approximately one meter of iron shielding in the extraction channel region over ER-1 would greatly increase the tolerance for error in the beam transport to the LANSCE target. However, the structural modifications needed to support the additional weight are a major complication. Nevertheless, design studies of the changes required for additional shielding of this magnitude are now underway with high priority.

Variations and drifts of the beams, both to and from PSR, can arise from a number of sources including the linac and the beam transport. The beam from the linac changes slightly a few times per shift; these changes are commensurate with our long term experience at LAMPF and can be large enough to have a significant effect at PSR. However, by the end of cycle 52, it became clear that a large portion of the beam changes which affected PSR resulted from poor stability of magnet set points in the Line D transport. A factor of 5 to 10 improvement in magnet-power-supply stability is underway. Longer term, we aim for 0.01% set-point reproducibility, which implies additional improvement in power-supply regulation.

### 3. Beam Losses<sup>2</sup>

Beam losses during accumulation are far and away the most serious barrier to higher-current operation. In the present operation with  $35\mu\text{A}$  at 20 Hz, the losses produce activation at the limit for hands-

on maintenance of the ring. As we shall demonstrate shortly, the losses at  $100\mu\text{A}$  would be an order of magnitude higher if nothing is done to reduce them.

### 3.1. General Characteristics of the Accumulation Losses

Slow losses are measured to  $\sim 30\%$  accuracy with a series of scintillator-based radiation detectors located on the outside wall of the tunnel at beam height opposite each ring dipole. Detector gains are all identical; signals from each as well as a sum signal of all detectors are used for loss measurements. The sum signal is calibrated by allowing a measured quantity of beam to be completely lost. Fast analog current signals, obtained directly from the phototubes, are available in the control room for detailed analysis of the time structure.

The sum-current signal is a measure of the beam loss rate,  $\dot{L}(t)$ . A trace from normal operation is shown in Fig. 3 along with a signal from a current monitor that senses the circulating beam current,  $I(t)$ . The ring current is a ramp because beam is continually injected during an injection period of  $375\ \mu\text{s}$ . Fig. 3 shows that  $\dot{L}$  is nearly proportional to the stored beam intensity. Total losses,  $L = \int \dot{L} dt$ , will then be quadratic in time. To increase the average current to  $100\ \mu\text{A}$  we need to inject for  $\sim 1000\ \mu\text{s}$ , but the losses under these conditions are an order of magnitude higher than for the present operation at  $375\ \mu\text{s}$ , which already produces the maximum acceptable activation of ring components.

Losses for an extended period of accumulation can arise from those occurring at the time of injection as well as from continual losses of the stored beam. The two components can be separated in an experiment where beam is accumulated for a short time ( $\sim 100\ \mu\text{s}$ ) and stored for a much longer period ( $\sim 1000\ \mu\text{s}$ ) before extraction. Loss rates and circulating current signals from one such experiment for a coasting beam (RF buncher off) are shown in Fig. 4. The discontinuity at the end of injection is caused by the cessation of "first-turn" or injection losses and amounts to  $\sim 2 \times 10^{-8}$  of the injected beam current. The loss rate during storage is a slowly increasing function of storage time with a fractional loss rate of  $\sim 1.3 \times 10^{-8}$  per proton per turn at the end of the  $100\text{-}\mu\text{s}$  injection period.

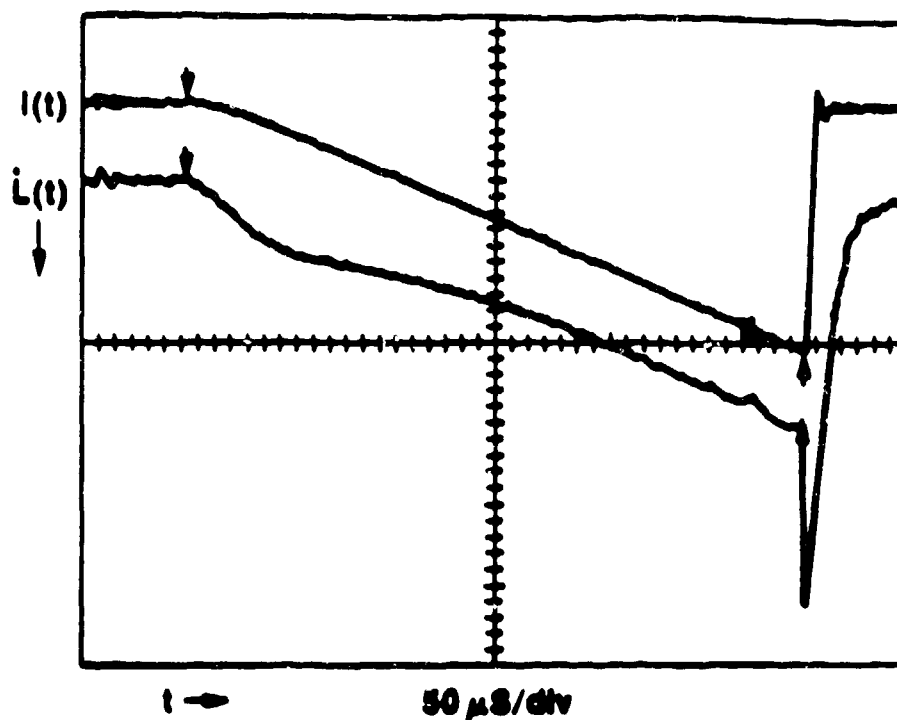


Fig. 3. Loss rate during normal operation.

The significant loss observed during injection and the continual losses thereafter suggest that the injected beam somewhat more than fills the acceptance of PSR. This is corroborated by halo plate scans of the horizontal beam profile in the ring in which a thick plate is scanned across the ring aperture and the fraction of the beam intercepted by the plate is obtained by measuring the scattered beam intensity in the sum of several loss monitors. The signal is normalised to unity when all of the beam is intercepted. This technique is especially useful for measuring the beam distribution in the extremities of the beam. Data from one scan are shown in Fig. 5 for the situation where beam is extracted shortly ( $10 \mu s$ ) after the end of  $100 \mu s$  of accumulation. The scan provides a good measure of the beam distribution just after capture in the ring and before foil scattering can cause appreciable emittance growth. In Fig. 5 it is readily apparent that the beam distribution extends to about 38 mm, which corresponds to the value of the limiting aperture defined by the extraction septum. Note that

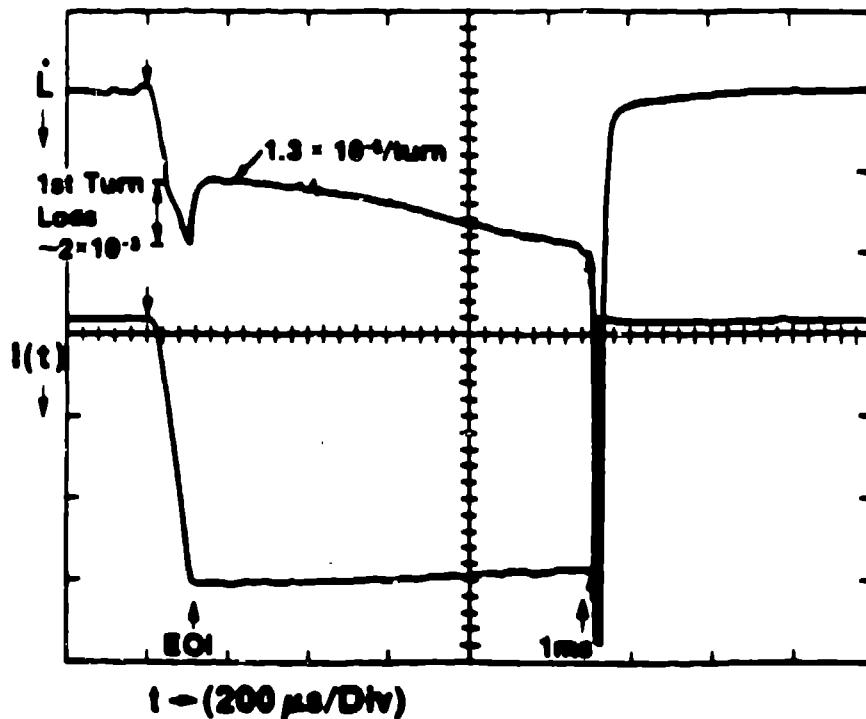


Fig. 4. Loss rate for 1 ms storage.

the beta functions at the septum and at the halo plate are nearly equal.

The mismatched Gaussian (MM GAUSS in Fig. 5), described in the next section, fits the distribution of Fig. 5 very well.

### 3.2. Emittance Growth and Losses During Injection

It may seem surprising that the beam fills the horizontal acceptance at injection since the acceptance of PSR,  $\sim 130\pi$  mm-mrad, is so much larger than the rms emittance,  $\sim 0.5\pi$  mm-mrad, of the  $H^-$  beam from LAMPF. The momentum spread (rms) of the  $H^-$  beam is also small with  $\Delta p/p \simeq 5 \times 10^{-4}$ . Two main factors contribute to emittance growth in the injection process: 1) an increase in horizontal divergence in the stripper magnet when  $H^-$  is converted to  $H^0$  and 2) a large horizontal optics mismatch of the  $H^0$  beam to the PSR acceptance.



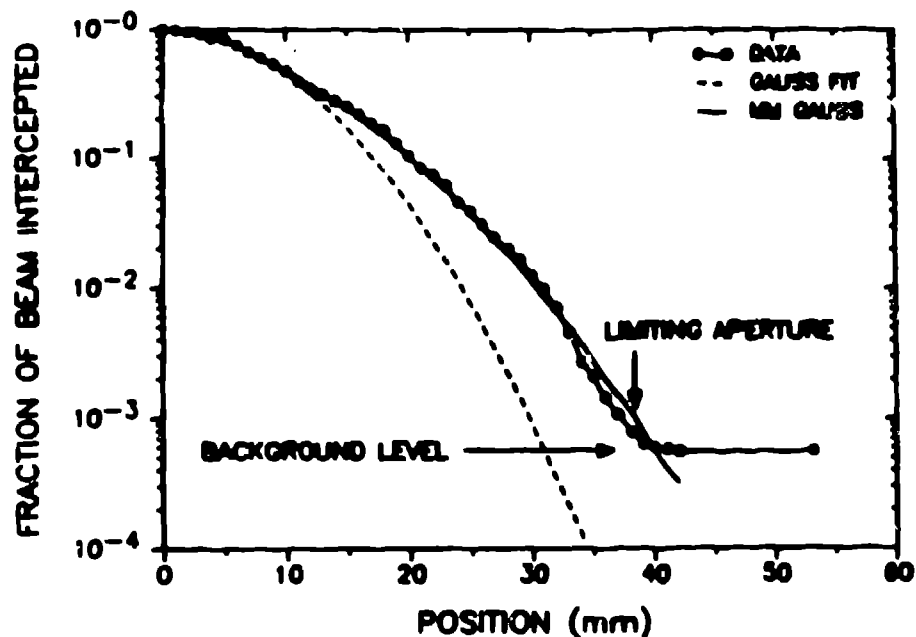


Fig. 5. Horizontal halo-plate scan.

A Gaussian fits the core of the beam but fails to fit the extremities. Stripping of the  $H^-$  in a high magnetic field is a stochastic process which leads to random fluctuations in the point of conversion and thus an increase in  $H^0$ -beam divergence. Calculations of the angular distribution for a pencil beam of  $H^-$  are shown in Fig. 6 for two different vertical entrance positions ( $y = 0$  at midplane and  $y = -4$  mm). The calculation used the measured field map of the stripper magnet and a parameterization of the  $H^-$  lifetime from earlier Los Alamos work.<sup>3</sup> Emittance growth in the stripper magnet is minimized by use of a small gap magnet with a high field gradient at the entrance and by optics which produce a very small spot in both  $x$  and  $y$  at the stripper magnet. Even with this optimization the horizontal emittance of the  $H^0$  is three (3) times larger than that of the incoming  $H^-$  beam.

An optics mismatch at injection, shown in Fig. 7, is an additional consequence of magnetic stripping. The  $H^0$  is constrained to diverge from a small spot at the stripper magnet and cannot be matched simultaneously in the  $(X, X')$  and  $(Y, Y')$  planes at the standard location of the foil stripper where the  $H^0$  is reasonably well matched in  $(Y, Y')$  but badly mismatched in the  $(X, X')$  plane.

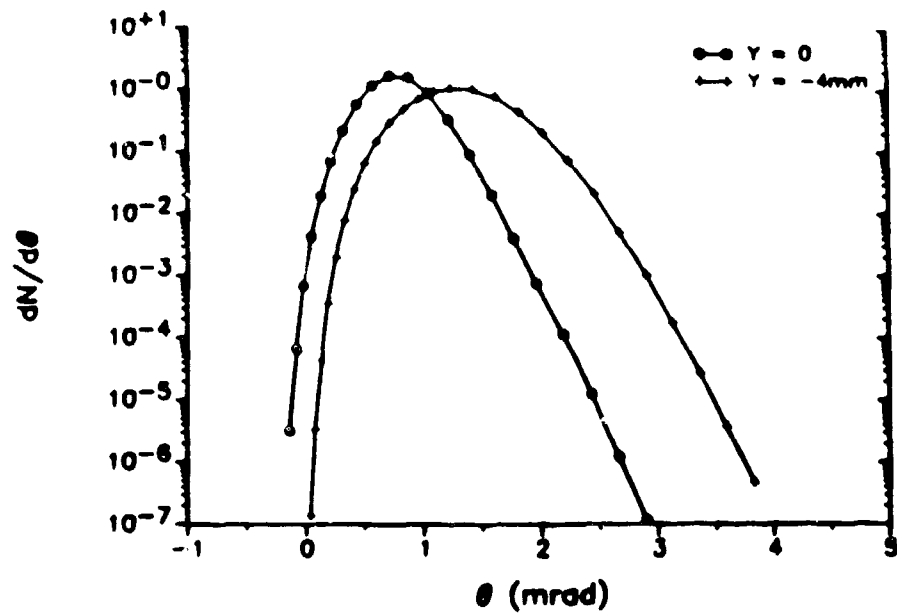


Fig. 6.  $H^+$  distribution after stripper magnet.

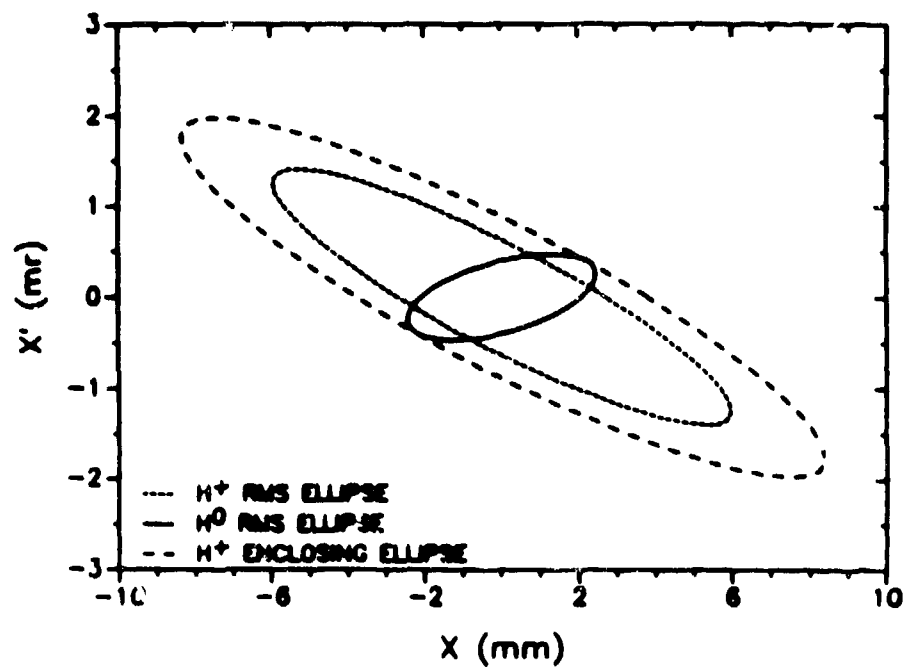


Fig. 7. Injection mismatch in horizontal plane.

The mismatch factor,  $C = \{\beta_o \gamma_R + \beta_R \gamma_o - 2\alpha_o \alpha_R\}/2$ , (subscript  $o$  refers to  $H^o$  and  $R$  to the ring) has a value of 3.8 indicating a further increase of 3.8 in the rms emittance of the stored beam. The mismatch also changes the beam distribution; for a Gaussian beam injected on axis, one can easily obtain the following closed form for the distribution of the invariant betatron amplitude,  $y$ :

$$P(y)dy = \frac{1}{\epsilon_o} e^{-\frac{Cy^2}{2\epsilon_o}} I_o\left(\frac{y^2}{2\epsilon_o} \sqrt{C^2 - 1}\right) y dy$$

where  $\epsilon_o$  is the rms emittance of the incoming  $H^o$  beam and  $I_o$  is a modified Bessel Function.<sup>4</sup> The rms emittance for this distribution is  $C\epsilon_o$ . This distribution has longer "tails" than a Gaussian with the same rms emittance, thereby increasing still further the size of the beam near the limiting apertures. The non-Gaussian tails are readily apparent at PSR in the halo-plate scan shown in Fig. 5 and in wire-scanner profiles of the extracted beam taken at the end of short (100  $\mu$ s) accumulation as shown in Fig. 8. The "mismatched" Gaussian distribution derived from equation (1) fits the data very well whereas a Gaussian with the same rms width fits poorly, especially at large  $X$ .

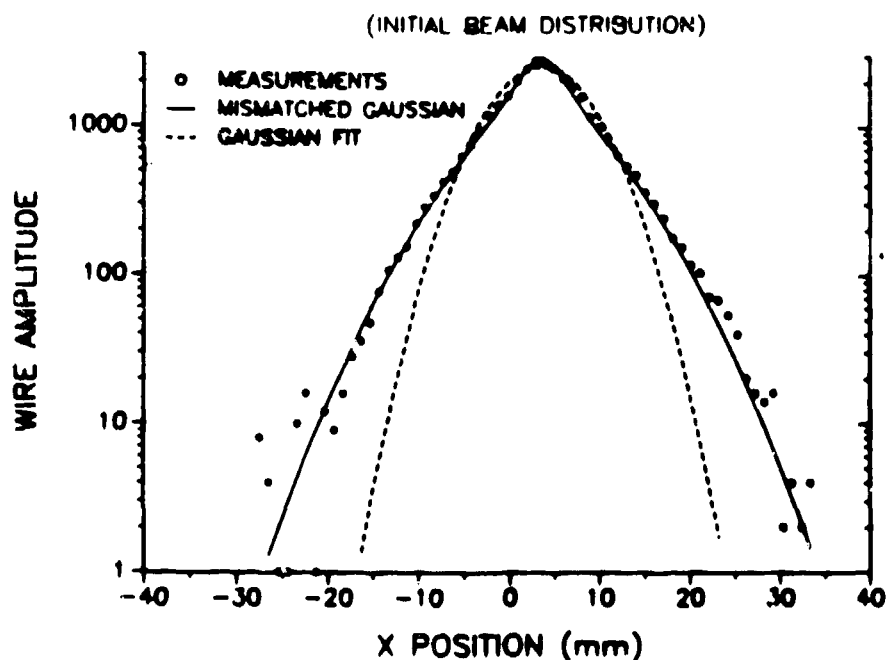


Fig. 8. Extraction wire-scanner profile.

Integration of the distribution described by equation (1) for the region outside of the limiting aperture provides an estimate of injection or "first-turn" losses. A value of 2 to 4 x 10<sup>-3</sup> is obtained which is in good agreement with the observed value of ~ 2 x 10<sup>-3</sup> considering the high sensitivity of the result to the size of the limiting aperture.

### 3.3 Emittance Growth and Losses During Storage

A typical proton in PSR traverses the injection foil during about half of its revolutions. Multiple Coulomb scattering in the foil will cause emittance growth (rms) given by  $\epsilon(t) = \epsilon_0 + \beta_f \theta_1^2 f N(t)/2$  where  $\epsilon_0$  is the initial rms emittance,  $\beta_f$  the beta function at the foil,  $\theta_1$  the rms scattering angle from a single foil traversal and  $fN(t)$  the number of foil traversals in N turns up to time t. The rms emittance is defined as  $\sqrt{\langle X^2 \rangle \langle \theta^2 \rangle - \langle X\theta \rangle^2}$  where  $\langle \rangle$  indicates expectation value and  $\theta = X'$ . Measurements of beam sizes as a function of storage time shown in Fig. 9 are well fit by the above equation for  $\epsilon(t)$  and show nearly a factor of three increase of emittance (proportional to square of the spot size) during 1 ms of storage.

To accurately estimate losses from multiple Coulomb scattering requires more than knowledge of the rms emittance growth; one must calculate the evolution of the distribution function with time. We have made estimates using two different methods which produce similar results in reasonable agreement with measurements. The first method used a Fokker-Planck equation

$$\frac{1}{K} \frac{\partial P}{\partial t}(t, y) = \frac{\partial}{\partial y} \left[ y \frac{\partial}{\partial y} \left( \frac{P(y)}{y} \right) \right] \quad (2)$$

which was derived for estimating beam lifetimes in the presence of Coulomb scattering by residual gases.<sup>5</sup> Here y is the invariant betatron amplitude and K a constant. Solutions for the distribution function, P, are obtained as a Fourier-Bessel series and integrated to obtain the losses.

Similar results are obtained with the Monte Carlo tracking code, ARCHSIM, developed for modeling circular machines.<sup>6</sup> The tracking code simulates emittance growth in the stripper magnet and treats scattering in the stripper foil as a combination of multiple Coulomb scattering with single Coulomb and nuclear tails.

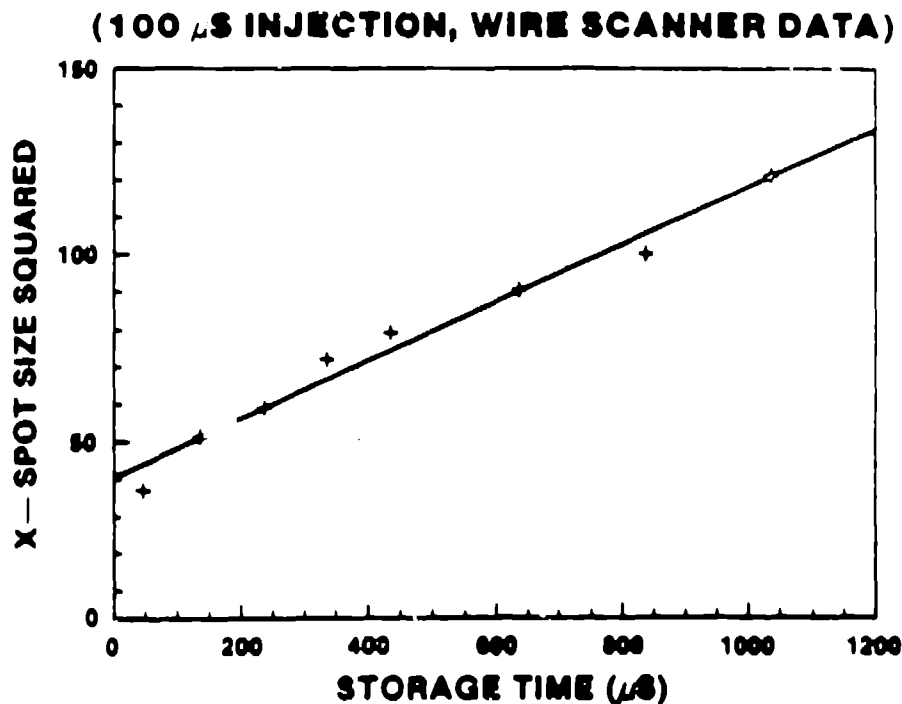


Fig. 9. Emittance as a function of storage time.

Results from the simulation and from solutions of the Fokker-Planck equation made using measured values of parameters in the models are compared in Fig. 10 with measured data on loss rates. The loss rates obtained using solutions of equation (2) were augmented with a constant term which takes account of nuclear scattering and large-angle single Coulomb scattering. Agreement between calculations and measurements are within the calibration uncertainties of the losses and the errors on parameters in the calculations. Losses are sensitive to several parameters including the mismatch factor, the  $H^{\circ}$  distribution, the probability for traversing the foil, and to the size of the limiting aperture. With small adjustments of parameters, within errors, both calculations can be made to agree completely with the loss-rate data.

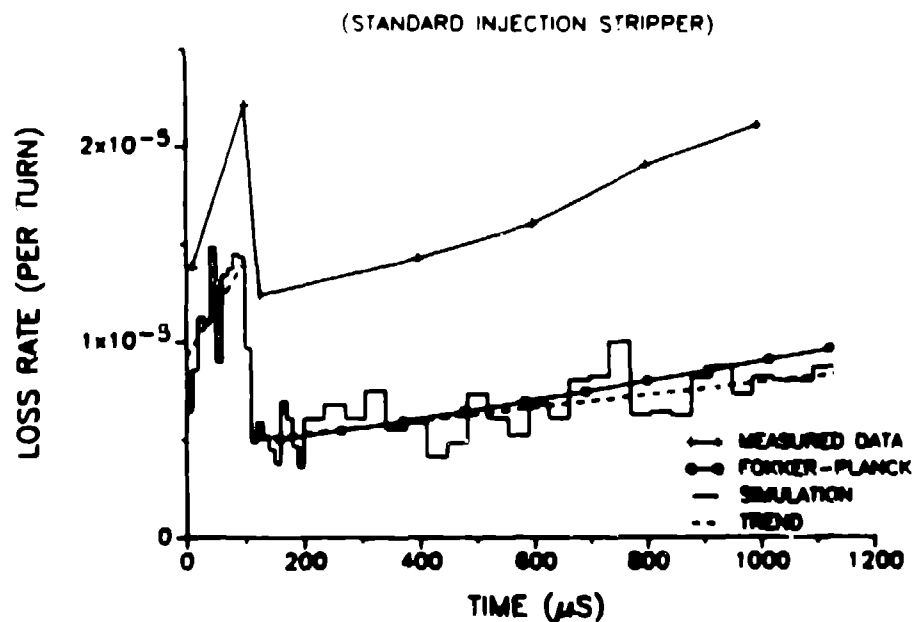


Fig. 10. Loss-rate calculations and measurements.

### 3.4 Effect of the RF Buncher

An RF buncher is used to maintain an empty gap to accommodate the extraction-kicker rise time. Synchrotron motion induced by the buncher increases the momentum spread to  $\sim 0.3\%$ ; because of dispersion the beam size increases by several mm and also contributes to beam losses. For long storage, this shows up as a striking modulation of the loss rate with a frequency twice that of the synchrotron oscillations as shown in Fig. 11. Losses are increased by about 45% when the RF is on at typical operating set points.

### 3.5 Other Contributions

Losses from nuclear scattering are readily estimated from the total cross section as  $3.3 \times 10^{-6}$  per foil traversal. The contribution from large-angle single Coulomb scattering is often overlooked. Because the cross section falls off only as a power law, rather than as an exponential, it contributes a long tail to any beam distribution. This was seen at PSR when the injection foil location was

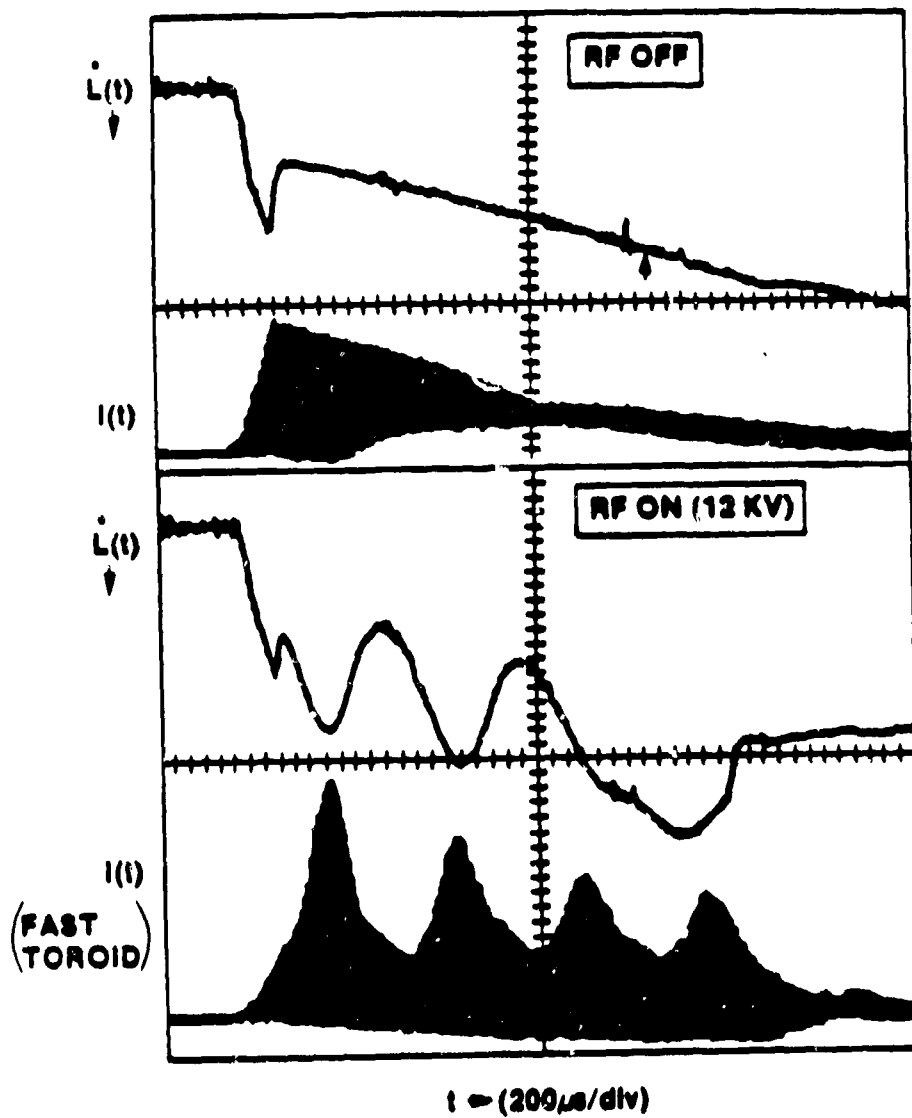


Fig. 11. Effect of RF buncher on loss rate.

changed to provide a better match in the  $(X, X')$  plane. The halo-plate scan of the beam distribution (after a short accumulation) plotted in Fig. 12 shows the expected reduction in size of the core of the beam. Also seen is a tail extending to the limiting aperture. The size and shape of the tail agrees with analytical and Monte Carlo calculations of the contribution from single Coulomb

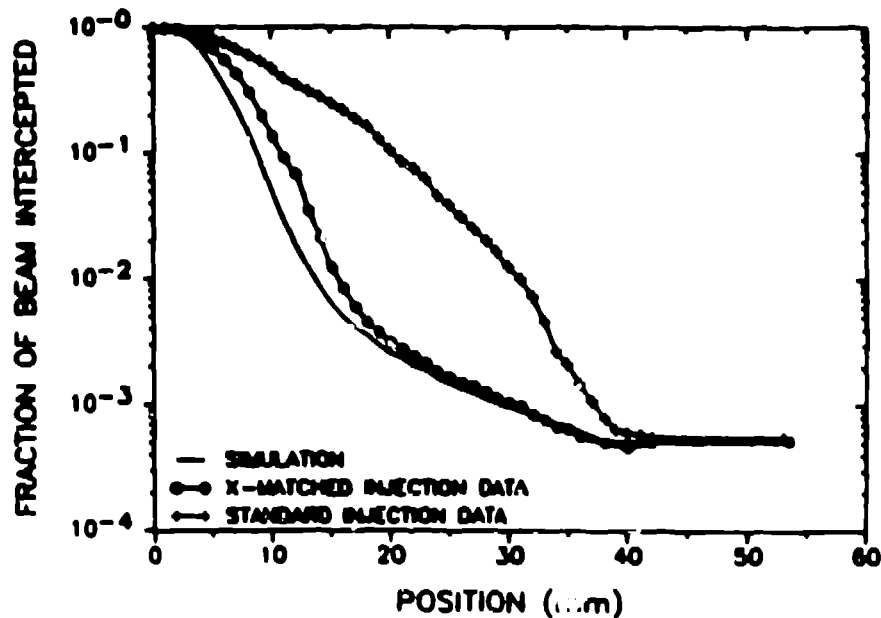


Fig. 12. Evidence for single Coulomb scattering.

scattering. At PSR large-angle Coulomb scattering contributes a loss rate of  $\sim 2 \times 10^{-6}$  per foil traversal for a  $\delta$  function initial distribution and more for a beam of finite emittance.

### 3.6 Summary of Losses During Accumulation

The composition of accumulation losses during standard operation of PSR (375  $\mu$ s injection period) can be determined from the data and analysis presented here. Results are listed below:

"First-Turn"	0.2%
Nuclear and Large-Angle Coulomb Scattering	0.2%
Emittance Growth in Absence of RF	0.6%
Effect of RF	<u>0.5%</u>
Total	1.5%

### 4. Upgrade of PSR to Reach 100 $\mu$ A

Increasing the operating current of PSR is a high priority goal for the Los Alamos National Laboratory. Management is committed to providing the upgrades needed to reach 100  $\mu$ A with beam avail-



ability of 75% or more. Our present understanding of the causes and mechanisms of the slow losses has pointed to several promising measures for significantly reducing or controlling the losses in the PSR. These are sketched below.

#### 4.1. Ring Halo Collimation System

Initial design studies assumed that a collimation system would be used to control the location of losses in the ring but none were designed or implemented in the initial construction. Plans for experimental study of the problem last summer were preempted by the more urgent need to improve reliability. The basic idea is to make scrapers or collimators the limiting apertures of the ring in such a way that the losses are moved from a critical component, such as the extraction septum, which is the present limiting aperture, to passive absorbers that are designed to deal with higher activation. These would be passive devices which would not need frequent service and would be located in less congested areas where activated components are more easily dealt with.

The two basic concepts are illustrated in Fig. 13a and b. In one (a) a high Z, movable scraper, such as 10 mm of tungsten, intercepts the beam halo and defines the limiting aperture. It is not thick enough to completely absorb the incident beam but scatters it by a relatively large amount so that most of the intercepted beam is caught by the downstream thick absorber, which is not a limiting aperture. A small fraction (perhaps 10%) of the intercepted and scattered beam goes through the opening of the absorber and is caught on a "cleanup" absorber or is lost elsewhere in the ring. If much of the beam intercepted by the scraper is beam that would have been lost elsewhere, such as at the extraction septum, then this system would be effective in reducing the losses elsewhere in the ring.

In the second concept (Fig. 13b), a moveable absorber also intercepts the beam halo and defines the limiting aperture. It is thick enough to absorb most of the incident beam. The difficulty with this concept is the "slit scattering" which occurs from the large surface of the moveable absorber struck by beam particles at grazing incidence. The amount of scattering and the fraction of

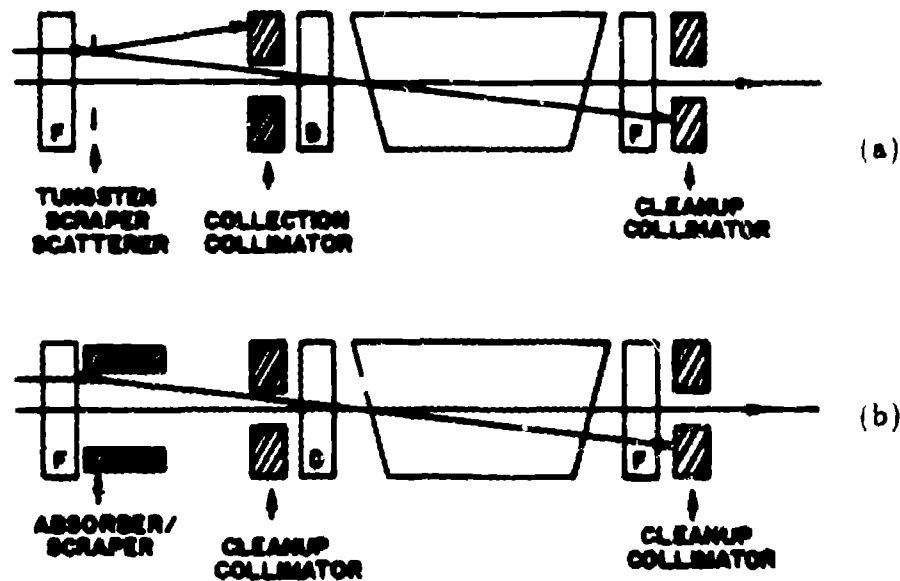


Fig. 13. Halo collimation concepts.

the scattered beam that spills elsewhere in the ring are not easily estimated.

More detailed study of these options is needed to determine which is best for PSR. Performance of the first option is more readily estimated. It has the advantage that the large scattering angles spread out the heat load on the absorber such that it may not need water cooling. The small moving scraper is a simpler mechanical device that is lightweight and probably does not need water cooling. Depending upon the amount of slit scattering, the second option may be more the efficient one in localizing the losses. However, it does have some disadvantages; the heat load is concentrated near the inner surface of the moveable absorber and it may well need water cooling. A large, moveable, water-cooled absorber is a complicated mechanical system that may require more frequent servicing, thus compromising the goal of containing the activation in highly reliable, passive devices that would seldom need servicing or removal.

## 4.2. Options for Improved Injection

It is now clearly understood that the key to reducing losses is reducing the number of times a stored proton traverses the stripping foil. In the present operation the probability for a stored beam particle to traverse the foil is between 50 to 100% per turn. A major goal for the upgrade is reducing this to around 5% or less primarily by improving the injected beam tune (some times called "match" or "matching"), improving injection "painting" in transverse phase space, and increasing the horizontal aperture of the ring.

### 4.2.1. Improved Painting in Phase Space

Injection "Painting" refers to procedures such as fixed offsets or programmed bumps used to control the beam density or other aspects of the way injected beam fills the phase-space acceptance of a ring. It can be used to reduce the number of foil traversals by the stored beam.

A fixed offset allows betatron motion to fill an interior region of phase space. A fixed vertical offset, which is depicted in Fig. 14, is presently in use at PSR. It was intended that the edge of the foil be on the vertical closed orbit of the ring and two standard deviations below the center of the  $H^+$  beam. This should result in a 50% probability per turn for the stored beam to intercept the foil. At PSR we have had, in the past, a good deal of uncertainty regarding the parameters of the  $H^+$  beam at the foil and thus the probability for the stored beam to hit the foil. With improved diagnostics and improved analysis procedures, we expected to resolve this issue in the coming running period.

A programmed closed-orbit bump is essentially a way to introduce an offset that varies with time. It can be used to move the stored beam off the foil so that some of it will not be able to hit the foil thereafter. The time profile of the bump can be chosen to optimise the beam spatial distribution or the foil hitting probability. For a given acceptance, the use of optimised programmed bumps improves both the beam density distribution and the foil-hitting probability compared with a fixed offset.

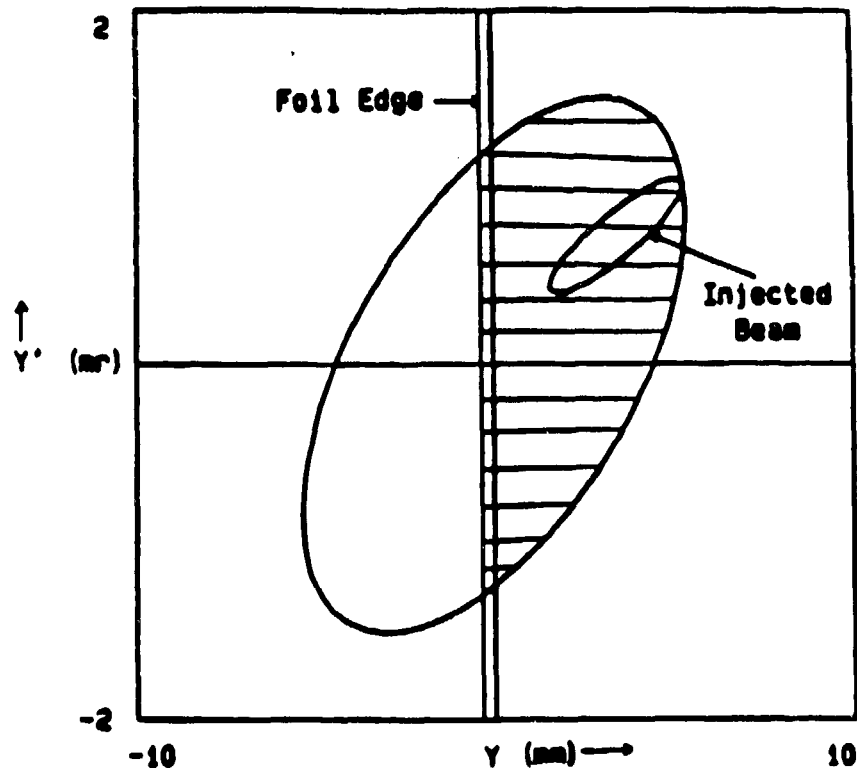


Fig. 14. Standard  $H^0$  injection at PSR with vertical offset.

#### 4.2.2. Improved Injected-Beam Tune

From an examination of Fig. 14, it is obvious that the foil hitting probability can be reduced by changing the shape and orientation of the  $H^0$  ellipse. Without changing the area of either the  $H^0$  or  $H^+$  beam ellipses, and while changing only the shape to a narrower, upright ellipse, the foil-hitting probability can be reduced by a significant factor ( $\sim 4$ ) as illustrated in Fig. 15. Unfortunately, such a tune of the  $H^0$  beam cannot be achieved with our system for generating  $H^0$ , given the location of the stripper magnet and the injection foil

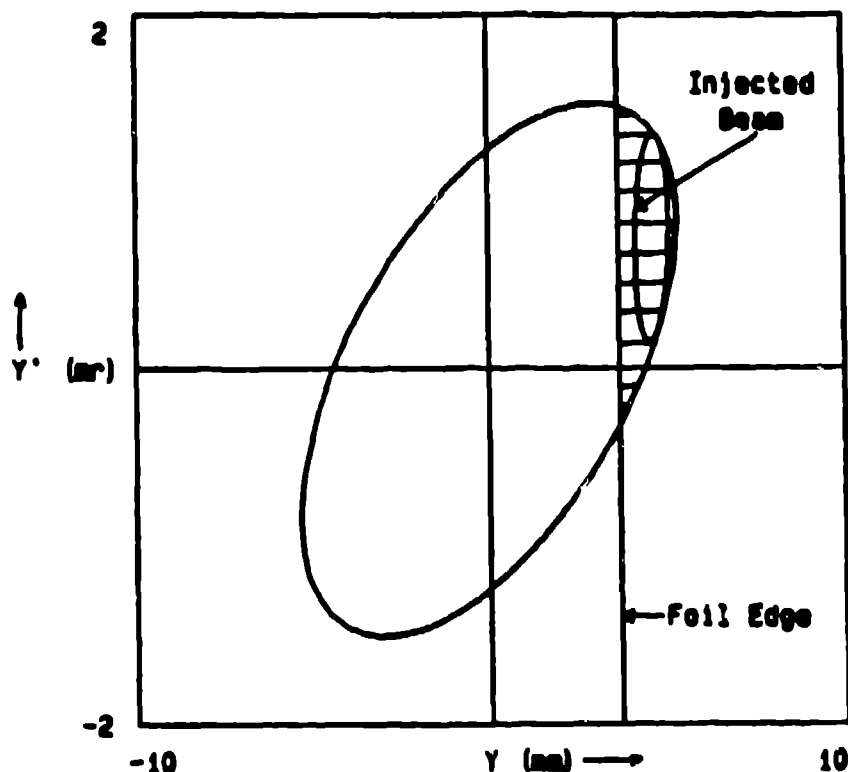


Fig. 15. Offset injection with the  $H^+$  tune optimized to reduce foil traversals by the stored beam.

#### 4.2.3. Improved Injection Foils

The carbon foils presently used at PSR are mounted on a C-shaped frame that supports the foil on three sides leaving a horizontal edge unsupported. The foil is positioned vertically to cover all of the vertically offset  $H^+$  beam but not all of the stored  $H^+$  beam. Thus, the foil covers the full horizontal aperture of the ring while in the vertical it covers less than the full aperture. An ideal foil for reducing losses would have a massless support with stripping material only in the region of the  $H^+$  beam spot.

A number of suggestions have been made for improving the foil support in ways that should reduce the probability for the stored beam to hit the foil. Yamane<sup>7</sup> at KEK has proposed "corner" foils for the JHF Compressor/Stretcher Ring. His foils have two un-

ported edges and can be positioned to cover an  $H^0$  beam offset in both dimensions while intercepting less of the stored beam. He has successfully tested corner foils with a low-energy nitrogen beam. This is a promising development for PSR and we will collaborate with KEK on tests of corner foils and other improvements to  $H^0$  injection.

Another concept being investigated at PSR is the use of very fine carbon filaments (4- to 5-microns diameter) to support carbon foils. This is work carried out in collaboration with a team from Westinghouse who have facilities at Hanford, Washington to fabricate foils supported in this manner. We expect to test fiber-supported foils in the beam during the 1989 running period.

#### 4.2.4. Improved $H^0$ Injection

The present method of injection using  $H^0$  can be improved using the techniques described above. However, it is much more difficult to improve the  $H^0$  beam tune at the foil since it is not possible to focus a neutral beam. One can only manipulate the  $H^-$  beam before it is converted to  $H^0$  or change the ring lattice so that the  $H^+$  beam (ring ellipse) better "matches" the fixed  $H^0$  beam. The constraints at the stripper magnet with its small gap severely limit the tuning of  $H^-$ . One can improve the match of  $H^0$  to the ring by moving the stripper foil to a location just upstream of the focusing quadrupole. Rotation of the stripper magnet, as proposed by Yamane,<sup>7</sup> can also help.

The important question is whether  $H^0$  injection can be improved sufficiently to meet our goal of reducing losses by an order of magnitude. We expect to answer this question with further analysis and experiment this summer.

#### 4.2.5. Direct $H^-$ Injection

$H^0$  injection suffers from two disadvantages: (a) the growth of emittance (about a factor of 3 for PSR) in the bend plane of the stripper magnet and (b) lack of flexibility in tuning the beam for optimum beam parameters at the injection foil. A way around

both of these difficulties is to inject the  $H^-$  beam directly. A scheme for doing this at PSR is shown in Figs. 16 and 17. The current in the two ring dipoles on either side of the injection straight section is reduced about 10% so that each bends the protons  $3^\circ$  less. The closed orbit of the stored beam is restored by the addition of a low-field dipole which bends protons by  $6^\circ$ . The field of this dipole is about 3.8 kG, which is low enough to cause negligible stripping of the  $H^-$  beam. An  $H^-$  beam can be transported to enter the low-field dipole in such a way that the  $H^-$  emerges from the dipole on top of and aligned with the stored  $H^+$  beam. A stripper foil to convert  $H^-$  to  $H^+$  follows. Some  $H^0$  will emerge

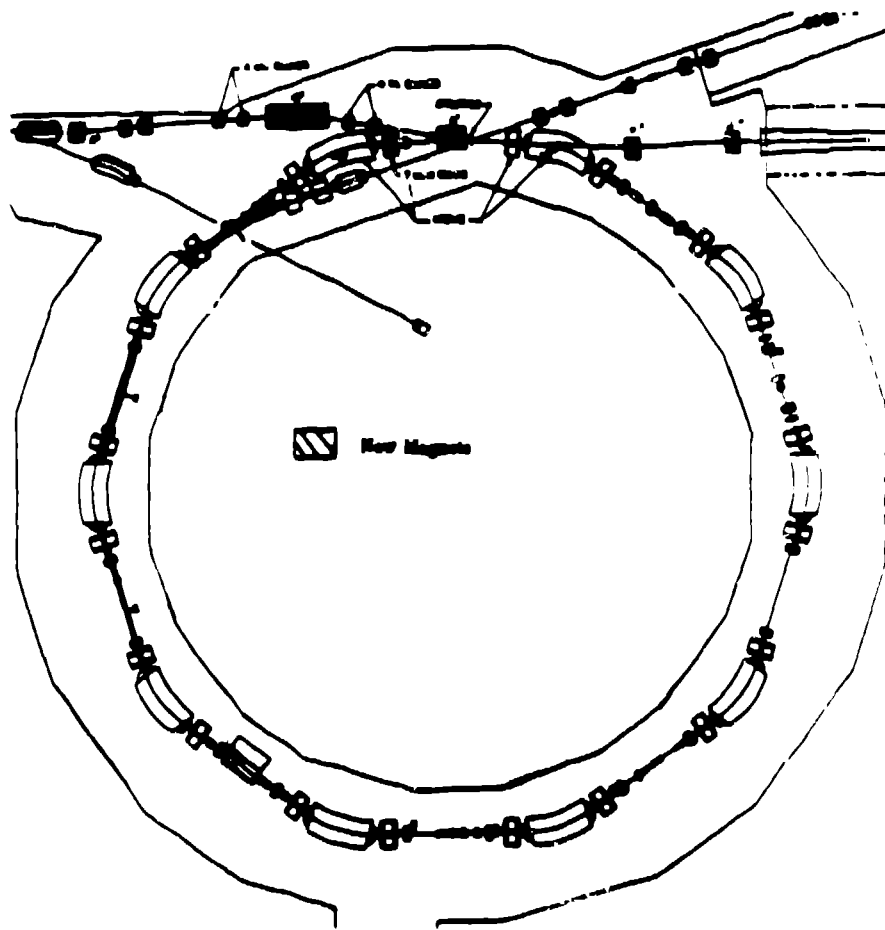


Fig. 16. Layout of PSR with direct  $H^-$  injection.

from the stripper foil; in addition, some  $H^-$  will miss the foil and be stripped to  $H^0$  in the fringe field of the ring dipole. Provisions are made to transport both  $H^0$  beams to the existing  $H^0$  beam dump.

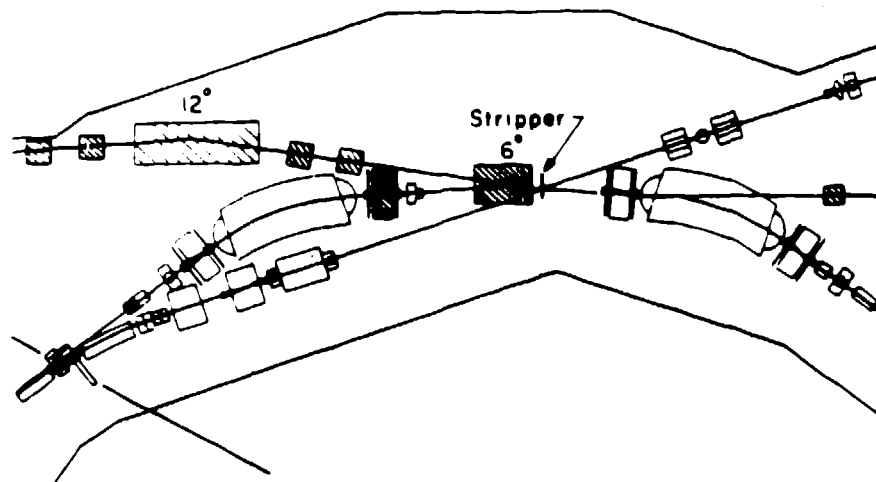


Fig. 17. Injection region for direct  $H^-$  injection.

Design studies are underway to find the optimum injection parameters for direct  $H^-$  injection and to estimate the improvement expected with respect to beam losses. Our planning for the upgrade assumes direct  $H^-$  injection since it offers greater promise for the needed reduction in losses. However, if it can be shown that the needed improvement is possible with less costly modifications of the  $H^0$  injection, then we would proceed in that direction. More study is needed before a final decision is made.

#### 4.3. Increased Aperture

Much of the beam loss occurs at the extraction septum, which is the limiting aperture in the horizontal plane. The rest of the ring has considerably more aperture; both the quadrupoles and the dipoles have larger horizontal apertures. The septum is a limit because the present extraction kickers are unable to provide a larger kick. A 50% larger kick (about 18 mrad) would allow the septum to be placed further from the stored beam and thereby increase the aperture by 50% and result in a factor of two larger acceptance of the ring in the horizontal phase plane.



Options which would provide the larger kick needed for full aperture extraction are under study. R & D on a ferrite kicker system is underway; a prototype pulser has been designed and is being fabricated at SAIC. The goal is a ferrite kicker system which provides 18 mrad of kick from ferrite magnets which occupy only one section of the ring instead of two. With the larger kick one may also need to replace the dipole and quadrupole just downstream of the kicker with ones of larger aperture to insure that the extracted beam is not distorted by nonlinear fields.

The larger aperture has two main advantages. The increased acceptance can be used to make painting more effective in keeping the beam off the foil for either  $H^0$  injection or direct  $H^-$  injection schemes. In the process of using the increased aperture to improve painting, the horizontal beam size will increase thereby reducing beam density and associated space-charge effects.

#### **4.4. Other Means of Reducing Losses**

Other methods to reduce losses include increasing the  $H^-$  beam intensity from the linac and/or increasing beam brightness by reducing emittance and beam halos. Increased intensity will reduce losses by reducing the accumulation time, hence, the number of foil traversals needed to achieve a given average current from the ring. Reduced emittance increases the effectiveness of all injection painting methods in keeping the stored beam off the injection foil.

Some efforts are underway to develop a higher intensity  $H^-$  source. These are not considered part of the present upgrade, but, as longer range studies aimed at longer-range improvements. If additional reduction in losses is needed for the upgrade, these efforts might be accelerated.

#### **4.5. Improved Beam Diagnostics**

Good beam-diagnostic instrumentation is necessary for a variety of reasons. Reliable, accurate, and well-understood instruments are needed for precise control of high-intensity beams and for conducting an efficient operation. They are also essential tools for effective experimental studies of beam dynamics issues. The present beam-position monitor (BPM) system needs improvement; it is sensitive to only the 201-MHz component of the beam. This is suitable

for use in the transport lines from the linac and for sensing the freshly injected beam at PSR, but not for locating the stored beam in the ring or in the extraction line. The present BPM's are also of limited use for studying broad-band phenomena such as the transverse instability. A program of BPM development is underway to develop instruments that satisfy these needs.

Knowledge of the distribution of  $H^-$  beam in transverse phase space is needed for careful setup of injection conditions. Present methods of reconstructing only the rms emittance are proving to be major limitations to a good optimisation of injection parameters. It is likely that a slit and collector method will need to be implemented to directly measure the phase-space distributions.

#### **4.6. Role of the Transverse Instability**

A coherent transverse instability has been seen at higher peak intensities at PSR. It is described in more detail elsewhere.<sup>8</sup> It is generally believed that we can run at  $3 \times 10^{13}$  ppp without the need for new hardware, such as an active damper, to control the instability. Some experimental studies have shown more or less stable operation at up to  $4 \times 10^{13}$  ppp using existing hardware to control the instability primarily by Landau damping. The techniques to enhance Landau damping, such as use of sextupoles and octupoles, generally increase the slow losses. In planning for the upgrade we assume that the instability is under control with the present hardware. However, more detailed experience with high peak currents is warranted and may change the present perception of the importance of the instability to the 100- $\mu$ A goal.

#### **4.7. Goals and Status of the Upgrade**

The goals of the upgrade are to develop and implement changes to PSR which will result in reliable delivery of 100 $\mu$ A at 20 Hz with beam availability greater than 75%. It is also a goal to complete the upgrade over the next three years and have it commissioned by the end of 1991. The planning for the upgrade is at the stage where numerous options are still being studied and R&D work on certain issues is underway. The scope of the project is known but much work remains before all choices are finalised. A conservative plan would include collimation in the ring, direct  $H^-$  injection,

increased aperture, and improved diagnostics carried as far as the present technologies permit. Budget realities cause us to seek the most cost-effective solution which meets our goals.

## **5. Perspective on the Storage Ring Option**

Enough experience has been gathered from PSR to offer some perspective on the storage- or compressor-ring option as the driver for an advanced neutron source. One must be careful to separate the generally applicable features of the experience from those which are due to local factors that are not particularly relevant elsewhere.

### **5.1. Reliability**

Poor reliability has become a stronger issue at PSR than it should be in general for a dc storage ring. It reflects past budget constraints coupled with changing requirements for the ring. The so called "short-burst mode" was the technically more challenging problem that drove many choices. That mode was discontinued late in the construction after numerous choices had been made. There was not an opportunity to redo the optimisation for the needs of the long-burst mode.

Good reliability was never an articulated, high-priority design goal for the PSR. It was and is too easy to compromise reliability to reduce initial construction costs. To some extent this will always happen but if reliability is a high-priority goal it should be included in the basic design goals.

### **5.2. Losses**

Losses are a difficult technical problem for most high-intensity proton machines. There is not a well-established theory for dealing with losses. Apart from the meson factories, there is not much experience to draw on. From the PSR experience, we can say that losses can be understood; but it requires careful, detailed work. We can also say that losses cannot be ignored; they, too, must be treated as a fundamental requirement in the design.

### **5.3. H<sup>0</sup> Injection**

With the benefit of hindsight, we would not recommend H<sup>0</sup> injection for a high-intensity accumulator or compressor ring. We do

not imply that  $H^0$  injection cannot work, but rather, that direct  $H^-$  injection is better. It does not suffer the significant emittance growth inherent in the use of magnetic stripping and a charged beam is much more easily manipulated to meet the various requirements for an optimised tune at the stripper foil.

#### 5.4. Conclusions

While there have been disappointments in the experience with PSR, they do not discredit the compressor-ring option as a driver for an advanced spallation neutron source. Compared to a ring that must accelerate as well as accumulate, the storage ring is intrinsically simpler. The one drawback is that injection losses in a storage ring, such as PSR, occur at the full energy rather than at a lower energy as is the case for a rapid cycling synchrotron typified by ISIS. One can tolerate and handle larger losses at lower energy.

There are several promising options for reducing or controlling losses at PSR. We are confident that a subset of these will enable PSR to reach  $100\mu A$  at 20 Hz. We expect to report operation with enhanced reliability and good beam availability in 1989 and increasing currents thereafter.

#### Acknowledgements

This work was performed under the auspices of the U. S. Department of Energy.

#### References

1. G. Lawrence, "The Performance of the Los Alamos Proton Storage Ring," Proc 1987 IEEE Particle Accelerator Conference, pp. 825-829.
2. R. Macek, D. H. Fitzgerald, R. L. Hutson, M. A. Plum, and H. A. Thiessen, "Analysis of Beam Losses at PSR," Proceedings European Particle Accelerator Conference, Rome, June 7-11, 1988. To be published
3. A. Jason, D. Hudgins, and O. van Dyck, "Neutralization of  $H^-$  Beams by Magnetic Stripping," IEEE Trans. Nucl. Sci., NS-28, pp. 2704-2706 (1981).

4. R. Macek, "PSR Beam Distributions II: Mismatched Gaussian," Los Alamos National Laboratory PSR Technical Note #153, October 1987.
5. H. Bruck, "Circular Particle Accelerators," LA-TR-72-10 Rev., Chap XIV (1972). Translation from French original "Accélérateur Circulaires de Particules" (1966).
6. H. A. Thiessen, "ARCHSIM Primer," Los Alamos National Laboratory, PSR Technical Note 89-002, March 1989.
7. I. Yamane, K. Kitagawa, H. Someya, and Y. Yano, "Injection of 1 GeV  $H^-$  Beam into the JHF I-A Ring," KEK Report 88-8, November 1988. Also I. Yamane, "JHP Compressor/Stretching Ring and Its Injection Scheme," invited talk at 1989 AHF Accelerator Design Workshop, Los Alamos, February 20-25, 1989, KEK Preprint 88-121, January 1989.
8. D. Neuffer, E. Colton, G. Swain, H. Thiessen, B. Blind, R. Hardekopf, A. Jason, G. Lawrence, R. Shafer, T. Hardek, J. Hurd, and R. Macek, "Transverse Collective Instability in the PSR," Particle Accelerators, 1988, Vol 23, pp 133-148.

## Shielding concerns at a spallation source

*G. J. Russell, H. Robinson, G. L. Legate, and R. Woods*  
Los Alamos Neutron Scattering Center  
Los Alamos, New Mexico 87545 USA

**ABSTRACT:** Neutrons produced by 800-MeV proton reactions at the Los Alamos Neutron Scattering Center spallation neutron source cause a variety of challenging shielding problems. We identify several characteristics distinctly different from reactor shielding and compute the dose attenuation through an infinite slab/shield composed of iron (100 cm) and borated polyethylene (15 cm). Our calculations show that (for an incident spallation spectrum characteristic of neutrons leaking from a tungsten target at 90°) the dose through the shield is a complex mixture of neutrons and gamma rays. High-energy (> 20 MeV) neutron production from the target is ≈5% of the total, yet causes ≈68% of the dose at the shield surface. Primary low-energy (< 20 MeV) neutrons from the target contribute negligibly (≈0.5%) to the dose at the shield surface yet cause gamma rays, which contribute ≈31% to the total dose at the shield surface. Low-energy neutrons from spallation reactions behave similarly to neutrons with a fission spectrum distribution.

### 1. Introduction

The Los Alamos Neutron Scattering Center (LANSCE)<sup>(1)</sup> uses 800-MeV protons from the Clinton P. Anderson Meson Physics Facility (LAMPF)<sup>(2)</sup> to produce neutrons for basic materials science and nuclear physics research.<sup>(3)</sup> Because it is a spallation source, LANSCE produces neutrons covering about 14 decades in energy (sub-meV to 800 MeV) and experiences shielding problems common to all such sources, but different from those of fission sources. We discuss the principles of spallation source shielding through a detailed calculation of a geometrically simple shield, and, using the same example, contrast spallation source spectrum problems with a fission spectrum neutron source.

At Los Alamos, we have a powerful Monte Carlo computational capability applicable to spallation neutron source design.<sup>(4)</sup> We have used this computational tool for various LANSCE shield designs including: a) proton beam line; b) target; and c) neutron beam line and beam stop.

### 2. Spallation Neutron Source Shielding Issues

#### 2.1 High-Energy Neutrons

For spallation reactions, we divide energy into two regions: low-energy (< 20 MeV) and high-energy (> 20 MeV). Low-energy neutrons are basically produced in three

ways: a) directly from intranuclear cascade processes; b) by evaporation; and c) from fission. These low-energy neutrons are emitted "more-or-less" isotropically and cause shielding problems like those for fission reactors. High-energy neutrons, resulting from nucleon-nucleon reactions, have a strong angular dependence and cause unique shielding problems. At  $0^\circ$  to the proton beam, high-energy neutrons can have energies up to the incident proton energy. As the angle with respect to the proton beam increases, the high-energy neutron spectrum softens considerably. *The presence of these high-energy neutrons and their strong angle-dependence are two reasons why shielding a spallation source is quite different than shielding a reactor source.*

## 2.2 Thin and Thick Targets

On its way to LANSCE, the LAMPF proton beam can strike a variety of objects (targets), ranging from proton beam transport pipe and magnets to the LANSCE target itself. Each of these "sources" presents different neutron spectrum and intensity to an adjacent shield, causing the effectiveness of the shield to be significantly dependent on the spill point.

For 800-MeV protons incident on stainless steel (one atom thick), the calculated double differential (energy and angle) neutron production spectra are illustrated in Fig. 1. One can see the strong angular dependence of the high-energy neutrons, but the low-energy neutrons are nearly isotropic.

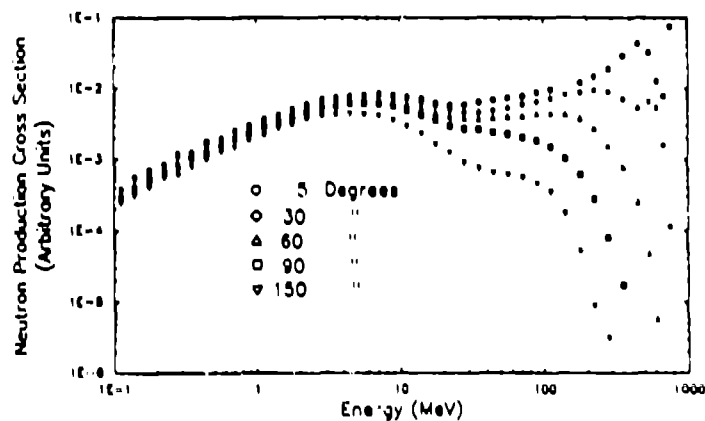


Fig. 1. Calculated neutron production spectra for 800-MeV protons on stainless steel.

For a thick target, both the shape and magnitude of the leakage neutron spectrum and the ratio of high-energy to low-energy neutrons can change dramatically from one target to another. The target itself "moderates", "self-shields", and "amplifies" the neutrons produced. The neutron spectrum (integrated over all angles) from a mild steel thick-target (50-cm-thick and 20-cm-diam) is shown in Fig. 2. In contrast, the

equivalent spectrum from a thin-target (0.3-cm-thick and 20-cm-diam) of the same material is also shown in Fig.2. The dramatic difference (both in intensity and energy) between the two leakage spectra is evident. Figure 2 also gives the neutron spectrum from a 30-cm-thick and 10-cm-diam tungsten target (a typical LANSCE target). For this target, low-energy neutrons account for 95.3% of the total neutron production, and high-energy neutrons 4.7%.

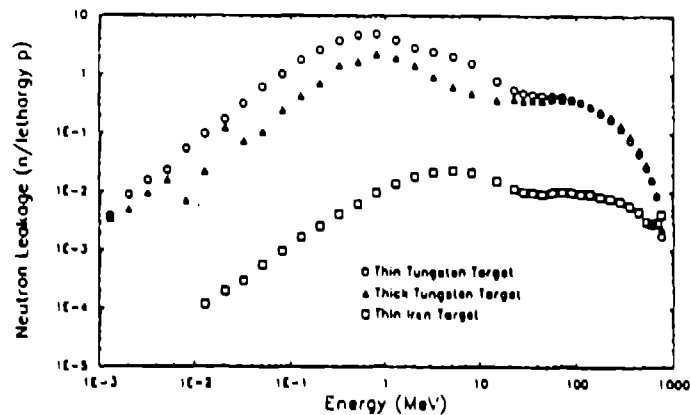


Fig. 2. Calculated neutron yields from thin and thick targets for 800-MeV protons.

*This is another reason why shielding a spallation source is more complex than shielding a reactor source: different leakage neutron spectra are produced depending upon whether the proton beam strikes a thin or thick target; neutron production is also material dependent.*

### 2.3 Thin and Thick Shields

In a particular shielding application, the distinction between "thin" and "thick" shields can be important and may affect the applicability of simplistic formalisms for estimating the neutron doses at the shield surface. If primary low-energy neutrons contribute significantly (either directly or by producing gamma-rays) to the total dose at the outer shield surface, we define the shield to be thin. Two other components contributing to the neutron dose are: a) high-energy neutrons, and b) secondary low-energy (evaporation) neutrons produced by high-energy neutron interactions in the shield itself. These secondary low-energy neutrons are distributed throughout the shield, and arise from the disappearance (attenuation) of high-energy neutrons as they "penetrate" the shield. Both the high-energy and secondary low-energy neutrons produce gamma-rays, which also contribute to the total dose at the shield surface.

*This is another complexity arising in shielding a spallation source relative to a reactor source: when a shield attenuates high-energy neutrons, low-energy neutrons are produced, i.e., the shield itself becomes a neutron source. Depending on the application, the*



high-energy neutrons plus progeny may dominate the dose at a shield surface.

## 2.4 Flux-to-Dose Conversion Factors

Another shielding complication has to do with flux-to-dose conversion factors for neutrons and gamma-rays. The flux required to produce one mrem per hour of dose is energy dependent as shown in Fig. 3.<sup>(5)</sup> It takes a flux of  $\approx 5.5$  n/cm<sup>2</sup>-s of 100 MeV neutrons to produce 1 mrem/hr of dose, compared to a flux of  $\approx 220$  n/cm<sup>2</sup>-s of 1 eV neutrons. At 1 MeV, it takes  $\approx 60$  times more gamma-ray flux than neutron flux to produce 1 mrem/hr. Thus, the energies of neutrons and gamma rays leaking through a shield can have profound effects on the total dose at the shield surface. The rapid change of the flux-to-dose conversion factors can cause significant errors in dose estimation, if the spectra are not well known.

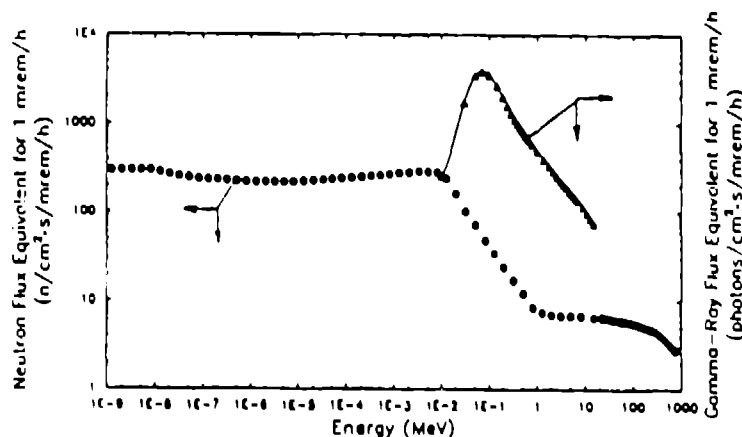


Fig. 3. Neutron and gamma-ray flux-to-dose conversions.

## 2.5 Flux and Dose

Neutron and gamma-ray fluxes are related to the physical number of neutrons and photons, respectively. Detectors used in LANSCE scientific instruments respond to flux; unwanted neutrons and gamma rays can cause background problems. However, these detectors are inside instrument shielding and their response includes the effects of the instrument shield on the incident neutrons and gamma rays. Dose, on the other hand, is also relevant because it is related to human biological response to radiation.

Because flux-to-dose conversion factors are energy dependent, flux and dose are attenuated differently by a shield. When a shield "attenuates" low-energy neutrons, it moderates (slows down) the neutrons within the shield (decreasing the neutron dose) and captures neutrons and produces gamma rays. Whether attenuation of flux or dose dominates the criteria for a shield design depends on the particular shield application.

Flux is important when shielding detectors; dose is important when shielding people.

## 2.6 Gamma Rays

Biologically, we need to concern ourselves with the total dose (neutron plus gamma rays) at the shield surface. Detectors also respond to both neutrons and gamma-rays, therefore, gamma rays must be accounted for when designing detector shielding. All low-energy neutrons that do not undergo particle reactions, such as  $(n,xn)$ ,  $(n,p)$ , etc., with nuclei are eventually captured in the shield or leak from it. In addition to capture and inelastic scattering gamma rays from low-energy neutron interactions, additional gamma rays are produced from the spallation process itself. These latter gamma rays may or may not be important in a particular shield application.

*We have identified another difference between spallation and fission source shielding to be an additional gamma-ray source from the spallation process itself.* Depending on the application, one may need to account for all three neutron components (primary low-energy, primary high-energy, and secondary low-energy) plus gamma rays when designing a shield for a spallation neutron source.

## 2.7 The Calculated High-Energy Neutron Source

A complication in using calculated high-energy neutron spectra in shield design is the potential that the computed angle-dependent spectra are incorrect both in magnitude and shape compared to measured results. There have been both excellent agreement and major disagreement between measured and calculated double-differential high-energy neutron production. In general, calculations underpredict measured cross section values. Until these problems are resolved, one may (in some shield calculations) multiply the calculated high-energy neutron production by some factor to account for these uncertainties. Such a bias may be consequential when deciding the relative importance between primary and secondary low-energy neutrons in a particular shield design.

## 3. LANSCE Shielding Concerns

LANSCE shielding issues can be broadly summarized as follows: a) adequate definition of the neutron source; b) proton beam line; c) service cell; d) target/moderator/reflector; e) target area; f) neutron collimator; g) longitudinal neutron beam line; h) transverse neutron beam line; i) neutron instrument; and j) neutron beam stop. We have used our Monte Carlo code package to address many of these shielding concerns.

## 4. Calculations for an Infinite Iron/Polyethylene Slab Shield

### 4.1 Problem Definition

To help understand the complexities of spallation source shielding, we chose a geometrically simple shield model (infinite slab). The shield (see Fig. 4) was composed of 100 cm of iron (mild steel) followed by 15 cm of borated polyethylene

(5 wt% natural boron) with a monodirectional point source of neutrons incident normal to the iron shield surface. The attendant neutron and gamma-ray progeny sum to give the total dose at various locations throughout the shield. By primary high-energy gamma rays, we mean those gamma rays produced by high-energy neutron interactions. Secondary low-energy gamma rays result from secondary low-energy neutron interactions. These two gamma-ray components sum to give a segment we call spallation gamma rays. Primary low-energy neutron interactions produce primary low-energy gamma rays. No gamma rays were assumed incident on the shield.

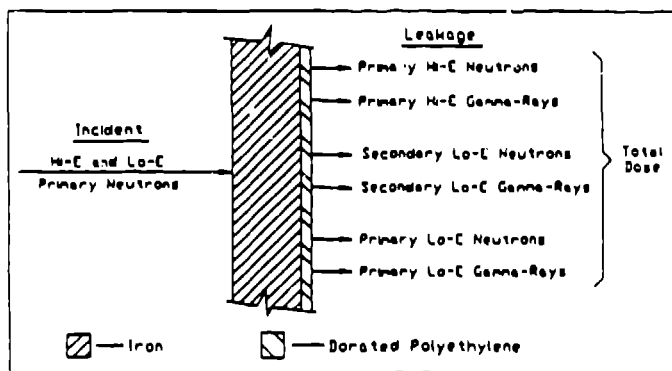


Fig. 4. Infinite slab shield mockup geometry.

A unit source of spallation neutrons calculated at  $90^\circ$  to the axis of a 10-cm-diam by 30-cm-thick tungsten target (see Fig. 5) was used as the primary incident spallation spectrum. In addition, we used a unit Watt fission spectrum, which is also depicted in Fig. 5.

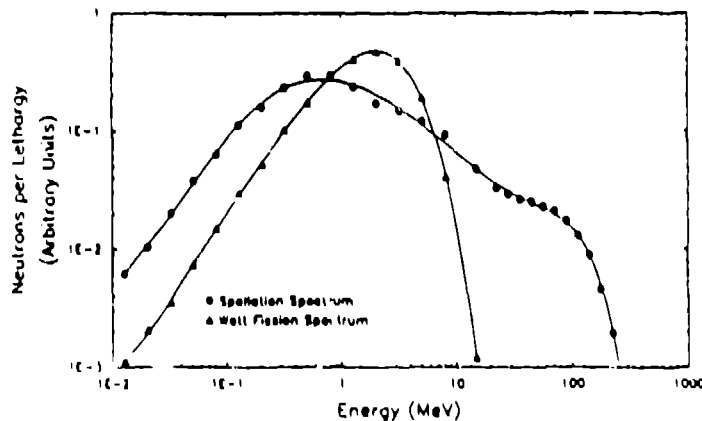


Fig. 5. Unit source spectra used in shield calculations.

## 4.2 Results

For the tungsten spallation neutron-spectrum in Fig. 5, primary low-energy neutrons account for 95.3% of the total neutron leakage from the target; primary high-energy neutrons account for 4.7%. Using this spallation neutron spectrum, we show calculated neutron and gamma-ray doses throughout the shield and at the shield surfaces in Figs. 6 and 7. Secondary low-energy neutron production is depicted in Fig. 6.

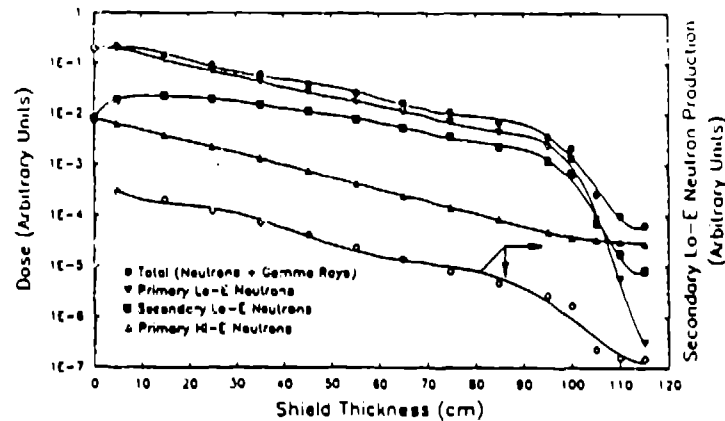


Fig. 6. Relative neutron and total dose through the iron/polyethylene shield for an incident spallation spectrum.

In Fig. 6, you can see the buildup of the secondary low-energy neutron dose as the high-energy neutrons are attenuated by the shield. The high-energy neutrons are attenuated very little by the polyethylene; secondary low-energy neutron production falls as well. At the outer surfaces of the iron shield low-energy neutron doses fall rapidly, due to neutron capture, enhanced moderation, and lack of isotropic reflection. The same arguments hold for the secondary low-energy neutrons; in addition, the source of these neutrons decreases rapidly. The doses at the shield surface are detailed in Table I.

The gamma-ray dose is further illustrated in Fig. 7. Gamma-ray production starts to increase at the iron/polyethylene interface and continues into the first part of the polyethylene. This increase is caused by the removal of neutrons via neutron capture and inelastic processes showing why, for some materials, it is important to account for gamma rays as well as neutrons in shield designs.

The effects of a unit Wau fission spectrum on neutron and gamma-ray doses for the same shield are shown in Fig. 8. A similar dose attenuation is observed here as for the primary low-energy neutrons in Fig. 6. At the shield surface in Fig. 8, the dose is essentially all caused by gamma rays. The complexity of spallation neutron source shielding compared to fission source shielding is seen in comparing Figs. 6 and 8.

Table I. Doses at the Surface of a Fe/CH<sub>2</sub> (5% B) 100/15 cm Shield

Dose Type	% of Total Dose	% of Incident Neutrons (W @ 90°)
Primary Hi-E Neutrons	43.0	4.7
Secondary Lo-E Neutrons	12.8	
Gamma-Rays from Primary Hi-E and Secondary Lo-E Neutrons	<u>11.4</u>	
Subtotal	68.1	
Primary Lo-E Neutrons	0.5	95.3
Gamma-Rays from Primary Lo-E Neutrons	<u>31.4</u>	
Subtotal	31.9	
Total	<u>100.0</u>	

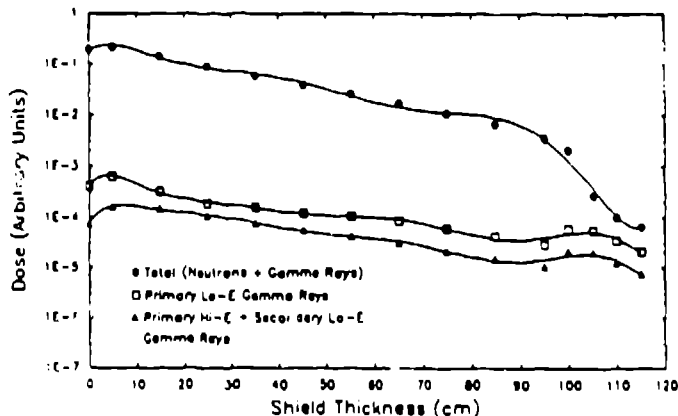


Fig. 7. Relative gamma-ray and total dose through the iron/polyethylene shield for an incident spallation spectrum.

Shielding calculations for spherical shields are underway.<sup>[6]</sup> One might expect spherical shields to behave neutronically different than infinite slab shields. One reason is that, for the infinite slab shield discussed here, ~79% of the primary low-energy neutrons incident on the inner shield surface are removed by back scattering and do not contribute to the dose at the outer shield surface. For a spherical shield, these "albedo" neutrons are incident on the opposite side of the shield, and, consequently, have repeated opportunities to contribute to the dose at the outer shield surface. Thus, depending on shield particulars, primary low-energy neutrons can contribute significantly to the dose at the outer surface of a spherical shield.

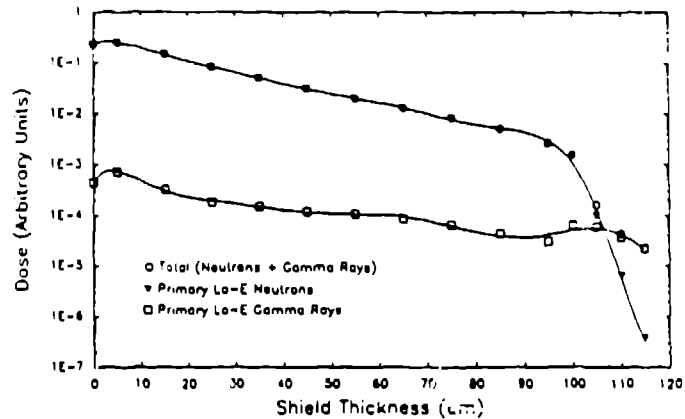


Fig.8. Relative neutron and gamma-ray dose through the iron/polyethylene shield for an incident Watt fission spectrum.

## 5. Conclusions

A spallation neutron source presents more difficult shielding problems than those posed by a reactor source. We demonstrated the basic differences between the two and showed the increased complexity of spallation-source shielding through a calculation for an iron/polyethylene shield. This example illustrates basic shielding principles for a spallation source; the particulars depend on the specific shielding problem. Shielding a fission source is similar to shielding the primary low-energy neutrons at a spallation source. The incident neutron spectrum and the shield geometry, composition, and thickness determine whether high-energy or low-energy neutrons dominate the neutron dose at the shield surface, and the relative importance of gamma rays.

## 6. Acknowledgements

We appreciate useful discussions with Tom Booth, John Hendricks, Bob Schrandt, Jerry Miller, Mike Howe, and Bob Mundis. We acknowledge the help of Dick Prael and Henry Lichtenstein. Many thanks to Dianne Hyer for reading the manuscript, and to Teri Cordova for typing help. We thank Roger Pynn for his support of this work.

This research was performed under the auspices of the U.S. Department of Energy, Office of Basic Energy Sciences.

## 7. References

1. G. J. Russell, H. Robinson, G. L. Legate, R. Woods, E. R. Whitaker, A. Bridge, and K. J. Hughes, the LANSCE Target System. In the Proceedings of the 9th Meeting of the International Collaboration on Advanced Neutron Sources, eds., F. Atchison and W. Fischer, September 22-26, 1986, SIN, Villigen, Switzerland, ISBN 3-907998-01-4, July 1987, pp. 177-244.
2. M. S. Livingston, LAMPF, a Nuclear Research Facility. Los Alamos National Laboratory Report, LA-6878-MS (1977).
3. F. A. Morse, Status Report on LANSCE, 1986. In Proceedings of the 9th Meeting of the International Collaboration on Advanced Neutron Sources, eds., F. Atchison and W. Fischer, September 22-26, 1986, SIN, Villigen, Switzerland, ISBN 3-907998-01-4, July 1987, pp.31-43.
4. R. E. Prael, High-Energy Particle Monte Carlo at Los Alamos. In Monte Carlo Methods and Applications in Neutronics, Photonics, and Statistical Physics, eds., R. Alcouffe, R. Dautray, A. Forster, G. Ledanois, and B. Mercier, Springer-Verlag Publisher, Berlin/Heidelberg, 1985, pp. 196-206.
5. A. J. Miller, Los Alamos National Laboratory (private communication).
6. G. J. Russell, et al., High Performance Shields, in these proceedings.

## Target system materials and engineering problems

*W. E. Fischer*  
Paul Scherrer Institute (PSI)  
CH-5232 Villigen  
SWITZERLAND

### 1 INTRODUCTION

As a model for our discussion we consider a spallation source which is fed by a high power proton beam of the order of one Megawatt (pulsed or continuous). Such a source will have roughly the following flux performance:

- i) pulsed  $\phi_{max} \geq 10^{16} n/cm^2s$
- ii) continuous  $\bar{\phi} \geq 10^{14} n/cm^2s$

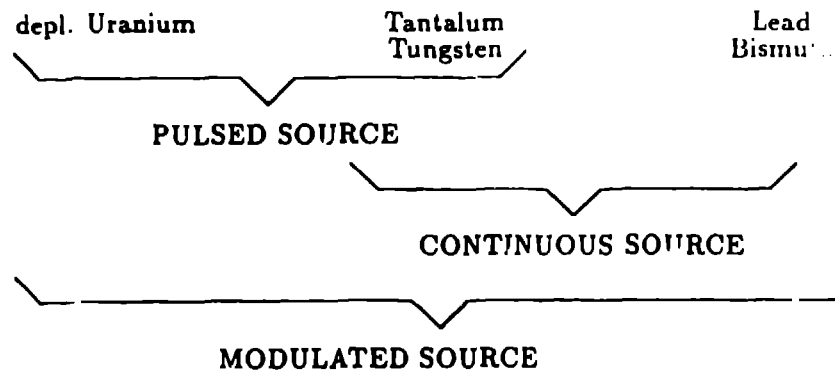
The materials used for the target stations and particularly for the spallation target itself depend on the source concept we are aiming for — that is, whether the source is built for

- pulsed
- modulated
- or continuous operation

The difference of the materials used is mainly determined by the neutronics considerations. Depending on the choice of the materials for the target systems, the characters of materials problems met, are of somewhat different nature.

For spallation sources realized or planned up to now, the following choices for the target materials have been taken (or considered).





In this paper we refrain from considering the booster-target concept.

The typical materials problems for the engineering of the various spallation targets can be summarized as follows:

- |                                   |   |
|-----------------------------------|---|
| Depl. Uranium                     | - Heat density, Thermal stress                    |
|                                   | - Phase transitions (temperature range)           |
|                                   | - Disturbance of material properties by radiation |
|                                   | - Micro- and Macro-Cyclic Stress                  |
|                                   | - Cladding  |
| Tantalum<br>Tungsten              | - Heat density, Thermal Stresses                  |
|                                   | - Disturbance of material properties by radiation |
|                                   | - Micro- and Macro-Cyclic Stress                  |
|                                   | - Cladding ?                                      |
| Lead<br>Bismuth --- Liquid target | - Heat density                                    |

We assume that for the case of a liquid target a target window is needed in any case - even e.g. if the proton beam is injected from above. Out-gassing of volatile spallation products at higher target temperature can not be avoided. Hence a separation between target material, beam line - and accelerator - vacuum is necessary.

The material problems for this target version become therefore the problems for the

target window — Heat density, Thermal stress  
 Disturbance of material properties by radiation  
 Compatibility between liquid and solid metal  
 Macro-Cyclic Stress

We recognize that for each target version quite specific difficulties have to be overcome. On the other hand there is a whole set of problems which is common to all the target versions.

These are:

- i) heat load in the region of proton beam interaction
- ii) Thermal stress and cycling
- iii) Radiation Damage

## 2 POWER DENSITY IN TARGETS

For the discussion of the heat load of the target we use the following semiempirical data:

- i) parameters of the proton beam

The proton beam is characterized by the two parameters - total beam current ( $I_p$ ) and a parameter for the beam width. For gaussian profiles we write

$$\frac{dI}{df} = \frac{I_p}{\pi\sigma^2} e^{-r^2/\sigma^2}$$

If a parabolic profile is assumed we use

$$\frac{dI}{df} = \frac{2I_p}{\pi r_0^2} \left[ 1 - \frac{r^2}{r_0^2} \right]$$

The maximal current density for the first case is given by

$$j_{max} = \frac{I_p}{\pi\sigma^2}$$

The same maximal current density is obtained for the second case if we put

$$r_0 = \sqrt{2} \cdot \sigma$$

- ii) power density in the material

For the power density we use

$$h(z) = \alpha \cdot \frac{\sum E \cdot j_p}{\exp(-\sum H(E))} \cdot e^{-Ez}$$

$$\Sigma = \frac{\rho}{A} \cdot 6 \cdot 10^{23} \cdot \sigma_{tot} [cm^{-1}]$$

total macroscopic cross section  
of protons with kinetic energy E  
in a material of density  $\rho$   
and atomic number A

$$R(E) = 233 \cdot \rho^{-1} Z^{0.23} (E[GeV] - 0.032)^{1.4}$$

This is the range of protons in this target material. The parameter  $\alpha$  depends on the target geometry.  $(1-\alpha)$  expresses essentially that part of the energy which escapes the target as kinetic energy of secondary particles. From Monte Carlo investigations of the cascade process we know that  $\alpha = 0.6 - 0.8$ ; here we assume  $\alpha = \frac{2}{3}$ .

iii) Neutron yield (non fissile)

$$Y = 0.1(A + 20) (E[GeV] - 0.12)$$

The contribution of fast fission in uranium targets depends rather strongly on the material distribution and the size of the target. We do not need it here.

As a typical example we consider tungsten as target material ( $Z = 74$ ,  $A = 184$ ) and a proton beam energy of 1 GeV.

The range of the protons is

$$R(\rho) := \frac{600}{\rho} [cm]$$

$\rho$  is here the effective density of the target material including the cooling medium.

The yield is  $Y = 18 \frac{n}{p}$

For a beam current density of  $20 \frac{\mu A}{cm^2}$  (typical) the maximal heat load in a target plate becomes

$$h_{max} = 1.42 \frac{kW}{cm^2}$$

These are the typical values which have to be considered.

**A comparison of the heat load with a beam-tube reactor**

The thermal flux in the reflector of a research reactor has the following property

$$\phi = \frac{P}{A} = \frac{P}{V^{2/3}} = P^{1/3} \left( \frac{P}{V} \right)^{2/3} = P^{1/3} \cdot \rho^{2/3}$$

P is the total core power, A and V the core surface and volume resp. and

p the power density in the reactor core.

The corresponding relationship for a spallation-source is very roughly

$$\phi \sim \frac{P_p}{r^{1/2}}$$

$P_p$  is the power of the proton beam and r the radius of the target. For pulsed sources  $\phi$  depends strongly on details of the geometry and materials used for the moderator. We have also to keep in mind that  $\phi$  is not the only figure of merit for a pulsed source.

From these relations we conclude that

- i) the reactor design aims rather for high power density, then for high total power
- ii) For a spallation source we essentially aim for high beam power. Decreasing the target size would increase the power density on a window like  $p_w \sim \frac{P_p}{r^2}$

### The Problem of Power Density

As general orientation we give here some data for a few prominent neutron sources (operational or planned)

	P[MW]	V(active)[l]	$\bar{p}[\frac{MW}{t}]$	$\phi_{th}[\frac{n}{cm^2s}]$	$\frac{n}{cm^2s}$ per MW
ILL	57	35	1.6	$1.5 \cdot 10^{18}$	$2.6 \cdot 10^{13}$
Oak Ridge	270	35	8.6	$10^{18}$	$3.7 \cdot 10^{13}$
SINQ	1	3	0.33	$1.5 \cdot 10^{14}$	$1.5 \cdot 10^{14}$

From these numbers it is evident that SINQ has a very high "neutronic efficiency". In an attempt to push this type of source towards higher flux the average power density will not be the main problem. This favorite situation is caused by:

- i) the low power deposition per neutron produced by the spallation reaction  $55 \frac{MeV}{n}$  as compared to  $140 \frac{MeV}{n}$  in a fission reactor
- ii) the compact target

iii) virtual absence of flux depression

However, if we want to achieve a flux of e.g.  $5 \cdot 10^{16} \frac{n}{cm^2 s}$ , we have to feed a SING-type source with a beam current of  $J_p \simeq 30 \text{ mA}$ , leading to a current density of  $400 \frac{\mu A}{cm^2}$  from the proton beam. The power density in a stationary target-window or-plate becomes larger than  $20 \frac{MW}{cm^2}$ . Hence a moving target including target-window seems to be unavoidable.

We admit that for a pulsed source the peak flux  $\phi_{max}$  is for a large class of experiments equivalent to the continuous flux  $\phi$  of a steady source. The IPNS II proposal [1] considers a pulsed proton beam (60 Hz) with a current of  $I_p = 500 \mu A$  at an energy of 800 MeV. With an uranium target the system could provide a peak flux of  $10^{16} \frac{n}{cm^2 s}$  with a time average of  $1.8 \cdot 10^{13} \frac{n}{cm^2 s}$ .

The power density in the first target plate would be  $p_{max} \simeq 2 \frac{kW}{cm^2} (2 MW \text{ all } l)$ . This is comparable to the power density in the ILL-reactor and therefore does not seem to be unfeasible. However, in view of the thermal cycling problems and the radiation damage due to the high energy proton beam, we may have some doubt concerning a sufficiently long lifetime of this target.

### 3 RADIATION DAMAGE

Radiation damage is certainly one of the main causes limiting the lifetime of a target and the structure material in its vicinity. Although the damage produced by the radiation field escaping the target has to be considered the most severe effect is produced by the proton beam in the material exposed to it. While the heat load relative to the neutron source strength in a spallation environment is lower than in a fission reactor, radiation damage effects might be more severe in a spallation neutron source due to the presence of high energy particles.

An estimate for the number of displacements in the materials is given by

$$S \left[ \frac{dpa}{s} \right] = \eta \cdot \frac{\sigma E_D}{2 E_d} \cdot \phi \cdot 10^{-13}$$

$E_D$  and  $E_d$  are the damage and displacement energies,  $\eta = 0.8$  is the collision efficiency factor and  $\phi$  the particle flux  $(cm^{-2} \cdot s^{-1})$ . For the damage rate due to the proton beam we can write accordingly

$$S \left[ \frac{dpa}{s} \right] = 3.26 \cdot 10^9 \cdot \frac{\sigma E_D}{E_d \cdot D^2} \cdot I_p \text{ (mA)}$$

where D is the beam diameter

An idea about the gas production - for our case He and H have the main significance - can be obtained by

$$P = \sigma \cdot \phi \cdot 10^{18} = \frac{7.95 \cdot 10^{-3} \cdot \sigma \cdot I(mA)}{D^2}$$

The relevant parameters for a proton energy of 800 MeV for a few materials are given in the following table

	$(\sigma E_D)[b \cdot keV]$	$E_d[eV]$	$\sigma_{He}[b]$	$\sigma_H[b]$
Al	63	40	0.21	0.86
Steel	300	40	0.32	2.52
Cu	330	30	0.40	2.58
Mo	900	58	0.58	4.00
V	1430	65	0.58	5.13

Let us now estimate the expected damage in a window or a first target plate after a running time of 6000 hours. We assume a maximal current density in the proton beam of  $20 \frac{\mu A}{cm^2}$ . This corresponds to the operation conditions of one year at SINQ.

	Material	dpa	He(appm)	H(appm)
Window:	steel	8	820	6500
	tungsten	24	1500	13200

For material in the immediate vicinity of the spallation-target, exposed to the secondary radiation field but not to the proton beam, we obtain:

	Material	dpa	He(appm)	H(appm)
	steel	0.9	6	31
	aluminium	0.2	4	11

The numbers of this table have been extracted from actual measurements of the He gas production in test samples in the TRIGA neutron station <sup>2</sup> and from Monte Carlo calculations <sup>3</sup>.

We are now confronted with the everlasting question: "What do these numbers tell us about the actual macroscopic properties of the material?"

The only statement we can make at this place is the following (optimistic version): If the window lasts safely for one operational year, the structure material in the vicinity should have a lifetime of more than ten years.

In order to obtain quantitative information about the behaviour of the irradiated material experimental tests of the macroscopic material properties are needed. There is no other choice today. Such an attempt is shown in the following.

This data was taken at LANL for a window-material test for the SINQ-target [4]. The irradiation was made at samples which were in contact with molten Pb/Bi - the SINQ target material - in order to search for corrosion effects. The samples were irradiated by the proton beam up to estimated damage parameters:

$$S = 1.7 \text{ dpa} \quad P_{He} = 173 \text{ appm} \quad P_H = 1360 \text{ appm}$$

The performance of Fe, Ta and the steels Fe - 2.25 Cr - 1 Mo, Fe - 12 Cr - 1 Mo (HT9) are shown in Fig. 1 - 3. As rather expected, the pure metals lose their ductility, while the steel samples perform well. These type of steel is therefore a genuine candidate for the target-window and -container material. Further testes, up to higher radiation damage are however in preparation.

Investigation about swelling of irradiated materials has mainly be done in reactors. This radiation environment leads mainly to dpa-dominated swelling. Its onset starts for steels between 20 - 30 dpa. Due to the presence of high energy particles in the radiation field of spallation targets, material test with high  $\frac{He}{dpa}$ -ratio are more relevant. Useful data is still rather rare.

Much information about the damage problems of uranium targets could be gathered from the operational experience of the ISIS-target. Two targets have been used up to end of life and subsequently analysed. These matters are discussed elsewhere at this conference [5] - we hence restrain from any further discussion.

## 4 THERMAL STRESSES

As a reference case for our discussion we assume a plate irradiated by a proton beam whose power deposition is given as discussed in chapter 2. The cooling medium is assumed to cover either

- 1) the front- and back side of the plate (possibly also the periphery) as a model for a target plate - or

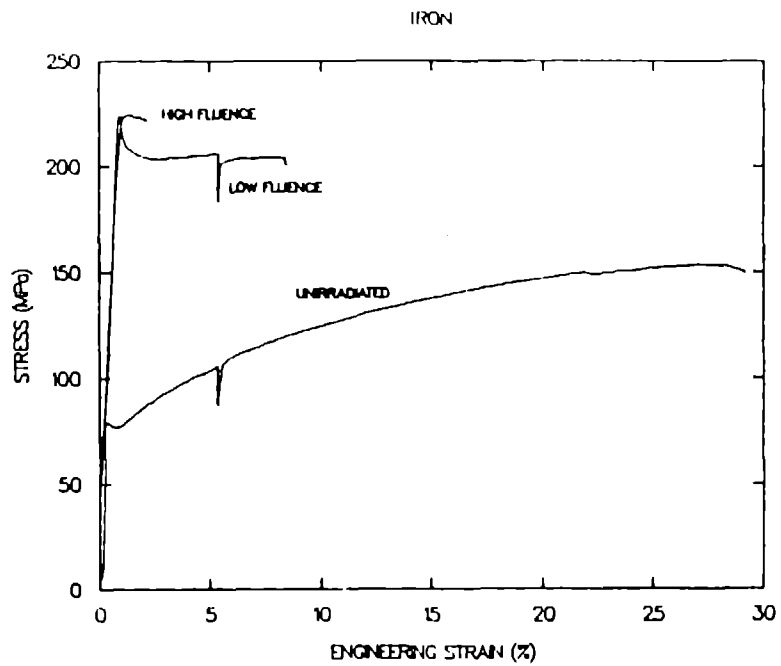


Fig. 1 Stress-strain behavior of pure iron after irradiation with 800-MeV protons. Low fluence:  $4.8 \times 10^{19}$  p/cm<sup>2</sup>; High fluence:  $5.4 \times 10^{20}$  p/cm<sup>2</sup>; Sample temperature was 400°C.

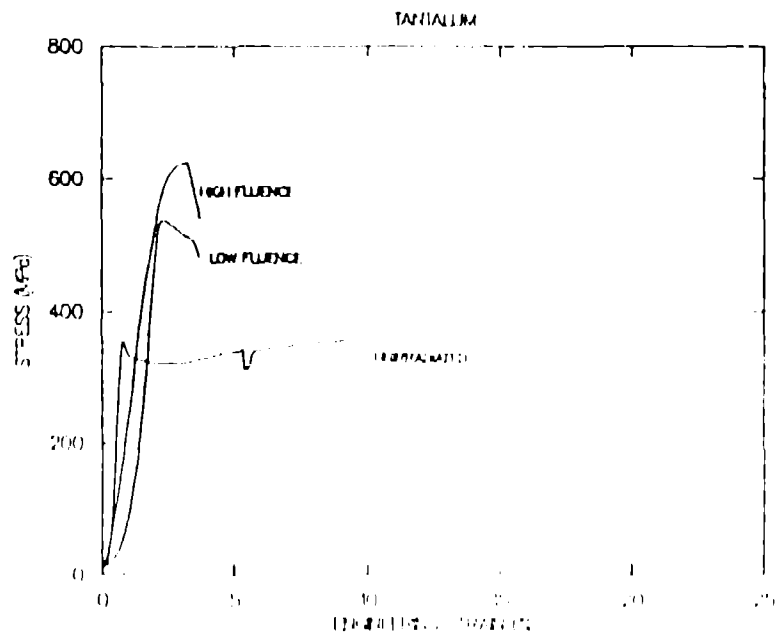


Fig. 2 Same as Fig. 1. Material: tantalum



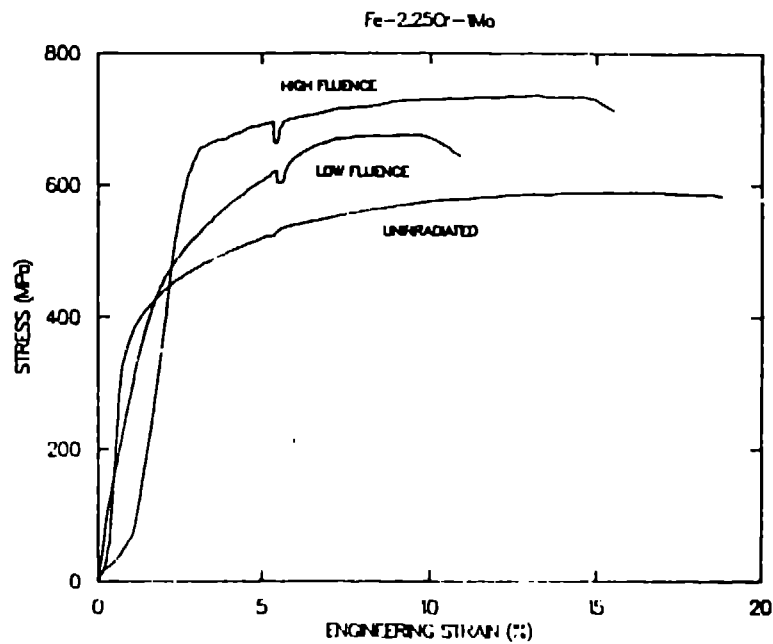


Fig. 3 Same as Fig. 1. Material: Fe - 12 Cr - 1 Mo steel.

ii) the back-side only as a model for a target window

Depending on the plate thickness, the temperature of the cooling medium and the heat-transfer from the plate to the cooling medium, we obtain temperature gradients in the plate, which may lead to considerable thermal stresses.

Furthermore, for a pulsed source the thermal stresses are not stationary - they follow "micro cycles" corresponding to the pulse-sequences of the proton beam. An other source for non stationary loads is the "macro-cycling" due to instabilities in the operation of the accelerator. As a consequence the target material deteriorates due to thermal cycling growth. This effect is particularly strong in materials which go through phase transitions within the temperature range covered during a cycle (e.g. uranium). Synergetic effects with swelling due to gaseous fission and spallation products as well as He gas production have to be taken into consideration also.

In principle the thermal stress is determined by

- symmetry properties and kinematics
- Hook's law

- equilibrium conditions

if the temperature distribution in the material is known. For a cylindrical plate we obtain

$$\sigma_r = \frac{\beta E}{1-\nu} \int_{r'}^R \frac{dr'}{r'^3} \left[ \int_0^{r'} \rho^2 \frac{dT}{d\rho} d\rho \right] = \sigma_\phi$$

$$\sigma_s = E\beta \left[ T - \frac{2}{R^2} \int_0^R T r dr \right] + \nu \left[ (\sigma_r + \sigma_\phi) - \frac{2}{R^2} \int_0^R (\sigma_r + \sigma_\phi) r dr \right]$$

E is Young's modulus,  $\nu$  the Poisson contraction ratio and  $\beta$  the parameter for thermal expansion. R is the radius of the plate.

The problem can be solved either by the powerful method of finite elements for more complicated geometries or under certain circumstances even analytically; e.g. in the present case the transversal problem, layer by layer in s-dimension. The T(r) - distribution is then given by a Fourier-Bessel serie [6]. If T(r) is not too narrow, that is the proton beam is sufficiently broad, one to two terms are sufficient for a 1 % precision.

As typical examples we show here data from the

- LANCE II, W-target [7]
- SINQ, window [6]
- IPNS II, U-target [1]

LANCE II, Fig. 4 - 6

beam power 1 MWatt

target plate: diameter 10 cm, thickness 1 cm

heat transfer to cooling medium is  $1.4 \frac{\text{Watt}}{\text{cm}^2}$  °C.

The maximal temperature in the center of the target plate is 900°C. The stress distribution contains components reaching values up to  $5500 \frac{\text{kg}}{\text{cm}^2}$  (550 MPa). These correspond to 70 % of the tensile yields of the material.

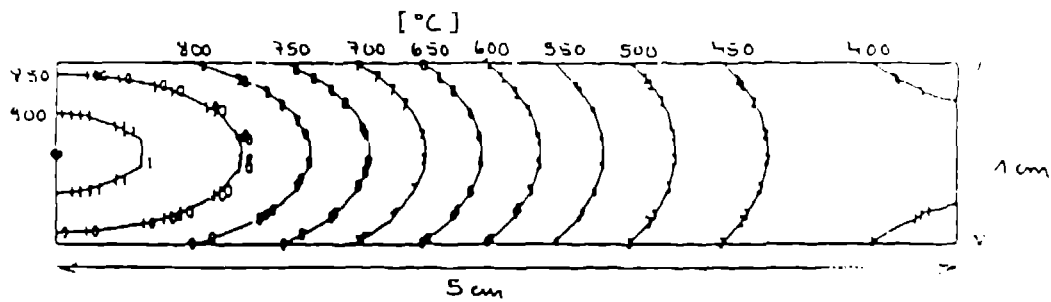
SINQ Fig. 7 - 8

beam power 0.9 MWatt

target plate: diameter 16 cm, thickness 0.6 cm

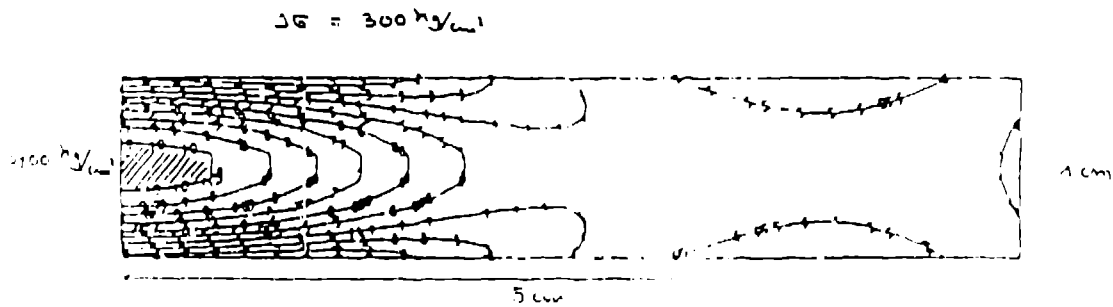
heat transfer to the cooling medium on one side of the plate (window) is assumed to be  $3.9 \frac{\text{Watt}}{\text{cm}^2}$  [8]. This performance

is based on model measurements



AHF, SPALLATION NEUTRON TARGET, W, 1 MICROSEC PULSES

Fig. 4 Temperature distribution in a tungsten target plate for a beam power of 1 MWatt. Cooling is on both plate sides with  $1.4 \text{ W/cm}^2 \text{ } ^\circ\text{C}$ .



AHF, SPALLATION NEUTRON TARGET, W, 1 MICROSEC PULSES

Fig. 5 Stress distribution for the same target plate as Fig. 4.

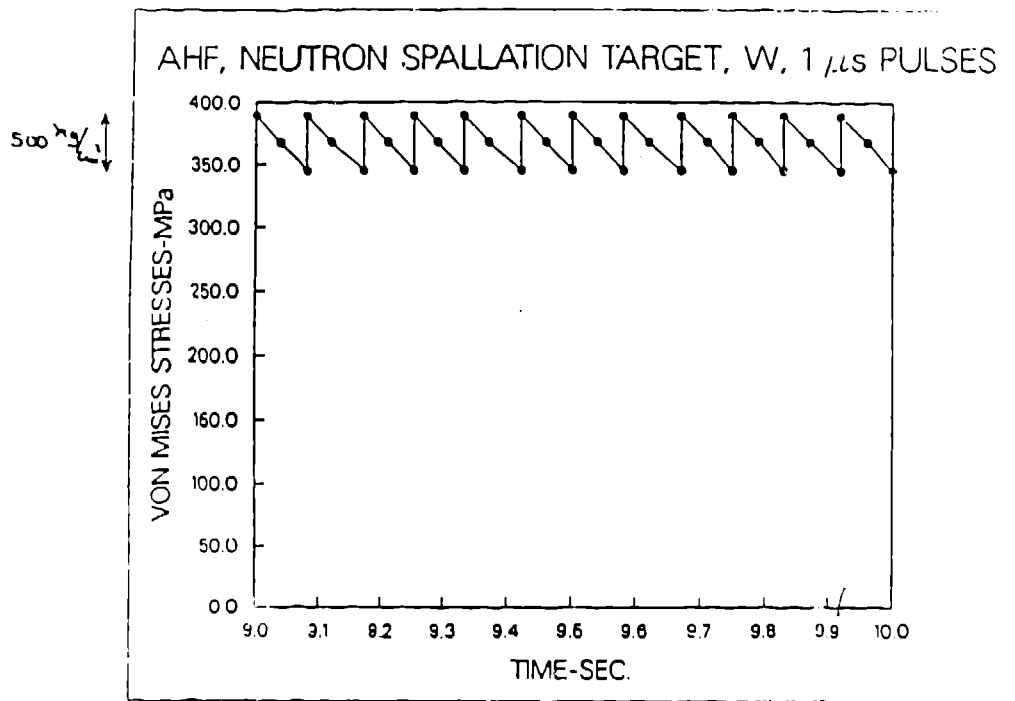


Fig. 6 Thermal cycling of the maximal von Mises-stress (a measure for yielding) due to the pulsed proton beam.

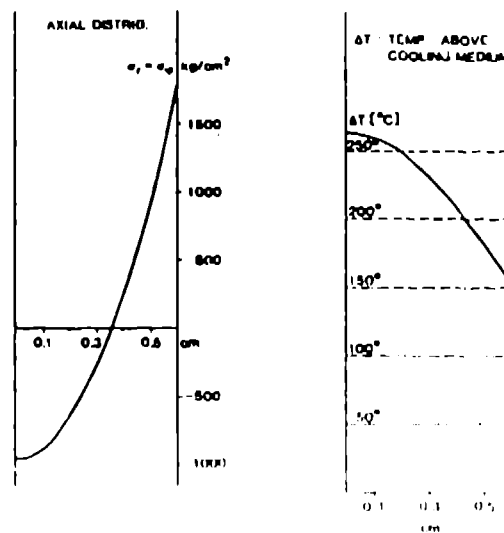
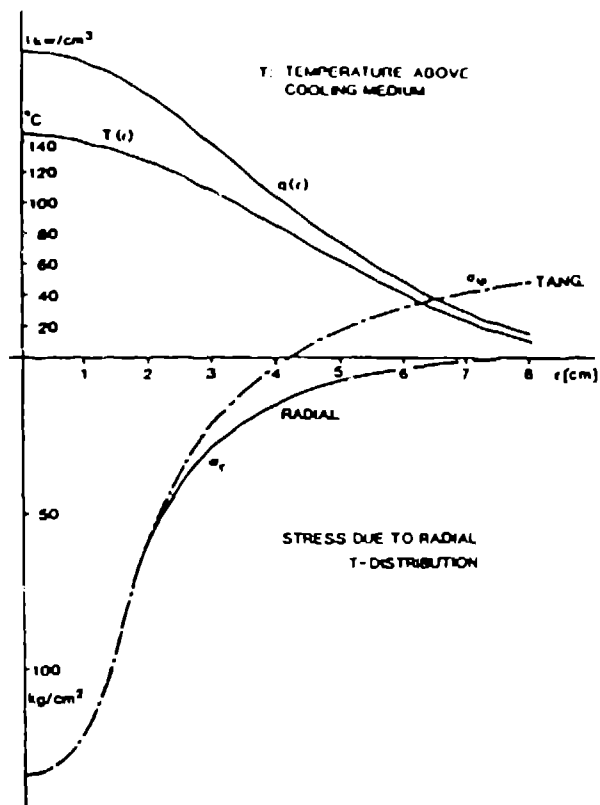


Fig. 7 Longitudinal temperature--and stress-distribution in a tungsten plate cooled at one side only. Heating is with a proton beam of 600-MeV energy and a current of 1.5 mA. Heat transition at the cooled surface is 3.9 W/cm<sup>2</sup> °C.



**Fig. 8** Radial temperature--and stress distribution at the cooled back side of the tungsten plate due to a proton beam of 600-MeV energy and a current of 1.5 mA. The radial beam profile is a Gaussian with  $\sigma = 5$  cm.

Due to the relatively large beam diameter (10 cm) the maximal current-density on the plate is  $20 \frac{\mu A}{cm^2}$ . The corresponding maximal temperature becomes 380 °C. The stress distribution reaches -1100  $\frac{kg}{cm^2}$  (radial and tangential compression) at the front of the plate and 1630  $\frac{kg}{cm^2}$  at the back (tensile)

IPNS II Fig. 9 - 11

beam power 400 kWatt

parabolic beam profile, truncated at 3 cm radius

The performance of the plate cooling has to be such, to keep the maximal temperature of the (U - 10 % W) plate below 400 °C.

$$k \partial_r T = h(T_{Mat} - T_{cool}) \quad k = 15.25 \frac{W}{cm^2 \cdot ^\circ C}$$

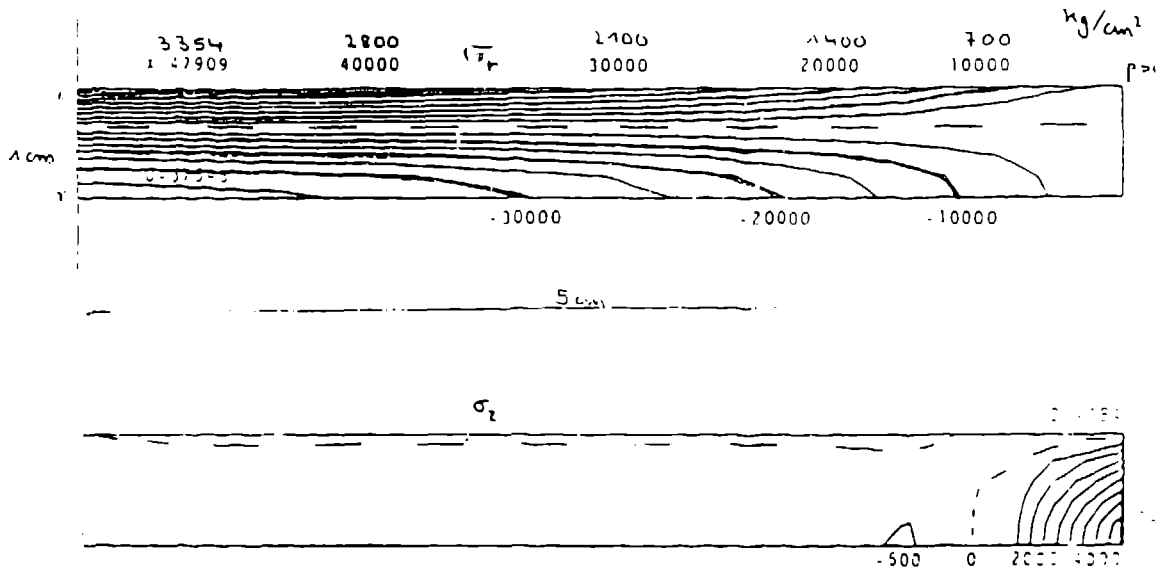


Fig. 9 Isostress lines for the radial and longitudinal stress distribution in a uranium-molybdenum disk. Beam power is 0.4 MWatt.

The cooling medium would be Na - K.

The result is a maximal temperature of 360 °C. The stress distribution contains radial and tangential compression of  $-2800 \frac{\text{kg}}{\text{cm}^2}$  in the center and a tensile stress of  $+2800 \frac{\text{kg}}{\text{cm}^2}$  at the back- and frontside of the plate.

While these stresses are well within the yield of the U - 10 % W-target material, they exceed at  $r \approx 0 \text{ cm}$  the yield of the Zirkaloy cladding. In view of the experience with the ISIS-target concerning swelling due to thermal cycling, this case seems to us at the ultimate limit of feasibility.

## 5 CONCLUSIONS

We tried to discuss the common problems of target design.

- power load
- radiation damage
- thermal stress

While each of these problems may find a more or less simple solution, the challenge for the engineers starts with the attempt to solve these problems simultaneously. The following kind of dialectics has then to be considered

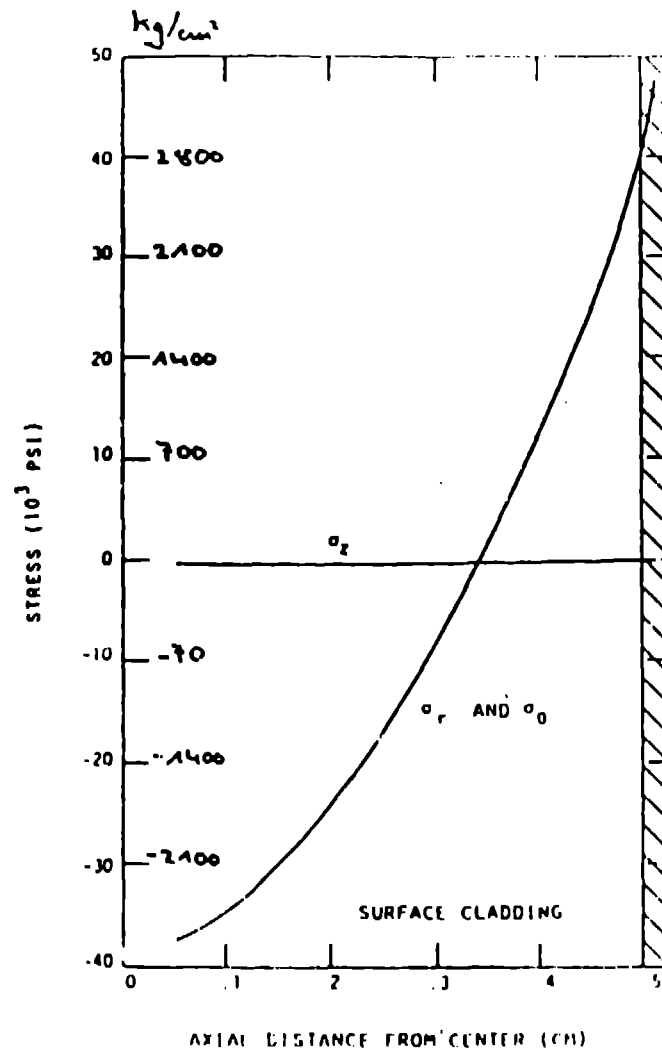
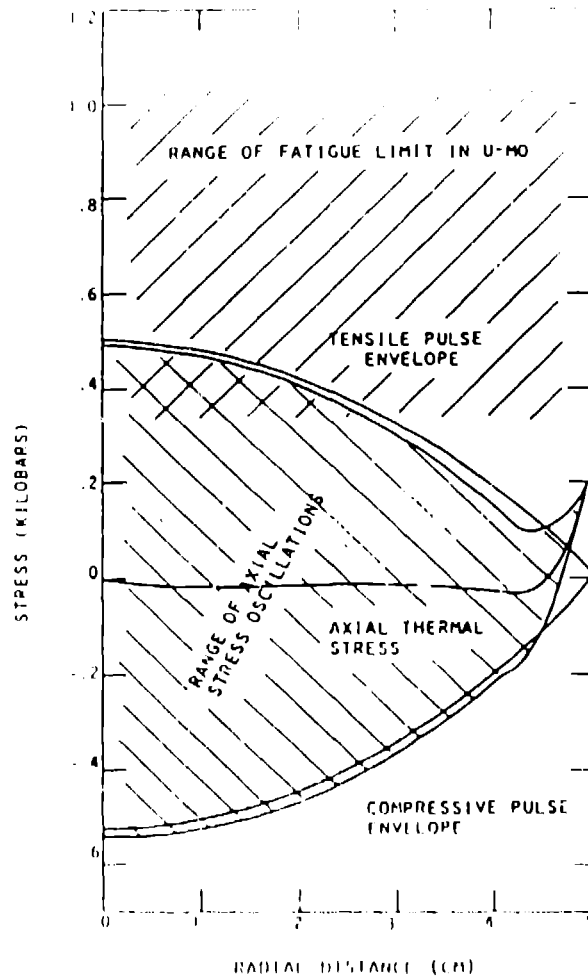


Fig. 10 Thermal stress along axial elements of Zircaloy-clad uranium-molybdenum disk.

- Temperature limits can always be taken into consideration but
- Strong dilution of the heavy target material by cooling media has to be avoided

or

- Uranium is concerning the neutronics a favorite material, but
- Uranium leads to high heat load and has to be operated at very low



**Fig. 11** Oscillation range of the axial thermal stress due to pulsation of the proton beam in the uranium-molybdenum target plate. In the center of the plate the fatigue limit is exceeded in the tensile phase of the pulse.

temperature ( $\leq 400^\circ\text{C}$ ) since it has the most miserable material properties of all given candidates

or

- (Nearly) all problems can be avoided with the choice of the concept of a liquid metal target, but
- A beam entrance window is needed



This dialectic becomes even more nasty, when considering radiation damage as well. Even if a solution has been found, the next question which comes up is: How long does it last?

The material properties change with operation time due to the influence of radiation damage. How does it?

This depends strongly on the solution chosen to solve the problems concerning power load and thermal stress.

We have shown that solutions to the whole package of problems up to a beam power of 0 (1 MWatt) have been found. But what next?  
e.g. 0 (10 MWatt)

The whole effort concentrates onto the region of the first few centimeters of beam penetration into the target. Two solutions have been proposed:

- i) Keep the power of the proton beam limited and produce the neutrons elsewhere in the target. This is probably the only argument for a (high intensity) booster.
- ii) Dilute the power by moving mechanically the target and the window. This proposal has been worked out in considerable detail for the late SNQ-project. If higher power sources turn out to be the way to go, this version should ultimately be taken up again.

#### References

1. IPNS II, 1988, "A National Facility for Condensed Matter Research, ANL-78-88.
2. Green, W. V., Hegedus, F., and Olivo, B. M., EIR, AN-22-84-44.
3. Atchison, F., personal communication.
4. Brown, R. D., Wechsler, M. S., and Tschalar, C., 1988, 13th Int. Symp. on Effects of Radiation on Matter, June 23-25, Seattle.
5. Carne, A., 1988, "The ISIS-Target", this conference.
6. Fischer, W. E., SINQ, 821/FIN-803.
7. International Workshop on Hadron Facility Technology, 1987, LA-11130-C, Feb. 2-5, Santa Fe.
8. Wimblett, R. W., et al., 1979, ICANS III, Los Alamos.

## Cold moderator scattering kernels

*R. E. MacFarlane*  
Applied Nuclear Science Group  
Los Alamos National Laboratory  
Los Alamos, New Mexico 87545  
USA

**ABSTRACT:** New thermal-scattering-law files in ENDF format have been developed for solid methane, liquid methane, liquid ortho- and para-hydrogen, and liquid ortho- and para-deuterium using up-to-date models that include such effects as incoherent elastic scattering in the solid, diffusion and hindered vibration and rotations in the liquids, and spin correlations for the hydrogen and deuterium. These files were generated with the new LEAPR module of the NJOY Nuclear Data Processing System. Other modules of this system were used to produce cross sections for these moderators in the correct format for the continuous-energy Monte Carlo code (MCNP) being used for cold-moderator-design calculations at the Los Alamos Neutron Scattering Center (LANSCE).

### INTRODUCTION

When Gary Russell needed cold moderator cross sections to use with the MCNP continuous energy Monte Carlo code<sup>1</sup> during the design of the liquid hydrogen moderator for the Los Alamos Neutron Scattering Center (LANSCE), he naturally came to the Applied Nuclear Data group, because we provide the other cross sections for MCNP. As a starting point, he provided us with FORTRAN coding from Dr. Guy Robert at Grenoble that implemented the Young and Koppel model<sup>2</sup> for ortho and para hydrogen. We implemented the calculation in the THERMR module of the NJOY Nuclear Data Processing System<sup>3</sup> and results obtained using cross sections produced in this way were reported at the last ICANS conference.<sup>4</sup> Subsequently, a need developed for deuterium cross sections. A later version of the European coding for the Young and Koppel model was obtained from Dr. Rolf Neef at Jülich, and the NJOY code was updated to be able to process para and ortho deuterium. Before this new capability was ever used, Gary became interested in liquid and solid methane as moderator materials. He obtained a version of the LEAP+ADDELT code that had been especially modified for cold methane calculations by Dr. Dave Pieton.<sup>5</sup>

This part of the development was considerably more complex than the earlier steps. Instead of directly computing the differential cross section  $\sigma(E \rightarrow E', \mu)$  from a (comparatively) simple formula, it became necessary to compute the scattering law  $S(\alpha, \beta)$  in the Evaluated Nuclear Data Files (ENDF) format and feed it into the THERMR module of NJOY. Our initial results with the LEAP code were so encouraging, that we decided to use it as the basis for a new LEAPR module for the NJOY system. This involved modifying the code for consistency with NJOY standards, making some "improvements", and doing a careful study of the theory of the method. The result is a new general purpose code for producing scattering law files in ENDF-6 format<sup>6</sup> for both cold moderators and normal reactor moderators.

The final step in this long history was to make use of the knowledge gained from the liquid methane model and the LEAPR code to improve the data for liquid hydrogen and deuterium. The Young and Koppel model assumed that the molecular translations were free, but a number of experimental studies have shown the presence of quasi-elastic scattering that appears to obey a diffusive law. Following the procedures outlined by Keinert and Sax,<sup>7</sup> we replaced the free-gas law in the Young and Koppel formula with a new scattering law that attempts to represent the hindered motions of each hydrogen or deuterium molecule in its clump of local neighbors and the diffusive motions of these clumps through the liquid. Because of spin correlations, it was necessary to extend the ENDF-6 format and the NJOY code to handle asymmetric scattering laws, that is  $S(\alpha, \beta) \neq S(\alpha, -\beta)$ .

In the rest of this paper, we will give a short review of the theory of the LEAPR module of NJOY, and then describe the actual models used for solid methane, liquid methane, liquid hydrogen, and liquid deuterium.

### LEAPR THEORY

The British code LEAP+ADDELT was originally written by McLatchie at Harwell,<sup>8</sup> then implemented by Butland at Winfrith,<sup>9</sup> and finally modified to work better for cold moderators as part of the Ph.D. thesis of D. J. Picton. The major modifications made while turning LEAP+ADDELT into LEAPR were extensive reworking of the coding and comments, the provision of output in ENDF-6 format, a capability to include either coherent or incoherent elastic scattering, a significant speedup for the diffusion calculation, and the liquid hydrogen/deuterium model.

In many practical moderator materials, the presence of some essential randomness (such as of position, spin orientation, isotopic content, or crystallite orienta-

tion) allows scattering of thermal neutrons to be described as "incoherent". It is shown in standard references<sup>10</sup> that the double differential scattering cross section of thermal neutrons by gases, liquids, or solids consisting of randomly ordered crystals can be written as

$$\sigma(E \rightarrow E', \mu) = \frac{\sigma_b}{2kT} \sqrt{\frac{E'}{E}} e^{-\beta/2} S(\alpha, \beta), \quad (1)$$

where  $E$  and  $E'$  are the incident and secondary neutron energies in the laboratory system,  $\mu$  is the cosine of the scattering angle in the laboratory,  $\sigma_b$  is the characteristic bound scattering cross section for the material,  $kT$  is the thermal energy in eV, and  $S$  is the scattering law. The scattering law depends on only two variables: the momentum transfer

$$\alpha = \frac{E' + E - 2\sqrt{E'E}\mu}{AkT}, \quad (2)$$

where  $A$  is the ratio of scatterer mass to the neutron mass, and the energy transfer

$$\beta = \frac{E' - E}{kT}. \quad (3)$$

Note that  $\beta$  is positive for energy gain and negative for energy loss. Except in the case of the hydrogen molecule,  $S$  is symmetric in  $\beta$  and only the part for positive values is tabulated in the ENDF format.

It turns out that the scattering law depends on the frequency spectrum of excitations in the system. In general, this spectrum can be expressed as a weighted sum of a number of simple spectra,

$$\rho(\beta) = \sum_{j=1}^K w_j \rho_j(\beta), \quad (4)$$

where some of the possibilities are:

$$\rho_j(\beta) = \delta(\beta_j) \text{ discrete oscillator} \quad (5)$$

$$\rho_j(\beta) = \rho_f(\beta) \text{ free translation} \quad (6)$$

$$\rho_j(\beta) = \rho_s(\beta) \text{ solid-type spectrum} \quad (7)$$

$$\rho_j(\beta) = \rho_d(\beta) \text{ diffusion-type spectrum} \quad (8)$$

The weights sum to one, and all the individual distributions are normalized. The scattering law for this sum of spectra can be expressed as a recursion based

on convolutions:

$$S(\alpha, \beta) = S^{(K)}(\alpha, \beta),$$

where

$$S^{(J)}(\alpha, \beta) = \int_{-\infty}^{\infty} S_J(\alpha, \beta') S^{(J-1)}(\alpha, \beta - \beta') d\beta'. \quad (10)$$

where  $S_J$  is the scattering law for partial spectrum  $J$ , and  $S^{(J-1)}$  is the composite scattering law including all partial distributions with  $j < J$ . As an example of the use of this recursive procedure, consider a case like solid methane where the desired spectrum is a combination of  $\rho_s$  and several discrete oscillators. First calculate  $S^{(1)} = S_1$  using  $\rho_s$ . Then calculate  $S_2$  using  $\rho(\beta_1)$ , the distribution for the first discrete oscillator, and convolve  $S_2$  with  $S^{(1)}$  to obtain  $S^{(2)}$ , the composite scattering law for the first two partial distributions. Repeat the process with the rest of the discrete oscillators, one at a time, to obtain the full distribution.

### The Phonon Expansion

The two main methods available for computing the scattering law for solid-type spectra are the time integration of the intermediate scattering function used by GASKET<sup>11</sup> and the phonon expansion used by LEAP. Our tests indicate that the LEAP method is faster and more stable, especially for the very high values of  $\alpha$  and  $\beta$  found in low-temperature problems. Therefore, we decided to use the phonon expansion for our new thermal module. The resulting formula for  $S_s(\alpha, \beta)$  is

$$S_s(\alpha, \beta) = e^{-\alpha\lambda} \sum_{n=0}^{\infty} \frac{1}{n!} (\alpha B)^n T_n(\beta), \quad (11)$$

where

$$\lambda = \int_{-\infty}^{\infty} P_s(\beta) e^{-\beta/2} d\beta \quad (12)$$

is the Debye-Waller factor,

$$B = \int_{-\infty}^{\infty} P_s(\beta) d\beta, \quad (13)$$

is a constant,

$$T_0(\beta) = \delta(\beta), \quad (14)$$

$$T_1(\beta) = \frac{1}{B} P_s(\beta), \quad (15)$$

and in general,

$$T_n(\beta) = \int_{-\infty}^{\infty} T_{n-1}(\beta') T_1(\beta - \beta') d\beta'. \quad (16)$$

In these formulas,

$$P_n(\beta) = \frac{\rho_n(\beta) e^{-\beta/2}}{2\beta \sinh(\beta/2)}. \quad (17)$$

The coefficients are precomputed using this convolution process for  $n$  up through 20. It is then a simple process to compute  $S$  for any desired value of  $\alpha$  or  $\beta$  using eq.(11). For high values of  $\alpha$  and  $\beta$  the sum may not converge adequately with only 20 terms. It is then possible to extend the sum to higher values of  $n$  using an approximation for the  $T_n$ , or the code can choose to use the "Short Collision Time" (SCT) approximation. We are still exploring the various strategies for making use of these approximations.

### Diffusion

The neutron scattering from many important liquids, including water and liquid methane, can be represented using a solid-type spectrum of rotational and vibrational modes combined with a diffusion term. Egelstaff and Schofield have proposed an especially simple model for diffusion called the "effective width model." It has the advantage of having analytic forms for both  $S_d(\alpha, \beta)$  and the associated spectrum  $\rho_d(\beta)$ :

$$S_d(\alpha, \beta) = \frac{2d\alpha}{\pi} e^{2d\alpha} \frac{\sqrt{c^2 + .25}}{\sqrt{\beta^2 + 4d^2\alpha^2}} K_1\left\{\sqrt{c^2 + .25}\sqrt{\beta^2 + 4d^2\alpha^2}\right\}, \quad (18)$$

and

$$\rho_d(\beta) = \frac{4d}{\pi\beta} \sqrt{c^2 + .25} \sinh(\beta/2) K_1\left\{\sqrt{c^2 + .25}\beta\right\}. \quad (19)$$

In these equations,  $K_1(x)$  is a modified Bessel function of the second kind, and the diffusion constant  $c$  and parameter  $d$  (usually  $w_d c$ ) are provided as inputs.

In LEAPR,  $S_s(\alpha, \beta)$ , the scattering law for the solid-type modes, is calculated using the phonon expansion as described above. The diffusive contribution  $S_d(\alpha, \beta)$  is then calculated using the formula above on a  $\beta$  grid chosen to represent its shape fairly well. The combined scattering law is then obtained by convolution as follows:

$$S(\alpha, \beta) = S_d(\alpha, \beta) + \int_{-\infty}^{\infty} S_d(\alpha, \beta') S_s(\alpha, \beta - \beta') d\beta'. \quad (20)$$

The first term arises from the delta function in eq.(11), which isn't included in the numerical results for the phonon series calculation. The values for  $S_d(\beta)$  and  $S_d(\beta-\beta')$  are obtained from the precomputed functions by interpolation. This makes LEAPR run much faster than LEAP + ADDELT for diffusive cases, because the original code did direct recalculations of the solid-type scattering law for all the desired values of  $\beta-\beta'$ . It also had to take pains to compute  $S_d$  on a  $\beta$  grid that was commensurate with the input grid. This often resulted in more points for  $S_d$  than were necessary to obtain useful accuracy for the convolutions.

### Discrete Oscillators

The scattering law for a discrete oscillator term  $w_i\delta(\beta_i)$  is known to be

$$S_i(\alpha, \beta) = e^{-\alpha\lambda_i} \sum_{n=-\infty}^{\infty} I_n\left(\frac{w_i\alpha}{\beta_i \sinh(\beta_i/2)}\right) \delta(\beta - n\beta_i), \quad (21)$$

where

$$\lambda_i = w_i \frac{\coth(\beta_i/2)}{\beta_i}, \quad (22)$$

and  $I_n(x)$  is a modified Bessel function of the first kind and n-th order. As discussed in connection with eq.(10), the net  $S(\alpha, \beta)$  for a complex distribution consisting of a smooth part and several discrete oscillators is obtained by convolving each oscillator in turn with the  $S(\alpha, \beta)$  resulting from all the previous parts of the distribution. The  $\delta$ -function makes the convolution trivial.

A variation of this procedure used for liquid hydrogen and deuterium will be discussed below.

### ENDF-6 Output

The Evaluated Nuclear Data Files (ENDF) format originated in the U. S., but it is now being used throughout the world. Thermal data is recorded in "File 7", and the new ENDF-6 version of the File 7 format is capable of representing the following types of data.

- *Incoherent Inelastic.* This type is important for all materials, and it requires  $S(\alpha, \beta)$  vs  $T$  and some auxiliary information such as bound scattering cross section and effective temperatures.
- *Coherent Elastic.* This type is important for crystalline materials like graphite and beryllium, and it requires information on the position and strengths of

the Bragg edges, a characteristic coherent cross section, and a Debye-Waller function.

- *Incoherent Elastic.* This type is important for hydrogenous solids like polyethylene, zirconium hydride, and solid methane, and it requires a characteristic cross section plus a Debye-Waller function.

The calculation of  $S(\alpha, \beta)$  was described above. The ENDF output subroutine of LEAPR simply stores it in the correct format. Effective temperatures for the ENDF Short-Collision-Time approximation can be determined from integrals performed by LEAPR, and they are also added to the file.

Coherent elastic parameters can be computed for the three materials graphite, beryllium, and beryllium oxide using methods based on the HEXSCAT code.<sup>12</sup> The Debye-Waller function needed to determine the temperature dependence of coherent elastic scattering is obtained from the LEAPR calculation of  $S(\alpha, \beta)$  for the material. Similarly, the Debye-Waller function for incoherent elastic scattering in hydrogenous materials is obtained from the LEAPR calculation of the inelastic scattering law for that material.

The speed and simplicity of the LEAP method for computing  $S(\alpha, \beta)$  combined with the comprehensive capabilities of the ENDF output routine make LEAPR a very useful module for all problems involving thermal neutron scattering.

### SOLID METHANE

The methane molecule consists of an atom of carbon surrounded by four atoms of hydrogen placed on the corners of a tetrahedron. The carbon atom is at the center of mass of the system; because of its symmetry, the methane molecule is often called a "spherical top". Optical measurements of methane in the gas phase show four fairly well defined vibrational modes at 162, 190, 361, and 374 meV. Following the lead of Picton, they have been included in this model as discrete oscillators with weights equal to .308, .186, .042, and .144, respectively.

Specific heat measurements in solid methane near one atmosphere show three phases with transitions at 8K and 20.4K. The melting point is about 89K. X-ray measurements show that the carbon atoms are arranged on an fcc lattice for both of the higher two phases; it has been speculated that the phase transition is due to a change in the degree of rotational order, or perhaps due to the onset of a self-diffusion behavior. Because of this interesting question, a series of slow



neutron inelastic scattering experiments were carried out with samples in each of the phases.<sup>13</sup> Because hydrogen is an incoherent scatterer, it was possible to analyze the data to obtain a frequency spectrum for hydrogen in solid methane. The results didn't really explain what was happening in the 20K phase transition, but they did provide us with just the data needed for our calculation.

Again following Picton, we chose the spectrum for 22.1K for our model. Instead of using Picton's numbers directly, we digitized the curve from the graph in the reference, plotted it on a large scale, and then smoothed it by hand. Care was taken to use an  $\omega^2$  variation for low energies. The resulting spectrum is shown in Figure 1. As discussed by Harker and Brugger, the appropriate normalization for this curve is 0.32.

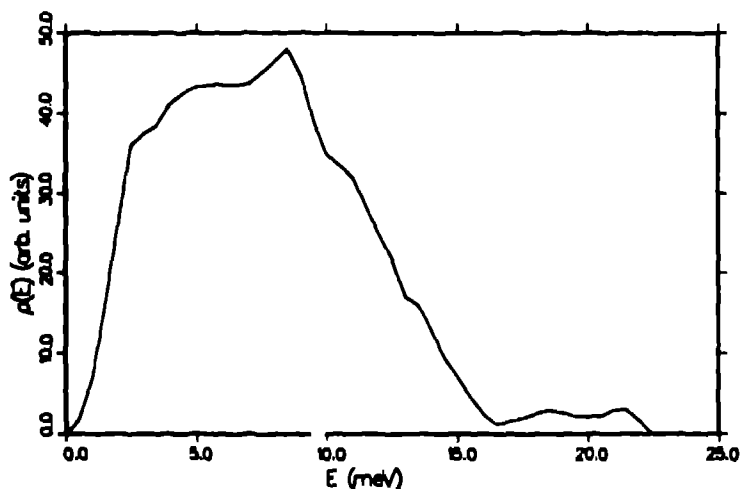


Figure 1: The Harker-Brugger frequency spectrum used for solid methane. Note the quadratic shape at low energies.

This spectrum and the four discrete oscillators were then used to calculate  $S(\alpha, \beta)$  with LEAPR using the  $\alpha$  and  $\beta$  grids of Picton. During this calculation, the moments of  $T_n$  and  $S(\alpha, \beta)$  were checked and the errors were modest. The output listing was examined carefully to see that the  $\alpha$  and  $\beta$  ranges were sufficient, and no obvious problems were found. LEAPR automatically prepared an output file in rNDF-6 format, including both incoherent elastic and incoherent inelastic representations, and complete with descriptive comments on the resulting evaluation. Plots of  $S(\alpha, \beta)$  versus  $\alpha$  for several values of  $\beta$  are give in Figure 2.

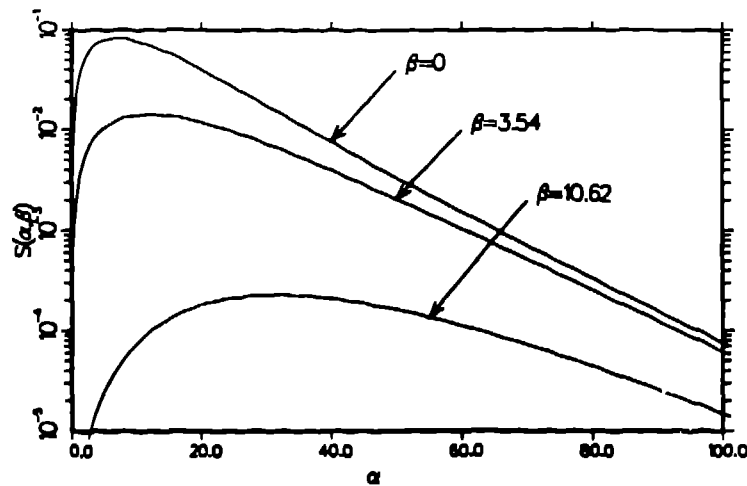


Figure 2:  $S(\alpha, \beta)$  for solid methane shown as a function of  $\alpha$  for several values of  $\beta$ .

Next, the new evaluation for  $S(\alpha, \beta)$  was processed into integrated cross sections and double differential cross sections using the THERMR module of NJOY. It was necessary to slightly modify the code to allow for the very large values of  $\beta$  appropriate to these low temperatures (note that  $\beta$  is inversely proportional to  $kT$  for a given energy transfer); it is necessary to keep values of  $S$  as small as  $1 \times 10^{-80}$  for this evaluation. This is quite a dynamic range! Plots of the integrated cross sections for the elastic and inelastic processes are given in Figure 3, and plots of the outgoing neutron spectrum integrated over angle at several incident energies are given in Figure 4.

Finally, the output of THERMR was passed to the ACER module of NJOY for conversion to ACE format for the MCNP Continuous-Energy Monte-Carlo code. The result of this step was made available to Group X 6 for addition to the standard MCNP thermal library.

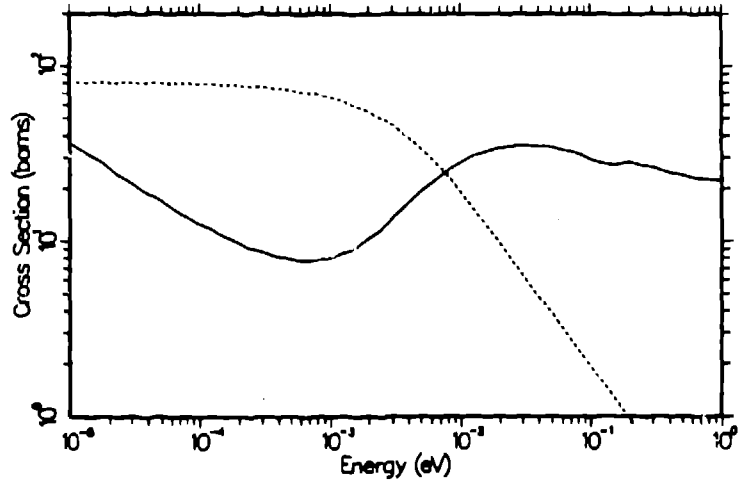


Figure 3: Incoherent inelastic cross section (solid) and incoherent elastic cross section (dashed) for solid methane.

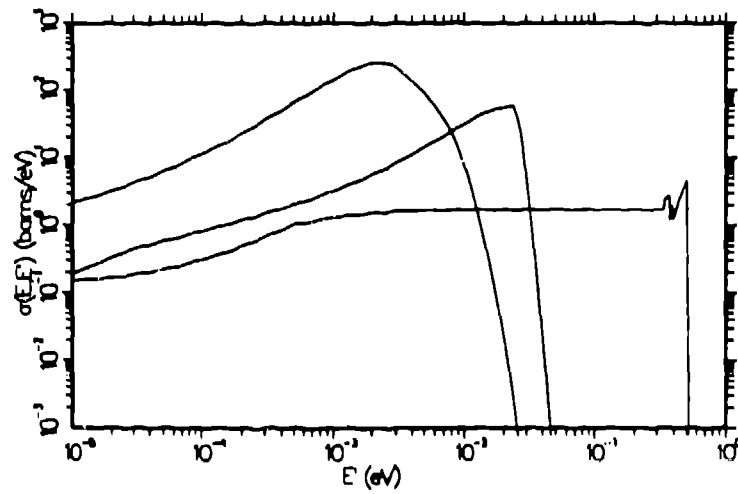


Figure 4: Neutron spectra  $\sigma(E \rightarrow E')$  for solid methane shown for  $E = 0.0001, .0253, \text{ and } .503 \text{ eV}$ .

## LIQUID METHANE

The preparation of a model for liquid methane at 90K was a little more difficult. Once again, we use the four discrete oscillators to represent the the molecular vibrations. In addition, we need a continuous frequency distribution to represent the molecular rotations, and a pair of parameters  $d$  and  $c$  to represent diffusion. This latter component was omitted from Picton's model, but we felt that it might be needed to obtain a reasonable quasi-elastic peak in the spectrum of scattered neutrons. Therefore, we couldn't use the Picton input directly, and we had to refer to his source.<sup>14</sup> Agrawal and Yip divided the problem into two parts: translations and rotations.

For translations, they proposed a model that matches the expected diffusive behavior at long times and provides an oscillatory behavior at short times. Each methane molecule is assumed to move in a "cage" formed by its neighbors, and the cage itself is allowed to relax with time. As Agrawal and Yip point out, the molecule will oscillate initially, but gradually as the restoring forces decay into a frictional background, it will go over into diffusive motions. The resulting analytic expression for the frequency spectrum is

$$f_t(\omega) = \frac{2}{\pi} \frac{\omega_0^2/\tau_0}{\omega^2 - \omega_0^2 + (\omega/\tau_0)^2} \quad (23)$$

The fact that  $f_t(\omega)$  is nonzero at  $\omega=0$  indicates that the molecules are capable of diffusion.

For rotations, they establish that the rotational excitations are related to the "dipole correlation function". The same function appears in the classical limit of the theory of optical line shapes for infrared absorption as presented by Gordon,<sup>15</sup> and he has used this method to compute the correlation function for liquid methane at 98K based on the infrared data of Ewing.<sup>16</sup> The desired spectrum of rotational excitations,  $\rho_r(\omega)$  can be obtained by transforming the function graphed by Gordon.

The net result is shown in Figure 5, together with the translational frequency distribution discussed above. These numbers were generated by digitizing the curve from Agrawal and Yip. The fact that the distribution is nonzero at zero energy transfer indicates that diffusion is present. Agrawal and Yip compared

their model with both double-differential and integrated cross sections, with very good agreement.

Unfortunately, this model does not match the requirements of LEAPR. The only type of frequency distribution that is nonzero at  $\omega=0$  that can be used by the code is the diffusive law of Eyring and Schofield, which does not have the short-time oscillatory behavior of eq.(23). Our main reason for using the diffusion term in our model for liquid methane was to improve the "quasi-elastic" peak, which depends mostly on the small- $\omega$  part of the frequency distribution. Therefore, it seemed reasonable to select diffusion parameters  $d$  and  $c$  that gave a reasonable representation for the full width at half maximum of the quasi-elastic peak, to subtract the result  $f_d$  from the sum of the two curves shown in Figure 5, and to use the difference to represent both the translational oscillatory modes and the rotational modes. Figure 6 shows this breakdown. Once again, there has been some hand smoothing, and the low energy part of the distribution was forced to follow an  $\omega^2$  law. The final breakdown was 1.5% diffusion, 30.5% rotation, and 68% molecular vibrations.

LEAPR was run with this input taking advantage of the much accelerated diffusion calculation discussed above. Once again the moments of  $T_n$  and  $S(\beta)$  were checked, and no great problems were seen. These checks help to prove that the  $\omega$  grid for the input frequency spectrum and the  $\beta$  grid for calculating  $S$  are reasonable. We also checked the range of  $\alpha$  and  $\beta$  to be sure that no significant cross section contributions were being cut off. The results seem to be good for all energy transfers possible with incident neutron energies up to 1 eV. Once again, LEAPR produced an output file in ENDF-6 format. This time, there was no elastic contribution at all. Plots of  $S(\alpha, \beta)$  versus  $\alpha$  for several values of  $\beta$  are shown in Figure 7. Note that the behavior of the curves for small  $\beta$  is quite different than in Figure 2. This reflects the presence of the diffusive component.

The new evaluation for liquid methane was run through the THERMR module of NJOY to produce integrated and differential cross sections. Sample results are given in Figures 8 and 9. The integrated cross section is compared with experimental data at 110K that was quoted in the Agrawal and Yip paper. The THERMR output was then processed by ACER to obtain the final MCNP library for Group X-6.

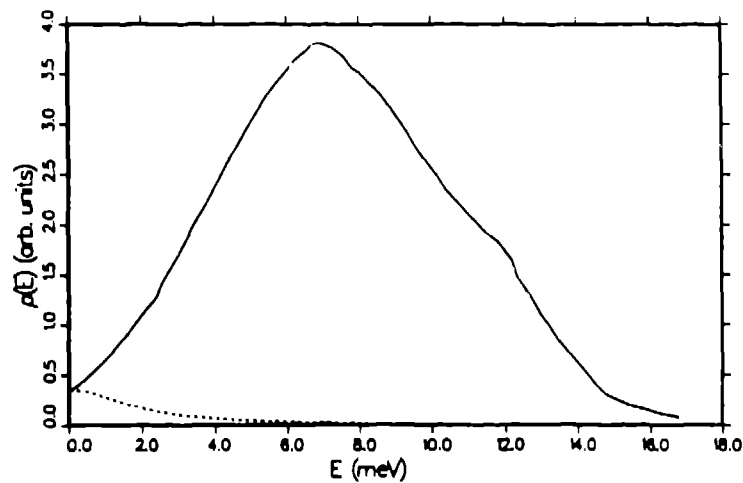


Figure 5: Frequency spectrum for liquid methane (solid) as given by Agrawal and Yip, including an analytic translational part (dashed) and a rotational part based on Gordon's analysis of the optical measurements of Ewing.

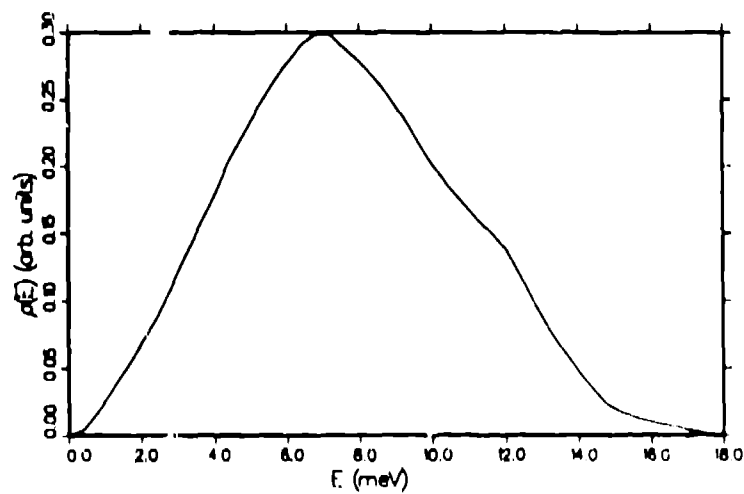


Figure 6: Effective frequency spectrum for methane including both translational and rotational modes, but not including diffusive modes.

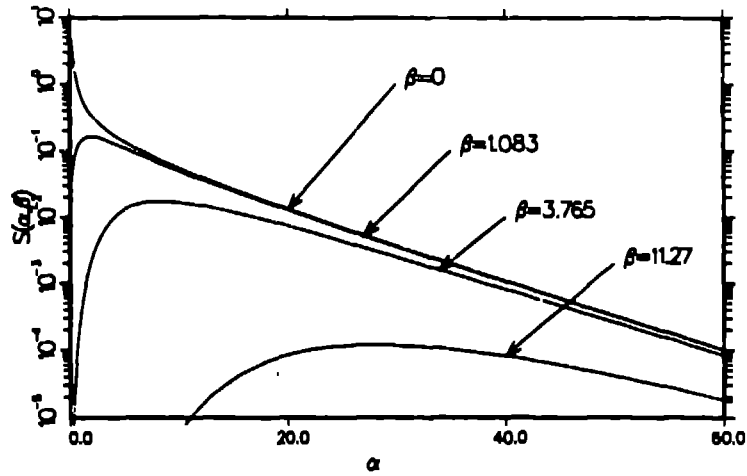


Figure 7:  $S(\alpha, \beta)$  curves for liquid methane. Note the diffusive behavior at low  $\alpha$  and  $\beta$ .

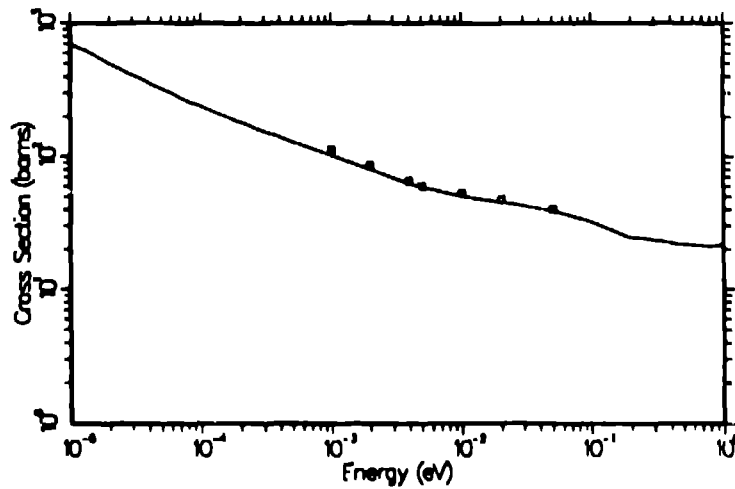


Figure 8: The computed cross section for liquid methane at 100K (solid) is compared to experimental data (squares) by Whittemore and by Rogalska as quoted by Agrawal and Yip.

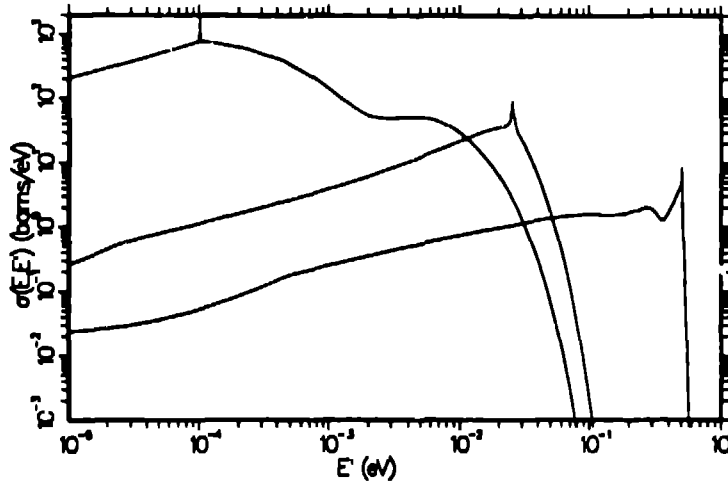


Figure 9: Neutron spectra  $\sigma(E \rightarrow E')$  are shown for  $E = .0001, .0253,$  and  $.503$  meV. Note the sharp quasi-elastic peak that results from the diffusive term in the theory used here.

## LIQUID HYDROGEN AND DEUTERIUM

Materials containing hydrogen or deuterium molecules violate the assumption that spins are distributed randomly that underlies the incoherent approximation used for eq.(11), and an explicitly quantum-mechanical formula is required to take account of the correlations between the spins of two atoms in the same molecule. This problem was considered by Young and Koppel, who gave the formulas for that were incorporated into the European coding that we originally received from Robert and Neef. Changing to our notation, the formulas for the hydrogen molecule (neglecting vibrations) become

$$S_{\text{para}}(\alpha, \beta) = \sum_{J=0,2,4,\dots} P_J \quad (24)$$

$$\times \frac{4\pi}{\sigma_b} \left[ a_c^2 \sum_{J'=0,2,4,\dots} + a_i^2 \sum_{J'=1,3,5,\dots} \right] (2J' + 1) \quad (25)$$

$$\times S_J(\alpha/2, \beta + \beta_{JJ'}) e^{-\beta_{JJ'}/2} \quad (26)$$

$$\times \sum_{\ell=|J'-J|}^{J'+J} 4j_\ell^2(y) \epsilon^{-2}(JJ'\ell; 00), \quad (27)$$



and

$$S_{\text{ortho}}(\alpha, \beta) = \sum_{J=1,3,5,\dots} P_J \quad (28)$$

$$\times \frac{4\pi}{\sigma_b} \left[ \frac{a_c^2}{3} \sum_{J'=0,2,4,\dots} + \frac{3a_c^2 + 2a_i^2}{3} \sum_{J'=1,3,5,\dots} \right] (2J' + 1) \quad (29)$$

$$\times S_J(\alpha/2, \beta + \beta_{JJ'}) e^{-\beta_{JJ'}/2} \quad (30)$$

$$\times \sum_{\ell=|J'-J|}^{J'+J} 4j_\ell^2(y) C^2(JJ'\ell; 00), \quad (31)$$

where  $a_c$  and  $a_i$  are the coherent and incoherent scattering lengths (note that the characteristic bound cross section  $\sigma_b = 4\pi[a_c^2 + a_i^2]$ ),  $P_J$  is the statistical weight factor,  $\beta_{JJ'} = (E_{J'} - E_J)/kT$  is the energy transfer for a rotational transition,  $j_\ell(x)$  is a spherical Bessel function of order  $\ell$ , and  $C(JJ'\ell; 00)$  is a Clebsch-Gordan coefficient. The parameter  $y$  is given by  $\kappa a/2 = (a/2)\sqrt{4MkT}/a$ , where  $a$  is the interatomic distance in the molecule. The sums over  $J'$  are treated as operators into order to keep the notation compact.

Young and Koppel assumed that the molecular translations were free, so the equations contain

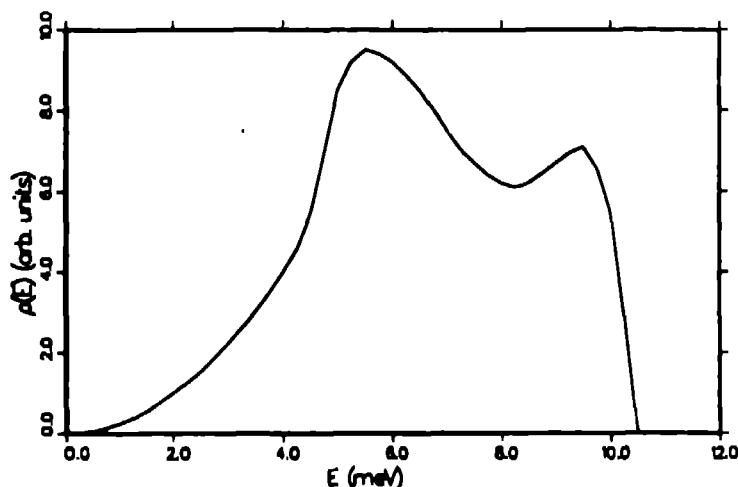
$$f(\alpha, \beta) = \frac{1}{\sqrt{4\pi\alpha}} \exp\left[-\frac{\alpha^2 + \beta^2}{4\alpha}\right], \quad (32)$$

the free-atom scattering function. Note that  $\alpha$  is divided by two when this equation is used to make the formula apply to a molecule containing two atoms. That is, the normalization of the translational part is 0.5.

These formulas as stated are appropriate for a gas of hydrogen molecules. In a liquid, there are two additional effects to be considered: interference between the neutron waves scattered from different molecules, and the fact that the recoil of the hydrogen molecule is not really free. So far, we have only considered the latter effect. Experiments by Egelstaff, Haywood, and Webb at Harwell<sup>17</sup> and Schott at Karlsruhe<sup>18</sup> showed appreciable broadening of the quasi-elastic scattering peak for liquid hydrogen, and both groups ascribed this to diffusive effects. Later, Utsuro of Kyoto University constructed a simple analytic model<sup>19</sup> that included both diffusion and intermolecular vibrations and showed good agreement with experiment. More recently, Keinert and Sax of the University of Stuttgart proposed the model<sup>7</sup> that we follow here.

They suggested that the free translation term in the Young and Koppel formu

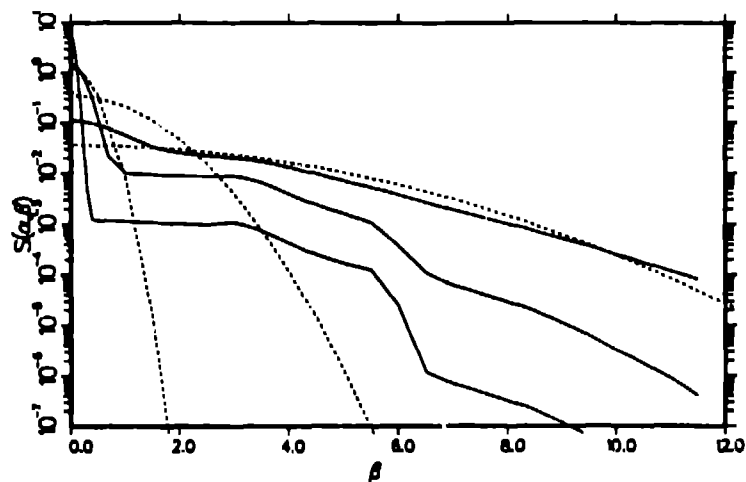
las be replaced by the superposition of a solid-state like motion and a diffusive law. One can picture a hydrogen molecule bound in a cluster of about 20 molecules and undergoing vibrations similar to those of a hydrogen molecule in a solid. These clumps then diffuse through the liquid (hindered translations) according to the Egelstaff-Schofield effective width model discussed above. The Keinert-Sax distribution function is shown in Figure 10. They assumed a weight of 0.025 for the hindered translation, leaving a value of 0.475 for the solid-like distribution.



**Figure 10:** The Keinert-Sax frequency distribution for the effective translational modes of liquid hydrogen.

This model was then used in LEAPR. Some results for the effective translational  $S(\alpha, \beta)$  to be used in the Young and Koppel formulas are shown in Figure 11 along with the corresponding free translation curves. A new subroutine was added to LEAPR to carry out the rest of operations in the Young and Koppel formulas. Because of the spin correlations,  $S(\alpha, \beta) \neq S(\alpha, -\beta)$ , and it is necessary to calculate both sides of the function. These results were then passed to the ENDF output subroutine. Here again, it was necessary to make a slight modification to allow for asymmetric scattering functions. A new parameter called "LASYM" was added to the File 7 format (it is in the "L1" position of the head card for MF=7, MT=4). When LASYM=1, the  $\beta$  grid in File 7 starts with  $-\beta_{\max}$  and increases through zero to  $+\beta_{\max}$ . Of course, it was also necessary to modify the THERMR module of NJOY to recognize the LASYM=1 option. This turned out to be very easy, and

some examples of cross sections and energy distributions computed by THERMR are shown in Figures 12 and 13.



Figures 11: The effective translational  $S(\alpha, \beta)$  for liquid hydrogen (solid) compared with the corresponding free translation curves (dashed). The  $\alpha$  values shown are 0.1, 1, and 10 (broadest).

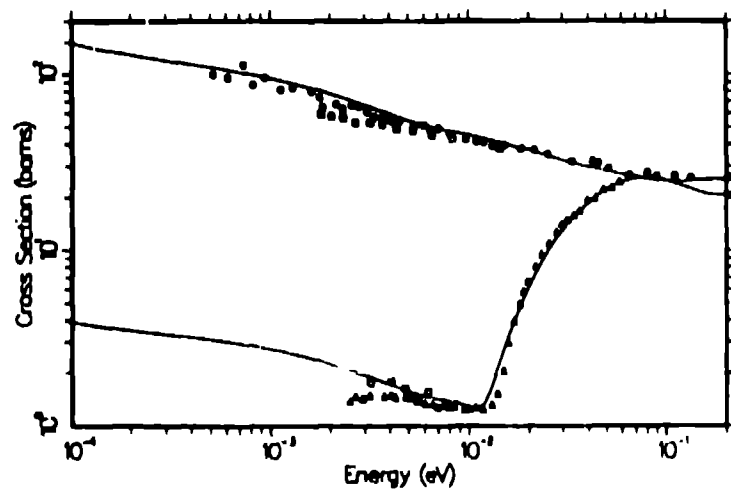


Figure 12: The cross sections for liquid ortho hydrogen (upper curve) and liquid para hydrogen (lower curve) at 20 K are compared with experimental data<sup>20</sup> due to Squires (gas) at 20K (squares), Whittemore at 20K (circles), and Seiffert at 14K (triangles).

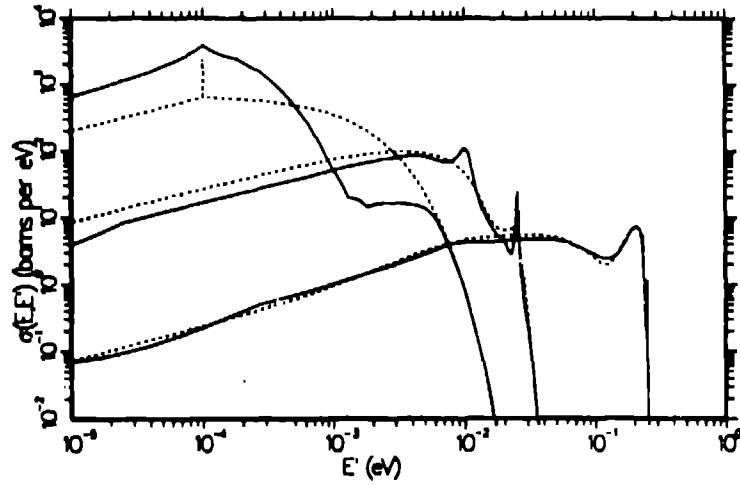


Figure 13: The spectra  $\sigma(E-E')$  for liquid para hydrogen are shown for  $E = .0001, .0253, \text{ and } .251 \text{ eV}$ . Note the sharp quasi-elastic peak arising from the diffusion treatment. The dashed lines show the free translation results from the original Young and Koppell formulas.

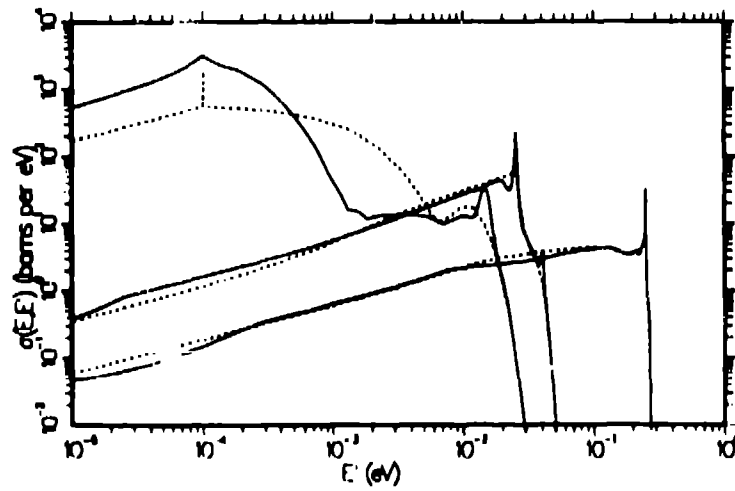


Figure 14: The spectra  $\sigma(E-E')$  for liquid ortho hydrogen are shown for  $E = .0001, .0253, \text{ and } .251 \text{ eV}$ . Again note the sharp quasi-elastic peak arising from the diffusion treatment. The dashed lines show the free translation result.

## CONCLUSIONS

The result of this work is set of state-of-the-art scattering law files for ortho and para liquid hydrogen, ortho and para liquid deuterium, liquid methane, and solid methane that can be used with the NJOY Nuclear Data Processing System to produce thermal scattering data for both continuous-energy Monte Carlo and multigroup applications. As a very useful spin-off, we have the LEAPR module, which can be used to produce new scattering law files for the traditional reactor moderators for the upcoming ENDF/B-VI library of evaluated nuclear data.

## REFERENCES

1. Judith F. Briesmeister, Ed., "MCNP-A General Monte Carlo Code for Neutron and Photon Transport, Version 3A," Los Alamos National Laboratory report LA-7396-M (September 1986).
2. James A. Young and Juan U. Koppel, *Phys. Rev.* **135**, A603(1964).
3. R. E. MacFarlane, D. W. Muir, and R. M. Boicourt, "The NJOY Nuclear Data Processing System, Volume I: User's Manual," and "The NJOY Nuclear Data Processing System, Volume II: The NJOY, RECONR, HEATR, and THERMR Modules," Los Alamos National Laboratory reports LA-9303-M, Vols. I and II (May 1982). R. E. MacFarlane and D. W. Muir, "The NJOY Nuclear Data Processing System, Volume III: The GROUPE, GAMINR, and MODER Modules," Los Alamos National Laboratory report LA-9303-M, Vol. III (October 1987). D. W. Muir and R. E. MacFarlane, "The NJOY Nuclear Data Processing System, Volume IV: The ERRORR and COVR Modules," Los Alamos National Laboratory report LA-9303-M, Vol. IV (December 1985).
4. G. J. Russell, H. Robinson, G. L. Legate, R. Woods, E. R. Whitaker, A. Bridge, K. J. Hughes, and R. D. Neef, "The LANSCE Target System," ICANS-IX, Proc. of the Ninth Meeting of the International Collaboration on Advanced Neutron Sources, Villigen, Switzerland, 22-26 September 1986.
5. Private communication from D. J. Picton to G. J. Russell, September 1987.
6. P. F. Rose and C. L. Dunford, Eds., "ENDF-102, Data Formats and Procedures for the Evaluated Nuclear Data File, ENDF," preliminary version available from the National Nuclear Data Center, Brookhaven National Laboratory, Upton, NY.
7. J. Keinert and J. Sax, "Investigation of Neutron Scattering Dynamics in Liquid Hydrogen and Deuterium for Cold Neutron Sources," *Kerntechnik* **51**, 19 (1987).
8. R. C. F. McLatchie, 1962, unpublished.

9. A. T. Butland, "LEAP and ADDEL, A Users Guide to Two Complementary Codes on the ICL-470 for Calculating The Scattering law From a Phonon Frequency Function," Atomic Energy Establishment Winfrith report AEEW-M-1200, 1973.
10. D. E. Parks, M. S. Nelkin, J. R. Beyster, and N. F. Wikner, Slow Neutron Scattering and Thermalization, W. A. Benjamin, Inc. (New York, 1970).
11. J. U. Koppel, J. R. Triplett, and Y. D. Naliboff, "GASKET, A Unified Code for Thermal Neutron Scattering," General Atomic report GA-7417 (Rev.) (March 1967).
12. Y. D. Naliboff and J. U. Koppel, "Coherent Elastic Scattering of Neutrons by Hexagonal Lattices," General Atomic report GA-6026(1964).
13. Y. D. Harker and R. M. Brugger, "Investigation of the Low-Temperature Phase Transitions in Solid Methane by Slow Neutron Inelastic Scattering," J. Chem. Phys. **46**, 2201(1967).
14. Ashok K. Agrawal and Sidney Yip, "Slow-Neutron Scattering by Molecular Liquids," Nucl. Sci. Eng. **37**, 368(1969).
15. R. G. Gordon, J. Chem. Phys. **43**,1307(1965).
16. G. E. Ewing, J. Chem. Phys. **40**, 179(1964).
17. P. A. Egelstaff, B. C. Haywood, and F. J. Webb, Proc. Phys. Soc., **90**, 681(1967).
18. Wolfgang Schott, Z.Physik **231**, 243(1970).
19. Masahiko Utsuro, Z. Physik B **27**, 111(1977).
20. This data was obtained from the paper of Kelnert and Sax<sup>7</sup> and converted to the numbers shown by subtracting the hydrogen absorption cross section. The ortho cross sections were converted from normal H<sub>2</sub> cross sections using the theoretical ortho and para cross sections to produce a conversion factor. The original references are G. L. Squires and A. T. Stewart, Proc. Roy. Soc. **A230**, 19(1955), W. L. Whittemore and A. W. McReynolds, "Differential Neutron Thermalization," Genral Atomic report GA-2505 (1961), and W. D. Seiffert, "Messung der Streuquerschnitte von flüssigem und festem Wasserstoff, Deuterium, und Deuteriumhydrid für thermische Neutronen," EUR-5566d (1970).

## Cold moderators for spallation sources

*A. T. Lucas*  
Rutherford-Appleton Laboratory  
Chilton, Didcot, Oxon  
UNITED KINGDOM

*H. Robinson*  
Los Alamos Neutron Scattering Center  
Los Alamos National Laboratory  
Los Alamos, New Mexico  
USA

**ABSTRACT:** Moderators using both liquid and solid methane and liquid hydrogen are currently in use at major spallation neutron sources. Los Alamos Neutron Scattering Center (LANSCE) is planning the use of liquid methane as part of a major update program planned in about three years time. This report presents an overview of some of these devices and outlines the general engineering design of the proposed LANSCE moderator, including some suggested solutions to the radiation damage problems of methane. Also included is a brief overview of a possible combined  $H_2/CH_4$  moderator for high-intensity proton beams, which is covered in more detail in a separate paper.

### General overview

- Argonne National Laboratory has two liquid moderators and one of solid methane. The solid moderator is a foam-filled vessel of aluminum with a one-sixteenth-in. wall thickness at the viewed face. Cooling is provided by a heat exchanger coil carrying cold helium gas from a Koch model 1400 refrigerator.

The two liquid moderators operate in a closed loop using a room-temperature-positive-displacement pump. All the methane is warmed up to room temperature in a heat exchanger, which subsequently re-cools the fluid on its return to the main loop on each pass. A liquid-nitrogen-cooled helium loop, used to cool a reflector, also supplies a secondary loop on its return leg, which in turn cools the methane heat exchangers. Supercooled liquid methane fed to the moderators is temperature-controlled by varying the flow rate of cold helium gas through the helium/methane heat exchanger. The methane is maintained at a pressure of 2 bar absolute (see Fig. 1).

- KENS also has a solid-methane moderator that is directly cooled by a helium circuit, including a refrigerator. The moderator is an aluminum canister containing four plates, about 10 mm apart, that are in contact with the cooled sides of the vessel to assist heat transfer from the methane (see Fig. 2).

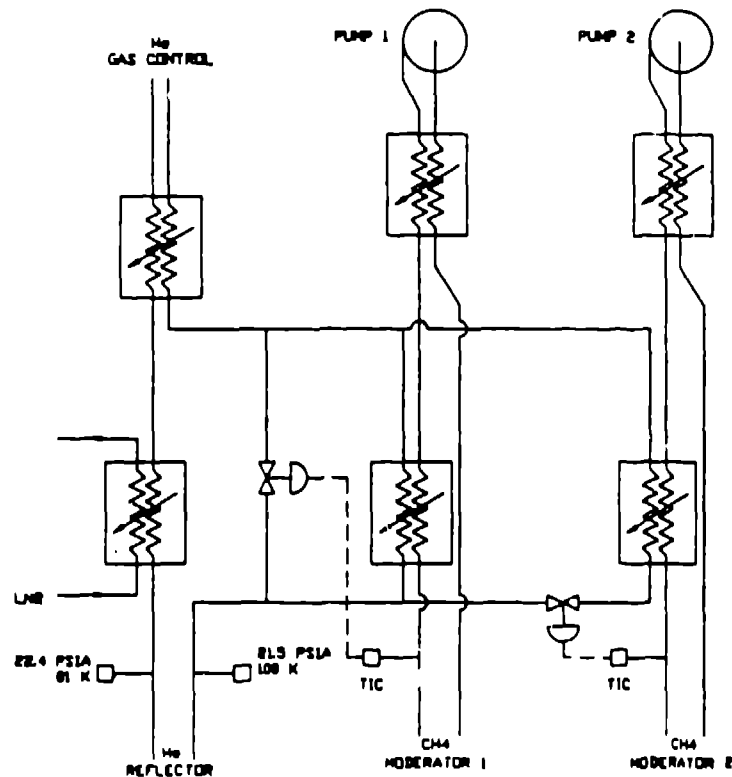


Fig. 1 Argonne National Laboratory CH<sub>4</sub> moderator flow schematic.

- ISIS has a liquid-hydrogen and a liquid-methane moderator, which function as completely independent systems. The hydrogen system was designed to operate in the supercritical region at 25 K and 15 bar absolute pressure. However, the current operating pressure is about 8 bar absolute since no boiling problems have been observed. The refrigerator is built by Sulzer and uses an oil-free reciprocating compressor and two series-connected high-speed turbines. Temperature control is provided by an electrical heater in the helium refrigerant circuit powered in response to a germanium diode sensor in the hydrogen loop and powered through a three-term controller. The hydrogen pressure is controlled within  $\pm \frac{1}{2}$  bar of its setpoint by a pressure control system, and the hydrogen is circulated by a high-speed centrifugal pump in the return leg of the circuit.

The liquid-methane system is cooled by a Phillips-Stirling cycle machine capable of about 1000 W at 100 K. The methane pressure is controlled at 4 bar absolute to raise its boiling temperature to 130 K. Circulation is provided by a high-speed centrifugal pump in the flow side of the circuit. Two 50-micron filters are built into the circuit return leg, and temperature control is provided by



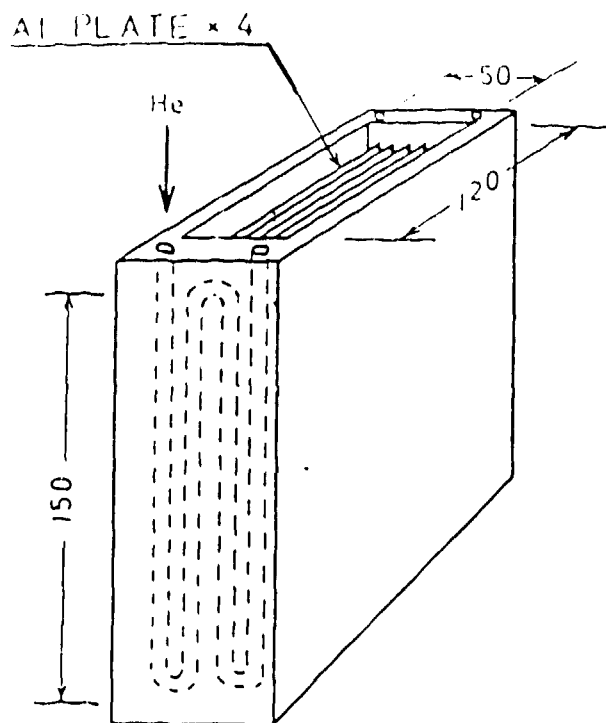


Fig. 2 KENS solid  $\text{CH}_4$  moderator.

an electrical heater driven through a three-term controller in response to a platinum thermometer sensor.

Both systems incorporate a spare circulator that can be valved into line by remotely operated valves. A faulty unit can then be isolated, purged, and subsequently removed without shutting down the system. The same applies to the filters in the methane system (see Figs. 3 and 4).

- LANSCE has a single liquid-hydrogen moderator operating at 20 K and a pressure of about 6 bar absolute. The refrigerator is a CTI unit, modified for the purpose, which uses two compressors with oil separators and two reciprocating expansion engines. Hydrogen is circulated by a 3000 RPM centrifugal pump, which is in the outlet line of the system. Temperature control is provided by an electrical heater powered through a three-term controller in response to a germanium-diode temperature sensor. Temperature measurement at the moderator itself is measured by a hydrogen-vapor pressure bulb. The cold box containing the heat exchanger, which interfaces the hydrogen loop with the helium refrigerant, together with the control heater and temperature sensors, is sited within the service cell above the target top plate.

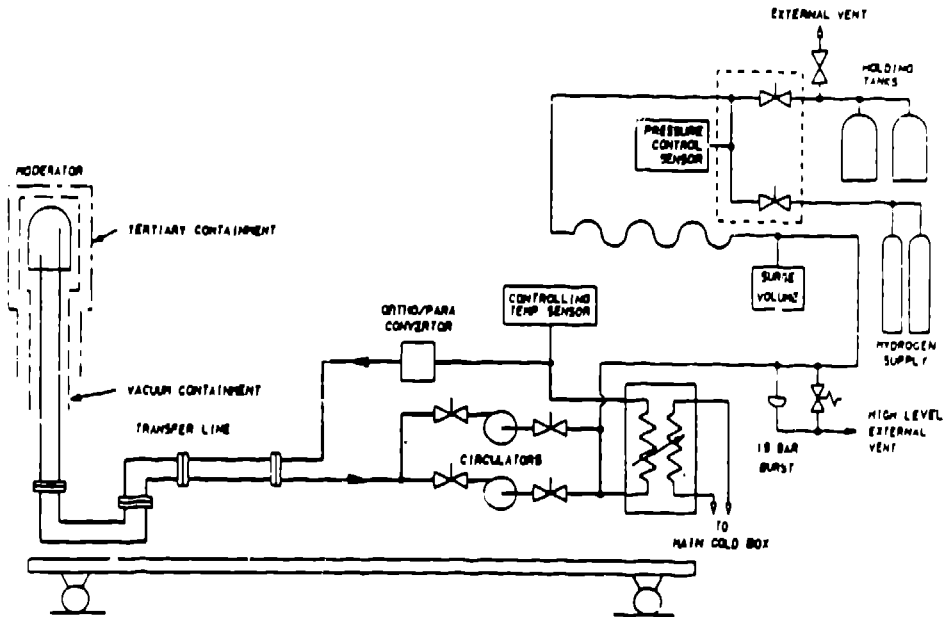


Fig. 3 ISIS H<sub>2</sub> moderator flow schematic.

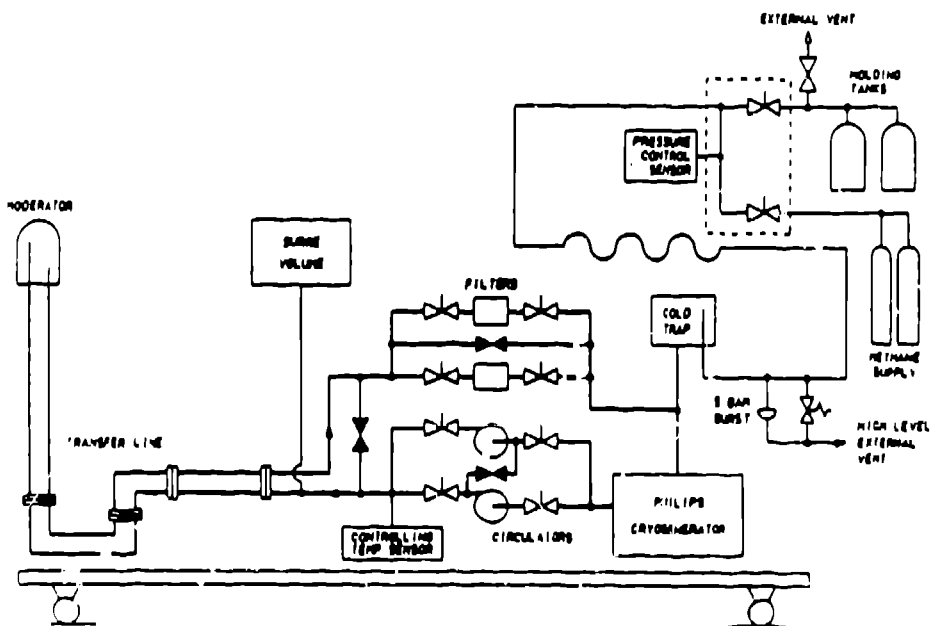


Fig. 4 ISIS CH<sub>4</sub> moderator flow schematic.

levels of  $30 \mu\text{A}$ , no radiation damage problems have been experienced in three years of operation. However, it is planned to re-site the cold box outside of the shielding during the major re-work of the target shielding in about three years time (see Fig. 5).

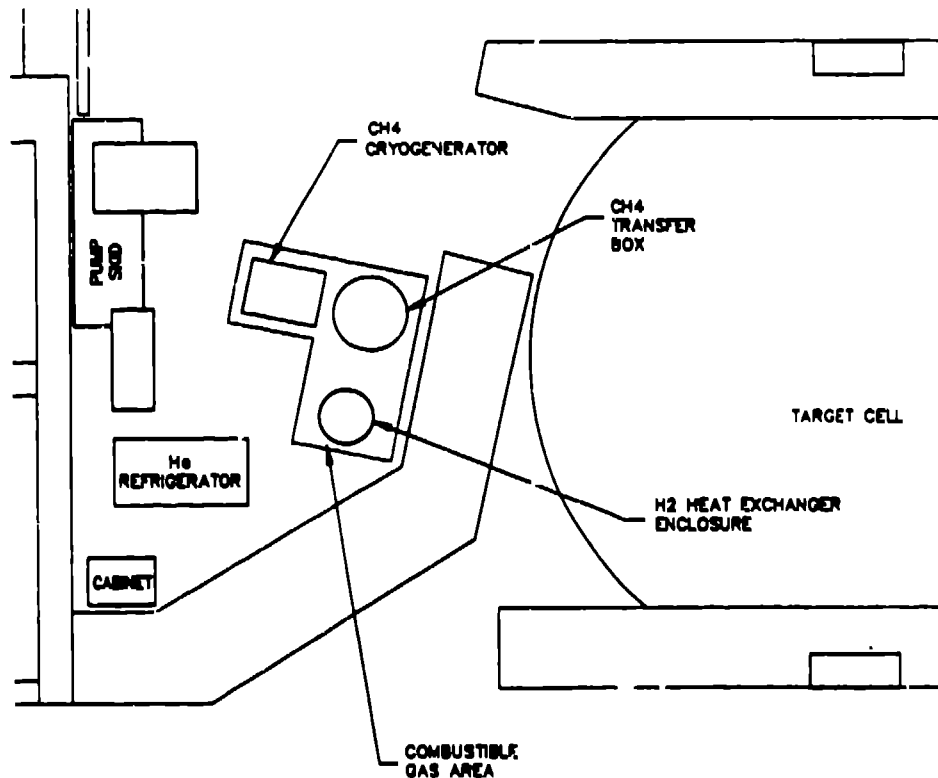


Fig. 5 LANSCE cryogenic equipment layout.

### LANSCE update

The LANSCE update will involve restructuring of the target-moderator-reflector (TMR) upper shielding and possibly some of the lower shielding. This will afford the opportunity to regroup the various feed pipes and transfer lines to improve the integrity of the upper shielding. It will also enable more preferred routes to be taken for the transfer lines to improve their flow characteristics.

The existing four-flux-trap-moderator windows might be reconfigured for cryogenic devices, depending on the experimental program requirements. The two moderator windows adjacent to the upper tungsten target will probably be opened up, also (see Fig. 6). Two or four methane moderators are possible, operating in one or two pairs. Each pair would share a refrigerator representing a heat load of about 1200 W at 100 K.

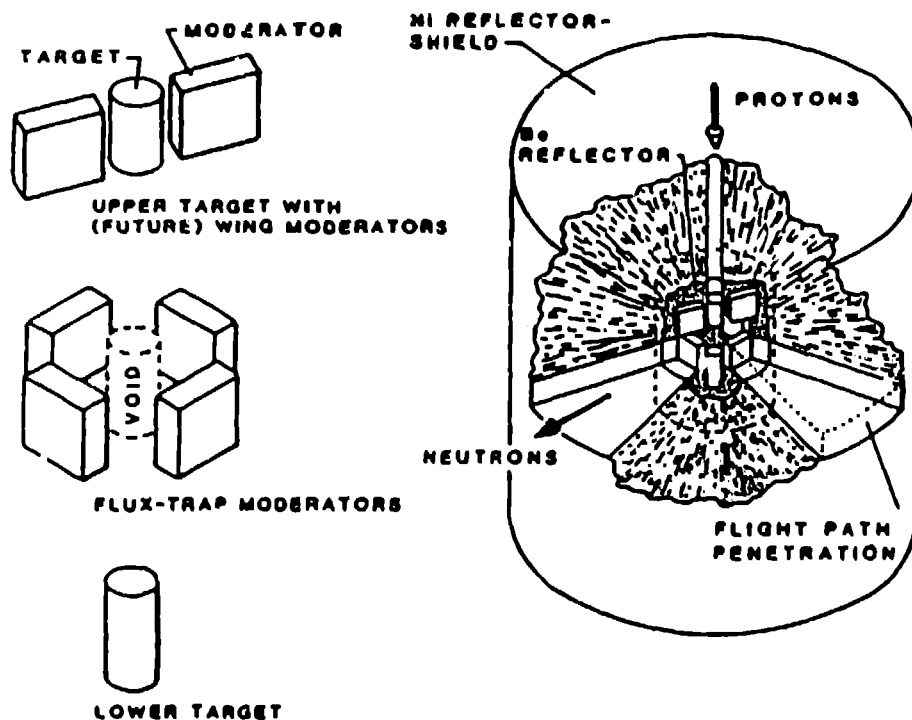


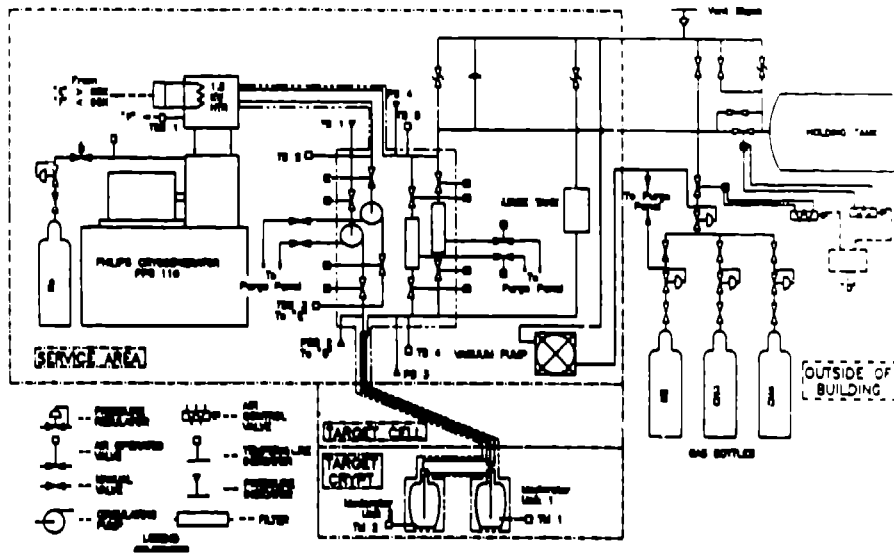
Fig. 6 LANSCE target system.

A complete design study of a liquid-methane system has been made, which indicates that by using a common transfer line for two moderators coupled in series, a Philips-Stirling cycle refrigerator with a listed output of 1500 W at 100 K would be sufficient (see Fig. 7).

A number of modifications to the ISIS refrigerator were found necessary to suit the particular application.

The heat exchanger is in the form of an annulus with the return liquid entering at the top center of the cold head. The outlet pipe was on the lower side of the annulus. This caused a variable flow pattern, which resulted in changes in heat transfer to the methane. The changes seemed to occur in response to some form of local turbulence, as the effect could be reversed by changing the flow or pressure of the liquid methane. A reasonably successful remedy was to insert fixed valves into the inlet pipe to create a rotary motion of the liquid. A second problem was local freezing of methane in the cold head during the initial cool down, as mass flow during the gas phase is very low. An electrical heater was eventually fitted in response to a sensor on the cold head. The powder insulation was also removed and the head vacuum insulated.

The LANSCE machine will be delivered suitably modified to avoid these requirements. The heat exchanger will be of a coiled pipe design with a heater wound



• Fig. 7 LANSCE facility liquid methane moderator flow schematic.

between the coils during manufacture. A vacuum-insulated head will have both inlet and outlet pipes from the cooling coil brought out through a common side port in the vacuum chamber, which will enable the vacuum chamber to be integrated into the main pumping system. Various additional interlocks will also be added to a remote control facility for the helium gas refrigerant pressure (see Fig. 8).

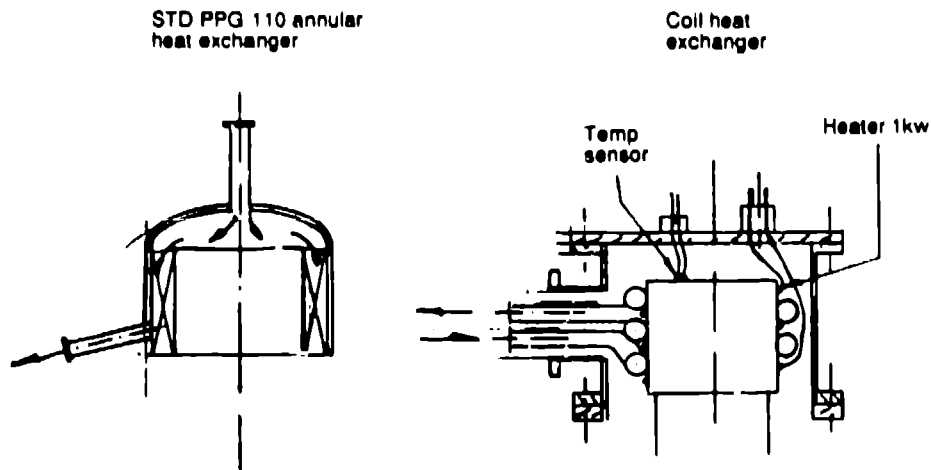


Fig. 8 LANSCE  $\text{CH}_4$  refrigerant heat exchanger concepts.

## Circulators for cryogenic liquid

The circulators used for both of the ISIS cryogenic moderators were developed from Philips units originally designed for pumping high-pressure cold helium gas in heat-transfer circuits. They use a standard high-quality 50-Hz three-phase motor operating at 300 Hz to give a rotational speed of 1800° RPM. An extension of the motor shaft carries the overhung pump impeller. The unit is built into a pressure vessel because it operates in methane gas, which forms a static pocket connected to the main system. A secondary containment filled with an inert gas was originally required as a safety measure in the event of a methane leak. The complete outer vessel was later redesigned to incorporate this gas jacket, greatly improving ease of servicing. The greater duty of pumping relatively heavy liquids resulted in bearing-slip within the mountings, which caused high temperatures and loss of lubricant with premature bearing failure. The remedy was to clamp both inner and outer bearing races with ring nuts—the bearing assembly furthest from the impeller being carried by a thin metal diaphragm to accommodate thermal axial movement. Unfortunately, this thermally isolated the bearing and led to overheating. The source of this heat, however, is probably not purely frictional but might well derive from the waveform generated by a newly installed model frequency inverter. This is now under investigation (see Fig. 9).

The circulator used for liquid hydrogen in the LANSCE moderator runs at a much lower speed. The impeller is correspondingly larger, but in place of the overhung shaft is a long drive shaft with a cold bearing at the impeller end. This bearing makes the whole design much more flexible and results in a device with a much longer life and greater reliability. The bearing is manufactured by *Barden Precision* and is primarily for high-temperature application. A dry lubricant is sintered into the cage material, which sheds dry lubricant in operation. The LANSCE circulator remained serviceable after approximately 10,000 hours operation. The maximum bearing life achieved with the ISIS high-speed unit is around 2500 hours, but the average is much less. On the other hand, the latter are smaller, lighter, and easy to replace.

A circulator similar to that used for the LANSCE hydrogen system has been ordered for the methane moderator but in a modified form to enable replacement without breaking into the vacuum system. The impeller will also be modified to better help the cool-down operation through the two-phase flow stage (see Fig. 10).

## General layout of LANSCE cryogenic equipment

The hydrogen and methane cryogenic service equipment will be sited side by side in the service area. A new control cabin is to be built on the roof of the LANSCE target area accessible from the upper plant room. This will contain monitoring and control equipment. Adjacent to the cabin will be the methane gas-handling plant and operation panel (see Fig. 11).

## Radiation damage to methane

Liquid methane undergoes molecular changes in ionizing radiation. Long chain hydrocarbons are formed initially taking the form of yellow oils belonging to the

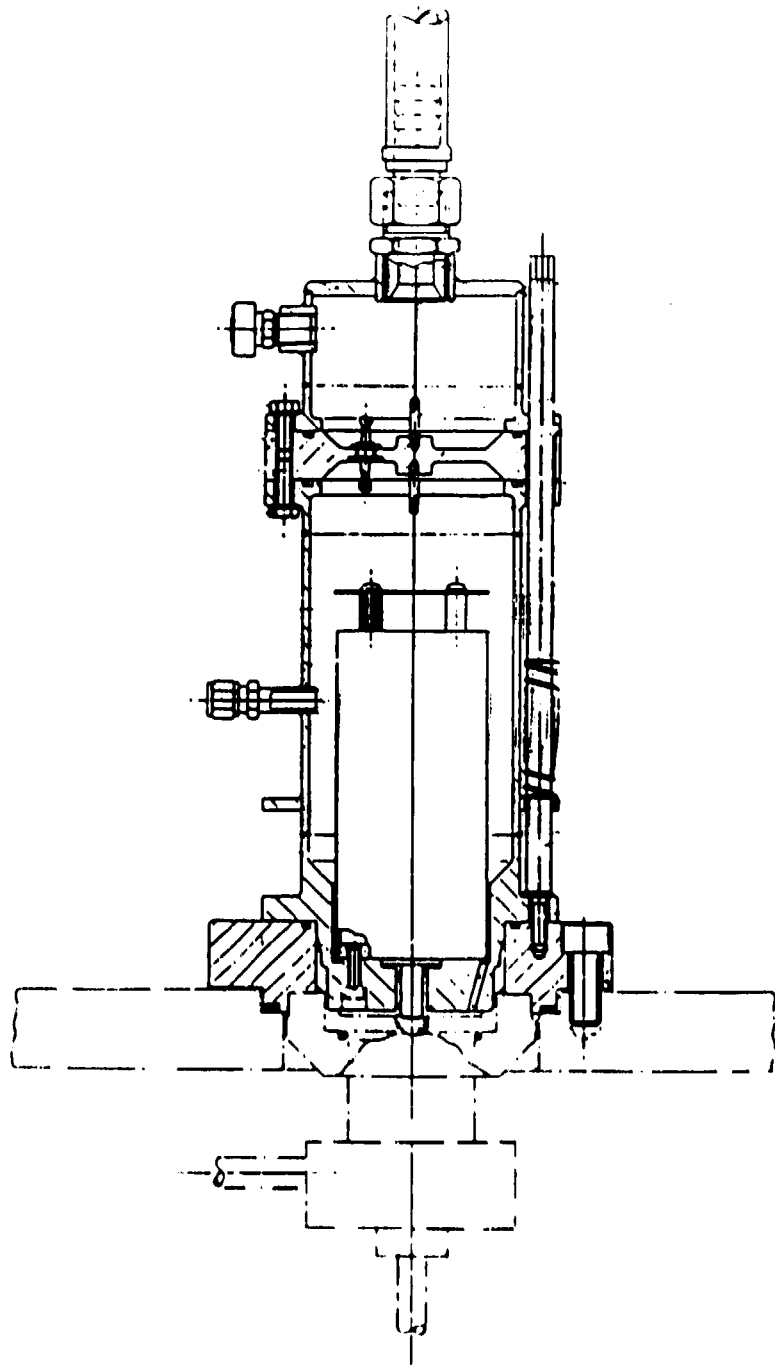


Fig. 9 ISIS CH<sub>4</sub> circulating pump.

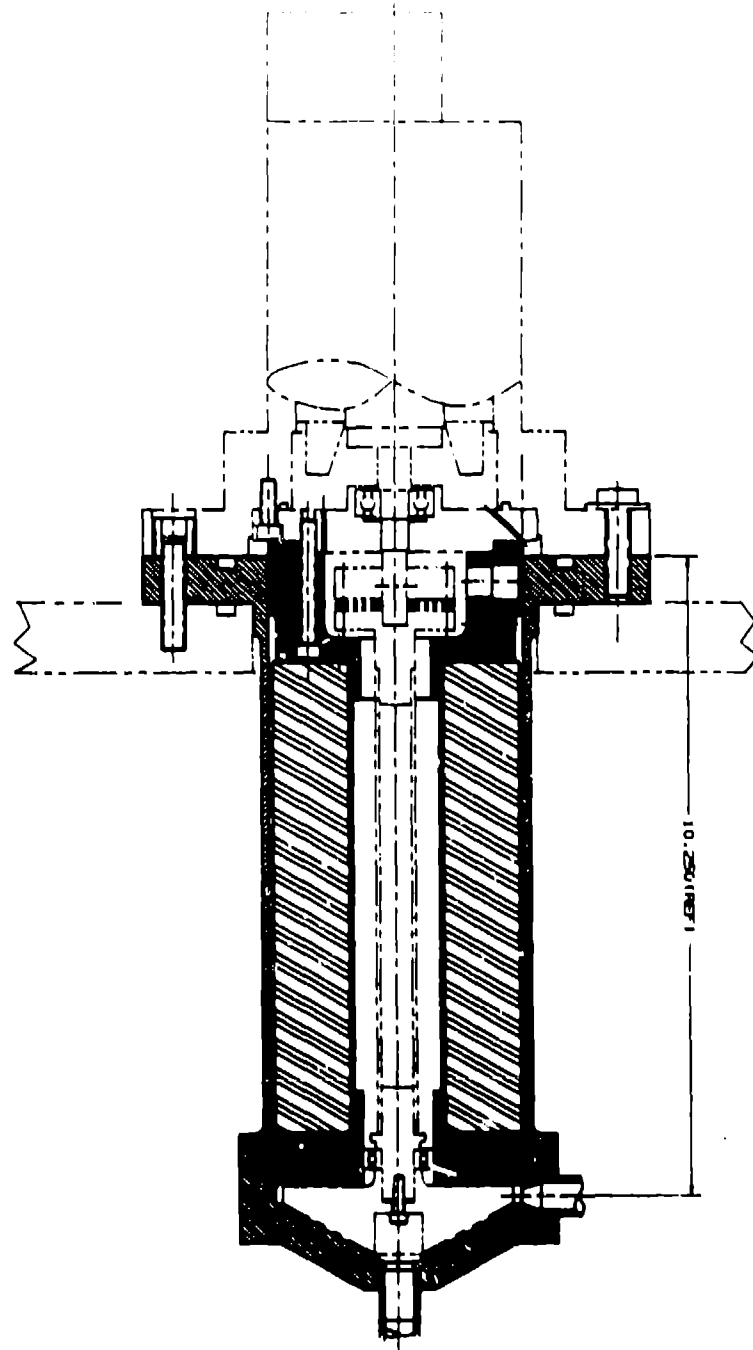


Fig. 10 LANSCE CH<sub>4</sub> circulating pump.



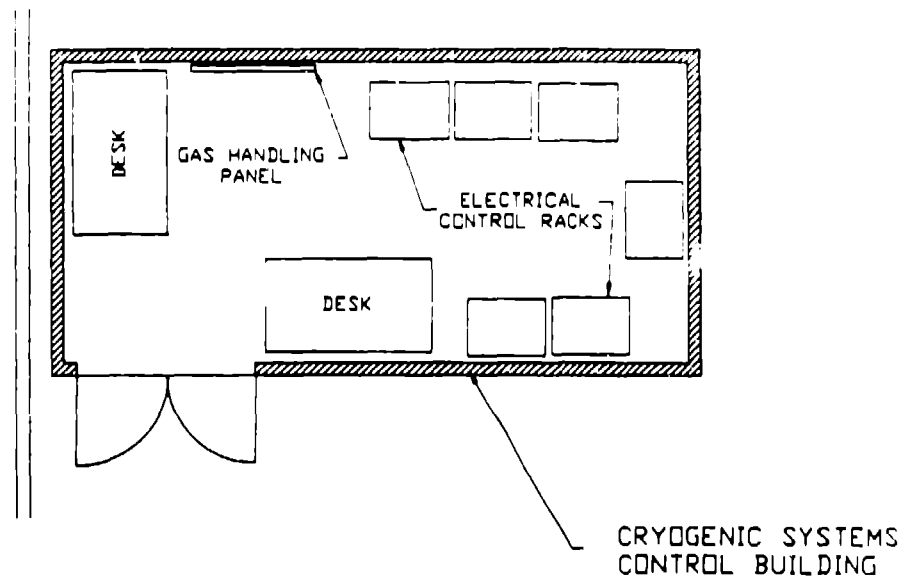


Fig. 11 LANSCE cryogenic control building.

paraffin group. Further radiation would probably result in the eventual formation of solids. The beam current at ISIS is now  $100 \mu\text{A}$ , and substantial levels of these paraffins are being produced. This does not appear to impair the neutronic efficiency of the moderator, but will ultimately result in a blockage that will be extremely difficult to remove. Most of the impurities are probably in solution with the methane liquid, but on warming up, the methane will be boiled off leaving the impurities behind as viscous liquid. Furthermore, it is likely that supersaturated levels of impurities will be produced. The present filters are, therefore, of limited value under such conditions, as some form of continuous separation and removal is required. This could be made possible by vaporizing the methane by raising its temperature or lowering its pressure and isolating the liquid impurities (see Figs. 12 and 13). However, either of these options would require development funds. A simpler method could be to centrifuge the liquids and remove the heavier fraction with a Pitot tube. This is worthy of examination because relatively small development costs would be required (see Fig. 14).

#### Combined $\text{CH}_4/\text{H}_2$ moderator

A separate report has been written about the idea of a combined  $\text{CH}_4/\text{H}_2$  moderator, which is based on some elementary calculations that indicate such a system is feasible thermodynamically. However, considerable experimentation and development would be needed to turn the idea into a working system, and a study of the neutronic gains would have to be evaluated before a decision can be made (see Fig. 15).

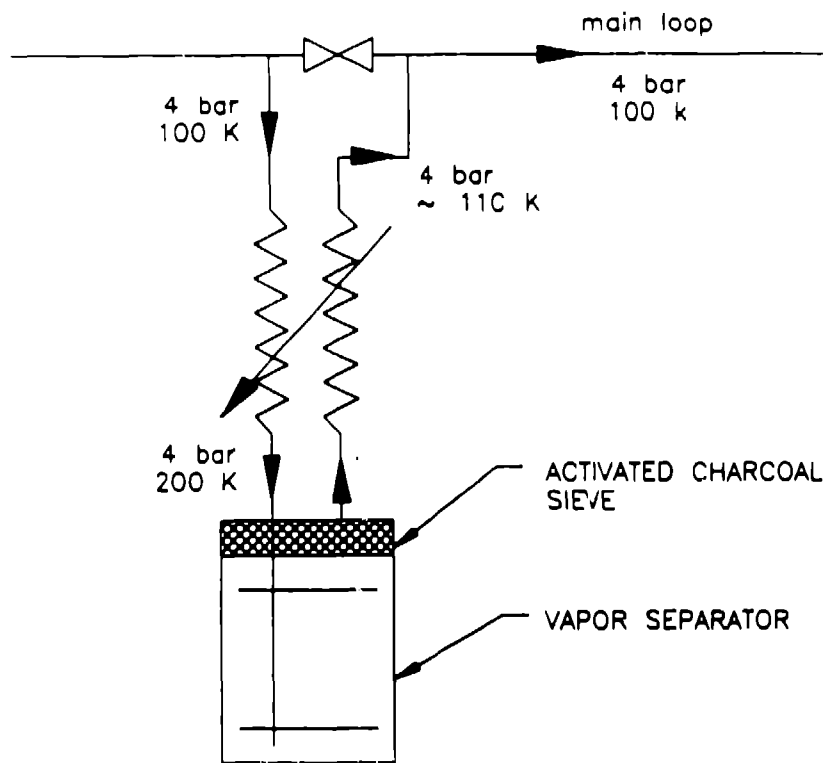


Fig. 12 Temperature vapor separator.

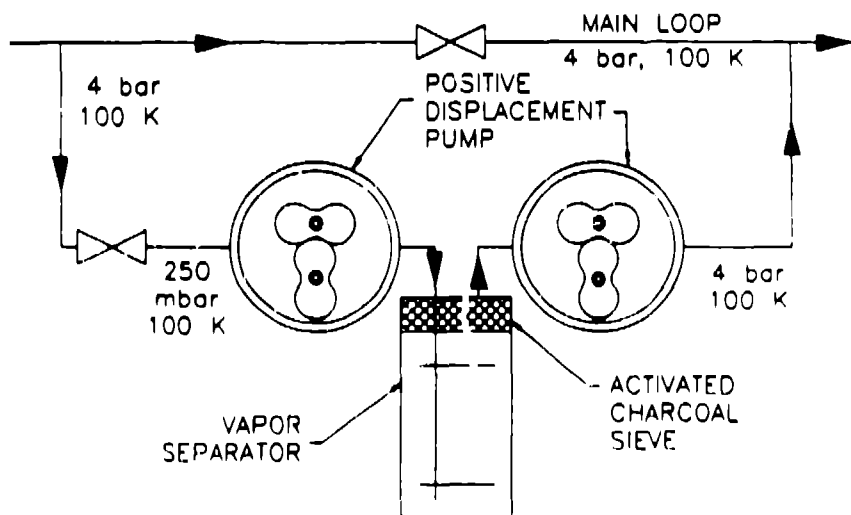


Fig. 13 Pressure vapor separator.

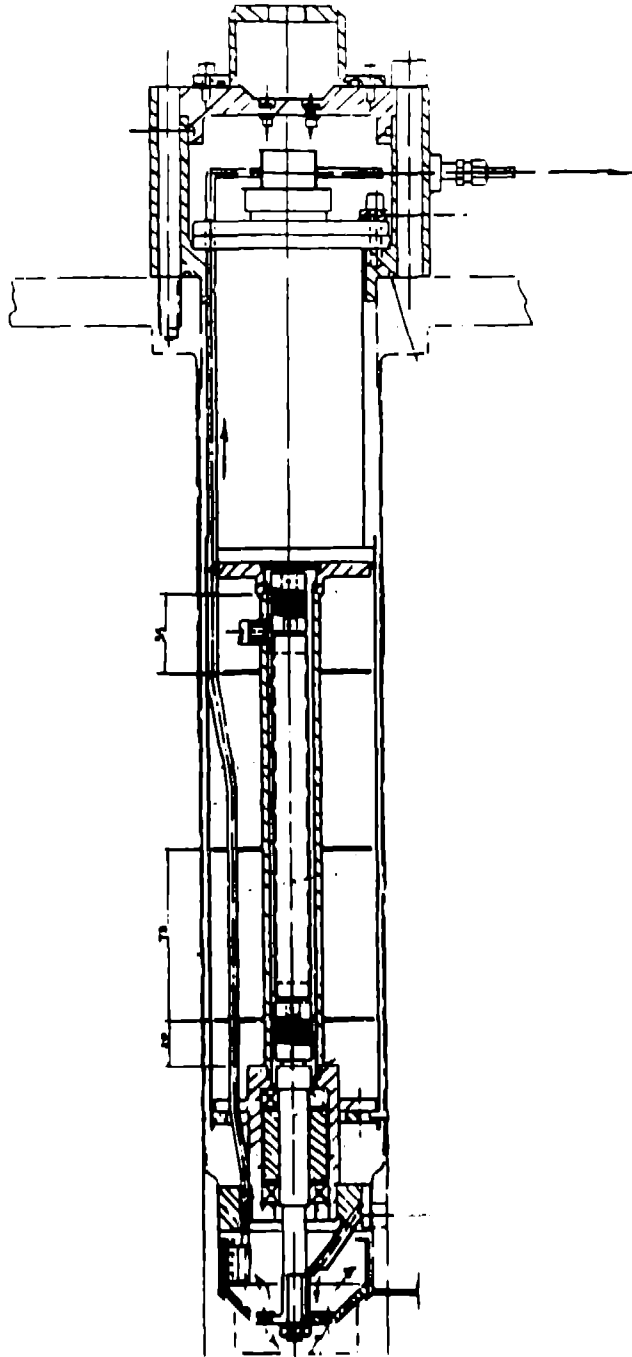


Fig. 14 Proposed centrifuge separator.

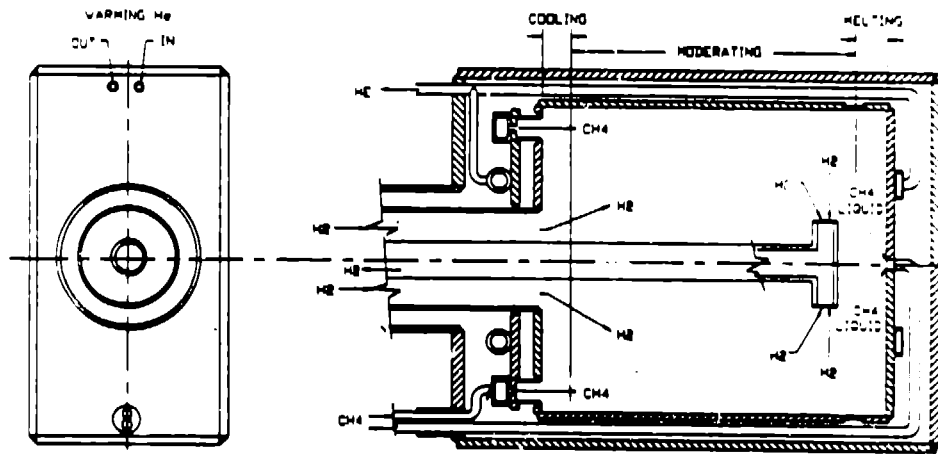


Fig. 15 Combined CH<sub>4</sub>/H<sub>2</sub> moderator.

## The advanced MAPLE reactor concept

*R. F. Lidstone, A. G. Lee, G. E. Gillespie and H. J. Smith*  
Atomic Energy of Canada Limited  
Pinawa, Manitoba  
CANADA

### Introduction

Over the next ten to twenty years, a major expansion in the utilization of intense neutron fields is anticipated, subject to the availability of an appropriate mix of medium-, high-, and ultra-high-flux neutron sources. At the leading edge in terms of flux intensity, an ultra-high-flux neutron source, such as the proposed ANS facility<sup>(1,2)</sup>, is needed to generate neutron fluxes approaching  $1 \times 10^{20}$  n/m<sup>2</sup>s for difficult experiments in condensed-matter physics and for the large-scale production of transuranium isotopes. Considering the saturated utilization of the existing high-flux reactors at Grenoble, Brookhaven, and Oak Ridge, new facilities with peak-available neutron fluxes of 0.5 to  $2 \times 10^{19}$  n/m<sup>2</sup>s will substantially augment the world's capability in materials testing for advanced fission and fusion reactors and in advanced basic and applied research using extracted neutron beams. Furthermore, the real key to global access to the peaceful benefits of nuclear science and technology is an international network of modern medium-flux (peak fluxes of 1 to  $5 \times 10^{18}$  n/m<sup>2</sup>s) neutron sources to facilitate practical applications in areas ranging from neutron scattering and nuclear physics in support of national research programs, to materials testing and manpower training in support of power-generation programs, to materials analysis and the production of key radioisotopes in support of medicine, industry, and agriculture.

Notwithstanding the exciting pace of development in accelerator technology<sup>(1,3)</sup>, fission-based systems are likely to continue to dominate the overall neutron-source population for the next decade or two. While accelerator-driven spallation sources are regarded as somewhat less difficult to site than comparable fission-reactor sources, their capital and operating costs are substantially higher than for conventional reactor sources<sup>(1)</sup>. Moreover, the research and development program required to establish an ultra-high-flux facility is judged to be "moderately large" for a spallation source, compared to "modest" for the current ANS concept<sup>(1)</sup>.

In Canada the need for advanced neutron sources has long been recognized. Between 1963 and 1967, AECL study teams investigated the accelerator-based ING (Intense Neutron Generator) concept<sup>(4,5)</sup>, whose objective was to generate peak-unperturbed thermal-neutron fluxes of about  $1 \times 10^{20}$  n/m<sup>2</sup>s, which would have yielded a factor of 25 improvement over the best performance since achieved in the NRU reactor.

During the past several years, AECL has been developing the new MAPLE multipurpose reactor concept<sup>(3,6,7)</sup>, which is capable of generating peak thermal neutron fluxes of up to  $3 \times 10^{18}$  n/m<sup>2</sup>s in its heavy water reflector at a nominal

thermal power level of 15 MW<sub>th</sub>. AECL will commercially produce key short-lived radioisotopes, such as <sup>99</sup>Mo, and demonstrate MAPLE technology in the prototype 10 MW<sub>th</sub> MAPLE-X10 facility now being constructed at its Chalk River Nuclear Laboratories.

Also, the Canadian Institute for Neutron Scattering (CINS) has recently made recommendations to the Natural Sciences and Engineering Research Council (NSERC) regarding the new and upgraded facilities necessary to sustain neutron scattering research in Canada<sup>(6)</sup>. Featured in the recommendations are the near-term upgrading of the McMaster Nuclear Reactor with a 5-MW<sub>th</sub> MAPLE reactor and the study of mid-term options to strengthen Canadian access to high and ultra-high neutron fluxes—including a MAPLE-based high-flux neutron source. McMaster University is currently seeking NSERC funding for the MAPLE upgrade. Additionally, AECL has just commissioned studies to compare an advanced D<sub>2</sub>O-cooled MAPLE reactor with an accelerator-based neutron source as prospective successors to NRU.

#### **A new Canadian high-flux neutron source**

To date, the MAPLE program has focused on the development of a modest-cost multipurpose medium-flux neutron source to meet contemporary requirements for applied and basic research using neutron beams, for small-scale materials testing and analysis, and for radioisotope production. The basic MAPLE concept incorporates a compact light-water cooled and moderated core within a heavy-water primary reflector to generate strong neutron flux levels in a variety of irradiation facilities. Its major design features are:

- 1. Compact, Light-Water-Cooled and -Moderated Core.** The MAPLE core volume is limited to about 63 liters (nineteen 600-mm long fuel assemblies), which results in the generation of very strong fast and intermediate neutron fluxes within the core and the availability of unusually strong thermal-neutron fluxes at irradiation facilities in the core and surrounding reflector. For example, the peak-unperturbed thermal-neutron flux is  $4 \times 10^{17}$  n/m<sup>2</sup>s/MW in a central flux trap and  $2 \times 10^{17}$  n/m<sup>2</sup>s/MW in the heavy-water reflector.
- 2. LEU-Silicide Fuel Particles Dispersed in Aluminum Rods.** MAPLE fuel meat is low-enrichment (about 19.7 weight percent <sup>235</sup>U in total uranium) U<sub>3</sub>Si particles dispersed in an aluminum matrix; it is coextrusion clad with aluminum to form finned rods. This fuel has been developed by AECL, as part of the international RERTR (Reduced Enrichment for Research and Test Reactors) program, for use in the NRU, MAPLE-X10 and other MAPLE reactors.
- 3. Heavy-Water Primary Reflector.** The MAPLE reactor concept employs heavy water as the primary reflector, which provides optimum transmission of neutrons from the core to the horizontal beam ports and various vertical facilities used for neutron activation analysis, radioisotope production, etc.

- ⊕
4. **Customized Beam-Tube Arrangement.** A variety of beam-tube arrangements can be accommodated in the MAPLE reactor assembly. The number and orientation of the beam tubes are adjusted to meet the specifications and requirements of facility users.
  5. **MAPLE Safety Features.** The MAPLE design relies on diverse safety measures to assure protection of operating staff and members of the public in the event of conceivable accidents. For example, the core is deliberately undermoderated so that all important reactivity coefficients are appropriately negative. Also, one reactor shutdown system is physically separated and the second is functionally isolated from the reactor regulation system, and fuel changing can proceed without the need to disable the control or shutdown systems.

In view of the renewed Canadian interest in a high-flux-neutron source, the MAPLE group has begun to explore advanced concepts based on AECL's experience with heavy-water reactors. The overall objective is to define a high-flux facility that will support materials testing for advanced power reactors, new developments in extracted neutron-beam applications, and/or production of selected radioisotopes. The design target is to attain similar performance levels to HFR-Grenoble, HFBR, and HFIR in a new D<sub>2</sub>O-cooled, -moderated, and -reflected reactor based on rodged LEU fuel. To minimize capital and incremental development costs, the design concept uses MAPLE reactor technology to the greatest extent practicable.

⊕

The main performance goals for the new advanced MAPLE-D<sub>2</sub>O reactor are a peak thermal-neutron flux of about  $1 \times 10^{19}$  n/m<sup>2</sup>s in the heavy water reflector and a peak fast-neutron flux of  $2 \times 10^{18}$  n/m<sup>2</sup>s in a central irradiation facility for a core configuration in which the maximum linear fuel rod rating is less than 120 kW/m.

#### **Description of the MAPLE-D<sub>2</sub>O reactor**

The MAPLE-D<sub>2</sub>O reactor (Figs. 1 and 2) is a tank-type reactor employing heavy water for cooling, moderation, and reflection. Within the stainless-steel tank (3.0 m tall by 2.2 m diameter), a 19-site MAPLE grid plate structure is installed to form an inlet plenum/lower reflector in the bottom meter of the tank. Hexagonal zirconium-alloy MAPLE flow tubes, lengthened to accept 1.0-m-long fuel assemblies thread and lock into the grid-plate sites; non-fuel modules, such as irradiation rigs, may be similarly attached to the grid plate. Heavy water from the primary heat exchangers enters the lower reflector region of the tank and is forced upwards through the flow tubes to cool the fuel; it then mixes in an outlet chimney and passes through apertures to the primary reflector region, which connects via exit nozzles and outlet piping to the primary coolant pumps. The main reactor specifications are presented in Table 1.

Included in Table 1 are fuel specifications. The MAPLE-D<sub>2</sub>O fuel assembly uses 1000-mm lengths of NRU-type U<sub>3</sub>Si-Al fuel rods in a 60-rod fuel assembly; however, the standard NRU sheath thickness is reduced from 0.76 mm to 0.38 mm. The performance of the U<sub>3</sub>Si-Al fuel rods has been excellent, with up to 93 percent burnup of initial fissile material being achieved at very high linear power ratings (up

⊕

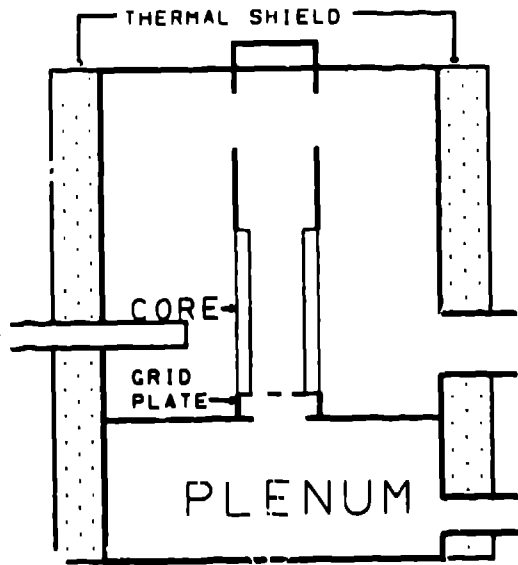


Fig. 1 Vertical MAPLE-D<sub>2</sub>O layout.

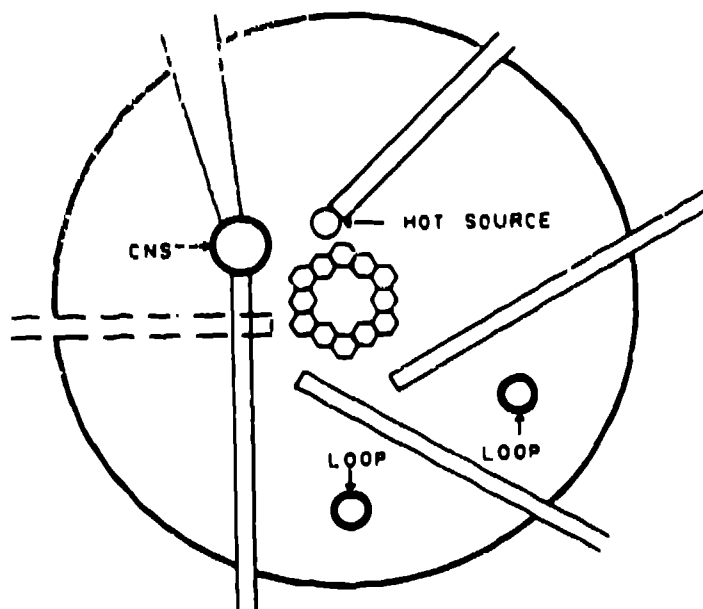


Fig. 2 Horizontal MAPLE-D<sub>2</sub>O layout.



Table 1 MAPLE-D<sub>2</sub>O specifications

General	
1. Reactor type	Tank type; low-enriched (19.7 %) uranium fuel; heavy-water cooled, moderated, and reflected
2. Nominal power	50 MW
3. Purpose	extracted neutron-beam applications; advanced materials testing; radioisotope production
Reactor Physics	
4. Core Parameters	$k_{eff} = 1.215$
5. Thermal neutron flux	Maximum in island: $1.0 \times 10^{19} \text{ n}\cdot\text{m}^{-2}\cdot\text{s}^{-1}$ in reflector: $1.2 \times 10^{19} \text{ n}\cdot\text{m}^{-2}\cdot\text{s}^{-1}$
6. Reactivity balance	Burnup 91 mk Xe & Sm 53 mk Experiments 25 mk Reserve 8 mk
Core	
7. Shape & dimensions	Irregular hollow hexagon, 1000 mm high, maximum diameter 400 mm
8. Number of subassemblies	12 hexagonal zirconium-alloy flow channels, 77.6 mm (externally) across the flats, 1.6 mm thick, containing 60-rod fuel assemblies
9. Lattice	Hexagonal, pitch approx. 80 mm
10. Core fissile load	Approx. 10.6 kg <sup>235</sup> U
11. Power density	Average 750 kW l <sup>-1</sup> Maximum 1300 kW l <sup>-1</sup>
12. Operating cycle	40 d
13. Burnup	Average 22 % of initial <sup>235</sup> U
14. Moderator	Heavy water
Fuel Assemblies	
15. Subassemblies	60 rods plus central support shaft in a hexagonal array, pitch 9.5 mm
16. Form & Composition	NRU-type U <sub>3</sub> SiAl rods coextrusion clad with finned aluminum alloy; fuel meat 5.48 mm diameter by 1000 mm long; cladding thickness 0.38 mm; six fins per rod 1.02 mm high by 0.76 mm wide; Enrichment 19.7 % <sup>235</sup> U in U, by weight;
17. Uranium content	0.88 kg <sup>235</sup> U; 4.47 kg U

Table 1 MAPLE-D<sub>2</sub>O specifications (continued)

<b>Core Heat Transfer</b>	
18. Heat transfer area	Total 22.9 m <sup>2</sup> , including fins
19. Heat flux	Average 2.18 MW m <sup>-2</sup> Peak 3.77 MW m <sup>-2</sup>
20. Fuel rod temperatures	218°C maximum in fuel 138°C maximum at clad surface
21. Coolant	heavy water
22. Core flow	Velocity 12 m s <sup>-1</sup> Total mass flow 420 kg·s <sup>-1</sup>
23. Coolant pressures & temperatures	Inlet 1000 kPa, 38°C Outlet 370 kPa, 57°C
<b>Control</b>	
24. Regulating system	Single PROTROL (industrial EC-based) digital control computer; six V-shaped Hf absorber blades attached above to stepper-motor-driven shafts; blade surface 92 mm wide by 1100 mm high, total reactivity worth 307 mk
25. Shutdown System #1	Six U-shaped Hf absorber blades attached above to hydraulically-actuated shafts, blade surface 138 mm wide by 1100 mm high
26. Shutdown System #2	Magnetic-clutch override of regulating system
<b>Reflector</b>	
27. Material & dimensions	heavy water surrounding core, 2.2 m diameter by 3.0 m high
<b>Reactor Vessel</b>	
28. Material, form & dimensions	Stainless-steel right-circular cylinder, 2.2 m inner diameter by 3.0 m high, 12 mm thick
<b>Experimental Facilities</b>	
29. Horizontal beams	Six to nine rectangular zirconium-alloy tubes, 60 mm wide by 150 mm high; Accessing thermal neutron fluxes of $8 \times 10^{18}$ n·m <sup>-2</sup> ·s <sup>-1</sup> to $1.0 \times 10^{19}$ n·m <sup>-2</sup> ·s <sup>-1</sup>
30. Cold source	To be specified, possibly a liquid hydrogen-deuterium mixture optimized for a cylindrical source of 200 mm diameter,
<b>Shielding</b>	
31. Radial	600 mm thermal shield: 70% iron, 30% water; 1350 mm ilmenite concrete biological shield
32. Radiation fields	gamma: 20 micro Sv·h <sup>-1</sup> neutron: less than 0.2 micro Sv·h <sup>-1</sup>

to 100 kW/m) with acceptable swelling behavior and no defects. For low burnup fuel, maximum linear power ratings of 120 kW/m have been found acceptable.

Hafnium absorber blades are inserted immediately outside the core for reactivity control, generally following the contours of the core. When deployed, the absorber blades isolate the fuel from the heavy water outside of the core. The principal reactor shutdown system hydraulically actuates a set of six U-shaped absorber blades that fit around the corner sites of the 19-site core. A set of six V-shaped absorber blades are normally operated by the reactor regulating system using stepper motors to position mechanically-driven absorber shafts; a second independent shutdown can override the regulating system by releasing magnetic latches to insert its reactivity-control absorbers.

The reactor regulating system utilizes a digital computer system to initiate and maintain selected reactor flux and power levels and to acquire, record, and display process information. Its automatic-control algorithm-effects reactor changes in minimal time from current set point while avoiding overshoot and the violation of rules governing minimum reactor period and maximum acceptable rate of absorber withdrawal.

The reflector tank is penetrated vertically by appropriate fuel-test loops, cold and/or hot sources, and irradiation rigs and horizontally by a set of zirconium-alloy beam-tubes. It is expected that most MAPLE-D<sub>2</sub>O beam tubes will be rectangular in cross section; the nominal specification is 150 mm high by 60 mm wide.

To limit beam-tube length while reducing neutron and  $\gamma$  fields to acceptable levels, the reactor tank is closely surrounded by a thick (600 mm) thermal shield, whose average composition, by volume, is seventy percent iron and thirty percent water. At a thermal power level of 60 MW, the radiation fields are reduced to 25  $\mu$ Sv/h by an additional 1350 mm of ilmenite concrete. Accordingly, typical distances from the nose of the beam tube to the working face are approximately 3 m.

## MAPLE-D<sub>2</sub>O studies

1. **Physics Studies.** Scoping calculations for MAPLE-D<sub>2</sub>O reactor were performed for two alternative core configurations: eighteen fueled sites with the central site unfueled; and twelve outer sites fueled with the central seven sites unfueled. The 3DDT three-dimensional multigroup diffusion code<sup>(9)</sup> was employed with two neutron-energy groups: a thermal group with  $E \leq 0.626$  eV, and a fast group with  $E > 0.625$  eV. Cell-averaged cross sections were prepared using the supercell option of the WIMS-CRNL code<sup>(10)</sup> to model the cell of interest in its local environment and an 89-group library derived from the ENDF/B-V data file.

The scoping calculations confirmed that the twelve-site annular core incorporated sufficient reactivity margins to support a practical fuel cycle and could attain the targeted fast-neutron flux in a central rig. For the same maximum linear fuel rating, the twelve-site core generated substantially better peak-thermal-neutron fluxes in the reflector—49 percent higher than the eighteen-site core. Accordingly, no efforts were made to achieve higher fluxes by flattening the power shape of the eighteen-site core

and subsequent calculations focused exclusively on the flux-trap arrangement formed by the twelve-site core.

Additional 3DDT calculations were performed for 30 MW and 50 MW twelve-site cores using the following five neutron-energy group structure:

FAST	$E > 0.8 \text{ MeV}$
GROUP 2	$9 \text{ keV} < E < 0.8 \text{ MeV}$
GROUP 3	$4 \text{ eV} < E < 9 \text{ keV}$
GROUP 4	$0.626 \text{ eV} < E < 4 \text{ eV}$
THERMAL	$E < 0.625 \text{ eV}$

The same WIMS-CRNL modeling strategy was used to prepare the cell-averaged cross sections for 3DDT. The 3DDT calculations were verified by repeating the fresh-core calculations with the MCNP code<sup>(11)</sup>, which uses a general-geometry package and Monte Carlo theory to solve the transport equations in three dimensions with minimal compromise in the realism of the modeling. MCNP relies on a continuous-energy library based on the ENDF/B-V data file.

Table 1 shows the computed reactivity balance for the twelve-site core at 50 MW. The excess reactivity in a fresh core is 177 mk. The estimated short-lived-fission-product load is about 51 mk. Allowing 25 mk for beam ports and irradiation sites in the heavy-water reflector and 8 mk as a reserve, the expected core lifetime is 40 full-power days. The corresponding average fuel burnup is estimated at 22% <sup>235</sup>U for a whole core replacement scheme. Alternative fuel management schemes will be investigated in future studies.

Fig. 3 shows the 3DDT-computed radial distribution of the fast and thermal-neutron fluxes at 50 MW for the horizontal plane of maximum thermal flux. The unperturbed-peak-thermal flux is  $1.2 \times 10^{19} \text{ n/m}^2/\text{s}$ . For three 50 mm x 150 mm tangential beam tubes at distances of 100 mm, 150 mm, 200 mm from the core wall, the MCNP-computed perturbed-thermal fluxes are  $9 \times 10^{18} \text{ n/m}^2/\text{s}$ ,  $1.0 \times 10^{19} \text{ n/m}^2/\text{s}$  and  $9 \times 10^{18} \text{ n/m}^2/\text{s}$ , respectively; the average computed ratio of perturbed to unperturbed flux at the beam-tube noses is 0.85.

Figure 4 shows the axial-thermal-neutron flux distributions for 50 MW at distances of 120 mm and 500 mm from the core edge. The flux skewing is caused by deployment of the regulating-system absorber blades to the core midplane; accordingly, the horizontal beam tubes should be located somewhat below the core midplane to minimize flux shifts during the operating cycle. At 500 mm from the core edge, the peak-unperturbed-thermal flux is roughly  $4 \times 10^{18} \text{ n/m}^2/\text{s}$ , which corresponds to the maximum available in NRU, and the flux length at half peak extends over about 1.3 m. Hence, although the effect of fueled sites in the reflector have not yet been evaluated, the outer reflector regions appear suitable for high-pressure, high-temperature fuel-test loops. Furthermore, it is planned to investigate the prospects for creating local regions of elevated fast flux for materials-damage studies via fast-neutron loops nearer the reflector flux peak.

Fast-neutron fluxes that could be produced in a central materials irradiation facility have also been investigated. For a zirconium-walled rig displacing a cylinder of

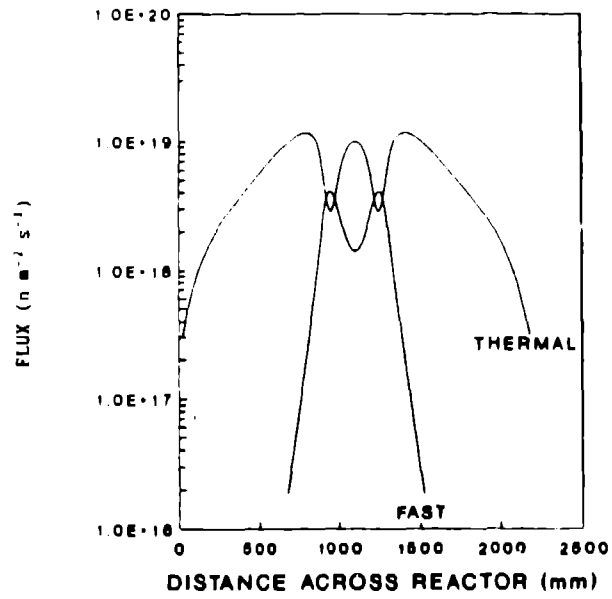


Fig. 3 MAPLE-D<sub>2</sub>O radial neutron flux distributions at 50 MW.

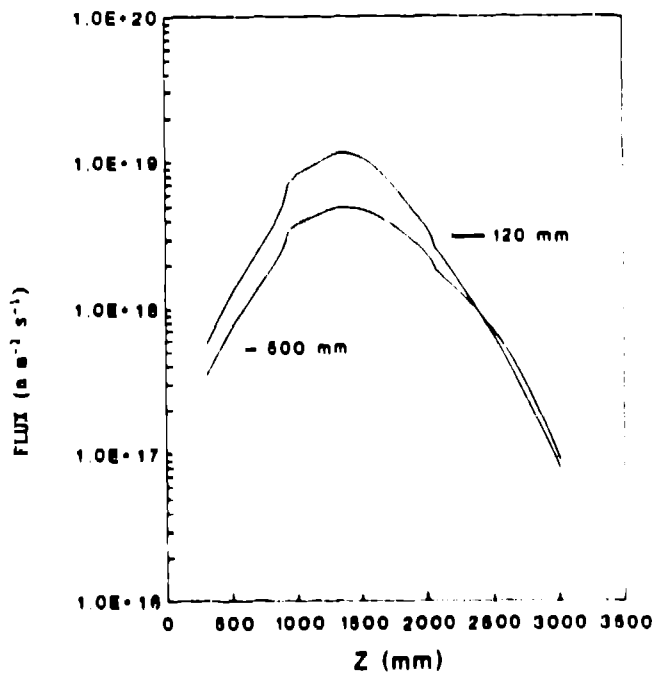


Fig. 4 MAPLE-D<sub>2</sub>O axial thermal flux distributions at 50 MW.

heavy water 1000 mm long by 90 mm diameter, the fast ( $> 0.8$  MeV) neutron flux in a strongly absorbing steel rod is estimated to be  $2.4 \times 10^{18}$  n/m<sup>2</sup>/s<sup>-1</sup>. This flux level is comparable to that available in a major facility such as OSIRIS, which generates fast neutron fluxes of  $2 \times 10^{18}$  n/m<sup>2</sup>/s<sup>-1</sup> in a cylindrical volume 520 mm long by 30 mm diameter at a power output of 70 MW<sub>th</sub>.

**2. Shielding Studies.** A brief survey of MAPLE-D<sub>2</sub>O shielding requirements was conducted using the one-dimensional discrete-ordinates transport code, XSDRNPM-S<sup>[12]</sup> and the SCALE 27n-18γ cross-section library<sup>[13]</sup>. Spherical geometry was assumed with S<sub>16</sub> angular quadrature, and P<sub>3</sub> anisotropic scattering. The MAPLE core was represented by a spherically homogenized (volume preserved) core with the central island assumed to be voided. The thickness of surrounding D<sub>2</sub>O, the tank wall, and the shields was preserved in the calculations. Peak heating in the concrete and the neutron and γ fields at the shield surface were estimated for a range of concrete and thermal-shield thicknesses.

For a thermal power output of 60 MW<sub>th</sub>, peak heating rates in the concrete are less than 1 W/1 for thermal shields thicker than 0.26 m. For the same power output and a total dose rate of 2.5 μSv h<sup>-1</sup>, the required thickness of ilmenite concrete is 1.71 m for a 0.40-m thick thermal shield and 1.35 m for a 0.60-m-thick thermal shield. The radiation fields at the shield surface are predominantly due to γs (ignoring the effects of shield penetrations); the neutron contribution to the overall dose rate is less than one percent.

**3. Thermalhydraulics Studies.** MAPLE-D<sub>2</sub>O fluid-flow and heat-transfer requirements were assessed with a one-dimensional thermalhydraulics code<sup>[14]</sup> that analyzes transient and steady-state conditions for piping networks associated with pool-type and low-pressure tank-type reactors. The heat-transfer package contains correlations that describe all the heat-transfer regimes of a boiling curve. A fully-implicit finite-difference scheme is used to solve the transient heat-conduction equation for a single fuel rod. The finned rods were conservatively modeled by choosing the sheath outer radius to preserve the total sheath mass.

The coolant flow requirement was determined by limiting the maximum operating heat flux for a fuel rod with a linear power rating of 120 kW m<sup>-1</sup> to less than two-thirds (actually 58%) of the heat flux at the point of onset of nucleate boiling. For an inlet pressure of 1.0 MPa and an inlet temperature of 38°C, the required flow velocity is 12 m s<sup>-1</sup>, which implies a core mass flow of about 420 kg s<sup>-1</sup>. The corresponding peak-fuel temperature is 218°C and the estimated outlet pressure is 370 kPa.

## Conclusions

This assessment of the MAPLE-D<sub>2</sub>O concept has identified a viable new concept that can be developed to play several roles:

- Provide a successor to NRU. The reference annular core concept produces thermal fluxes that exceed those currently available in NRE by a factor of three to five at about half the thermal power output. Fast neutron fluxes three

- times higher than the best achievable in NRE can be generated in a larger irradiation volume than is feasible in NRE.
- Enhance the global availability of high-flux-neutron sources. The reference concept produces comparable accessible thermal-neutron fluxes to those achieved in ISS, HFBR and HFIR.
  - Complement the proposed ANS reactor by enabling the building of similar instrumentation for a compatible facility generating ten to twenty percent of the targeted ANS conditions.
  - Extend the current MAPLE reactor family via a high-powered multipurpose reactor design for materials testing, radioisotope production, and extracted neutron-beam applications.






This preliminary study of the MAPLE-D<sub>2</sub>O reactor shows that a 12-site annular core meets all major requirements for a high-flux multipurpose reactor facility. As the study is based on a cursory examination of the performance potential, more detailed investigations are required to gain a better understanding of its capabilities. Accordingly, AECL is further exploring the feasibility of developing this promising concept.

#### **A. knowledgements**

The authors wish to acknowledge the assistance of G. B. Wilken and P. J. Mills of AECL who performed the shielding and the thermalhydraulics computations, respectively.

#### **References**

1. Proceedings of Workshop on Advanced Steady State Neutron Facility, Dec. 1985, 1986, in Nuclear Instruments and Methods **A249**, 1-131.
2. West, C. D., "The U.S. Advanced Neutron Source", Proc. of ICANS-X.
3. IAEA Publication STI/PUB/694, 1985, Proc. of the Conference on Neutron Scattering in the Nineties, Julich, FRG, Jan. 14-18, 1985.
4. Bartholomew, G. A. and Tunnicliffe, P. R. (eds.), 1966, "The AECL Study for an Intense Neutron Generator", Atomic Energy of Canada Limited Report AECL-2600.
5. Church, T. G., (ed.), 1967, "ING Status Report July 1967", Atomic Energy of Canada Limited Report AECL-2750.
6. Lidstone, R. F., 1984, "MAPLE: A Canadian Multipurpose Reactor Concept for National Nuclear Development", Atomic Energy of Canada Limited Report AECL-7826.
7. Lidstone, R. F. and Saroudis, J. I., 1986, "MAPLE: A New Multipurpose Reactor for National Nuclear Development in the 1990s", in Proc. of an International Symposium on the Significance and Impact of Nuclear Research in Developing Countries, Athens, Greece, Sept. 8-12, IAEA-SM-291/19, 245-259.
8. Egelstaff, P. A. (ed.), 1988, "Neutron Sources in the Canadian Context", Canadian Institute of Neutron Scattering Report, ICDN/CINS/R1.
9. Vigil, J. T., 1970, "3DDT, A Three-Dimensional Multigroup Diffusion - Burnup Program", Los Alamos Scientific Laboratory Report LA-4396.
10. Donnelly, J. V., 1986, "WIMS-CRNL—A User's Manual for the Chalk River Version of WIMS", Atomic Energy of Canada Report AECL-8955.

- 
- 
- 
- 
- 
11. Los Alamos Radiation Transport Group, 1981, "MCNP - A General Monte Carlo Code for Neutron and Photon Transport", Los Alamos National Laboratory Report LA-7396-M.
  12. Green, N. M., and L. M. Petrie, 1983, "XSDRNPM-S: A One-Dimensional Discrete-Ordinates Code for Transport Analysis", NUREG/CR-0200, Rev. 1, V. 2, Sec. F3.
  13. Bucholz, J. A., Knight, J. R., Parks, C. V., Petrie, L. M., Turner, J. C., and Westfall, R. M., 1984, "Standard Composition Library", NUREG/CR-0200, Rev. 2, V. 3, Sec. M8.
  14. Shim, S. Y., P. J. Mills, and Meyer, S., 1987, "SPORTS-M: A Thermalhydraulics Computer Model for Pool-Type Reactors", Proc of 5th International Conf. on Numerical Methods in Thermal Problems, Montreal, June.



## Design calculations for the ANS cold source

*R. A. Lillie and R. G. Alsmiller*  
Engineering Physics and Mathematics Division  
Oak Ridge National Laboratory  
Oak Ridge, Tennessee  
USA

**ABSTRACT:** The calculational procedure, based on discrete ordinates transport methods, that is being used to carry out design calculations for the Advanced Neutron Source cold source is described. Calculated results on the gain in cold neutron flux produced by a liquid-deuterium cold source are compared with experimental data and with calculated data previously obtained by P. Ageron, *et al.*, at the Institute Max von Laue-Paul Langevin in Grenoble, France. Calculated results are also presented that indicate how the flux of cold neutrons vary with cold-source parameters.

### Introduction

The Advanced Neutron Source (ANS) is a new experimental facility being planned by the Oak Ridge National Laboratory to meet the national need for an intense steady-state source of neutrons<sup>(1,2,3)</sup>. The facility will be built around a new research reactor and will have the largest neutron flux available anywhere in the world. The ANS will be equipped with advanced neutron scattering and nuclear physics research facilities, with isotope production facilities, and with facilities for the study of materials in strong radiation fields.

A major purpose of the ANS is to provide a high flux of cold ( $\leq 10^{-2}$  eV) neutrons for experiments. High fluxes of such cold neutrons can be obtained from a liquid deuterium ( $\sim 20$  K) region in the reflector tank outside of a high-flux reactor. Such a system has been in operation for some time at the Institute Max von Laue-Paul Langevin (ILL) in Grenoble, France<sup>(4)</sup>. In this paper some of the calculations that have been done to aid in the design of a liquid-deuterium cold source for the ANS will be described and the results discussed.

### ANS geometry and method of calculation

**ANS reactor and reflector.** The ANS is in the preconceptual design stage. The base concept for the ANS reactor is a very compact core (30 to 40 L active volume) with a very high-density fuel of  $U_3Si_2$  in an aluminum matrix. The coolant and reflector/moderator surrounding the core are heavy water. Preliminary calculations show an unperturbed peak thermal flux of  $\sim 10^{20}$  n/m<sup>2</sup>s at a power level of  $\sim 300$  MW and give a core life of approximately 14 d<sup>(5)</sup>.

A preconceptual reactor design for the ANS in a single-core configuration has been developed by the Oak Ridge National Laboratory (ORNL) and in a split-core

configuration by the Idaho National Engineering Laboratory (INEL)<sup>(6,7)</sup>. Both designs were analyzed independently by both laboratories and very satisfactory agreement was obtained. As part of these studies, the neutron flux per unit energy throughout the reflector region was calculated at ORNL using the discrete ordinates transport code DORT<sup>(8)</sup>. In the remainder of this paper, these calculated flux values for the INEL split-core design will be used as the basis for the calculations.

More details of the work that has been done to date and the design and performance calculations will be found in Refs. 2, 3, 6, 7, 9-11.

**Reactor geometry, cold-source geometry, and coupling surfaces.** To simplify the calculations as much as possible, they will be carried out in a two-dimensional  $r$ - $z$  geometry. In Fig. 1 two cylindrical geometries—the reactor geometry and the cold-source geometry—are depicted. The reactor geometry, in the absence of the cold source, has cylindrical symmetry about the reactor  $z$ -axis; it is the geometry in which the neutron flux throughout the reflector was calculated previously and is available for use in the calculations described here. The cold-source geometry has cylindrical symmetry about the cold-source  $z$ -axis that is perpendicular to the reactor-geometry  $z$ -axis.

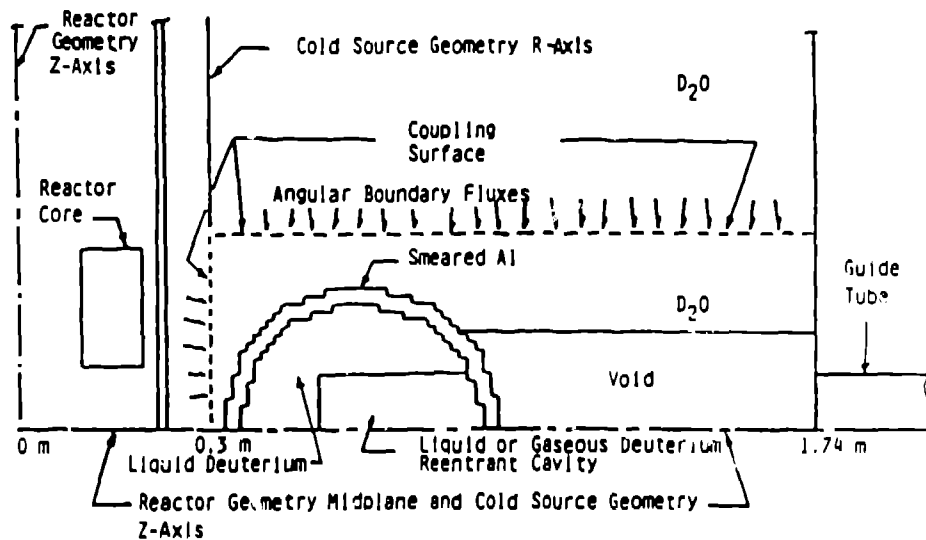


Fig. 1 Reactor and cold-source geometries with coupling surface.

An auxiliary code has been developed to transform particle fluxes from discrete ordinates calculations between between two  $r$ - $z$  geometries, such as those shown in Fig. 1. The transformation code constructs the boundary angular fluxes needed to perform a cold-source calculation from the volume-distributed angular fluxes determined in a reactor geometry. The method consists of performing a spatial and angular transformation to equate the angular fluxes at each radial, azimuthal and axial boundary mesh point to the angular flux at the closest mesh point and angular

direction in the reactor geometry. Azimuthal symmetry is taken into account by employing a one-dimensional Gaussian quadrature to integrate over the azimuthal mesh points. Because of the relatively small number of angular directions employed in most discrete ordinates calculations, the boundary angular fluxes obtained using this nearest neighbor approach do not, in general, conserve boundary leakage. Therefore, boundary angular currents both before and after the transformation are calculated and employed to scale the output boundary fluxes. The boundary fluxes at the coupling surface (dashed lines in Fig. 1) are approximate because they were determined from the angular flux per unit energy that exist in the absence of the cold source and are used in the presence of the cold source. Also in the cold-source geometry, azimuthal symmetry is assumed; this symmetry does not exist in the reactor geometry. To test the validity of these approximations, the thermal neutron flux, as a function of distance along the cold-source z-axis as obtained in the reactor geometry and in the cold source geometry when the cold source, void tube, etc., are replaced by D<sub>2</sub>O have been compared and found to be in good agreement.

**Transport calculations.** The cold-source transport calculations were carried out for the geometry inside the dashed lines in Fig. 1. This geometry begins at a distance of 0.30 m from the reactor-geometry z-axis and extends to 1.44 m along the cold-source z-axis and 0.45 m along the cold-source r-axis. The value of  $z \approx 1.74$  m in Fig. 1 is approximately the position where the neutron guide tubes will begin. Only liquid deuterium is considered as the cold-source material. The liquid-deuterium region is shown as approximately circular in Fig. 1, but may be any shape. In the remainder of this paper, a cylindrical guide tube with its axis along the axis of the cold source will be considered. The re-entrant cavity is for the purpose of studying the effect of such a cavity on the cold-source performance because this effect has been found to be significant<sup>(4,12,13)</sup>.

The quantity of primary interest is the flux of cold neutrons that emerge from the guide tubes at the experiment stations. The reflection properties of the guide tubes are such that cold neutrons at grazing angles with respect to the walls of the guide tubes will be reflected and, thus, transported over quite long distances to the experimental stations<sup>(14)</sup>. The quantity of interest in the calculations is, therefore, the angular leakage of cold neutrons that exit the void region behind the cold source and enter the guide tube (see Fig. 1), or more precisely, the cold neutrons that enter the guide tube at small angles (~ few degrees) with respect to the cold source z-axis.

The transport calculations were carried out using the two-dimensional discrete ordinates code DORT<sup>(8)</sup> and the last flight code FALSTF<sup>(15)</sup>. All of the DORT calculations were carried out using an S<sub>8</sub> symmetric angular quadrature and a P<sub>3</sub> angular expansion of the scattering cross section. To obtain the angular neutron leakage at small angles, the code FALSTF was used because the symmetric S<sub>8</sub> angular quadrature set employed in the DORT calculations does not contain discrete directions pointed down the axis of the void region. FALSTF calculated the flux at point detectors located outside the DORT calculational geometry using the final scattering source distribution produced by DORT. With a thin layer of black absorber located in the cold-source geometry to ensure that only neutrons which pass through the entrance of the guide tube are counted, the neutron flux at a point detector located a large distance R from the entrance to the guide cavity is simply the angular

neutron leakage into the guide cavity entrance divided by  $R^2$ . Thus, multiplying the neutron flux at a number of point detectors located at different distances from the z-axis by  $R^2$  yields the directional angular neutron leakage into the guide cavity.

**Cross section data.** A coupled neutron-photon multigroup cross-section library designated ANSL-V (for Advanced Neutron Source Library based on ENDF/B-V) has been developed for use in ANS studies<sup>(16,17)</sup>. A fine-group library containing 99 neutron- and 44 photon-groups and a broad-group library containing 39 neutron- and 44 photon-groups have been generated. For low energy studies of particular interest here, the fine-group library contains 29 neutron groups between  $1.00 \times 10^{-5}$  and 3.00 eV and the broad-group library contains 25 groups in this energy range.

Of particular interest here is the cross-section model used to describe the very low temperature scattering of neutrons by ortho- and para-deuterium. The model used is not yet documented, but is not appreciably different from the free gas model developed by J. A. Young and J. U. Koppel<sup>(18,19)</sup>. The calculated cross sections deviate significantly from available experimental data<sup>(20)</sup> at energies below approximately  $2 \times 10^{-3}$  eV. It has been established by the work of W. Bernini, *et al.*<sup>(21)</sup>, and M. Utsuro<sup>(22)</sup> that this discrepancy can be substantially reduced by the use of a liquid rather than a gas model, but results from this more accurate model have not yet been incorporated into the ANSL-V library.

For many of the studies considered here, it was convenient to use fewer than 39 neutron groups. When this was the case, the 39-group library was collapsed with XSDRN<sup>(23)</sup> and a one-dimensional model of ANS.

## Results and discussion

The gain factor may be defined to be the ratio of the angular leakage of neutrons, with a given wavelength, from the cold source into the guide tube (see Fig. 1) to this angular leakage when the cold-source material is replaced by  $D_2O$ . In Fig. 2 the calculated and measured gain factor for a liquid-deuterium-filled spherical cold source with a radius of 190 mm is shown<sup>(12)</sup>. In Fig. 2 the calculated results of P. Ageron, *et al.*<sup>(4,12,13)</sup>, as well as those reported here are shown.

In the calculations reported here, the geometry used is that shown in Fig. 1. A guide tube radius of 55 mm, which corresponds to that used in the experiment, was used. This geometry differs in detail from the experimental geometry, but the differences are not thought to have an appreciable effect on the results. Also, the neutron source used in the calculations is that used throughout the paper since the actual source distribution in the experiment is not available. Since the gain factor that is compared involves a ratio, the details of the source may not have a significant effect on the results.

The histogram in the figure is for an angle of  $0^\circ$ . The calculated results for an angle of  $3^\circ$  is very similar to that for  $0^\circ$  and is, therefore, not shown. The angular range of  $0^\circ$  to  $3^\circ$  is chosen to cover the wavelength range of interest ( $\sim 0.1$  to 1 nm) for the possible guide-tube materials<sup>(14)</sup>. The calculated results obtained here are slightly

higher than those obtained by P. Ageron, *et al.*, but are somewhat lower than the measured values.

Calculations carried out using the 39 neutron groups, as in Fig. 2, require very long computing times, which are much too long for design calculations that must be repeated many times. For routine use, the 39-group cross sections have been reduced to a 6-group cross-section set. In Table 1 calculated results of the neutron angular leakage at  $0^\circ$  into the guide tube obtained with the 39-group and the 6-group cross sections are presented. The geometry used in obtaining the results in Table 1 is that shown in Fig. 1 with a spherical liquid-deuterium cold source with a radius of 190 mm. The void-tube radius was 146 mm, the guide-tube radius was 85 mm, and there was no cavity. In the results shown in Table 1 and throughout the remainder of this paper, the liquid deuterium used will be taken to have a density of 0.8 of the theoretical density to account for the fact that gaseous deuterium will be present; also, the liquid deuterium is assumed to be uniformly distributed over the cold-source volume.

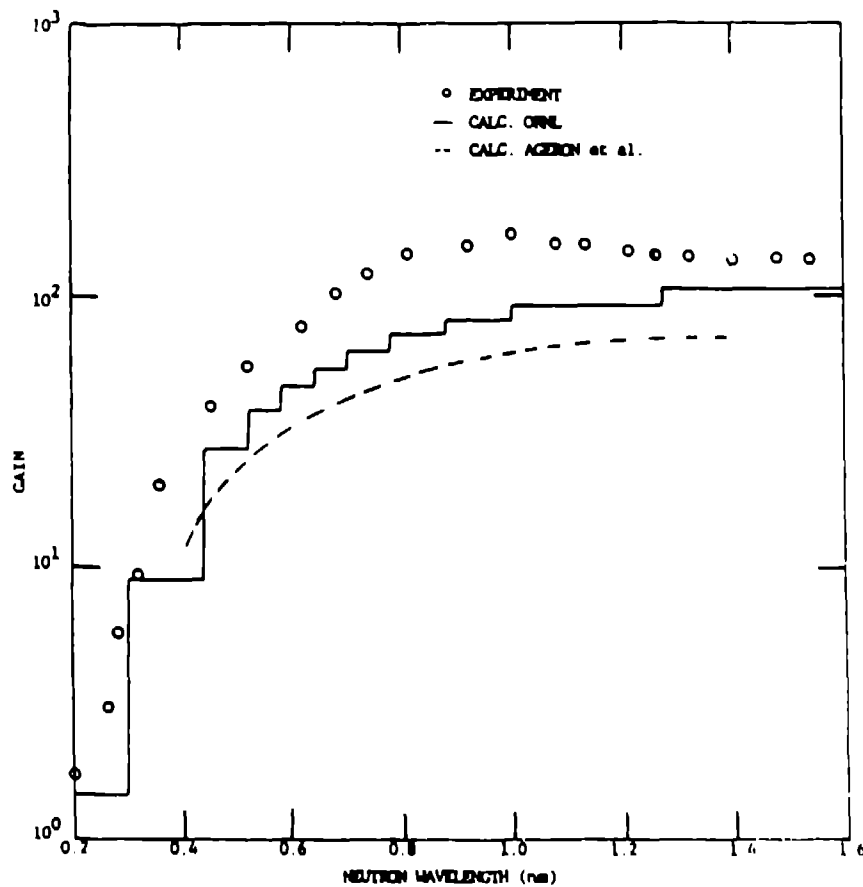


Fig. 2 Gain vs. neutron wavelength.

Angle from Cold Source Centerline = 0 Degree.  
(neut./ster)

Neutron Group	Upper <sup>1</sup> Energy (eV)	Lower <sup>2</sup> Wavelength (nm)	39 Group Calc.	Sum 39 Group Calc.	6 Group Calc.	Sum 39 Group 6 Group
1 (1)	2.00+7 <sup>3</sup>	6.40-6	1.84+13	3.33+14	2.27+14	1.47
2	6.43+6	1.13-5	9.79+13			
3	3.00+6	1.65-5	7.05+13			
4	1.85+6	2.10-5	2.37+13			
5	1.40+6	2.42-5	1.96+13			
6	9.00+5	3.02-5	2.58+13			
7	4.00+5	4.52-5	7.74-13			
8 (2)	1.00+5	9.05-5	2.09+14	1.39+15	1.80+15	0.77
9	1.70+4	2.19-4	3.00+14			
10	3.00+3	5.22-4	3.91+14			
11	5.50+2	1.22-3	4.93+14			
12 (3)	1.00+2	2.86-3	3.98+14	4.03+15	1.64+16	0.25
13	3.00+1	5.22-3	4.03+14			
14	1.00+1	9.05-3	5.11+14			
15	3.00+0	1.65-2	5.87+14			
16	1.77+0	2.15-2	4.75+14			
17	1.30+0	2.51-2	4.38+14			
18	1.00+0	2.86-2	5.70+14			
19	7.65-1	3.27-2	6.44+14			
20 (4)	5.88-1	3.73-2	4.99+14	4.20+16	3.79+16	1.11
21	4.79-1	4.13-2	4.31+14			
22	3.97-1	4.54-2	4.96+14			
23	3.30-1	4.98-2	4.58+14			
24	2.70-1	5.51-2	6.64+14			
25	2.15-1	6.17-2	9.58+14			
26	1.62-1	7.11-2	1.72+15			
27	1.04-1	8.87-2	6.69+15			
28	5.00-2	1.28-1	8.12+15	4.07+16	3.44+16	1.18
29	3.00-2	1.65-1	2.20+16			
30 (5)	1.00-2	2.86-1	2.16+16			
31	4.45-3	4.29-1	8.34+15			
32	3.25-3	5.02-1	4.84+15			
33	2.60-3	3.61-1	3.38+15	8.05+15	6.40+15	1.25
34	2.15-3	6.17-1	2.52+15			
35 (6)	1.80-3	6.74-1	2.40+15			
36	1.45-3	7.51-1	1.87+15			
37	1.15-3	8.44-1	1.61+15			
38	8.50-4	9.81-1	1.24+15			
39	5.50-4	1.22+0	9.47+14			

<sup>1</sup> Lower energy of Group 39 is 1.00-5 eV.

<sup>2</sup> Upper wavelength of Group 39 is 9.03 nm.

<sup>3</sup> 2.00+7 read as 2.00x10<sup>7</sup>.

Table 1 Neutron angular leakage into neutron guides (spherical liquid deuterium cold source with radius = 190 mm, void tube radius = 148 mm, guide tube radius = 85 mm, no cavity).

In Table 1 the energy group and corresponding wavelength-group boundaries are shown. For purposes of comparison, the appropriate 39-group results have been summed; these summed results are also given in Table 1. There are significant differences between the 39-group and the 6-group results, but the differences are not so major as to make the 6-group results completely untrustworthy. Calculated results similar to those in Table 1, for an angle of  $3^\circ$  have also been obtained and are not appreciably different from the results shown in Table 1.

The results discussed above were all for a guide tube of radius 85 mm. In Table 2, the calculated angular leakage at  $0^\circ$  and  $3^\circ$  is presented for a range of guide-tube radii. The case considered is as before, i.e., a spherical liquid-deuterium cold source with a radius of 190 mm and a void tube radius of 146 mm. As indicated in the table, guide-tube radii of 37, 61, 85, and 146 mm are considered.

Neutron Energy Group	Upper <sup>1</sup> Energy (eV)	Lower Wavelength (nm)	Neutrons/s/Ster			
			Neutron Guide Tube Radius (mm)			
			37	61	85	146
Angle from Cold Source Centerline = $0^\circ$						
1	2.00+7 <sup>2</sup>	6.40-6	3.88+13	1.13+14	2.27+14	6.94+14
2	1.00+5	9.05-5	3.07+14	8.94+14	1.78+15	5.66+15
3	1.00+2	2.86-3	2.85+15	8.19+15	1.64+16	5.21+16
4	5.88-1	3.73-2	6.81+15	1.90+16	3.79+16	1.20+17
5	1.00-2	2.86-1	6.12+15	1.75+16	3.44+16	1.01+17
6	1.80-3	6.74-1	1.13+15	3.25+15	6.40+15	1.83+16
Angle from Cold Source Centerline = $3^\circ$						
1	2.00+7	6.40-6	4.13+13	1.13+14	2.31+14	5.31+14
2	1.00+5	9.05-5	3.15+14	9.04+14	1.88+15	4.33+15
3	1.00+2	2.86-3	4.15+15	9.64+15	1.87+16	4.13+16
4	5.88-1	3.73-2	6.64+15	1.97+16	4.11+16	9.23+16
5	1.00-2	2.86-1	5.72+15	1.73+16	3.54+16	7.73+16
6	1.80-3	6.74-1	1.07+15	3.21+15	6.52+15	1.41+16

<sup>1</sup>Lower energy of Group 6 is 1.00-5 eV.

<sup>2</sup>Upper wavelength of Group 6 is 9.0<sup>4</sup> nm.

<sup>3</sup>2.00+7 read as  $2.00 \times 10^7$ .

**Table 2** Neutron angular leakage into guide tubes of different radii (spherical liquid deuterium cold source with radius = 190 mm, void tube radius = 146 mm, no cavity).

The values in the table are given for completeness, but can be compared more readily by taking ratios. First, it is clear that the leakage into the guide tube is nearly proportional to the area of the guide tube. To remove this effect, the values in Table 2 must be divided by the guide-tube cross sectional area. Second, the angular leakage in a given energy group for a guide tube of 85 mm will be taken as a normalizing factor, and the results for the other guide tubes will be divided by this normalizing value. The results, when this is done, are shown in Fig. 3 as a function of guide-tube radius for the lowest three energy groups considered. The plotted points indicate

the calculated values. The curves are only for guidance and, particularly in the 3° case, are somewhat arbitrary.

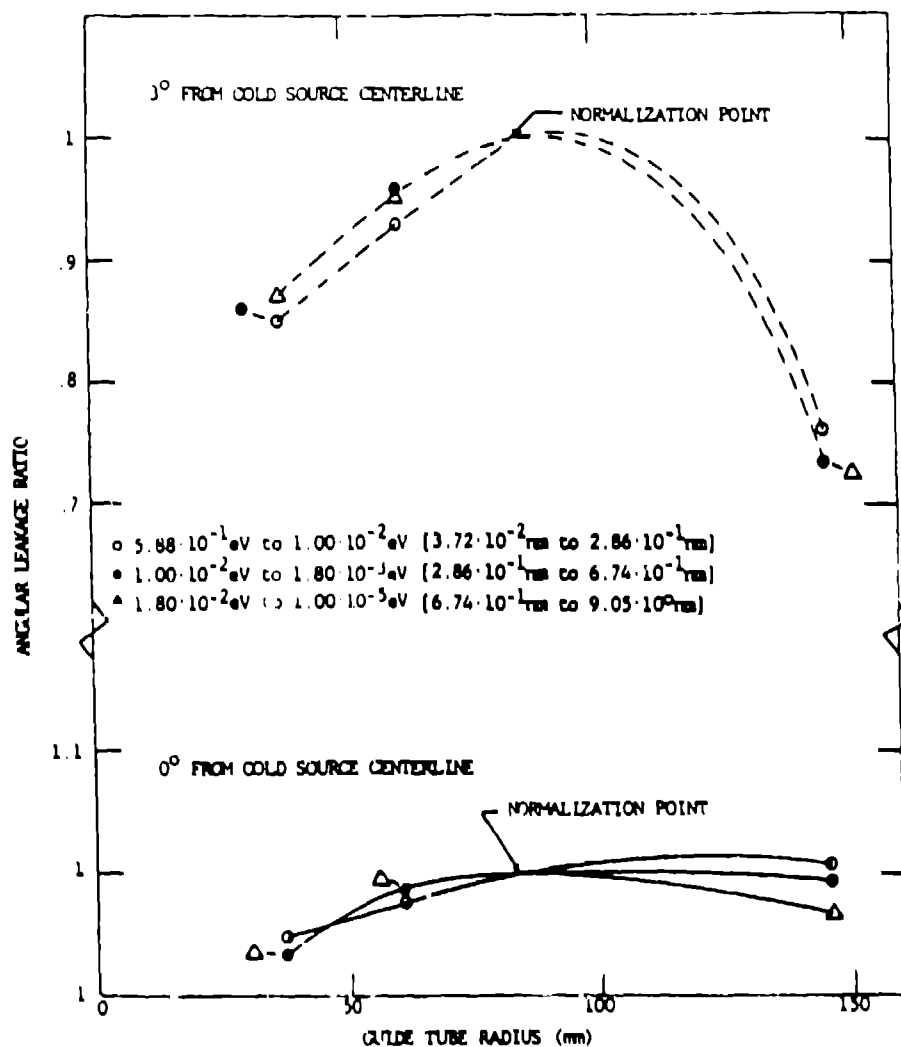


Fig. 3 Ratio of angular leakage in a given energy range into a guide tube of specified radius to angular leakage into guide tube of radius 85 mm vs. guide tube radius. (Spherical cold source with radius = 190 mm, void tube radius = 146 mm, no cavity.)

In the 0° case, the change of the leakage with guide-tube radius is not large. For each of the energy groups considered, there appears to be an optimum guide-tube radius, but not a very precise one. In the 3° case, the variation of the leakage with guide-tube radius is larger than the 1° case. It is also clear that there is an optimum guide-tube radius for each of the groups considered; but with only the points that are shown



in Fig. 3, it is not possible to estimate the position of the optimum or the magnitude of leakage at the optimum.

At the ILL it has been found that a re-entrant cavity, such as that shown in Fig. 1, can significantly increase the flux of cold neutrons in the guide<sup>[4,12,13]</sup>. A series of calculations with a spherical cold source of radius 190 mm and various re-entrant cavities has been carried out to study this phenomena. The neutron source and void-tube radius are the same as that used previously. The cavity radius and the guide-tube radius are taken to be the same and equal to 85 mm. Cavity lengths of 134 mm, 219 mm, and 256 mm are considered.

In Fig. 4 the calculated neutron flux in the energy range  $1.8 \times 10^{-3}$  eV to  $1.0 \times 10^{-2}$  eV is shown along the cold-source centerline as a function of distance from the front, i.e., the reactor side, of the cold source. In the figure, results are shown for the three different re-entrant tube lengths and for the case when there is no cavity.

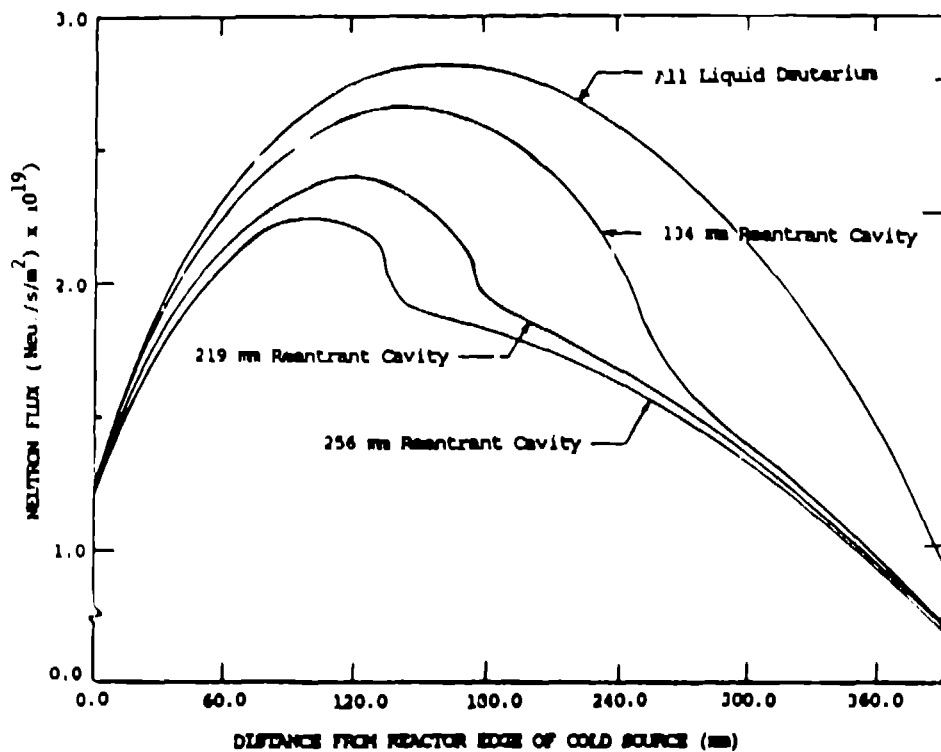


Fig. 4 Low energy flux ( $1.8 \times 10^{-3}$  eV  $< E < 1.0 \times 10^{-2}$  eV) profiles through center of spherical cold source.

In all cases, the flux reaches a maximum and then decreases. As the length of the cavity increases (see Fig. 1), the maximum value of the flux decreases and the position of the maximum value is closer to the front of the cold source. In the three curves for the re-entrant cavities, the position to the right of the flux peak, where the curves have a change in slope, is the position of the interface between the liquid deuterium and the cavity. Note that the flux at the entrance to the cavities is larger than the flux at the entrance to the void tube in the case of no cavity.

In Table 3 the angular leakage into the guide tube is shown for the three cavities considered and the case of no cavity. In the table, results are given for all energy groups and for angles 0°, 1°, 2° and 3°. The values in the table are again given for completeness, but can be more readily understood by considering ratios.

Neutron Energy Group	Upper <sup>1</sup> Energy (eV)	Lower <sup>2</sup> Wavelength (nm)	(neutrons/s/star)			
			Angle from Beam Tube Centerline (degrees)			
			0	1	2	3
All liquid deuterium						
1	2.00+7 <sup>3</sup>	6.40-6	2.27+14	2.23+14	2.26+14	2.31+14
2	1.00+5	9.05-5	1.78+15	1.79+15	1.81+15	1.88+15
3	1.00+2	2.86-3	1.64+16	1.64+16	1.67+16	1.87+16
4	5.88-1	3.73-2	3.79+16	3.82+16	3.91+16	4.11+16
5	1.00-2	2.86-1	3.44+16	3.44+16	3.49+16	3.54+16
6	1.80-3	6.74-1	6.40+15	6.40+15	6.48+15	6.52+15
134 mm reentrant cavity						
1	2.00+7	6.40-6	5.61+14	5.02+14	4.71+14	4.31+14
2	1.00+5	9.05-5	3.98+15	3.59+15	3.37+15	3.19+15
3	1.00+2	2.86-3	2.95+16	2.71+16	2.59+16	2.64+16
4	5.88-1	3.73-2	4.32+16	4.15+16	4.16+16	4.41+16
5	1.00-2	2.86-1	4.35+16	4.06+16	3.89+16	3.94+16
6	1.80-3	6.74-1	9.18+15	8.41+15	7.87+15	7.78+15
219 mm reentrant cavity						
1	2.00+7	6.40-6	9.89+14	8.65+14	7.87+14	6.73+14
2	1.00+5	9.05-5	6.74+15	5.89+15	5.35+15	4.65+15
3	1.00+2	2.86-3	4.43+16	3.93+16	3.65+16	3.42+16
4	5.88-1	3.73-2	4.97+16	4.67+16	4.63+16	4.60+16
5	1.00-2	2.86-1	4.26+16	3.96+16	3.80+16	3.60+16
6	1.80-3	6.74-1	9.14+15	8.31+15	7.78+15	7.06+15
254 mm reentrant cavity						
1	2.00+7	6.40-6	1.74+15	1.07+15	9.57+14	6.12+14
2	1.00+5	9.05-5	7.06+15	7.14+15	6.38+15	5.51+15
3	1.00+2	2.86-3	5.28+16	4.58+16	4.16+16	3.85+16
4	5.88-1	3.73-2	5.30+16	4.93+16	4.87+16	4.80+16
5	1.00-2	2.86-1	3.92+16	3.68+16	3.54+16	3.42+16
6	1.80-3	6.74-1	8.33+15	7.64+15	7.25+15	6.61+15

<sup>1</sup>Lower energy of group 6 is 1.00-5 eV.  
<sup>2</sup>Upper wavelength of group 6 is 9.05 nm.  
<sup>3</sup>2.00+7 read as 2.00x10<sup>7</sup>.

Table 3 Neutron angular leakage into 85.3 mm radius neutron guide tube (void tube radius = 146.3 mm, cavity radius = 85.3 mm).

In Fig. 5 the ratio of the angular leakage in a given energy range with a cavity present to the corresponding angular leakage with no cavity is shown as a function of cavity length. Results are shown for angles of  $0^\circ$  and  $3^\circ$ . At  $0^\circ$  the maximum value of the ratio obtained is slightly less than 1.5 and is for the highest energy group shown that is group 4. For group 5, the maximum value obtained is considerably smaller; for group 6, the maximum value obtained is slightly smaller. For groups 4 and 5, the maximum value of the ratio occurs between lengths 134 mm and 219 mm; but for group 6, the maximum value occurs at the largest cavity length considered. At  $3^\circ$  the ratios have similar behavior, but the values are, in general, smaller than at  $0^\circ$ ; for groups 4 and 5, the maximum value of the ratio occurs at smaller values of the cavity length.

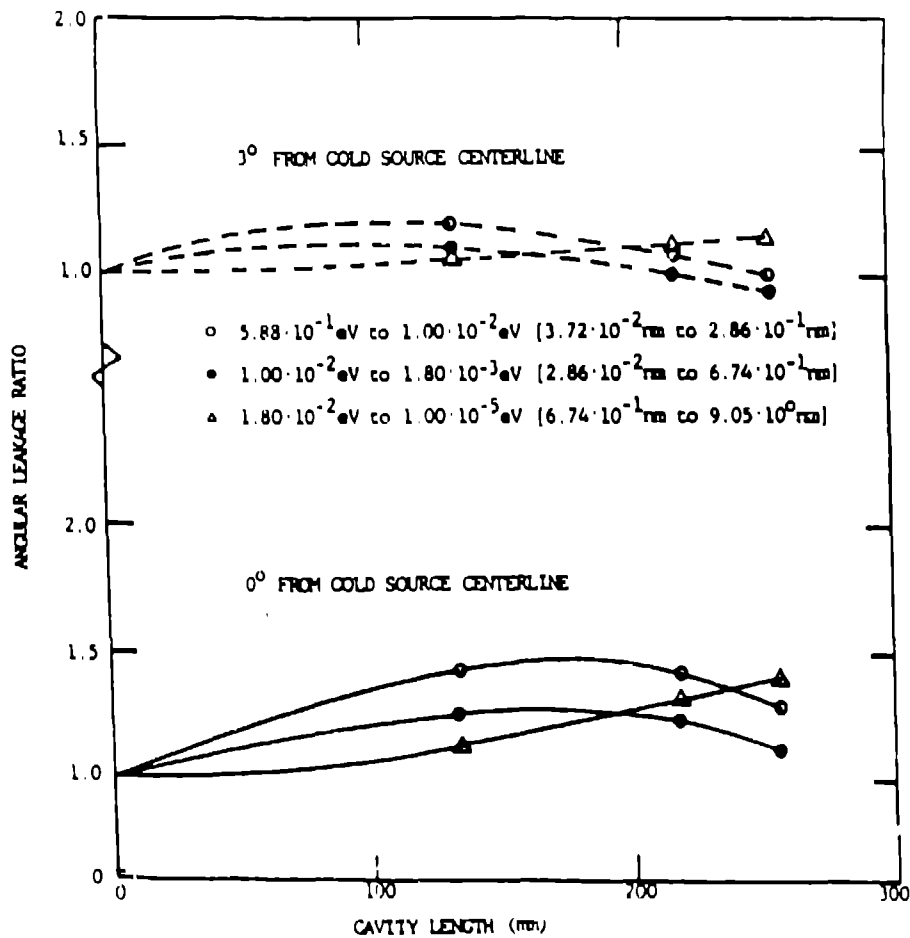


Fig. 5 Ratio of angular leakage in a given energy range from cold source with re-entrant cavity to angular leakage from cold source with no cavity vs. cavity length. (Spherical cold source with radius = 190 mm, void tube radius = 148 mm, cavity radius = 85 mm, guide tube radius = 85 mm.)

P. Ageron has presented both measurements and calculations of the effects of re-entrant cavities on the flux of cold neutrons produced by liquid-deuterium cold sources. Detailed calculations from ORNL for comparison with these results are not yet available, but from the preliminary results that have been obtained, it is clear that the ORNL results will not agree well with those of Ageron, *et al.* In general, the results in Refs. 4, 11, and 12 indicate improvements in the wavelength range 0.1 to 1 nm due to cavities to be factors of 1.5 and above, and our calculation gives values such as those in Fig. 5 of 1.5 or significantly less.

### Acknowledgements

The authors are very grateful to P. Ageron of the ILL for his very helpful comments. This research was sponsored by the Office of Basic Energy Sciences, U. S. Department of Energy under contract number DE-AC05-84OR21400 with Martin Marietta Energy Systems, Inc.

### References

1. A. Zucker, "The Advanced Neutron Source - An Ultrahigh Flux Research Reactor," presented at the International Symposium on the Utilization of Multi-Purpose Research Reactors and Related International Cooperation, Grenoble, France.
2. D. L. Selby, *et al.*, 1987, "ORNL Contributions to the Advanced Neutron Source (ANS) Project for October 1986 - March 1987", Oak Ridge National Laboratory ORNL/TM-10579.
3. D. L. Selby, *et al.*, 1988, "ORNL Contributions to the Advanced Neutron Source (ANS) Project for October 1986 - March 1987", Oak Ridge National Laboratory ORNL/TM-10860.
4. P. Ageron, "Special Neutron Sources", 1985, Proceedings of Conference on Neutron Scattering in the Nineties", organized by the International Atomic Energy Agency and held at Jülich Nuclear Research Center, January 14-18, IAEA-CN-46/16.
5. C. D. West, 1988, "Overview of the ANS Project", to be presented at the American Nuclear Society/European Nuclear Society 1988 International Conference, Washington, D. C., October 30 - November 3, and included in the transactions.
6. D. L. Selby and J. L. Lake, 1988, "ANS Core Comparison Workshop Summary", Oak Ridge National Laboratory ORNL/ANS/INT-4.
7. J. M. Ryskamp, *et al.*, 1988, "Comparison of Single and Split Core Concepts for the Advanced Neutron Source", to be presented at the Topical Meeting on Reactor Physics, Jackson Hole, Wyoming, September 18-22, and published in the proceedings.
8. DORT is the CRAY computer version of the DOT-IV code. See W. A. Rhoades and R. L. Childs, "An Updated Version of the DOT 4 One- and Two-Dimensional Neutron/Photon".
9. J. M. Ryskamp, D. K. Parsons, and J. A. Lake, 1986, "Ultrahigh Flux Double Donut Research Reactor Design", Proc. Topl. Mtg. Reactor Physics and Safety, Saratoga Springs, New York, September 17-19, 1986, NURE/3/CP-0080, 2, 780, U.S. Nuclear Regulatory Commission.

10. F. C. Difilippo, *et al.*, 1986, "An Intense Steady-State Neutron Source - The CNR Reactor", Proc. Topl. Mtg. Reactor Physics and Safety, Saratoga Springs, New York, September 17-19, 1986, NUREG/CP-0080 2, 792, U.S. Nuclear Regulatory Commission.
11. J. M. Ryskamp, 1969, "Preconceptual Core Design of the Advanced Neutron Source", to be presented at the American Nuclear Society/European Nuclear Society 1988 International Conference, Washington, D.C. October 30 - November 3, and included in the transactions.
12. P. Ageron, *et al.*, 1969, "Experimental and Theoretical Study of Cold Neutron Sources of Liquid Hydrogen and Liquid Deuterium", *Cryogenics* 42.
13. P. Ageron, 1978, "Neutron Flux Calculations for the Deuterium Cold Sources in Siloette and in HFR", Institut Max Von Laue-Paul Langevin, DTE-781650-PA/ngd.
14. C. D. West, *et al.*, 1986, "Center for Neutron Research Project Status Report", Oak Ridge National Laboratory ORNL/TM-10065.
15. "FALSTF, Informal Notes", 1979, CCC-351, Radiation Shielding Information Center, Oak Ridge National Laboratory.
16. J. W. Arwood, *et al.*, 1987, "Preparation and Benchmarking of ANSL-V Cross Section Library for Advanced Neutron Source Reactor Studies", Transactions of the 1987 Winter Meeting of the American Nuclear Society, November 15-19, Los Angeles, California.
17. D. L. Selby, *et al.*, 1987, "ORNL Contributions to the Advanced Neutron Source Project for October 1986-March 1987, Oak Ridge National Laboratory ORNL/TM-10579.
18. J. A. Young and J. U. Koppel, 1964, "Slow Neutron Scattering by Molecular Hydrogen and Deuterium", *Phys. Rev.* A135, 603.
19. M. W. Waddell, 1987, private communication.
20. N. D. Seiffert, 1970, "Measurement of Scattering Cross Sections of Liquid and Solid Hydrogen Deuterium and Deuterium-Hydride", EUR4455d.
21. W. Bernnat, 1988, "Evaluation of Neutron Cross Sections for Liquid Hydrogen and Deuterium for the Design of Cold Neutron Source", Proc. of International Conference on Nuclear Data for Science and Technology, Mito, Japan, May 30-June 3.
22. M. Utsuro, 1977, "Slow Neutron Scattering and Intermolecular Excitation in Liquid Hydrogen", *Z. Physik* B27, 111.
23. N. M. Greene and C. N. Craven, *et al.*, 1969, "XSDRN, A Discrete Ordinates Spectral Averaging Code", Oak Ridge National Laboratory ORNL/TM-2500.

## **Opportunities for research program development at LANSCE**

*C. D. Bowman*  
Physics Division  
Los Alamos National Laboratory  
Los Alamos, New Mexico 87544

**ABSTRACT:** The availability of intense neutron beams from facilities associated with the Proton Storage Ring and LANSCE has stimulated the development of neutron research well beyond the mainstream of neutron scattering. A description of this extended program is given along with prospects for further growth.

### **Introduction**

The Proton Storage Ring (PSR) project originally was launched for nuclear physics research. As the opportunities for neutron scattering research were recognized, capabilities were included in the PSR design to accommodate both programs. However as the scope of both programs grew it became clear that the PSR could not be satisfactorily multiplexed between them. As a result, the PSR was finally constructed with a several hundred nanosecond pulse width which was most suitable for neutron scattering research, and other means were devised to obtain a sub-nanosecond pulse width for MeV neutron nuclear physics at a different target station. These two modes also could be readily multiplexed allowing both programs to run simultaneously and thereby greatly enhancing the research output across the full energy spectrum of neutron spectroscopy. Upon completion of the PSR, its powerful capabilities for nuclear physics research were also recognized. The success of this extended neutron research program<sup>1</sup> has provided the base for suggesting in this paper further major augmentation of the facilities by adding an experimental cell capable of receiving a small fraction of the PSR beam and arranged so that the PSR proton pulse can be brought directly to experimental apparatus. The views expressed here regarding prospects for the future are my own and do not necessarily represent those of the Laboratory.

### **Neutron Nuclear Physics at the LANSCE Complex**

The scope of the neutron nuclear physics program at the LANSCE complex is perhaps best illustrated by the following list of experiments approved by the Internal Program Advisory Committee for Neutron Research (IPAC) for 1988.

Gamma Ray Production Measurements by keV and MeV Neutrons.

Neutron-Induced Fission Cross Section From 1 to 400 MeV.

Neutron-induced Pion and Photon Production from Nuclei.

Charge Exchange Reactions in Neutron Physics.

Giant Resonance Studies Using Neutron Capture Gamma Rays.

Neutron-Proton Bremsstrahlung.

Accurate  $^{235}\text{U}$  Fission Cross Section from 1 to 200 MeV.

Nuclear Level Density through (n,p) and (n,alpha) Reactions.

Response of BGO to neutrons from 1 to 200 MeV.

Differential Cross Sections for (p,xn) Reactions at 800 MeV.

Continuum Excitation by the (p,n) Reaction at 900 MeV.

Neutron Cross Sections on Radioactive Nuclei.

Fundamental Symmetry Experiments using Resonance Neutrons.

Electric Polarizability of the Neutron Using eV Neutrons.

Neutron-induced Optical Photon Emission.

Benchmark Neutron Transport Experiments.

The substantial Los Alamos staff which participated in this program in 1988 is listed in Table I. The P-3 staff devoted essentially full time to the program while most of the other staff members worked part time. The many other institutions which contributed to these experiments are listed in Table II.

#### **A. MeV Neutron Nuclear Physics Facilities**

The key to MeV neutron nuclear physics at LANSCE was the realization<sup>2</sup> that a world class MeV neutron source could be developed at LANSCE at very

modest cost by directing single micropulses, with width as small as 0.3 nanosecond at a small tungsten target and energy analyzing the white-spectrum neutrons by nanosecond time-of-flight techniques. The low cost arose from (1) use of the PSR injector for injecting well separated H<sup>-</sup> beam micropulses into the LAMPF accelerator simultaneously, (2) accelerating them simultaneously with the high current H<sup>+</sup> (3) separating the two charges at the end of the accelerator in an existing magnet, and (4) transporting them to the MeV spallation target using much of the same beam line used to transport LANSCE beam.

The main cost in adding this capability, referred to as Target 4, was in constructing the target and associated beam lines. This construction is now complete and is shown in Fig. 1. Neutron drift tubes radiate from two target locations<sup>3</sup>. The dashed-line tubes are located about 2.5 M below and in a plane parallel to the other drift tubes. Altogether there are 14 drift tube locations of which eight have already been brought into frequent use. Each beam line has its own stand-alone Microvax data collection system. This facility provides the world's most intense neutron beams in the 1 to 800 MeV range. By increasing the rate of LAMPF macropulse delivery to Target 4 and improving the H<sup>-</sup> injection into LAMPF, the neutron intensity could be increased by a factor of three or more. Research on this facility is well established with substantial staff, a large external user group, and an exciting array of research problems.

Presently the major fraction of neutron nuclear physics is conducted at Target 4. However a program using 0.025 to 10,000 eV neutrons has begun at LANSCE with substantial growth potential. Also additional facilities could be added making possible an even broader spectrum of research opportunities. The remainder of this paper will be devoted to a discussion of PSR-based nuclear research and program expansion beyond the confines of conventional pulsed neutron scattering techniques.

#### **B. eV Neutron Nuclear Physics at LANSCE**

The width of the proton pulse from the PSR is 0.25 microseconds which corresponds to the moderation time in a water moderator for 15-eV neutrons. Therefore for neutrons with energy below 15 eV the resolution is not appreciably worsened by the beam pulse width. Above that energy effective neutron spectroscopy still can be performed despite some resolution broadening introduced by the PSR pulse width. These properties along with the low repetition rate of 12-15 Hz and very high average intensity make LANSCE a powerful source for eV neutron spectroscopy. We describe here several experiments already performed which illustrate this power.



**Table I. Los Alamos Staff Members Participating in Neutron Nuclear Physics Research at LANSCE-related Facilities in 1988.**

R. Nelson	P-3 (Facility and Research Program Responsibility)
S. Seestrom-Morris	
S. Wender	
J. Ullmann	
P. Lisowski	
P. Koehler	
H. O'Brien	
C. Bowman	
R. Byrd	P-2
G. Morgan	P-15
N. King	
R. Haight	
J. D. Bowman	MP-4
J. Szymanski	
B. Tippins	
D. Lee	
J. McGill	MP-5
C. Morris	MP-10
C. Goulding	N-2
C. Moss	
R. Reedy	ESS-8
M. Meier	ESS-9
D. Drake	
J. Wilhelmy	INC-11
M. Fowler	

**Table II. Universities and Laboratories Participating in Neutron Nuclear Physics Research at LANSCE-related Facilities in 1988.**

University of Colorado

University of Hanover

ORNL

NBS-Washington

Ohio University

University of California-Davis

-Irvine

-Los Angeles

-Riverside

CEBAF

University of New Mexico

Temple University

William and Mary University

Uppsala University

LLNL

KEK

Kyoto University

TRIUMF

University of Technology-Delft

GKSS Research Center-FRG

Princeton

Harvard

AERE-Harwell

TUNL

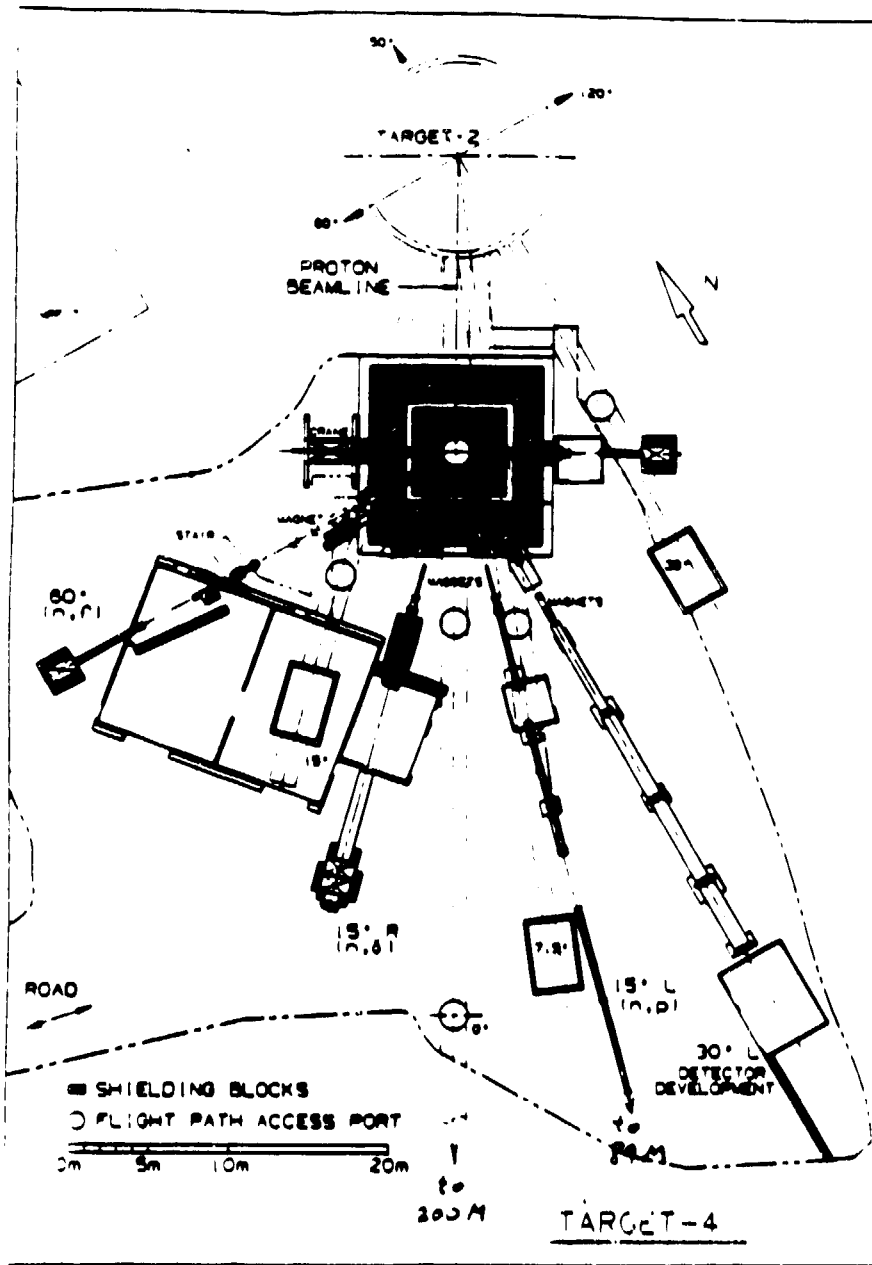


Fig. 1 Facilities for MeV neutron nuclear physics research.

## 1. Cross Sections on Radioactive Samples

Perhaps the most dramatic example of the power of LANSCE for neutron nuclear physics is in the measurement of reaction cross sections on highly radioactive nuclei. The problem with such experiments in the past has been the decay products which overload the detector and obscure the detector response to the neutron-induced reaction products such as protons, alphas, and gammas. The sheer intensity of the LANSCE eV beam allows the use of samples smaller by about a factor of 1000 than previously practical (i. e. in the nanogram and microgram range) and the low repetition rate at which the neutrons are delivered to the sample produces a high signal-to-noise ratio.

Our first successful measurements<sup>4</sup>, conducted on FP-4 when the first LANSCE beam became available in 1986, were done using 100 nanograms of  $^7\text{Be}$ , which has a 53-day half-life. The measurements extended from thermal to about 50,000 eV. The apparatus shown in Fig. 2 includes a beam line with collimation for a 3-mm diameter beam, an aluminum foil on which the sample is placed, a solid-state charged particle detector to detect the reaction products, and a second detector downstream (not shown) to collect alphas and tritons from a second foil with a small amount of  $^6\text{Li}$  used as a flux monitor.

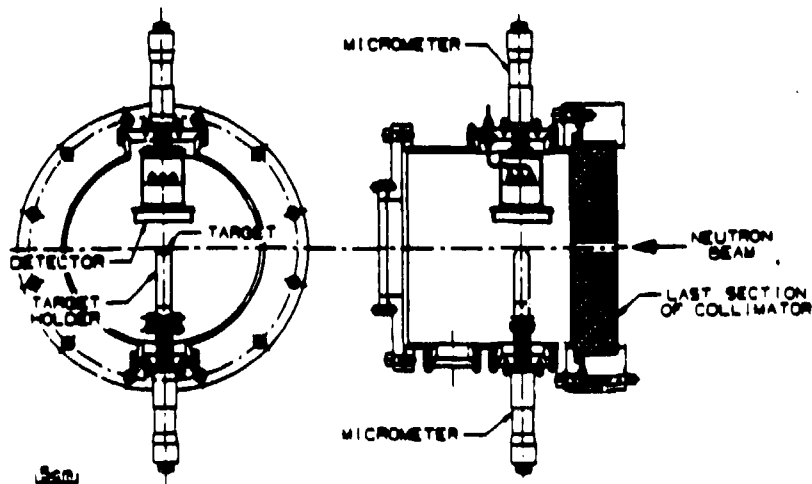


Fig. 2 Arrangement for neutron reaction cross section measurements on highly radioactive targets.

The flight path length is about 7 M. The samples studied to date include  $^7\text{Be}$ ,  $^{22}\text{Na}$ ,  $^{26}\text{Al}$ ,  $^{35}\text{Cl}$ ,  $^{36}\text{Cl}$ , and  $^{57}\text{Co}$ . The results for  $^{36}\text{Cl}$  are shown in Fig. 3. A new detector is under construction which will allow capture cross section measurements on this class of samples by gamma detection. Measurements will become possible on more than 100 nuclei previously inaccessible to study. The primary basic research interest for this work is in nuclear astrophysics.

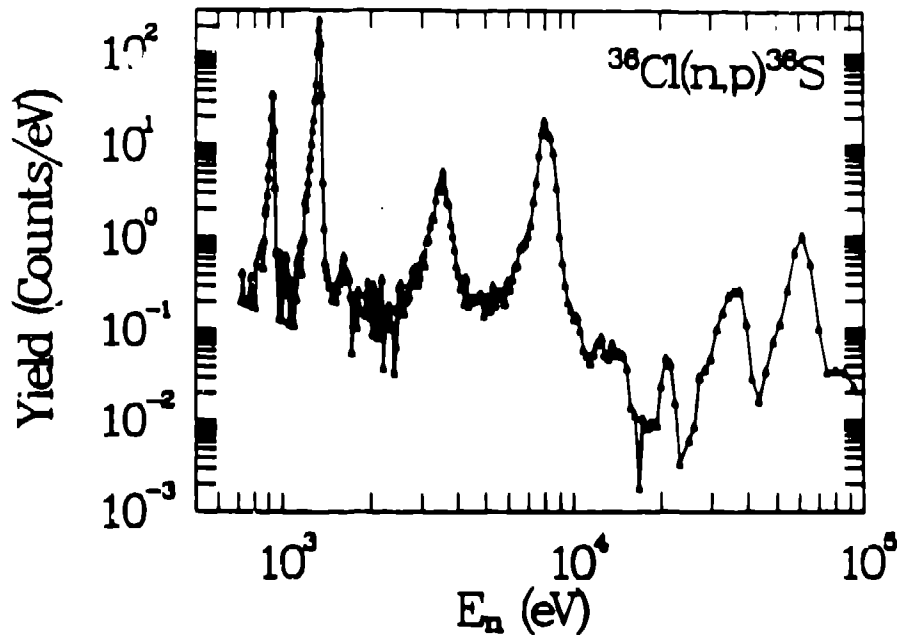


Fig. 3 The  $^{36}\text{Cl}(n,p)^{36}\text{S}$  yield as a function of neutron energy measured at a 7 meter flight path.

## 2. Neutron Transport Benchmarks

A facility also has been established on FP-2 at LANSCE for neutron transport studies. The assembly for this study includes a fission neutron detector incorporating detection by proton recoil and the elimination of gamma detection by pulse shape discrimination. It is located at the end of a 60-M flight path. Successful experiments require the presence of fissile material and a neutron life time in the assembly which is short compared to the drift time of the neutron along the flight path. The latter condition is satisfied in small assemblies for neutrons with energy less than 1000 eV. An example of a very simple assembly is shown in Fig.4. A comparison of the results for two thicknesses of  $^{235}\text{U}$  is shown in Fig. 5. This particular geometry is highly sensitive to the capture-to-fission ratio and has been used to improve the

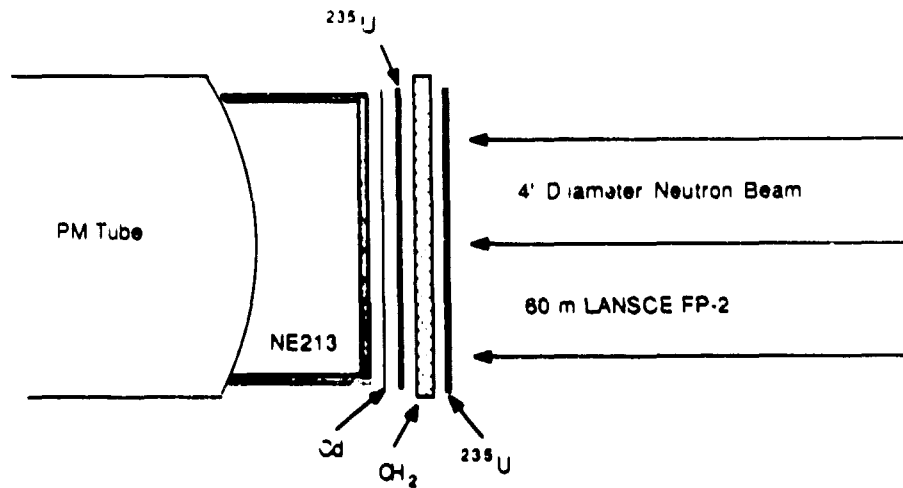


Fig. 4 Benchmark neutron transport assembly. Neutrons impinge from the right on an assembly in this case consisting simply of a layer of  $^{235}\text{U}$  and a layer of Cd. Fission neutrons produced in the  $^{235}\text{U}$  are detected by proton recoil in the hydrogenous scintillator viewed by the photomultiplier tube. The flight path length is 60 meters.

accuracy of the  $^{235}\text{U}$  resonance parameter characterization of the cross section in the energy region below 1000 eV in a joint effort with the Theoretical Physics Division of Los Alamos and the ORELA Group at the Oak Ridge National Laboratory.

### 3. Polarized Neutrons for Fundamental Symmetry Studies

It is now well established that p-wave resonances in the eV range exhibit parity violation (P-violation) enhanced over the nucleon-nucleon experiments by several orders of magnitude<sup>5</sup>. Similar enhancements are also expected for time reversal invariance violation (T-violation)<sup>6</sup>. Since P-violation is a property of the weak force, detection of this effect as a general phenomenon in neutron resonances would provide the only opportunity for studying systematics of the weak force in nuclei. Among the many ways in which the P-violation experiment might be done, perhaps the simplest is the transmission of longitudinally polarized neutrons. The detection of a difference in transmission for the two helicities is unambiguous evidence for P-violation.

Our first experiments however were done without polarized neutrons<sup>7</sup>. Since in the presence of P-violation the transmission (cross section) depends on the

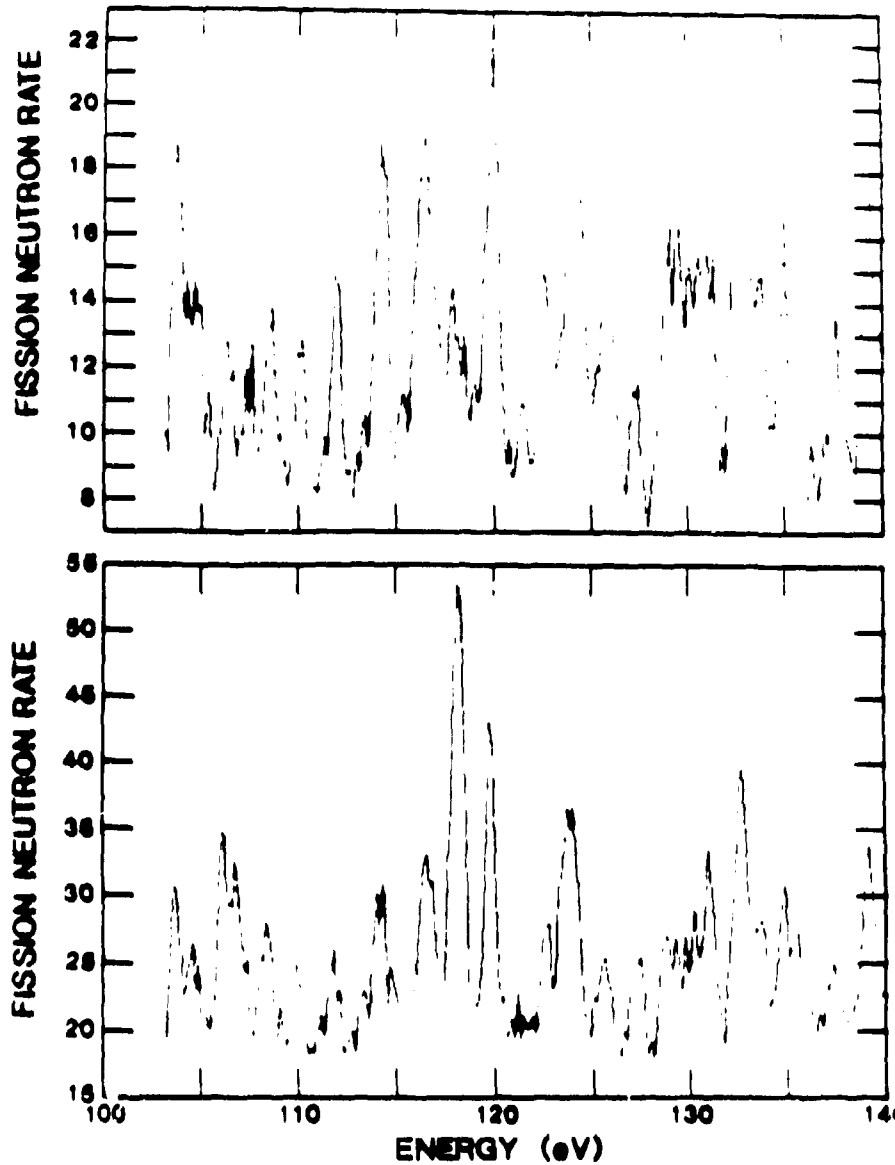


Fig. 5 A comparison of fission neutron rate for two thicknesses of  $^{235}\text{U}$  as a function of neutron energy. The measurements, which extended up to 1 keV and required eight hours, illustrate the power in resolution and intensity for eV range neutron spectroscopy at a modern spallation source.

neutron helicity, likewise polarization will be introduced into the beam when an unpolarized beam traverses a sample exhibiting parity-mixed neutron interactions. We demonstrated this effect using the geometry illustrated in Fig. 6. The unpolarized beam was first transmitted through a La sample which has a P-violating resonance at 0.73 eV. It was then passed through a magnetic device which flipped the longitudinal polarization introduced by the resonance in the first sample. The neutron beam was then passed through a second sample of the same material and neutrons detected in a detector at a flight path of 11.3 M. If the detected rate is different for the two states of the flipper, the presence of polarization in the neutron beam after traversing the first sample is established.

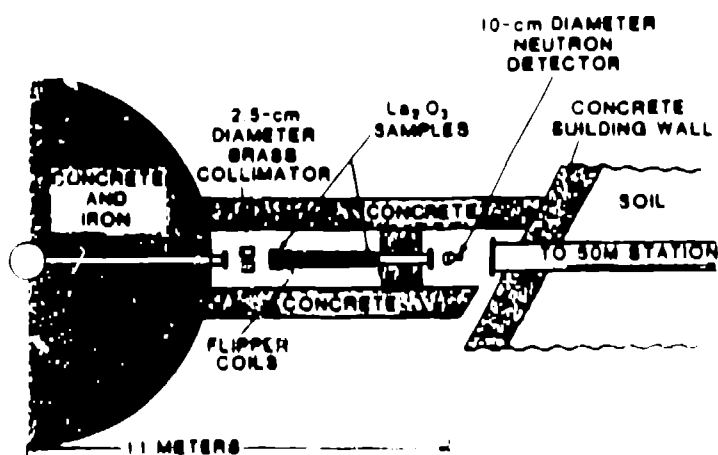


Fig. 6 Plan view of the arrangement for first measurements of parity violation without the use of polarized neutrons. Our next experiments were conducted using polarized neutrons produced by transmission through laser-polarized  $^3\text{He}$ . The  $^3\text{He}$  is polarized by bathing a mixture of helium gas and a small amount of vaporized rubidium with polarized laser light<sup>8</sup>. The alkali vapor is polarized in the optical pumping process and the polarization transferred to the helium nuclei by the spin-spin interaction. We typically achieve an 70%  $^3\text{He}$  polarization in a 10 atmosphere-cm<sup>3</sup> volume. The area of the cell was 0.75 cm<sup>2</sup> with a length of 4 cm, and a pressure of 3.3 atmospheres. It was located at a flight path distance of 7 meters.

The technique has the advantage over a polarized hydrogen target<sup>9</sup> of little loss in neutron intensity in the polarization process, easy neutron spin flipping by flipping the  $^3\text{He}$  by adiabatic fast passage, eight-hour polarization decay time in the absence of laser pumping, no cryogenics, and no strong magnetic field. At its present stage the beam area is small and useful neutron



polarization experiments are limited to the energy region below 1 eV. Progress in the amount of polarized  $^3\text{He}$  has moved rapidly and depends primarily on a better understanding of wall depolarization effects and on increasing the laser power. The power on the cell was about 0.5 watts. A comparison of what we have achieved and what should be possible for a  $3\text{ cm}^2$  beam area with an increase in laser power by a factor of ten is shown in Fig. 7. This performance would be of substantial interest to the neutron scattering community. We are also studying the possibility of a laser-polarized  $^3\text{He}$  detector which would offer interesting advantages for polarized neutron research.

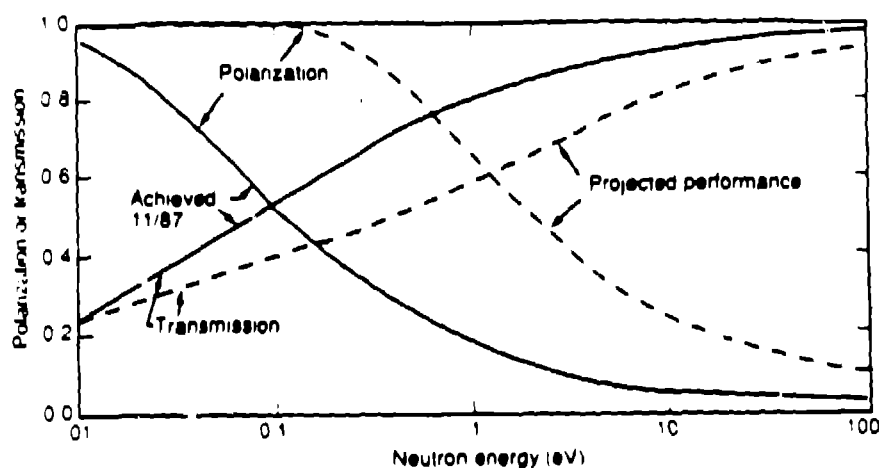


Fig. 7 Performance of the first  $^3\text{He}$  spin filter in terms of filter transmission and polarization as a function of neutron energy and improvements resulting from a factor ten increase in polarized laser light intensity.

In order to reach polarization of about 60 % over an area of  $10\text{ cm}^2$  and throughout the eV range, we brought on line for 1988 a polarized hydrogen transmission filter of conventional design using lanthanum magnesium nitrate crystals as the filter<sup>5</sup>. The transmission of the neutron beam through the filter was about 0.18. P-Violation data was collected using a  $100\text{-cm}^2$  detector located at 11 M or a  $700\text{-cm}^2$  detector at 60 M. An example of the P-violation data collected on  $^{139}\text{La}$  in 1.5 hours is shown in Fig. 8. A spectrum for  $^{238}\text{U}$  is shown in Fig. 9. The p-wave resonances are readily seen; a resonance at 89 eV appears to show substantial P-violation. For 1989 we hope to switch over to an organic filter and to improve our beam area by at least a factor of two, make some improvements in polarization, and increase the transmission by perhaps a factor of two.

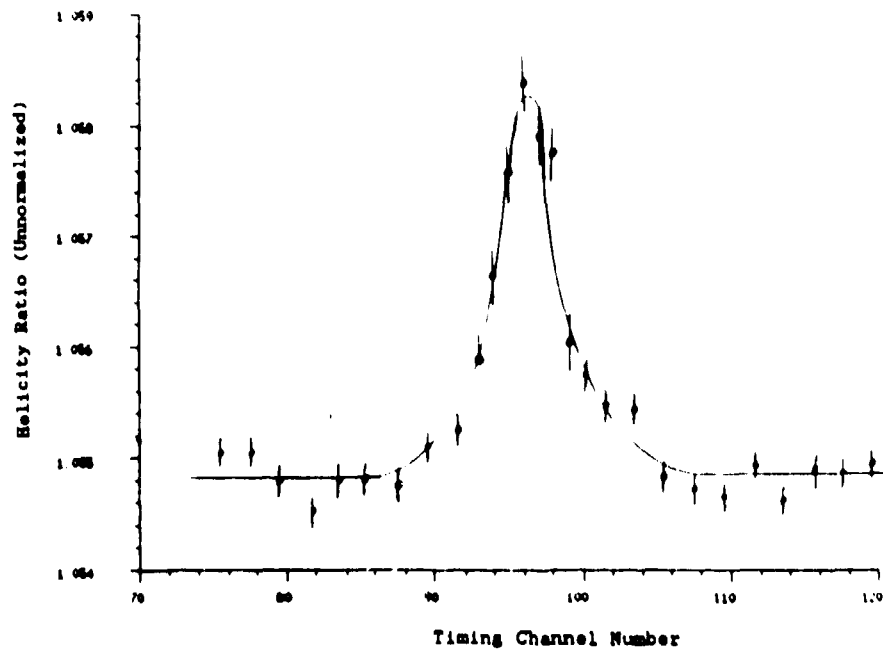


Fig. 8 A measurement of parity violation in a resonance at 0.734 eV in  $^{139}\text{La}$ . The ordinate is the ratio of transmission for neutrons polarized along and opposite to the direction of neutron propagation. The measuring time was 1.5 hours.

The counting rate in these transmission experiments exceeds  $10^{10}$  per second and it is therefore not possible to count individual neutrons. We have therefore developed current-mode counting to accommodate the rates. The apparatus and an example of the data is shown in Fig. 10. A 1-cm thick detector of  $^6\text{Li}$ -loaded glass is attached to the face of a photomultiplier tube with separate high capacity power supplies for each of the higher dynodes to assure that the voltage on these dynodes doesn't sag under high current loading. The signal may be averaged and then fed into a transient digitizer. This unit measures the current 8096 times in one cycle with a dwell time as short as 1/8 microsecond. Each of these 8096 values is added to an 8096-channel summing memory after each beam pulse. The result for three LANSCE beam pulses (1/5 s running time) is shown for transmission on a Ho sample. Note that even weak p-wave resonances in Ho are beginning to appear already in the wings of the much stronger s-wave resonances. Being able to handle these enormously high counting rates might make Bragg-edge diffraction competitive with conventional high resolution powder

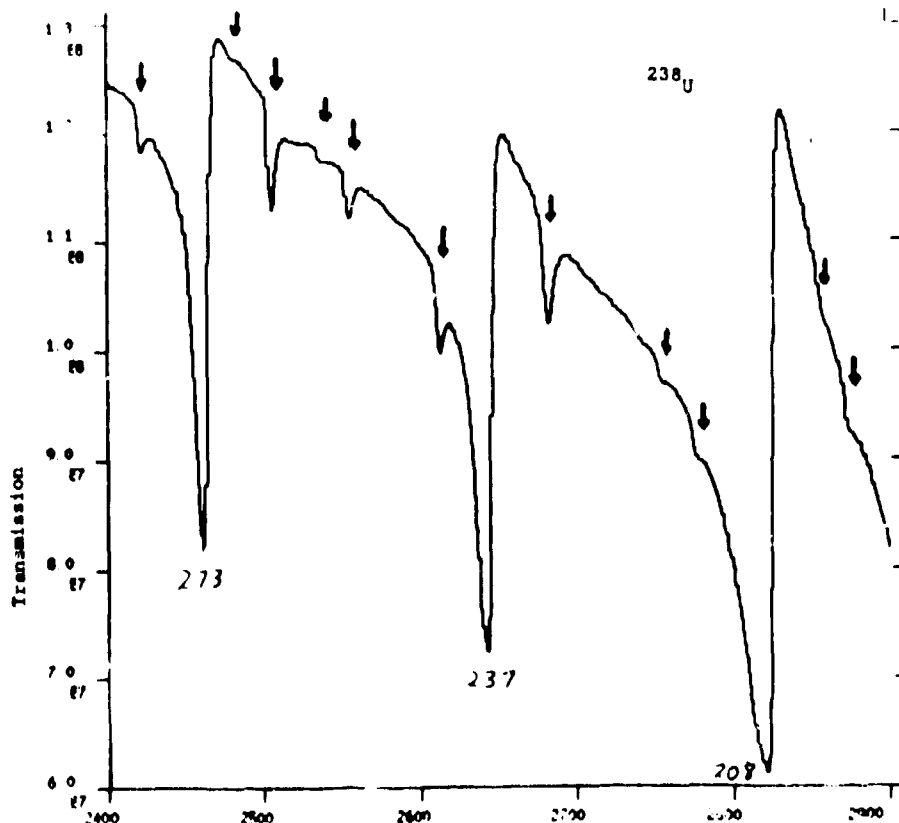


Fig. 9 Transmission measurements on  $^{238}\text{U}$  using polarized neutrons for parity violation studies. The ordinate is proportional to transmission and the abscissa is the neutron time of flight channel. The numbers at the dips are the  $s$ -wave resonance energies in eV. The arrows indicate the position of the weak  $p$ -wave resonances.

diffractometers. This possibility is discussed for some specific experiments below.

#### Neutron Scattering Science Related to Neutron Nuclear Physics

Both neutron scattering and neutron nuclear physics originated at nuclear reactors. While neutron scattering focused on the exploitation of thermal neutrons and the science possible with them, most of the nuclear physics moved on to higher energies using electron linacs which produce intensities of

higher energy neutrons. However the advent of intense spallation sources provides epithermal neutron intensity higher by several orders of magnitude and has begun to attract nuclear physicists back to the lower energy range. One may therefore expect a synergism with nuclear physics which might hasten the exploitation of some parts of the pulsed neutron scattering field. This section gives some examples of prospective condensed matter science growing out of neutron nuclear research.

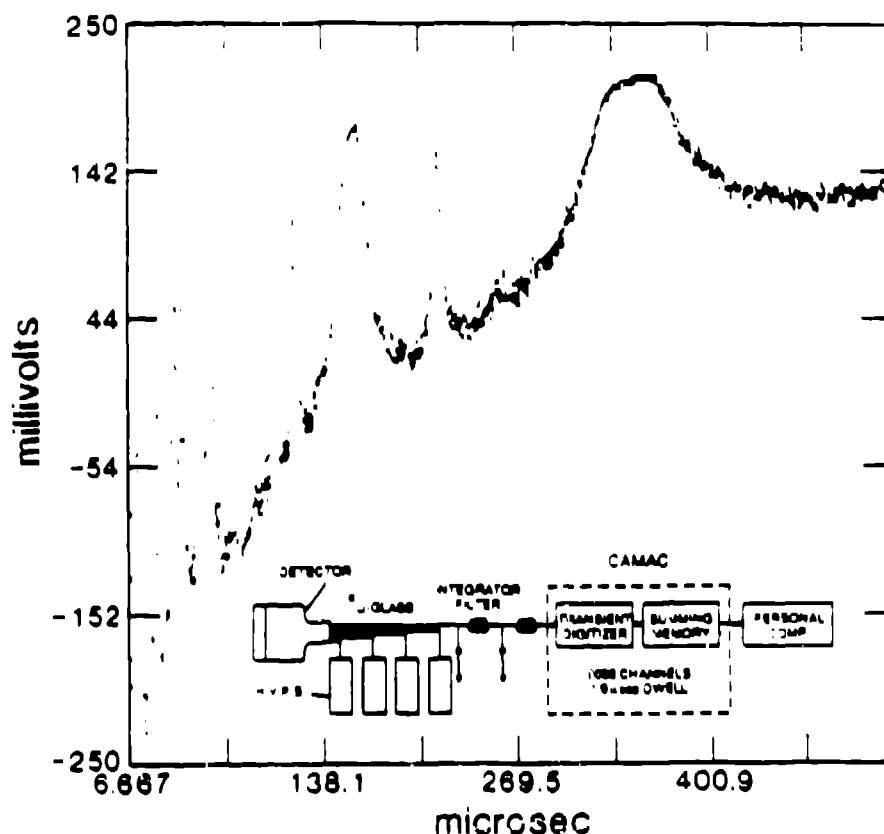


Fig. 10 Current-mode neutron detection. The spectrum shown was collected in about 0.3 seconds. See text for details.

#### A. Bragg-Edge Diffraction

Several years ago demonstration experiments<sup>10</sup> were reported which suggested the use of Bragg-edge diffraction for extending the power and breadth of neutron diffraction research. Fig. 11 shows an example of such a measurement on a 2-cm thick slab of iron. The sharpness of the peaks allows a measure of

the internal stress and the relative sizes allowed a determination of the texture. This approach offers high resolution because of the absence of scattering angle and sample thickness contributions to the resolution. The geometry is simple since it is a straightforward transmission experiment and the angular structure of the detector need not be dealt with in data collection. The transmission geometry also allows the collection of position-sensitive data on the sample so that high resolution position-sensitive stress distributions, etc could be measured. The natural geometry for this experiment is substantially different from the scattering geometry in that the few  $\text{cm}^2$  sample should be placed relatively close to the source and a large area detector placed far away for best resolution.

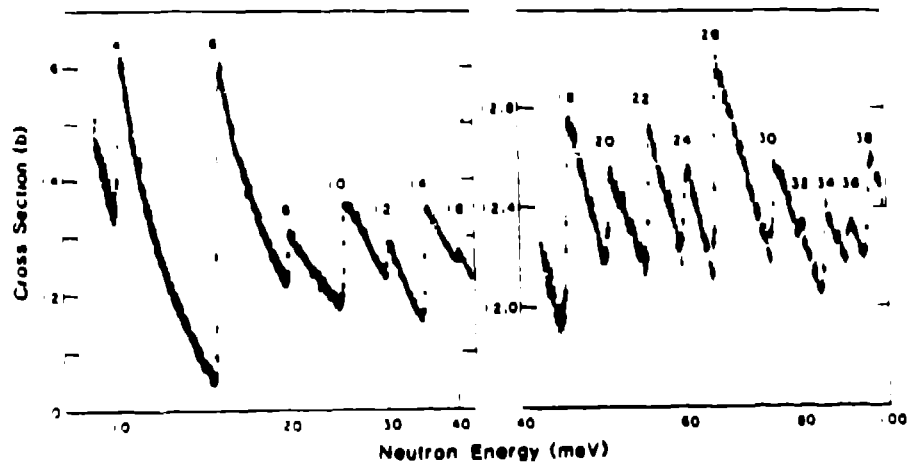


Fig. 11 Bragg-edge diffraction measurement on a 2-cm thickness of natural iron. The numbers at the edges in the figure are the sum of the squares of the Miller indices for the various scattering planes.

### 1. High Resolution Diffraction

The geometry of the P-violation experiment described above is essentially that required for high resolution Bragg-edge diffraction. The 60-M detector should make possible resolution equivalent to a scattering geometry path length of 120 M. Also the current-mode large area neutron detector is operational and make possible data collection at the high rates necessary for practical diffraction experiments in transmission geometry.

## 2. Diffraction Using Polarized Neutrons

Polarized neutrons are available on this beam line along with spin flippers and polarization transport apparatus. The LMN transmission filter is not the most effective neutron polarizer for the thermal range. The rising cross section of hydrogen as the energy decreases into the thermal range improves the polarization substantially above the eV range value of about 55%. However the transmission of the neutrons decreases rapidly as the neutron energy decreases. The practicality of polarized neutron diffraction remains to be demonstrated with the present system. Of course planned improvements in the system using filter materials such as butanol could improve the polarized neutron intensity in the thermal range. The full development of the potential of the laser-polarized  $^3\text{He}$  should make this geometry highly effective for this field of work.

## 3. Stress Distribution Studies

The Bragg-edge geometry has the feature that the sharpness of the edges is different as a function of position on the sample if the stress distribution varies over the sample. This position information can be measured with either of two position-sensitive detector arrangements. In either case the incident neutron beam should be as nearly parallel as possible and the neutron detector should be located close behind the sample to reduce parallax. Data could be collected at a short flight path by scanning a small current-mode detector across the sample with position resolution determined by the detector size. This geometry would be suitable where low wavelength and position resolution is adequate and high measurement speed is important.

Alternatively a high efficiency position-sensitive detector<sup>11</sup> could be used with resolution as good as 0.5 mm. The data collection rate for this class of detector is usually too low for use in the direct beam at LANSCE unless the sample and detector are placed a long way from the moderator. Therefore this mode would make possible better wavelength and position resolution but with much longer measurement time. Position-sensitive stress measurements could prove valuable for industrial application such as stress distribution in welds.

## 4. Strong Transient Diffraction

Strong transient diffraction is defined here as the study of the response of a sample to a sudden change in its condition such as would be caused by sudden heating by a strong current pulse or by sudden compression from a hammer blow. Obtaining the time history of a phase transition induced by these means might be the objective of such an experiment. Another might be to study the time history of the stress under such transient conditions. It appears that LANSCE now has the capability to conduct such experiments using a single

PSR pulse. The experiment requires the very high pulsed neutron intensity of the PSR, the Bragg-edge geometry, and current-mode neutron detection.

The idea is to look at the change in position and shape of a sequence of Bragg edges as the transient is imposed upon the sample. Each edge therefore provides both strain and compression information. Since the neutrons arrive at the sample at different times for each Bragg edge, a time sequence of this information can be obtained with a single PSP. pulse for a transient which takes the sample to destruction. Table III lists parameters for such an experiment on a 1-cm<sup>2</sup> area by 2-cm thick iron sample located at a flight path length of 6 meters using a collimated beam on a detector which collects all neutrons transmitted through the sample. Counting rate estimates indicate that seven frames could be measured over a time interval (at the sample) extending from 2.2 to 6.2 milliseconds after a particular PSR pulse. The typical size of a Bragg-edge step in transmission is about 0.3 and ten points across each edge could be obtained with a statistical accuracy of 0.01. It is of interest to note that the time required for a sound wave to cross the sample is about 4 microseconds.

Table III. Parameters for Strong Transient Diffraction Experiment.

Target Yield in Thermal Range	0.4 n/p- $\mu$ -eV
Solid Angle (1cm <sup>2</sup> at 6 meters)	$2.8 \times 10^{-6}$
Protons per pulse (12 Hz)	$5 \times 10^{13}$
Channel Width (eV) (2dL/L)E	$2.2 \times 10^{-4}$

Incident Neutrons =  $1.2 \times 10^4$

Statistical Accuracy = 0.01

Transmission Change at 2.1.1 peak of 1-cm iron = 0.65

<u>Multiple Frames per Pulse</u>	<u>Indices</u>	<u>Time microseconds</u>
	3,2,1	2200
	2,2,2	2550
	3,1,0	2800
	2,2,0	3100
	2,1,1	3600
	2,0,0	4350
	1,1,0	6200

### B. eV Inelastic Neutron Scattering

The ability to measure energy transfers in the eV range at low momentum transfers would be a powerful addition to the array of experimental techniques available at pulsed sources. Attempts<sup>12</sup> to establish this capability using

materials possessing narrow neutron resonances in transmission or capture geometry have not been entirely successful because of both limited intensity and the resolution limit of a few percent. However enough has been learned that it is clear that a resolution of a few tenths percent with adequate intensity would probably have a major impact on condensed matter physics studies.

Two new avenues are available at LANSCE for attempted improvements. The first involves the use of the LANSCE through-tube which makes possible the emplacement of a resonance scatterer near the moderator which would scatter down the flight path only neutrons at the resonance energy. The resolution of the neutron pulse is determined by the resonance shape and not by the time of flight. By appropriately filtering this pulse it might be possible to improve the resolution into the interesting range while maintaining adequate intensity and low background.

The second possibility is the use of polarized beams, spin rotation and polarized detectors to develop a means of high resolution neutron spectroscopy similar in some ways to the spin-echo technique<sup>13</sup>. At LANSCE the ingredients available for testing such an idea include high intensities of eV polarized neutrons, high current spin rotation solenoids, long drift tubes, and prospects for a polarized <sup>3</sup>He neutron detector.

### **C. Resonance Neutron Radiography**

Resonance neutron radiography takes advantage of the distinctive resonance properties of materials for quantitative assay of samples in both a chemical and isotopic sense and for distribution assay of samples with a position resolution of 0.5mm. The practicality of resonance neutron radiography has been demonstrated using neutron sources far weaker than modern spallation sources. However the implementation of a facility which can make available the power of the method at a spallation source for a broad spectrum of applications remains to be done. The full development of the potential of the method probably requires the active involvement of staff with extensive experience in neutron nuclear spectroscopy in the eV and keV range.

### **Extensions for Neutron Nuclear Physics at LANSCE**

In this section new experiments in nuclear physics for spallation sources will be described. The power of the polarized beam facility on FP-2 and the unstable target facilities on FP-4 at LANSCE and also the demand for time on these beam lines forecloses the possibility of expanding the scope of the neutron nuclear physics effort at LANSCE for the foreseeable future except through the implementation of at least one new flight path. This flight path should have the potential for extension to 300 M and eventually to 600 M. Apparently



FP-15 at LANSCE is the only unoccupied flight path which can be extended to these distances.

#### **A. Electric Polarizability of the Neutron**

In the absence of T-violation the neutron has no static electric dipole moment. However an induced dipole moment appears as the neutron closely approaches the strong field of a heavy nucleus such as lead. The field induces a moment through which the neutron and the nucleus can interact. There is as a result a small contribution to the scattering cross section which in principle can be detected either in the total or the scattering cross section at back angles<sup>14</sup>. The size of this cross section has been estimated<sup>15</sup> using quark models both for the neutron and the proton and the polarizability appears to be measurable for both particles. The proton polarizability is being measured in high energy electron scattering experiments. LANSCE appears to be an excellent neutron source for studying the neutron. Preliminary evaluations of the experiment indicate the need for a flight path of 100- to 150-M length and that a sensitivity three to ten times smaller than the predicted polarizability could be achieved at LANSCE. This would be quark physics using eV neutrons!

#### **B. Neutron Gravitation**

Interest continues on a comparison of the value of small  $g$  for the neutron compared with that for macroscopic objects. The value of small  $g$  has been measured by comparing the value of a scattering length measurement using a reflectometer with that from other methods. An accuracy of  $3 \times 10^{-4}$  is claimed<sup>16</sup> for a value of  $g$ , which agrees with the geophysical value. By taking advantage of the high intensity at LANSCE and a flight path of 300 M it should be possible to extend the accuracy to  $1 \times 10^{-5}$ . If the flight path were extended across a 100-meter deep by 200-meter wide canyon to about 600 meters, the first "fifth force" experiment looking for a short range contribution to the gravitational field for an elementary particle might be performed. Both experiments would likely be viewed as milestone experiments in the field of gravitation.

#### **C. Neutron Capture Gamma Ray Spectroscopy**

The field of neutron capture gamma ray spectroscopy has been rather well studied with thermal neutrons. However the scope of the experiments in terms of scientific questions is greatly expanded by studies using resonance neutrons. Such studies at electron linacs have been greatly hampered by the low neutron intensity and the intense gamma flash. Both limitations can be resolved by using a LANSCE-class spallation source for studies in the eV and keV range. By working at longer flight paths the duty cycle advantage of the linac is also

substantially overcome. It seems likely therefore that this field could be greatly advanced by experiments conducted using 100- to 200-M flight path distances.

#### **D. eV and keV Spectroscopy**

The field of neutron resonance spectroscopy advances steadily through a variety of experiments. The research is driven by the interests of basic science and the continuing need for nuclear data for technology. Most experiments could be done better at LANSCE than at the best electron linacs in current use. One could therefore envisage a broad program of eV and keV neutron spectroscopy conducted on a long flight path equipped with several experimental stations. Highlight experiments in neutron electric polarizability and neutron gravitation would be supplemented with applied studies such as resonance neutron radiography.

#### **Experimental Cell for PSR Beam**

The PSR now provides the world's most intense bursts of protons and neutrons. When the PSR improvement program reaches design specs, the intensity will be still higher by a factor of three with an instantaneous current of 25 amperes, and a proton power level of 30,000 megawatts. The parameters of the intense pulse are summarized in Table IV.

**Table IV. Proton Storage Ring Output Beam Parameters**

Proton Energy	800 MeV
Pulse Width	0.27 microseconds
Stored protons	$5 \times 10^{13}$
Instantaneous Current	25 A
Proton Power Level	30 GW
Neutrons per pulse	$10^{15}$
Total Proton energy	8 kJ

Presently there is no available experimental area for direct access to this intense proton pulse. Such space would make possible a number of noteworthy experiments which would not be practical anywhere else. These experiments would typically use only a small part of the PSR output and many might fall

into the class of single pulse experiments. Frequent and close access to the experimental apparatus by personnel would be a characteristic of the required experimental cell. Some of the experiments which might be conducted are briefly described below.

#### **A. PSR-Driven Neutron Multiplier**

Neutron production from spallation reactions can be multiplied by large factors using a fission multiplying assembly. These assemblies range from high repetition rate devices such as the new multiplier at Argonne<sup>17</sup> with modest effective neutron amplification of a factor of three to slower devices with greater amplification and even conceptual designs with multiplication by 1000 which allow for core disassembly during the multiplication process while still maintaining a slow repetition rate capability<sup>18</sup>. Using a spallation driver also provides more control over pulse width and delayed neutron backgrounds, and more flexibility in some aspects of mechanical design for pulsed reactors.

The concept most likely of interest to Los Alamos would be a facility operating at an average power level of less than 1 MW with high multiplication and therefore repetition rate of 1 to 0.001 Hz. The impact on LANSCE neutron production would be negligible while the intensity of the neutron pulses would be much larger than those at LANSCE and close access to the source could be available. One can imagine a broad array of studies in condensed matter and nuclear research, radiation effects, and radiography.

#### **B. Ultracold Neutron Facility**

The ultimate storage density of ultracold neutrons depends on the highest instantaneous density of cold neutrons which can be produced. Realization of advantages from pulsed neutron sources requires the use of synchronized reciprocating collectors which have been demonstrated<sup>19</sup>. The collection efficiency also can be enhanced if the facility geometry allows close access to the proton beam line or to a multiplier assembly<sup>20</sup>. Stored neutron quantities substantially exceeding that available at the best reactors are in principle possible if one takes advantage of all the features of the most intense spallation sources and of any associated multiplier assemblies.

A broad array of experiments would be possible with higher densities of ultracold neutrons than presently available including the search for the neutron electric dipole moment, the search for T-violation in neutron decay, improved accuracy for the neutron half-life, more than an order of magnitude improvement on the measurement of small  $g$  for the neutron including the search for a gravitational spin dependence, neutron-antineutron oscillations, improving the limit on the neutron charge, and surface studies in condensed matter physics.

### C. Lead Slowing-Down Spectrometer

The lead slowing-down spectrometer provides a means of greatly enhancing the neutron intensity available for some classes of neutron spectroscopy in the eV and keV range. A cube of lead usually about 1 meter on a side is driven with a pulse of MeV neutrons. As the neutrons moderate, a correlation develops between the neutron energy in the block and the time after the block was pulsed. The intensity gain over a conventional drift tube experiment at 7 meters can be four orders of magnitude while giving up a factor of ten in resolution. The PSR could drive such an assembly with four orders of magnitude more average or pulsed intensity than has been used up to the present<sup>21</sup>. Such a facility offers its best advantage in measurements of very small neutron reaction cross sections or measurements on very small samples.

### D. Neutron-Neutron Scattering

The neutron-neutron (n-n) scattering length has never been directly measured and a value to an accuracy of a few percent is of great interest. Experiments on the edge of practicality have been proposed for steady state thermal neutron sources. Since the scattering rate in an n-n scattering length measurement depends on the square of the neutron flux, the spallation pulsed source has a decided advantage over the steady state reactor.

A cavity could be built close to a spallation source or better yet close to a neutron multiplier assembly containing a gas of thermal neutrons which is viewed by a detector through a collimated path which does not allow the detector to see the cavity walls. With a cavity containing a low pressure of hydrogen gas, the scattering rate will be proportional to the neutron flux so that the flux may be measured. The n-n scattering rate may be separated from residual gas scattering by measurement of the scattering rate for different pulse intensities. Although a calculation has not been done for a spallation source, it has been done for a pulsed reactor<sup>22</sup>. For a flux of  $10^{17}$  n/cm<sup>2</sup>-sec, a cavity 10-cm long, and 10-cm in radius, a detector distance of 12 meters, a detector radius of 10 cm, and a pulse width of 6 milliseconds, the detected n-n scattering rate is 30 neutrons per pulse.

### E. Optical, X-ray, and Gamma-ray Lasers

The 30,000 megawatt power level of the PSR proton pulse offers substantial potential for use in driving a wide spectrum of laser types. Optical lasers certainly could be driven and an experiment already has begun<sup>23</sup> at LANSCE to do this in front of the tune-up beam dump in the PSR hall. Of greater interest would be driving an x-ray laser through the electron excitation produced by the proton beam or a gamma-ray laser through nuclear

excitations created by the protons directly or perhaps through the neutrons generated by the beam.

An x-ray or gamma-ray laser driven by the same facility used in neutron production would be a powerful adjunct to condensed matter physics. Undoubtedly many new experimental techniques not possible with synchrotron radiation could be developed and many conventional experiments could be done better with a super-intense high coherence keV photon beam. It seems likely that many experiments in fundamental physics such as quantum mechanics tests, etc. might also be possible using a beam with such characteristics.

### Conclusion

The spectrum of neutron nuclear science, which stretches from 0.01 eV to 800 MeV, is clearly a rich field of research which is ripe for development and facilities are now in place at Los Alamos for studies throughout the energy range. So far, however, no spallation facility includes a cell providing direct access to the intense pulsed proton beams. Such a capability would broaden much further the power of the spallation source for research. Hopefully the ICANS community will encourage exploration of the full spectrum of science which the Advanced Neutron Sources make accessible in order to provide the strongest possible case for the next advance in pulsed neutron intensity.

### References

- <sup>1</sup> For earlier descriptions of LANSCE-related facilities for neutron nuclear physics research and research progress see: C. D. Bowman, "Spallation Sources for Neutron Nuclear Physics", in Properties of Neutron Sources, Proceedings of an IAEA Conference, Leningrad, USSR, IAEA-TECDOC-410, 396 (1986). Also P. W. Lisowski, S. A. Wender, and G. F. Auchampaugh, Proceedings of a Conference, "Nuclear Data for Basic and Applied Science", Santa Fe, NM, Gordon and Breach, New York, NY, p. 1245 (1986). Also C. D. Bowman, "New Opportunities in Neutron Capture Research Using Advanced Pulsed Neutron Sources", Inst. Phys. Conf. Ser. No. 88/ J. Phys G: Nucl Phys. 14 Suppl. S339 (1988). Also C. D. Bowman, "New Neutron Physics Using Spallation Sources", Proceedings of the International Conference on Nuclear Data for Science and Technology, Mito City, JAPAN, (1988)
- <sup>2</sup> C. D. Bowman, S. A. Wender, and G. F. Auchampaugh, AIP Conference Proceedings No. 184, "Neutron-Nucleus Collisions, A Probe of Nuclear Structure", Burr Oak State Park, Ohio, p. 259 (1984)

- 5 S. A. Wender and P. W. Lisowski, Nucl. Inst. and Meth. B24/25, 897 (1987)
- 6 P. E. Koehler, C. D. Bowman, F. J. Steinkruger, D. C. Moody, G. M. Hale, J. W. Starner, S. A. Wender, R. C. Haight, P. W. Lisowski, and W. L. Talbert, Phys. Rev. C37, 917 (1988)
- 7 V. P. Alfimenkov et. al. Sov. J. Nucl. Phys. 39, 665 (1984)
- 8 P. Kabir, Phys. Rev., D25,2013 (1982)
- 9 C. D. Bowman, J. D. Bowman, and V. W. Yuan, "Parity Violation in the 0.734 eV Neutron Resonance in  $^{139}\text{La}$ " Submitted to Phys. Rev. (1988)
- 10 K. P. Coulter, T. E. Chupp, A. B. McDonald, C. D. Bowman, J. D. Bowman, J. Szymanski, V. W. Yuan, G. Cates, D. R. Benton and E. D. Earle "Neutron Polarization with a Polarized  $^3\text{He}$  Spin Filter", Submitted to Phys. Rev. (1988)
- 11 G. A. Keyworth, et. al., Phys. Rev. C2, 2352 (1973)
- 12 R. G. Johnson and C. D. Bowman, "High Resolution Powder Diffraction by White Source Transmission Measurements", Argonne Conference on Neutron Scattering, 1981. Am. Inst. Phys. Conf. Proc. 89 (1982)
- 13 R. A. Schrack, International Advances in Non-destructive Testing, Vol II, pp 219-249, Gordon and Breach (1985)
- 14 R. G. Johnson and C. D. Bowman, Phys. Rev. Letters 49, 797 (1982)
- 15 F. Mezel, Nucl. Instrum. and Meth. 164, 153 (1979)
- 16 J. Schmiedmayer, H. Rauch, and P. Rieha, "Measurement of the Electric Polarizability of the Neutron" Submitted to Phys. Rev. Letters (1988)
- 17 G. Dattoli, G. Matone, and D. Prosperi, Lettere al Nuovo Cimento 19,601 (1977)
- 18 L. Koester, Phys. Rev. D14, 907 (1976)
- 19 J. M. Carpenter, "Booster Targets and Moderator Characteristics" These proceedings
- 20 L. D. P. King, "Disposable-core Fast Burst Reactors", Proceedings of the National Topical Meeting on Fast Burst Reactors held at The

University of New Mexico, Albuquerque, Jan 28-30, 1969, USAEC 15  
Symposium Series.

- <sup>10</sup>J. W. Lynn, W. A. Miller, T. W. Dombek, G. R. Ringo, V. E. Krohn, and  
M. S. Freedman, *Physica* 120B, 114 (1983)
- <sup>20</sup>H. Yoshiki, S. Ishimoto, and M. Utsuro, *Z. Phys.* B67, 161 (1987)
- <sup>21</sup>R. C. Block, R. W. Hockenbury, D. S. Cramer, E. Bean, and R. E. Slovacek,  
NBS Special Publication 425, Nuclear Cross Sections and Technology,  
p. 93 (1975)
- <sup>22</sup>W. C. Dickenson, E. M. Lent, and C. D. Bowman, "An Analysis of a  
Proposed n-n Scattering Experiment", UCRL Report 50848 (1970)
- <sup>23</sup>M. V. Hynes, Private Communication (1988)

# Introduction to maximum entropy

*D. S. Sivia*

Theoretical Division and Los Alamos Neutron Scattering Center  
Los Alamos National Laboratory  
Los Alamos, New Mexico 87545  
USA

**ABSTRACT:** The maximum entropy (MaxEnt) principle has been successfully used in image reconstruction in a wide variety of fields. We review the need for such methods in data analysis and show, by use of a very simple example, why MaxEnt is to be preferred over other regularising functions. This leads to a more general interpretation of the MaxEnt method, and its use is illustrated with several different examples. Practical difficulties with non-linear problems still remain, this being highlighted by the notorious phase problem in crystallography. We conclude with an example from neutron scattering, using data from a filter difference spectrometer to contrast MaxEnt with a conventional deconvolution.

## 1. Introduction

In many scientific experiments, the quantity of interest  $f$  is related to the data  $d$  through some transformation  $O$  and noise  $\sigma$ :

$$d = O.f + \sigma.$$

For example,  $f$  might be the radio-flux distribution of an astronomical source, the momentum distribution of atoms in liquid helium, or the scattering law in a neutron scattering experiment, and so on. The transformation operator  $O$  might represent a Fourier transform or a convolution with an instrumental resolution function. The job of data analysis is to infer the desired quantity  $f$  from the data  $d$ .

The simplest way of deriving an estimate of  $f$ ,  $\hat{f}$ , from the data is to apply the inverse transform  $O^{-1}$  to the data:  $\hat{f} = O^{-1} . d$ . In many cases, however, we cannot do this because the inverse operator does not exist, often because we have missing data. We cannot Fourier transform a data set, for example, if we have unmeasured data. Even if we can compute the inverse transform, our reconstruction will have many artifacts because we have not taken into account the fact that the data were noisy:

$$\hat{f} = O^{-1} . d = f + O^{-1} . \sigma .$$

We will illustrate the effects of noise on the direct inverse graphically in Section 6.

The fact that the data are both noisy and incomplete means that our problem is fundamentally ill-posed—there are many reconstructions of  $f$  permitted by the data. We can consider all the reconstructions that would give data consistent with those





actually measured by setting up a misfit statistic— $\chi^2$  is often appropriate:

$$\chi^2 = \sum_{k=1}^N \frac{|\hat{d}_k - d_k|^2}{\sigma_k^2},$$

where  $d_k$  is the  $k^{\text{th}}$  measured datum, with error-bar  $\sigma_k$ , and  $\hat{d}_k$  is the corresponding datum that a trial reconstruction  $\hat{f}$  would produce in the absence of noise:  $\hat{d}_k = [O \cdot \hat{f}]_k$ . Those reconstructions that give  $\chi^2 \leq N$  are deemed to have "fit the data" and constitute the *feasible set* of  $\hat{f}$ . This *feasible set*, however, is incomprehensibly large: suppose we wish to reconstruct a 2-d image on an 8x8 pixel grid with just 16 grey levels; this gives a total number of  $10^{77}$  possible reconstructions. Even if the data restricted the intensity of each pixel to vary only by ( $\pm$ ) one level on average, the *feasible set* would still consist of  $10^{30}$  possible reconstructions. This is enormous if you compare it with age of the universe, which is only  $10^{17}$  seconds. Real problems are typically 128x128 pixel grids with 256 grey levels!

As we cannot even comprehend the total number of solutions, let alone compute and display them, we are forced to make a selection. We would like to say this is our ("best") estimate of the true  $f$ . Which solution should we select?

## 2. The principle of maximum entropy

If  $f$  is a *positive* and *additive* quantity—for example, a probability density function, or the intensity distribution of an optical picture, or the radio-flux distribution of an astronomical source—then the MaxEnt principle states we should choose that solution which maximises the Shannon-Jaynes entropy  $S$  (Jaynes 1983, Skilling 1988):

$$S = - \sum_j f_j \cdot m_j \cdot f_j \log(f_j/m_j),$$

where  $f_j$  is the flux in the  $j^{\text{th}}$  pixel of the digitized reconstruction of  $f$ , and  $(m_j)$  is a starting model which incorporates any prior knowledge we have about  $f$ ; in the absence of any such knowledge, all the  $m_j$  are set equal. If  $f$  is a normalised quantity such that  $\sum f_j = 1$  and  $(m_j)$  is constant, then entropy reduces to the more familiar form  $-\sum f_j \log(f_j)$ .

But why should we choose the MaxEnt solution? We shall try to answer this question by using a specific and very simple, example and then give a more general interpretation of the MaxEnt choice.

### 2.1 The kangaroo problem

MaxEnt is not the only regularising function used in image reconstruction: several



have been recommended. We will follow Gull & Skilling (1983) in using the *kangaroo problem* to demonstrate our preference for the MaxEnt choice over the alternatives. It is a physicists' perversion of a mathematical argument given by Shore & Johnson (1980), where they formally show that MaxEnt is the only regularising function that yields self-consistent results when the same information is used in different ways. The *kangaroo problem* is as follows:

- Information:** (1) One third of kangaroos have blue eyes.  
 (2) One third of kangaroos are left-handed.
- Question:** On the basis of this information alone, estimate the proportion of kangaroos that are both blue-eyed and left-handed.

Clearly, we do not have enough information to know the correct answer: all solutions of the type shown in the 2x2 contingency table of Fig. 1 (a) fit the data—these constitute the *feasible set* of solutions, each of which is equally likely. Figs. 1(b)-(d) show three of the myriads of feasible solutions: namely, the one with no correlation and the ones with the maximum positive and negative correlations, respectively. Although the data do not allow us to say which is the *correct* solution, our common sense compels us to the uncorrelated solution if we are forced to make a choice—no other single choice is defensible.

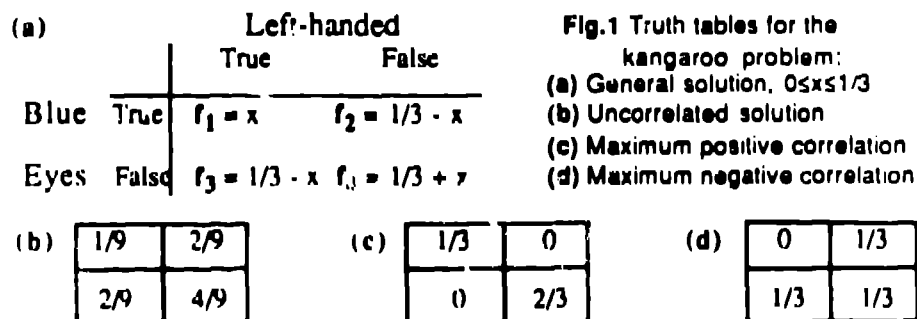


Table 1 shows the result of selecting the solution by maximising four commonly used regularising functions. For this very simple example, where common sense tells us the "best" answer when faced with insufficient (but noise-free) data, it is only the Shannon-Jaynes entropy that yields a sensible answer!

Table 1

Regularisation function	Proportion blue-eyed and left-handed (x)	Correlation
$-\sum f_j \log(f_j)$	1/9	Uncorrelated
$-\sum f_j^2$	1/12	Negative
$\sum \log(f_j)$	0.13013	Positive
$\sum f_j^{1/2}$	0.12176	Positive



Can we interpret the MaxEnt choice more generally?

## 2.2 The monkey argument

Our common sense recommended the uncorrelated solution because, intuitively, we knew that this was the least committal choice. The data itself did not rule out correlation but, without actual evidence, it was (*a priori*) more likely that the genes controlling handedness and eye-colour were on different chromosomes than on the same one. Although we cannot usually appeal to specific knowledge like genes and chromosomes, we can use the *monkey argument* of Gull & Daniell (1978) to see more generally that the MaxEnt choice is the one that is *maximally non-committal* about the information we do not have. The monkey argument can (again) be thought of as a physicists' perversion of the formal work of Shannon (1948) showing that entropy was a unique measure of information content. The monkey argument is as follows:

Imagine a large team of monkeys who make images ( $\hat{f}$ ), at random, by throwing small balls of flux at a (rectangular) grid. Eventually, they will generate all possible images. If we have some data relating to an object ( $f$ ), we can reject most of the monkey images because they will not give data consistent with the experimental measurements. Those images that are not rejected constitute the *feasible set*. If we are to select just one image from this *feasible set*, the image that the monkeys generate most often would be a sensible choice. This is because our hypothetical team of monkeys have no particular bias, and so this choice represents that image which is consistent with the measured data but, at the same time, is *least committal* about the data we do not have. This *preferred* image is the MaxEnt solution.

## 3. Model-fitting and least squares

The quantity of interest  $f$  is usually a continuous quantity. For computational purposes, however, we digitize it into a discrete set of pixels  $\{f_j\}$ . This is not a limitation because we can digitize as finely as we like, but it does result in us having to estimate a large number of parameters (flux in each pixel) from a relatively small number of data. The problem tends to be grossly under-determined and, hence, we use MaxEnt to help us.

Sometimes we are more fortunate in that we have a functional model for  $f$ —the sum of six  $\delta$ -functions, or two Gaussians, for example. In this case  $f$  can be parameterised by a handful of variables. We now have to estimate a small number of parameters from a relatively large number of data—the problem is over-determined. In these cases, and with suitable assumptions, the method of least squares is usually appropriate.

If we have a sound basis for our model, then model-fitting with least squares will give more accurate results than MaxEnt—we are using much more *prior* knowledge in the model-fitting procedure than we are in MaxEnt. If we do not have a functional model, or if our model is *ad hoc* ("try fitting Gaussians"), then we are better off using MaxEnt. It is possible, and perhaps to be recommended, that we combine the use of MaxEnt and model-fitting: use MaxEnt to obtain an initial reconstruction to get an



overall picture; if the MaxEnt reconstruction and our prior physical knowledge suggest a functional model, then use this in a least squares sense for further quantitative analysis.

#### 4. General examples

We refer the reader to a comprehensive review by Gull & Skilling (1984) for numerous examples of the applications of MaxEnt. With their kind permission, a small selection of these are reproduced in Fig. 2. They illustrate the wide range of problems to which MaxEnt is now applied—forensic imaging, radio astronomy, plasma diagnostics, medical tomography, and blind deconvolution.

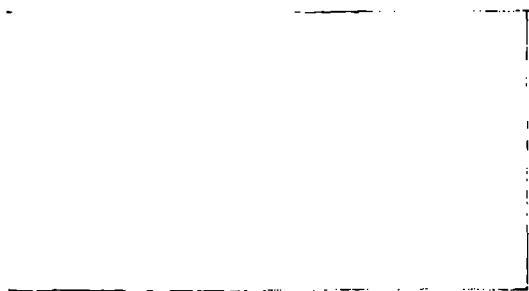
#### 5. Difficult problems

The principle of MaxEnt is quite general and can be applied to any problem where the object of interest is a positive and additive quantity. Actually, finding the MaxEnt solution can be very difficult for non-linear problems because there are many local minima of  $\chi^2$  in a large parameter-space (typically  $10^5$  pixels). A particularly well-known example is the notorious Fourier *phase problem* in crystallography, the gravity of the situation being graphically illustrated in Fig. 3. We will not pursue this topic any further here except to state that, in general, the use of additional prior knowledge is essential for these problems (see, for example, Sivia 1987).

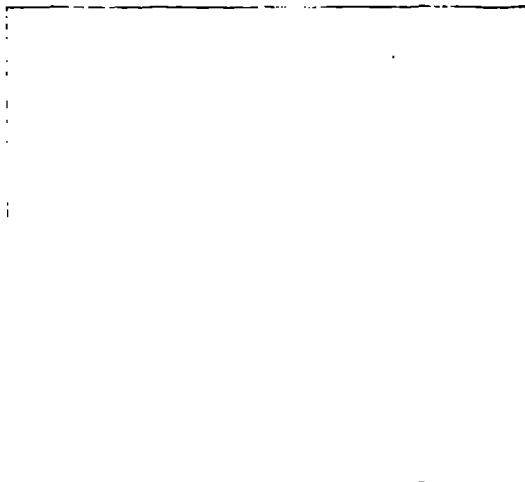
#### 6. The Filter Difference Spectrometer

We now give an explicit example from neutron scattering—the deconvolution of data from a filter difference spectrometer (FDS). For the experimental and spectrometer details, the reader is referred to Taylor, *et al.*, (1984). The essential point for our purposes is that the FDS has a resolution function with a fairly sharp edge and a long decaying tail. The Cambridge algorithm was used throughout to maximise the entropy (Skilling & Bryan, 1984).

We start with simple simulations to highlight the differences between MaxEnt and a conventional direct inverse under "controlled" conditions. They do not mimic the FDS exactly but capture its salient features. For these simulations, the true spectrum  $f(x)$  (scattering law) is shown in Fig. 4(e): it consists of two spikes separated by a low plateau on the left and a much broader peak on the right. This "truth" was generated on a grid of 128 pixels and convolved with a sharp-edged exponential  $e^{-x/\tau}$ , where  $\tau = 15$  pixels, shown in Fig. 4(b), to create a noiseless data set of 128 points. A constant ("known") background equal to 10% of the peak datum was used and Gaussian random noise with a standard deviation equal to the square root of each datum was added. Fig. 4(b) shows this simulated data set when the peak datum was  $10^8$  (counts)—essentially noiseless. For this case, both MaxEnt and the direct inverse ( $O^{-1} \cdot d$ ) gave reconstructions indistinguishable from the truth (Fig. 4a). Figures 5 and 6 show the corresponding results when the data were made more noisy (lower counts). The quality of the reconstructions deteriorates for both methods. Since the direct inverse does not take into account the fact that the data are noisy (Section 1), it produces numerous artifacts and deteriorates much more rapidly than MaxEnt.



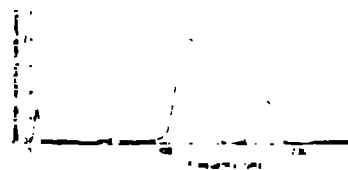
before after  
Maximum entropy deconvolution  
(UK Home Office)



SNR Cas A at 5 GHz - 1024<sup>2</sup> ME image  
(5-km telescope MRAO, Cambridge)



ME X-ray tomography  
(skull in perspex, FMI Ltd)



mm-wave Michelson interfero-  
meter spectrum of cyclotron  
emission from DITE tokamak  
(Culham Laboratory)

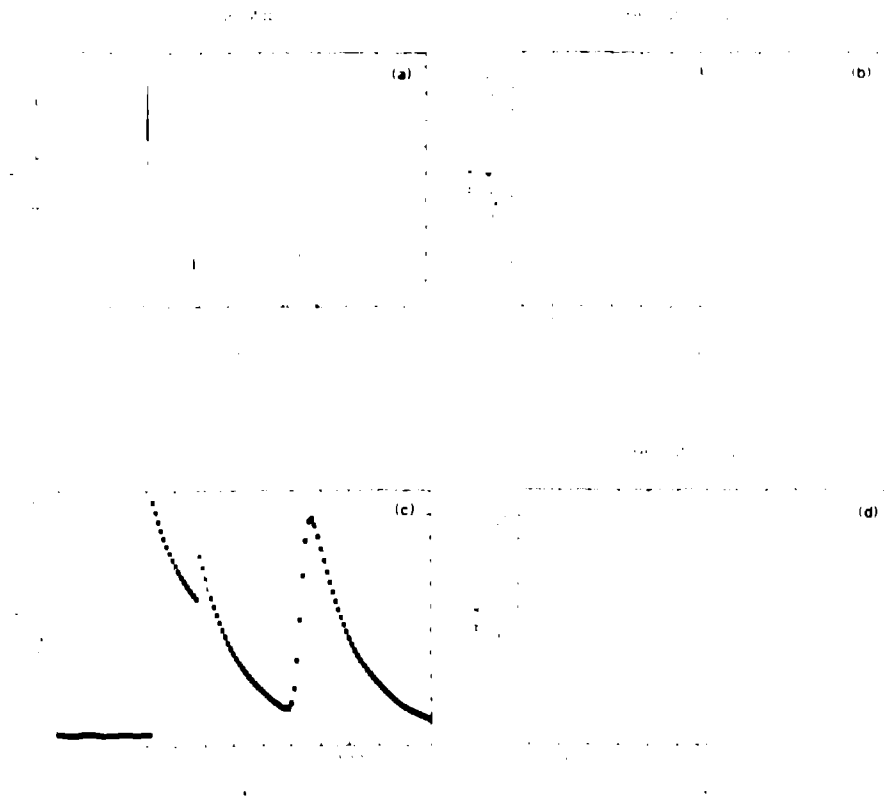
"Blind" deconvolution of  
unknown blurring.

(left) true image & blurring

(middle) data as given to  
ME program

(right) reconstructions  
(T.J. Newton)

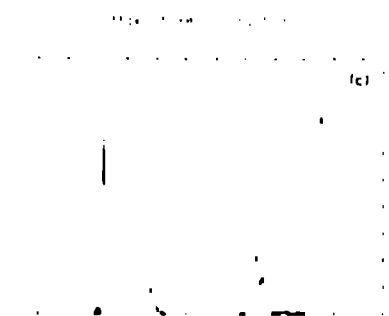
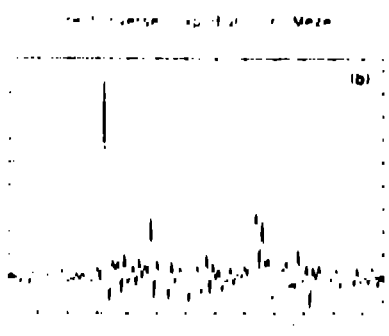
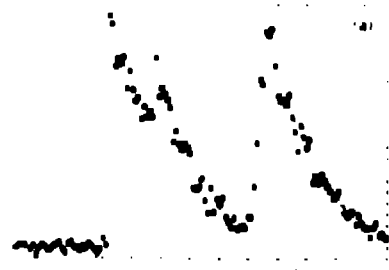
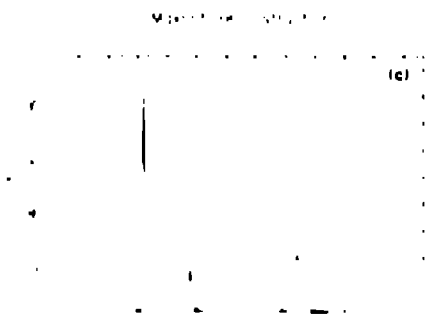
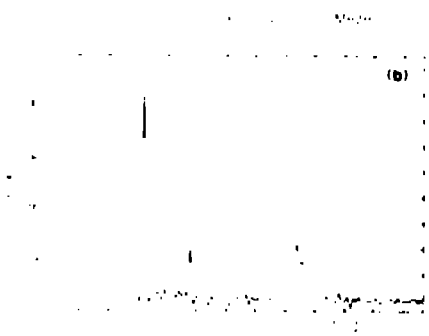
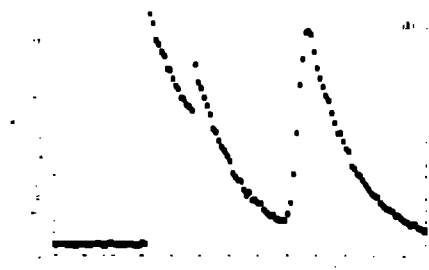
Fig. 2 General examples of MaxEnt image reconstruction. Reproduced by courtesy of Drs. Gull and Skilling.



**Fig. 4** (a) Spectrum of idealised scattering law, used in the FDS simulations. (b) A first approximation to the FDS resolution function: a sharp-edged exponential. (c) simulated data set with very good statistics. (d) A better approximation to the FDS resolution function: sharp-edged exponential convolved with a narrow Gaussian.



**Fig. 3** A graphic illustration of the phase problem: (a) and (b) are the original images. (c) is the (Fourier) reconstruction which has the Fourier phases of (a) and Fourier amplitudes of (b); (d) is the reconstruction with the phases of (b) and the amplitudes of (a).

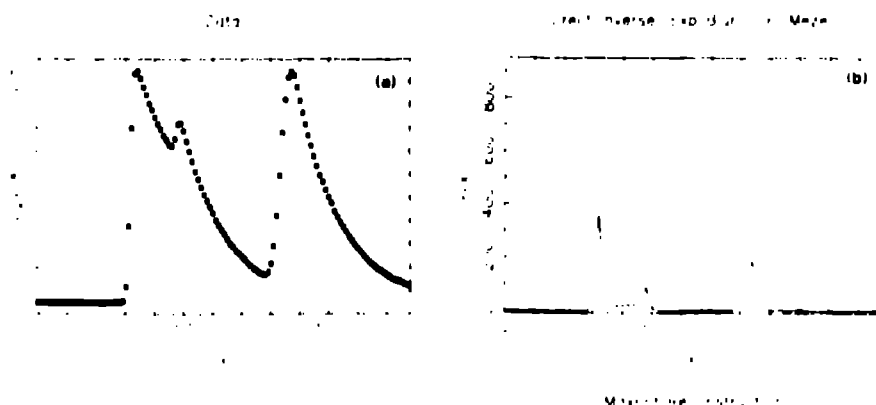


**Fig. 5** (a) Simulated FDS data with some noise. (b) Direct inverse. (c) MaxEnt reconstruction.

**Fig. 6** (a) Simulated FDS data with a lot of noise. (b) Direct inverse. (c) MaxEnt reconstruction.

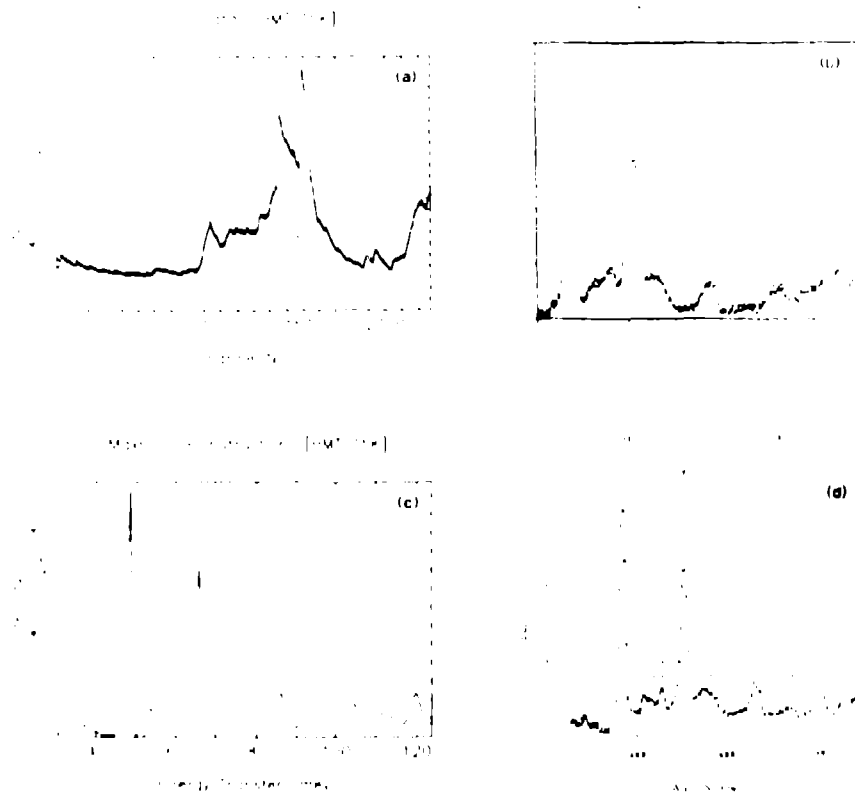


Rather than use the sharp-edged exponential above (Fig. 4b), we obtain a better approximation to the FDS resolution function if we convolve it with a narrow Gaussian (standard deviation of one pixel). The resulting simulated data, with good statistics, is shown in Fig. 7(a). Although we can deconvolve this new resolution function with the direct method in principle, we will only deconvolve the exponential component as is done in practice (Mezei & Vorderwisch 1989). This is because the inverse is easy to calculate if there is a sharp edge (by direct substitution), but more so because the inverse becomes badly conditioned (very sensitive to noise in the data) when the Gaussian component is included. With MaxEnt, however, we can safely deconvolve the "smoothed" resolution function. The inverse and MaxEnt reconstructions are shown in Figs. 7(b) & (c), respectively. The MaxEnt reconstruction shows much improved resolution and some noise suppression over the direct inverse.



**Fig. 7** (a) Simulated FDS data, with good statistics, using the exponential convolved with a narrow Gaussian resolution function (Fig. 4d). (b) Direct inverse deconvolution of the exponential component, or "Mezei method" reconstruction. (c) MaxEnt reconstruction, showing that the Gaussian component can be safely deconvolved to give improved image resolution.

Finally, we show the result of using MaxEnt on a real FDS data set. The data and resolution function were provided by Vorderwisch, experimental and analysis details being given in forthcoming papers (Vorderwisch 1989, and Sivia *et al.*, 1989). Fig. 8(a) shows the Be data for hexamethylene-tetramine (HMT) at 15 K taken at the Los Alamos Neutron Scattering Center (LANSCE). Fig. 8(b) shows the conventional *Filter Difference* spectrum: a crude hardware deconvolution obtained by subtracting the data obtained with Be and BeO filters. Fig. 8(c) shows the MaxEnt reconstruction, and Fig. 8(d) shows this overlaid on the direct inverse reconstruction



**Fig. 8** (a) FDS data for Hexamethylene-Tetramine, at 15 K, taken with the Be filter at LANSCE. The channels are in increasing time-of-flight, or decreasing energy transfer. (b) The Filter Difference spectrum, or a crude hardware deconvolution obtained by subtracting data obtained with Be and BeO filters. (c) The MaxEnt reconstruction. (d) The direct inverse, or "Mezei method", reconstruction (dots) overlaid on the MaxEnt reconstruction.

mentioned above. As expected, we find that MaxEnt has improved the resolution and reduced the noise. The improvement is obvious, but not dramatic, in this particular example, because we had good statistics and the intrinsic Gaussian-like contribution to the resolution function is very narrow with little effect.

### 7. Concluding remarks

We have shown that MaxEnt provides an optimal criterion for selecting a positive image when faced with incomplete and noisy data. The MaxEnt choice can be interpreted as the maximally non-committal solution that is consistent with the data. As such, it tends to be less noisy and has fewer artifacts than conventional methods, thus making it easier to interpret the results.

We mention in passing that a unified approach to all data analysis (MaxEnt, model-fitting, or whatever) can be achieved by casting all such problems in the probabilistic framework of a Bayesian analysis. This not only gives us the way to select the optimal answer to any given problem, but it also tells us how to estimate the reliability of that solution; unfortunately, however, the error analysis is usually impossible to implement in practice except for the smallest of problems. The difficulty does not arise because we are using MaxEnt, but because we are trying to estimate a large number of parameters.

### Acknowledgements

The approach to MaxEnt provided here is due almost entirely to Steve Gull and John Skilling, who brought me up on a good dose of MaxEnt and Bayes' theorem. Many thanks to Richard Silver and Roger Pynn for their support and encouragement in applying MaxEnt to neutron scattering problems in general, and to Peter Vorderwisch for working with me on the FDS example.

### References

- Gull, S. F. & Daniell, G. J., 1978, *Nature*, **272**, 686-690.  
Gull, S. F. & Skilling, J., 1984, *IEE Proc.*, **131E**, 646-659.  
Jaynes, E. T., 1983, (Collected Works) *Papers on Probability, Statistics and Statistical Physics*, ed. by R.D. Rosenkrantz, Dordrecht Holland, Reidel.  
Mezei, F. & Vorderwisch, P., *Physica B*, in press.  
Shannon, C. E., 1948, *Bell System Tech. J.*, **27**, 379-423 and 623-656.  
Shore, J. E. & Johnson, R. W., 1980, *IEEE Trans., information Theory*, Vol. 1, **IT-26**, No. 1, 26-37.  
Sivia, D. S., 1987, *Phase Extension Methods*, Ph.D. Thesis, Cambridge University.  
Sivia, D. S., Vorderwisch, P., Silver, R. N., 1989, "Maximum Entropy Deconvolution of the Filter Difference Spectrometer," in preparation.  
Skilling, J., 1988, "The Axioms of Maximum Entropy," in *Maximum Entropy & Bayesian Methods in Science and Engineering* (Vol. 1), ed. by G. Erickson and C. R. Smith.  
Skilling, J. and Bryan, R.K., 1984, *Mon. Not. R. Astr. Soc.*, **211**, 114-124.  
Taylor, A. D., Wood, E. J., Goldstone, J. A., and Eckert, J., 1984, *Nucl. Instr. and Meth.*, **221**, 408-418.  
Vorderwisch, P., 1989, "The Resolution Function of the Filter Difference Spectrometer," in preparation.

## New Instruments at IPNS: POSY II and SAD II

*R. K. Crawford, G. P. Felcher, R. Kleb, J. E. Epperson, and P. Thiyagarajan*  
Argonne National Laboratory  
Argonne, Illinois  
USA

### Introduction

Three new instruments are currently in varying degrees of development/construction at IPNS. One of these, the Glass, Liquid, and Amorphous Materials Diffractometer (GLAD) is the subject of a separate paper<sup>(1)</sup> in these proceedings and so will not be discussed further here. The other two, a second neutron reflectometer (POSY II) and a second small-angle diffractometer (SAD II), are described briefly below.

### POSY II

The polarized neutron reflectometer (POSY) has been operating at IPNS since 1984<sup>(2)</sup>. Recently, it was shown that by utilizing the large difference in scattering from H and D to measure chemical profiles rather than the magnetic profiles for which POSY was designed, such a neutron reflectometer could measure chemical density profiles with resolution unmatched by other techniques<sup>(3)</sup>. Users in the polymer science community indicated a real need for such an instrument—they could provide enough problems to saturate the time available at POSY. Typical problems include interdiffusion of two similar polymers; concentration gradients for polymers in solutions both at the surface and at solid boundaries; and the mixing of chemically different polymers, or polymeric chains with a head and a tail, such as block copolymers—all over a length scale (  $\mu\text{m}$  ) not easily probed by other techniques.

To help satisfy such a greatly expanded user community and because POSY had been conceived and optimized for magnetic studies and, consequently, is not best suited for polymer work, it was decided to split the neutron beam at beam line C2, which serviced only POSY, for use by both POSY and a new instrument (POSY II) that is dedicated totally to polymer research. Figure 1 shows the arrangement of the two instruments on the two beams brought out through the single bulk-shielding penetration. (Beam penetrations in the IPNS bulk shielding are 30 to 35 cm wide, allowing these two narrow beams to achieve an angular separation of  $3.7^\circ$  within the same penetration.) This construction effort, with half of its cost being financed by IBM, is well along, and POSY II and the rebuilt POSY are scheduled for commissioning in Fall 1988. Table I gives some parameters of the two instruments.

In the new arrangement the original POSY will be restructured, implementing modifications previously tested. The sample will not view the direct beam because this will be doubly reflected by a pair of polarizing supermirrors. These mirrors are made of layers of cobalt and titanium of progressive thickness on an anti-reflecting backing of gadolinium and were prepared by Dr. O. Schärpf at Grenoble on accurately polished borosilicate glass. The pair of mirrors are part of a newly

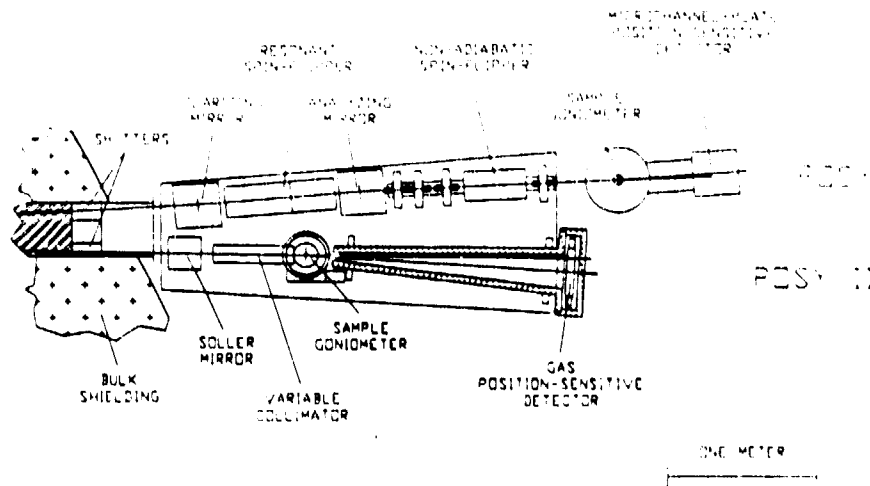


Fig. 1 The reflectometer complex at the IPNS beam line C2. The heavy-duty sample goniometer on POSY can accommodate an electromagnet, a cryostat, or an ultrahigh vacuum chamber, while that on POSY II is a high-precision Huber goniometer to support a temperature-controlled polymer sample cell.

developed "resonant spin flipper" (Fig. 1) to reject neutrons whose wavelengths do not correspond to their nominal time-of-flight, thus sharpening the resolution and improving the background. This device consists of a supermirror spin polarizer, a Drabkin flipper resonantly scanned to flip spins only of the correct wavelength for the current flight time, and a supermirror spin analyzer to reject the unflipped spins<sup>(2)</sup>. POSY will still use its original microchannel-plate detector. Appropriately placed collimators (not shown in the figure) in the external portion of the incident beam will allow its tailoring to the size of the sample. Samples of magnetic interest are expected to exhibit surfaces of the order of 1 to 2 cm<sup>2</sup>.

The design of POSY II reflects the requirements for polymer work. The samples used here have surfaces of several tens of cm<sup>2</sup>. The reflectivity will be measured over a wide range of momentum transfers. Because of the increased surface size, slightly relaxed collimation, and absence of polarization analyzers, POSY II should have data rates several times those of POSY.

Table I

	POSY	POSY II
Source-sample distance (cm)	831	623
Sample-detector distance (cm)	60	178
Detector horizontal range (cm)	2.5	20
Detector resolution (mm)	0.5	2
Wave-vector range ( $\text{\AA}^{-1}$ )	0.0 - 0.07	0.0 - 0.25
Wave-vector resolution ( $\text{\AA}^{-1}$ FWHM)	-0.003	-0.003
Beam size at moderator (cm <sup>2</sup> )	2.6 x 10.3	2.6 x 10.3
Beam size at bulk-shield exit (cm <sup>2</sup> )	0.54 x 5.8	0.84 x 6.4

Particular attention has been given to making POSY II easy to operate by external users. Thus, for instance, the counter consists of a linear-position-sensitive detector fixed in a preselected location. This counter has an active area of 5 cm x 20 cm and a one-dimensional position resolution (along the long axis) of 2 mm (Ordela, Inc., Oak Ridge). The detector is of the gas-proportional type, filled with a  $^3\text{He-CF}_4$  mixture, giving an efficiency of 81% at 3 Å.

For this instrument as well, the sample will not be in the direct beam from the source. However, it was desired to eliminate the transmission filter used in the past (beryllium-cooled by liquid nitrogen) to avoid the small-angle scattering from the sintered beryllium and to extend the dynamical range of neutrons to span the maximum neutron flux from the solid moderator ("soller mirrors"). Each of the mirrors will consist of a disk of silicon 10 cm in diameter and 0.4 mm thick. Both faces are covered with 800 Å of  $^{58}\text{Ni}$ . The whole soller mirror consists of 24 such disks, enclosed between flat reference plates, and set at an angle with the incident beam to ensure total reflection for  $\lambda = 3$  Å.

The portions of the POSY and POSY II flight paths within the collimation in the bulk shielding will be evacuated, while most portions of the external flight paths for both instruments will be He-filled. Both instruments will be equipped with heavy-duty sample goniometers capable of supporting a variety of sample mountings and environments.

## SAD II

The Small Angle Diffractometer (SAD) has been operating at IPNS since 1982 and has been in essentially its current configuration since 1984. This instrument has been severely oversubscribed for several years, with proposals exceeding operating time by a factor of two to three. Instrument oversubscription and our experience led us to believe we could now build a significantly improved instrument; therefore, consideration of a second SANS instrument at IPNS was begun in early 1986. Development of the new instrument (currently designated as SAD II) is under way, and the assessment of the final parameters should be completed in 1989. Many of the features of the new instrument will be, at least initially, similar to those of SAD. However, the new instrument is intended to have a much better detector system and more varied collimation options, leading to greater Q range, and is also intended to have a more convenient sample environment than does the present SAD.

In particular, the instrument will occupy the C3 beam line, where it will view the same solid  $\text{CH}_4$  (or liquid  $\text{H}_2$ ) moderator viewed by SAD. The moderator-to-sample distance will be 7.5 m, as in SAD; this is roughly the minimum distance that allows room for filters, shielding, interchangeable collimation, etc. The instrument will be, at least initially, a filtered-direct-beam instrument in which the moderator, sample, and detector are in a direct line. A filter (MgO as in SAD, or oriented single-crystal sapphire, probably at 77 K) in the incident beam line will reduce the fast neutron flux by roughly two orders of magnitude, while having a transmission of greater than 50% for the neutrons of interest ( $\sim 1.4$  Å). A second filter of oriented single-crystal bismuth will be used to attenuate the gamma rays from the source, if necessary. An alternate option, a "beam-bender" that would "bend" the trajectories of the long-wavelength neutrons (greater than  $\sim 1.5$  Å) away from the main beam of fast

neutrons and gamma rays, was considered but does not appear to permit transmission to wavelengths as short as those allowed by the filters. The apertures that define the beam from the moderator to the face of the bulk-shielding monolith for the initial filtered-direct-beam instrument have now been installed, and the necessary modifications have been made in the beam gate to accommodate the filter(s).

A two-dimensional position-sensitive gas-proportional counter detector of nominally 40 cm x 40 cm active area with 4 mm x 4 mm resolution (Ordela, Inc., Oak Ridge) was purchased for this instrument and was received in spring, 1988. This detector is filled with  $^3\text{He}$  and  $\text{CF}_4$  to provide the desired position resolution and neutron efficiency (61% at 2 Å) while having a low gamma sensitivity. (For comparison, the SAD detector has an active area of 17 cm x 17 cm and a resolution of ~4 mm x 4 mm). The position and time-encoding electronics for this detector, as well as the rest of the data acquisition system for this instrument, are similar to those on SAD and have already been acquired. Data acquisition will initially utilize a PDP-11/24 computer, which will be replaced with a microVax when the instrument development is further along.

The remainder of the development of the new instrument is expected to proceed in stages. Temporary beam-transport, collimation, and sample-environment components have been fabricated and will be installed in fall, 1988. These will permit detailed testing of the new detector and will also serve as a testbed for the development of other instrument components. Of primary importance in this regard are shielding to reduce the background to satisfactory levels, the filters discussed above, and the angular collimation system for the incident beam. Design and construction of the final instrument will depend in part on the outcome of the development and testing efforts with this temporary version.

To achieve the necessary angular collimation in the incident beam while utilizing the full source size (~1 cm diameter) requires the use of converging multiple-aperture collimation. If the collimation channels are all focused to the same point on the detector, then a large sample size will not affect  $Q_{\text{min}}$  or the Q-resolution<sup>(4)</sup>, even if the sample-to-detector distance is short. In SAD such focusing multiple-aperture collimation is done with crossed-converging soller collimators, which define ~400 converging beam channels with essentially no "dead" space between them. This entire collimator system occupies only a distance of ~60 cm along the incident flight path, while providing angular collimation of 0.003 radians FWHM. This system has worked quite well, producing resolutions in good agreement with the calculated values, and the collimators presently in use have produced a cleanly collimated beam. These collimators, and improvements needed in such soller collimator systems, are discussed elsewhere in these proceedings<sup>(5)</sup>. One of the uses of the initial temporary flight path will be to test (and develop, if necessary) satisfactory collimators to provide even tighter resolution than this.

The practical  $Q_{\text{min}}$  with the present set of collimators is ~0.005 Å<sup>-1</sup>. With the detector spatial resolution noted above,  $Q_{\text{min}}$  and Q-resolution down to ~0.002 Å<sup>-1</sup> can be achieved with the 1.5 m sample-to-detector distance simply by installing different incident beam collimators with the desired angular divergence in each channel. If satisfactory collimators can be produced, several such collimators will be

provided in a "cassette" arrangement to permit easy changes in resolution and  $Q_{\min}$ . A further decrease in  $Q_{\min}$  and resolution will require moving the detector further from the sample, with a Q-resolution of  $\sim 0.001 \text{ \AA}^{-1}$  achievable with this detector resolution and at a sample-to-detector distance of 3 to 3.5 m, if the incident beam collimation can be made to match. (With the moderator and path lengths being considered, the source pulse width is too short to contribute appreciably to the resolution for the cases considered here.) The count rate will fall at least as fast as the square of the resolution, so it will not be desirable to try to push the resolution this far for most cases. Since the multiple-aperture collimation must focus on the detector, a different collimator is needed for each sample-to-detector distance; therefore, there is no point in having a continuously variable sample-to-detector distance in this instrument.

With a filter in the beam, the minimum usable wavelength will be  $\sim 1 \text{ \AA}$ . With the detector at 1.5 m from the sample and centered on the beam, this will yield usable intensity at a  $Q_{\max}$  of  $\sim 0.6 \text{ \AA}^{-1}$ . When the detector is operated with the beam near the edge of its active area, this could be increased to  $Q_{\max} \sim 1 \text{ \AA}^{-1}$ , at some cost in intensity at the smaller Q values. However, in some cases it is desirable to have  $Q_{\max}$  even larger than this, and in most cases it is desirable to be able to include measurements over a wide range of wavelengths in the high-Q data, so the ability to cover even higher scattering angles will be incorporated into the instrument. This will be done either by providing a means of rotating the detector about the sample position or by supplementing the main two-dimensional detector by an array of linear position-sensitive detectors (LPSDs) at higher angles, using the technology for position- and time-encoding of such detectors, which has already been developed for GLAD. Roughly 40 LPSDs at 1.5 m from the sample would extend continuous angular coverage out to a scattering angle of  $30^\circ$  and a  $Q_{\max} \sim 1.6 \text{ \AA}^{-1}$ .

Even without the new enriched-uranium target just installed at IPNS in 1988, the new instrument would have a much higher data rate at high Q than does the present SAD (up to a factor of 10 increase at the highest Q presently obtained on the SAD), and a  $Q_{\max}$  more than four times that of the present SAD. Under the same conditions, at low Q the new instrument would have a data rate comparable to that of the present SAD at the same resolution. By tightening the collimation or by changing both the collimation and detector position,  $Q_{\min}$  down to 0.001 to 0.002  $\text{\AA}^{-1}$  should be achievable, with a corresponding data rate reduction. However, the factor of three increase in source intensity expected from the enriched-uranium target should mean that the time required for such higher-resolution measurements will not be unreasonable in many cases.




#### Acknowledgements

Work supported by U.S. Department of Energy, BES, Contract No. W-31-109-ENG-38.

#### References

1. R. K. Crawford, D. L. Price, J. R. Haumann, R. Kleb, D. G. Montague, J. M. Carpenter, S. Susman, and R. J. Dejus, in these proceedings.



- 
- 
- 
2. G. P. Felcher, R. O. Hilleke, R. K. Crawford, J. Haumann, R. Kleb, and G. Ostrowski, 1987, *Rev. Sci. Instrum.* 58, 609-619.
  3. T. P. Russell, A. Karim, A. Mansour, and G. P. Felcher, 1988, *Macromolecules* 21, 1890.
  4. A. C. Nunes, 1974, *Nucl. Instrum Methods* 119, 291-293.
  5. R. K. Crawford, J. E. Epperson, and P. Thiyagarajan, in these proceedings.



## The ASPUN project

*R. L. Kustom*  
Argonne National Laboratory  
Argonne, Illinois  
USA

### Introduction

A study of a pulsed spallation neutron source<sup>(1)</sup> that could deliver fluxes in excess of  $1 \times 10^{17}$  N/cm<sup>2</sup>-s began at Argonne in 1981. A review of various accelerator concepts to act as an intense charged-particle source to generate spallation neutrons resulted in the selection of a Fixed-Field Alternating-Gradient<sup>(2)</sup> (FFAG) accelerator as the preferred device.

There are several features of an FFAG accelerator that make it well suited to be the charged-particle accelerator for a  $10^{17}$  N/cm<sup>2</sup>-s pulsed source. Since the main magnets are dc operated, injection time can be long enough to provide for efficient injection and adiabatic capture, the rf system can be optimized for maximum use of the accelerating voltage, the repetition rate can reach hundreds of hertz because there are no  $\frac{dB}{dt}$  effects in the magnets or vacuum chamber, and large transverse and momentum acceptances are possible. The large momentum acceptance and rapid acceleration helps avoid some of the instability problems.

The conceptual design has evolved from a spiral-type FFAG with strong edge focussing<sup>(3)</sup> to a radial-type FFAG<sup>(4)</sup>. The radial-type FFAG allows easier installation of the rf cavities at the expense of higher magnetic fields. Since the magnets are dc operated, the higher field can be achieved with superconducting coils.

Repetition rates of 200 to 300 Hz are possible and reasonable with an FFAG accelerator; however, the scientific users would prefer a repetition rate less than 100 Hz. The earliest FFAG designs considered internal stacking in energy space of several injected pulses at an energy near the extraction energy and then final acceleration of the stacked pulses to full energy and extraction as a single pulse. This technique was successfully demonstrated on the early MURA-FFAG accelerators<sup>(2)</sup>. However, some problems are encountered when applying this technique to a spallation source driver in which the goal for efficiency of extracted beam to inject beam is 99.9% or better. In order to stack at an intermediate energy, the energy spread of the injected beam is limited to be able to stack several bunches into the acceptance of the rf bucket. This potentially could reduce the threshold for the microwave instability at injection to where beam losses could occur. Also, the stacking technique requires adiabatically debunching, merging, and rebunching, with virtually no losses, several injected bunches that are accelerated to the stacking energy before final acceleration and extraction of the single stacked bunch. A technically

less demanding concept using one or two external pulse accumulation rings is presently proposed.

### Fixed-field alternating-gradient accelerator design

The guide field in an FFAG accelerator as a function of radius is given by

$$B = B_0(R/R_0)^k,$$

where  $R$  is the average radius given by the integrated path length of the accelerated particle divided by  $2\pi$ , and  $B_0$  is the magnetic field at a reference radius  $R_0$ . Each lattice cell consists of horizontally focussing and defocussing magnets, the latter being of weaker field. Meads and Wüstefeld suggest a DFD combination<sup>(4)</sup> in which the horizontally positive and negative bending fields occupy equal lengths along the circumference, but the field of negative bending section is half the field in the positive bending section and divided in two equal lengths before and after the positive bending section. The magnetic field profile along the particle path is shown in Fig. 1.

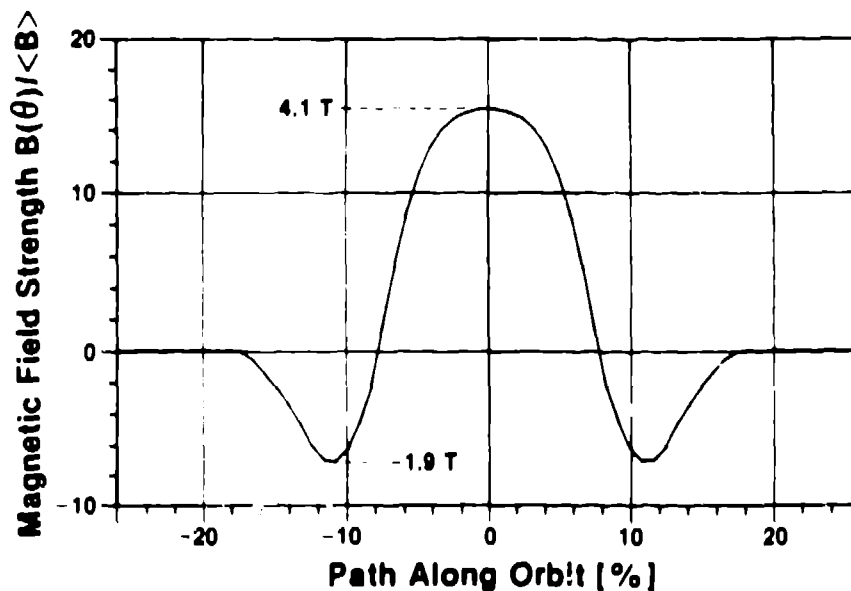


Fig. 1 Azimuthal profile of magnetic field along the path of one cell.

Figure 2 shows the plan view of a 1500-MeV radial-FFAG accelerator presented by Meads and Wüstefeld at the 1985 Particle Accelerator Conference<sup>(4)</sup>. There are 20 identical bending magnet sectors that occupy about 35% of the circumference of the ring. The value of the field index,  $k$ , is 13.4. The parameters for an FFAG accelerator for ASPUN are given in Table 1. The transverse  $\beta$ -functions for a half-sector are shown in Fig. 3. Deviations of the actual radial position from the mean orbit described by a circle with radius,  $R$ , are shown in Fig. 4 as a function of position along the orbit.

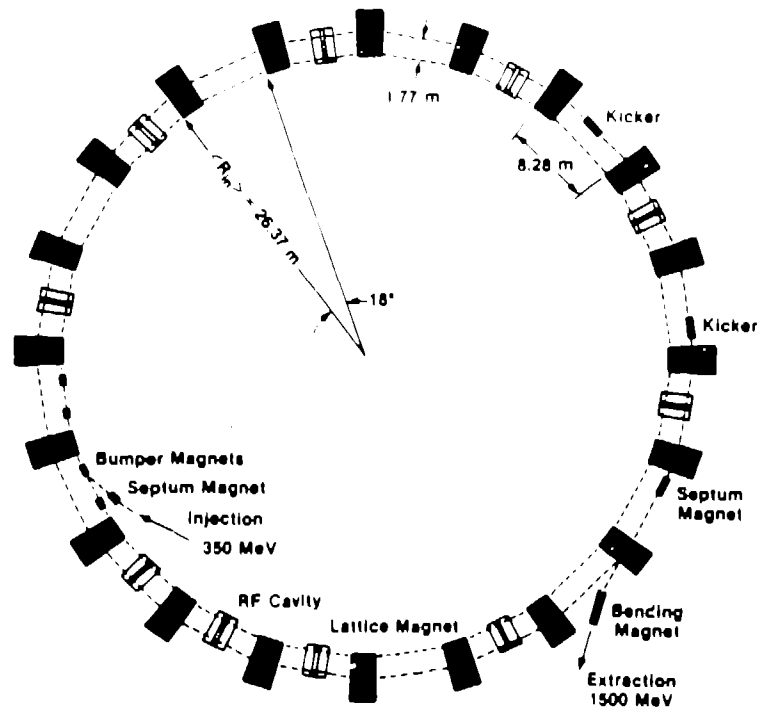


Fig. 2 Layout of radial-sector FFAG for ASPUN.

Table 1. Parameters for the FFAG accelerator

Extraction Energy, MeV	1500
Extraction Radius, $\int ds/2\pi$ , m	28.14 m
Injection Energy, MeV	350
Injection Radius, $\int ds/2\pi$ , m	26.37
Field Index, k	13.4
Peak Positive Bending Field @ Extraction, T	4.1
Peak Negative Bending Field @ Extraction, T	1.9
Peak Positive Bending Field @ Injection, T	1.717
Peak Negative Bending Field @ Injection, T	0.796
Horizontal Tune	4.25
Vertical Tune	3.25
Horizontal Emittance, mmmr	$650 \pi$
Vertical Emittance, mmmr	$500 \pi$
Repetition Rate, Hz	250
Maximum RF Voltage, kV	400
Maximum RF Frequency (Extraction), MHz	1.565
Maximum RF Frequency (Injection), MHz	1.241

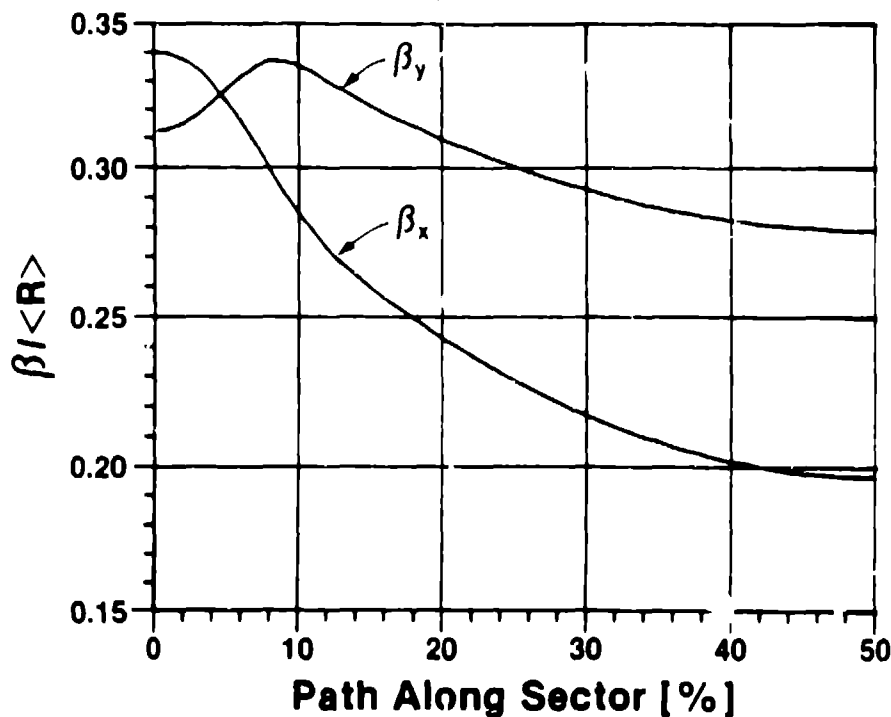


Fig. 3 Horizontal and vertical beta functions normalized to the average radius.

Since the magnetic fields of an FFAG accelerator are highly nonlinear, it is necessary to ensure that the beam emittances are well within the stability limits defined by the nonlinear terms. A computer program written by Meads<sup>[9]</sup> was used to calculate the limits in the vertical and horizontal planes. The 500- $\pi$ mmmr vertical emittance and 650- $\pi$ mmmr horizontal emittance are shown in relation to the calculated stability limits in Figs. 5 and 6, respectively.

$H^-$  beam is injected from a linac on the inside radius of the accelerator. Four bumper magnets are used to locally deflect the closed orbit onto a stripper foil for stripping the  $H^-$  to  $H^+$ . The fields of the bumper magnets are reduced during injection so the beam is more uniformly distributed over phase space. Approximately 38.5 mA of  $H^-$  beam is injected over a 500- $\mu$ s period in order to reach  $1.2 \times 10^{14}$  protons.

The proposed injection energy is 350 MeV. The incoherent space charge limit for number of injected particles,  $N$ , is given by

$$N = \frac{\pi(e_s + \sqrt{(v_x e_x e_x) v_x}) B^2 \gamma^3 \Delta v_x B_l}{r_p F}$$

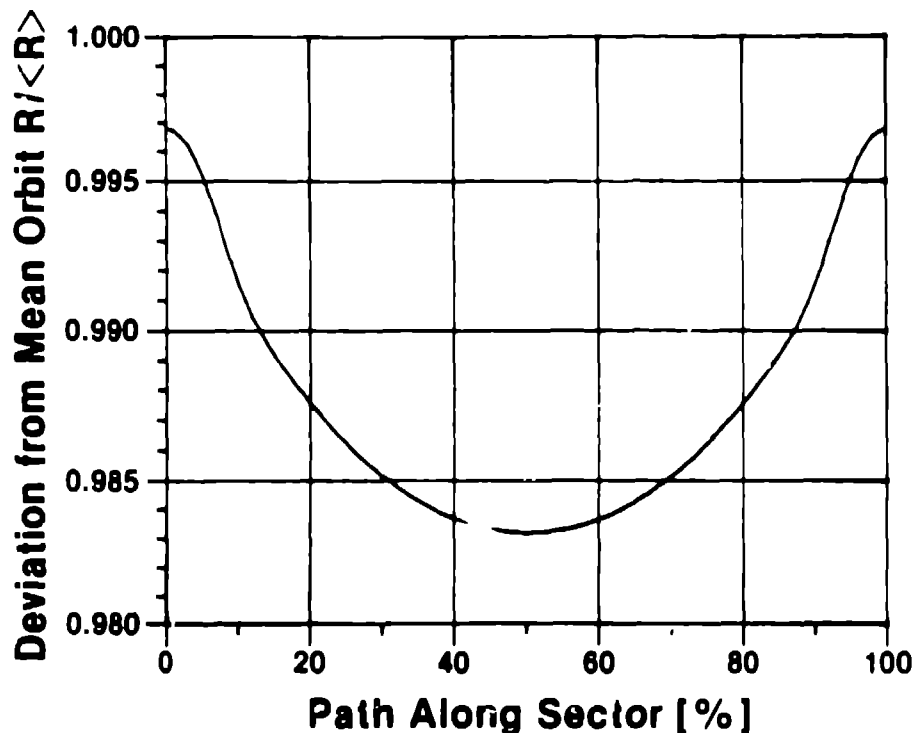


Fig. 4 Deviation of orbit from a circle of average radius,  $R$ , over a single cell length.

where  $\epsilon_x$  and  $\epsilon_y$  are the horizontal and vertical emittances,  $\beta$  is the relativistic velocity of the injected particle,  $\gamma$  is the relativistic mass of the injected particle  $\Delta\nu_z$  is the allowable tune shift,  $B_f$  is the circumferential bunching factor,  $r_p$  is  $1.54 \times 10^{-18}$  m, and  $l^2$  is the transverse bunching factor.

It is planned to program the rf during capture and initial acceleration to keep  $B_f$  at 0.375 or larger. It is assumed that the horizontal beam distribution can be made reasonably uniform and that the distribution in vertical space will be nearly quadratic. These conditions lead to a value of  $F$  equal to 1.35. If the allowable tune shift is 0.25, the space charge limit should be about  $1.72 \times 10^{14}$  protons per pulse. The proposed operating level is about 70% of the calculated space-charge limit.

Acceleration to full energy of 1500 MeV is accomplished in about 2.5 ms, requiring an average accelerating voltage of about 260 kV. The design is for a maximum voltage of 400 kV to operate at a stable phase angle of  $40^\circ$ . The first 250  $\mu$ s after injection are used for adiabatic capture of the beam during which time the rf voltage increases to about 150 kV. Operation at full voltage does not start immediately after the capture period to avoid bunching the beam too rapidly. The rf voltage increases from 150 kV to the full 400 kV in about 700  $\mu$ s. The whole cycle from start of injection to extraction takes 4 ms. During the 500- $\mu$ s injection period, the cavity is retuned to the injection frequency, 1.241 MHz.

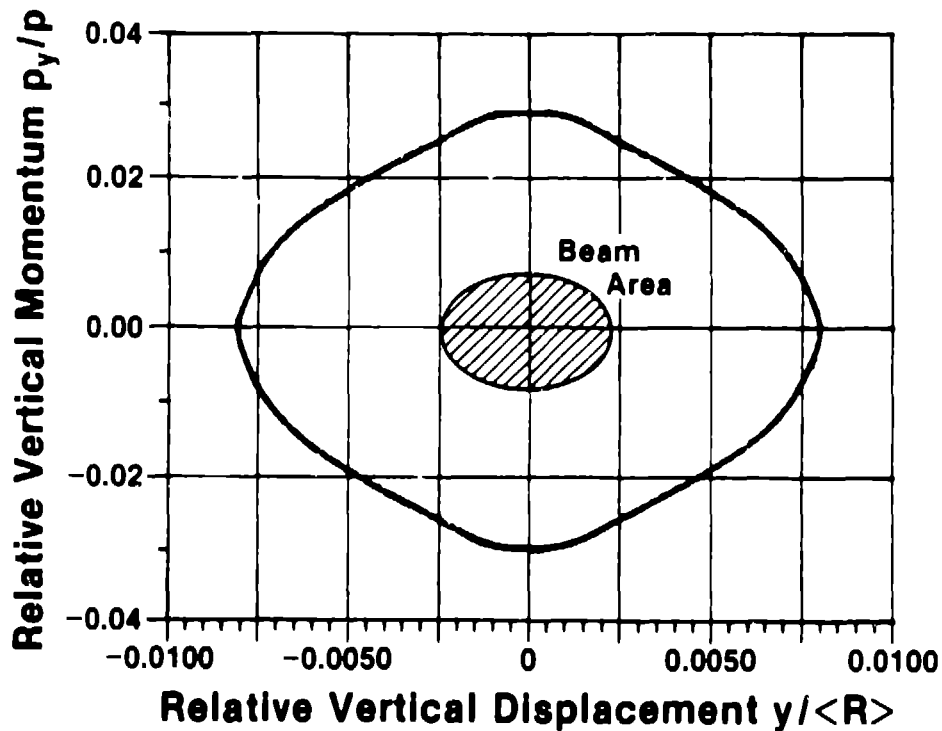


Fig. 5 Limit of beam stability in the vertical plane due to magnet nonlinearities with the  $500\text{-}\pi\text{mmmr}$  emittance shown in shaded area.

The average accelerating voltage per length of straight section is  $10\text{ kV/m}$  for ferrite-loaded cavities. Ten straight sections are used for 20 rf cavities developing  $20\text{ kV}$  each. The beam loading is fairly large with roughly 20% to 30% of the total stored energy delivered in each passage of the beam. However, a number of techniques have been suggested for handling beam loading at this level<sup>(6-8)</sup>.

Extraction of the beam is performed in one turn using ferrite kicker magnets located on the outside radius of the accelerator. The extracted beam pulse should be about 160 to 200-ns long. Allowing for some dilution in transverse space that might occur during acceleration, the design values for emittances in transverse space are  $\epsilon_x = 410\text{ }\pi\text{mmmr}$  and  $\epsilon_y = 315\text{ }\pi\text{mmmr}$  at 1500 MeV.

#### Pulse accumulation to lower repetition rate on target

The repetition rate on the target is reduced and the charge per pulse increased with the use of two external pulse accumulation rings. No design work has been done on these rings; however, a conceptual design for an isochronous compressor ring for proton beams (IKOR) was done for the SNQ project in 1981<sup>(9)</sup> and can be considered as a proof-of-principle to achieve what is necessary for the ASPUN rings.

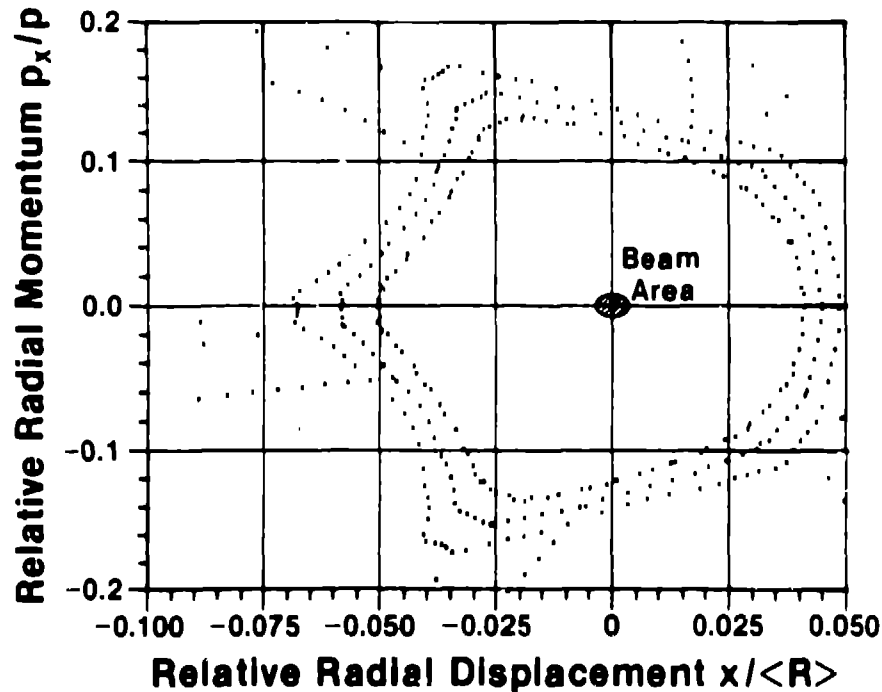


Fig. 6 Limits of beam stability in horizontal plane due to magnet nonlinearities with the  $65\text{-}\mu\text{m}\text{mmr}$  beam emittance shown in shaded area.

The radius of the IKOR ring is 32.2 m. This is compatible with the FFAG for ASPUN, which extends to 28.14 m plus another meter or so for the return yoke. IKOR was designed for  $\text{H}^-$  to  $\text{H}^+$  injection and a smaller emittance, whereas for ASPUN, the injection would be with two consecutive 150 to 200-ns-long pulses. There would be two pulses with about 90-ns spacing in the ring. The fast injection kickers must have a 10% to 90% rise and fall time of about 75 to 80 ns and a 200 ns flattop. The extraction kicker magnet needs a 75-80 nanosecond risetime and 500 to 600 ns flattop. These requirements are within the present technology for ferrite-type kicker magnets.

The IKOR ring was designed to store  $2.7 \times 10^{14}$  protons at 1100 MeV. Similar rings for ASPUN would only need to store  $2.4 \times 10^{14}$  protons at 1100 MeV. The ASPUN rings would have to be isochronous at 1500 MeV and would require larger magnet apertures, but there is no reason this couldn't be done.

Four out of every five ASPUN pulses would be stored in the accumulator rings. The fifth pulse would be directed to the ASPUN target followed sequentially by the pulses stored in the accumulating rings. This would mean a train of five pulses arrive on target over about a 1.5- $\mu\text{s}$  period. This pulse length is acceptable with regard to moderation times for epithermal neutrons.



## Conclusion

While the conceptual design for an accelerating system presented here is, in principle, able to deliver the required charge per pulse, many features still need to be developed. The whole question of controlled losses to  $10^{-3}$  or  $10^{-4}$  per pulse needs to be explored in depth. The goal is to be able to do hands-on maintenance on most of the accelerator components and to greatly limit the number of components that will get activated to a degree that more elaborate handling schemes are needed.

No target design has been undertaken at Argonne. The DIANNE target of SNQ<sup>(10)</sup> was taken as a proof-of-principle, but that development effort has been stopped. A major development effort is needed on the targets and modulators.

No engineering design has been undertaken for the individual accelerator components. There are no components for which the requirement exceeds the limits of the present state-of-art. However, the demands on these components are challenging and require careful design and considerable prototyping to ensure satisfactory performance.

## References

1. J. M. Carpenter and David L. Price, 1975, "An Intense Neutron Source for Argonne National Laboratory," *IEEE Trans. on Nuclear Science* NS-22 No. 3, June.
2. F. T. Cole, et al., 1957, "Electron Model Fixed Field Alternating Gradient Pulsed Neutron Source," *Rev. Sci. Instru.* 28.
3. T. K. Khoe and R. L. Guston, 1983, "ASPUN, Design for an Argonne Super Intense Pulsed Neutron Source," *IEEE Trans. on Nuclear Science* NS-30 No. 4, August.
4. P. F. Meads, Jr. and G. Wüstefeld, 1985, "An FFAG Compressor and Accelerator Ring Studied for the German Spallation Neutron Source," *IEEE Trans. on Nuclear Science* NS-32 No. 5, October.
5. Philip F. Meads, Jr., 1985, "A New FFAG Orbit Code," *IEEE Trans. on Nuclear Science* NS-32 No. 5, October.
6. Thomas W. Hardek and William E. Chyna, 1979, "Common Anode Amplifier Development," *IEEE Trans. on Nuclear Science* NS-26 No. 3 June.
7. A. Luccio and M. Puglisi, 1981, "Behavior of Single-Ended vs. Push-Pull Amplifiers for the Accelerating Systems of High-Current Beam Storage Rings," *Particle Accelerators* 11.
8. F. Pederson, 1985, "A Novel RF Cavity Tuning Feedback Scheme for Heavy Beam Loading," *IEEE Trans. on Nuclear Science* NS-32 No. 5, October.
9. G. Schaffer, ed., 1982, "IKOR, An Isochronous Compressor Ring for Proton Beams," Jul-Spez-114, ISSN 0343-7639, Kernforschungsanlage, Jülich-Kernforschungszentrum, Karlsruhe, June.
10. G. S. Bauer, 1983, "The SNQ Project Status Report as of August 1983," *Proceedings of the Seventh Meeting of the International Collaboration on Advance Neutron Sources, Chalk River Nuclear Laboratories* (Sept. 13-16).

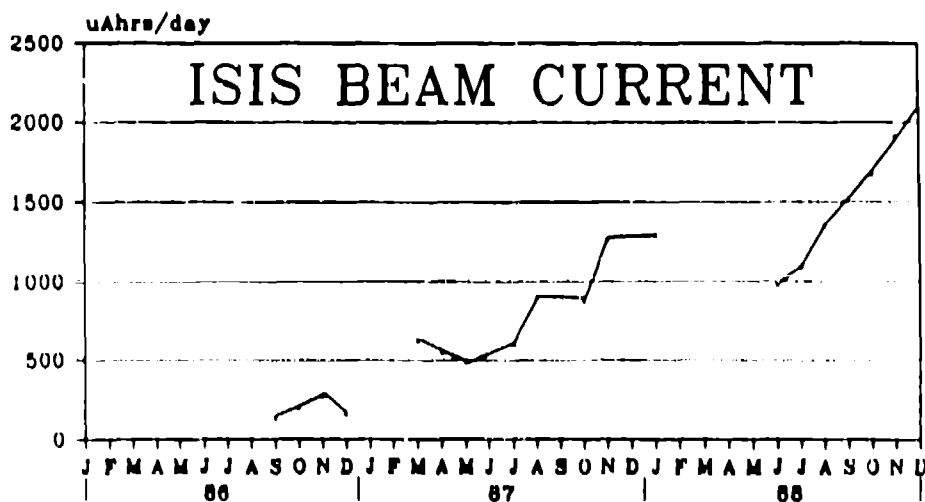
## Developments in inelastic instrumentation at ISIS

*A. D. Taylor, Z. A. Bowden, C. J. Carlile, M. E. Hagen, A. C. Hannon,  
R. S. Holt, J. Mayers, R. Osborn, M. P. Paoli, S. T. Robertson, A. Smith,  
U. Steigenberger, J. Tomkinson, and W. G. Williams*  
Rutherford Appleton Laboratory  
Chilton, Didcot, Oxon OX11 0QX  
UNITED KINGDOM

**ABSTRACT:** We summarise developments on the three scheduled inelastic spectrometers HET, TFXA and IRIS and illustrate their scientific programme with some recent highlights. We give details of commissioning experiments on PRISMA and discuss the status of the eVS and polarisation programmes. The status of the MARI project is reviewed.

### Introduction

ISIS, the world's most powerful pulsed neutron source, is now operating regularly at proton currents of 100  $\mu\text{A}$ . There has been a ten-fold increase in neutron production in the last two years, see Fig. 1. This is reflected in both the quality and quantity of the scientific programme. Of the 14 beamlines in use, see Fig. 2, nine have fully scheduled instruments with over-subscription factors varying from two to four. The inelastic instrument suite comprises three fully scheduled spectrometers (HET, TFXA and IRIS), two instruments at advanced stages of commissioning (PRISMA and eVS) and one (MARI) in the final stages of construction. This paper discusses the current state of these instruments together with the polarisation programme at ISIS.



**Fig. 1** The increase in ISIS beam current over the past three years measured as a  $\mu\text{A}\cdot\text{hr}$  per day.

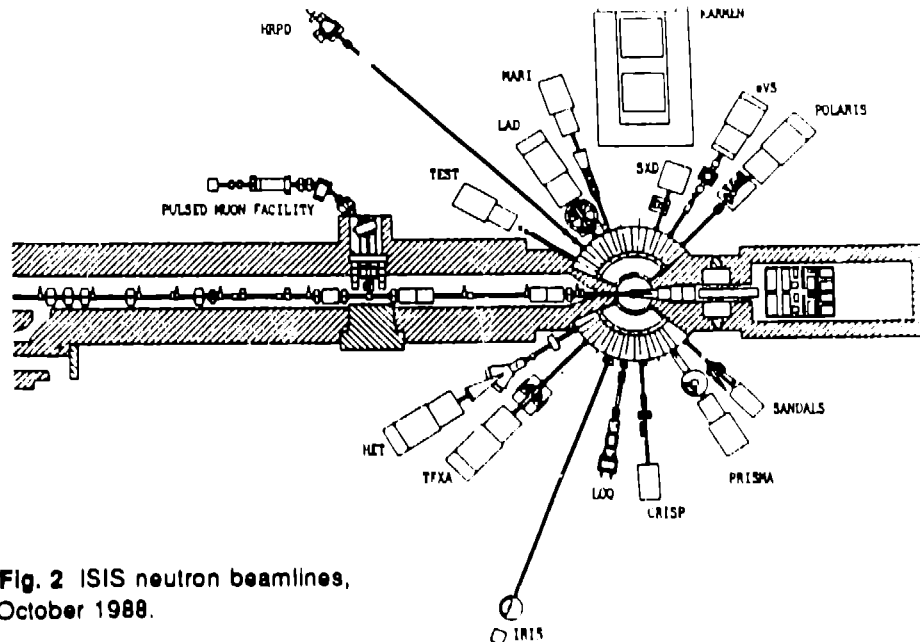


Fig. 2 ISIS neutron beamlines, October 1988.

### HET: High energy inelastic spectrometer

The HET instrument is a direct geometry chopper spectrometer designed specifically to study inelastic scattering at high energy transfer with low associated momentum transfer and good energy transfer resolution<sup>(1)</sup>. There has been a diverse scientific programme on HET with experiments on localised and itinerant magnetism, vibrational density of states, particularly of the new high  $T_C$  superconductors and momentum density measurements in model systems.

The major project on HET this year has been the upgrade of the intermediate angular range detector between  $9^\circ$  and  $29^\circ$ . The new thin window arrangement with its eight-fold azimuthal symmetry is designed to accommodate 256 high pressure  $^3\text{He}$  detectors (Fig. 3). Installation of this array involved a substantial rebuild of the secondary spectrometer during the three month long shutdown of ISIS in Spring 1988. The incident energy range of the spectrometer has been successfully extended with a new chopper slit package designed to operate at energies as low as 35 meV. All the chopper systems have been very reliable. With the substantial increase in flux from ISIS during the year, the major time loss became the pumpdown time after a sample change. This has been halved by the use of a larger turbo pump and a more efficient roughing device. Designs for a top loading cryostat with an air lock to allow "bare" samples to be changed quickly while still minimising scattering from the sample environment device are well advanced.

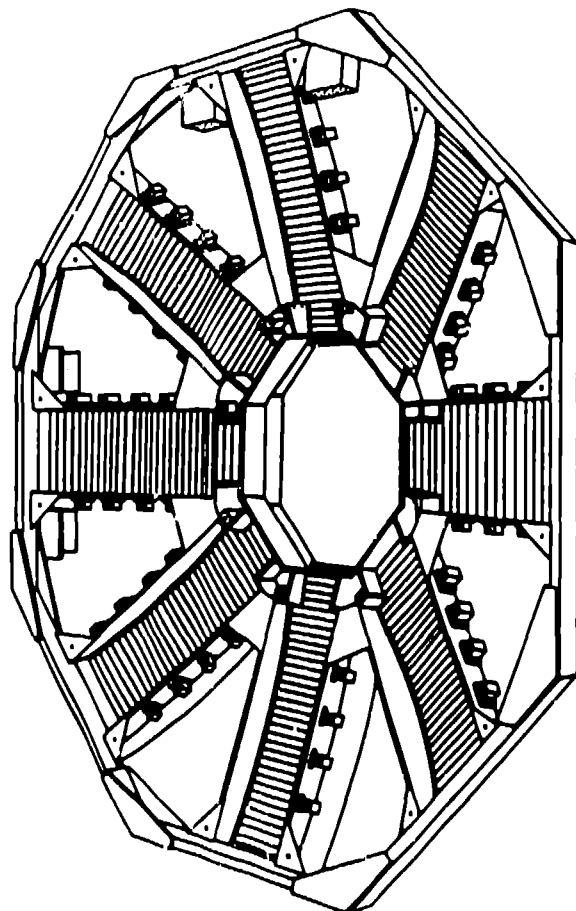


Fig. 3 The eight-fold array of 256  $^3\text{He}$  detectors, which covers the intermediate angular range on HET.

### Highlights of the scientific programme on HET

#### Magnetism

The main thrust of the HET programme was in the field of magnetic scattering. The intermultiplet transition in praseodymium at 260 meV was easily observed in a specially purified sample of the metal. The  $Q$  dependence of this  $^3\text{H}_4 \rightarrow ^1\text{H}_4$  transition confirmed its magnetic origin. Such an observation was only possible because of the excellent low background of the  $^3\text{He}$  gas detectors. The same system gave a new record for high energy inelastic magnetic scattering with energy transfers in excess of 800 meV being observed<sup>[2]</sup>. The neutrons induce excitations from the ground state of the  $4f^2$  ion to excited states with different  $LSJ$  quantum numbers. Several such intermultiplet transitions were found, see Fig. 4, and this more than

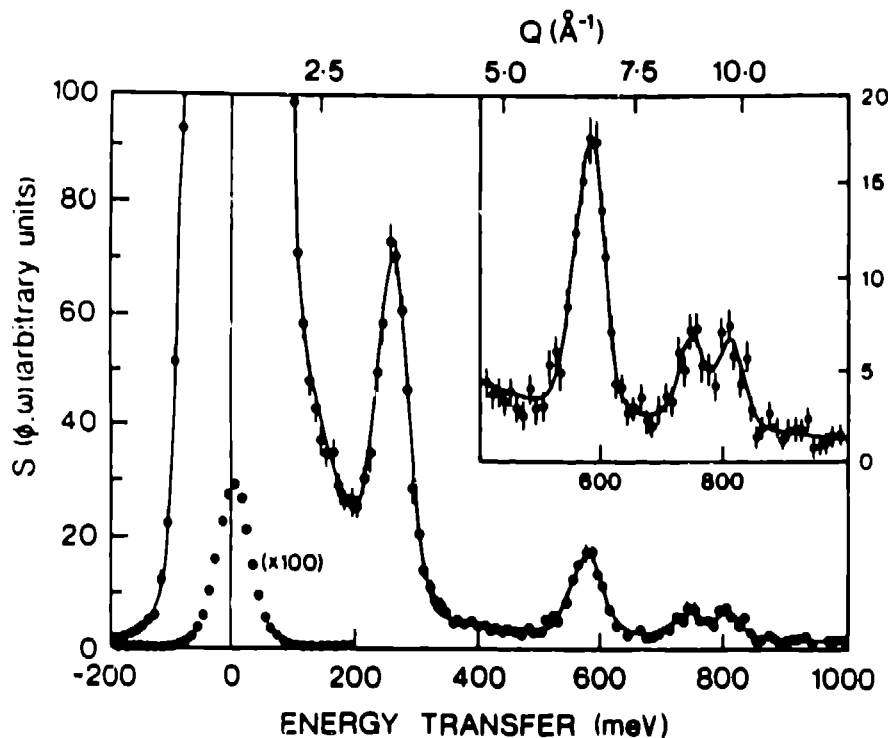
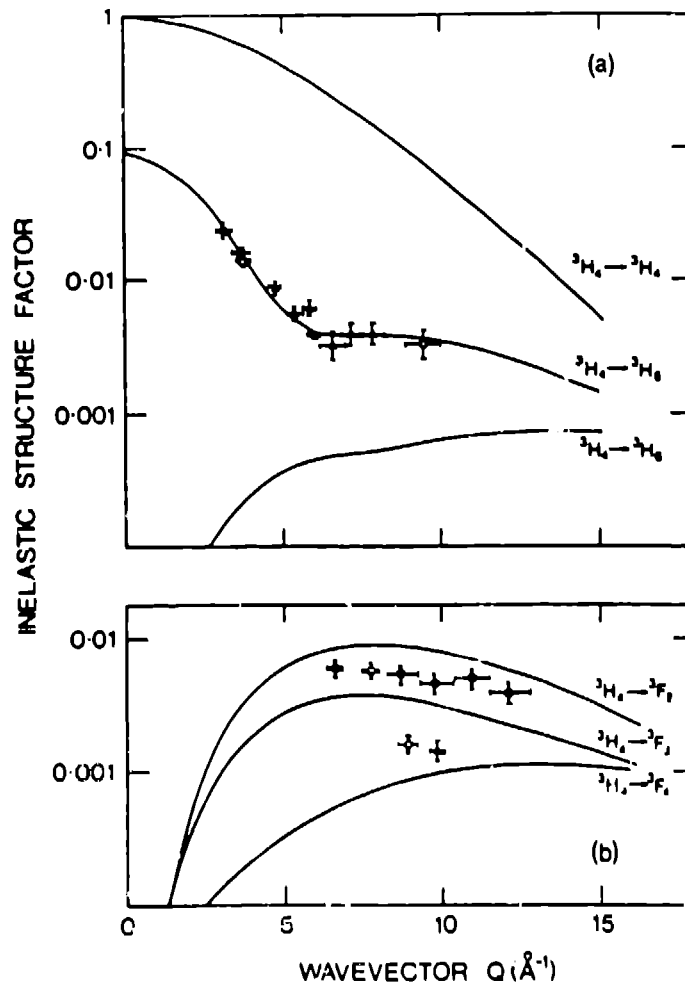


Fig. 4 Neutron scattering cross section of praseodymium at 17 K, measured at an angle of  $5^\circ$  with an incident neutron energy of 1300 meV. The change in the scattering vector across the spectrum is shown along the top axis. The data have been fitted by four Gaussians and a tail of low energy scattering.

doubles the energy range over which magnetic excitations have been observed by inelastic neutron scattering.

The momentum transfer dependence of the intensities was found to be in good agreement with calculated, free-ion inelastic structure factors. These are not simple functions of momentum transfer, see Fig. 5. Dipole and higher order multiple excitations have been identified with the aid of these calculations. Transitions to a different value of orbital angular momentum were found to be shifted significantly from the free ion value. These results will lead to a better understanding of the interactions between localised f-electrons and delocalised conduction electrons in these rare-earth metallic systems. Again such measurements were only possible because of the excellent resolution and signal to noise achievable on a pulsed neutron source.

The high energy spin dynamics of the transition metal ferromagnets is a subject of strong current interest. A team from Cambridge University was able to measure the spin waves in cobalt to only half of their predicted maximum energy using neutrons from the hot source at the Institute Laue-Langevin (ILL). The same team have now successfully completed their measurements using a single crystal of hexagonal cobalt



**Fig. 5** Neutron inelastic structure factors for transitions (a) within the  ${}^3H$  term, (b) from the  ${}^3H$  to the  ${}^3F$  term. The lines represent calculated intensities of the transitions. The structure factors are normalised to the  ${}^3H_4 \rightarrow {}^3H_4$  intensity at  $Q = 0$ , which has a cross section of 620 mb/sr.

on HET at ISIS, observing the spin waves to energies of up to 310 meV, see Fig. 6<sup>(3)</sup>. (It is essential to observe the full energy range of the excitations in order to distinguish between the various theoretical models). The nature of the time-of-flight scan complicates interpretation of these data somewhat, but this is more than compensated for by the good resolution and excellent signal to noise obtained by this technique, see Fig. 7. Further data analysis to extract widths and absolute intensities is in progress.

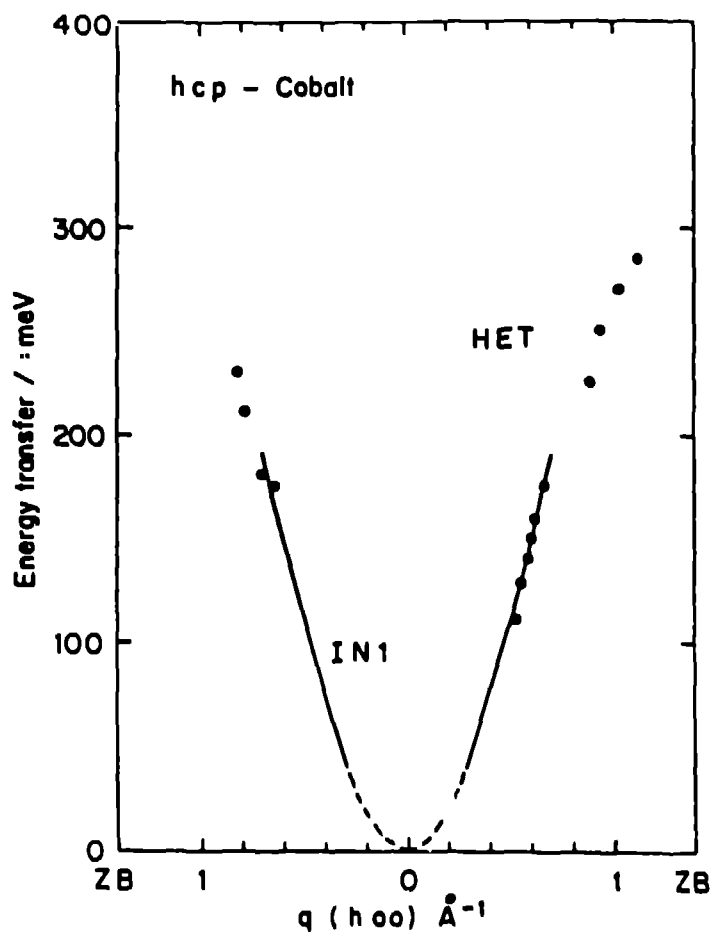
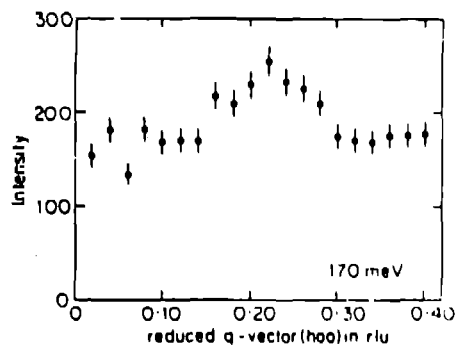
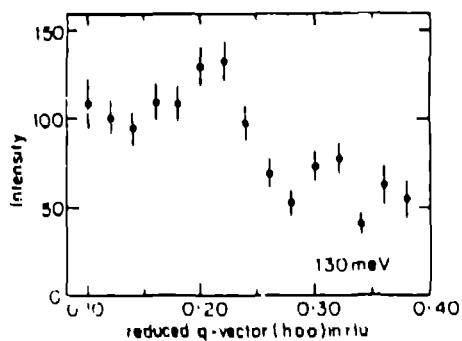
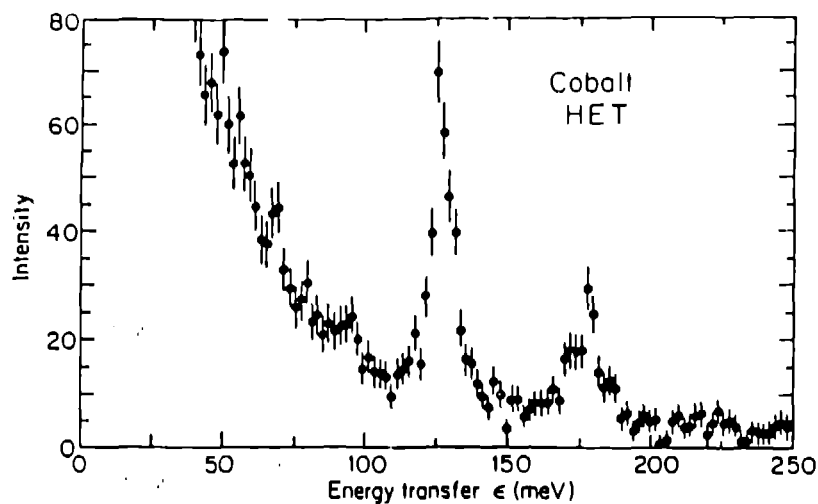


Fig. 6 The magnon dispersion relation for hcp-cobalt along the [h00] direction measured on IN1 at the ILL (line) and on HET at ISIS (dots).

Work on localised high energy magnetic excitations has continued with studies of the crystal field potential in UOS where transitions were observed up to an energy of 80 meV both above and below the antiferromagnetic ordering transition at 55 K. As in the case of  $UO_2$  both the energy and intensity of the crystal field splittings support a level scheme calculated from a point charge model<sup>[4]</sup>. In an experiment designed to refine the crystal field potential within the new ceramic superconductors<sup>[5]</sup>, the heavy rare earth ions Ho, Er and Dy were substituted for Y in the 1-2-3 compound  $YBa_2Cu_3O_{7.8}$ . Clearly resolved magnetic excitations were observed between 10 and 100 meV and their temperature dependence measured. The results show that the parameters of the potential can be scaled across the rare-earth series.



**Fig. 7** The 130 meV and 170 meV spin waves in hcp-cobalt measured on (a) HET and (b,c) IN1 illustrating the improved resolution and signal-to-noise obtained with the time-of-flight method.

### Vibrational spectroscopy

Work on metal hydride systems continued with a detailed study of the alpha phase  $YH_{0.11}$ . A high energy measurement, Fig. 8, illustrates the nearly harmonic behaviour of the degenerate a-b modes at 135 meV in the tetrahedral site and the extremely anharmonic behaviour of the c-axis mode at 100 meV<sup>(6)</sup>. Using a lower incident energy, a high resolution measurement revealed a splitting of this mode due to H-H pairing along the c-axis. These subtle features require a more sophisticated quantum mechanical description of the interstitial hydrogens than the perturbed simple harmonic oscillator which has until now been adequate.



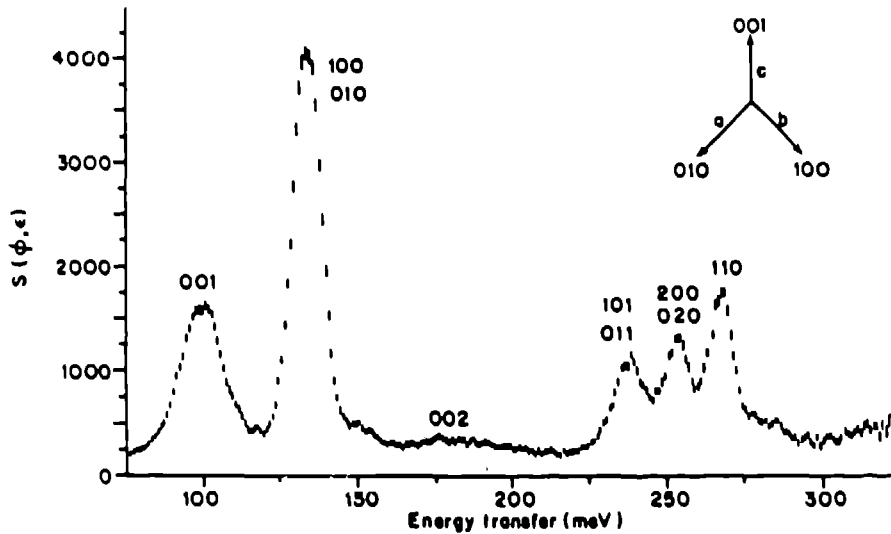


Fig. 8 The inelastic spectrum of YH<sub>0.11</sub> measured on HET with an incident energy of 330 meV. The simple harmonic quantum numbers are given for each transition.

Studies of the dynamical structure factor of amorphous boron<sup>(7)</sup> were successful despite the limited angular range of detectors available, see Fig. 9. Such problems will benefit significantly from the newly installed detector array and these results bode well for the future of such experiments on MARI.

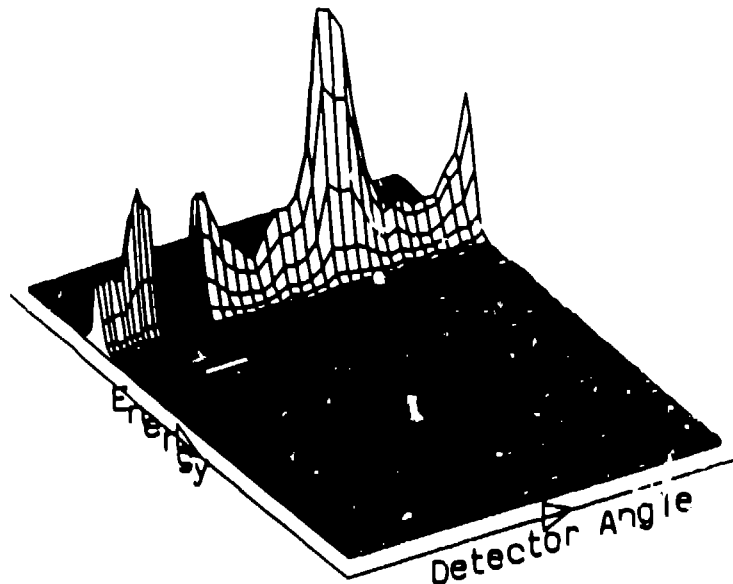


Fig. 9 The scattering function for amorphous boron determined using an incident energy of 360 meV. The angular range covered is 7° to 7° and 10° to 30°.

### TFXA: The time-focussed crystal analyser spectrometer

TFXA is an inverted geometry neutron inelastic scattering spectrometer<sup>(8)</sup>. The sample, at 12 m from the source, is illuminated with pulses of white radiation. Neutrons lose energy by exciting vibrations in the sample, and some are scattered towards the analyser crystals. These graphite crystals are set to reflect neutrons of  $\sim 4$  meV toward the detectors. The more energetic neutrons arrive at the sample first and energy analysis is by time of flight. The spectrum was converted from neutrons per channel to  $S(Q, \epsilon)$  per energy transfer, by standard programs. The spectrometer has excellent resolution, see Fig. 10,  $\Delta\epsilon/\epsilon \leq 2\%$  and  $\Delta|Q| \sim 0.2 \text{ \AA}^{-1}$ . The fixed locus through  $Q$ - $\epsilon$  space effectively follows  $Q^2 \sim \epsilon/2 \text{ (\AA}^2\text{-meV}^{1/2}\text{)}$ .

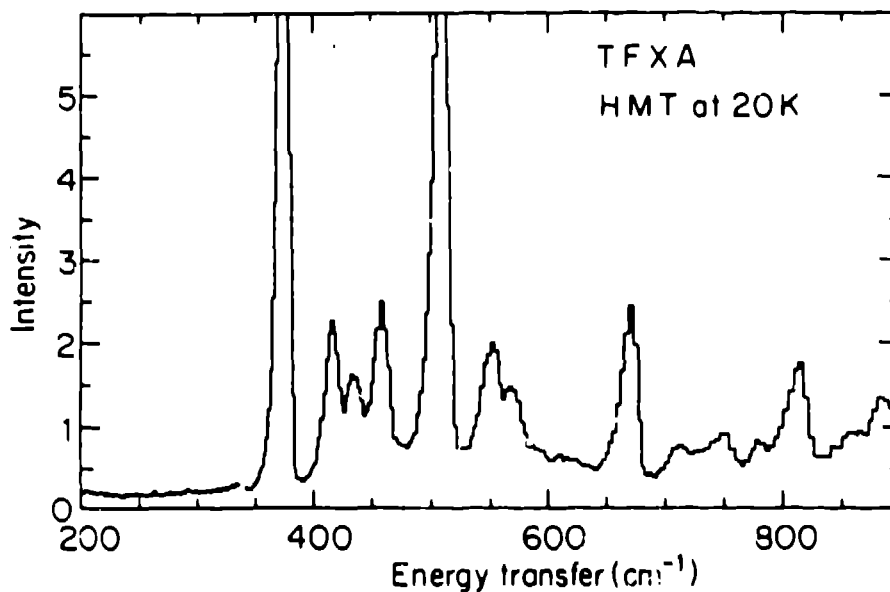


Fig. 10 Part of the inelastic spectrum of hexamethylene tetramine (HMT) measured on TFXA. These high resolution data should be compared with the MaxEnt reconstruction given in these proceedings by D. Sivia.

Samples are held as flat plates perpendicular to the incident beam. Therefore, for energy transfers greater than  $\sim 30$  meV the momentum transfer vector  $Q$  is also perpendicular to the sample. This can be put to significant advantage in the study of some hydrogenous single crystals.

We have already reported that TFXA is almost free of the effects of multiple scattering<sup>(9)</sup>. In the case of single crystal spectra this requires some qualification. The effects of multiple scattering in single crystals is to produce spectra which are more "powder" like. Hydrogenous crystals which are ca 1 mm thick scattering ca 5% of the neutrons should not introduce significant multiple scattering problems.

## Spectrometer Improvements

Since the last ICANS meeting, TFXA has seen several improvements. Principle amongst these are improvements in resolution, flux and background.

- (i) The resolution has been improved by obtaining detectors whose active thickness was matched to the secondary spectrometer. These are 6 mm thick squashed Helium tubes. At 5 bars filling pressure they are as inefficient as  $\text{BF}_3$  tubes at detecting high energy neutrons thus slightly reducing the noise.
- (ii) The count rate has been improved by obtaining thicker graphite crystals, with larger mosaic spread. There is a slight degradation in resolution attendant upon this change—but this occurs in the elastic peak region.
- (iii) The background has been improved by coating all exposed metal surfaces by cadmium. The sample is also heavily encased in cadmium. The reflection geometry of TFXA has simplified opting for this solution.

The calibration of TFXA has traditionally been based upon Hexamine (HMT) which produces a very strong inelastic line at  $\sim 390 \text{ cm}^{-1}$ , see Fig. 11. We anticipate that this choice of calibrant will have to change. This is because it produces a strong (111) Bragg reflection at the elastic energy. With our reduced elastic resolution we are no longer able to resolve the coherent and incoherent contributions to the elastic line. A systematic error introduced by this effect leads to an underestimation of the energy transfer values. This underestimate is not greater than  $4 \text{ cm}^{-1}$ .

## Data treatment

Because there are no spectral variables open to choice on the TFXA spectrometer we have instituted an automatic standard analysis program. The experimentalist automatically launches this by ending his data collection. It has the advantage of producing standard files, avoids wasting time and prevents inexperienced users from producing very badly analysed data.

Molecular spectroscopists are making good use of the CLIMAX program. This is analogous to the Rietveld fitting programs for diffraction. Working with G. J. Kearley (ILL) we have produced a version of CLIMAX which fits phonon wings out to eighth order.

The effects of recoil scattering has also been identified on TFXA. In the context of molecular vibrations recoil is an exaggerated and smooth phonon wing. It is present when the lattice forces restricting small molecules are very weak. Useful, if limited, parameters can be extracted from the recoil spectra of simple molecules, e.g., recoil mass, average lattice energy.

## Scientific highlight on TFXA: Hydrodesulphurisation catalysts

The high sulphur content found in North Sea oils can be reduced by the hydrodesulphurisation process. The presence of sulphur poisons the surface of normal active metal catalysts in the cracking and reforming reactions necessary to

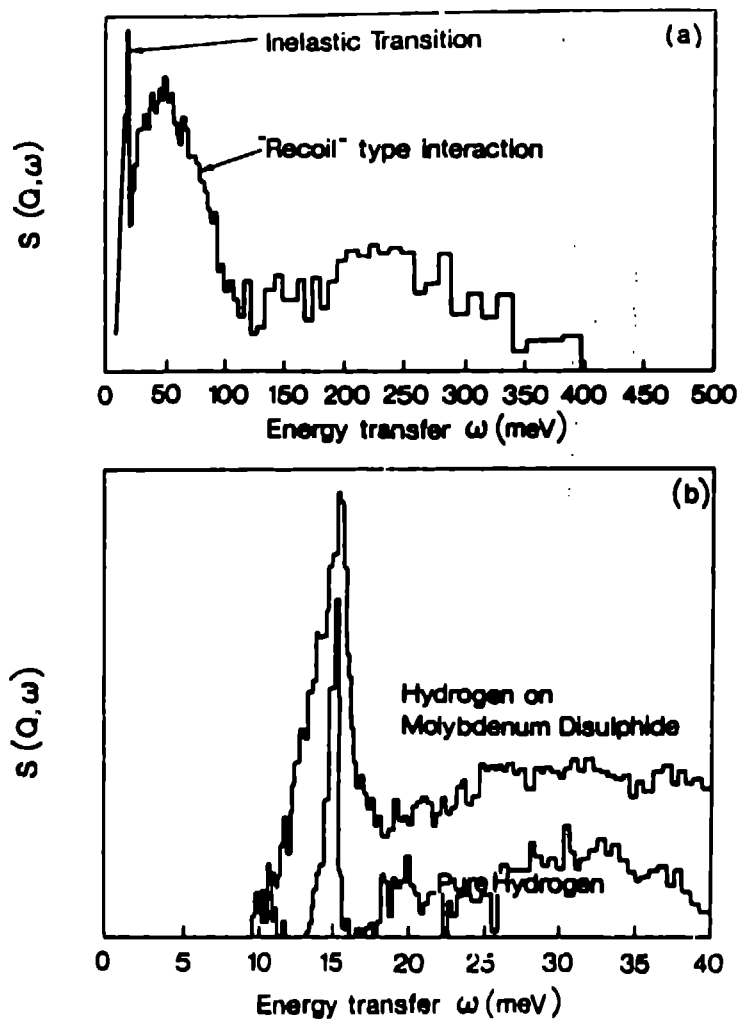


Fig. 11a TFXA data for H<sub>2</sub> on tungsten disulphide at 50 bar.

Fig. 11b TFXA data for H<sub>2</sub> on molybdenum disulphide at 50 bar showing the sharp  $0 \rightarrow 1$  rotational transition.

refine the oil. An understanding of the desulphurisation reaction is essential for the efficient use of expensive hydrogen.

Following earlier neutron studies on the sorption of H<sub>2</sub> on MoS<sub>2</sub>, work on H<sub>2</sub> + MoS<sub>2</sub> and H<sub>2</sub> + WS<sub>2</sub> has been extended to higher pressures<sup>(10)</sup>. The original high pressure results produced convincing evidence that more than one absorption site was present in MoS<sub>2</sub>. The second absorption site was associated with a spectral feature at 50 meV. This site saturates at 50 bar. Kinetic data shows that the

hydrosulphurisation reaction over  $\text{MoS}_2$  is first order in hydrogen partial pressures up to 50 bar. It was assumed that the second absorption site was responsible for the behaviour of the hydrogen in this important industrial process. The 50 meV band was understood to be due to atomic hydrogen.

The TFXA data for  $\text{H}_2$  on tungsten disulphide may be compared with those obtained from solid  $\text{H}_2$  in Fig. 11. The theoretical response of a 'recoiling'  $\text{H}_2$  molecule is also shown. The TFXA results show clearly that non-dissociated  $\text{H}_2$  molecules are involved. This is confirmed by the very sharp transition at 14.7 meV which is the 0-1 rotational transition of molecular hydrogen. The spectra obtained, however, are not simply those of solid  $\text{H}_2$  condensed on the sample. This demonstration of the molecular nature of the adsorbed hydrogen as distinct from the atomic nature previously accepted has far-reaching consequences in understanding these important chemical reaction mechanisms.

### **IRIS: The high resolution inelastic spectrometer**

IRIS is an inverse geometry crystal analyser spectrometer optimised for high resolutions (15  $\mu\text{eV}$ ) up to moderate energy transfers (0-10 meV)<sup>(11)</sup>. It was commissioned during the second half of 1987 and is now in routine operation, although a number of major items are still being installed.

#### **Instrument description**

The spectrometer views the ISIS liquid hydrogen cold source via a 34 m long curved neutron guide which terminates with a 2.5 m long supermirror-coated converging guide. At 6Å the flux at the sample is enhanced by a factor of 2.8 due to the converging guide. The sample position is at 36.54 m from the moderator and the measured flux at 100  $\mu\text{Amp}$  operation of ISIS is  $5 \times 10^6$  n/cm<sup>2</sup>/sec over a sample area of  $3.5 \times 2.5$  cm<sup>2</sup>.

At 6.4 m from the moderator a variable aperture disc chopper serves to prevent frame overlap at the detector and to eliminate ISIS pulses when a wider energy transfer range is required. At full ISIS frequency the wavelength window at the sample is 2.0 Å. The energy transfer range spanned depends upon the phase of the chopper with respect to the ISIS pulse. If the wavelength window is centred on the elastic line an energy transfer range from +0.65 meV to -0.45 meV can be observed. In downscattering only to the elastic line an energy transfer range from +1.85 meV to 0.0 meV can be observed. Decreasing the chopper speed to 25 Hz increases the measuring window to 11.1 meV. The maximum energy transfer range is limited by the short wavelength cut-off of the curved guide to a value of approximately 15 meV. At this energy transfer the resolution is ~80  $\mu\text{eV}$  compared to 15  $\mu\text{eV}$  at the elastic line.

It is a feature of inverted geometry spectrometers that the measuring range in neutron energy loss is very large compared with a direct geometry spectrometer as a result of the opposite handedness of the (Q- $\epsilon$ ) loci, see Fig. 12. Direct geometry machines (such as IN5) achieve high resolutions by reducing the incident neutron energy such that in the limiting case a very narrow energy transfer range with only a small

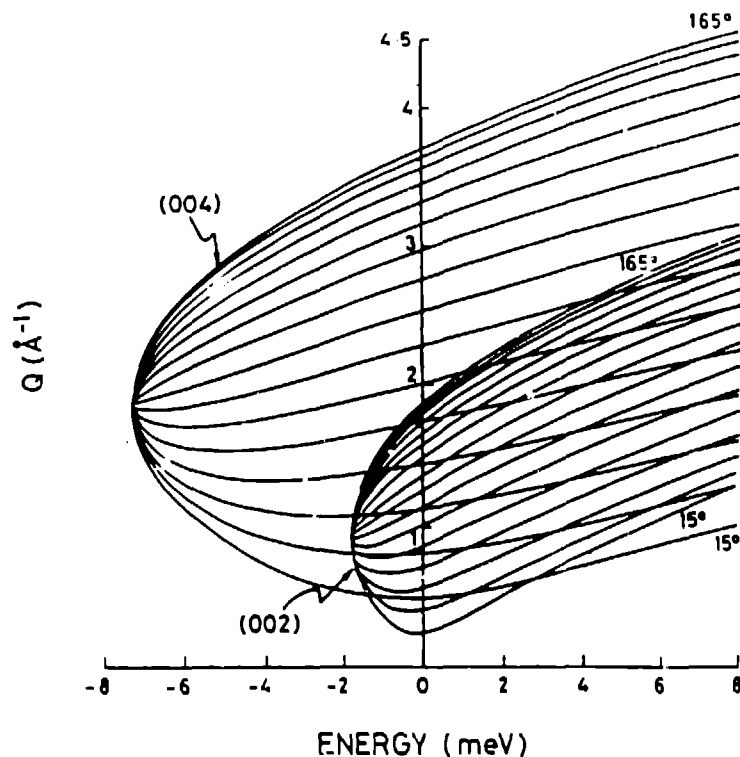


Fig. 12 The Q- $\epsilon$  range available on IRIS from the 002 and 004 reflections of PG. The elastic resolution is 15  $\mu\text{eV}$  and 45  $\mu\text{eV}$ , respectively.

momentum transfer range is observable. Inverse geometry machines suffer from no such conflict. This feature is a great advantage when attempting to assign level schemes in tunnelling spectroscopy and crystalline electric field spectroscopy with very cold samples in their ground states.

### Planned upgrades

A new ZnS scintillator is presently being installed. This does not suffer from gamma sensitivity in the manner which the present detector does. As a result a significant contribution to the spectral background derives from the effects of neutron absorption in the sample and whilst hydrogenous sample could be studied routinely non-hydrogenous samples containing significant absorbing species proved impossible to measure. A gamma insensitive detector will also be a great relief in that we can now resort to the flexibility of shielding using cadmium!

At the same time we are installing a radial collimator between sample and analyser bank. This should reduce considerably background effects due to sample environment windows and stray neutrons, although it will also have an effect on the signal.

During 1989 we shall install a cooled beryllium filter between the sample and analyser bank. Financial constraints allow us to purchase only sufficient beryllium to cover half the analyser. This however should not be a severe restriction since it will mainly be utilised for inelastic spectroscopy where full Q coverage is not absolutely necessary initially. It will be installed to cover  $90^{\circ}$ - $165^{\circ}$  angles of scattering with the possibility of switching this to the low angle analysers for crystal field excitations if required.

### Future developments

We have tested the idea of a mica analyser with a mock-up array which was by no means optimised. An elastic resolution using the (004) mica reflection of  $5.5 \mu\text{eV}$  was recorded at an analysing energy  $833 \mu\text{eV}$ , see Fig. 13. Compare this with  $15.5 \mu\text{eV}$  presently available from the (002) pyrolytic graphite reflection analysing at  $1.835 \text{ meV}$  with a count rate  $\sim 25 \times$  higher. Despite this reduction in counting times, it was possible to observe tunnelling peaks at  $\pm 15 \mu\text{eV}$  and  $+150 \mu\text{eV}$  in 4-methyl pyridine zinc chloride, never previously observed, in a 16 hour run. We believe the  $15 \mu\text{eV}$  peaks are the lowest energy transfers observed to date at a pulsed neutron source. Theoretically it is possible to use the (002) mica reflection to obtain resolutions of the order 1 to  $2 \mu\text{eV}$  at an analysing energy of  $208 \mu\text{eV}$  but we were not able to observe the elastic line due to frame overlap problems. (The (002) reflection is detected on IRIS 10 pulses after the neutrons left the moderator!). This may seem an impossible goal but we are planning to build a large area mica analyser (at least 10 times larger than the prototype) focusing onto a single detector for use in inelastic spectroscopy for operation in late 1989. We also plan to investigate methods of increasing the mica reflectivity. The 4-MPZnCl<sub>2</sub> could then be collected in 1 1/2 hours (or 45 minutes at  $200 \mu\text{Amps}$ ) and the transition to the mica (002) reflection with its 1-2  $\mu\text{eV}$  resolution is becoming attainable. (It should be remembered that run times on IN10 are typically 24 hours.)

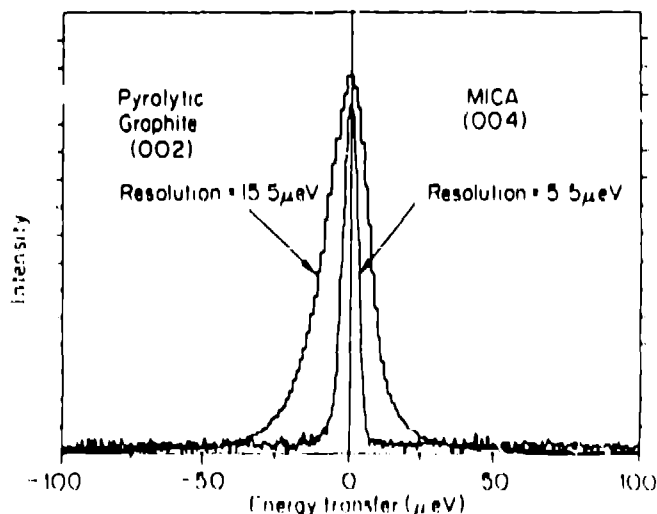


Fig. 13 Test data on IRIS comparing the  $5.5\text{-}\mu\text{eV}$  resolution available from Mica (004) with the standard  $15\text{-}\mu\text{eV}$  resolution of PG (002).

### Scientific highlight on IRIS: Intermolecular coupling in 4-methyl-pyridine

$C_5NH_4 \cdot CH_3$  have been revealed by neutron scattering on the IRIS spectrometer. The tunnel level in 4-methyl-pyridine at  $520 \mu\text{eV}$ , very close to the free rotor limit for a methyl group of  $665 \mu\text{eV}$ , is one of the few examples of an almost-free rotor found in the solid state. Instead of a single tunnel level expected from a molecule which is non-interacting with its surroundings, the tunnel spectra of 4-methyl-pyridine measured on IRIS exhibits four discrete components centred around  $520 \mu\text{eV}$ , see Fig. 14. In an attempt to unravel the cause of the complex spectrum, a series of experiments have been performed on IRIS varying both temperature and the dilution of the hydrogenated molecules with fully deuterated molecules. Both increased temperature and increased dilution clearly weaken the coupling between neighbouring molecules giving rise to an anomalous rise in the tunnelling frequency as a function of temperature at low concentrations. The results are being modelled theoretically using the concepts of dynamic and static coupling of methyl groups employing gauge theory<sup>[12]</sup> and by utilising the sine-Gordon formalism which proposes the existence of soliton-antisoliton waves<sup>[13]</sup>.

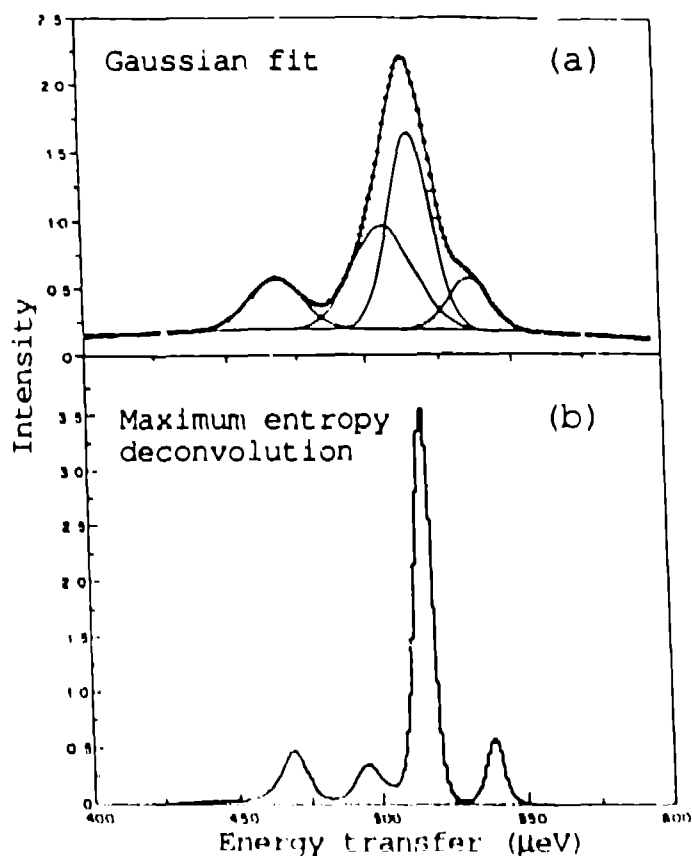


Fig. 14 Decomposition of the  $520 \text{ meV}$  tunnel level in 4-methyl-pyridine into four components (a) by Gaussian fitting and (b) by the maximum entropy method.



## PRISMA:

### A high-symmetry inelastic spectrometer

PRISMA stands for **PR**ogetto dell'Istituto di Struttura della **MA**teria del CNR. Under an international collaboration signed in 1985 between SERC and the Consiglio Nazionale delle Ricerche, CNR, Frascati, Italy, PRISMA has been provided by Italy for installation on ISIS.

PRISMA is designed to measure coherent excitations in single crystals<sup>(14)</sup>. The scattering function  $S(Q, \epsilon)$  is measured along a high-symmetry direction in reciprocal space to be determined by the experimentalist. With the present set of germanium analysers the energy transfer range reaches up to 200 meV (depending on the choice of wavevector  $Q$ ).

The instrument operates in inverted geometry, i.e., it has a white incident neutron beam. The energy change of the scattered neutrons is analysed by 16 independent analysers, each equipped with a detector. The angular separation between the individual detectors is  $2^\circ$ , so a total  $\phi$ -range of  $30^\circ$  is covered, see Fig. 15. Keeping the ratio  $(\sin\phi_i/\sin\Theta_{A_i})$  constant for all analysers ensures that every analyser-detector arm records  $S(Q, \epsilon)$  along the same  $Q$ -direction in reciprocal space. The positioning of all analyser and detector motors, as well as of the motors for the sample angles  $\phi$  and  $\Psi$  and the sample goniometer, are controlled by a dedicated PC.

An elaborate software package has been developed for communication between the PRISMA control programme, the standard ISIS data acquisition, CAMAC software and the IBM personal computer which controls the 34 positioning motors (16 analysers, 16 detectors, the rotating collimator and the  $\phi$ -arm). This allows to set up the spectrometer by computer in every desired configuration. Also a single motor or a physical quantity (like the analysing energy of an analyser) can be driven and scanned individually. A simulation program including a graphics display enables the experimenter to select in advance the most favourable configuration for an experiment.

Within the past few weeks, commissioning experiments have yielded very promising data, demonstrating clearly the power of this instrument to measure dispersion curves. As an example we show the phonon dispersions along the  $[1,0,0]$  direction of a single crystal of copper. Figure 16 summarises the results from all the available detectors. The curved solid lines indicate the time-of-flight loci of the 16 detectors, with the thick line marking the detector whose spectrum is shown in Fig. 17. The measurements were performed at room temperature and therefore phonons in energy gain and energy loss were observed. We would like to stress that this dispersion curve was the result of a single setting of the instrument. The data were obtained in 1.6 mA-hr, equivalent to less than a day running at current ISIS conditions. It is also evident from Fig. 17 that instrumental resolution effects influence strongly the shape of the spectra. Therefore a powerful software programme is required and is at present under development, in order to analyse the data in an appropriate way.

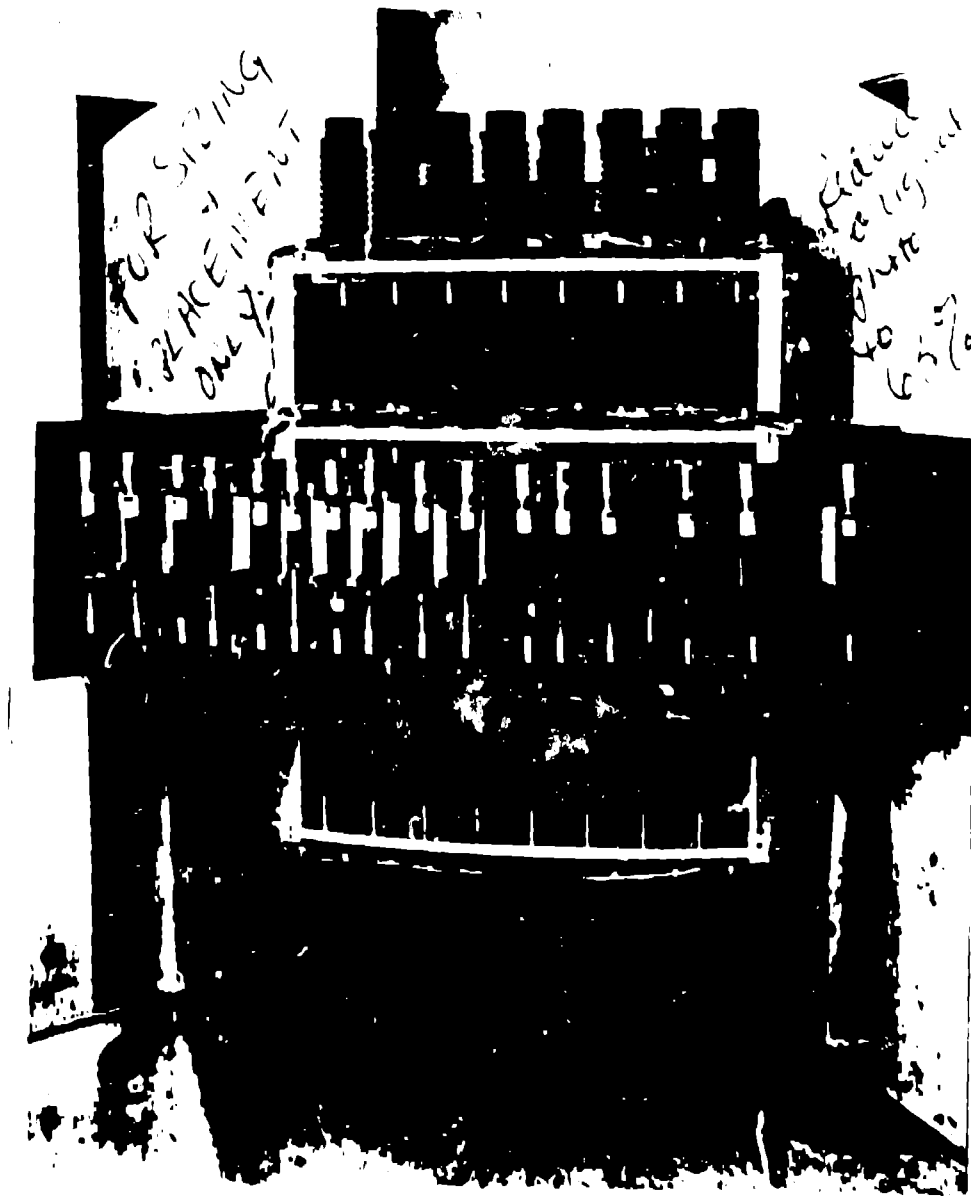


Fig. 15 The PRISMA spectrometer with part of the shielding removed to show the  $\phi$ -arm with the 16 analyser-detector arms and the pathway of the  $\phi$ -arm through the shielding.

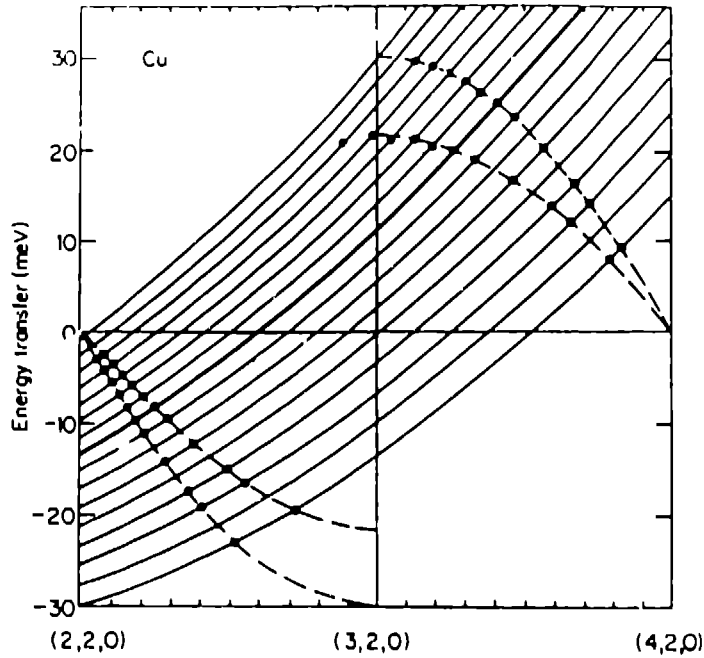


Fig. 16 The phonon dispersion relation measured along the [100] direction in a single crystal of copper during early tests on PRISMA. The solid lines are the loci in  $(Q, \epsilon)$  space scanned by each detector, while the dashed lines indicate the known dispersion relation. The locus corresponding to detector no. 9 is highlighted.

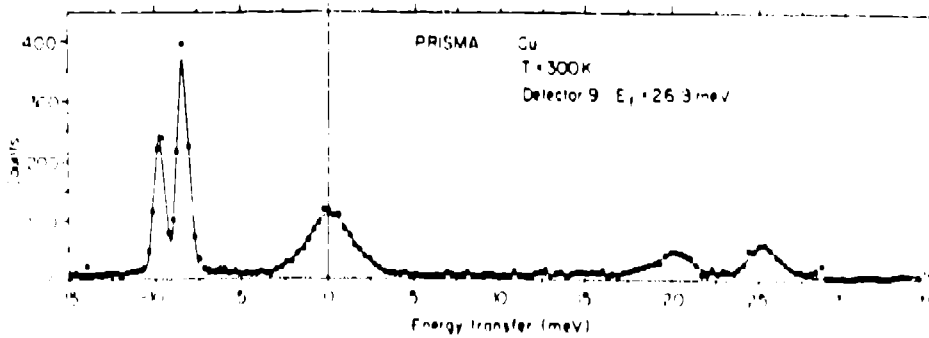


Fig. 17 The spectrum of one individual detector (no. 9). Phonons in both energy gain and loss are clearly seen.

## eVS: The electron volt spectrometer

### Low-Q programme

The original goal of eVS was to explore high energy transfer scattering at low values of associated momentum transfer using  $(n,\gamma)$  detectors<sup>[15]</sup>. A review held in Spring 1988 concluded that below 500 meV transfer, chopper spectrometers such as HET had significantly better resolution and count rate than was achievable by this method. (Figure 18 compares the observation of intermultiplet transitions in praseodymium on HET and eVS). Above 1000 meV transfer this conclusion would be reversed, but the interesting cross-sections such as those associated with interband electronic excitations are predicted to be far too small to be observable with current instrumentation. As a result of this review the high energy transfer, low Q programme on eVS has been terminated.

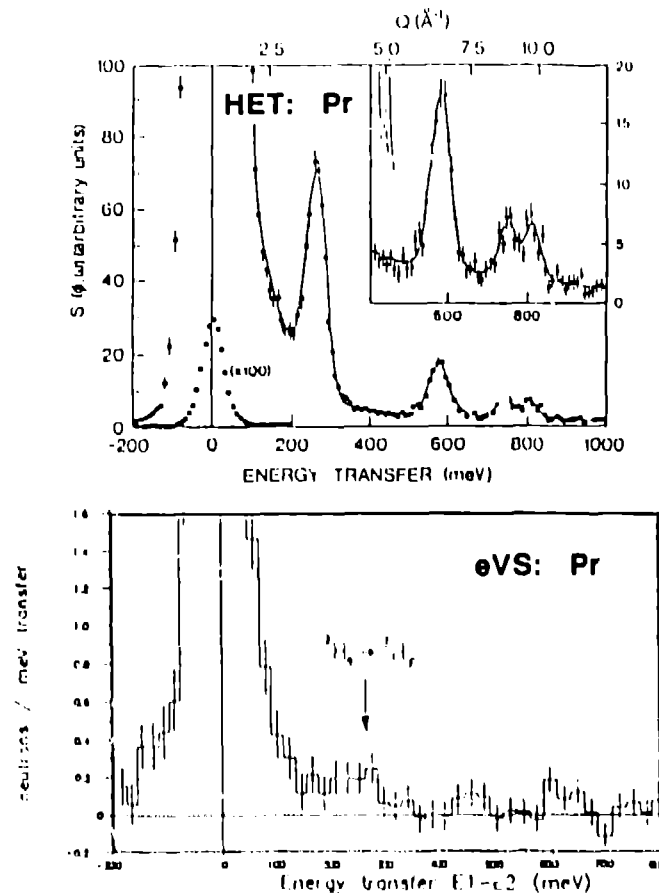


Fig. 18 Intermultiplet transitions in metallic Pr observed in 1300  $\mu\text{A}\cdot\text{hr}$  on HET (top) and in 7000  $\mu\text{A}\cdot\text{hr}$  on eVS (bottom).

### High-Q programme

Progress on the high Q programme of eVS has continued with the development of a multidetector system based on the  $(n,\gamma)$  capture resonance in thin foils. An array of seven Bismuth Germanate (BGO) photon detectors was installed and commissioned using Ta annular analysing foils ( $E_r = 4.28$  eV, 10.3 eV and 23.9 eV) with a range of thicknesses between 10  $\mu\text{m}$  and 50  $\mu\text{m}$ . Measurements have been undertaken at high energy and momentum transfers which allows the momentum density of the recoiling atoms to be obtained within the impulse approximation. Several experiments within this regime have been carried out on polycrystalline graphite and a comparison between the single and multidetector systems made in terms of the signal count rates and signal to noise. The signal count rate is 20 times greater for the multidetector system albeit with a small loss in overall signal to background compared to a single detector system. In further measurements on polycrystalline Be the counting statistics were sufficient to allow data to be analysed using all three main resonances in Ta. Figure 19 shows the recoil scattering spectra from Be and the Al sample container on an energy transfer scale using the 4.28 eV resonance. Also shown is a two-Gaussian fit to the data. Measurements undertaken at 16 K on the same sample have clearly indicated the corresponding decrease in the mean atomic kinetic energy (extracted from the recoil width) in agreement with theoretical models based on the phonon density of states. Recent data have been analysed using the method of  $\gamma$ -scaling where it has been possible to compare directly recoil scattering data obtained on both eVS and HET.

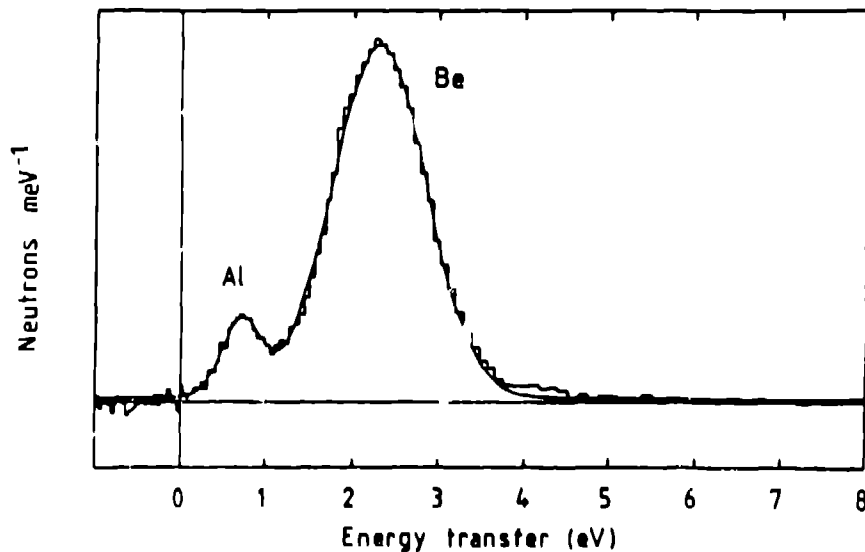
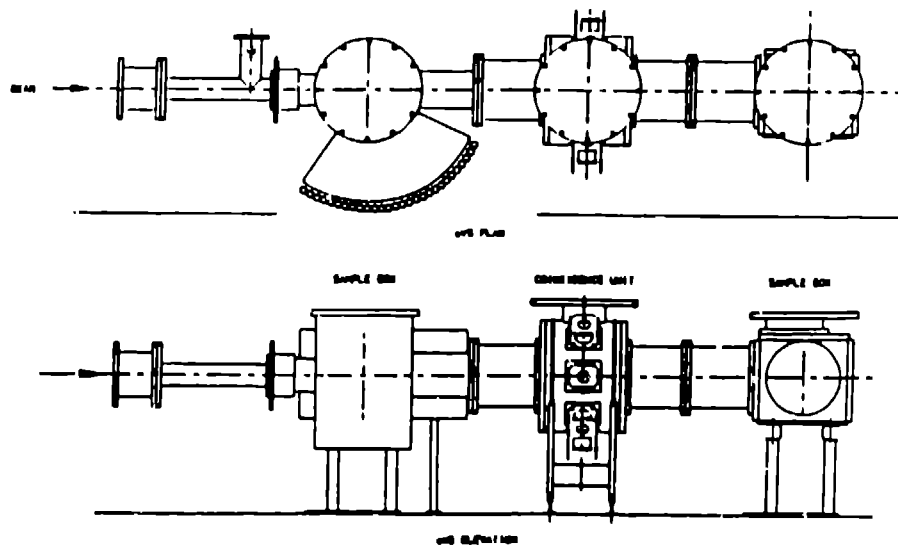


Fig. 19 The recoil spectrum from polycrystalline beryllium obtained on eVS with the 4.28 eV resonance in Ta.

Due to an increase in the demand for studies of momentum distributions on ISIS the present eVS system has been modified and extended to undertake recoil scattering from hydrogenous materials. The fixed high-angle system imposes kinematical constraints which does not allow recoil scattering from mass 1 particles. An intermediate angle recoil spectrometer has therefore been developed to cover the angular range  $30^{\circ}$ - $120^{\circ}$  using  $30 \text{ He}^3$  detectors positioned  $0.5 \text{ m}$  away from the sample. Figure 20 shows the new eVS spectrometer on ISIS. Curved analyser foils of Ta and Au are available providing a range of energy and momentum transfers. The resonance filter difference method will be used to obtain the recoil scattering spectra. Preliminary trial measurements on  $\text{ZrH}_2$  with Ta and Au have produced some promising results in terms of both signal count count and signal to noise. A user programme for the study of hydrogenous samples is already scheduled on this spectrometer.



**Fig. 20** The intermediate angle spectrometer on eVS, which is optimised for recoil scattering from mass 1 and mass 2 systems. Energy analysis is performed using tantalum or gold resonance difference techniques.

### Future developments

In an attempt to return to the original goals of the eVS programme, namely the study of high energy excitations at low values of associated momentum transfer, a new spectrometer design is being investigated. Drawing on experience from HET, it would be a high resolution direct geometry spectrometer which would cater to the existing demand for high resolution magnetic scattering and would allow Brillouin scattering in amorphous systems to be explored, see Fig. 21. In addition a parallel development programme on high energy monochromating choppers and tests on polarised beams on chopper spectrometers could be performed. Detailed studies of the feasibility of constructing such a spectrometer at modest cost utilising existing

equipment are in progress. Sources of external funding for this project are also being explored.

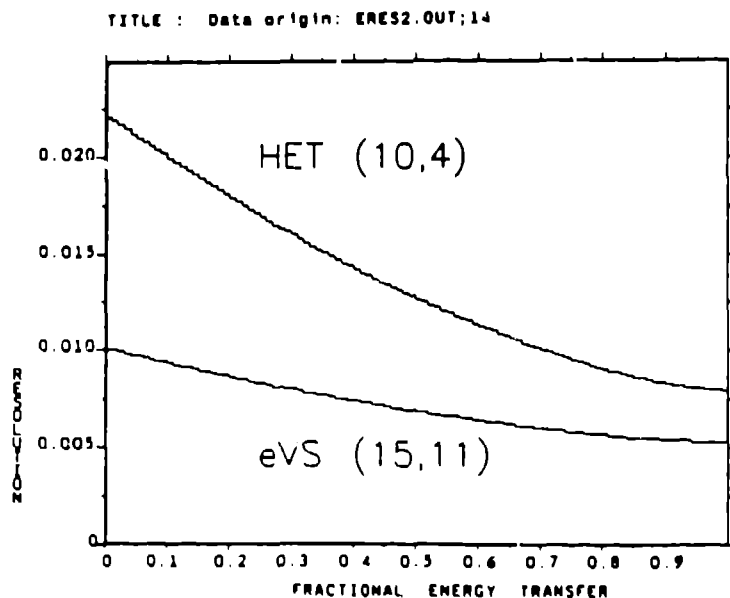


Fig. 21 The energy transfer resolution ( $\Delta E/E_i$ ) of the proposed high resolution spectrometer (Primary flight path 15 m, Secondary flight path 11 m) as a function of fractional energy transfer ( $\epsilon/E_i$ ) compared with HET.

### MARI: The multi-angle rotor Instrument

The MARI project, a joint collaborative venture between RAL and the Japanese National Laboratory of High Energy Physics (KEK), is now under construction at the ISIS facility. The instrument is based on a fast Fermi chopper device, similar to that used on HET, providing energy transfer resolutions,  $\Delta E/E_i \sim 1\%$ . The chopper system, manufactured by Uranit GmbH at Julich, was recently delivered to RAL. An identical chopper system and associated rotor package has been manufactured for KEK. The spectrometer will view the 100 K liquid methane moderator and will use incident energies in the range 50-1000 meV. A unique feature of this new spectrometer will be that it will record inelastic scattering processes in the vertical plane using a large angular array of helium detectors with a coverage between  $\pm 10^\circ$  and  $10^\circ$ - $135^\circ$  (see Fig. 22). This will provide an accurate interpolation from  $S(\phi, t)$  to  $S(Q, \epsilon)$ . The low angle octagonal bank and the large detector vessel, containing three  $^3\text{He}$  detectors at each angle, forms a continuous angular coverage and is well shielded internally with  $\text{B}_4\text{C}$  plates and collimation vanes. This large angular range together with the high resolution will enable science to be undertaken in areas such as molecular spectroscopy, magnetic excitations, measurements of  $S(Q, \epsilon)$  and momentum distributions. It is anticipated that commissioning experiments will begin in the spring of 1990.

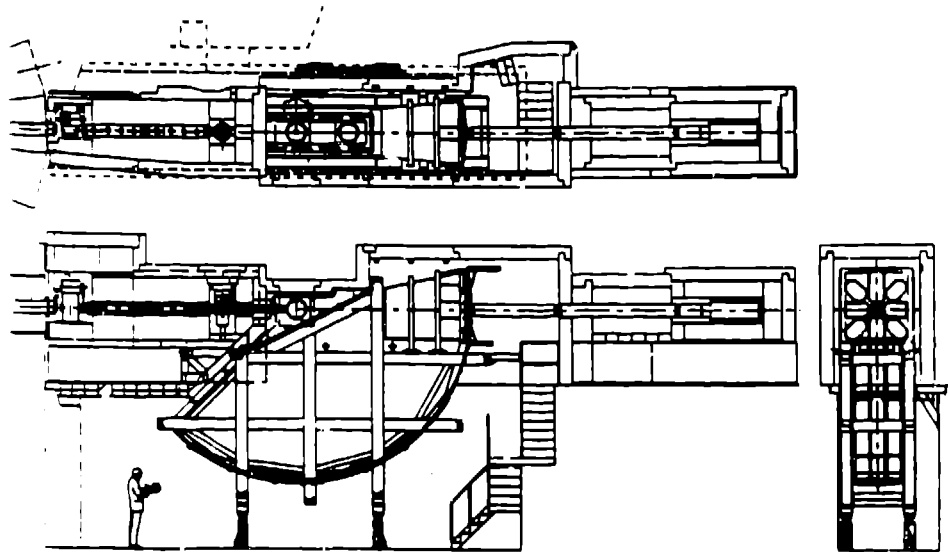


Fig. 22 Plan and elevation views of the MARI spectrometer.

### The polarisation programme at ISIS

A series of measurements made in 1985-86 on a sintered  $\text{SmCo}_5$  filter showed that this material has very good intrinsic properties as a neutron polariser at all neutron energies up to about 160 meV. The polarising efficiency in this energy range varied between 98% and 70% with corresponding transmittances between 10% and 30%. These results were obtained at approximately 1% of the ISIS design current ( $\sim 2 \mu\text{A}$ ).

Later measurements at 10% of the full ISIS current showed significant filter heating effects. The polarising efficiency at the  $^{149}\text{Sm}$  resonance peak energy (97 meV) was reduced to 65% and the transmittance to 5%. This corresponds to a nuclear spin temperature in the filter of  $\sim 70$  mK, whereas an independent measurement of the dilution refrigerator temperature by Co nuclear orientation thermometry gave 13 mK. Subsequent tests showed that this heating was caused by poor thermal contact between the filter material and the mixing chamber of the dilution refrigerator.

Considerable effort was put into achieving a good metal-metal contact between the filter material and the copper filter holder. A successful solution to this problem was found first by ion implanting copper on to the surface of the filter, and then soldering this to a copper plate which formed part of the mixing chamber base. A filter prepared in this way was found to be well-coupled to the mixing chamber and the limiting factor determining the performance of the filter was then found to be the cooling power of the refrigerator. Two observations supported this deduction: (i) the filter temperatures measured by neutrons was equal to the mixing chamber temperature measured by Co nuclear orientation, and (ii) the time constant for cooling the filter was longer than in previous filters, and equal to the cooling time of



the fridge. The cooling power of the dilution refrigerator used in this test was  $\sim 1$   $\mu$ watt at 20 mK (the temperature required for an effective filter performance), and from this it was concluded that a 40  $\mu$ watt dilution refrigerator (which is now commercially available) is required for effective filter operation in the incident beam on the Polaris beam with ISIS operating at 100  $\mu$ A.

This development programme has been discontinued for the present. Although only partially successful we can conclude that: (i) it is feasible to construct a large area polarisation analyser using the permanent magnetic material  $\text{SmCo}_5$  for neutron energies  $E < 200$  meV (the advantages of not requiring an applied field are self evident) and (ii) the method can also be used in the primary beam on a pulsed source chopper monochromator, since monochromatic fluxes would not be sufficient to heat the filter.








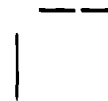
The current plans for polarisation work at ISIS are to construct a polarising bender made from Co/Ti supermirrors with Gd/Ti antireflecting layers. The device designed has a length  $\sim 1.2$  m with a critical wavelength  $\lambda^* \sim 0.87 \text{ \AA}$  ( $E^* \sim 110$  meV) and is similar in design to the bender on the LOQ spectrometer. It is expected to be available for first tests towards the end of 1989.

### Acknowledgements

We would like to thank the engineers, physicists and operations crews of ISIS and our technical support staff for their hard work and dedication.

### References

- [1] A D Taylor, B C Boland, Z A Bowden and T J L Jones, Rutherford Appleton Laboratory Report RAL-87-012 (1987)
- [2] A D Taylor, R Osborn, K A McEwen, W G Stirling, Z A Bowden, W G Williams, E Balcar and S W Lovesey, Phys Rev Lett **61**, (1988) 1309-1312
- [3] T G Perring and G L Squires, ISIS Experimental Report RB/140, p A119 in 'ISIS 88' RAL-88-050
- [4] G Amoretti, A Blaise, J M Fournier, R Caciuffo, J Larroque, R Osborn, A D Taylor and Z A Bowden, J Magnetism and Magnetic Materials **77/78** (1988)
- [5] B D Raituord, D McK Paul, S Culverhouse and R Osborn, ISIS Experimental Report RB/414, p A114 in 'ISIS 88' RAL-88-050
- [6] S M Bennington, D K Ross, M J Benham, A D Taylor and Z A Bowden, Z Physik 1989 (in press)
- [7] U Danlborg, R G Delaplane and A C Hannon, ISIS Experimental Report RB/250, p A111 in 'ISIS 88' RAL-88-050
- [8] J Penfold and J Tomkinson, Rutherford Laboratory Report RAL-86-019 (1986)
- [9] P S Goyal, J Penfold and J Tomkinson, Rutherford Laboratory Report RAL-86-070 (1986)
- [10] P N Jones, E Knozinger, W Langel, R B Moyes and J Tomkinson, Surface Sc **207** (1988) 159
- [11] C J Carlile, Nucl Inst and Meth (in preparation) 1989
- [12] C J Carlile, S Cough, A J Horsewill and A Smith, submitted to Chemical Physics 1989

- 
- 
- 
- [13] F Fillaux and C J Carlile (in preparation) 1989  
[14] C Andreani, C J Carlile, F Cilloco, C Pettillo, F Sacchetti, G C Stirling and C G Windsor, Nucl Inst and Meth A254,(1987) 333.  
[15] M P Paoli, D Phil Thesis, Oxford University 1988
- 
- 
- 
- 
- 

## Development of a chopper spectrometer at KENS

*M. Arai, M. Kohgi\**, *M. Itoh\**, *H. Iwasa\*\**, *N. Watanabe, S. Ikeda, and Y. Endoh\**  
National Laboratory for High Energy Physics  
Oho-Machi, Tsukuba-gun  
Ibaraki-Ken, 305  
JAPAN

\*Department of Physics, Tohoku University

\*\*Department of Engineering, Hokkaido University

### 1. Introduction

A direct geometry chopper spectrometer combined with an advanced pulsed neutron source has a promising feasibility for its wide accessible dynamic range in  $Q$ - $\omega$  space and for the applicable various fields of high energy magnetic excitations, molecular dynamics and dynamics of liquids and glasses. The recent scientific requirements of measuring high energy excitations caused the decision to build a chopper spectrometer at KENS.

The development of a sophisticated magnetic bearing made it possible to realize a short chopper burst, due to the high speed revolution, as narrow as the neutron pulse width from a moderator in the epithermal neutron region, providing higher momentum and energy resolution with less sacrifice in intensity.

In this report we discuss a spectrometer called INC, which is under construction at KENS, aiming at neutron scattering with an energy transfer from 20 to 1000 meV and a momentum transfer from  $0.3$  to  $40 \text{ \AA}^{-1}$ .

### 2. Design Performance

INC was installed at beam hole H-6, which views a polyethylene moderator at room temperature. This beam line has the widest and longest available space, so that INC can perform at its highest ability by arranging the detector arrays at a wide scattering angle. However, the flight path of 7m from the bulk shield with 4m thick was the most important restriction for designing the spectrometer. We tried to find optimal parameters to achieve better performance under this restriction. We adopted a horizontal layout rather than a vertical one, and took the parameters  $L_1=7\text{m}$ , the distance between the moderator and the monochromating chopper,  $L_2=1.3$  or  $2.5\text{m}$ , between the sample and the detector, and  $L_3=1\text{m}$ , between the chopper and the sample. ( $L_2$  is  $2.5\text{m}$  for the scattering angle  $5^\circ$ - $25^\circ$  for the lefthand side detector bank and  $5^\circ$ - $40^\circ$  for the righthand side detector bank from the downstream point of view, while  $1.3\text{m}$  for  $40^\circ$ - $130^\circ$ .) These parameters satisfy most of our required performance as discussed below.

## 2.1. Accessible Range in Q- $\omega$ Space

The detectors cover the scattering angle from 5° to 130° and give a wide accessible range in Q- $\omega$  Space. Figure 1 shows the accessible Q- $\omega$  space at the scattering angles of 5°, 11°, 25°, 40°, 80° and 130° with the incident energies of 100, 400 and 1000 meV. As it is well known, due to the kinematic constraint of neutrons, small angle scattering with high energy neutrons is indispensable in measuring the scattering with high energy transfer at smaller Q, which is especially important in high energy magnetic excitations.

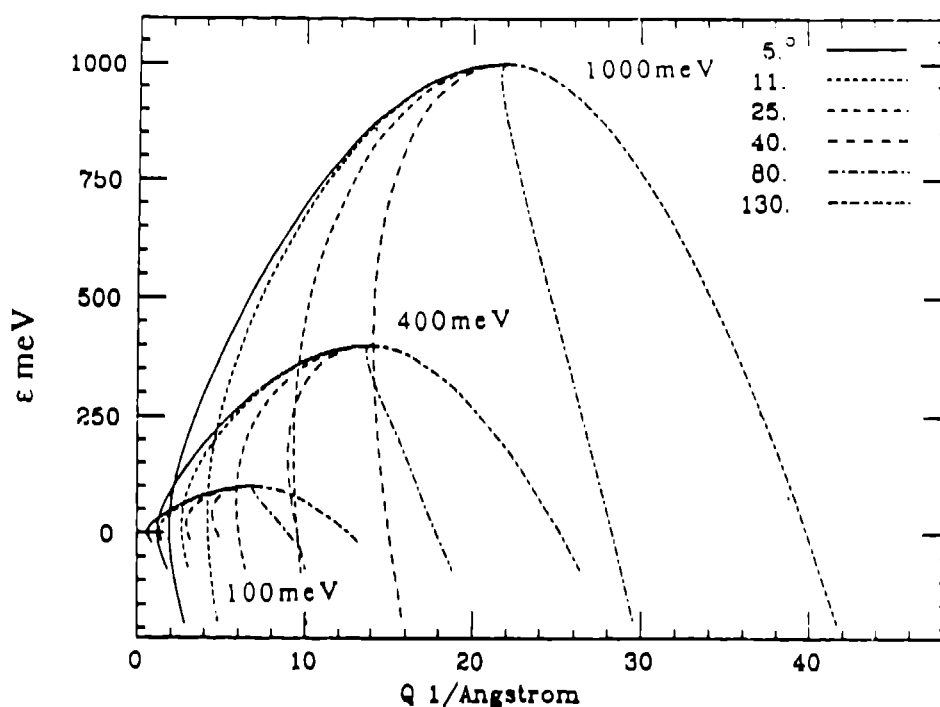


Fig. 1 The Q- $\omega$  space accessible with scattering angles of 5°, 11°, 25°, 40°, 80° and 130° for the incident energies of 100, 400, and 1000 meV.

## 2.2. Resolutions

The energy resolution is essentially determined by two dispersive parts of R1 and R2 due to the chopper opening time width and the neutron burst pulse width at the moderator, as described below, and can be expressed in a good approximation as<sup>1)</sup>,

$$\frac{\Delta E}{E_i} = \left[ \left( 2R_1 \left[ 1 + \frac{L_1 + L_2}{L_2} \left( 1 - \frac{E}{E_i} \right)^{3/2} \right] \right)^2 + \left( 2R_2 \left[ 1 + \frac{L_1}{L_2} \left( 1 - \frac{E}{E_i} \right)^{3/2} \right] \right)^2 \right]^{1/2}$$

Then the momentum resolution is described using the energy resolution as,

$$\frac{\Delta Q}{Q} = \frac{2mE_i}{h^2 Q^2} \left( \frac{E_i}{4E_f} (\cos(\Phi_0) - \sqrt{\frac{E_f}{E_i}})^2 \left( \frac{\Delta e}{E_i} \right)^2 + \frac{E_f}{E_i} \sin^2(\Phi_0) \Delta\Phi^2 \right)^{1/2},$$

where

$$R_1 = \Delta t_{ch}/t_{ch}, \quad R_2 = \Delta t_m/t_{ch} = \delta_m/L_1, \quad \Delta t_{ch} = \frac{W}{2v_p} P(u),$$

$$P(u) = 1 + \frac{u}{4} \quad \text{for} \quad 0 < u < 0.8$$

$$P(u) = 2 + u - (4u - u^2)^{1/2} \quad \text{for} \quad 0.8 < u < 2$$

$$P(u) = u \quad \text{for} \quad 2 < u$$

$$u = \frac{W_{minet}}{L_1} / \frac{W}{D}$$

$$W_{minet} = W_m (\cos(\alpha) - \frac{2\pi L_1 f \sin(\alpha)}{v_0}).$$

The notations used in the above equations are defined below, and shown in Fig.2.

- $\Delta t_m$  : neutron pulse width
- $\delta_m$  : moderator effective thickness
- $\alpha$  : moderator rotation angle
- $W_m$  : moderator width
- $L_1$  : flight path length from the moderator to the chopper
- $L_2$  : flight path length from the sample to the detector
- $L_3$  : flight path length from the chopper to the sample
- $D$  : chopper rotor diameter (assumed to be 10cm)
- $W$  : chopper rotor slit width
- $t_{ch}$  : time of flight at the chopper
- $\Delta t_{ch}$  : chopper burst time width
- $f$  : revolution frequency of the chopper (assumed to be 600Hz)
- $v_p$  : chopper peripheral speed ( $v_p = \pi D f$ )
- $\Phi_0$  : scattering angle
- $\Delta\Phi$  : angular ambiguity by a detector (detector diameter 2.5cm)
- $v_0$  : velocity of incident neutrons
- $E_i$  : incident energy of neutrons
- $E_f$  : final energy of neutrons
- $e$  : energy transfer
- $\Delta e$  : ambiguity in energy
- $k_i$  : wave number of incident neutrons
- $Q$  : momentum transfer
- $\Delta Q$  : ambiguity in momentum

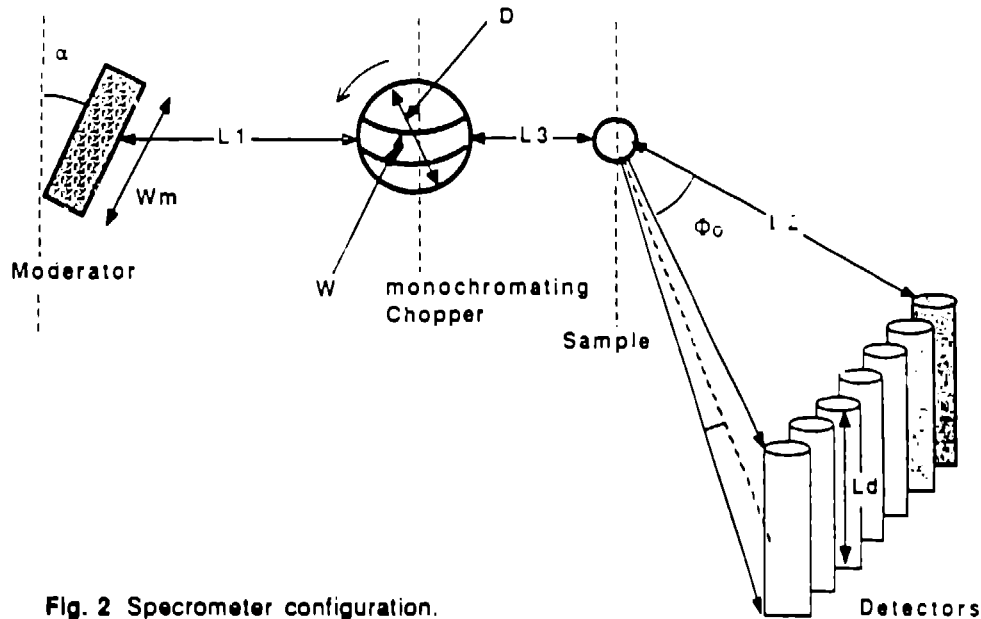


Fig. 2 Specrometer configuration.

For the room temperature moderator in KENS, a neutron pulse width of  $\Delta t_m = 1.5/\sqrt{E}$  [eV]  $\mu s$  is a good approximation in the epithermal neutron range above 250meV, which gives 2.1cm for  $\delta_m$ , but becomes longer with an asymmetric long tail below 250meV. For example, it is about 10 $\mu s$  at  $E_i=100$ meV. The moderator has angle clockwise by 15° to the H-6 beam line, and this configuration gives the optimal time focusing for 500meV. The moderator width  $W_m$  is 8cm. The slit width  $W$  of the chopper rotor is determined from  $\Delta t_{ch} = W/v_p$ , with the optimizing condition  $\Delta t_{ch} = \Delta t_m$ . For example at the incident energy of 300meV, the slit width becomes 0.10cm.

In Fig.3 the energy resolution  $\Delta e/E_i$  is plotted as a function of  $e/E_i$ . The solid line is for  $L_2=2.5$ m, and the upper broken line is for  $L_2=1.3$ m. The resolution of HET (high resolution chopper spectrometer at ISIS, RAL) is also plotted as a reference.

Figure 4 shows  $\Delta Q/Q$  at an  $e$  of  $0.2E_i$ ,  $0.4E_i$ ,  $0.6E_i$  and  $0.8E_i$  as a function of  $Q/k_i$ . The discontinuities at  $Q/k_i=0.7$  correspond to  $\Phi=40^\circ$ , where  $L_2$  changes from 2.5m to 1.3m.

### 2.3. Required Resolution

Here we do calculations using actual scientific examples to estimate the feasibility with the designed resolutions.

#### i) High Energy Magnetic Excitations

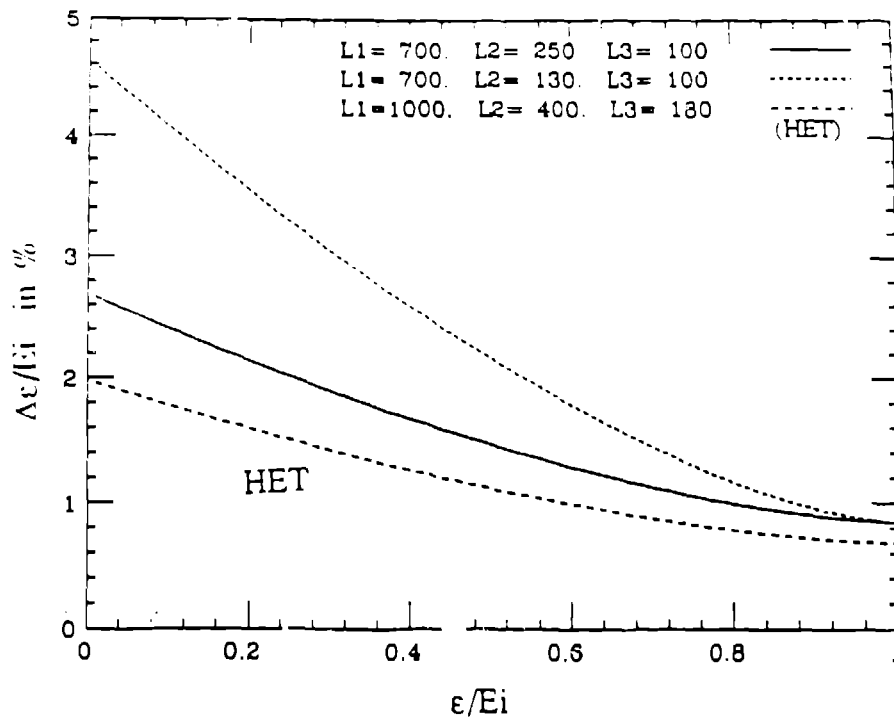


Fig. 3 The energy resolution  $\Delta\epsilon/E_i$  as a function of  $\epsilon/E_i$ . The solid line is  $L_2 = 2.5$  m and upper broken line is  $L_2 = 1.3$  m. The resolution of HET is also plotted as a reference ( $L_1 = 10$ ,  $L_2 = 4$  and  $L_3 = 1.8$  m).

We consider the crystal field splitting in  $UO_2$  demonstrated by HET<sup>2)</sup>. They observed excitations around 150meV with FWHM about 6meV. Now we suppose  $E_i = 250$ meV and  $\epsilon = 150$ meV with  $Q < 4.5 \text{ \AA}^{-1}$ . For this condition the scattering angle  $\Phi < 12^\circ$  is required, and the result is shown in the table below. We can resolve those excitations by a close shave.

$E_i$	$\Phi$	$L_2$	$\epsilon$	$\Delta\epsilon(\text{calc.})$	FWHM(obs.)
250meV	$< 12^\circ$	2.5m	150meV	3meV	6meV

#### ii) $S(Q, \omega)$ of glassy materials

We examine the following extreme examples, although glassy materials in general do not have sharp structure in  $Q-\omega$  space<sup>3)</sup>.

$SiS_2$  glass has an exceptionally sharp excitation as measured in the Raman spectrum at  $420\text{cm}^{-1}$  (52meV) with FWHM =  $20\text{cm}^{-1}$  (2.4meV)<sup>4)</sup> corresponding to the A1 mode. When  $E_i = 100$ meV, the resolutions are as follows.

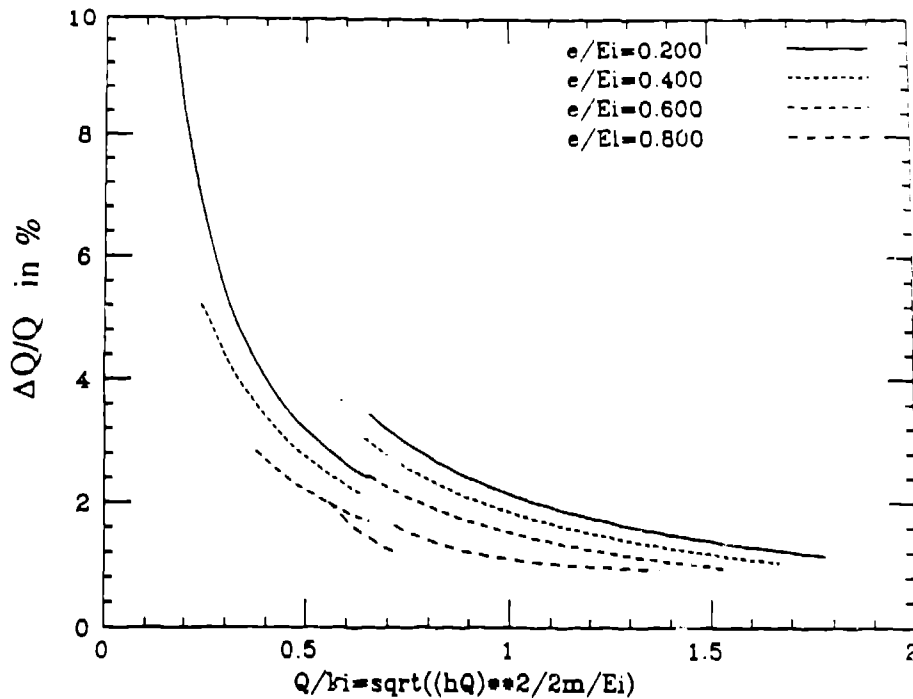


Fig. 4 The momentum resolution  $\Delta Q/Q$  at  $e$  of 0.2  $E_i$ , 0.4  $E_i$ , 0.6  $E_i$  and 0.8  $E_i$ , as a function of  $Q/k_i$ . The discontinuities at  $Q/k_i = 0.7$  correspond to the scattering angle  $\phi = 40^\circ$ , where  $L_2$  changes from 2.5 m to 1.3 m.

$E_i$	$L_2$	$e$	$\Delta e(\text{calc.})$	FWHM(obs.)
100meV	1.3m	52meV	4.0meV	2.4meV
100meV	2.5m	52	2.8	2.4

The energy resolution  $\Delta e$  for  $L_2 = 2.5\text{m}$  is just comparable to the natural width of the excitation.

In some glasses<sup>5)</sup>, there is a first sharp diffraction peak (FSDP) in  $S(Q)$  at around  $1 \text{ \AA}^{-1}$  with FWHM =  $0.2 \text{ \AA}^{-1}$ . When we take  $E_i = 100\text{meV}$ , although this condition is not optimal for measuring elastic scattering at  $Q = 1 \text{ \AA}^{-1}$ , the momentum resolution  $\Delta Q$  is again comparable to the FWHM of the FSDP as shown in the table below. From the considerations above, we believe that the resolution of INC are reasonable for usual case.

$E_i$	$\phi$	$L_2$	$Q$	$\Delta Q(\text{calc.})$	FWHM(obs.)
100 meV	$8^\circ$	2.5m	$1.0 \text{ \AA}^{-1}$	$0.15 \text{ \AA}^{-1}$	$0.2 \text{ \AA}^{-1}$



### 3. Chopper System

#### 3.1. Monochromating Chopper and Background Suppression Chopper

A chopper system is supplied from RAL as a part of the UK-Japan collaboration. The chopper is equipped with a magnetic bearing system developed at KFA, Jülich<sup>6</sup>. The chopper is almost the same as that of MARI (multi-angle rotor instrument at ISIS). The rotor can be spun at 600Hz with  $\pm 0.2\mu\text{s}$  phase ambiguity for fixed frequency operation, and is designed to rotate clockwise when viewed from the top in order to realize time focusing. We will have four rotors with different slit packages, which are optimized to  $E_i = 50, 100, 200$  and  $500\text{meV}$ . The beam aperture of the chopper is  $6 \times 6\text{cm}^2$ .

In order to suppress delayed fast neutrons from the uranium target as well as fast burst neutrons, a background suppression chopper is indispensable for INC. We are developing a mechanical chopper system for this purpose.

#### 3.2. Phasing

In order to achieve the required resolution, the chopper rotor must be phased accurately with the accelerator having a time ambiguity of about  $\pm 5\mu\text{s}$  in successive beam extractions. We have developed electronics to solve this problem.<sup>7)</sup> There is an acceptable time band for the extraction of the proton beam from the Booster synchrotron of about  $\pm 50\mu\text{s}$  centered at the peak magnetic field. Within the acceptable band, the beam can be extracted according to a request signal from the chopper. Otherwise, the beam is extracted automatically at the end of the band. Figure 5 shows typical results of the phasing experiment using the Harwell Mk VIII rotor spinning head at a rotor revolution speed of 500rev/s. In the figure the distribution of the extraction time after request signal is plotted. The results show that the beam extraction time is phased to the request signal with a time ambiguity of  $\pm 0.4\mu\text{s}$  and a duty factor of 99%. These values are sufficient for practical operation.

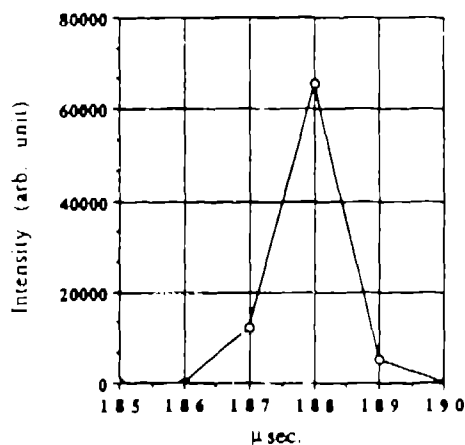


Fig. 5 Typical results of a phasing experiment using Harwell Mk VIII rotor spinning head at a rotor revolution speed of 500 rev/s. The distribution of the extraction time after request signal is plotted.

#### 4. Collimator System

The design of a collimator system was essentially based on the ray diagram consideration<sup>8</sup>). The collimator system consists of two parts. The inner collimator in the bulk shield and the outer collimator between the two choppers consist of sintered  $B_4C$ , steel and borated resin (boric-acid 40%, polyethylene-beads 40%, epoxy-adhesive 20% in weight) making an image  $6 \times 6 \text{ cm}^2$  at the sample position. They were designed so that the iron soften fast neutron spectrum, the hydrogenous compound slows down neutrons to be absorbed by the boron, and the scattered neutrons are captured by  $B_4C$  scraper projecting inward in the collimator. Figure 6 shows the details of the collimators.

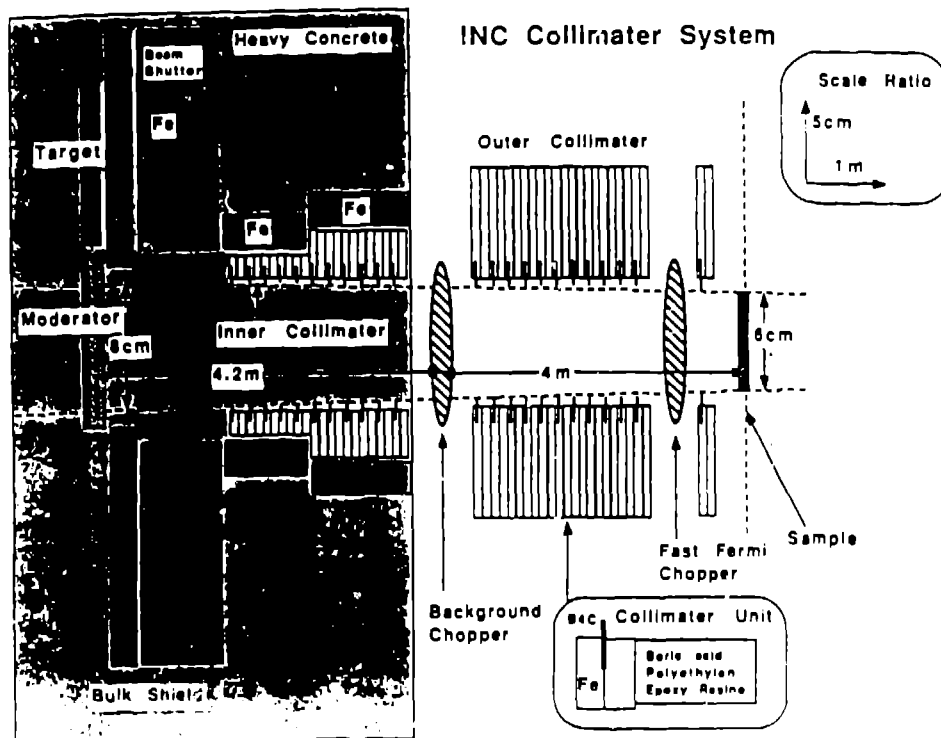


Fig. 6 Details of the collimators. The inner collimator in the bulk shield and the outer collimator between two choppers consist of sintered  $B_4C$ , steel and borated resin.

#### 5. Spectrometer

The spectrometer shield enclosing the scattering chamber is mainly made of borated resin (boric-acid polyethylene-beads epoxy-adhesive combination, 45, 45, 10% in weight) 30 - 40cm thick, and partly made of ordinary concrete 30 - 50cm thick. The thickness of these shields was determined by dose measurements under

actual conditions. The shield has a shield door for access to the detectors, and there is a sliding overhead shield for access to the sample.

Figures 7 (a) and (b) show the layout of INC. The scattering chamber consists of two parts; a sample chamber (high vacuum) and a detector chamber (low vacuum). They are separated by a thin aluminum window 0.1mm thick. The detector chamber has 13 detector-windows of aluminum plates 2mm thick. The low angle bank has a flight path length of 2.5m with six-fold detector arrays covering scattering angles from 5° to 11°, which can accommodate 80 detectors (6", 8", 10" and 12" in length, 1" in diameter). The medium angle bank consists of 50 detectors (12" in length, 1" in diameter) in single detector arrays, which extend from 11° to 25° at the lefthand side and from 11° to 40° at the righthand side from the downstream point of view. The high angle bank has a flight path of 1.3m, covering scattering angles from 40° to 130°, and can accommodate up to 80 detectors (12" in length, 1" in diameter). In order to cover the angles between the detector banks, there are insertion detector banks in the detector chamber.

The inside of the detector chamber is completely covered by B<sub>4</sub>C resin tiles 10mm thick, so that the detectors see only the sample.

## 6. Data Acquisition System

### 6.1. Compact Charge-Sensitive Amplifier

We have developed low-cost high-performance charge-sensitive amplifier for multi-detector use<sup>9)</sup>, which has excellent performance of very low noise with very high counting rate. The amplifier includes a charge-sensitive preamplifier, a pulse shaping amplifier and a discriminator. The size is very compact and is 3 × 7 × 10cm<sup>3</sup>. This made it possible to make 200 detectors for INC at a low cost.

### 6.2. Data Acquisition Electronics

We have developed new data acquisition electronics. The time boundary of the time analyzer can be set in arbitrary way by computer to minimize the time resolution to fit with the other contributions such as neutron burst pulse width and chopper burst width, and can be used very flexibly. The details are described in Ref. 10.

## 7. Discussions

### 7.1. Intensity and Background

Here we show the estimated counting rate from U<sup>4+</sup> (UO<sub>2</sub>) in the INC, comparing with the measured background level and the results from the HET<sup>2)</sup>.

The cross section for crystal field splitting averaged over all direction is given by<sup>11)</sup>

$$\frac{d^2\sigma}{d\Omega dk} = r_0 \frac{k_f}{k_i} P_n ( a j_0^2 + b j_0 j_2 + c j_2^2 + \dots ) \delta(e - E_n + E_n).$$

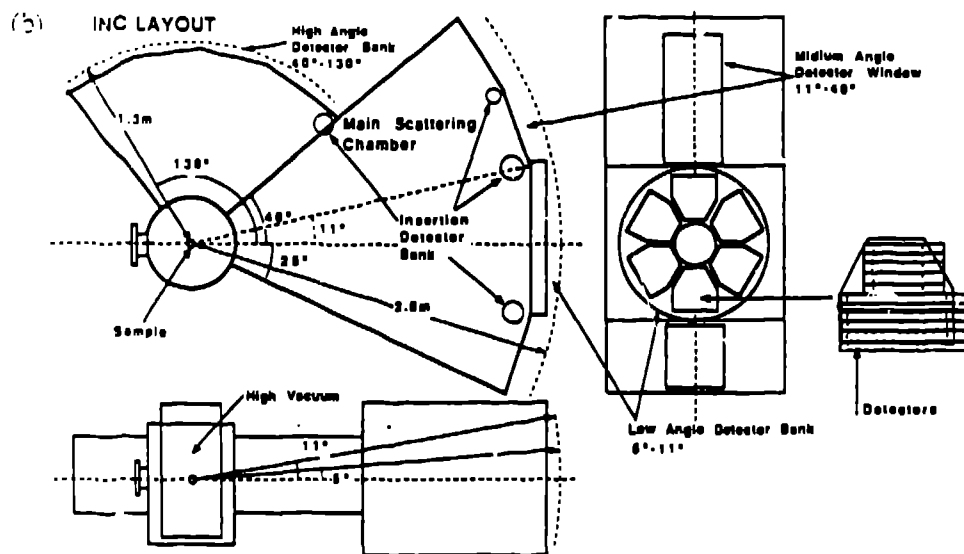
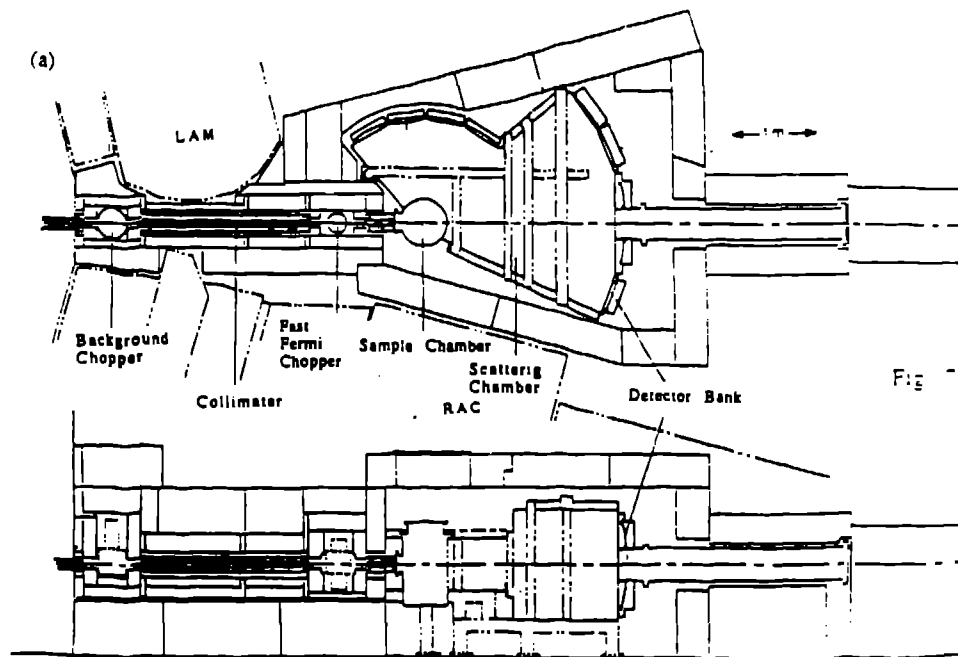


Fig. 7 Layout of the INC.

Here,  $j_k$  is the spherical Bessel function of order  $k$ . We consider the case of the  $\Gamma_5 \rightarrow \Gamma_3$  transition, i.e. from the ground level ( $n=5$ ) to the first excitation level ( $n=3$ ) with  $e=180\text{meV}$ .  $P_3$  is product of the degeneracy and the population factor, which is about  $1/3$ .  $a$  is the matrix element for the transition, and is 1.28.  $r_0$  is  $\left(\frac{e^2}{m_e c^2}\right)^2 = 0.29 \times 10^{-24}$ . In case that the total momentum is a good quantum number, the zeroth Bessel function is dominant and the cross section can be written by

$$\frac{d^2\sigma}{d\Omega de} = r_0 \frac{k_f}{k_i} P_3 a j_0^2 \delta(e - E_5 + E_3).$$

We take  $E_i=300\text{meV}$  ( $k_i=12.2\text{\AA}^{-1}$ ),  $E_f=120\text{meV}$  and  $e=180\text{meV}$ . The cross section at  $Q=4.5\text{\AA}^{-1}$  (measured by the  $5^\circ$  detector) with  $j_0 = 0.6$  is

$$\begin{aligned} \left\langle \frac{d^2\sigma}{d\Omega de} \right\rangle &= (-0.54 \times 10^{-12})^2 \frac{1}{3} \sqrt{E_f/E_i} \times 1.28 \times 0.6^2 \delta(e - E_5 + E_3) \\ &= 0.0256 \times 10^{-24} \delta(e - E_5 + E_3) \quad [\text{cm}^2/\text{meV}/\text{sr}] \end{aligned}$$

Then the counting rate (integrated intensity of  $I(e)$ ) at a detector is

$$\begin{aligned} \int I(e) de &= \int de i(E_i) N \left\langle \frac{d^2\sigma}{d\Omega de} \right\rangle T(E_i) f(E_f) P C d\Omega \\ &= 15.6 \text{ [n/day/detector}/\mu\text{A}] \end{aligned}$$

The flux intensity at the sample position  $i(E_i)$  is expressed as,

$$i(E_i) = r / (L_1 + L_3)^2 \Delta e / E_i \quad [\text{n}/\text{cm}^2/\text{p}].$$

The values used are as follows,

- the intensity of neutrons from a moderator per steradian per eV at  $E_i$  per proton expressed by  $r$  is

$$r = 1.0 \times 10^{-2} \times \left( \frac{E_i(0.3\text{eV})}{E_i(1\text{eV})} \right)^{-0.88} \quad [\text{n}/\text{sr}/\text{eV}/\text{p}] \quad \text{for } E_i = 300\text{meV}.$$

- $\Delta e/E_i = 1.3\%$  at  $180\text{meV}$ , i.e.  $\Delta e = 3.9\text{meV}$  or  $\Delta t = 8\mu\text{s}$  at  $t = 516\mu\text{s}$ .
- sample amount is  $N = 0.3\text{mol}$  ( $1.8 \times 10^{23}$  U atoms) assuming 10% scatterer and the beam size of  $60(\text{wide}) \times 60(\text{long}) \times 2(\text{thick})\text{mm}^3$ .
- $T(E_i)$  is the transmission of the chopper, typically 0.5.
- $f(E_f)$  is the detector efficiency, 0.8.
- $P$  is the number of proton pulses in a day,  $1224 \times 10^3$  pulses/day.
- $C$  is the number of protons per proton pulse per  $\mu\text{A}$ ,  $3.1 \times 10^{11}$  ppp $\mu\text{A}$ .
- $d\Omega$  is the solid angle subtended by a detector ( $2.5 \times 30\text{cm}^2$ ) at the  $2.5\text{m}$  position,  $1.2 \times 10^{-3}$  sr.

If the counting rate estimated above is spread over 20 meV (50 $\mu$ s), we have 0.33cnt/day/ $\mu$ A/detector/ $\mu$ A. This value should be compared with the background counts, 0.034 cnt/day/ $\mu$ A/detector/ $\mu$ A, which was obtained with a reference detector surrounded by 2cm thick B<sub>4</sub>C resin and 30cm thick boric acid.

The counting rates from UO<sub>2</sub> measured in the HET were scaled by the parameters of KENS, and are 0.18 for the signal and 0.056 for the background. The counting rate 0.33 estimated above shows fairly good agreement with the scaled value of HET measurement. The thickness of the constructed shield seems to be good enough for distinguishing the signal from the background.

## 7.2. Counting Rate

It turns out that the performances of INC satisfy most of the requirements for the targeted scientific fields. The counting rate per unit solid angle of INC,  $I(e)_{INC}$ , is compared in a Table below with HET and MARI,

	$L_1$ (m)	$L_3$ (m)	$L_2$ (m)	$P$ ( $\mu$ A)	$M$	$A$ (cm <sup>2</sup> )	$I(e)/I(e)_{INC}$
INC	7.2	1	2.5	8	2	6 x 6	1
HET	10	1.8	4	200	1	5 x 5	1.2
MARI	10	1	4	200	1	6 x 6	2.0

where  $I(e) = 1/(L_1+L_3)^2/L_2^2 \Delta e/E_1 \times P \times M \times A$ .  $P$  is the proton current,  $M$  is the target-moderator coupling factor,  $A$  is the sample area and  $I(e)/I(e)_{INC}$  is the ratio of the expected intensity at a detector for the spectrometer to that of INC.









As we see here, the counting rate per unit area at the detector position in INC has encouraging value even compared with that in HET and MARI in spite of the lower proton current at KENS. Therefore INC could produce reasonable scientific output with a slightly lower resolution.

## Acknowledgements

We acknowledge Dr. C.K. Loong for the helpful advice in the early stage of the design work. We also acknowledge Dr. A.D. Taylor, R. Ward and Mr. T.J.L. Jones for stimulating discussions on the chopper spectrometer and the chopper system.

## References

- 1) C. J. Carlile, A. D. Taylor and W. G. Williams; MARS - A Multi-Angle Rotor Spectrometer for SNS, RAL-85-052.
- 2) A. D. Taylor, B. C. Boland, Z. A. Bowden and T. J. L. Jones; HET The High Energy Inelastic Spectrometer at ISIS, RAL-87-012.
- 3) M. Aral, D. L. Price, S. Sussman, K. J. Volin and U. Walter, Phys. Rev. B37, 1988, 4240.
- 4) M. Tenkover, M. A. Haste and R. K. Grasselli, Phys. Rev. Lett. 51, 1983, 404.
- 5) R. W. Johnson, D. L. Price, S. Sussman, M. Aral, T. I. Morrison and G. K. Shenoy J. Non-Cryst. Solids 75, 1986, 57

- 
- 
- 
- 
- 
- 
- 
- 
- 6) T. J. L. Jones, J. H. Parker, I. Davidson, K. Boden and J. K. Fremerly, Proc. ICANS VIII 1985 at RAL, UK, p707.  
7) M. Arai, M. Kohgi, Y. Arakida and M. Hosoda, KENS report VI 1987 KEK p68.  
8) W. S. Howells, Proc. ICNAS-IV 1980 at KEK, Japan, p359  
9) M. Arai, M. Hosoda and M. Kohgi, unpublished  
10) M. Arai, M. Furusaka, M.W. Johnson and S. Satoh, KENS report VII 1988 KEK p24.  
11) S. W. Lovesey; Theory of neutron scattering from condensed matter. 1984, Vol. 2, p242.

# On the kinematics and resolution of spectrometers for neutron Brillouin scattering

*R. A. Robinson*  
Los Alamos Neutron Scattering Center  
Los Alamos National Laboratory  
Los Alamos, New Mexico 87545  
USA

**ABSTRACT:** Neutron Brillouin scattering involves measurement of excitations at smaller  $Q$  values than is currently customary. We outline the kinematic constraints on scattering angle and incident energy for excitations with both linear dispersion (sound waves) and parabolic dispersion (ferromagnetic spin waves), and discuss the resolution characteristics of the chopper spectrometer proposed for LANSCE which should be suitable for such studies. In particular, we demonstrate that longitudinal resolution focussing can be exploited both in neutron energy gain and in neutron energy loss.

## 1. Introduction

In general, measurements of sound velocity by means of inelastic neutron scattering have been made in higher-order Brillouin zones (i.e., not at the reciprocal-space origin) of single crystals using reactor triple-axis spectrometers<sup>(1)</sup>. If single crystals are unavailable, this method cannot be used. Nor can it be used for amorphous solids, liquids or gases, in which there is no translational symmetry and hence no reciprocal lattice. In these cases, it is necessary to work close to the wave-vector space origin, in a manner analogous to conventional optical Brillouin scattering. Some measurements of this type have been made on triple-axis spectrometers<sup>(2)</sup> as well as reactor time-of-flight machines<sup>(3)</sup>, but the momentum transfers reached have been relatively large. This necessitates the use of neutron energies rather large in comparison with the energy of the acoustic phonon concerned and very small scattering angles. This is a demanding combination: the use of high neutron energies means that the resolution requirements are tight, while working close to the straight-through beam, and its attendant background will degrade the signal-to-noise ratio of the experiment. However, with the new high-intensity accelerator-based sources such as LANSCE at Los Alamos and ISIS at Rutherford Appleton Laboratory, these experiments should be feasible.

It must be added that the requirement for high incident energies and small scattering angles arises in other areas, for instance, the measurement of highly dispersive spin waves in amorphous magnets<sup>(4)</sup>. It is the purpose of this article to address the general question of kinematics and resolution for a neutron Brillouin scattering spectrometer and to propose a specific configuration that could be implemented at one of the new high-intensity spallation sources.



For the purpose of discussion, we will consider two sound wave and two magnetic cases: firstly, a material with sound velocity of  $1000 \text{ ms}^{-1}$  down to a wave-vector  $Q = 0.05 \text{ \AA}^{-1}$  and secondly, a material with sound velocity of  $6000 \text{ ms}^{-1}$  down to  $Q = 0.3 \text{ \AA}^{-1}$ . The former corresponds loosely to a typical liquid, while the latter corresponds to the longitudinal sound velocity in a fairly hard solid like aluminium, a case that has been considered previously by Reichardt<sup>(9)</sup> for SNQ. In both of these cases, we will find that one requires scattering angles in the vicinity of  $1^\circ$ . In addition we consider ferromagnets with spin wave stiffnesses  $D$  of  $30 \text{ meV\AA}^2$  and  $300 \text{ meV\AA}^2$ . The former of these corresponds loosely to a weak itinerant ferromagnet like  $\text{Ni}_2\text{Al}$ <sup>(6)</sup>, and the latter corresponds loosely to a strong itinerant ferromagnet like iron or nickel<sup>(7,8)</sup>.

An abbreviated version of this work has already appeared elsewhere<sup>(9)</sup>.

## 2. General kinematical considerations

In general, when designing a spectrometer or deciding how to perform a given experiment, one has some idea of the excitation energy  $E$  and the wave-vector  $Q$  that one would like to reach. The normal energy and momentum conservation laws for a neutron scattered by an angle  $\phi$  then determine the incident energy  $E_1$  that must be used:

$$E_1 = \frac{\hbar^2}{4m \sin^2 \phi} \left\{ (Q^2 + \epsilon \sin^2 \phi) \pm \cos(\phi) \sqrt{Q^4 - \epsilon^2 \sin^2 \phi} \right\} \quad (1)$$

where

$$\epsilon = \frac{2mE}{\hbar^2} \quad (2)$$

These equations are perfectly general and are not specific to Brillouin scattering or time-of-flight instruments. There are two solutions to eq.(1). However, they are not always both physical. For instance, in the case of elastic scattering ( $\epsilon \rightarrow 0$ ), the positive root gives

$$E_1 = \frac{\hbar^2 Q^2}{2m \sin^2 \left( \frac{\phi}{2} \right)} \quad (3)$$

which corresponds to Bragg's Law, while the negative root gives

$$E_1 = \frac{\hbar^2 Q^2}{2m \cos^2 \left( \frac{\phi}{2} \right)} \quad (4)$$

which is clearly unphysical. In fact, it can be shown that the negative root is unphysical if  $|k| < Q^2$  (see appendices for proof.) This constraint is shown in Fig. 1, along with the dispersion relations for sound waves with  $v = 1000, 2000$  and  $6000 \text{ ms}^{-1}$ . For any value of  $Q$  in the Brillouin scattering regime, one has two solutions and the negative root is to be preferred as it gives the lower incident energy. For ferromagnetic spin waves, with a dispersion relation  $E = DQ^2$ , there are two solutions if  $D > 2m/\hbar^2$  ( $0.4826 \text{ meV \AA}^2$ ). As most systems are stiffer than this, again one is in the two-solution regime and the negative root is to be preferred. In other words, although the relative energy changes in Brillouin scattering are small, it is not a small perturbation on Bragg scattering, or one can say that Brillouin scattering is closer to the  $\phi \rightarrow 0$  limit than the  $E \rightarrow 0$  limit.

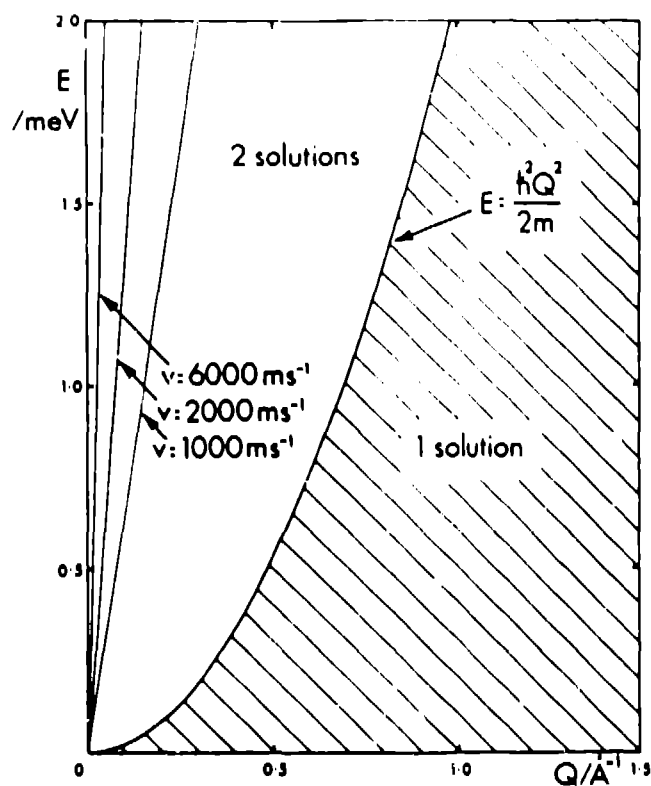


Fig. 1 The region of phase space in which there are two physical solutions to Eq. (1) and in which there is only one. While the high-energy solution is the only one for elastic scattering ( $E = 0$ ), for any  $Q$ -values and sound velocities appropriate for Brillouin scattering, both solutions to Eq. (1) are physical and the low-energy solution is preferred.

For any given E and Q, there is a maximum possible scattering angle  $\phi_{\max}$  given by

$$\sin^2 \phi_{\max} = \frac{Q^4}{\epsilon^2} \quad (5)$$

and a corresponding incident energy  $E_I(\phi_{\max})$  given by

$$E_I(\phi_{\max}) = \frac{\hbar^2}{4m} \left( \frac{\epsilon^2}{Q^2} + \epsilon \right) \quad (6)$$

In addition, there is a minimum possible incident energy  $E_{I_{\min}}$ , corresponding to forward scattering ( $\phi = 0$ ), given by

$$E_{I_{\min}} = \frac{\hbar^2}{8mQ^2} (\epsilon + Q^2)^2 \quad (7)$$

Equations (5), (6) and (7) serve to define the broad angular and energy range within which one must work for any given value of E and Q.

### 3. Application to sound waves

For excitations, like sound waves, with a dispersion relation  $\epsilon = \hbar v Q$ , Equations (5), (6) and (7) become

$$\sin^2 \phi_{\max} = \frac{\hbar^2 Q^2}{4m^2 v^2} \quad (8)$$

$$E_I(\phi_{\max}) = mv^2 + \frac{\hbar v Q}{2} \quad (9)$$

and

$$E_{I_{\min}} = \frac{\hbar^2}{8mQ^2} \left\{ \frac{2mvQ}{\hbar} + Q^2 \right\}^2 \quad (10)$$

As  $Q \rightarrow 0$ ,

$$E_I(\phi_{\max}) \rightarrow mv^2 \quad \text{and} \quad E_{I_{\min}} \rightarrow \frac{mv^2}{2} \quad (11)$$

In other words, the incident energy scale is proportional to  $v^2$  and there is a factor of two available in the choice of  $E_I$ , but no more than that.

The variation of  $E_I$  with  $\phi$  is shown in Figs. 2 and 3 for sound velocities of  $1000 \text{ ms}^{-1}$  and  $6000 \text{ ms}^{-1}$ , respectively.

#### 4. Application to ferromagnetic spin waves

For ferromagnetic spin waves with  $E = DQ^2$ , Equation (1) can be written in the simplified form

$$E_I = \frac{\hbar^2 Q^2}{4m \sin^2 \phi} \left\{ 1 + \frac{2mD \sin^2 \phi}{\hbar^2} \pm \cos(\phi) \sqrt{1 - \frac{4m^2 D^2 \sin^2 \phi}{\hbar^4}} \right\} \quad (12)$$

Clearly,  $E_I$  is simply proportional to  $Q^2$  and, as is well known<sup>(10)</sup>,  $\phi_{\max}$  is independent of  $Q$ :

$$\sin^2 \phi_{\max} = \frac{\hbar^4}{4m^2 D^2} \quad (13)$$

Equations (6) and (7) become

$$E_I(\phi_{\max}) = \frac{\hbar^2 Q^2}{4m} \left\{ \frac{4m^2 D}{\hbar^4} + \frac{2mD}{\hbar^2} \right\} \quad (14)$$

and

$$E_{I_{\min}} = \frac{\hbar^2 Q^2}{8m} \left( \frac{2mD}{\hbar^2} + 1 \right)^2 \quad (15)$$

Note that while the angular range available is independent of  $Q$ , the incident energies required for such experiments rise in proportion to  $Q^2$ .

The variation of  $E_I$  with  $\phi$  is shown in Figs. 4 and 5 for spin wave stiffnesses of  $30 \text{ meV \AA}^2$  and  $300 \text{ meV \AA}^2$ , respectively.

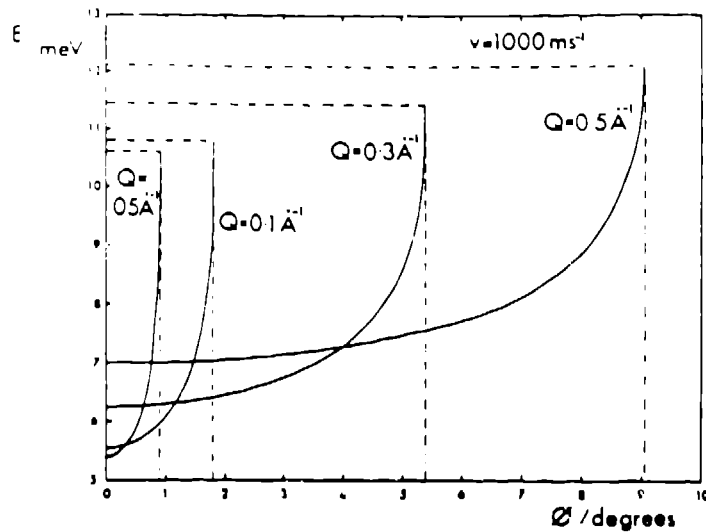


Fig. 2 Plot of Incident energy  $E_1$  versus scattering angle  $\phi$  for a sound velocity of  $1000 \text{ ms}^{-1}$ . The low-energy solution of Eq. (1) is plotted for  $Q = 0.05, 0.1, 0.3$  and  $0.5 \text{ \AA}^{-1}$ . The corresponding energies are  $0.33, 0.66, 1.97$  and  $3.29 \text{ meV}$  respectively. The dashed lines extend to  $\phi_{\text{max}}$  and  $E_1(\phi_{\text{max}})$ , respectively. This figure shows the possible trade-off between incident energy and scattering angle for the chosen value of  $Q$  and the value of  $E$  determined by the choice of  $Q$  and  $v$ .

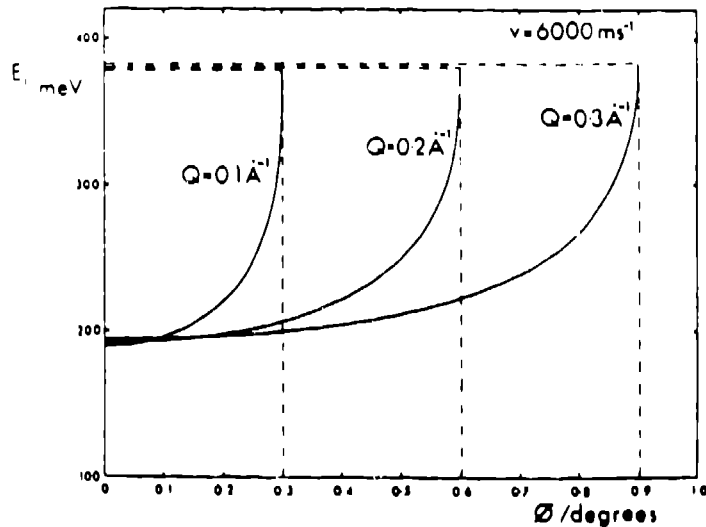


Fig. 3 Plot of incident energy  $E_1$  versus scattering angle  $\phi$  for a sound velocity of  $6000 \text{ ms}^{-1}$ . The low-energy solution of Eqn. 1 is plotted for  $Q = 0.1, 0.2$  and  $0.3 \text{ \AA}^{-1}$ . The corresponding energies are  $3.95, 7.9$  and  $11.85 \text{ meV}$ , respectively. The dashed lines extend to  $\phi_{\text{max}}$  and  $E_1(\phi_{\text{max}})$  respectively. This figure shows the possible trade-off between incident energy and scattering angle for the chosen value of  $Q$  and the value of  $E$  determined by the choice of  $Q$  and  $v$ .

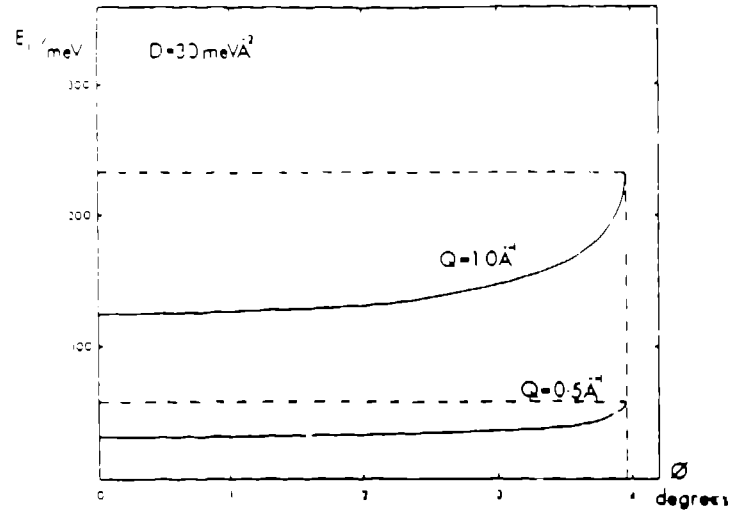


Fig. 4 Plot of incident energy  $E_1$  versus scattering angle  $\phi$  for a spin wave stiffness of  $30 \text{ meV \AA}^2$ . The low-energy solution of Eq. (1) is plotted for  $Q = 0.5$  and  $1.0 \text{ \AA}^{-1}$ . The corresponding energies are 7.5 and 30 meV, respectively. The dashed lines extend to  $\phi_{\text{max}}$  and  $E_1(\phi_{\text{max}})$ , respectively. This figure shows the possible trade-off between incident energy and scattering angle for the chosen value of  $Q$  and the value of  $E$  determined by the choice of  $Q$  and  $D$ .

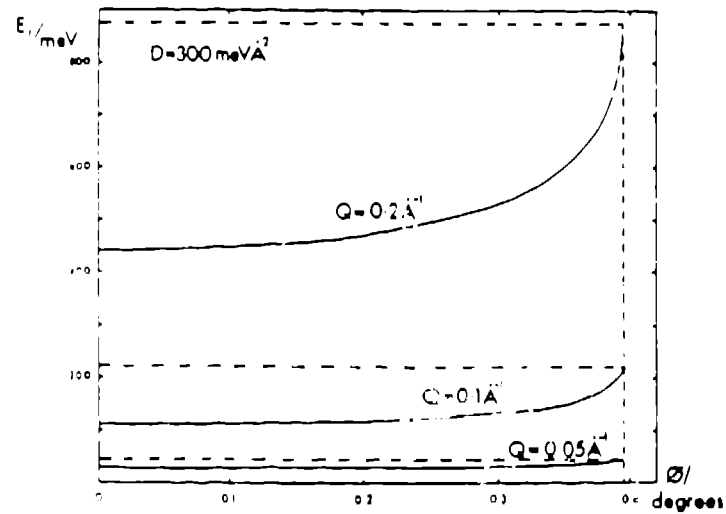


Fig. 5 Plot of incident energy  $E_1$  versus scattering angle  $\phi$  for a spin-wave stiffness of  $300 \text{ meV \AA}^2$ . The low-energy solution of Eq. (1) is plotted for  $Q = 0.05$ ,  $0.1$  and  $0.2 \text{ \AA}^{-1}$ . The corresponding energies are 0.75, 3 and 12 meV, respectively. The dashed lines extend to  $\phi_{\text{max}}$  and  $E_1(\phi_{\text{max}})$ , respectively. This figure shows the possible trade-off between incident energy and scattering angle for the chosen value of  $Q$  and the value of  $E$  determined by the choice of  $Q$  and  $D$ .

## 5 The Instrument

The configuration proposed here is the low-angle flight path of a general-purpose high-resolution chopper spectrometer<sup>(11)</sup> being built at LANSCE. The spectrometer characteristics are given in Table 1. Neutrons emanate from a methane moderator and are monochromated by a 600-Hz phased chopper at a distance of 19 m before striking the sample at 20 m. The secondary flight path will extend a further 10 m for small scattering angles. In the epithermal regime, the incident energy resolution will be approximately 0.5%. This approach contrasts with that proposed by Egelstaff<sup>(3)</sup>, in which a crystal monochromator is used to deflect neutrons out of the direct beam, the hope being that this will reduce the background.

## 6. Resolution considerations

In calculating the full resolution function for an experiment of this type, it is important to know the value of  $\phi_Q$ , defined in Fig. 6 as the angle between  $\underline{Q}$  and the incident wave-vector  $\underline{k}_i$ .  $\phi_Q$  is given, by the sine and cosine rules respectively, as

$$\sin(\phi_Q) = \frac{k_F}{Q} \sin(\phi) \quad (16)$$

and

$$\cos(\phi_Q) = \frac{k_i^2 + Q^2 - k_F^2}{2k_i Q} \quad (17)$$

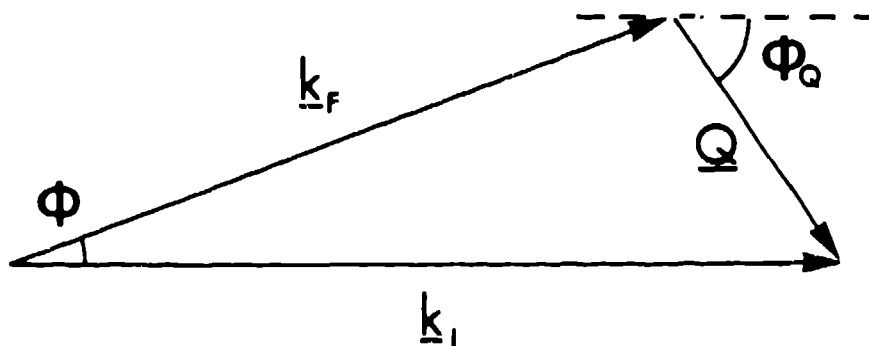


Fig. 6 A scattering triangle showing the definition of  $\phi_Q$ .

The variation of  $\phi_Q$  with  $E$  at fixed scattering angle is shown for one particular case in Fig. 7. For forward scattering ( $\phi = 0$ ),  $\phi_Q \rightarrow 0$  for neutron energy loss, while  $\phi_Q \rightarrow 180^\circ$  for neutron energy gain. When  $\phi = \phi_{\text{max}}$ ,

$$\sin(\phi_Q)^{\phi = \phi_{max}} = \sqrt{\frac{1}{2} \frac{Q^2}{2\epsilon}} \quad (18)$$

For neutron energy loss, this means that  $\phi_Q$  is less than  $45^\circ$ . Clearly,  $\phi_Q$  can be greater than  $45^\circ$ , as shown in Fig. 7, but in that case one can reach the same energy transfer and  $Q$  using a lower incident energy.

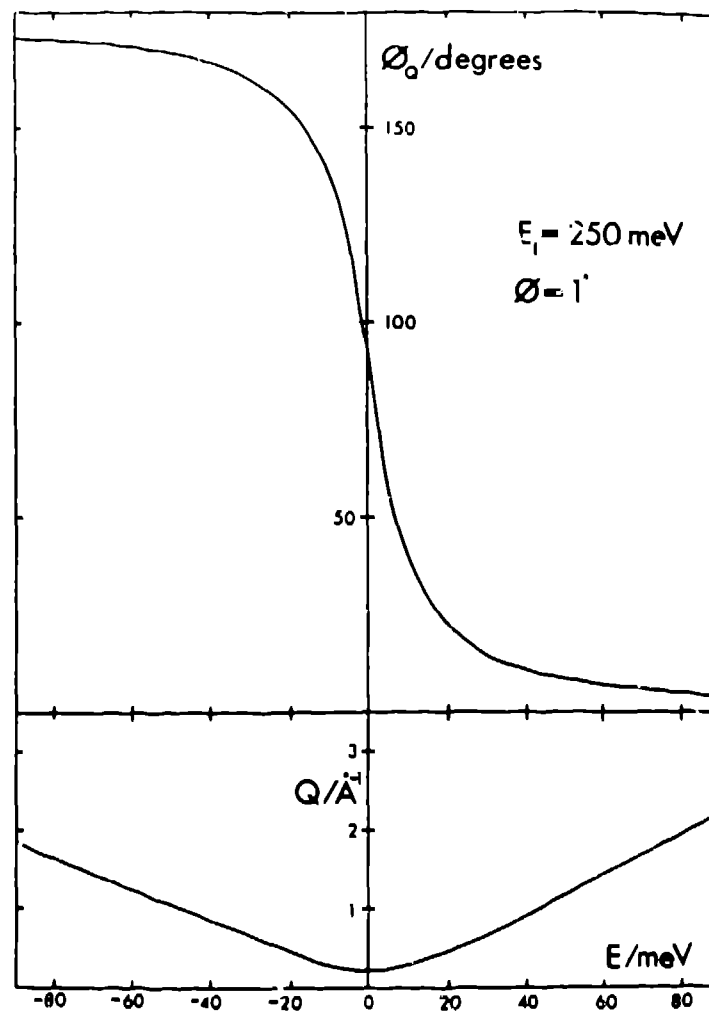


Fig. 7 The variation of (a)  $Q$  and (b)  $\phi_Q$  within a time-of-flight scan at constant angle  $\phi = 1^\circ$  and constant incident energy, as might be observed in a single detector element in an experiment.



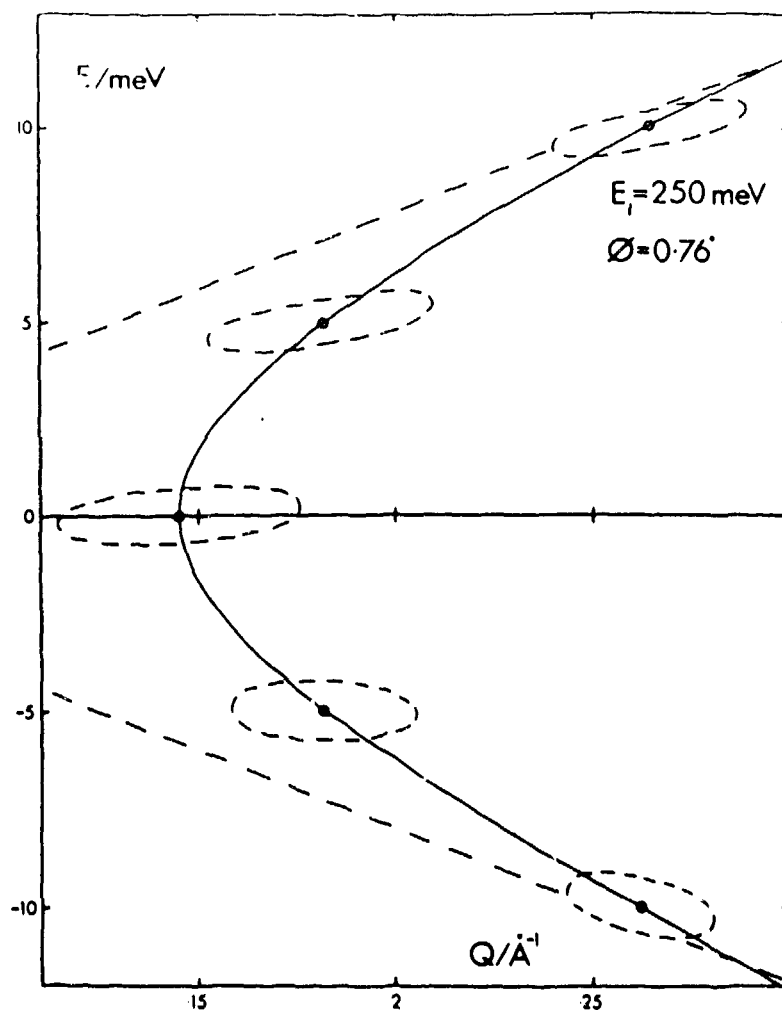
We have done a Monte-Carlo simulation of the instrument for the moderator, chopper and sample characteristics listed in Table 1. The sample thickness is ignored, as is

TABLE 1	
Moderator-Chopper Distance	19 m
Chopper-Sample Distance	1 m
Sample-Detector Distance	4 m between $10^\circ$ and $140^\circ$ up to 10 m between $-10^\circ$ and $+10^\circ$
Moderator	$12.5 \times 12.5 \text{ cm}^2$ liquid methane
Source Repetition Frequency	12 or 24 Hz
Chopper Frequency	600 Hz
Chopper Diameter	10 cm
Chopper Slit Spacing	1 mm or more
Sample Size	up to 5 cm x 7.5 cm

appropriate for small-angle scattering. The detector is assumed to have circular symmetry about the straight-through beam and perfect angular and time resolution. Results for  $E_i = 250 \text{ meV}$  and  $\phi = 0.76^\circ$  are shown in Fig. 8. Clearly, both the energy and the Q resolution are sufficient for this case. Furthermore, the  $t$  and  $\phi$  resolution is such that 2.5-cm-diam. position sensitive detectors at 10 m from the sample will easily have sufficient angular resolution for this experiment. It is also rather striking that there is some focusing (i.e., the resolution ellipse is oriented almost parallel to the dispersion surface for acoustic phonons) both in neutron energy loss and in neutron energy gain. In fact, the focusing is even more enhanced at larger Q values. This type of focusing has been discussed previously for Brillouin scattering experiments on triple-axis spectrometers<sup>(13)</sup>. As one would expect, the  $t$  and  $\phi$  resolution is almost constant over this range of the scan, and the changes in Fig. 8 are mainly due to the fact that  $f_Q$  changes so dramatically, as in Fig. 7. In going from energy loss to energy gain,  $\phi_Q$  goes from being parallel to  $k_x$  to being anti-parallel. Clearly, this type of focusing is not peculiar to chopper spectrometers or even constant- $E_i$  instruments. It will occur on any instrument for which monochromatization uncertainties dominate the resolution and when  $\phi_Q$  is close to  $0^\circ$  or  $180^\circ$ . In principle, this focusing can be exploited in a Brillouin scattering measurement to improve the resolution without loss of intensity. However, the dispersion relation is almost tangential to the time-of-flight locus, so one needs to make constant-Q scans (or some other type of scan, for instance perpendicular to the dispersion curve) to exploit this focusing. This means that one would require rather good angular resolution, which would in turn permit reliable interpolation or two-dimensional rebinning.

## 7. Conclusions

We have discussed the kinematic constraints on doing neutron Brillouin scattering experiments: all the essential information is contained in the negative root of Eq. (1).



**Fig. 8** The  $Q_{||}, E$  resolution for the proposed Los Alamos spectrometer with an incident energy of 250 meV and  $\phi = 0.76^\circ$ . This corresponds to  $v = 6000 \text{ m s}^{-1}$  and  $Q = 0.3 \text{ \AA}^{-1}$ , one of the special cases mentioned in the introduction. The solid curved line is the time-of-flight locus for these parameters and the straight dashed lines are the dispersion relations in neutron energy loss and gain for sound waves with  $v = 6000 \text{ m s}^{-1}$ . The dashed ellipses represent contours at one standard deviation away from maximum assuming scattering from a delta-function in  $Q$  and  $E$ . The total energy widths are in good agreement with the standard analytic expressions given in Ref. 8. Note there is longitudinal resolution focusing both in energy loss and in energy gain. The physical origin of this effect is explained in the text.

For sound waves, the incident energies required are proportional to  $v^2$  while the angular range is proportional to  $Q/v$ . For spin waves, the incident energies required are proportional to  $Q^2$  while the angular range is independent of  $Q$ . Experiments on sound waves become progressively more difficult as  $Q$  decreases, because the scattering angle decreases. In contrast, those on spin waves become more difficult as  $Q$  increases because the incident energy increases very rapidly.

We have shown that the proposed LANSCE spectrometer will have sufficient  $E$  and  $Q$  resolution to perform such experiments and that there is some focusing, could be exploited in such experiments. Finally, the major unresolved question concerns background levels in such experiments, whether they be due to working close to the straight-through beam or to multiple scattering in the sample and its environment.

### Acknowledgements

We are glad to acknowledge a number of fruitful discussions with Drs. J. M. Carpenter and R. Pynn. This work was supported, in part, by the division of Basic Energy Sciences of the U.S. Department of Energy.

### Appendix: A Simple Graphical Proof that there are 2 physical roots to Equation 1 if $\epsilon > Q^2$ , but that only the positive root is physical for $\epsilon < Q^2$ .

Strictly speaking Eqn. 1 should be written with the  $\cos^2\phi$  factor within the square root:

$$E_1 = \frac{\hbar^2}{4m \sin^2\phi} \left\{ (Q^2 + \epsilon \sin^2\phi) \pm \sqrt{(Q^4 - \epsilon^2 \sin^2\phi) \cos^2\phi} \right\} \quad (19)$$

This is the solution for  $E_1$  (or  $k_1$ ), for given  $E$ ,  $\phi$  and  $Q$ . It is the properties of this equation that we shall now examine graphically.

Firstly, consider scattering triangles for which only the scattering angle  $\phi$  and wave-vector transfer  $Q$  are fixed. The allowed incident wave-vectors  $k_1$  trace out a circle, as shown in Fig. 9a. Of course the energy transfer  $E$  increases as one moves around the circle in a clockwise fashion and the smaller circular arc (below the vector  $Q$ ) corresponds to scattering angle  $\pi - \phi$  rather than  $\phi$ .

Secondly, while remaining in the same space, consider scattering triangles for which only the energy transfer  $E$  and wave-vector transfer  $Q$  are fixed. From conservation of energy and conservation of momentum, it is straightforward to show that

$$k_1 \cdot Q = \frac{1}{2} (\epsilon + Q^2) \quad (20)$$

which is constant for given  $E$  and  $Q$ . In other words, the component of  $k_1$  parallel to

$Q$  is constant, so that the allowed values of  $k_1$  lie on a straight line like that shown in Fig. 9b. Of course the scattering angle  $\phi$  varies as one moves along this line.

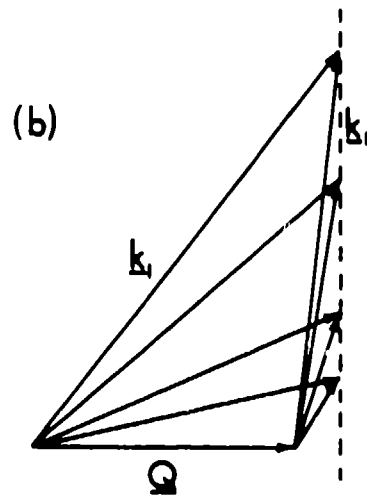
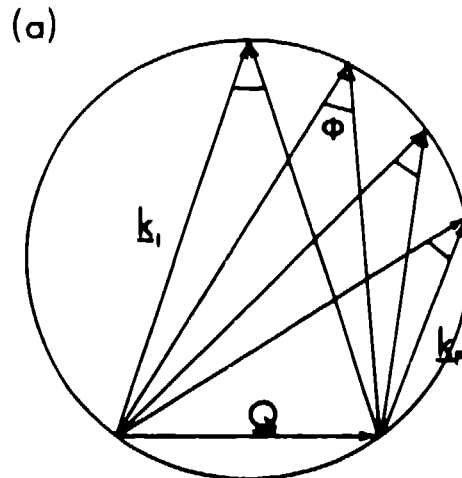


Fig. 9 (a) Allowed scattering triangles for constant  $Q$  and  $\phi$ .  $k_1$  lies on a circle of radius  $Q/(2\sin \phi)$ . (b) Allowed scattering triangles for constant  $Q$  and  $E$ .  $k_1$  lies on the dashed line.

Now, the values of  $E_1$  given by Eqns. 1 and 19 are for constant  $E$ ,  $Q$  and  $\phi$ . These are then simply given by the intersections between the circular locus of Fig. 9a and the straight line of Fig. 9b. Fig. 10a shows a case where there are 2 allowed solutions, with scattering angle  $\phi$ . In contrast, for the case shown in Fig. 10b, there are still 2 solutions, but the smaller triangle corresponds to a scattering angle of  $\pi$ .

$\phi$ . As  $k_i$  is smaller for this triangle, it corresponds to the negative "unphysical" root of Eqn. 1. The ambiguity within Eqns. 1 and 19 lies in the fact that both

$$\sin^2\phi = \sin^2(\pi - \phi) \quad (20)$$

and

$$\cos^2\phi = \cos^2(\pi - \phi) \quad (21)$$

so that Eqn. 19 is ambiguous between  $\phi$  and  $\pi - \phi$ . In other words, it describes the full circle in Fig. 9a, and not just the upper arc corresponding to scattering angle  $\phi$ .

Finally, the transition between a single physical root and two roots occurs for the right-angled triangle shown in Fig. 10c. By Pythagoras' Theorem,  $Q^2 = k_f^2 - k_i^2$ , but conservation of energy gives  $\epsilon = k_f^2 - k_i^2$ , so the limiting condition is that  $\epsilon = Q^2$ .

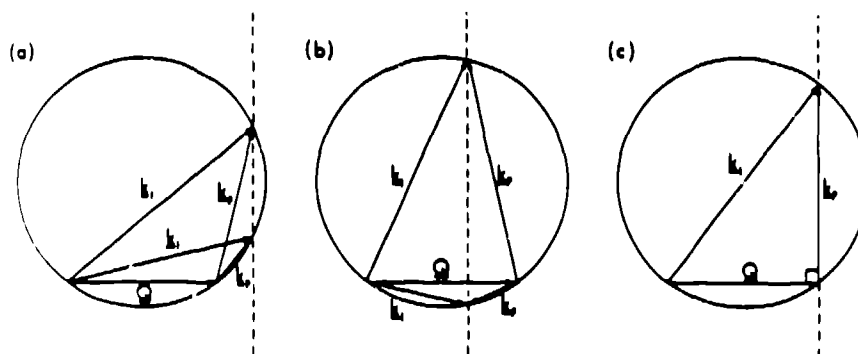


Fig. 10 Allowed scattering triangles for constant  $Q$ ,  $\phi$  and  $E$ , corresponding to the solutions of Eqns. (1) and (19). (a) for  $\epsilon > Q^2$ , (b) for  $\epsilon < Q^2$  and (c) for  $\epsilon = Q^2$ .

## References

1. J. Skalyo and Y. Endoh, *Phys. Rev.* **B7** (1973) 4670. N. A. Lurie, G. Shirane and J. Skalyo, *Phys. Rev.* **B9** (1974) 2661. R. A. Robinson, J. D. Axe, A. I. Goldman, Z. Fisk, J. L. Smith and H. R. Ott, *Phys. Rev.* **B33** (1986) 6488.
2. B. Dörner, Th. Pleßner and H. Sülzer, *Discussions of the Faraday Society* **43** (1967) 160. O. Söderström, J. R. D. Copley, J. -B. Suck and B. Dörner, *J. Phys.* **F10** (1980) L151. J. Teixeira, M. C. Bellissent-Funel, S. H. Chen and B. Dörner, *Phys. Rev. Lett.* **54** (1985) 2681.
3. P. A. Egelstaff in *Proceedings of the Eighth meeting of ICANS, Oxford 8 - 12th July 1985*, Rutherford Appleton Laboratory Report RAL-85-110 Vol II p. 546.
4. J. R. D. Copley, W. Gläser, W. S. Howells, D. L. Price, I. J. Rhyne, K. Sköld and C. Wagner, in *Proceedings of Workshop on "Scientific Opportunities with Advanced Facilities for Neutron Scattering"*, Shelter Island, October 23-26 1984, CONF-8410256, p. 83.

5. W. Reichardt, in Proceedings of the Workshop on Neutron Scattering Instrumentation for SNQ, Maria Laach 3-5th September 1984, ed. R. Scherm and H. Stiller, Jülich Report Jül-1954, p. 312.
6. N. R. Bernhoeft, G. G. Lonzarich, D. McK. Paul and P. W. Mitchell, Physica **136B** (1986) 443.
7. H. A. Mook and R. M. Nicklow, Phys. Rev. **B7** (1973) 336.
8. P. W. Mitchell and D. McK. Paul, Phys. Rev. **B32** (1985) 3272.
9. R. A. Robinson, Physica **B156** (1989) 557.
10. M. W. Stringfellow, J. Phys. **C1** (1968) 950.
11. J. M. Carpenter, K. Crawford, R. Kleb, C. -K. Loong, G. Ostrowski, D. L. Price, M. Nutter, R. Pynn, R. A. Robinson, R. N. Silver, J. M. Rowe, P. Sokol and A. D. Taylor, Los Alamos Report LA-UR-87-2582 (1987).
12. J. M. Carpenter, D. L. Price and N. J. Swanson, Argonne National Laboratory Report ANL-78-88 (1978) p. 78.
13. B. Dornier and H. H. Stiller, in "Instrumentation for Neutron Inelastic Scattering Research", I. A. E. A. Vienna (1970) p. 19.

## Neutron Brillouin scattering in dense nitrogen gas

*P. A. Egelstaff<sup>1</sup>, G. Kearley<sup>2</sup>, J. B. Suck<sup>3</sup>, and J. P. A. Youden<sup>1</sup>*

<sup>1</sup>Physics Department, University of Guelph, CANADA

<sup>2</sup>Institut Laue-Langevin, Grenoble, FRANCE

<sup>3</sup>Institut für Nukleare Festkörperphysik, Kernforschungszentrum, Karlsruhe,  
FEDERAL REPUBLIC OF GERMANY

**ABSTRACT:** In order to develop the field of neutron Brillouin scattering, we have assembled a new neutron spectrometer system and have used it to study the scattering from dense nitrogen gas at wave numbers from 0.05 to 0.15  $\text{\AA}^{-1}$ . We have demonstrated both that the new system is efficient and successful, and that these new data conform to existing theory.

# The effects of chopper jitter on the time-dependent intensity transmitted by multiple-slot multiple disk chopper systems

*J. R. D. Copley*  
University of Maryland  
College Park, Maryland 20742  
and  
National Institute of Standards and Technology  
Gaithersburg, Maryland 20899  
USA

**ABSTRACT:** We present Monte Carlo calculations of the time dependence of the intensity transmitted by single- and multiple-slot multiple disk chopper assemblies, taking into account the effects of chopper jitter. In the case of multiple-slot systems, where each of at least two choppers and a mask is fitted with two or more slots, a switching function is employed to suppress contaminated pulses, i.e., pulses in which neutrons can pass through slots that would never line up in the absence of jitter. Such pulses, if accepted, would degrade the time resolution of the system. Our results for the time-integrated intensity are in good agreement with previously reported semi-analytic calculations. The need to reject contaminated pulses in multiple-slot systems is emphasized.

## Introduction

One of the standard ways to pulse a thermal neutron beam is to use a disk chopper spinning about an axis parallel to the beam<sup>(1)</sup>. The burst time and the intensity transmitted by this type of device depend, *inter alia*, on the width of the beam, the width of the slot in the chopper, and the speed with which the slot passes through the beam. In very high-resolution (short burst time) applications, the slot is narrower than the beam, and the beam is masked down to the width of the slot, as shown in Fig. 1(a), in order to achieve the desired performance. (It is assumed throughout this discussion that the chopper is turning at maximum speed.)

A necessary consequence of the masking of the beam is a reduction in the transmitted intensity, but the intensity can be effectively doubled, with no change in the burst time, using two counter-rotating choppers and, at the same time, doubling the slot widths in the choppers and the mask, as illustrated in Fig. 1(b). This idea is employed in the MIBEMOL spectrometer at the Orphee reactor<sup>(2)</sup> and in the time-of-flight spectrometer that is presently under construction at the Hahn-Meitner Institut reactor in Berlin<sup>(3)</sup>.

A further doubling in intensity (with no change in burst time) is, in principle, achievable<sup>(4)</sup> using two counter-rotating choppers and a stationary mask, each fitted with two slots whose centres are separated by a distance that is at least twice the



width of the individual slots (Fig. 1(c)). This concept can be extended still further with the next stage being a system of three choppers and a mask, each fitted with four slots, as shown in Fig. 1(d): in this case the relative speeds of the choppers are +1, -1, and 1/2, and again the intensity is doubled with no change in the burst time of the system.

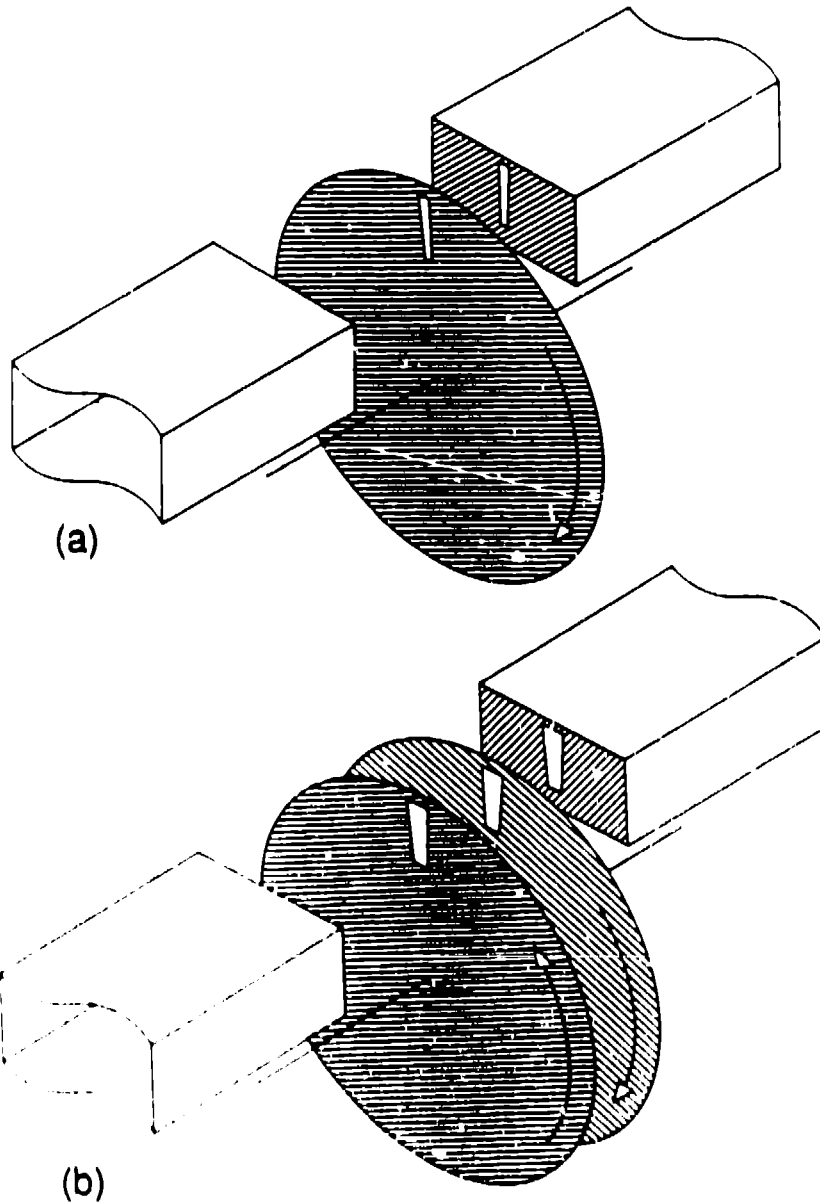
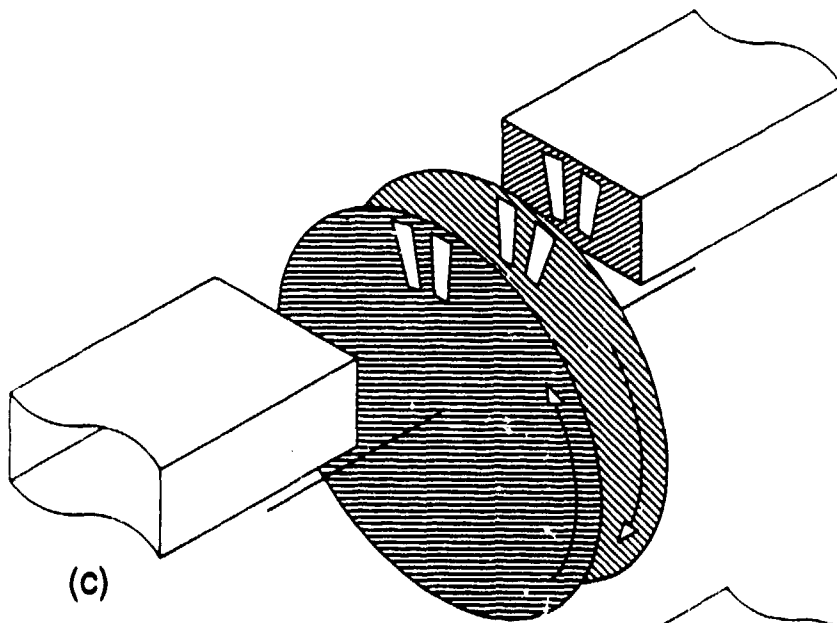
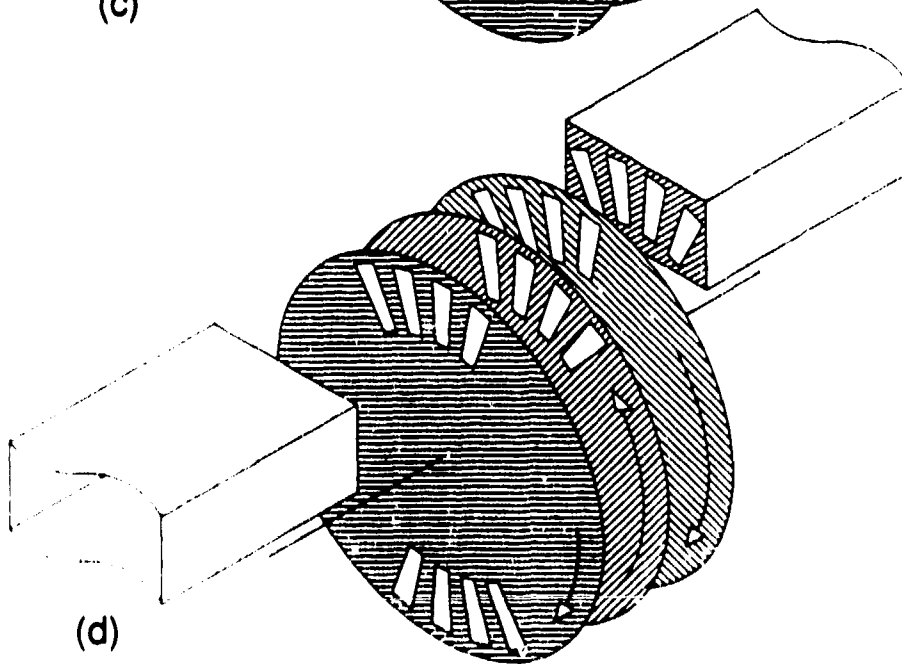


Fig. 1 (continued on next page).



(c)



(d)

**Fig. 1** Schematic views of several chopper assemblies. The width of the neutron guide is exaggerated for clarity. In (a) the single-slot single chopper arrangement is shown: note that the slots are one-half the width of the slots in the other systems. The one-slot and two-slot two chopper setups are shown in (b) and (c) respectively. The four-slot three chopper arrangement is illustrated in (d): in this case the third chopper is spinning at one-half the speed of the other choppers. It is fitted with a second set of slots so that there is still one pulse per revolution of the faster choppers.



The gains in intensity described in the previous two paragraphs only occur if the overall width of the slot system is no greater than the available beam width and if the choppers remain exactly phased. In practice the choppers jitter, causing phase deviations to occur, and in the remainder of this paper we shall discuss the consequences of this departure from ideal behaviour.

In a previous paper<sup>(4)</sup> we described semi-analytic calculations of the effects of chopper phase deviations on the transmitted intensity in the two-slot two chopper and the four-slot three chopper systems. Here we shall describe Monte Carlo calculations which, though less accurate and in some cases much more time-consuming, are very much easier to formulate and code. The time dependence of the transmitted intensity is calculated, and the total intensity per pulse is obtained by integration over time.

### Calculations

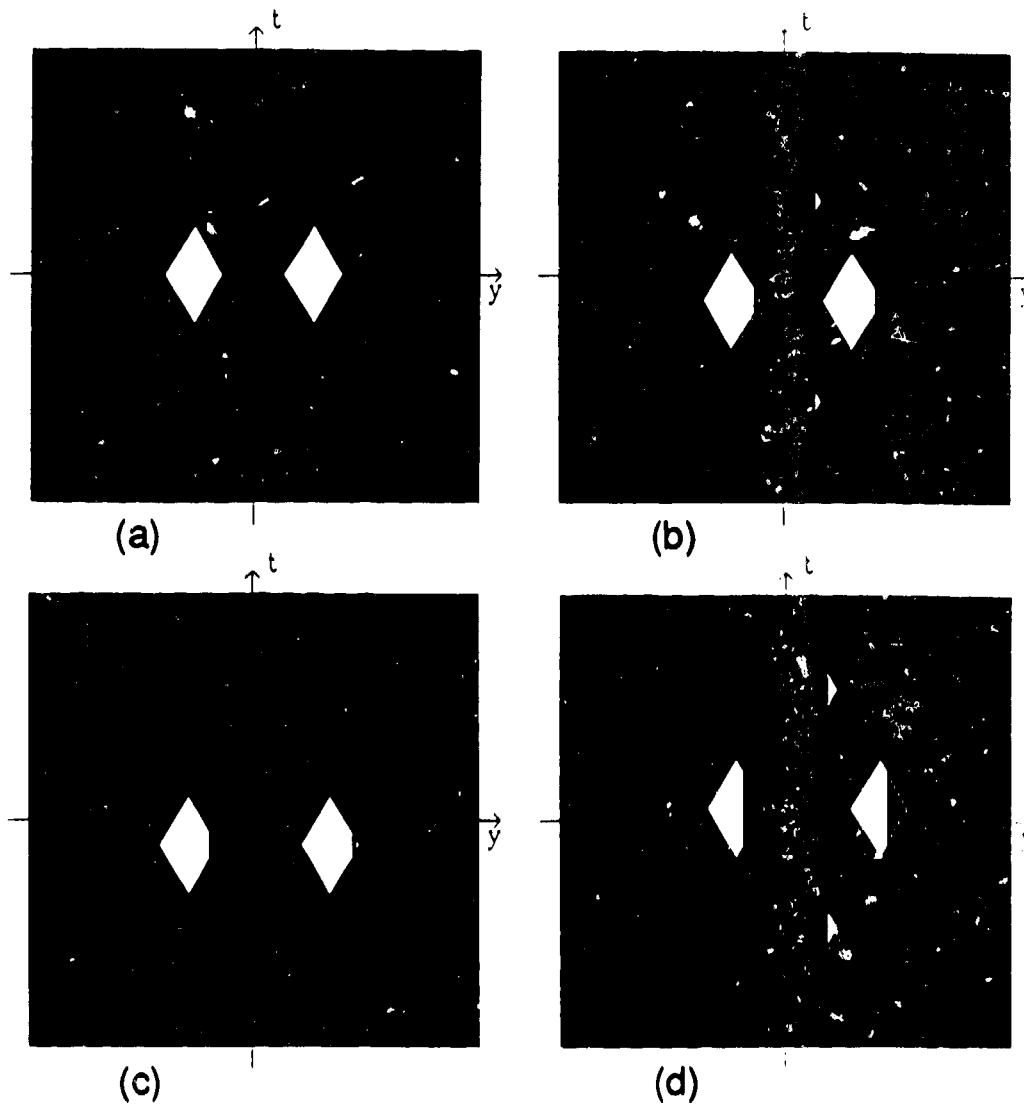
Whereas the semi-analytic calculations<sup>(4)</sup> were formulated in dimensionless units, the present Monte Carlo calculations are expressed in real units. We consider 50-cm diameter disks spinning at 19,100 rpm (9,550 rpm for the slower chopper in the three chopper system), with slots of full width 0.5 cm (0.25 cm for the single chopper system) and negligible radial extent, placed on the circumference of the disk. The peripheral velocity  $V$  of the slots in the faster choppers is therefore 500 m/s, and the burst time is  $5 \mu\text{s}$  (full width at half maximum height, FWHM). We assume that the separation between the disks in the multiple chopper systems may be neglected.

In order to define phasing deviations, we postulate a reference clock with fixed period  $T_0$ . Each disk, labelled  $k$ , is fitted with a magnetic spot that is detected by a fixed pickup at times  $t_k(i) = \Delta t_k + iT_0 + \delta t_k(i)$ , where  $\Delta t_k$  is a constant delay,  $i$  is an integer, and  $\delta t_k(i)$  is the time deviation of the  $i$ 'th pulse. The function that defines the probability that  $\delta t_k$  has the value  $x$  is assumed to be the (normalized) Gaussian function  $G(\sigma_k, x)$ , which has zero mean and standard deviation  $\sigma_k$ . With no loss in generality, we may mentally position the magnetic spots and pickups so that  $\Delta t_k = 0$  for each disk.

Before proceeding any further we need to explain the concept of contaminated pulses in multiple-slot chopper systems. As an example we consider the two-slot system illustrated in Fig. 1(c). The movement of the slots in the choppers (and the lack of movement of the slots in the mask) is illustrated in Fig. 2(a), for the case of perfect phasing ( $\delta t_1 = \delta t_2 = 0$ ). If both choppers are delayed the same length of time (i.e., if  $\delta t_1 = \delta t_2 \neq 0$ ), the intensity is unchanged, but the burst does not occur at the intended time. If the delays are different, as illustrated in Fig. 2(b), there is in general a decrease in the intensity of the two principal components and an associated appearance of intensity in two satellite components. Principal and satellite components are due to neutrons that, respectively, do and do not pass through corresponding slots in the choppers and the mask. A contaminated pulse is defined to be a pulse that has a non-zero satellite component to the intensity. If the width of a slot is  $2b$  and the center-to-center slot separation is  $2B$ , then if  $B = 2b$  all pulses with non-zero relative time deviation must be contaminated and, therefore, unacceptable. To reduce the likelihood of a contaminated pulse it is necessary to

there is  
plus  
sign  
between  
 $\delta t_k(i)$   
attachment  
k-3





**Fig. 2** Diagrams illustrating tangential chopper displacements  $y$  as a function of time  $t$  for the two-slot two chopper system illustrated in Fig. 1(c). In (a) and (b) the center-to-center slot separation  $2B$  is exactly twice the slot width  $2b$ , whereas in (c) and (d) the ratio  $\chi$ , i.e.,  $B/2b$ , is greater than unity. In (a) the choppers are exactly phased but in (b) they are not, and satellite intensity is evident: the pulse is contaminated. In (c) the phase deviations are the same as in (b), but there is no satellite intensity because of the increased value of  $\chi$ . On the other hand, the phase deviations in (d) are sufficiently large that the pulse is contaminated.

make  $B$  somewhat greater than  $2b$ . There is then a range of relative time deviations for which no contamination occurs, whereas contaminated pulses will be produced if the relative time deviation is sufficiently great, as indicated in Figs. 2(c) and 2(d). In order to exclude the possibility of degradation of the resolution by contaminated pulses, the phases of the choppers should be continuously monitored, and contaminated pulses should be rejected by the data acquisition system. Similar considerations apply to the case of the three chopper system illustrated in Fig. 1(d).

The rejection of contaminated pulses may be mathematically represented by a switching function, as has been previously discussed<sup>(4)</sup>. For the two-slot two chopper system the function is unity for  $|\xi| < \chi^{-1}$ , where  $\xi = -V(\delta t_1 - \delta t_2)/4b$  and  $\chi = B/2b$ , and otherwise it is zero. For the four-slot three chopper system it is unity if one or the other of the following sets of conditions is satisfied:

- (i)  $|\xi| < \chi^{-1}$  and  $\xi\zeta > 0$  and  $|(\xi + \zeta)/2| < \chi^{-1}$
- (ii)  $|\xi| < \chi^{-1}$  and  $\xi\zeta \leq 0$  and  $|(2\xi + \zeta)/2| < \chi^{-1}$ .

Here  $\zeta = -V(\delta t_1 + \delta t_2 - 2\delta t_3)/4b$ . If neither of these conditions is satisfied, the switching function is zero.

The first step in each of the calculations was to select standard deviations  $\sigma_x$  for each of the choppers. Standard deviations were made equal for choppers rotating at the same speed (i.e.,  $\sigma_2$  was made equal to  $\sigma_1$ ), whereas the standard deviation for the slower chopper in the three chopper system was assumed to be either the same as, or else twice that of, the faster choppers (i.e.,  $\sigma_3/\sigma_1$  was set to either 1 or 2): the latter choice is equivalent to making the standard deviations of the angular distributions of the three choppers identical. A time deviation  $\delta t_x$  was then selected for each of the choppers from the appropriate Gaussian distribution, and the transmission of the system was computed as a function of time. The procedure was repeated many times, for different choices of the time deviations  $\delta t_x$ , in order to achieve the desired statistical precision. Calculations were made either with respect to the reference clock or with respect to the mean delay time of the pickup pulses from the choppers (ignoring that of the slower chopper in the case of the three chopper system). In the case of multiple-slot systems, time distributions were computed for various choices of the parameter  $\chi$ , and calculations were performed both with and without the contaminated pulse-switching function described above.

## Results

We shall use  $I_C(\sigma, t)$  and  $I_P(\sigma, t)$  to denote transmitted intensities, time being measured with respect to the reference clock and with respect to the mean pickup pulse (as described above), respectively. The corresponding time-integrated intensities  $I_C(\sigma)$  and  $I_P(\sigma)$  are identical, and the shorter notation  $I(\sigma)$  will be used. We shall drop the subscript on  $\sigma$  except in cases where doing so would introduce ambiguity.

For all systems examined with the contaminated pulse-switching function activated,  $I_P(\sigma, t)$  is only non-zero for time differences less than the burst time of the assembly, whereas  $I_C(\sigma, t)$  is (for  $\sigma > 0$ ) a broader function with undesirable tails. For

example,  $I_p(\sigma, t)$  for the single chopper system is a triangular distribution with an FWHM of  $5 \mu\text{s}$ , independent of  $\sigma$ ; whereas  $I_c(\sigma, t)$  is the convolution of  $I_p(\sigma, t)$  with  $G(\sigma t)$ :  $I(\sigma)/I(0) = 1$  for all values of  $\sigma$ . In view of the above it is clearly advisable (and it is normal practice) to relate the start time of a data acquisition cycle to the mean pickup pulse rather than to the system clock. We shall not discuss  $I_c(\sigma, t)$  any further.

The function  $I_p(\sigma, t)$  for the single-slot two chopper system is shown in Fig. 3 for several choices of  $\sigma$ . Similar rounded triangular line shapes are found for the time distributions  $I_p(\sigma, t)$  for all of the multiple-slot systems we have studied. For example, Fig. 4(a) shows results for the two-slot two chopper system with  $\gamma = 1.1$ : note that as  $\sigma$  is increased, the intensity drops more rapidly than in the case of the one-slot two chopper system shown in Fig. 3. In Fig. 4(b) we show time distributions for the same system, for  $\sigma = 1 \mu\text{s}$  and  $\sigma = 2 \mu\text{s}$ , with and without the contaminated-pulse-switching function activated. The switching function reduces the transmitted intensity significantly, but little intensity appears in the satellites if it is turned off. For example, the integrated intensity ratio  $I_p(\sigma)/I_p(0)$  is reduced from  $\sim 0.99$  to  $\sim 0.83$  when  $\sigma = 1 \mu\text{s}$  ( $\sim 0.97$  to  $\sim 0.53$  when  $\sigma = 2 \mu\text{s}$ ), but the contribution to the integrated intensity in the satellites (with the switching function turned off) is only  $\sim 0.0006$  ( $\sim 0.012$ ). This is because the switching function rejects all contaminated pulses, even though almost all of the intensity in these pulses is in the principal component.

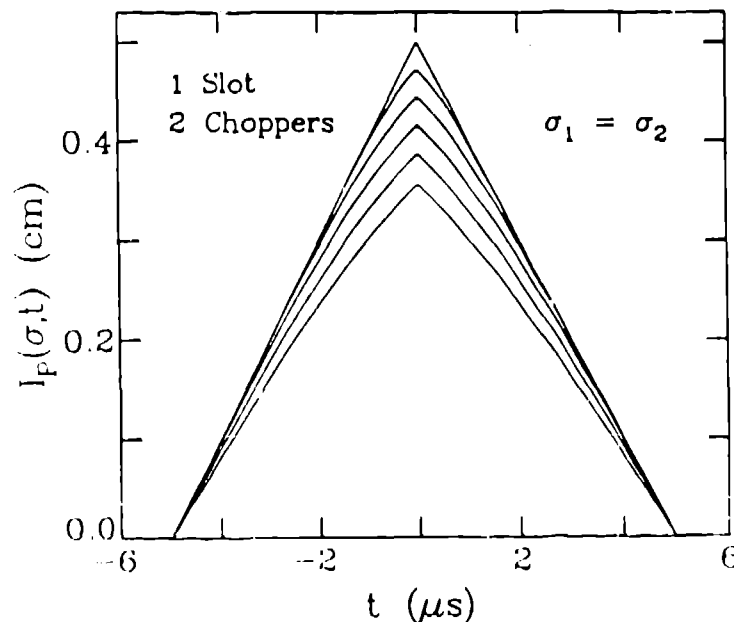
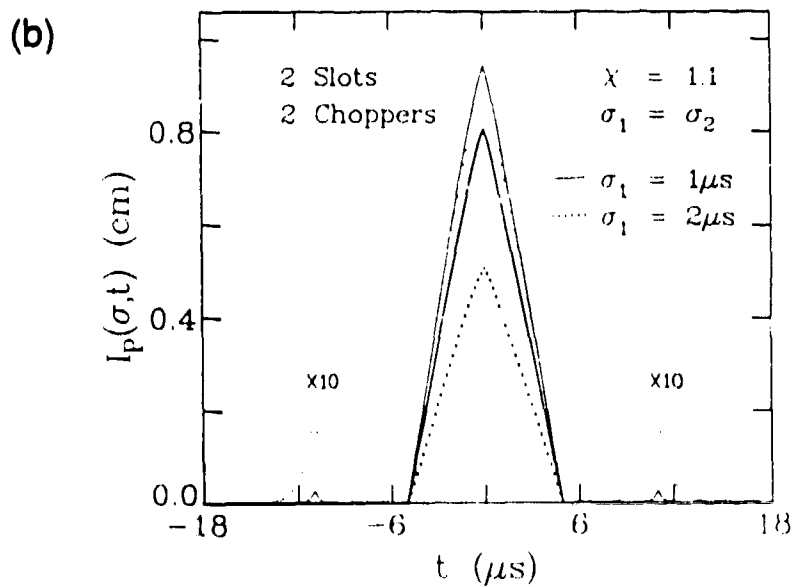
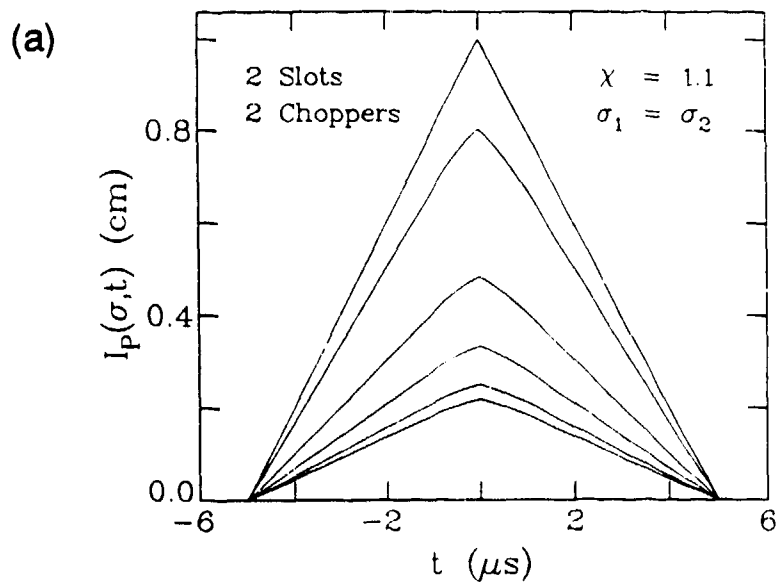


Fig. 3 Transmitted intensities  $I_p(\sigma, t)$  for the single-slot two chopper system. The intensity is expressed in units of length. For example, when  $\sigma = 0$  and  $t = 0$ , neutrons are transmitted over the full width of the slots,  $0.5 \text{ cm}$ . Successive plots, starting from the top, correspond to  $\sigma = 0, 1, 2, 3, 4,$  and  $5 \mu\text{s}$ .



**Fig. 4** Transmitted intensities  $I_p(\sigma, t)$  for the two-slot two chopper system. The unit of intensity is explained in the caption to Fig. 3. Results for  $\chi = 1.1$  are shown in (a). Successive plots, starting from the top, correspond to  $\sigma = 0, 1, 2, 3, 4,$  and  $5 \mu s$ . Intensities for  $\chi = 1.1$ , for  $\sigma = 1 \mu s$  and  $\sigma = 2 \mu s$ , are shown in (b). The darker and lighter lines represent the results of calculations where the contaminated pulse switching function is on and off, respectively. The scale of the satellite intensities is increased by a factor of 10 to make them more apparent.

Integrated intensities for the two-slot two chopper system are compared with our earlier semi-analytic results in Fig. 5: the agreement is good. The ratio  $I(\sigma)/I(0)$  for the one-slot two chopper system is identical to  $I(\sigma)/I(0)$  for the two-slot two chopper system with  $\chi = \infty$ , being the convolution of the function  $f_1(\xi)$ , introduced in reference 4 (appendix 1), with  $G(\sigma\xi)$ . In Table 1 we present selected results for  $I(\sigma)/I(0)$  for the two-slot system, derived from the semi-analytic calculations.

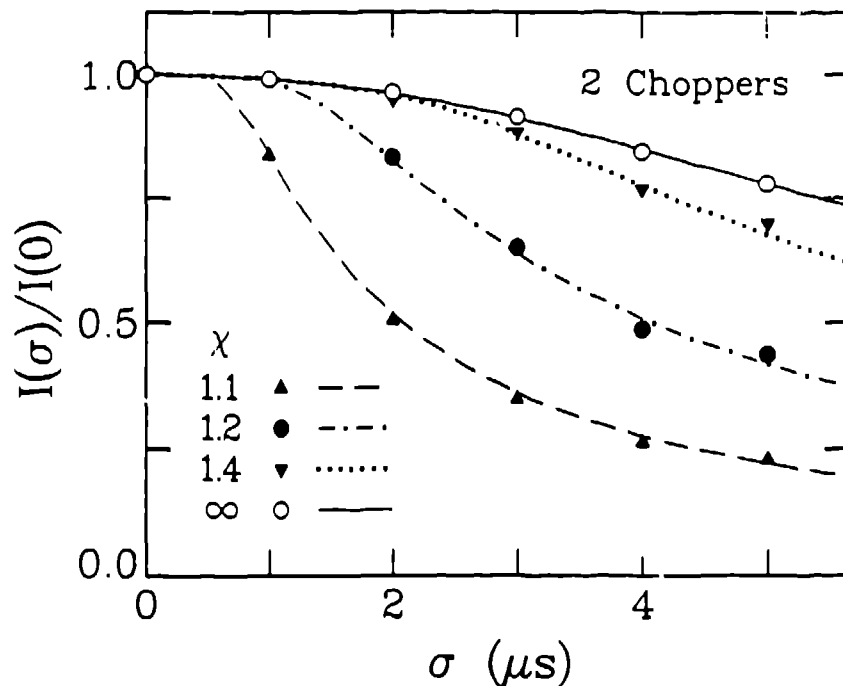


Fig. 5 The time-integrated intensity ratio for the two-slot two chopper system, for various choices of  $\chi$ . The symbols represent the present Monte Carlo calculations whereas the lines show the results of earlier semi-analytic calculations<sup>[4]</sup>. The line labelled  $\chi = \infty$  also represents the integrated intensity ratio for the single-slot two chopper system.

In Fig. 6 we show results for  $I_p(\sigma, t)$ , for the four-slot three chopper system with  $\sigma_3 = \sigma_1 = 1 \mu s$  and  $2 \mu s$  and  $\chi = 1.1$ , with and without the contaminated-pulse-switching function activated: again the switching function reduces the intensity very significantly, but there is little intensity in the satellites when the switching function is turned off. Intensity ratios  $I(\sigma)/I(0)$  for this system, for  $\sigma_3/\sigma_1 = 1$  and  $2$ , are again in good agreement with the earlier semi-analytic calculations, and selected results from the latter calculations are given in Table 2.



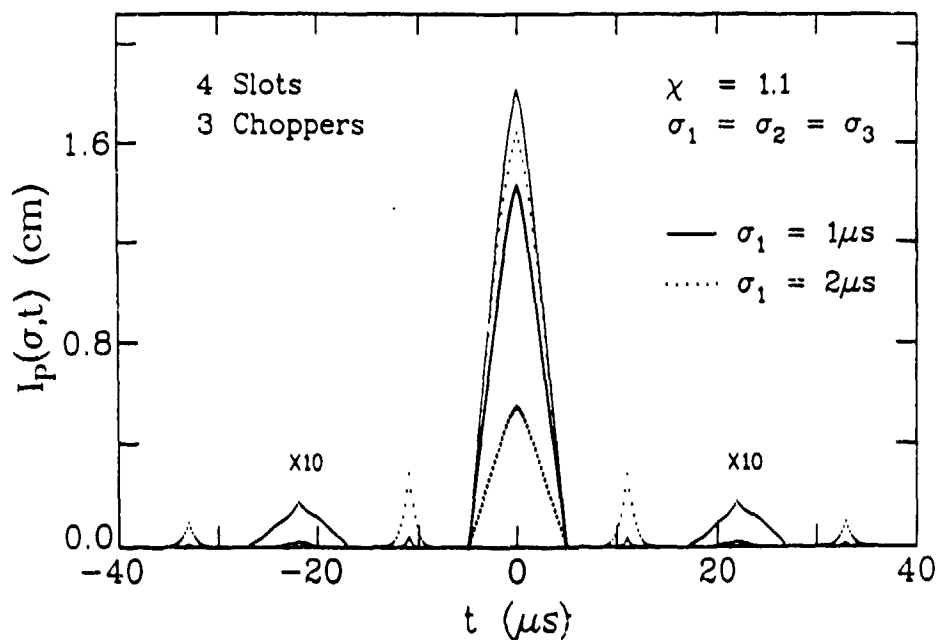


Fig. 6 The time-dependent intensity  $I_p(\sigma, t)$  for the four-slot three chopper system with  $\chi = 1.1$ ,  $\sigma_1 = \sigma_3$ , and  $\sigma_1 = 1 \mu s$  and  $\sigma_1 = 2 \mu s$ . The darker and lighter lines represent the results of calculations, where the contaminated-pulse-switching function is on and off, respectively. The scale of the satellite intensities is increased by a factor of 10 to make them more apparent. The unit of intensity is explained in the caption to Fig.3.

**Table 1.** Values of the integrated intensity ratio for the two-slot two chopper system for selected values of  $\chi = B/2b$ . The column for  $\chi = \infty$  also represents the integrated intensity ratio for the single-slot two chopper system. The quantity  $\sigma_\xi$  is given<sup>[4]</sup> by  $\sigma_\xi^2 = (V/4b)^2(\sigma_1^2 + \sigma_2^2)$  so that, for the system studied in this paper,  $\sigma_1 = 14.14\sigma_\xi \mu\text{s}$ .

$\chi$ $\sigma_\xi$	1.100	1.200	1.300	1.400	$\infty$
0.00	1.000	1.000	1.000	1.000	1.000
0.02	0.999	0.999	0.999	0.999	0.999
0.04	0.985	0.997	0.997	0.997	0.997
0.06	0.900	0.992	0.993	0.993	0.993
0.08	0.785	0.976	0.987	0.987	0.987
0.10	0.679	0.940	0.978	0.980	0.980
0.12	0.592	0.888	0.962	0.971	0.971
0.14	0.522	0.830	0.937	0.958	0.961
0.16	0.465	0.772	0.904	0.942	0.949
0.18	0.419	0.717	0.867	0.920	0.935
0.20	0.381	0.667	0.828	0.895	0.920
0.24	0.321	0.581	0.750	0.838	0.887
0.28	0.277	0.512	0.679	0.779	0.850
0.32	0.244	0.456	0.617	0.721	0.811
0.36	0.217	0.411	0.563	0.667	0.772
0.40	0.196	0.373	0.516	0.619	0.734
0.50	0.157	0.303	0.426	0.520	0.645
0.60	0.132	0.254	0.361	0.445	0.570

Table 2. Values of the integrated intensity ratio  $I(\sigma)/I(0)$  for the three chopper system for selected values of  $\chi = B/2b$ , for  $\sigma_3/\sigma_1 = 1$  and 2. The quantity  $\sigma_\xi$  is given<sup>(4)</sup> by  $\sigma_\xi^2 = (V/4b)^2(\sigma_1^2 + \sigma_2^2)$ .

$\chi$	1.100	1.200	1.300	1.400	1.100	1.200	1.300	1.400
$\sigma_\xi$	$\sigma_3/\sigma_1 = 1$				$\sigma_3/\sigma_1 = 2$			
0.00	1.000	1.000	1.000	1.000	1.000	1.000	1.000	1.000
0.02	0.998	0.998	0.998	0.998	0.995	0.996	0.996	0.996
0.04	0.975	0.992	0.992	0.992	0.884	0.984	0.985	0.985
0.06	0.844	0.979	0.981	0.981	0.677	0.940	0.965	0.966
0.08	0.674	0.946	0.966	0.966	0.497	0.852	0.931	0.940
0.10	0.528	0.880	0.945	0.948	0.367	0.742	0.877	0.906
0.12	0.416	0.795	0.913	0.926	0.278	0.634	0.811	0.863
0.14	0.333	0.705	0.869	0.899	0.215	0.537	0.740	0.813
0.16	0.270	0.621	0.816	0.867	0.171	0.455	0.668	0.759
0.18	0.223	0.546	0.759	0.830	0.138	0.388	0.600	0.704
0.20	0.186	0.481	0.701	0.789	0.114	0.332	0.538	0.649
0.25	0.125	0.354	0.567	0.680	0.075	0.233	0.409	0.525
0.30	0.089	0.268	0.458	0.577	0.053	0.170	0.316	0.424
0.35	0.067	0.208	0.373	0.488	0.039	0.129	0.248	0.344
0.40	0.052	0.165	0.307	0.414	0.030	0.101	0.199	0.283
0.50	0.034	0.110	0.215	0.303	0.020	0.066	0.135	0.197
0.60	0.023	0.079	0.158	0.228	0.014	0.047	0.096	0.144

### Discussion

We have described Monte Carlo calculations of the time-dependent intensity and the integrated intensity transmitted by single- and multiple-slot chopper systems. The results of earlier calculations<sup>(4)</sup> of the integrated intensity are fully confirmed. This in itself justifies the present calculations, since the earlier calculations were quite complicated in their formulation. In the course of the present work, an error was discovered (prior to publication) in one of the equations of reference 4. This lends credence to the argument that Monte Carlo calculations may be used to check analytic calculations, and *vice versa*.

Figures 4(b) and 6 demonstrate the effects of activating the contaminant-pulse-switching function with multiple-slot chopper systems. The loss in intensity is considerable, especially when  $\sigma$  is large; but the pulse is perfectly clean. The satellite peaks, which appear when the switching function is not used, have potentially disastrous implications with respect to the interpretation of time-of-flight data acquired under such circumstances. The best course of action is to use very stable choppers, e.g., with a  $\sigma$  of order 10% or less of the burst time, and to reject all contaminated pulses.

It is our intention to build a high-resolution multiple-disk-chopper time-of-flight spectrometer in the neutron guide hall of the Cold Neutron Research Facility at the National Institute of Standards and Technology (formerly the National Bureau of Standards). The design specification requires burst times of the order of 5 - 10  $\mu$ s, and the available guide dimensions are such that we may well decide to include an option to use the two-slot double chopper arrangement illustrated in Fig. 1(c). We expect to operate the choppers at a maximum speed of 20,000 rpm, and the mean chopper disk diameter will be of order 50 cm. The calculations described in this paper and in our previous publication<sup>[4]</sup> suggest that  $\sigma$  for each of the choppers should be no greater than 1  $\mu$ s if  $\chi = 1.2$ . Recent measurements<sup>[5]</sup> of this quantity, using a chopper system built at the KFA (Jülich, Federal Republic of Germany) research center, indicate that values of  $\sigma$  of the order of 50 - 100 ns may be achieved. It, therefore, seems that the necessary technology already exists so that we can exploit the multiple-slot chopper concept and, thereby, realize a significant gain in instrumental throughput.

### Acknowledgements

Helpful discussions with R. Lechner, J. Raebiger and J. K. Fremerey are gratefully acknowledged.

### References

1. F. Douchin, R. E. Lechner and R. Scherm, (unpublished). For a short description of the IN5 spectrometer see the report Neutron Research Facilities at the ILL High Flux Reactor (Institut Laue-Langevin, Grenoble, France, December 1983, pp. 75-77 (unpublished).
2. S. Hautecler, E. Legrand, L. Vansteelandt, P. d'Hooghe, G. Rooms, A. Seeger, W. Schalt and G. Gobert, 1985, Proc. Conf. Neutron Scattering in the Nineties, Jülich, (IAEA, Vienna, 1985) p. 211.
3. R. E. Lechner, private communication.
4. J. R. D. Copley, 1988, Nucl. Instrum. Meth. (in press).
5. J. Raebiger, J. K. Fremerey, R. Lechner and J. R. D. Copley, unpublished results.

## Application of eV neutron scattering and eV neutron absorption techniques

*Susumu Ikeda*

National Laboratory for High Energy Physics  
Oho, Tsukuba-shi, Ibaraki-ken, 305  
JAPAN

Intense spallation neutron sources can provide a useful eV neutron flux in the energy range 1-100 eV, which is much more intense than has ever been available from steady state sources, and makes two fruitful techniques possible. One is an eV neutron scattering technique, which allows the impulse approximation limit to be approached. In this limit, the scattering function is simply related to the momentum distribution  $n(p)$  of the struck particle (mass  $M$ ) by [1,2]

$$S(Q, \hbar\omega - R) = \int dp \delta(\hbar\omega - R - \hbar Q \cdot p/M) n(p), \quad (1)$$

where  $\hbar Q$  is the momentum transfer and  $R = \hbar^2 Q^2 / 2M$  the recoil energy. If  $n(p)$  is Gaussian,  $S(Q, \hbar\omega - R)$  can be written as

$$S(Q, \hbar\omega - R) = (\sqrt{2\pi}\sigma_R)^{-1} \exp(-(\hbar\omega - R)^2 / 2\sigma_R^2). \quad (2)$$

In this equation,  $\sigma_R = \sqrt{2Rk_B T_{eff}}$  and  $k_B T_{eff} = (2/3) \langle K \rangle$ , where  $\langle K \rangle$  and  $T_{eff}$  are the mean kinetic energy and the effective temperature, respectively. The mean kinetic energy and the effective temperature are related to the density-of-state  $f(E)$ . Thus,

$$k_B T_{eff} = (2/3) \langle K \rangle = (1/2) \int_0^{E_D} E f(E) \coth(E/2k_B T) dE. \quad (3)$$

$T$  is the real temperature of a sample and  $E_D$  the maximum energy of  $f(E)$ . If  $f(E) \propto E^2$  (Debye model),  $T_{eff}$  is given by

$$k_B T_{eff} = (3/2) \int_0^{k_B \theta_D} E^3 \coth(E/2k_B T) dE / (k_B \theta_D)^3, \quad (4)$$

where  $\theta_D$  is the Debye temperature. This method has been applied to measure

ments of the momentum distribution in pyrolytic graphite, superfluid helium and metal hydrides. Some successful results have already been obtained [3,4,5]. In eV neutron scattering, atoms in a solid are considered to be "free atoms". Hence, the overall scattering function,  $S_{total}$ , for a mixed system, such as compounds and alloys, should be written as a sum of the scattering functions of atoms A,B,C...:

$$S_{total} = \sum_{i=A,B,C...} \sigma_S^{(i)} \cdot N_d^{(i)} \cdot S^{(i)}(Q, \hbar\omega - R_{(i)}), \quad (5)$$

where  $R_{(i)}$ ,  $\sigma_S^{(i)}$  and  $N_d^{(i)}$  are the recoil energy, neutron scattering cross section and number density. Let's consider a compound composed of two kinds of atoms (A and B;  $M_B > M_A$ ). If  $R_A \gg R_B$ ,  $S_{total}$  has two distinct peaks around  $\hbar\omega = R_A$  and  $\hbar\omega = R_B$ , corresponding to scattering from atoms A and B. This unique nature of eV neutron scattering provides an opportunity for the direct observation of the motion of a specific atom, separated from the others.

Another one is an eV neutron absorption technique. Many heavy atoms, such as Ta, U, Sb, Ba and Ho, have large neutron resonant absorption in the energy range 1-100 eV, and the cross section of neutron absorption,  $\sigma$ , is also described using the effective temperature in the weak binding approximation, as follows [6]:

$$\sigma = \sigma_0 \xi (2\sqrt{\pi})^{-1} \int dy \exp[-(\xi/2)^2 (x - y)^2 / (1 + y^2)], \quad (6)$$

where  $x = 2(E - E_0 - R)/\Gamma$ ,  $\xi = \Gamma/\Delta$ ,  $R = (m/M)E_0$  and  $\Delta = 2\sqrt{Rk_B T_{eff}}$ . Here,  $m$  is the neutron mass and  $\sigma_0$  the peak cross section of neutron absorption. The intrinsic line width,  $\Gamma$ , is defined as the full width at half-maximum of the resonance. Since a specific atom is identified by the resonance energy,  $E_0$ , one can measure the effective temperature of the specific atom by using the width of the resonance peak, apart from the other atoms in a mixed system. The finite thickness of the absorbing material leads to self-shielding effects, and the probability for neutron absorption is given by [6]

$$P_A(E) = 1 - \exp(-n_A \sigma), \quad (7)$$

where  $n_d$  is the number density of the resonant absorbing atoms per unit area perpendicular to the neutron beam.

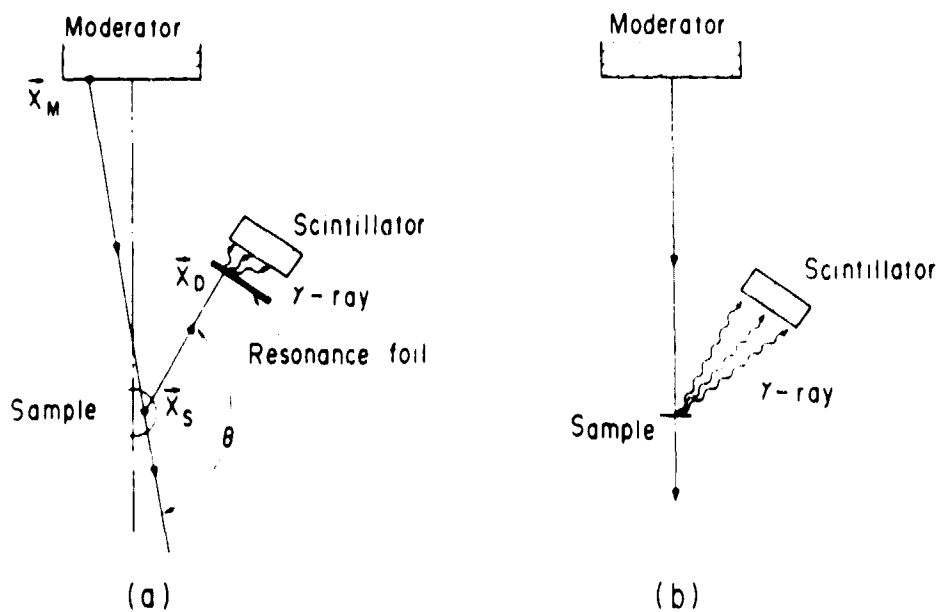
A schematic layout of an eV neutron scattering spectrometer is shown in Fig.1(a). Pulsed white neutrons produced at  $t_0$  on the moderator are scattered by a sample, and the scattered neutrons of final energy  $E_f$  are captured by a resonance foil. The probability of neutron absorption of the resonance foil also can be described by  $P_A(E_f)$  in Eq.(7). Promptly after the neutron capture, a  $\gamma$ -cascade is emitted from the resonance foil, which is detected by a scintillator. The energy of the incoming neutrons is determined by the time-of-flight(TOF). In this geometry, the TOF scattering spectrum  $I_S(t)$  is given by

$$I_S(t) = \int dX_M dX_S dX_D dE_i dt_0 P_A(E_f) I(E_i, t_0) \delta(t - t_0 - l_i/v_i - l_f/v_f) \\ \times \sqrt{E_f/E_i} \cdot S(Q, \omega - R), \quad (8)$$

where  $l_i = |X_m - X_s|$ ,  $l_f = |X_s - X_D|$ ,  $\cos \theta = (X_M - X_S) \cdot (X_S - X_D) / l_i l_f$  and  $(M/m)R = \hbar^2 Q^2 / 2m = E_i + E_f - 2\sqrt{E_i E_f} \cos \theta$ . Here,  $I(E_i, t_0)$  is the neutron intensity of energy  $E_i$  at the emission time  $t_0$  on the moderator.  $E, v$  and  $l$  are the neutron energy, neutron velocity and flight path length, respectively, and  $i$  and  $f$  refer to incoming and scattered neutrons.  $X_M, X_S$  and  $X_D$  represent positions on the moderator, the sample and the detector, respectively. Fig.1(b) shows a schematic layout of the neutron absorption spectrometer. The prompt capture  $\gamma$ -cascade produced in the sample is detected by a scintillator and the energy of the incoming neutrons is determined by TOF. The TOF spectrum of the resonant neutron absorption,  $I_A(t)$ , is given by

$$I_A(t) = \int dE_f dE_i dt_0 P_A(E_f) I(E_i, t_0) \delta(t - t_0 - l/v_i) \quad (9)$$

The discovery of superconductivity in the temperature range 30-100 K for the La-Cu-O system [7] and the Y-Ba-Cu-O system [8,9] is one of the most exciting events in the recent solid state physics. Many attempts to explain such



**Fig. 1** Layout of an eV neutron scattering spectrometer (a) and a neutron absorption spectrometer (b).

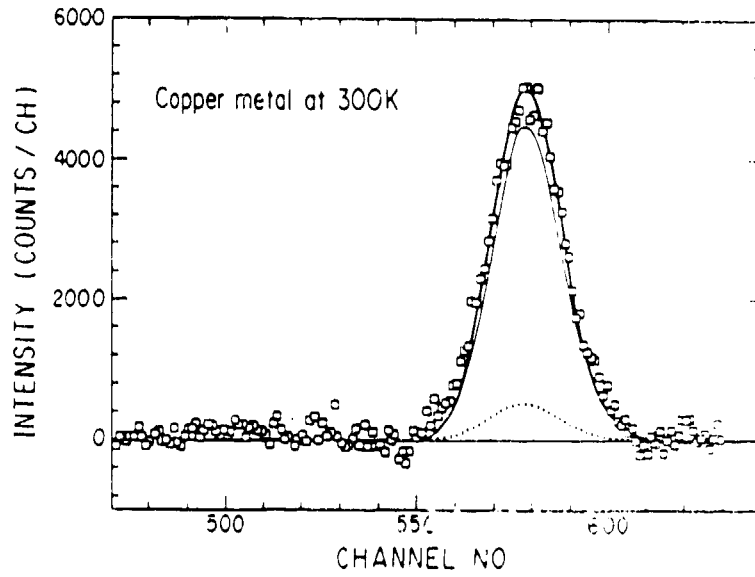
extraordinarily high  $T_c$  values have been made with the conventional electron-phonon coupling theory [10,11] as well as with non-phonon mechanisms [12]. The most direct test for such theories is to look for the predicted excitations by using inelastic neutron scattering techniques. Actually, many experiments have been performed using thermal and epithermal neutrons in the energy range  $E_i \ll 1$  eV [13,14]. As mentioned above, the eV neutron scattering and eV neutron absorption experiments also can provide new important information for the understanding of the high- $T_c$  mechanism, which has never been obtained by ordinary neutron scattering experiments. For the first time, I applied these methods to the observation of the motions of the specific atoms in La-Cu-O and Y-Ba-Cu-O systems. In this paper, I will report a procedure of the application.

Each powder sample of copper metal,  $\text{CuO}$ ,  $\text{La}_2\text{CuO}_4$  and  $\text{YBa}_2\text{Cu}_3\text{O}_7$ , was held in a zirconium cell of 10 mm diameter, 8 cm height and 50- $\mu\text{m}$  thickness, and set at a distance of 8.361 m from the moderator surface. A resonance foil of tantalum (5 cm  $\times$  5 cm) at room temperature was installed at a distance

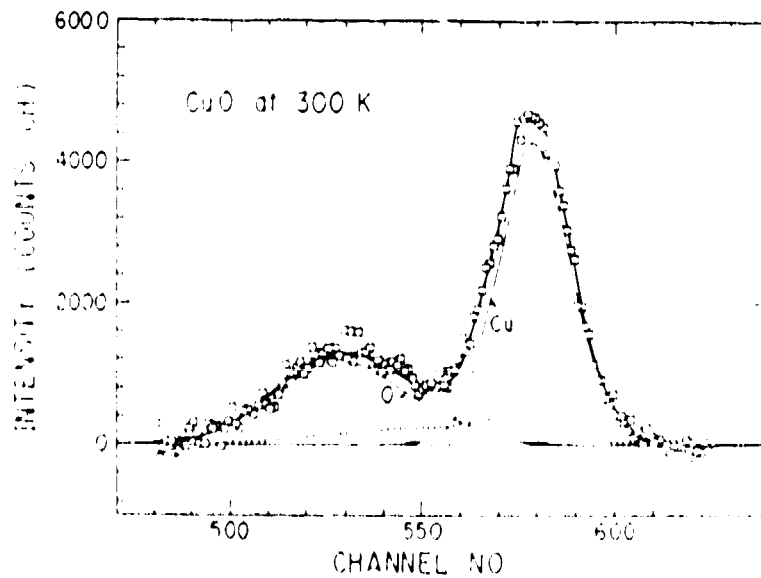


of 0.15 m from the sample with fixed at an angle of 159 degrees. Scattered neutrons with a final energy of  $E_f = 4.28$  eV were detected by a tantalum foil with a scintillator. In these conditions,  $Q \sim 90 \text{ \AA}^{-1}$  was realized. Figs.2, 3, 4 and 5 show the neutron scattering TOF spectra of copper metal,  $\text{CuO}$ ,  $\text{La}_2\text{CuO}_4$  and  $\text{YBa}_2\text{Cu}_3\text{O}_7$ , in which the background has been subtracted. These TOF spectra were measured at a channel width of  $0.5 \mu\text{sec}$ . I calculated the single scattering and multiple scattering TOF spectra and plotted them in Figs.2, 3, 4 and 5 as solid and dotted lines. In these figures, the thin solid lines, the dotted lines and the thick solid lines represent the single scattering spectra calculated by Eq.(8), calculated double scattering spectra and the sum of those, respectively. In the case of copper metal, the effective temperature at  $T = 300$  K was calculated to be 319 K using the Debye temperature of copper metal,  $\theta_D = 343$  K (see Eq.(4)). The TOF spectrum was calculated with  $T_{\text{eff}} = 319$  K and compared with the measured data. Good agreement between the calculated spectrum and the measured data was obtained, as shown in Fig.2. This result suggests that the Debye temperature can be well estimated from the effective temperature using Eq.(4). For a mixed system, such as  $\text{CuO}$ , the TOF spectrum should be calculated using Eqs.(5) and (8). A fit was made to the measured spectrum using the effective temperatures of  $\text{Cu}$  and  $\text{O}$  as parameters. A satisfactory fit to the measured spectrum was obtained with  $T_{\text{eff}} = 375$  K for  $\text{Cu}$  and  $T_{\text{eff}} = 550$  K for  $\text{O}$ , as shown in Fig.3. For a more complicated compound, such as  $\text{La}_2\text{CuO}_4$ , the TOF spectrum can also be calculated by using Eqs.(5) and (8). The total scattering  $S_{\text{total}}$  in Eq.8 should be written as the sum of three components. A similar fit was made to the measured spectrum of  $\text{La}_2\text{CuO}_4$  using the effective temperatures of  $\text{Cu}$ ,  $\text{O}$  and  $\text{La}$  as parameters. A good fit was obtained with  $T_{\text{eff}} = 600$  K for  $\text{Cu}$ ,  $T_{\text{eff}} = 550$  K for  $\text{O}$  and  $T_{\text{eff}} = 500$  K for  $\text{La}$ , as shown in Fig.4.

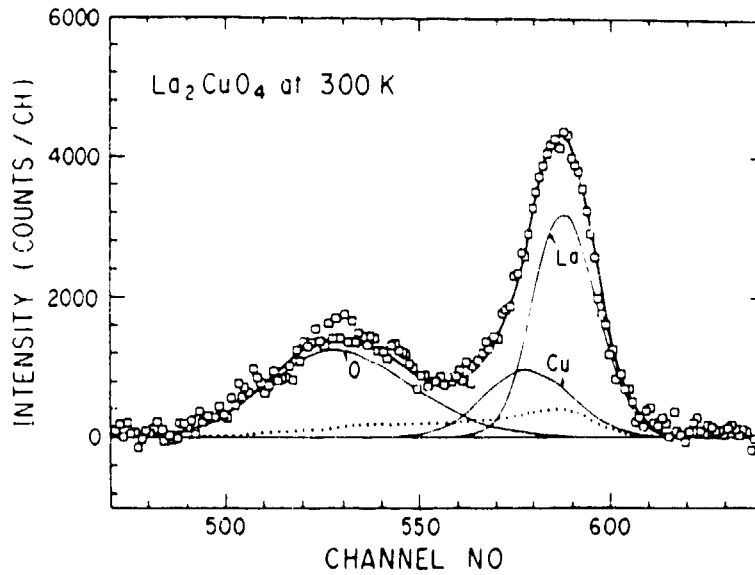
$\text{YBa}_2\text{Cu}_3\text{O}_7$  is a very complicated system comprising four kinds of atoms. It is, of course, possible to perform a similar fit with many parameters, though a precise determination of the effective temperatures seems to be very difficult. Therefore, I tried, at first, to determine the effective temperatures of  $\text{Ba}$  and  $\text{Y}$



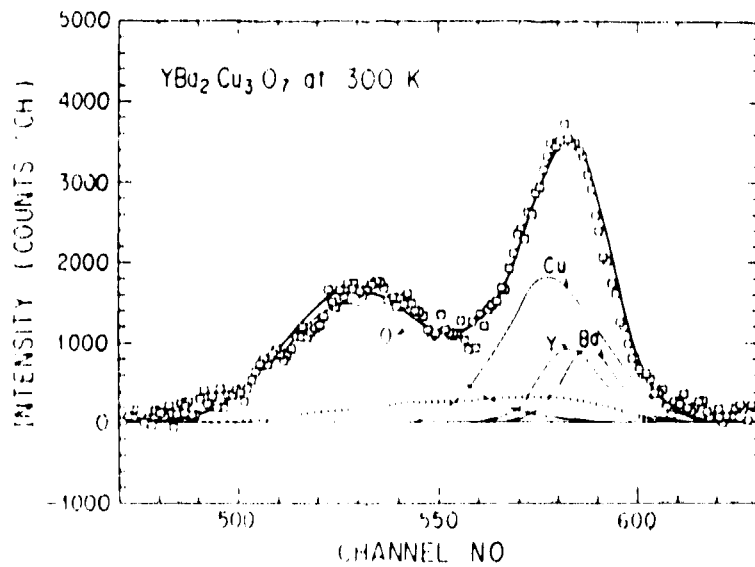
**Fig. 2** Neutron scattering spectrum of copper metal at 300 K. The thick solid line is a calculated spectrum with  $T_{eff}=319$  K. The thin solid line and dotted line are calculated single and multiple scattering, respectively.



**Fig. 3** Neutron scattering spectrum of CuO at 300 K. The thick solid line is a calculated spectrum with  $T_{eff}=375$  K (Cu) and  $T_{eff}=550$  K (O). The thin solid line and the dotted line are calculated single and multiple scattering, respectively.



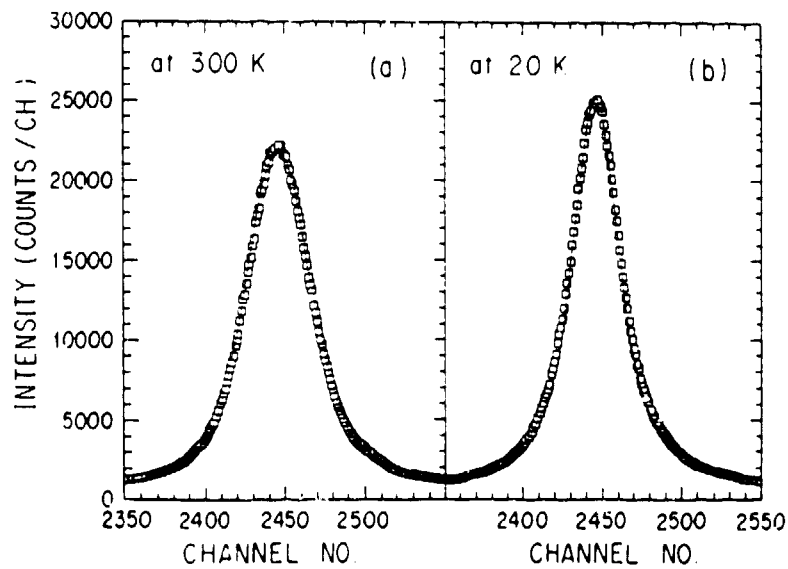
**Fig. 4** Neutron scattering spectrum of La<sub>2</sub>CuO<sub>4</sub> at 300 K. The thick solid line is a calculated spectrum with  $T_{eff}=600$  K (Cu),  $T_{eff}=550$  K (O) and  $T_{eff}=500$  K (La). The thin solid lines and the dotted line are calculated single and multiple scattering, respectively.



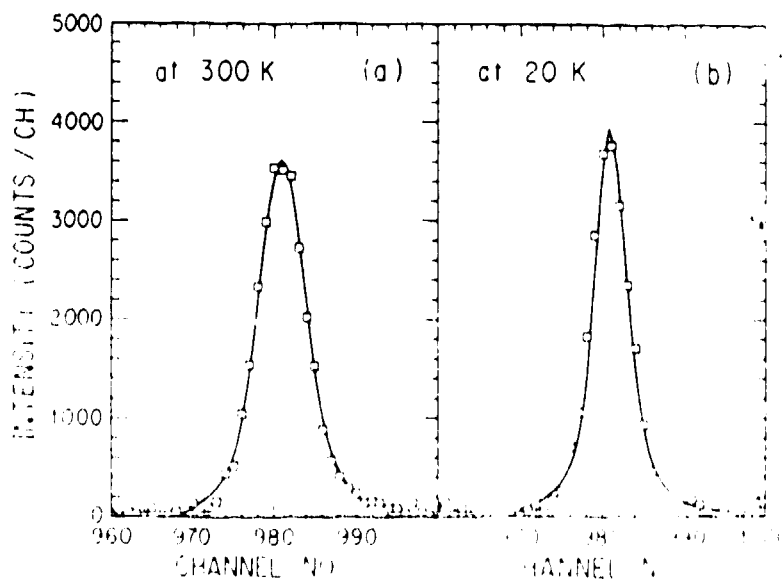
**Fig. 5** Neutron scattering spectrum of YBa<sub>2</sub>Cu<sub>3</sub>O<sub>7</sub> at 300 K. The thick solid line is a calculated spectrum with  $T_{eff}=750$  K (Cu),  $T_{eff}=550$  K (O),  $T_{eff}=300$  K (Ba) and  $T_{eff}=300$  K (Y). The thick solid lines and the dotted line are calculated single and multiple scattering, respectively.

by neutron absorption experiments, and then to fit to the measured data using only two effective temperatures of  $Cu$  and  $O$  as parameters. I performed neutron absorption experiments on  $HoBa_2Cu_3O_7$  instead of  $YBa_2Cu_3O_7$ , since  $^{165}Ho$  and  $^{135}Ba$  have very large neutron resonant absorptions at 3.92 eV and 24.4 eV, respectively. However,  $Y$  has no neutron resonant absorption in the energy range 1-100 eV.  $HoBa_2Cu_3O_7$  is isostructural to  $YBa_2Cu_3O_7$ , and its transition temperature is the same as that of  $YBa_2Cu_3O_7$  [15]. Therefore, the effective temperatures of  $Ho$  and  $Ba$  in  $HoBa_2Cu_3O_7$  is considered to be the same as those of  $Y$  and  $Ba$  in  $YBa_2Cu_3O_7$ . In order to test the neutron absorption spectrometer, neutron absorption experiments were performed on holmium metal foil (5 cm  $\times$  5 cm, 25  $\mu m$ ) at 300 and 20 K. The TOF spectra,  $I_A(t)$ , was calculated by Eq.(9) and fitted to the measured spectra using the effective temperature of  $Ho$  as a parameter. Excellent fits to the measured spectra at 300 and 20 K were obtained with  $T_{eff} = 300$  K and  $T_{eff} = 80$  K, respectively. In the calculation of  $I_A(t)$ , I used  $\Gamma_i = 87$  meV and  $\sigma_0 = 9510$  barn, which were taken from ref.(16), and  $n_d = 7.95 \times 10^{19} \text{ cm}^{-2}$  which was calculated from the foil thickness. These results were consistent with a previous measurement [17].

I prepared a sample of  $HoBa_2Cu_3O_7$  (2 cm  $\times$  2 cm and 0.2 mm thick) and set it on the sample position.  $n_d$ 's of  $Ho$  and  $Ba$  in this sample, were  $6.5 \times 10^{19} \text{ cm}^{-2}$  and  $13 \times 10^{19} \text{ cm}^{-2}$ , respectively. Figs.6 and 7 show the TOF neutron absorption spectra of  $Ho$  and  $Ba$  in  $HoBa_2Cu_3O_7$ , which were simultaneously measured at 300 and 20 K. The channel width was 0.125  $\mu sec$ .  $I_A(t)$  for  $Ho$  in  $HoBa_2Cu_3O_7$  was calculated with the same values of  $\Gamma_i$  and  $\sigma_0$  as those used in the calculation for holmium metal. The solid lines in Figs.6(a) and (b) were calculated with  $T_{eff} = 300$  K and  $T_{eff} = 80$  K, respectively. Excellent agreement with the measured spectra was obtained. Note that the effective temperatures of  $Ho$  in  $HoBa_2Cu_3O_7$  are the same as those of holmium metal at both 20 and 300 K. These results indicate that the Debye temperature of  $Ho$  in  $HoBa_2Cu_3O_7$  is the same as that of holmium metal.  $I_A(t)$  for  $Ba$  in  $HoBa_2Cu_3O_7$  was also calculated using  $\Gamma_i = 124$  meV and  $\sigma_0 = 4680$  barn, taken from ref.(16). Since the Debye temperature of barium metal is 116 K,



**Fig. 6** Neutron absorption spectra of Ho in  $\text{HoBa}_2\text{Cu}_3\text{O}_7$  at 300 K and 20 K. The solid lines are the calculated spectra with  $T_{\text{eff}}=300$  K (a) and  $T_{\text{eff}}=80$  K (b), respectively.



**Fig. 7** Neutron absorption spectra of Ba in  $\text{HoBa}_2\text{Cu}_3\text{O}_7$  at 300 K and 20 K. The solid lines are calculated spectra with  $T_{\text{eff}}=300$  K (a) and  $T_{\text{eff}}=45$  K (b), respectively.

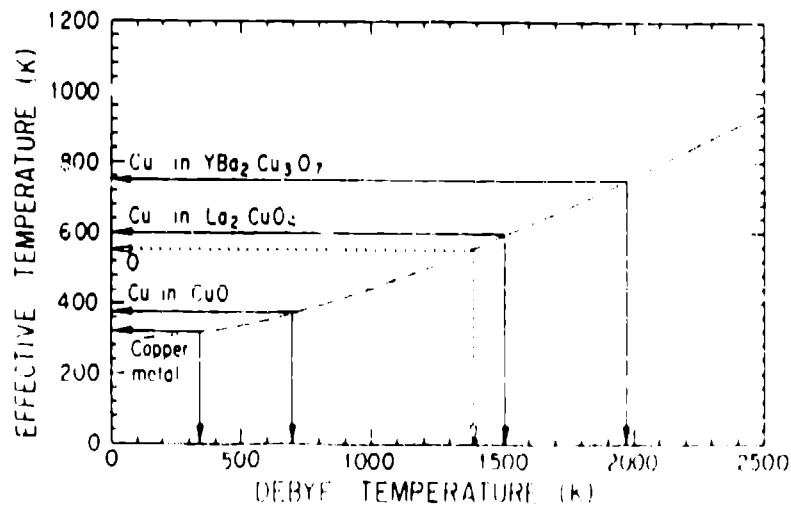
the effective temperatures of barium metal at  $T = 20$  K and  $T = 300$  K were calculated to be 45 and 300 K, respectively. The solid lines in Figs.7(a) and (b) were calculated with  $T_{eff} = 300$  K and  $T_{eff} = 45$  K, respectively. Good agreement with the measured spectra was obtained. These results also indicate that the Debye temperature of Ba in  $HoBa_2Cu_3O_7$  is the same as that of barium metal. From these results, the effective temperatures of Y and Ba in  $YBa_2Cu_3O_7$  at  $T = 300$  K were assumed to be  $T_{eff} = 300$  K. Then, the effective temperatures of Y and Ba were fixed and a fit was made to the neutron scattering spectrum of  $YBa_2Cu_3O_7$  using the effective temperatures of Cu and O as parameters. A satisfactory fit to the measured spectrum was obtained with  $T_{eff} = 750$  K for Cu and  $T_{eff} = 550$  K for O, as shown in Fig.5.

Table I shows the effective temperatures of O and Cu in copper metal, CuO,  $La_2CuO_4$  and  $YBa_2Cu_3O_7$ , obtained by the present experiments. Note that the effective temperature of O is 550 K in CuO,  $La_2CuO_4$  and  $YBa_2Cu_3O_7$ . This value is almost the same as the effective temperature of O in  $H_2O$  at  $T = 300$  K,  $T_{eff} = 500$  K [5]. My results may suggest that the effective temperature of O is almost independent of the structure and the bonding atom. The most interesting result in my experiments is that the effective temperatures of Cu in  $La_2CuO_4$  and  $YBa_2Cu_3O_7$  are much larger than those of CuO and copper metal, and that the effective temperature of Cu in  $YBa_2Cu_3O_7$  is larger than that in  $La_2CuO_4$ . The neutron absorption spectra of Ta in TaC and  $Ta_2O_5$  were measured in order to determine the effective temperatures of Ta. The results show that the effective temperatures of Ta are almost the same as that of tantalum metal in a wide temperature range of 40 - 300 K [17]. Generally, the effective temperature of a heavy atom in a compound with light atoms is considered to be the same as that of the pure heavy atom's metal, independently of the bonding atoms. My results for Cu in  $La_2CuO_4$  and  $YBa_2Cu_3O_7$  are opposed to 'the sound consideration'. This suggests that the Cu vibration is abnormal in  $La_2CuO_4$  and  $YBa_2Cu_3O_7$ . It might be interesting to calculate the Debye temperature by Eq.(4) in order to make a rough estimate of the density-of-state. The dashed line in Fig.8 shows the relation between the Debye

temperature and the effective temperature at  $T = 300$  K. By this relation, the Debye temperature of O was determined to be about 1400 K, and the Debye temperatures of Cu in  $La_2CuO_4$  and  $YBa_2Cu_3O_7$  were determined to be about 1500 and 2000 K, respectively. This indicates that the O vibration spectrum extends to 120 meV in  $CuO$ ,  $La_2CuO_4$  and  $YBa_2Cu_3O_7$ , and that Cu vibrations in  $La_2CuO_4$  and  $YBa_2Cu_3O_7$  may extend to 130 and 170 meV, respectively.

	O $T_{eff} (K) / \theta_D (K)$	Cu $T_{eff} (K) / \theta_D (K)$
Copper metal	—	319 / 343
CuO	550 / 1400	375 / 700
$La_2CuO_4$	550 / 1400	600 / 1500
$YBa_2Cu_3O_7$	550 / 1400	750 / 2000

**Table I** Effective temperatures and the Debye temperatures of O and Cu.



**Fig. 8** Relation between the effective temperature and the Debye temperature at 300 K.

## References

1. P.C. Hohenberg and P.M. Platzman, *Phys. Rev.* 152(1966) 196.
2. M.S. Nelkin and D.E. Parks, *Phys. Rev.* 119(1960) 1060.
3. H. Rauh and N. Watanabe, *Phys. Lett. A* 100 (1984) 244.
4. S. Ikeda and N. Watanabe, *Phys. Lett. A* 121 (1987) 34.
5. A.D. Taylor, *Proceedings of the 1984 Workshop on High-Energy Excitations in Condensed Matter* (Feb., 1984, Los Alamos) p.512.
6. W.E. Lamb, *Phys. Rev.* 55 (1939) 190.
7. J.G. Bednors and K.A. Muller, *Z Phys. B* 64 (1986) 18.
8. M.K. Wu, J.R. Ashburn, C.J. Torng and P.H. Hor, R.L. Meng, L. Gao, Z.J. Huang, Y.Q. Wang and C.W. Chu, *Phys. Rev. Lett.* 58 (1987) 405.
9. C. Politis, J. Greek, M. Dietrich, B. Obst and H.L. Luo, *Z. Phys. B* 66 (1987) 279.
10. L.F. Mattheis, *Phys. Rev. Lett.* 58 (1987) 1028.
11. W. Weber, *Phys. Rev. Lett.* 58 (1987) 1371.
12. P.W. Anderson, *Science* 235 (1987) 1196.
13. B. Renker, F. Gompf, N. Nucker, D. Ewert, W. Reichardt and H. Rietschel, *Z. Phys. B* 67 (1987) 15.
14. B. Renker, F. Gompf, E. Gering, G. Roth, D. Ewert, W. Reichardt and H. Rietschel, *Physica C* 153-155 (1988) 272.
15. H. Asano, K. Takita, T. Ishigaki, H. Akinaga, H. Katoh, K. Masuda, F. Izumi and N. Watanabe, *Jpn. J. Appl. Phys.* 26 (1987) L1341.
16. *Neutron cross sections*, 3rd Ed., BNL 325 (1973).
17. H. Rauh and N. Watanabe, *Nucl. Instrum. Methods* 222 (1983) 507.



## Future perspectives for liquids and amorphous materials diffraction at ISIS

A. K. Soper  
Neutron Science Division  
Rutherford Appleton Laboratory  
Chilton, Didcot, Oxon, OX11 0QX  
UNITED KINGDOM

**ABSTRACT:** A review is given of the current state of neutron diffraction from liquids and amorphous materials at ISIS. In particular the justification and status of the SANDALS diffractometer, which is now undergoing detailed design and construction, is reviewed, and compared with competing diffractometers in Europe and the U.S.A.. A general description of this instrument is included.

### 1. Introduction

In the last three years the proton current at ISIS has increased steadily so that it now operates routinely at 100 $\mu$ A. Although this is still below the design current of 200 $\mu$ A, it has become apparent that the majority of working neutron instruments are performing at least as well as originally planned and in some cases much better than expected. For liquids and amorphous materials diffraction the Liquids and Amorphous Diffractometer (LAD) was originally designed as the main workhorse for structure factor  $S(Q)$  measurements, and it has produced high quality datasets on such diverse materials as deuterium gas, superionic glasses, molten salts, molecular liquids, and aqueous solutions. Figures 1 and 2 show the measured structure factor and pair correlation function,  $g(r)$ , for amorphous boron as measured on LAD (R G Delaplane and U Dahlborg, 1987, unpublished data). Table I lists the experiments accomplished since May 1988. Recently the solid angle of the lower scattering angle detector banks on LAD was increased by a factor of 8 and this, combined with the high proton currents, means that more difficult experiments such as isotope substitution experiments have been tackled successfully.

ISIS and therefore LAD have come rather late in the field of disordered materials diffraction because intense reactor neutron facilities have been available in Europe since the early 1970's for this type of work. The ILL at Grenoble and the Orphée reactor at Saclay, both in France, have high count rate liquids instruments available, and several other European institutions have useful albeit lower flux facilities. Additionally in the time it has taken to bring ISIS on line liquids diffraction facilities at the ILL have undergone several upgrades with substantial rises in count rate. In the case of liquids or amorphous materials, where structural features are intrinsically broad the most difficult experiment that can be attempted correlates directly with the number of neutrons per measuring bin accumulated in the course of an experiment. ILL with its diffractometers D4B and D20, has generally taken the lead in terms of count rate, it being routine to obtain  $10^7$  counts in a Q-bin of width of say  $0.05\text{\AA}^{-1}$  in a few hours of running time. As a result there have

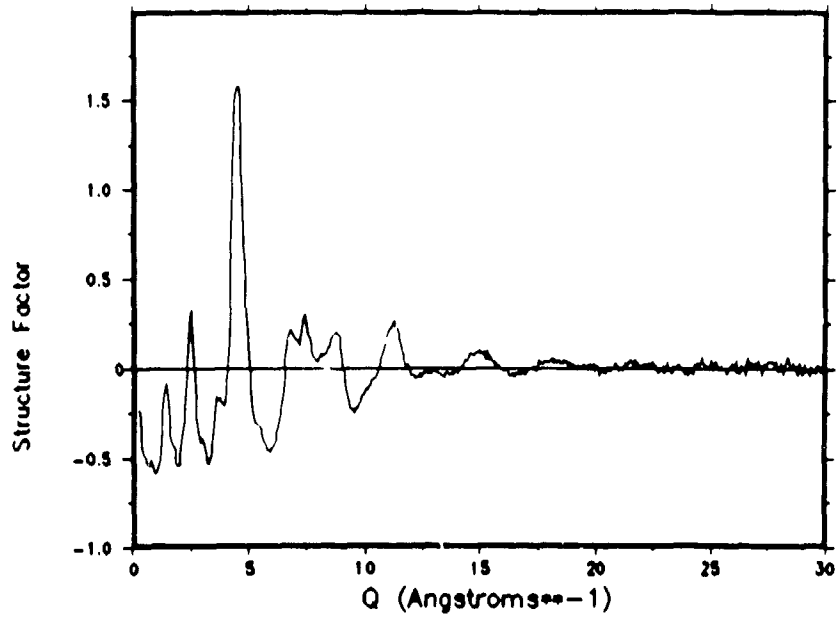


Figure 1. Measured structure factor for amorphous boron on LAD at room temperature.

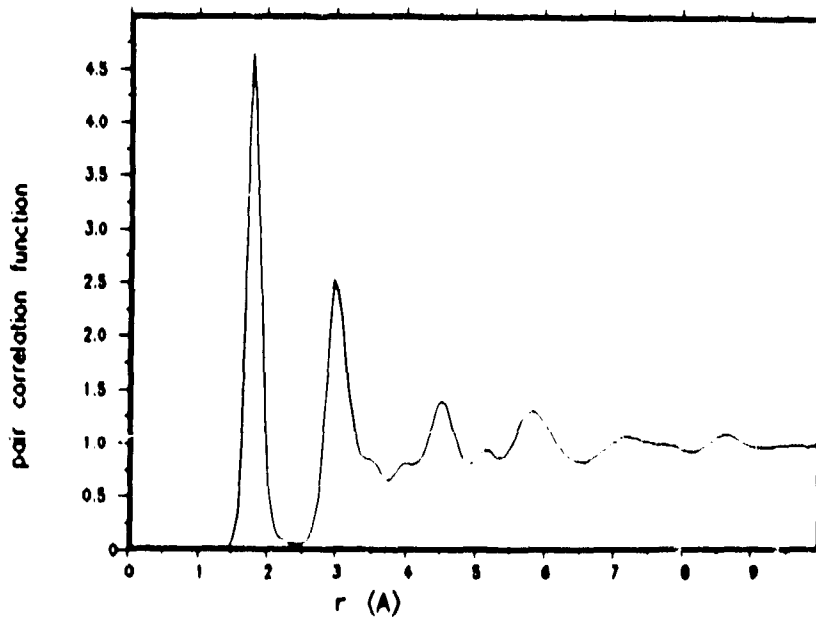


Figure 2. Calculated pair correlation function for amorphous boron, based on the structure data of figure 1. The coordination number of the first peak is 6, indicative of the icosahedral packing which has been proposed for this material.

been several significant achievements in liquid and amorphous diffraction at ILL: perhaps the most important contribution is that isotope substitution has become a routine technique for probing complex materials. It has for example revolutionized the study of ions in melts and aqueous solutions.

TABLE I Experiments on LAD May - September 1988

<u>Investigator</u>	<u>Institution</u>	<u>Sample</u>
Wood/Hove	Leicester University	molten KCl/ZnCl <sub>2</sub>
Borjesson/Torell	Chalmers U., Sweden	superionic glasses
Wright/Sinclair	Reading/Harwell	Pb-germanate glasses
Neilson/Sandstrom	Bristol/Stockholm	Cr-perchlorate solutions
Dupuy	Lyon, France	LiCl.6D <sub>2</sub> O glasses
Skipper	Oxford	Ni-vermicullite.3H <sub>2</sub> O
Fontana	Parma, Italy	Cu-nitrate solutions
Dahlborg	Stockholm, Sweden	iso-propanol glasses
Bermejo	Madrid, Spain	butane, methanthiol
Burgess	ICX	battery polymer
Orton	Brunel	molten antimony
Neilson/Adya	Bristol	molten ammonium nitrate
Yamaguchi	Fokoda, Japan	lanthanide perchlorate solutions

Therefore the case for using a pulsed source for diffraction on liquids and amorphous materials is based not on count rate, at which reactor sources have traditionally excelled, but on two intrinsic weaknesses of the reactor experiment which are unavoidable. First of all the region of Q over which it operates, typically in the region of  $0.4\text{\AA}^{-1}$  to  $17\text{\AA}^{-1}$  for D4B (wavelength =  $0.7\text{\AA}$ ) is always finite. This range can be extended by using several wavelengths but that reduces the effective count rate by a factor of 2 or 3. Also the reactor experiment necessarily involves a scan in scattering angle at fixed incident energy. This means that recoil or Placzek effects (Placzek 1952) deteriorate with increasing Q value resulting in great controversies about to how to cope with the corrections. (See for example the various attempts to measure the partial structure factors in liquid water: Thiessen and Narten, 1982; Soper 1984; Dore, 1985)

For time-of-flight diffraction, which uses fixed scattering angles, the range of Q values available is much broader, (for example LAD has a range in Q from  $-0.15\text{\AA}^{-1}$  to  $>50\text{\AA}^{-1}$ ) and the recoil correction is nearly independent of Q at small scattering angles (see figure 3). It will be noted that the correction is particularly small for scattering angles below  $20^\circ$ .

The LAD diffractometer at ISIS has detectors at scattering angles of  $5^\circ$ ,  $10^\circ$ ,  $20^\circ$ ,  $35^\circ$ ,  $58^\circ$ ,  $90^\circ$  and  $150^\circ$ , and resolutions ( $\Delta Q/Q$ ) at  $20^\circ$  of  $\sim 2\%$  and at  $150^\circ$   $\sim 0.5\%$ , Howells (1980). These are certainly good for most applications concerning disordered structures. In fact in the past LAD has doubled as a good medium resolution powder diffractometer. In addition the background is exceptionally low, the beam-on, no-sample count rate being essentially zero, due to the high degree of collimation in the scattered beam. Figure 4 shows a diagram of the instrument.

However this high degree of secondary flight path collimation ultimately limits the usefulness of LAD because it imposes detector solid angle

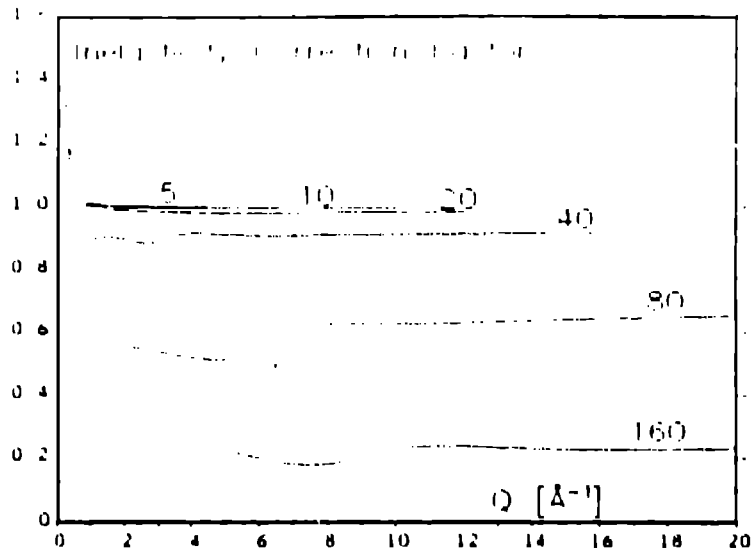


Figure 3. Calculated single atom scattering for a free particle of mass 2 at 40K. The number on each line refers to the scattering angle.

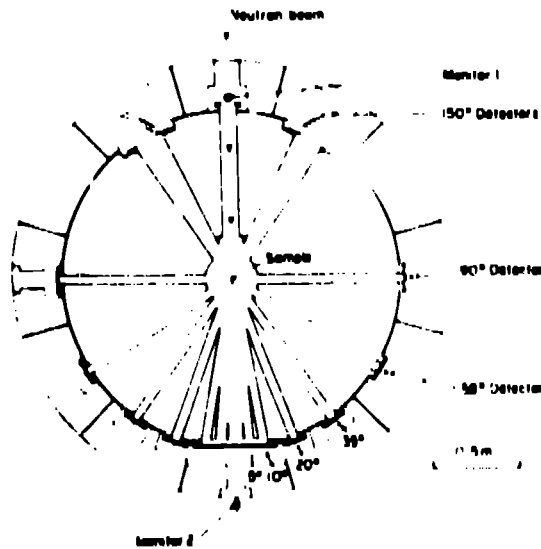


Figure 4. Layout of LAD. The unshaded region between scattered flight tubes is filled with shielding wax. The solid angle of two 20° banks combined is 0.02 sr.

constraints which mean the count rate is only as good as the ILL diffractometers over a rather limited range of  $Q$  near  $Q=1\text{\AA}^{-1}$ . (See discussion in Section 3 and Figure 5.) Therefore several years ago a proposal was made to complement LAD with a Small Angle Neutron Diffractometer for Amorphous and Liquid Samples (SANDALS) which would emphasize the small angle scattering region. By doing so it would reduce even further the smallest  $Q$  attainable to approximately  $0.05\text{\AA}^{-1}$  (this is crucial for experiments, such as those aiming at determining the pair potential, where accurate pair correlation functions are required), at the same time as reducing recoil (or Placzek) corrections by performing the whole diffraction measurement at small scattering angles. Subsequently two further conditions were established: to be viable SANDALS would have to be very competitive with ILL in terms of count rate. Also there has been a long-standing interest in the possibilities of exploiting the anomalous dispersion of the neutron scattering length near a nuclear resonance to tackle the problem of extracting partial structure factors from multicomponent systems; this would require a continuous span of detectors with scattering angle. These added requirements have necessitated several redesigns, but the various ideas have now converged to a final design which is currently under construction. The present schedule calls for the main detector tank and part of the detector bank to be in operation by the end of 1989.

This article therefore is devoted for the most part to a review of the ideas that have lead to the final SANDALS proposal.

## 2. Tests with the SANDALS prototype

Before final design of SANDALS could proceed it was necessary to check certain key aspects of the instrument, in particular the detector performance, the beam collimation and the count rate, and also to gain experience with data analysis with a large number of detectors. The original proposal called for a 14m flight path and since much of the collimator and beam stop had already been purchased these were installed on the beamline. A tank (volume  $1\text{m}^3$ ) from the NINROD accelerator was filled with argon and used as a detector tank; the detectors were two glass scintillator optically encoded modules, formerly from the LOQ instrument, making a total of 1120 detectors. These detectors subtended scattering angles of  $4^\circ - 8^\circ$  and  $11^\circ - 26^\circ$  respectively at the sample position. In addition several other detector types and configurations were tested. One experiment, on the water correlation functions in concentrated solutions of urea, was completed, Finney, Soper and Turner (1988).

The prototype produced the expected count rate based on known moderator parameters. However backgrounds were quite severe at high neutron energies ( $>1\text{eV}$ ), particularly at the smallest scattering angles. Comparison with other ISIS instruments indicated that there was a similar problem although much scaled down on LAD at  $5^\circ$  scattering angle and also on MET (with both choppers removed) at small scattering angles. In all three cases the problem appears to be related to the fact that the  $B_4C$  used in the collimator becomes a partial scatterer of neutrons and is less efficient at neutron capture at high neutron energies. As a result since the small angle detectors are difficult to shield they may view this  $B_4C$  and the background problem becomes exacerbated. Therefore careful attention has been paid in the SANDALS design to the final collimation stage.

The other main achievement of the prototype was to test various detectors. On the assumption that it would be prohibitively expensive to build the final detector bank from  $^3\text{He}$  tubes, then the only practical alternative was scintillator detectors, which could be built for a fraction of the cost of  $^3\text{He}$

tubes. Because they have not been tested nearly so extensively in neutron scattering applications, scintillator detectors inevitably require a longer development time. Two types of scintillator detector have been tested: glass scintillator and zinc sulphide scintillator. Both rely on  $^6\text{Li}$  for initial neutron capture. The former have an intrinsic deadtime, on the order of 100ns, but have a high background, on the order of  $0.5\text{cts/s/cm}^2$ , and more importantly cannot be made completely  $\gamma$ -insensitive. The latter property turns out to be serious for liquids and amorphous solids diffraction since many potential samples are likely to be sources of  $\gamma$  radiation when in a neutron beam. It is particularly serious for SANDALS where the demand for high efficiency detectors means thick scintillators are needed.

On the other hand the zinc sulphide scintillator which is built from a sandwich of scintillator materials between glass sheets, to assist light extraction, had  $\gamma$  sensitivity only marginally higher than a  $^3\text{He}$  tube and had a very low intrinsic background. Its deadtime was on the same order as a  $^3\text{He}$  tube. However the count rate in an individual module on SANDALS is unlikely to be sufficient that dead time would be important for these detectors. The zinc sulphide detector, has the important advantage that it can be made more efficient than a  $^3\text{He}$  tube at epithermal energies: a module 20mm deep can be made 30% efficient at a neutron energy of 10eV, which is twice as efficient as the corresponding  $^3\text{He}$  tube. Therefore it was decided to employ the zinc sulphide scintillator for SANDALS.

### 3. Count rate calculation and comparison of instruments

For liquids and amorphous materials diffraction, irrespective of whether it is constant wavelength or time-of-flight diffraction, the structure factor  $S(Q)$  is measured versus the momentum transfer,  $hQ/2\pi$ , where for elastic scattering

$$Q = 4\pi \sin \theta / \lambda \quad (1)$$

and  $2\theta$  is the scattering angle and  $\lambda$  the neutron wavelength. Because the features in  $S(Q)$  are rather broad (compared to crystalline powder diffraction) the requirements for resolution are relatively relaxed, but an adequate count rate can be crucial to obtaining a useful result, particularly for those experiments which involve differencing datasets as a function of pressure, temperature, isotope, etc. In these cases the differential behaviour is usually more important than the total scattering pattern. Therefore count rate is almost always the primary quantity of interest. Typically the data for  $S(Q)$  are mapped out in bins of width  $0.05\text{\AA}^{-1}$ , and the quantity of interest in rating the performance of a diffractometer is therefore the count rate per Q-bin per unit volume of standard scatterer which is normally vanadium:-

$$\text{neutrons / s / } 0.05\text{\AA}^{-1} / \text{cm}^3 \text{ of vanadium} \quad (2).$$

This definition serves to normalize out differences between instruments which are purely geometric in origin, (usually the size and shape of the beam at the sample position). This number is also useful to know for a given diffractometer: a rough estimate of the count rate for a given sample can be obtained by multiplying it by the volume of sample times the ratio of sample scattering cross section to vanadium scattering cross section. It would be helpful therefore if this number could be specified for all liquids diffractometers so that realistic intercomparisons could be made. For convenience I shall refer to the count rate number according to (2) as the "C number" for a given diffractometer.

For reactor experiments the count rate is almost independent of  $Q$ , but for pulsed sources the spectrum falls as  $1/Q$  in the epithermal region. In addition the detector efficiency is proportional to  $\lambda \sim 1/Q$ , so the measured count rate falls as  $1/Q^2$ . In practice efficiency corrections mean that the intensity falls more like  $1/Q^{1.7}$ , but even so there is a dramatic fall in measured count rate with increasing  $Q$ , as shown in figure 5, where the measured spectrum for LAD at a scattering angle of  $20^\circ$  is displayed.

TITLE : C-Number for LAD at 20 deg.

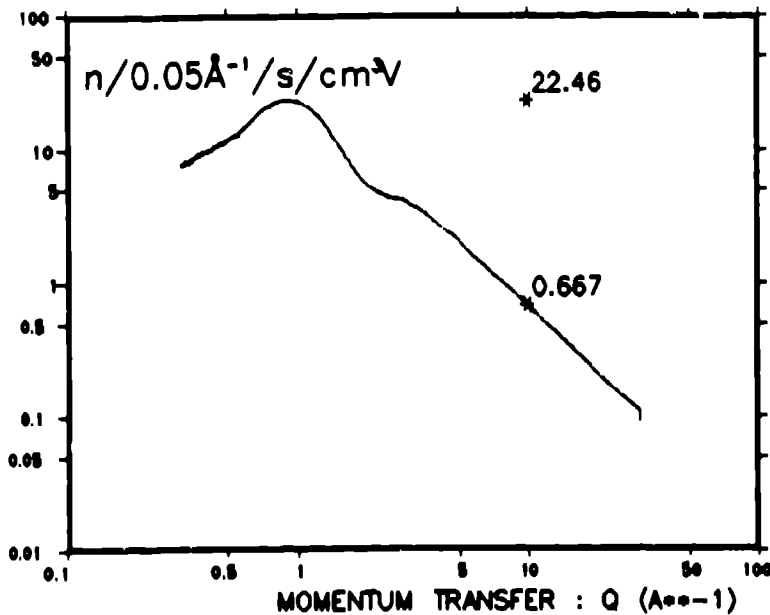


Figure 5. Measured count rate (or "C-number" -- see text) for LAD at  $20^\circ$  scattering angle as a function of  $Q$ . Note the log a .

For the methane moderator at ISIS, the parameter that describes the epithermal flux is  $\phi_0$  and at 100 $\mu$ A proton current and 750 MeV energy, this has the value for a moderator area of 10<sup>2</sup> square cm, Taylor (1984)

$$dI/dE = \phi_0 = 2.7 \times 10^{12}/E^{0.92} n/\text{eV}/\text{sr}/100\text{cm}^2/\text{s} \quad (3).$$

$$\begin{aligned} \text{Now } E &= Q^2 \text{ so } dI/dQ = 2(E/Q)dI/dE = 5.4 \times 10^{12}/Q n/\text{\AA}^{-1}/\text{sr}/100\text{cm}^2/\text{s} \\ &= 2.7 \times 10^{11}/Q n/0.05\text{\AA}^{-1}/\text{sr}/100\text{cm}^2/\text{s} \quad (4). \end{aligned}$$

Using these values the expected count rate on LAD can be estimated. It is assumed that:

- (i) the collimator views most of the active area of moderator;
- (ii) the incident flight path is 10m;

- (iii) the sample is a cube of vanadium,  $10 \times 10 \times 10 \text{mm}^3$  in volume (corresponding to a 30% scatterer);
- (iv) detector is 30% efficient (corresponds to a  $^3\text{He}$  tube at 2eV, and  $Q=10\text{\AA}^{-1}$  for  $20^\circ$  scattering angle);

then the scattered count rate per unit detector solid angle is

$$\begin{array}{ccccccc}
 2.7 \times 10^{11} & \times & 0.3 & \times & 1.0 \times 10^{-6} & \times & 0.3 / 4\pi Q \\
 \uparrow & & \uparrow & & \uparrow & & \uparrow \\
 \text{moderator} & & \text{fraction} & & \text{sample} & & \text{Detector} \\
 & & \text{scattered} & & \text{solid} & & \text{efficiency} \\
 & & \text{by sample} & & \text{angle} & & \\
 & & & & \text{at} & & \\
 & & & & \text{moderator} & & \\
 \end{array}$$

$$= 1940/Q \text{ n}/0.05\text{\AA}^{-1}/\text{sr}/\text{s}/\text{cm}^3\text{V}. \quad (5)$$

It will be noted that this number, which of course applies strictly only to the epithermal region of the spectrum, is independent of scattering angle for a given Q value. The fact that count rates vary for different scattering angles and different Q values in practice arises because the thermal part of the spectrum eventually takes over at low neutron energies and in any case the detector efficiency will be different for the same Q value at different scattering angles. For LAD at  $2\theta = 20^\circ$  the detector area is  $2 \times 0.04 \times 0.2 \text{m}^2$  and the final flight path is 1.0m, and so for  $Q = 10\text{\AA}^{-1}$  the C-number is  $3.1\text{n}/0.05\text{\AA}^{-1}/\text{s}/\text{cm}^3\text{V}$ . I quote the C-number at  $Q = 10\text{\AA}^{-1}$  since it is important to remember the very rapid decline in count rate at a pulsed diffractometer with increasing Q value.

Figure 5 shows that the measured C-number is much lower at  $-0.7\text{n}/0.05\text{\AA}^{-1}/\text{s}/\text{cm}^3\text{V}$  for this Q value (and  $-22\text{n}/0.05\text{\AA}^{-1}/\text{s}/\text{cm}^3\text{V}$  at  $Q = 1\text{\AA}^{-1}$ ), and the reason for this disagreement is not clear at the present time. It should be born in mind of course that for most experiments several LAD detector banks can be combined so that the count rate should be multiplied by a factor of  $\sim 2-3$  to get a realistic estimate of likely count rates. Even so the very rapid fall in count rate with increasing Q is clear from figure 5.

For the new glass diffractometer at IPNS, GLAD, the estimated C-number assuming a full complement of detectors at the same Q value is  $\sim 20 - 25\text{n}/0.05\text{\AA}^{-1}/\text{s}/\text{cm}^3\text{V}$  at  $Q = 10\text{\AA}^{-1}$ , Montague and Price (1988), which includes the factor of 2.5 enhancement which has taken place since the booster target was installed.

Finally for the D4B diffractometer at ILL the measured neutron flux on the sample is  $4 \times 10^7 \text{ n}/\text{cm}^2/\text{s}$  for a wavelength of  $0.7\text{\AA}$ , so the C-number for the standard cube of vanadium would be

$$\begin{array}{ccccccc}
 4 \times 10^7 & \times & 0.3 & \times & 5.5 \times 10^{-4} & \times & 0.67 & \times & 0.15 / 4\pi \\
 \uparrow & & \uparrow & & \uparrow & & \uparrow & & \uparrow \\
 \text{flux} & & \text{fraction} & & \text{detector} & & \text{detector} & & \text{sampling} \\
 & & \text{scattered} & & \text{solid} & & \text{effic.} & & \text{factor} \\
 & & \text{by} & & \text{angle} & & & & \\
 & & \text{sample} & & \text{for } 0.05\text{\AA}^{-1} & & & & \\
 & & & & \text{bins} & & & & \\
 \end{array}$$

$$= 53 \text{ n}/0.05\text{\AA}^{-1}/\text{s}/\text{cm}^3\text{V}. \quad (6)$$



The sampling factor arises here because the present detector does not scan all scattering angles simultaneously. This number is entirely in accord with the observed count rate from a sample of vanadium placed in the neutron beam on D4B (A C Barnes, 1988, private communication). Comparison of this C-number with figure 5 shows that when several angles are combined the LAD diffractometer is already as intense as D4B, but only in a narrow region of Q, around  $Q=1\text{\AA}^{-1}$ . Outside this region the intensity falls off rapidly.

#### 4. Design of SANDALS

The count rate numbers of the previous section tell their own story: whatever the cause for the measured count rate on LAD being lower than the number based on moderator performance figures there was no avoiding the conclusion that the count rate on LAD was inherently lower than on competing diffractometers over a range of important Q values, i.e.  $Q = 5\text{\AA}^{-1}$  to  $20\text{\AA}^{-1}$ . This was a key result which has directed the design of SANDALS. The principal goal has been to strive for the maximum solid angle of detector in the "small" angle region (i.e. for  $2\theta < 40^\circ$ ), with a continuous span in scattering angle, that can be achieved within the engineering constraints imposed by allowed sizes of vacuum tanks and windows and the restrictions imposed by including some shielding in the scattered flight path. As a result the available solid angle will be approximately 40% of the theoretically maximum. As seen in table II this still will ensure that SANDALS is highly competitive in count rate if the full detector complement is available.

TABLE II Some Design Specifications for SANDALS

Moderator:	Kethane, 100K
Incident Flight Path:	11m
Beam Cross Section:	Circular
Maximum Beam Aperture:	32mm (diameter)
Final Flight Path:	0.75m - 4.0m
Detectors:	Zinc sulphide sandwich detectors 200 (high) x 10 (wide) x 2 (deep) mm 30% efficient at 10eV

Range In <u><math>2\theta</math></u> (deg.)	Detector <u>Solid Angle</u> (sr)	<u>High Resolution</u>		<u>Low Resolution</u>	
		<u>Resolution</u> $\Delta Q/Q$ (%)	<u>C-number</u> (at $Q=10\text{\AA}^{-1}$ )	<u>Resolution</u> $\Delta Q/Q$ (%)	<u>C-number</u> (at $Q=10\text{\AA}^{-1}$ )
3 - 11	0.043	11 - 2	0.3	16 - 4	7
11 - 21	0.121	2	1.6	4 - 3	35
19 - 31	0.222	1.5	3.9	3	84
29 - 41	0.301	1.3	6.1	2.5	131

The projected count rates have been achieved by shortening the original proposed flight path from 14m to 11m, by opening up the beam from 10mm diameter to 32mm diameter and by increasing the detector solid angle from the original SANDALS proposal (Appendix to NBRC 9-85, 1985). Of course there is a penalty in resolution that has been paid in doing so, although this is not likely to be serious for the high count rate, isotope substitution diffraction work which is likely to feature very frequently in the SANDALS experimental program. However since there will undoubtedly be some experiments which require better resolution than the default resolution, provision is being made to narrow the beam and view a smaller area of moderator if so desired, by placing beam defining apertures of 24mm and 16mm at 6.25m and 9m from the target respectively. Although these will give lower count rates, they will double the resolution in the small angle region. As a further provision the sample tank will include windows for detectors at larger scattering angles up to 120° in the event that better resolution is needed in the future.

An obvious problem that arises at small angles when dealing with large arrays of detectors is that the resolution can vary sharply with scattering angle, which can make combining detectors from different angles problematic if resolution effects are apparent. Therefore a further feature of the design is that the detectors lie on a trajectory of continuous and nearly constant resolution. At small scattering angles this trajectory corresponds approximately to the surface of a cylinder whose axis is coincident with the transmitted beam. With this geometry the resolution varies by a factor of  $\sim 2$  over the scattering angle range 10° - 40°.

Table II lists the principal characteristics of the proposed SANDALS diffractometer and figures 6 and 7 show two views of the sample vacuum tank. It will be noted that the reduction of count rate from low resolution to high resolution options is on the order of a factor of 20: this is because the resolution of the instrument at small angles is dominated by the angular divergence of the incident beam. The only way to improve this resolution is to restrict the aperture of the beam with a consequent large reduction in count rate. To build the "ideal" geometry with equal contributions to the resolution from moderator, sample and detector would require a much larger area of detector than the present proposal, would increase the linear dimension of the instrument by a factor of at least 1.5, would lead to increasing difficulties with frame overlap at the ISIS repetition rate of 50Hz, and would escalate the cost significantly above the present allocation. To compensate for the increased cost there would have to be reduced solid angle coverage which would correspondingly negate the advantages of the larger instrument. It is felt that the present design is probably optimal given the conflicting demands of count rate, resolution, cost and engineering constraints. It should also be noted that in the high count rate/low resolution mode SANDALS will remain competitive in count rate with ILL even if further proposed modifications to D4B are implemented.

Outside the vacuum tank the scattered flight path to the detector modules will be filled with argon gas to reduce air scattering. The gas will be contained in boxes lined with B<sub>4</sub>C baffles to reduce neutron backgrounds from sources other than the sample. The detectors themselves will be surrounded in B<sub>4</sub>C (except in the direction of the sample!) Finally the entire instrument will be entombed in wax shielding to remove external sources of background. It is anticipated that the full array of sample environment equipment which is used on the other ISIS instruments will be available for use on SANDALS as well.

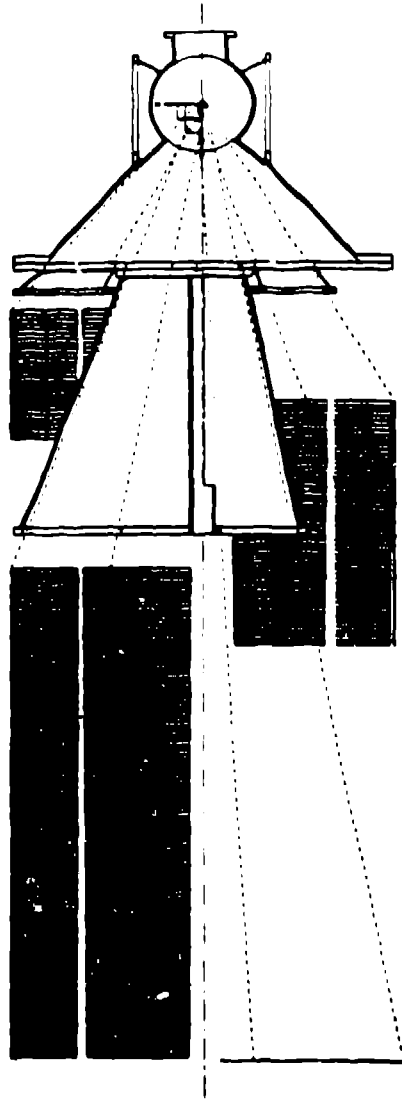
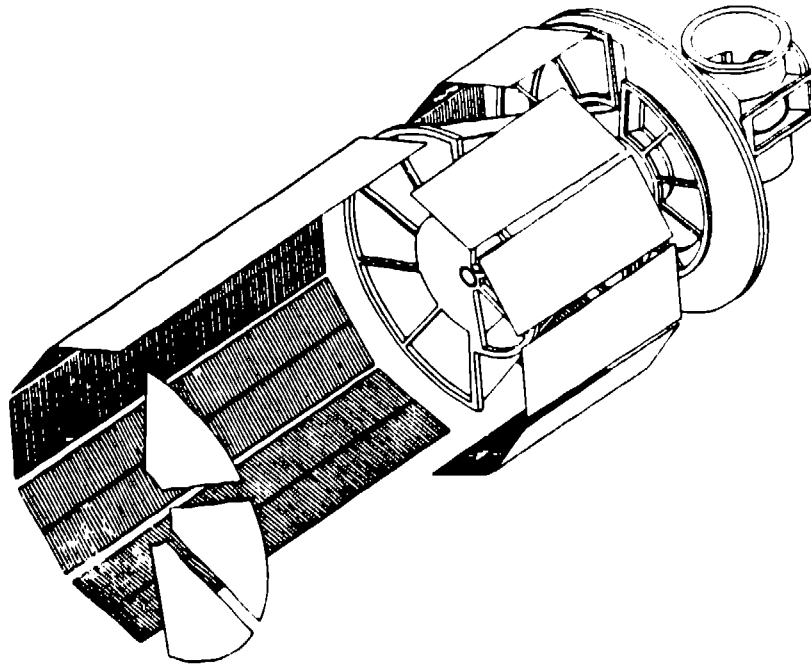


Figure 6 Plan layout of the SANDALS sample tank and detectors. The beam enters the tank at the top of the diagram and leaves at the bottom, and the sample is placed at the centre of the circular tank. The distance from sample to small angle detector is 4m, and the other detector banks are 0.75m from the transmitted beam axis.



**Figure 7** Three-dimensional view of the SANDALS detector tanks. The beam enters at the upper rightmost corner of the diagram and exits at lower left. The scintillator detectors lie on the surface of a cylinder of radius 0.75m.

#### **5. Conclusion - Beyond SANDALS**

The availability of high count rate diffractometers has increased the complexity of systems that can be investigated. This complexity increases roughly as the square root of the count rate and so there will in the future, as count rates are pushed even higher, be a trend to look at more technologically interesting materials, such as liquids under extremes of pressure and temperature, local coordination in dilute mixtures, complex molecular fluids, and fluids at surfaces. For example the structural changes which occur near the glass transition are real but rather subtle and would greatly benefit from the detail possible with isotope substitution. In this sense therefore the field of liquid and amorphous material diffraction is unlimited in scope. However the limiting factor at the present time is not count rate, but detector stability and sample preparation; count rate is only useful if the sample is good enough to withstand the precise investigation possible with higher statistics and the detector efficiency fluctuations over the course of an entire experiment are no worse than the statistical precision. It is not clear whether either condition is being met for the instruments presently available, although it is likely that as count rates improve still further they will necessarily drive a demand for better characterised samples and more stable detectors.

The data analysis stage is also crucial, and whilst it is essentially routine to proceed from measured diffraction data to a reliable pair correlation function, this is really only the first stage of the experiment: the real job is to interpret the correlation functions. At present the only practical way to achieve this is to computer model the system under investigation because the process of going from assumed potential function to correlation functions is extremely non-linear. Current methods centre mostly on assuming pair-wise forces, a serious limitation which will have to be removed in the future. Since the process of data analysis yields advances over a period of time it likely that the techniques of instrument development and data handling will develop concurrently.

If the past is an indication of the future then it is clear that worldwide there has been a continuing interest in the structure of the fluid and amorphous states for many years now. This interest is fueled by unresolved fundamental and technological issues. Neutron diffraction is therefore likely to remain an important tool in the rather large array of techniques that can be applied to this problem because it yields accurate, absolute values for the underlying correlation functions.

In this article I have attempted to outline the existing "state of the art" for liquids and amorphous diffraction at ISIS, and the reasons for having adopted the current specification for SANDALS. It is clear that the proposed instrument will probably make optimal use of the present ISIS neutron source. It will form a unique facility for liquids and amorphous diffraction by providing a wider range of Q values, and by reducing recoil corrections, compared to equivalent reactor based instruments. At the same time the count rate on SANDALS will be highly competitive with other liquids diffraction facilities around the world.

Because SANDALS will fully exploit the current ISIS neutron source, the next generation of liquids diffractometers must look towards a revised source and moderator configuration. Assuming the cost of building a diffractometer is not the limiting factor the primary constraints imposed by the present source for this work are the repetition rate, which as discussed above leads to an instrument which is too small to make full use of the available neutron flux, and the neutron pulse width, which currently makes a negligible contribution to the resolution. Increases in both resolution and count rate could be achieved with a lower repetition rate source, and a moderator which produces broader neutron pulses.

References

- Dore J C, 1985, in "Water Science Reviews", ed. by F. Franks (Cambridge University Press, 1985), Vol. 1, Chap. 1.
- Finney J L, Soper A K and Turner J Z, 1988, Proceedings of the International Conference on Neutron Scattering, Grenoble, to be published in Physica.
- Hovells W S, 1980, RAL report RL-80-017
- Montague D G and Price D L, 1987, "Preliminary conceptual design of the GLAD scattered flight path", D.L.Price and D.G.Montague, Argonne. Natl. Lab., communicated on Dec 21 1987 to the GLAD participating research team.
- Placzek G, 1952, Phys. Rev. 86, 377
- Soper A K, 1984, Chem. Phys. 88, 187
- Taylor A D, 1984, RAL report RAL-84-120
- Thiessen W E and Narten A H, 1982, J. Chem. Phys. 77, 2656

# A comparison of germanium and copper analyzers for pulsed-source crystal-analyzer spectrometers

M. Yethiraj and R. A. Robinson  
Los Alamos Neutron Scattering Center  
Los Alamos National Laboratory  
Los Alamos, New Mexico 87545  
USA

**ABSTRACT:** We describe the new copper "organ-pipe" analyzer installed on the Los Alamos Constant-Q Spectrometer<sup>(1)</sup> and compare its performance with the previous germanium analyzer. In addition, we discuss the implications of our experience for pulsed-source crystal-analyzer spectrometers in general.

## 1. Introduction

It has long been realized<sup>(2)</sup> that, for thermal and hot neutrons, beryllium is the material of choice for crystal monochromators and analyzers. On the basis of reflectivities, copper and silicon are next best, but the silicon coherent scattering cross-section is so small that silicon monochromators and analyzers would be impractically large (in thickness)<sup>(2)</sup>. Given that it is only recently that single crystal beryllium has been grown reproducibly with sufficient quality for neutron monochromators<sup>(3)</sup>, copper is still the most practical choice for most thermal and hot neutron applications. On the other hand, if second-order contamination is a problem, the odd-index reflections (like (111), (113), (331) etc.) of a diamond-structure material like germanium can be used. The second-order reflections are systematically absent. However, a significant price will be paid in reflectivity (and hence intensity at the detector) when compared with a copper monochromator or analyzer. Within the neutron scattering community, a folklore has built up that order contamination is a significant problem on crystal-analyzer spectrometers and that one must therefore use germanium as an analyzer, even though the orders of reflection are separated by normal time-of-flight analysis. It seems that this belief has its origins in early experiments<sup>(4,5)</sup> in which the (004) or (006) reflections of pyrolytic graphite were used. It is straightforward<sup>(6,1)</sup> to show that, for an analyzing energy  $E_F$  and a primary to secondary flight path ratio  $L_1/L_F$ , the limiting condition for observing an excitation of energy transfer  $E$  in the presence of  $n$ th-order elastic contamination is:

$$\frac{E}{E_F} \leq \left[ \frac{n}{1 - (n-1)(L_F/L_1)} \right]^2 - 1 \quad (1)$$

While this is not the whole story, in that the corresponding  $n$ th-order energy gain processes (from thermally populated phonons or magnons) and the effects of finite resolution are not included, it does provide a reasonable estimate of the constraints imposed by order contamination. For second order contamination ( $n = 2$ ) and  $L_i/L_F = 3.5$ , which is roughly what we now have on the Los Alamos Constant-Q Spectrometer, this gives  $E_i/E_F \leq 6.9$ . Since one would not normally consider transferring much more than half of the incident energy to the sample, second-order contamination should not be a problem. Together with the fact that we had already done successful experiments with the germanium (220) reflection, which does have second-order contamination, this line of argument led us back to copper as an analyzer material

## 2. The analyzer

The "organ-pipe" analyzer geometry employed on the Los Alamos Constant-Q Spectrometer has been described previously<sup>(1)</sup> and is illustrated schematically in Fig. 1. It has three advantages over the conventional disc geometry:

1. the combination of (a) having the cylinder axes parallel to the  $[1\bar{1}0]$  axis and (b) pressing the original single crystal blocks parallel to the  $[110]$  axis, as described in Ref. [1], means that one has a large horizontal and narrow vertical mosaic spread for all reflections of the type  $(h k)$ .
2. the whole analyzer is used all of the time, in contrast to the disc geometry. This means that the minimum amount of material is used.
3. the analyzer thickness can be varied as a function of scattering angle, so as to optimize the reflectivity, as shown in Fig. 1.

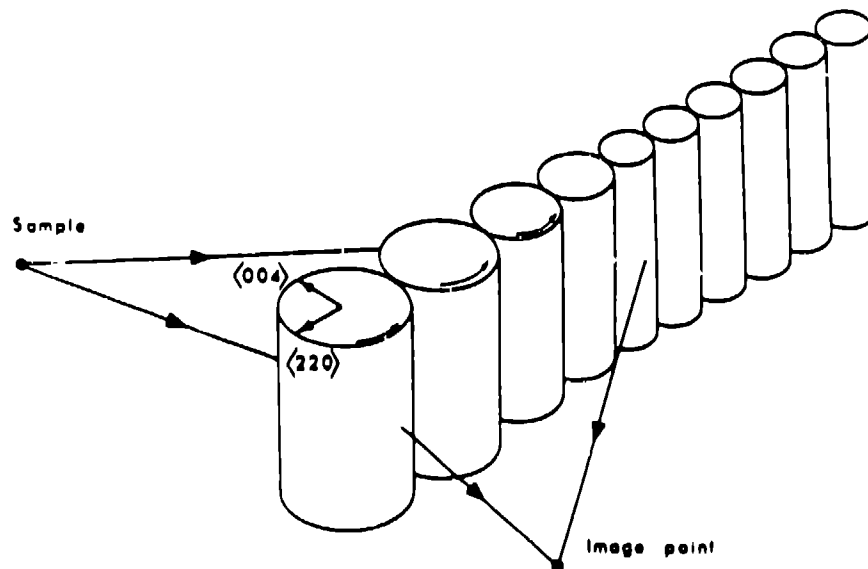


Fig. 1 A schematic figure showing the "organ-pipe" geometry.



The photograph in Fig. 2a shows our original germanium analyzer. The original oriented germanium single crystals, of size 4 x 4 x 8 cm were bought from Eagle Picher Industries and hot-pressed in situ on a  $\gamma$ -ray diffractometer at the Institut Laue Langevin, Grenoble. The mosaic spread is approximately 30'FWHM. Unfortunately, the original single crystals had significant small-angle grain boundaries, as detected in  $\gamma$ -ray scans and the boundaries widened in angle during deformation. Some of the mosaic spread is therefore non-uniform. The germanium cylinders were then diamond core-drilled from the rectangular blocks used for pressing. These crystals were then oriented on a two-axis diffractometer at the University of Missouri Research Reactor and glued, with dental cement, on to the mount shown in Fig. 2a. This consists of a set of vertical shafts driven by a worm and gear system from two horizontal shafts geared to a stepping motor. We wished to locate the crystals as close together as possible and this necessitated the use of two horizontal shafts rather than one. This system has worked well. The only problem encountered with it was that one of the horizontal shafts slipped, along its axis, relative to the other, with the consequence that the even crystals were misoriented by about 1° with respect to the odd crystals. We believe that this was due to incorrect seating of one of the bearings during assembly. This manifested itself in the form of double peaks in scans with an elastic incoherent elastic scatterer and the system was realigned on a two-axis diffractometer at the Omega West Reactor at Los Alamos.

Figure 2b shows the copper analyzer, which was constructed in a similar fashion. Again, plastic deformation was performed in Grenoble, cylinders were spark-eroded from the original boules and the analyzer was assembled on a two-axis neutron diffractometer at Missouri. In this case, we found that the optimum thickness varied much less strongly than for germanium. We therefore decided to use a single diameter (15 mm) for the cylinders. This gives us more flexibility in positioning the analyzer, as it is no longer optimized for specific scattering angles. In addition, optical encoders were installed on the horizontal shafts to aid in diagnosis of problems like that described above. The mosaic spread was approximately 20' FWHM.

### 3. Results

For comparison purposes, we show results for the elastic line from a standard  $ZrH_2$  sample with both the germanium (331) and the copper (220) reflections. The d-spacings for these reflections are 1.2979 Å and 1.2780 Å respectively. Sections of representative scans are shown in Fig. 3. Figure 4 shows the variation of integrated intensity as a function of scattering angle within our spectrometer. The normalized integrated intensity is about 4.5 times greater for the copper analyzer. This is a much greater difference than the 70% increase calculated using the program MONO<sup>(7)</sup>. In addition, the lineshape (see Fig. 3) is much cleaner. This is due to a more ideal mosaic spread in the case of the copper analyzer. There was no significant difference in the background levels with the two analyzers.

### 4. Discussion

Returning to Eqn. 1, one is very unlikely to build a spectrometer with  $L_p$  outside the limits  $0 < L_p < L_1$ . The corresponding energy ratios,  $E/E_p$ , lie between 3 and

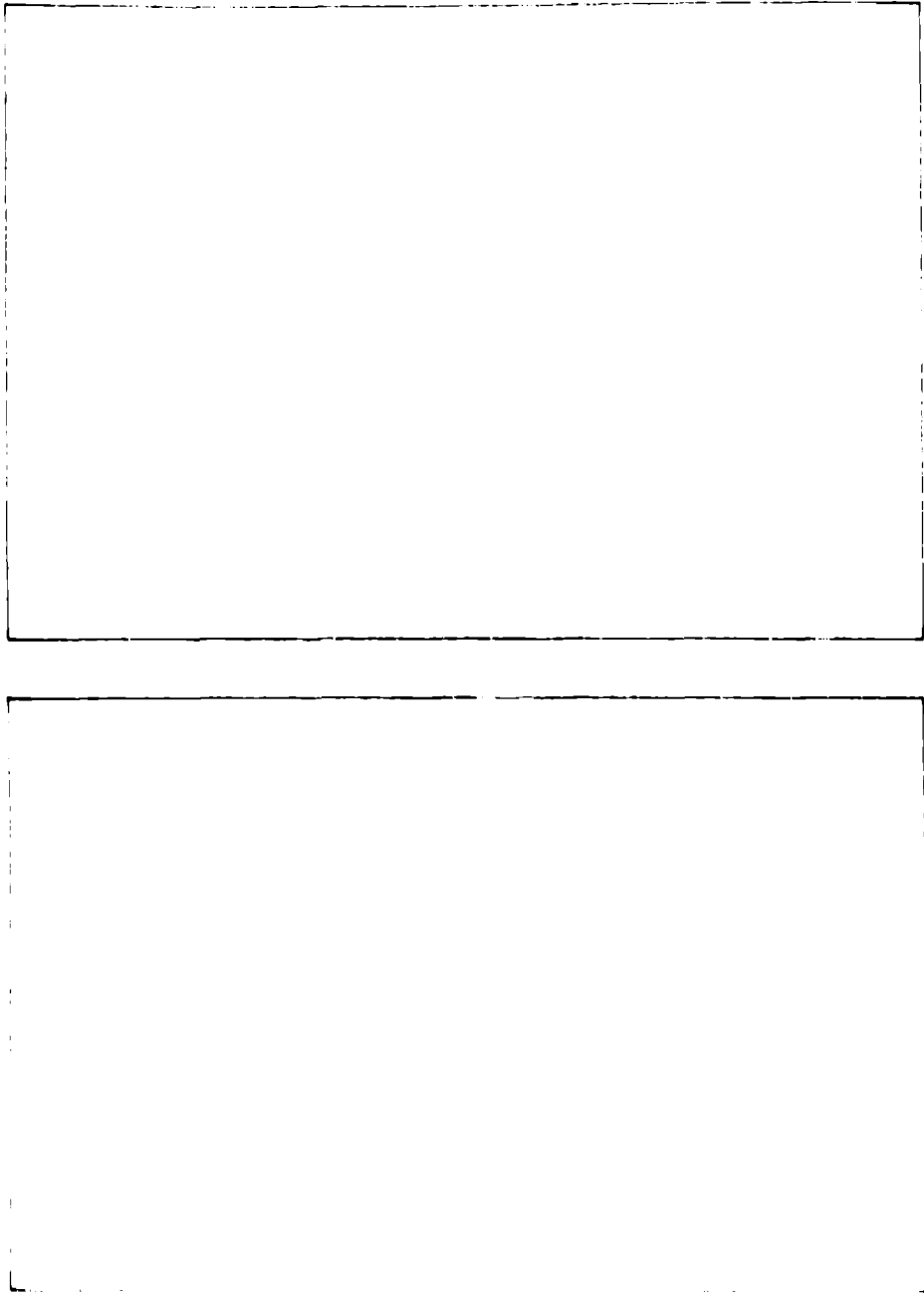


Fig.2 Photographs of (a) the germanium analyzer and (b) the copper analyzer.

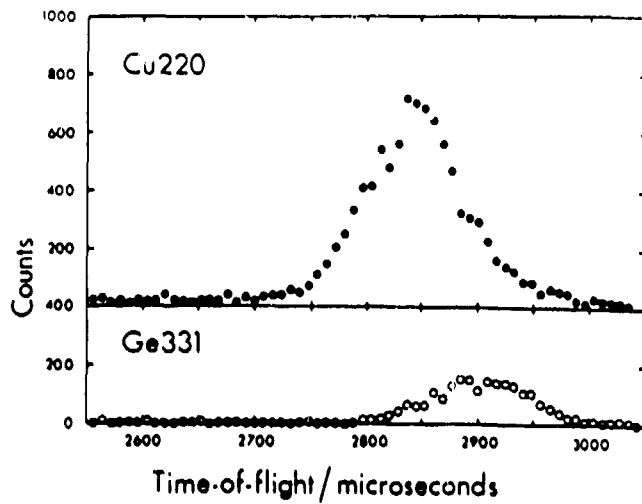


Fig.3 A typical time-of-flight scan through the incoherent elastic peak from  $ZrH_2$  for Cu(220) and Ge(331) analyzers. The d-spacings differ by less than 2% and the monitor count was approximately 10% greater for the germanium run.

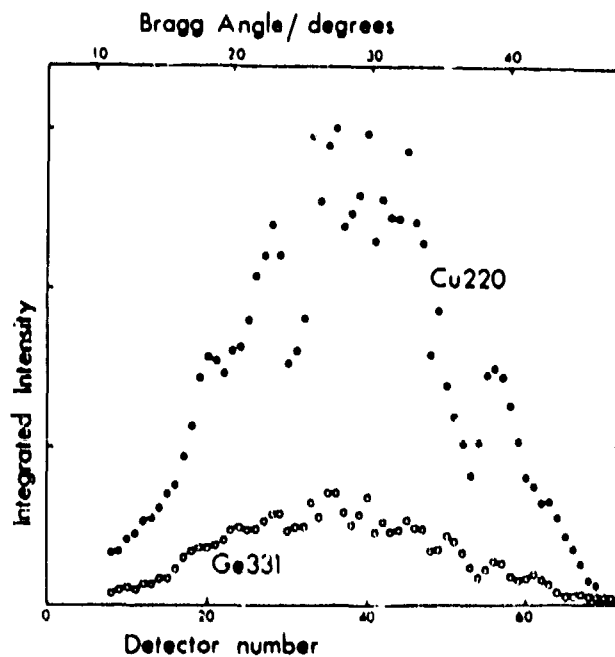


Fig.4 Integrated intensities (normalized to the same monitor count) for a wide range of detectors and the two analyzers Cu(220) and Ge(331).

infinity, for  $n=2$ . So, even in the worst case, second-order contamination should not be a problem, although it is fair to state that the longer the secondary flight path is, the less of a problem one has with order contamination. We conclude that there is no compelling reason to use diamond structure analyzer materials on pulsed-source crystal-analyzer spectrometers, unless one is consistently depositing most of the energy in the sample. One can always achieve a higher reflectivity with copper and the relative performance will be even better than one calculates. This is simply because it is easier to achieve good plastic deformation with the latter and, as a consequence, one is closer to the ideal mosaic model and the observed copper reflectivities will be nearer to the calculated values. Even on existing spectrometers with germanium analyzers it is simple to check the points raised above: use of reflections like (220), which are contaminated by second-order, should give more intensity than the odd-indexed reflections as the structure factor is twice as large.

### Acknowledgements

We are indebted to A. K. Freund for numerous discussions and invaluable assistance in the fabrication of both analyzers. We are also grateful to the staffs of both the Institut Laue-Langevin and the University of Missouri Research Reactor for assistance in deforming and mounting the analyzer components. This work was supported, in part, by the division of Basic Energy Sciences of the US Department of Energy.

### References

1. R. A. Robinson, R. Pynn and J. Eckert, 1985, Nucl. Inst. Meth. A241, 312.
2. A. K. Freund and J. B. Forsyth, 1979, in "Neutron Scattering in Materials Science", ed. G. Kostorz, Academic Press, p.477.
3. A. K. Freund, S. Jönsson, S. Sultz and G. Petzow, 1984, J. Nucl. Mater. 124, 215.
4. C. G. Windsor, R. K. Heenan, B. C. Boland and D. F. R. Mildner, 1978, Nucl. Inst. Meth. 151, 477.
5. R. Pynn and C. G. Windsor, private communication.
6. C. G. Windsor, 1981, "Pulsed Neutron Scattering", Taylor and Francis, London, ch. 9.
7. R. A. Robinson and A. K. Freund, 1985, Institut Laue-Langevin Report 85FR13T.

## Recent results with the Los Alamos Constant-Q Spectrometer

*M. Yethiraj and R. A. Robinson*  
Los Alamos Neutron Scattering Center  
Los Alamos National Laboratory  
Los Alamos, New Mexico 87545  
USA

### 1. Introduction

The Constant-Q geometry for measuring collective excitations on pulsed-neutron sources was proposed and tested by Windsor et al.,<sup>(1)</sup> in 1978. By 1985, a second improved Constant-Q spectrometer had been built at Los Alamos<sup>(2)</sup>, and improvements over Windsor's version were listed in a previous ICANS proceedings<sup>(3)</sup>. In this article, we list further improvements made to the Los Alamos spectrometer and give a brief account of other progress on it.

### 2. Improvements since 1985

- (a) Following the flight-path nomenclature in Ref. 2,  $L_2$  was increased from 200 mm to 400 mm. This was made possible with the large multi-element analysers described elsewhere in these proceedings<sup>(4)</sup>. It had effect in reducing backgrounds and diminishing contamination from nearby reflections in the analyser.
- (b) We installed a new copper "organ-pipe" analyser, described elsewhere in these proceedings<sup>(4)</sup>, which gave intensity increases of a factor 3 to 5.
- (c) The detector complement was increased further from 64 to 96. The angular range now covered is from  $7^\circ$  to  $62^\circ$ .
- (d) The line-up detector system was modified so that the three detectors now have independent preamplifiers and independent channels in the multiplexer. Summing is now done in software, although the signals can also be added directly and fed to a rate meter and simple counting chain for manual alignment of samples.
- (e) Some improvements were made to the shielding in the region of the image point, mainly by using low-albedo materials (like  $B_4C$  and  $^{10}B-AI$ ) in well-engineered containers. In addition, the image point can now be flushed with argon gas.

### 3. Calibration procedures

By measuring Bragg peaks from a nickel powder sample at the image point, we calibrate the flight path distances as well as the initial angle and the angular increment. Further, the scattering through the analyser of a  $ZrF_2$  powder at the sample position is a check of the initial calibration; in this case, the elastic peak should also correspond to zero energy transfer if the calibration is correct.

The above procedure was further tested by running with a KBr powder at the sample position using the 220 reflection in Ge for analysing the final energy of the neutron. In this case, the 111 Bragg reflection in KBr is within the Q-range of the instrument. It can be easily shown that the Bragg peak should appear at  $Q_{11} = 0.51 \text{ \AA}^{-1}$ . As can be seen in Fig. 1, the scattering from this sample is an ellipse centered about zero energy transfer and  $Q_{11} \approx 0.5 \text{ \AA}^{-1}$ . Thus the Q calibration of the instrument is satisfactory.

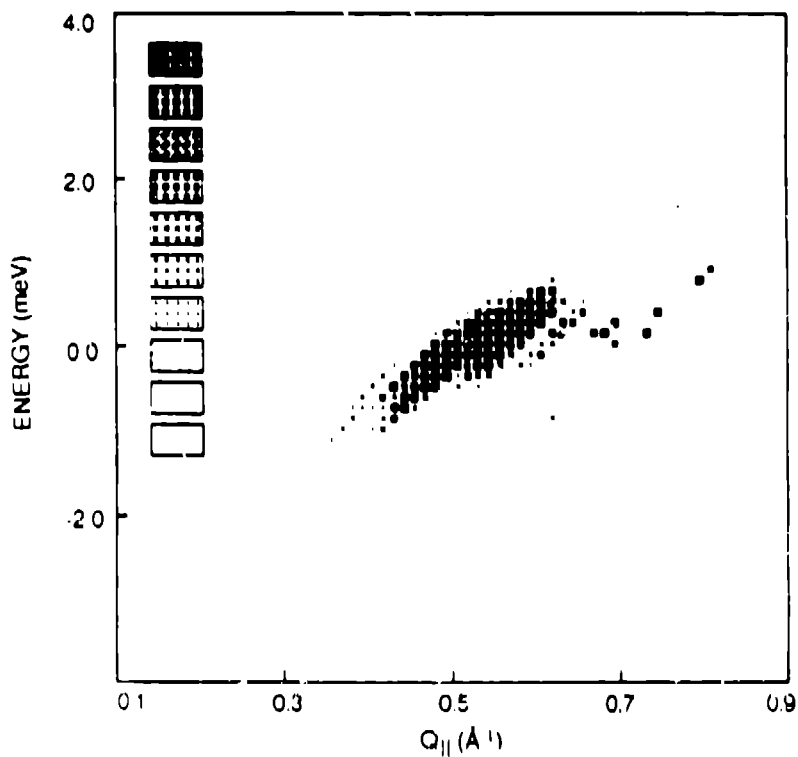


Fig. 1 The resolution of the spectrometer mapped out in the  $(Q_{11}, E)$  plane using a KBr powder sample and a Ge 220 analyser. The calculated peak position for the 111 Bragg peak in KBr is  $Q_{11} = 0.51 \text{ \AA}^{-1}$ ,  $E = 0$ . This is a good check of the momentum transfer calibration of the spectrometer.

#### 4. Measurement of spin waves in Iron<sup>51</sup>

Inelastic neutron scattering measurements have been made on a single crystal of Fe<sup>54</sup> (12 at.% Si) that weighed ~166 gms. The spectrometer locus in Q-space for a representative run is shown in Fig. 2(a). This scan was through the 110 Bragg peak in Fe and within 10.9° of a [200] direction. Figure 2(b) indicates the available range in energy transfer as a function of Q<sub>||</sub>. A typical time-of-flight spectrum from a

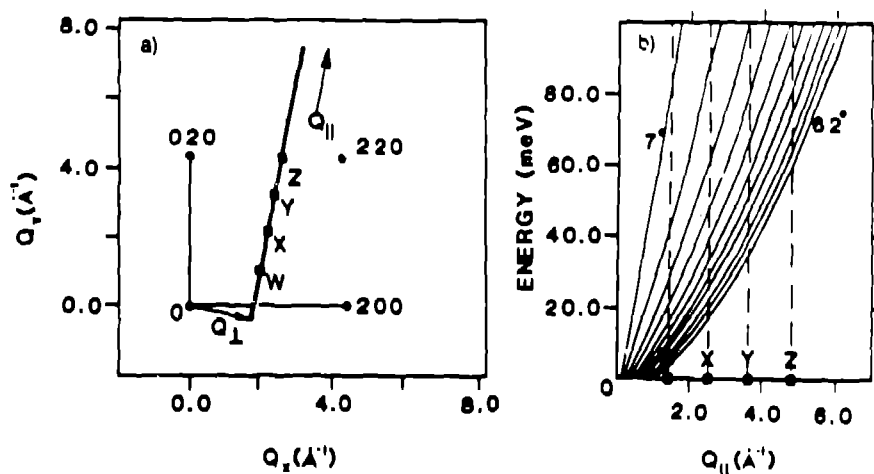


Fig. 2 The kinematics of the scan used for Fe (Cu 002 analyser). Figure 2(a) shows a section of the (hk0) zone in the reciprocal lattice of Fe. The bold line indicates the spectrometer locus along which Q<sub>||</sub> increases. The scan passes through the 110 reciprocal lattice point, which is marked X. Figure 2(b) shows the available energy range as a function of Q<sub>||</sub>, for angles between 7° and 62°. The values of Q<sub>||</sub> marked W, X, Y and Z correspond to the points indicated in Fig. 2(a).

single detector is shown in Fig. 3. The three inelastic peaks seen in the data can be identified as the transverse acoustic phonon, the longitudinal acoustic phonon (which is unresolved from a magnon), and a second magnon mode, in order of increasing energy transfer. The individual detector scans were fitted with three Gaussians and the centers of each of the Gaussians are plotted in Fig. 4 against the corresponding value of Q<sub>||</sub>. The dashed line is the calculated position, using the relation:  $E(q) = Dq^2$  where the value of D used is 230 meV Å<sup>2</sup>, which was obtained in Ref. 6. Since the system is isotropic, this relation should still be valid even though the scan is not along a high symmetry direction. A very respectable agreement between the calculated and observed values is to be noted. We point out that this analysis is preliminary and that we have presented a limited portion of the data that we have taken.

Measurements were also made at room temperature, but the background at higher energies (which is presumably due to multi-phonon scattering) was significantly reduced in the low temperature data shown here.

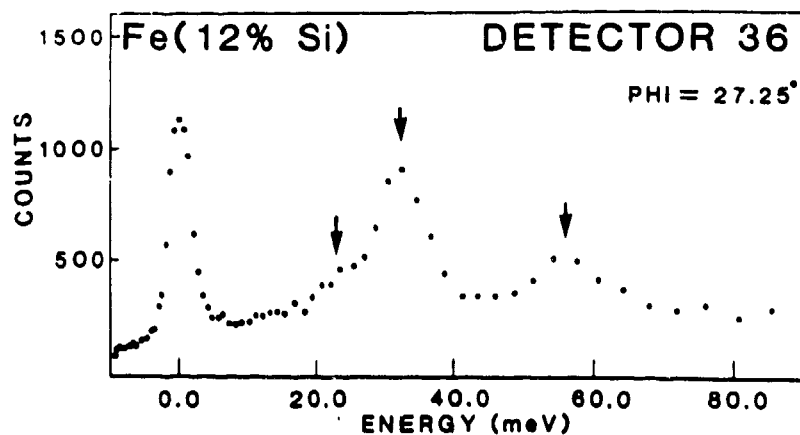


Fig. 3 A representative time-of-flight spectrum, from a single detector, for a 166-g sample  $^{54}\text{Fe}$  (12at. % Si) at 10 K, with a Cu 002 analyser. This scan, which took three days to run, corresponds to the configuration shown in Fig. 2. Three inelastic features can be seen and these are marked by arrows. The excitation at approximately 55 meV is a magnon, which corresponds to  $Q_{\parallel} = 3.0 \text{ \AA}^{-1}$ .

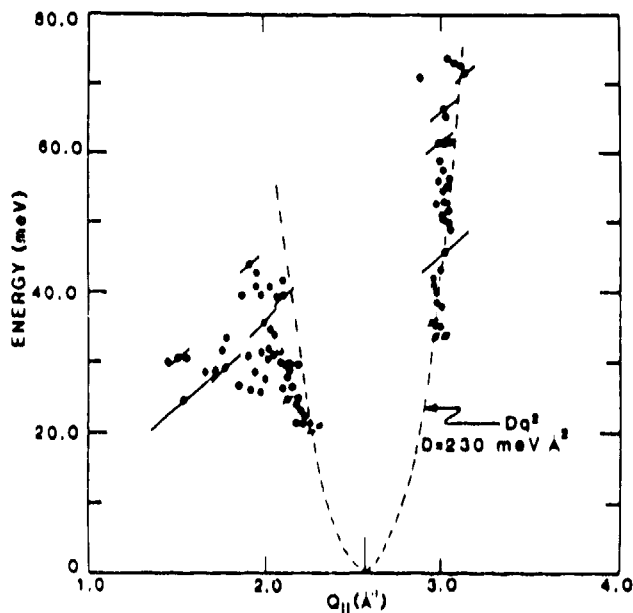


Fig. 4 The dispersion curve obtained for Fe from scans like the one shown in Fig. 3. The inelastic peaks were fitted with Gaussians and the centers of these Gaussians are plotted here against the corresponding  $Q_{\parallel}$ . The dashed line represents the parabolic spin wave dispersion measured previously by Lynn<sup>(6)</sup>; ( $D = 230 \text{ meV \AA}^2$ ). The spin waves branch on the right is well resolved, but that on the left is poorly resolved from low-lying phonons, as can be seen in Fig. 3.



## 5. Graphite

We have also made a study of phonons in pyrolytic graphite. The spectrometer locus in Q-space for a representative run is shown in Fig. 5(a). This scan was through the 005 Bragg peak and  $31.7^\circ$  away from the [001] direction. Figure 5(b) indicates the available range in energy transfer as a function of  $Q_{||}$ . A typical time-of-flight spectrum from a single detector is shown in Fig. 6.

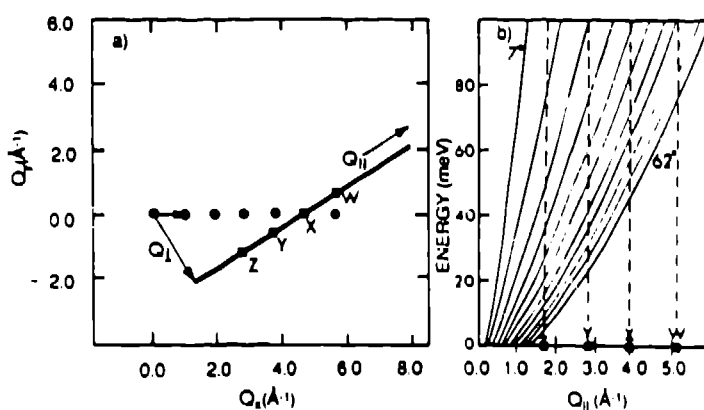


Fig. 5 The kinematics of the scan used for graphite (Cu 220 analyser). Figure 5(a) shows a section of the reciprocal lattice of graphite. The bold line indicates the spectrometer locus along which  $Q_{||}$  increases. The scan direction is along this line, where the point marked X is the 005 Bragg reflection.  $Q_x$  is along the  $c^*$  axis and  $Q_y$  is in the basal plane of the sample. Figure 5(b) shows the available energy range as a function of  $Q_{||}$ , for angles between  $7^\circ$  and  $62^\circ$ . The values of  $Q_{||}$  marked W, X, Y and Z correspond to the points indicated in Fig. 5(a).

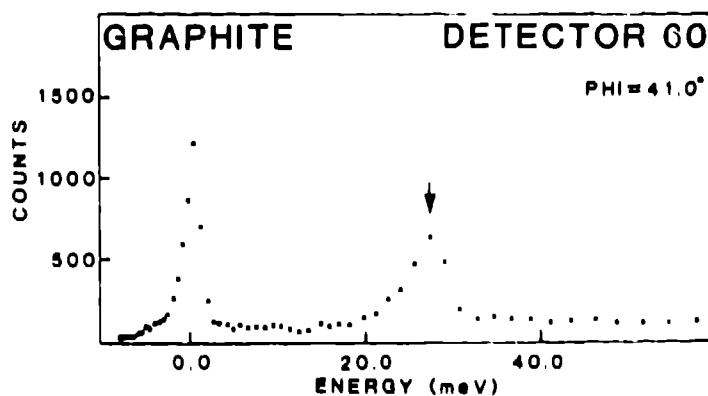


Fig. 6 A representative time-of-flight spectrum, from a single detector, for a sample of pyrolytic graphite with a Cu (220) analyser. This scan, which took two days to run, corresponds to the configuration shown in Fig. 5. A phonon can be seen at approximately 28 meV, which corresponds to  $Q_{||} = 2.16 \text{ \AA}^{-1}$ .

A phonon can be seen clearly at approximately 28 meV. By finding the center of the peak and plotting the energy against the corresponding Q-vector, a dispersion curve is obtained. In addition, by looking at the contribution of each detector in any given energy window and normalising the intensity against the  $ZrH_2$  elastic peak intensity, detector by detector, constant-E scans can be obtained. An example of a constant-E scan at  $E = 28$  meV is shown in Fig. 7. The dispersion curve resulting from a series of constant-energy scans between 20 meV and 40 meV (with 2 meV bandwidths) is shown (open circles) in Fig. 8, as is the dispersion relation obtained directly from individual detector peaks (dots). It should be noted that this is a preliminary analysis. Again, this is part of a more extended study of the phonons in graphite, but we have not yet had time to complete the full analysis.

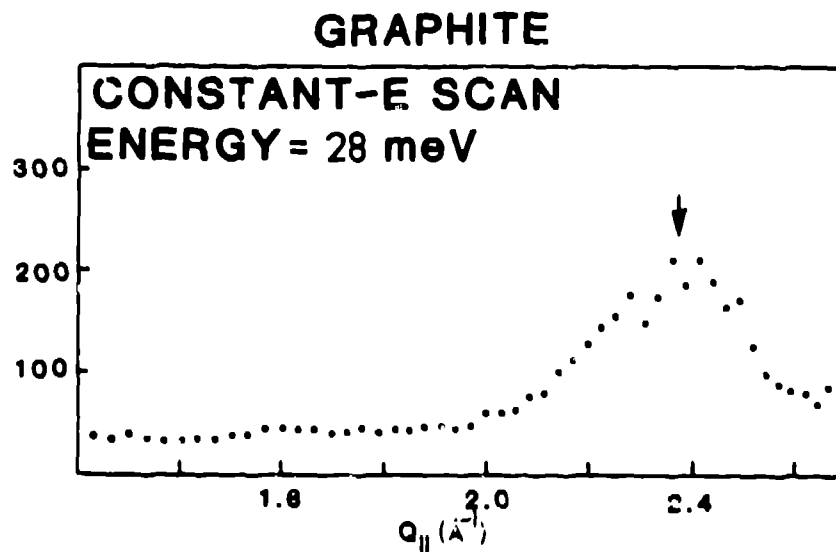


Fig. 7 A constant-E scan for the configuration shown in Fig. 5. This scan was obtained from raw data, like that shown in Fig. 6, with an energy transfer of  $28 (\pm 1)$  meV. The peak is centered at  $Q_{||} = 2.35 \text{ \AA}^{-1}$ . This procedure was carried out for several different energies and the results can be seen in Fig. 8.

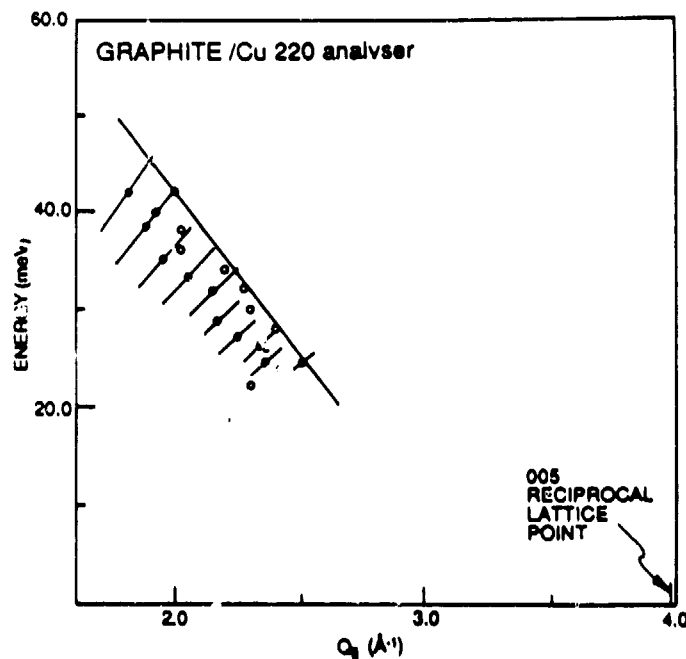


Fig. 8 The dispersion curve for graphite obtained from the scan described in Fig. 5. The solid circles represent peaks in time-of-flight scans and the open circles were obtained from constant-E scans, like that shown in Fig. 7. It can be seen that the agreement between the two is well within the estimated error. The 005 reciprocal lattice point lies at  $Q_{||} = 3.98 \text{ \AA}^{-1}$ . The solid line shows the dispersion curve for the [110] transverse acoustic phonon branch as measured by Nicklow et al.<sup>(7)</sup>

## 6. Conclusions

There are a number of fundamental features of this type of spectrometer that we have found troublesome and which may severely limit its usefulness.

- (a) Firstly, the fact that the scattering angle is tied to the analyser Bragg angle is very constraining. The only choice one has in reaching a given momentum transfer  $\hbar Q_{||}$  is in the choice of analyser d-spacing. This gives one very little latitude in manipulating the resolution function to obtain focusing. This constraint is peculiar to the constant-Q geometry and does not apply to the other pulsed-source crystal analyser spectrometer, the high-symmetry spectrometer<sup>(7)</sup>, which has one more degree of freedom in its operation.
- (b) Secondly, even for constant-energy transfers, the energy resolution varies as a function of scattering angle. This is because the analyser Bragg angle (and therefore  $E_p$ ) vary with scattering angle. This is also true in the high-symmetry configuration<sup>(8)</sup>, but is not for conventional constant-E<sub>i</sub> machines (like chopper spectrometers) or reactor triple-axis spectrometers.

- (c) Thirdly, the sample-analyser distance is relatively small (20 cm) in our case, even with a very large analyser array. While vertical collimation can be installed fairly readily in this section of the spectrometer, it is impossible to include divergent horizontal collimation without severely reducing the amount of sample viewed by the analyser, with a consequent unacceptable loss in intensity. This means that the shielding in this part of the spectrometer is weak and that background levels are higher than in spectrometers with well-collimated beams everywhere. This problem is peculiar to the constant-Q geometry.

On the other hand, the surface on which the constant-Q spectrometer measures is a simple one, in contrast to that for constant-E<sub>1</sub> machines (see Fig. 1 of Ref. 2). Even though the latter appear to give better signal-to-noise ratios, it is not yet clear whether single crystal data taken on them can really be analysed.

### References

1. C. G. Windsor, R. K. Keenan, B. C. Boland and D. F. R. Mildner, 1978, Nucl. Instrum. Methods 151, 477.
2. R. A. Robinson, R. Pynn and J. Eckert, 1985, Nucl. Instrum. Methods A241, 312.
3. R. A. Robinson, R. Pynn, J. Eckert and J. A. Goldstone, 1985, in Proceedings of VIIIth meeting of ICANS, Oxford 8-12th July 1985, Rutherford-Appleton Laboratory Report RAL-85-110 Vol.II, p.600.
4. M. Yethiraj and R. A. Robinson, 1988, in these proceedings. Los Alamos preprint LA-UR-88-3060.
5. M. Yethiraj, R. A. Robinson, J. W. Lynn and H. A. Mook, to be published.
6. J. W. Lynn, 1975, Phys. Rev. B11, 2624.
7. R. Nicklow, N. Wakabayashi and H. G. Smith, 1972, Phys. Rev. B5, 4951.
8. K. Tajima, Y. Ishikawa, K. Kanai, C. G. Windsor and S. Tomiyoshi, 1982, Nucl. Instrum. Methods 201, 491.

## The new chopper spectrometer at LANSCE, PHAROS

*R. A. Robinson, M. Nutter, R. N. Silver, D. T. Hooten, and R. L. Ricketts*  
Los Alamos National Laboratory  
Los Alamos, New Mexico 87545  
USA

**ABSTRACT:** We describe the new chopper spectrometer PHAROS under design at Los Alamos. It is intended to provide 0.5% incident energy resolution for incident energies between 50 meV and 2 eV. This will be achieved with a methane moderator and a 20-m incident flight path on Flight Path 16 of the Los Alamos Neutron Scattering Center. The secondary flight path will be 4 m for scattering angles between  $10^\circ$  and  $140^\circ$ . For small scattering angles (down to  $0.5^\circ$ ), the secondary flight path can be extended to 10 m. We include results of preliminary tests on phasing a prototype chopper and the Proton Storage Ring. These show that phasing can be achieved and that the width of the transmitted neutron pulse is in reasonable agreement with calculation.

### 1. Description of the proposed spectrometer

A new chopper spectrometer is currently under design at the Los Alamos Neutron Scattering Center. In March 1987, a workshop was held at the Argonne National Laboratory to define the parameters of the spectrometer, and the present design does not differ greatly from the thinking expressed in the report<sup>(1)</sup> of that workshop. The configuration of the spectrometer is shown schematically in Fig. 1 and the proposed instrument parameters are given in Table 1. A more detailed scale drawing showing chopper positions and building constraints is shown in Fig. 2.

Moderator-Chopper Distance	18.5 m
Chopper-Sample Distance	1.5 m
Sample-Detector Distance	4 m between $10^\circ$ and $140^\circ$ up to 10 m between $-10^\circ$ and $+10^\circ$
Moderator	$12.5 \times 12.5 \text{ cm}^2$ liquid methane
Source Repetition Frequency	12 or 24 Hz
Chopper Frequency	600 Hz
Chopper Diameter	10 cm
Chopper Slit Spacing	1 mm or more
Sample Size	up to 5 cm x 7.5 cm

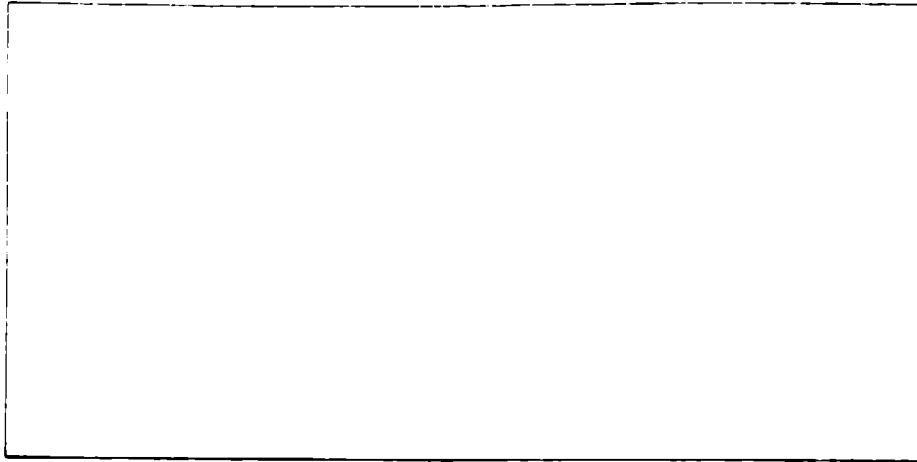


Fig. 1 A schematic diagram of the proposed LANSCE chopper spectrometer

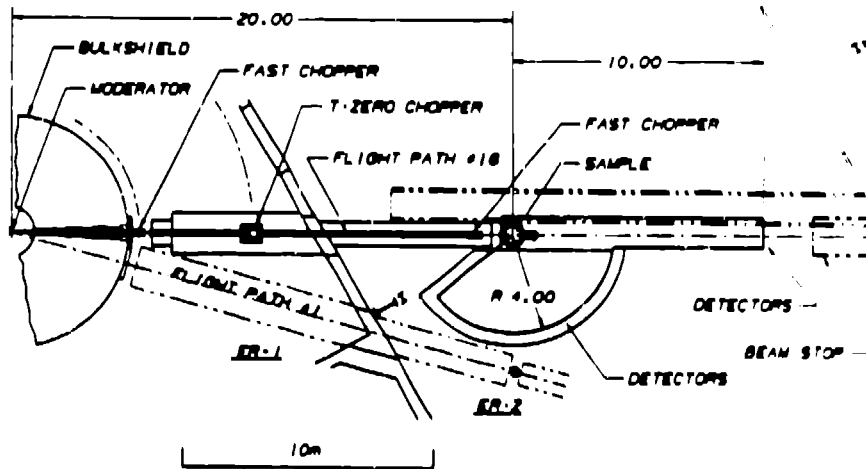
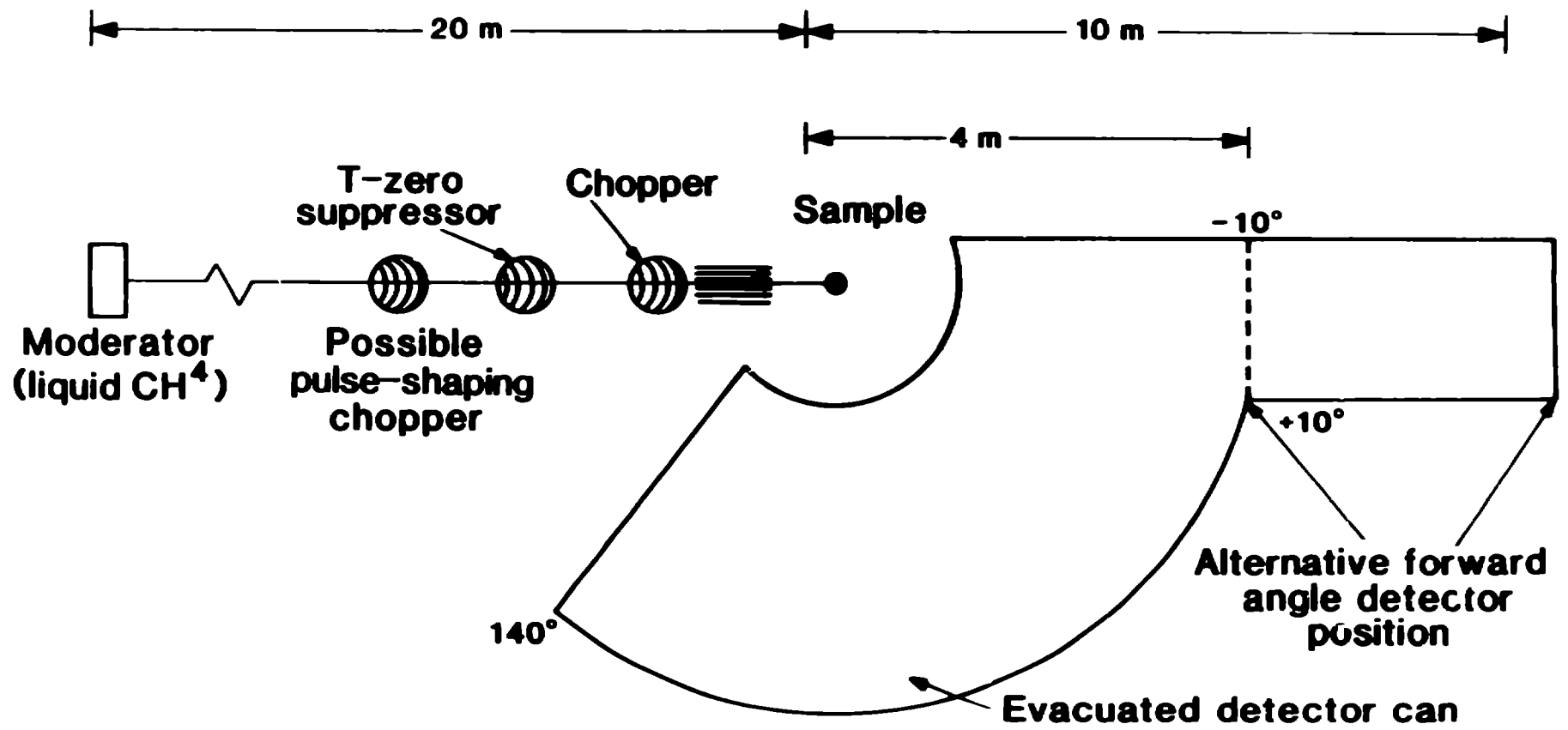


Fig. 2 A scale drawing showing the position of the choppers and the spectrometer footprint in the LANSCE facility. The primary chopper sample and secondary flight path will all be in the new Experimental Hall ER-2, while the T-zero chopper and a possible pulse-shaping chopper will be in the old experimental hall ER-1.

The spectrometer will be installed on Flight Path 16, which currently views a water moderator (in the flux-trap geometry) at  $15^\circ$  from the normal to its surface. This will be replaced by a liquid methane moderator by 1992. Up to three choppers will be placed in the incident beam. The most important of these is the primary chopper, which is closest to the sample position. It is an aluminium-bodied chopper mounted on a magnetic-bearing system, which has been described previously<sup>[2]</sup>, with a borated



**Fig. 1**

slit package. Secondly, there will be a T-zero suppressor, which is intended to block the beam line when protons hit the target, but be completely removed from the beam by the time 2eV neutrons (the highest energy we currently envisage using) reach it. While it would be best, from a background point of view, to place the T-zero suppressor as close to the source as possible, it will be 10 m from the source to have the beam fully open in time for 2eV neutrons. Thirdly, there will be provision for yet another chopper to be placed, at some later date, close to the bulk shield. This will be a fast chopper, similar to the primary chopper, and its purpose will be to clean up the spectrometer resolution function and/or to improve the time resolution beyond that of the moderation time. As the beam size in this position is larger than at the sample position, it would be best if this chopper could contain an aperture significantly larger than the sample size.

Our philosophy is very similar to that which has been employed at ISIS, namely that we will have a fast magnetic-bearing chopper for monochromation purposes, with a slower nickel-alloy T-zero suppressing device upstream to reduce backgrounds. In contrast, the practice to date at IPNS has been to employ one Be-bodied chopper, on mechanical bearings, for both purposes.

The secondary flight path will be evacuated, with the detectors placed outside the vacuum behind thin aluminium alloy windows. It will extend to 4 m for scattering angles between  $10^\circ$  and  $140^\circ$  and can be extended to a maximum of 10m in the forward direction. The purpose is for experiments at small momentum transfers (and, hence, small scattering angles), like neutron Brillouin scattering<sup>(3,4)</sup>. We plan to reach scattering angles as low as  $0.5^\circ$ , although we will need additional collimation between sample and chopper to achieve this cleanly. In all probability, the low-angle option will be ready before the wide-angle flight path, and we plan to build it in such a way that the spectrometer can be used solely in that mode at first.

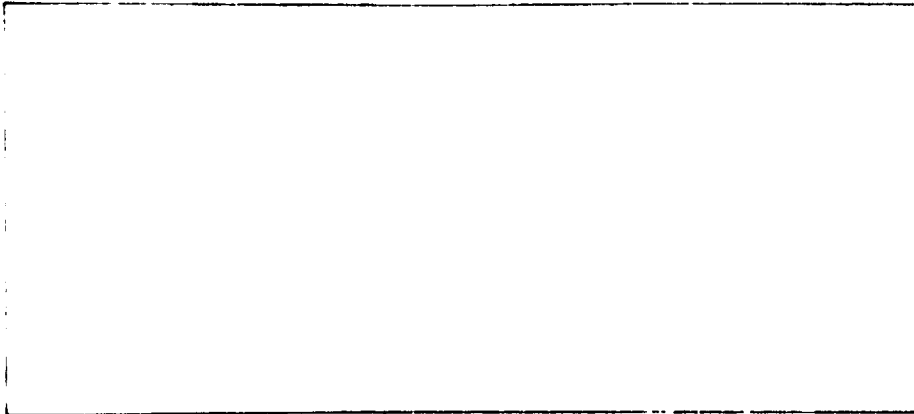
The spectrometer will use 10 atmosphere  $^3\text{He}$  proportional counters throughout, most probably 2.5-cm-diam., 90-cm active-length linear position-sensitive detectors. We are currently working on window designs for the vacuum vessel, which are compatible with this detector configuration, while minimising the dead angle due to structural window panes.

Current beam profile and chopper apertures are such that samples of size up to 5 cm may be used. This is significantly larger than beam sizes at ISIS, but smaller than those on LRMECS and HRMECS at IPNS.

## 2. Primary tests of the chopper system

Figure 3 shows the components of our rotor immediately prior to assembly. We have run the primary chopper at 8 m from the moderator on a test beam line, Flight Path 5, at LANSCE. This flight path is considerably shorter than that proposed for the final spectrometer and it views a low-resolution ambient water moderator. The results are shown in Fig. 4. Figure 4(a) shows the relative phasing of the LAMPF accelerator to our chopper, without phasing the Proton Storage Ring (PSR)<sup>(5)</sup> to the chopper. This distribution is very broad, with the tails clearly extending to  $\pm 150 \mu\text{s}$ . We believe that this is mainly due to inaccuracies introduced in the zero-crossing





**Fig. 3** Components of the 600-Hz rotor prior to assembly. The slit package consists of 0.71-mm-thick boron-fibre epoxy resin slats with 0.76-mm open slits between, all on a 1.5-m radius.

circuitry that triggers LAMPF. However, the proton beam can be held in the PSR for up to 150  $\mu$ s, with extraction on a trigger from the chopper. Results in this mode are shown in Figs. 4(b) through (d). Figure 4(b) shows the signal from a magnetic pick-up on the rotor; these data are directly comparable with Fig. 4(a). There is a small tail on the distribution, which we believe is due to the 150- $\mu$ s window being insufficient in some cases. Figures 4(c) and (d) show transmitted neutron signals in two downstream monitors: the first of which is immediately after the chopper and the second is 3.1 m further downstream. The peak in Figure 4(c) has a standard deviation of 3.60  $\mu$ s. If one calculates the width one should observe, based on the chopper parameters, the result in Fig. 4(b), and the monitor thickness, one arrives at a standard deviation of 3.2  $\mu$ s. Given the imprecision of the measurement in Fig. 4(b), this is reasonable agreement. The width of the peak in the downstream monitor is dominated by dispersion of the neutron pulse, which is mainly due to the moderator pulse width.

These results show definitively that we can phase the chopper and the PSR.

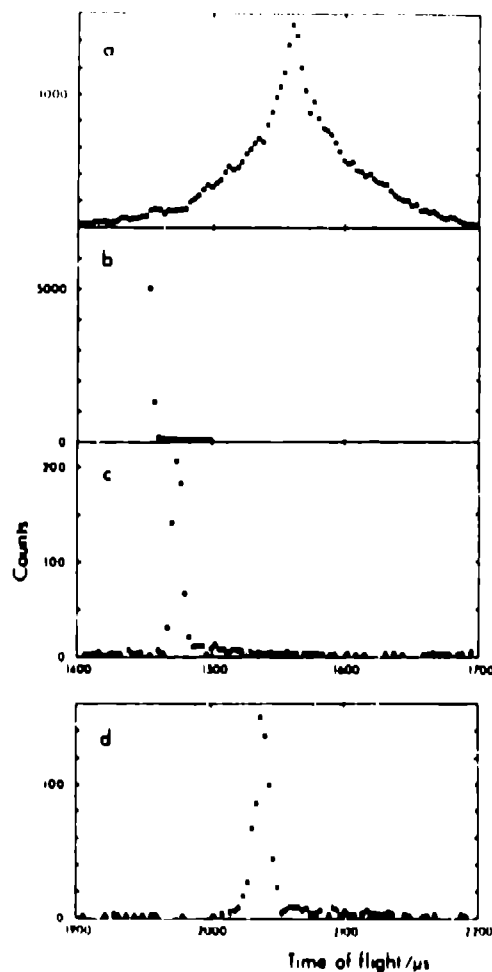
### **Acknowledgements**

We are glad to acknowledge a number of fruitful discussions with Drs. J. M. Carpenter, A. D. Taylor and R. Pynn. This work was supported, in part, by the division of Basic Energy Sciences of the U.S. Department of Energy.

### **References**

1. J. M. Carpenter, K. Crawford, R. Kleb, C. -K. Loong, G. Ostrowski, D. L. Price, M. Nutter, R. Pynn, R. A. Robinson, R. N. Silver, J. M. Rowe, P. Sokol and A. D. Taylor, 1987, Los Alamos Report LA-UR-87-2582.
2. M. Nutter, L. Lewis, S. Tepper, R. N. Silver and R. H. Heffner, 1988, in Proceedings of VIIIth meeting of ICANS, Oxford 8-12th July 1985, Rutherford

- Appleton Laboratory Report RAL-85-110 Vol.III, p. 697.
3. R. A. Robinson, in Proceedings of International Conference on Neutron Scattering, Grenoble, France, 12-15th July 1988, to be published in Physica B. Los Alamos preprint LA-UR-88-1573.
  4. R. A. Robinson, 1988, in these proceedings, Los Alamos preprint LA-UR-88-3099.
  5. G. P. Lawrence, R. Cooper, D. W. Hudgings, G. Spalek, A. J. Jason, E. F. Higgins and R. E. Gillis, 1980, *Experientia Supplementum* **40**, 103 (proc. 11th Int. Conf. on High Energy Acceleration, Geneva (1980) p.103).



**Fig. 4** Time-of-flight spectra for the chopper system on flight path 5 at LANSCE.  
 (a) The magnetic pick-up signal on the rotor, with the chopper following the LAMPF accelerator trigger signal. This represents the time jitter in the accelerator trigger signal. The FWHM is approximately 42  $\mu$ s, but with very substantial tails to the distribution.  
 (b) Magnetic pick-up signal as in (a), but with the proton beam held in the PSR

until kicked out on a trigger from the chopper control signal. The standard deviation of this distribution is approximately  $1.9 \mu\text{s}$ , the time bin-width ( $3.2 \mu\text{s}$ ) being insufficient to determine this quantity accurately.

(c) Signal in a beam monitor immediately after the chopper, with extraction from the PSR triggered by the chopper. The standard deviation of this distribution is  $3.60 \pm 0.12 \mu\text{s}$ .

(d) Signal in a downstream monitor, with extraction from the PSR triggered by the chopper. The standard deviation of this distribution is  $5.50 \pm 0.22 \mu\text{s}$ .

# Time-of-flight small-angle-neutron-scattering data reduction and analysis at LANSCE with program SMR

*Rex P. Hjelm, Jr. and Philip A. Seeger*  
Los Alamos Neutron Scattering Center  
Physics Division  
Los Alamos National Laboratory  
Los Alamos, New Mexico 87545  
USA

**ABSTRACT:** A user-friendly, integrated system, SMR, for the display, reduction and analysis of data from time-of-flight small-angle neutron diffractometers is described. Its purpose is to provide facilities for data display and assessment and to provide these facilities in near real time. This allows the results of each scattering measurement to be available almost immediately, and enables the experimenter to use the results of a measurement as a basis for other measurements in the same instrument allocation.

## Introduction

Neutron diffractometers at pulsed sources use time-of-flight (TOF) to calculate the magnitude of each neutron momentum,  $p$ . Due to the broad distribution of  $p$  from pulsed sources, a single measurement accesses a large domain of momentum transfer space, given as  $Q = (2p/\hbar) \sin \theta$  ( $\hbar$  is Planck's constant divided by  $2\pi$ , and  $\theta$  is half the scattering angle). This gives considerable advantage in data acquisition over similar instruments using monochromated neutron beams as a source.

In a small-angle TOF instrument with a two-dimensional position-sensitive detector, the data are taken as counts in three dimensional cells,  $C_{i,j,n}$ , where  $i$  and  $j$  refer to the  $x$  and  $y$  channels of the detector at which the scattering event is detected and  $n$  refers to the TOF channel. The number of data points is, thus, very large. For example, in the present configuration of the Low-Q Diffractometer (LQD) at the Los Alamos Neutron Scattering Center (LANSCE), there are 128 each of  $x$  and  $y$  channels and 147 TOF channels for a total of over  $2.4 \times 10^6$  cells. The data must be remapped into physically meaningful one- or two-dimensional momentum transfer spaces as differential cross sections,  $d\Sigma(Q)/d\Omega$  or  $d\Sigma(Q)/d\Omega$ , respectively. In this, the broad-band nature of the source introduces aspects of data reduction that must be considered carefully. These have been discussed in earlier papers<sup>(1-3)</sup>, but are still an active area of research. It is likely that the reduction procedure will depend on the sample and the requirements of the analysis that will be used. By recording and storing all data for each measurement, we provide maximum flexibility for data reduction and analysis. Thus, as a consequence of the use of TOF measurement and the broad-band nature of the source, data reduction on TOF small-angle instruments is more complicated but has greater flexibility than on similar instruments that use monochromated neutron sources.

There are three primary functions that are supported in our system SMR (Show Me and Reduce). These are data display, reduction, and analysis all of which are required for the user to assess the data and draw some conclusions from it. Because of the large size of the data sets, a graphics display of data is essential. This should be interactive, allowing information to be returned to the program. Furthermore, our state of understanding the data reduction demands that the procedures should have flexibility built in to suit the needs of a particular measurement. Also, functions should be present that allow assessment of the data-reduction procedures.

Of major importance in the design of our system is that we have taken the point of view that near-real-time data display and reduction are an essential part of a neutron scattering experiment. Thus, facilities should be available during data acquisition, as well as after the measurement. This offers the possibility that the results of a measurement can be immediately available, allowing them to be used as a bases on which to plan the next measurement. The ability to assess the data quickly allows the well-prepared user to make optimal use of the current allocation and may save having to redo parts of an experiment at a later date. This is important at a scheduled user instrument because the user may have to wait several months for additional measurement time.

Therefore, the objectives for SMR are the following:

- (1) Provide tools for assessment of TOF small-angle data as it is being acquired, which includes display of raw data and fast data reduction (not necessarily highly accurate in this mode).
- (2) Provide data reduction to  $d\Sigma(Q)/d\Omega$  and  $d\Sigma(Q)/d\Omega$  in absolute units. In addition, tools should be provided to assess the efficacy of the data-reduction procedure itself. The program should thus be useable as a tool to research data reduction procedures.
- (3) Provide basic data-manipulation functions and analysis procedures with appropriate interactive displays.
- (4) All of this must be in the framework of a fast, user-friendly program that is easy to learn and use, and provides sufficient flexibility to meet the needs of all types of measurements. This implies that no knowledge of the data-acquisition-computer-operating system, beyond a list of simple operations, should be required, and that these operations should be readily available as menu options and/or commands.

We have found that these objectives are best met by an integrated system that automates most of the communications needed for the function of the different program parts, thus minimizing the amount of user interaction and input.

### Organization

SMR must allow the user to retrieve and manipulate data from the instrument detectors in a manner that is transparent to the user. The different instrument detectors and the relationship with other parts of the data acquisition system are shown in Fig. 1. The LQD uses three detectors: the main, position-sensitive area detector; an upstream incident-beam monitor; and a downstream transmission monitor (currently under development).<sup>(4,5)</sup> The signals from the detectors are collected and

processed by FASTBUS acquisition hardware and stored as histograms in the acquisition system BULKSTORE module. The FASTBUS crate is interfaced to a dedicated DEC  $\mu$ VAX workstation/GPX operating under VMS. A complete description of the data acquisition hardware and software is given elsewhere.<sup>[6]</sup>

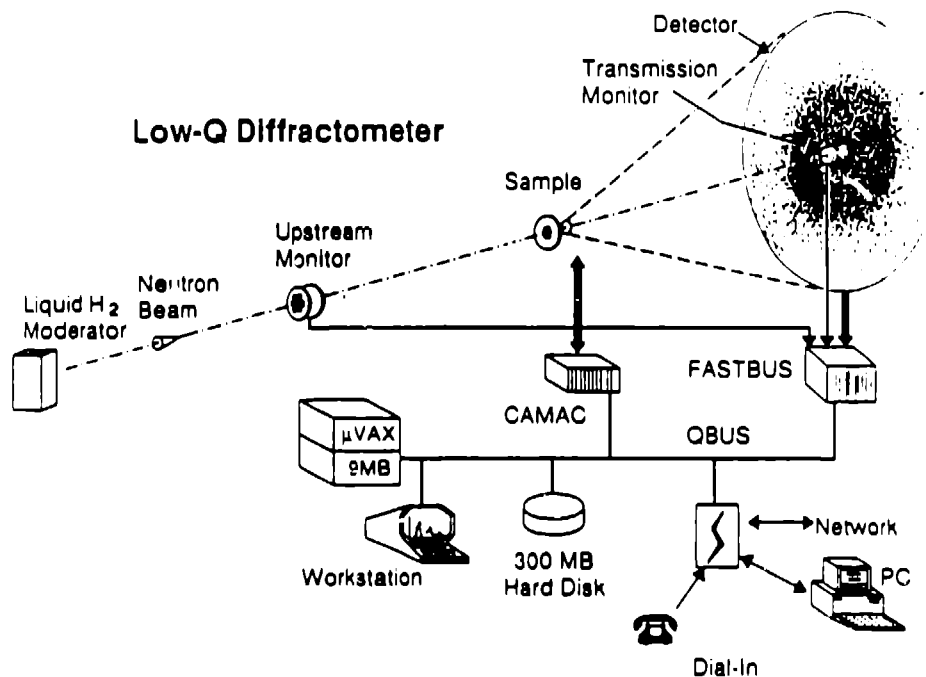
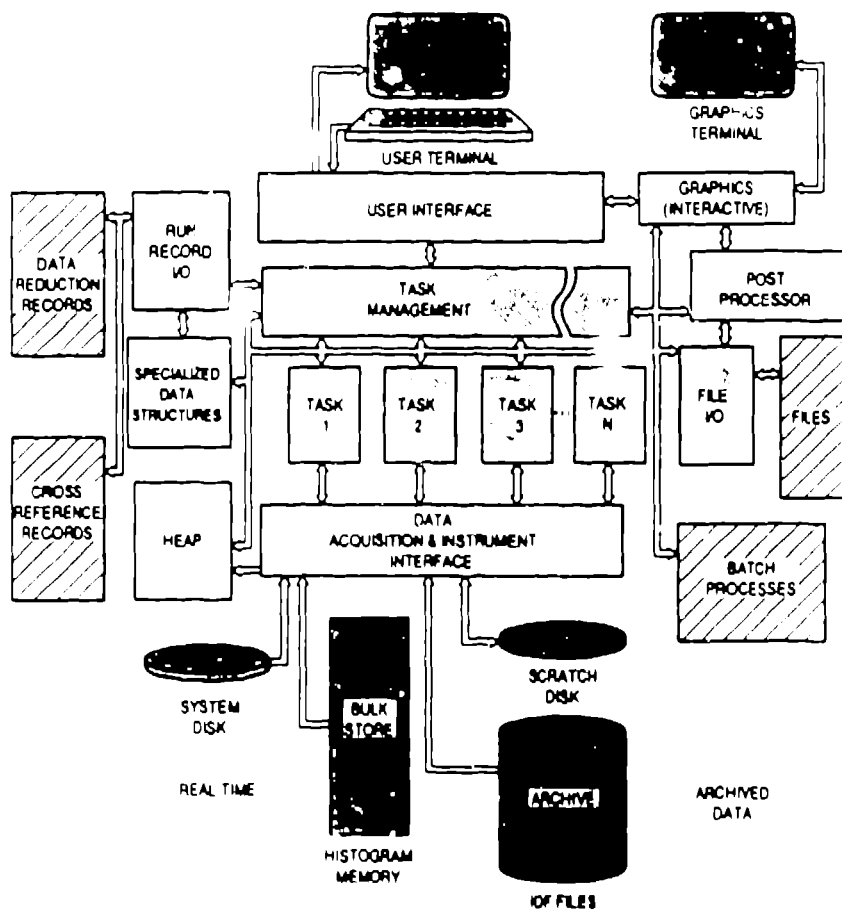


Fig. 1 The Low-Q Diffractometer at LANSCE and the integration of its components with the data acquisition system. The geometry of the LQD is shown with the positions of the different detectors and sensors. The upstream monitor is used to monitor the incident beam intensity just after the collimator entrance aperture. The sample position is located about 4 m downstream. A second transmission monitor is planned, which will be placed in the beam stop just in front of the main position-sensitive detector. Signals from the beam monitors and main detector are passed to the FASTBUS crate where they are mapped and stored in the bulkstore module. Sample environment information is passed to the CAMAC crate. The data in the CAMAC scalars and FASTBUS bulkstore are transferred to the dedicated  $\mu$ VAX via the QBUS. The  $\mu$ VAX, however, is not involved in the data acquisition per se, but in setting up the measurement and in data transfer. Communication with the data acquisition system is also through the  $\mu$ VAX. Data is passed between the computer and other devices by the QBUS.

SMR consists of a core of central tasks and a periphery of extensions and enhancements. The core of SMR is organized into four major subsystems as illustrated in Fig. 2. These are the user interface, the task management module, the task subsystem, and the data acquisition and instrument interface. The subsystems are further partitioned into modules and segments associated with specific tasks or program functions. This design is intended to ease the evolution of the system as functions are added, deleted, or redefined.

## ORGANIZATIONAL OUTLINE FOR SMR



**Fig. 2** The organization of SMR. Each of the major subsystems of SMR is illustrated by a light-shaded block. Files are represented by hatch blocks, physical devices by dark shading. Internal data structures are represented by open blocks. Tracks having arrows at both ends represent bidirectional information flow between the connected units and the different data structures, files, and devices. Single arrows indicate uni-directional flow.

The major peripheral subsystems are the interactive graphics, postprocessor and file I/O modules. All are organized with the same philosophy as the core subsystems. The postprocessor is an extension of SMR to provide flexible operations on reduced or raw data in analysis, normalization, scaling, background subtraction, averaging, and related functions. Its organization is like that of SMR (Fig. 2) except there is no instrument interface.

## User Interface

User requests are communicated through the user interface. The various modules supporting different functions and options are organized as menus and submenus in a tree-like hierarchy. The branches of the tree correspond to the different program functions and their options. The user interface supports different interactive modes, depending on the type of terminal connected to the process. This interface includes a menu driver that can be used on DEC terminals or emulators and a command line interpreter for use on other terminals. Terminals are polled as to their capabilities and the appropriate part of the user interface is run. Future versions of the user interface will also use more advanced facilities that are under development for VAX workstations by the data acquisition section at LANSCE.<sup>(6)</sup>

## Task management module

The requests generated by the user interface are organized by the task-management module. The task manager invokes the functions of SMR, after polling the control flags set up by the user interface, and passes control to the required functions that are organized into task modules (labeled in Fig. 2 as 1 through N). Appropriate data structures containing values obtained from the cross-reference records, data-reduction records, and the user interface are passed to the routines. The results of the computation are placed in data structures or passed by the task manager to the interactive graphics display facility or to file I/O routines, depending on user request. Control is then passed back to the user interface along with any other numerical results that should be reviewed by the user. Some of the calculations in data-reduction tasks require considerable computation times. Thus, there is an option for the task manager to pass these to detached processes run in batch mode (Fig. 2), returning control immediately to the user and informing him when the calculation is complete.

## Task subsystem

The computational functions of SMR are set up in the different task modules of the system. Thus, functionality in SMR is easily altered by changing or adding modules. Raw data is obtained by these functions from the different bulk-storage devices through the data acquisition and instrument interface. Other preprocessed data and intermediate results are communicated between modules and between the main process and any tasks relegated to batch processes by way of file I/O procedures. The programs normally run in batch modes are non-interactive subsets of SMR.

All computations and tasks are supported internally by several data structures. The HEAP is a linked list of data structures.<sup>(6)</sup> A similar data structure containing information pertinent to the TOF measurement, instrument geometry, and detector configuration is maintained on the system disk during data acquisition<sup>(6)</sup>, and a copy is stored as part of the archive file when the run is saved. The run information in the system or run HEAP is copied directly into the local HEAP and then used for data reduction, display, and analysis. Other data structures tailored to specific tasks and functions are also used, which include data for the interactive graphics facilities as well as parameters and cross references to files used in data reduction and analysis. The data in these structures are maintained in external data-reduction record files and



in cross reference record files (Fig. 2) for later reference. These can be reviewed at any time. This recall is necessary as data reduction involves a number of options and values that may need to be changed if later assessment of the data reduction shows it to be faulty. The files are also used to communicate data-reduction information to batch processes.

### **Instrument and data acquisition interface**

The modules of the instrument and data acquisition interface retrieve data from the different bulk storage and data acquisition devices. The bulkstore memory of the FASTBUS retain data currently being acquired. The system disk maintains run configuration information on the current run in the HEAP. Previously acquired data is stored in compressed form as an Instrument Data File (IDF) on the user disk or remotely on an archive disk. The modules of this interface determine the physical location of the requested data, retrieve the data, and pass it back to the calling routine. The interface searches the data archive using criteria supplied through the user interface, which may include run number, experimenter name, instrument name, experiment title and/or IDF file name. In this way the entire data archive, which consists of remotely mounted optical disks with a planned total storage capacity of 0.5 terabytes, is accessible for analysis or display in a manner transparent to the user. Accessed archived data are retrieved to a local scratch disk in global data areas to increase access speed. The basic-data retrieval functions are recovery of raw data for each time channel from the upstream monitor, the transmission monitor, and the main detector.

### **The peripheral subsystems: graphics, postprocessor and file I/O**

The graphics output has several display options that support one- and two-dimensional displays. The current versions of the one-dimensional graphics and two-dimensional contour plotting routines use TEK4010/4016 graphics, which may be emulated on a wide variety of terminals. Two-dimensional color graphics is currently done by outputting to an IBM PC, which displays the data using programs developed by John Hayter of Oak Ridge National Laboratory. The graphics subsystem is in an early stage of development and will be expanded to accommodate other graphics systems and standards as determined by the LANSCE data acquisition section. User interaction with the graphics subsystem is used to pass information back to SMR for other data acquisition, reduction, and analysis tasks.

The interactive graphics is closely tied to the postprocessor of SMR, which contains the data analysis package. All sample-dependent data manipulation, e.g., scaling, is done in this part of SMR. Other tasks presently available in the postprocessor are regression analysis, free-formatted data manipulation (arithmetic operations on data sets and binary operations with data sets as arguments), and input and output in different file formats. This facility, which is also implemented in a stand-alone form, has organization like that of SMR. It is intended to give some flexibility in data treatment; it can be used to manipulate all SMR output, and is portable to VMS 4.6 and later versions.

The computational results (reduction or analysis) or raw data can be sent to an output file at the user's request. In addition, some procedures generate intermediate data files that may be found and used by subsequent tasks and detached processes. These output tasks are supported by the file I/O facility. We plan to support several file formats for user output to suit the needs of the experimenter. Our standard output file is block-formatted ASCII, including an abstract containing run identification, run-configuration information, and a running account of the various operations performed on the raw data sets, followed by labeled data blocks and the statistical (rms) precision of the data. The rms Q-precision of the differential cross section is included when appropriate. Descriptions of this format along with descriptions of subroutines available to read it are given in Appendix A.

## Functions

Here we present a partial list of the various functions presently implemented in SMR, with an emphasis on those that allow assessment of raw and reduced data. As the number of data can be quite large, even in reduced form, there is a strong reliance on graphics.

Figure 3 illustrates the main menu and two submenus of the core user interphase of SMR, which give examples of some of the functions available. Selections are made by moving the cursor to a line by either typing the character indicated by bold (underscored in this rendition) on the menu or by using the cursor keys, arrows, return, tabs, spaces or backspace, then typing <ENTER>, <DO>, or <CTRL>-G. These illustrations are for a terminal supporting ANSI control sequences; otherwise (or if the "M" option (Fig. 3) is toggled), the same functions are achieved with a command line format (Fig. 4). The two submenus shown are for raw data Display and for data Reduction. In the particular example shown, an archived file has been accessed. This could also have been data in the FASTBUS bulkstore, and the same functions would have been available.

Raw-data display options currently available are, in order: a detector map for selected time slices projected onto either one or two dimensions; detector counts mapped into two-dimensional space defined by detector radius and time (R-T); and one-dimensional displays of the counts as a function of TOF channel for the integrated detector, upstream, or transmission monitors. Computation of the center of scattering intensity on the detector or entry of the beam center by the user is also available, as is a display of the contents of scalers.

The different data-reduction functions are also illustrated in Fig. 3. The first entry is the computation of the wavelength-dependent transmission coefficients of the sample. Next is the basic function of mapping the data into  $d\Sigma(Q)/d\Omega$  and  $d\Sigma(Q)/d\Omega$  spaces. These are output on an absolute scale (see below). The "quick and dirty" version of this is for quick reduction of data over a limited number of time channels (strictly for quick assessment of the data). The Q-lambda map is a normalized and scaled form of an R-T map and is used for assessment of the normalization and background subtraction of the reduced data. The Theta-T map is similar to the Q-lambda map except that the two-dimensional space is defined by the independent variable in Q, scattering angle, and TOF. The flux, as measured by the main detector and downstream (transmission) monitor, is also available. The two options for the beam

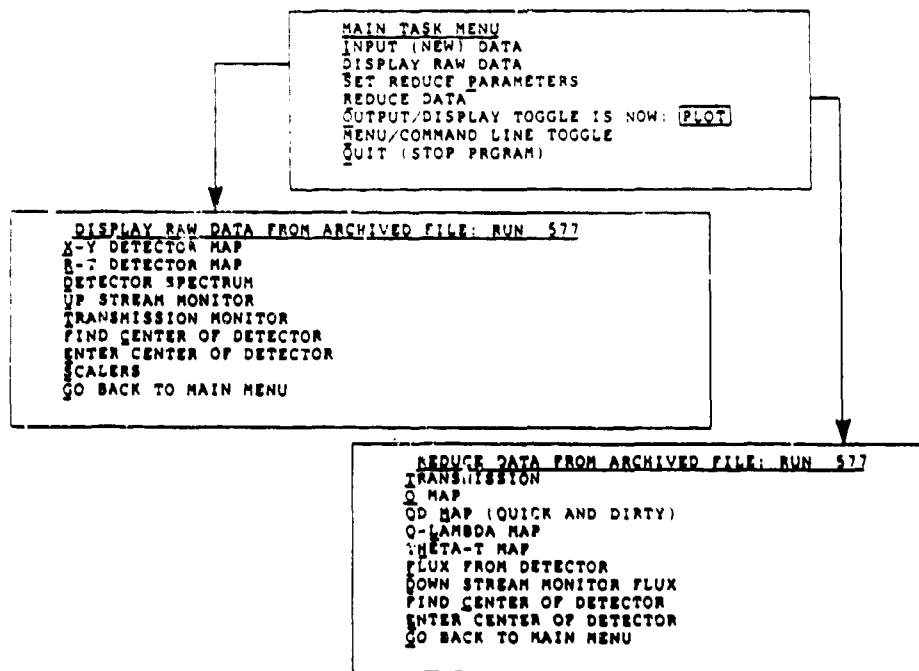


Fig. 3 An example from the main menu and two submenus of the SMR user interface. The main menu of the user interface is shown here, which illustrates the various options available to the user. Characters that appear in bold are underscored in this rendition. The data reduction and raw-data display submenus are also shown. The interaction with the menus is supported by a driver written in C.

BINNING PARAMETERS

COMMAND	PARAMETER	OPTION
+0	60	Number of (radial) Q-bins
+1	55	Number of radial detector bins used in detector and RT maps
+2	0.000 A	Lower limit for Q-map
+3	0.350 A	Upper limit for Q-map
+4	5 det ele	Smallest radius used on detector
+5	60 det ele	Largest radius used on detector
+6	0.00638	Instrument scaling constant
+0a	1.000	Fraction of background to be subtracted
+7	0.500	Position in the time channels from which the nominal value is taken.
+8	1.500	Position in the spatial channels from which the nominal value is taken.
+9		Go back (no further changes)
+0 1 5 +4 0 0		

Fig. 4 The command line interpreter. An alternate interactive mode of the user interface is illustrated. This segment is from a facility for altering entries in the data-reduction options table for  $d\Sigma(Q)/d\Omega$  and  $d\Sigma(Q)/d\Omega$  maps. It illustrates the general form of this mode, in which a key followed by a parameter is entered into a command line. The display shows the options available, the parameter to be entered, if needed, and the default value, if any.

center are identical to those in the raw-data display menu and are needed to support the mapping functions of SMR.

Figure 4 is an example of the command line mode of the SMR user interface. In this case, the user has made a request to alter the values in the parameter table (a specialized data structure in Fig. 2) for the binning parameters for data reduction to a Q-map. The display for this mode includes a menu of the commands, the parameter to be entered and its default values (if applicable), and the resulting option invoked. A typical entry is shown, in which the number of Q-bins is changed to 175 and the smallest radius used on the detector is altered to be 10 detector elements. These become the new defaults for the duration of the computing session.

An example from the graphics and postprocessor user interface is shown in Fig. 5. This subsystem is used to manipulate and analyze output from the core functions of SMR in a flexible manner. It is also implemented as a stand-alone facility. Here the menu for file I/O, data manipulation, and analysis menus are shown, along with two submenus. On the left are the currently available analysis routines. On the right are the data manipulation routines. Here, three previously computed, background-subtracted  $d\Sigma(Q)/d\Omega$  maps for measurements 263, 591 and 588 are being compared. One has been selected and its ordinate values are to be scaled by dividing by 10. Data arrays can be added to, subtracted from, multiplied or divided by each other in the postprocessor.

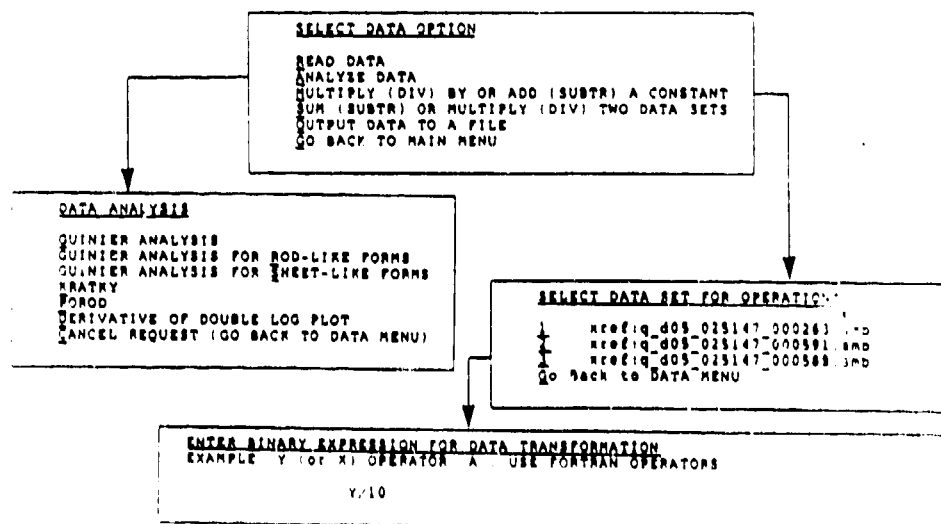


Fig. 5 An example from the postprocessor menu. The different options currently available in the postprocessor menu are illustrated, including data analysis and file-manipulation options.

## Examples

The basic function of SMR is to provide the maps,  $d\Sigma(Q)/d\Omega$  and  $d\Sigma(Q)/d\Omega$ . In this, the counts detected in each  $i, j^{\text{th}}$  detector element in each  $n^{\text{th}}$  time channel,  $C_{i,j,n}$ , are placed into a bin,  $K$ , with a domain in  $Q$  (or  $Q$ ) covering that of the  $i, j, n^{\text{th}}$  cell. Each counts in cell is converted to an absolute differential cross section times the area density of scatterers by division with an appropriate normalization factor; thus, the map is given by the expression<sup>(1,3)</sup>:

$$N/A [d\Sigma/d\Omega]_K = \sum_{\{K\} \supseteq \{i,j,n\}} C_{i,j,n} / \sum_{\{K\} \supseteq \{i,j,n\}} \Delta\Omega_{i,j} I_n \epsilon_n \eta_{i,j}, \quad (1)$$

where the differential cross section is in units of area and  $N/A$  is the number of scatterers per unit area. Here  $\Delta\Omega_{i,j}$  is the solid angle of the  $i, j^{\text{th}}$  detector element, and  $\eta_{i,j}$  is its counting efficiency;  $\epsilon_n$  refers to the response of the detector to the neutrons in the  $n^{\text{th}}$  time channel.<sup>(4)</sup>  $I_n$  is the number of neutrons that passed through the sample neither scattered nor absorbed. Equation (1) is a statistically weighted average of the contributing cells, which optimizes the precision in  $Q$  and in differential cross section<sup>(1,3)</sup>.

The measurement of  $I_n \epsilon_n$  is critical to proper normalization of each cell. Errors in its determination can lead to distortions in the scattering curve. On the LQD,  $I_n \epsilon_n$  is presently determined by making a separate measurement of the transmitted beam using a Cd mask as an attenuator, normalized to the upstream monitor. We are developing a transmission monitor in the beam stop to make this measurement concurrently with the scattering measurement.<sup>(4,5)</sup>

An example of the efficacy of the calculation represented in Eq. (1) is shown in Fig. 6 (from a display generated by the postprocessor), which compares data from a standard sample consisting of a mixture of deuterated and protonated polystyrene (PSD/PSH = 0.48<sup>(7)</sup>) measured on the LQD and the 30-m SANS at Oak Ridge National Laboratory. The shapes of the curves are, for all practical purposes, the same. Some differences are seen in the low- $Q$  region, and this is likely to be the result of multiple scattering of the long wavelength neutrons which contribute to this part of the map. Inspection of the transmission coefficients at long wavelengths illustrates this (Fig. 7) and indicates a useful application of data reduction to transmission coefficients.

Displays available from SMR for  $d\Sigma(Q)/d\Omega$  and  $d\Sigma(Q)/d\Omega$  maps are shown in Figs. 8 and 9 which show data for polystyrene latex spheres in  $D_2O$ . The Guinier analysis given by the postprocessor (not shown) gives the radius of gyration as 143 Å, in good agreement with the known diameter of 380 Å for these particles. Figure 9 is a shaded monochrome rendition of the two-dimensional color graphics display.

Figure 10 illustrates a diagnostic raw-data display, the R-T map. From this, some idea of the parts of the histogram that are contributing signal can be determined. An example of a normalized theta-lambda map is given in Fig. 11. The lines, which are contours of constant  $d\Sigma(Q)/d\Omega$ , will be straight on this double log display if the scattering is invariant at constant  $Q$ , which should be the case. Curvature in the

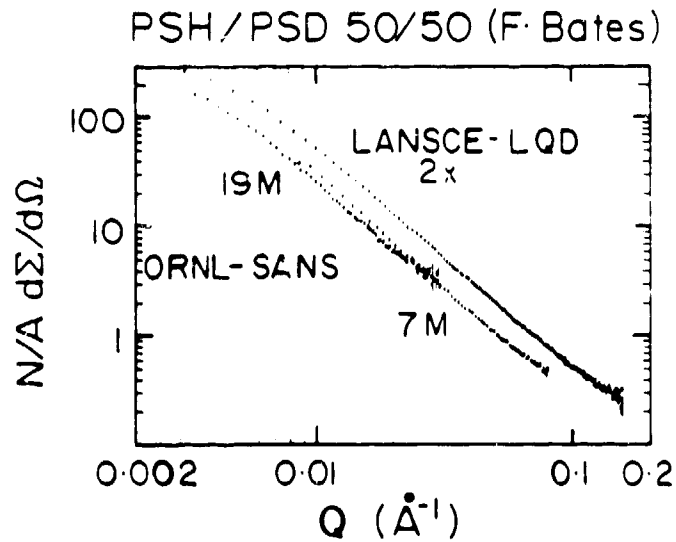


Fig. 6 A comparison of a map computed for a mixed perdeuterated/protonated polystyrene (PSD/PSH) sample and data taken for the same sample on the Oak Ridge SANS instrument. This figure is from a display generated by the postprocessor. Data taken on the ORNL 30-m SANS instrument at the 19-m and 7-m positions are indicated. Scattering computed from data taken on the LQD at LANSCE is scaled by a factor of two for clarity.

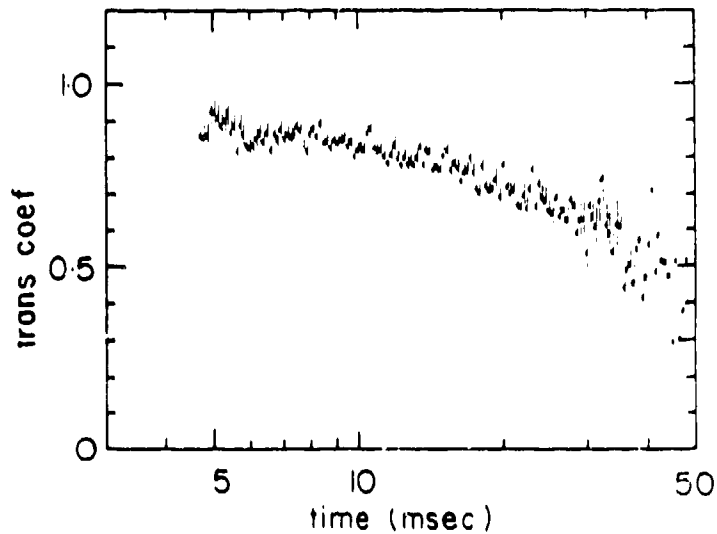
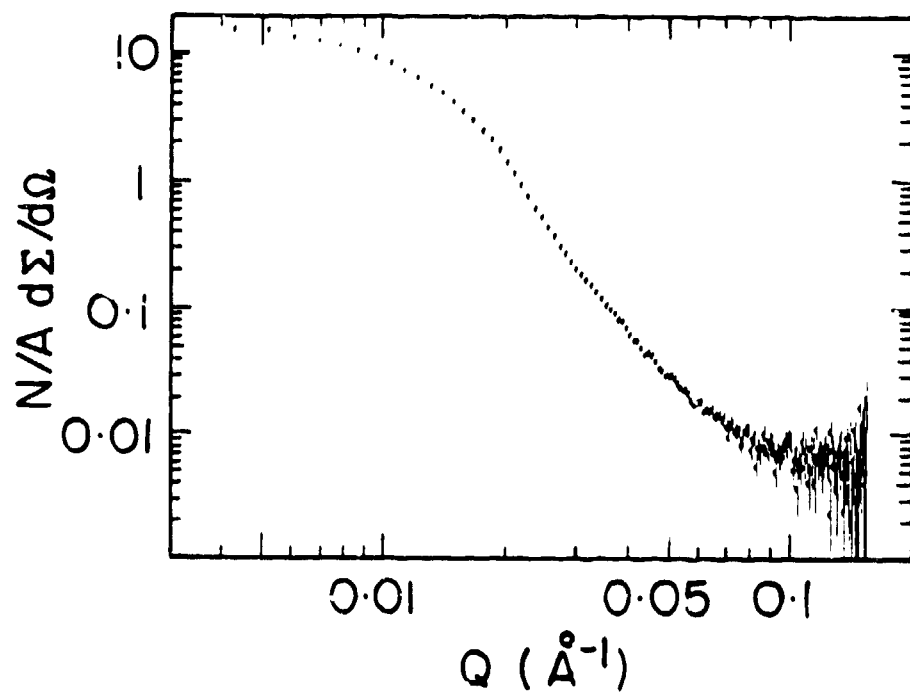


Fig. 7 Transmission of the PSD/PSH standard polystyrene sample. This is from the interactive graphics display generated by the transmission coefficient option of the reduce data submenu. Plotted are the transmission coefficients for each time-of-flight channel. These numbers are not used directly in computing Q-maps, but serve a function in assessing the possible presence of multiple scattering in the mapped data.



**Fig. 8** An  $N/A \frac{d\Sigma(Q)}{d\Omega}$  map of polystyrene latex spheres in  $D_2O$ . This is from the output generated by the Q-map option of the data reduction submenu using the one-dimensional output option. The test particles are spheres approximately 38 nm diameter.

# 584: polystyrene latex in D2O

Q max = 0.16000 1/A

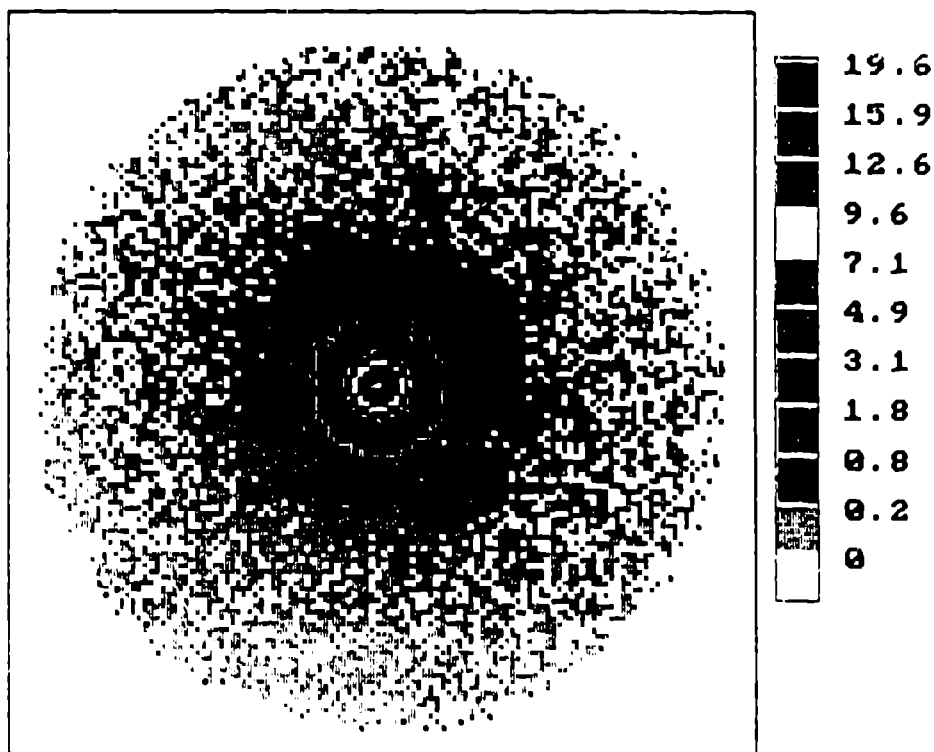


Fig. 9 An  $N/A \, d\Sigma(Q)/d\Omega$  map of scattering from polystyrene latex spheres in  $D_2O$ . A monochrome reproduction of output generated by the Q-map option of the data reduction submenu using the two-dimensional color graphics option. Here, the values of  $N/A \, d\Sigma/d\Omega$  are shown for each  $Q_y, Q_x$  cell. Values are indicated on the scale to the right. The values of the differential cross section increase monotonically toward the Q origin at the center.



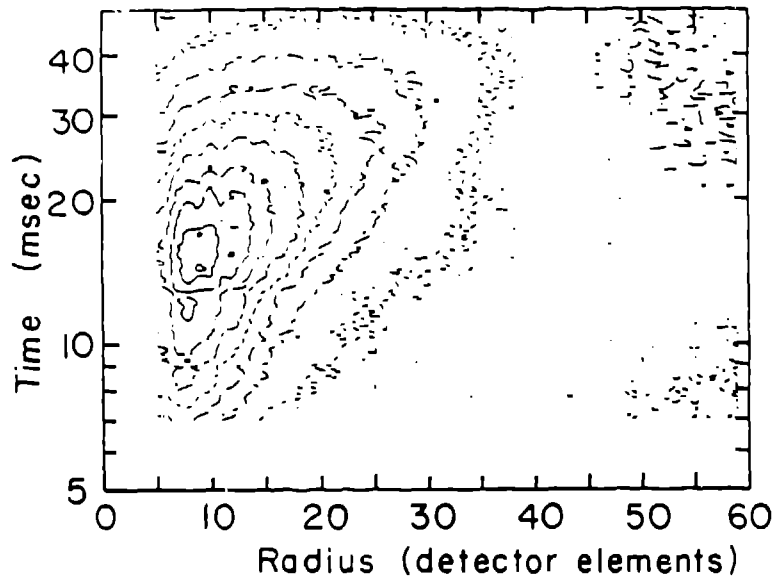


Fig. 10 A radius-TOF map of raw data taken from latex spheres in  $D_2O$ . This is from the output obtained from the R-T Map option of the Raw Data Display submenu using the contour map display option. In this, the counts in each radial-TOF cell are contoured at levels of 1% (—), 4% (---), 9% (---), 16% (---), 25% (---), 36% (---), 49% (---), 64% (---), and 81% (---) of the maximum value.

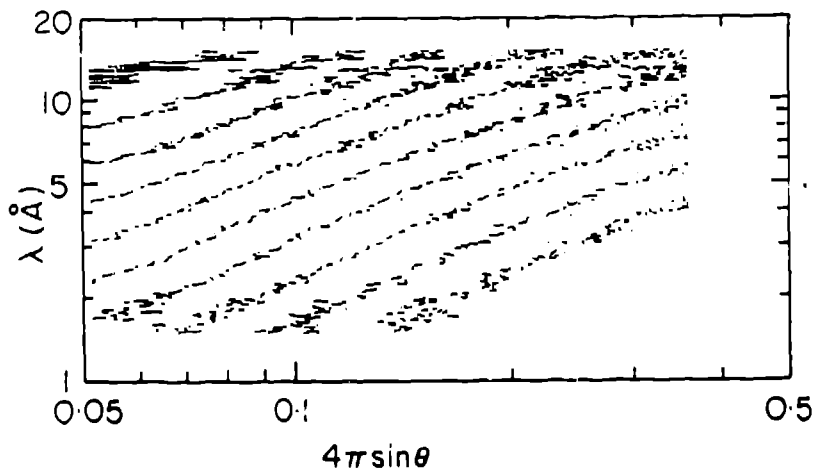


Fig. 11 A theta-wavelength map of data reduced from PSH/PSD. This is from output obtained from the Theta-Lambda option of the Reduce Data submenu using the contour display option. Here lines of constant  $N/A \frac{d\Sigma(Q)}{d\Omega}$  are plotted for the wavelength and  $4\pi \sin\theta$  using the same contouring intervals as in Fig 10. Wavelength is on a logarithmic scale, as is  $4\pi \sin\theta$ .

lines is indicative of problems in normalization, background subtraction or instrumental effects, such as detector non-linearity or instrument resolution effects.<sup>[1-3]</sup> Sample dependent effects, such as multiple scattering<sup>[2]</sup> or inelastic effects<sup>[3]</sup>, may also be seen from such plots.

### Future directions

The basic features of SMR have now been outlined and future developments will involve the implementation of other facilities, particularly interactive graphics and data analysis. A major concern is improving the speed of the calculations. Presently, some of the maps require about 60 minutes of CPU time to calculate, necessitating that some tasks be relegated to batch processes. This clearly cannot be accepted given the objectives of SMR. Some improvements in speed can be obtained by more efficient code. However, acceptable computation times can only be obtained with hardware improvements such as attached processors. When such devices are available, it will be straightforward to alter the interface modules to use these, and near-real-time data assessment and analysis will then be possible.

### References

1. Seeger, P.A., and Pynn, R., 1986, "Resolution of Pulsed-Source Small-Angle Neutron Scattering", Nucl. Instr. Meth., **A245**, 115-124.
2. Hjelm, R.P., Jr., 1987, "Resolution of Time-of-Flight Small-Angle Neutron Diffractometers", J. Appl. Cryst., **20**, 273-279.
3. Hjelm, R.P., Jr., 1988, "The Resolution of TOF Low-Q Diffractometers: Instrumental, Data Acquisition and Reduction Factors", J. Appl. Cryst., **21**, 618-628.
4. Seeger, P.A., 1988, "Neutron Detection Systems for Small-Angle Scattering", J. Appl. Cryst., **21**, 613-617.
5. Seeger, P.A., Hjelm, R.P., Jr., and Nutter, M.J., 1989, "The Low-Q Diffractometer at the Los Alamos Neutron Scattering Center", Mol. Cryst. Liq. Cryst., (in press).
6. Nelson, R.O., Cort, G., Gjovig, A., Goldstone, J.A., McMillan, D.E., Ross, J., Seal, J., and Machen, D.R., 1987, "The Los Alamos Neutron Scattering Center Data Acquisition System", IEEE Trans. Nucl. Sci., **NS-34**, 1017-1032.
7. Wignall, G.D., and Bates, F.S., 1987, "Absolute Calibration of Small-Angle Neutron Scattering Data", J. Appl. Cryst., **20**, 28-40.
8. Copley, J.R.D., 1988, "The Significance of Multiple Scattering in the Determination of Small-Angle Neutron Scattering Experiments", J. Appl. Cryst., **21**, 639-644.

## APPENDIX A:

### Block-formatted ASCII files

Standard output data files from the LQD consist of a three-record abstract and a number of blocks of data, all in directly readable ASCII strings. A data block consists of a series of numbers that may include decimal points and/or exponent fields, which are separated by commas or blanks and terminated by '/' followed by a zero byte (ASCII <NUL>). For ease of printing, the string includes <CR><LF> sequences after every 126 or fewer characters, and the first character on the line is generally a blank. The subroutine REALOUT (ARRAY, NDATA, NUNIT) is provided to write these blocks. The string is designed to be read by a FORTRAN unformatted read statement, into a real array at least as long as the number of data. The array should be zeroed (or appropriately initialized) before the read statement, as null fields will not be modified during reading. The terminal zero byte has been included to assist parsing in other languages.

#### Abstract Record 1

Bytes 1-4, File type (e.g., 'LOGT' or 'RT'). For 1-D spectra, the type generally specifies the independent variable.

Bytes 6-45, Title of run, usually terminated with '\$'

Bytes 47-63, File ID; the instrument, date, and time at which data was saved, as assigned by the data-acquisition system; e.g., 'LQD\_881002\_183520'

Bytes 64-73, Integrated current ( $\mu\text{A}\cdot\text{h}$ ), real format (may be blank).

#### Abstract Record 2

This record is an ordered block (as defined above) of up to 100 parameters. Several parameters have been defined for use by various analysis programs (especially MPLLOT and QBIN); these are as follows:

1. Number of channels in data blocks. This parameter is always required.
2.  $dt/t$  for the logarithmic time scale
3. Clock tick ( $\mu\text{s}$ ); usually  $0.1 \mu\text{s}$
4. First time-channel boundary ( $\mu\text{s}$ )
5. Time delay of detector electronics ( $\mu\text{s}$ )
6. Source-to-sample distance (m)
7. Sample-to-detector distance (m)
8. Size of one detector element (mm)
9. X-position of beam center, in detector elements
10. Y-position of beam center, in detector elements
11. Power of units: 1 (default) for raw data, 0 for ratio
12. Number of bins that have been combined; usually 1
13. Number of bins per decade for uniform log scale
14. Incident energy for direct-geometry inelastic scattering (eV)
15. Final energy for inverse-geometry inelastic scattering (eV)
16.  $dQ/Q$  for Q bins below the switch point
17. Q at which bins switch from log to linear ( $\text{\AA}^{-1}$ )

18. Width factor in Q-binning: radial bins wider than this factor times the Q-bin width are deleted.
19. Fraction of total neutrons kept during Q binning.

### Abstract Record 3

This record is an algebraic expression of operations that have been performed on the data. Initially, it is a brief spectrum identifier enclosed in parentheses, with byte 1 blank. For instance, '(586, 25-147)' represents radially averaged detector time slices 25-147 of run 586, '(256,M1)' is the corresponding upstream monitor spectrum, and '(585, R=0-5)' is the sum of the central 5 radial zones of the detector for run 585, which was a transmission run. There must be no embedded blanks; the first blank after column 1 terminates the string. (The terminating blank may be followed by an ASCII <NUL>.) The string is divided into "lines" by a <CR><LF> after every 80 characters. Total length allowed is 720 characters (9 lines).

Byte 1 is blank if the term will not need parentheses added when another operation is appended,  
is '+' if the last operation was + or -, and  
is '\*' if the last operation was \* or /.

All data blocks following the abstract have keyword identifiers in the first record. If the first four characters aren't one of the standard identifiers listed below, the record is assumed to be the type identifier of a new abstract. A blank record should be used to separate data files within a file.

### 'POINTS' or 'BINS'

An optional block giving the values of the independent variable (POINTS) or of the boundaries of histogram bins (BINS). The number of points should equal the value given in the second abstract record; the number of bin boundaries is one greater than this number. This block may be omitted if the independent variable is the channel number, or if it is time of flight that may be computed from parameters 2-5 of the abstract. For two-dimensional data, the first block will refer to the X coordinate and the second (if any) to Y. The dimension of the second block is not included in the abstract.

### 'AREA'

An optional block of normalizing factors to be divided into the data. This is useful if the data are raw histogram counts. For two-dimensional data, the first block will refer to the X coordinate and the second to Y.

### 'RMSBIN'

An optional block giving the rms of the values of the independent variable, for instance, when finding an average of data within a bin. For two-dimensional data, the first AREA or RMSBINS block will refer to the X coordinate and the second to Y. Note that the read subroutines described

below do not allow having both AREA and RMSBIN blocks associated with the same variable.

**'DATA'**

The dependent variable of a one-dimensional file (must not occur in a two-dimensional file). The number of data should agree with parameter 1 in the abstract.

**'Y = nnn'**

The identifier for this block has an '=' anywhere within the first four characters and an integer within characters 5 to 15. The integer is the row number in a two-dimensional array (i.e., the Y coordinate). The number of data in the block should agree with parameter 1 in the abstract (the X coordinate).

**'STDDEV'**

Standard deviations of the data. This block should immediately follow the 'DATA' or the 'Y=' block to which it applies. May be omitted only if the data have Poisson statistics; i.e., for raw histograms or simple sums of channels.

Two standardized FORTRAN subroutines are available for reading these files, respectively, for one-dimensional and two-dimensional data. Both are written in Fortran 77 and should be highly transportable.

Subroutine READ\_1D(IUNIT, TYPE, TITLE, FILEID, UAHR,  
PARAMS, NP, HEADER, NH,  
X, DX, Y, DY, IFLAG, IERROR)

Searches logical unit IUNIT for the next data file of type TYPE, or for any one-dimensional file if TYPE = ' '. Returns all abstract information and the arrays X, DX, Y, and DY. X is always converted to bin boundaries and DY defaults to SQRT(Y) if the STDDEV block was omitted. DX may be a normalizing factor (i.e., bin area) or the rms of points included in the bin (in which case IFLAG = 1).

Variables in calling sequence:

IUNIT	Integer	Input	Fortran unit number
TYPE	Char*4	In/Out	Type to search for, or type found
TITLE	Char*40	Output	Title from first record of abstract
FILEID	Char*17	Output	Instrument_Date_Time identifier
UAHR	Real	Output	Integrated beam current
PARAMS	Real(NP)	In/Out	Parameters in the abstract. May be preinitialized if missing from data file.
NP	Integer	Input	Maximum number of parameters to return
HEADER	Char(9)*80	Output	Character string describing operations previously performed on data

NH	Integer	Output	Number of characters in HEADER
X	Real(*)	Output	Bin boundaries (channels + 1)
DX	REAL(*)	Output	Normalizing function or rms of bins (see IFLAG)
Y	Real(*)	Output	Data values summed or averaged over bins
DY	Real(*)	Output	Standard deviations of Y
IFLAG	Integer	Output	0 if DX is normalization, 1 if rms, or -1 if neither
IERROR	Integer	Output	0 for successful read, -1 for end-of-file, or system-dependent message number.

Subroutine READ\_2D(IUNIT, TYPE, TITLE, FILEID, U/HR, PARAMS, NP, HEADER, NH, X, DX, Y, DY, NY, Z, DZ, NXZ, IFLAG, IERROR)

Searches logical unit IUNIT for the next data file of type TYPE, or for any two-dimensional file if TYPE = ' '. Returns all abstract information, the one-dimensional arrays X, DX, Y, and DY, the two-dimensional arrays Z and DZ. X and Y are always converted to bin boundaries, and DX and DY may either be normalizing factors (i.e., bin areas) or the rms of the bins; IFLAG = 1 if DX is rms, 2 if DY is rms, or 3 if both, or defaults to -1 if no AREA or RMS3INS blocks were read.

Variables in calling sequence (see also READ\_1D):

X	Real(*)	Output	Bin boundaries (channels + 1)
DX	Real(*)	Output	Normalizing function OR rms of bins
Y	Real(*)	Output	Bin boundaries (channels + 1)
DY	Real(*)	Output	Normalizing function OR rms of bins
NY	Integer	Input	Maximum value allowed for Y index
Z	Real(NXZ,*)	Output	2-D data array
DZ	Real(NXZ,*)	Output	Standard deviations of Z
NXZ	Integer	Input	First dimension of Z in calling program
IFLAG	Integer	Output	1 if DX is rms, 2 if DY is rms, 3 if both, 0 if neither; -1 if no blocks were read.
IERROR	Integer	Output	0 for successful read, -1 if end-of-file, or system-dependent error number

The following examples include a monitor spectrum, a portion of a two-dimensional (RT) data set, and a completely reduced I(Q) data set.



LOGT PS Spheres in 020\$  
 147.0.016.0.1.4766.4.3570.4.522/  
 (586.M1)

LQ0\_001002\_103520

DATA

39330,39577,39931,40154,42306,35093,43607,47696,48769,46142,53731,58027,64273,68768,64012,72744,88508,93455,98329,102520,  
 99068,100849,95782,93260,94170,90025,89228,88547,86527,86744,82825,82224,82731,80713,74823,75558,72254,72746,70022,66343,  
 64183,65638,63261,60258,57851,55409,52779,51917,48913,45940,42879,41453,36471,37038,34921,32356,31038,29203,27277,25627,  
 24056,23515,22097,20390,19016,18146,17182,16183,15108,14568,13989,12519,12469,11358,10758,10121,9878,9326,8651,8254,7943,  
 7335,6910,6815,6118,6091,5723,5206,4847,5023,4459,4358,4109,3945,3746,3532,3332,3142,2916,2909,2641,2383,2357,2074,1900,2017,  
 1751,1829,1508,1402,1329,1220,1109,1061,928,984,954,773,767,685,668,596,555,454,527,472,466,432,405,401,569,493,498,467,433,  
 477,307,237,218,195,228,171,173,244,211,201,187/

RT PS Spheres in 020\$

LQ0\_001002\_103520

55.0.016.0.1.4766.4.0.56.4.16.4.00.63.80.65.46.1.1/  
 (586.60-67)

BINS

5,6,7,8,9,10,11,12,13,14,15,16,17,18,19,20,21,22,23,24,25,26,27,28,29,30,31,32,33,34,35,36,37,38,39,40,41,42,43,44,45,46,47,  
 48,49,50,51,52,53,54,55,56,57,58,59,60/

AREA

36,41,45,55,61,64,72,78,89,87,87,107,111,117,118,130,137,141,147,151,164,167,170,178,186,198,199,200,212,219,225,223,239,245,  
 217,253,256,274,269,280,286,292,305,297,312,318,329,332,327,342,352,357,363,363,380/

T= 60

410,637,718,840,828,666,544,484,404,289,222,169,109,84,80,76,87,55,55,47,49,41,46,33,41,27,33,24,26,27,25,32,31,21,23,33,21,  
 31,33,27,29,28,33,26,32,21,27,25,25,34,29,23,38,36,33/

T= 61

463,644,711,782,791,661,603,475,395,290,254,162,121,129,87,77,61,53,59,43,54,41,50,52,45,38,44,36,27,33,19,30,24,28,32,20,22,  
 35,35,26,28,34,25,27,26,32,20,27,26,35,22,24,25,31,38/

T= 62

423,612,695,706,708,597,569,492,382,292,257,184,146,105,82,72,86,50,59,62,58,47,42,34,32,42,44,25,32,32,32,27,28,28,25,26,26,  
 25,34,21,24,26,23,27,30,29,39,21,27,28,24,28,35,31,23/

T= 63

413,580,656,787,708,651,564,509,408,253,304,201,148,142,89,100,74,44,68,38,46,44,33,39,33,29,39,28,27,27,34,28,17,20,32,25,  
 31,26,26,29,24,21,43,22,16,21,30,32,23,24,29,28,24,42,39/

T= 64

492,683,798,898,840,713,640,490,450,348,284,216,157,134,109,81,72,63,57,48,49,46,53,47,33,32,32,26,34,39,23,26,39,24,28,19,  
 23,30,27,25,24,21,30,28,29,23,33,15,30,18,28,38,29,21,28/

T= 65

563,716,873,959,961,817,743,626,528,412,327,250,199,133,118,93,88,76,69,66,58,42,42,42,55,39,34,32,32,23,21,28,38,24,27,27,  
 25,31,30,20,24,24,29,22,22,39,29,32,31,27,31,35,32,31,20/

T= 66

542,722,820,999,989,817,776,613,529,383,338,270,191,146,124,100,86,70,60,54,57,53,37,45,48,38,29,47,42,34,19,31,31,35,29,24,  
 22,26,29,32,26,28,28,24,28,30,33,35,29,30,20,29,35,32,38/

T= 67

537,744,878,1049,1043,829,734,690,597,447,379,298,203,166,136,108,88,75,62,66,64,55,32,46,41,49,31,39,36,34,33,32,24,27,28,  
 29,22,24,28,31,34,22,29,27,19,31,27,33,26,29,23,23,32,28,39/





Q PS Spheres in 020, less backgrounds Q0 001002\_183520  
 175.0.016.0.1.4766.4.0.56.4.16.4.64.38.69.32.0.001.1/  
 00630(((506.25-147)/(506.M1))((266.25-147)/(266.M1)))/((505.R=0.5)/(505.M1)) (26  
 6.R=0.5)/(266.M1))(((531.25-147)/(531.M1))((266.25-147)/(266.M1)))/((530.R=0.5)/  
 (530.M1))((266.R=0.5)/(266.M1)))

POINTS

00436530, 00525520, 00614510, 00703507, 00792497, 00881487, 00970476, 0105947, 0114848, 0123745, 0132644, 0141542, 0150441,  
 015934, 0168239, 0177138, 0186037, 0194936, 0203835, 0212734, 0221633, 0230532, 0239431, 024833, 0257229, 0266128, 0275027,  
 0283926, 0292825, 0301724, 0310623, 0319522, 0328421, 033732, 0346219, 0355118, 0364017, 0372916, 0381815, 0390714, 0399612,  
 0408511, 041741, 0426309, 0435208, 0444107, 0453006, 0461905, 0470804, 0479703, 0488602, 0497501, 05064, 0515299, 0524198,  
 0533097, 0541996, 0550895, 0559794, 0568693, 0577592, 0586491, 059539, 0604289, 0613188, 0622087, 0630986, 0639885, 0648784,  
 0657682, 0666581, 067548, 0684379, 0693278, 0702177, 0711076, 0719975, 0728874, 0737773, 0746672, 0755571, 076447, 0773369,  
 0782268, 0791167, 0800066, 0808965, 0817864, 0826763, 0835662, 0844561, 085346, 0862359, 0871258, 0880157, 0889056, 0897955,  
 0906854, 0915753, 0924651, 093355, 0942449, 0951348, 0960247, 0969146, 0978045, 0986944, 0995843, 1004742, 1013641, 102254,  
 1031439, 1040338, 1049237, 1058136, 1067035, 1075934, 1084833, 1093732, 1102631, 111153, 1120429, 1129328, 1138227, 1147126,  
 1156025, 1164924, 1173823, 1182722, 119162, 1200519, 1209418, 1218317, 1227216, 1236115, 1245014, 1253913, 1262812, 1271711,  
 128061, 1289509, 1298408, 1307307, 1316206, 1325105, 1334004, 1342903, 1351802, 1360701, 13696, 1378499, 1387398, 1396297,  
 1405196, 1414095, 1422994, 1431893, 1440791, 144969, 1458589, 1467488, 1476387, 1485286, 1494185, 1503084, 1511983, 1520882,  
 1529781, 153868, 1547579, 1556478, 1565377, 1574276, 1583175, 1592074/  
 DATA

15.80074, 15.70131, 14.02314, 12.94971, 12.01633, 10.90089, 9.88711, 8.75951, 7.62483, 6.49195, 5.7565, 5.04184, 4.27975, 3.63639,  
 3.05901, 2.538635, 2.137722, 1.783712, 1.453642, 1.175721, .8618, .776271, .626827, .540689, .439182, .379775, .3173052, .2743633,  
 .2390564, .2112663, .1909863, .1699791, .1552704, .1380089, .1214706, .1087911, .1000655, .9322941, .8844205, .8799719, .8707361, .8630396,  
 .8577417, .8540938, .8486642, .8424202, .8461346, .8431875, .8386537, .8343012, .8329244, .8302312, .8301376, .8300853, .8281162,  
 .8257065, .824313, .8236099, .8233133, .8218402, .8191824, .8182961, .8183907, .8186263, .8189339, .8196874, .8169997, .8154298,  
 .8161082, .8140396, .8143637, .8146013, .8139907, .8140963, .811789, .8097659, .8125943, .811823, .810508, .8105019, .8105475, .8083306,  
 .8090731, .8110781, .8110899, .8108139, .8076473, .8093324, .8096139, .8095737, .8080336, .8070772, .8079294, .8104317, .8080095,  
 .8073824, .8090125, .8087587, .8073846, .8090881, .8073839, .806638, .8066199, .8077734, .8077057, .8089273, .807893, .8101264, .8089383,  
 .8089899, .809316, .8084653, .8085707, .8073507, .808131, .8054478, .8086602, .80896, .8098243, .8077263, .8089932, .8041055, .8043105,  
 .8080414, .8052919, .8077864, .8041736, .8112402, .8062016, .8070163, .8070968, .8063963, .8068116, .8075996, .8079357, .806434, .8064708,  
 .8023693, .8110927, .8076639, .8099024, .8096123, .8073587, .8093503, .8073997, .8081882, .8081521, .8046909, .8029071, .8090546,  
 .8059774, .8097346, .8049154, .803091, .8100641, .8019913, .8024025, .806469, .1.78600E-04, .8113137, .8048981, .8042873, .8024871,  
 .807595, .8168763, .8073621, .810987, .8062251, .8130425, .8027488, .8041678, .8026424, .8074962, .8129264, /

STDEV

.717393, .349422, .2101421, .1454645, .1064218, .0836344, .0669984, .0549952, .0449675, .037833, .0319837, .027756, .0240273, .0209081,  
 .0182982, .0158739, .0139862, .0122865, .0106711, .00931963, .00818983, .00716184, .00639088, .00571524, .00506366, .00461365, .00416449,  
 .00383874, .00359489, .0033412, .00311823, .00292196, .00277942, .00261999, .00249129, .00232701, .00221927, .00213281, .0020397,  
 .0019822, .00187294, .00179929, .00171158, .00169016, .00161864, .00154967, .00146608, .00132939, .00147013, .00139441, .00139347,  
 .00133801, .00134727, .00133599, .0013169, .00130099, .00129497, .00127077, .00125066, .0012423, .00121886, .00120157, .00119817,  
 .00121128, .00120842, .00117917, .00119801, .0012098, .00118833, .00117883, .00118129, .0011879, .00118169, .00123311, .00118962,  
 .00118007, .00120034, .00122497, .0012059, .00121199, .00123146, .00122012, .00121736, .0012874, .00128462, .00127746, .00123269,  
 .00129147, .00128648, .00124811, .00129979, .00129783, .00130087, .00136043, .00130496, .00132162, .00132959, .0013478, .00139684,  
 .00132136, .00139982, .00139966, .00140159, .00142109, .00143483, .00146811, .00146246, .00150942, .00148799, .00150284, .00148924,  
 .0015071, .00151189, .00150778, .00154961, .00153915, .0015797, .00170647, .00160487, .00169968, .00163201, .0016236, .001637, .00179939,  
 .00171264, .00182931, .00179939, .0018796, .00187974, .00192172, .00191429, .00188781, .00196929, .00202823, .00206681, .00201908,  
 .0020889, .00202889, .00230308, .00217688, .00224997, .0022908, .0022238, .00229992, .00238641, .00259722, .0025974, .0025894, .00264852,  
 .00278881, .00287466, .00297029, .0030018, .00308228, .00318072, .0032793, .0032908, .00361471, .00347813, .00360099, .00418799,  
 .0048916, .00418767, .00484813, .00627943, .00499898, .00692287, .00912681, .00714899, .0068759, .00686036, .00947017, .00738788,  
 .00991103, /





## Some considerations on TOF-NSE

*S. Ikeda*  
National Laboratory for High Energy Physics  
Oho, Tsukuba-shi, Ibaraki-ken, 305  
JAPAN

Recently a future plan of a huge spallation neutron source has been proposed in a framework of the Japan Hadron Project (JHP), in which accelerated protons with 100-200  $\mu\text{A}$  and 1-2 GeV will be used for the production of neutrons. Here, as a new concept, a unique cold moderator is considered, which can produce high intense pulsed-cold-neutrons with the extreme wide burst-width. If it will be realized, it will confer benefits on elastic scattering TOF-instruments, such as SAN in KENS, which does not require high time-resolution. However, it is a "devil" for ordinary inelastic scattering TOF-spectrometers with high energy-resolution, such as LAM in KENS. In these inelastic spectrometers, high time-resolution is required and the energy-resolution is approximately given by  $2(\text{burst-width})/(\text{time-of-flight})$ . It means that the ordinary inelastic scattering spectrometer with  $e/E_1 = 0.005$  must be constructed much farther from this moderator, at about 300 m.

Because the area of JHP is very small, it is hard to prepare such a long flight path. Even if it could be constructed with the long flight path, the available band-width of neutron wavelength becomes very small. For our future plan, many attempts should be performed to "invent" a new type of the TOF-spectrometer, which can realize the high energy-resolution even in the condition of a short distance and a wide burst-width on various spectrometers, including the ordinary one.

The TOF spin-echo method (TOF-NSE) is one candidate for these trials. The pure spin-echo method<sup>[1]</sup> has been already realized on the steady state sources, and many low energy excitations in magnetic systems, polymers and so on, have been observed. TOF-NSE was proposed by Mezei in 1979<sup>[2]</sup> but not still realized at the spallation neutron sources. At KENS, we constructed a test machine of TOF-NSE in 1983.

If incident polarized neutrons with velocity  $V_1$  is used in NSE, the polarization observe dby the analyzer,  $P(V_1)$ , can be written as

$$P(V_1) = \int dt S(t) \cos(\omega_1 t_1 - \omega_2 t_2), \quad (1)$$



where  $\epsilon = m(V_1^2 - V_2^2)/2$ ,  $t_1 = l_1/V_1$ ,  $t_2 = l_2/V_2$  and  $\omega_{1,2} = \gamma H_{1,2}$ .  $m$  is the neutron mass,  $H_{1,2}$  a magnetic field in precession section I and II, and  $V_2$  is the velocity of scattered neutrons.  $S(\epsilon)$  is a scattering function of a sample. If  $V_1 - V_2 \ll V_1$  and  $l = l_1 = l_2$  and  $H = H_1 = H_2$ , Eq.(1) is written as

$$P(V_1) = \int d\epsilon S(\epsilon) \cos(\tau\epsilon) = S'(\tau), \quad (2)$$

where  $\tau = \gamma l / (mV_1^3) \cdot H$ . In principle, it is possible to measure  $S'(\tau)$  in two kinds of neutron sources; the steady state source and the pulsed source. In the case of the steady state source,  $\tau$  can be represented as a function of  $H$  because of  $V_1 = \text{constant}$ , and  $S'(\tau)_{\text{steady}}$  can be observed by changing magnetic field  $H$ . In the case of the pulsed source, pulsed white neutrons are used as incident neutrons. Here,  $V_1$  is determined as  $V_1 = L/t$  and  $\tau$  can be written as  $\tau = \gamma H l / (mL^3) \cdot t^3$ , where  $L$  is the total flight-path length and  $t$  the time-of-flight. This means  $S'(\tau)_{\text{TOF}}$  can be automatically observed as a function of  $t^3$  in the constant magnetic field  $H$ . This is a most useful nature of TOF-NSE.



A schematic layout of TOF-NSE is shown in Fig.1. Here we assume that  $\pi$ -turner and  $\pi/2$ -turners perfectly work for every neutron velocity, and that  $l_3 = l_4 = l_5 = l_6 = l_7 = 0$  and  $\delta l_0 = 0$  in order to simplify the equation. The observed TOF-spectrum,  $I(t)$ , is written as

$$I(t) = 1/2 \int P^i P_1^i P_2^i P_1^w P_2^w \delta(t - t_0 - t_1 - t_2) (1 + \cos(\omega_1 t_1 - \omega_2 t_2)) S(\epsilon) \delta(E_i - E_f - \epsilon) dt_0 dt_1 dt_2 d\omega_1 d\omega_2 \epsilon. \quad (3)$$

Here,  $P_{1,2}^i$  and  $P_{1,2}^w$  represent are fluctuations of the lengths and the precession frequency in precession sections ( $i = 1,2$ ), respectively.  $E_i$  and  $E_f$  are incident and scattered neutron energies, respectively.  $P^i$  is a pulse shape function of the neutron burst. Let's represent  $P_{1,2}^i$ ,  $P_{1,2}^w$  and  $P^i$  by Gaussian as



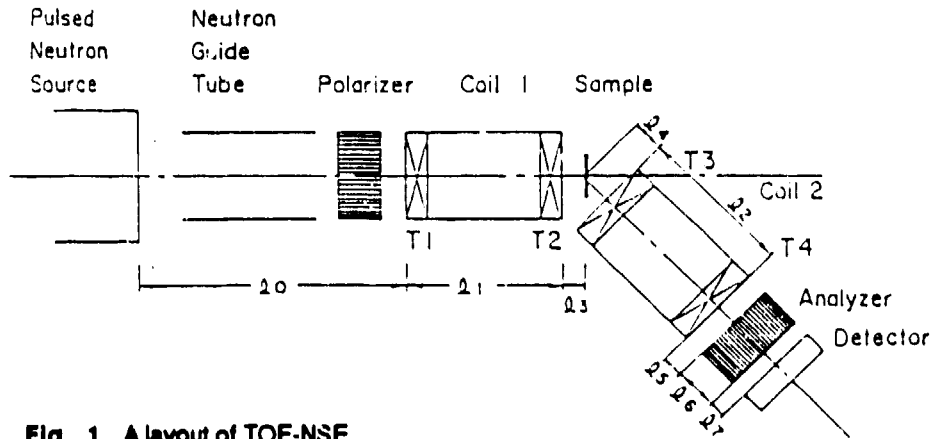


Fig. 1 A layout of TOF-NSE.

$$P^t = (\sqrt{2\pi}\sigma_t)^{-1} \exp(-(t_0 - t_0^0)^2 / 2\sigma_0^2), \quad (4)$$

$$P_{1,2}^\omega = (\sqrt{2\pi}\sigma_{\omega_{1,2}})^{-1} \exp(-(\omega_{1,2} - \omega_{1,2}^0)^2 / 2\sigma_{\omega_{1,2}}^2) \quad (5)$$

and

$$P_{1,2}^l = (\sqrt{2\pi}\sigma_{l_{1,2}})^{-1} \exp(-(l_{1,2} - l_{1,2}^0)^2 / 2\sigma_{l_{1,2}}^2), \quad (6)$$

where  $t_0^0$ ,  $\omega_{1,2}^0$  and  $l_{1,2}^0$  are mean values of  $t_0$ ,  $\omega_{1,2}$  and  $l_{1,2}$ .  $\sigma_0$  corresponds to the neutron burst-width. If  $\sigma_{l_{1,2}}/V_1 \ll \sigma_0$ ,  $I(t)$  can be written as

$$I(t) = (2\sqrt{2\pi}\sigma_0)^{-1} \int dt_0 d\epsilon \exp(-(t - t_0^0 - t_1^0 - t_2^0)^2 / 2\sigma_0^2) \\ [1 + \Psi(a_1, a_2)\Phi(a_1, a_2)] S(\epsilon) \delta(E_i - E_f - \epsilon). \quad (7)$$

Here,

$$\Psi(a_1, a_2) = a_1 a_2 / \sqrt{(a_1^2 + g_1^2 h_1^2)(a_2^2 + g_2^2 h_2^2)} \\ \cdot \exp(-(g_1^2 + h_1^2)/(a_1^2 + g_1^2 h_1^2) + (g_2^2 + h_2^2)/(a_2^2 + g_2^2 h_2^2)) \quad (8)$$

and

$$\Phi(a_1, a_2) = \cos(a_1/(a_1^2 + g_1^2 h_1^2) - a_2/(a_2^2 + g_2^2 h_2^2)) \quad (9)$$

where  $t_0^0 = l_0/V_1$ ,  $a_i = V_i/\omega_i^0 t_0^0 = 1/\omega_i^0 t_0^0$ ,  $g_i = \sigma_i^l/l_0^0$  and  $h_i = \sigma_i^w/\omega_i^0$ .

$\Psi(a_1, a_2)$  and  $\Phi(a_1, a_2)$  are a damping factor and an oscillation factor, respectively. Since  $V_1 \sim V_2$ ,  $\Psi(a_1, a_2)$  is described by

$$\Psi(a_1, a_2) = \Psi_g(a_1) = a_1^2/(a_1^2 + g^4) \exp(-2g^2/(a_1^2 + g^4)). \quad (10)$$

where  $g = g_1 = g_2 = h_1 = h_2$  is assumed in order to simplify.  $\Psi_g(a_1)$  was calculated as a function of  $H \cdot l$  in the case of  $\lambda_1 = 9 \text{ \AA}$ , and is shown in Fig. 2. Here,  $\lambda_1$  is a wavelength of incident neutron. Furthermore  $\Psi_g(a_1)$  was calculated as a function of  $\lambda_1$  in the case of  $H \cdot l = 120 \text{ Oe}$ , and is shown in Fig. 3. If  $g > 10^{-4}$ ,  $\Psi_g(a_1)$  goes down drastically as  $\lambda_1$  or  $H \cdot l$  increase. These results indicate  $g < 10^{-4}$  is required to obtain a good neutron economy. In the same assumption, the oscillation factor  $\Phi$  is described by

$$\Phi(a_1, a_2) = \Phi_g(a_1, a_2) = \cos(a_1/(a_1^2 + g^4) - a_2/(a_2^2 + g^4)). \quad (11)$$

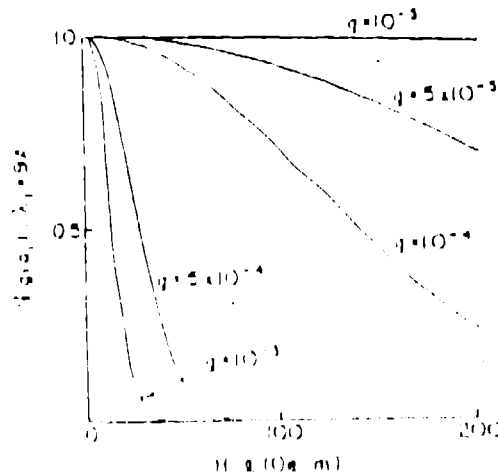
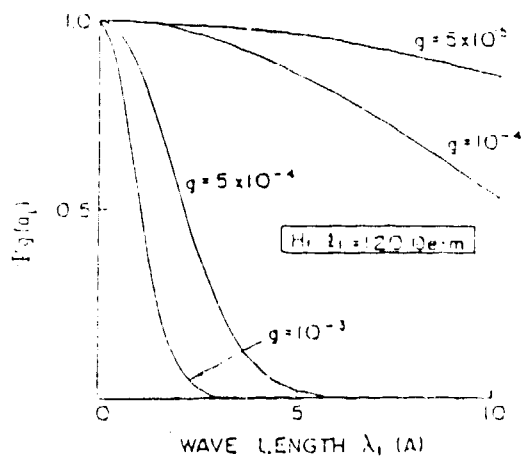
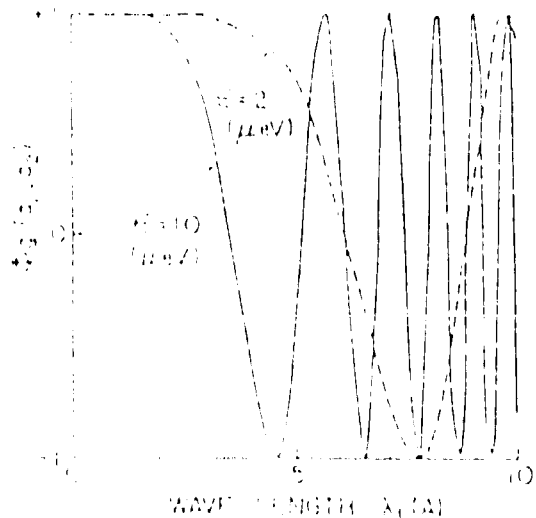


Fig. 2 Damping factor  $\Psi_g$  and  $H \cdot l$ . The solid lines are calculated with  $\lambda_1 = 9 \text{ \AA}$ .



**Fig. 3** Damping factor  $\Psi_g$  and wavelength  $\lambda_1$ . The solid lines are calculated with  $H \cdot l = 1200 e \cdot m$ .

In the case of  $S(\epsilon) = (\delta(\epsilon - \epsilon_0) + \delta(\epsilon + \epsilon_0))/2$ ,  $H \cdot l = 1200 e \cdot m$  and  $g = 10^{-4}$ ,  $\Phi_g(a_1, a_2)$  was calculated with  $\epsilon_0 = 2 \mu eV$  and  $\epsilon_0 = 10 \mu eV$  and shown in Fig. 4. This results show the oscillation of  $\Phi_g(a_1, a_2)$  with  $\epsilon > 2 \mu eV$  can be observed in the range  $2.5 \text{\AA} < \lambda_1 < 10 \text{\AA}$ .



**Fig. 4** Oscillation factor  $\Phi_g$  and wavelength  $\lambda_1$ . The solid line is calculated with  $\epsilon = 10 \mu eV$  and  $H \cdot l = 1200 e \cdot m$ . The dashed line is calculated with  $\epsilon = 2 \mu eV$  and  $H \cdot l = 1200 e \cdot m$ .

The effect of the burst-width on the TOF-NSE should be discussed using Eq.(7). As is obvious from this equation, if the burst-width is much smaller than a period of  $\Phi_g$ , one can expect no effects on TOF-NSE spectrum. Since  $\Psi_g$  changes very slowly under  $g = 10^{-4}$  as shown in Figs.2 and 3, it is possible to consider that  $\Psi_g$  is not affected by the burst-width. In order to observe a clear oscillation of  $S'(\tau)_{TOF}$  under  $l_0 = 18m$  and  $0 < \lambda_1 < 9A$ , the following condition is at least required:

$$3\omega l \cdot (\text{burst} - \text{width}) / (2l_0 \cdot 1000) \sim 0.1 \ll 1 \quad (12)$$

In the case of  $(\text{burst} - \text{width}) \sim 260\mu\text{sec}$  (KENS-I) and  $H \cdot l = 120Oe \cdot m$ , the 'no effect' can be realized in the range  $\epsilon < 17\mu\text{eV}$ . Under these results, our test machine was designed with  $g \sim 10^{-4}$  and  $H \cdot l = 120Oe \cdot m$ . It is shown by the photograph (see Fig.5). In the case of  $(\text{burst} - \text{width}) \sim 1000\mu\text{sec}$  (JHP) and  $H \cdot l = 120Oe \cdot m$ , one can observe the clear oscillation only in the range  $\epsilon < 3\mu\text{eV}$ . These results indicate that the TOF-NSE spectrum is much affected by the burst-width and can give correct information on  $S(\epsilon)$  only in very small range. If one constructs TOF-NSE under the wide burst-width, the complete determination of many parameters mentioned above and the precise data correction will be necessary.

## References

1. F. Mezei, Z. Physik 255 (1976) 146.
2. F. Mezei, Nucl. Instru. Methods 164 (1979) 153.

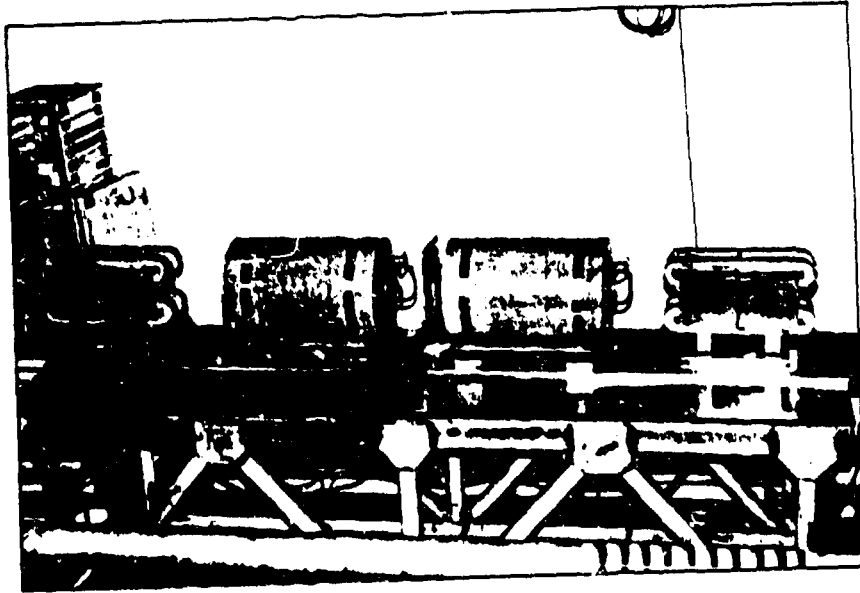


Fig. 5 Photograph of the test machine.

## Optimal Larmor precession magnets: application to neutron spin echo

*C. M. E. Zeyen*

Institut Laue Langevin BP 156 F-38042 Grenoble-Cedex  
FRANCE

*P. C. Rem, R. A. Hartmann, H. H. J. ten Kate and L. J. M. van de Klundert*

University of Twente, Faculty of Applied Physics

P. O. Box 217 NL-7500 Ae Enschede

THE NETHERLANDS

**ABSTRACT:** Resolution characteristics of neutron spectrometers using Larmor precession of the neutron spin are presently limited by magnetic field homogeneities of a special type. The line integral of the modulus of the magnetic induction  $\int^L |B| dl$  along a neutron trajectory of length  $L$  is a measure of the amount of precession performed by the neutron. Hence, it should be precisely the same for all neutrons of the same energy in a diverging beam. We present an analytical solution to the variational problem  $\int^L |B| dl = \text{constant}$  for the case of cylindrical magnets coaxial to the beam axis. This solution describes the best irrotational field shape along the beam axis  $z$ . The optimal homogeneity is significantly better than for a simple solenoid of comparable dimensions. Improved neutron economy can be achieved because our magnets can be made much shorter than solenoids. For realistic lengths  $L$  and beam radii  $r$ , it is, however, not good enough for high-resolution spectroscopy. Therefore, we studied a way to correct both for the residual inhomogeneities of cylinder magnets and the line-integral variations caused by pathlength differences, which result from finite angular beam divergence. Such corrections can only be done by introducing current distributions in the beam. Their optimal distributions can also be calculated analytically, and we present a way of implementing them in practice. In addition, we discuss the application of the same correction technique to other magnets, demonstrating that it is useful in general for cylinder-symmetric magnets such as solenoids. With magnets designed and corrected this way, the Larmor phase angle is a unique measure of the neutron energy and the resolution of spectroscopic methods using Larmor precession, such as LPS, which allows spectrum determination before or after scattering, or more sophisticated techniques, such as NSE and NMS\*, for example, is not influenced by corrections or other limitations caused by imperfect magnets. With the two novel concepts of optimal magnets (OFS) and pathlength corrections described here, the resolution properties of Larmor precession techniques can be pushed to their intrinsic limits. As further results of the correction technique introduced here, wider angular divergencies can be used, resulting in substantially improved neutron economy.

\*Spectroscopy techniques using Larmor precession (LPS) are:

NSE: neutron spin echo, NSM: neutron spectral modulation and just LPS.





**Acknowledgements**

Work supported by NATO Grant 86/0217



## Soller collimators for small angle neutron scattering

*R. K. Crawford, J. E. Epperson, and P. Thiyagarajan*  
Argonne National Laboratory  
Argonne, Illinois  
USA

### The collimation system at the IPNS small angle diffractometer

Small angle diffractometers at pulsed sources need to have fairly short flight paths if they are to make use of the long-wavelength portion of the spectrum without encountering problems from frame overlap or sacrificing intensity with band-limiting or pulse-removing choppers. With such short flight paths, achieving the necessary angular collimation in the incident beam while utilizing the full source size (~10 cm diameter) and a reasonable sample size (~1 cm diameter) requires the use of converging multiple-aperture collimation<sup>(1)</sup>. If the collimation channels are all focussed to the same point on the detector, then the large sample size will not affect  $Q_{\min}$  or the Q-resolution<sup>(2)</sup>, even if the sample-to-detector distance is short. The Small Angle Diffractometer (SAD) at IPNS uses crossed-converging soller collimators to provide focussing multiple-aperture collimation having ~400 converging beam channels with essentially no "dead" space between them. This entire collimator system occupies a distance of only ~60 cm along the incident flight path, while providing angular collimation of 0.003 radians FWHM. These collimators are shown schematically in Fig. 1. The dimensions for the SAD upstream collimator are  $L_c = 32.8$  cm,  $d_1 = 0.974$  mm,  $d_2 = 0.851$  mm, while for the SAD downstream collimator  $L_c = 25.0$  cm,  $d_1 = 0.844$  mm,  $d_2 = 0.750$  mm. Each of these collimators has 20 blades defining 21 horizontal or vertical channels.

These collimators use blades of stretched mylar coated with  $^{10}\text{B}$  in a suitable binder<sup>(3)</sup>, and are commercially available (Cidic, Ltd., Cheltenham, England). For the initial set of such collimators provided to IPNS for SAD, the coating was brushed on in a layer ~10 microns thick on each side of the mylar. This set of collimators had adequate absorbing power to define the beam quite cleanly at the calculated geometrical limits when using 1 Å neutrons. However, at longer wavelengths "wings" began to appear on the transmission pattern, resulting in appreciable intensity appearing at the detector well outside the geometrical beam penumbra. Figure 2 shows a typical pattern of these "wings", with no sample or other scatterer in the beam, and Fig. 3 shows how the total "wing" intensity outside the beamstop (which was slightly larger than the geometrical beam penumbra) varied with wavelength. Note that even in the worst case, the "wing" intensity was only  $\sim 3 \times 10^{-5}$  of the main beam intensity, so although this collimator-produced background was large enough to be easily seen on the SAD and to interfere with the lowest Q data from weakly-scattering samples, this was really a very small effect.

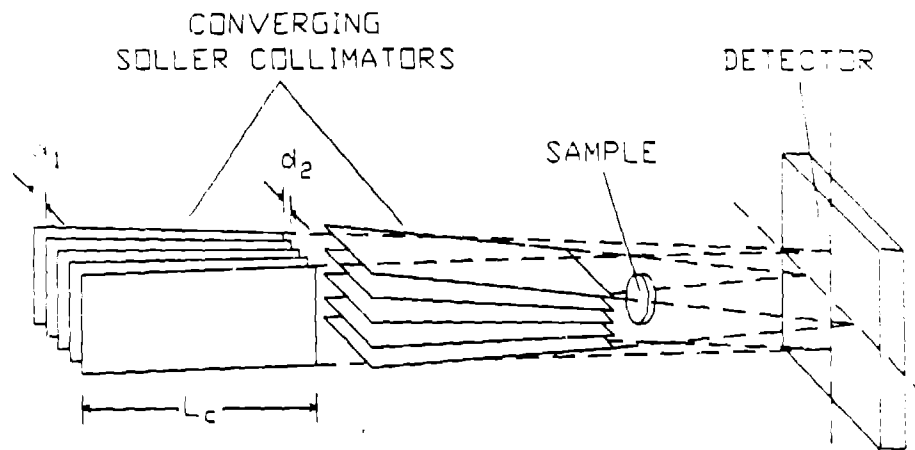


Fig. 1 Schematic representation of a crossed converging soller collimator system.

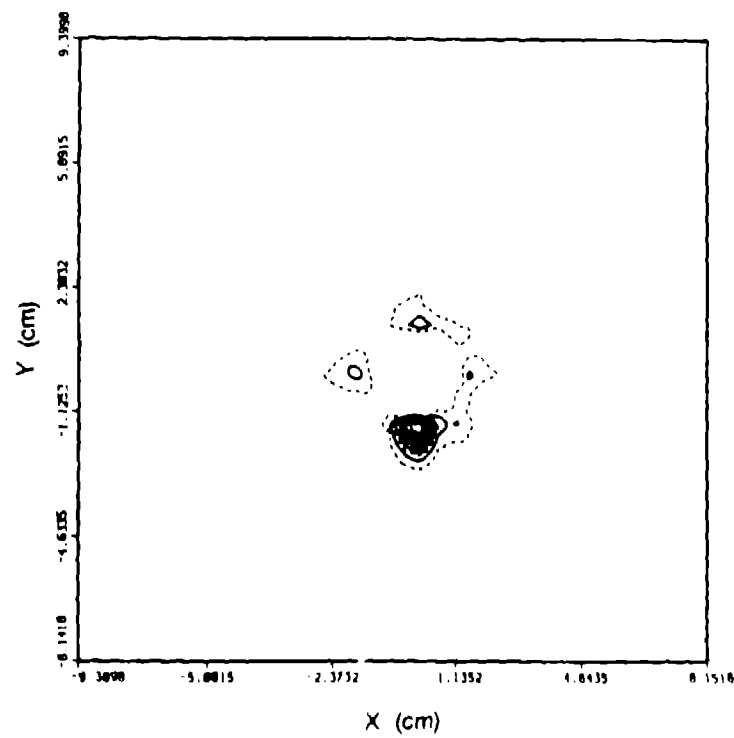


Fig. 2 Contour plot of total empty-beam background intensity on the SAD detector, showing the background "wings" observed about the main transmitted beam. The main beam has been absorbed by a beamstop and so is not seen in this figure.

### Reflectivities of absorbing materials

The wavelength dependence exhibited in Fig. 3 suggested that this "wing" phenomena was probably due to reflections from the collimator blades. The reflectivity  $R$  of a flat surface of homogeneous material is given by<sup>(4)</sup>

$$R = \left| \frac{1 - \sqrt{(n^2 - \cos^2\theta)/\sin^2\theta}}{1 + \sqrt{(n^2 - \cos^2\theta)/\sin^2\theta}} \right| \quad (1)$$

Where  $\theta$  is the angle of incidence, and the complex index of refraction  $n$  can be written as

$$n^2 = n_r^2 - n_i^2 + i2n_r n_i \approx 1 - \frac{N\lambda^2}{\pi} \bar{b}_r + i \frac{N\lambda^2}{\pi} \bar{b}_i \quad (2)$$

where  $\bar{b}_r$  and  $\bar{b}_i$  are the average real and imaginary components of the scattering length for the material, and  $N$  is the number density of the material. Applying Eq. 2 to Eq. 1 and assuming that  $\theta$  is small leads to

$$R = \frac{1 - 2 \left[ (E + \sqrt{E^2 + F^2})/2 \right]^{1/2} + \sqrt{E^2 + F^2}}{1 + 2 \left[ (E + \sqrt{E^2 + F^2})/2 \right]^{1/2} + \sqrt{E^2 + F^2}} \quad (3)$$

with

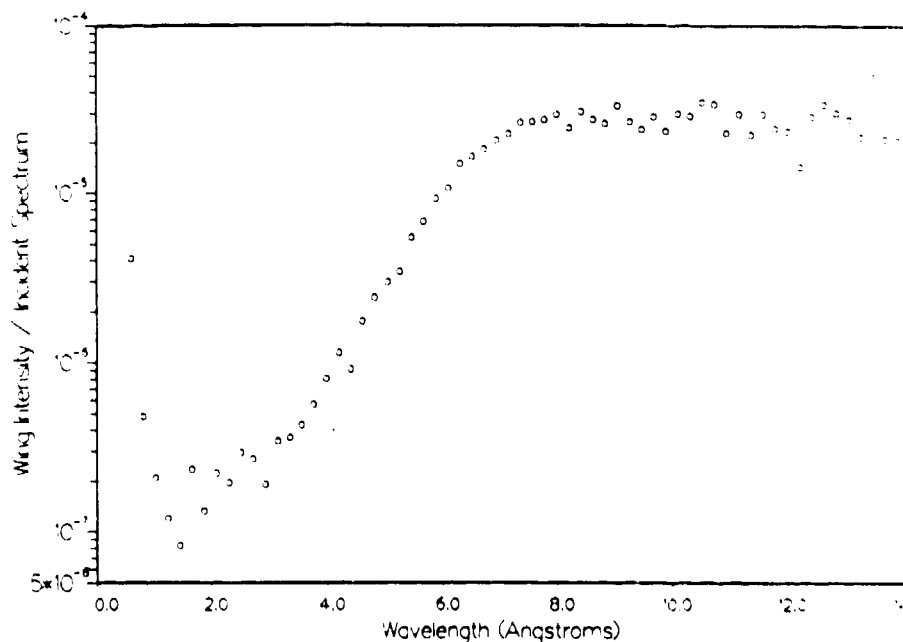
$$E = \frac{N\lambda^2}{\pi \sin^2\theta} \bar{b}_r \quad (4)$$

$$F = \frac{N\lambda^2}{\pi \sin^2\theta} \bar{b}_i \quad (5)$$

The "critical angle"  $\theta_c$  is the angle which makes  $E = 0$ .

$$\sin^2\theta_c = \frac{N\lambda^2}{\pi} \bar{b}_r \quad (6)$$

In the case where  $F = 0$  (no absorption),  $R = 1$  for angles less than  $\theta_c$ , and total reflection occurs. If  $\bar{b}_r < 0$ ,  $\theta_c$  is not defined and total reflection does not occur. However, the reflectivity always approaches 1 as  $\theta$  approaches 0 or  $\lambda$  approaches  $\infty$ , so it can still be substantial at small angles or large wavelengths.



**Fig.3** Observed ratio of collimator-produced "wing" background to main beam intensity for the original SAD soller collimators.

Figure 4 shows the minimum reflectivity which results from varying  $E$  at constant  $F$ , as a function of  $F$ . Two features can be noted: (1) very small reflectivities can only be obtained for  $F$  near 0, and hence for small values of  $\bar{\sigma}_i$  (implying small total cross-section) and/or small wavelengths and/or large angles. This means that within the framework of this theory, namely treatment of the medium as homogeneous and ignoring resonance effects, every good absorber is also at least a fairly good reflector at small angles and/or large wavelengths. (2) For any given  $F$  there is an optimum value for  $E$ , and hence for any given  $\bar{\sigma}_i$  there is an optimum value  $\bar{\sigma}_r$ , which will minimize the reflectivity. Thus there is some room for optimization by changing the material constituents to vary  $\bar{\sigma}_r$  even when  $\bar{\sigma}_i$  must remain large and fixed (as is the case when a material of a certain total absorption is required, but it is desired that this material have as low reflectivity as possible).

A large value for the absorption cross-section leads to a large magnitude for  $\bar{\sigma}_i$ , and hence to a large value for  $F$ , giving a relatively large reflectivity. Thus it is desirable to have a value for  $\bar{\sigma}_i$  no larger than necessary, as determined by the total absorption required. The best that could be done to minimize the reflectivity (within the framework of this homogeneous model) for the SAD collimators, while still providing adequate absorption, would be to coat them with a material having the approximate parameters

$$N\bar{b}_r \sim -1.4 \times 10^9 \text{ cm}^{-2} \quad (7)$$

$$N\bar{b}_i \sim -(2.8) \times 10^8 \text{ cm}^{-2} \quad (8)$$

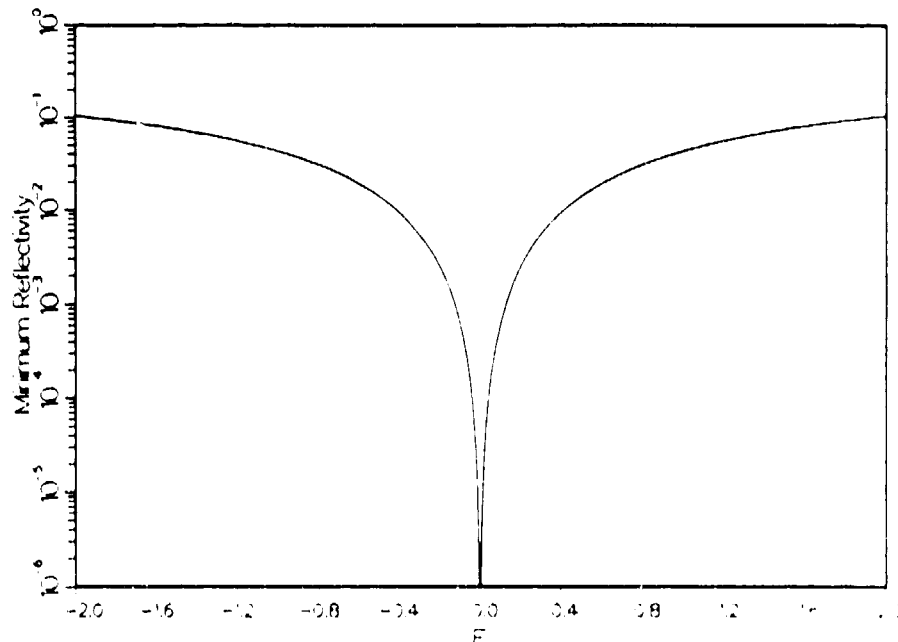


Fig. 4 Minimum reflectivity resulting from varying E (related to the real component of the scattering length - see text) at constant F (related to the imaginary component of the scattering length - see text) as a function of F.

#### Monte Carlo simulation of Soller collimators

The Monte Carlo simulation program SOLLER was written to simulate the transmission of neutrons through a converging or straight soller collimator. The program simulates just one channel of such a collimator, and treats the problem in two dimensions only. The blade surfaces were simulated by randomly chosen connected straight line segments. Because it was found that a few individual facets which were properly oriented for reflection could cause pronounced features in the pattern observed on the detector, new surfaces were generated several times during the simulation so that the results were averaged over different sets of surfaces. Both reflection probabilities, given by Eq. 3, and scattering probabilities were considered whenever a neutron path intersected one of these surfaces.

The downstream SAD collimator was simulated using the dimensions given above, and with the material parameters

$$b_r = -0.0221 \times 10^{-12} \text{ cm},$$

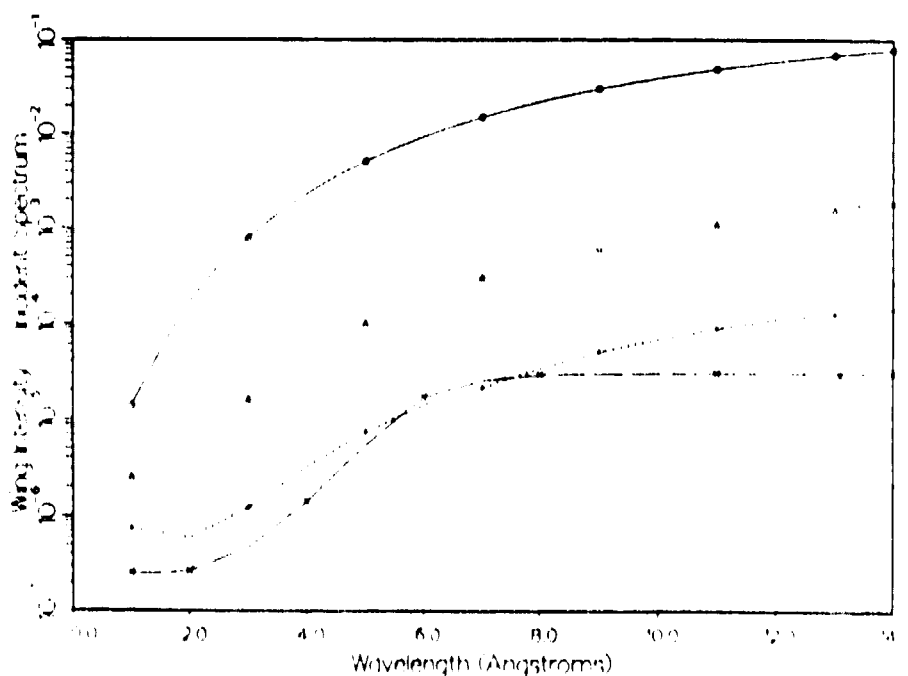
$$b_i = (-0.0556 - 0.0441/\lambda) \times 10^{-12} \text{ cm},$$

$$\sigma_{inc} = 26.73 \text{ barns, and}$$

$$N = 1.222 \times 10^{23} \text{ per cm}^3.$$

(These parameters were derived on the assumption of a 50-50 (by volume) mixture of  $^{10}\text{B}$  and  $\text{CH}_2$ , the latter simulating the binder.) A smooth surface and two different rough surfaces were simulated. For the rough surfaces the ends of the surface segments were allowed to vary  $\pm 0.02$  mm from the nominal surface line, and the mean surface segment lengths were set to 0.2 mm (0.1 rough) and 0.04 mm (0.5 rough) respectively (the second case being the "rougher" surface, with the rms angular variation of surface segments in the second being 5 times that in the first). A "roughness" value is defined here as the ratio of maximum segment end displacement to mean segment length.

Figure 5 shows the ratios of the calculated "wing" probabilities to the main beam probabilities as functions of wavelength for each of these three surface roughness cases. For wavelengths  $> 2 \text{ \AA}$ , the collimator-produced background was due almost entirely to reflection from the blade surface facets, while for wavelengths  $< 2 \text{ \AA}$  incoherent scattering from the blade surfaces began to dominate. Also shown in Fig. 5 are the ratio of "wing" events to main beam events observed for the real SAD collimator. The 0.5 rough surface produced an absolute magnitude and a shape versus  $\lambda$  for the "wing" background very similar to that experimentally observed at SAD. (Simulated segment sizes in the 0.5 rough case approached realistic physical dimensions, with a  $40\mu$  average length and a  $\pm 20\mu$  maximum end displacement.)



**Fig. 5** Monte Carlo simulation of collimator-produced "wing" background with different blade surface roughnesses and different material parameters. Solid - smooth blade surface; dotted - 0.1 rough blade surface; dashed - 0.5 rough blade surface; chain - dot - observed behavior for the original SAD collimators, taken from Fig. 3.

The "wing" background fraction was also calculated using the SOLLER program for a 0.1 rough surface with the "optimized" parameters of Eqs. 7 and 8. A factor of 10 - 20 decrease in this background fraction, relative to that calculated above for the same roughness with the 50 - 50 mixture, was obtained by the use of the optimized materials, but small shifts ( $\pm 0.004 \times 10^{-12}$  cm) in  $\bar{b}$ , from the optimum value resulted in a factor of  $\sim 2$  increase in the calculated collimator-produced background. Thus although significant gains can be achieved by optimizing the material parameters, these parameters must be adjusted quite closed to the optimum values in order for these gains to be realized.

As can be seen in Fig. 5, surface roughness had a pronounced effect on the number of neutrons reflected out of the beam by the collimators. A decrease in "roughness" from 0.5 to 0.1 resulted in more than a factor of 10 increase in the "wing" background fraction, and the further decrease in roughness from 0.1 to 0.0 (smooth) increased this fraction by another factor of  $\sim 50$ . However, there was very little change in the wavelength dependence of these fractions except for  $\lambda \leq 2 \text{ \AA}$ , where the incoherent scattering starts to dominate the results.

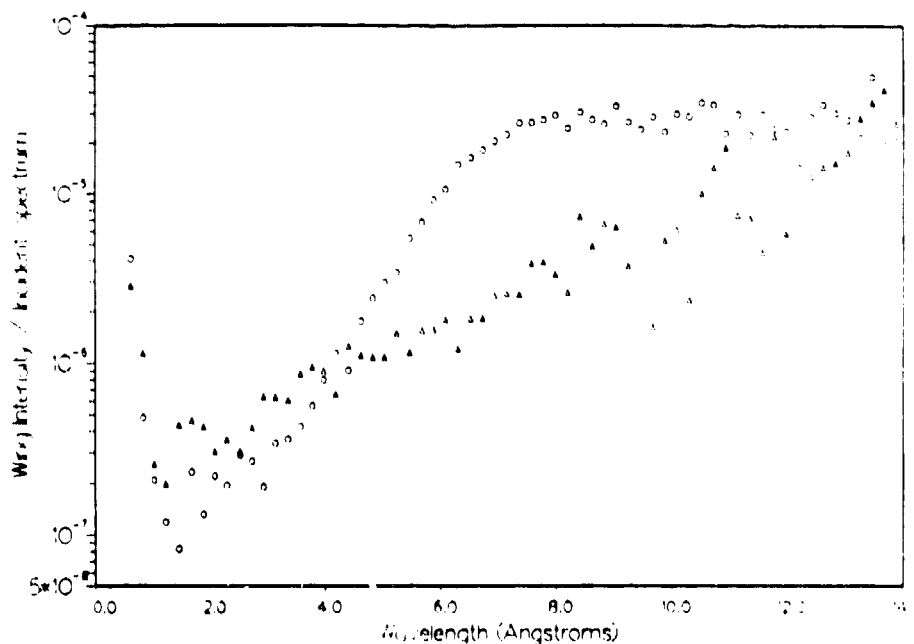
### New collimators

Based on the results of the Monte Carlo simulations and on the considerations of reflectivities of practical absorbing materials, it was concluded that significant improvements in soller collimator performance would be easier to achieve by improving the surface roughness, rather than by optimizing the absorbing coatings to minimize reflectivity. Fortunately, in the interim Cidic had developed a method for applying "matte" coatings, rather than the original brushed coatings, of the  $^{10}\text{B}$ -plus-binder to the surfaces of their mylar collimator blades. Thus a second set of collimators was obtained, geometrically identical to the first SAD collimators, but this time with the boron applied in two matte-finish coatings on each surface. These new collimator blade surfaces appeared distinctly rougher, and had significantly less optical "shine" than did the originals when viewed at grazing incidence. These new collimators were installed on SAD in May, 1988, and were much improved over the originals. No "wings" could be observed at all, and the background over the remainder of the detector was reduced as well. Figure 6 compares the "wing" background (obtained by integrating over the same set of detector cells used for calculating the original "wing" intensities) observed with these new collimators to that produced by the originals. Further testing of these new collimators will occur in Fall, 1988, but it is already clear that the rough surface has resulted in a significant improvement beam quality with no measurable reduction in main-beam intensity.

### Summary

The neutron beam transmitted through the soller collimators on the SAD instrument at IPNS showed "wings" about the main beam. These "wings" were quite weak, but were sufficient to interfere with the low-Q scattering data. General considerations of the theory of reflection from homogeneous absorbing media, combined with the results from a Monte Carlo simulation, suggested that these "wings" were due to specular reflection of neutrons from the absorbing material on the surfaces of the collimator blades. The simulations showed that "roughness" of the surface was extremely important, with "wing" background variations of three orders of magnitude





**Fig. 6** Measured ratio of collimator-produced "wing" background to main beam intensity (triangles) for the new "rough-surface" SAD collimators. The observed behavior (circles) of the original SAD collimators is shown for comparison.

being observed with the range of roughness values used in the simulations.

Based on the results of these simulations, new collimators for SAD were produced with a much rougher <sup>10</sup>B-binder surface coating on the blades. These new collimators were determined to be significantly better than the original SAD collimators. This work suggests that any soler collimators designed for use with long wavelengths should be fabricated with such a rough surface coating, in order to eliminate (or at least minimize) the undesirable reflection effects which otherwise seem certain to occur.

#### **Acknowledgements**

This work was supported by the U.S. Department of Energy, BES, contract No. W-31-109-ENG-38.

#### **References**

1. R. K. Crawford and J. M. Carpenter, 1988, *J. Appl. Cryst.*, in press.
2. A. C. Nunes, 1974, *Nucl. Instrum. Methods* **119**, 219-293.
3. C. J. Carlile, J. Penfold, and W. G. Williams, 1978, *J. Phys. E: Sci. Instrum.* **11**, 837-838.
4. G. E. Bacon, 1975, *Neutron Diffraction, Third Edition*, Clarendon Press.

## GLAD: the IPNS Glass, Liquid, and Amorphous Materials Diffractometer

*R. K. Crawford, D. L. Price, J. R. Haumann, R. Kleb, D. G. Montague,  
J. M. Carpenter, S. Susman and R. J. Dejus*  
Argonne National Laboratory  
Argonne, IL  
USA

### Introduction

A number of years of experience in diffraction from amorphous materials has now been accumulated at various pulsed neutron sources. Workshops at IPNS and elsewhere have distilled some of this experience to provide a set of criteria for a new diffractometer dedicated to and optimized for structural studies of amorphous materials. These criteria include:

1. All Q values should be measured with as short wavelengths and small scattering angles as possible to minimize both inelasticity and attenuation corrections for highly absorbing samples. The workshops suggested that a wavelength range of  $\sim 0.2 - 2 \text{ \AA}$  would be appropriate. A large solid-angle detector at small scattering angles is required to make an efficient instrument under these conditions.
2. Wavelength and angle information should be kept separate (no time-focusing) until wavelength-dependent corrections have been made.
3. The instrument should provide a high incident flux and a large scattered solid-angle coverage so that reasonable data rates can be achieved with small samples and a rapid turnaround time is possible with larger samples.
4. Resolution should be adequate for the problems but no greater than necessary to keep the data rates as high as possible. The workshops suggested that resolutions ranging from  $\Delta Q = 0.005 \text{ \AA}^{-1}$  at  $Q = 0.05 \text{ \AA}^{-1}$  to  $\Delta Q = 0.15 \text{ \AA}^{-1}$  at  $Q = 20 \text{ \AA}^{-1}$  would be appropriate. The implications of these resolution requirements are discussed further below.

This paper discusses the instrument GLAD (Glass, Liquid, and Amorphous Materials Diffractometer) which has been designed to meet these criteria and is now being built at IPNS. This instrument involves the use of relatively short-wavelength neutrons and a sophisticated neutron detection and acquisition system. A preliminary, simplified version of the instrument has been constructed while the final version is still under design, in order to develop the data acquisition and analysis techniques and to develop methods for collection of data with adequate quality (low background) at short wavelengths. This paper will briefly outline the final instrument envisioned and its calculated performance, but will focus mostly on the details of the detection/acquisition system and the calibration and data collection procedures which have been developed. The brief operating experience which has been gained to date with the preliminary instrument version will also be summarized.

#### Conceptual Design and Projected Performance

The design criteria noted above have led directly to several features of GLAD. In particular, the incident flight path should be short to provide high intensities. Angular considerations rather than wavelength uncertainties dominate the resolution at the small scattering angles of interest here, so the incident path can be as short as is permitted by the space constraints at IPNS. Soller collimators can be used to provide the necessary angular resolution for the incident beam, so a relatively large sample size and the full moderator size can be utilized with no loss in resolution.

Figure 1 shows a sketch of the final version of GLAD as currently conceived. This instrument will have a 9.0 m incident flight path (the minimum value consistent with spatial constraints on the beamline chosen at IPNS), and a 3.0 m "diameter" scattered flight path. Two sample positions are provided. The 9-meter "high-resolution" position is located where the beam enters the scattered flight path, and the "high-intensity" position is located 1.5 m further downstream at the center of the scattered flight path. Converging soller collimators, focused at the point where the beam exits the scattered flight path (3.0 m from the high-resolution sample position), provide incident beam collimation of 0.007 rad FWHM in the horizontal and vertical directions. The circular detector locus then eliminates the sample size as a factor in the resolution when the sample is located at the high resolution position.<sup>1</sup> At the high intensity position this focusing is still effective for small scattering angles, but is ineffective at the higher scattering angles. However, using this sample position places the sample much closer to the detectors and hence provides a much greater solid angle for detection of the scattered neutrons - thus the name "high-intensity". As shown in the figure, the detector positions

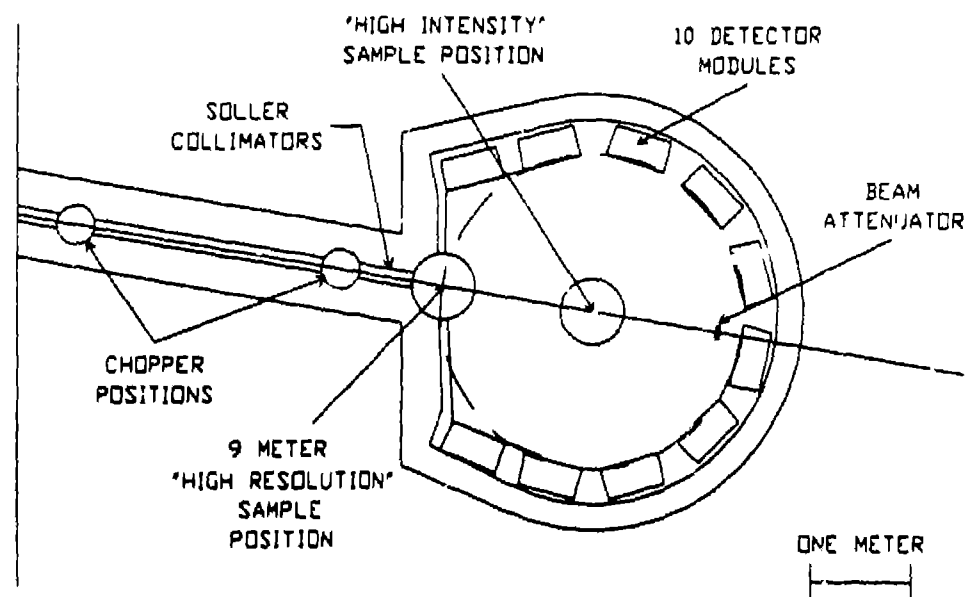
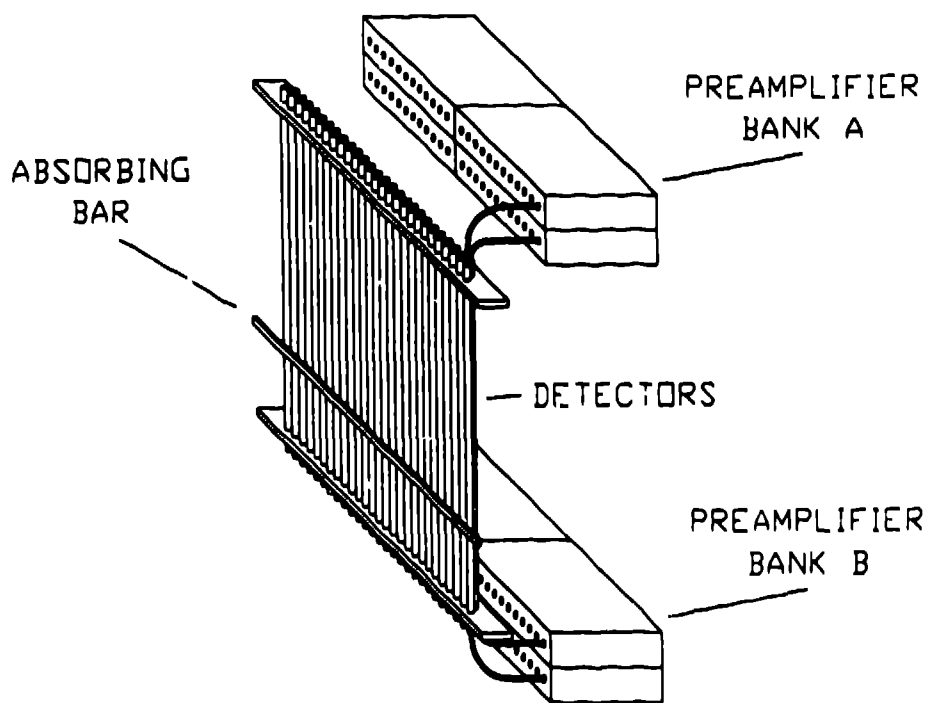


Fig. 1 Plan view of the GLAD instrument.

nearest the high-resolution sample position deviate somewhat from the circular locus, reducing the detector size contributions to the resolution to acceptable values.

With this flight path configuration the desired resolution can be achieved (for the high-resolution position) by using detectors which are  $\sim 1$  cm in diameter. At small scattering angles the spatial resolution along the axes of the detectors must be of comparable magnitude, so position-sensitive detectors must be used. Two-dimensional proportional counters suffer from data rate limitations, so we have chosen to use cylindrical linear position-sensitive detectors (PSD). The position encoding scheme used for these detectors is discussed below. The detectors are located in a controlled atmosphere, outside the scattered-flight-path vacuum and separated from the vacuum by thin Al windows. The detectors are mounted with their axes normal to and centered on the scattering plane, in "modules" which each contain  $\sim 40$ -60 detectors and a mechanism for providing absolute position calibration. This position-calibration mechanism consists of a neutron-absorbing bar which can be driven to various known positions in front of the detectors by a stepping-motor system. Individual detector positions within each module are chosen to provide as nearly continuous angular coverage as possible while preventing "shadowing" by adjacent detectors when either sample position is used. As shown in Fig. 1, the locations of the detector modules are not symmetrical about the incident

beam, so that detectors on one side will cover the gaps in angular range on the other side necessitated by the flight path structural components and detector calibration mechanisms. Figure 2 shows a typical mounting arrangement for the detectors, preamplifiers, and detector calibration mechanism in one detector module. A beam "attenuator" upstream from the flight path exit window absorbs most of the direct beam before it reaches the detectors, allowing the PSD bank to operate in the forward-scattering direction.



**Fig. 2** Schematic representation of the detector module intended for the forward scattering direction, showing detectors, preamplifiers, and the absorbing bar for position calibration. Modules for other scattering angles are similar, although detector shadowing considerations lead to location of detectors in a single row, rather than the staggered double row shown here, for most of the higher-angle modules. For clarity, only two of the sets of coaxial cables between the detectors and preamplifiers are shown, and the drive mechanism for the absorbing bar is omitted from the drawing.

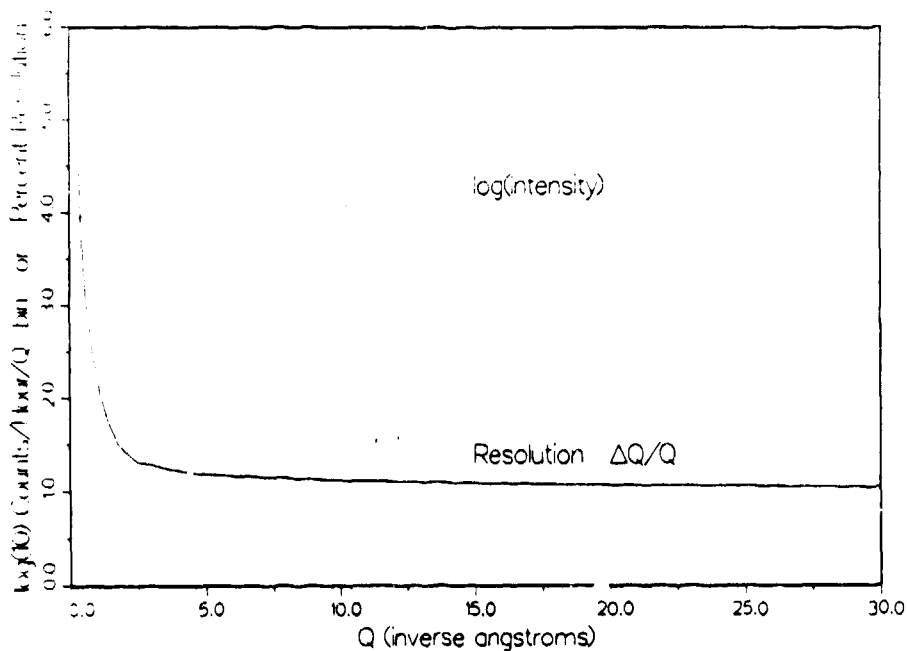
The scattered flight path will be evacuated, and in cases where sample environment is not of particular importance, samples can be mounted directly in the flight path vacuum with no other windows to contribute to the scattering. When sample environment must be controlled, as for cryostats or furnaces, a thin-windowed "well" can be used to separate the sample environment from the flight path vacuum.

As can be seen in Fig. 1, the incident beamline includes provisions for the installation of Fermi choppers when desired. Since the use of a chopper will drastically reduce the overall data rate, this is not expected to be the normal operating mode. However this capability will allow the collection of elastic-scattering rather than total-scattering data when required for specific problems. It is also possible that a second, somewhat different chopper may be needed in the incident beam to suppress background originating from the prompt pulse or from scattering in the main chopper, so two different chopper locations have been provided.

Figure 3 shows the calculated performance for this instrument. These data are based on Monte Carlo simulations which trace neutron paths from the moderator, through the collimators and sample, and into the detectors. The results presented here include effects of the Soller collimators. The simulations predict values of resolution which are nearly equal for each detector position-element with the same Q-value, independent of the scattering angle and the vertical position on the detector. The resolution  $\Delta Q/Q$  shown in Fig. 3 is in line with the resolution goals stated above. For low values of Q,  $\Delta Q/Q$  increases rapidly as Q decreases, while it reaches a nearly constant value slightly larger than 1% for Q greater than  $5 \text{ \AA}^{-1}$ . These results were calculated by summing, with equal weight, all detector elements contributing to the same range of Q. The resolution for the individual detector elements is somewhat better, but since the angular coverage for each element is slightly different, the summing process degrades the resolution. Estimates of count rate are based on measurements done on the Special Purpose Powder Diffractometer (SEPD) at IPNS. This estimate of intensity is the sum of all elements with the same average Q-value, assuming ~ 450 detectors in the 10 modules as shown, and corresponds to the composite resolution  $\Delta Q/Q$  shown in the lower curve in Fig. 3.

#### Temporary Flightpath

Because of the long lead time required for design and procurement of the vacuum flight path for this instrument, it was decided to begin with a temporary flight path while the final unit is still under design. This will

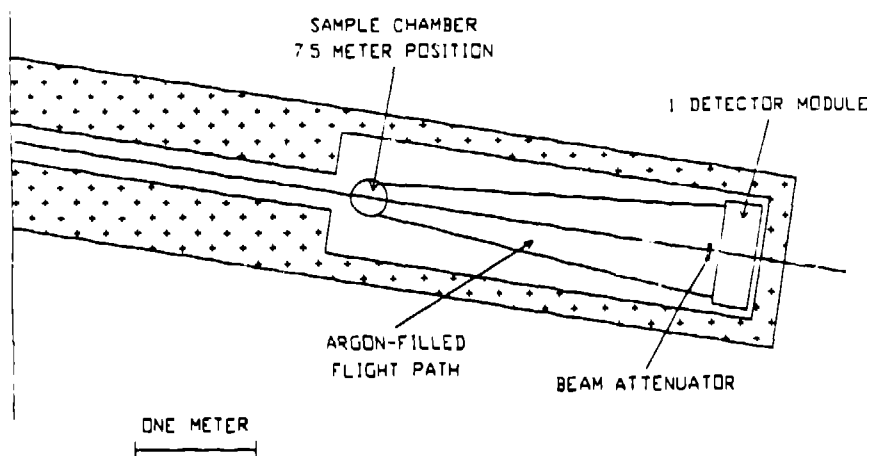


**Fig. 3** Calculated resolution (FWHM) and intensity for GLAD. The calculated values are based on a 1 cm square x 1 mm thick vanadium sample at the high-resolution sample position, and are for an instrument geometry and detector locations approximately as shown in Fig. 1.

enable us to gain experience in the use of the rather complicated detector/data-acquisition system envisioned, to begin work on reducing the backgrounds at short wavelengths, and to develop methods for handling and analyzing data sets of the expected magnitude (see below for projections). The temporary flight path is shown schematically in Fig. 4. This path allows the use of one complete detector module with 55 detectors, as shown in Fig. 2, providing scattering angles up to  $\pm 9^\circ$ . An evacuable chamber is provided so that samples can be in cryogenic or other environments, but the scattered flight path is Ar-filled rather than evacuated. To increase intensities, the incident flight path for this temporary version was chosen to be 7.5 m rather than the 5 m planned for the final instrument. Otherwise, the temporary version provides a reasonably good simulation of the planned final unit.

#### Detectors and Position Encoding

The position-sensitive detectors selected are 1.27 cm dia x 60 cm active length  $^3\text{He}$ -filled gas proportional counters, containing 10 atm of  $^3\text{He}$  plus



**Fig. 4** Temporary GLAD flight path used to gain experience while the flight path shown in Fig. 1 is being fabricated.

additional stopping and quench gases. The resolution specifications require that these detectors be capable of  $\sim 1$  cm resolution along their length, which is compatible with encoding each detector into 64 segments. The intrinsic detector resolution due to the stopping range of the fill gas is  $\sim 0.5$  cm, and the contribution due to the noise in the encoding electronics should be kept to a comparable amount to ensure the desired overall resolution.

The charge-division method is used for position encoding. The neutron detection process starts with the absorption of a neutron at a distance  $x$  from end A of the detector. The absorption reaction is



The resulting proton and triton ionize the stopping-gas molecules, depositing the 765 keV of kinetic energy within a short distance ( $\sim 0.5$  cm) of the initial absorption. Gas amplification from the proportional mode operation then leads to a sizable charge being deposited on the anode at position  $x'$ , which is the projection of the center of the ionization cloud produced by the proton and triton and so may differ from  $x$  (by at most  $\sim 0.5$  cm for this fill-gas mixture). If  $V_A$  and  $V_B$  are respectively the peak voltages output by the charge-sensitive preamplifiers at ends A and B of the detector of length  $L$ , then the encoded quantity is

$$\frac{x'}{L} = \frac{V_B}{V_A + V_B} \quad (2)$$



### Data Acquisition Requirements

Based on the final instrument design and the source flux available at IPNS with the new multiplying target, it was estimated that the data acquisition system must meet the following criteria:

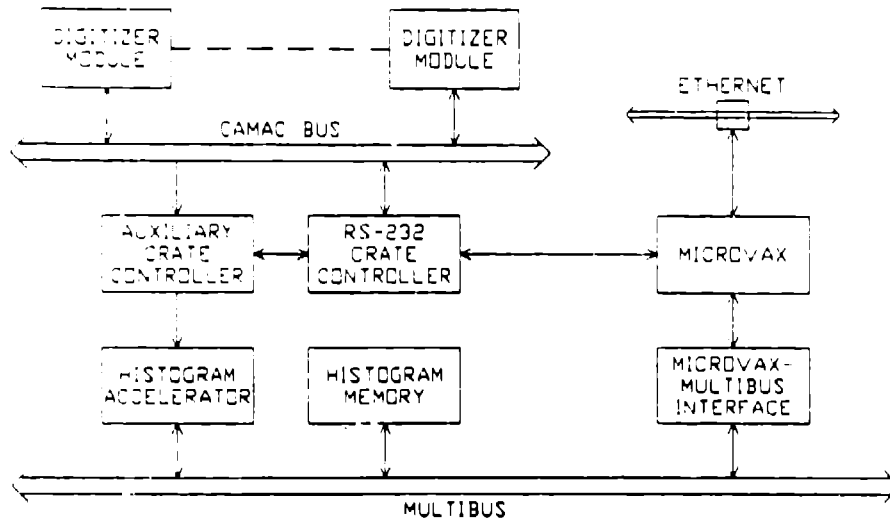
Maximum instantaneous data rate per detector	- $5 \times 10^4$ n/sec/det
Maximum time-averaged data rate per detector	- $1 \times 10^3$ n/sec/det
Maximum number of detector elements	- 450 detectors
64 elements/detector	- 29,000 elements
Maximum total time-averaged data rate	- $4.5 \times 10^5$ n/sec
Maximum number of time-channels per detector element	- 1000 channels
Histogram memory per channel	2 or 4 bytes
Maximum histogram memory required with no grouping	
- $29 \times 10^6$ channels	- 60-120 Mbytes

The last result implies that the data acquisition system must group on the average of at least - 10 elements per channel on the fly in order to reduce the single-histogram size to a manageable value of - 10 Mbytes or less. Strategies for accomplishing this are discussed below.

### Data Acquisition

To handle the high instantaneous and time-averaged data rates expected for GLAD, we have developed a new FAST Data Acquisition System (FASTDAS) for use at IPNS. This system is capable of histogramming data in a fashion similar to the present microprocessor-based data acquisition systems in use at IPNS, but can build the histograms at a 300 kHz rate and can handle up to 65,536 detector elements. If higher rates prove necessary, multiple FASTDAS systems can be used.

An overview of the system is sketched in Fig. 5, and individual components are shown schematically in Figs. 6-8. This system is made up of Camac digitizer modules (1 for each 4 position-sensitive detectors or 1 for each 8 standard detectors), a special Camac auxiliary crate controller module, a custom designed Histogram Accelerator Multibus board coupled to a Multibus memory array, and a microVax computer also coupled to the Multibus and to a

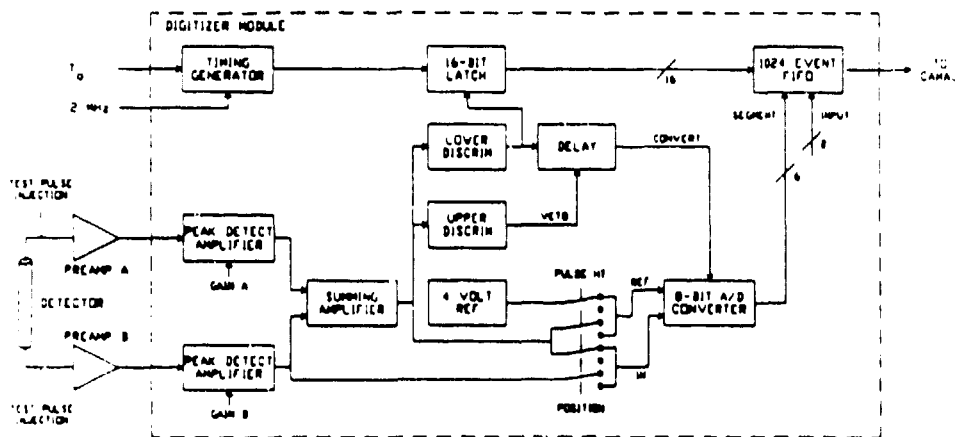


**Fig. 5** Block diagram of the GLAD data acquisition system.

Camac crate controller. The microVax computer is also attached to an Ethernet network allowing data files to be sent to other computer systems for analysis.

#### Camac Digitizer Modules

The Camac digitizer modules (Fig. 6) are custom designed for the particular detectors being used and use a standard Camac interface design. The position-sensitive-detector modules currently in use with FASTDAS can each encode four separate detectors concurrently. "Flash" analog-to-digital converter chips are used to provide rapid encoding. The precision limits of available converters (0.5 bit in 8 bits) result in roughly a 10 percent variation in the encoded position-channel widths, but this does not pose a serious problem and is accounted for in the calibration process. These modules contain built in first in-first out (FIFO) event buffers with depths of 1024 events, each event made up of 8 bits of detector element ID (encoding 64 positions along each of four detectors) and 16 bits of time information. When an event is stored in the module FIFO the look-at-me (LAM) signal for that module is raised to indicate that that module requires service. The encoding of an event by one of these PSD modules occupies only the detector producing the event and the chain of encoding electronics ("encoding path") associated with that detector, and requires a deadtime on that encoding path of 10  $\mu$ sec. Thus each detector is completely independent as far as deadtime is concerned, and that coupled with this fast encoding means that the system can handle quite high instantaneous



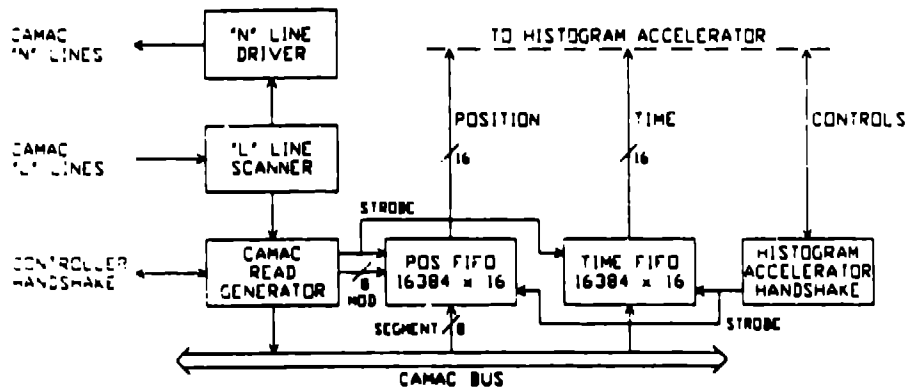
**Fig. 6** Schematic representation of the position encoding for one PSD at GLAD, including the detector, preamplifiers, and one of four encoding-paths in a PSD digitizing module. Also shown are the points at which test pulses from pulse generators can be injected for calibration purposes. The digitizer module also provides "offset" and "span" adjustments, but these have been omitted from the drawing for clarity.

data rates without significant deadtime losses. (The projected maximum instantaneous rate per detector of 50000 n/sec/det would lead to deadtime corrections of ~ 40 percent, which is not acceptable. This rate is expected to occur only in rare cases, and then only over a limited time range, but even so, some development efforts will be directed toward reducing this encoding deadtime.)

A useful feature of the PSD digitizing modules is a software-selectable option which allows them to collect data in a 64 channel pulse-height mode for each detector, rather than the usual 64 position mode. This feature greatly facilitates the initial adjustments of the PSD modules and the monitoring of the subsequent performance of individual detectors and encoding paths (see below).

#### Camac Auxiliary-Crate Controller

A specially designed auxiliary crate controller module (Fig. 7) has been built to scan the 20 digitizer modules within the crate at a 1.982 rate. When the controller finds a LAM set it transfers one data word from the digitizer module FIFO to its internal FIFO. This internal FIFO has a depth of 16.984 12 bit "events". In addition to the time and element ID from the module, the controller stores the crate and slot number of the module in its FIFO. Thus



**Fig. 7** Block diagram of the Camac auxiliary-crate-controller used with the FASTDAS system.

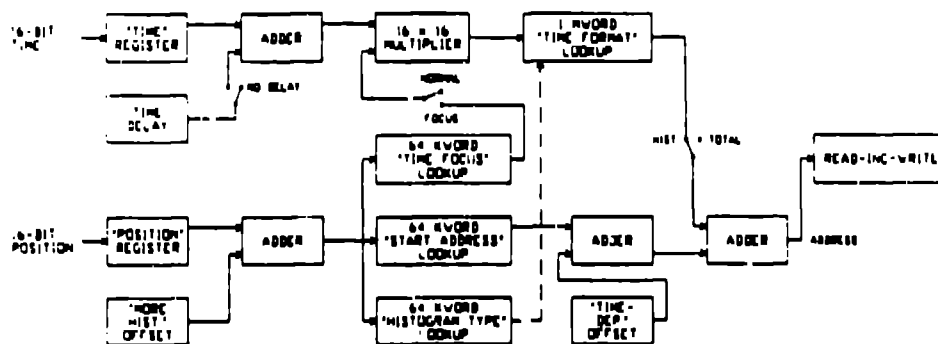
the controller FIFO contains 16 bits of ID and 16 bits of time for each event. A 32-bit event is supplied from the controller FIFO to the Histogram Accelerator when requested by the latter.

With each module being scanned every 20  $\mu$ sec the average data rate per Camac module is limited to 50 kHz or 1666 events per IPNS pulse. Since each module contains a 1024-event FIFO the peak data rate per module can be much higher, limited by the module and detector deadtime for a burst of at least 1024 events.

#### Histogram Accelerator

The FASTDAS Histogram Accelerator (Fig. 8) is a hardware device which contains fast RAM-based lookup tables, adders, and read-increment-write logic for the Multibus memory. This device is implemented on a single Multibus board. All RAM memory on this board is loadable from the microVax computer through the Multibus address space. Using the configuration shown in the block diagram the Histogram Accelerator can duplicate nearly all the features of the software-controlled histogramming system presently in operation at IPNS,<sup>2,3</sup> including multiple histogramming of each event, rapid switching between histograms for real-time measurements, flexible choice of time channels and detector element grouping, and on-the-fly time focusing. The focusing feature is not currently intended for use with GLAD, but has been designed in so the FASTDAS system can be used on other IPNS instruments, as well.

At the start of a histogramming cycle, the Histogram Accelerator requests a 32-bit event from the Camac auxiliary-crate-controller FIFO. The 16 bits of



**Fig. 8** Block diagram of the FASTDAS Histogram Accelerator. The focus and time-delay options are not intended for use with GLAD, but are included for compatibility with other IPNS instruments.

detector-element ID in this event address a 64 kword lookup table ("start address" table) which contains the "starting address" of the time histogram for that detector element. This "starting address" is the upper 16 bits of a 24-bit address, so each time histogram must start on a 256-byte boundary. The 16 bits of element ID also address a 64 kword lookup table ("histogram type" table) which is used to select different binning algorithms from the time-binning ("time format") table. This histogram type table also contains flags indicating whether data from this ID are to be binned, whether each event from this ID is to be binned in more than one histogram, and whether "on-the-fly time focusing" is to be applied to events from this ID.

The 16 bits of time data first has a constant added to it (contents of the "constant delay" register set to 0 for GLAD) and, if time focusing is enabled, is multiplied by a constant obtained from a 64 kword lookup table ("time focus" table) addressed by ID. This result is then used to address a lookup table ("time format" table) which contains the various binning algorithms, using 64 kwords per algorithm with a maximum possible 1 Mwords or 16 algorithms. Each algorithm in this table provides a channel offset number for each 16-bit "modified time value" input to it. A lookup value of zero in this table indicates that the time is out of range and therefore should not be histogrammed. This scheme provides complete flexibility in time binning, permitting conversion of the raw time information to varying numbers of channels per time histogram and different channel widths at different time values.

If the event is to be histogrammed, the address of the 32-bit totalizing counter (which is the time histogram starting address for this ID), is incremented first. Then the address calculated by adding the channel offset number obtained from the time format table is also incremented. A jumper

selectable option allows the histogramming to occur in either 16-bit channels or in 32-bit channels. In the 16-bit case, any overflows which occur because of these increments will be recorded in a FIFO (not yet implemented), and attached to the data set when it is read out by the microVax.

Once the Histogram Accelerator has completed all required histogramming for this event it immediately requests another event from the auxiliary-crate-controller FIFO, so the Histogram Accelerator is the controlling factor in the overall histogramming rate. The table lookups and memory incrementing are limited mainly by the Multibus access time and the memory cycle time of the Multibus memory used. With the current 400 nS cycle time memories, a time-averaged histogramming rate of over 300 kHz has been measured. This is already close to the estimated maximum rate of 450 kHz for GLAD, and so should be adequate for some time to come. (Two such systems could be used to double the histogramming rate if necessary.) The Histogram Accelerator has the capability of multiplexing data from eight Camac auxiliary-crate-controllers, thus allowing for a total of 160 digitizing modules (640 linear PSDs) in a system.

#### Multibus System

The Multibus system is of the same type as is currently used in the other IPNS data acquisition systems.<sup>2,1</sup> The Multibus has 24 memory address lines which allows for the addressing of up to 16 Mbytes of memory (1 "Mbyte" is really  $2^{20}$  or 1,048,576 bytes). Of this 16 Mbytes, 1.5 Mbytes are needed to address the Histogram Accelerator lookup tables (nearly 3 Mbytes are used for these tables, but since word-addressing is used on the Histogram Accelerator board this requires only 1.5 Mbytes of Multibus "address space"), thereby leaving 14.5 Mbytes available for histogram data. Multibus memory, including the lookup tables on the Histogram Accelerator board, is accessible by the microVax-to-Multibus interface which can address all 24 bits of address space. This interface is nearly the same as that currently used with the PDP computers on the other IPNS instruments,<sup>2</sup> requiring only minor switch selectable modifications. However, the software driver for this interface had to be modified for use on a microVax.

#### MicroVax to Camac Interface

Unlike the microprocessor based system used on other IPNS instruments, the FACEDAS Histogram Accelerator issues no commands to the Camac system. Instead, a microVax to Camac interface has been included to provide the capability to initialize Camac modules and control data acquisition directly from the microVax. Since there are no speed dependent functions which must occur via

this link, this interface is via an RS-232 Camac crate controller for simplicity.

#### PSD Adjustment, Calibration, and Monitoring

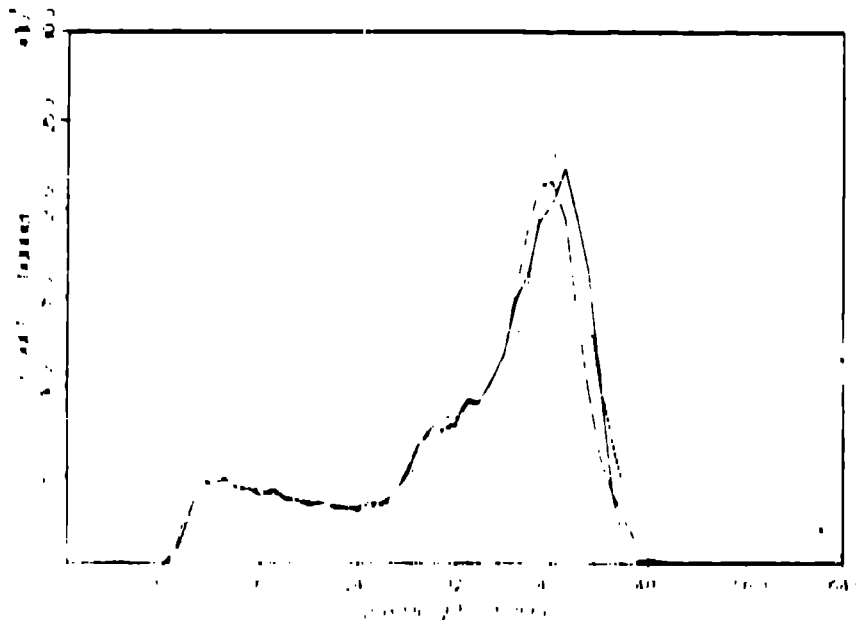
With such a large number of detectors, an efficient calibration procedure and the associated hardware and software features to facilitate calibration and to ensure the reliability of this calibration are very important. In developing these, we have benefited considerably from the previous experience with PSDs at the University of Missouri<sup>4</sup> and at IPNS.

A number of hardware features intended to aid in PSD adjustment, calibration, and monitoring have been incorporated into the GLAD system from the outset. Two of these, the position calibration mechanism which is an integral part of each detector module and the pulse-height data acquisition mode for the PSD digitizer modules, have already been noted above. In addition, separate power supplies have been provided for the upper (A) and lower (B) banks of preamplifiers, allowing either bank to be turned on or off independently and remotely; test-pulse input points are connected to each A and B preamplifier; and programmable tail-pulse generators allow independent injection of test pulses of known amplitudes into either the A or B (or both) banks of preamplifiers. The procedures for PSD adjustment, calibration, and monitoring based on these hardware capabilities (and correspondingly developed software) are outlined briefly below. With all these features in place, the operation and maintenance of the ~ 450 detectors encoded into ~ 29,000 position elements should be relatively painless and quite reliable.

#### Initial Adjustment Procedure for Camac PSD Digitizing Modules

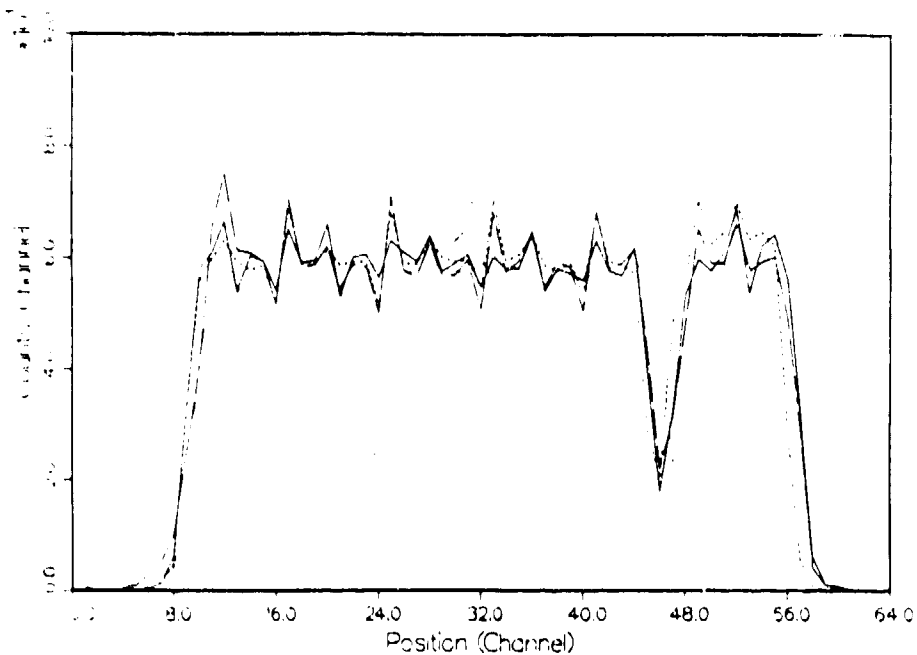
This procedure must be carried out whenever a new detector, preamplifier, or PSD digitizing module is installed, but need be repeated only infrequently otherwise. These steps can be followed concurrently for any number of detectors. First the gains must be set and balanced for the A and B signals for each detector. This is done with the detectors illuminated with neutrons from a strongly scattering sample placed in the beam or from a <sup>252</sup>Cf source placed in the sample position or near the detectors. First, only the A preamplifiers are powered, the PSD modules are operated in pulse height mode, and the gain of each input is adjusted to give the desired pulse height spectrum. The same is then done with only the B preamplifiers powered. Next, both A and B preamplifiers are powered with the PSD module still in pulse height mode, and the lower discriminator level is adjusted to cut off the

pulse height spectra at the desired level (upper discriminator levels are not adjustable). An example of such pulse height data at this stage is shown in Fig. 9. Finally, the PSD modules are switched to position mode and position spectra are acquired with the absorbing bar in two different locations ( $-1/4$  and  $-3/4$  of the detector length) between the neutron source and the detectors. This last step is repeated while adjusting the "Offset" and "Span" controls on the PSD modules until the bar shows up in the same position channels on all detectors. Figure 10 shows such position calibration data for several detectors for one position of the absorbing bar. These data were collected before the final "Offset" and "Span" adjustments had been completed, so some unused channels occur at each end of the range and the absorbing bar does not appear at quite the same channels for each detector.



**Fig. 9** Pulse-height data simultaneously collected from four different detectors, using a PuBe neutron source, after the initial PSD adjustments have been performed. These variations among detectors are typical.





**Fig. 10** Position data simultaneously collected from four different detectors, using a PuBe neutron source, after the initial PSD adjustments have been performed but before the final "Offset" and "Span" adjustments have been completed. The absorbing bar was positioned in front of the detectors, and its shadow is seen to be in nearly the same position on all four detectors even though the adjustments were not yet complete. The variation of intensity with channel for channels away from the bar position is due to irregularities in channel widths introduced by the limited precision of the analog-to-digital converters.

#### Determination of the Absolute Channel-to-Position Mapping

This needs to be done after the initial adjustment, and repeated only occasionally as a check against drifts. This procedure requires a smoothly-varying known distribution of neutrons (a uniform distribution is best), which can again be provided by a strongly scattering sample in the beam or by a PuBe source at the sample position. It is necessary to record position spectra in all detectors with the absorbing bar in several different known positions. These data are fit to determine the detector resolution and the positions corresponding to the boundaries of each position channel for each detector. These results are then stored in an instrument calibration file, for subsequent use by the data analysis routines as noted below.

## Automatic Monitoring of Calibration Drifts

No neutrons are needed for this. Before the automatic monitoring can be implemented, it is first necessary to provide an information base for this purpose. This can be generated with only a minimum of manual intervention, and should be done immediately following the initial adjustment procedure. The first item in this information base is a record of all the individual encoding-path gains (each end of each detector). This is obtained by powering each preamplifier bank (A or B), one at a time, injecting test pulses of known magnitude, and recording the pulse-height channels which accumulate these pulses for each detector. The second item is a record of discriminator settings for each detector. To obtain this, both preamplifier banks are powered, test pulses spanning a range of amplitudes are injected into one preamplifier bank, and for each detector the lowest test-pulse amplitude which is accumulated is recorded. The third and final item is an indication of the relative position mapping for each detector. This is obtained by powering both preamplifier banks, injecting test pulses of different known amplitudes into banks A and B, and recording for each detector the position channels into which these events are accumulated. This provides a record of the overall position mapping.

Once this information base is available, it can be used to test automatically all the detectors and encoding electronics to ensure that no drifts have occurred since the initial calibration. The basic test is a repeat measurement of the relative position mapping data (the third set of measurements in the information base), comparing the results with the values recorded in the information base for each detector. If further information is desired, either or both of the first two sets of measurements in the information base can be repeated and the results compared with the values previously recorded. All of this can be done automatically in a relatively short time with no user intervention, and so can be included as part of a standard startup procedure at the start of each run or other suitable interval. If any values have shifted by more than the allowed limits, the user can be warned and any other desired action (such as refusing to start the run) can be taken.

## Data Handling and Analysis

### Data Collection Strategies

The philosophy for the initial data analysis assumes elastic scattering, i.e.,  $k_1 = k_0 = 2\pi/\lambda$ . Inelasticity effects are considered as a correction to

be made later. We consider two types of sample. The simpler case is an isotropic sample, for which data are required only as a function of the scalar variable.

$$Q = \frac{4\pi}{\lambda} \sin \theta \quad (3)$$

where  $\theta$  is the scattering angle between incident and scattered wavevectors. The more complicated case is that of a full three-dimensional structure, e.g., of a single crystal or of a bulk glass or film with orientational effects. In this case the data are required as a function of the vector variable

$$Q = \frac{2\pi}{\lambda} (1 - \cos \psi \cos \phi, -\cos \psi \sin \phi, -\sin \psi) \quad (4)$$

where  $\psi$  and  $\phi$  are polar coordinates of a detector element (see Fig. 11). These are related to  $\theta$  by

$$\cos 2\theta = \cos \psi \cos \phi. \quad (5)$$

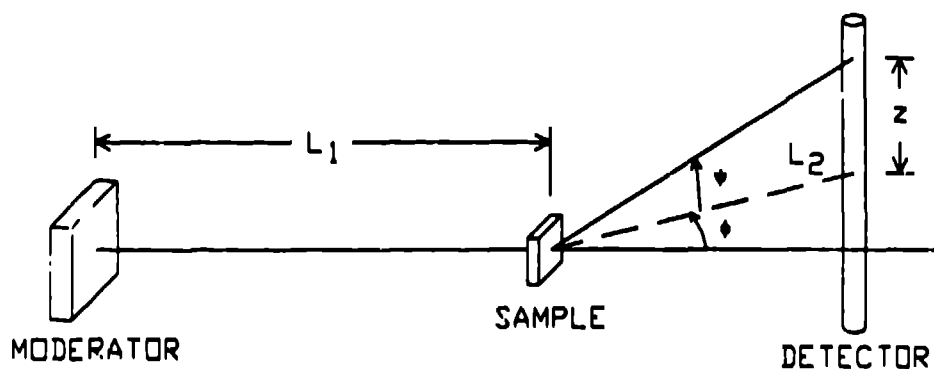


Fig. 11 Geometry for data analysis.

The data must be histogrammed so as to meet the requirements that (a) the size of the data sets is manageable, (b) the channel widths in both time and angle do not make a significant contribution to the experimental resolution, and (c) the outcome of the experiment should be as insensitive as possible to failure of single components. As is usually the case, these requirements are not strictly compatible: (b) and (c) would dictate that each vertical element in each detector is binned into a separate time histogram, but as noted earlier this requires on the order of 60 Mbytes per measurement, which exceeds the available memory on the present system and in any case would be unmanageably large. Some compression of the data must therefore be made on line in order to stay within the memory limits and also to keep the data sets to a reasonable

size. For example, it would be convenient to be able to store onto a single magnetic tape the output from a series of, say, eight samples inserted into an automatically cycling sample changer, which implies a maximum of around 15 Mbytes per sample; and even smaller sets would further simplify the tasks of data transfer, analysis, and archiving.

For the case of isotropic samples, the obvious way to compress the data at collection time is to bin the detector elements into a histogram of scattering angle  $2\theta \pm \Delta\theta$ , with events from all elements lying within this angular range being binned in a single time histogram. The bin width  $2\Delta\theta$  will then introduce a contribution of  $0.68 \Delta\theta \cot \theta$  into the FWHM  $\Delta Q/Q$  resolution. Choosing these bin widths to make this contribution somewhat smaller than the calculated  $\Delta Q/Q$  resolution due to other geometrical effects in the present design requires ~ 315  $2\theta$  channels to cover the entire angular range ( $0.3^\circ$  to  $90^\circ$ ).

Actually, this mode of histogramming provides more compression than would be required initially at data collection time. Thus it is proposed that during the data collection the elements contributing to a given  $2\theta$  bin be grouped with a separate time histogram for each set of such elements arising from the same detector (or small subset of the detectors). Advantages of this are: (a) deadtime corrections can be readily applied since, in a given detector, these depend on the count rate up to that time over all elements in the detector; (b) a faulty detector may be dropped without jeopardizing the whole  $2\theta$  bin; (c) the variation in flight path length is greatly reduced if only elements in a single detector are involved, so this contribution to the resolution is minimized; and (d) the same conceptual scheme (but with different grouping to provide the desired coverage of  $\phi, \psi$  space defined in Fig. 11) may be used for anisotropic samples.

#### Calibration Procedure

For a neutron travelling a total path length  $L$  and detected at time  $t$  from its point of origin, the wavelength can in principle be determined from

$$\lambda = \frac{ht}{mL} \quad (6)$$

In practice, the neutron production and moderation processes make it impossible to determine  $t$  and  $L$  absolutely. Ikeda and Carpenter<sup>5</sup> developed detailed descriptions of the time distributions of neutron emission from the moderator. In the Ikeda-Carpenter description the emission time  $t_n$ , which is the delay between the time origin (the " $t_0$ " pulse" at IPNS) and the mean of the time distribution for emission of neutrons of wavelength  $\lambda$ , can be written as

$$t_e = t_0 + 3m\lambda/hE(\lambda) + \exp(-\lambda_0^2/\lambda^2)/\beta \quad (7)$$

where  $t_0$  is a fixed time-triggering offset,  $E(\lambda) = (s_1 + s_2\lambda^2)^{1/2}$ ,  $\lambda_0 = (h^2/2mE_0)^{1/2}$ , and  $s_1$ ,  $s_2$ ,  $E_0$  and  $\beta$  are constants defined by Ikeda and Carpenter and subject to measurement for a particular moderator. For a neutron recorded in a time channel centered at a time  $t'$  relative to the time origin, Eq. (6) must thus be replaced by

$$\lambda = h \frac{[t' - t_0 - 3m\lambda/hE(\lambda) - \exp(-\lambda_0^2/\lambda^2)/\beta]}{mL} \quad (8)$$

(or by a corresponding equation if a different formulation is used to represent the emission-time delay).

Sinclair, Tasker, Clare, and Wright<sup>6</sup> describe the procedure for determining  $L$  and  $t_0$  for a given detector element. This procedure involves the careful measurement of powder diffraction patterns from known samples as well as the use of a series of sharp wavelength markers, such as resonant absorbers, single-crystal Bragg reflections, or polycrystal Bragg edges, in the incident beam. The GLAD incident beamline will include provision for easy insertion of such filters for calibration.

In determining the angle  $\psi$  for each detector element, the absorbing bar calibration procedure described above is used to obtain values  $z(\ell, m)$  for the height (above or below the instrument midplane) of each element ( $m$ ) in each detector ( $\ell$ ). The angle  $\psi(\ell, m)$  is then given by

$$\psi(\ell, m) = \tan^{-1} \left( \frac{z(\ell, m)}{L_2(\ell)} \right) \quad (9)$$

where  $L_2(\ell)$  is the distance from sample center to the center of the  $\ell$ th detector on the instrument midplane, which is determined by measurement after construction of the flightpath. The value of  $L(\ell, m)$  is then obtained from

$$L(\ell, m) = |L_1 + L_2(\ell)| + [L_2^2(\ell) + z^2(\ell, m)]^{1/2} - L_2(\ell) \quad (10)$$

The set of quantities  $\{t_0, s_1, s_2, E_0, \beta, \psi(\ell), L(\ell, m), \psi(\ell, m)\}$  will be stored on the microVax as the basic calibration file for the instrument. It should be updated periodically to allow for changes in detector calibration, changes in moderator properties, changes in geometry due to shifts in the floor, and other factors which alter with time.

### Data Analysis

In a given run, an intensity histogram  $I(\ell, k, n)$  is measured as a function of detector ( $\ell$ ), angle group ( $k$ ), and time channel ( $n$ ). Each  $I(\ell, k, n)$  will be affected by deadtime, the effect being related to the count rate in the preceding time channels summed over all elements for that detector. Since the deadtime will have a fixed value (8  $\mu$ sec) which has been set in the electronics design, the effect can be calculated to give a deadtime-corrected histogram  $I_c(\ell, k, n)$ . The wavelength  $\lambda(\ell, k, n)$  associated with each time channel for each detector element can be determined by iteratively solving Eq. (8) for a given time-histogram setup. These results can then be averaged to provide an average wavelength  $\lambda(\ell, k, n)$  for each detector, angle group, and time-channel combination. A typical experiment includes a number of runs measuring samples, backgrounds, empty containers, and vanadium for normalization, leading to a "primary" data set consisting of

$$S_1 = \{I_{c1}(\ell, k, n), \dots, I_{cp}(\ell, k, n), \lambda(\ell, k, n), \Theta(\ell, k), \psi(\ell, k)\} \quad (11)$$

where the indices  $1 \dots p$  extend over all the runs in this experiment.

For isotropic samples, it is not necessary to retain the identity of the detector, so the histograms can be summed over  $\ell$  to give  $I_c(k, n)$ ; similarly, the  $\Theta(k)$  and  $\lambda(k, n)$  can be obtained by appropriate averaging. The "secondary" data set for isotropic samples can then be taken as

$$S_2 = \{I_{c1}(k, n), \dots, I_{cp}(k, n), \lambda(k, n), \Theta(k)\} \quad (12)$$

This can be expected to be the level at which most users will transfer their data.

In the final stage of analysis, all the remaining corrections must be considered, including multiple scattering, absorption, background and container partially debugged, and hope to begin commissioning of this instrument in earnest at that time. We have also received the soller collimators (Cidic, Ltd., Cheltenham, England) and hope to install them, along with some additional incident beamline components, later this fall. We will then be able to test essentially the complete incident beamline (excluding choppers) to be used on the final version of the instrument.

The design is nearly complete for the final version of the GLAD scattered flight path. We hope to have this flight path built, and to provide enough detectors and electronics for two more detector modules to go with this path, during the coming year. At the same time, we are beginning to develop the

ancillary devices, such as cryogenic and high-temperature environments with sample changers, necessary for the performance of quality science at such an instrument. Thus by the end of 1989 the final version of GLAD should be in place with a complement of ~160 detectors, and should be beginning commissioning. This detector complement should be adequate for many of the envisioned scientific problems, and we expect scientific research on GLAD to begin on a routine basis in 1990, although the choppers for elastic scattering studies may not yet be in place at that time. Additional detectors will be added as funding permits until the full complement of ~450 detectors is reached.

The data acquisition system is close to meeting the design goals set forth earlier in this paper, but several additional development steps remain to bring the final instrument up to its ultimate level of performance. New preamplifiers must be developed to improve the PSD position resolution while retaining or increasing the encoding speed. The present resolution is ~ 1.6 cm FWHM, while a resolution of ~ 1 cm is desired. We would also like to develop faster encoding (preamplifiers and/or digitizing modules) to reduce the deadtime below the present 8 usec per event per detector, to reduce deadtime losses to acceptable levels at the estimated maximum instantaneous data rates. The 300 kHz histogramming speed is already adequate for all but the most demanding situations anticipated, but may need to be increased somewhat by the time the full complement of detectors is installed. It would be desirable to develop software techniques to reduce the time required to calculate and download the histogramming tables and start a run, since with the present software this can be several minutes per time-binning table if many channels scattering, and Placzek corrections. These depend on both  $\lambda$  and  $\theta$ . Routines used at this stage will be similar to those currently in use for glass data from SEPD and GPPD at IPNS. The final data set for isotropic samples then has the form

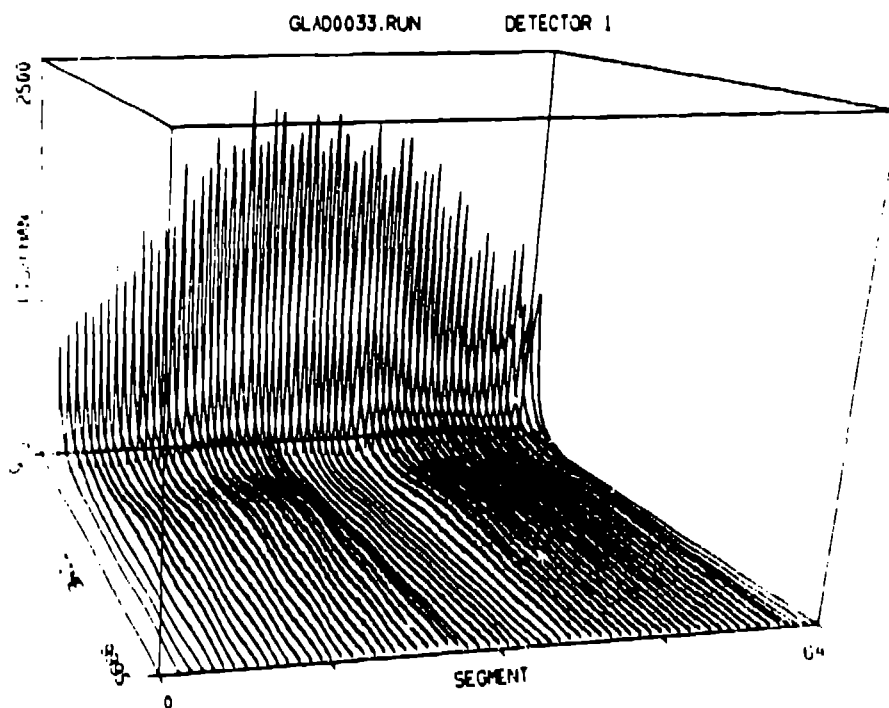
$$S_j = \{I_1(j), \dots, I_p(j), Q(j)\} \quad (13)$$

where the index  $j$  runs over all the  $Q$  bins used in this analysis.

#### Status and Results

The temporary flightpath for GLAD was installed in May, 1988, allowing data collection for ~ 2 weeks before the summer shutdown of IPNS (only 12 of the 55 detectors were in place for this period). During this running period we were able to perform the initial PSD adjustments (see above and data in Figs. 9-10) and to verify that the FASTDAS system, the position and time encoding of the

the PSDs, and the basic microVax data acquisition software all worked satisfactorily. We also confirmed that the PSDs could be operated satisfactorily in line with the direct beam, with the beam being attenuated only by a 2.5 cm thick  $B_4C$ /epoxy "beam attenuator" directly in front of the detectors. Detector recovery problems were apparent at times shorter than 500  $\mu$ s after the prompt pulse, but recovery was nearly complete by 500  $\mu$ s (which is the time-of-flight for 0.19  $\text{\AA}$  neutrons). Figure 12 shows time-of-flight data from the individual segments for the detector centered on the beam. These data were collected while there was still a significant amount of air in the scattered flight path, and so show a strong air-scattering background reflecting the spectral shape of the incident spectrum. The shadow of the beam attenuator is clearly evident in this figure.



**Fig. 12** Example of initial time-of-flight data from a single detector (64-segments) with the GLAD temporary flight path. A strong background at short times is seen, while the spectral features at longer times are primarily due to neutrons scattered from residual air in the flight path, and reflect the incident neutron spectrum. This detector was centered on the neutron beam, with the beam being attenuated only by the "beam attenuator". No adverse effects from this beam loading are seen at times  $> 500 \mu$ s, but the beam attenuator is clearly seen as a shadow in the air-background scattering.



The limited amount of running time did not permit a thorough background study, but did pinpoint a number of potential problems. Several shielding modifications were made during the summer, which should reduce the background from some of these sources. During the summer, we also installed the additional detectors and electronics to bring the single detector module up to its full complement of 55 detectors. Thus we will begin the Fall, 1988, running period with the temporary instrument version fully assembled and a long time range are used. We would also like to reduce the time required to save data to a file, since this can be significant for the large data sets contemplated. Because of the size of the run files, we will also need to develop new techniques for archiving of run files and/or partially reduced  $I(\theta, \lambda)$  data. We expect that most of these problems will be solved by the time the final flight path is installed.

A significant remaining problem is background, particularly the background at short times which is so evident in Fig. 12. Much of the running time with the temporary flight path is expected to be devoted to the development of effective techniques for background reduction.

## Acknowledgements

The authors would like to thank D. Bohringer and R. Stefiuk for their work on the design of the temporary GLAD flight paths and M. Faber for his work with the GLAD detector systems. A large number of people from the IPNS operations and accelerator groups were involved in the construction of the temporary GLAD instrument and the fabrication of the detector electronics, and we gratefully acknowledge these efforts. Discussions with R. Berliner and D. F. R. Mildner at the University of Missouri were very helpful in the initial design of the position-sensitive-detection electronics and the position-calibration procedures. This work was supported by the U.S. Department of Energy, BES, contract No. W-31-109-ENG-38.

## References

1. A. C. Nunes, Nucl. Instrum. Methods, 119, 291-293 (1974).
2. J. R. Haumann, R. T. Daly, T. G. Worlton, and R. K. Crawford, IEEE Trans. Nucl. Sci., NS-29, 62-66 (1982).
3. J. R. Haumann and R. K. Crawford, IEEE Trans. Nucl. Sci., NS-34, 984-953 (1987).
4. R. Berliner, D. F. R. Mildner, O. A. Pringle, and J. S. King, Nucl. Instrum. Methods, 185, 481-495 (1981).
5. S. Ikeda and J. M. Carpenter, Nucl. Instrum. Methods, A239, 536-544 (1985).
6. R. N. Sinclair, C. G. Tasker, A. G. Clare, and A. C. Wright, Nucl. Instrum. Methods, A240, 199-202 (1985).

## Workshop summary on inelastic and elastic scattering

*R. K. Crawford*  
Argonne National Laboratory  
Argonne, Illinois  
USA

This workshop session was designed to be non-selective in subject matter, but with an emphasis on description of scattering instruments (as opposed to instrument components or data analysis). As such, it attracted a large number of papers. To accommodate these papers, the workshop format was abandoned to a large extent, discussion periods were limited, and the session was run primarily as a formal presentation session. Even with these restrictions, the presentations carried over through the first thirty minutes originally scheduled for the following session. Although this arrangement was more formal than originally intended or desired, it did provide an opportunity for presentation of a wide variety of topics at an early stage of the conference, which it is hoped stimulated subsequent private discussions.

The first presentation was by Andrew Taylor, who discussed the status and performance of the ISIS inelastic instruments: HET (high-resolution high-energy chopper spectrometer), TFXA (crystal analyzer spectrometer), IRIS (high-resolution backscattering spectrometer)—all of which are operational and regularly scheduled; and EVS (electron-volt resonance spectrometer), PRISMA (multi-angle crystal analyzer spectrometer for single-crystal excitation), and MARI (multi-angle chopper spectrometer), all of which are in various stages of development or construction. Details of these instruments are provided in the paper, "Developments in Inelastic Instrumentation at ISIS" by A. D. Taylor, C. J. Carlile, Z. A. Bowden, M. Hagen, R. S. Holt, J. Mayers, R. Osborn, U. Steigenberger, Y. Todute, J. Tomkinson, and W. G. Williams in these proceedings.

Next, Masa Arai discussed the new chopper spectrometer INC under construction at KENS. Despite the severe spatial constraints imposed by adjacent instruments and the intensity limitations of the KENS source, Masa estimated that when completed, this instrument will provide an intensity similar to that of HET at ISIS, while having an energy resolution that is only 1.5 times that of HET. This instrument is described in detail in the paper "Chopper Spectrometer at KENS" by M. Arai, in these proceedings.

Rob Robinson discussed the kinematics and resolution of a chopper instrument for Brillouin scattering at relatively high neutron energies. These kinematics impose severe constraints upon an instrument designed for this purpose and, in particular, require very small scattering angles. The chopper spectrometer PHAROS being designed at LANSCE is intended to operate at scattering angles down to  $0.5^\circ$  both to cover this Brillouin-scattering regime and to serve as a more general-purpose chopper spectrometer. This work is presented in the paper "On the Kinematics and

Resolution of Spectrometers for Neutron Brillouin Scattering" by R. A. Robinson, in these proceedings. Details of the PHAROS chopper spectrometer can be found elsewhere in these proceedings.

Following Rob's paper, Peter Egelstaff presented some general comments on Brillouin scattering and showed some low-energy Brillouin scattering data he had recently collected. This experiment and data have been submitted for publication elsewhere ("Neutron Brillouin Scattering in Dense Nitrogen Gas" by P. A. Egelstaff, G. Kearlye, J. B. Suck, and J. P. A. Youden), and so will only be summarized here. Peter suggested that there are three distinct regimes for neutron Brillouin scattering:

- (a)  $\gamma \sim 5 \text{ \AA}$ , for which a reasonable instrument can be made by placing the ILL D11 area detector in the forward-scattering direction at the ILL IN5 instrument. This can be used to study systems with sound velocities  $\sim 600$  m/s.
- (b)  $\gamma \sim 2 \text{ \AA}$ , for which a reasonable instrument could be made by placing the ILL D17 detector system (detector and movable mount) on the ILL IN4 instrument. This could be used to study systems whose sound velocities are  $\sim 1000$  m/s.
- (c)  $\gamma \sim 0.65 \text{ \AA}$ , which would require modifications of the HET instrument at ISIS to achieve the small scattering angles necessary. This regime, which could presumably also be studied by the PHAROS instrument at LANSCE when it comes on line, is appropriate for the study of systems with sound velocities  $\sim 4500$  m/s.

If a minimum scattering angle of  $1^\circ$  can be achieved in each case, the  $Q_{\min}$  is  $\sim 0.02$  for case (a),  $\sim 0.05$  for case (b), and  $\sim 0.15$  for case (c). Peter and collaborators managed to convince the ILL management to make the instrument rearrangement necessary to achieve case (a). The IN5 chopper system produced a neutron beam with  $\sim 100\text{-}\mu\text{eV}$  bandwidth and  $0.5^\circ$  collimation. The  $65 \text{ cm} \times 65 \text{ cm}$  area detector from D11 was centered on this beam at a distance of 4 m downstream from the sample. Figure 1 shows typical Brillouin scattering data they obtained from  $\text{N}_2$  gas at two different pressures, and Fig. 2 summarizes the dispersion relations measured for the two gas pressures. This experiment shows that good Brillouin scattering data can indeed be generated, at least in the low energy case, if an instrument can be configured to provide low-background data at sufficiently small scattering angles. Extension of the technique to the higher energy cases awaits the development of new instruments, such as PHAROS, or the modification of existing instruments, such as those indicated in cases (b) or (c) above.

This Brillouin-scattering discussion was followed by John Copley's presentation of techniques for improving the intensity transmitted through a disk-chopper system on a neutron guide. In particular, John discussed the gains that might be achieved by using multiple-slot disk shippers and presented an analysis of some of the problems that are unique to such multiple-slot choppers. This work can be found in the paper "The Effects of Chopper Jitter on the Time-Dependent Intensity Transmitted by Multiple-Slot Multiple Disk Chopper Systems" by J. R. D. Copley in these proceedings.

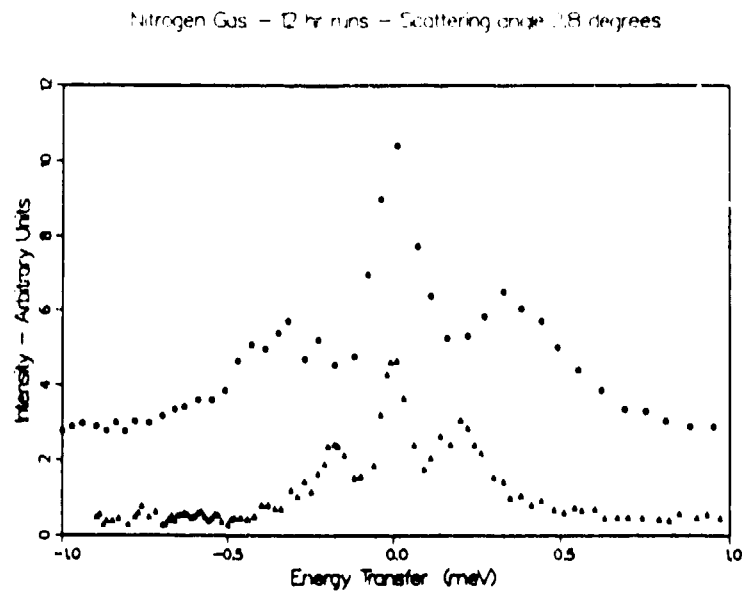


Fig. 1 Typical Brillouin scattering data (from Peter Egelstaff). Circles are data at  $\gamma = 4.7 \text{ \AA}$  and a gas pressure  $P = 51 \text{ MPa}$ . Triangles are for  $\gamma = 6.0 \text{ \AA}$  and  $P = 27 \text{ MPa}$ .

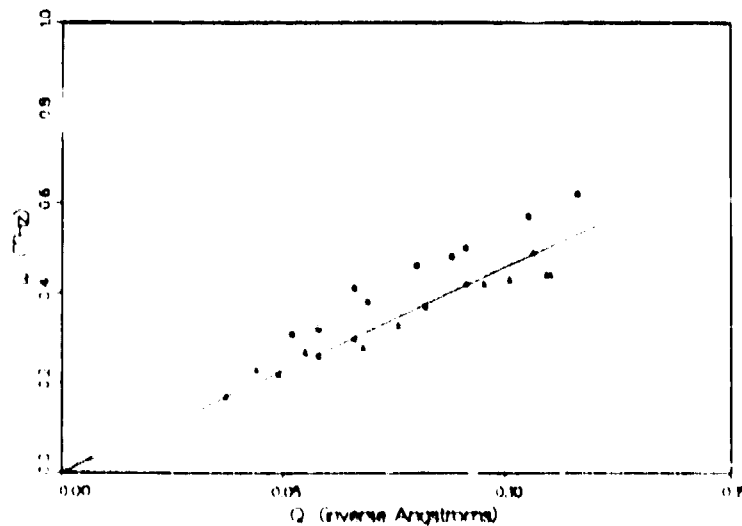


Fig. 2 Dispersion relations in dense  $\text{N}_2$  gas (from Peter Egelstaff). Circles are for  $P = 51 \text{ MPa}$  and triangle are for  $P = 27 \text{ MPa}$ . Lines are extrapolations of the sound velocity relations for these pressures.

Susumu Ikeda then indicated how the complementary techniques of resonance absorption of eV neutrons by the sample and resonance detection of eV neutrons scattered by the sample could be used to determine the kinetic energy of each of the individual types of atoms in a multi-component system. The method was illustrated by data obtained on the RAT instrument at KENS for the high-temperature superconductors  $\text{La}_2\text{CuO}_4$  and  $\text{YBa}_2\text{Cu}_3\text{O}_7$ . The techniques and results can be found in the paper "Application of eV Neutron Scattering and eV Neutron Absorption Techniques" by S. Ikeda in these proceedings.

Alan Soper discussed the current performance of the liquid and amorphous materials diffractometer (LAD) at ISIS. He then described the SANDALS instrument being constructed at ISIS and discussed the features of SANDALS that should make it much better than LAD. SANDALS will use the new ZnS scintillator detectors being developed at ISIS to cover a much greater angular range than in LAD; it will also have much greater data rates than those of LAD. These instruments are described in the paper "Future Perspectives of Liquids and Amorphous Materials Diffraction at ISIS" by A. K. Soper in these proceedings.

Michihiro Furusaka outlined one alternative being considered for small-angle scattering instrumentation at the proposed new Japanese pulsed-neutron source KENS II. This alternative involves two instruments: an 11-m flight path medium-resolution instrument, ( $Q_{\text{min}} = 0.006 \text{ \AA}^{-1}$ ), and a 40-m flight path high-resolution instrument, ( $Q_{\text{min}} = 0.002 \text{ \AA}^{-1}$ ).

Finally, Rex Hjelm discussed the important features of the newly developed user-interface software for the LQD small-angle diffractometer at LANSCE. This comprehensive software package provides for on-line assessment of the data, data reduction in absolute units, basic data manipulation and analysis procedures, and corresponding graphic representations—all within a user friendly framework. This system is described in the paper "Time-of-flight Small-Angle-Neutron-Scattering Data Reduction and Analysis at LANSCE with Program SMR" by R. Hjelm in these proceedings. Rex's paper served as a natural lead into the following workshop session on detectors and data acquisition.




**Monte Carlo simulation of the LANSCE  
target/moderator/reflector/shield geometry**


*H. Grady Hughes, III*  
Group X-6, MS B226  
Los Alamos National Laboratory  
Los Alamos, NM 87545

**ABSTRACT:** We present a detailed computer model of the existing LANSCE Target/Moderator/Reflector/Shield system. We describe the HETC/MCNP Monte Carlo code system used with this model, and we introduce a calculation designed to make comparisons with experimental results.

**Introduction**




The Target/Moderator/Reflector/Shield<sup>1</sup> (TMRS) system of the Los Alamos Neutron Scattering Center<sup>2</sup> (LANSCE) has been extensively described in the meetings and Proceedings of the International Collaboration on Advanced Neutron Sources. This paper presents a detailed computer simulation of the TMRS geometry and describes Monte Carlo particle transport calculations using this simulation. The purpose of this investigation is twofold: we wish to compare calculated fluxes in the flight paths to experimental measurements; and we wish to have available a standard Monte Carlo model both for parameter studies of the existing LANSCE facility, and for accurate studies of possible future modifications and upgrades.<sup>3</sup>



**The HETC/MCNP Code System at Los Alamos**

Our computational tool for these calculations is the HETC Code System,<sup>4</sup> the Los Alamos version of a computer program for the transport of nucleons, pions, and muons, based on the high-energy Monte Carlo code HETC,<sup>5</sup> originally developed at Oak Ridge National Laboratory (ORNL). The HETC code uses the Monte Carlo intranuclear cascade model of Bertini and the evaporation model of Drenner to describe the physics of nuclear interactions. Particles are transported between interactions through material and void regions in space, as defined with three-dimensional general geometry, with charged particles losing energy according to the continuous-slowing-down model. In the Los Alamos version, the geometric transport capability is that of the continuous energy neutron/photon Monte Carlo code MCNP.<sup>6</sup> HETC currently includes as user options two models for fission induced by high-energy interactions: the ORNL model by Altmüller and others,<sup>7</sup> and the Rutherford Appleton Laboratory (RAL) model by Atkinson.<sup>8</sup>



The philosophy of the HETC code is to treat all interactions by protons, pions, and muons within HETC, but to treat neutron interactions only above a cutoff energy, typically 20 MeV at Los Alamos. Any neutron emerging from a reaction with energy below the cutoff has its kinematic parameters recorded on a neutron file for subsequent transport by a Monte Carlo code utilizing ENDF/B-based neutron cross-section libraries. At Los Alamos, a version of MCNP modified to accept the neutron file as an input source is used to complete the particle transport; at other installations, the MORSE code is often used.

Calculational results from the MCNP phase of the computation can be obtained directly from the standard MCNP tallies, and a number of modified output edits appropriate to accelerator problems have been provided. In addition, both HETC and MCNP can write history files containing a (nearly) complete description of events occurring during the computations. Edited tallies of the initial HETC run, the subsequent MCNP run, or both runs in combination are obtained by using the HTAPE code to process data recorded on the history files. The edit options available with HTAPE include surface current and flux, cell-averaged neutron flux, particle production spectra, residual mass production and mean excitation, energy deposition by cell or material, mass-energy balance by cell or material, pulse shape analysis of surface current, gas production by cell or material, and global emission spectrum recorded in polar and azimuthal bins.

The MCNP phase of the computation can be executed as a coupled neutron/photon problem; however, obtaining a photon source from the high-energy interactions computed by HETC requires executing the PIIT code. PIIT accepts the history file as input and produces a gamma file containing a photon source for MCNP in the same format as the neutron file. In the current version, the gamma source arises from two processes: 1) decay of neutral pions produced in the intranuclear cascade and 2) de-excitation of residual nuclei after particle evaporation.

The neutron file and the gamma file can be merged to serve as a source for MCNP in a coupled neutron/photon problem that describes the transport of the entire gamma-ray source in the system. Alternatively, the two source files can be processed separately to analyze the effects of gammas arising from the high-energy interactions, and the effects of gammas arising from neutron-induced reactions (below 20 MeV).

HETC can also be used to compute cross sections directly. With this option, the transport is turned off and the primary particle is assumed to interact directly with the specified material at the incident energy. The resulting history file is then processed with the XSEX code to generate double-differential particle production cross sections. Tabulated and plotted output of the generated cross sections is available.

It is well known that the intranuclear cascade model, which provides the principal nuclear physics description for HETC, does not reproduce particularly well the angular spectrum for production of secondary particles observed in experiments. Nevertheless, the choice of HETC is dictated by its three-dimensional capability and its self-contained physics models. HETC is not dependent on the availability of complete nuclear physics data libraries. Undoubtedly, we could obtain more reliable results if we had extensive evaluated nuclear data libraries combining known experimental data with the most sophisticated model calculations. Efforts in that direction are now underway.

### The TMRS Geometry Model

Both MCNP and the Los Alamos version of HETC use a very general and robust method for modeling three-dimensional geometry. In this method, one specifies a collection of surfaces, selecting from any number of planes, spheres, cylinders, cones, tori, and general quadratic surfaces. One then describes a complete geometry by defining three-dimensional cells as the unions and intersections of regions bounded by these surfaces. The cells thus defined may contain voids, or may represent real materials by the use of appropriate cross-section sets for the Monte Carlo transport calculation.

The geometric model of the TMRS system is a fairly complex one, requiring 323 cells defined by 340 surfaces, and making use of 21 different cross-section sets to represent 14 distinct materials. Table I shows the 14 materials used in this simulation. In the upper part of the table, the atom fraction (i.e. the fraction by number of nuclei) of each constituent isotope is given for every material. In the lower part of the table, the corresponding mass fractions are given.

Figures 1-2 show, respectively, a horizontal and a vertical cut-away view of the LANSCE geometry. Many of the unique features of the TMRS system are shown in these pictures. For example, in Fig. 1 one can see the "high-resolution" water moderator serving flight paths 1 and 2, with its gadolinium poison at 1.5 cm and its complete decoupler/liner of cadmium and boron. By contrast, the cadmium and boron layers for the two "high-intensity" water moderators serving flight paths 3, 4, 5 and 6, 7, 8, are present only in the outer walls of the lines of sight. For these moderators, the gadolinium poison is at 2.5 cm. The cold moderator containing liquid para hydrogen at 20° K has no poison, and flight path walls similar to the two high-intensity moderators. In Fig. 2, one can see the two unequal segments of the target, the flux-trap arrangement of the moderators (not adjacent to the target), and additional details of the beryllium and nickel reflector/shield design. All of these details and more are present in the geometric model used in the Monte Carlo simulation.

Figure 3 shows the four flight paths studied in the present investigation. These are flight path 1, viewing the high-resolution moderator, and flight paths 3,



TABLE I. Materials used in the TMRS model.

Material	Component nuclides and atom fractions.			
M1	Ni: 1.00000			
M2	C: 0.00460	Si: 0.01968	Cr: 0.18075	<sup>55</sup> Mn: 0.02013
	Fe: 0.64742	Ni: 0.11302	Mo: 0.01441	
M3	<sup>1</sup> H: 0.66666	<sup>16</sup> O: 0.33334		
M4	Fe: 0.02782	Ni: 0.06174	W: 0.91044	
M5	<sup>9</sup> Be: 1.00000			
M6	Gd: 1.00000			
M7	Cd: 1.00000			
M8	<sup>10</sup> B: 0.08174	<sup>11</sup> B: 0.37237	C: 0.11353	<sup>27</sup> Al: 0.43236
M9	<sup>1</sup> H: 1.00000			
M10	Mg: 0.01112	<sup>27</sup> Al: 0.98075	Si: 0.00577	Cr: 0.00131
	Cu: 0.00106			
M11	<sup>10</sup> B: 1.00000			
M12	<sup>1</sup> H: 0.05111	<sup>9</sup> Be: 0.92333	<sup>16</sup> O: 0.02556	
M13	<sup>1</sup> H: 0.06732	<sup>16</sup> O: 0.03366	Ni: 0.99902	
M14	<sup>1</sup> H: 0.29139	<sup>16</sup> O: 0.14570	Fe: 0.56291	

Material	Component nuclides and mass fractions.			
M1	Ni: 1.00000			
M2	C: 0.00100	Si: 0.01000	Cr: 0.17000	<sup>55</sup> Mn: 0.02001
	Fe: 0.65401	Ni: 0.11998	Mo: 0.02500	
M3	<sup>1</sup> H: 0.11191	<sup>16</sup> O: 0.88809		
M4	Fe: 0.00900	Ni: 0.02100	W: 0.97000	
M5	<sup>9</sup> Be: 1.00000			
M6	Gd: 1.00000			
M7	Cd: 1.00000			
M8	<sup>10</sup> B: 0.04560	<sup>11</sup> B: 0.22844	C: 0.07591	<sup>27</sup> Al: 0.65005
M9	<sup>1</sup> H: 1.00000			
M10	Mg: 0.01000	<sup>27</sup> Al: 0.97898	Si: 0.00600	Cr: 0.00251
	Cu: 0.00251			
M11	<sup>10</sup> B: 1.00000			
M12	<sup>1</sup> H: 0.00587	<sup>9</sup> Be: 0.94758	<sup>16</sup> O: 0.04655	
M13	<sup>1</sup> H: 0.00127	<sup>16</sup> O: 0.01009	Ni: 0.98864	
M14	<sup>1</sup> H: 0.00862	<sup>16</sup> O: 0.06842	Fe: 0.92296	

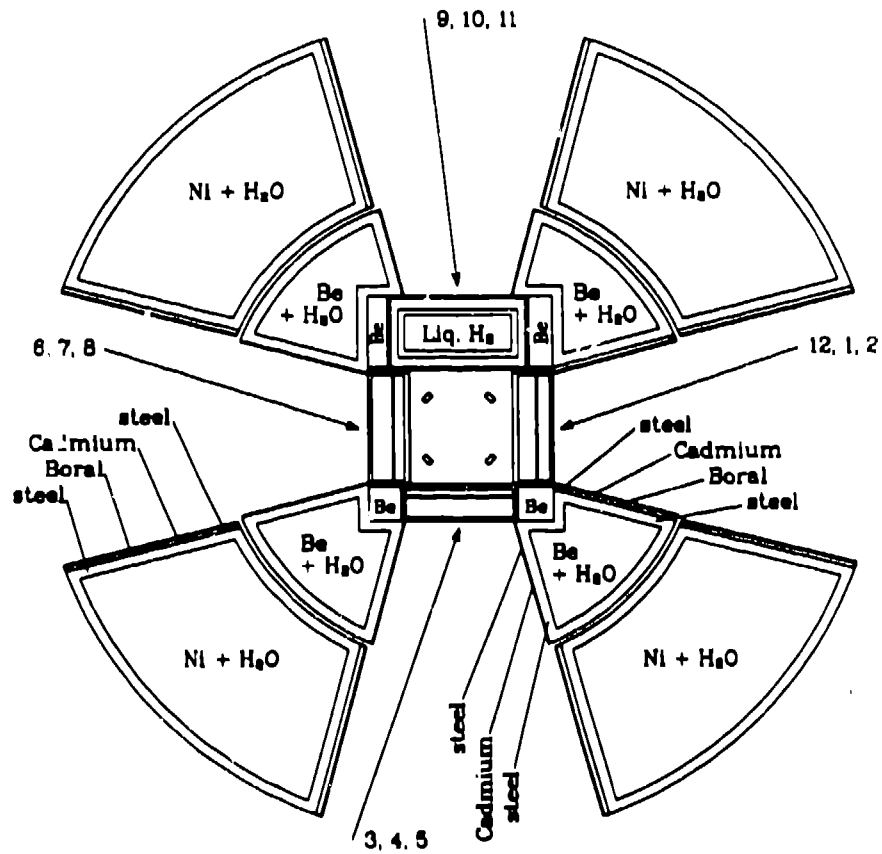
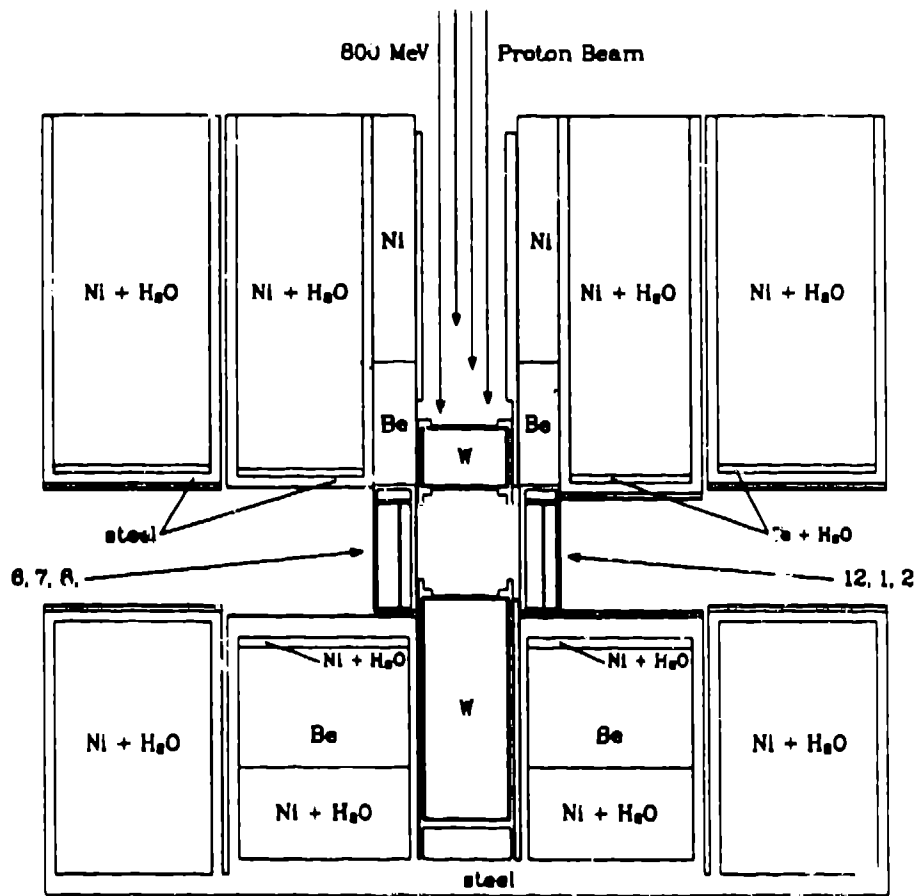
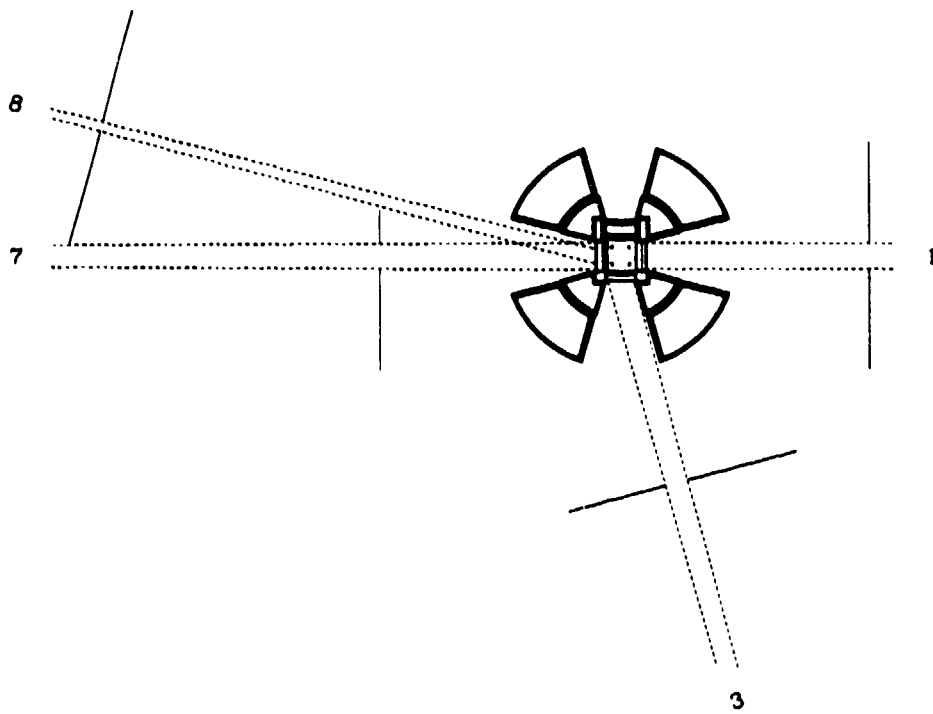


Fig. 1 Horizontal cut-away view of the LANSCE TMRS system. The layer of Boral (material 8 in Table I) is present in the outer walls of all four flight paths, but in the inner wall only for flight path (12, 1, 2).



**Fig. 2** Vertical cut-away view of the LANSCE TMRS system. As in Fig. 1, the linings of the flight paths consist of steel/Boral/cadmium/steel for all outer flight paths and for the inner path (12, 1, 2), but only steel/cadmium/steel for the other inner paths.



**Fig. 3** The four lines of sight calculated in the present investigation. The limits of the lines of sight are shown in dashed lines, and the artificial, zero-importance cells used to simulate the apertures are shown in solid lines. The lines of sight are either on-axis or offset at  $15^\circ$ .

7, and 8, viewing the two high-intensity moderators. Calculations of point detector responses at appropriate locations on the flight paths simulate experimental measurements of neutron fluxes. We will return to the subject of point detectors and the modeling of apertures in the next section.

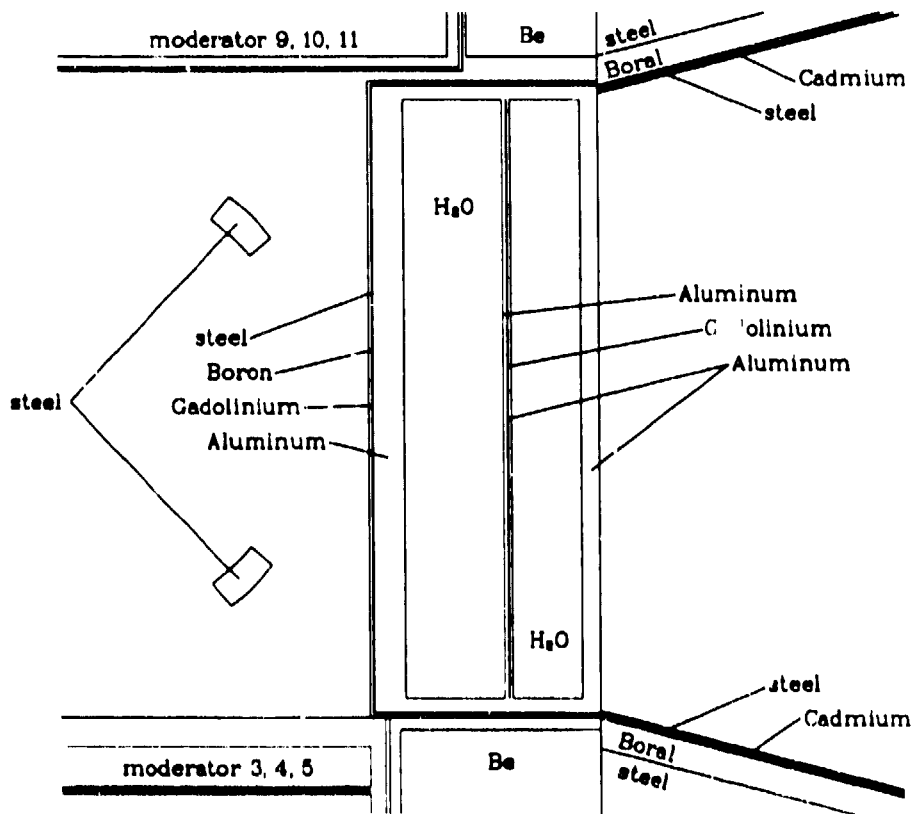
At an expanded scale, Figs. 4-7 show, in order, the high-resolution moderator serving flight paths 12, 1, and 2; the high-intensity moderator serving 3, 4, and 5; the high-intensity moderator serving 6, 7, and 8; and the cold moderator serving 9, 10, and 11. The previously mentioned features of these moderators are more easily seen (and labeled) in these pictures. To facilitate comparison, these four figures are all presented at the same scale.

### The Monte Carlo Calculation

One purpose of this investigation was to compare calculated fluxes in the flight paths with experimental measurements. The experiments consisted of measurements of the 1-eV flux from gold foil activation. These measurements were made in flight paths 1, 3, 7, and 8, at various distances from the moderators, and with various fields of view. The experimental situation is described in more detail in Ref. 9.

To simulate each flux measurement, a point detector tally was used in the MCNP phase of the Monte Carlo calculation. The detector was placed on the center line of the flight path, at a distance from the moderator corresponding to the location of the foil. In a point detector calculation, every interaction of a neutron in specified cells makes a virtual contribution to the detector tally, even when the probability of a neutron actually reaching the detector is small. Thus the response of a small, distant detector may be calculated accurately for situations in which the direct (analogue) simulation of the transport would be prohibitively expensive. The point detector is a tally option of MCNP which is not implemented in HETC. Fortunately, all of the neutron transport below 20 MeV is handled by the MCNP phase, so that this tally is available in the present situation.

In addition, the apertures defining the fields of view for the four measurements were simulated in the Monte Carlo calculations. This was done by the introduction of artificial cells outside the TMRS geometry to represent the shielding material blocking the neutrons outside of the fields of view. The artificial cells were given zero importance, which instructs the Monte Carlo code to terminate any entering particle history. Thus only neutrons passing through the open aperture are allowed to contribute to the point detectors. This arrangement is illustrated in Fig. 3, showing the constraining zero-importance cells outside the TMRS. The limits of the lines of sight thereby defined are shown as dashed lines.



**Fig. 4** Horizontal cut-away view of the high-resolution water moderator serving flight paths 12, 1, and 2. The moderator is heterogeneously poisoned with gadolinium at 1.5 cm, and has the boron and cadmium liner previously seen in Figs. 1 and 2.

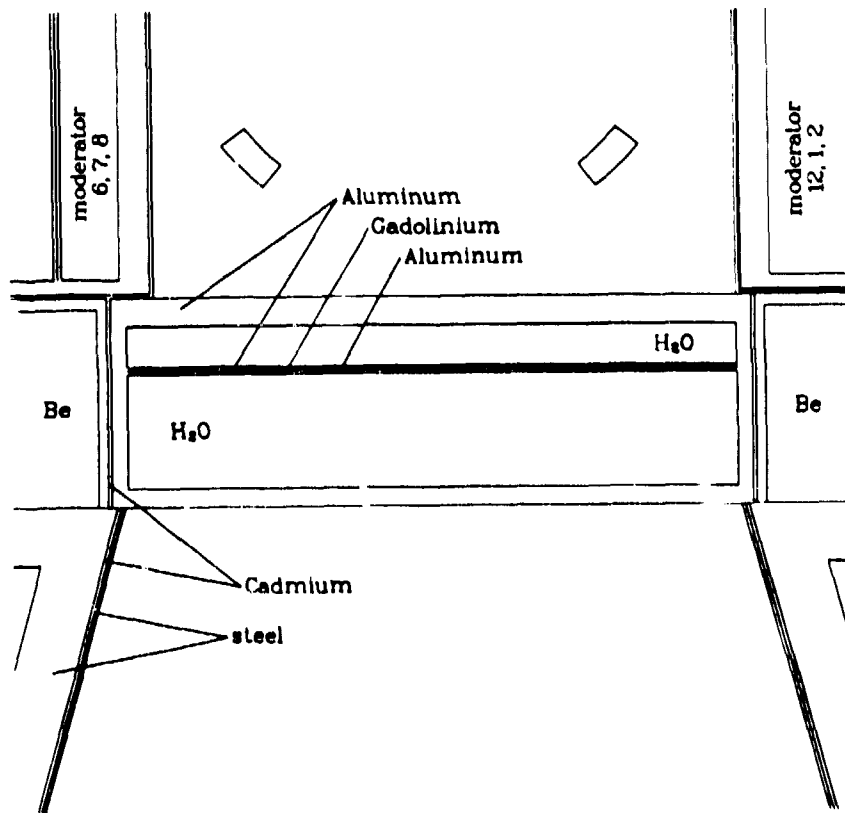
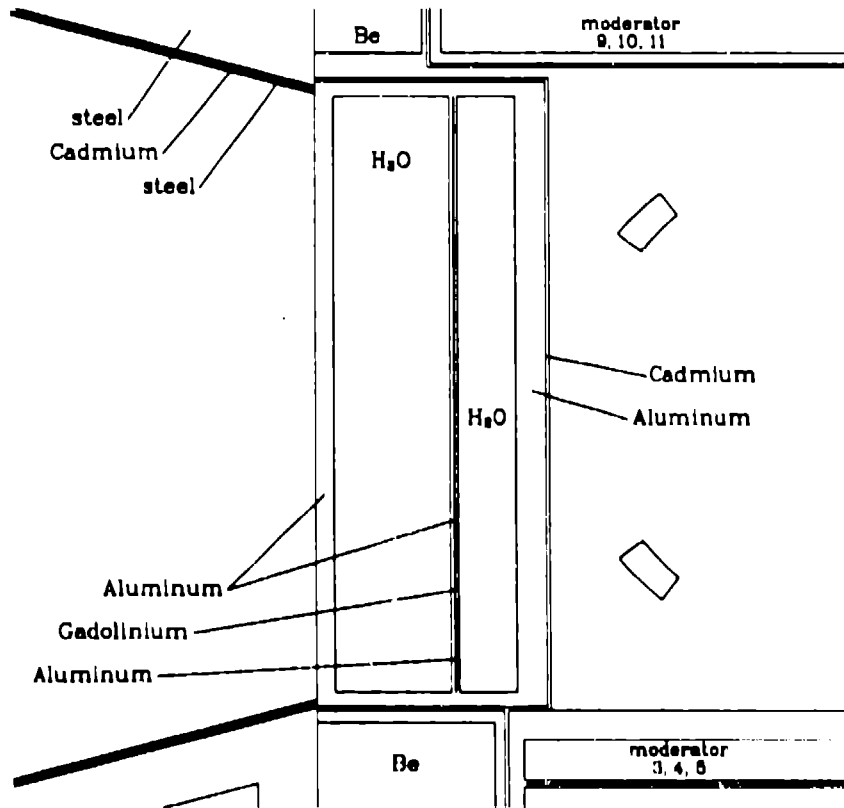
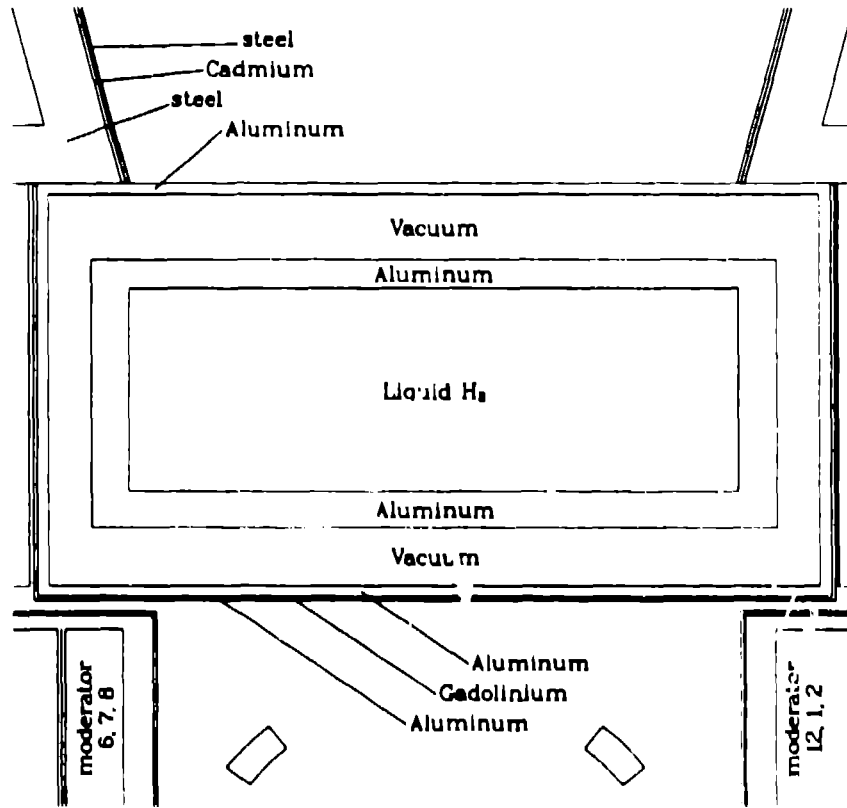


Fig. 5 Horizontal cut-away view of the high-intensity water moderator serving flight paths 3, 4, and 5. This moderator is heterogeneously poisoned with gadolinium at 2.5 cm, and has only a cadmium liner in the inner flight path.



**Fig. 6** Horizontal cut-away view of the high-intensity water moderator serving flight paths 6, 7, and 8. The poison and liner are similar to those in the other high-intensity moderator, shown in Fig. 5.





**Fig. 7** Horizontal cut-away view of the cold moderator serving flight paths 9, 10, and 11. This moderator contains liquid para hydrogen at 20° K, and has a cadmium liner in the inner flight path.

An additional refinement in the calculation was the use of  $S(\alpha, \beta)$  cross-section sets for beryllium, water, and liquid hydrogen. The  $S(\alpha, \beta)$  cross-section set provides a more accurate representation of the cross-section at low energies, and is especially important when neutron thermalization becomes significant. The  $S(\alpha, \beta)$  set used in these calculations for liquid hydrogen is a recent improvement to previous studies.

Table II shows the results of the four calculations of 1-eV flux at the foils. Column 1 gives the flight path number. Column 2 is the distance from the center of the outer surface of the moderator to the simulated foil. Column 3 is the distance from the outer surface of the moderator to the center of the aperture. The field of view in column 4 is not the field of view at the moderator, but the actual open surface at the aperture, since that is the quantity that is actually incorporated in the calculation. This field of view is related to the field of view at the moderator by a simple  $R^2/\cos\theta$  factor. The measured and calculated values for the 1-eV flux are shown in columns 5 and 6. The units for these quantities are, of course,  $10^{-9}/\text{eV cm}^2 \text{ p}$ . These results and some of their implications are discussed in some detail in Ref. 10.

**TABLE II. Experimental and Theoretical Fluxes.**

Flight Path	Moderator-to-foil distance	Moderator-to-aperture distance	Aperture field-of-view	Measured 1-eV Flux	Calculated 1-eV Flux
1	3175 cm	98 cm	132.8 cm <sup>2</sup>	0.44	0.49
3	900 cm	93.56 cm	101.9 cm <sup>2</sup>	5.26	7.66
7	1300 cm	94.43 cm	120.3 cm <sup>2</sup>	2.61	3.93
8	660 cm	224 cm	21.4 cm <sup>2</sup>	3.40	5.90

### Acknowledgments

I appreciate many useful discussions with R. J. Brewton, J. S. Gilmore, and G. J. Russell.

This work was performed under the auspices of the U. S. Department of Energy, Office of Basic Energy Sciences.

### References

1. G. J. Russell, C. D. Bowman, E. R. Whitaker, H. Robinson, and M. M. Meier, "LANSCE High-Power (200  $\mu\text{A}$ ) Target-Moderator-Reflector Shield," *ICANS-VIII, Proceedings of the Eighth Meeting of the International Collaboration on Advanced Neutron Sources*, Oxford, England, July 8-12, 1985, RAL 85-110, pp. 272-293 (1985).

2. F. A. Morse, "Status Report on LANSCE, 1986," *ICANS-IX. Proceedings of the Ninth Meeting of the International Collaboration on Advanced Neutron Sources*, SIN, Villigen, Switzerland, September 22-26, 1986, ISBN 3-907998-01-4, pp. 31-43 (July 1987).
3. G. J. Russell, H. Robinson, G. L. Legate, R. Woods, E. R. Whitaker, A. Bridge, K. J. Hughes, and R. D. Neef, "The LANSCE Target System," *ICANS-IX, Proceedings of the Ninth Meeting of the International Collaboration on Advanced Neutron Sources*, SIN, Villigen, Switzerland, September 22-26, 1986, ISBN 3-907998-01-4, pp. 177-244 (July 1987).
4. R. E. Prael, and H. Lichtenstein, "User Guide to the HETC Code System," Los Alamos National Laboratory interim documentation (June 15, 1987).
5. Radiation Shielding Information Center, "RSIC Computer Code Collection: HETC, Monte Carlo High-Energy Nucleon-Meson Transport Code," Oak Ridge National Laboratory report CCC-178, Rev. (August 1977).
6. J. F. Briesmeister, editor, "MCNP — A General Monte Carlo Code for Neutron and Photon Transport," Los Alamos National Laboratory report LA-7396 M, Rev. 2 (September 1986).
7. J. Barish, T. A. Gabriel, F. S. Alsmiller, and R. G. Alsmiller, Jr., "HET-FIS High-Energy Nucleon-Meson Transport Code with Fission," Oak Ridge National Laboratory report ORNL/TM-7882 (July 1981).
8. F. Atchison, "Spallation and Fission in Heavy Metal Nuclei under Medium Energy Proton Bombardment," in *Targets for Neutron Beam Spallation Sources*, Jül-Conf-34, Kernforschungsanlage Jülich GmbH (June 1980).
9. J. S. Gilmore, R. A. Robinson, and G. J. Russell, "Experimental Determination of Neutron Beam Fluxes at LANSCE from Gold Foil Activation," in these proceedings.
10. G. J. Russell, J. S. Gilmore, H. Robinson, G. L. Legate, A. Bridge, R. J. Sanchez, R. J. Brewton, R. Woods, and H. G. Hughes, III, "LANSCE Target System Performance," in these proceedings.

## Experimental determination of neutron beam fluxes at LANSCE from gold foil activation

*J. S. Gilmore, R. A. Robinson, and G. J. Russell*  
Los Alamos National Laboratory  
Los Alamos, New Mexico 87545  
USA

### Introduction

The purpose of this work was threefold: (1) to measure fluxes at the experimental locations for more efficient design and use of the instruments; (2) to compare measured fluxes with those predicted by state-of-the-art Monte Carlo computer code calculations incorporating a detailed mockup of the LANSCE target-moderator-reflector-shield geometry; and (3) to compare the fluxes from the unique flux-trap design with more conventional target-moderator systems of ISIS and ZING-P.

In measurements taken at Rutherford-Appleton Laboratory, T. G. Perring, A. D. Taylor, and D. R. Perry<sup>(1)</sup> emphasized the thermal neutrons by suppressing the epithermal neutron activation through self-shielding in very thick gold foils. The experimenters then matched the activations with those calculated from independent, experimentally determined neutron-spectral shapes to calculate the 1 eV neutron fluxes.

T. G. Worlton and J. M. Carpenter<sup>(2)</sup> at Argonne measured the 1-eV fluxes directly by using cadmium-shielded 22.56-mg/cm<sup>2</sup> thick gold foils. They determined the necessary self-shielding corrections by irradiating a stack of three foils. Preliminary corrections were applied to the specific activities of the foils using the following approximation for the self-shielding correction  $g$ :

$$g(\tau) = e^{-\tau/2} [I_0(\tau/2) + I_1(\tau/2)],$$

where  $\tau$  is the thickness  $\sigma \sigma x$ ,  $\sigma$  is the Doppler-broadened peak capture cross section (27,370 b), and  $I_0$  and  $I_1$  are modified Bessel functions of the first kind.

Their final values for the corrected specific activities were then determined by extrapolating the proximate results as a function of foil thickness to zero thickness.

Our measurements at LANSCE parallel these latter experiments for the 1-eV flux. We have, however, irradiated bare Au foils for additional data on the subcadmium flux. In the future we plan to use a modified cadmium-difference method, taking into

account the undermoderated spectrum from a pulsed-spallation source, which is rich in epithermal neutrons.

### Measurement location

The measurements were made of flight paths (FP) 1, 3, 7 and 8 at LANSCE. The moderator configuration has been described previously by Russell, et al<sup>(3)</sup>. All of these flight paths view water moderators poisoned heterogeneously with gadolinium. FP 1 views a "high-resolution" moderator, with a boron decoupler/liner. FP 3 views a "high-intensity" moderator, which is decoupled with cadmium. FP 7 and 8 both view a second "high-intensity" moderator.

### Proton beam monitor and normalization

The LANSCE experiments consisted of three successive irradiations in which we determined the relative number of protons from a current monitor that recorded the output of the Proton Storage Ring (input minus loss). In the last experiment we also determined the absolute number of protons from the number of reactions that occurred in an aluminum-monitor foil packet irradiated in a harp box ~3 m in front of the bending magnet for vertical insertion into the target. After irradiation the packet, which consisted of 0.025-mm-thick Al foil sandwiched between two 0.025-mm Al recoil compensating foils, remained in the box but out of the beam for an additional 12 days to avoid opening the beam line during the run cycle. Of the three reaction products we measured, the yields of <sup>22</sup>Na and <sup>24</sup>Na were clearly augmented by secondary low-energy neutron reactions, and only the <sup>27</sup>Al(p,x)<sup>7</sup>Be reaction, where the product is removed from the target nucleus in Z and A, gave a valid result. The number of protons may still be an upper limit because the beam is defocused before it enters the tungsten target.

Two Au samples separated vertically by 1.27 cm were irradiated at the experimental location in each of the flight paths we studied. The upper foil was always a bare 0.0127-mm-thick foil for use as a monitor. In the first irradiation the lower sample consisted of a stack of three 0.0127-mm-thick Au foils in a 0.76-mm-thick cadmium cover. In the second run, and in FP 8 in the third run, both the upper and lower samples were bare gold.

The Au monitor foils indicated that while the relative neutron production per proton viewed by FP 8 was constant in all three runs, production for FP 1 and 3 were lower by 12% and 9%, respectively, in Run 1 than in Run 2, presumably because of poorer beam quality, which improved with changes in steering and focusing. The final number of protons based on the Al monitor foil and relative integrated beam current from the current monitor were, therefore, also normalized for beam quality through the Au monitors.

### Calculation of epithermal flux

The neutron flux at 1 eV at the experimental location, normalized to the number of protons is given by the following:

$$I(E)_{1 \text{ eV}} = \frac{{}^{198}\text{N}}{{}^{197}\text{N} a_{\text{Cd}} g N_p \text{RI} (1 + 0.029/g)}$$

where  ${}^{198}\text{N}/{}^{197}\text{N}$  = the number of  ${}^{198}\text{Au}$  atoms produced per atom of Au in the foil  
 $a_{\text{Cd}}$  = attenuation correction for the cadmium cover for 4,906-eV neutrons  
 $g$  = gold self-shielding correction  
 $N_p$  = number of protons for the irradiation  
 $\text{RI}$  =  $1.71 \times 10^{-21} \text{ cm}^2$ , resonance integral for Au in a neutron spectrum, which we assumed had the form  $I(E) = I(E^*) [E/E^*]^{-0.92}$ .

Our value for the self-shielding correction for Au from stacked foil data differed from the measurement of Worlton and Carpenter by less than 1% for the same foil thickness. The quantity 0.029/g is the contribution of the  $1/v$  part of the Au capture cross section to the total activations.

### Results and conclusions

The results are given in Table 1. Columns 1 and 2 delineate the flight path number and moderator type. Columns 3 and 4 give the flight-path lengths (from moderator to foil) and moderator field-of-view (i.e., the effective area of moderator viewed by the foil). This area, A, is obtained simply by projecting the limiting upstream thermal-neutron aperture (i.e., the aperture closest to the moderator) from a point in the foil plane on to the moderator surface. As the foils in each beam line were identical, the intensities measured should be proportional to a  $\cos\theta/L^2$ , where  $\theta$  is the angle between the flight path and the moderator normal.

Table 1. Measured epithermal neutron-beam fluxes at LANSCE.

Flight Path	Moderator Type	Foil Position L (cm)	Moderator Field-of-view A (cm <sup>2</sup> )	Cadmium Ratio	1 eV Flux, I(E)	
					at L (10 <sup>9</sup> /eV cm <sup>2</sup> p)	at moderator* (10 <sup>10</sup> /eV sr $\mu$ A s)
1	High Resolution H <sub>2</sub> O	3175	141.2	1.09	0.44	2.82
3	High Intensity H <sub>2</sub> O A	900	131.5	1.29	5.26	3.01
7	High Intensity H <sub>2</sub> O B	1300	139.8	1.13	2.61	2.84
8	High Intensity H <sub>2</sub> O B	660	50.8	1.37	3.40	2.71

\*For a 12 x 12 cm field of view.

Column 5 gives the cadmium ratios for each flight path. These were obtained with thick Au foils (22.6 mg/cm<sup>2</sup>); the values for thin foils would be closer to unity. There appear to be significant differences between flight paths, even for FF 7 and 8, which view the same moderator. For these two beam lines, we have also examined the spectra measured by low-efficiency BF<sub>3</sub> monitors. The spectra were fitted to the standard spectral function previously used by Carpenter, et al.<sup>(4)</sup> The result of this

analysis is that the epithermal-to-Maxwellian ratios for FP 7 and 8 agree to within 1%. It is, therefore, very unclear whether the differences in cadmium ratio are significant.

In columns 6 and 7, we list the epithermal fluxes at the foil position and moderator surface, respectively. In the latter case, we have corrected for the solid angle of the measurement. One would expect the epithermal fluxes to be similar for all four flight paths and, indeed, the agreement is very good. For comparison with calculations, see reference 5.

### **Acknowledgements**

This work was supported, in part, by the division of Basic Energy Sciences of the U.S. Department of Energy. We acknowledge the support of R. Woods for this work, and the help of H. Robinson, G. L. Legate, A. Bridge, R. Sanchez, and K. J. Hughes in conducting the experiment. We appreciate the support of the counting room personnel in the Los Alamos Nuclear and Radiochemistry Group.

### **References**

1. Perring, T. G., Taylor, A. D., and Perry, D. R., 1985, "Absolute Neutronic Performance of SNS from Gold Foil Activation," Rutherford Appleton Laboratory RAL-85-029.
2. Worlton, T. G. and Carpenter, J. M., "Technique for Epithermal Beam Current Measurements at Spallation Neutron Source," IPNS Note 14 (unpublished).
3. Russell, G. J., Bowman, C. D., Whitaker, E. R., Robinson, H., and Meier M. M., 1985, in Proceedings of Eighth meeting of ICANS, Oxford 8th-12th, July 1985, Rutherford-Appleton Laboratory Report RAL-85-110, 1, 277.
4. Carpenter, J. M., Robinson, R. A., Taylor, A. D., and Picton, D. J., 1985, Nucl. Instrum. Methods **A234**, 542.
5. Russell, G. J., et al., "LANSCE Neutronic Performance," in these proceedings.

# The D<sub>2</sub> cold-neutron source for SINQ

*F. Atchison, W. Bucher, A. Höchli, I. Horvath and L. Nordström*  
Paul Scherrer Institute  
CH-5232 Villigen  
SWITZERLAND

## 1. Introduction

This report describes the present state of the design for a D<sub>2</sub> cold neutron source for SINQ. The source is to provide neutrons in the wavelength range 2 to 12 Å for a guide-system<sup>(1)</sup> and at two beam ports. The basis of the design is an adaptation of the "horizontally" mounted thermosyphon as used for the second cold-source at the ILL, Grenoble<sup>(2)</sup>. The principal advantages of the thermosyphon are as follows:

- High heat-transfer rates at cryogenic temperatures are easily achieved.
- The system is basically passive and self-regulating.
- Minimization of the cooling power required by allowing, for instance, the condenser/phase-separator system to be removed from the high heating region.

So far, work has been concentrated on the cryogenic part of the source, which is in the region of the bulk shield. The main considerations for the design are outlined in the following section and specific points given in section 3. The layout of the beam-tubes and cold-source plugs is shown in Fig. 6 and details of the present D<sub>2</sub> source layout in Fig. 7.

## 2. Design considerations

The practical design (dimension specification, services, etc.) comes from a synthesis of requirements (often conflicting) from the following principal areas.

**2.1 Neutronics.** The aim is to produce the highest "cold" neutron flux, which requires that the source is as close to the thermal flux maximum as is possible, has as large a volume of D<sub>2</sub> as possible, and there is as little as possible material in the path between D<sub>2</sub> and the user. The beam tubes need to view the source at the position that gives the best "cold" flux.

A practicable D<sub>2</sub> source will always be too small to allow complete rethermalization of the neutrons. The thermal neutrons from the D<sub>2</sub>O are to be induced to lose about a factor of 10 in energy; but because the scattering is determined by the dynamics of the deuterium molecule, the slowing-down rate is considerably reduced compared to that at "higher" energies, and about 10 collisions are required.



Neutron transport studies have been carried out using Monte Carlo with a scattering kernel derived from differential cross sections calculated using the Young and Koppe model<sup>(3)</sup>. The calculated total scattering cross sections together with the measured values of Sieffert<sup>(4)</sup> are shown in Fig. 1; the agreement with the Sieffert results (liquid D<sub>2</sub> at 19 K) is generally good down to about 3 meV. Below this energy, coherent scattering starts to become significant; but as the main effect will be felt only in the long-wavelength (e.g., VCN) region, it has not been included.

We should expect, at best, a spectrum with a mean energy rather higher than the 25 K physical temperature (this is observed with the cold sources at the ILL, Grenoble): this may be seen from the plot of mean-scattered energy as a function of incident energy shown in Fig. 2. An equilibrium will occur at about the energy where the average scattered energy equals the incident, which is 3.8 meV (44 K) for ortho- and 5.0 meV (58 K) for para-deuterium.

The best cold flux will be at a position some distance from the entry point of the neutron into the D<sub>2</sub>. The cold neutron intensities for a window 80 mm wide and 120 mm high, at three positions along the cylindrical surface and for various re-entrant windows, are shown in Fig. 3.

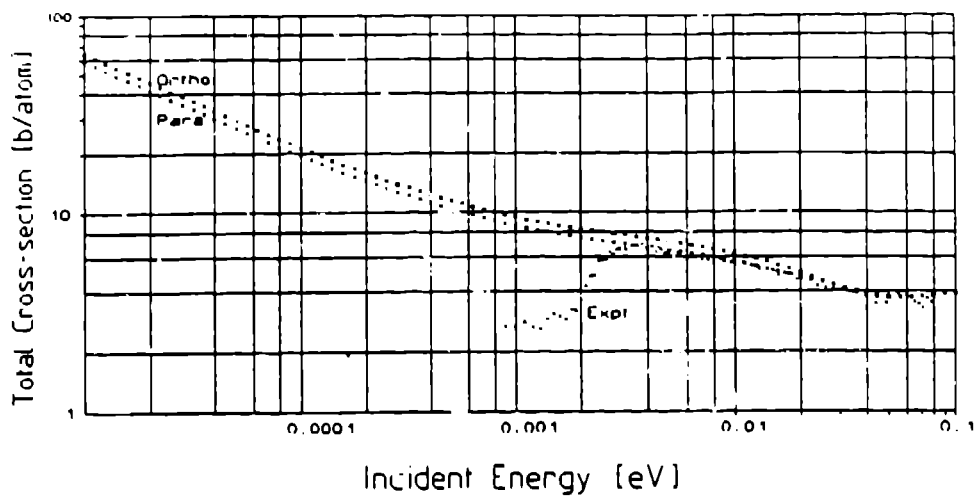
The results indicate that a re-entrant hole leaving 10 to 15 cm of D<sub>2</sub> between the two windows and located approximately 15 cm from the target-end of the source cell is about optimum. The neutron intensity gain over a window on the surface could be in the region of 50%. A calculated spectrum of the neutrons leaving the D<sub>2</sub> is shown in Fig. 4.

Flux loss will be caused by materials in the path of the cold-neutron beams. These may be split into two categories:

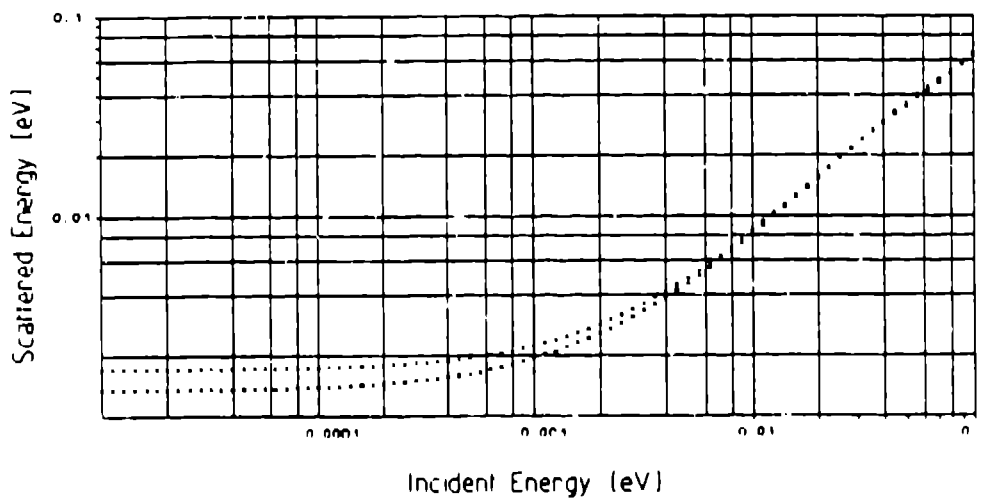
- (i) unavoidable: material that must be present (container walls, safety windows, etc.)
- (ii) avoidable: material that may be removed, but with consequences on other aspects of the SINQ design.

The actual losses will come from three effects—direct absorption, scattering of the neutrons to outside the acceptance of the beam tube, and upscattering. A particularly unfortunate material to have in the path of the beam is D<sub>2</sub>O, as it is a good upscatterer. The spectra for neutrons transmitted through various thickness D<sub>2</sub>O layers (and averaged over all escapes, irrespective of position) has been calculated. The results are presented in Fig. 5 as the ratio of the intensity per unit wavelength in the transmitted spectrum to that in the incident spectrum.

**2.2 Cryogenics.** We have a cold box that can give about 2.4 kW cooling power at 15 K, but which must also provide cooling for an H<sub>2</sub> source (it is possible that a higher temperature for the helium gas will be used with consequent gain of cooling power). Preliminary estimates for the heating of the inner parts of the D<sub>2</sub> source (cooled by liquid deuterium) is 1.5 to 2 kW/mA. The actual heating will be a function of the final design (wall thickness, actual position of the source cell in the moderator tank, etc.)



**Fig. 1** The calculated total cross section for scattering of neutrons from deuterium molecules at 25 K. The measured results are from W.D. Sieffert<sup>(4)</sup> and are for liquid D<sub>2</sub> at 19 K.



**Fig. 2** The average energy of neutrons scattered by deuterium molecules at 25 K as a function of incident neutron's energy.

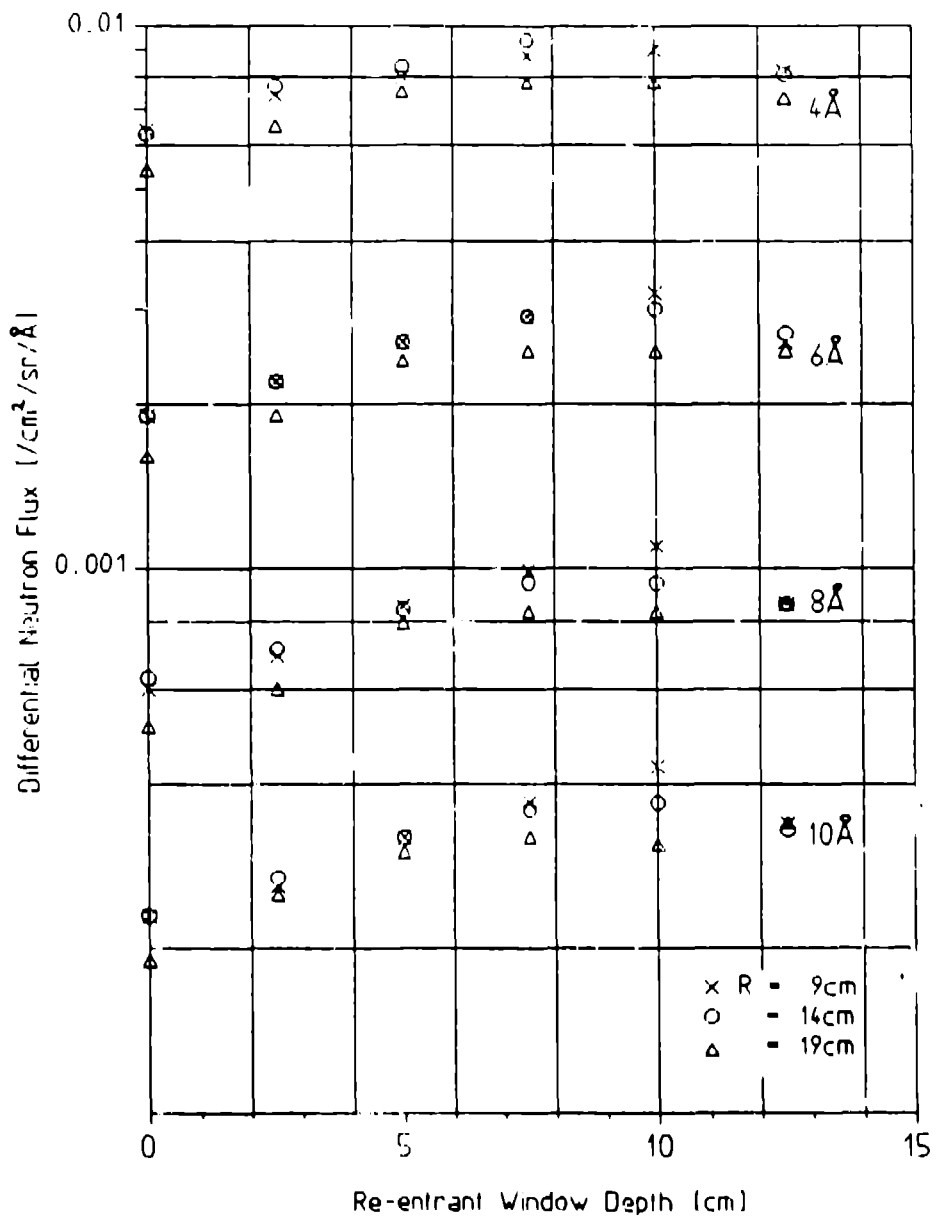


Fig. 3 The variation of cold neutron intensity at given wavelengths as a function of beam window position and depth of re-entrant window. The intensities are normalised to unit thermal flux at the position of the flat surface of the cylinder nearest to the target.

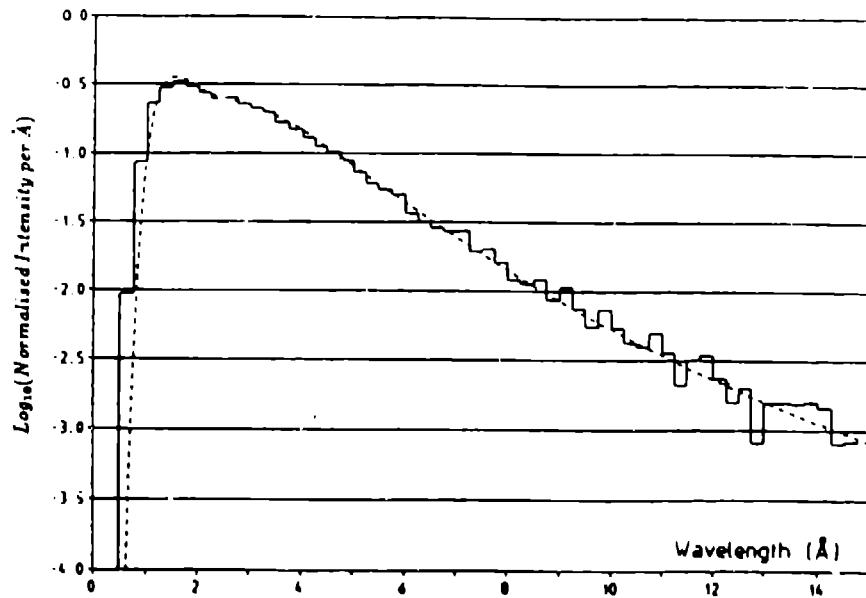


Fig. 4 The calculated neutron escape spectrum from the  $D_2$  cold-source (histogram) for a 80-mm-wide beam window centered 90 mm from the end of the source nearest the target and re-entrant to a depth of 25 mm, together with the result of a two-component Maxwellian fit to the data in the region 1.25 to 9.75 Å.

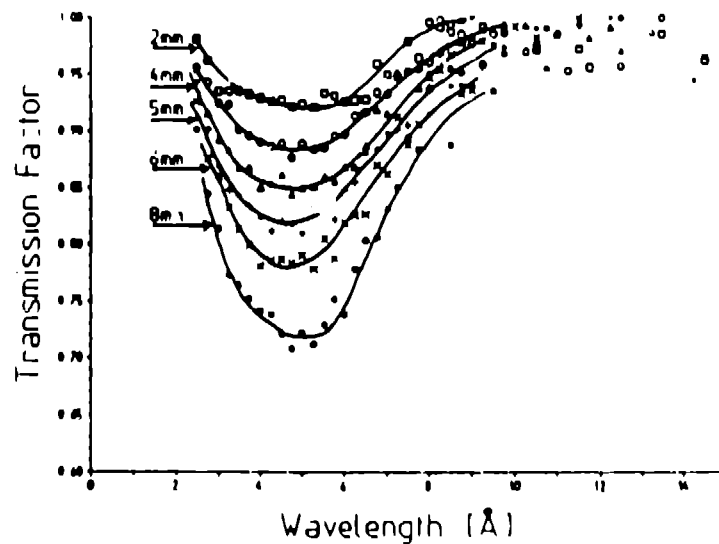


Fig. 5 The ratio of the transmitted to incident intensity per unit wavelength as a function of wavelength for various thickness layers of  $D_2O$ .

The liquid part of the system (at about 25 K) requires a vacuum insulation layer with a pressure =  $10^{-5}$  Torr.

**2.3 Thermohydraulics.** The main parameter to be fixed is the hydrostatic head for the thermosyphon circuit. The aim should be to have as short and smooth a path as possible between cell and condenser but against this are the following:

- (i) chicanes in the transfer line to limit streaming paths in the shielding;
- (ii) putting enough distance so that connections and components are in low heating and low activation regions; and
- (iii) making things accessible for maintenance.

The  $D_2$  mass-flow to transfer the heat is about 7 g/s (1.5 mA operation), that is about 2.2 litres/s of gas flowing to the condenser and 50 cm<sup>3</sup> of liquid  $D_2$  in the return path. The hydraulic losses will be compensated by the liquid- $D_2$  head to the condenser, but estimation of the required height is complicated by:

- A variable degree of two-phase flow in the return line (i.e., the actual  $D_2$  mass-flow will be higher due to a liquid/vapor mix being present).
- The needs to include bends (a) to turn the transfer lines into the vertical and (b) to minimize the length of direct streaming paths through the shielding.
- Pressure loss through the  $D_2$ -cell itself.

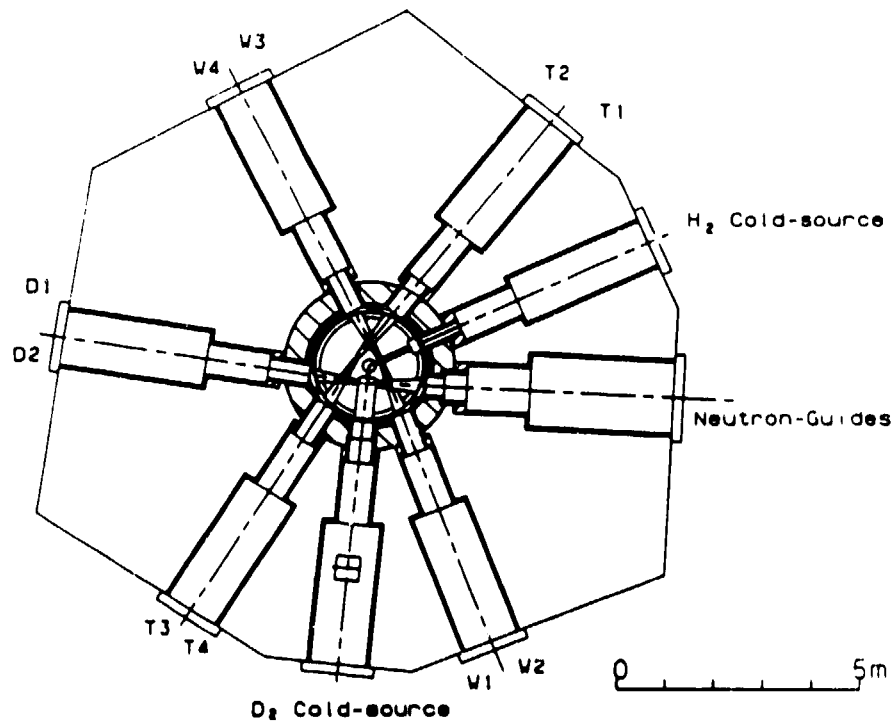
**2.4 Shielding and Induced activation.** The axis of the source is in direct line with the target and, hence, looks directly at the high-energy neutron source. The shield design has two main aims:

- (i) to reduce activation in the region of the change from horizontal to vertical so that "hands on" maintenance can be used (see Section 3.1); and
- (ii) to reduce the dose rate at the outer surface of the assembly to  $\leq 0.5$  mrem/hour, but to do this within the geometrical limits of the bulk-shield to avoid loss of operating space for instruments on the adjacent beam ports (see Fig. 6).

The transfer-line connections in the plug assembly include chicanes to limit the length of direct streaming paths, and a final large homogeneous shielding plug can be inserted behind.

The inner parts of the cold-source system will become highly activated during operation and a shielded container to extract the source into and for its transport to a suitable place for repair will be required. Where possible, materials that give the lowest possible post-irradiation dose are to be selected.

**2.5 Radiation damage.** Radiation damage will change material properties during the lifetime of the source and needs to be taken into account in the engineering design of the source-cell and auxiliary containers (items in the highest radiation field). The choice of "auxiliary" materials (for seals, etc.) will also be made with due regard for the radiation field where they are to be located, so as not to have the operational life of the source limited by such auxiliary materials.



**Fig. 6** Layout of the beam tubes and plugs for the cold sources.

**2.6 Safety.** The three major concerns are (i) deuterium explosion or fire, (ii) overpressure, and (iii) radiation. The principal safety measures planned are as follows:

- (a) A minimum of three walls between liquid deuterium and any source of oxygen (or uncontrolled atmosphere). The two outer regions will contain a controlled inert atmosphere. For the (warm) gaseous deuterium parts of the system, we plan to use one less wall.
- (b) The use of high-purity deuterium and stringent operational procedures so that this purity is maintained.

These measures are to prevent (i) oxygen and deuterium coming into contact, (ii) blockage of the thermosyphon system by frozen contaminants, and (iii) containment for tritium.

Pressure transients that result from reasonable operational equipment failures will be limited by provision of bursting discs and by including in the choice of sizes for transfer lines (cryogenic, gas line to the buffer volume, vacuum, etc.) the need for a suitably high gas conductance.

During operation there will be production of about 150 Ci/year tritium by neutron capture in the  $D_2$ . This requires that the complete  $D_2$  system be surrounded by a controlled atmosphere with tritium monitoring, and that all pump exhausts, emergency  $D_2$  dumping arrangements, pressure relief systems, etc., have appropriate venting arrangements.

### 3. Source layout

**3.1 Bulk shield insert.** The  $D_2$  cold-source is to be inserted into a gas-tight box built into the bulk shield between beam-tube pairs T3/4 and W1/2 (see Fig. 7). The box has a vacuum liner that extends into the beam-tube assembly in the moderator tank and gives the vacuum insulation for the cryogenic parts of the source. It will be cooled over the first meter or so and is also the second wall for the containment; the third wall is provided by the inner helium containment system for SINQ. The insert itself has the source cell (a cylindrical flask of about 300 mm diameter and 300 mm length), an auxiliary  $D_2O$  tank mounted behind the source cell to reduce flux depression and the shielding plug with the transfer lines. The inner parts of the shielding block will require forced cooling. The overall shielding is complete by a large mobile block.

The region about 4200 mm from the target center line has the changeover to the vertically mounted section. This has a system of flanges to allow source insertion and extraction. The details of this region may be seen in Fig. 8, which shows the principal operations of a plug change.

**3.2 Vertical insert.** This consists of the vertical part of the transfer lines and the condenser/phase-separator system. These are mounted in a chimney through the fixed part of the bulk shield with a continuation of the vacuum system and a cover gas system (possibly nitrogen), which is independent from the helium of the horizontal part. Access to these parts will be from above (the upper part of the bulk shield consists of "loose" blocks). The transfer lines (deuterium-gas, vacuum, cold-helium, etc.) will cross to a plant area located just off the bulk shield with the cold-box, vacuum pumps, etc.

### References

1. I. S. Anderson and F. Atchison, in these proceedings.
2. J. M. Anstruc and K. H. Gobrecht, 1987, Proc. 17th Int. Conf. on Cryogenic Techniques, Vienna.
3. J. A. Young and J. U. Koppel, 1964, Phys. Rev. **135**, A603.  
J. U. Koppel and J. A. Young, 1966, Nukleonik **8**, 40.
4. W. D. Sieffert, 1970, Euratom Report EUR 4455d.

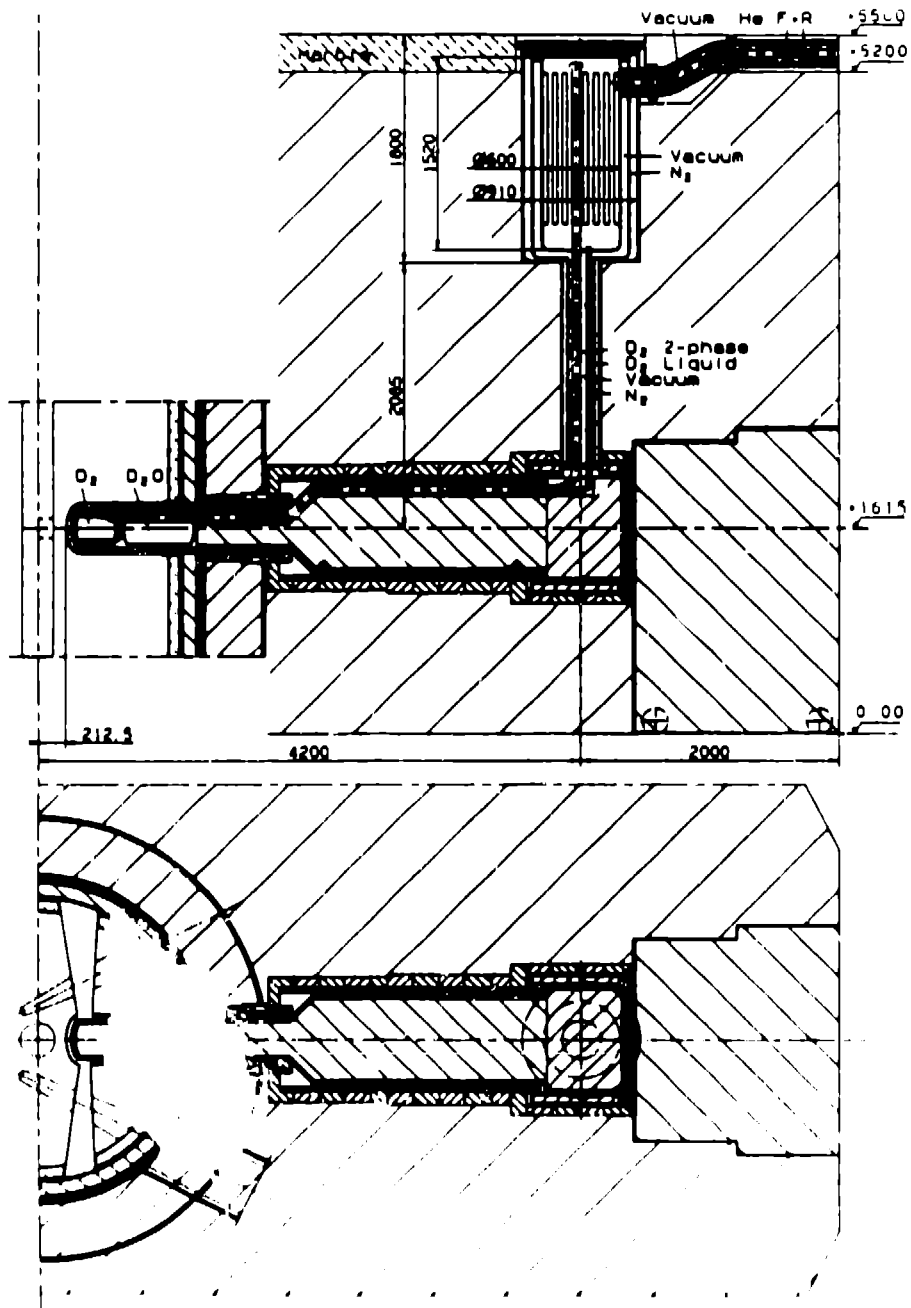


Fig. 7. The layout of the  $D_2$  source in the bulk shield.



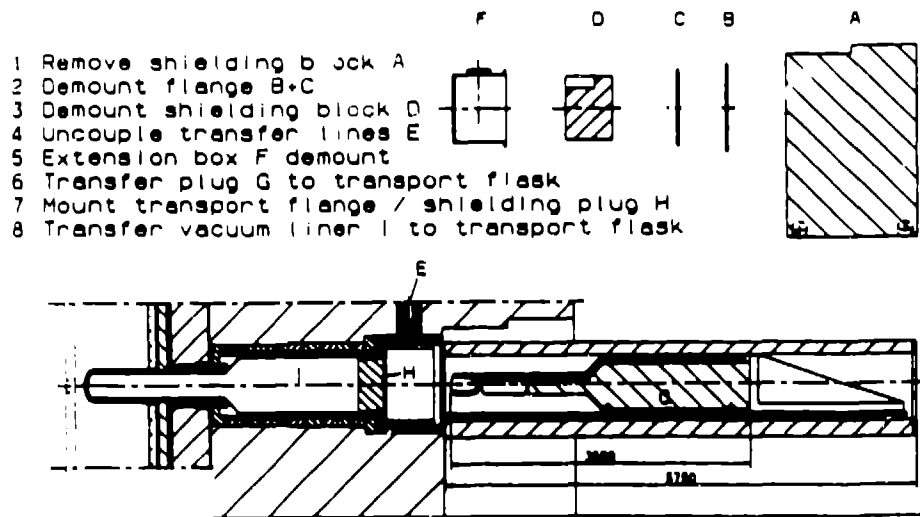


Fig. 8 Details of the plug change operation.

## LANSCCE steady-state unperturbed thermal neutron fluxes at 100 $\mu$ A

G. J. Russell  
Los Alamos Neutron Scattering Center  
Los Alamos, New Mexico 87545 U.S.A.

**ABSTRACT:** The "maximum" unperturbed, steady-state thermal neutron flux for LANSCE is calculated to be  $2 \times 10^{13}$  n/cm<sup>2</sup>-s for 100  $\mu$ A of 800-MeV protons. This LANSCE neutron flux is a comparable entity to a steady-state reactor thermal neutron flux. LANSCE perturbed steady state thermal neutron fluxes have also been calculated. Because LANSCE is a *pulsed* neutron source, much higher "peak" (in time) neutron fluxes can be generated than at a steady-state reactor source.

### Introduction

The intercomparison of pulsed-spallation-neutron-source and reactor-source performance is complex and ultimately has to be based on individual experiment/instrument particulars. Carpenter defined an "effective peak flux" to describe the performance of a pulsed neutron source.<sup>(1)</sup> Care should be used in quantitatively applying the "effective peak flux" concept to characterize pulsed neutron-source performance. However, for a pulsed spallation source, a "thermal" neutron flux can be calculated which is similar to a steady-state reactor thermal neutron flux. This spallation source neutron flux is the spatial maximum of the unperturbed steady state thermal neutron ( $E < 0.625$  eV) flux inside a moderator.

### Approach

The LANSCE spallation neutron source has been described elsewhere.<sup>(2)</sup> An expanded plan view of the LANSCE target/moderator arrangement is depicted in Fig. 1. Some nomenclature is in order. Liners eliminate neutron "crosstalk" between the moderator surface viewed by a flight path and the reflector/shield. Decouplers neutronically isolate the moderator per se from the reflector/shield. Poisons define an "effective" moderator volume for thermal and cold-neutron production. The neutron energies at which liners, decouplers, and poisons are neutronically effective depend on the material type and thicknesses.

At Los Alamos, we have a powerful Monte Carlo computational capability applicable to spallation-neutron-source-performance computations.<sup>(3)</sup> I used this computational tool to calculate a variety of thermal neutron fluxes for the LANSCE target system. Thermal neutrons are defined to include all neutrons with energies below 0.625 eV. This is how thermal neutron fluxes are being quoted for the Advanced Neutron Source and for the ILL reactor;<sup>(4)</sup> the ILL is basically the "world standard" to which other neutron producing facilities are compared.

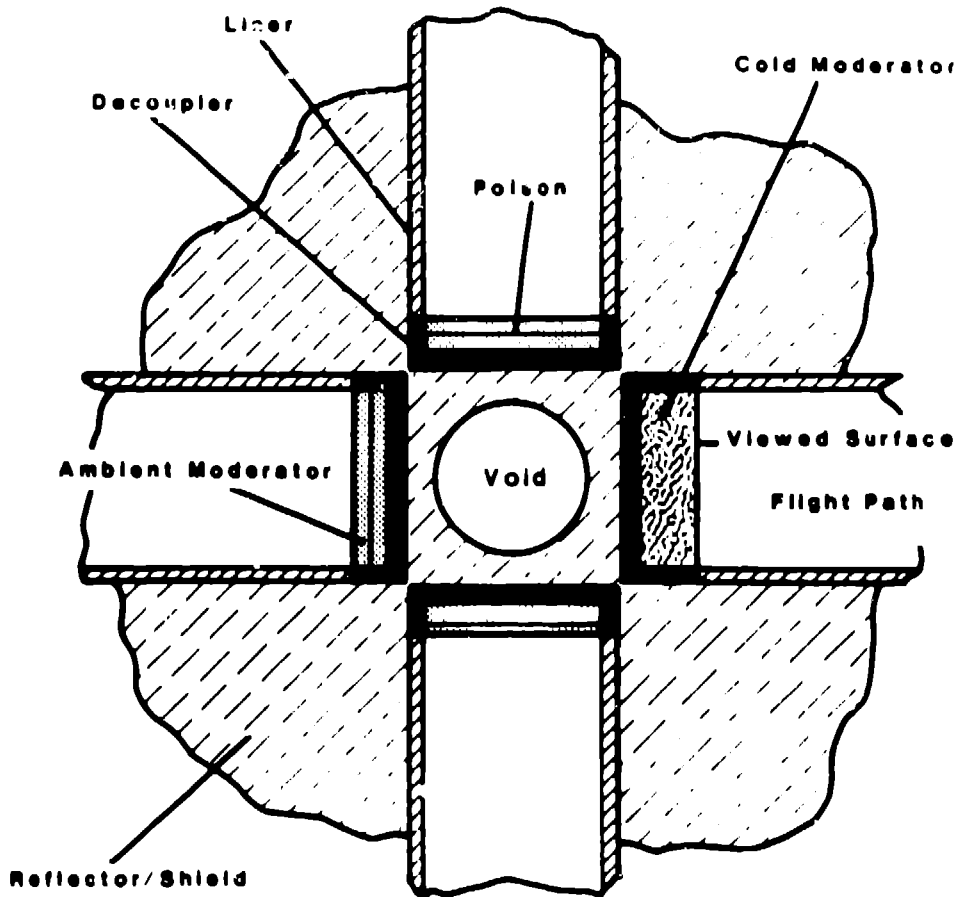


Fig. 1 Expanded plan-view schematic diagram of the LANSCE target/moderator arrangement. The liquid-hydrogen moderator is depicted on the right side.

Simplistically, LANSCE moderator neutron fluxes are *perturbed* in two ways: 1) neutronicly—with liners, decouplers, or poisons, and 2) spatially—by the intrusion of void spaces through the reflector/shield to extract neutron beams for experiments. I define a *decoupled* LANSCE moderator to be one in which poisons, decouplers, or liners are used. Conversely, a *coupled* LANSCE moderator is one where no poisons, decouplers, and liners are utilized. A *coupled/perturbed* moderator is perturbed by the void space used to extract neutron beams. A *coupled/unperturbed* moderator does not have a void space for neutron beam extraction. At present, LANSCE operates with four decoupled/perturbed moderators;<sup>[2]</sup> the thickness of the LANSCE H<sub>2</sub>O moderators is a nominal 3.5 cm.

## Results

A plot of the average thermal neutron flux at the surface of a LANSCE moderator viewed by an instrument is shown in Fig. 2 as a function of moderator thickness.

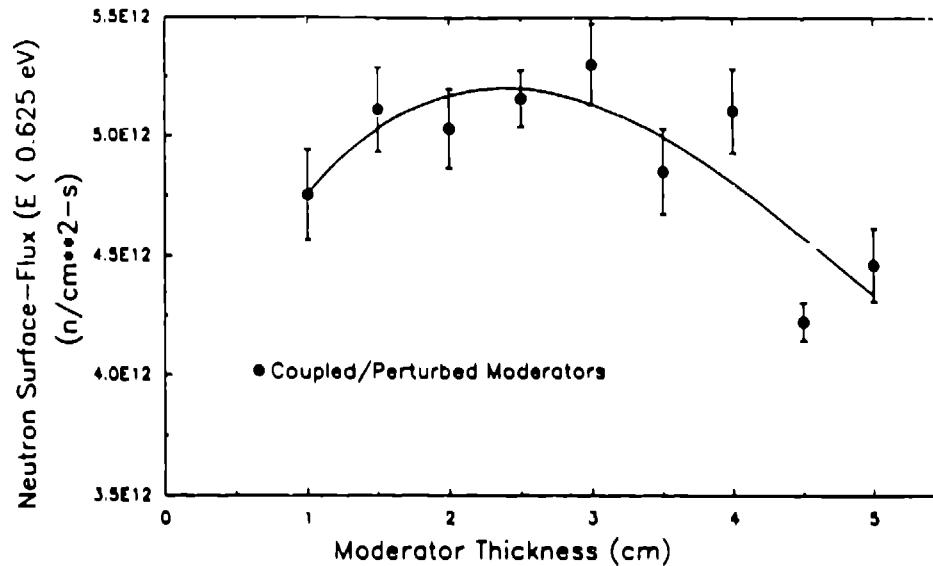


Fig. 2 LANSCE thermal neutron flux at a water moderator surface as viewed by an experiment, for 100  $\mu$ A of proton current.

These data are for coupled/perturbed 13 by 13 cm H<sub>2</sub>O moderators; the neutron flux is averaged over the 13 x 13 cm surface. The fluxes are, therefore, "useful" fluxes in a practical sense because they are averaged over a 169 cm<sup>2</sup> area. A polynomial fit to the data shows a broad peak in the range 1.5 to 3.5 cm.

I calculated the spatial distribution of thermal neutrons inside 2.5- and 3.5-cm-thick coupled moderators, for both perturbed and unperturbed cases. The results are shown in Figs. 3 and 4. For the 3.5-cm-thick moderator, the maximum thermal neutron flux is about  $2 \times 10^{13}$  n/cm<sup>2</sup>·s. This is to be compared to the ILL value of  $1.5 \times 10^{13}$  (see Ref. 4). Even though the surface fluxes (for the moderator surface viewed by an instrument) are similar for the two moderator thicknesses, there may be an advantage for the thicker moderator because of potential gain from the use of "honeycomb" moderators,<sup>[5]</sup> etc.

The thermal neutron flux from a LANSCE decoupled/perturbed H<sub>2</sub>O moderator is compared to that from coupled/perturbed and coupled/unperturbed H<sub>2</sub>O moderators in Fig. 5. One can see the gain (of about 6) in going from a decoupled to a coupled moderator. A further gain would be realized by removing the poison from within the decoupled moderator.<sup>[2]</sup>

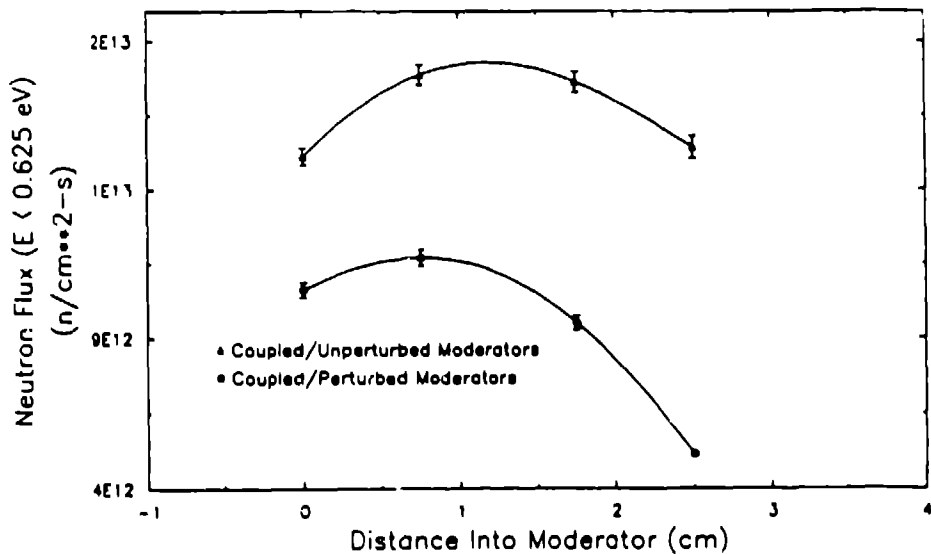


Fig. 3 Spatial distribution of thermal neutron flux for a 2.5-cm-thick LANSCE water moderator, for 100  $\mu$ A of proton current.

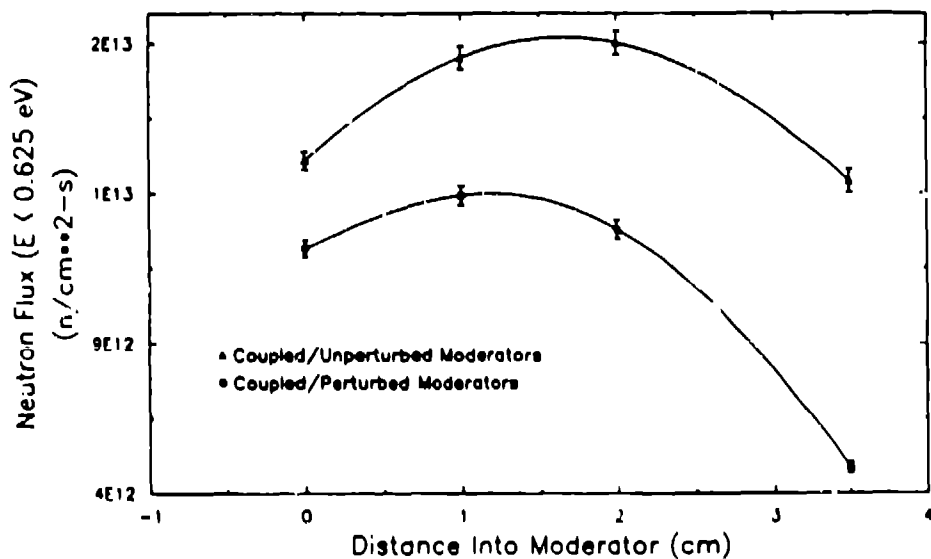


Fig. 4 Spatial distribution of thermal neutron flux for a 3.5-cm-thick LANSCE water moderator, for 100  $\mu$ A of proton current.

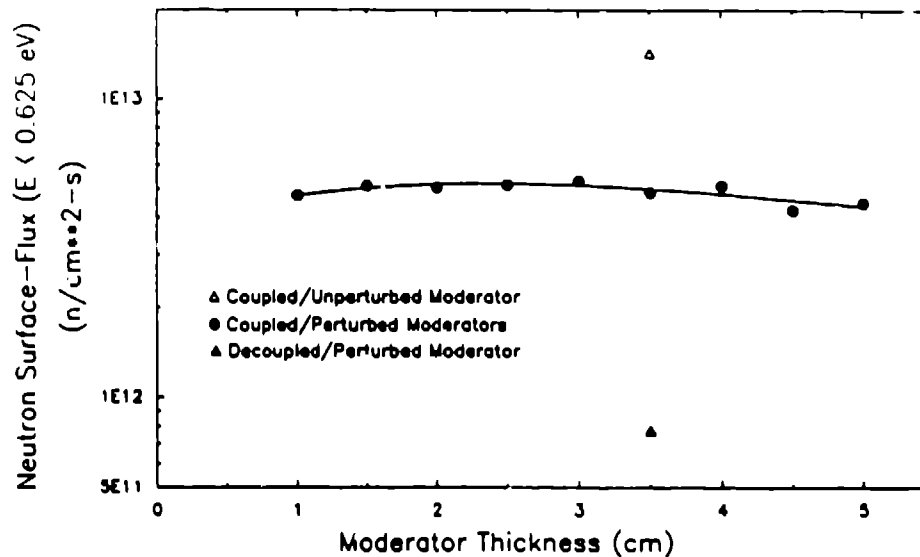


Fig. 5 Thermal neutron flux at the surface of various LANSCE water moderators, for 100  $\mu$ A of proton current.

## Conclusions

Thermal neutron fluxes have been calculated for the LANSCE spallation neutron source. The steady-state thermal neutron flux value of  $2 \times 10^{13}$  is similar to a steady-state reactor thermal neutron flux. Because LANSCE is a pulsed-spallation neutron source, much higher peak (in time) thermal neutron fluxes are generated than at a steady-state reactor. Intercomparing the performance of a pulsed neutron source with a steady-state reactor source is complicated and dependent on experiment/instrument particulars.

Because of engineering realities associated with high-power source design, care should be exercised in extrapolating LANSCE thermal neutron flux values for 100  $\mu$ A of 800-MeV protons to higher proton currents and energies.



## Acknowledgements

I appreciate useful discussions with André Michaudon, Roger Pynn, Gerald Garvey, and Gail Legate. I acknowledge the support of Dick Woods for this work. Many thanks to Teri Cordova for her typing help.

This work was performed under the auspices of the U.S. Department of Energy, Office of Basic Energy Sciences.



## References

1. J. M. Carpenter, et al., "IPNS—A National Facility for Condensed Matter Research", Argonne National Laboratory report ANL-78-88 (November 1978).
  2. G. J. Russell, et al., "The LANSCE Target System", ICANS-IX Proceedings of the 9th Meeting of the International Collaboration on Advanced Neutron Sources, Villigen, Switzerland, September 22-26, 1986, ISBN 3-907998-01-4, pp. 177-244 (April 1987).
  3. R. E. Prael, "High-Energy Particle Monte Carlo at Los Alamos", Monte Carlo Methods and Applications in Neutronics, Photonics, and Statistical Physics, eds., R. Alcouffe, R. Dautray, A. Forster, G. Ledanois, and B. Mercier, Springer-Verlag Publisher, Berlin/Heidelberg, 1985, pp. 177-244 (April 1987).
  4. C. D. West, "The U. S. Advanced Neutron Source", these proceedings.
  5. R. E. Mayer, et al., these proceedings.
- 
- 

## LANSCE target system performance

*G. J. Russell, J. S. Gilmore, H. Robinson, G. L. Legate, A. Bridge, R. J. Sanchez,  
R. J. Brewton, and R. Woods*  
Los Alamos Neutron Scattering Center  
Los Alamos, New Mexico 87545 U.S.A.

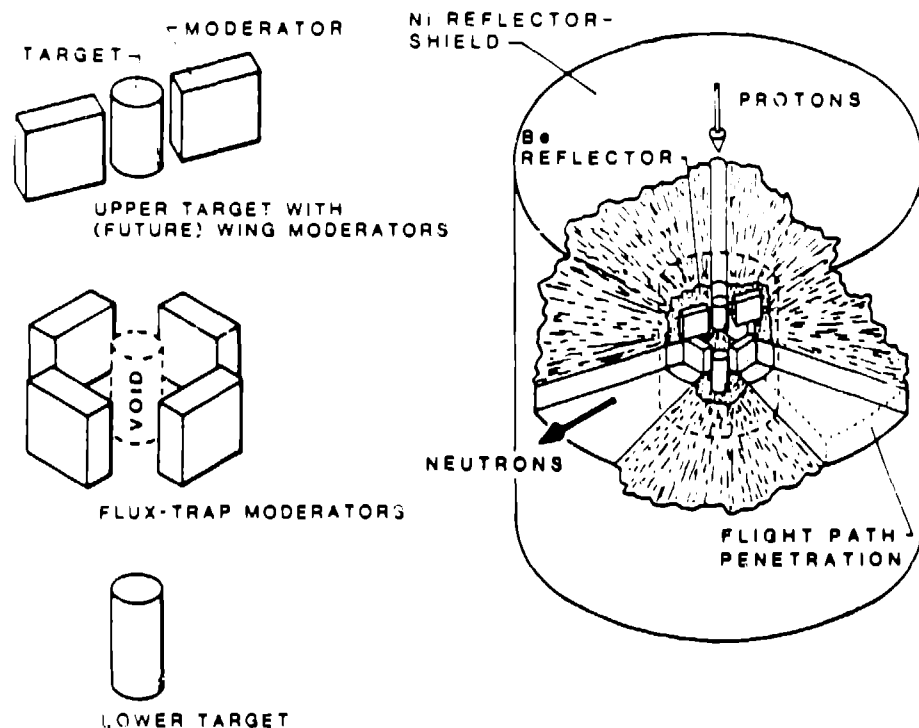
*H. G. Hughes, III*  
Radiation Transport Group, X-6  
Los Alamos, New Mexico 87545 U.S.A.

**ABSTRACT:** We measured neutron beam fluxes at LANSCE using gold foil activation techniques. We did an extensive computer simulation of the as-built LANSCE Target/Moderator/Reflector/Shield geometry. We used this mockup in a Monte Carlo calculation to predict LANSCE neutronic performance for comparison with measured results. For neutron beam fluxes at 1 eV, the ratio of measured data to calculated varies from  $\approx 0.6$ -0.9. The computed 1 eV neutron leakage at the moderator surface is  $2.9 \times 10^{10}$  n/eV-sr-s- $\mu$ A for LANSCE high-intensity water moderator and the corresponding values for the LANSCE high-resolution water moderator and the liquid hydrogen moderator are 3.3 and  $2.9 \times 10^{10}$ , respectively. LANSCE predicted moderator intensities (per proton) for a tungsten target are essentially the same as ISIS predicted moderator intensities for a depleted uranium target. The calculated LANSCE steady state unperturbed thermal ( $E < 0.625$  eV) neutron flux (at 100  $\mu$ A of 800 MeV-protons) is  $2 \times 10^{13}$  n/cm<sup>2</sup>-s. The unique LANSCE split-target/flux-gap-moderator system is performing exceedingly well. The system has operated without a target or moderator change for over three years at nominal proton currents of  $\approx 0.5$   $\mu$ A of 800-MeV protons.

### 1. Introduction

The Manuel Lujan, Jr. Neutron Scattering Center (LANSCE)<sup>(1)</sup> is a state-of-the-art pulsed spallation neutron source. The origin of the 800-MeV protons for LANSCE is the Clinton P. Anderson Meson Physics Facility (LAMPF)<sup>(2)</sup>. LAMPF 800-MeV protons feed the Proton Storage Ring (PSR)<sup>(3)</sup> which produces short (270 ns), intense proton pulses for LANSCE. An international user community utilizes LANSCE for condensed matter and nuclear physics research. The LANSCE target system needs to be operated efficiently, and continually upgraded to remain competitive worldwide. The LANSCE Target/Moderator/Reflector/Shield (TMRS)<sup>(4)</sup> provides spectrometers with potent neutron beams with appropriate time-structure and energy-spectral distributions.





**Fig. 1** Illustration of the LANSCE target system consisting of a split-target, an inner beryllium/nickel reflector region, and an outer nickel reflector/shield. Three water slab-moderators and a liquid hydrogen slab-moderator are in flux-trap geometry between two tungsten targets. The system is one meter in diameter and one meter high.

The LANSCE TMRS is depicted in Fig. 1. Presently, there are four slab-moderators in flux-trap geometry between the split targets. The four flux-trap moderators service twelve existing flight paths. Two additional moderators are envisioned adjacent to the upper target (in either wing- or slab-geometry) to service four new neutron flight paths. These two "upper-moderators" are part of the LANSCE upgrade project, scheduled for completion in 1992.

The LANSCE TMRS has four unique features:

- There is *no cryp* per se (void region) surrounding the TMRS.
- The target is *not in one piece*, but split into two unequal segments separated by a void.
- Moderators are *not* located adjacent to the target as in the more conventional

wing-geometry design. In the LANSCE target system, the moderators are in slab-geometry located in a flux-trap arrangement where there is no target material. They lie *between* the two target segments and surround a central void region.

- A conventional all-beryllium reflector is *not used*; the LANSCE TMRS employs a composite (beryllium/nickel) reflector/shield arrangement.

One significant advantage of our flux-trap geometry is that all four flux-trap moderators are high-intensity. This is in contrast to conventional wing-geometry moderators employed at ISIS<sup>[5]</sup> and IPNS<sup>[6]</sup>. At the latter spallation sources, moderators are located at both the front and back of the target to increase the number of flight paths serviced simultaneously. Because neutron production from spallation targets is strongly dependent on axial location, moderators in the fore position are nominally a factor of two more intense than aft placed moderators. This relative performance of fore and aft moderators in wing-geometry has been predicted theoretically<sup>[7]</sup> and observed experimentally. LANSCE flux-trap moderator performance should be akin to high-intensity, wing-moderator performance.

The twelve existing LANSCE neutron flight paths are depicted in Fig. 2. The four LANSCE TMRS flux-trap moderators are shown in Fig. 3; each moderator services three flight paths. Three of the moderators are ambient temperature water. Two of the water moderators are heterogeneously poisoned at 2.5 cm from the exit face with gadolinium and have cadmium decoupler/liners. We call these two moderators "high-intensity" moderators. The third water moderator is heterogeneously poisoned with gadolinium at 1.5 cm and has a boron decoupler/liner (1/e transmission at ~3 eV). We refer to this moderator as the "high-resolution" moderator.

For thermal neutrons, the *poison* neutronically defines the thickness of a moderator viewed by an experiment. *Decouplers* surround a moderator and neutronically isolate it from the reflector. *Liners* neutronically isolate the moderator "viewed surface" from the reflector/shield.

We recognize the importance of cold neutrons in condensed matter research, and our fourth flux-trap moderator is liquid para hydrogen at ~20 K. The liquid hydrogen moderator has no poison, a gadolinium decoupler, and a cadmium liner.<sup>[4]</sup>

The LANSCE TMRS was installed in August 1985, and has operated reliably (with no target or moderator changes) since its inauguration. Proton currents over the 3-year period were a nominal 25  $\mu$ A. During the run cycle recently completed, the average proton current to LANSCE was ~35  $\mu$ A.

## 2. Approach

Because the LANSCE TMRS is an innovative design (unique worldwide) for a

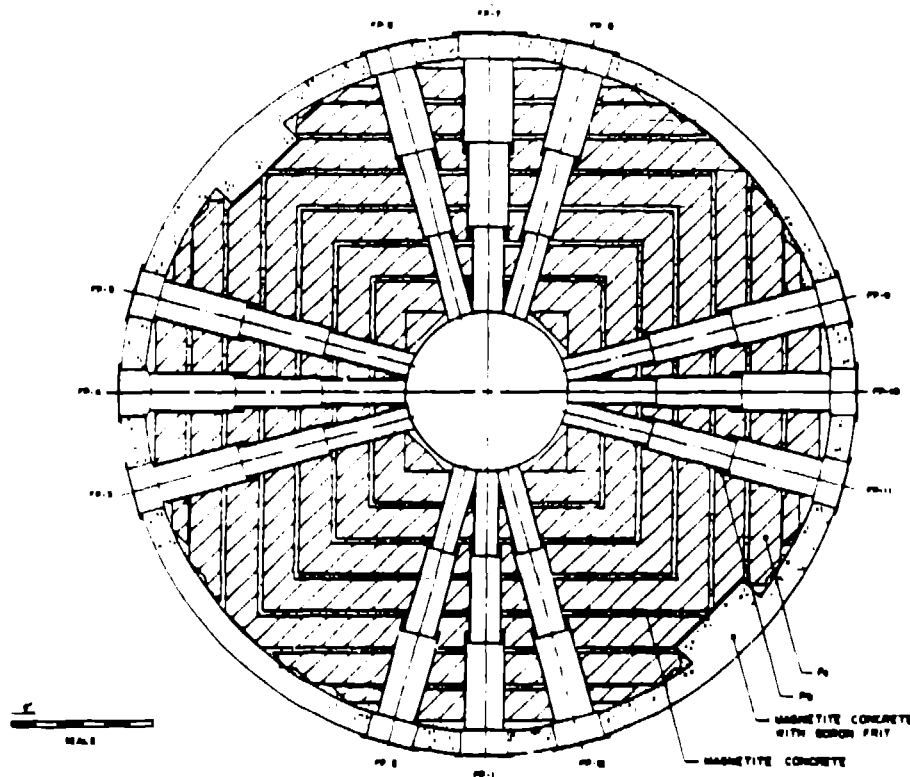


Fig. 2 Plan view of the LANSCE moderator and flight path arrangement.

spallation neutron source, it is imperative that we measure and calculate the neutronic performance of the as-built LANSCE target system. We must also compare the LANSCE absolute neutronic performance with those spallation neutron sources using conventional wing-geometry design.

We measured neutron beam fluxes using gold foil activation techniques. The details of these measurements are given in Ref. 8; the measurements were carried out on flight paths 1, 3, 7, and 8. During the design phase of the LANSCE target system, Russell<sup>(4,7)</sup> did preliminary calculations to estimate the neutronic performance. In order to directly compare measured and calculated neutron performance, Hughes<sup>(9)</sup> did a very detailed geometric mockup of the as-built LANSCE TMRS, and used the powerful Los Alamos Monte Carlo code system<sup>(10)</sup> to calculate the neutronic performance of LANSCE.

In this paper we concentrate only on neutron intensity, but the time behavior of neutrons is of paramount importance for a pulsed neutron source.

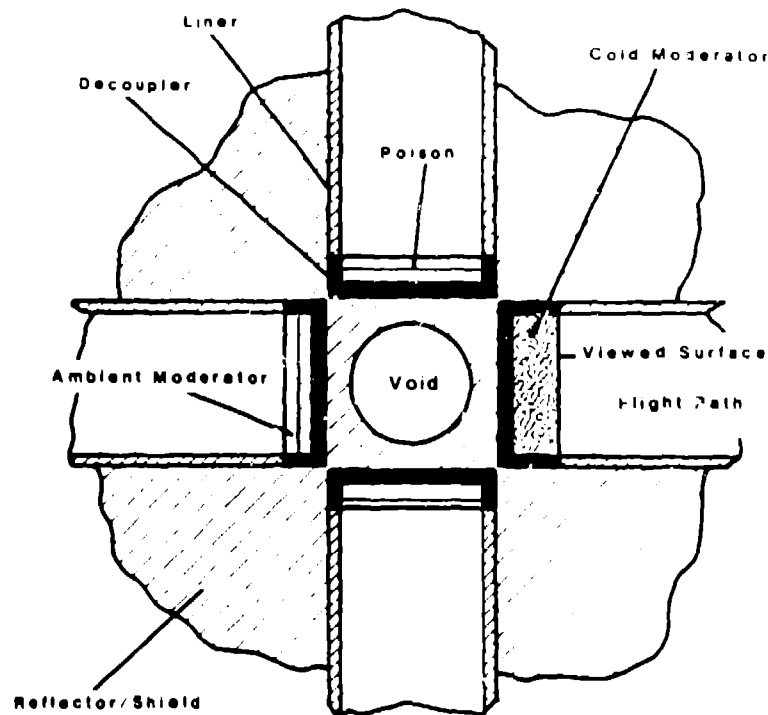


Fig. 3 Expanded plan view schematic of the LANSCE target/moderator arrangement. The liquid hydrogen moderator is depicted on the right side.

### 3. Results

#### 3.1 LANSCE Neutron Beam Fluxes

LANSCE instrument designer/users are interested in the *neutron beam flux* at their sample location. We measured LANSCE neutron beam fluxes for flight paths 1, 3, 7, and 8<sup>(8)</sup>, and did a detailed calculation of the corresponding neutron beam fluxes.<sup>(9)</sup> The results are shown in Table I.

In Table I, one can see that the ratio of measurement/calculation varies from 0.58-0.90. These are slightly larger variations than the preliminary values presented at the ICANS-X meeting. The differences are due to our changes in the assumed moderator field-of-view for each flight path. Subsequent to the ICANS-X meeting, Robinson<sup>(8)</sup> redetermined the moderator fields-of-view for each flight path where measurements were taken. He reviewed the actual flight path drawings, and applied a consistent definition of moderator field-of-view to all the flight paths. Hughes<sup>(9)</sup> recalculated the neutronic performance using the new fields-of-view.

Flight Path	Moderator Type	Moderator Field-of-View (cm <sup>2</sup> )	1eV Neutron Beam Flux		Ratio Measured to Calculated
			Measured (n/eV·cm <sup>2</sup> ·p)×10 <sup>9</sup>	Calculated (n/eV·cm <sup>2</sup> ·p)×10 <sup>9</sup>	
1	High-Resolution H <sub>2</sub> O	141.2	0.44	0.49	0.90
3	High-Intensity H <sub>2</sub> O	131.5	5.26	7.66	0.69
7	High-Intensity H <sub>2</sub> O	139.8	2.61	3.93	0.66
8	High-Intensity H <sub>2</sub> O	50.8	3.40	5.90	0.58

There are several variables that strongly influence the agreement between measured and calculated neutron beam fluxes. They are:

- The number, spatial distribution, and position of protons striking the target.
- The flight path collimation system and the resulting moderator field-of-view.
- The alignment of the flight path collimation system within the LANSCE bulk shield.
- Flux depression, multiple scattering, effective cross section corrections, etc. to the measured data.

At LANSCE, we presently have no direct measurement of the number, spatial distribution, and position of protons striking the LANSCE target. Gilmore<sup>(1)</sup> overestimated the number of protons striking the LANSCE target by assuming that *all* the protons passing through his aluminum monitoring foil struck the LANSCE target. The proton monitoring foil was located in the LANSCE beam line upstream from the LANSCE 90° bending magnet system. This conservative position would underestimate measured LANSCE neutron beam fluxes. Discrepancies in determining flight path collimation or the practical alignment of a collimation system in the LANSCE bulk shield will affect both measured and calculated data. Also, more work needs to be done using calculated neutron spectra to ascertain appropriate correction factors for the measured gold foil data.

### 3.2 LANSCE Neutron Source Intensities

Spallation neutron source designers typically quote *neutron source intensity*, which is the angle dependent neutron leakage at the moderator surface. Calculated neutron leakage at 1 eV and  $E < 0.625$  eV (thermal neutrons) are shown in Table II for 1  $\mu$ A of protons. The 1 eV neutron leakage is  $3.9 \times 10^{10}$  n/eV-sr-s- $\mu$ A for the two LANSCE high-intensity water moderators. The corresponding values for the LANSCE high-resolution and liquid hydrogen moderators are 3.3 and  $2.9 \times 10^{10}$ , respectively. These LANSCE neutron leakages are respectable values for a spallation

Table II Calculated Neutron Leakage Currents at Various LANSCE Moderator Surfaces for a 12x12 cm Field-of-View

Flight Paths	Moderator Type	1eV Neutron Leakage Current (n/eV·sr·s· $\mu$ A) $\times 10^{-10}$	Thermal(<0.625eV) Neutron Leakage Current (n/sr·s· $\mu$ A) $\times 10^{-11}$
1, 2, 12	High Resolution H <sub>2</sub> O	3.3 $\pm$ 0.4	0.98 $\pm$ 0.07
3, 4, 5	High-Intensity H <sub>2</sub> O	3.9 $\pm$ 0.5	2.0 $\pm$ 0.1
6, 7, 8	High-Intensity H <sub>2</sub> O	3.9 $\pm$ 0.5	1.9 $\pm$ 0.1
9, 10, 11	Liquid Hydrogen	2.9 $\pm$ 0.4	1.7 $\pm$ 0.1

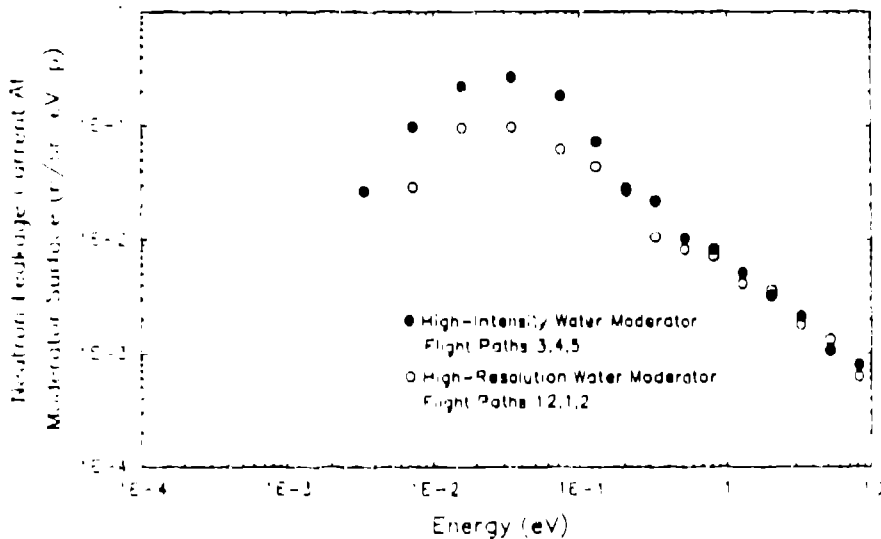
Table III Calculated Neutron Leakage Currents at Various LANSCE Moderator Surfaces for a 12x12 cm Field-of-View

Flight Paths	Moderator Type	1eV Neutron Leakage Current (n/eV·sr·p) $\times 10^3$	Thermal(<0.625eV) Neutron Leakage Current (n/sr·p) $\times 10^2$
1, 2, 12	High Resolution H <sub>2</sub> O	5.3 $\pm$ 0.7	1.6 $\pm$ 0.1
3, 4, 5	High-Intensity H <sub>2</sub> O	6.3 $\pm$ 0.7	3.2 $\pm$ 0.2
6, 7, 8	High-Intensity H <sub>2</sub> O	6.3 $\pm$ 0.7	3.1 $\pm$ 0.2
9, 10, 11	Liquid Hydrogen	4.7 $\pm$ 0.6	2.7 $\pm$ 0.1

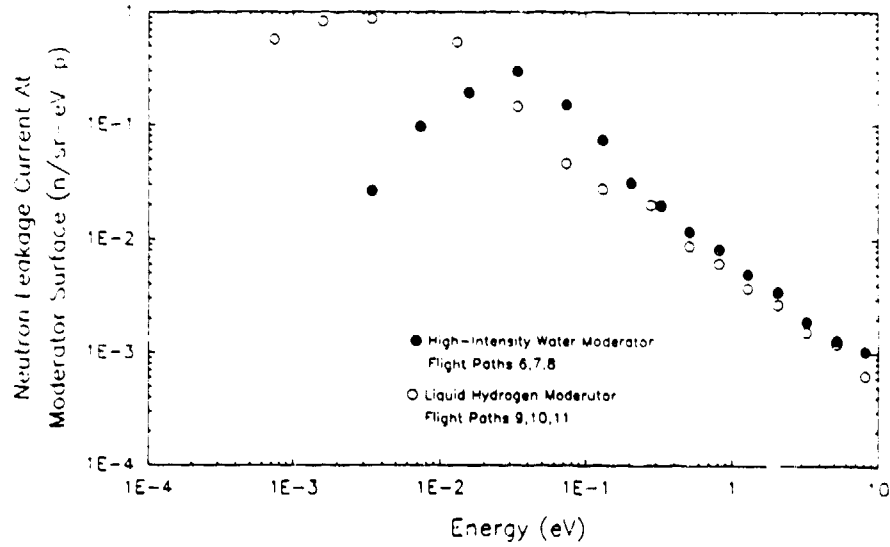
source employing a tungsten target. Thermal neutron leakages for a spallation neutron source are not usually quoted. The LANSCE moderator neutron leakage values are given in Table III on a per proton basis.

In the design of the LANSCE TMRS, Russell<sup>(4)</sup> used a simplified mockup employing only two (not four) flux-trap moderators. He also did not dilute material atom densities with cooling passages. A "rule-of-thumb" engineering factor of 0.7 was assumed to estimate the as-built LANSCE TMRS performance from the simplified mockup. The actual factor is 0.62, as derived by comparing results from Russell's simplified mockup with the detailed simulation by Hughes.<sup>(9)</sup>

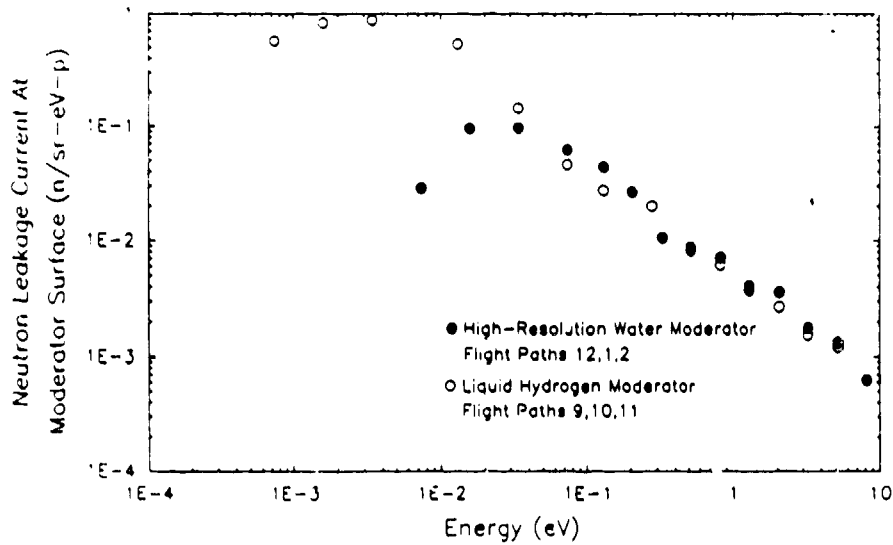
We show computed neutron leakage spectra at the LANSCE moderator surfaces in Figs. 4-6. In Fig. 4, we compare the performance of a LANSCE high-intensity water moderator to the high-resolution water moderator. The effect on thermal neutron flux of tailoring moderator performance for resolution is shown in Fig. 4. The ratio of high-intensity/high-resolution thermal neutron leakage is about a factor of 2. However, the neutron pulse widths for the high-resolution moderator are narrower. The calculated neutron leakage spectra from the LANSCE liquid hydrogen, high-intensity, and high-resolution moderators are shown in Figs. 5 and 6. Cold moderators are used at pulsed spallation sources for two reasons: a) to extend the slowing-down (1/E) region to lower energies thereby retaining narrow neutron pulse widths; and b) to produce low-energy neutrons. The ability of the LANSCE liquid hydrogen moderator to produce low-energy neutrons is evident in Figs. 5 and 6.



**Fig. 4** Calculated neutron leakage spectra for LANSCE moderators showing the differences between high-intensity and high-resolution water moderators.

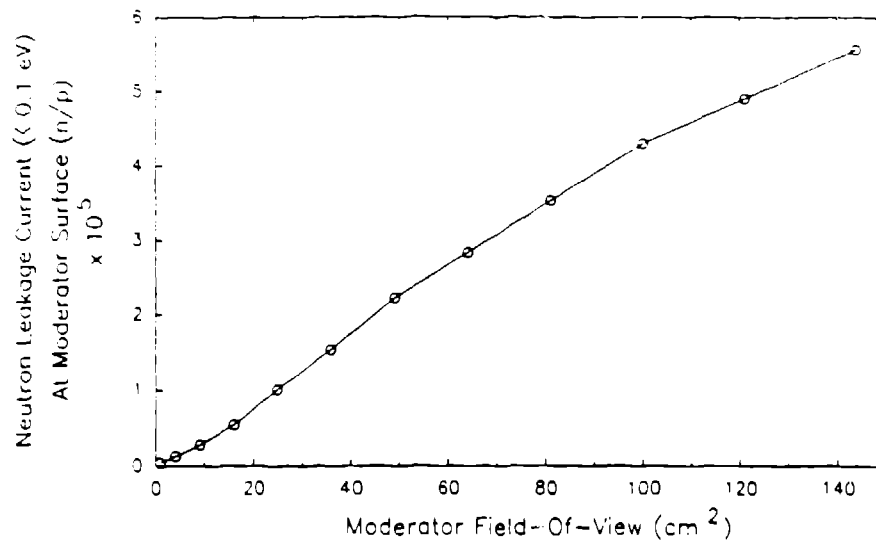


**Fig. 5** Calculated neutron leakage spectra for LANSCE moderators comparing a high-intensity ambient temperature water moderator with the liquid hydrogen moderator at  $\approx 20$  K.



**Fig. 6** Calculated neutron leakage spectra for LANSCE moderators comparing the high-resolution ambient temperature water moderator with the liquid hydrogen moderator at  $\approx 20$  K.





**Fig. 7** Calculated neutron leakage current from a high-intensity ambient temperature water moderator showing the effects of different moderator fields-of-view.

### 3.3 LANSCE Moderator Field-of-View Study

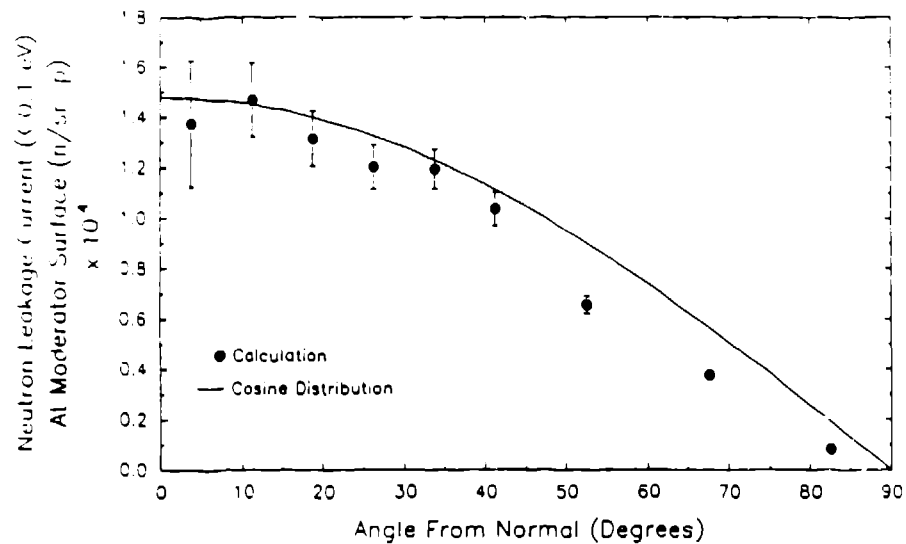
One advantage of the LANSCE flux-trap moderators is that they are in slab-geometry without directly looking at the target (see Fig. 3). This allows significant gains to be made to neutron intensities by using larger fields-of-view at the moderator. The neutron leakage current from a LANSCE high-intensity water moderator as a function of the moderator field-of-view is given in Fig.7. For example, an increase in the field-of-view from 100 to 144 cm<sup>2</sup> augments the neutron intensity < 0.1 eV by ~30%.

### 3.4 LANSCE Angle-Dependent Neutron Flux at a Moderator

We looked at the angular distribution of leakage neutrons < 0.1 eV relative to the normal to the moderator surface. The results of the calculation are shown in Fig. 8. For angles < ~40 degrees, the distribution is cosine-like; at larger angles, the intensities appear to fall off more rapidly than a cosine function.

### 3.5 LANSCE Steady State Unperturbed Thermal Neutron Flux

For a pulsed spallation neutron source, a "thermal" ( $E < 0.625$  eV) neutron flux can be calculated which is a comparable entity to a steady state reactor "thermal" neutron flux. This spallation source neutron flux is the spatial maximum of the unperturbed steady state thermal ( $E < 0.625$  eV) neutron flux inside a moderator.<sup>(11)</sup> For LANSCE at 100  $\mu$ A of 800 MeV protons, this calculated flux is  $2 \times 10^{13}$  n/cm<sup>2</sup>·s.<sup>(11)</sup>



**Fig. 8** Calculated angle-dependence of neutrons leaking from a LANSCE high-intensity ambient temperature water moderator. The angle is relative to the surface normal.

#### 4. Conclusions

The Monte Carlo computer codes used to predict low-energy neutron transport give sensible agreement with a variety of measured data.<sup>[12-14]</sup> This provides reason to believe that calculated predictions of 1 eV neutron beam fluxes should correspond to measured results to within ~20%. Not all the LANSCE measured and calculated neutron beam fluxes agree to this accuracy.

The strong dependence of LANSCE calculated neutron beam fluxes on the moderator field-of-view emphasizes the importance of collimation systems and their correct alignment (in a practical sense). One possible scenario for explaining the discrepancies between LANSCE measured and calculated neutron beam fluxes is that some flight path collimation systems are either misaligned or misunderstood. Also, at LANSCE the number, spatial distribution, and position of protons striking the target is uncertain; this situation needs improvement. The discrepancies between LANSCE measured and calculated neutron beam fluxes could also be real, requiring further explanation.

The LANSCE target system employs a tungsten target; the ISIS target system uses a depleted uranium target. Calculated LANSCE neutron leakages (per proton) at the various moderator surfaces are essentially the same as moderator leakages predicted for ISIS<sup>[15-17]</sup>.

*Given that the LANSCE TMRS is complicated and unique worldwide, the measured and calculated absolute neutron intensities for the as-built TMRS are particularly gratifying.*

The LANSCE target system has performed admirably for over three years. We intend to continue to understand and improve the neutronic performance of LANSCE; the calculational tools recently developed will aid those endeavors. We plan further measurements of neutron beam fluxes as new neutron beam lines are developed.

The LANSCE upgrade (which will add two new moderators adjacent to the upper target) is scheduled for completion in 1992. Our current thinking (subject to change) is to employ the following moderators at upgrade: a) two liquid methane moderators at  $\sim 77$  K; b) two liquid hydrogen moderators at  $\sim 20$  K; and c) two ambient temperature water moderators.





## **5. Acknowledgements**








We acknowledge the continued support of Roger Pynn for this work, and for the typing help of Teri Cordova. We (G. J. Russell) appreciate useful discussions with Walter Fischer.

This work was performed under the auspices of the U.S. Department of Energy, Office of Basic Energy Sciences.

## **6. References**

1. R. Pynn, "Recent Progress at LANSCE", in these proceedings.
2. M.S. Livingston, LAMPF, a Nuclear Physics Research Facility, Los Alamos National Laboratory Report, LA-6878-MS (1977).
3. R. J. Macek, "The Proton Storage Ring: Problems and Solutions", in these proceedings.
4. G. J. Russell, H. Robinson, G. L. Legate, R. Woods, E. R. Whitaker, A. Bridge, K. J. Hughes, and R. D. Neef "The LANSCE Target System", ICANS-IX Proceedings of the 9th Meeting of the International Collaboration on Advanced Neutron Sources", F. Atchison and W. Fischer, eds., September 22-26, 1986, SIN, Villigen, Switzerland, ISBN 3-907998-01-4, July 1987, pp. 177-244.
5. A. Carne, "Review of the SNS Target Station," ICANS-IV, Proc. of the Fourth Meeting of the International Collaboration on Advanced Neutron Sources, Tsukuba, Japan, October 20-24, 1980, KENS Report II, pp. 136-153 (March 1981).

- 
- 
- 
6. J. M. Carpenter, C. W. Potts, and G. H. Lander, "Intense Pulsed Neutron Source (IPNS) at Argonne National Laboratory (ANL): A Status Report as of June 1982", ICANS-VI, Proceedings of the Sixth Meeting of the International Conference on Advanced Neutron Sources, Argonne National Laboratory, June 28 - July 2, 1982, ANL-82-80 (January 1983).
  7. G. J. Russell, C. D. Bowman, E. R. Whitaker, H. Robinson, and M. M. Meier, "LANSCE High Power (200  $\mu$ A) Target-Moderator-Reflector-Shield", ICANS-VIII, Proc. of the Eighth Meeting of the International Collaboration on Advanced Neutron Sources, Oxford, England, July 8-12, 1985, RAL-85-110, pp. 272-293 (1985).
  8. J. S. Gilmore, R. A. Robinson, and G. J. Russell, "Experimental Determination of Neutron Beam Fluxes at LANSCE from Gold Foil Activation", in these proceedings.
  9. H. G. Hughes, III, "Monte Carlo Simulations of the As-Built LANSCE Target/Moderator/Reflector/Shield Geometry", in these proceedings.
  10. R. E. Prael, "High-Energy Particle Monte Carlo at Los Alamos". In Monte Carlo Methods and Applications in Neutronics, Photonics, and Statistical Physics, R. Alcouffe, R. Dautray, A. Forster, G. Ledanovis, and B. Mercier, eds., Springer-Verlag Publisher, Berlin/Heidelberg, 1985, pp. 196-206.
  11. G. J. Russell, "LANSCE Steady State Unperturbed Thermal Neutron Fluxes at 100  $\mu$ A", in these proceedings.
  12. G. J. Russell, M. M. Meier, J. S. Gilmore, R. E. Prael, H. Robinson, and A. D. Taylor, "Measurements of Spallation Target-Moderator-Reflector Neutronics at the Weapons Neutron Research Facility", ICANS-IV, Proceedings of the 4th Meeting of the International Collaboration on Advanced Neutron Sources, KEK, Tsukuba, Japan, October 20-24, 1980, KENS Report II, pp. 210-241 (March 1981).
  13. G. J. Russell, M. M. Meier, H. Robinson, and A. D. Taylor, "Preliminary Neutronics of a Reflected T-Shape Premoderator/Moderator for the Weapons Neutron Research Facility", ICANS-V, Proceedings of the 5th Meeting of the International Collaboration on Advanced Neutron Sources, Juelich, West Germany, June 22-26, 1981, Jul-Conf-45, ISSN 0344-5789, pp. 389-418 (October 1981).
  14. J. S. Gilmore, G. J. Russell, H. Robinson, and R. E. Prael, "Fertile-to-Fissile and Fission Measurements for Depleted Uranium and Thorium Bombarded by 800-MeV Protons", Nucl. Sci. and Engr., 99, 41-52 (1988).
- 

- 
- 
- 
15. A. D. Taylor, "SNS Moderator Performance Predictions", Rutherford Appleton Laboratory Report RAL-84-120 (December 1984).
  16. T. G. Perring, A. D. Taylor, and D. R. Perry, "Absolute Neutronic Performance of SNS from Gold Foil Activation", Rutherford Appleton Laboratory Report RAL-85-029 (May 1985).
  17. A. J. Leadbetter, et al., "First Neutron Results from SNS", Rutherford Appleton Laboratory Report RAL-85-030 (May 1985).
- 
- 
- 
- 

## Scattering cross sections and transport properties of $H_2$ and $D_2$ as obtained from a synthetic model

*J. R. Granada, V. H. Gillette, M. M. Scaffoni and R. E. Mayer*  
Centro Atomico Bariloche and Instituto Balseiro  
8400 S. C. de Bariloche (RN)  
ARGENTINA

**ABSTRACT:** In the frame of a synthetic scattering function, the interaction of slow neutrons with  $H_2$  and  $D_2$  is described in a simple way. The main advantage of the synthetic model is contained in the analytical expressions it produces for the total cross section and the isotropic and anisotropic energy-transfer kernels. They allow a very fast evaluation of neutron scattering and transport properties in liquid hydrogen and deuterium, including variation of the concentration in the ortho and para forms. The calculations are compared with available experimental data, showing very good agreement. The results presented here are relevant to cold neutron source design.

### Introduction

As examples of simple molecular systems, liquid hydrogen and deuterium have attracted considerable interest from a theoretical point of view, whereas their unique neutronic properties have made them a natural choice as moderating materials for the production of cold neutrons.

After the early total cross-section measurements performed by Squires and Steward<sup>(1)</sup> on liquid  $H_2$  and the theoretical work of Sarma<sup>(2)</sup>, many calculational techniques were developed, most of them based on the gas model of Young and Koppel<sup>(3)</sup>. As a consequence, the differentiating feature of those bound atom models has been in the treatment of the translational motion of the molecular unit, some of them<sup>(4,5)</sup> following the lines of the Egelsstaff-Schofield prescription for liquid systems<sup>(6)</sup>, while others have adopted a continuous frequency spectrum for this mode<sup>(7,8)</sup>. However, there is still a lack of experimental information on the neutron field behavior in those systems<sup>(9)</sup>.

The transformation properties of the total wavefunction in a homonuclear diatomic molecule causes the total nuclear spin  $I$  and the total angular momentum  $J$  to be correlated, thus producing a well-defined "selection rule" that governs the transitions between states corresponding to those quantum numbers<sup>(10)</sup>. Those correlations are especially important in the case of  $H_2$  and  $D_2$  at low temperatures, where not many rotational levels are excited and, consequently significant interference effects show up in the neutron cross sections for the ortho and para forms.

A knowledge of the full molecular dynamics is generally required to compute the cross sections for the neutron-molecule interaction. However, many neutron

properties can be evaluated through the use of a simplified scheme to represent the actual frequency spectrum, and this is the basic idea behind the development of the Synthetic Scattering Law<sup>(11)</sup>. The latter has been successfully applied to the description of neutron scattering and transport properties in several hydrogenous materials<sup>(12)</sup>. We present here some results of the synthetic model for H<sub>2</sub> and D<sub>2</sub> and compare them with available information.

### The model for H<sub>2</sub> and D<sub>2</sub>

The basic hypotheses borne into the synthetic scattering function have already been described<sup>(11,12)</sup>, so that only its main characteristics will be briefly commented upon here. The actual frequency spectrum of the system is lumped into discrete harmonic oscillator modes, each of these having an occupation number for the excited levels controlled by the system's temperature and an associated effective mass, which is a measure of its relative weight. Furthermore, collision-induced transitions between those levels are allowed in the neutron-molecule interaction, which in turn depends on the incident neutron energy E<sub>0</sub>. In this way, a synthetic scattering function T(Q, w, E<sub>0</sub>) is obtained, where the effects of the molecular dynamics on the cross sections is represented through the variation of an effective mass, temperature and vibrational factor.

Our model for H<sub>2</sub> and D<sub>2</sub> is built on the basis of the Young-Koppel<sup>(3)</sup> formalism to describe the rotational elastic and one-phonon inelastic cross sections, together with the prescriptions of the general synthetic model for the vibrational and translational forms of the molecular scattering function. Concerning this latter mode, an additional Einstein oscillator was introduced to represent the low-energy collective excitations, as it is well known that a simple gas model is not adequate to predict some scattering properties at low neutron energies<sup>(4,5,13)</sup>. The complete set of input parameters for our model calculations has been given elsewhere<sup>(14)</sup>.

Intermolecular interference effects show up in the measured total cross section of liquid H<sub>2</sub> and D<sub>2</sub> at low energies (~0.003 eV)<sup>(15)</sup>, where they partially cancel the intramolecular interference contribution for neutron wavelengths longer than the average distance between molecular centers. We have taken this behavior into account in a crude manner by imposing a complete cancellation of the coherent elastic scattering, whereas a more rigorous treatment of these effects should be based on the consideration of the static structure factor of the liquid system<sup>(16)</sup>.

By virtue of its simple form, the synthetic model produces analytical expressions for several magnitudes of interest in neutron thermalization problems, and consequently evaluations involving changes of parameters (ortho:para concentration, density, temperature, weighting spectrum) can be easily performed in a fast and accurate manner.

### Results

We show in Fig. 1 the results of our model, together with the experimental data of Seiffert<sup>(15)</sup> for the total cross section of para- and normal-hydrogen. The discrepancies observed at the low energy side are due to the crudeness in the treatment of the

translational motion in the case of n-H<sub>2</sub> and the forced neutralization of scattering components in the other case (p-H<sub>2</sub>). Besides those differences, the overall agreement is reasonably good.

The total cross-section data of Seiffert for liquid D<sub>2</sub> are compared in Fig. 2 with the synthetic model results for ortho- and normal deuterium. The agreement between experiment and calculation in this case is not as good as for H<sub>2</sub>, but still quite satisfactory.

Figure 3 shows the evaluated energy-transfer kernel for liquid H<sub>2</sub> at an incident neutron energy E<sub>0</sub> = 0.018 eV. It is observed that o-H<sub>2</sub> presents an almost gas-like behavior at this energy, while p-H<sub>2</sub> shows the effect of the J = 0 ≥ 1 flipping transition through a pronounced down-scattering contribution.

We used the analytically generated scattering kernels to evaluate some other integral properties. The slowing down power  $\xi\sigma$  (per atom) of ortho- and para-hydrogen is shown in Fig. 4, while the results corresponding to deuterium are presented in Fig. 5. In the case of o-H<sub>2</sub> (Fig.4), the large negative values of  $\xi\sigma$  even at energies above 0.001 eV, reflect the importance of upscattering processes through the transition J = 1 ≥ 0.

Besides the macroscopic density, neutron transport parameters are strongly dependent on the ortho:para ratio as well as on the neutron spectrum. We have adopted a Maxwellian distribution as a first order approximation to the actual spectrum, with different characteristic temperatures T<sub>M</sub> to simulate the spectrum hardening due to leakage in large buckling geometries. The results of our model for the neutron-transport-mean-free path  $\lambda_{tr}$  in liquid hydrogen and deuterium are shown in Figs. 6 and 7, respectively, over temperature ranges centered around the accepted equivalent Maxwellian temperature<sup>(17)</sup>.

The dependence of  $\lambda_{tr}$  on the ortho:para concentration in H<sub>2</sub> is shown in Fig. 8, where our results (T<sub>M</sub> = 37 K<sup>(17)</sup>) are compared with Würz's calculations. A satisfactory agreement between both evaluations is observed over most of the range, except in the high para- concentration limit where our model gives larger values.

Finally, Fig. 9 shows calculated scalar fluxes for two concentrations of parahydrogen in liquid H<sub>2</sub> at 20 K, together with Maxwellian distributions corresponding to T = 37 K.

### Conclusions

We have applied the synthetic scattering formalism to produce a simple model to describe neutron scattering and transport in liquid H<sub>2</sub> and D<sub>2</sub>. Based on the analytical expressions derived from the model, we evaluated several magnitudes of interest in cold neutron source design. From the comparison of its predictions with the available information and its ability to produce in a fast way the scattering matrices for any desired physical condition, we believe that this model could be a useful tool for the above mentioned design and optimization work.



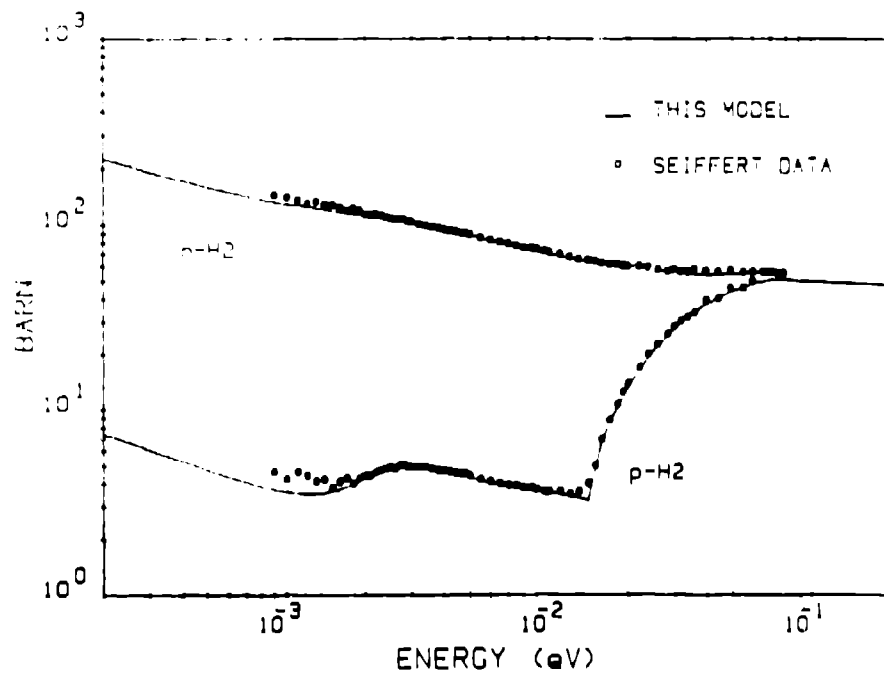


Fig. 1 Total cross section of normal and para hydrogen.

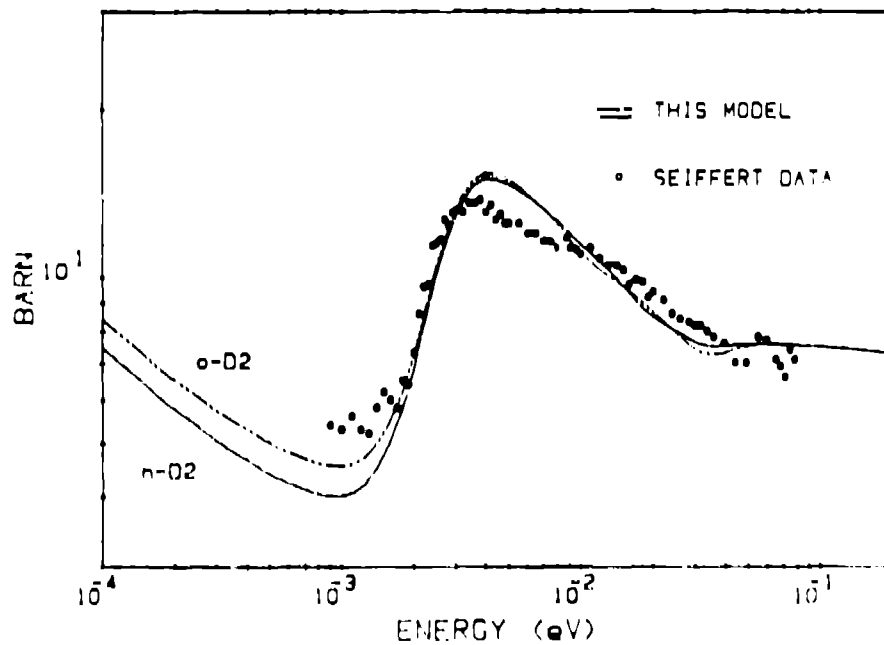


Fig. 2 Total cross section of normal and ortho deuterium.

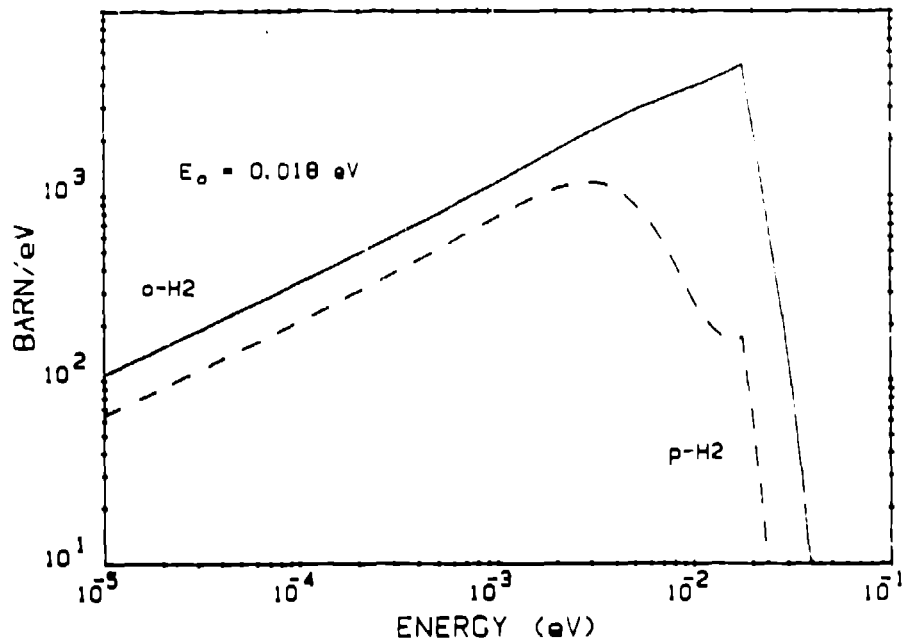


Fig. 3 Energy-transfer kernels for  $H_2$  at  $E_0 = 0.018 \text{ eV}$ .

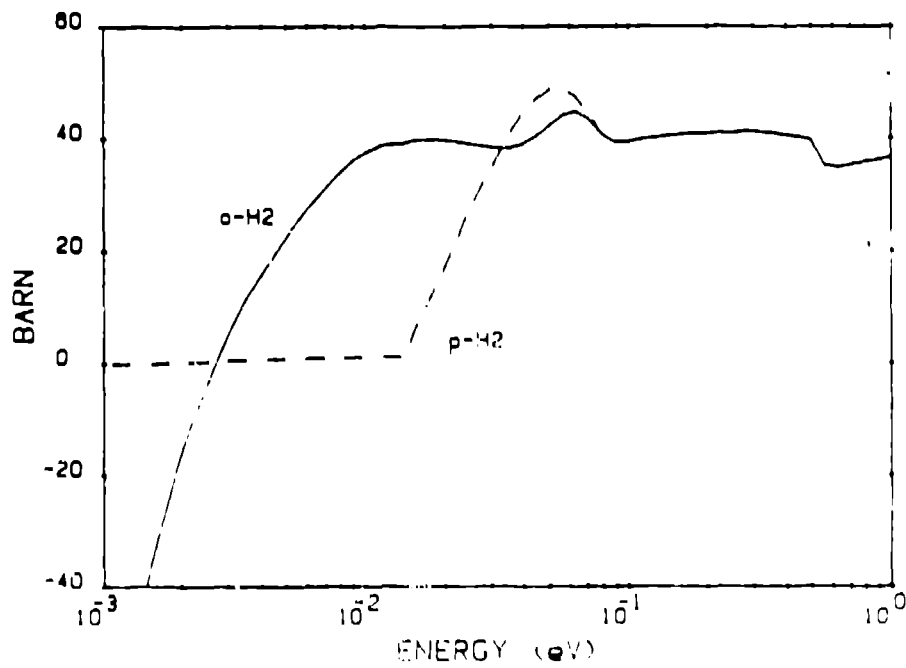


Fig. 4 Slowing down power of liquid  $H_2$ .

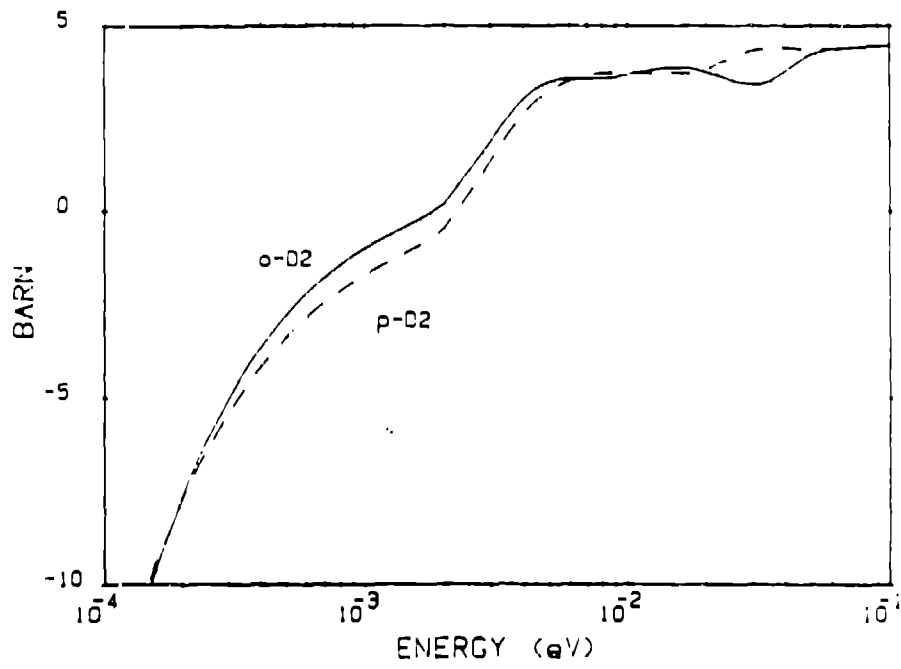


Fig. 5 Slowing down power of liquid D<sub>2</sub>.

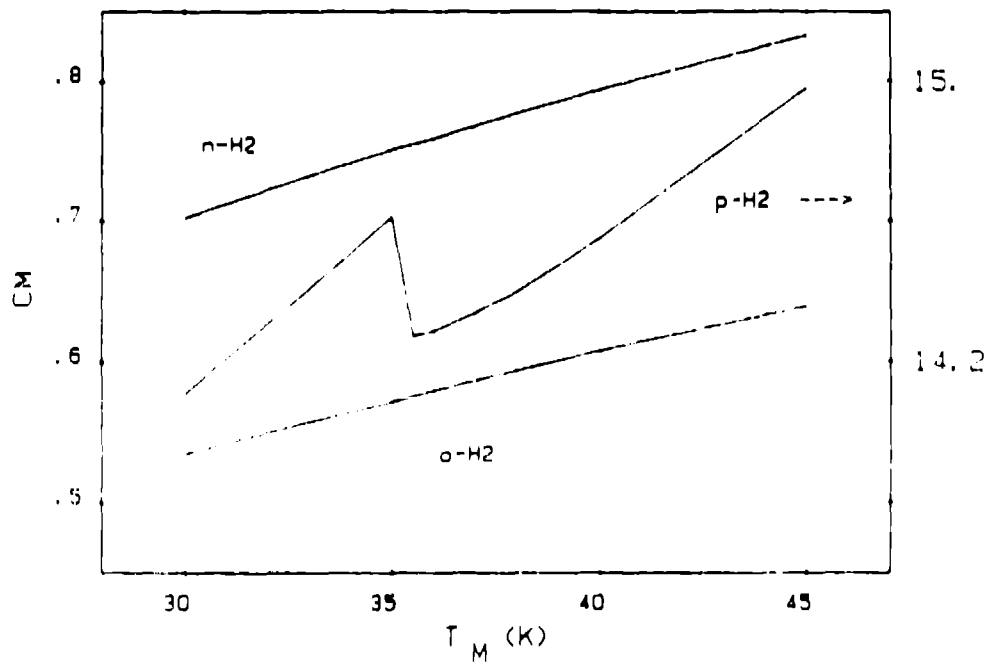


Fig. 6 Mean free path in H<sub>2</sub> vs. spectrum "temperature" (see test for details).

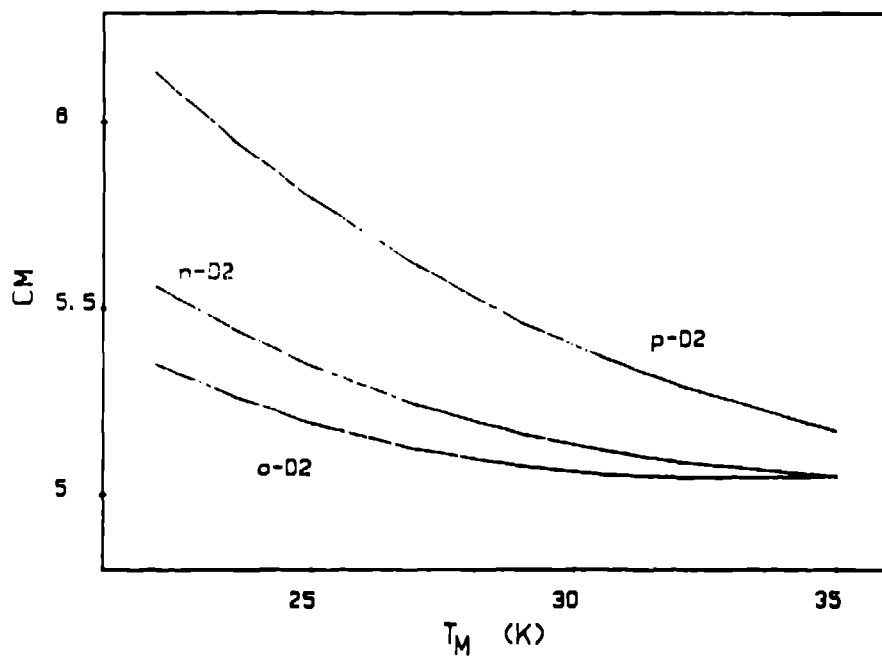


Fig. 7 Same as Fig. 6. but for  $D_2$ .

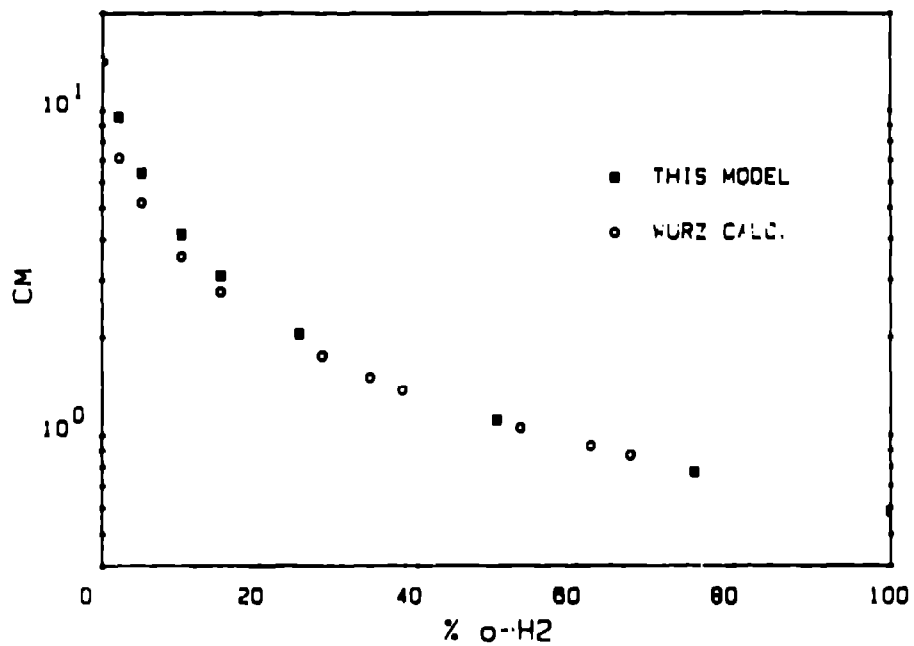


Fig. 8 Mean free path in  $H_2$  vs. ortho:para concentration.

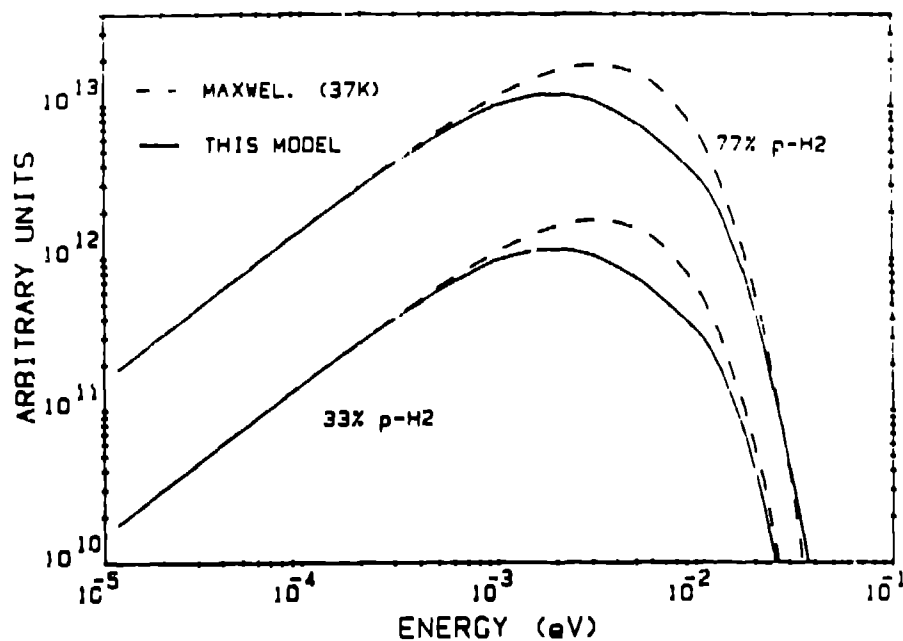


Fig. 9 Calculated scalar flux in liquid hydrogen at 20 K.

#### References

1. G. L. Squires and A. T. Steward, 1955, Proc. Roy. Soc. (London) **A230**, 19.
2. G. Sarma, 1960, Proc. Int. Symp. Inel. Scatt. of Neutrons, IAEA, Vienna.
3. J. A. Young and J. U. Koppel, 1964, Phys. Rev. **A135**, 603.
4. M. Utsuro, 1977, Z. Phys. **B27**, 111.
5. H. Würz, 1973, Report KFK 1697.
6. P. A. Egelstaff and P. Schofield, 1962, Nucl. Sci. Eng. **12**, 260.
7. W. Schott, 1970, Z. Phys. **231**, 243.
8. J. Keinert and J. Spix, 1987, Kerntech. **51**, 19;  
W. Bernnat, et al., 1988, Int. Conf. Nucl. Data for Sci. & Techn., Mito, Japan.
9. J. M. Carpenter, et al., 1981, Nucl. Instr. Meth. **189**, 485.
10. S. W. Lovesey, 1984, Theory of Neutron Scattering from Condensed Matter, **1**, Clarendon Press p. 269.
11. J. R. Granada, 1985, Phys. Rev. **B31**, 4167.
12. J. R. Granada, et al., 1987, Phys. Rev. **A26**, 5585 (I & II).
13. S. P. Tewari and K. Swaminathan, 1980, Phys. Rev. Lett. **45**, 1344.
14. J. R. Granada, 1988, Int. Conf. Nucl. Data for Sci. & Techn., Mito, Japan.
15. W. D. Seiffert, 1970, Report EUR 4455d.
16. M. Utsuro and M. Heltzelt, 1977, Neutron Inel. Scatt., **1**, IAEA, Vienna.
17. P. Carter and D. M. Jones, 1972, J. Nucl. En. **26**, 237.

## Upgrading of the reactor BER II

A. Axmann  
Hahn-Meitner Institut Berlin GmbH  
Glienicke Str. 100, D-1000 Berlin 39  
FEDERAL REPUBLIC OF GERMANY

The Berlin Research Reactor BER II at the Hahn-Meitner Institut is a swimming pool reactor. The BER II was operated at a power of 5 MW from December 1973 until it was shut down in August 1985 for a general physical and technical improvement and upgrading.

The neutron fluxes available at the beam tube positions in the reflector will be about  $10^{14}$  n/cm<sup>2</sup>sec. The upgraded BER II will be a medium-flux neutron source for standard applications, such as neutron scattering, materials research, and activation analysis, the latter of which is used mainly for medical problems.

The increase of the usable reflector-flux density by a factor of 10 is the result of the following:

- The power of the reactor will be increased from 5 to 10 MW.
- The fission density will be increased by reducing the core size from 64 to 42 MTR fuel-element positions.
- The reflection efficiency will be increased by a beryllium reflector. The beryllium reflector, which is 30-cm thick, surrounds the core and produces a well pronounced flux peak about 5 cm from the core edge. To this flux maximum, 10 beam tubes will be adapted (a horizontal cut through the reactor is seen in Fig. 1).

The flux density of cold neutrons will be further increased by a factor of 13 by a cold neutron source. Six neutron guides will feed a new neutron guide hall of approximately 1200 m<sup>2</sup>.

The licensing authorities require backfitting according to current regulations for science and technology for technical improvement. A large number of guidelines and regulations concerning design, construction and operation of nuclear power plants have had to be followed. Thus, planning permission had to cover the energy supply system, cranes, fire protection system, the security system, the reactor control and safety system, and the storage facilities of fresh unirradiated fuel elements as well as spent-fuel elements.

The upgrading program will be completed in 1988 and the operating license is expected in 1989.

The Hahn-Meitner Institut is one of the 13 national research centers in the Federal Republic of Germany. Basic research in close operation with the Berlin universities is the main task of the Institute. Thus, BER II is an important facility in this program.

The following neutron scattering instruments will be installed in the experimental hall (E) and neutron guide hall (V) respectively (see Fig. 2):

No.	I N S T R U M E N T   A N D   P R O G R A M	L O C A T I O N
1.	<u>3-Axis-Diffractometer for Polarised Neutrons</u>	E1
2.	<u>Flat-cone Diffractometer and Neutron-Photography</u>	E2
3.	<u>Powder Diffractometer with Multicounter</u>	E3
4.	<u>2-Axis-Diffractometer</u>	E4
5.	<u>Four-Circle-Diffractometer</u>	E5
6.	<u>High Resolution Processing Single Crystal Diffractometer with Multicounter</u>	E6
7.	<u>3-Axis-Spectrometer</u>	E7
8.	<u>Diffractometer with Multidetector for Biological Membranes</u>	V1
9.	<u>Small Angle Scattering</u>	V4
10.	<u>3-Axis-Spectrometer for Cold Neutrons</u>	V2
11.	<u>Time-of-Flight Spectrometer</u>	V3
12.	<u>Spin-Echo Spectrometer</u>	V5

The upgraded BER II will continue to operate with HEU fuel (93.5 weight percent <sup>235</sup>U). However, the conversion to LEU fuel (less than 20 weight percent <sup>235</sup>U in total uranium) is planned for the future.

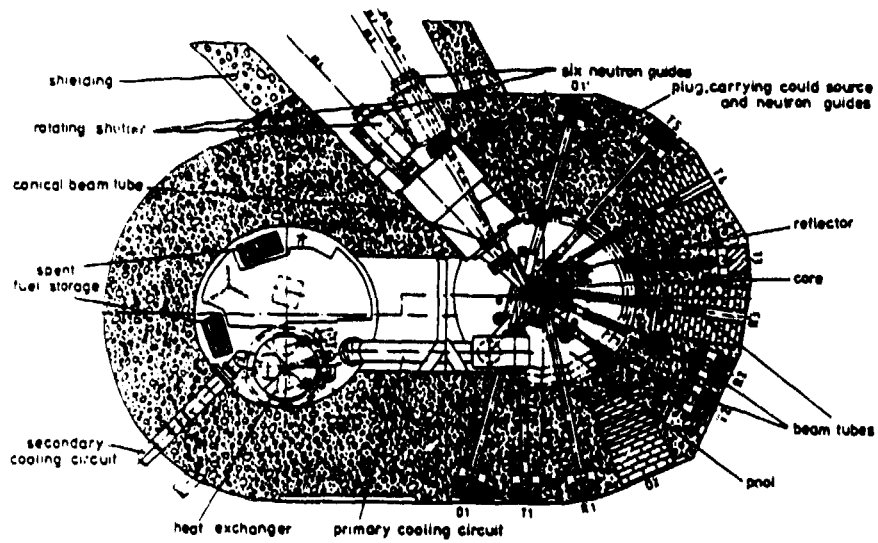


Fig. 1 BER II—horizontal cut.

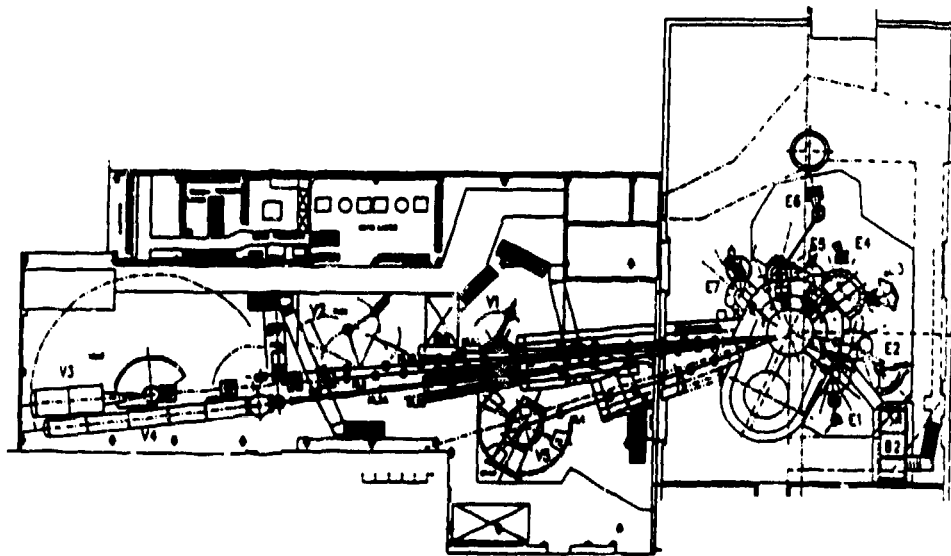


Fig. 2 BER II experimental hall and neutron guide hall.



## New moderator for pulsed neutron diffraction

R. E. Mayer, J. R. Granada, V. H. Gillette and J. Dawidowski  
Centro Atomico Bariloche and Instituto Balseiro  
8400 S. C. de Bariloche (RN)  
ARGENTINA

**ABSTRACT:** Experiments of neutron diffraction, leakage spectrum and pulse decay have been carried out on a new geometry, heterogeneously poisoned, set of moderators and on conventional "sandwich" and slab moderators for comparison purposes. For a given time pulse width, great increase in neutron leakage intensity has been found in these assemblies, up to 2.7 times that of a sandwich moderator. Clues to implementation of desired time-response in moderator design and of further increases in neutron yields are suggested by present results.

### Introduction

Since the early days of pulsed neutron diffraction, efforts have been aimed at producing ever more efficient devices to moderate the fast neutrons from an accelerator's target down to the wanted range of energies<sup>(1,2)</sup>.

Development has found its way in different directions through the cooling of the moderator<sup>(3)</sup>, or new geometries<sup>(4)</sup> and even new materials<sup>(5)</sup>. Even old moderators have been restudied<sup>(6)</sup> recently.

Considering the subject is still open for innovation, we have undertaken the testing of a set of moderators based on a completely different design conception from those that are widely used today in pulsed neutron diffraction work.

### The moderator

From our previous experience with thin moderators, we became convinced that their lateral dimensions are the determining parameters as far as time response is concerned. Consequently, a new system was conceived consisting of an array of small moderators placed side by side and decoupled by cadmium strips. The actual moderator concept is based on a Cd square grid with moderating material in the form of square base prisms inserted in the spaces defined by the grid.

The present array differs from that studied by Day and Sinclair<sup>(2)</sup>, which they found to be of no benefit in realistic experimental conditions, in that the depth of moderator elements is not restricted by the lateral size because they *are not* defined as cubes.

Throughout this work we will characterize each of the arrays tested by  $(a \times a \times b)$ , where  $a$  and  $b$  are the lateral dimension (or "grid spacing") and the moderator depth, respectively, both given as their most approximate value in inches for mnemonic

reasons. Also, the same symbol will identify each moderator in the graphs, as given in Table 1.

Tabel 1

MODERATOR	SYMBOL
SLAB	⌘
( 2 x 2 x 1 )	◇
( 1 x 1 x 2 )	■
( 1 x 1 x 1 )	▲
( 1 x 1 x 1/2 )	●
SANDWICH	⌘
( 1/2 x 1/2 x 2 )	□
( 1/2 x 1/2 x 5/4 )	△
( 1/2 x 1/2 x 3/4 )	○

The "sandwich" consists of a polypropylene pre-moderator slab 20 x 20 x 1.8 cm<sup>3</sup>, and a thin circular post-moderator 15 cm in diameter and 0.6 cm thick, decoupled from the pre-moderator by a 0.6 mm thick Cd sheet. The slab is polypropylene 20 x 20 x 2.4 cm<sup>3</sup>.

The grids are filled with paraffin because of ease of manufacturing, and their exact measures taken individually. Except on their emitting faces, all moderator systems were wrapped in 0.8 mm thick cadmium.

### Experimental

Three types of experiments were performed:

- neutron leakage spectrum, measured by time of flight;
- thermal neutron pulse decay, as seen by a <sup>235</sup>U miniature fission chamber placed in the vicinity of each moderator; and
- neutron diffraction on a powdered copper sample.

We will report here the results from the last experiment (c). Neutron diffraction measurements were done using our wide-angle backscattering diffractometer, which has a bank of 32 He-3 tubes arranged on a conical geometry dictated by a focussing

concept<sup>(7)</sup>. The powder diffraction patterns were fitted with the use of a peak shape function developed some time ago<sup>(8)</sup>.

The pulsed neutron source is based on a 25 MeV electron linac with a cooled lead target. All moderators were placed at the same position within centimeters of the target in such a way that fast neutrons reached the assemblies from a face opposite to the emitting one (not as in a "wing configuration").

### Results

A part of the diffraction spectrum corresponding to the thickest representative of each moderator "family" (same  $a$ ) is plotted in Fig. 1, where it is clearly seen that resolution varies with the value of  $a$  (or grid spacing) in an expected manner.

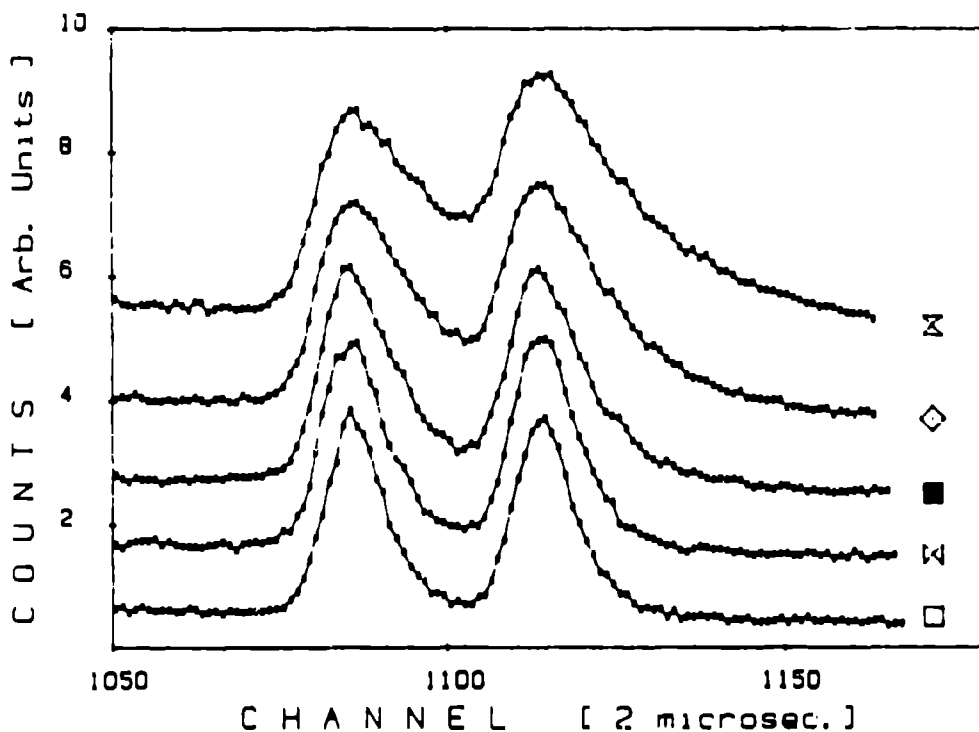


Fig. 1 Part of the diffraction spectra of powder copper as obtained with different moderators. Symbols are listed in Table 1. Lines are guides for the eye. Spectra have been arbitrarily displaced vertically for display purposes.

The second result is not so obvious. Our peak shape function has two resolution parameters<sup>(8)</sup>:

- i) *sigma*, which collects the effects of all symmetrical contributions to the time distribution, and
- ii) *alpha*, which takes account of all non-symmetrical contributions and...

besides some minor effects—strongly reflects the time response of the moderator.

As shown in Fig. 2, the alpha values naturally group into families belonging to each grid family, thus showing a clear tendency to grow with grid spacing rather than with moderator thickness.

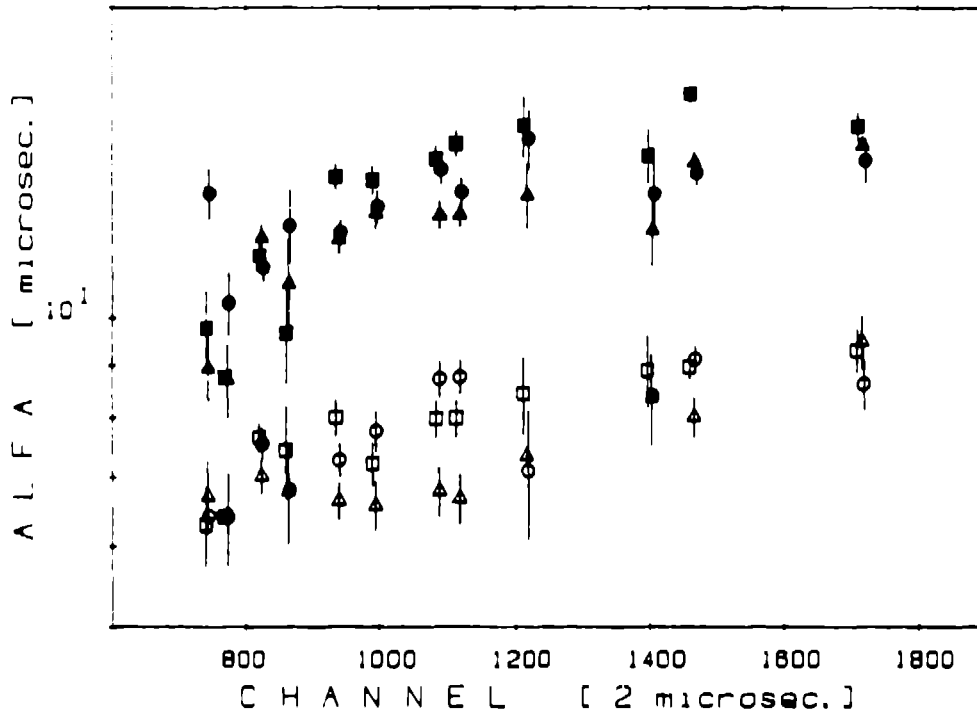


Fig. 2 Fitted ALFA values for different moderators of two grid families (conventional symbols).

The sigma values are all rather similar, as should be expected; nevertheless, they also show this "family" behavior and tend to grow in the same sense as the alphas, rendering a greater overall resolution for the smaller grid spacing systems than is accounted for by alpha alone.

The moderators tested in this experiment do not reach a complete constant value of alpha in the lower side of the observed momentum transfer range. Nevertheless, a mean alpha value can be associated to the "quasi-plateau" region for each moderator, and those are shown in Fig. 3 as "ALFA<sub>m</sub>". The well-defined tendency observed as a function of grid spacing constitutes one of the main results of this study, as it suggests the possibility of selecting the adequate value of (a) to match any desired time response for our moderator systems. For comparison purposes, the alpha value corresponding to our standard sandwich moderator is also included in Fig. 3.

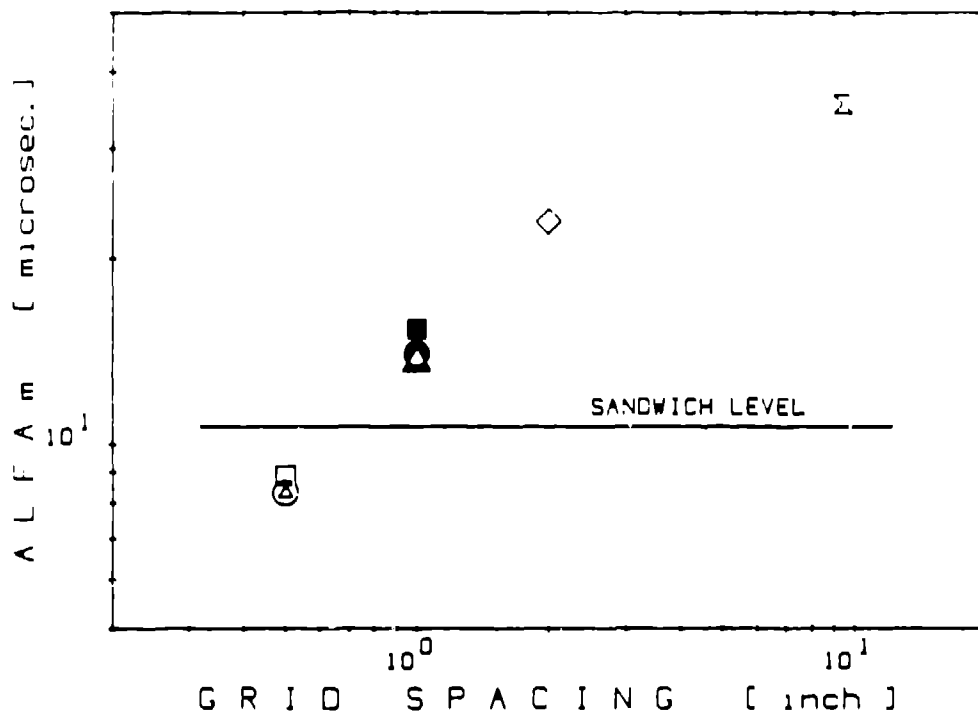


Fig. 3 Trend of ALFAM with lateral dimensions of grid or of slab (see text for details).

Finally, the relative neutron production is represented in Fig. 4. The areas of 13 diffraction peaks, divided by monitor counts and normalized by the corresponding values for the sandwich, were summed up to give one point in the graph for each moderator. This magnitude still shows a tendency to grow with moderator thickness so that greater intensities can be expected for each grid with no important increase in time spread (Fig. 3).

No *figure of merit* is proposed in this work, as it is not intended to find "the best" moderator; instead its purpose is to display the behavior of these moderator systems in terms of parameters that are relevant to design and optimization for specific situations.

#### References

1. R. G. Fluharty, et al., 1969, Nucl. Sci. Eng. **35**, 45.
2. D. H. Day and R. N. Sinclair, 1969, Nucl. Inst. Meth. **72**, 237.
3. D. F. R. Mildner, et al., 1978, Nucl. Inst. Meth. **152**, 437.
4. Y. Kiyonagi, 1984, J. Nucl. Sci. Techn. **21**, 735.
5. D. J. Picton, D. K. Ross and A. D. Taylor, 1982, J. Phys. **D15**, 2369.
6. S. Ikeda and J. M. Carpenter, 1985, Nucl. Inst. Meth. **A232**, 536

7. F. Kropff, 1986, Nucl. Inst. Meth. A245, 125.
8. F. Kropff, J. R. Granada and R. E. Mayer, 1982, Nucl. Inst. Meth. 198, 515.

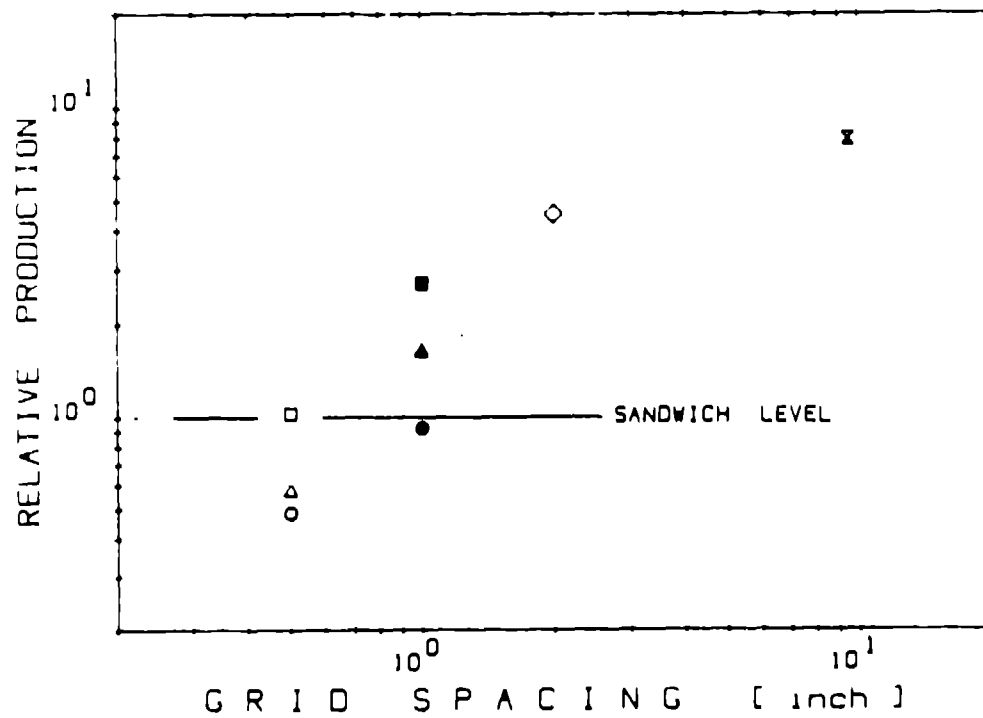


Fig. 4 Trend of the relative neutron production as defined in the text, with lateral dimensions of grid or of slab.

## Workshop summary on targets and moderators

*W. E. Fischer*  
Paul Scherrer Institut  
CH-5232 Villigen  
SWITZERLAND

Two subjects have been discussed quite in detail at this session:

1. The neutronics performance of the LANSCE-target/moderator system by Grady Hughes and Jim Gilmore (LANL), and
2. the cold-neutron D<sub>2</sub> source at SINQ by F. Atchison (PSI).

For the LANSCE target system, a very detailed Monte-Carlo mockup has been set up. The fluxes for neutrons at 1 eV have been calculated in absolute terms, i.e.,  $\frac{n}{\text{cm}^2 \cdot \text{p}}$  for various flight paths.

Furthermore, using activation technique, the fluxes have also been measured. Remarkable agreement has been achieved as is shown in the following table:

Flight Path	Detection Distance (cm)	Measured $\frac{n}{\text{cm}^2 \cdot \text{p}}$ at 1 eV	Calculated $\frac{n}{\text{cm}^2 \cdot \text{p}}$ at 1 eV
1	3175	$4.4 \times 10^{-10}$	$4.95 \times 10^{-10}$
3	900	$5.2 \times 10^{-9}$	$6.17 \times 10^{-9}$
7	1300	$2.61 \times 10^{-9}$	$2.71 \times 10^{-9}$

In view of the complicated geometry of the LANSCE system, this agreement is satisfactory, indeed. Consider that this system consists of a split tungsten target with moderators the height of the target gap in slab arrangement, embedded in a nickel reflector.

The essential points of these results are the following:

- The fluxes per proton are more or less the same as those given for IPNS and ISIS, which both have uranium targets and moderators in wing-geometry. Hence, it seems, that the higher source strength of the uranium target is compensated by the stronger coupling of the moderators in slab arrangement. In the LANSCE system, the moderators view the target void.

Hence, there is some hope that the background will be as low as for the other systems. This remains, however, still to be shown.

- The SINQ D<sub>2</sub> cold-neutron source is a typical installation for a steady-state neutron source. Dimensions and design are, therefore, hardly different from a reactor source. The basis of the design is an adaptation of the horizontally-mounted thermosyphon as used for the second cold-source at the ILL, Grenoble.
- An essential aim in the design of the cold source for SINQ is to exploit the advantage of the lower heating of the vicinity of a spallation target. Therefore, special considerations of several items are worthwhile:
  - (i) material distribution and flux optimization (e.g., re-entrance hole);
  - (ii) cryogenics and thermohydraulics; and
  - (iii) shielding and induced activations.



## Detector development at the ISIS facility

*P. L. Davidson, E. M. Mott, N. J. Rhodes, and M. W. Johnson*  
Rutherford-Appleton Laboratory  
Chilton, Didcot, Oxon, OX11 0QX  
UNITED KINGDOM

### 1. INTRODUCTION

For many years the Rutherford Appleton Laboratory has had a neutron detector development programme. It was undertaken to see if the limitations inherent in conventional  $\text{He}^3$  detectors (their speed, efficiency at high neutron energies and rigid geometry) could be overcome by scintillator technologies. It was also underpinned by the fact that it can cost tens of millions of pounds to double the intensity of a neutron source but a few thousand pounds can in some cases double the performance of a neutron scattering instrument if its detection system is improved.

The detectors developed up to the present date have been based on  $\text{Li}^6$  doped glass scintillator and have been successfully installed and run routinely on the HRPD, LAD and IRIS instruments at ISIS. In fact all the present ISIS instruments make use of the  $\text{Li}^6$  glass scintillator technique within their monitors - which comprise small beads of scintillator supported on fine glass filaments in a reflecting housing and viewed directly by a single photomultiplier tube (PMT). The glass scintillators have performed well, with intrinsic backgrounds and  $\gamma$  sensitivities within original specifications. However, it has become clear that on many instruments the neutron background is so low, it is these quantities that are the most important in determining the ultimate signal to noise achievable.

To overcome the background and  $\gamma$  sensitivity problems studies have been made of  $\text{Li}^6$  loaded ZnS scintillator. This has proved so successful that it is likely this technology will form the basis of our detector programme over the next few years.

### 2. THE TECHNOLOGY

Zinc sulphide and  $\text{Li}^6$  (as  $\text{LiF}$  - 25% by weight) are held in a resin in 0.5 mm

sheets. We now have a company in the UK who can supply this material at - £0.15/cm<sup>2</sup>. The resultant material is largely opaque (only about 10% of normally incident light is transmitted) but - 20% of the light from a scintillation event at the centre emerges, and the figure is of course higher as the event nears the surface. It is therefore preferable to view both sides of the scintillator if possible. Despite the relative opacity the method works well because each neutron event produces - 50,000 photons, a figure about 10 times higher than than for the Li loaded glass scintillator.

If a single sheet of ZnS scintillator is viewed directly by a photomultiplier tube the n efficiency is - 20% at a wavelength of 1Å, while the  $\gamma$ -sensitivity and intrinsic background are essentially zero. This is because the pulse height of the neutron event is very large compared to that for  $\gamma$ s (see Figure 1) and by suitable choice of discriminator level the  $\gamma$  sensitivity can be reduced to  $10^{-7}$  or  $10^{-8}$  without substantially lowering the neutron count. For detectors that use more complex geometries, the light received by the PMT is very much reduced. This results in a train of single photo-electron pulses from the PMT that must be integrated to identify neutron event reject  $\gamma$  events. This type of design has slightly worse gamma rejection ( $10^{-6}$ ), and longer dead times (2-5  $\mu$ sec), but can provide detectors with high spatial resolution - 3 mm and detectors with high neutron detection efficiency.

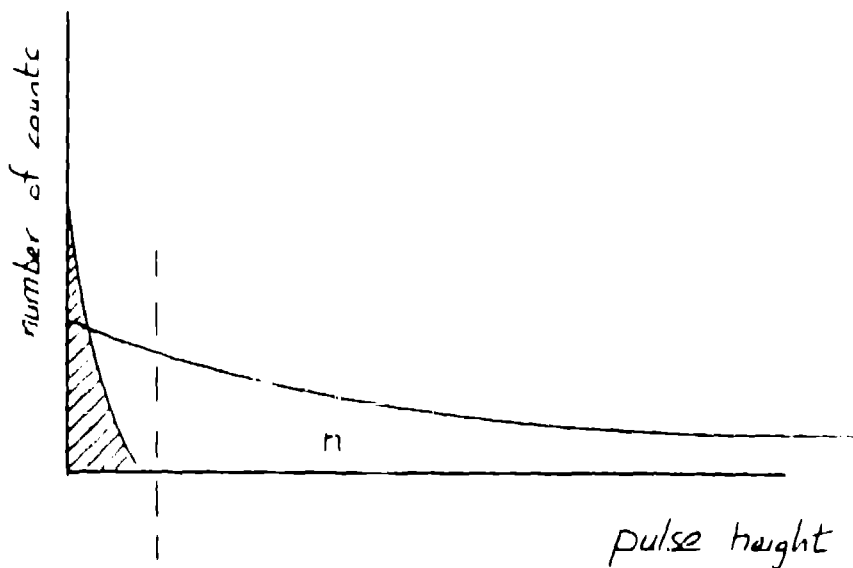


Fig. 1 Pulse height of neutron event.

### 3. APPLICATIONS

Test modules currently being constructed for the SANDALS instrument which requires very good efficiencies at high neutron energies together with a need for large detector areas (a total of  $3 \text{ m}^2$  is required). The result is the module shown in Figure 2. Interestingly the light emitted from the scintillator elements scatters between the parallel sheets at a grazing angle with good efficiency. Figure 3 shows the relative efficiency of such a device compared with a  $\text{He}^3$  tube. It has an absolute efficiency of 50% at 10 eV, representing a gain of  $\sim 3.5$  over a conventional  $\text{He}^3$  tube. It is also relatively cheap to make. Estimates of component costs are in the range £110 per  $20 \times 1 \text{ cm}$  detector, plus £80 for electronics and HT supplies.

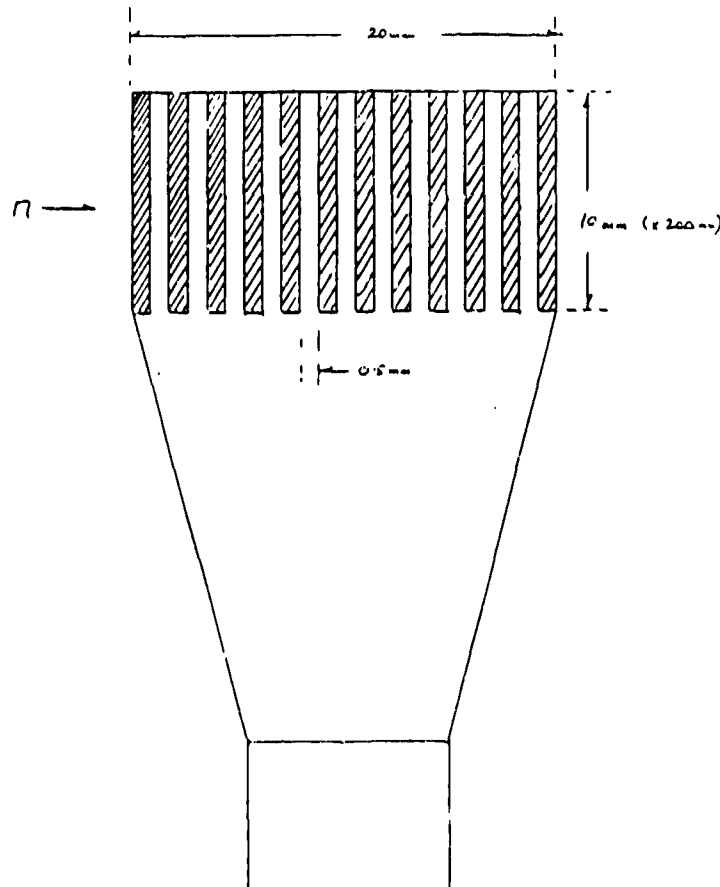


Fig. 2 Test module for the SANDALS instrument.

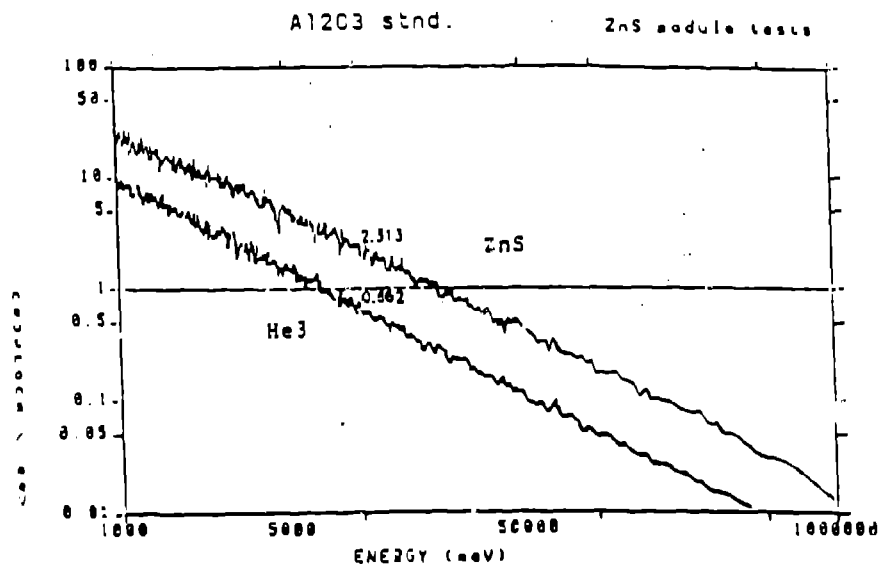


Fig 3. Relative efficiency comparison.

Finally, it should be pointed out that the ZnS scintillator is highly suitable as a material for constructing area position sensitive detectors. We have built a prototype area detector with 5 mm resolution over an area of 100x100 mm, in which individual detector elements are viewed by optic fibres. This compares very favourably with the glass scintillator Anger Camera technique, as shown in Figure 4, where the (0 0 20) from SrF<sub>2</sub> is shown as an observable peak when recorded by the ZnS detector. Signal to background ratios are often in the region of several thousand to one and this is illustrated in Figure 5 where the (001) reflections from SrF<sub>2</sub> are shown on a log scale. As final illustration of the low noise characteristics, Figure 6 shows an inelastic feature recorded on the ZnS module in an off-Bragg position. As far as we know peaks of this sort have not been recorded in position sensitive area detectors for single crystal samples before.

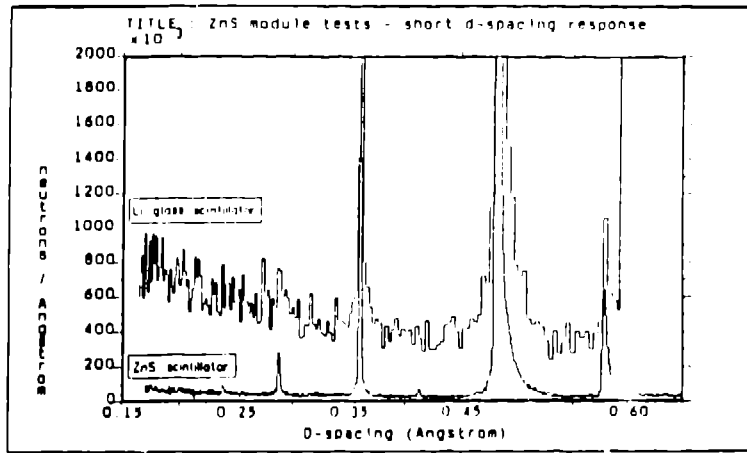


Fig. 4

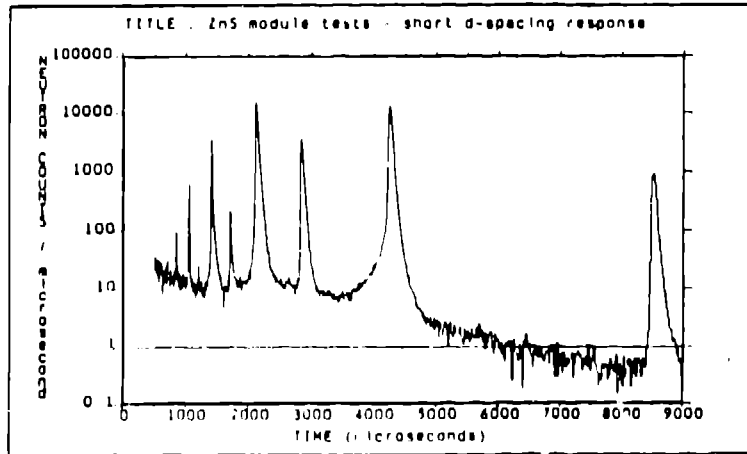


Fig. 5

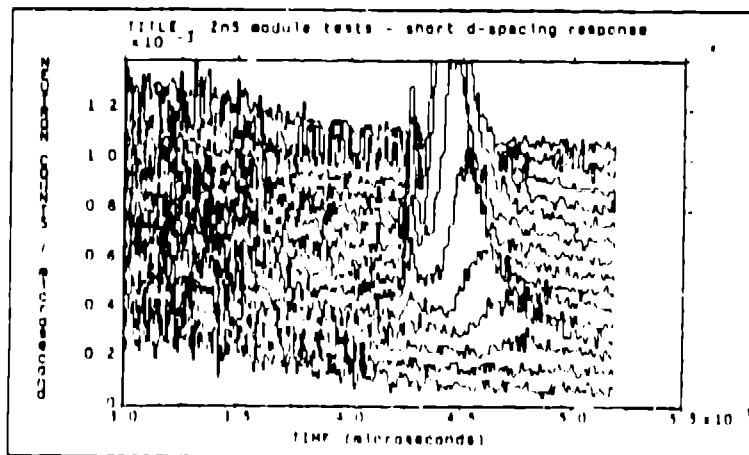


Fig. 6

#### 4. CONCLUSION

The use of zinc sulphide scintillators opens the possibility of building cheap, efficient neutron detectors which should have a profound effect on the performance of future neutron scattering instruments. If the potential for building two dimensional position sensitive detectors is realised it will provide a tremendous step forward for single crystal instrumentation.

## **New KENS data acquisition system**

*M. Arai, M. Furusaka, and S. Satoh*  
National Laboratory for High Energy Physics  
1-1 Oho, Tsukuba-shi, Ibaraki 305  
JAPAN

### **1. Introduction**

Measurements made using the pulsed neutron technique have the advantage of a wide dynamical range in  $Q$ - $\omega$  space with multiple scans along the loci defined by the kinematic constraint. The measured TOF data, however, do not give direct results in  $Q$ - $\omega$  space because the data is obtained as a function of time-of-flight (TOF) and modulated by the incident neutron spectrum; also, the scanning path does not have simple loci in  $Q$ - $\omega$  space. This is clearly different from a measurement at a reactor using a constant wavelength technique. Therefore, it is important to make on-line analysis during the data acquisition phase of an experiment to understand the results obtained.

The best science often requires that a number of neutron techniques are used on the same material. Sometimes it becomes necessary to use two or more spectrometers for a given sample because most instruments at a pulsed-neutron facility are optimized to make measurements in specific areas of  $Q$ - $\omega$  space. Thus, it is also important to have a data acquisition system with the same user interface for all spectrometers.

Furthermore, it is helpful for visiting experimenters to finish the necessary data corrections during their stay at the facility and take the data in a reduced form to their home institute for further analysis because data obtained back at a pulsed-neutron facility usually include enormous amounts of bytes and various wave-dependent correction factors. For this purpose adequate CPU power is required.

By satisfying the above requirements on a data collection and manipulation system, a pulsed-neutron facility can be more easily used by outside users and is more competitive against a continuous neutron source.

Experimenters need various capabilities both during and after a run to facilitate the discussion of results and the preparation of manuscripts. Some of these capabilities include word-processing programs, drawing and quick-graphing software, and a method for conveniently doing calculations. For all these purposes, we need intelligent and user-friendly workstations.

In this report we discuss a data acquisition system, KENSnet, which is newly introduced to the KENS facility.

## 2. Required performances for a data acquisition system

To estimate the required disk storage and CPU power, we consider the data collection rate and turn-around time for preliminary data analysis in the case of the small-angle neutron-scattering instrument SAN, which gives the highest data-collection rate (word/hour) at KENS.

### 2.1 Data collection rate

We show the data-collection rate at KENS in Table 1, where 4 bytes are allocated per channel. One histogram of about 0.36 Mbytes (91 K channels x 4 bytes) is taken within 1.5 hours, and the accumulated data becomes 650 Mbytes per year. Data are usually analyzed within three months, so roughly 160 Mbytes are necessary for temporary disk storage.

Instrument	SAN	TOP	LAM	HRP	MRP	RAT	PEN	MAX	HIT	WIT	FOX	INC
nd of SD	6	3	19	9	6	2	16	16	50	16		200
nt of SD	512	512	512	16,000	8,000	8,000	512	512	1,000	512		4,000
no. of PSD	43	4										1
nd of PSD	2,752	256										128
nt of PSD	32	32										512
n = nd*nt	91,136	9,728	9,728	144,000	48,000	16,000	8,192	8,192	50,000	8,192	65,536	800,000
Typical time to obtain one histogram (h)	1.50	2	6	20	4	10	3	40	2	2	5	20
Data Collection Rate:												
Words/hour	60,757	4,864	1,621	7,200	12,000	1,600	2,731	205	25,000	4,096	13,107	40,000
Mbyte/day	4.86	0.39	0.13	0.38	0.96	0.13	0.23	0.02	2.00	0.33	1.05	3.20
Mbyte/year	656	53	18	78	130	17	29	2	270	44	143	432

Table 1 Data collection rate in the KENS. nt is the number of time channels, nd is the number of detectors. SD is a single detector. PSD stands for a linear position-sensitive detector.

During the measurement, the two-dimensional data of 0.36 Mbytes are to be converted to  $S(Q)$  in a short time, e.g., one minute. This requires 1 MIPS of CPU power from our experience.

So we put criteria at about 1MIPS for CPU speed and 150 Mbytes for storage capacity for a computer per spectrometer.

## 3. Data acquisition system

### 3.1. Computing system

We chose models from the VAX family of computers with their proprietary operating system, VMS. The computers are made by the Digital Equipment Corporation and used world wide by other neutron scattering facilities. Most important, the VMS operating system has a very user friendly interface and is well suited to instrument control applications. A hub computer, VAX 8350, has 16 Mbytes of main memory, about one Gbyte of disk storage, and about 2.5 MIPS of CPU speed. Data acquisition computers (DAC) are VAX station II/GPX's. They control the data acquisition electronics (DAE). There are eight DAC's, which have



the following: 5 Mbytes of main memory, one or two of 140 Mbytes disk storage, and about 1 MIPS of CPU speed. The CPU power of the DAC is enough to make preliminary data analysis during the experiment to understand the results. The disk storage of DAC is enough for the required data amount. The layout of the total system is shown in Fig. 1.

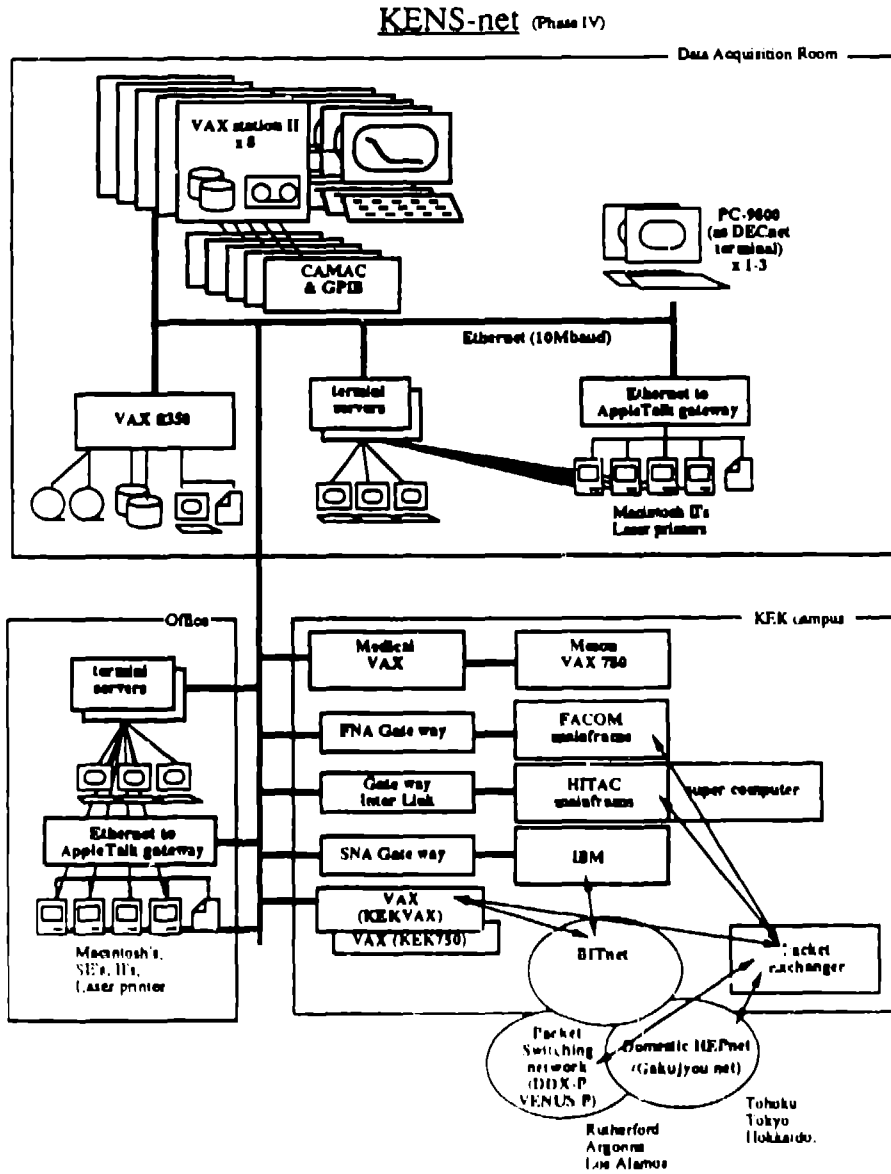


Fig. 1 Diagram of the new data acquisition system KENSnet.

These computers are connected by a network (Ethernet; 10 Mbps) and form a local area VAX cluster (LAVc). An operating system (VAX/VMS) resides only on the hub computer (boot member), and all the other DAC's (satellite members) use the operating system through the network. Therefore, maintenance is done only on the operating system of the boot member, and this saves a lot of time and man power for system management. On the occasion of the shutdown of the boot member, the satellite member can start up by itself. Therefore, there is no risk of cluster-wide failure caused by a single machine. The LAVc is also very convenient because any disk in the cluster can be accessed from any VAX as if it were a local disk of its own. Each CPU is shared flexibly by batch jobs entered within the local area cluster, which gives effective use of the total CPU power.

The front-end computers (FEC), Apple Macintosh Plus and Macintosh II, were chosen for their user-friendly manipulation and intelligence. These are connected to AppleTalk or Ethernet (Fig. 2). Users can manipulate very easily plotting and drawing tools, and can do convenient calculations using results corrected by the DAC for discussion and other considerations. Both word processing for manuscripts and controlling DAC's using emulated terminals (VT100 / Tektronics 4014 emulation) on behalf of experiments can be done. These functions of the front-end computer, so-called "work stations," are important to achieving efficient experiments.

### 3.2 Networking

The VAX computers are connected by a DECnet network mediated by Ethernet; Macintosh computers are connected by AppleTalk. By introducing a gateway, KINETICS's FastPath, and a communication program, Alisa-System's AlisaTalk, both types of computers can communicate with each other. Certain files on a VAX disk can be accessed from the Macintosh, and applications software for the Macintosh can be down-loaded to the VAX.

Laser printers on the AppleTalk network can be used from both the Macintosh and VAX computers. The Macintosh controls the DAC through a terminal server on Ethernet or through Ethernet directly using TCP/IP protocols.

On the other hand DECnet extends to the central VAX computers in the Laboratory and to the world through HEPnet (network for High Energy Physics). We can communicate with other foreign institutes. The Ethernet also links us to the mainframes (HITAC, FACOM) of the Central Computer Division, and those are used for heavier calculations, analysis, and Bitnet services.

Users in outside institutes can access KENSnet through telephone modem links, a packet-switching network (DDX-P), or HEPnet.

### 3.3 Data acquisition electronics (DAE)

We have developed new CAMAC-based data acquisition electronics (Fig. 3). A Gate module receives a signal of proton extraction time from the accelerator and checks the veto signals from the sample environment equipment (vacuum, temperature, chopper phasing, etc.). Then the enable signal is issued to a Delay-Time module. A Time-Control module starts timing from the delayed start signal from the Delay-

## Micro- to Mini- Link

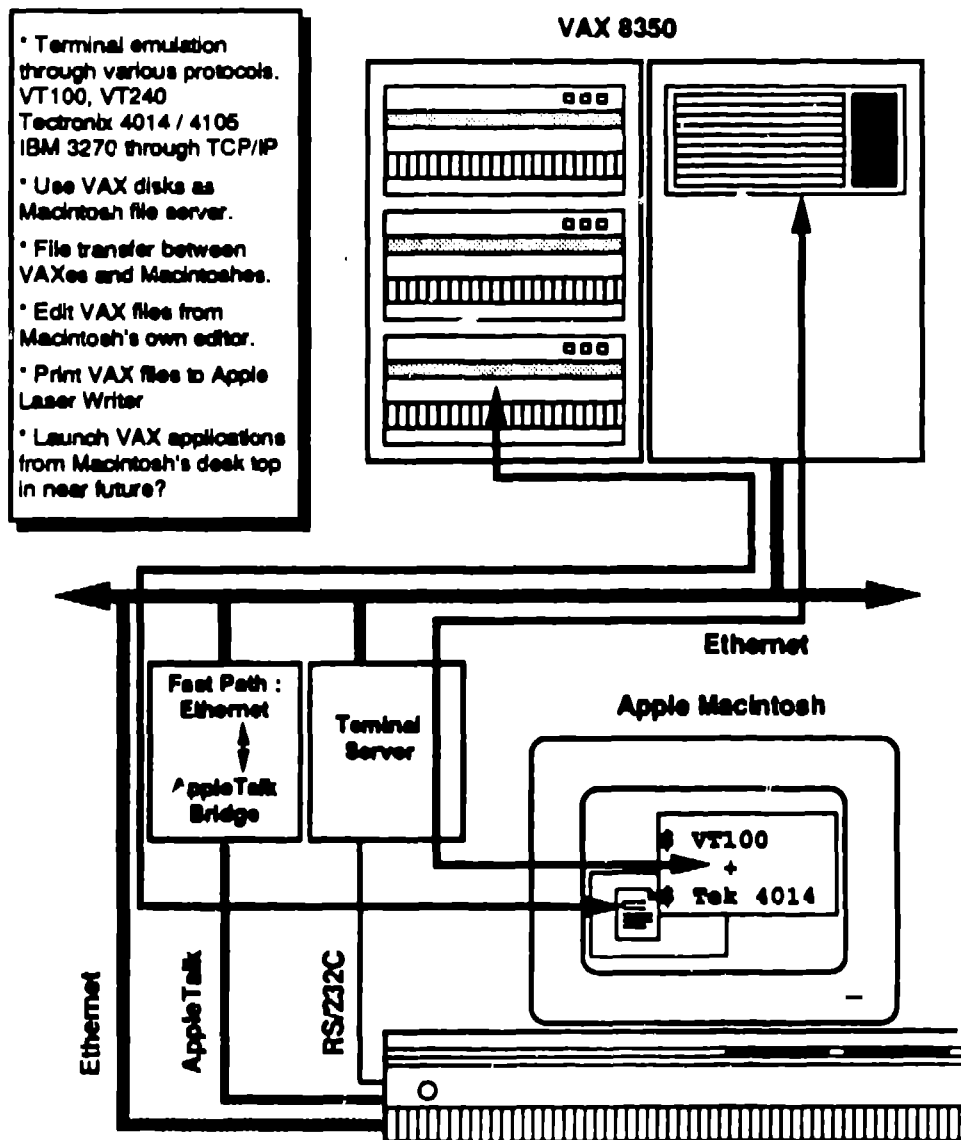


Fig. 2 Diagram of Macintosh/VAX link.

Time module and distributes an encoded time-boundary address to Memory modules at the preset times, enabling the Memory modules to accumulate data histograms. There are two types of Memory modules, which have 4 or 8 inputs for a detector signal. One Memory module has 16 K words (16 or 24 bits), which is shared by 2 to 4 or 8 histograms. To match the time resolution with other contributions, the time boundary of the Time-Control module and the delay time of the Delay-Time module can be set by the DAC flexibly in arbitrary width with the minimum step of 62.5 ns and minimum base width of 0.5 or 1  $\mu$ s.

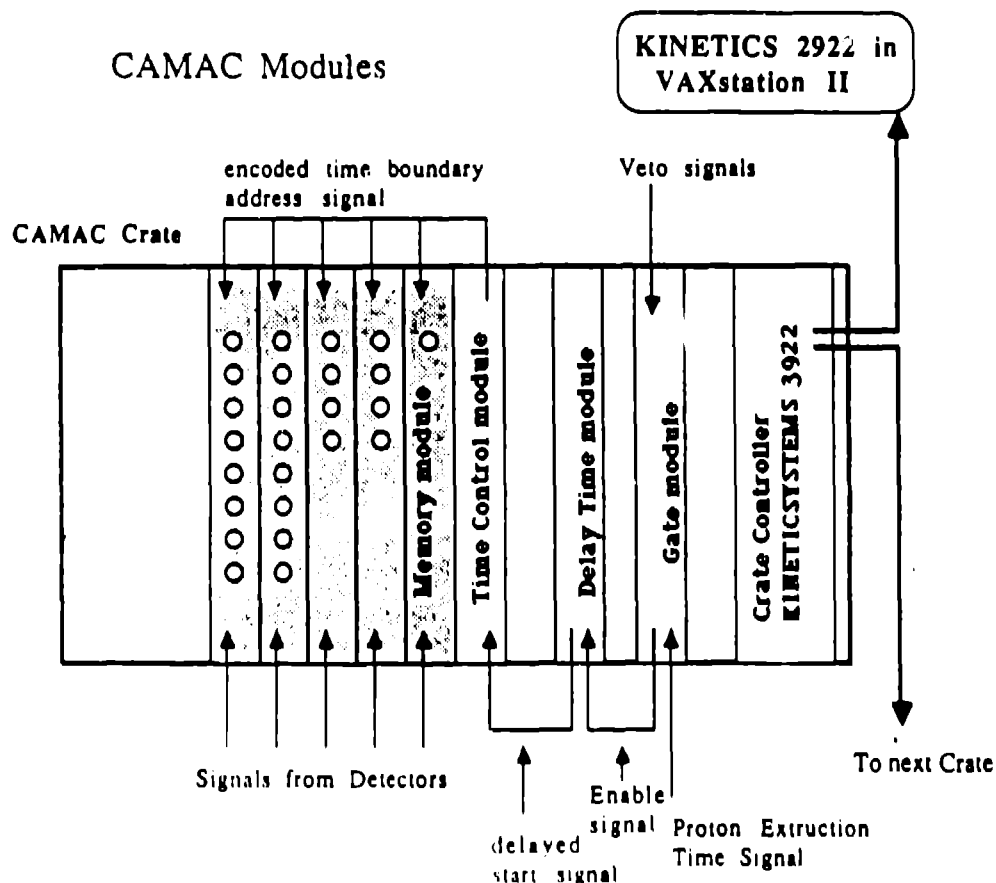


Fig. 3 Diagram of the new data acquisition electronics.

We inherited the traditional concept in KENS data acquisition electronics, i.e., one-to-one correspondence of detector-to-histogram relation. This method needs enormous data storage in some cases; however, our low-cost, high-performance memory modules enable us to realize the above concept. We can manipulate the data and reduce them for certain purposes after the experiment, which provides a high degree of flexibility in the data analysis and reduces a risk of troubles from noisy detectors.

CAMAC crates are connected to the DACs via a pair of KINETICSYSTEMS CAMAC Crate Controllers and Q-Bus Adapters, which lets us put CAMAC crates up to 150 meters from the computers. We can accommodate up to eight crates.

Sample-environment control is done by GP-IB devices, which are connected to the DAC via GP-IB extenders, enabling very long cables (up to 1.8 km) to be used. Sample environments, such as temperature and magnetic field, can easily be controlled by commercially available GP-IB devices.

### 3.4 Software of new data acquisition system

The data acquisition control program (ICP) and the general data analysis program (Genie) were both developed at ISIS<sup>(1,2)</sup> and have been installed in the new data acquisition system. They give the experimenter "user-friendly" data acquisition and a good environment for data manipulation. The ICP controls the DAE and transfers the histogram data into the computers.

The hardware-dependent parts in the ICP were modified to fit the DAE system at KENS. The modified ICP allows the use of different kinds of DAE depending on the detector system, e.g., position-sensitive or single detectors. As Genie is independent of hardware environment, only minor changes were performed to the data size.

All of the software used on the Macintosh computers is commercially available: terminal emulation software for the VT100 and Tektronics 4014, which controls DAC as a terminal and transfer files between FEC and DAC; DECnet AppleTalk linking software, which allows communication between FEC and DAC and gives file-serving and print-spooling environments. Also, spread-sheet and quick-graphing software conveniently manipulates corrected and reduced data.

## 4. Discussion

The compatibility with ISIS in data acquisition and analysis is very important in achieving excellent UK-Japan collaboration. Japanese scientists can immediately start their experiments at ISIS, and the analysis of data taken at ISIS can be continued in Japan. This system saves a lot of time for the scientists in the preliminary steps of an experiment and in the later stages of data analysis.

Now all the pulsed spallation neutron facilities—ISIS, ANL, LANSCE and KENS—have the same proprietary operating system, the VAX/VMS. We can circulate or exchange analysis programs between the facilities and run them without any difficulties.

Intelligent work stations are a great convenience to the experimenter. So far, data acquisition systems have been designed only for controlling data acquisition electronics and analyzing data. However, we often need quick graphing, curve-fitting, and calculations to determine the next direction of the experiment. Much excellent software for these purposes is commercially available for the Macintosh computer. We can use such functions without writing any programs. By combining these general-purpose, convenient programs for the FEC and the data acquisition programs for the DAC, we create a high performance and very effective

data acquisition system. This set-up represents the most significant difference found between us and other neutron facilities.

### **Acknowledgements**

We acknowledge Dr. M. W. Johnson for stimulating discussion on data acquisition systems and his great effort and help for introducing the ICP and Genie system to KENSnet. We also acknowledge Mr. K. J. Knowles for his help on introducing the ICP and Genie systems.

### **References**

1. M. W. Johnson, J. A. Goldstone, and A. D. Taylor, 1982, Los Alamos National Laboratory Report LA-9099-MS.
2. W. I. F David, M. W. Johnson, K. J. Knowles, C. M. Moreton-Smith, G. D. Crosbie, E. P. Campbell, S. P. Graham, and J. S. Lyall, 1986, Rutherford-Appelton Laboratory Report RAL-86-102.

## Future data acquisition at ISIS

*W. C. A. Pulford, S. P. H. Quinton, M. W. Johnson and J. Norris*  
Rutherford Appleton Laboratory  
Chilton, Didcot, Oxon  
UNITED KINGDOM

### Introduction

To some extent at ISIS we are becoming the victims of our own success. Over the past year ISIS beam intensity has increased steadily to 100 microamps during periods of good running. With the instrument users finding it comparatively easy to set up data-collection runs, we are facing an ever increasing volume of incoming data. Table 1 illustrates this point by showing the data volumes collected by the scheduled instruments during the weekend of September 10 and 11, 1988.

Note that the figures for HRPD do not include contributions from the now functional 90° detector bank, which might easily triple the data volume from this instrument. Moreover, the problems involved with digesting this data input will be exacerbated by the introduction of new instruments, such as the single crystal diffractometer (SXD) and the high intensity powder diffractometer (HIPD, still at the design stage)—both of which have large area detectors, up to 100,000 elements in the latter case. The data format of these instruments has been discussed in a paper delivered by M. W. Johnson at ICANS-IX. Greatly improved detector technology, mainly involving large areas of zinc sulfide phosphor, are expected to contribute much to the capacity of these instruments as well as provide an enhancement path for many of the existing ones. It is clear that we are fast reaching the point where if we continue to use our current technology data collection techniques, our computer systems will no longer be able to migrate the data to long-term storage, let alone enable their analysis at a speed compatible with continuous use of the ISIS instruments.

### Overcoming the data volume barrier

Before describing the methods that we will employ to overcome the data problem, I will briefly refer to our current data acquisition electronics (DAE 1) and migration path. These are illustrated schematically in Figures 1 and 2. This system does work extremely effectively, but experience has indicated a number of inherent difficulties:

- (a) Seven instruments are still equipped with VAX 11/730 computers as their Front End Minicomputers (FEM). Unfortunately, these machines usually possess insufficient processor power to perform some of the more complex initial data reduction. This frequently means that the raw data have necessarily to be networked to the HUB computer before analysis may be performed. Currently, we send all data to the HUB, anyway, as a matter of policy.

**Table 1** Data volumes at ISIS for 10-9-88 and 11-9-88.

Instrument	Type of instrument		Number of datasets	Approx. size of datasets	Total data volume(blocks)
	E-elastic	I-inelastic			
HRPD	E	High resolution powder diffractometer	119	3,000	390,000
HET	I	High energy transfer spectrometer	17	3,100	54,000
LOQ	E	Low angle spectrometer	15	4,400	65,700
IRIS	I	High resolution inelastic spectrometer	5	4,400	22,000
TFXA	I	Time focussed analyzer	3	650	1,950
CRISP	E	Neutron surface reflectometer	25	50	1,350
LAD	I	Liquid and amorphous diffractometer	1	1,570	1,570
POLARIS	I/E	Polarized neutron diffractometer	4	1,000	4,000
	Total		540,570 (270 Mbytes)		

- b) The size of the bulk store memory, in which histograms are stored, is restricted to 16 Mbytes by the 24-bit address field of the Multibus in the system crate. This limits the complexity of experiments available to the instrument scientists.
- c) The DAE error detection and analysis system of the FEM is crude and renders the process of monitoring and correcting hardware errors non-straightforward.

It is clear that the most effective method to improve on this situation is to reduce the data volume flowing between the DAE and the FEM and to provide facilities to monitor data acquisition within the DAE. For these purposes we must incorporate processing power closer to the point of data collection. Our preliminary thoughts as to how we might proceed are set out in the ICANS paper previously mentioned.

#### **The next generation data acquisition electronics (DAE 2)**

We have now decided to implement the processing elements within DAE 2 in the form of intelligent memory boards illustrated schematically in Fig. 3. The CPU



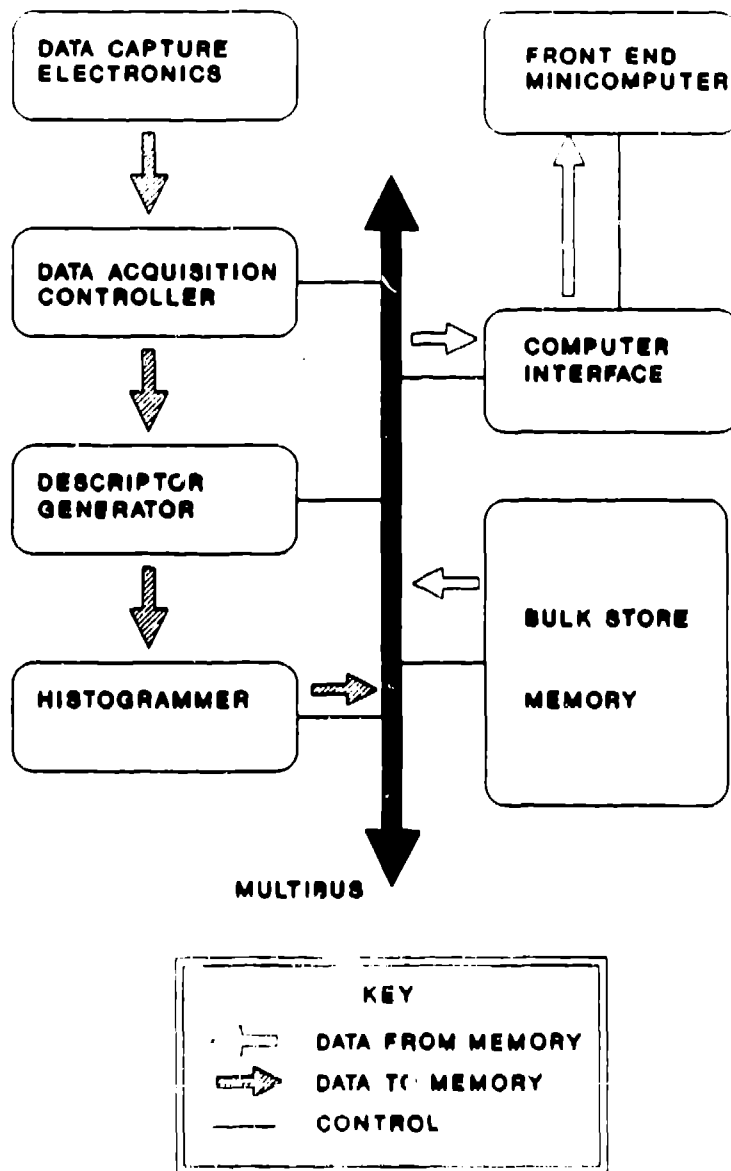


Fig. 1 Existing data acquisition electronics.

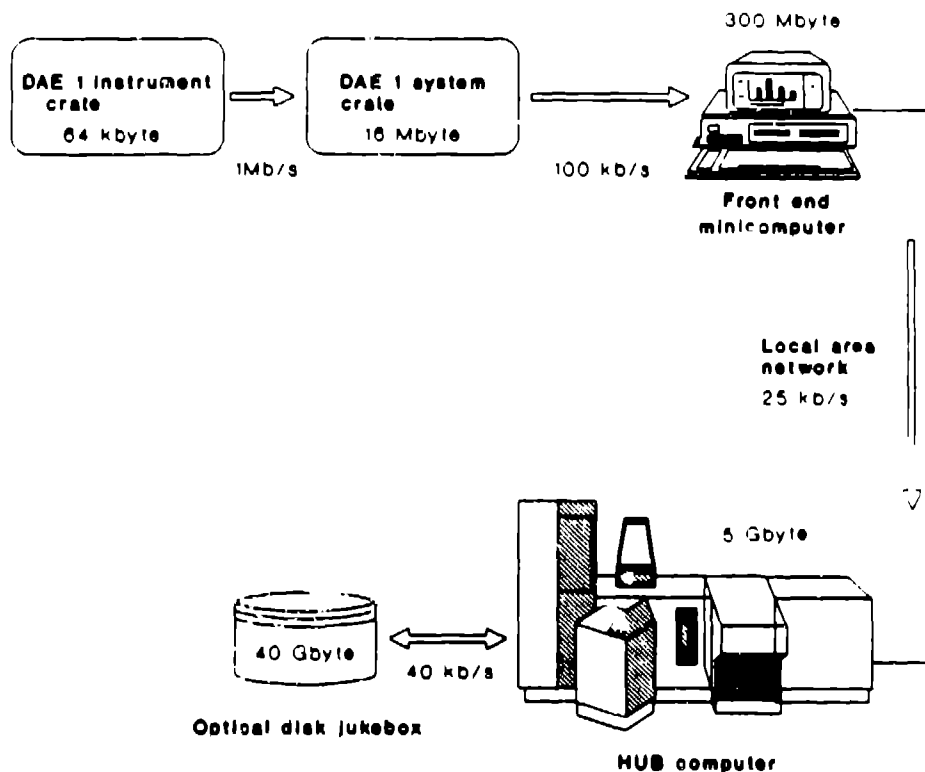


Fig. 2 Current ISIS data migration path.

engines to be employed are TRANSPUTERS rather than Motorola 680x0 or National Semiconductor NS32032, mainly because we have not been able to find a commercially supported multiprocessing and multiprocessor operating system for the latter serial processors; whereas, from the second quarter of 1988, a variety have been available for the T4 and T8 transputers. Moreover, transputer architecture automatically lends itself to increasing overall processing performance by simply configuring further transputers in parallel using the links. Despite the flexibility of the transputer-link architecture, it was deemed necessary that the DAE 1a remains based on a databus because the 300 ns read/modify/write cycle of the T800 and the peak link speed of 1.5 Mbytes/second would impose too great a practical limitation on the allowed data collection speed should only the links be available.

The major enhancements desired for DAE 2 compared with DAE 1 are as follows:

- a) The address bus should be at least 32 bits wide to enable enough memory to be configured for all experiments in the future.
- b) The databus components should be capable of read/modify/write cycles at greater than 4 Mhz in anticipation of future data rates in excess of the current value of 1 Mhz. The higher bus speed would also prevent online

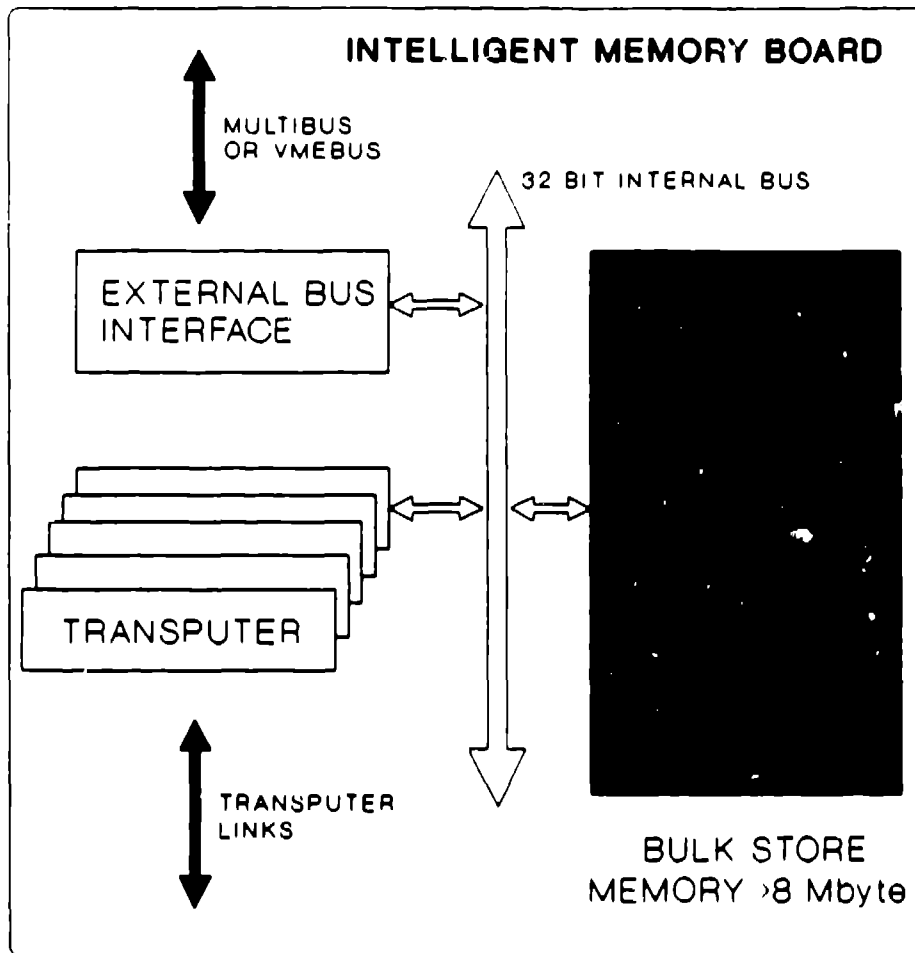


Fig. 3 New intelligent DAE board.

data analysis from competing with data collection for the available bus bandwidth.

- c) It may eventually be necessary to install a software programmable unit (descriptor processor), which maps the time of arrival and the position on the detector of a neutron event to the memory location to be incremented. This is occasioned by such instruments as HIPD, which have the capacity to map uneconomically large amounts of memory using the current relatively inflexible descriptor generator technology. Plans for the descriptor processor unit are not far advanced at this point, but it is reasonable to expect to use digital signal processors such as the Motorola DSP 56000, which are efficient at performing the type of multiply/accumulate functions we will require.

- d) Scientists increasingly need to inspect the data as they are accumulated, particularly with reference to finding peaks and assessing the optimum duration of a run. With this in view, it is planned to incorporate a real time graphics display within DAE 2.

These requirements lead to the probable future DAE layout illustrated schematically in Fig. 4.

### **Our current evaluation systems**

In implementing DAE 2, we are attempting to preserve as much of our original intellectual and financial investment in DAE 1 as possible. Consequently, for the moment we have concentrated our efforts primarily on the system crate. This crate is the part of the data acquisition system interfaced to the FEM that controls data collection processes, 40-bit neutron event descriptors from the instrument crate, and histograms them in bulk memory. Our first evaluation system, known as DAE 1a is illustrated schematically in Fig. 5. Here we have made the minimum change necessary consistent with the overall plan since we have replaced the Multibus bulk store memory with in-house designed intelligent memory boards, each containing 1 Mbyte of RAM and one transputer. This enhancement is currently operational and will be available to ISIS instruments from the start to 1989. I expect this to be a major platform on which the necessary advanced software will be developed. We selected the CAPLIN QT0 as the interface between the transputer and the VAX mainly because it was the only one available that fulfilled our requirements. Nevertheless, this technically advanced board does have valuable properties, such as the ability to support three transputer systems, and a reasonably fast link to QBUS data rate. An interesting feature of DAE 1 is that it offers two routes for the transfer of data to the FEM, via the original computer interface (CI) or using the transputer link. The best attainable data rates for the two routes are 120 Kbytes/second for the CI and about 100 Kbytes/second for the link.

At the same time as developing DAE 1a, a closer approximation to DAE 2 is being assembled. It is shown schematically in Fig. 6. The VME bus was chosen for the following reasons:

- a) It has 32 bit addressing and, in principle, supports bus speeds well in excess of the required 4 Mhz. The bus also supports read/modify/write as a single bus operation.
- b) There is considerable commercial support for VME technology, particularly for the provision of functional boards. This may be important in the choice of graphics processors.
- c) VME systems are much less expensive than the main competitor, which is FASTBUS.

The intelligent memory board used in this DAE 2 is the commercial INMOS BOO11 board, which has stations for three transputers but has only 2 Mbytes of onboard RAM. The shortage of RAM in the BOO11 or the need to reduce costs may eventually cause us to build an analogous board possible with fewer processors and at least 8 Mbytes of memory. Apart from this, the first major hardware design effort will be to produce a VME-based memory incrementer capable of receiving the output

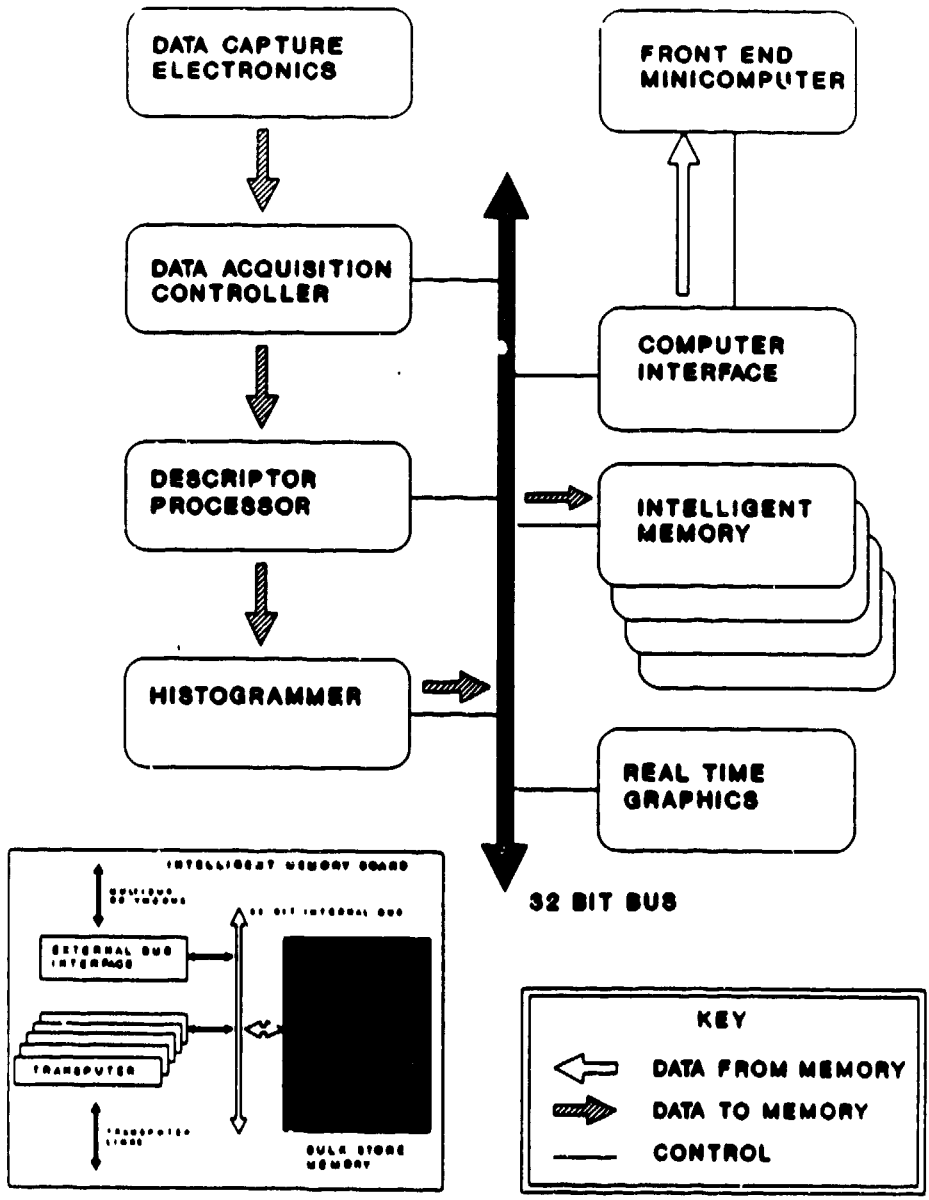


Fig. 4 Probably future DAE layout.

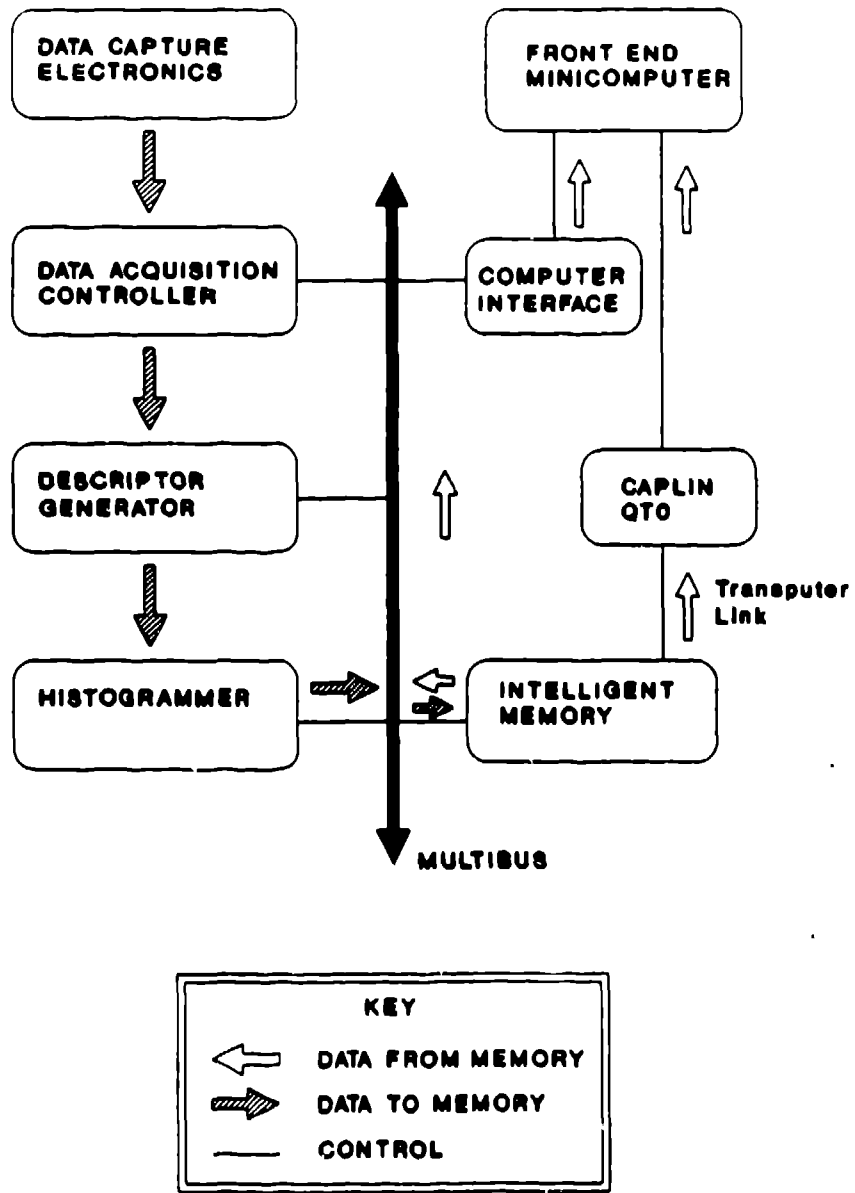


Fig. 5 Evaluation system 1.

of the current descriptor generator. The future migration path away from DAE 1 to DAE 2 is clearly to reimplement the functional boards from the Multibus crate to the VME crate in bottom to top order in Fig. 6. This process may hopefully be accomplished gradually and with the minimum of disruption to the instruments' operation.

### **DAE 2 software**

We propose to write most of the software within the advanced DAE using a parallel implementation of the C language called multi-C. This supports multiple C processes programmed on an arbitrary configuration of transputers. The C language was chosen rather than the major alternative, OCCAM 2, for two reasons:

- a) Many more of us are conversant with the language.
- b) OCCAM 2 is generally supported by a system called TDS. We found this system to be extremely awkward to use, particularly from its normal host, the IBM PC. The folding editor, although elegant in concept, does not appear to us to be conducive in association with the language itself in producing major software systems.

In developing the software, we must pay great attention to trends within the computer industry, particularly with respect to user interfaces. In the systems area, it would be valuable if the DAE 2 were cluster sharable. An entertaining area might be to implement an MSCP analogue on the DAE 2 processor responsible for communications. (MSCP is Digital's proprietary mass-storage subsystem protocol.) To facilitate user applications for the DAE processing power, it may be valuable to implement at least part of the X-windows X protocol. This implementation would be supported by DEC themselves in the C language by the DEC-windows migration package.

The required software functionality changes, depending on the time domain of operation. While data are being collected, the main functions would be:

- a) Supporting interactive peak searching for the purposes of monitoring data collection; checking instrument alignment and estimating optimum run duration.
- b) Performing hardware-system-error checking. This would entail such activity as checking for time-dependent inconsistencies in the data as collection proceeds.

At the completion of a run, the emphasis of the software changes to compression and/or analysis of the collected data. In the cases of some instruments the data analysis doubles as a very powerful data compression. Two examples illustrate this point. On HRPD, spectra of adjacent detectors have similar profiles, but are phase-shifted by an amount dictated by the geometry of the machine. Large reductions in data storage requirements may be achieved by performing this phase shift using the DAE processors prior to data migration to the FEM. (This shift may eventually be accomplished using the programmable descriptor processor mentioned in Fig. 4.) With access to large amounts of processing power, it would also be possible to peak

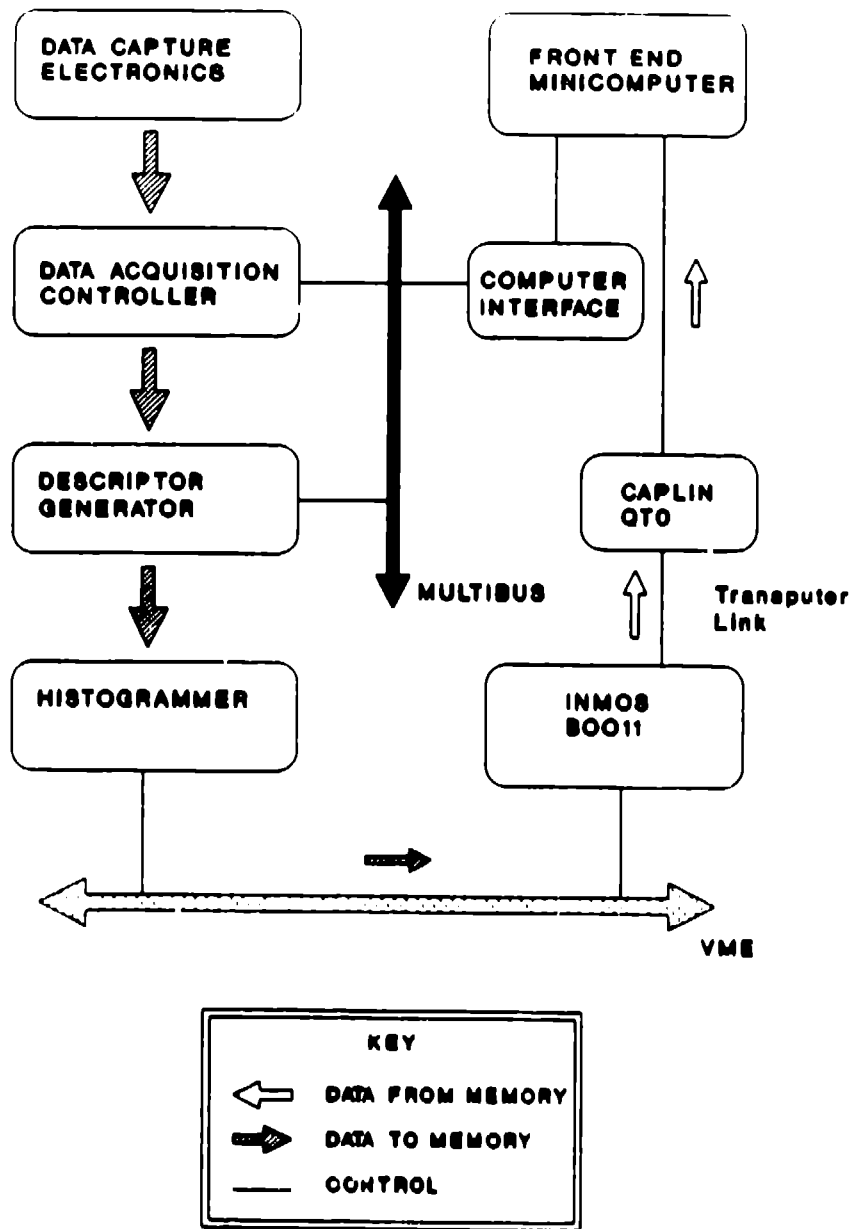


Fig. 6 Evaluation system 2.



search the sparse data collected by a single crystal diffractometer and produce a potentially enormous reduction in data volume. However, even in less helpful situations, much compression may be performed by empirical methods, which make few prior assumptions about the data. The two most promising methods investigated so far are storing the data in a format analogous to a VMS descriptor and incremental byte packing. In the former case contiguous data points with the same value are not all stored but rather are abbreviated to a descriptor defining the data type (e. g., BYTE, WORD, LONG\_WORD), a value count and a value field. The strategy may be extended to values which differ by less than the standard deviation from their mean, provided care is taken not to miss weak trends in the data. The second compression strategy depends on the difference between any two adjacent data points, not exceeding 256 for byte operations. Here only the initial value is stored in a whole word and the remaining data are stored as incremental bytes.

I expect the DAE 2 processing power to be used not only for the above-mentioned tasks, but also for analysis functions such as Rietvelt-profile refinements. To this end it is the intention to provide a set of software tools resident within the transputer domain but accessible to the instrument user, quite possibly via the popular GENIE data-reduction suite. This package is currently being rewritten to include better functionality, particularly with respect to access to windowing; hence the suggestion of an X-windows interface to DAE 2.

## Workshop summary on data acquisition

*R. Nelson*  
Los Alamos Neutron Scattering Center  
Los Alamos, New Mexico 87545  
USA

Two presentations were given during the data acquisition session of the ICANS X conference. Bill Pulford of the Rutherford Laboratory and Gary Cort from Los Alamos delivered formal talks. The latter included a demonstration using a DEC workstation.

Generalizing the presentations and ensuing discussions, I feel that the first generation of data acquisition systems for pulsed neutrons sources may expect some significant changes in the next two years. There are principally four factors driving these changes. First, neutron scattering facilities have been operating now for several years and experience with higher neutron intensities has revealed certain operational problems. Second, the computer technology underlying our data acquisition systems continues to advance rapidly and to offer better alternatives for our applications. Couple technology changes to the imagination of users and system implementers, and change is inevitable unless constrained by the costs for change. Thus, imagination and cost are the third and fourth factors contributing to predicted changes for data acquisition systems.

In the hardware area, changes will be significant. First, systems using Multibus I modules, e.g., IPNS and ISIS, are experiencing growing pains as memory requirements push into the 16 Mbyte memory addressing limit imposed by this architecture. Memory demands are rising with the increased use of position-sensitive detectors. Large memory capacity is a common requirement in data acquisition systems, and designers should expect to provide systems supporting 32-bit addressing. Costs for memory continue to decline as technology delivers ever higher densities in RAM chips.

Second, processing power at the front end is too limited. Either the performance is sufficient but data handling is inflexible, or performance is inadequate but flexible. Currently, processor performance problems are apparent in two roles: descriptor generation and data formatting. Increased memory utilization further aggravates the problems for both of these functions. For descriptor generation, users want to see in real-time or near-time meaningful results for experiments in transformed physical coordinates. Waiting several minutes for the host to prepare an image is not acceptable. Data formatting at the end of the run is becoming a bottleneck for data acquisition. With increased intensity, the runs are becoming short enough that spending 3 to 5 minutes saving the data can consume 25-50% of the beam time allocated to an experiment. Additional front-end processors may alleviate this difficulty. While the cost of the microprocessors decreases as their computational

power increases, there remains some expensive software to be written to realize these potential benefits.

Third, on-line archive capacity for stored data will be greatly increased by exploiting optical disk technology. With access times for arbitrary files under 20 seconds, automated robotic systems with capacities of up to 500 to 1000 Gbyte will be available. Such systems would cost on the order of \$1000K a few years ago, but today can be found for one quarter of that cost.

The last major impact of hardware change is strongly coupled to software change as well. Expect to replace terminals with graphics-oriented interactive workstations. Generally, such workstations include a multi-window work surface (screen) and a pointing device (mouse). The computation power in a single workstation today rivals that of the VAX 8600, which is often dedicated as the centralized data analysis computer. The graphics capability enables the use of alternative interfaces frequently regarded as significantly more friendly to the novice user, e.g., the Macintosh interface. Because old ways will die hard and experts will want shortcuts around menu-driven protocols, terminal-like commands must be included in all future software-interface strategies. While the costs of workstations will exceed the costs of graphics terminals by a factor of four, keep in mind that the requirements for the central analysis computer will significantly diminish. Costs for the user friendly interface may be high initially as we mount the learning curve of this new technology.

In conclusion, technology has provided feasible and affordable solutions to many problems posed by the neutron-scattering community. But there is mounting evidence that some "cultural" changes may be required. While it may be feasible to capture and save a 50 Mbyte data file five times an hour, is it a reasonable thing to do? Perhaps science is adequately served by saving some derived quantities, and discarding most of the raw data. Combining and reducing histograms may not only be desirable but essential, lest the experimenter be hopelessly buried in data. Equally well, can the neutron-scattering community evolve from a terminal-oriented society as earlier it evolved from a card-punch society?

## Upgrades to the ISIS moderator configuration

A. D. Taylor  
Rutherford Appleton Laboratory  
Chilton, Didcot, Oxon, OX11 0QX  
UNITED KINGDOM

**ABSTRACT:** Possible upgrades to the ISIS moderator configuration are discussed in the light of the current and projected instrument suite.

### Introduction

The current ISIS moderator configuration, shown in Fig. 1, was designed in 1980 to provide a flexible set of beams for a hypothetical instrument suite. The use of fluid moderators at three different temperatures offering six faces to the instruments, see Table I, has proved to be effective.<sup>[1]</sup> In this paper we discuss an upgrade of these moderators in the light of the current and projected instrument configuration.

**Table I** ISIS moderator-instrument configuration

<u>Beam</u>	<u>Moderator</u>	<u>Instrument</u>
S1	H <sub>2</sub> O (Gd at 3.0 cm)	POLARIS
S2	H <sub>2</sub> O (Gd at 3.0 cm)	eVS
S3	H <sub>2</sub> O (Gd at 3.0 cm)	SXD
S4	H <sub>2</sub> O (Gd at 2.2 cm)	—
S5	H <sub>2</sub> O (Gd at 2.2 cm)	—
S6	CH <sub>4</sub> at 100 K	MARI
S7	CH <sub>4</sub> at 100 K	LAD
S8	CH <sub>4</sub> at 100 K	HRPD
S9	CH <sub>4</sub> at 100 K	TEST
N1	CH <sub>4</sub> at 100 K	SANDALS
N2	CH <sub>4</sub> at 100 K	PRISMA
N3	CH <sub>4</sub> at 100 K	—
N4	H <sub>2</sub> at 25 K	CRISP
N5	H <sub>2</sub> at 25 K	LOQ
N6	H <sub>2</sub> at 25 K	IRIS
N7	H <sub>2</sub> O (Gd at 1.5 cm)	—
N8	H <sub>2</sub> O (Gd at 1.5 cm)	TFXA
N9	H <sub>2</sub> O (Gd at 1.5 cm)	HET

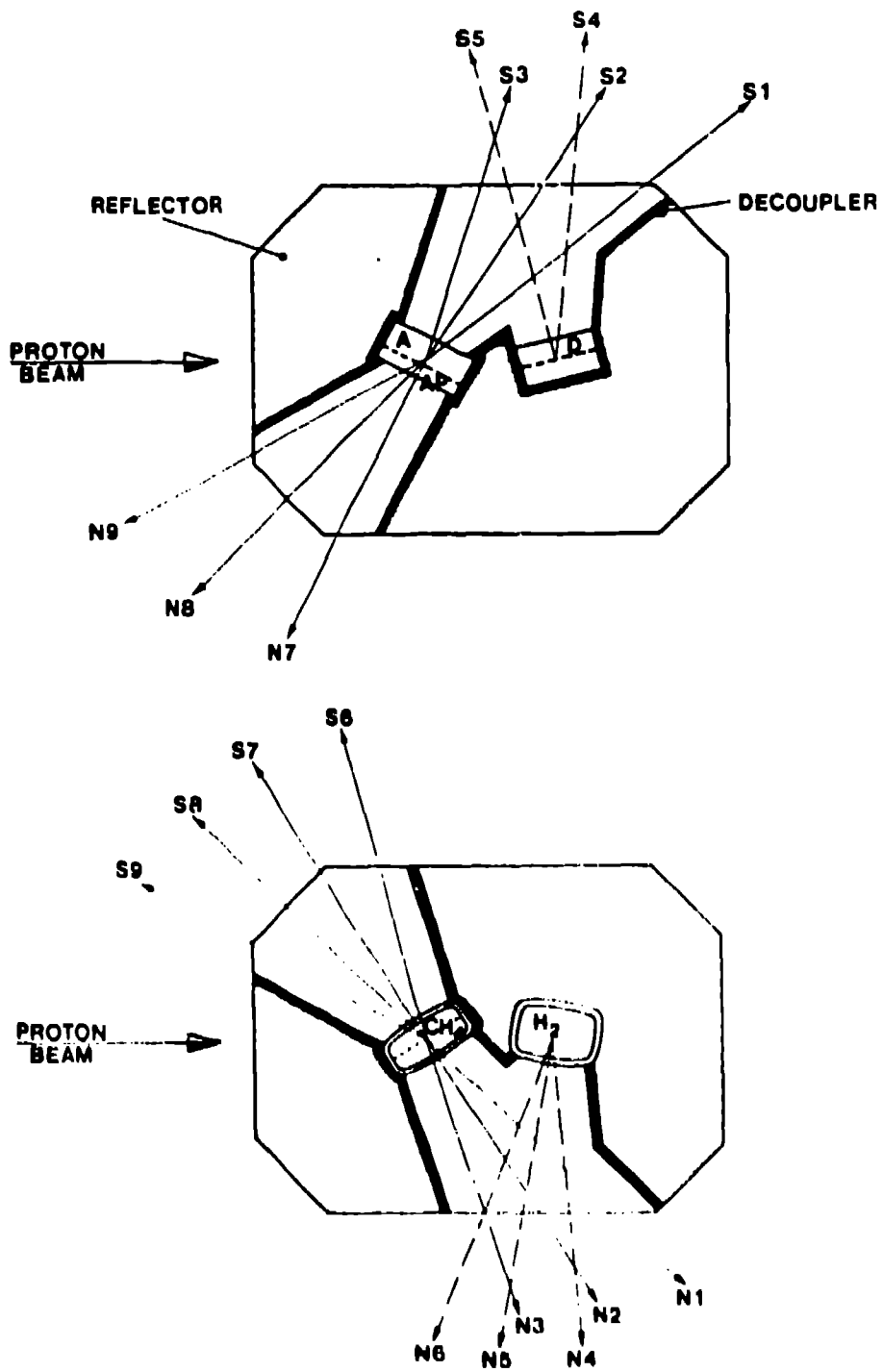


Fig. 1 Current configuration.

### **Change in poison depth for beams S1, S2 and S3**

The southwest corner group S1, S2, S3 currently views an ambient water moderator poisoned at a depth of 3 cm. This group was designed to optimise the thermal intensity at the expense of lineshape. This was originally felt to be the appropriate configuration for polarisation tests on POLARIS and the development of single crystal studies on SXD. The eVS spectrometer only utilises the slowing down part of the spectrum, which is independent of poison depth.

The new use of POLARIS is as a medium-resolution powder diffractometer. This would greatly benefit from having the lineshape in the thermal region improved from the current 30- $\mu$ s decay to a 20- $\mu$ s decay (see Figs. 2 and 3). SXD would similarly be improved. Neither of these diffractometers is intensity-limited at 100  $\mu$ A operation. Again current uses of eVS are neutral to such a change.

We propose to reduce the poison depth on the south side of the ambient water moderator from 3 cm to 1.5 cm. This will be accomplished by replacing the entire moderator vessel early in 1989.

### **Cold beam lines at ISIS**

Successful instruments have been built on all three of the beam lines that view the 25 K hydrogen moderator. The construction of a double guide on the IRIS beam is a long-term option to provide a new cold beam, but there is an immediate demand for a new cold beam for CRISP-II (a reflectometer optimised for liquids work with \*10 the intensity of the current CRISP). It would be possible to site CRISP-II on S4 if this beam could view the back of the hydrogen moderator. The initial flexibility of the ISIS moderator assembly allows each line to view any moderator. The beryllium/D<sub>2</sub>O reflector layer in the plane of the lower moderators would have to be replaced, see Fig. 4, and the window on the target station void altered to permit S4 to view a lower moderator. Such changes were anticipated on the original design. The change in performance of the front face of the hydrogen moderator would be less than 10%.<sup>[2]</sup>

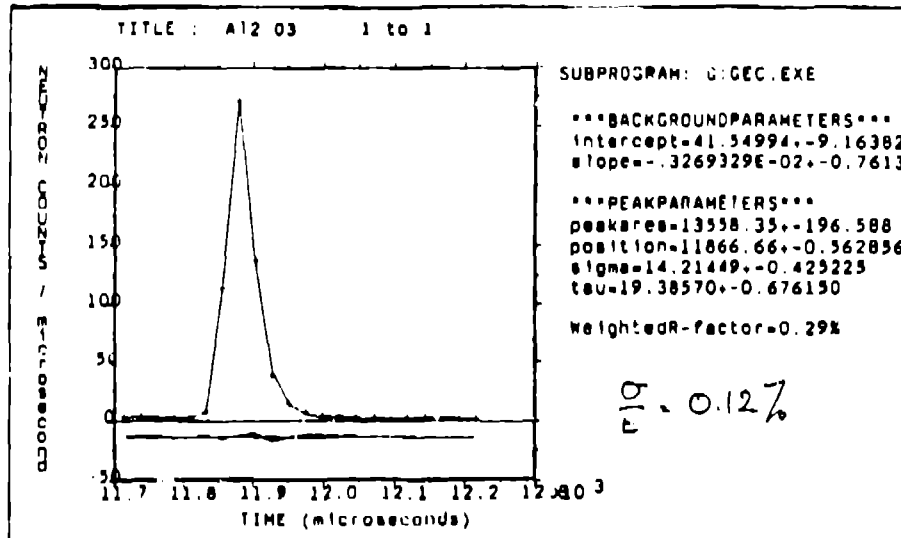
A design study will begin shortly on a new reflector layer to allow S4 to view the back of the hydrogen moderator.

### **Improved pulse shape for HRPD**

HRPD currently has a 35- $\mu$ s decay constant in the thermal region. A significant improvement in its performance could be obtained if this were reduced to say below 20  $\mu$ s. This is possible in two ways.

Firstly, by reducing the poison depth. Studies show (see Fig. 5)<sup>[1]</sup> that a 1-cm poison depth would give a decay of less than 20  $\mu$ s at the expense of a factor of two in thermal flux. The effect of this on LAD, MARI and S9 would have to be determined. Such a change is not as simple as altering an ambient moderator and might require the development of significant remote handling expertise.

INSTRUMENT: HET USER: Z A Q  
RUN NUMBER: 691 RUN START TIME: 6-JUL-1988 11:37:45  
SPECTRUM: 67 PLOT DATE: THU 27-OCT-1988 14:49:05  
NO GROUPING OF BINS  
LOCATION: HETDISK:[HETMGR.RESTORE]HET00691.RAW



INSTRUMENT: POLARIS USER: JH/ACH  
RUN NUMBER: 1593 RUN START TIME: 9-JUN-1988 21:34:30  
SPECTRUM: 1 PLOT DATE: THU 27-OCT-1988 14:50:58  
NO GROUPING OF BINS  
LOCATION: POLDISK:[POLMGR.DATA]POL01593.RAW

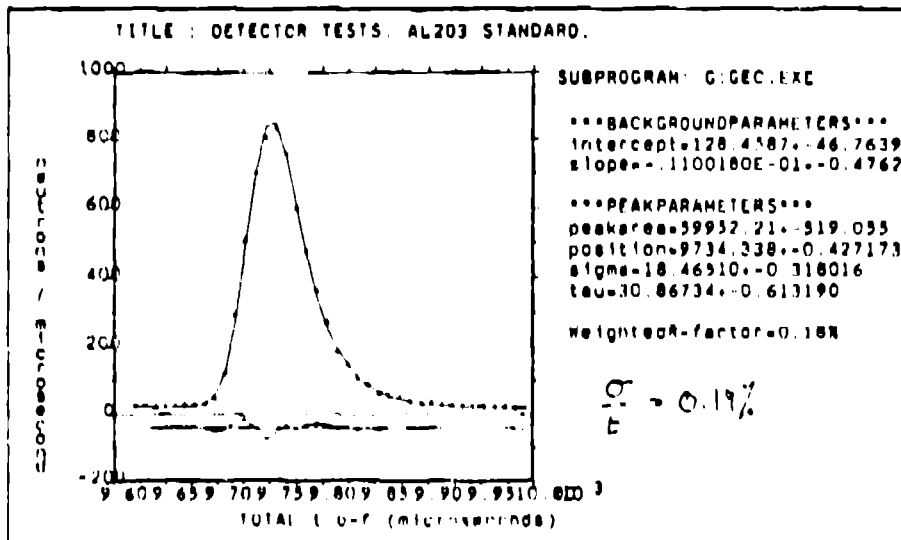


Fig. 2 Lineshape analysis of the same Al<sub>2</sub>O<sub>3</sub> reflection as measured on HET and POLARIS. Note the reduction in width and decay constant.

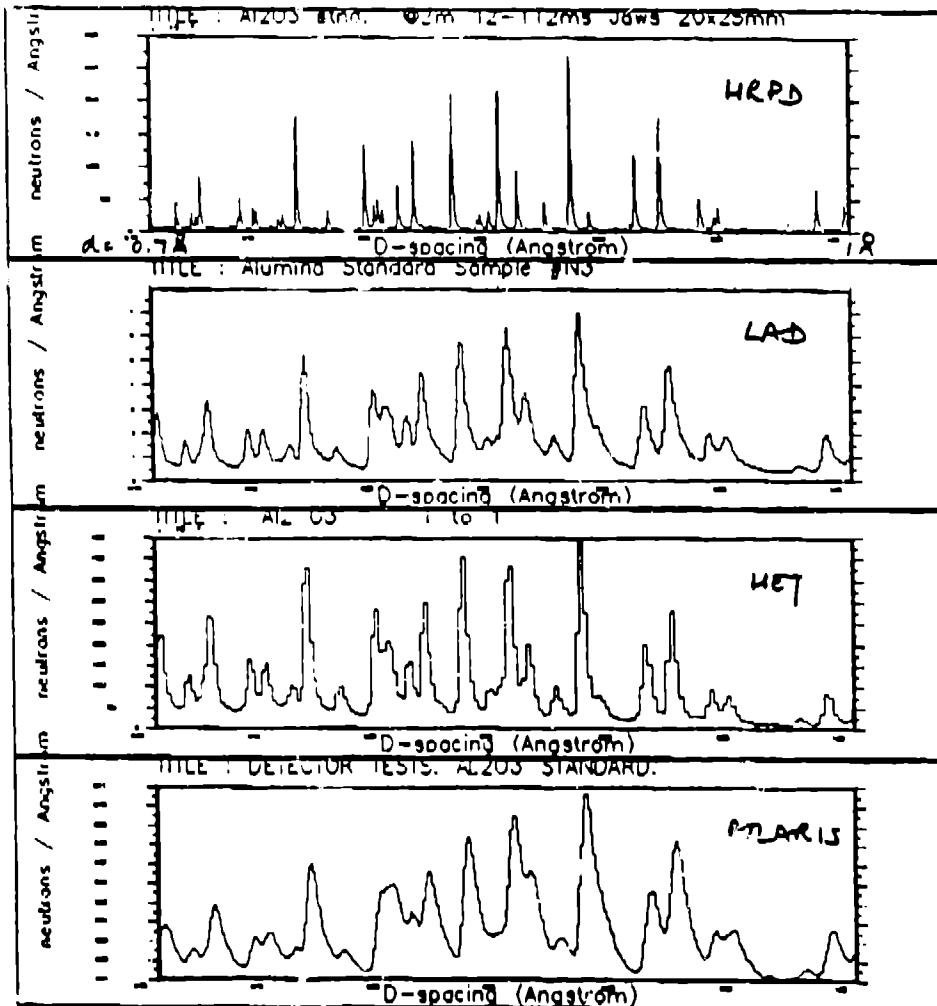


Fig. 3 A comparison of the lineshape from the various diffractometers at ISIS. The advantages of the 1.5 cm poison depth (HET) over the 3 cm poison depth (POLARIS) are obvious.

A second approach is to change the moderator material from 95 K liquid methane to a 20 K methane slurry in liquid hydrogen or a liquid-hydrogen-cooled metal hydride. Such moderators would suppress the effects of thermalisation but might still maintain the high hydrogen density necessary for a good epithermal pulse shape. These concepts would require a major development programme on new moderator materials.

The impact of a reduced poison depth on LAD and MARI will be investigated as will the potential of high-density, low-temperature moderating materials.



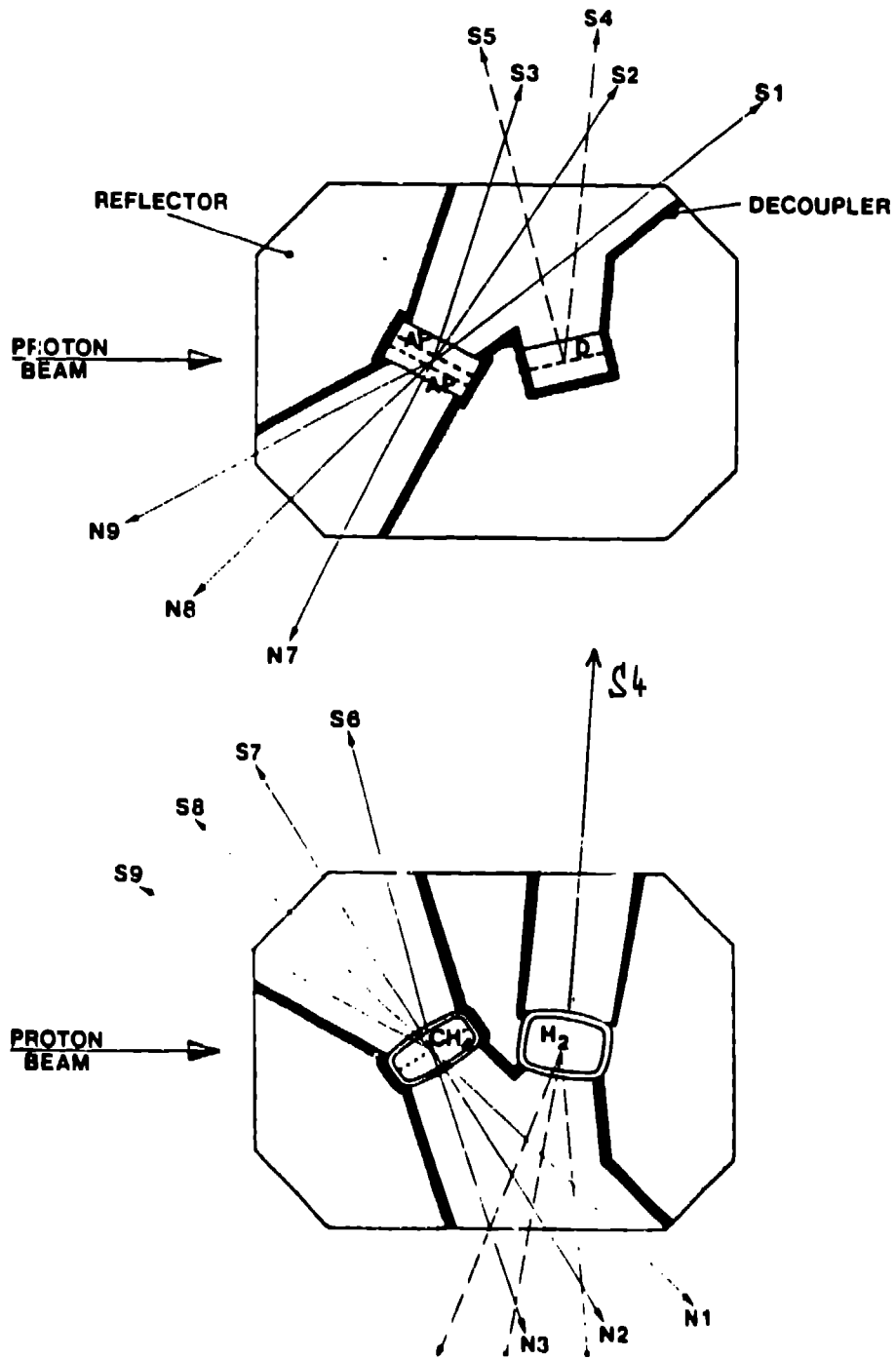


Fig. 4 Proposed configuration.

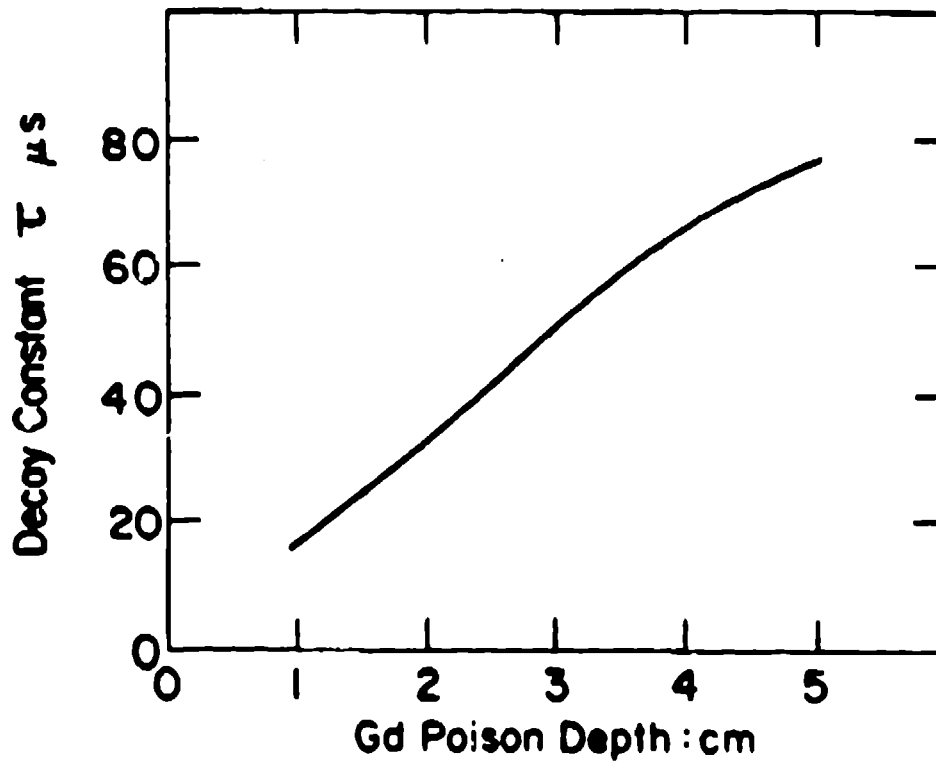


Fig. 5 The calculated behaviour of the exponential decay constant  $\tau$  as a function of the gadolinium poison depth in a  $10 \times 10 \times 5 \text{ cm}^3$  liquid methane moderator.

#### References

1. A. D. Taylor, "SNS Moderator Performance Predictions," RAL-84-120.
2. A. D. Taylor, "Neutron Transport from Target to Moderators," RL-81-007.
3. J. M. Carpenter, R. A. Robinson, A. K. Taylor, and D. J. Picton, 1985, "Measurement and Fitting of Spectrum and Pulse Shapes of a Liquid Methane Moderator," Nucl. Inst. and Meth. A234, 542-551.

## A combined H<sub>2</sub>/CH<sub>4</sub> cold moderator for a short pulsed neutron source

*K. D. Williamson*  
Los Alamos National Laboratory  
Los Alamos, New Mexico  
USA

*A.T. Lucas*  
Rutherford-Appleton Laboratory  
Chilton, Didcot  
Oxon  
UNITED KINGDOM

### Foreword

Both the ISIS (Rutherford-Appleton Laboratory) spallation source and the Los Alamos Neutron Scattering Center (LANSCE) were designed to produce neutrons as a result of an 800-MeV proton beam being incident on a target. Both systems are intended to accept beam intensities up to 200  $\mu$ A.

Cryogenic moderators of liquid hydrogen and methane are either in use or are planned for service at both facilities. Very low temperature methane would be an ideal moderating material as it has a high hydrogen density and many low frequency modes, which facilitate thermalization. Such moderators are in service at two major world facilities, KEK (Japan) and Argonne National Laboratory (USA).

Unfortunately, solid methane has very low thermal conductivity (see Fig. 1) and is subject to radiation damage making a moderator of this type impractical for use in high-intensity beam, such as indicated above. This report outlines a possible alternative using small spheres of solid methane in a matrix of supercritical hydrogen at 25 K.

### General approach

A novel method of building a low-temperature methane moderator might be to use small spheres in a flowing medium of supercritical hydrogen at 25 K. Initial calculations indicate that a diameter of 1.5 mm is about the optimum size. At 200  $\mu$ A, such a sphere would receive about 1.0 mW of neutron energy. The heat flux from the inner core to the outer surface, assuming a temperature gradient of 30 K, would be about 1.25 mW for an outer surface temperature of 25 K. This would mean a maximum temperature within the sphere of about 55 K, which is 35 K below the freezing point. Unless neutronically unacceptable, this assumption would seem to form a reasonable base for subsequent design calculations. The temperature gradients in present solid moderators are not known, but it is suspected that they might not be too different from the figure mentioned above.

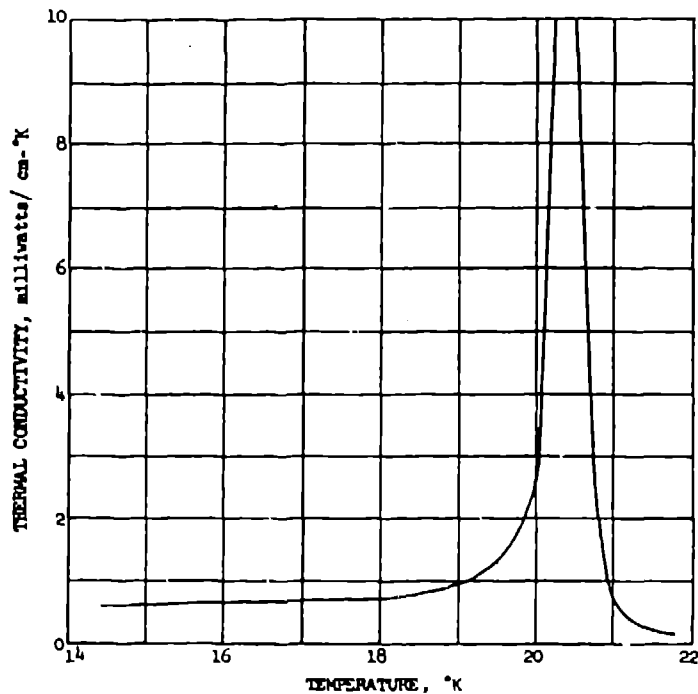
Source of Data:

Gerritsen, A.H. and van der Star, P., *Physica*, 9, 503-12 (1942).

Commun. Kamerlingh Onnes Lab. Univ. Leiden, Commun. No. 265a.

Comments:

In the graph below the discontinuity that occurs at the transition temperature (20.4°K) is similar to that found for the specific heat.



KDT/VJJ Issued: 8/20/59

Fig. 1 Thermal conductivity of solid methane (15° to 21°K).

### Proposed system of operation

Uniformly sized spheres can theoretically be packed to a density of better than 73%. However, for practical purposes, an estimated density of 60% has been assumed. The hydrogen density of this mixture would be 0.05 atoms/Å<sup>3</sup>, which is intermediate between methane and hydrogen (i.e., 0.06 and 0.042 atoms/Å<sup>3</sup>).

To transport a mixed fluid of this density through pipework into a moderator would be impossible. Therefore, the only recourse is to generate the spheres within the moderator vessel. This would require a cooling region at the top of the vessel outside of the neutron flux large enough to freeze and cool incoming liquid methane. Liquid methane at 95 K would be injected through nozzles in short bursts to form spheres naturally by surface tension. To maintain repeatability would require careful attention to such factors as "duration of burst" and nozzle diameter. Cooling such a

sphere to 25 K throughout would require 210 mJ. Because the heat flux is limited to 1.25 mJ/s, the time required in the cooling region would be about three minutes. This figure can now be used to give a methane flow rate and a sphere production rate, which works out to be 250 spheres per second for a moderator volume of one liter. Each sphere, assuming uniformity of flow, would then remain in the moderating region for about 20 minutes.

To assist a steady downward movement of the spheres and prevent block-ups, a vibrator would be attached to the moderator vessel. Such devices are driven by gas and operate by the oscillation of a steel ball in a circular cell. They are available commercially, though not specifically for use at cryogenic temperatures; this should not present a problem if stainless steel is used throughout.

The above sphere-production rate represents a liquid flow of 30 cm<sup>3</sup>/min, which is too low for a continuous flow system. It would be better, therefore, to maintain a liquid-methane flow of ~150 cm<sup>3</sup>/s and pass the majority through a bypass restrictor. A gas-operated cryo-valve (see Fig. 2) would admit liquid to the nozzles as required, and a second cryo-valve in the outlet methane pipe would be used during the initial start up of the system as described later. Pulsations in the flow of the methane would be provided by a motor-driven oscillator connected into the flow line. Together with the liquid-methane circulator, this would produce pressure cycles ranging from zero to double the steady-state pressure produced by the circulator.

All equipment at the moderator would obviously have to be radiation hard making the use of inorganic materials essential.

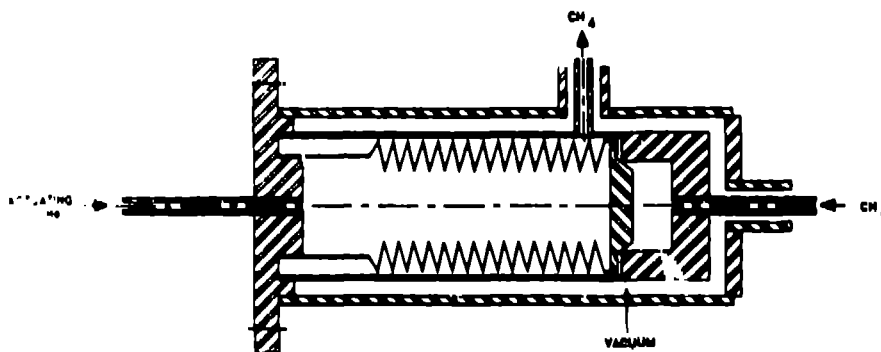


Fig. 2 Remotely operable cryo-valve.

### Construction

The moderator vessel would constitute a vertical chamber with outward curving sides on account of the high operating pressure of 15 bar absolute. An additional height of ~25 mm outside the neutron beam would rob the target of reflector material. Likewise, a liquification region at the bottom would represent a further loss of ~12 mm in length. Unfortunately, this is the price to be paid for such a system and it must be balanced against the neutronic gains to be made.

Hydrogen would enter at the top of the vessel and exit through the end of the central vertical tube terminating just above the bottom of the moderating region. A strainer across the open tube would prevent the entry of methane particles. Methane would also enter at the top through a series of nozzles. Fully cooled spheres would then progress down the vessel, be melted off in a pool at the bottom, then drawn off into the return pipe. The flow-rate of hydrogen would probably be around  $500 \text{ cm}^3/\text{s}$ , although this could be increased to improve the skin coefficient of heat transfer of the sphere surfaces if necessary. A heating block to raise the sphere temperature above  $90 \text{ K}$  would be attached to the bottom of the vessel using warmed helium gas in a closed loop. Because the vessel wall would have a temperature gradient of  $65 \text{ K}$ , a thermal break in the form of a local thinning of the wall would be machined into the vessel. Also, the vessel would be tapered outwards by  $\sim 3 \text{ mm}$  over its height to assist the steady fall of the spheres (see Fig. 3).

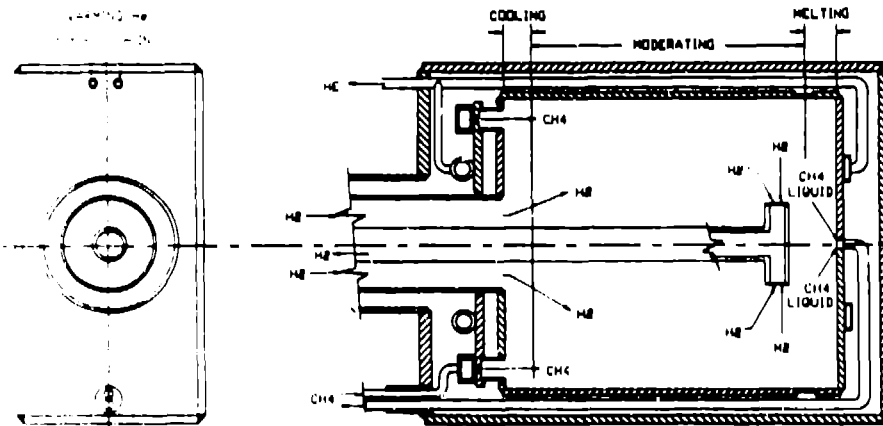


Fig. 3 Moderator canister.

### Refrigeration

The hydrogen refrigerator would be called upon to freeze and cool the methane spheres and also to remove nuclear heating during moderation. The calculated total load at  $25 \text{ K}$  would be about  $510 \text{ W}$ . The methane heat load would only represent transport losses plus losses incurred during purification, i.e.,  $200 \text{ W}$  at  $95 \text{ K}$ . This heat load would probably be removed by the same refrigerator by tapping into the circuit at an earlier stage (see Fig. 4).

### Installation and operation

The complete system would involve a complex of several feed and return loops. In addition to the hydrogen and methane systems, there would also be helium gas supplies to the warming block, the cryogenic valves, and the vibrator unit.

The most difficult operation would be that of initial start up. The two cryogenic methane valves would remain shut, though the methane circuit could be cooled

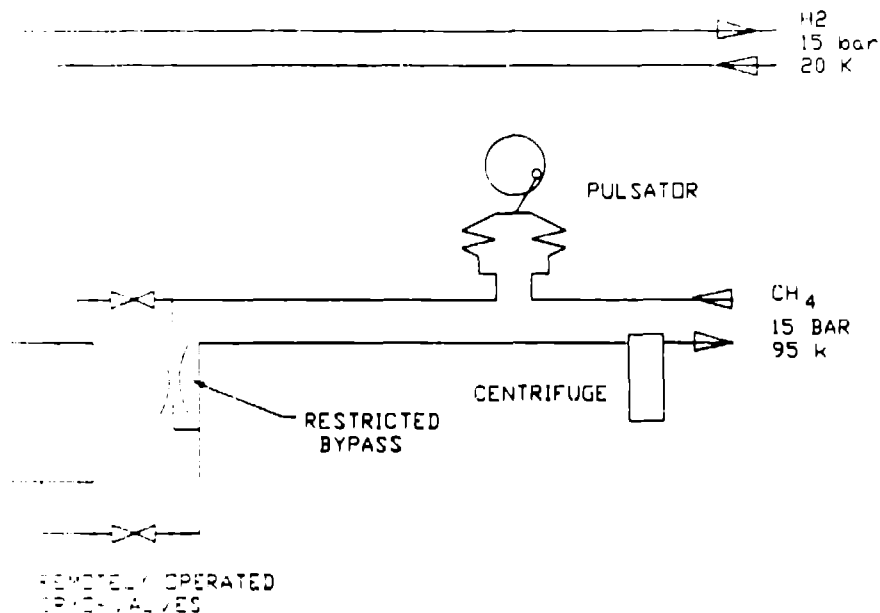


Fig. 4 Flow diagram.

through its bypass, while the full compliment of hydrogen at 15 bar absolute and 25 K was generated. The methane inlet valve would now be opened with the pulsator operating and the spheres formed. A careful check on the methane gas added together with a check on the hydrogen displaced would enable a good evaluation to be made of the progress. When "full", the exit/return methane valve would be opened. Confirmation of the existence of a pool of liquid at the bottom would be provided by a thermocouple able to differentiate liquid from gas; or, perhaps a platinum thermometer mounted vertically could actually measure the depth of liquid. Once the system was operational, the inlet valve would be opened and closed automatically in response to the liquid methane pressure or the liquid-level indicator. Under normal operation, liquid would prevent any hydrogen entering the methane exit, but during start up, any hydrogen penetrating the methane would be expelled as gas (at 95 K at the refrigerator end of the system).

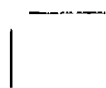

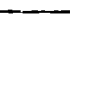
#### Development

The design of such a system could only be entertained with the backup of considerable experimentation. Initial work on sphere formation could be readily carried out using water in liquid nitrogen. This would ultimately have its limitations as the spheres would have a density of about  $0.9 \text{ gms/cm}^3$  in a fluid of  $0.8 \text{ gms/cm}^3$  density. The density of solid methane is  $0.522 \text{ gms/cm}^3$  and that of supercritical hydrogen only  $0.0669 \text{ gms/cm}^3$ . Further work could be done using water in helium gas at 25 K and 10 bar absolute with a density of  $0.025 \text{ gms/cm}^3$ . Finally, methane in helium would give a close approximation of the true fluid state.



## Conclusion

The overall challenge would be of a high order, but what calculations have been done indicate that thermodynamically such a system is feasible. If realized, such a system would provide significant improvements in the shape of the neutron pulse that is desired for pulsed source diffractometers.





## Pulsed-neutron production at the Brookhaven 200-MeV linac

*T. E. Ward, J. Alessi, J. Brennan, P. Grand, R. Lankshear, P. Montemurro,  
C. L. Snead, Jr., and N. Tsoupras*  
Department of Nuclear Energy  
Brookhaven National Laboratory  
Upton, New York 11973  
USA

**ABSTRACT:** The new 750-kV RFQ preinjector and double chopper system capable of selecting single nanosecond micropulses with repetition rates of 0.1 to 20 MHz has been installed at the Brookhaven 200-MeV proton linac. The micropulse intensity is approximately  $1 \times 10^9$  p/ $\mu$ pulse. Neutron time-of-flight path lengths of 30 to 100 meters at  $0^\circ$ ,  $12^\circ$ ,  $30^\circ$ ,  $45^\circ$ ,  $90^\circ$  and  $135^\circ$  are available as well as a zero-degree beam swinger capable of an angular range of  $0^\circ$  to  $25^\circ$ . Pulsed neutron beams of monoenergetic ( $p^7\text{Li} \rightarrow n^7\text{Be}$ ) and spallation ( $p^{238}\text{U} \rightarrow nx$ ) sources will be discussed in the present paper as well as detailing the chopped-beam capabilities.

### Introduction

The replacement of one of the Cockcroft-Walton preinjectors<sup>(1-3)</sup> with a new high-current 750-keV radiofrequency quadrupole (RFQ) will improve substantially the H<sup>+</sup> capabilities of the Brookhaven 200-MeV Linac<sup>(1-3)</sup>. In conjunction with the new RFQ, a double chopper capable of single micropulse selection (pulse width < 1 ns) with periods ranging from 100 ns to greater than 10  $\mu$ s will be installed. The new double-chopper RFQ system is detailed in the present paper as well as the neutron-time-of-flight (NTOF) capabilities that exist at the 200-MeV linac complex. Future improvements and upgrades that will also be described include a  $0^\circ$  to  $25^\circ$  beam swinger on the zero-degree line and intense pulsed monoenergetic and spallation neutron sources for use in nuclear physics and radiation-effects studies.

### The double-chopper RFQ system

The RFQ Linac input is from a 35-keV H<sup>+</sup> magnetron ion source modified to produce an axially symmetric beam matched to the RFQ. The RFQ parameters are summarized in Table I. Operational tests have routinely produced outputs of 50 mA from the RFQ, whereas the design current limit is rated at  $\sim$ 100 mA. The RFQ emittance at 50 mA was optimized for transport to the 200-meV linac.

Figure 1 shows an illustration of the double-chopper RFQ system. A fast beam chopper (Chop I) located between the ion source and the RFQ can variably bunch the beam with frequencies of 2.5 MHz or less. The first chopper is a slow-wave electrostatic deflection device that rejects the beam at a small aperture located before the RFQ. The second chopper (Chop II) is located after the RFQ and is phase-

locked to the RFQ. Chop II is a fixed-frequency sine-wave located after the RFQ and is phase-locked to the RFQ. Chop II is a fixed-frequency sine-wave chopper that selects single microbunches (440-ps width) of the 200-MHz RFQ linac. The duty factor of the double chopper is adjustable from one bunch every 100 ns to one bunch per 450- $\mu$ s macropulse. The macropulse frequency is 5 Hz. The standard 200-MHz micropulse intensity with 50-mA averaged current is  $1.2 \times 10^9$  protons/ $\mu$ pulse. The dc-averaged beam current with 10- $\mu$ s repetition rate and 5-Hz macrostructure is 50 nA, a value comparable with a 10- $\mu$ sec 200-MeV pulsed beam from a cyclotron such as the Indiana University Cyclotron.

Table 1  
RFQ Parameters:

Ion	H <sup>+</sup> H <sup>-</sup>
Input Energy	35 keV
Output Energy	753 keV
Current Limit	~100 mA
Operating Frequency	201.25 MHz
Peak Cavity Power	100 kW
Stored Energy	0.5 Joules
Duty Factor	0.007
Structure	4-vane, ringed
Vane Length	1.62 m

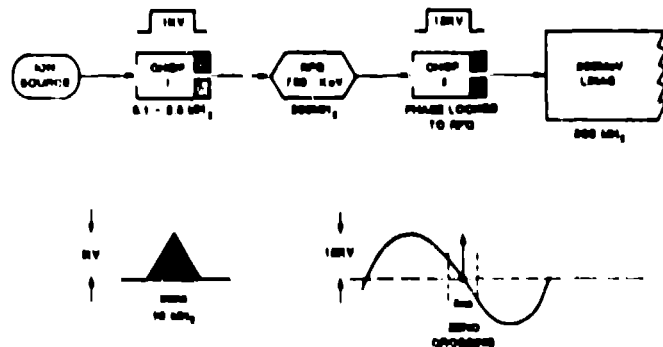


Fig. 1 Double-chopper RFQ showing single-micropulse selection.

### 200-MeV linac performance

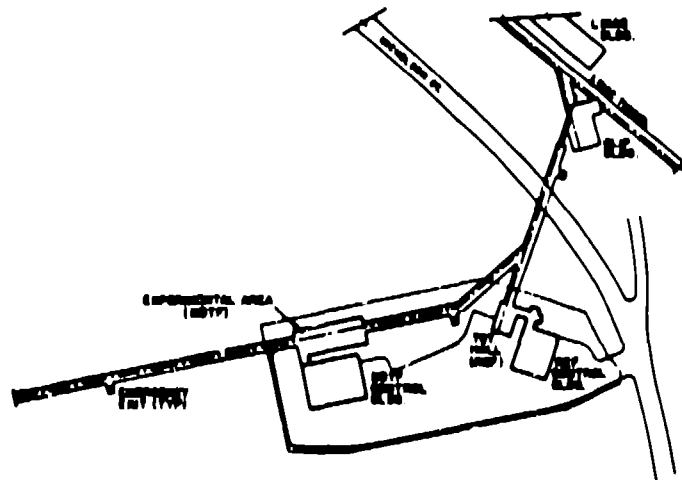
The linac can accelerate H<sup>+</sup> or H<sup>-</sup> beams of 92.6, 116.5, 139.0, 160.5, 181.0 and 200.3 MeV with an energy spread of about 140 keV at 200 MeV.<sup>(1)</sup> The standard operating beam at 200 MeV is a 30-mA peak current and 450- $\mu$ s-wide macropulse. The repetition rate is currently 5 pps, but can be increased to 7-8 pps. The

microstructure is 200 MHz or 1  $\mu$ pulse every 5 ns with a  $\mu$ pulse with  $<1$  ns. The typical beam spot is 1.5 cm FWHM Gaussian in both vertical and horizontal dimensions yielding a flux of approximately  $9 \times 10^{12}$  p/s  $\text{cm}^2$ .<sup>[2]</sup> The maximum total beam current per macropulse is about 10  $\mu$ A dc-averaged.

The adjustable parameters are the macropulse (5  $\mu$ s to 500  $\mu$ s), the peak current (1 mA to 30 mA), the transported beam (1 nA to 10 A) and beam size (3  $\text{cm}^2$  to 7850  $\text{cm}^2$ ) delivered to the target areas of the Radiation Effects Facility (REF) and Neutral Beam Test Facility (NBTF).

### **NTOF facilities and performance**

The 200-MeV linac complex consists of NTOF facilities at the Radiation Effects Facility (REF) and Neutral Beam Test Facility (NBTF) as shown in Fig. 2. The REF has 30 to 100-m flight paths at 12°, 30°, 45°, 90°, and 135° with approximately 30 m of earth shielding (12" tubes through shielding). The zero-degree line located at the NBTF consists of a 3-m-diameter underground tunnel with a present length of 100 m, a zero-degree sweep and dump magnet, and a collimation wall (3-m thick).



**Fig. 2** BNL 200-MeV Linac Complex.

The momentum spread in the beam ( $\Delta p/p = 7 \times 10^{-4}$ ), coupled with the 125-m beam transport into the REF and NBTF, increases the width of the micropulse to about 1 ns from the intrinsic width of 440 ps that results from the linac acceleration. The overall NTOF energy resolution ( $\Delta E_n$ ) that results from a combination of the micropulse width ( $\sim 1$  ns), detector-timing resolution (0.8 ns), and the detector width (see Ref. 4 for details) is shown in Fig. 3 for various flight paths and neutron energies. The detector width contributes 58 - 82% to the uncertainty in the 200 to 10-MeV neutron-energy range, respectively.<sup>[4,6]</sup> The overall resolution is somewhat less than that of other intermediate-energy (p, n) facilities, but uniquely provides high

dc-averaged beam currents with repetition rates of 100 ns to 10  $\mu$ s or greater. These low-frequency micropulse modes, with 100-kHz rates and 100-m path lengths, allow the NTOF spectral range of  $E_n = 1$ -200 MeV to be acquired without troublesome wrap-around backgrounds.

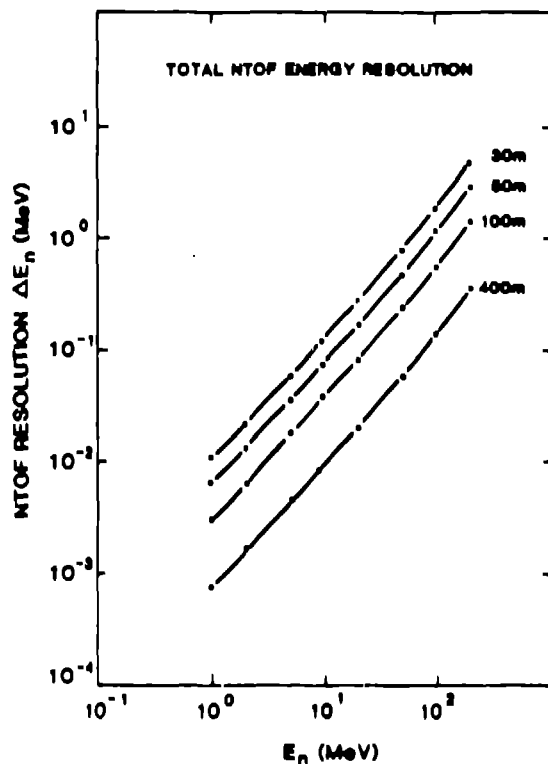


Fig. 3 NTOF energy resolution as a function of neutron energy and flight path.

The zero-degree NTOF sweep magnet in the NBTf line is a large-aperture (3.15-cm gap) high-field magnet (1.9 T) that allows target insertion along the beam trajectory, permitting the forward neutron angles of 1-25° to be selected. The protons, after interacting with the target, are transported to a proton Faraday cup shielded in the target hall. The forward-directed neutrons emerge through a collimation wall (3-m width) for transport in vacuum through the 100-m TOF tunnel.

#### Monoenergetic and spallation pulsed-neutron beams

The facility can produce intense pulsed monoenergetic neutron beams of 93 to 200 MeV. The nearly monoenergetic neutrons are produced in the  ${}^7\text{Li}(p, n){}^7\text{Be}$  (0.0 and 0.43 MeV) charge-exchange reaction. Lithium produces copious quantities of neutrons, has only one excited state, and little continuum neutron production. The differential cross section for  $E_p = 120$  MeV is shown in Fig. 4 (ref. 7). The reaction

is strongly forward-peaked, has a total reaction-cross-section dependence on the proton energy of  $E_p^{-1.13}$  in the  $E_p = 600\text{-}800\text{-MeV}$  range<sup>[8]</sup>, and a zero-degree cross section of  $d\sigma/d\Omega = 35 \pm 1 \text{ mb/sr}$ . The maximum neutron yield from a  $210 \text{ mg/cm}^2$   ${}^7\text{Li}$  metal target would be  $1.5 \times 10^6 \text{ n/sr}$  per micropulse or about  $7.5 \times 10^5 \text{ n/sr s}$ .

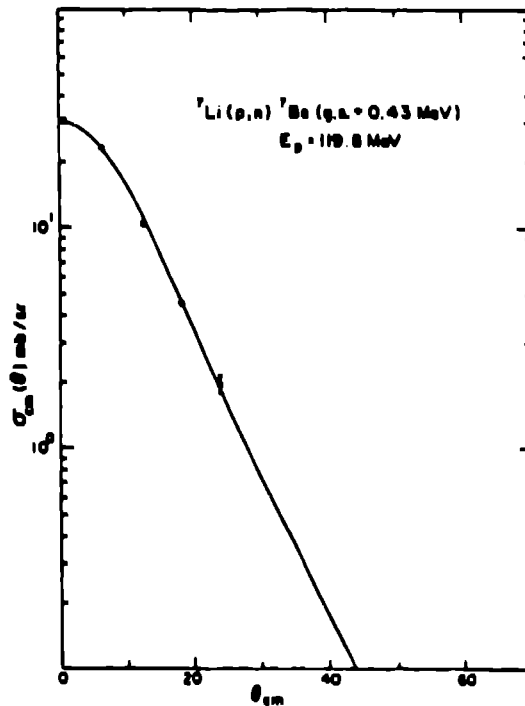


Fig. 4 Angular distribution for the  ${}^7\text{Li}(p, n){}^7\text{Be}$  (g.s. + 0.43 MeV) reaction obtained at  $E_p = 120 \text{ MeV}$  (ref. 7).

The 200-MeV proton beam at the BNS Radiation Effects Facility (REF) can also produce an intense fission-spallation spectrum of neutrons. This is accomplished by using a depleted uranium ( ${}^{238}\text{U}$ ) target to stop the beam. The spectral comparison<sup>[9]</sup> with a pure thermal fission spectrum are shown in Fig. 5, where the main difference between an actual thermal fission spectrum are the high-energy spallation (p, n) direct components. The direct-components' yields are typically (5-10%) of the total neutron yield. The spallation target consists of a  $15 \text{ cm} \times 15 \text{ cm} \times 4 \text{ cm}$  slab of depleted  ${}^{238}\text{U}$  that has an area density of  $74 \text{ g/cm}^2$ , which is greater than 110% of the range of a 200-MeV proton. The  ${}^{238}\text{U}$  (p, fission) cross section is essentially constant at energies greater than  $E_p = 20 \text{ MeV}$  and is given as  $1.44 \pm 0.10 \text{ b}$ .<sup>[10]</sup> The total inelastic (fission and spallation) cross section is  $1.91 \text{ b}$ .<sup>[11]</sup> The total neutron yield is approximately  $6.4 \times 10^{10} \text{ n/sr}$  per micropulse or  $3 \times 10^{15} \text{ n/sr s}$  for full beam intensity.

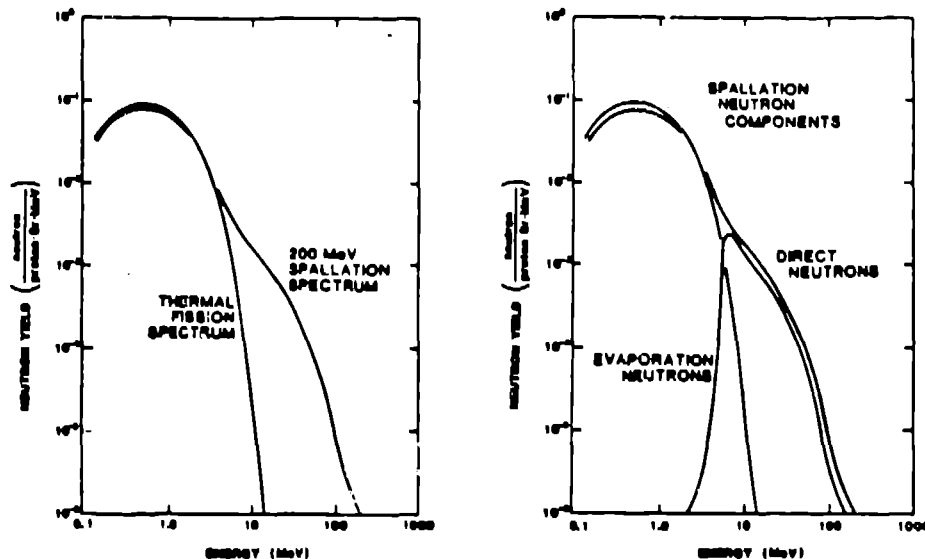


Fig. 5 Comparison of  $^{235}\text{U}$  thermal fission neutron spectrum and 200 MeV  $p + ^{238}\text{U}$  spallation neutron spectrum.

Pulsed monoenergetic or spallation (fission) source neutron beams are of considerable current interest in intermediate-energy (n, p) nuclear-physics research, for use in radiation-effects studies of electronics or other material flown in space, or research on materials used in fusion or fission reactors. The BNL radiation-effects facilities (REF and NBTF) can provide for a wide range of experimental conditions, the advantages of the user facility being:

1. **Controlled Radiation Environment.** Beam size and intensity can vary to meet wide range experimenters' needs.
2. **Reproducibility.** Experiments can be readily repeated to assure reproducible results.
3. **Flexible User Experimental Schedule.** Beam available on demand with reasonable short-lead times.

In summary, the REF/NBTF complex can uniquely provide high-intensity pulsed ( $< 1$  ns) and macropulse (500  $\mu\text{s}$ ) proton beams of 93 to 200 MeV. Furthermore, the use of appropriate targets of  $^7\text{Li}$  or  $^{238}\text{U}$  can produce monoenergetic and spallation neutron beams, respectively, that can likewise be pulsed or macropulsed. These beams can be expanded from 2 cm to 1 m in diameter in radiation-effects studies of systems, subsystems, or components.

#### Acknowledgements

Work performed under the auspices of the U.S. Department of Energy under Contract No. DE-AC-02-76CH00016.

### References

1. Gough, R. et al., "Design of an RFQ for BNL/FNAL", 1986 Linac Conference, Abstr. #WE 3-8, to be published.
2. Alessi, J. G. et al., 1987, Proc. IEEE Part. Accel. Conf. **1**, 276 and **1**, 304.
3. Wheeler, G. W., Batchelor, K., Chasman, R., Grand, P., and Sheehan, J., 1979, PLACBD **2**, 1.
4. Taddeucci, T. N., 1985, "Proc. AIP Conf. #124, 394, Rapaport, J., Finlay, R.W., Grimes, S. and Deitrich, F. (eds.), (AIP, NY 1985).
5. Goodman, C. D., Rapaport, J., Bainum, D., Greenfield, M., and Goulding, C., 1978, IEEE NS-**25**, 577.
6. Goodman, C. D., Rapaport, J., Bainum, and Brient, C., 1978, NIM **151**, 125.
7. Goulding, C. A., Greenfield, M. B., Foster, C. C., Ward, T. E., Rapaport, J., Bainum, D. E., and Goodman, C. D., 1979, Nucl. Phys. **A331**, 29.
8. Auria, J. D., Danbsky, M., Moritz, L., Ruth, T., Sheffer, G., Ward, T. E., Foster, C. C., Watson, J., Anderson, B., and Rapaport, J., 1984, Phys. Rev. **C30**, 1999.
9. "Monte Carlo High Energy Nucleon-Meson Transport Code System," 1977, HETC, ORNL-CCC-178.
10. Hyde, E. K. (ed.), 1964, "The Nuclear Properties of the Theory Elements", **III**, Fission Phenomena, Prentice Hall, Chapter 7 Sec. 4, *Ibid*, Chapter 9, *Ibid*, Chapter 11, Sec. 6.
11. Karol, P. J., 1975, Phys. Rev. **C11**, 1203.

## Workshop summary on high power targets and target assembly developments

A. Carne  
Rutherford-Appleton Laboratory  
Chilton, Nr Didcot, Oxon  
UNITED KINGDOM

There were four presentations in this session under the broad heading of High Power Targets and Target Assembly Developments.

The first paper was from Andrew Taylor (RAL) proposing upgrades to some of the ISIS moderators following several years' running experience and feedback from the instrument users. The ISIS target assembly was based on the best obtainable specification at the time, where 'best' in my book means optimum match between physics requirements and engineering realities, giving also good operational reliability and maintainability. Operating experience now suggests modifications to some moderators to give improvements mainly to pulse shape, resulting in improved resolution. These are, in descending order of priority but increasing order of technical difficulty :

- i) Change poison depth in front H<sub>2</sub>O moderator
- ii) Modify reflector to open up to second face of H<sub>2</sub>-moderator (CRISP)
- iii) Change poison depth in CH<sub>4</sub> moderator (subject to agreement of HRPD, LAD, MARI, TEST).

The question was raised of using H<sub>2</sub> instead of CH<sub>4</sub> for the front cold moderator, iii) above. It was pointed out that with hydrogen densities of 0.06 in liquid CH<sub>4</sub> and 0.042 in liquid H<sub>2</sub>, a better pulse shape and resolution were obtainable from liquid CH<sub>4</sub>. We shall return to this point again.

The second paper was from Trevor Lucas (RAL/LANSCE) on a possible mixed solid CH<sub>4</sub> in liquid H<sub>2</sub> moderator at 20K. This represents a fun challenge to cryogenics engineers and some first-shot thermodynamics calculations looked reasonable (e.g. 3 mm CH<sub>4</sub> pellets in liquid H<sub>2</sub>, pellet centre temperature ~ 50K at ISIS type energies). However there remain several tricky problems on pellet formation, the risk of clogging, the difficulty of pumping the "slurry" with a high density of CH<sub>4</sub>, and the size of the operational device.



But just how good is this slurry neutronically? For example, if the pellet centres are at 50K and the liquid hydrogen at 25k, what is the spectral temperature of the mix? Even with 60% CH<sub>4</sub> in the mix (as in the thermodynamics example) the average hydrogen density is only about 25% greater than liquid hydrogen. At what percentage mix does the gain justify the engineering complexities? Is CH<sub>4</sub> soluble in H<sub>2</sub>? Why not add Krypton to make the methane lattice bigger and "unfreeze" the rotational modes? Krypton is also a natural poison when used this way.

In the discussions on this topic there were two offers of help: the first in the best tradition of ICANS, where Gary Russell offered to model a CH<sub>4</sub>/H<sub>2</sub> moderator to determine the neutron output spectrum as a function of the ratio of CH<sub>4</sub> to H<sub>2</sub>; and the second with our new colleagues from reactor sources, where Colin West (ANS at ORNL) offered the use of a cryogenic test-bed for slurry moderator testing.

The third paper was from Noboru Vatanabe (KEK) who reviewed the efficiency of accelerator based cold neutron sources, with the goal of achieving an efficiency comparable with the ILL cold source. Efficiency here is defined as

$$\int_{\lambda} \phi_c(\lambda) d\lambda / n_f$$

A fully decoupled high power moderator, like ISIS, has an efficiency ~ 6 x 10<sup>-5</sup> compared with 3 x 10<sup>-4</sup> for the ILL cold source. With such large differences accelerator based cold sources are not competitive, especially in the important area of SAS. How can accelerator based sources be improved?

One possibility to improve on the pulsed source performance would be to follow the intensity modulated source practice proposed at SNO, i.e. to use a decoupled moderator and exploit both the bandwidth and time structure. KENS-II may have such a moderator, in addition to short pulse moderators, but its competitiveness depends crucially on the gain that might be achieved from exploiting the time structure. Ideally KENS-II would like an efficiency 10X that of ILL. There were, however, worries whether such a gain might be achievable.

Other features of an SAS instrument include:

resolution obtainable with a beamline about 30 m long; long tails to the neutron pulses might be removed by the use of phased choppers; the use of focusing guides is being considered. The performance of SAS instruments would benefit from a p.r.f. lower than 50 Hz: one case, at least, to support

the contention raised at the Conference of the value of a very low (~ 1 Hz!) p.r.f.

The final paper was from Gary Russell (LANCSE) on the THRS upgrade. The present LANCSE THRS is an elegant flux trap target system with 4 moderators in "slab" geometry located between the upper and lower target tungsten blocks. It can be upgraded by opening up the upper reflector to add two more moderators and so provide perhaps four more beamlines into the new experimental hall.

There are several geometric possibilities for the two new moderators, beyond the initial thought of having them in wing configuration: the moderators could be in slab in the same plane as the upper target block, or they could be in slab and slightly above the upper target block to operate as flux trap moderators in a similar way to the present moderators. The suggestion was raised that the upper target block itself might be of slab type (as was proposed for the SNQ target) to improve the solid angle coupling to the moderators, especially in wing geometry. "Tuning" of the target lengths was done on the original assembly and clearly it would be worthwhile to do this again. LANCSE is fortunate to have such computing resources to make such studies!

To the question of what materials for the moderators, the first thoughts were for one water moderator and one liquid methane. The choice will depend on user demand. On ISIS we were fortunate to have at a quite early stage a clear specification of moderator types, canvassed from the user requirements. I offer the recommendation of a similar canvassing exercise for the LANCSE upgrade in order to clear the way for the necessary technical developments.

A good meeting, some interesting challenges and some good examples of collaboration within and beyond ICANS!

## The LANSCE target data collection system

*A. K. Kernodle*  
Los Alamos Neutron Scattering Center  
Los Alamos, New Mexico 87545 USA

**ABSTRACT:** The Los Alamos Neutron Scattering Center (LANSCE) Target Data Collection System is the result of an effort to provide a base of information from which to draw conclusions on the performance and operational condition of the overall LANSCE target system. During the conceptualization of the system, several goals were defined. A survey was made of both custom-made and off-the-shelf hardware and software that were capable of meeting these goals. The first stage of the system was successfully implemented for the LANSCE run cycle 52. From the operational experience gained thus far, it appears that the LANSCE Target Data Collection System will meet all of the previously defined requirements.

The goals of the LANSCE Target Data Collection System are listed in the order in which it was deemed the system was to evolve. Each goal builds upon the data collected and confidence built by the accomplishment of the previous goal.

- Develop a data base of the operational parameters relating to the performance of the target and moderator systems as well as their support systems.
- Extract trend and normal range parameters for the data points of prime interest and then for all data points.
- Implement a means of automatic warning and alarm in cases where a particular data point has exceeded its normal range or has reached a level that poses a threat to the continued safe operation of the system.
- Provide for the intervention of the data collection system in the operation of the target and moderator systems to avert unnecessary system shutdown.

Having defined the capabilities and direction the system was to take, a preliminary survey was made of both custom-made and off-the-shelf hardware and software that were capable of meeting these goals. Additional criteria for the system were then defined as follows.

- All system components were to be standard products offered for sale by established firms.
- All system components would provide a high degree of operational reliability and accuracy while affording the lowest possible cost.
- All system components would provide for easy expansion capability beyond the presently defined number of data points.

A final survey of available system components was then made. Each product was screened in accordance with all the preceding goals and criteria. The union of products from four different vendors seemed to offer a system that would provide the versatility to meet all of our previous requirements. Trade-offs and initial procurements were made.

Contained within the following paragraphs is a brief description of the capabilities of each system component, followed by a summary of our experience with the system so far, and then a look into the potential of this system for the future.

- The first component is an IBM PC AT compatible computer manufactured by Dell Computer Corporation—the System 200 model, set up with the following:
  - Intel 80286 microprocessor running at 12.5 MHz
  - Intel 80287 math coprocessor
  - 640K Bytes of RAM
  - 40MB 28ms hard disk
  - 1.2MB floppy disk
  - 360MB floppy disk
  - EGA graphics adapter and monitor
  - Real-time clock with battery backup
  - 2400 baud internal modem
- The second component is a hardware data acquisition and control system manufactured by OPTO 22. This system, called Optomux, is a family of digital and analog input and output units. The Optomux system can handle up to 255 different digital or analog module racks, which are all serially connected via one cable of two twisted pairs. Each module rack can support up to 16 input or output modules (any mix). Control of the serial system, which can extend 5000 feet without an additional repeater, is accomplished via an interface card that plugs into the Dell System motherboard.
- The third component in the system is a voice-synthesized warning system built by RACO Manufacturing and Engineering Company. This device, called the Verbatim Automatic Dialing Remote Monitoring System, or "the Verbatim", is capable of monitoring eight different contact-closure channels. Each channel's unique user-recorded message is stored in nonvolatile memory. Upon detecting an alarm condition, the Verbatim unit will dial up to eight different phone numbers up to twenty times to report the channel-specific prerecorded message.

- The last component in the system is the software package that runs on the Dell System 200 PC. Developed by Intec Controls Corporation, the software Paragon Control is a graphics-interface-process-control package optimized for real-time process control and data acquisition. Paragon Control can support up to 800 data points and can display both real-time trend information and store selected data points for archival purposes. The package provides the capability to set operational limits for all signals and respond to alarm conditions by message display on the screen of the computer. It also activates other warning devices thru the OPTO22 hardware output system.

During the LANSCE run cycle 52, the first stage of this system was successfully implemented. Approximately 40 different data points were monitored at a rate of 0.25 s per sample and stored for archival purposes at a rate of 1 to 5 samples per minute. Several liquid-hydrogen-moderator-system shutdowns were averted. The archived data has helped solve several other unexplained system shutdowns that occurred during times when the system was unattended.

For run cycle 53, the LANSCE Target Data Collection System is scheduled to monitor some 100 data points. The Verbatim alarm system will be implemented and operational. Signal trending will be emphasized. The data collection system has been given the prime responsibility to monitor the liquid-hydrogen moderator system and report any out-of-range operating conditions via both the Verbatim automatic voice-synthesized phone-calling system and local warning lights and alarms in the attending technician's work area. From our experience thus far, it appears this system will meet all of our previously defined goals and will provide the versatility needed to meet future requirements.

## Liquid-hydrogen-control-system modifications

*T. Summers*

Los Alamos Neutron Scattering Center  
Los Alamos, New Mexico 87545 USA

**ABSTRACT:** By late 1987, the Los Alamos Neutron Scattering Center (LANSCE) liquid-hydrogen-control-system electronics had evolved to a functionally adequate stage, but occasionally showed signs that rebuilding was needed. The rebuild offered opportunity to redesign the external features of the system, which are described in this paper along with some technical features.

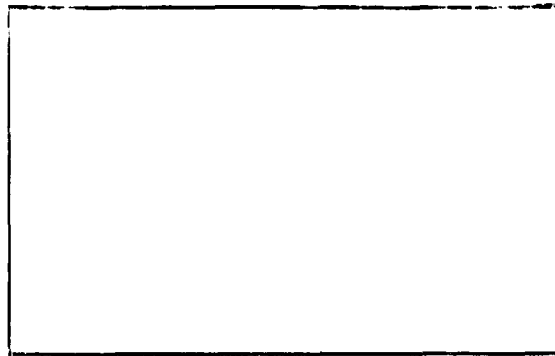
The LANSCE liquid-hydrogen control system had grown during the years and reached a stage, by late 1987, where major revisions were needed. A main feature of the rebuild was the ergonomic aspects of the front control panel. The design changes that were implemented with considerable success were as follows.

1. All push-button controls are now lighted in red or green. The normal state-of-the-function is indicated by green illumination in the upper half of the square button, with the illuminated legend indicating status (e.g., "open"). Thus, when all valves, etc., are in their normal state, the control panel shows only green across the tops of all the buttons (see Fig. 1).
2. If any function is in an abnormal state, a red light within a schematic of the system is illuminated (see Fig. 2).
3. Any transient condition that can lead to a safety dump of the liquid hydrogen is latched in an indicator panel until reset (Fig. 2).

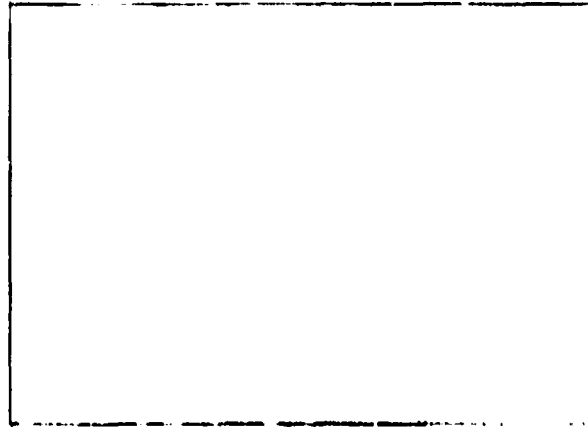
The consequences of these changes have exceeded our expectations. System troubleshooting is almost "at a glance". The ability of new personnel to learn the system has been enhanced, and the solid construction has increased reliability.

Most of the subsystems in the hydrogen control system provide for remote readout—the exception being the thermocouple vacuum gauges. Because of poor history with electromechanical gauges, it was decided to build an all electronic vacuum gauge to meet our needs. Two designs were made: one for the four-wire thermocouple gauge, such as the Varian series; and one for three-wire gauges as provided by Hastings.

A thermocouple vacuum gauge applies a heating current to a fine wire exposed to the vacuum to be measured. A thermocouple attached to the heated wire records the temperature of the wire, which rises as vacuum improves (less convective cooling). In an electromechanical gauge, the thermocouple directly drives a meter. The meter scale is marked off to account for the peculiar calibration curve of the gauge. Typical



**Fig. 1** Control switches.



**Fig. 2** Alarm hatch panel and status panel.

constants for a three-wire Hastings tube are 20 ma heater current and 10 mv (300° C) thermocouple output. The principal problem in an electronic gauge is matching a non-linear circuit to the calibration curve of the tube used. We accomplished this by using a linear amplifier with two break points to achieve a 0 to :999 micron vacuum range. The amplifier circuit is shown in Fig. 3 and, once adjusted, conformance with a McLeod gauge is shown in Fig. 4.

In addition to the above, the corrected output is applied to a voltage-to-current converter making three separate outputs available that convert 0 to 2000 microns to 0 to 1 ma of output with approximately 7 volts of compliance.

The entire revised system has all critical functions (defined as those functions that can lead to venting of the liquid hydrogen due to safety) operating on two sealed gel-cell batteries. In the event of a power failure, all systems will stay alive for more than an hour. Note that when the helium compressors associated with the hydrogen

refrigerator go off because of power loss, the system warms and must be vented in six minutes to avoid possible excess pressure.

The revised hydrogen control system has been very successful in attaining its objectives. Corrective actions are more rapidly determined and down time caused by control-system failure appears to be a thing of the past.

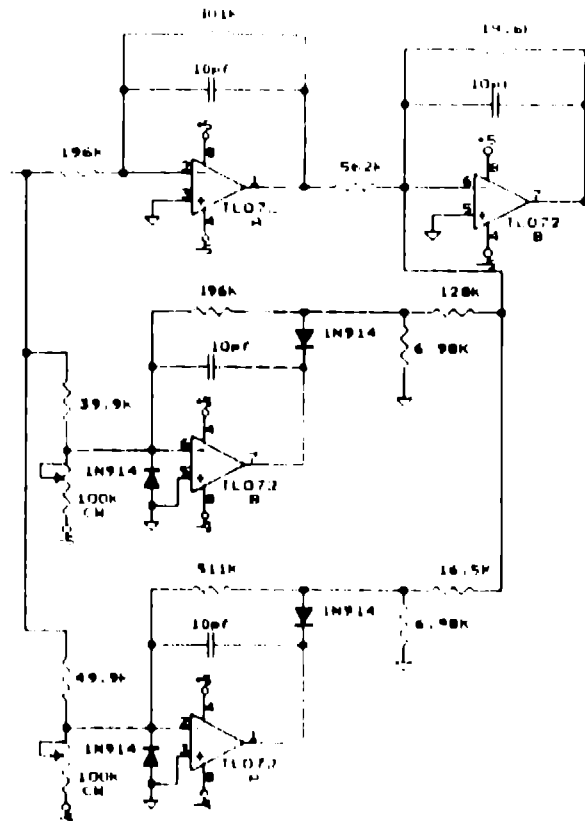


Fig. 3 Amplifier with break points.

### Acknowledgements

The design features described here were implemented by John Quicksilver and Alan Kernodle, who did a magnificent job of putting high quality into the finished systems.



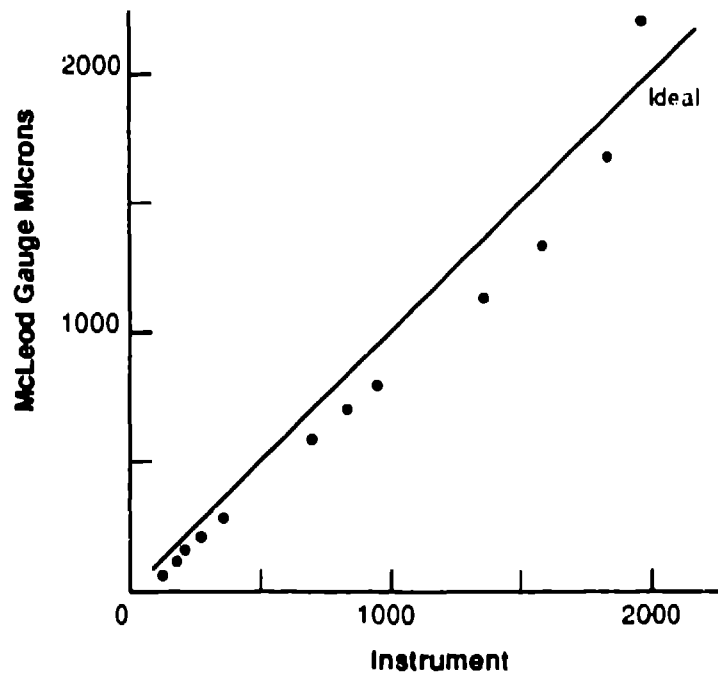


Fig. 4 Measured response after first adjustment.

## Remote handling for an ISIS target change

*T. A. Broome and M. Holding*  
Rutherford Appleton Laboratory  
Chilton, Didcot, Oxford  
UNITED KINGDOM

### 1. Introduction

During 1987 two ISIS targets were changed. This document describes the main features of the remote handling aspects of the work. Many people took part in the job, either directly or indirectly, and their considerable efforts are gratefully acknowledged.

All the work has to be carried out using remote handling techniques. The radiation level measured on the surface of the reflector when the second target had been removed was about 800 mGy/h demonstrating that 'hands on' operations on any part of the target reflector moderator assembly is not practical.

The target changes were the first large scale operations in the Target Station Remote Handling Cell and a great deal was learned about both equipment and working practices. Some general principles emerged which are applicable to other active handling tasks on facilities like ISIS and these are discussed below.

The sequence of operations for the remote handling is given in appendix A as an aid to understanding the video film of the work

### 2. The remote handling cell

Figure 1 shows the layout of the Target Station. In operation the target is positioned in the centre of the biological shield. For all maintenance work the target with its associated shield plug, cryogenic and ambient water services trolleys is moved back to position the target reflector and moderator assembly in the Remote Handling Cell as shown in Fig. 2.

A plan view of the RHC is shown in Fig. 3. The cell is equipped with two pairs of VNE 80 master slave manipulators, a remotely controlled crane of capacity 1 tonne and viewing is through two zinc bromide windows 1.6m thick.

For target changes video cameras are installed to improve the view for the operators. There are three fixed cameras, one on each side of the cell (positions A and B on Fig. 2) and one at high level (position C). All of these fixed cameras were equipped with remotely operated pan, tilt, zoom and focus. In addition two small cameras were used which could be held by the manipulators to give a view of areas not well covered by

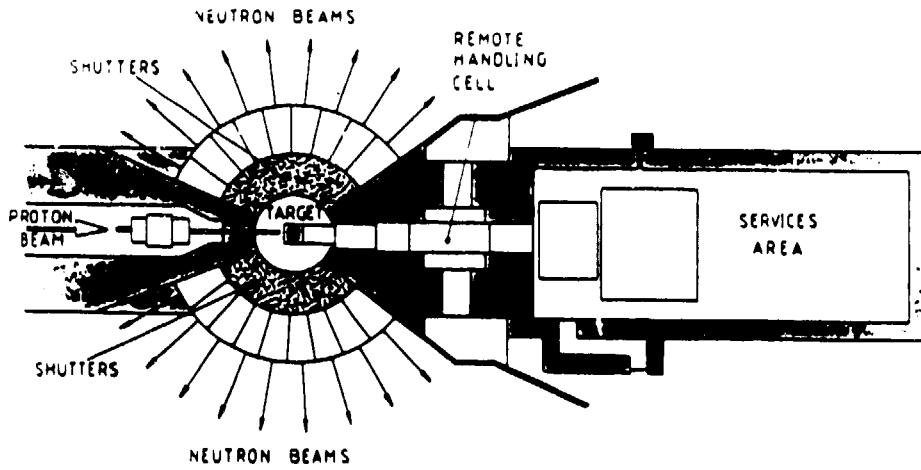


Fig. 1 Layout of target station.

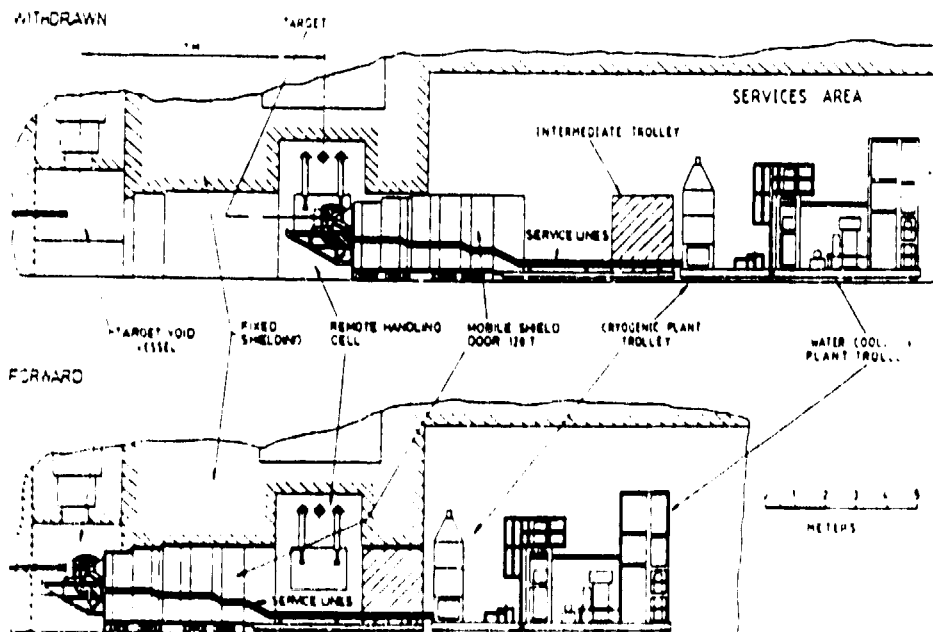


Fig. 2 Target assembly and services trolley.

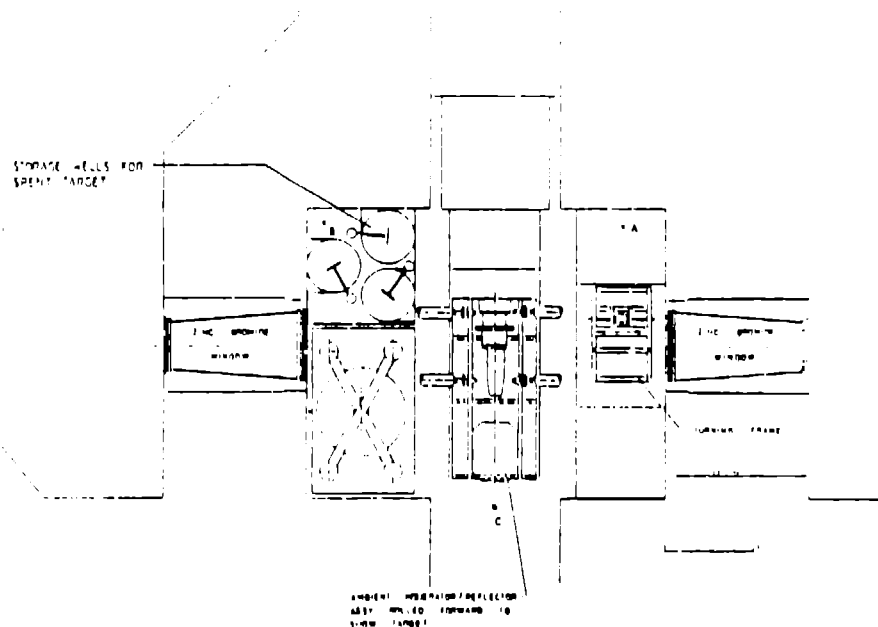


Fig. 3 Remote handling cell - plan view.

the windows or the other cameras. Pictures from the cameras were displayed on monitors in the manipulator rooms and were also recorded on video tape.

An intercom system allowed the operators in the two manipulator rooms to talk to each other and to listen to the sound inside the RHC.

### 3. Tools

The desirability to test the remote handling equipment in dummy runs or a mock-up before it is installed was recognised but there was only time and resources in the installation schedules to prove the overall concepts. Also the first target failed somewhat earlier than had been expected so the equipping of the cell and provision of tools was, of necessity, done in a very short time which inevitably led to some compromises and development during the job.

Ordinary open ended and ring spanners were used for tightening and loosening nuts. They were fitted with special grips for the manipulator jaws. An air operated wrench was tested before the first change on a spare target flange bolt. However, the nut seized possibly because the rotational speed of the wrench was too high so it was decided not to use it on the real job.

The only specialist tool, the cropper for the thermocouple umbilical, worked well although some redesign of its support on the crane would make it easier to align.

#### 4. Management of the work

Effective management of the work was essential to its efficiency and success. The responsibilities were split into two areas—safety, and control of the actual remote handling operations.

##### 4.1 Control of safety

In general the day to day problems of radiation protection on ISIS are the responsibility of a 'Radiation Protection Supervisor' who is normally the leader of the operations crew on duty. It was felt that the demands of the task of changing a target were sufficient to require a full time Radiation Protection Supervisor who was appointed for the duration of the job.

In particular his duties involved:

- (i) Controlling access to the various areas of the Target Station namely:  
Services Area  
Remote Handling Cell  
South Tunnel  
Manipulator Rooms
- (ii) Issuing of 'Permits to Work' which are required for personnel to work in areas where the dose rate is greater than 250  $\mu\text{Sv/h}$
- (iii) Issuing 'Permits' to allow people to work in the Remote Handling Cell which is defined as a 'confined space' i. e., an enclosed volume with only one access
- (iv) Keeping a detailed log of the work

The RPS was based at the Target Station throughout the target change and he was in very close liaison with the person controlling the work, although these two people have independent and distinct roles. For the second target change the RPS had a television screen showing the work in progress in the Remote Handling Cell. In addition there were taped video tapes from the first change available for reference.

It is also necessary to keep the operations staff informed of the progress of the work and the state of the Target Station when it is left unoccupied. It was convenient for the Radiation Protection Supervisor to do this. Also he was the natural person to keep the Laboratory Safety Officer fully informed and to consult him when necessary.

##### 4.2 Control of the work

This task was performed by a person independent of the Radiation Protection Supervisor. The manipulator rooms are small and it was found important to limit the number of people in them to the minimum required to perform the task in hand. For most of the time only four people were permitted to be in each room—two to operate the manipulators, one to operate the cameras and a fourth person to operate the crane. For this reason the progress of the job was monitored and controlled in

conjunction with the RPS, much use being made of the remote television pictures in the target change control office.

The work was planned to be carried out in set elements following the written procedures. Generally this worked well but on occasions, particularly during the first target change there was a tendency to press on. It is important to remember that remote handling is physically and mentally taxing and the person in charge must be aware of fatigue setting in. If individual tasks are not going according to the procedures laid down the work should be stopped and the problem considered away from the working area and the master video tape referred to. This was done several times during the second target change and proved to be a successful method of working. The target change control office was found to be the most convenient place to discuss problems.

##### **5. General comments on the target changes**


The target changes carried out were generally very satisfactory. However, neither change went entirely to plan and it can be anticipated that future target changes will have their own special problems.

Very little testing of the principles and equipment needed to change a target remotely had been possible before the original installation so the two target changes represented the first chance to develop the system. Before starting to change target number one as much mock-up work as practical was carried out. The target storage was checked completely with a spare target and the positions of the cameras in the cell checked, as far as possible, to ensure that they would provide the required views for the various operations.

One main general problem was the unreliability of the VNE 80 manipulators. There is one pair on each side of the cell and all four became unserviceable at some time during the work. In fact, both target changes had to be stopped for the manufacturer to repair the manipulators. The manipulators are absolutely crucial to the work and steps have been taken in conjunction with the manufacturer to improve their reliability.

Before the first target change there was very little experience with manipulators at RAL. A specialist from Harwell Laboratories assisted with both target changes and his comments were very useful and appreciated. By the end of the second change several of the RAL team had become very proficient in the use of manipulators and it is not expected that external specialist operators will be necessary in the future.

The design of the tools, particularly their handling fixtures, was improved a great deal between the two target changes. Experience is showing what type of attachments are best for each tool to make them convenient for use with the manipulators. Getting the spanners properly located on the nuts was frequently quite difficult. They all fitted the nuts slightly too well and they will be machined, with a lead in, before the next target change. Also some of the spanners were quite heavy and tiring to use. Aluminium alloy spanners will be tested as an alternative to the current steel ones. All the tools were fitted with chains. This was to aid retrieval when they were dropped.




Detailed check lists of equipment for use in the cell were produced which proved to be most important. In addition to the tools expected, a range of others was put in to cater for the unforeseen. In both target changes all the tools were used and more had to be put in as well so the provision of tools will need careful review before the next change.

The positions of the video cameras in the cell, and their mounting arrangements can be improved. In the second change the overhead camera (position C in Fig. 3) was fitted with remote pan, tilt, zoom, and focus which it did not have in the first change and this made the work considerably easier and resulted in the the small cameras with flying leads being used somewhat less in the second change than in the first. A colour camera was used in the second change and it was generally felt that it gave a better view than black and white.

Video recordings were taken continuously during both target changes which is a practice which will be continued in the future. When a problem occurs the relevant film from previous changes can be viewed which may well present a solution. The master film will need to be updated after each target change to make sure it includes not only the work which went according to plan but also the techniques and methods found useful for dealing with any unexpected difficulties.

The intercom system which allowed the operators on the two sides talk to each other was essential for many operations particularly when using the crane to move equipment when a good view could only be obtained from one side or the other. It was found that the use of the intercom required some discipline to avoid a general babble with at least four and sometimes more people being able to talk at the same time.




## 6. Essential Improvements

The margin between success and failure for both target changes was at times small. For example, on the first target change there were difficulties in removing the old target and on the second change it was necessary to replace the pipe and flanges feeding the casing circuit. It is quite likely that future target changes will present new problems. While it is difficult to anticipate exactly what these will be several improvements were identified, regarded as essential, which should make the job easier and give greater scope for dealing with any difficulties.

The main single improvement needed is the provision of a posting port for introducing small items of equipment into the remote handling cell. The design of the cell included posting ports but they have yet to be installed.

The tools while mainly adequate can certainly be improved. It is felt to be important to have some power operated spanners and to find more convenient methods of applying known torques when tightening nuts.

Some design changes are necessary. The attachment of the thermocouple connector to the main shield door was extremely difficult in both changes and this has already been redesigned. Also the bayonet connectors on the water pipes will be strengthened



to avoid the problems encountered in the second change when one of them was damaged and had to be replaced.

## **7. Remote handling general**

During the two target changes several principles became evident which it was felt would be applicable to general remote handling tasks.

- a. A comprehensive list of all items required, no matter how trivial, is vital
- b. Spares of all components which could need to be replaced should be available before the job starts
- c. Only one operation or function at a time should be attempted
- d. Good location should be achieved first before any locking or tightening is attempted. i. e., the task should involve a change to one dimension only at a time.
- e. When dowel location is used the dowels should be of unequal lengths to enable the component to be fitted in one plane at a time.
- f. Hexagon shapes appear to be easier to handle than round shapes with two flats
- g. A video film of detailed operations is a very useful tool, this is different from a publicity film
- h. It is not always possible to 'feel' things with manipulators particularly at extended reach

## **APPENDIX 1. Outline of the Remote Handling Procedure**

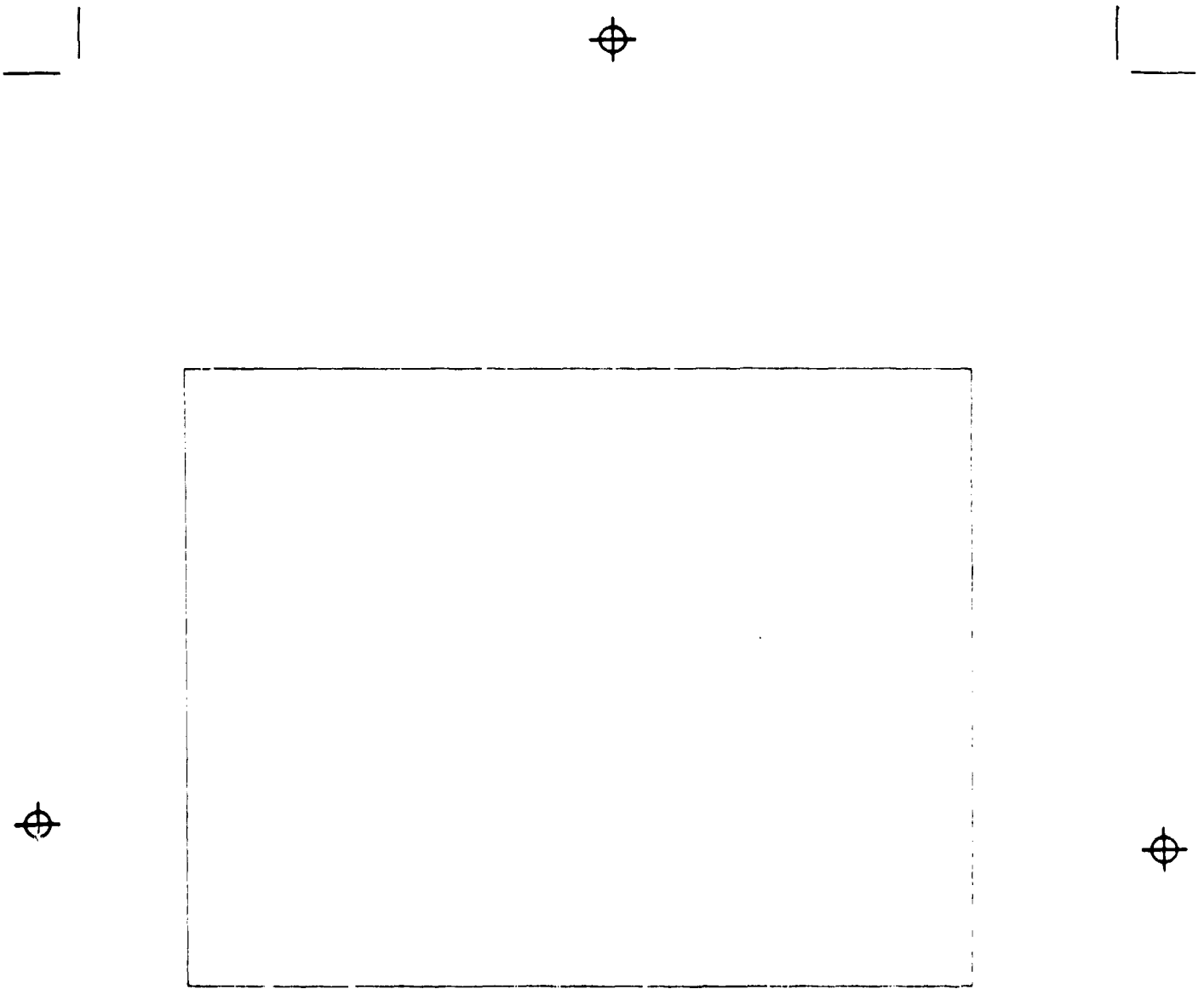
As an aid to understanding the operations shown in the video film the components of the target reflector and moderator assembly referred to in the procedure below are illustrated in Figs. 4 to 8. Figures 4 and 5 show the target reflector moderator assembly during initial installation. Also visible in the bottom left hand corner of the photograph of the top of one of the wells for storing used targets. Figures 6, 7 and 8 show various features of the assembly mentioned in the procedure below.

A video film showing the stages in replacing a target has been produced by editing film recorded during the two target changes. It should be noted that the object of these recordings was to aid the work in progress and to help with future changes. Thus the camera pictures chosen during the operation were those which best supplemented the direct view of the job via the windows rather than the one which itself gave the best view of the task. Much of the remote handling was, in fact, done without the need for camera pictures at all.

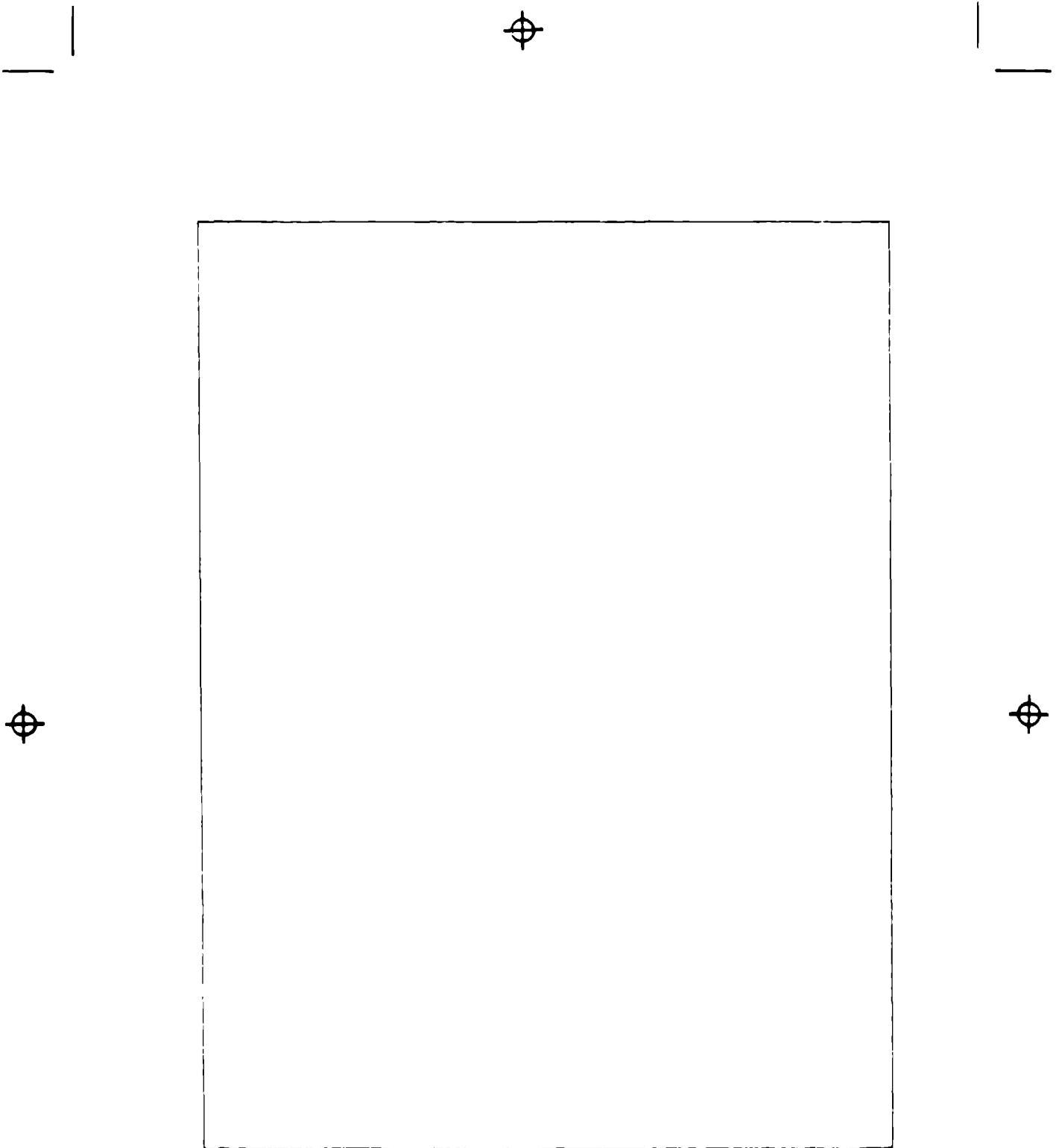
The process of changing a target can be split into eight basic parts.

1. Exposing the target by rolling back the upper section of the reflector
2. Draining the remaining water from the target
3. Unbolting the target and thermocouple connector
4. Preparing the target for storage
5. Storing the target
6. Bolting on a new target and thermocouple connector
7. Reconnecting the cooling systems
8. Replacing the upper section of reflector

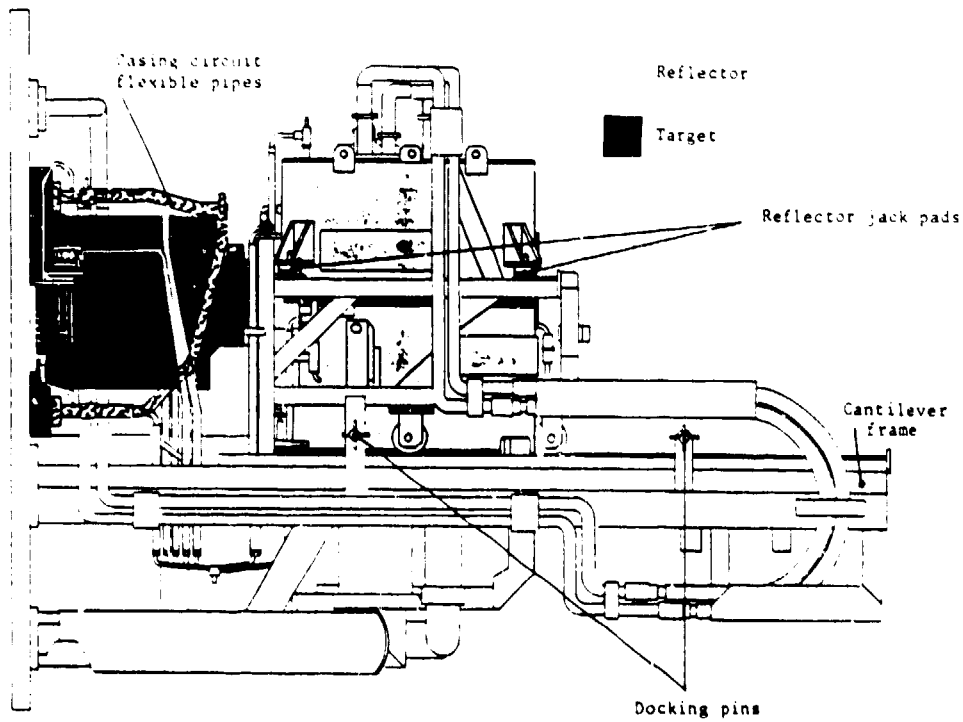




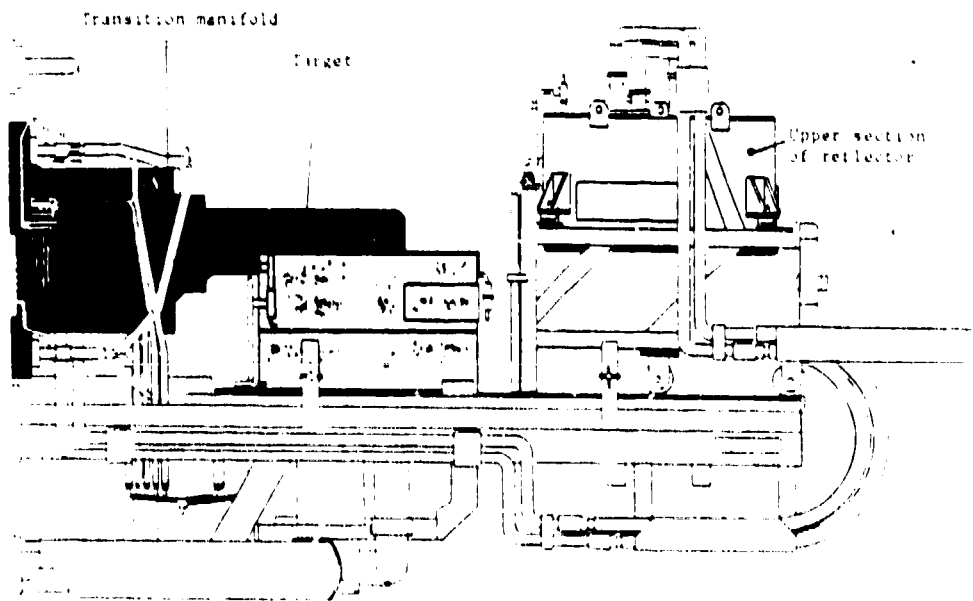
**Fig. 4 Target reflector moderator assembly during construction.**



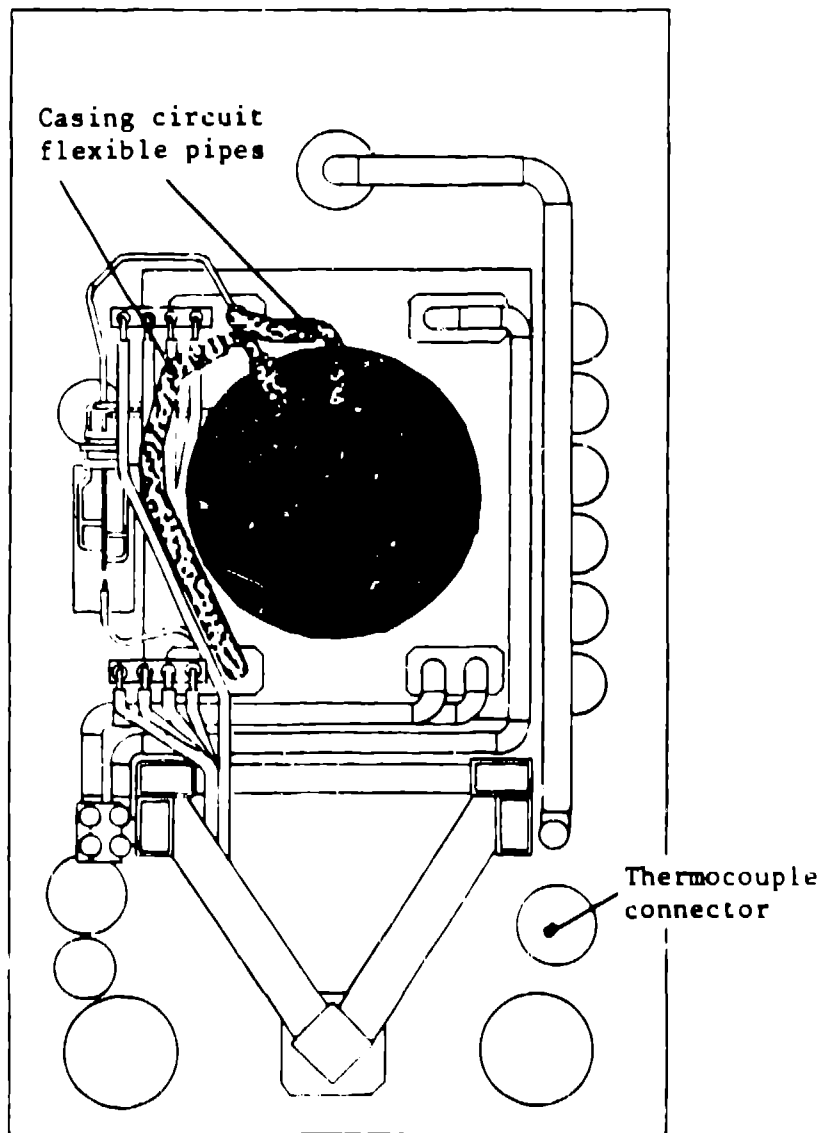
**Fig. 5** Target reflector moderator assembly during construction.



**Fig. 6** Target reflector moderator assembly in operational configuration.



**Fig. 7** Target reflector moderator assembly with upper section of reflector in maintenance position.








**Fig. 8** Section through target reflector assembly showing connections for casing circuit.










The following list describes the operation in more detail.

- A.1 Move the shielding door and associated trolley assemblies to position the reflector between the manipulators directly in front of the windows.
- A.2 Pick up the halo monitor assembly from the front of the reflector trolley using the manipulators and place it in the cradle on the cantilever frame
- A.3 Pick up the reflector lifting frame on the crane and locate the three hooks of the frame into the lifting eyes of the top piece of the reflector. Raise the reflector above the fixed jack pads by 20 mm, which is sufficient to allow the four pads to be rotated through 90 degrees using the manipulators.
- A.4 Lower the reflector onto the rotated jack pads and remove the lifting frame from the reflector and replace it on the vertical motion table.
- A.5 Remove the operating position docking pin on the cantilever frame and move the reflector trolley towards the end of the frame.
- A.6 When the trolley reaches the end of the cantilever frame engage the servicing position docking pin into the hole in the reflector trolley.
- A.7 Remove the drain blank from the target assembly and connect the drain hose and bottle to the outlet pipe. Open the drain valve and blow out the heavy water that remains in the target casing with nitrogen.
- A.8 Remove the Drain Hose and replace the Drain Blank.
- A.9 Disconnect the two flexible coolant pipes that feed the target case cooling circuit from the intermediate manifold and position the free ends out of the way.
- A.10 Pick up the target handling frame from the the vertical motion table and position it on the rails of the cantilever frame over the target and lower half of the reflector assembly.
- A.11 Remove the lifting dowel locking pins and push the dowels and beam window plug of the lifting frame into the target assembly locations and insert the locking pins.
- A.12 Release the vee clamp bolt retaining the thermocouple connector, retract the assembly from the door flange and place the thermocouple connector in a convenient position.
- A.13 Release the main target flange tee bolts fully and rotate the heads to align with the slots in the transition manifold.
- A.14 Roll the handling frame and target away from the mounting manifold to clear the location dowels.



- 
- 
- 
- 
- 
- A.15 Lift the handling frame and target and position on the target turning frame the Target Flange facing away from the Void Vessel.
- A.16 Rotate the target to a convenient angle and crop off the thermocouple umbilical as close to the outlet from the target vessel as possible.
- A.17 Rotate the target until it is vertical and fix the target sealing flange to the target
- A.18 Lift off the lid from the storage well and place it on the Access Door
- A.19 Pick up the target assembly lifting beam on the crane and locate the lifting bars in the slots of the intermediate manifold, rotating them into the 'lifting' position.
- A.20 Lift the target from the handling frame and lower it into the opened storage well locating it on the pins. Rotate the lifting bars to remove them from the slots and lift the Target Lifting Beam clear.
- A.21 Replace the Storage Well Lid.
- A.22 Bring the replacement target into the cell in its handling frame on the transfer platform.
- A.23 Pick up the target and frame from the transfer platform and place it on the target turning frame on the lifting table.
- A.24 Move the shielding plug trolley to position the lower part of the reflector between the manipulators and in front of the windows.
- A.25 Pick up the target and frame from the turning frame and lower it over the lower half of the reflector until the wheels rest on the rails of the cantilever frame.
- A.26 Remove the seal protection plate and roll the target and frame towards the mounting manifold so that it is located on the dowels and against the seal face.
- A.27 Turn the tee bolts to the 'fastening' position and tighten them to the required setting.
- A.28 Use the manipulators to pick up the thermocouple connector housing from the cradle on the handling frame and position it on the connector flange, reassembling and tightening the vee clamp bolt to the required setting.
- A.29 Remove the lifting dowel locking pins and roll the frame away to release the target.

- 
- 
- 
- A.30 Lift the Frame away relocating it on the target turning frame on the lifting table.
- A.31 Reconnect the two flexible coolant pipes to the case cooling connector flanges and tighten them to the required setting.
- A.32 Roll the reflector trolley back to the operating position , and insert the operating position docking pin into the hole in the reflector trolley.
- A.33 Raise the reflector above the fixed jack pads by 20 mm and rotate them through 90 degrees using the manipulators.
- A.34 Lower the reflector down into the operating position and remove the lifting frame.
- A.35 Pick up the halo monitor from its cradle on the cantilever frame using the manipulators and reposition it in its operational position on the front of the reflector Trolley.
- 
- 
- 
- 

## LANSCE target calculations

*D. L. Grisham and R. D. Brown*  
Los Alamos National Laboratory  
Los Alamos, New Mexico 87545  
USA

The LANSCE target presently operates at a beam current of 30  $\mu\text{A}$ . We present here the results of the finite-element calculations for the temperatures and stresses in the present target operated at 100  $\mu\text{A}$ . The calculations were run using the ABAQUS finite-element code. All finite-element codes require as input both the boundary conditions for the material being heated and such material properties as the thermal conductivity, specific heat, and the elastic modulus. For the LANSCE target, the boundary conditions involve knowing the power deposition from the beam, and the heat-transfer coefficients between the tungsten-alloy cylinder and the cooling water. We believe that these numbers are quite well established.

The target material is a powder metallurgy alloy of tungsten, iron, and nickel (96.2% W, 3.8% Fe and Ni). Although the properties of pure tungsten are well known, the properties of this particular alloy have not been found in the literature. Figures 1, 2, and 3 show the available literature information on pure tungsten and a few tungsten alloys.

Calculations were run for both the steady-state and transient conditions. The former allowed us to determine the equilibrium temperature and stresses; the latter allowed us to decide whether thermal shock might be a problem. In the steady-state case, the power deposition, thermal conductivity, and the cooling rate determine the temperature. The maximum heat-up rate for the transient case is determined by the power deposition and the specific heat.

The heat-up rate in the transient calculation is far below the rate required to produce thermal shock. The thermal expansion, which is dependent on temperature and the expansion coefficient, determines the stress in the target. The calculations were done using the material properties identified in Figures 1-3 as "LANSCE CALC", and the beam parameters were 12 pulses per second with a total heat deposition of 25.78 kW in a pattern furnished by Gary Russell of LANSCE. Figure 4 shows the equilibrium temperature of 860 K calculated in the pulsing mode at the hottest point.

Figure 5 is the temperature distribution of the entire target in the steady-state condition. Figure 6 shows the steady-state stress distribution, which should be compared with the yield stress of 690 MPa. Since the highest stress value, 730 MPa, is above the yield strength but below the ultimate strength of 980 MPa, some local yielding would occur. Both strength values were furnished by the vendor. These conditions would not result in a catastrophic failure, but would probably cause some local surface cracking.



# THERMAL EXPANSION TUNGSTEN AND ALLOYS

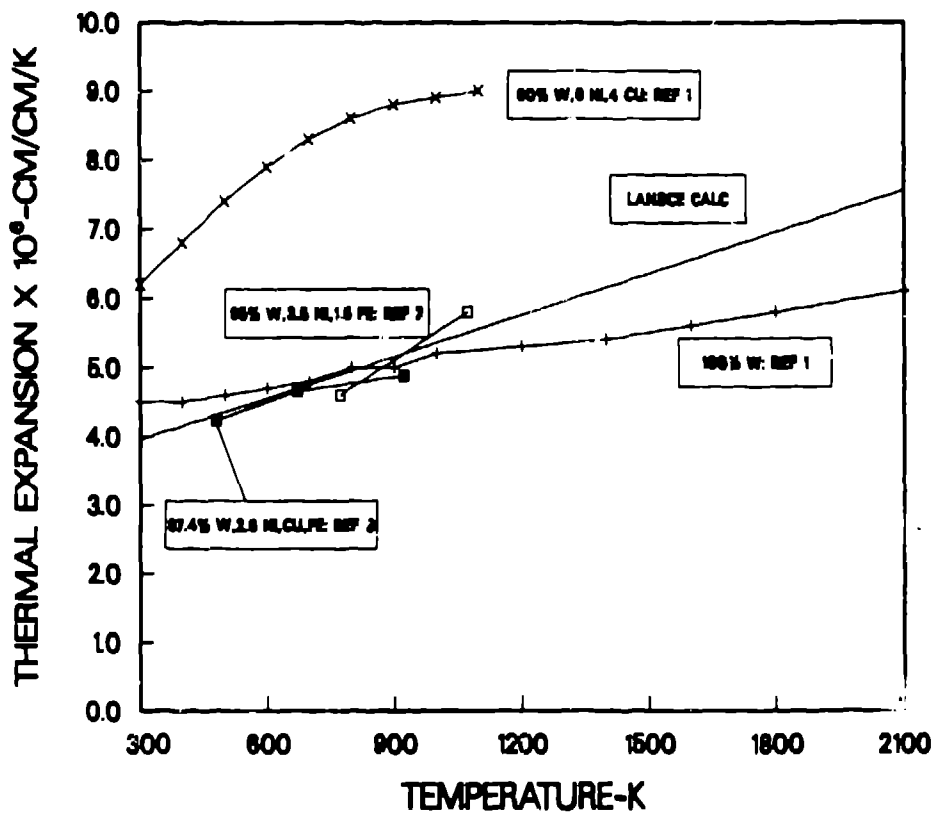


Fig. 1 Thermal expansion coefficients versus temperature for tungsten and three alloys.

# THERMAL CONDUCTIVITY TUNGSTEN AND ALLOYS

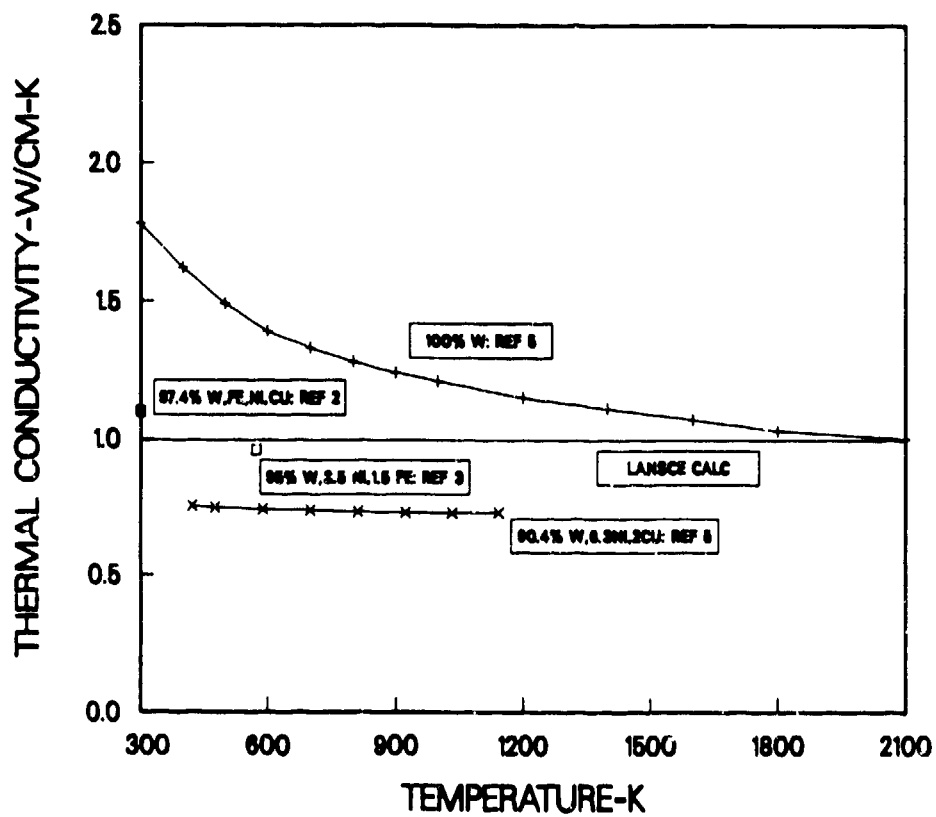


Fig. 2 The thermal conductivity for tungsten and three alloys.

# SPECIFIC HEAT TUNGSTEN AND ALLOYS

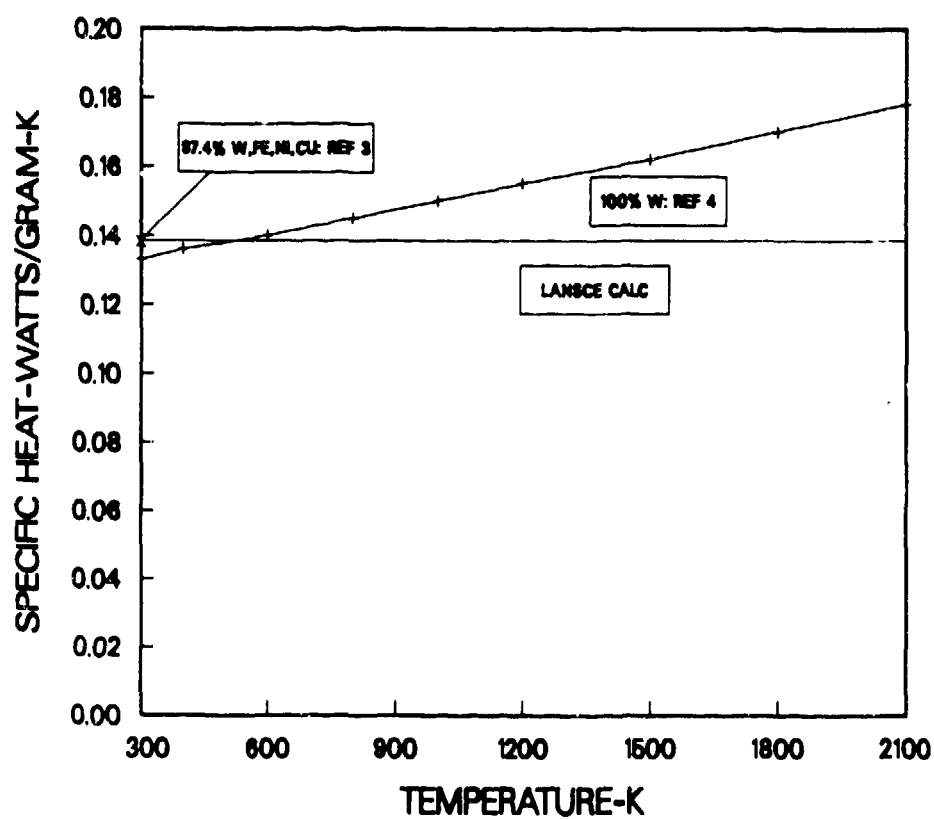


Fig. 3 The specific heat for tungsten and a single alloy.

# LANSCCE TARGET, 100 $\mu$ A, 1-89

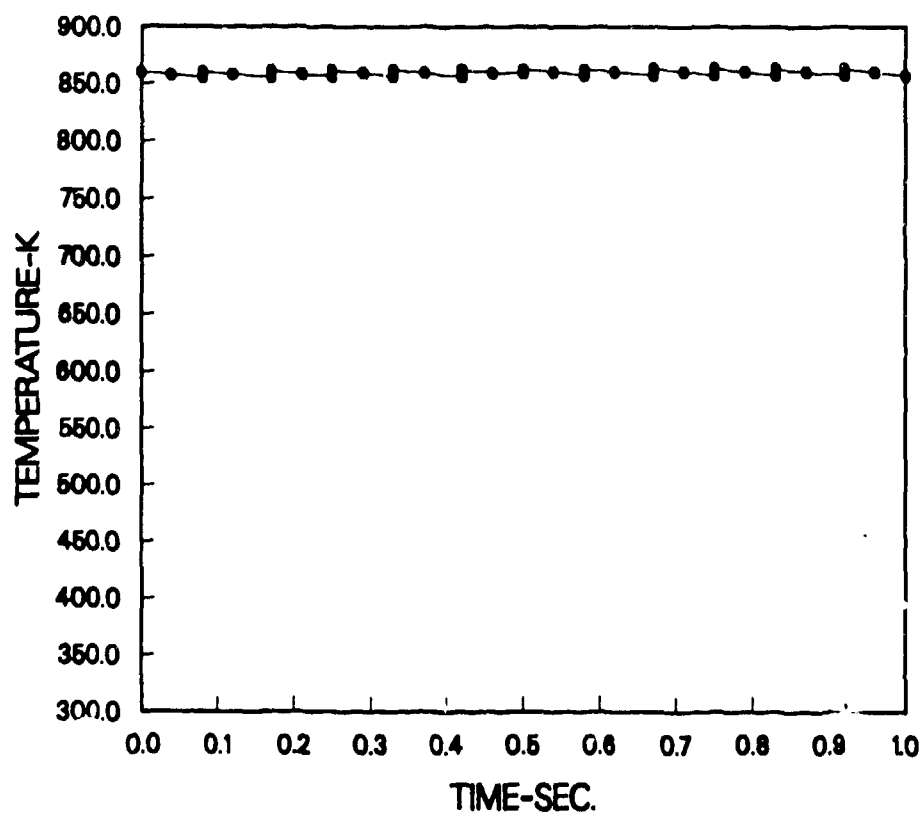


Fig. 4 The maximum target temperature near equilibrium for the transient (pulsed) calculation.

# LANSCE TARGET, 100 $\mu$ A, 1-89

TEMPERATURE-K

1	300.
2	360.
3	420.
4	480.
5	540.
6	600.
7	660.
8	720.
9	780.
10	840.
11	900.

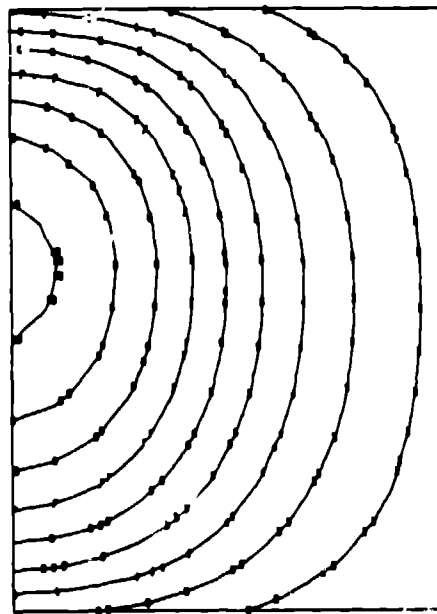


Fig. 5 The steady-state temperature distribution for the entire target.

# LANSCCE TARGET, 100 $\mu$ A, 1-89

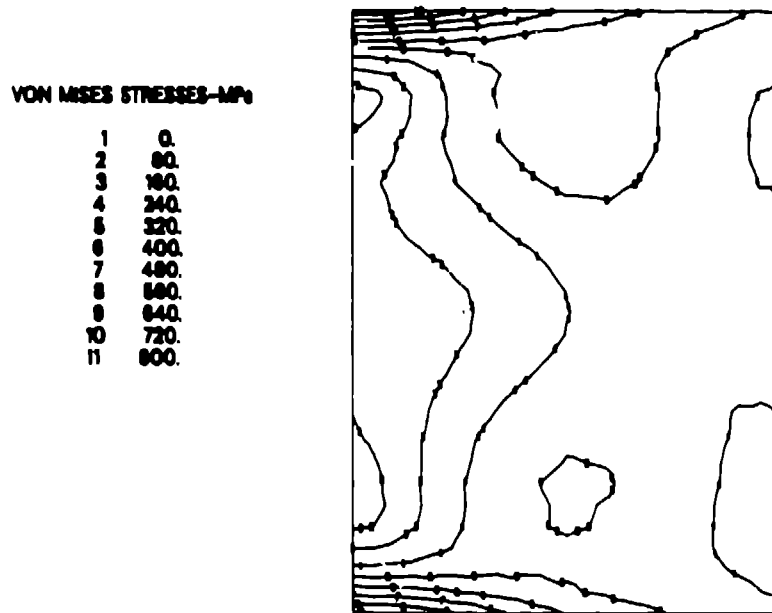


Fig. 6 The steady-state distribution for the entire target. The cylinder axis is the left vertical side, with the beam centered on this axis. The maximum stresses occur at the cooled end faces.

These calculations are done with both physical and thermal properties that have not been determined for the particular alloy being used. LANSCE is now preparing to have the real properties measured, at which point the calculations will be redone using the measured properties. Only at that point can the effect of the 100- $\mu$ A beam current on the existing LANSCE target be properly determined.

### References

1. Touloukian, Y. S., Kirby, R. H., Taylor, R. E., and Desai, P. D., eds., 1970, Thermophysical Properties of Matter, Volume 12, Thermal Expansion, IFI/Plenum, New York.
2. Contacts, Metals, and Welding, Inc., High Density Refractory Metals, Series 700, Indianapolis, Indiana 46206.
3. Kennametal, Inc., Machinable Heavy Tungsten Alloys, Latrobe, Pennsylvania 15650.
4. Touloukian, Y. S. and Ruycy, E. H., eds., 1970, Thermophysical Properties of Matter, Volume 5, Specific Heat, IFI/Plenum, New York.
5. Touloukian, Y. S., Powell, R. W., Ho, C. Y., and Klemens, P. G., eds., 1970, Thermophysical Properties of Matter, Volume 1, Thermal Conductivity, IFI/Plenum, New York.

## Workshop summary on target systems

*R. Woods*  
Los Alamos Neutron Scattering Center  
Los Alamos, New Mexico 87545 USA

This session focused on operational experience with target systems and subsequent improvements to such systems. The ISIS target failed twice in 1987 providing the unwanted, but very useful, experience of changing the target. An excellent presentation by Tim Broome and an accompanying video of the actual target changing provided a very complete description of the process, the tools required, the human interface to their remote handling cell, and the increased time required when doing work through a remote handling system. The management of the human element, particularly the personnel operating the remote handling, provided valuable information for other facilities facing a target change in the future. The process allowed ISIS to improve the tooling and the process between the two changes. They discovered that advanced planning is extremely crucial and determines the efficiency of the actual process.

The LANSCE target section presented three papers dealing with operation of the LANSCE target-moderator-reflector-shield and calculations of the heat profiles in the tungsten target material. Tom Summers discussed the electronics for controlling the liquid-hydrogen moderator. When the cryogenic system shuts down, one has about six minutes to get it going again before it vents, which then requires the eight-hour cool-down procedure. The human interface to determine the failure quickly combined with an easily understood system graphic has allowed even inexperienced personnel to recover before venting.

Alan Kemodle discussed the monitoring system based on a personal computer. The purposes of the monitoring are to both sense trends that could lead to breakdowns and provide a diagnostic history preceding a breakdown to determine the cause of failure.

The heat-transfer properties of target materials determine the temperatures reached within a system. This is complicated at LANSCE by the low-duty-factor pulsed structure of the heat source—the proton beam and subsequent spallation processes. To design higher power targets, the validity of heat-transfer calculations is crucial. These calculations are compared to operating values to develop proper calculational methods.



## Summary of contribution to the ICANS-X panel discussion

*C. D. Bowman*  
Physics Division  
Los Alamos National Laboratory  
Los Alamos, New Mexico 87545  
USA

I have spent the past three years developing neutron nuclear physics research at LANSCE with attention to applied science and fundamental symmetry studies in the energy range from thermal to 10,000 eV. I am, therefore, the only panel member who is not working full time in a neutron scattering program, although I am strongly interested in the subject. Therefore, my perspective on the development of spallation neutron research might be substantially different from the rest of the panel. Also, the views expressed here are personal and are not necessarily those of the Laboratory. My first remarks are related to spallation-source development in general.

First, I assert that the field of neutron-scattering research still is dominated by reactor science although spallation sources have made some inroads. As long as the pulsed sources focus major attention on duplicating the powerful capabilities already in place at reactors, the real potential of the pulsed sources will fail to develop. We must emphasize our advantages of time-of-flight techniques and the very intense epithermal portion of our neutron spectrum. Pulse widths of hundreds of microseconds and cold neutrons should not dominate the planning for future spallation sources unless it becomes impractical to build new reactor sources or it becomes clear that these features put spallation sources substantially ahead of the best reactors.

Turning now to future relationships between spallation sources, I wish to emphasize that each laboratory is unique in important ways and that we all lose by pushing toward some norm rather than taking advantage of our individuality. I will illustrate this by some remarks about the challenge to Los Alamos from other spallation sources and by suggesting a response.

We have heard the reports at this meeting of the excellent reliability records of IPNS and ISIS at 90% and higher, of the significant achievements in proton intensity on target at those facilities, and of an impressive array of spectrometers on line. Where does this leave Los Alamos? At first glance, not very well off. With regard to reliability, even with the PSR operating at 95%, the typical LAMPF condition of 85% leaves a net reliability of about 80%, which is a factor of three worse in unreliability than IPNS. With regard to intensity, even when we meet our 100-microamp specification, we will have no dominating advantage over our competitors.

We also fall short in terms of number and variety of spectrometers. With fewer spectrometers, only moderate intensity advantage, limited annual operating hours, and

most important, inferior reliability, we have to worry that most users who can do their experiments elsewhere will go elsewhere.

The key to the future at Los Alamos is to establish the capability to do experiments that cannot be done anywhere else. This means instruments built for the highest resolution, or for the highest intensity, making the utmost of our low repetition rate and high pulse intensity, and instruments that work in the extremes of the energy range—in particular, the higher energies. Not only would we be able to do experiments that would be nearly impossible elsewhere, we also would be opening up new areas of science. We place ourselves firmly in the avant-garde of neutron scattering and build our image around the innovative and creative. Users will come here in spite of unreliability problems for forefront science that can only be done here.

Fortunately, we are still well positioned to take this direction. The intensity of our neutron pulses, even now, is unmatched, and this advantage will improve substantially. Our target design offers advantages in flexibility and effective moderated neutron intensity. Our spectrometer construction is just beginning, and it is still possible to avoid duplication of instruments elsewhere. Our existing high-intensity powder diffractometer and the Be-filter difference spectrometer already are focused on intensity-limited experiments. We have the world lead in production of polarized beams. We are the only laboratory dealing with high counting rate by measuring neutron-detector current. We have in close proximity experimentalists with long experience in epithermal neutron spectroscopy.

We have strong institutional advantages as well. Our PSR/Line-D complex of Targets 1, 2 and 4 provides solid capabilities simultaneously for neutron scattering, neutron nuclear physics, and defense science. Together, these three make up the most comprehensive neutron-research program anywhere covering almost twelve decades of energy from cold to 800-MeV neutrons. Each of these programs has major growth potential. When the time is right, we have the best in linac and storage-ring technology at Los Alamos to take the next step in neutron intensity for all three programs and also, finally, to eliminate the reliability issue.

Critics will emphasize the risks in the program I advocate, which, I agree, are present. However, duplicating reactor capabilities, following the lead of reactor science, and emphasizing mid-range and general purpose instrumentation that aim at the present average user expose us in an unacceptable competitive position. Prudent risk-taking is the safest route to the future for Los Alamos.

As emphasized earlier, other spallation sources will adopt different positions for sound reasons that are special to their situations. We are probably all better off if the different spallation research programs do not look the same.

## Summary of contribution to the ICANS-X panel discussion

*K. Crawford*  
Argonne National Laboratory  
Argonne, IL  
USA

In general, users don't care about the source characteristics or even the type of source—what they care about is the performance of specific instruments for specific experiments. It is the instrument designers who dictate what source characteristics are necessary or desirable to achieve specific levels of instrument performance. From an instrument designer's point of view, the time-structure (pulse shape and repetition frequency) of the source and the time-averaged intensity as a function of wavelength are the two most important source parameters. Clearly, the source time-structure is of fundamental importance to those instruments based on traditional time-of-flight techniques. However, source time-structure can also be of considerable importance to some instruments that traditionally have been operated in a steady-state mode. If new sources are being designed, some of these traditional techniques should be reexamined from this point of view.

Many instruments are now operated with a less-than-optimum source time-structure and could achieve significant performance improvements if the source time-structure were optimized. Consider, for example, the small-angle scattering instruments currently operating at pulsed spallation neutron sources. For these instruments, the pulses are typically much narrower than required, so lengthening the pulses could lead to significant gains in data rates with no appreciable loss in resolution. Another example is the triple-axis spectrometers, which have been so important at steady-state sources. Introduction of a non-steady-state source time-structure could permit the use of time-gating techniques to eliminate higher-order monochromator and analyzer reflections, and so eliminate many spurious effects from the data. All instruments involve tradeoffs between intensity and resolution. Source time-structure optimization in many cases allows some of these tradeoffs to be made at the source rather than in the instruments, so that fewer unwanted neutrons escape to contribute to the background.

One of the great advantages of pulsed sources is the flexibility they provide in optimizing source time-structure and intensity-vs-wavelength characteristics. Moderators can be cold, hot, small and decoupled, or large and coupled. Several of these can coexist around a single target. If more than one target station were driven by the accelerator, preferably at different repetition rates, still greater flexibility could be achieved and a greater number of instruments could be physically accommodated. Such a dual- or multi-target facility should be seriously considered when a new pulsed neutron source is planned.




## Summary of contribution to the ICANS-X panel discussion

G. Dolling  
Atomic Energy of Canada Limited  
Chalk River, Ontario  
CANADA

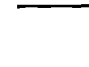

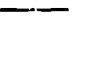
My role on this panel is to represent that group of users who wish to measure  $S(\vec{Q}, \omega)$  at specified, pre-selected values of  $\vec{Q}$  and  $\omega$ . Until now this kind of measurement has always been reasonably easy to do with a triple axis crystal spectrometer (TACS) at a continuous source of neutrons, and rather more difficult to do with a time-of-flight (TOF) machine at a pulsed source. Only those physicists who were extraordinarily hard-working and persistent managed to get any useful specific  $s(Q, \omega)$  data, using TOF methods. The lazy physicist (like me) simply emigrated to a place where triple axis spectrometers were located, or where he could build new ones. Well over 90% of all specific  $(Q, \omega)$  research has been done the easy way during the past 30 years. Human nature being what it is, I suspect there will continue to be a group of physicists who want the spectrometer to do all the work for them, requiring little or no advance planning and presenting them with results that can be fully comprehended with essentially no data analysis. They can then devote all their attention to the physics of the problem at hand. This is the essence of the TACS: Long Live Bert Brockhouse!

It has not so far been feasible to use a conventional TACS at a pulsed neutron source because there is insufficient time-averaged intensity. The pulsed source user is obliged to use TOF methods, so naturally there has been much effort devoted to making it possible to do specific  $(Q, \omega)$  measurements with a TOF spectrometer. One of the better examples along these lines is right here at Los Alamos—the Constant Q Spectrometer; PRISMA at ISIS is another excellent example. There are, however, significant limitations to the flexibility of these instruments, which I do not have space to discuss here. It seems likely that they will not be capable of supplanting the conventional TACS for a substantial body of fundamental research work. (Anyone who wants more details is welcome to contact me.)

I wonder whether it might be worthwhile, just for fun, to put a TACS at a spare beam port at LANSCE? Is the TACS that John Yamell used to use at the Omega West reactor still available? One recalls the truly superb work he did, for example, on phonons in diamond. The only modification to a conventional TACS that would be nice to have would be a computer-controlled gating system for allowing the single detector to accept neutrons only for a suitably chosen 100- $\mu$ s period, at a time after the machine pulse that would only allow the incident and then the scattered neutrons, at their calculated speeds, to travel the known distance from the source to the detector. This way one could easily suppress most of the background noise and all the order contamination problems, which can be quite a nuisance to TACS users at steady state



neutron sources. Of course, for optimum results one should really use a different pulse structure at the spallation source: broad pulses (~200 to 300  $\mu$ sec) at 50 to 100 Hz would be good enough for order elimination and background reduction, and would permit much better thermalization of the fast neutrons in the target. The time-averaged flux could be 20 times better than it is for a target-moderator system designed for sharp pulses. Is it too late now to redesign the Swiss SINQ so as to produce a suitable broad-pulse time structure without sacrificing any time-averaged intensity? This would surely make it a much better neutron source for TACS users! Is anyone prepared to give this idea a try?



## User requirements as they impact spallation neutron source design

*P. A. Egelstaff*  
University of Guelph  
Guelph, Ontario  
CANADA

### General items

Experiments completed with the existing sources worldwide have shown that much good work can be done with present flux levels. In many cases the urgent need is for long-term stable running conditions. After this has been achieved there will be further requests for higher power levels, but again long-term stable running conditions will be emphasized as crucial to many experiments. In addition, many users work in other areas of physics and different disciplines and are not used to the problems of working in a "high-energy physics" environment. They need user friendly facilities and support services. Such services will also increase the productivity of all users and, therefore, should be regarded as essential.

The points made above require the continuous attention of administrators and managers and should be given priority over any features that have been introduced for administrative or managerial convenience.

### Variable slow neutron sources

As the experiments become more sophisticated, the source requirements become more extensive. Thus, at this meeting, we have heard requests for high-intensity wide-pulse sources and for sources giving very narrow pulses. The pulse repetition frequency has also to be varied to meet these needs from 100 Hz to 0.1 Hz without reduction of mean current.

The aspects of source control imply control over the storage ring's performance and a wide control over the moderator temperature (from  $k_B T - 10 E_n$  for intensity to  $k_B T - 0.1 E_n$  for narrow pulses, where  $E_n$  is the desired neutron energy.) The panel should discuss how the storage ring and moderator designers could develop designs that would give experimentalists control of this kind. Included in this discussion should be how one might achieve such results in reasonable cost and time frames.

"Reasonableness" will become an important requirement as discussions of the above items are pursued, and both experimentalists and designers should take part in a joint dialogue to define this concept.

## Summary of the Contributions to the ICANS-X panel discussion

*F. Mezei*

Hahn-Meitner Institute Berlin GmbH  
Glienicke Str. 100, D-1000 Berlin 39  
FEDERAL REPUBLIC OF GERMANY

The field of high-resolution inelastic spectroscopy at pulsed neutron sources is still at its beginnings. However, a closer analysis of the opportunities reveals that in this particular field of applications, the pulsed nature of these sources offers distinct advantages compared to continuous sources. Assuming that the resolution improvement is achieved by using longer flight paths (which is well feasible without undue intensity losses, even for relatively short wavelengths, by the application of ordinary or supermirror coated neutron guides), the intensity penalty turns out to be just proportional to the resolution increase, because either the pulse length or the wavelength band can be kept constant. This is in contrast to losses increasing with higher powers of the resolution gain on continuous sources.

In any case, the main limiting factor in inelastic spectroscopy, in general, and in high-resolution spectroscopy, in particular, is the neutron intensity. Therefore, flexibility of resolution is crucial to obtain the optimal resolution-intensity compromise for the particular feature studied. The asymmetric resolution functions often encountered on pulsed sources offer a fortunate (and rather surprising) possibility, which is fully understood and tested by now. In a wide variety of cases, we can simultaneously derive advantage from both the better resolution offered by the sharper edge and the higher intensity corresponding to the full width of the resolution function by extracting all information from the measured spectra using proper mathematical approaches.

The main implications of these considerations concerning the characteristics of an optimally adapted neutron source are: (a) low pulse repetition rate is to be preferred (some 10 Hz or less) to allow the use of long flightpaths; and (b) best flexibility for optimizing resolution and intensity is provided by maximum intensity, unpoisoned, and coupled ("big fat") moderators and pulse-shaping choppers.

By now it is perfectly clear that the best performance in the next generation of neutron sources can be expected from advanced pulsed sources as opposed to reactors, not only at short wavelengths where pulsed sources have already proved to be superior, but over the whole spectrum of wavelengths and applications. A pulsed source offering some hundred times the effective useful flux of ILL might be within the realm of the possible by the turn of the century.

## Summary of contribution to the ICANS-X panel discussion

*A. D. Taylor*  
Rutherford Appleton Laboratory  
Chilton, Didcot, Oxon, OX11 0QX  
UNITED KINGDOM

Users are a nuisance, but they are essential to ensure the long-term funding and optimum utilisation of research facilities as expensive as advanced neutron sources. Users are also naive, and so we should follow the tradition set by Lord Reith, the founder of the BBC, and give them what is good for them rather than what they want! The typical user wants ten times more flux, ten times better resolution and ten times more beam time! But the history of neutron scattering shows that advances are instrument-led rather than science-led. This is perhaps inevitable in a field such as condensed matter studies where neutron scattering is but one (albeit a very important one) of the techniques available.

The current generation of accelerator-based pulsed neutron sources represent one such major advance giving, as we have seen at this conference, significant improvements in resolution (from the sharpness of the pulses) and signal-to-noise (from the time discrimination of fast and thermal neutron). Source reliability at greater than the 80% level is essential for efficient scheduling of a user programme, and that has now been shown to be achievable. Powerful computing tools are also essential to allow the user to extract the meaningful information from the deluge of data, and these will continue to be developed in a user friendly way. One promise held out by pulsed sources is the exploitation of the fixed-scattering geometry to allow the use of exotic sample environment. Development funds spent in this area will be well rewarded.

For the next generation neutron source we should try to combine the newly discovered advantages of the high resolution, sharp pulse spallation sources with the experience built up over the years of steady state sources. The SDI programme has shown that the current generation of accelerators are nowhere near their technological limit. A relatively modest increase in proton current, to say 1-2 mA, would not only boost the performance of traditional time-of-flight instruments but also give sufficient flux from an unpoisoned moderator to compete effectively as a steady state source whilst retaining all the advantages of a pulsed source. Incorporation of time discrimination for order and background suppression on a triple-axis crystal spectrometer is a truly exciting prospect.



# Advanced spallation sources; scientific opportunities and technical feasibility

*Günter S. Bauer*  
Paul Scherrer Institute  
CH-5234 Villigen  
SWITZERLAND and  
Kernforschungsanlage Jülich  
D517 Jülich  
GERMANY

## 1 The Scientific Case for an Advanced Neutron Source

Neutrons, among several other methods, are a scientific tool in the quest to understand the laws governing the behaviour and interaction of many particles in closed or open systems. While the properties of the individual particles in question (ions and electrons) are quite well understood and relatively simple in nature, the net effect of their interaction is the full complexity of matter and its macroscopic properties, which, to a large extent, still evade our understanding.

Traditionally, several distinctive fields of research used to deal with this complexity and to try to unveil its secrets:

- physics
- chemistry
- molecular biology and
- microbiology.

In a certain sense, although dealing with different degrees of complexity, their common goal is to understand the laws that govern the interaction of many particles in a system and - ultimately - to exploit this knowledge for increasingly sophisticated technologies to produce substances with new and predetermined properties. In most cases in the past such progress has been made in a heuristic fashion by trial and error but in recent years detailed understanding of the underlying laws has played an ever increasing role in this process. Nevertheless there remain vast num

bers of phenomena and effects which are not yet fully understood and which require continuing efforts and scientific scrutiny together with the use of a variety of tools and techniques for their solution. Important examples are:

- the formation and transformation of structures and order in physical, chemical and biological systems
- the interplay of order and chaos
- the dynamics of states far from equilibrium
- and many more.

Understanding of such problems will come about in tiny steps and will require the use of whatever clue is available, an important one being the scattering of radiation from the constituents of the system in question. Since these constituents tend to respond differently to different types of radiation the possibility to apply the various types of radiation depends on the ability to couple to the phenomena in question and on the resolution that can be obtained to extract the desired information. X-rays, or light in general, and neutrons are two typical examples of such complementary tools which, in some cases many furnish equivalent information, in others reveal completely different aspects of a given problem. Despite a rapidly growing range of applications of light scattering as brought about by the advent of new and powerful light sources, there remain a number of cases in which neutrons, due to their very physical properties cannot be substituted (see also: D. Moncton, 1988). The most important ones of these properties are:

- the simplicity of the interaction of the neutron with matter, which leaves little ambiguity in the interpretation of measured data
- the isotope-specific scattering amplitude for neutrons which does not depend in a regular fashion on atomic mass or charge and hence allows distinction of nuclear species which are difficult to distinguish otherwise. This property is frequently used for contrast variation by isotopic substitution.
- the weak interaction of neutrons with matter, which not only allows investigation of bulk properties in thick samples but also makes extreme environmental conditions possible, often requiring massive sample containers.

- the fact that neutrons not only interact with nuclei but also with magnetic moments, which makes them the best available tool for the study of collective magnetic phenomena on a microscopic scale.
- the fact that not only the wavelength of thermal neutrons is in the range of atomic distances in condensed matter but also their kinetic energy is of the same order of magnitude as the energies of elementary excitations, which makes structural and dynamic studies possible at the same time.

For several decades it was a fact that neutrons are much more expensive than X-rays, but this situation is about to change with the advent of the synchrotron light sources, which are not much cheaper than neutron sources any more and which require instruments of a degree of sophistication which is at least comparable to, if not more demanding than, present day neutron spectrometers.

This fact, and the uniqueness of the neutrons as a scientific tool, together with the fact that neutrons are making their way also towards more routine technical and industrial applications not only justifies but makes it mandatory to give some thought to the question, how the full spectrum of neutron scattering techniques can be improved and made available to a growing community of users in the future.

## 2 Directions of Progress

Although generally hard to predict, the likely development of the scientific needs and the instrumental techniques is an important factor when contemplating the layout and design of a possible future neutron source. While a certain flexibility to adopt upcoming new ideas must always be retained, several trends are clearly observable at present:

### Improved resolution

As the information extracted from scattering experiments becomes more and more detailed, the need for continuous improvement in resolution becomes more and more obvious. Since it is not possible to produce monoenergetic neutrons, the desired energies have to be selected from a wide band, with a corresponding loss in intensity and hence counting statistics as the resolution is improved. On cw sources this

tradeoff between intensity and resolution is unavoidable. The idea with pulsed sources has been to provide the higher resolution by time of flight techniques and compress as much as possible of the total intensity into those time bins actually used. This led to the lengthy discussions on an optimum moderator design which have dominated much of the previous ICANS meetings.

#### **Smaller or more dilute samples and small cross sections**

In many cases the amount of sample material available can determine the duration of a measurement because of the limited luminosity of the source. While in some instances focussing techniques can help to to a certain extent, the problem is not much different from the resolution problem; we are just looking at different coordinates of phase space.

As for very dilute samples it is one of the beauties of neutron scattering that large volumes can be used if no strongly absorbing materials are present.

Small cross sections of the phenomena under investigation will require good enough statistics to separate off those events which are not of interest. This is sometimes a matter of resolution, some times of intensity but often also a question of the availability of the optimum measuring technique.

#### **Parametric studies**

Since transitions from one state to the other are among the most fascinating problems in many particle systems, it often becomes necessary to measure the scattering as a function of several external or internal parameters of the system, or, even more difficult, as a function of the rate of change of these parameters. This is certainly a field where substantial progress is still ahead, provided we can sharpen our tool enough to tackle these problems.

### **More clear cut information**

Although neutron scattering in itself is comparatively easy to interpret and well understood, there remains one parameter which is usually not fully exploited and hence the interpretation of the scattering data often requires additional information. This parameter is the spin dependence of nuclear scattering which is the main cause for neutron scattering to be either coherent or incoherent. Separating these two types of scattering by analyzing the polarisation before and after scattering offers great potential but is on the expense of at least a factor 4 in intensity if done in the traditional way. However, recently some hope has been created that, on sources with a suitable time structure, this loss factor may be reduced by separating neutrons with the spin up and down in time and then flipping the spin of the ones coming in later (H. Rauch, 1985 / H. Rauch, 1986).

### **- Extended range of neutron energies**

The fact that the neutron's kinetic energy when in equilibrium with an ambient temperature moderator is in the range of the most common excitation energies in solids originally triggered the success of inelastic neutron scattering. However, excitation energies in many particle systems range from very low up to several eV or more. As a consequence, and also to be able to work around existing dispersion relations and conservation laws, the range of neutron energies used has been expanding continuously.

Mainly for practical reasons this expansion first went to the low energy side. Here it is now about to reach its limiting value with "ultra-cold" neutrons which can be stored in a vessel because they are totally reflected from the walls at all angles. Since the density which can be obtained with these neutrons depends on the phase space density and hence the flux level at which they are created, sources with time structure offer a potential for extra progress.

On the other end of the useful neutron spectrum, at epithermal energies, the expansion has been limited by experimental difficulties on cw-sources. These result from the difficulty of providing suitable phase space shaping devices such as high performance choppers and from the extremely small take off angles from monochromating crystals. Here, too, pulsed sources brought about substantial progress because (a) ep

ithermal neutrons are more abundant in their spectrum and (b) time-of-flight techniques are better suited in this energy range but require an intrinsically short pulse.

### 3 Ways of Improvement

The relatively short history of neutron scattering has seen a spectacular development both in the intensity available from the reactors, which are the traditional neutron sources, as well as in sophistication of the experimental techniques used. The new ANS project (C. West, 1988) represents the latest state of the development of fission neutron sources and, as far as one can see today, it is definitely exploiting the limits of what is considered as feasible with present day technologies.

On the other hand, the need to select only a small fraction of the neutrons produced for many of the experiments has triggered considerable thought, how the efficiency of neutron use could be improved. In many cases this is possible by moving away from an even time distribution of the neutron production and thus by exploiting an extra open parameter. Very significant advantage factors have been achieved in this way on the existing spallation neutron sources and we are presently in a situation where the pulsed source ISIS at the Rutherford-Appleton Laboratory can in several fields compete with or even outdo the thousand times more powerful high flux reactor in Grenoble. However, this spectacular success is limited to only a relatively narrow range of the spectrum of scientific activities in question. Also, in order to achieve this success, a specialisation on short pulse time-of-flight techniques was necessary. This generally means that only 5 % of the total possible flux is permitted to leave the moderators in order to obtain the desired short pulses. Still this figure compares favourably to the number around 0.01 % one would obtain if a similar TOF-resolution would be attempted on a cw source.

Thus, on the source side, two ways of improvement can be seen at present:

increase the neutron production rate and/or

improve the utilisation factor for the neutrons produced

For accelerator driven neutron sources, increasing the neutron production rate means either a more powerful accelerator or a higher yield target. While the first option is primarily a question of money, with a lot of progress possible both from a theoretical and a technical point of view, there is a physical limit to how high a target yield can be anticipated from the spallation process. Roughly speaking, this is about 20 n/p/GeV. If one wants to go beyond this number, one would have to resort to fission as a way of neutron multiplication. Although a viable option on low power sources (J. Carpenter, 1988), this introduces a qualitative difference from the concept of a spallation target in various respects:

- (a) For a SPNS (Short Pulse Neutron Source), thermal fission in the booster has to be avoided since this would lead to a source pulse whose length is determined by the decay constant of the thermal neutron field in the moderators. As a consequence, the target (1) has to be heavily decoupled to allow fast fission only and (2) becomes very massive and large due to the smaller probability for fast fission (G. Bauer, 1986).
- (b) A booster target will thus contain a substantial amount (up to more than 100 kg) of fissile material (U-235 or Pu) and hence will require a different operating license and safeguarding measures.
- (c) Most of the heat generated in a booster stems from fission and, depending on the desired multiplication, so do most of the neutrons, making the accelerator an expensive start-up source.
- (d) As a consequence of more severe engineering constraints and increased requirements to safety barriers, as well as the larger extension of the primary source, the effective flux gain from the moderators will be at least a factor of 2 less than the multiplication in the target.
- (e) Since the source multiplication is roughly given by

$$M = \frac{1}{k_{eff}}$$

it is necessary to operate a near critical arrangement to get a good increase in moderator leakage. This introduces a number of problems in avoiding criticality in all stages of manufacturing, installation, operation, removal and disposal.

- (f) The target lifetime is not determined by fission burn-up, but by damage due to irradiation and cyclic stresses. It is, therefore, very costly to replace and reprocess the targets at the intervals needed.
- (g) Since fission is the dominating process, delayed neutron precursors become abundant. Most of them are created during the pulse in proportion to the multiplication factor  $M$ . Since these neutrons will again be multiplied by a factor  $M$  as they decay between the pulses, the neutron background between pulses is likely to increase roughly as  $M^2$  (not relative to a tungsten target, where it is very low, but relative to a depleted uranium target!)
- (h) About 30 % of the neutrons escape from the moderator at high energies. These normally come during the  $t=0$  pulse and can be suppressed by gating the detectors. This is not true for the delayed unmoderated neutrons. These therefore constitute an extra background problem.
- (i) Reducing the problem of delayed neutron background between pulses either requires difficult to build background rotors at each beam line or a reactivity modulation for the target. The latter is technically very complicated although it does not have the same safety relevance as the reactivity modulator of a pulsed reactor.

In view of these facts the technical feasibility of a high-multiplication fissile target will not be discussed any further at this point. It seems more beneficial, at present, to review other possibilities, in which a time structure on the source flux can be exploited. (see also: G. Bauer and R. Scherm, 1986, R. Scherm and H. Stiller, 1984 and G. Bauer et al, 1981).

The most obvious and widely used way is separation of neutron energies by direct or inverted TOF which either requires intrinsically short pulses or suitable pulse-shaping devices which operate in phase with the source; the first option being clearly preferable.

Another obvious option which works on all methods that do not utilize neutron flight time is to take advantage of the short periods in which the desired neutrons arrive at the detector



to reduce backgrounds and higher order contaminations in the beam by a suitable time gate. This option can probably compensate a flux disadvantage factor of 2 to 3.

- Correlation time of flight techniques which are designed to use up to 50 % of the available beam are normally plagued by the fact that the smaller peaks of interest are sitting on a high background of "non-successful" correlations caused by more intense peaks in the spectrum. With a suitable time structure on the source this can be avoided by a coarse conventional TOF selection and a correlation interval restricted to the region of interest (see Fig. 1a and 1b).
- Phase space transformations by moving crystal devices can provide substantial intensity gains in many cases. Such devices usually work in a periodic fashion. The times, when the desired conditions are fulfilled can be synchronized to the pulses from the source, thus using the full time average intensity.
- Another technique, which becomes mainly important when TOF separation is not used in very high resolution work, is to delay neighboring neutron energies by one pulse width in time through an appropriate "detour" in space. In this way, the average flux of the source can be used several times between pulses.
- Finally, using electromagnetic forces on the neutron spin (frequently in conjunction with perfect crystals, H. Rauch, 1985 / H. Rauch, 1986) makes it possible to successively transform different phase space elements or spin orientations into the desired one. These devices require ramping of fields and hence also work in a periodic way with the resulting option of handling the full time average flux on a source with appropriate time structure.

It is important to note that, out of all the options mentioned only the first one requires really short pulses and hence makes it necessary to compromise between pulse length and time average flux. The other methods, some of which still require further development, can mostly handle pulses of a few hundred microseconds duration and actually depend very little on the shape of the pulse.

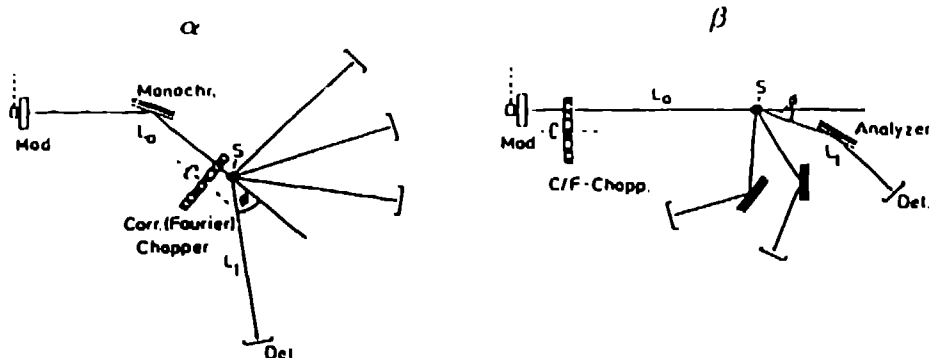


Fig. 1a Univariable correlation (or Fourier) spectrometer at a pulsed source with fixed incident ( $\alpha$ ) or fixed detected ( $\beta$ ) neutron wavelength. The source acts as a conventional chopper of a host spectrometer with coarse time resolution.

Obviously, the gains that can be expected from the various methods of using the time structure relative to a cw-source of equal time average flux vary and also depend on the details of the time structure available. They range from the full peak-to-average flux ratio (or more, considering the transmission losses in choppers) to about an order of magnitude or even less in other cases (R. Scherm and H. Stiller, 1984). Nevertheless, considering what it means to increase the source flux by an order of magnitude, these options should be taken into account when planning a second generation spallation neutron source.

#### 4 Outline of a Medium to High Power Target System

Cw-neutron sources are now aiming at a flux level of  $10^{16} \text{cm}^{-2} \text{sec}^{-1}$  (C. West, 1988). Nevertheless it seems appropriate to use the presently available flux level of  $10^{15} \text{cm}^{-2} \text{sec}^{-1}$  as a standard for comparison. This means that, in order to be competitive in the majority of neutron scattering techniques and significantly superior in all TOF-techniques one should aim at a time average flux of a coupled and unpoisoned moderator in the regime of a few times  $10^{14} \text{cm}^{-2} \text{sec}^{-1}$ . From various experimental and theoretical studies presented in detail in previous ICANS-meetings, it is clear that this requires about 1 MW of proton beam power on a pure spallation target.

Other demands to an advanced neutron source with the above characteristics and the resulting technical requirements are listed in Table 1.

Cross Correlation Technique on a cw Neutron Source and on an Intensity Modulated Neutron Source

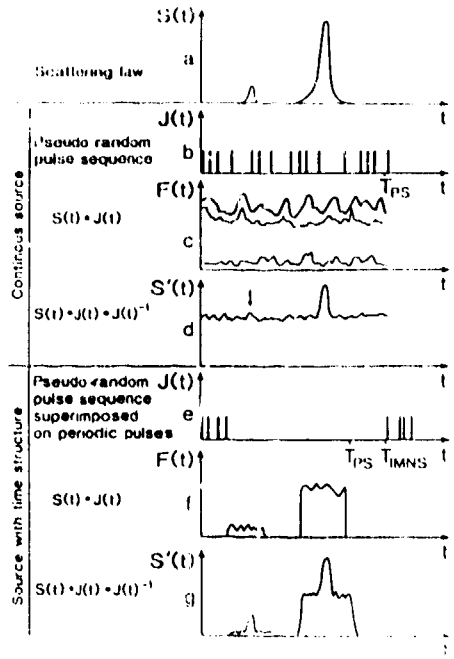


Fig. 15 Correlation spectroscopy on a spectrometer as shown in Fig. 1a

- (a) simple TOF spectrum of the sample showing a weak and a strong line
- (b) Pseudo random pulse sequence of duration  $T_{PS}$  on a cw source
- (c) Recorded spectrum at the detector composed from two components resulting from the two lines
- (d) Spectrum obtained by cross correlating b and c. The weak line is wiped out by the statistical fluctuations of the high constant level caused by the total intensity
- (e) Random pulsing of an intensity modulated source with a period  $T_{PS}$  which should not coincide with the source repetition rate  $T_{IMS}$ .
- (f) TOF spectrum consisting of two separated regions, obtained by conventional coarse time of flight analysis.
- (g) Cross correlating e and f results in a very much lower constant level under the weak peak, and hence the full gain of the cross correlation technique, obtained for weak as well as for strong lines.

It is obvious from looking at this list that there seem to be conflicting technical requirements especially in the moderator design. Fortunately, however, in contrast to the situation on a fission reactor, a spallation target does not depend on neutron return from the moderator. This gives substantial flexibility in arranging moderators of different characteristics around the target.

As a reference, let us assume that we have protons of 1.5 GeV, 750  $\mu$ A time average current which are delivered at a repetition rate of 25 Hz in pulses of 5  $\mu$ s duration. Such beam characteristics might result from acceleration in a linac or in an FFAG and injection into a post-accelerating system of rings like the CERN-booster with successive single-turn extraction from the rings.

Although, at the beam power chosen, an internally cooled tungsten target might still be feasible, it seems desirable to look for a system which has a perspective for further development and with no coolant present in the target region.

Since, as mentioned before, the precise needs which might arise in the future cannot be predicted, not even a possible shift of emphasis in known uses between now and the time when a new generation neutron source might go into operation, it is probably wise to retain as much configurational and operational flexibility as possible and fix those parameters only which require an immediate technical solution.

The configuration outlined in the following is by no means a technically mature proposal but it might indicate a route to follow when most of the above requirements are to be met.

The source shown schematically in Fig. 2 has a unified target-reflector and inner shield system of lead-bismuth or lead which is partly molten during operation with the liquid zone extending as far as required by the heat transport mechanism.

Lead-bismuth is the choice material from the point of view of operating temperature and expansion upon melting, but, if more detailed studies showed that the temperatures are not a crucial problem and that excessive materials loads due to melting and solidification can be avoided, lead might be preferable since virtually no  $\alpha$ -active products would be created.

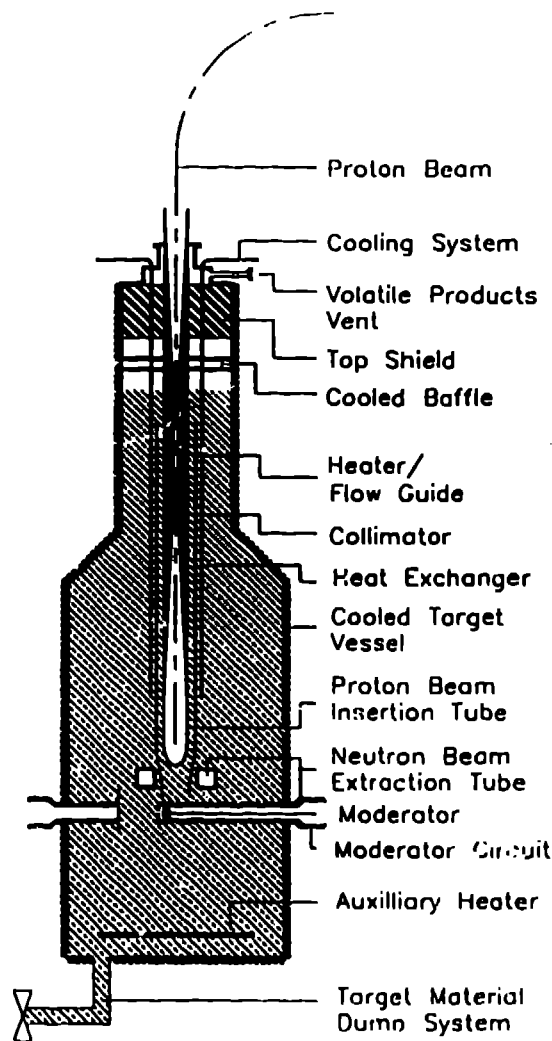


Fig. 2 Schematic representation of a spallation target with integrated heavy metal reflector and inner shield. The target material around the proton beam insertion tube can be melted by the concentric heater. Heat removal from the molten zone below the insertion tube can be either by natural convection (at relatively low power level) or by forced convection, if a pumping system is installed at the top. Cooling is effected by the vertical heat exchanger around the heater/flow guide. This concept allows efficient tailoring of the neutron spectrum by the position of the beam tubes relative to the tip of the beam insertion tube as well as by the choice of moderators inserted in the neutron beam extraction tubes. The extension of the molten zone depends on the proton beam power.

Into the vessel containing the heavy metal there intrude:

- the proton beam insertion tube from the top
- a heater system to melt the target before the proton beam is switched on
- a cooling system to remove the heat created in the interaction zone by natural convection or, if necessary by forced convection.
- several horizontal tubes which are designed to house the moderators and the neutron beam extraction tubes and which are held at low enough temperatures to be surrounded by a solid layer of target/reflector material.

The system also has a dump outlet at the bottom and an auxilliary heater to melt the whole contents of the vessel when it needs to be emptied.

With the proton beam inserted from the top, such a system has the following technical advantages:

- Only the beam insertion tube and the vertical heater are in contact with the liquid metal
- The only solid part with high temperature and high radiation load is the tip of the beam insertion tube. Its integrity can be monitored easily via the vacuum system. If it breaks, the only result is a rise of the target material in the tube.
- The volatile spallation products are collected in the space above the liquid target and hence do not constitute a hazard if the beam insertion tube breaks. They can also be removed continuously or in batches to minimize operational hazards even further.
- Exchange of the beam insertion tube can be accomplished relatively easily by first pulling it up when the target material is molten and then removing it when it is frozen again and all volatile spallation products have been trapped.

There is no need to ever change the target material

- The water cooling of the horizontal tubes can be used as pre-moderator if designed suitably.
- The design of the moderators can be varied according to the needs arising. They can be exchanged without access to the top of the target area.
- Beam tubes can be designed to serve widely different purposes; from cold neutron beams all the way to keV-beams or irradiation ports, if desired even in the very hard forward or the much softer backward spectrum.

Although it is desirable to have a cooling system at the outside of the target vessel which can be subjected to an internal pressure to help melting the whole target material if necessary, the vessel might be surrounded by a water layer to moderate and absorb neutrons escaping from the reflector-shield system in order to reduce the activation of the surrounding outer shield.

Cold and ambient moderators which are inserted into horizontal beam extraction tubes have been in operation for examples at the 23 MW research reactor FRJ-2 at KFA Jülich for many years and have been performing satisfactorily. Recently such a cold source has also been installed at the HFR in Grenoble.

The decision, whether a given moderator should be viewed from two sides and hence be placed in a through tube or should rather be surrounded by as much reflector material as possible has to be made in the frame of a detailed study.

It is beyond the scope of this paper to pursue the concept in more detail but it is likely that, if forced convection is used, such a system could work in the multi-megawatt range since the choice of the material for the beam insertion tube is neutronicly not critical and can be entirely determined by radiation and temperature resistance as well as by resistance to corrosion. The tube will have to be exchanged as a measure to prevent damage after a certain operating period.

## 5 Conclusions

In order to meet with the growing demands both for neutron scattering facilities as such and for more sophisticated experiments to obtain more detailed and clear cut information, a new generation of neutron sources is necessary which allows optimum use of the neutrons produced to give enough intensity for very high resolution work as well as for the investigation of phenomena with very low signal rates. Spallation neutron sources with a short primary neutron pulse and flexibly designed "fast" as well as coupled moderators together with a variety of imminent new phase space handling techniques have a prospect of satisfying the scientific needs also in the future. They are technically feasible both on the part of accelerators, which have not been dealt with in this paper and on the part of target systems, where new design routes can be followed.



Table 1 Demands and Resulting Requirements to the Constituents of an Advanced Spallation Neutron Source

Demand	Technical requirement
<b>Proton Beam</b>	
Short neutron pulses possible	Proton pulses no longer than a few $\mu\text{s}$
Moderately extended primary neutron source	Proton energy between 1 and 1,5 GeV optimum
Possibility of long flight path spectrometers	Repetition rate around 25 Hz
Average power on target around 1 MeV	Time average proton current around 0,7 to 1 mA
<b>Spallation target</b>	
High neutron yield from spallation	High Z material (Pb, Bi, Ta, W)
Moderately extended primary source	High density target (minimum amount of cooling channels)
Long target life time	Little susceptibility to damage from radiation and stress (liquid optimum)
High safety standard	Target design that prevents escape of radioactivity in case of damage
High beam power	Good heat removal properties
<b>Reflector</b>	
Short neutron pulses	High scattering cross section for fast neutrons. Reflector close to moderator. High density. Little moderation
High average neutron flux	Low absorption cross section for thermal and epithermal neutrons
High power dissipation	Good heat removal properties
<b>Moderators</b>	
Intrinsically short pulses	Good slowing down properties, low escape depth, cryogenic moderator
High average leakage flux	Low absorption, good escape probability
Long wavelength neutrons	Thermal equilibrium at low temperature, good escape probability
Epithermal neutrons	High escape probability at epithermal energies, short slowing down time

References:

- D. Moncton      1988    this conference
- H. Rauch        1985    "Novel Beam Bunching Methods by Perfect Crystals  
and Electromagnetic Means"  
in Neutron Scattering in the Nineties  
IAEA, CN-46, Vienna 1985, p. 35 - 52
- H. Rauch        1986    "Perfect Crystal and Magnetic Field Beam Tailoring"  
Proc. ICANS IX, Villigen 1986, p. 125 - 139
- C. West         1988    this conference
- J. Carpenter    1988    this conference
- G. Bauer et al   1986    "Enhanced Target-Moderator Concepts for ISIS"  
Proc. ICANS IX, Villigen 1986, p. 1 - 21
- G. Bauer and    1986    "Forthcoming Instrument Developments for  
R. Scherm        Improved Utilization of Neutron Beams"  
Physica 136 B 80 - 86
- R. Scherm and   1984    Proceeding of the Workshop on Neutron Scattering  
H. Stiller        Instrumentation for SNQ  
report Jül 1984, Jülich
- G. Bauer        1981    Realisierungsstudie zur  
H. Sebening      Spallations Neutronenquelle  
J.E. Vetter and   Jül Spez 113 and  
H. Willax, eds.    KfK 3175 p. 125 ff

## The U. S. Advanced Neutron Source

C. D. West  
Oak Ridge National Laboratory  
Oak Ridge, Tennessee  
USA

### The ANS project

The Advanced Neutron Source (ANS) is to be a new user experimental facility for all fields of neutron research. The most important scientific justification for the ANS Project<sup>(1,2)</sup> is to provide intense beams of neutrons for scattering and other experiments: neutron scattering is a primary tool of basic and applied materials science. Facilities will also be provided for engineering materials irradiation tests, isotope production (including transplutonium elements), and materials analysis. More than 1000 users per year are expected to carry out experiments at the ANS facility.

The source of neutrons will be a steady-state reactor designed to maximize the thermal neutron flux available outside the core, where it is accessible to neutron beam tubes and guides.

The objectives of the ANS Project are:

1. to design and construct the world's best research reactor for neutron scattering;
2. to provide isotope production facilities that are as good as, or better than the High Flux Isotope Reactor (HFIR); and
3. to provide materials irradiation facilities that are as good as, or better than, the HFIR.

In addition to these objectives, certain constraints have been placed on the reactor designers. Specifically, safety issues and technical risks are to be minimized by basing the reactor as far as possible on known technology; in particular, the design should not rely on the development of new technology to meet the minimum design criteria. However, research and development (R&D) work that could lead to further major improvements in performance will be identified and planned. Furthermore, a high availability of the reactor should be provided to users. This constraint implies a minimum core life of about 14 d that, in conjunction with an average shutdown of 3 d/cycle or 65 d/year, would give an availability of more than 80%.

The major design criteria for the ANS reactor (ANSR) are set by the user needs (Tables 1 and 2). The neutron beam experimenters, for example, want the highest possible flux of slow neutrons with a minimal contamination of the beam by fast particles. For irradiation testing of structural materials, especially for the fusion program, the opposite is required: a high fast flux with little thermal neutron content.

**Table 1. User requirements in six major fields of neutron research: neutron flux and spectrum characteristics**

	Hot/thermal/cold	Epithermal	Fast
Neutron beam experiments	High		Low
Isotope production	High		
Materials analysis	High		
Transuranium production	Medium	High	
Fuels irradiation	Medium		Medium
Structural materials irradiation	Low		High

**Table 2. User design criteria for the ANS**

Parameter	Minimum criteria
Peak thermal flux <sup>a</sup> in reflector	≥ 5
Thermal/fast ratio	≥ 80
Thermal flux at cold source position	≥ 2
Epithermal flux for transuranium production	≥ 0.6
Epithermal/thermal ratio	≥ 0.25
Thermal flux for isotope production	≥ 1.7
Fast flux for small materials tests	≥ 1.4
Fast/thermal ratio	
Fast flux for larger tests	≥ 0.5
Fast/thermal ratio	≥ 0.3

<sup>a</sup> All fluxes in units of  $10^{19}$  neutrons/(m<sup>2</sup>s<sup>-1</sup>), or  $10^{15}$  neutrons/(cm<sup>2</sup>s<sup>-1</sup>).

### Beam reactor design

Nuclear reactors produce large numbers of neutrons,  $\sim 8 \times 10^{16}$  neutrons/s for each megawatt of thermal power. These neutrons are born, within the core, with an energy of a few MeV, that is, they are fast neutrons. If the reactor core is small and does not contain an effective moderator material, most of these fast neutrons will escape into the surrounding medium, still with a high energy. If the surrounding medium is also a poor moderator and not an absorber, the fast neutrons will eventually be moderated down to thermal energies some distance outside the core. Some of these thermal neutrons will diffuse back into the core, maintaining the chain reaction; for this reason, the region outside the core is referred to as the reflector. Such a system has a high fast flux inside the core region and a high thermal flux some way outside it, with a volume of high epithermal flux in between. A reactor of this kind can simultaneously meet, in different zones, the seemingly conflicting requirements of the various user groups listed in Table 1.<sup>(1)</sup>

This design for a high flux beam reactor is typified by the world's most advanced

neutron-scattering facility, the Institut Laue Langevin (ILL) at Grenoble, France. The ILL reactor core is a compact annulus of aluminum-clad fuel plates occupying a volume of only about 46 L. The core is cooled by heavy water (a relatively poor moderator with low absorption), and the reflector is a large tank of heavy water surrounding the core. The power level is 57 MW, and the peak thermal flux—found in a region about 130 mm outside the fuel element—is  $\sim 1.5 \times 10^{19}$  neutrons/m<sup>2</sup>s<sup>-1</sup>.

### Technology for the ANSR

As indicated above, the secret of a high flux beam reactor is a small, high-power core in a low-absorption, low-moderation environment (perhaps 300 MW in a 40-L core, cooled and reflected by D<sub>2</sub>O for the ANSR). To build such a system, we require a fuel geometry that puts a large cooling surface in a small volume and also a high-density fuel form so that sufficient fissile material can be loaded to maintain criticality for at least 14 d at full power. The core design should optimize the thermal flux and spectrum in the reflector, while maintaining acceptable conditions of neutron flux and spectrum with acceptable gamma heating rates in the structural materials.

Fortunately, the required technology is found in the HFIR, at ILL, and other existing reactors or has been developed since those reactors were built. Thus, the annular, involute element of aluminum-clad, cermet fuel plates has been used with complete success for the past 20 years in the HFIR and at ILL (Table 3 and Fig. 1).

**Table 3.** Compact annular fuel elements similar to the ANSR design and used with complete success for 20 years on other reactors

Reactor	Fuel-plate thickness (mm)	Cladding thickness gap (mm)	Coolant channel length (mm)	Plate axial
ILL	1.27	0.38	1.80	880
HFIR	1.27	0.25	1.27	610
ANSR	1.27	0.25	1.27	235

The ANSR coolant and reflector will be heavy water; ILL and the High Flux Beam Reactor (HFBR) at Brookhaven are among the many research reactors that already use this technology.

The coolant velocity in the ANS reactor may be 27 m/s, only 23% greater than the 22 m/s that has been used at the Savannah River Plant; furthermore, experiments at Savannah River revealed no erosion problems for aluminum plates up to 30.5 m/s.

The fuel form selected, in the reference design, is U<sub>3</sub>Si<sub>2</sub>, which has been developed by Argonne National Laboratory and extensively tested in U. S., European, and Japanese reactors. In Fig. 2, the area to the left of and below the solid line is considered to be the "known region" of fuel loading and burnup, whose characteristics have been demonstrated by tests; the range of conditions expected within the ANSR, shown by the cross-hatched region, lies within the known region. However, special tests will be needed to verify that the fuel behavior is as expected under the very high rate of burnup expected in the ANSR.

Fig. 1 Involute (HFIR) fuel element.

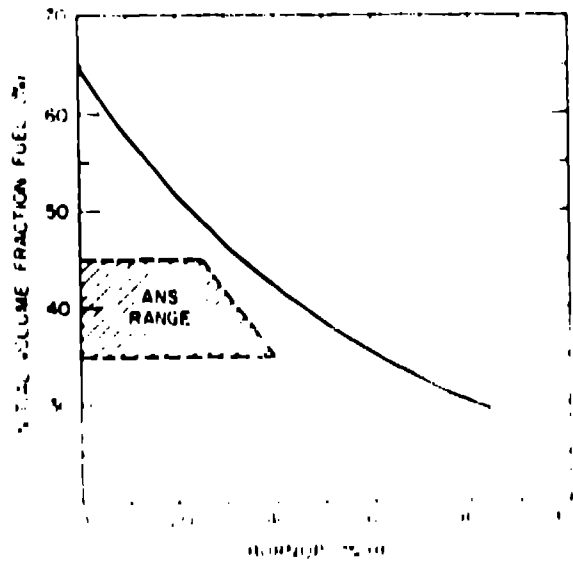


Fig. 2 Burnup and volume fraction of  $U_3Si_2$  fuel

The core is formed in two elements, separated by a heavy water gap. Compared with a core without the central gap, this arrangement (Fig. 3) provides efficient neutron production and reduces the gamma and fast neutron flux on the midplane. There are also some safety advantages. The National Institute of Standards and Technology reactor in Washington, D. C., already has an axially split core, and such a design is also proposed as an upgrade to the Jülich heavy water research reactor.

---

**Fig. 3** Reactor core and reflector tank assembly with cold sources.

### **Reactor safety**

The ANS Project intends to maximize inherent safety features of the reactor. For example, the large Department of Energy (DOE) reservation at Oak Ridge permits the reactor to be placed further from the site boundaries than even much larger power reactors. Compared with a typical power reactor, the low power level and fuel loading of the ANSR lead to a smaller fission product inventory and decay heat sources (Table 4). A large containment volume is needed to provide space for beam experiments, and this large volume ( $>100$  m<sup>3</sup>/MW of thermal power compared with only  $\sim 10$  m<sup>3</sup>/MW for a typical light-water power reactor) is a significant safety feature. Unlike a power reactor, the ANSR will be designed so that the coolant is below 100°C, so in the event of a pipe rupture the water will not flash into steam and challenge the containment integrity. Other features include the small core, which

limits the chemical energy available to drive an accident, and the large light-water shielding pool, which is an effective heat sink for accident mitigation and also would retain a large fraction of any fission products released below its surface. The relative simplicity of a research reactor, compared with an electrical generating plant, is also a safety advantage. The high power density of the core, however, means that the time available to reestablish core cooling under emergency conditions is less than that for a power reactor; thus, emergency core cooling is an especially important issue.

Table 4. Power levels and radionuclide inventories<sup>a</sup>

Reactor	Operating power [MW(t)]	Fuel mass (kg)	Radionuclide <sup>b</sup> inventory (10 <sup>7</sup> Ci) <sup>c</sup>	Decay heating rate at various times after shutdown (MW)	
				50s	10,000s
HFBR	60	12.4	2.1	2.7	0.5
EBR-II	62.5	345	7.6	2.3	0.6
HFIR	85	11.9	4.3	2.8	0.6
ATR	250	39-46	24	12.6	2.4
ANSR	300	25-30	9.0	9.9	2.2
FFTF	400	2,928	31	20	
PWR <sup>d</sup>	3,414	101,100	160	100	26
Savannah River <sup>e</sup>	2,915	113,000	220	154	63

<sup>a</sup> Data for reactors other than the ANS are taken from Table 1 of *Safety Issues at the DOE Test and Research Reactors*, National Academy Press, Washington, D. C., 1988

<sup>b</sup> Radiologically important isotopes of Kr, Xe, I, and Cs calculated at shutdown for refueling.

<sup>c</sup> 1 curie = 3.7 x 10<sup>10</sup> becquerel.

<sup>d</sup> Typical commercial pressurized-water reactor.

<sup>e</sup> Savannah River production reactor at full power.

The ANS Project has, from the beginning, taken a proactive approach to safety. The Safety Analysis Manager, even at the early stages when design detail was insufficient to carry out extensive calculations, was at the same management level as the R&D and Engineering managers, reporting to the Project Director. A safety philosophy was established early in the preconceptual design phase, documented (as a living draft), and widely distributed to project staff.

The design is based on the proven strong points of existing reactors and especially those of the HFIR, which has recently undergone multiple, extensive safety reviews. The ANSR design is fully responsive to the findings of those reviews.

A Probabilistic Risk Assessment (PRA) was initiated in the preconceptual design



phase and has already led to design changes that will enhance safety. The use of PRA to influence design at the preconceptual stage is unique and will continue throughout the design effort.

The containment design has a low-leakage, steel inner dome, separated from the hardened concrete outer dome by a ventilated plenum that exhausts through high-efficiency particulate air (HEPA) and charcoal filters (Fig. 4). With design criteria (outleakage from the inner containment of not more than 4%/d and removal of at least 99% of iodine from the outleakage by the filters) that are well within the current state of the art, the region for mandatory evacuation in case of the maximum postulated accident is entirely within the DOE reservation (Fig. 5).

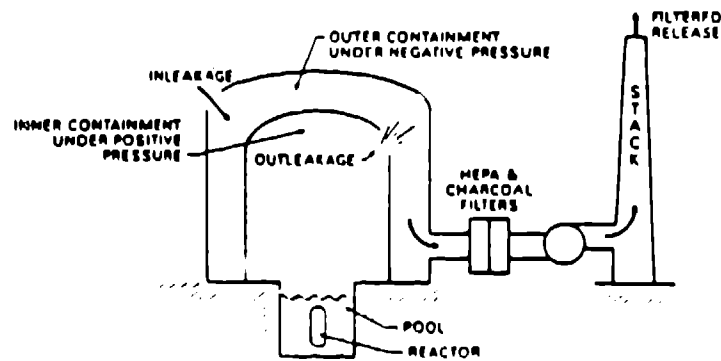


Fig. 4 Double containment with ventilated outer containment.

Fig. 5 Region for mandatory evacuation in case of maximum postulated ANS accident is entirely on the DOE reservation at Oak Ridge.

## Site layout

The facility architecture effectively separates the experiment areas from reactor operations areas. This approach provides control of personnel and contamination and makes it possible to establish appropriate security and ventilation zones. Noise and vibration control in experiment areas is also enhanced by separating the reactor coolant pumps and main heat exchangers from the neutron-scattering instruments.

A computer drawing of the facility layout is shown in Fig. 6. The main entrance lies between, and provides access to, the office building (which includes accommodation for the users) and the experimental guide hall. A security control center is located in the entrance area through which experimenters can be given access to the experimental floor in the reactor building and authorized personnel can be admitted to the reactor operations areas.

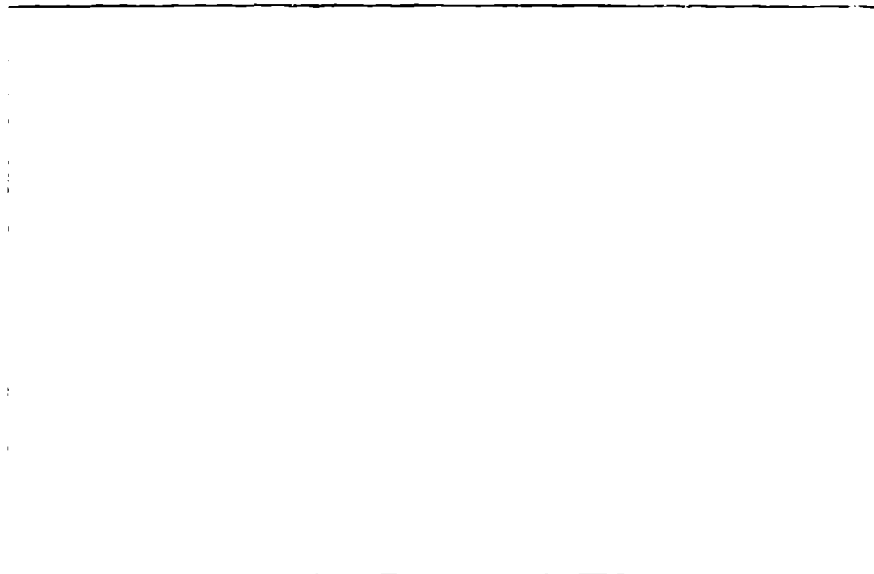


Fig. 5 Perspective of ANS facility.

## Fuel enrichment

Existing DOE orders address the physical protection of fissionable material and critical facilities. The sections of those orders relevant to the ANS Project do not distinguish between highly enriched and medium-enriched uranium fuel (HEU and MEU); that is, the precautions are no less stringent for MEU than for HEU. Low-enrichment fuel (LEU) could be stored, transported, and handled with fewer precautions. However, for the particular case of the ANSR located at Oak Ridge, the use of HEU poses very little extra cost for security and safeguards because the systems for transport and storage of weapons-grade material are already in place to support the Y-12 weapons component production plant in Oak Ridge. With these systems available, the extra cost of secure shipment of HEU for the ANSR would be only about \$100,000 per year, and the additional cost for security forces to provide

protection during refueling would be \$10,000 to \$100,000 per year.

Even for licensed research reactors, Nuclear Regulatory Commission (NRC) rules<sup>(4)</sup> (which do not presently apply to DOE facilities) provide for the use of highly enriched fuel where necessary to meet a "unique purpose." Examples given by NRC of unique purpose include "research projects based on neutron flux levels or spectra attainable only with HEU fuel," and "a reactor core of special design that could not perform its intended function without using HEU fuel." The ANSR falls in this category. For example, at 300 MW an HEU core will give ~65% more flux than an LEU one: the flux from HEU will be 5 to 10 x 10<sup>19</sup> neutrons/m<sup>2</sup>s, but from LEU only 3 to 6 x 10<sup>19</sup> neutrons/m<sup>2</sup>s. The additional cost of raising the power level to regain the flux lost by going from HEU to LEU is \$100 million in construction, and \$400 million in lifetime fuel and pumping power costs: these costs should be compared with the \$100,000 per year cost of providing security and protection for the HEU fuel. Furthermore, the higher power level of the LEU core brings the safety disadvantage of a much higher fission product inventory decay heat load. The present reference design therefore incorporates HEU as presently used at the other reactors in Oak Ridge.

### **Performance specifications**

The major performance parameters of the reference core are compared with the user design criteria in Table 5. Because the core design is still evolving in some respects the figures shown are approximate; nevertheless, it is clear that the design concept can meet and in most cases greatly exceed the minimum requirements of the user community.

### **R & D tasks**

"Feasibility R&D" addresses some basic assumptions about the behavior of certain components and materials that have so far been tested only under conditions that are less demanding than the ANSR. One example, mentioned previously, is the fuel behavior at high fission rates. Other examples include the fuel clad oxidation rate at very high heat flux and the thermal-hydraulic and structural stability of the involute core assemblies. In addition, further preconceptual design work is needed to establish the design criteria so that conceptual design can begin; for example, the control concepts, cooling system, site selection, facility and experimental instrument layout, and safety criteria must all be finished, or at least frozen, before conceptual design can begin.

Among the R&D areas identified as offering the potential for further major improvements in performance are (1) reduction of fuel clad corrosion rate, perhaps by surface modification, choice of materials, or water chemistry manipulation; (2) improvements in neutron mirror and neutron detector technology; and (3) enhancement of core cooling by introducing fresh coolant that has bypassed the first fuel element into the inlet of the second element in the gap between the two core halves.

Table 5. Approximate major performance parameters of the February 1988 reference core compared with the user design criteria

Parameter	Minimum criteria	Reference core <sup>a</sup>
Peak thermal flux in reflector <sup>b</sup>	> 5	10
Thermal/fast ratio	> 80	80
Thermal flux at cold source position	> 2	8
Epithermal flux for transuranium production	> 0.6	2
Epithermal/thermal ratio	> 0.25	2
Thermal flux for isotope production	> 1.7	4
Fast flux for small materials tests	> 1.4	6
Fast/thermal ratio	> 0.5	6
Fast flux for larger tests	> 0.5	1
Fast/thermal ratio	> 0.3	0.4

<sup>a</sup> Unperturbed at nominal power level

<sup>b</sup> All fluxes in units of  $10^{19}$  neutrons/(m<sup>2</sup>s<sup>-1</sup>), or  $10^{15}$  neutrons/(cm<sup>2</sup>s<sup>-1</sup>).

### Schedule and cost

Figure 7 shows the schedule that forms the project's current planning base. This schedule calls for congressional approval (and funding) to begin detailed design work in FY 1992, followed by approval and funding for construction to begin in FY 1993. The reactor would first go critical at the end of FY 1997. This is almost the fastest schedule that can now be imagined, and of course it depends upon timely availability of the funding for these activities, described in the previous section, that must precede conceptual and detailed design.

The spending plan associated with this schedule is presented in Fig. 8: the costs of detailed design and construction are presently estimated at \$412 million (1988 dollars), but until a conceptual design is completed, no validated construction cost estimate can be made.

### Summary

A reactor design based on previously developed technology can meet the minimum, and at least approach the maximum, performance criteria set by the user community for the ANS. The design approach, objectives, and organization of the ANS Project emphasize safety and minimize technical risk. Certain R&D issues that must be resolved to give full confidence that the design will meet performance criteria have been identified and are being addressed. Other R&D tasks that might further enhance performance or safety margins have been identified and are being addressed.

### Acknowledgements

Based on work performed at Oak Ridge National Laboratory, operated for the U. S. Department of Energy under contract DE-AC05-84OR21400 with the Martin Marietta Energy Systems, Inc.

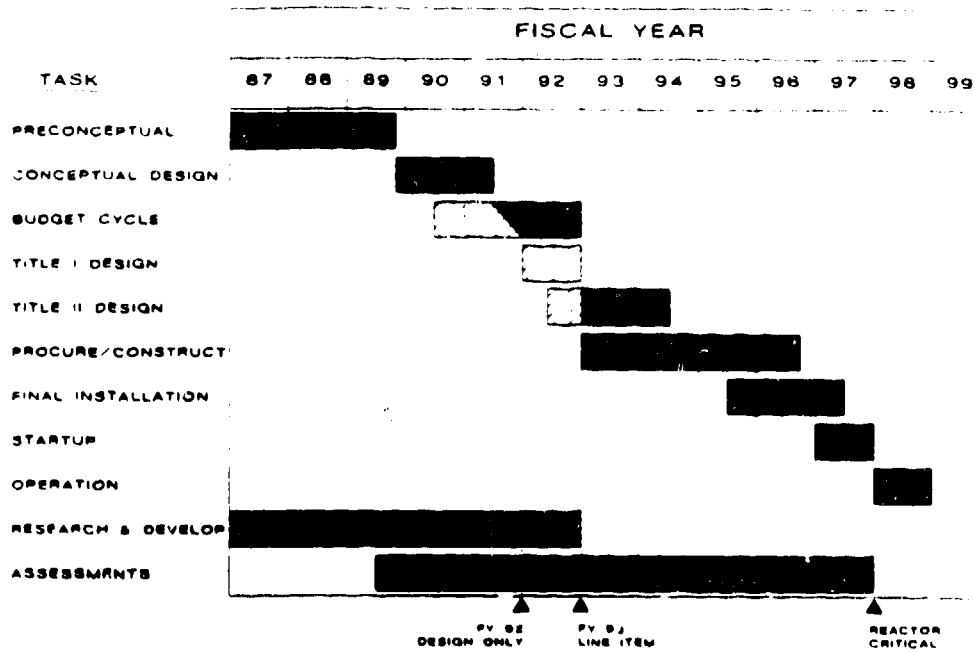


Fig. 7 Schedule for ANS project.

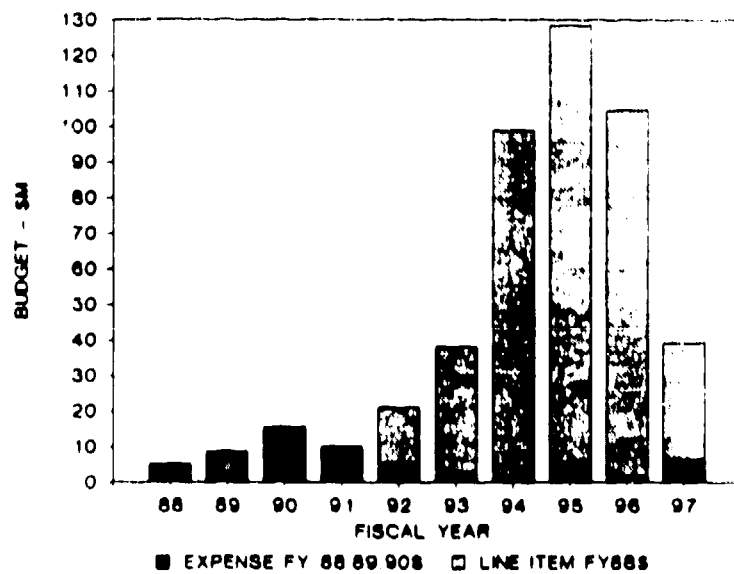




Fig. 8 ANS project spending plan.



## References

1. Major Materials Facilities Committee, National Research Council, 1984 *Major Facilities for Materials Research and Related Disciplines*, National Academy Press, Washington, D. C.
  2. Materials Ad Hoc Panel of ERAB, Review of National Research Council Report, 1985, "*Major Facilities for Materials Research and Related Disciplines*", DOE/S-0037, June.
  3. Proc. of the Workshop on An Advanced Steady-State Neutron Facility, 1986, Gaithersburg, Md., *Nucl. Instr. and Methods A249*.
  4. *Code of Federal Regulations*, 1987, 10 CFR 50.64, "Limitations on the Use of Highly Enriched Uranium (HEU) in Domestic Non-power Reactors".
- 
- 

⊕

## Progress report on measurement and fitting of pulse shapes of moderators at IPNS

*Russell L. Bywater, Jr. and  
Robert E. Williams*  
Department of Nuclear Engineering  
Iowa State University  
Ames, Iowa 50011  
USA

*John M. Carpenter*  
Intense Pulsed Neutron Source Division  
Argonne National Laboratory  
Argonne, Illinois 60439  
USA

⊕

### ABSTRACT

We present a progress report on measurements and fitting of pulse shapes for neutrons emerging from one solid and two liquid methane moderators in IPNS. A time-focused crystal spectrometer arrangement was used with a cooled Ge monochromator. Data analysis of one of the liquid methane moderators has shown the need for some generalization of the Ikeda-Carpenter function that worked well for fitting pulse shapes of polyethylene moderators. We describe attempts to model physical insight into the wavelength dependence of function parameters.

⊕

### 1. Introduction

At the time of this writing, the Intense Pulsed Neutron Source (IPNS) at Argonne National Laboratory is in its eighth year of successfully providing spectroscopists with slow ( $< 10\text{eV}$ ) neutrons. The IPNS uses solid and liquid methane moderators to slow down fast (MeV) neutrons from a depleted uranium primary

⊕

source. Fast neutrons are obtained by bombarding the depleted uranium target at 30 Hz with 80-ns bursts of 450 MeV protons. The fast neutrons are produced in pulses of the same frequency and approximate duration as the proton pulses. Thus, a convenient origin in time is established for neutron time-of-flight studies.

The neutrons emerge from the moderators in pulses also, but on quite a different time scale. The thermalization process in the moderators causes a substantial energy-dependent broadening of the neutron pulse which can amount to tens of microseconds. The end result is a fundamental limit of resolution established by the neutronic properties of the moderators. A quantitative understanding of the neutron emission-time distributions, or pulse shapes, for a moderator is necessary for neutron time-of-flight data analysis.

To this end, measurements were made of the neutron pulse shapes of the one solid and two liquid methane moderators in IPNS. This progress report briefly describes these measurements and the attempts made to fit mathematical functions to the data.

## 2. Measurements of Pulse Shapes

We measured the neutron pulse shapes of one solid and two heterogeneously poisoned liquid methane moderators. The solid methane "C" moderator measures  $7.9 \times 10.0 \times 10.5 \text{ cm}^3$  in size, has 1.95 cm deep grooves on the viewed face and can be cooled with liquid helium to temperatures as low as 10 K. The continuously-recirculated liquid methane "H" moderator measures  $5 \times 10 \times 10 \text{ cm}^3$ , is cooled to about 100 K, and is heterogeneously poisoned with a 0.5 mm Cd plate 2.5 cm below the viewed surface. The



liquid methane "F" moderator has the same dimensions and temperature but is poisoned with two Gd plates 1.7 cm below its two viewed surfaces. The beamports at IPNS used to view the moderators for these measurements were C3, H1, and F1, respectively.

The experimental procedure follows closely that outlined by Ikeda and Carpenter when they made similar measurements of polyethylene moderators at IPNS.<sup>1,2</sup> The arrangement calls for a crystal monochromator and a detector with the correct geometrical orientation to achieve time focusing. That is, only reflections of neutrons having the wavelengths allowed by the Bragg diffraction equation will be seen by the detector. In addition, the experimental geometry assures that the neutrons of each particular order of reflection have flight path lengths and Bragg angles such that they reach the detector in exactly the same amount of time. This is true in spite of the fact that considerable changes of position of origin on the moderator, position and angle of the scatterer from the crystal, and positions of interactions in the detector are accepted in the measurements, which enhance the intensity. Fig. 1 shows a diagram of the experimental arrangement.

The conditions for time focusing in this arrangement are as follows:

$$\begin{aligned}
 P &= L_f / L_i \\
 \tan \theta_m &= \sqrt{1+P} \cot \theta_B \\
 \tan \theta_D &= \sqrt{1+1/P} \cot \theta_B \\
 \cot \theta_c &= \frac{\cos \theta_D \tan \theta_m + \sin(2\theta_B + \theta_D)}{2 \sin \theta_B \sin(\theta_B + \theta_D)} \quad (1)
 \end{aligned}$$

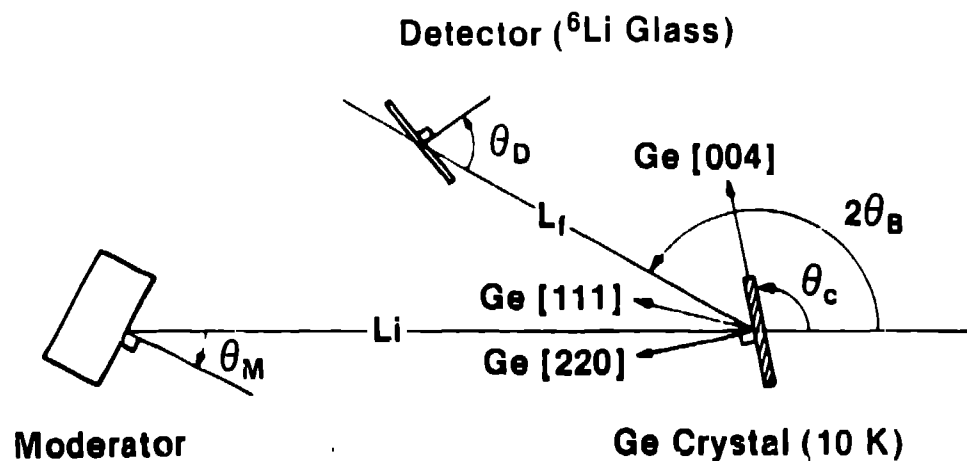


Fig. 1. Time-focused arrangement of moderator, monochromator, and detector used in these measurements.

The monochromator was a 1-mm thick, 25-mm diameter Ge crystal which had been cut parallel to (110) planes so that the (111) reflecting planes used were not parallel to the physical plane of the cut face. The Bragg angle was  $\theta_B=60^\circ$ . Each of the beam ports used views its moderator at the angle  $\theta_m=18^\circ$  (focusing cannot be accomplished when  $\theta_m=0^\circ$  except when  $\theta_B=90^\circ$  (backscattering).) The detector was a 2-mm thick, 75-mm diameter <sup>6</sup>Li glass scintillator and was placed to intercept neutrons scattered at  $2\theta_B=120^\circ$ . For each of the moderator measurements, the flight path lengths  $L_1$  and  $L_2$  were chosen so that their ratio  $F$  was equal to 0.1. For example, for the F moderator the crystal was positioned at a distance  $L_1=13.44$  m from the moderator and the detector was positioned at a distance  $L_2=1.34$  m from the crystal. This flight path ratio corresponds to a crystal angle,  $\theta_c=95^\circ$ , and a detector angle,  $\theta_D=73^\circ$ .

The Ge crystal was cooled to about 30 K to increase reflectivity and gain higher intensity for the high order

reflections. The refrigeration and vacuum equipment used, however, did not maintain a constant temperature and there was warming during each of the data collection runs of at least 10 K.

From the neutron time-of-flight spectra obtained for the F moderator, good data was available through the ninth order reflection (206 meV) and reflections were observed through the 15th order reflection (650 meV). The statistics for these higher order reflections are poor. This will be addressed again in the analysis section. There are several factors contributing to the low count rates for this measurement, including: the diminishing beam intensity for this long path length, and problems with cooling, vacuum, and geometrical alignment. Fig. 2 is a portion of the raw time-of-flight spectrum displaying six reflections. The Ge(444) reflection (1.41 Å) has the best statistics with nearly 1500 counts in the peak channel. Fig. 3 is an expanded view of the Ge(333) reflection (1.88 Å).

These high resolution measurements immediately reveal the very sharp rise in the leading edge. In the case of fig. 3, the 10-90% rise time is about 8 microseconds, a relative wavelength resolution of about 0.1% at this flight path length.

Spectra from the H moderator show pulses that look very similar (as expected, although not identical because of the different poisoning) to those of the F moderator. The exception is that because of better alignment, the peak integrals in the spectra from the H moderator are several times greater than those of the F moderator, so that the measurements from the H moderator are statistically more reliable.

Spectra from the solid methane C moderator show good peak statistics and clearly illustrate the presence of the physical

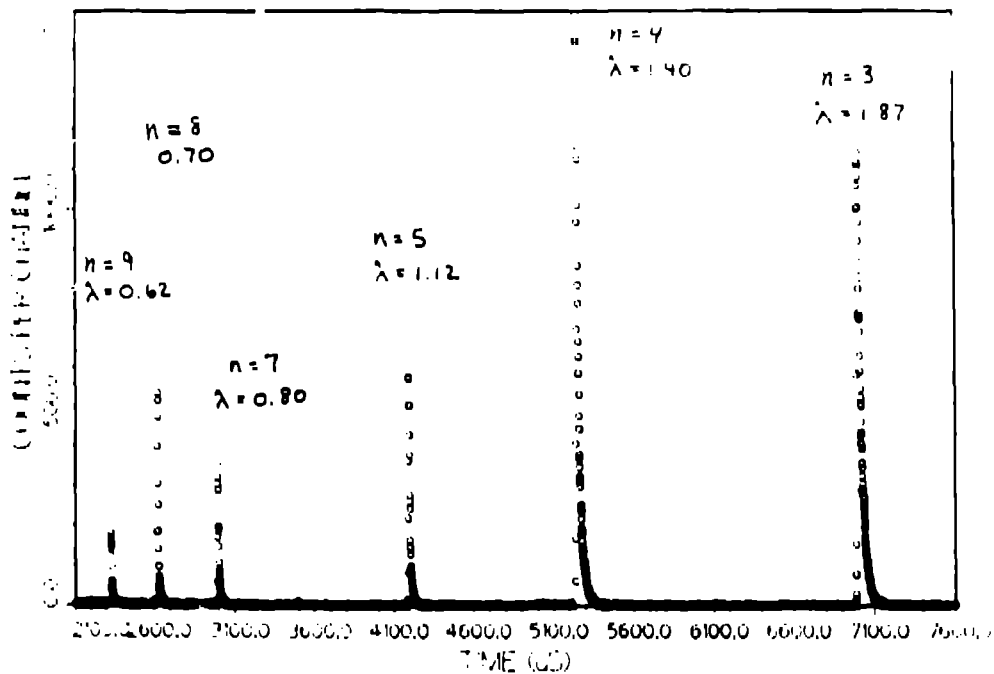


Fig. 2. Ge reflections observed in the F moderator measurement with  $L_1=13.4$  m,  $L_2=1.34$  m.

grooves in the moderator. Pulse shapes from this moderator are actually composed of two individual pulse shapes. The leading edge, or shoulder, represents the pulse of neutrons emerging from the top of the moderator "fins" and the second peak represents the pulse of neutrons of the same energy emerging from the bottom of the grooves. The second pulse is delayed by an amount of time equivalent to that required by the neutrons to travel the length of the grooves. Fig. 4 is a view of the Ge(444) reflection (1.41 Å) and clearly shows that the intensity of neutrons from a grooved moderator is greatest from the base of the grooves.

#### 1. Analysis and Discussion

To date, attempts to fit mathematical functions to the data

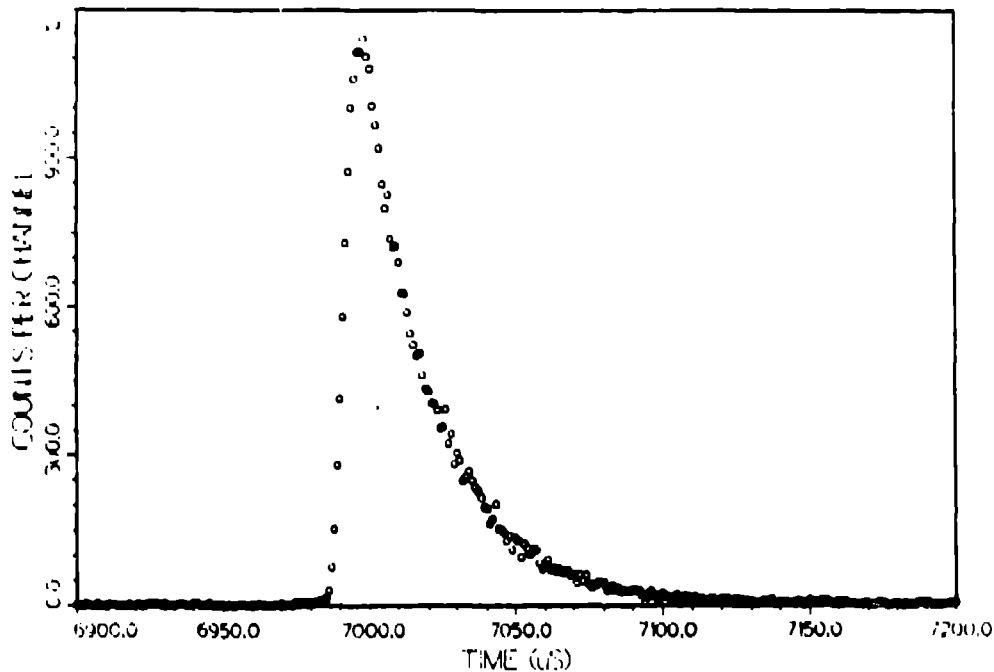


Fig. 3. Ge(3,3,3) reflection observed in F moderator measurement, 1.88 Å.

have been limited to the F moderator which, although having the least favorable counting statistics, were obtained first. Analysis of F moderator data was continued well after data had been collected from the similar H moderator. This may prove to have been unwise because several evolutionary steps have been made in the functions to provide better fits. These changes were based on results of analysis of the F moderator data without comparing function performance on the H moderator.

Ikeda and Carpenter<sup>1</sup> developed a function which fit the pulse shapes of polyethylene moderators extremely well. The function has four wavelength dependent parameters and attempts to model some of the physical processes that occur in neutron thermalization. The function has the form

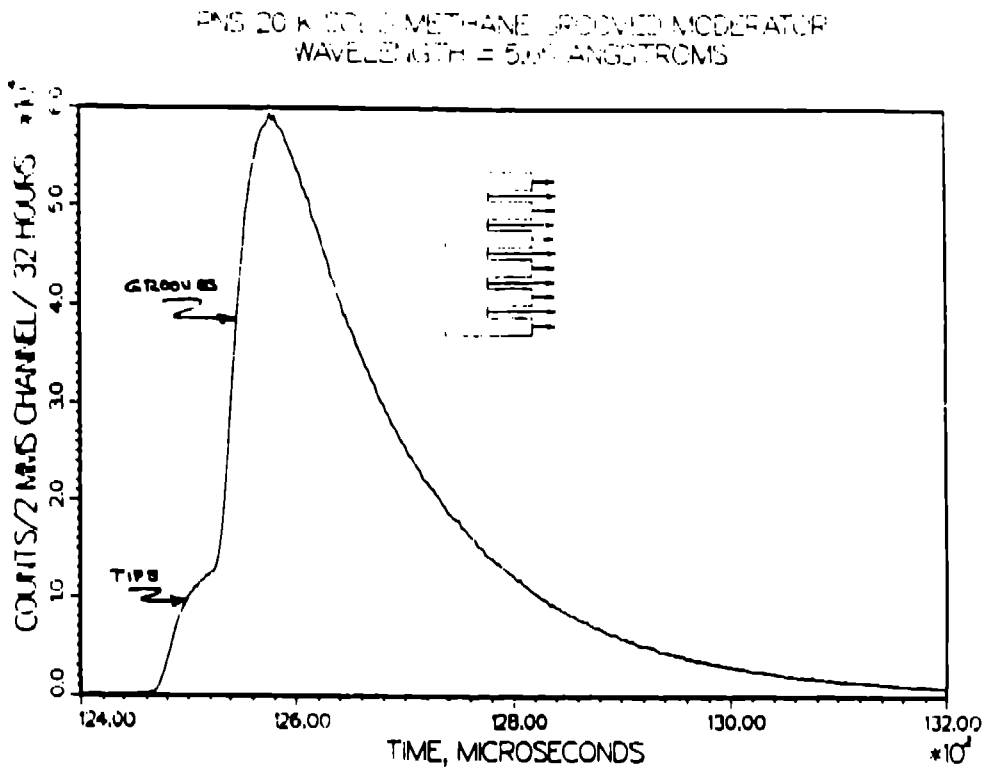


Fig. 4. Ge(4,4,4) reflection observed in C moderator measurement, 1.41 Å.

$$\begin{aligned}
 \psi(a, \beta, R, t) = & a/2 \{ (1-R)(at)^2 e^{-at} + 2Ra\beta / (a-\beta) \} \\
 & \times [ e^{-\beta t} - e^{-at} (1 + (a-\beta)t + \frac{1}{2}(a-\beta)^2 t^2) ] \quad (2)
 \end{aligned}$$

where,  $a = v[\Sigma_s]$  the neutron velocity times the macroscopic scattering cross section.

$R$  = fraction of the area of the peak in the 2nd term, the storage or thermalization term.

$\beta$  = a time constant characterizing the decay of the storage term

The function makes sense physically from the basics of neutron slowing down theory. Neutrons emerging from a pulsed moderator

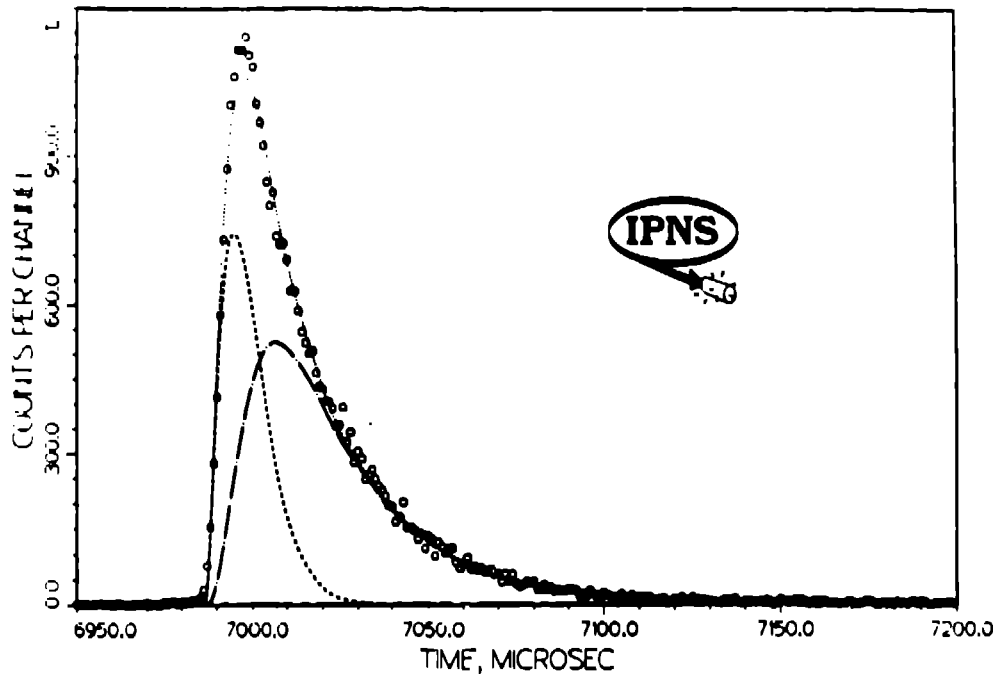


Fig. 5. Ge(3,3,3) reflection for F moderator. The dotted line is calculated by eq. (2) with parameters  $\Sigma=2.88 \text{ cm}^{-1}$ ,  $\beta=0.04/\mu\text{sec}$ , and  $R=0.85$ .

consist of two terms: a slowing-down component, representing neutrons that have emerged in the process of slowing down before thermalization, and a storage component, representing neutrons that have reached thermal equilibrium with the moderator and leak from it with a characteristic wavelength-independent decay constant  $\beta$ . The first term in eq. (2) represents the component of the pulse of a particular energy that is in the  $1/E$  slowing-down spectrum (slowing-down term) and the second term (storage term) represents the component of the pulse that is in the Maxwellian part of the spectrum. The function is the sum of a delta function and the decaying exponential storage term convoluted with the slowing-down function.

Pulse shapes of the F moderator were fitted using this function and maintaining the three parameters described above, a scale factor, and a delay time  $t_0$ , as free parameters of wavelength. The results of the fitting, while encouraging, were not spectacular. Fig. 5 shows the results of fitting the Deardorff-Carpenter (IC) function to the data for the Ge(333) (1.88 Å) F moderator reflection. The figure indicates that the slowing-down term is important in fitting the rising edge of the peak and the storage term is dominant in the decaying tail of the pulse shape for neutrons of this wavelength. Characteristic of these fits was a systematic underestimation of the height and integral of each peak. This experience suggested that some modification was needed in the IC function.

The slowing-down term in the IC function is the simple description of neutrons slowing down in an infinite medium of free protons (the "proton gas" model). We suggest that a generalization in the exponent in the slowing-down term from 2 be made to account for some of the molecular characteristics of thermalization. Such a generalization is plausible on the grounds of using the Sachs-Teller effective mass<sup>3</sup> to approximate the scatterers in a liquid, where molecular effects can be important, with gas atoms of mass greater than the physical mass.

The function maintains the form of its predecessor but is more general in that it contains the incomplete gamma function. The generalized IC function has the form

$$\Psi(a, \beta, \nu, R, t) = (1-R)\Phi(a, \nu, t) + R F(a, \beta, \nu, t) \quad (3)$$

$$\text{where: } F(a, \beta, \nu, t) = \left[ \beta a^{\nu+1} / \Gamma(\nu+1) \right] (a-\beta)^{-(\nu+1)} e^{-\beta t} \\ \times \gamma((\nu+1), (a-\beta)t) \quad (4)$$



is the slowing-down term and,

$$\delta(a, \nu, t) = [a/\Gamma(\nu+1)](at)^\nu e^{-at} \quad (5)$$

is the storage term.

Again, pulse shapes of the F moderator were fitted. The generalized IC function was used while maintaining the parameters  $a$ ,  $B$ ,  $\nu$ ,  $R$ , a scale factor, and  $t_0$  as free parameters of wavelength. The results showed improvement over previous fitting in that discrepancies between best fits of the function to the data and the peak integral were eliminated. An example of a fit using the generalized IC function for the Ge(333) F moderator reflection with no restraint on the fitting parameters is shown in fig. 6. Allowing freedom of the parameters during the

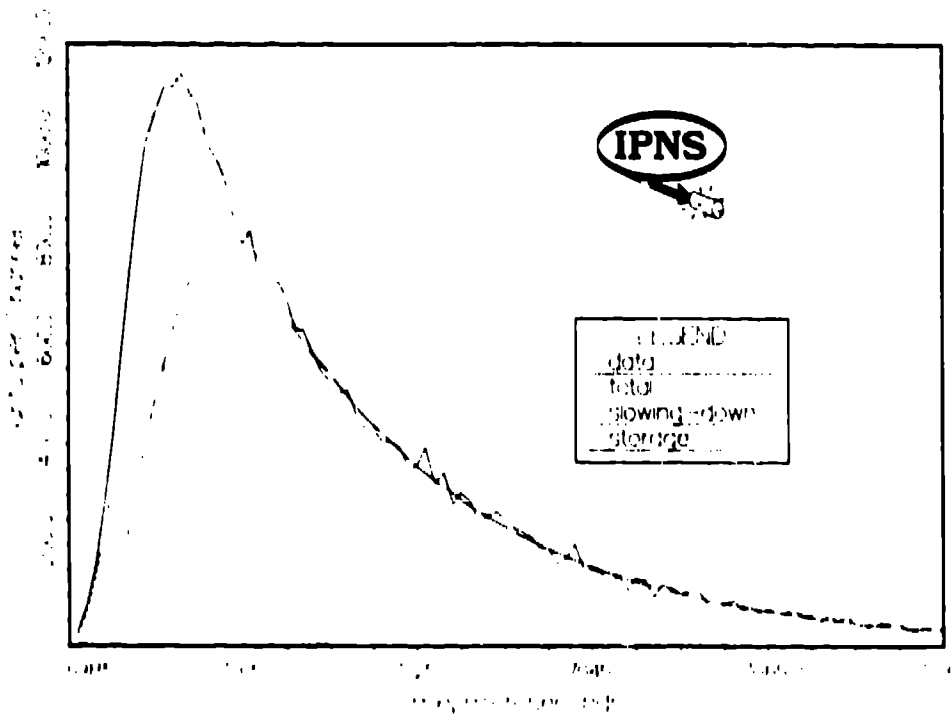


Fig. 6. Ge(3,3,3) reflection for F moderator. The dotted line is calculated by eq. (3) with parameters  $\nu=7.4$ ,  $\lambda=2.88 \text{ cm}^{-1}$ ,  $R=0.041 \text{ } \mu\text{sec}$ , and  $R=0.81$ . The estimated chi square value for this fit is 1.288.

fitting, however, produced some unexpected variations as a function of wavelength (energy). Most disturbing was the large fluctuation in the parameter  $\beta$ . This parameter represents the decay constant of the storage term which, to first approximation from slowing-down theory, should be representative of the fundamental eigenvalue of the Maxwellian and should be independent of energy.<sup>4</sup>

So as not to completely disregard the theory, the parameter  $\beta$  was "fixed" for all energies and fits were made again with the remaining four parameters maintained as free parameters for each wavelength. The results of this trial showed an interdependence of the parameters  $a$ ,  $\nu$ , and  $t_0$ . Fits of pulse shapes of a particular wavelength of almost equal quality (based on an estimation of the chi-square values for the fits; the least-squares iteration was not carried all the way to the minimum of  $\chi^2$ ) could be obtained with different triplet sets of  $a$ ,  $\nu$ , and  $t_0$ . A three-dimensional linear regression analysis for these parameters was performed for one of the peaks, which demonstrated their linear interdependence within a rather wide range of values of  $a$ ,  $\nu$ , and  $t_0$ . Rather than perform this task for each of the peaks, we chose to include a wavelength-dependent functional form for each of the parameters in the fitting routine and fit all the pulse shapes from the moderator data simultaneously.

The functional forms for the four wavelength-dependent parameters ( $\beta$  was a fitted parameter, but constant at all wavelengths) were chosen with the desire to implement a little knowledge of physics and provide for some physically believable parameters. The wavelength dependent functions were now of the form

$$t_0 = A + B\lambda, \quad (6)$$

$$a = v\Sigma_s, \quad (7)$$

where  $v$  = neutron velocity, and

$\Sigma_s$  = macroscopic scattering cross section

$$\Sigma_s = (S_1^2 + S_2^2 \lambda^2)^{1/2}, \quad (7')$$

$$R = \exp(-E/E_0), \text{ and} \quad (8)$$

$$\nu = 2. + c^2 \exp(-E/E') \quad (9)$$

This representation of the generalized IC function now called for fitting seven new wavelength-independent parameters to determine the four wavelength-dependent parameters for each peak and an eighth parameter for the wavelength-independent parameter  $\beta$  as before. Each peak was allowed its own amplitude factor. The time delay  $t_0$  shown in eq. (6) represents the flight time from moderator to detector plus a fixed shift of the time origin and is necessarily linear in form. The functional forms chosen for  $\Sigma_s$  and  $R$  have proven successful earlier.<sup>1</sup> The form for the exponent parameter  $\nu$  was chosen with the feeling that it should approach a lower limit of 2 for shorter wavelengths and should be in some fashion greater than two for longer wavelengths to account for the increasing Sachs-Teller effective mass.

Fits to the F moderator data using these functions presented another problem. The function was not adequately describing the decaying tail of the higher-order reflections; it was dying away too rapidly, underestimating the tails of the short wavelength pulse shapes. One explanation was the possibility of the existence of another decay constant corresponding to a higher-order energy or spatial eigenvalue of the moderator. (When  $\beta$  was a free parameter, best fits were obtained with different decay

constants for the higher-order reflections.) Another possibility was the need for a better representation of the parameter R than the simple Boltzmann function of eq. (8). The latter alternative was pursued by including the energy spectrum relationship of the slowing-down and storage terms of the generalized IC function. That is, representing the energy spectrum as a Maxwellian component smoothly joining with the 1/E slowing down component in the epithermal region. Here, use was made of a generalization of Westcott's<sup>5</sup> joining function

$$\Delta(E) = [1 + (E_{c0}/E)^s]^{-1} \quad (10)$$

where:  $E_{c0}$  = a cutoff energy corresponding to about  $5kT$  and,

$s$  = a parameter suggested by Westcott to be about seven.

The generalized IC function could then be written as

$$\Psi(a, \beta, \nu, \Delta, E_T, E, A, t) = (\Delta/E) \Phi(a, \nu, t) + A^2 e^{-E/E} EF(a, \beta, \nu, t) \quad (11)$$

where F and  $\Phi$  have their previous meanings and  $A^2$  is another amplitude factor.

The function did not perform as well as had been hoped on the F moderator data. In some respects it performed even worse, underestimating the peak integrals for the intermediate wavelength pulse shapes.

Shortly before the time of this writing a second decay constant (also independent of energy) was added. This created an entirely new storage term corresponding to an additional

moderator eigenvalue. The function describing the wavelength dependence of R was dropped and in its place, free independent coefficients for each of the three terms were incorporated. The new function has the form

$$\Psi(a, \nu, \beta_1, \beta_2, A_1, A_2, A_3, t) = A_1 \delta(a, \nu, t) + A_2 F(a, \beta_1, \nu, t) + A_3 F(a, \beta_2, \nu, t) \quad (12)$$

This pulse shape function provides the best fits to the F moderator data using simultaneous, multi-peak fitting of all attempts to date. A plot of the Ge(333) pulse shape fit with this function is shown in fig. 7; this does not produce as good a fit as when peaks were fit individually as was shown in fig 6.

#### 4. Concluding Remarks

Pulse shapes have been measured of the one solid and two liquid methane moderators at IPNS. Attempts to analyze data from the liquid methane F moderator have suggested the need for generalization of the Ikeda-Carpenter function and the inclusion of physical models of parameter wavelength dependence in the fitting process. Results may also indicate the need to include an additional decay constant for an additional moderator eigenvalue other than that of the fundamental mode.

The counting statistics for the F moderator are not of the same quality or as those obtained the H and C moderators. Future work will involve using the experience and lessons learned from analysis of the F data to complete the analysis of the remaining moderators.

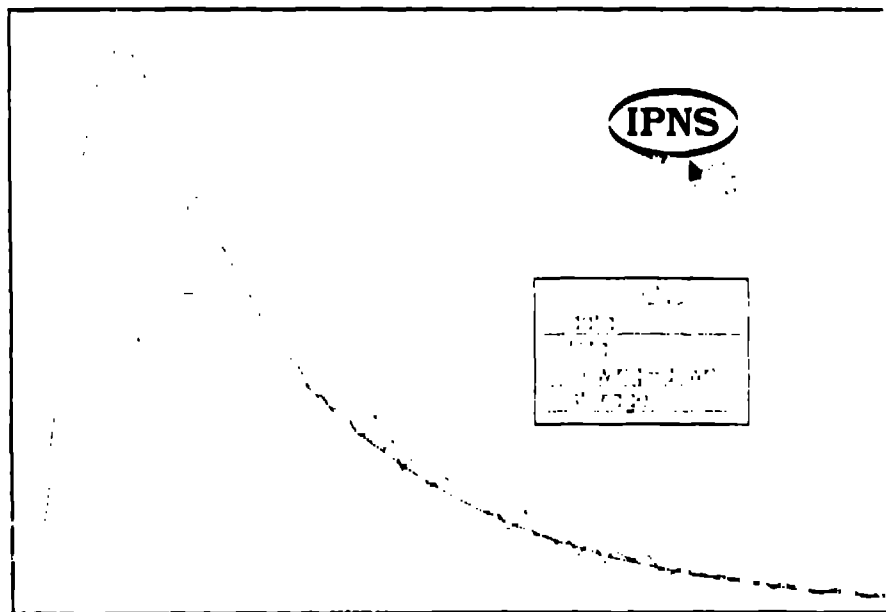


Fig. 7. Ge(3,3,3) reflection for F moderator. The dotted line is calculated by eq. (12) with parameters  $\nu=2.80$ ,  $\Sigma=1.53 \text{ cm}^{-1}$ ,  $B_1=0.042/\mu\text{sec}$ ,  $B_2=0.036/\mu\text{sec}$ ,  $A_1=0.282$ ,  $A_2=0.619$ ,  $A_3=0.099$ . The estimated chi-square value for this fit is 1.802. Parameters for this fit were calculated by simultaneously fitting reflections in the F moderator data (see text). The storage term shown is the sum of two individual storage terms with two decay constants.

#### ACKNOWLEDGMENTS

We thank the many members of the IPNS staff who have provided us with assistance many times during our data collection and analysis phases. Two of us (RLB and REW) express their gratitude to the Argonne Division of Educational Programs for support under the Student and Faculty Research Participation Programs.

**REFERENCES**

1. S. Ikeda and J.M. Carpenter, Nucl. Instr. and Meth. A239(1985) 536.
2. K. F. Graham and J.M. Carpenter, Nucl. Sci. and Eng. 49(1972) 418; Nucl. Instr. and Meth. 85(1970) 165.
3. R.G. Sachs and E. Teller, Phys. Rev. 60(1941) 18.
4. See, for example, M.M.R. Williams, The Slowing Down and Thermalization of Neutrons (North-Holland, Amsterdam, 1966).
5. C.H. Westcott, Chalk River Report Number CRRP-960 and AEC L-1101, 3rd ed. (1969).

## Information content of lineshapes

*R. N. Silver, D. S. Sivia, and R. Pynn*  
Theoretical Division and Los Alamos Neutron Scattering Center  
Los Alamos National Laboratory  
Los Alamos, New Mexico 87545  
U.S.A.

**ABSTRACT:** We examine the question of figures-of-merit for optimizing the lineshapes of neutron scattering sources, instruments and experiments. Using maximum entropy deconvolution of simulated data, we test the effects of various features of lineshapes including intensity, resolution (FWHM), shape, and background. We demonstrate that conventional figures-of-merit are of limited validity, and we suggest that bandwidth is an important criterion for optimization.

### Introduction

An outstanding problem in the development of neutron scattering sources, instruments and experiments is how to establish figures-of-merit (FOM) for optimizing designs. This is central to the wise allocation of the billions of dollars which have been, or are proposed to be, invested in neutron scattering facilities for condensed matter research [1]. Applications [2] would include comparing the relative performances of pulsed spallation and reactor neutron sources, choosing the poisoning of moderators at pulsed sources, making decisions to trade intensity for resolution or noise for signal in the conduct of an experiment, etc. Prior approaches to optimization have been primarily intuitive "seat-of-the-pants" judgments based on empirical experience in neutron scattering research. Although the goal should be to maximize the information gained in neutron scattering experiments, until now there has been little effort to address the problem from an information theory viewpoint. Optimization should consider the statistical problem of data analysis. In the present paper, we begin to remedy this oversight by providing some simulations of the ability to recover information from differing instrument response functions (or lineshapes). We wish to motivate the application of information theory to neutron scattering science and facility design.

Let us consider a one-dimensional neutron scattering experiment in which the data,  $D(x)$ , are a convolution of an instrument response function (or resolution function),  $R(x)$ , with the neutron scattering law,  $S(x)$ . Then

$$D(x) = \int_{-\infty}^{\infty} R(x-x') S(x') dx' + B(x) + \Sigma(x) \quad (1)$$



where  $B(x)$  is the background, and  $\Sigma(x)$  is the noise. The goal of any neutron scattering experiment is to infer the neutron scattering law,  $S(x)$ , from the data,  $D(x)$ .

In a representative neutron scattering experiment, the neutron scattering law,  $S(x)$ , we wish to measure may be as shown in Fig. 1(a). As a first approximation  $R(x)$  is usually assumed to be Gaussian, as the Central Limit Theorem suggests. Traditionally, an experimenter would select the Full Width Half Maximum (FWHM) of  $R(x)$  to be of the same magnitude as the width of the structure expected in  $S(x)$ . The corresponding typical data set,  $D(x)$ , is shown in Fig. 1(b), where there is broadening due to the instrument (of FWHM = 2.5 pixels as shown by the bar), noise governed by Poisson statistics, and background (chosen to be flat and equal to 5% of the peak signal). That is, experiments are typically optimized so that the raw data,  $D(x)$ , resembles a slightly broadened and noisy version of the  $S(x)$  neutron scatterers expect to measure. This "what-you-see-is-what-you-get" philosophy of optimization is based on the widely-held perception that, if the FWHM of  $R(x)$  is very broad, much sharper structure in  $S(x)$  is not recoverable.

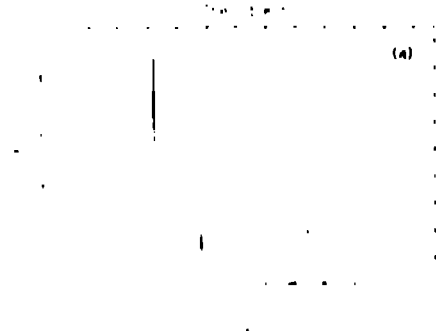


FIG. 1(a) - A representative neutron scattering law,  $S(x)$ , as a function of pixel (or channel) number,  $x$ .

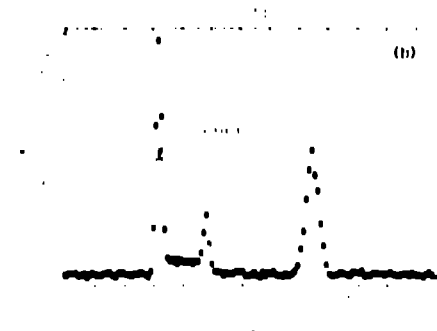


FIG. 1(b) - Typical neutron scattering data,  $D(x)$ , corresponding to the neutron scattering law in Fig. 1(a). The data are broadened by a Gaussian with FWHM of 2.5 pixels as shown, and with noise and 5% background added.

While neutron scattering is in general a Poisson process, in the limit of large numbers we can make an independent Gaussian approximation for  $\Sigma(x)$  in which

$$\Sigma(x) \approx \sigma \quad (2)$$

and

$$\Sigma(x) \Sigma(x') \approx \sigma^2 \delta(x-x') \left[ \int R(x-x') S(x') dx' + R(x) \right] \quad (3)$$

Here  $\langle \rangle$  denotes an average over all such experiments. A common data analysis procedure would be to estimate the parameters of a model for  $S(x)$  by minimizing

$$\chi^2 = \frac{1}{N} \sum_i \Delta x \frac{\left( D(x_i) - \sum_j \Delta x R(x_i - x_j) S(x_j) - B(x_i) \right)^2}{D(x_i)} \quad (4)$$

where we have broken the integral up into pixels of width  $\Delta x$ , and  $N$  is the number of pixels in the range of the experiment. The errors on the parameters would be determined from the variation of  $\chi^2$ .

Another popular perception is that the FOM for the design of spectrometers should be

$$F.O.M. = \frac{\text{Total Intensity}}{FWHM^2} \quad (5)$$

Instruments with the same FOM are supposed to have comparable performance for neutron scattering experiments. This FOM is rigorously correct for the problem of determining the position of a  $\delta$ -function broadened by a Gaussian  $R(x)$  by minimizing  $\chi^2$ . It has been proposed as a more general FOM for the problem of optimizing spectrometers for pulsed neutron sources [3].

We contend that both these popular perceptions are demonstrably false. A counterexample is provided by the Be Filter Difference Spectrometer at LANSCE, where features in  $S(x)$  orders of magnitude sharper than the FWHM have been recovered, using both direct inversion [4] and maximum entropy deconvolution [5], by taking advantage of the sharp leading edge of  $R(x)$ . The present paper generalizes this example to the overall problem of the optimization of neutron scattering experiments.

### Approach

We formulate the problem of inferring  $S(x)$  from  $D(x)$  in terms of Bayes' theorem [6], upon which all data analysis procedures are at least implicitly based. This states that the conditional probability of  $S(x)$  given  $D(x)$  is

$$P[S(x)|D(x)] \propto P[D(x)|S(x)] \times P[S(x)] \quad (6)$$

Here,  $P[D(x)|S(x)]$  is the probability of the measured data for a given scattering law, which is referred to as the *Likelihood* function. In our limit of independent Gaussian statistics, this reduces to the familiar form

$$P[D(x)|S(x)] \Rightarrow \exp \left( -\frac{\chi^2}{2} \right) \quad (7)$$

$P[S(x)]$  represents our state of knowledge about  $S(x)$  (or the lack of it) before we have any data, and it is referred to as the *Prior*. Eq. (6) states that the product of the Likelihood and the Prior is proportional to the *Posterior*, or our state of knowledge after we have measured the data. The best estimate of  $S(x)$  from the data is given by the maximum of the Posterior, and the errors in this estimate are given by its width. The data analysis procedure of parameter estimation by minimizing  $\chi^2$  (i.e. *maximum Likelihood*) is equivalent to maximizing the Posterior if the Prior is taken to be a uniform function of the parameters of the model. A less familiar procedure to neutron scatterers is deconvolution, in which an alternative form for the Prior is chosen. For example, in the maximum entropy method [7] the Prior is taken to be the exponential of the entropy of  $S(x)$  relative to a starting default model.

The present paper describes simulations of the effect of differing instrument responses ( $R(x)$ ,  $B$ ,  $\Sigma(x)$ ), on the ability to infer the scattering law,  $S(x)$ , from the data,  $D(x)$ . Altering the instrument response only alters the Likelihood function and not the Prior, so that our general conclusions will be independent of whether we attempt parameter estimation or deconvolution to infer  $S(x)$ . Similarly, since different deconvolution procedures only alter the Prior, our conclusions are also qualitatively independent of the choice of deconvolution method.

To be specific, we take the test  $S(x)$  (termed the *object*) shown in Fig. 1(a), and we create simulated data resulting from various instrument responses. Although such simulations could be attempted for any physical experiment, in this paper the choice of instrument responses will be limited to what we consider to be typical of neutron scattering spectrometers and sources. Unless otherwise stated, we set the background level at 5% of the peak signal. We perform a maximum entropy (MaxEnt) deconvolution of the data to recover an inferred  $S(x)$  (termed the *image*). Maximum entropy has been shown to be the preferred method for the deconvolution of positive additive distribution functions [7]. The MaxEnt deconvolution procedure will use a flat default model with a stopping criteria of  $\chi^2=1$ . We shall compare the image to the object, and we will exercise our subjective judgement about which images are more faithful to the object.

Our purpose is to be provocative rather than definitive. Therefore, we attempt to keep the argument simple by presuming that the instrument response parameters,  $R(x)$  and  $B(x)$ , are accurately known, although this is often not true in practice. Data analysis procedures exist for the cases where these are imperfectly known including: *calibration experiments* on a known sample,  $S(x)$ , which can be used to infer  $R(x)$ ; *blind deconvolution* which can be used to infer both  $R(x)$  and  $S(x)$ ; and, *two-channel deconvolution* which

can be used to infer  $B(x)$ . In principle a straightforward extension of our approach can include such complications, but we do not attempt that here.

### Simulations

First, it is important to establish some experience with deconvolution. We begin with the ubiquitous Gaussian instrument response function,  $R(x)$ . Figure 2(a) shows typical simulated data when the object of Fig. 1(a) is convoluted with a broad Gaussian  $R(x)$  of FWHM of 25 pixels, which is ten times the broadening of Fig. 1(b) and much broader than the structure in  $S(x)$ . Figure 2(b) shows the MaxEnt images corresponding to the data in Fig. 2(a) (dashed line), with 100 times the counts (solid line), and 10,000 times the counts (dotted line). Figure 2 demonstrates that deconvolution can resolve peaks which are not evident in the raw data, and that increasing statistical accuracy can improve the resolution of the image.

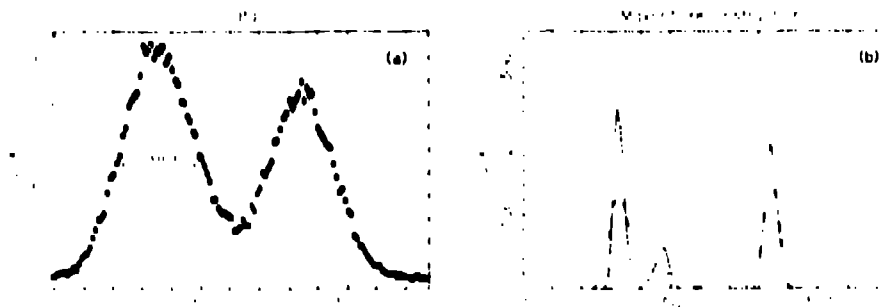
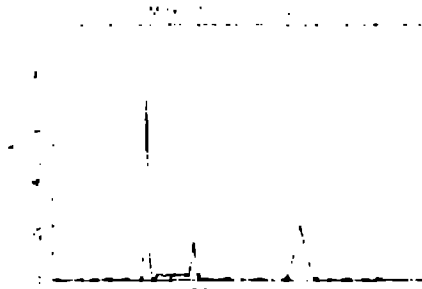


FIG. 2(a) - Gaussian broadened data with FWHM = 25 pixels, for the  $S(x)$  of Fig. 1(a).

FIG. 2(b) - Images of  $S(x)$  calculated by maximum entropy (MaxEnt) deconvolution of the data in Fig. 2(a) (dashed line), with 100 times the counts (solid line), and with 10,000 times the counts (dotted line).

Figure 3 shows images for the narrow Gaussian (FWHM of 2.5 pixels) broadening obtained by deconvoluting the data in Fig. 1(b) (solid line), and for the same experiment with 100 times the counts (dotted line). The sharp peaks on the left of the object are more highly resolved in the image with better statistical accuracy. The intrinsically broad peak on the right is unchanged. Figure 3 demonstrates that, even with a sharp  $R(x)$ , deconvolution can be useful because it can determine whether a peak is narrower than the instrument broadening.

FIG. 3 - MaxEnt images of  $S(x)$  for the narrow Gaussian broadened data in Fig. 1(a) (solid line), and with 100 times the counts (dashed line).



Moreover, Fig. 3 should be compared with Fig 2(b), which are the images created using data from the broad Gaussian  $R(x)$ . According to the popular FOM, Eq. (5), the solid line in Fig. 2(b) should be comparable to Fig. 3, and the dotted line should be much sharper. In fact, even with 10,000 times the peak intensity, a ten times broader Gaussian  $R(x)$  produces poorer images than the narrow Gaussian. This provides our first counterexample to this FOM.

Next we consider an  $R(x)$  constructed by convoluting the narrow Gaussian (of FWHM = 2.5 pixels) with a wide exponential of  $1/\tau = 1/15$  pixels with identical peak intensity to Fig. 1(b). This lineshape is common to the *unpoisoned* moderators of pulsed neutron sources. This  $R(x)$  is shown (solid line) in Fig. 4(a). Our initial expectation may be that the quality of the image would be severely degraded. The simulated data shown in Fig. 4(b) (pluses) do not resemble the object. Nevertheless, the quality of the image shown in Fig. 4(c) obtained by deconvolution (solid line) is almost equal to that obtained with the narrow Gaussian, shown as the solid line in Fig. 2 (note the change in vertical scale). We conclude that the correct FOM may not be very sensitive to the FWHM of  $R(x)$ , which also contradicts Eq. (5).

Figure 4 also shows a simulation analogous to the poisoning of moderators for pulsed neutron sources. Figure 4(a) shows a *poisoned*  $R(x)$  (dashed line) constructed by convoluting a narrower exponential of  $1/\tau = 1/2$  pixels with the same narrow Gaussian. Both the poisoned and unpoisoned  $R(x)$  have the same peak intensities, although in practice there would be some decrease in peak intensity with poisoning. In the conventional neutron scatterer's view, poisoning moderators has the desirable effect of making the data much more closely resemble the object, as shown in Fig. 4(b) (dots), and therefore improving the apparent resolution. Fig. 4(c) shows the corresponding image (dashed line). Both the poisoned and unpoisoned moderators in fact have almost identical resolving power. Poisoning moderators is questionable from an information content viewpoint! Moreover, if the object being measured is broader than the FWHM of  $R(x)$ , neutrons are lost by poisoning.

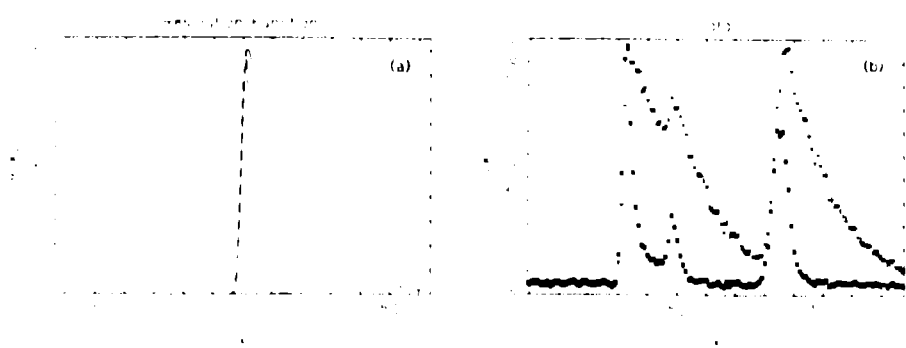


FIG. 4 - (a) Instrument response functions,  $R(x)$ , for a narrow Gaussian convoluted with a broad exponential (solid) and a narrow exponential (dashed); (b) corresponding data,  $D(x)$ , for broad (pluses) and narrow (dots)  $R(x)$ ; (c) corresponding MaxEnt images of the neutron scattering law,  $S(x)$ , for broad (solid) and narrow (dashed)  $R(x)$ .

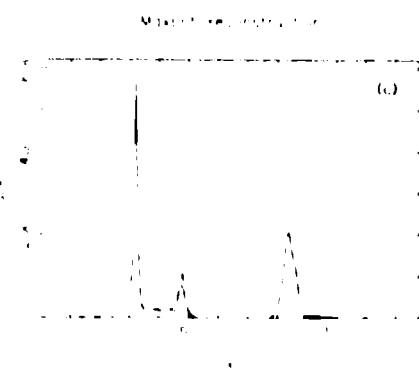
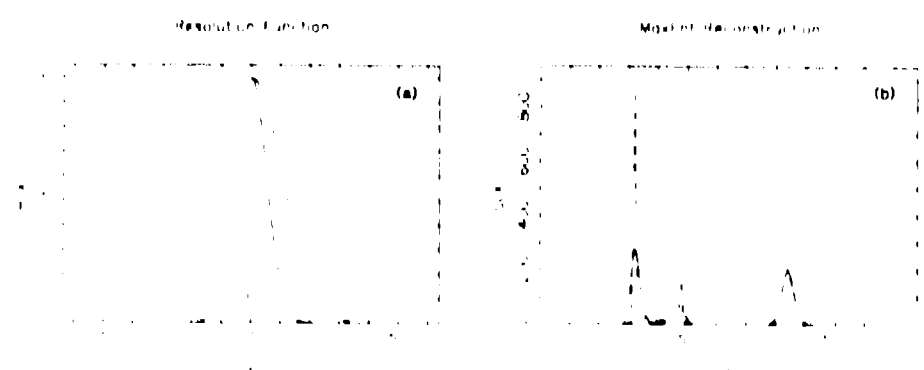


FIG. 5(a) - Two instrument response functions,  $R(x)$ , with the same figure-of-merit according to Eq. (5). The solid line is a Gaussian, and the dashed line is a half-Gaussian with the same FWHM.

FIG. 5(b) - MaxEnt images of  $S(x)$  for the two  $R(x)$  in Fig. 5(a). Solid line corresponds to the Gaussian  $R(x)$ , and the dashed line to the half-Gaussian  $R(x)$ .



The insensitivity of the FOM to the FWHM is further illustrated in Fig. 5. Figure 5(a) shows two different  $R(x)$  with identical FWHM and total intensity, and therefore identical FOM according to Eq. (5). One is a Gaussian (solid line) and the other is a half Gaussian (dashed line). Figure 5(b) shows the corresponding MaxEnt images. It is clear that the half Gaussian  $R(x)$  has much better resolving power.

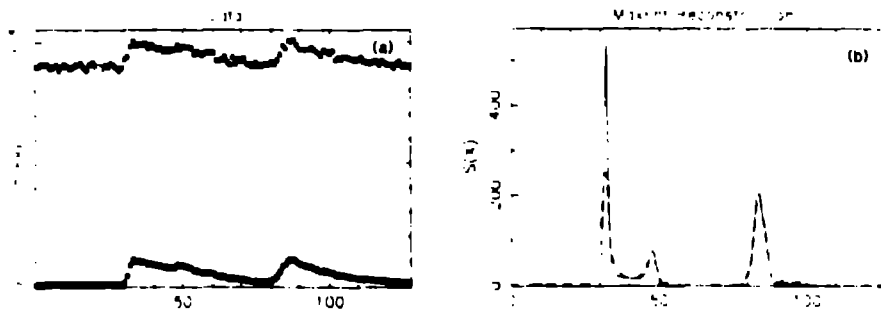


FIG. 6(a) - Study of the effect of background level, using the  $R(x)$  in Fig. 4(a). The bottom data (stars) is with the usual 5% background. The top data (dots) has much higher background with the same signal.

FIG. 6(b) - MaxEnt images of  $S(x)$  for the two  $D(x)$  in Fig. 6(a). Solid line corresponds to the low background data, and the dashed line to the high background data.

Finally, Fig. 6 illustrates that background is also important to the correct FOM for experiment optimization. We consider the same  $R(x)$  as the solid line in Fig. 4(a), but with two different levels of background. The data are shown in Fig. 6(a) and the corresponding MaxEnt images are shown in Fig. 6(b). Higher background degrades the ability to recover information from the experiment, as expected.

### Analysis

It should be clear from these simulations that the figure-of-merit is a much more complex object than suggested in Eq. (5). In particular, the sharpness of the structure in  $R(x)$  appears to be far more important than the FWHM.

An argument to support this observation may be most easily developed by considering the direct inversion of the data by Fourier transform. We define the transform by

$$R(k) = \int_{-\infty}^{\infty} e^{ikx} R(x) dx \quad (8)$$

Then the image,  $S_I(x)$ , formed by direct inversion is given by

$$S_I(x) = \int \frac{dk}{2\pi} e^{-ikx} \left[ \frac{D(k) - B(k)}{R(k)} \right] \quad (9)$$

Such an inversion would satisfy  $\chi^2 = 0$ . If we average over all such experiments in the same sense as Eq. (2) and (3), we find that the expectation value of the image is given by

$$\langle S_I(x) \rangle = S(x) \quad (10)$$

as desired. However, this inversion is poorly conditioned because of the noise term,  $\Sigma(x)$ , in Eq. (1). Using Eq. (3), the variance of the image is given by

$$\langle \delta S_I(x) \delta S_I(x) \rangle = \int \frac{dk}{2\pi} \int \frac{dk'}{2\pi} \frac{e^{-i(k+k')x}}{R(k)R(k')} D_o(k+k') \quad (11)$$

where

$$D_o(k) = R(k) S(k) + B(k) \quad (12)$$

Since  $R(k)$  goes toward zero for  $k$ 's larger than some critical value, call it  $k_c$ , direct inversion amplifies the noise and the variance is divergent. The image for any particular experiment would appear to be noisy.

The solution of this problem is to condition the inversion by asking instead for a broadened image. This can be crudely done by cutting off the limits on the integrals in Eq. (9) and Eq. (11) at some critical value, say  $k_c$ . The image for any particular experiment would have the noise suppressed at the expense of a broadened image; that is, the variance would be well behaved.

The  $k_c$  may be chosen such that  $\chi^2 = 1$  for the image. It determines the achievable resolution by

$$\Delta x \approx \frac{2\pi}{k_c} \quad (13)$$

Sharp features in  $R(x)$  produce high Fourier components of  $R(k)$  which makes  $k_c$  large. A broad  $R(x)$  lacks high Fourier components and so  $k_c$  must be small. Figure 7 shows the  $R(k)$  of the resolution functions shown in Fig. 5(a). The full Gaussian does not have high Fourier components at large  $k$  while the half Gaussian has large Fourier components at high  $k$ . The corresponding MaxEnt images are shown in Fig. 5(b). The resolution of an experiment primarily depends on the Fourier spectrum of the instrument response function.



FIG. 7 - Fourier transforms of the instrument response functions,  $R(x)$ , for the Gaussian (solid line) and the half-Gaussian (dashed line) shown in Fig. 5(a).



### Conclusions

We have provided counterexamples to several of the popular perceptions in the neutron scattering community regarding the relation between the instrument response function and the resolution of an experiment. We have shown that the figure-of-merit of an instrument response function strongly depends on its Fourier spectrum, in addition to other more traditional variables such as intensity, background, etc. Our Bayes' theorem argument suggests that this qualitative conclusion will remain valid regardless of whether deconvolution or parameter estimation is used to infer the neutron scattering law from the data. It will also remain true regardless of the specific choice of deconvolution procedure or fitting model.

We have not proposed a specific new figure-of-merit to replace Eq. (5). However, we suggest that the ultimate answer may have much in common with the theory of communication. The characteristic Fourier variable,  $k_c$ , which governs the resolution of an experiment, is analogous to the *bandwidth* of a signal processing circuit. In this sense, the design of neutron scattering experiments is related to the theory of communication [8], in which the capacity of a channel to transmit information is proportional to the bandwidth. Neutron scatterers should adapt the extensive knowledge and experience in information theory to the design of neutron scattering experiments and sources. A statistical theory for spectrometer optimization will be published elsewhere [9].

### Acknowledgements

We thank R. Robinson for helpful discussions. This research was supported by the Office of Basic Energy Sciences of the U.S. Department of Energy.

### References

- [1] W. Seitz, D. Eastman, eds., *Major Facilities for Materials Research and Related Disciplines*, National Academy Press, Washington, D.C., 1984
- [2] G. H. Lander, V. J. Emery, eds., *Scientific Opportunities with Advanced Facilities for Neutron Scattering*, Shelter Island Workshop, Octo-

ber, 1984, Argonne National Laboratory CONF-8410256; see also prior proceedings of the *International Collaboration on Advanced Neutron Sources* (ICANS).

- [3] A. Michaudon, *Reactor Science and Technology* (Journal of Nuclear Energy Parts A/B), 17, 165-186 (1963); D. H. Day, R. N. Sinclair, *Nuclear Inst. Meth.* 72, 237-253 (1969); C. Windsor, *Pulsed Neutron Scattering*, Taylor & Francis, Ltd., London, 1981, p. 104ff
- [4] P. Vorderwisch, F. Mezei, J. Eckert, J. Goldstone, *Inst. Phys. Conf.* 81, 161-168 (1986)
- [5] D. Sivia, P. Vorderwisch, R. N. Silver, to be published; D. S. Sivia, this volume
- [6] H. Jeffreys, *Theory of Probability*, Cambridge University Press, 1939
- [7] S. F. Gull, J. Skilling, *IEE Proc.*, 131E, 646 (1984); D. S. Sivia, *ibid.*
- [8] C. E. Shannon, *Bell Systems Tech. J.*, 27, 379-423, 623-656 (1948)
- [9] R. N. Silver, D. S. Sivia, R. Pynn, to be published

## The performance of maximum entropy methods in spectral deconvolution

*M. W. Johnson and J. Lister*  
Rutherford-Appleton Laboratory  
Chilton, Didcot, Oxon OX11, 0QX  
UNITED KINGDOM

### Introduction

There have been a number of previous demonstrations of the use of the Maximum Entropy principle (MaxEnt) in the deconvolution of experimental spectra [1-3]. However, as far as we know, there have been no previous discussions of the problems that arise in applying MaxEnt methods in practice. When deconvoluting a known, model spectrum it is straightforward to show, by means of an R-factor, that you have reached good agreement with the intrinsic spectrum. When deconvoluting real data the experimentalist derives a result, but then does not know how much credence to place on the result. The question 'what are the error bars' is not appropriate since the errors on a deconvoluted spectrum are not uncorrelated, but the spirit of the question is valid. This paper addresses itself to that problem.

Our approach is purely pragmatic. In the first section we show the results of deconvoluting a Gaussian line shape from three different intrinsic line shapes. This demonstrates not only the quality of the deconvoluted spectrum that may be obtained, but also how the final R-factor varies as a function of the Gaussian width.

In the second section the procedure is repeated for doublet intrinsic peaks, and the criteria for separation established.

In the third section we demonstrate that line shapes other than Gaussian may be removed from broadened spectra and examine the effects of uncertainties in our knowledge of the broadening function.

Finally we demonstrate the use of MaxEnt on a real problem where the technique has been used to substantially improve the resolution of an inelastic spectrometer.

#### THE DECONVOLUTION OF GAUSSIAN LINE SHAPES

In all the computer experiments described below the following procedure and definitions were used.

An intrinsic spectrum is defined, corresponding to the result that would be measured by an instrument with perfect resolution and no statistical error. This intrinsic spectrum is broadened by the resolution function and noise (with Poisson statistics) is added to produce the observed spectrum. The METRIC [4] MaxEnt method is then used to deconvolute the observed spectrum using the broadening function to yield the deconvoluted spectrum. Clearly the broadening function should be identical to the resolution function, if the deconvoluted spectrum is to agree with the intrinsic spectrum.

The first computer deconvolutions were conducted to enable users of the method on real data to estimate the likely difference between the deconvoluted spectrum and the (unknown) intrinsic spectrum. In these experiments three different intrinsic spectra were used :

$$\text{GAUSSIAN } y = (1/\sigma\sqrt{2\pi}) e^{-x^2/2\sigma^2} + b$$

$$\text{CAUCHY } y = (1 + x^2/\lambda^2)/\pi\lambda + b$$

$$\text{GAMMA } y = u^3 x^2 e^{-ux/2} + b$$

Each were calculated over a time base from 0 to 1600  $\mu$ s using channels of width 8  $\mu$ s.

The tests were carried out with varying values for the background level (b) and different values for  $\sigma$ , the standard deviation of the Gaussian resolution function which was used to broaden the intrinsic spectra.

Figures 1, 2 and 3 (A-C) show sample results for each of the three types of intrinsic spectra with the following parameters

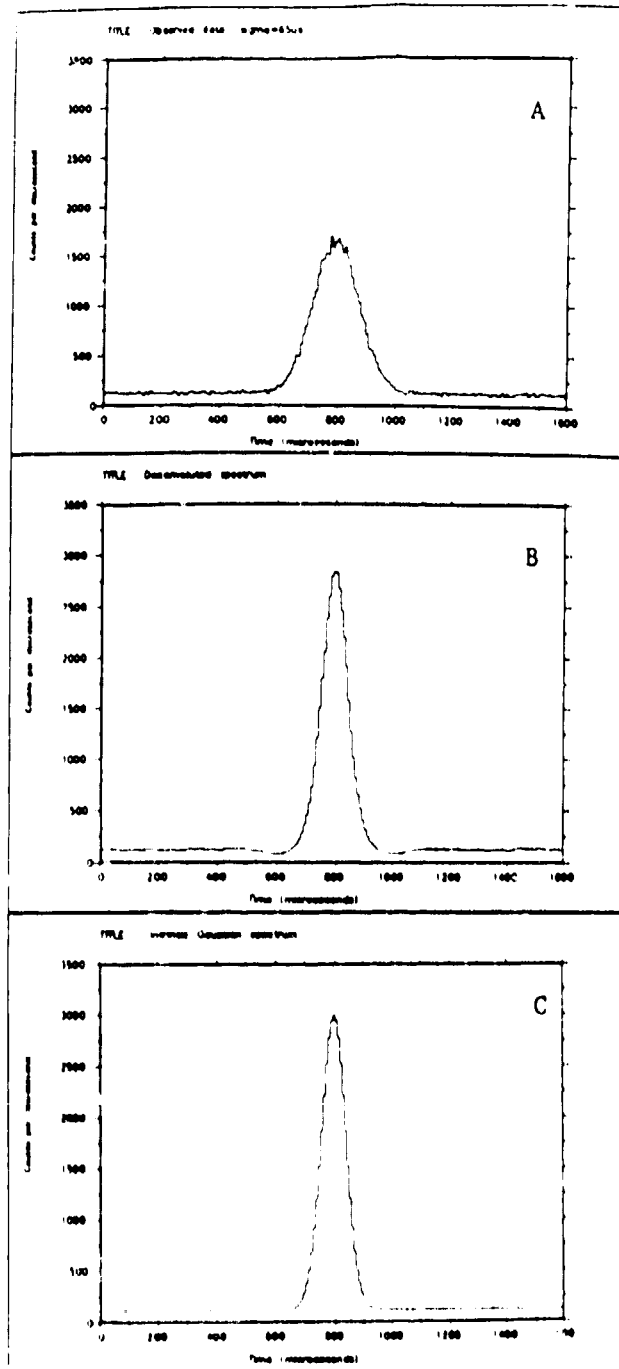


Figure 1

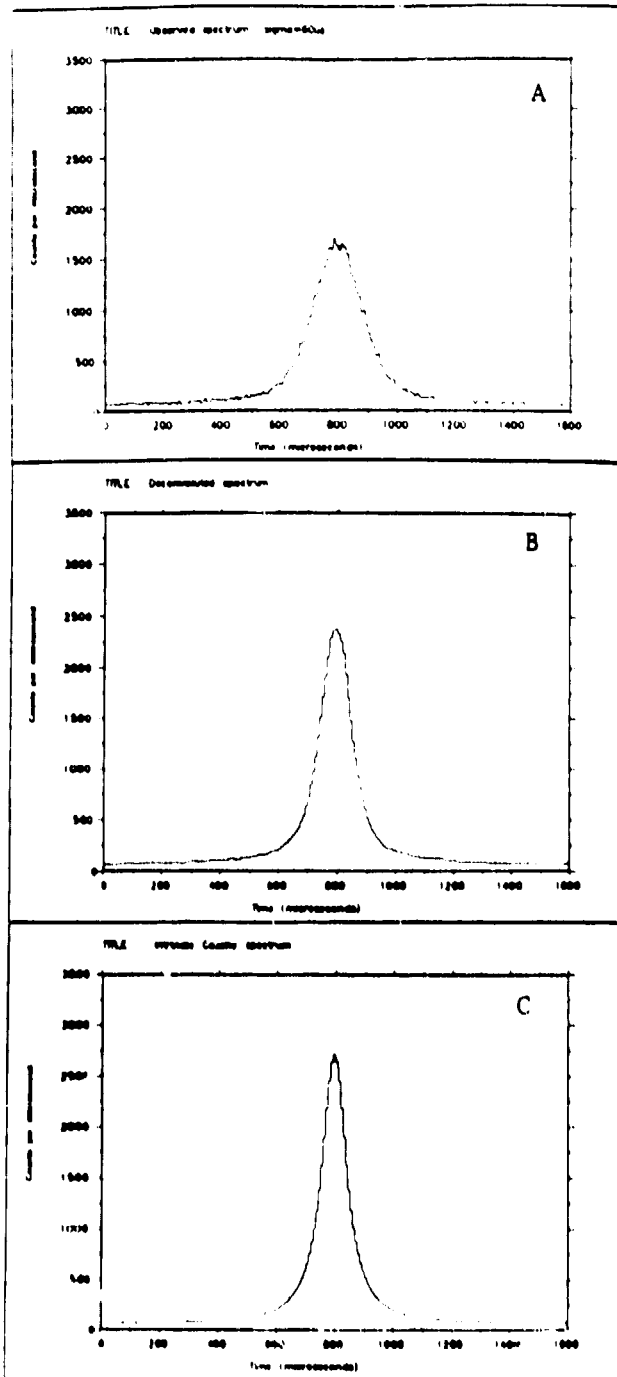


Figure 2

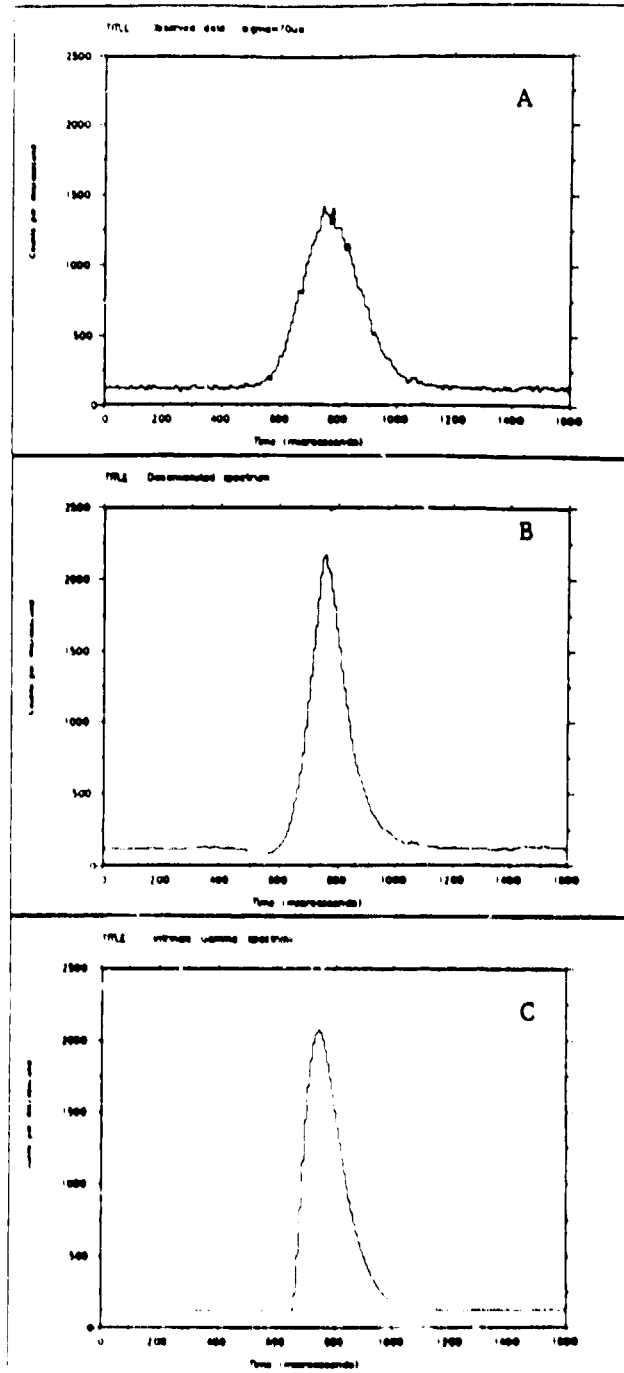


Figure 3

	<u>Intrinsic</u>	<u>FWHM (μs)</u> <u>intrinsic</u>	<u>σ<sub>r</sub></u> <u>(μs)</u>	<u>Background</u>
Figure 1	Gaussian	100	65	0.4
2	Cauchy	100	60	0.2
3	Gamma	140	70	0.4

The background is expressed as an area fraction of the total area.

In these figures A is the observed spectrum, B is the deconvoluted spectrum and C the intrinsic spectrum.

Defining the R-factor as :

$$R^2 = \frac{\sum (d_i - i_i)^2}{\sum i_i^2}$$

where  $d_i$  is the deconvoluted spectrum

$i_i$  is the intrinsic spectrum

We may plot R as a function of  $\sigma_r/\text{FWHM}_{\text{obs}}$ , assuming  $\sigma_r/\text{FWHM}_{\text{obs}}$  to be a measure of the 'difficulty' of the deconvolution. This is done in Figures 4, 5 and 6. It will be seen from these plots that :

- (a) The results are largely independent of the background level.
- (b) There is a general similarity between the R-factors when deconvoluting all peak shapes - especially those of Cauchy and Gamma distributions.
- (c) If the deconvolution problem lies in the range  $0 < \sigma_r/\text{FWHM}_{\text{obs}} < 0.2$  the final R-factor will be  $< 50$ .



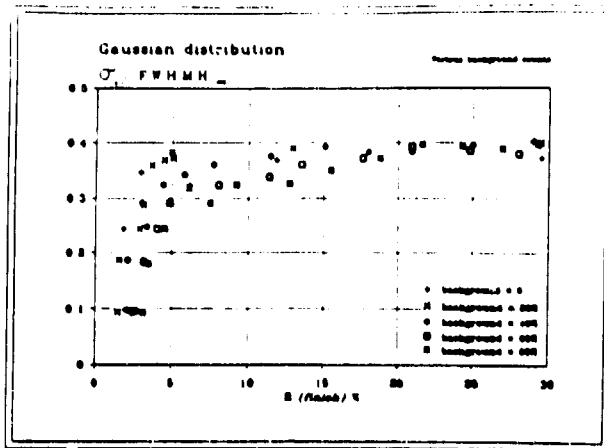


Figure 4

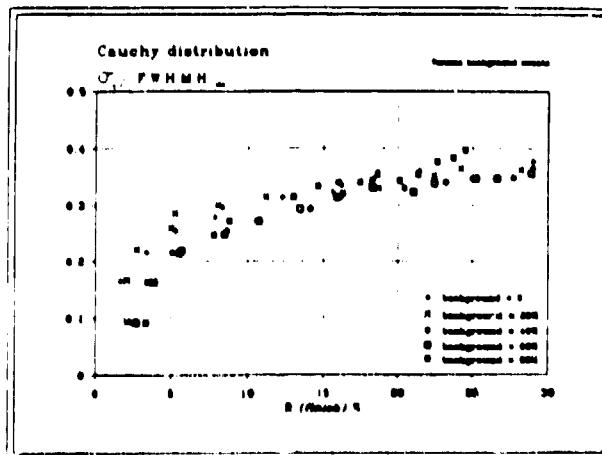


Figure 5

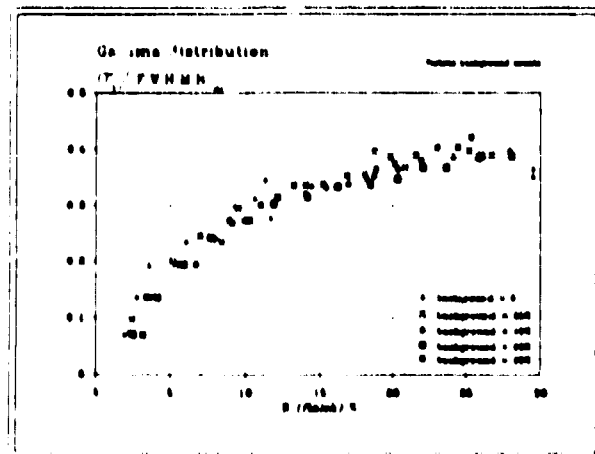


Figure 6

These results are useful in giving us confidence when deconvoluting peaks in this region. It also demonstrates that the method becomes unstable for  $\sigma_r/\text{FWHM}_{\text{obs}}$  ratios greater than 0.30 when the resolution function is Gaussian.

## 2. DOUBLET INTRINSIC PEAK SHAPES

The second series of tests used two peaks with a background count at a constant 20% of the total count, with  $\sigma_r$  in the range 10-80  $\mu\text{s}$ , and the separation between the peaks in the range 80-300  $\mu\text{s}$ .

Figures 7, 8 and 9 (A-C) show sample results for the following parameters :

<u>Figure</u>	<u>i</u>	<u>FWHM<sub>i</sub></u> <u>(<math>\mu\text{s}</math>)</u>	<u><math>\sigma_r</math></u> <u>(<math>\mu\text{s}</math>)</u>	<u>Separation</u> <u>(<math>\mu\text{s}</math>)</u>
7	Gaussian	100	60	132
8	Cauchy	100	60	165
9	Gamma	140	60	148

The R-factor results for the double peak deconvolutions are shown in Figures 10, 11 and 12. This shows the R-factor versus the peak separation for various values of  $\sigma_r$ . The results to the left of the vertical line on each Figure are those for which the two peaks are not resolved.

Again it becomes clear that there is a broad agreement of the region where separation will occur and the R-factors exhibit predictable, systematic variations which should be useful in indicating the likely results to be obtained when deconvoluting true experimental data.

## 3. NON GAUSSIAN RESOLUTION FUNCTIONS

In all the preceding experiments the resolution function has been Gaussian.

Figures 13-17 (A-D) show sample plots of results obtained using single and double peak intrinsic Gaussian

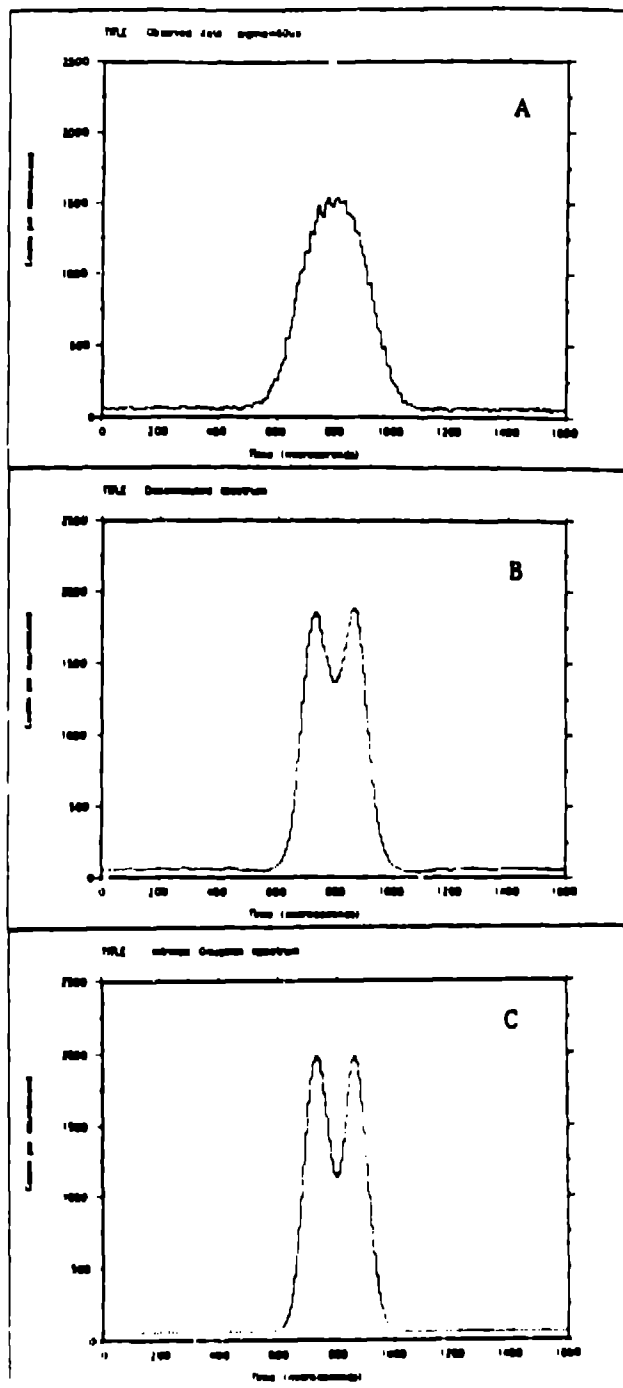


Figure 7

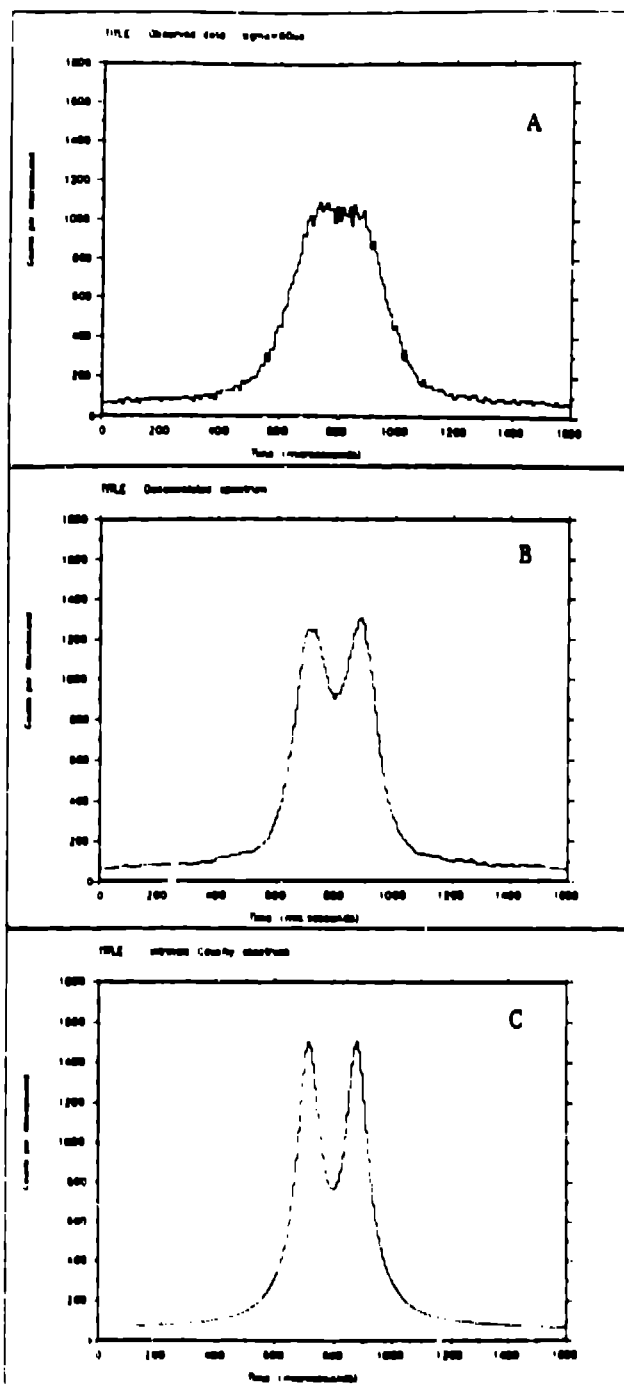


Figure 8

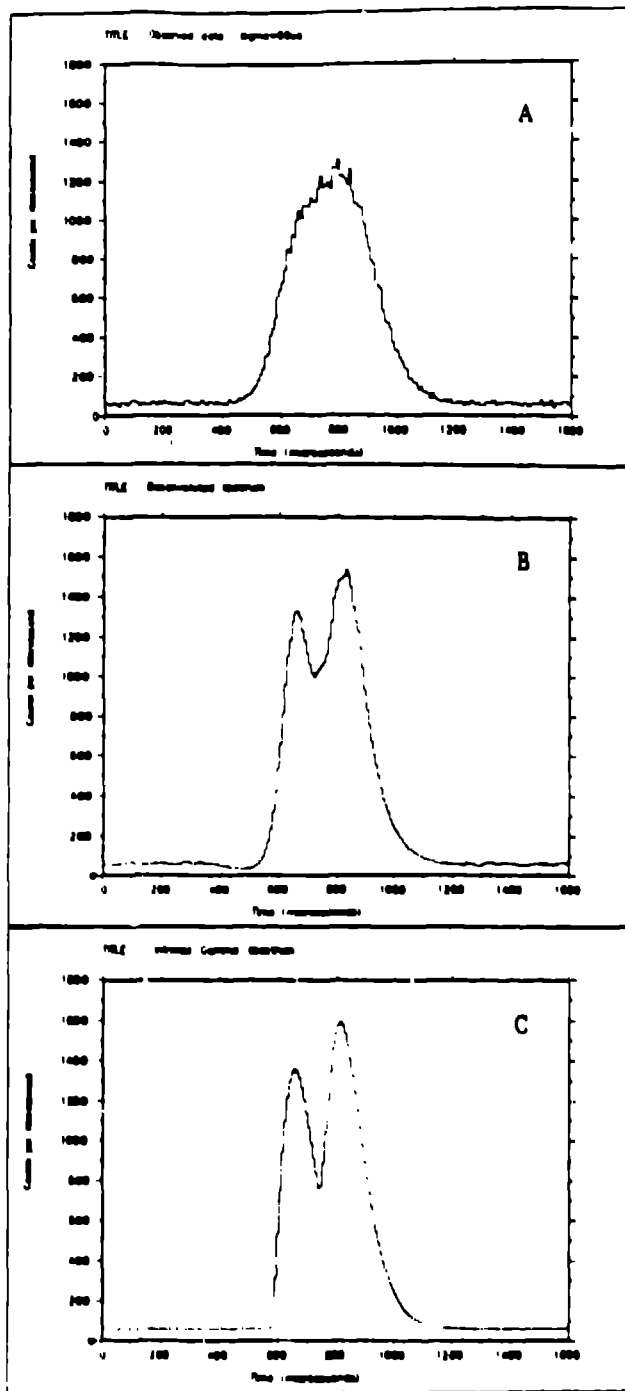


Figure 9

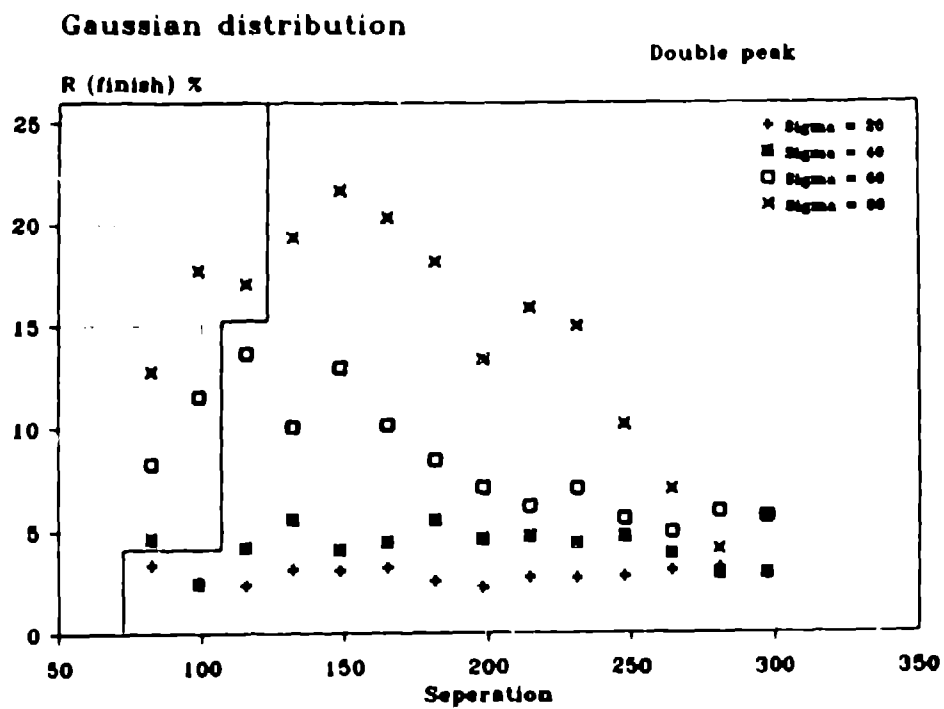


Figure 10

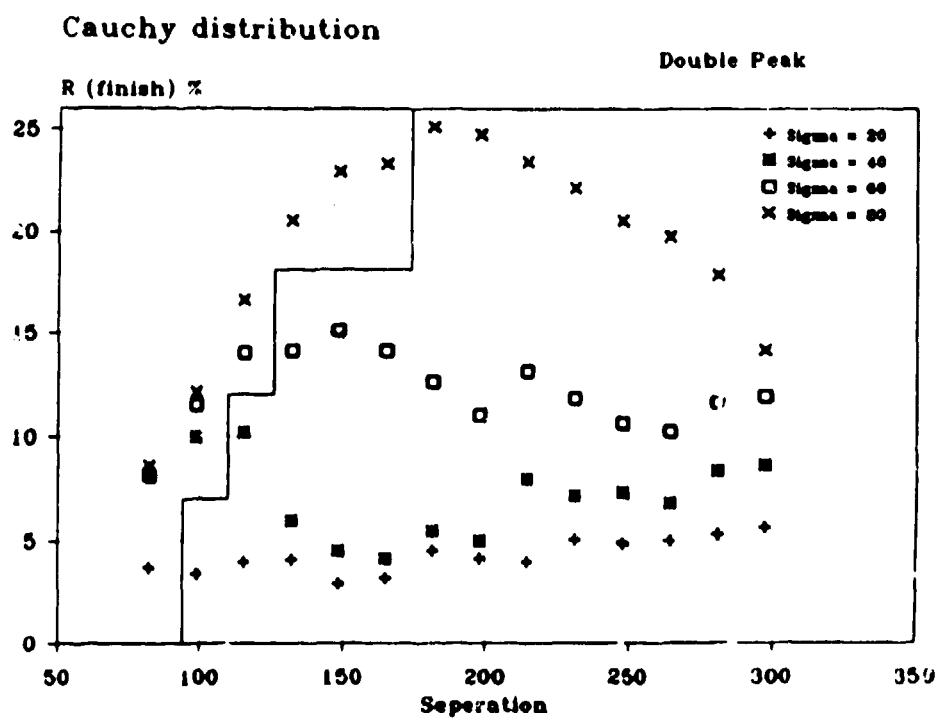


Figure 11

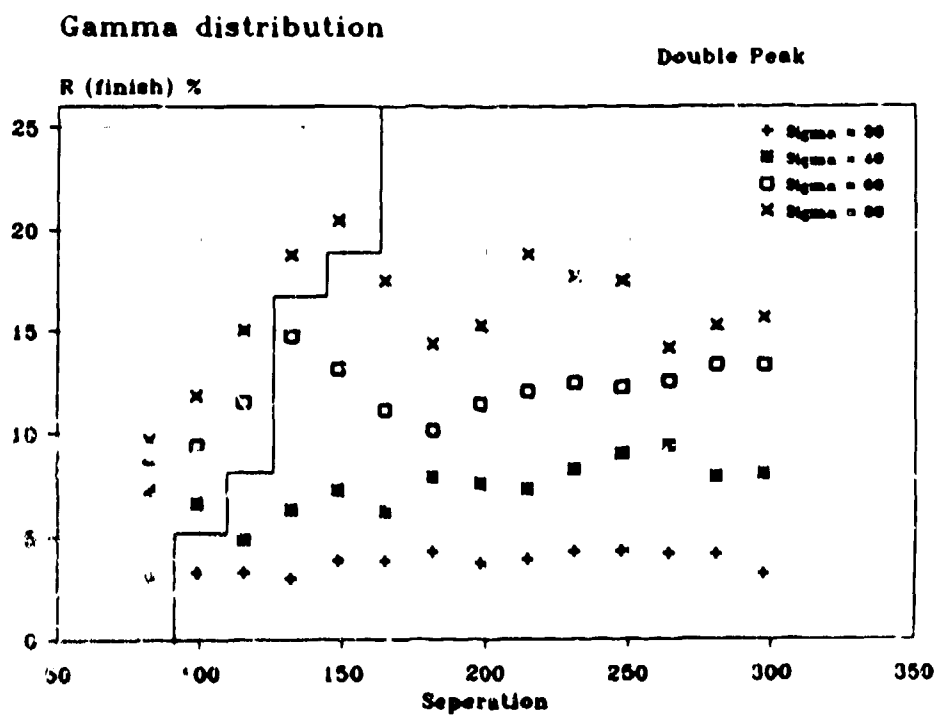


Figure 12



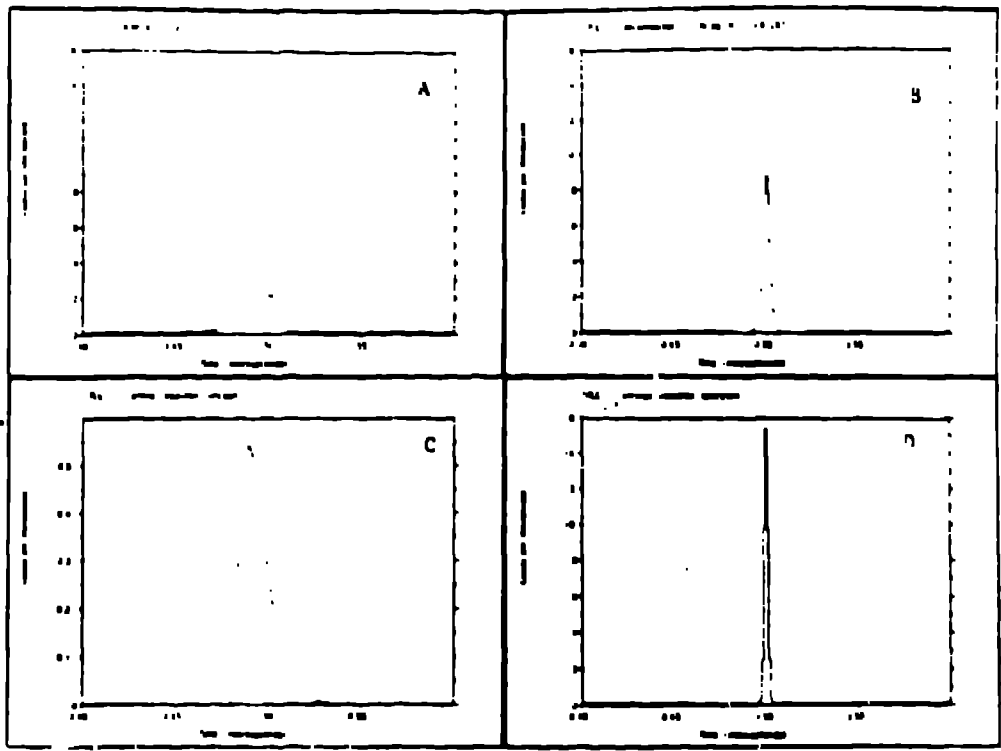


Figure 13

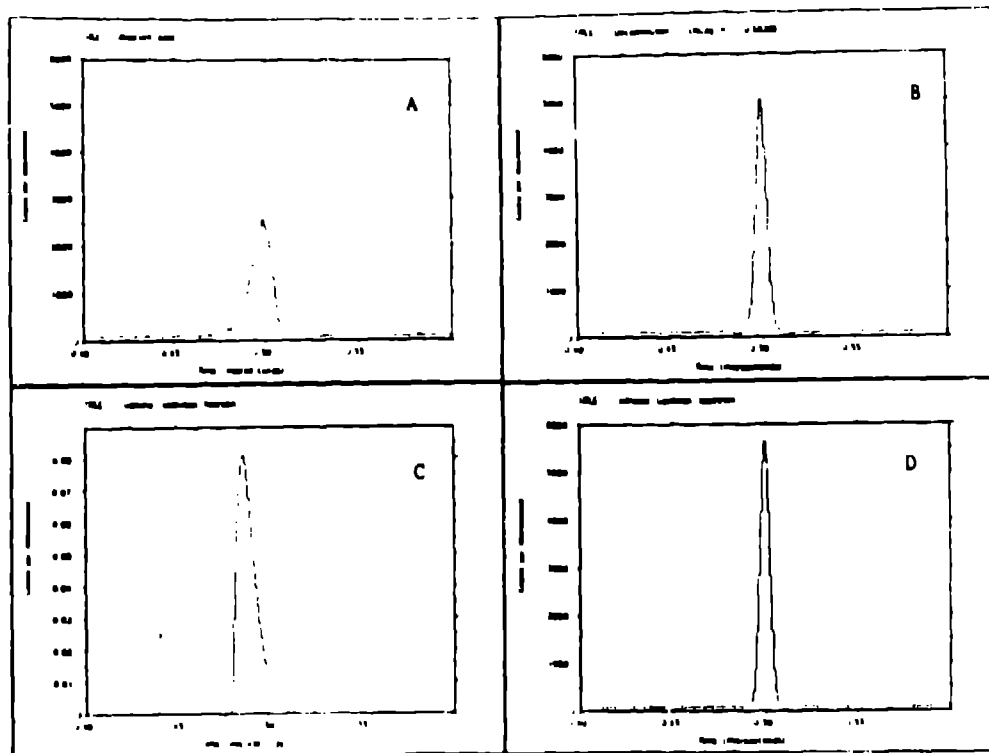


Figure 14

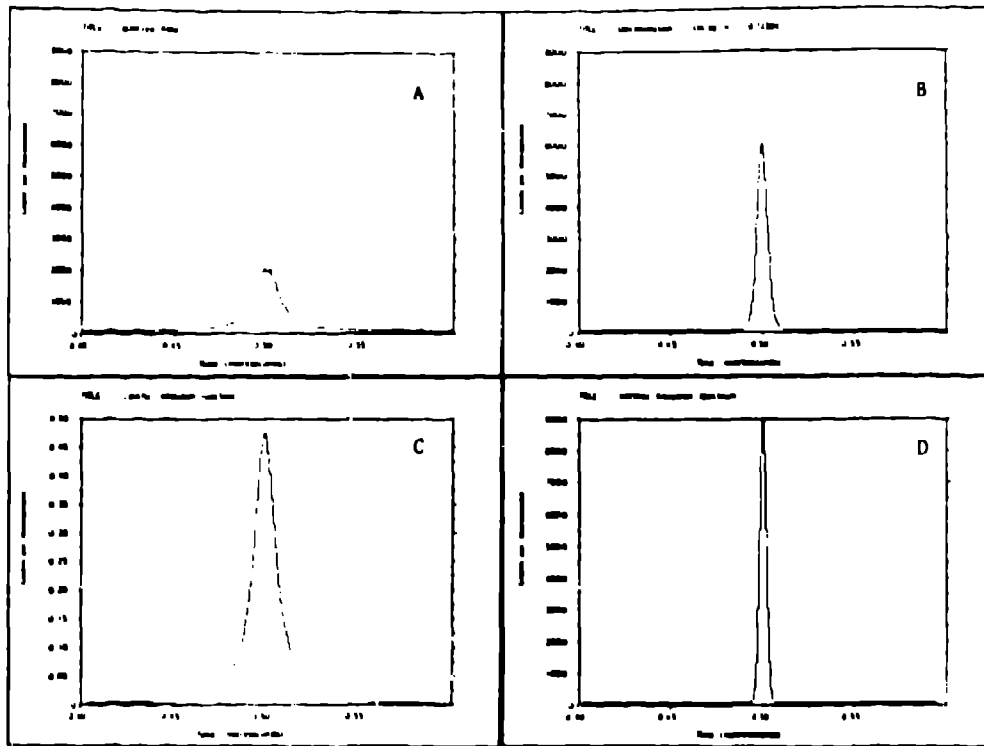


Figure 15

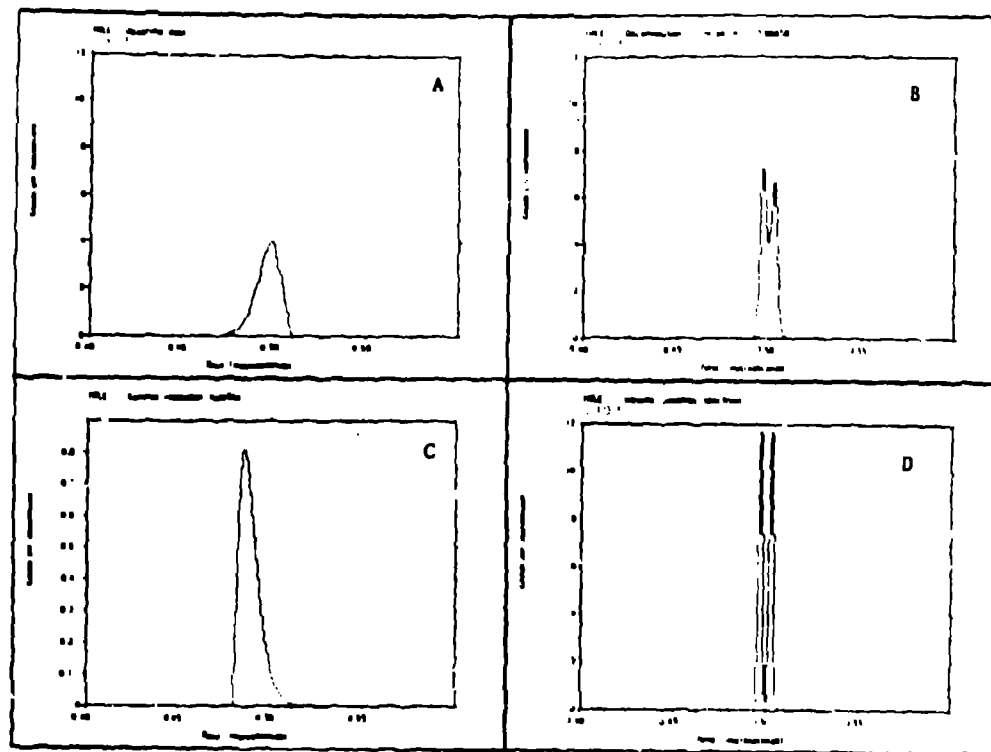


Figure 16

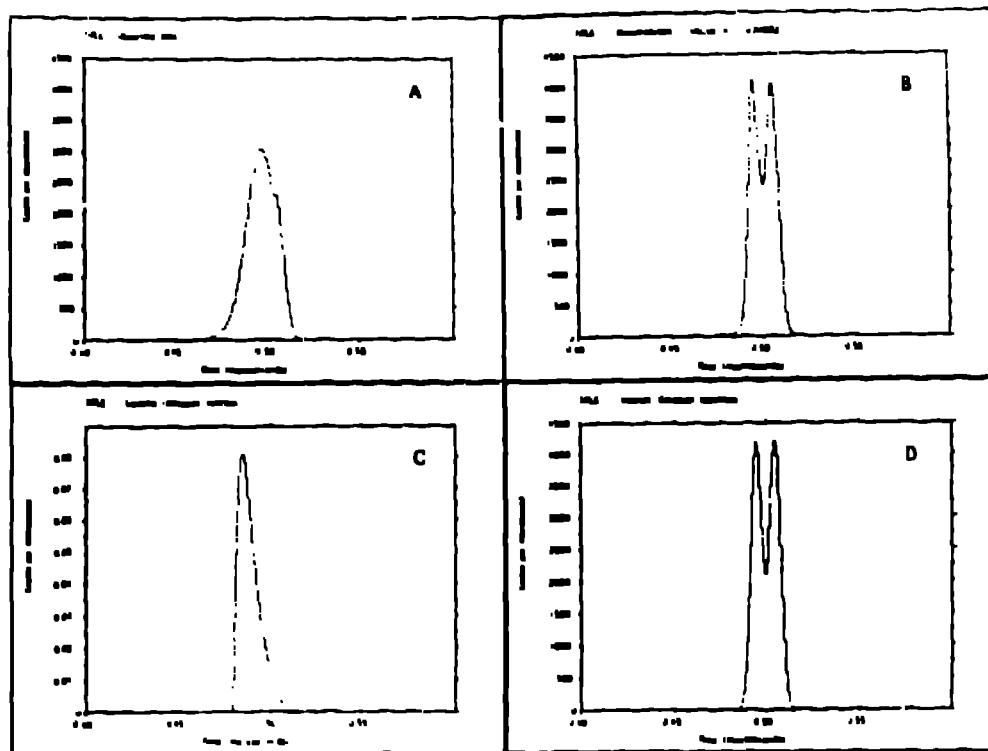


Figure 17

TABLE 1

Intrinsic : Gaussian  
 FWHM<sub>i</sub> : 9.4  
 Resolution : Gamma  
 FWHM<sub>r</sub> : 11.0  
 Background : 0.0

<u>Broadening</u> <u>FWHM</u>	$\chi^2$	<u>Iterations</u>	<u>Solution</u>
15.0	708	600	x
14.0	402	600	x
13.0	230	700	x
12.0	< 1	900	√
11.0*	< 1	500	√
10.0	< 1	500	√
9.0	< 1	400	√

TABLE 2

Intrinsic : Gaussian  
 FWHM<sub>i</sub> : 5.9  
 Resolution : Gamma  
 FWHM<sub>R</sub> : 11.0  
 Background : 0.33

<u>Broadening</u> <u>FWHM</u>	$\chi^2$	<u>Iterations</u>	<u>Solution</u>
15.0	8.4	20,000	x
14.0	4.3	20,000	x
13.0	< 1	1,800	√
12.0	< 1	1,000	√
11.0*	< 1	700	√
10.0	< 1	600	√
9.0	< 1	400	√

**TABLE 3**

Intrinsic : Gaussian Doublet  
 FWHM<sub>i</sub> : 7.1  
 Separation : 10.0  
 Resolution : Gamma  
 FWHM<sub>R</sub> : 11.0  
 Background : 0.0

<u>Broadening</u> <u>FWHM</u>	$\chi^2$	<u>Iterations</u>	<u>Solution</u>
14.0	5.2	20,000	x
13.0	1.6	20,000	x
12.0	< 1	1,700	✓
11.0	< 1	1,300	✓
10.0	< 1	1,000	✓
9.0	< 1	800	✓
9.0	< 1	800	✓



The  $\chi^2$  rapidly diverges as the broadening FWHM is increased beyond the 'true' value. In fact it is possible that, in the absence of any other information, this behaviour could be used to try to judge the width of the broadening function.

#### 5. TEST ON EXPERIMENTAL DATA

So far all the results discussed in this paper have been for computer simulated spectra. As a test of the method the algorithm was applied to data recorded on the IRIS spectrometer at the ISIS facility. The raw data is shown in Figure 18, and was obtained from a sample of 4-methyl pyridine. If the  $\text{CH}_3$  group in this molecule were a free rotator the spectrum would consist of a single line, broadened by the instrumental resolution.

In fact three peaks are easily seen and the deconvolution of the observed data (Figure 19) by a Gaussian broadening function ( $\sigma_b = 0.0064 \text{ meV}$ ) suggests that a fourth peak is in fact present as a shoulder to the central peak. This is agreement with the presence of four molecules in the unit cell.

#### 6. CONCLUSION

In this paper we have explored some of the issues that will have to be resolved if the MaxEnt method is to become a standard data analysis tool. The central problem hinges on the confidence levels to be assigned to the result, either when the broadening function is known precisely or when there may be some systematic error in its assumed value.

Since these confidence limits cannot be determined analytically the only method at present available is the empirical one. If one is deconvoluting a particular experimental spectrum the result can be used as the starting point of a series of computer experiments to determine the stability of the solution to a number of random or systematic errors.

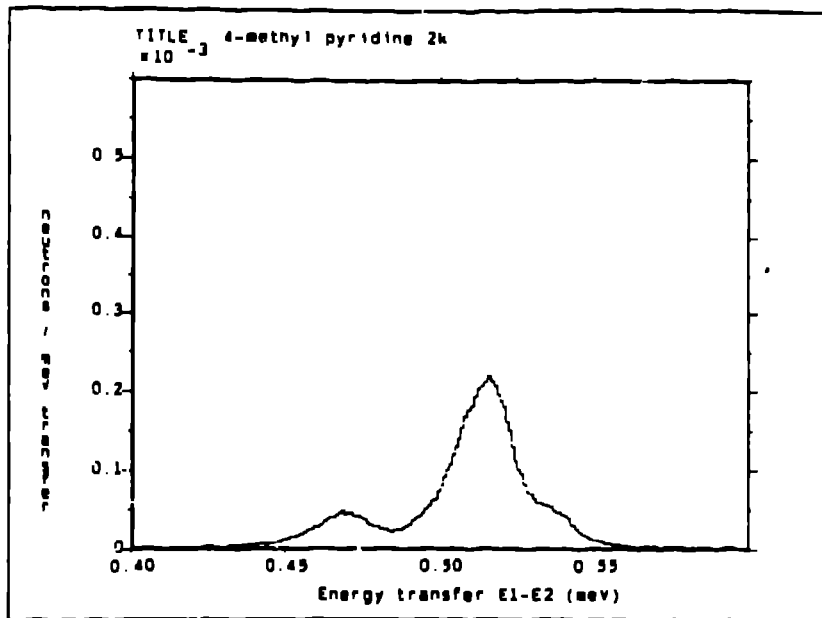


Figure 18

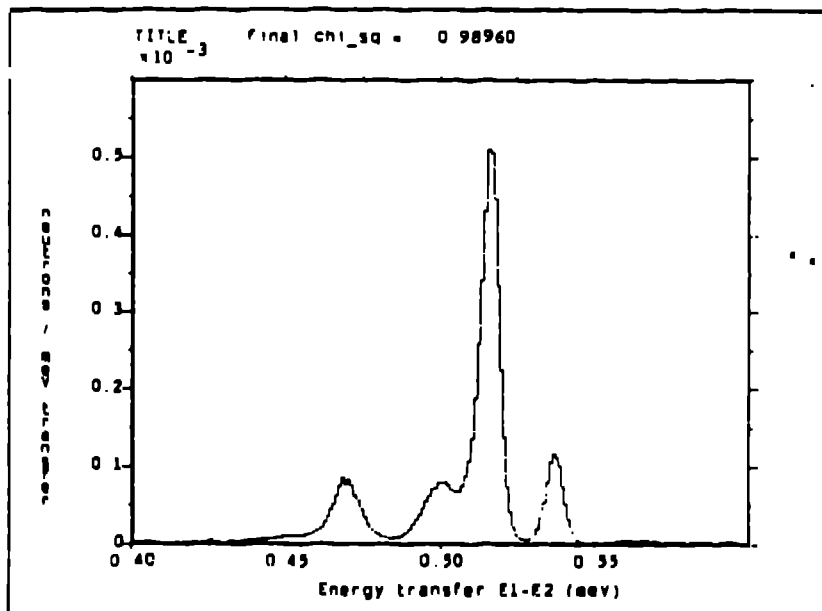


Figure 19



**References**

1. Burg J P (1967) Maximum-Entropy Spectral Analysis,  
Conf Paper reprinted in: Modern Spectrum Analysis, Ed  
D G Childers (New York, Wiley 1978)
2. Gull S F and Daniel G J (1978) Nature 272 686-90
3. Steinstrup S (1986) Conf Paper in: Neutron Scattering  
Data Analysis, Ed M W Johnson (IOP Conference Series  
81 1986)
4. Johnson M W (1987) Rutherford Appleton Laboratory  
Report RAL-87-058



# Maximum entropy methods in neutron scattering: application to the structure factor problem in disordered materials

A. K. Soper  
Neutron Science Division  
Rutherford Appleton Laboratory  
Chilton, Didcot, Oxon, OX11 0QX  
UNITED KINGDOM

**Abstract:** Maximum entropy methods are becoming increasingly important in the analysis of neutron scattering data, principally for the deconvolution of the instrumental resolution function from measured data, and for the inversion of structure factor data to pair correlation function. It is demonstrated that maximizing the entropy of the estimated distribution does not necessarily guarantee that the inverted distribution is free from artifacts associated with the truncation, noise and systematic effects in the data: the result can depend quite markedly on the assumed prior distribution used to calculate the entropy. For the structure problem a novel exponential weight on the Fourier coefficients is introduced which serves to ensure that the structure factor and its derivatives are continuous. The rate of exponential decay, which is related to the width of the narrowest peak in the structure factor is determined by an inverse correlation length that can be obtained from the data. In this way the results are markedly less dependent on the assumed prior distribution.

## 1. Introduction

A broad class of problems in neutron scattering involve the inversion of a set of measurements, the data  $D_i$ , to a desired distribution function  $N_j$ , the  $N_j$  being related to the  $D_i$  via a transform of some kind:-

$$D_i = \text{Tr} \left\{ N_j \right\}, \quad i, j = 0, 1, \dots, n \quad (1)$$

This inversion is often impossible or ill-conditioned for several reasons:-

- (a) the transform may not be linear;
- (b) the data may be incomplete,  $i=11 \dots i2$ ;
- (c) the data are measured at discrete points;
- (d) the data may be noisy;
- (e) the data may have systematic errors.

Because of the ill-conditioning it is likely that several or perhaps a large set of distributions  $N_j$  can be regarded as consistent with the measured data.

Over the years a large number of methods have evolved to cope with the variety of difficulties which arise in the inversion of incomplete data. Of these it is claimed, Jaynes (1982), that the Maximum Entropy (ME) approach, which attempts to avoid producing any information which is not justified by the data, provides an independent assessment of all the possible solutions to a particular problem, and so leads to that solution which is "maximally non-committal" with respect to the unmeasured data. This is achieved via an entropy metric which is usually defined as

$$H = - \sum_j N_j \ln (N_j/P_j) - \sum_j N_j - \sum_j P_j \quad (2)$$

where P represents a "prior" distribution which incorporates previous knowledge about the distribution not contained in the data. The second and third terms are introduced in (2) in the event that N and P are not normalizable distributions. In the absence of any other information the ME solution, which attempts to maximize H, is simply  $N = P$  for all j. When constrained by additional information, i.e. the measured data, the entropy falls below its maximum value. The object of the ME method therefore is to find that solution for N which satisfies the data but which also keeps H as near as possible to its maximum value. It will be seen that this definition of H only exists if  $N_j, P_j > 0$ .

The goodness of fit to the data is usually measured by a  $\chi$ -squared statistic or R-factor:

$$R_f^2 = \sum_i (D_i - M_i)^2 / \sum_i D_i^2 \quad (3)$$

where  $M_i$  is an estimate (or "model") of the i'th data point obtained from the estimated trial N distribution via (1). With this definition a "quality factor", or Q-factor, which represents how well a particular solution satisfies the dual constraints of entropy maximization and fit to the supplied data, is defined as

$$Q_f^2 = -H + xR_f^2, \quad (4)$$

where x is an undetermined positive multiplier which controls how closely the model fits the data. Therefore it is the Q-factor which is to be minimized, with x determined by constraining the R-factor to a predefined value.

In setting up the ME solution for a given experimental situation, there are two questions that need to be confronted. Firstly what is the most appropriate distribution space, the N distribution, in which entropy is to be calculated? Secondly, what is the most reasonable choice for the prior distribution, or P distribution. It is frequently assumed that the prior distribution should be uniform even though the existence of the data implies that the real distribution is anything but uniform. Unfortunately both of these questions are often ignored in the literature, there being an implicit assumption that somehow maximizing entropy will cover up all the difficulties. In the sections that follow I will apply the ME method to the problem of calculating the pair correlation function for a liquid or amorphous material from structure factor data. I will demonstrate that the obvious choice for the distribution N is in

fact quite inappropriate in this case, and that the result of ME analysis can depend markedly on the choice of prior distribution. Full details on the correct choice for the N and P distributions for the entropy estimation for this problem are given elsewhere. Soper (1988), but some examples of the results are shown here. The conclusions to be drawn are applicable to many other applications where ME techniques are used.

## 2. Solution of the Maximum Entropy Problem

The general solution of the ME problem is a highly non-linear problem and several solutions exist, mostly using sophisticated search procedures, Bryan and Skilling (1984). I have developed a Monte Carlo (MC) solution to this problem which has several attractive features. In particular it is simple to execute, can allow error bars on the calculated distributions to be estimated if needed, and by virtue of the stochastic process intrinsic to MC calculations is unlikely to get stuck in local phase space minima. The object of the MC calculation is to set up an ensemble of distributions such that each member occurs with probability

$$p(Q_f^2) = \exp(-\lambda Q_f^2) \quad (5)$$

with  $\lambda$  a positive multiplier which determines the size of the Q-factor and its fluctuations: as  $\lambda$  is made larger so the Q-factor is driven smaller and the fluctuations become smaller. Full details of this algorithm are given elsewhere, Soper (1988), and will not be elaborated further here. However it will be noted that in all the examples given below  $\lambda$  is kept as large as possible, so that fluctuations are held to a minimum and the individual trial distributions lie indistinguishably close to the ME solution. Typical run times for this algorithm, which might involve 500,000 individual moves, are 10 minutes of cpu on a VAX 8650, assuming 200 data points and 500 points in the N distribution.

## 3. The Structure Problem in Disordered Systems

The underlying transform in the structure of liquids and amorphous materials is in principle a straightforward Fourier transform:

$$S(Q) = 4\pi\rho \int_0^\infty r \{ g(r) - 1 \} \sin(Qr) dr \quad (6)$$

where  $S(Q)$  is the measured structure factor, as a function of wave vector transfer,  $Q$ , and  $g(r)$  is the underlying pair distribution function as a function of radial distance  $r$  from an atom at the origin. The atomic number density is  $\rho$ . Inverting this transform directly can lead to significant transform errors because the data can never be measured over a complete range of  $Q$  values and in any case invariably contain some form of error, statistical or systematic. Typically one introduces the constraint of only calculating  $g(r)$  at certain values of  $r$ , according to the Lado (1971) rules for Fourier transforms, i.e.  $\Delta r = \pi/Q_{\max}$ . Furthermore a "window" function is often invoked to further reduce the effects of noise in the calculated distribution function.

This problem is readily amenable to ME analysis. In particular there is apparently an obvious choice for the N distribution by virtue of the normalization

$$4\pi\rho \int_0^{\infty} r^2 (g(r)-1) dr = -1 + \rho\chi k_B T \quad (7)$$

where  $\chi$  is the isothermal compressibility and  $T$  is the absolute temperature. Hence the "obvious" choice for the  $N$  distribution is simply

$$N_j = N(r_j) = 4\pi\rho r_j^2 g(r_j) \Delta r \quad (8)$$

where  $\Delta r$  is the bin width of the discretized distribution. Figures 1 and 2 show the effects of applying ME analysis to the problem of transforming the hard sphere structure factor to pair correlation function. In this case the input  $S(Q)$  is known exactly within the Percus-Yevick approximation but is a particularly severe test of any transform method because  $g(r)$  for hard spheres is discontinuous at  $r=\sigma$ , the hard core diameter. In this case the density was chosen such that  $\rho\sigma^3 = 0.5$ , and a large  $Q$  limit of  $Q_{\max} = 15/\sigma$  was imposed on the  $S(Q)$  data, with  $\sigma = 1\text{\AA}$ . In figure 1 the prior distribution is

$$\begin{aligned} P_j &= 0 & \text{for } r_j < \sigma \\ P_j &= 4\pi\rho r_j^2 \Delta r & \text{for } r_j > \sigma, \end{aligned} \quad (9)$$

while for figure 2 the prior distribution is set at

$$\begin{aligned} P_j &= 0 & \text{for } r_j < 0.75\sigma \\ P_j &= 4\pi\rho r_j^2 \Delta r & \text{for } r_j > 0.75\sigma. \end{aligned} \quad (10)$$

In either case the fit to the data was the same, ( $R$ -factor = 1%); however it is readily apparent that the two results for  $g(r)$  are not the same. In particular the distribution in figure 2 has greater entropy than figure 1 (-2.064 for figure 2 compared to -2.534 for figure 1) when measured against the uniform prior, thus confirming that the algorithm has found the true maximum entropy solution for figure 2. This result is apparently at odds with our intuition which might tend to favour the one in figure 1 as being less "structured", if the word "structure" in this case is taken to indicate the number and size of peaks and valleys in the calculated distribution. In fact the distribution in figure 1 is very close to the known exact solution, Throop and Pearson (1965).

The difference between the two solutions is manifested in  $Q$  space not in the region of the input data, where the two solutions give equally good fits, but beyond the input region. Figure 3 shows the calculated structure factor for the distribution in figure 2, and also the difference between model and data. It is seen that immediately beyond the data ( $Q = 15-16 \text{\AA}^{-1}$ ) there is a strange cusp in the  $S(Q)$  from figure 2, a phenomenon which has been seen before, Root, Egelstaff and Nickel (1986). The ripples seen in figure 2 become suspect when it is realized they have a period of  $\sim 2\pi/Q_{\max}$ , where  $Q_{\max}$  is the largest  $Q$  value for the input data. Hence it is concluded that maximizing the entropy has not avoided the truncation ripples associated with the discontinuity in the input data at  $Q=Q_{\max}$ . For measured datasets which usually have a noise component, the discontinuities become important since there is effectively a discontinuity at every data point.

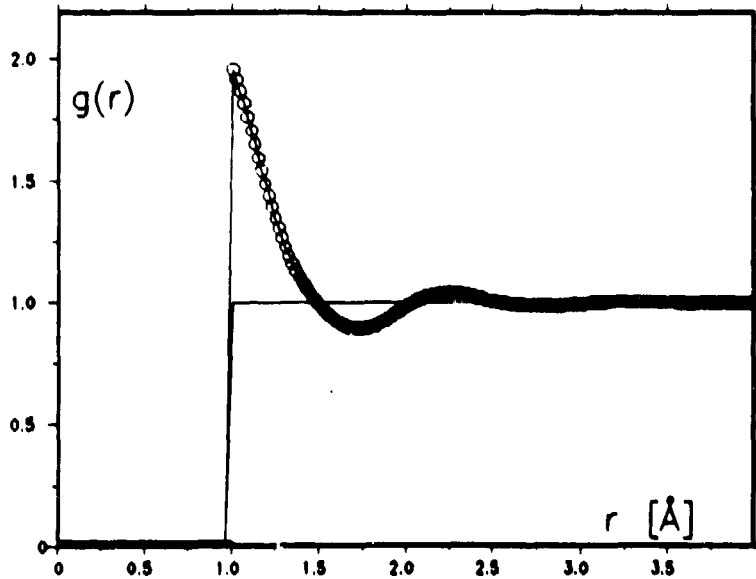


Figure 1 Maximum entropy pair correlation function derived from Percus Yevick hard sphere structure factor. The  $S(Q)$  data were truncated at  $Q = 15\text{\AA}^{-1}$ , and the prior distribution used is zero in the region  $r = 0$  to  $r = 1\text{\AA}$ . The circles show the calculated distribution and the line shows the prior.

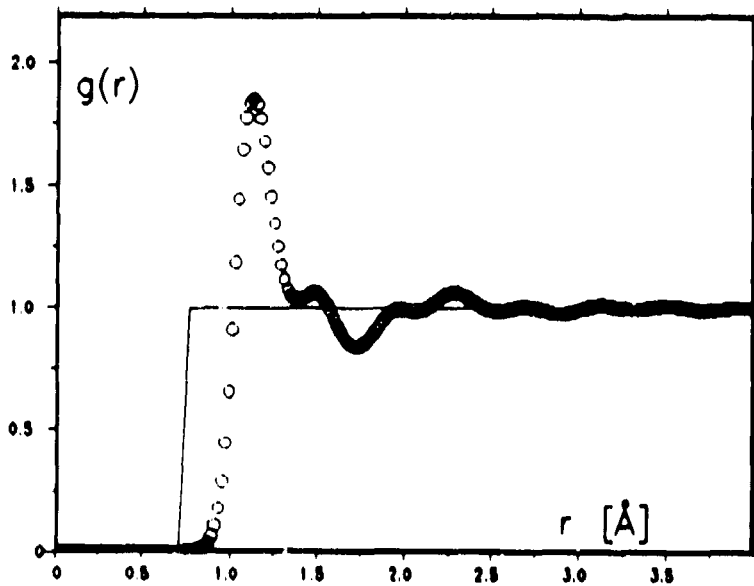


Figure 2 Same calculation and notation as for figure 1 except that the prior is zero in the region  $r = 0$  to  $r = 0.75\text{\AA}$ .



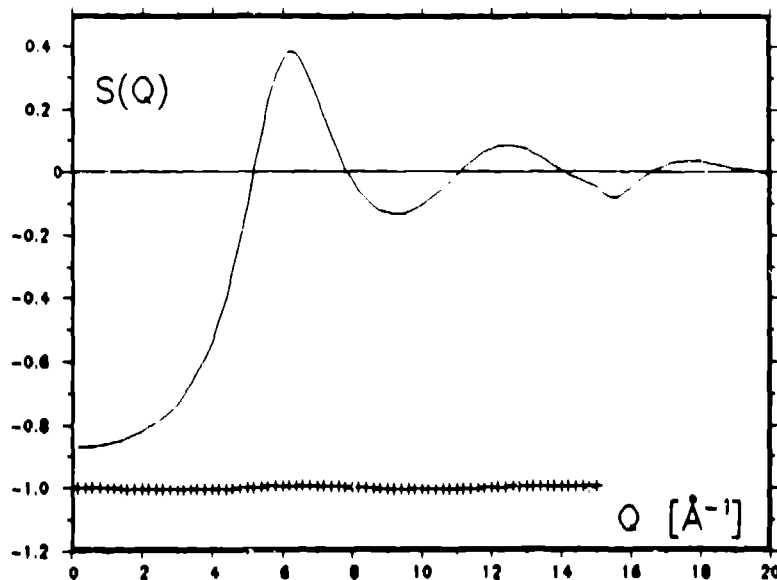


Figure 3 Maximum entropy structure factor corresponding to the correlation function of figure 2. The crosses show the residual between fit and data shifted below zero by unity.

#### 4. Solution of the Discontinuity Problem

I propose two solutions to the problem of discontinuities. The first is to effectively force  $S(Q)$  to be everywhere continuous and have continuous derivatives. To see how to do this a well known theorem from Fourier transforms is invoked, Lighthill (1959). From (6) it can be seen that the  $n$ 'th derivative of  $S(Q)$  is given by

$$S^n(Q) = 4\pi\rho(-1)^{n/2} \int_0^\infty r^{n+1} (g(r)-1) \sin(Qr) dr \quad \text{for } n\text{-even} \quad (11)$$

and

$$S^n(Q) = 4\pi\rho(-1)^{(n-1)/2} \int_0^\infty r^{n+1} (g(r)-1) \cos(Qr) dr \quad \text{for } n\text{-odd} \quad (12).$$

Therefore if  $(g(r)-1)$  converges slower than  $1/r^{n+2}$  as  $r \rightarrow \infty$ , there will be discontinuities in the  $n$ 'th derivative. On the other hand if  $\exp(-ar)(g(r)-1)$ , where  $a$  is a finite positive number, is convergent as  $r \rightarrow \infty$  then  $r^{n+2}(g(r)-1)$  is also convergent at large  $r$  for all  $n$ . For the hard sphere pair correlation function the exponential decay of  $(g(r)-1)$  with increasing  $r$  is an analytic consequence of the theory which describes the hard sphere structure factor, Perry and Throop (1972). For other liquid and amorphous structures the requirement that  $S(Q)$  be continuous and have continuous derivatives is a necessary consequence of there being no long range order in the material.

This exponential constraint leads to a simple revision of the definition of the N and F distributions, namely

$$N_j' = \exp(\alpha r_j) * N(r_j) = 4\pi\rho \exp(\alpha r_j) r_j^2 g(r_j) \Delta r \quad (13)$$

and

$$\begin{aligned} P_j' &= 0 && \text{for } r_j < \sigma \\ P_j' &= 4\pi\rho \exp(\alpha r_j) r_j^2 \Delta r && \text{for } r_j > \sigma. \end{aligned} \quad (14)$$

The primed distributions are used instead of the unprimed distributions in the definition of entropy, equation (2). Otherwise the calculation proceeds as before. The inverse correlation length,  $\alpha$ , is determined from the width of the narrowest peak in  $S(Q)$ , or by inspection of the large  $r$  behaviour of  $g(r)$ . Hence for a previously unknown dataset it may be necessary to redetermine its value once an initial solution has been achieved.

Figures 4 and 5 show the results of applying this exponential constraint in the definition of entropy, with  $\alpha = 1.8/\text{\AA}$ . It can be seen that the ripples in figure 2 have been largely eliminated in figure 4, and that the problem of the cusp in  $S(Q)$  at  $Q=Q_{\text{max}}$  has now been eradicated (figure 5). The fit is a good as before (R-factor = 1%), and the entropy is only marginally lower than for figure 2, being equal to  $-2.0\%$ .

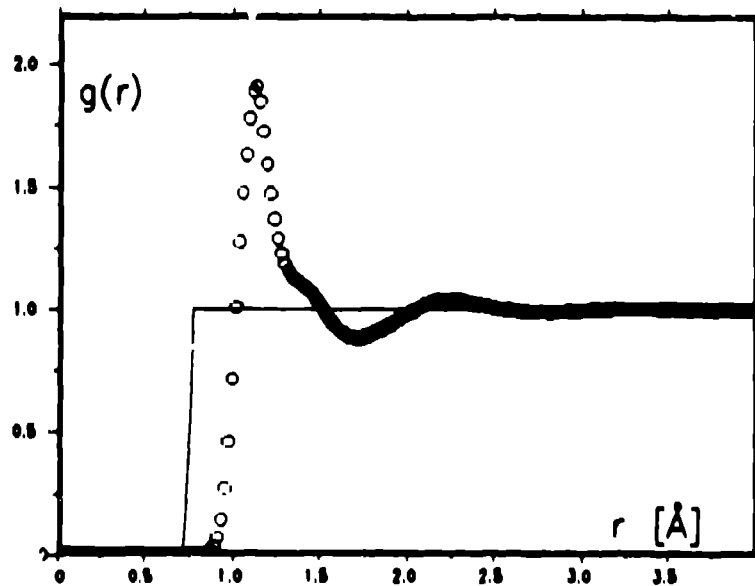


Figure 4 Maximum entropy pair correlation function as for figure 2, but this time derived using the exponential weighting on the distributions used to calculate the entropy, as described in the text.

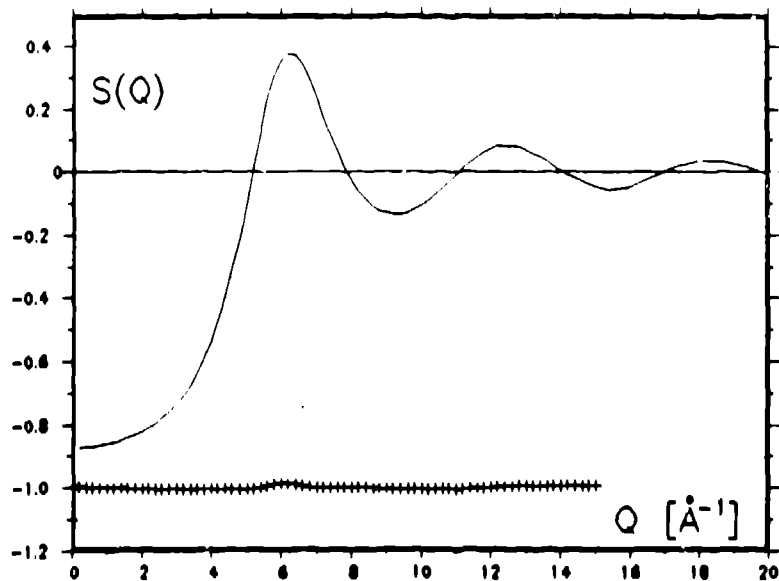


Figure 5 Maximum entropy structure factor corresponding to figure 4. Note that the cusp near  $Q = 15/\text{\AA}$  is absent in this case.

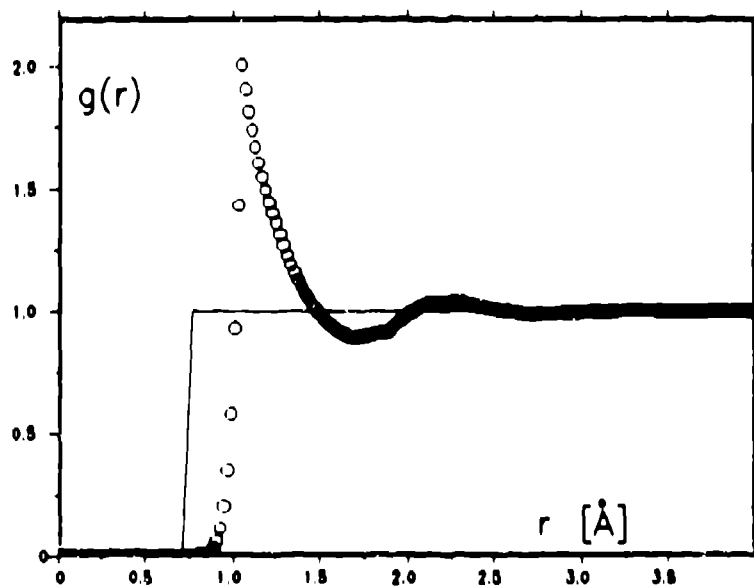


Figure 6 Maximum entropy pair correlation function as before, but this time using the fluctuations in the  $Q$ -factor linearly interpolated between the allowed discrete Fourier values.

## 5. Coping with Truncation Effects

It is apparent in figure 4 that some truncation effects may still be present in the estimated distribution functions. These arise because in estimating the change in Q-factor at each move, there is a sum over the input data which in effect is a Fourier transform of the difference  $D_i - M_i$ , Soper (1988). Since the change in Q-factor at each move is the driving force behind the calculation this Fourier transform can give rise to exactly the same truncation effects seen in a direct transform of the raw data. My solution to this difficulty is to evaluate the transform only at the allowed  $r$  values ( $r_j = j\pi/Q_{\max}$ ), and then interpolate the result onto the required grid of  $r$  values by linear interpolation.

Figure 6 shows the result of doing this for the same input dataset as before. Now it will be noted that truncation effects are diminished even further; the result is now approaching that of figure 1, but with greater entropy ( $H = -2.141$ ).

## 6. Conclusion

The foregoing text has described the application of the ME method to the calculation of the pair correlation function from structure factor data for liquid and amorphous materials. The main conclusion is that ME does not automatically guarantee that the results are free from artifacts associated with noise and truncation in the data. To avoid these artifacts it is necessary to build into the distributions used to calculate entropy known physical constraints which must be satisfied, whatever the detailed form the distributions are to take. For the structure factor problem these constraints include the requirement that the structure factor must everywhere be continuous and have continuous derivatives, and that the fluctuations in the distributions away from the prior distribution are not biased by the truncation of the input data. Further details and applications of the Monte Carlo algorithm used here are available elsewhere, Soper (1988), as well as a discussion of the present approach in the context of other recent attempts at the structure factor problem.

## 7. Acknowledgement

I would like to acknowledge invaluable discussions on the subject matter of this paper with S. Baer, T. Gaskell, and N. Rivier.

References

Bryan R K and Skilling J, 1984, Monthly Not. Astr. Soc., 211, 111

Jaynes E T, 1982, Proc. of the IEEE. 70, 939

Lado F, 1971, J. Comput. Phys. 8, 417

Lighthill M J, 1959, "Introduction to Fourier Analysis and Generalised Functions", Cambridge University Press.

Perry G and Throop G J, 1972, J.Chem. Phys. 57, 1827

Root J H, Egelstaff P A, and Nickel B G, 1986, Inst. of Phys. Conf. Ser. No. 81  
"Neutron Scattering Data Analysis, 1986", ed. by M W Johnson, IOP Bristol.

Soper A K, 1988, "Proceedings of the International Workshop on Static and Dynamic Properties of Liquids", June 27th-30th, Dubrovnik, Yugoslavia, ed. by M. Davidovich and A.K.Soper, to be published in Springer-Verlag Proceedings in Physics Series; also manuscript in preparation.

Throop G J and Bearman R J, 1965, J.Chem. Phys. 42, 2408

## Optimization of reconstruction algorithms using Monte Carlo simulation

*K. M. Hanson\**  
Los Alamos National Laboratory, MS P940  
Los Alamos, New Mexico 87545  
USA

**ABSTRACT:** A method for optimizing reconstruction algorithms is presented that is based on how well a specified task can be performed using the reconstructed images. Task performance is numerically assessed by a Monte Carlo simulation of the complete imaging process including the generation of scenes appropriate to the desired application, subsequent data taking, reconstruction, and performance of the stated task based on the final image. The use of this method is demonstrated through the optimization of the Algebraic Reconstruction Technique (ART), which reconstructs images from their projections by an iterative procedure. The optimization is accomplished by varying the relaxation factor employed in the updating procedure. In some of the imaging situations studied, it is found that the optimization of constrained ART, in which a nonnegativity constraint is invoked, can vastly increase the detectability of objects. There is little improvement attained for unconstrained ART. The general method presented may be applied to the problem of designing neutron-diffraction spectrometers.

### Introduction

The overall purpose of an imaging system is to provide information about the object or scene being imaged. For mission-oriented imaging systems, the type of scenes expected and the kind of information desired can frequently be specified. In such a case an imaging system should be optimized on the basis of how well the specified task can be performed using the resulting images. Here this approach to optimization is applied to only one aspect of the complete imaging system, that of the image reconstruction algorithm. It is shown that such an optimization is distinctly practical and can be extremely beneficial.

Several classes of measures have been employed in the past on which to base the optimization of reconstruction algorithms [1]. Some are based on the fidelity of the reconstructed images, such as the conventional measure of the

\*This work was supported by the United States Department of Energy under contract number W-7405-ENG-36.

rms difference between the reconstruction and the original image, simply called the rms error. Experience teaches us that this does not always seem to be correlated with the usefulness of images. There are alternative measures based on how closely the estimated reconstruction reproduces the measurement data, for example, the mean-square residual. Unfortunately, without further constraints reconstruction based on minimizing the mean-square residual is known to be ill-conditioned or even worse, ill-posed [1].

In the approach to algorithm optimization presented here, an algorithm is rated on the basis of how well one can perform stated tasks using the reconstructed images. As shown in Ref. [2], task performance in a well specified imaging situation is readily assessed numerically through a Monte Carlo technique that is used to simulate the complete imaging process. The optimization procedure involves maximizing task performance by varying whatever free parameters exist in the reconstruction algorithm.

This article closely follows one that appeared in conjunction with an SPIE conference [3]. The main thrust of the present article is the solution of the tomographic reconstruction problem in which a two-dimensional image is to be determined from a set of projections (line integrals) taken through it. However, the same kind of difficulties that exist in tomographic reconstruction are present in other image-recovery problems. That goes for the deblurring of blurred data in either one or two dimensions. The technique presented here for evaluation and optimization of a reconstruction algorithm has obvious applications to many of the questions that have been posed during this workshop regarding the best design of neutron-diffraction spectrometers. It is well to remember that the data-collection system includes both the spectrometer design and the subsequent data analysis, which includes any deblurring that might be deemed necessary. Optimization of the quality of the final data should also include the effects of the data processing that may be required for the proper interpretation of the data.

### Method to Calculate Task Performance

For linear imaging systems the effects of image noise on task performance can be predicted for a variety of simple tasks [4]. The same cannot be said of the effects of artifacts. The masking effects of measurement noise are truly random in nature. The random noise process results in each set of measurements being different, even when the scene being imaged does not change. However, reconstruction from limited data typically produces artifacts in the reconstructed images that behave differently than the fluctuations arising from random noise. They manifest themselves as seemingly unpredictable irregularities that look like noise, but in a strict sense, they are not. They are deterministic since they can be predicted from the combined knowledge of the measurement geometry, the scene, and the reconstruction algorithm. Since these artifacts depend on the scene, a single realization of a simple scene is plainly inadequate to judge a reconstruction algorithm. It is necessary to obtain a statistically meaningful

average of the response of an algorithm to many realizations of the ensemble of scenes with which it must cope.

A Monte Carlo technique, one that employs pseudo-random numbers to generate its results, is used to simulate the entire imaging process from scene generation to the final task performance, because it can readily provide the above variations within the ensemble.

The method requires first a complete specification of the entire problem in the following manner:

a) Define the class of scenes to be imaged with as much complexity as exists in the intended application.

b) Define the geometry of the measurements. The deficiencies in the measurements such as blur, uncertainties in the geometry, and uncertainties in the measurements (noise) should be specified.

c) Define clearly the task to be performed. Details concerning what is known about the signal and the background must be stated explicitly.

d) Define the method of task performance. This method should be consistent with the intended application and the *a priori* known information.

The simulation procedure is then performed by doing the following:

e) Create a representative scene and the corresponding measurement data by means of a Monte Carlo simulation technique.

f) Reconstruct the scene with the algorithm being tested.

g) Perform the specified task using the reconstructed image.

h) Repeat steps e) through g) a sufficient number of times to obtain the necessary statistics on the accuracy of the task performance.

Finally, determine how well the task has been performed:

i) Evaluate the task performance using the relevant measure of performance.

The advantage of this numerical approach is that it readily handles complex imaging situations, nonstationary imaging characteristics, and nonlinear reconstruction algorithms. Its major disadvantage is that it provides an evaluation that is valid only for the specific imaging situation investigated.

## ART

The Algebraic Reconstruction Technique (ART) [5] is an iterative algorithm that reconstructs a function from its projections. It has proven to be a very successful algorithm in tomographic reconstruction, particularly for estimating a function when there is a limited amount of data available. It is identical to the Kaczmarz algorithm [6], which provides a pseudoinverse solution to a singular system of linear equations [7] and works particularly well when the matrix is sparse. Assume that  $N$  projection measurements are made of the unknown function  $f$ , which will be considered a vector. As these measurements are linearly related to  $f$ , they may be written as

$$g_i = H_i f, \quad i = 1, \dots, N, \quad (1)$$



where  $g_i$  is the  $i$ th measurement and  $H_i$  is the corresponding row of the measurement matrix. The ART algorithm proceeds as follows. An initial guess is made, for example,  $f^0 = 0$ . Then the estimate is updated by iterating on the individual measurements taken in turn:

$$f^{k+1} = f^k + \lambda^k H_i^T \left[ \frac{g_i - H_i f^k}{H_i^T H_i} \right], \quad (2)$$

where  $i = k \bmod(N)+1$  and  $\lambda^k$  is a relaxation factor for the  $k$ th update. Any applicable constraints are invoked after each update. For example, for constrained ART in which a non-negativity constraint is enforced, when  $f^{k+1} < 0$ , set  $f^{k+1} = 0$ . In the absence of constraints, the normalization of such that when  $\lambda^k = 1$ ,  $f^{k+1}$  is guaranteed to satisfy the measurement equation (1). In the standard nomenclature one iteration is completed after the full set of  $N$  measurements has been processed. We use the index  $K$  to indicate the iteration number ( $K = \text{int}(k/N)$ ). Variable relaxation (or damping) factors are used here to attenuate successive updates during the reconstruction. We will express the relaxation factor as

$$\lambda^K = \lambda_0 (r_\lambda)^{K-1}. \quad (3)$$

The proper choice of the relaxation factor is the issue at hand. There is very little guidance on this choice in the literature. It is known [8] that if a solution to the measurement equations exists, the ART algorithm will converge to it in the limit of an infinite number of iterations provided that  $2 > \lambda_k > 0$ . A value of unity is often suggested. Censor *et al.* [9] have shown that unconstrained ART ultimately converges to a minimum-norm least-squares solution if the relaxation factor approaches zero slowly enough. However,  $\lambda^K$  will asymptotically approach zero for any value of  $r_\lambda < 1$ . The value appropriate to a finite number of iterations remains uncertain. In previous work the author has assumed for  $\lambda_0$  and  $r_\lambda$  the nominal values of 1.0 and 0.8 for problems involving a limited number of projections, and 0.2 and 0.8 for problems involving many ( $\sim 100$ ) views [2]. This choice for  $r_\lambda$  makes the final  $\lambda^K$  at ten iterations about seven times smaller than the initial one  $\lambda_0$ . In our experience unconstrained ART converges reasonably well in ten iterations. Next we discuss a way to find the best choice for the relaxation parameters for a given problem.

### Optimization of ART

The use of numerically calculated task performance will be demonstrated by searching for the optimum choice of  $\lambda_0$  and  $r_\lambda$  for the ART algorithm. For the present purpose, the class of scenes is assumed to consist of a number of non-overlapping discs placed on a zero background. For this example, each scene contains 10 high-contrast discs of amplitude 1.0 and 10 low-contrast discs with amplitude 0.1. The discs are randomly placed within a circle of reconstruction, which has a diameter of 128 pixels in the reconstructed image. The diameter

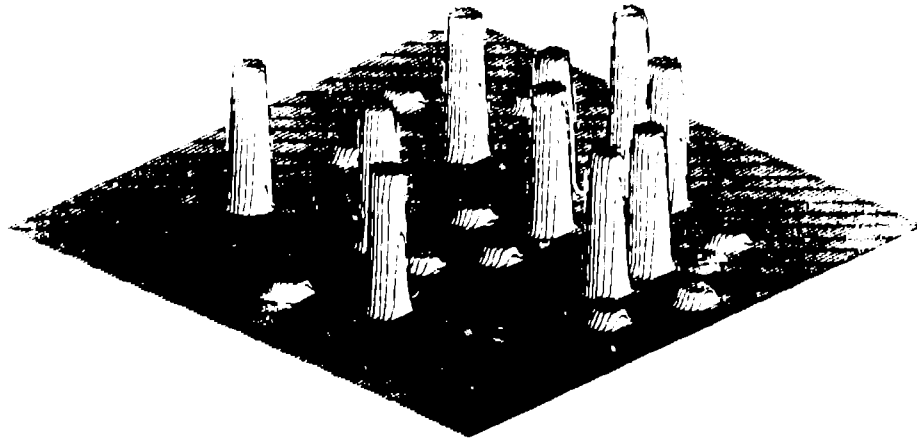


Figure 1: The first randomly generated scene consisting of 10 high-contrast and 10 low-contrast discs. The evaluation of task performance is based on an average over ten similar scenes.

of each disc is 8 pixels. The first of the series of images generated for these tests is shown in Fig. 1. In this computed tomographic (CT) problem, the measurements are assumed to consist of a specified number of parallel projections, each containing 128 samples. Ten iterations of ART are used in all of the present examples. It is assumed that the task to be performed is the detection of the low-contrast discs. To produce noisy data, random noise is added to the projection measurements using a Gaussian-distributed random number generator.

The result of reconstructing Fig. 1 from 12 noiseless views spanning  $180^\circ$  is shown in Fig. 2. The seemingly random fluctuations in the background are actually artifacts produced by the limited number of projections and arise mainly from the high-contrast discs. As the artifacts depend on the positions of the discs, it is important to allow for random placement of the discs to allow for the full range of artifacts. It appears that the nonnegativity constraint improves the reconstruction considerably in that it has reduced the confusion caused by the fluctuations in the background. However, upon careful examination, one finds that some of the low-contrast discs have not been reproduced. Also, there still remain many fluctuations in the background that may mislead one to suspect the presence of discs in places where none exist in reality. Thus, on the basis of this single example, one cannot say with certainty whether or not the detection of the low-contrast discs is improved by the nonnegativity constraint. A statistically significant comparison between reconstructions with and without the constraint must be made to assess its value.

The task to be performed is assumed to be the simple detection of the low-contrast discs. It is assumed that the position of a possible disc is known beforehand as is the background. To perform the stated task of detection, it is

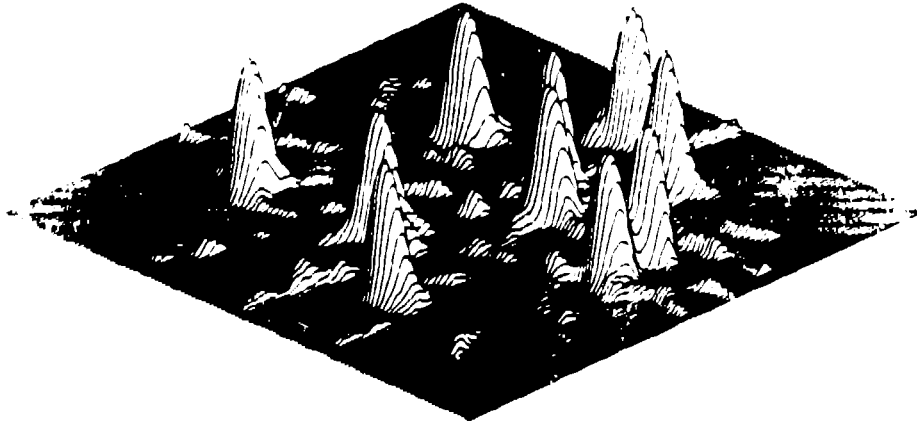
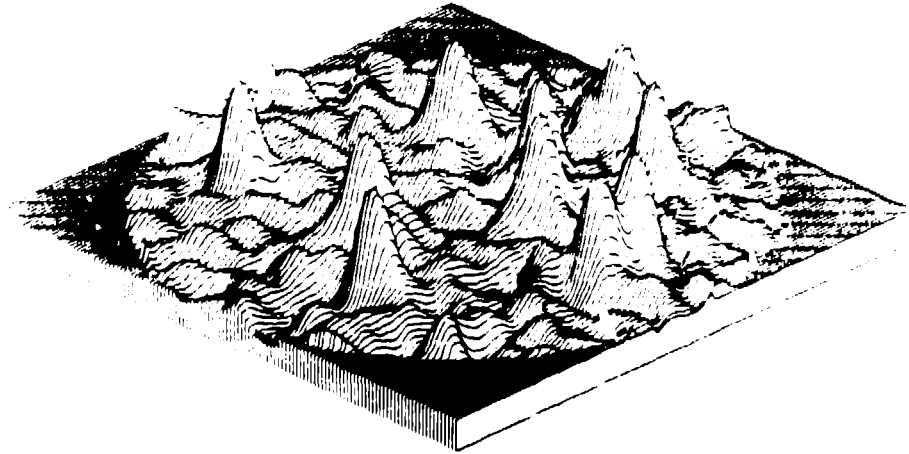


Figure 2: Reconstructions of Fig. 1 from 12 noiseless parallel projections subtending  $180^\circ$  obtained with 10 iterations of the ART algorithm (top) without and (bottom) with the nonnegativity constraint. These reconstructions were obtained with  $\lambda_0 = 1.0$  and  $r_\lambda = 0.8$ .

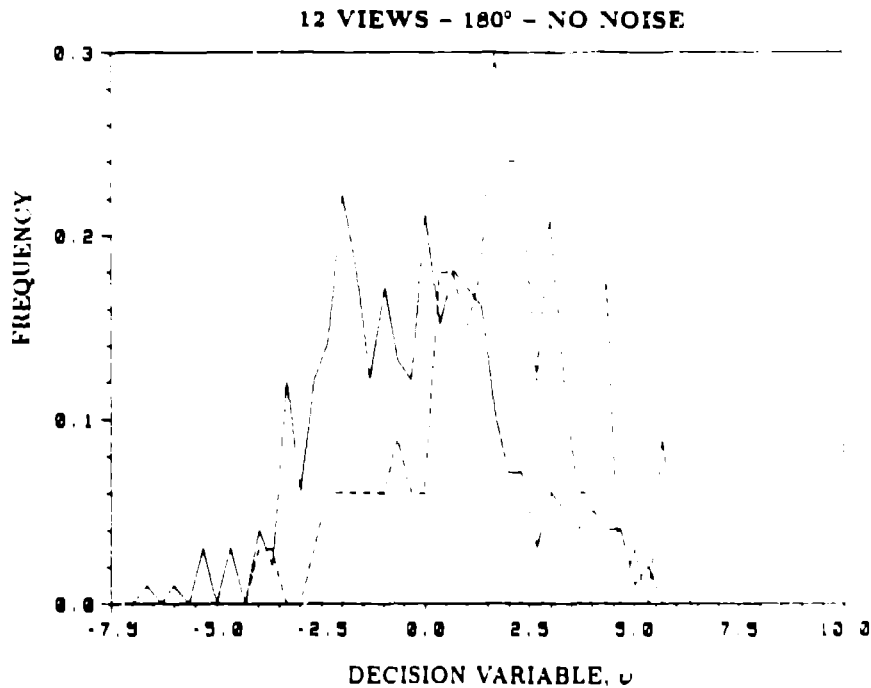


Figure 3: The frequency distributions of the decision variable (the sum over a circular region) evaluated where a low-contrast disc is known to exist (dashed line) and where none exists (solid line) for ART reconstructions without the nonnegativity constraint. These results summarize the detection performance obtained from reconstructions from 12 views for 10 randomly-generated scenes.

assumed that the sum over the area of the disc provides an appropriate decision variable  $\psi$ . This sum is an approximation to the matched filter, which is known to be the optimum decision variable when the image is corrupted by additive uncorrelated Gaussian noise [10]. Ignored is the blurring effects of the finite resolution of the discretely-sampled reconstruction. Neither is account taken of the known correlation in the noise in CT reconstructions [11] that have been derived from projections containing uncorrelated noise. After reconstruction, the sums over each region where the low-contrast objects are known to exist are calculated, as well as those over each region where none exist. These two data sets may be displayed as histograms in this decision variable as shown in Fig. 3. To perform the detection task, a disc will be said to be present at each location where the value of the decision variable is above a chosen threshold. The degree of separation between these two distributions is often characterized

by the detectability index  $d'$ , given by

$$d' = \frac{\psi_1 - \psi_0}{\sqrt{\frac{\sigma_1^2 + \sigma_0^2}{2}}}, \quad (4)$$

where  $\psi_1$  and  $\sigma_1$  are the mean and rms deviation of the frequency distribution when the object is present and those with the subscript 0 are when the object is not present. This quantity is sometimes called the signal-to-noise ratio (SNR) for detection. Clearly, larger  $d'$  implies better separation of the two distributions and hence better detectability. For the histograms shown in Fig. 3 obtained for unconstrained reconstructions,  $d'$  is 0.871. When the same analysis is carried out on reconstructions employing the nonnegativity constraint, a value of 2.054 is obtained. We conclude that the nonnegativity constraint has improved detectability. As noted in Ref. [2], the detectability index based on the area under the receiver operating characteristic curve  $d_A$  may be more appropriate for the binary decision task. But  $d'$  has better statistical accuracy than  $d_A$  and is more likely to be a continuous function of the parameters that can be varied in the reconstruction procedure. Thus  $d'$  is the preferred choice for the purpose of optimization.

Fig. 4 shows how two choices for optimization functions depend on  $\lambda_0$  and  $r_A$  for constrained ART. There is a definite minimum in these functions indicating optimum operating points for these two parameters. However, the minima are at different values of these parameters. Which operating point should we choose? Fig. 5 shows the reconstructions obtained using the relaxation parameters for optimization with respect to  $100/d'$  and the rms error in the reconstruction. There is an enormous improvement in the quality of both reconstructions over those shown in Fig. 2. Optimization with respect to  $100/d'$  appears to be preferable because it yields a  $d'$  that is twice as large as the optimization with respect to rms error. The latter also leads to annoying streak artifacts, which are quite visible in a good display of the reconstruction. The same kind of contour plots for unconstrained ART are relatively flat and uninteresting.

Fig. 6 shows reconstructions obtained from noisy data. Because of the large number of views, the data are complete. For the unconstrained and constrained reconstructions,  $d'$  is found to be 1.995 and 1.825, respectively. In this case the nonnegativity constraint has worsened detectability, contrary to what might be concluded from a first glance. The CPU time required to calculate these detectabilities took about one hour on a VAX 8700, which is about four times faster than a VAX 785.

The optimum values for  $\lambda_0$  and  $r_A$  were found for various conditions of data collection using a function minimizer from the NAG library<sup>1</sup> called E04JB. This routine finds the parameters for the minimum of a function after many evaluations of the function. From 20 to 100 function evaluations are required for the cases studied here. Table 1 tabulates the results obtained with unconstrained

<sup>1</sup>Numerical Algorithm Group, 7 Banbury Road, Oxford OX2 6NN, UK

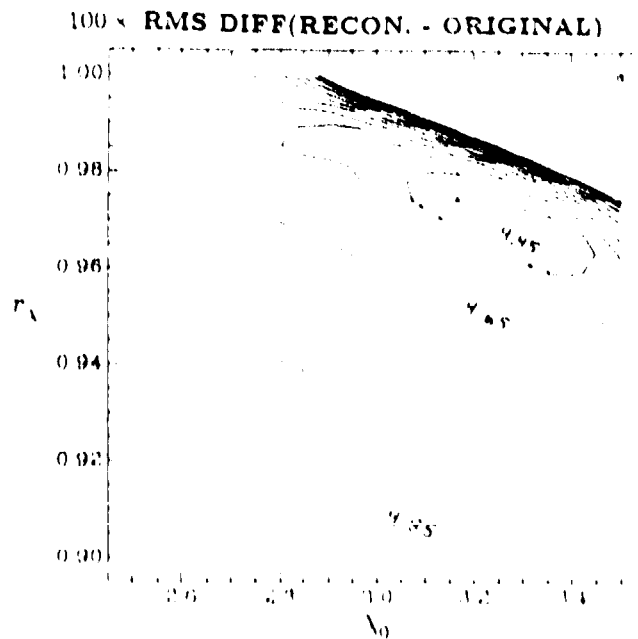
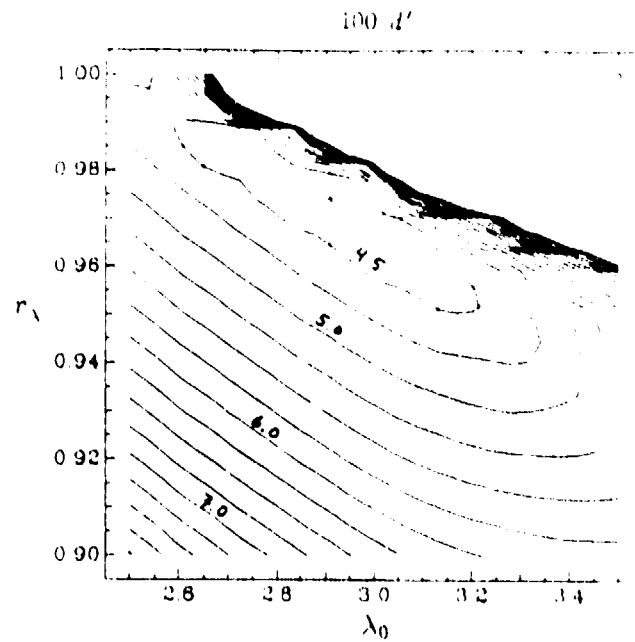


Figure 4: Contour plots of two optimization functions plotted as a function of the relaxation parameters  $\lambda_0$  and  $r_\lambda$  used in the constrained ART reconstruction algorithm. The measurements consist of 12 noiseless, parallel projections spanning  $180^\circ$ . The coarse sampling ( $10 \times 10$  points) of these functions, necessitated by the lengthy computation time required for each function evaluation, accounts for the scalloping effects.

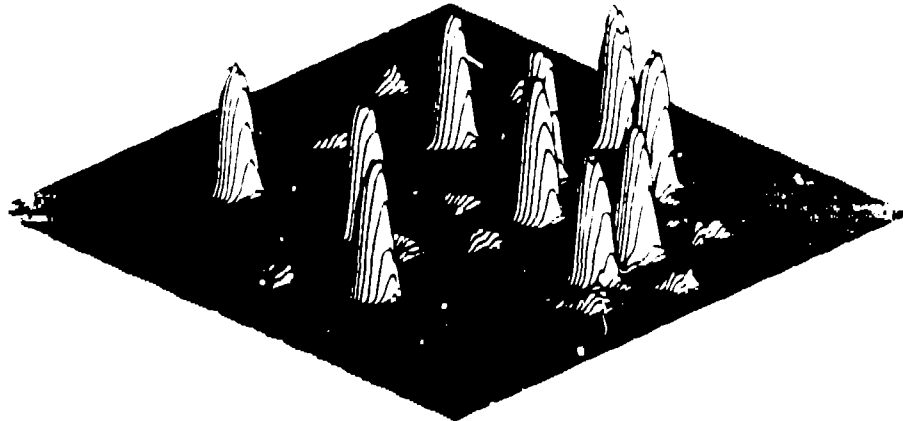
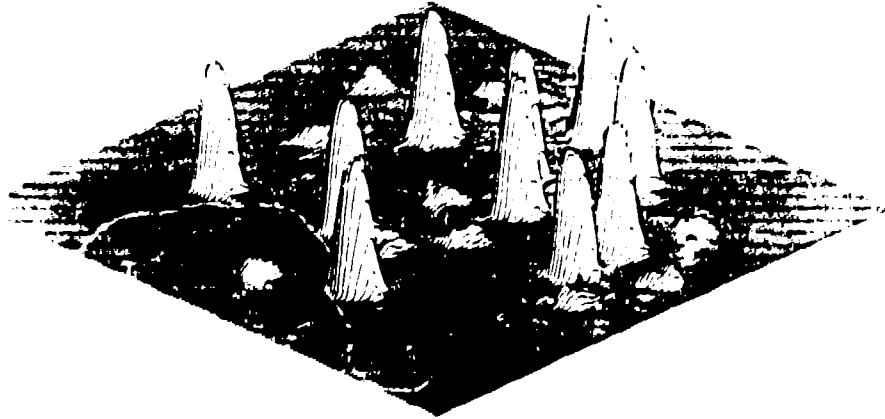


Figure 5: Optimized reconstructions of Fig. 1 from 12 noiseless parallel projections subtending  $180^\circ$  obtained with constrained ART. The reconstruction on the top is obtained with  $\lambda_0 = 2.96$  and  $r_A = 0.975$ , which is the optimum for detectability. The reconstruction on the bottom is obtained with  $\lambda_0 = 3.25$  and  $r_A = 0.975$ , which produces the smallest rms difference between the reconstruction and the original image. Although the rms error in the reconstruction is a common measure for the quality of reconstruction, it yields more visible artifacts and reduces  $d'$  from its optimum of 23.5 to 12.6.

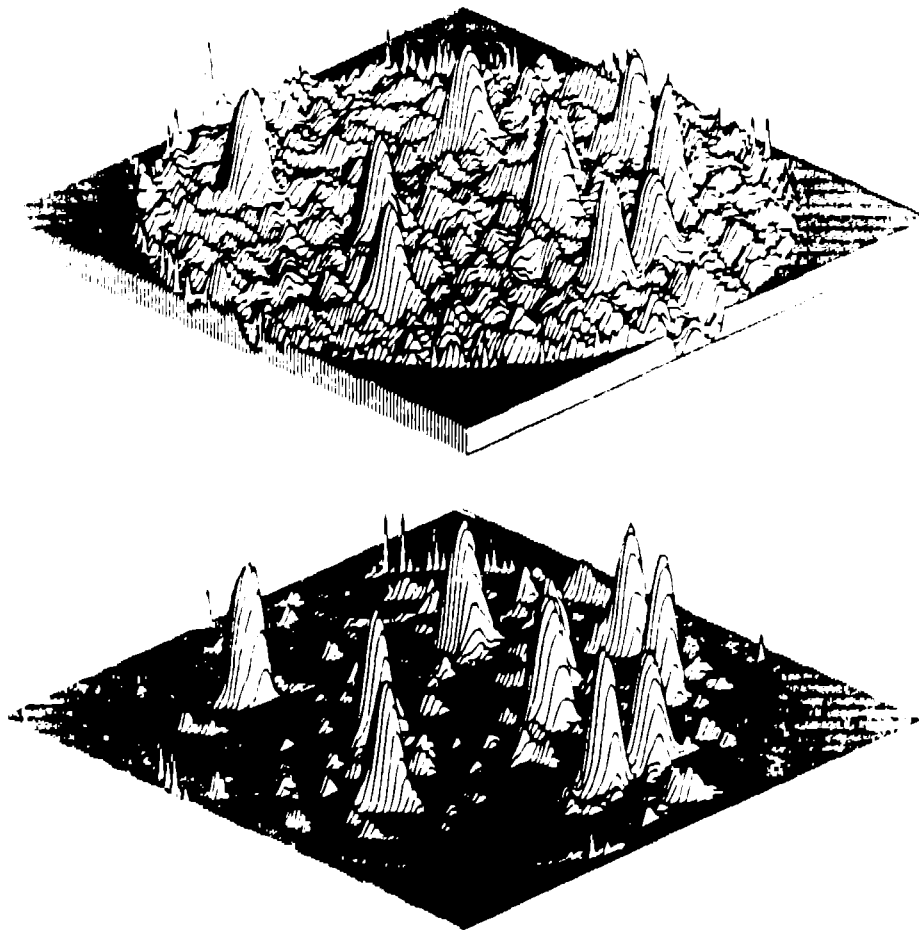


Figure 6: Reconstructions of Fig. 1 from 100 noisy parallel projections subtending  $180^\circ$  obtained with the ART algorithm (top) without and (bottom) with the nonnegativity constraint. The noise added to the projection measurements has an rms amplitude of 8, which is ten times the peak projection value for one of the low-contrast discs. These reconstructions were obtained with  $\lambda_0 = 0.2$  and  $r_\lambda = 0.8$ .



Table 1: Summary of the effect of optimization with respect to the detectability index  $d'$  on reconstructions obtained using 10 iterations of unconstrained ART. The optimum operating point was found by varying the parameters that control the relaxation factor used in the ART algorithm,  $\lambda_0$  and  $r_\lambda$ , as discussed in the text. There is generally little improvement in detectability.

number proj.	$\Delta\theta$ (deg.)	rms noise	nominal			optimized		
			$\lambda_0$	$r_\lambda$	$d'$	$\lambda_0$	$r_\lambda$	$d'$
100	180	8	0.2	0.8	1.995	0.107	0.820	2.013
8	180	0	1.0	0.8	0.464	0.915	0.463	0.485
12	180	0	1.0	0.8	0.871	0.427	0.729	0.932
16	180	0	1.0	0.8	1.960	1.047	0.998	1.969
16	90	0	1.0	0.8	1.122	1.714	0.993	1.202
16	180	2	1.0	0.8	1.653	2.247	0.635	1.662

Table 2: Summary of the effect of optimization with respect to the detectability index  $d'$  on ART reconstructions incorporating the nonnegativity constraint. When the measurement geometry limits the reconstruction rather than noise in the data, dramatic improvement in detectability is seen to be possible.

number proj.	$\Delta\theta$ (deg.)	rms noise	nominal			optimized		
			$\lambda_0$	$r_\lambda$	$d'$	$\lambda_0$	$r_\lambda$	$d'$
100	180	8	0.2	0.8	1.825	0.052	0.859	1.908
8	180	0	1.0	0.8	0.653	3.450	0.959	4.91
12	180	0	1.0	0.8	2.054	2.959	0.975	23.46
16	180	0	1.0	0.8	4.782	2.794	0.951	40.13
16	90	0	1.0	0.8	2.050	2.782	0.967	6.20
16	180	2	1.0	0.8	2.372	3.012	0.712	2.747

ART. In most cases relatively little improvement in detectability is achieved by optimization compared to that obtained with the nominal relaxation factors. In the noiseless cases, a value of unity for  $\lambda^k$  yields essentially the same results as the optimized values, a choice that is in agreement with common practice. However, for noisy data it seems desirable for  $r_\lambda$  to be less than unity and, when there are many views,  $\lambda_0$  should be small. These choices are reasonable as they promote significant averaging over all the views. As a rule of thumb, for noisy but complete data, the relaxation factor should be approximately equal to the reciprocal of the number of views for the last few iterations.

The results of optimizing constrained ART are presented in Table 2. The nonnegativity constraint is seen to be generally useful with the nominal relaxation factors, particularly when the data are limited by the measurement geometry. But with optimization, huge improvements in detectability are ob-

tained in these cases. Very large relaxation factors are preferred, in fact much larger than might be expected. However, when it is realized that the non-negativity constraint has the effect of undoing the agreement with each measurement that should result from an update, it seems reasonable that overrelaxation is needed. Neither the use of nonnegativity nor the optimization has much benefit when the data are complete but noisy. It is possible that this conclusion depends heavily on the type of task posed and the decision variable adopted for the performance of the detection task. It seems that the task of identification of the discs as separate entities might yield a different conclusion about the value of the nonnegativity constraint when the data are noisy.

### Discussion

In some of the imaging situations studied, the use of the nonnegativity constraint in ART significantly increases the detectability of objects, especially when the data consist of a limited number of noiseless projections. Optimization is accomplished by varying the relaxation factor, both in terms of its initial value and the rate of its decline with iteration number. The detectability in the reconstructions obtained with constrained ART is dramatically enhanced by the optimization procedure in some cases. It is found that optimization of ART with respect to conventional measures of reconstruction quality, such as rms difference from the original image, results in reconstructions with more artifacts and lower detectability. For unconstrained ART, little improvement was achieved through optimization.

It is concluded that it is important to optimize image-reconstruction algorithms on the basis of what is most important, which can often be defined in terms of a task that is to be performed using the final image. The approach taken here is based on a Monte Carlo simulation of the complete imaging process from the composition of the original scene to the final interpretation of the reconstructed image. This method is consistent with the assertion that an algorithm can only be properly evaluated by testing it on a statistically meaningful sample of trials in which all the uncontrollable variables in the problem are varied. This numerical simulation technique has several great advantages. It can be used to evaluate the net effect of complex scenes on the reconstructed images. It is particularly useful in situations that do not lend themselves to analytic analysis, as in nonlinear algorithms like constrained ART. It can optimize the performance of iterative algorithms for an arbitrary number of iterations. These issues cannot be addressed directly by theoretical approaches to optimization. The major disadvantage of relying on the Monte Carlo numerical technique is that each result applies only to the specific imaging situation tested and generalizations are seldom possible.

The method for optimizing tomographic reconstruction presented here suggests a way to evaluate and optimize the design of neutron-diffraction spectrometers together with the performance of the required data-unfolding schemes. For a postulated mix of broad and narrow peaks that occur on a variable back-

ground, one could determine how well the presence of each peak is detected. To push the technique further, it would be possible to ascertain how well one could estimate the various parameters associated with each peak (amplitude, width, position) from the final reconstructed data. This approach to data evaluation can provide a firm basis upon which to make decisions about spectrometer design.

## References

- [1] H. C. Andrews and B. R. Hunt. *Digital Image Restoration*. Prentice-Hall, Englewood Cliffs, New Jersey, 1977.
- [2] K. M. Hanson. Method to evaluate image-recovery algorithms based on task performance. *Proc. SPIE* 914, 336-343, 1988.
- [3] K. M. Hanson. POPART - Performance OPTimized Algebraic Reconstruction Technique. *Proc. SPIE* 1001, 318-325, 1988.
- [4] K. M. Hanson. Variations in task and the ideal observer. *Proc. SPIE* 419, 60-67, 1983.
- [5] R. Gordon, R. Bender, and G. Herman. Algebraic reconstruction techniques for three-dimensional electron microscopy and x-ray photography. *J. Theor. Biol.* 29, 471-481, 1970.
- [6] S. Kaczmarz. Angenährte Auflösung von Systemen linearer Gleichungen. *Bull. Acad. Polon. Sci. Lett.* A35, 355-357, 1937.
- [7] K. Tanabe. Projection method for solving a singular system of linear equations and its applications. *Numer. Math.* 17, 203-214, 1971.
- [8] G. T. Herman, A. Lent, and P. H. Luts. Relaxation methods for image reconstruction. *Commun. Assoc. Comput. Mach.* 21, 152-158, 1978.
- [9] Y. Censor, P. P. B. Eggermont, and D. Gordon. Strong underrelaxation in Kaczmarz's method for inconsistent systems. *Numer. Math.* 41, 83-92, 1983.
- [10] A. D. Whalen. *Detection of Signals*. Academic, New York, 1971.
- [11] K. M. Hanson. Detectability in computed tomographic images. *Med. Phys.* 6, 441-451, 1979.

## Workshop summary on data treatment and techniques

*R. N. Silver*  
Theoretical Division/Los Alamos Neutron Scattering Center  
Los Alamos National Laboratory  
Los Alamos, NM 87545  
USA

*M. W. Johnson*  
Rutherford-Appleton Laboratory  
Chilton, Didcot, Oxon, OX11 0QX  
UNITED KINGDOM

The goal of neutron scattering experiments is to measure the neutron scattering law, which is proportional to the correlation functions of the condensed matter systems of scientific interest. The data produced in neutron scattering experiments is equal to a convolution of the scattering law with a spectrometer resolution function, with the addition of Poisson noise due to the finite counting statistics and of background due to other physical processes taking place in the spectrometer. The data may be incomplete, may be measured at only a discrete set of points, and may have systematic errors. The problem of inferring the scattering law from such data is central to the extraction of information from the neutron scattering technique.

The simplest, and most popular, approach is to assume that the raw data provides a first approximation to the scattering law. However, the raw data may poorly represent the scattering law because of distortions due to the measurement process. Especially for the time-of-flight techniques used in pulsed neutron sources, the raw data may be presented in a space of instrument variables (e.g. scattering angle, time-of-flight channel) which is different from the space of physical variables (e.g. momentum transfer, energy transfer) of interest. The ability to accurately display data in physical variables may be critical to real-time decisions about the conduct of experiments.

To date, most neutron scattering experiments have been analyzed by fitting the data with models using a minimum of parameters which, at least implicitly, assumes specific physical processes underlying the neutron scattering law. Such parameter estimation procedures depend on the accuracy with which one knows the resolution functions and backgrounds of the spectrometer. The paper by Bywater, Williams, and Carpenter in this workshop addresses the measurement of the pulse shapes of moderators from pulsed neutron sources which dominates the instrument resolution functions. Parameter estimation also depends on the sensitivity of the data to the parameters one wishes to determine, and on the physical validity of the fitting model. Such

procedures can be well-controlled in many cases, e.g. the Rietveld profile refinement method for the analysis of powder diffraction data for neutron crystallography. They can also be poorly-controlled especially in cases where the prior physical knowledge is incorrect, e.g. fitting Gaussian peaks to data which are in fact Lorentzian broadened.

To go beyond these two traditional procedures for analyzing neutron scattering data, one can attempt to infer the scattering law directly from the data. Such statistical inference problems are inherently ill-conditioned because there may be an infinity of scattering laws all of which fit the data according to a chi-squared criterion. The problem is to use the data to make the best choice of scattering law, termed the *image*, including whatever prior information about the scattering law one has such as sum rules, positivity, physical properties, etc.

Such image processing problems are not unique to neutron scattering. Sophisticated data analysis methods have been developed to handle similar problems in other fields of research such as radio astronomy, magnetic resonance imaging, computed x-ray tomography, etc. The most successful of these are the maximum entropy and Bayesian methods. Bayes' theorem provides a systematic approach to statistical inference. It states that the probability of the image after an experiment (the *Posterior*) is the product of the probability of the image before the experiment (the *Prior*) times the modification of the image probability by the data (the *Likelihood*). In the maximum entropy (*MaxEnt*) method the Prior is the exponential of the Shannon/Jaynes entropy of the image relative to a starting model. The MaxEnt image reconstruction is obtained by maximizing the Posterior probability. The most important properties of MaxEnt are that it enforces the positivity of the scattering law, and it puts structure in the image only if it is warranted by the data. Moreover, it permits the incorporation of other forms of prior information such as physical knowledge and, therefore, it provides an iterative approach to image reconstruction. Because of the success of the maximum entropy method in other fields of research, and the obvious need for it in neutron scattering research, maximum entropy has recently been applied to time-of-flight experiments at the LANSCE and ISIS pulsed neutron sources. An excellent introduction with specific applications to pulsed neutron sources is presented by D. S. Sivia in these proceedings. This paper demonstrates that enormous improvements in image quality are obtainable with the maximum entropy method compared with the popular, "the raw data approximates the scattering law", philosophy.

Several of the workshop papers are concerned with more technical aspects of the application of maximum entropy method to pulsed neutron sources. The paper by Johnson and Litster provides empirical experience on the application of the maximum entropy method to the deconvolution of the typical spectra found in neutron scattering research. The paper by Soper addresses

the prior knowledge which must be incorporated in the maximum entropy method in order to reliably extract the radial distribution function of amorphous materials and liquids from the incomplete scattering data obtained in neutron diffraction experiments. The paper by Silver, Sivia, and Pynn uses the maximum entropy technique to assess the relative ability of various instrument resolution functions to convey information about the scattering law.

More broadly, we emphasize that the application of modern methods of data analysis to neutron scattering may lead to a sea-change in how we analyze and display data, and even revolutionize the criteria for optimizing neutron scattering instrumentation and neutron sources. The appropriate philosophy is stated in the paper by Hanson: "...the data collection system includes both the spectrometer design and the subsequent data analysis... Optimization of the quality of the final data should also include the effects of the data processing that may be required for the proper interpretation of the data." Hanson goes on to provide a specific example of data analysis algorithm optimization for the case of the Algebraic Reconstruction Technique. The paper by Sivia, Silver and Pynn demonstrates by simulations that the maximum entropy data analysis procedure leads to a different optimization of instrument resolution functions than the popular, "the raw data approximates the scattering law," philosophy.

Neutron scattering is an inherently signal limited and expensive technique, and therefore it is imperative to optimize spectrometers, sources and experiments. The use of modern data analysis methods can lead to improvements of an order-of-magnitude or more in the information which can be extracted from neutron scattering data. Optimization of spectrometers and neutron sources based on modern data analysis procedures can potentially lead to further orders-of-magnitude gains. An information theory of spectrometer design should be a high priority in neutron scattering research. Such *software* approaches to advancing the state-of-the-art in neutron scattering research can be far more cost-effective than the conventional *hardware* approaches (e.g., increasing proton currents from accelerators, boosted targets, etc.) which have dominated prior meetings of the International Collaboration on Advanced Neutron Sources.

We believe that modern data analysis methods, such as maximum entropy image processing, will become a dominant theme in the future development of the neutron scattering technique.

## Design for a second-generation proton storage ring at LAMPF

*E. P. Colton*  
Los Alamos National Laboratory  
Los Alamos, NM 87545  
USA

**ABSTRACT:** A conceptual design is presented for a second-generation proton storage ring complex at LAMPF. The facility would consist of two stacked racetrack-shaped machines. These machines would deliver a 1.2-mA beam of 1.6-GeV protons at 48 Hz. The pulse length would be 1.75  $\mu$ sec which represents a time compression of 570.

### 1. Introduction

There is some local interest for a 1.6-GeV proton storage ring (PSR) which will deliver nominally 2 MW of beam power at 48 Hz. The design for the present PSR is just 80 kW so the improvement is a factor of  $\sim 25$ . The 1.6-GeV kinetic energy would be obtained from an add-on linac to LAMPF. The flux requirement is  $1.5 \times 10^{14}$  ppp at 48 Hz; the beam would be sent alternately to neutron production, and neutrino production experiments, respectively. These facilities would each operate at 24 Hz.

This request can be met by using two stacked rings which are respectively fed with two successive LAMPF macropulses. Each ring would store  $7.5 \times 10^{13}$  protons. Thus, 96 of the 120 LAMPF macropulses normally available in 1 sec would be devoted to these ends. Additionally, the present  $H^-$  source would have to be upgraded by a factor of two. Protons would be fast extracted in a single turn from each ring and sent to the experiments in box-car fashion. The pulse length would be 1.75  $\mu$ sec, so the time compression is a factor of  $\sim 570$ . There are two constraints which must be met: (1) The slow losses which occur in the Los Alamos Proton Storage Ring (PSR) cannot take place in these rings.<sup>1</sup> (2) It is necessary to store beam in one of the rings for up to 8 msec, so the rings must be stable against coherent instability. In view of these

requirements, it appears to me that certain steps have to be taken—they are spelled out below.

1. The injection must be direct  $H^-$  to  $H^+$  in a stripping foil instead of the two-step process used in the PSR. The stripping magnet introduces extra beam divergence in the bend plane. The lack of control over the neutral beam is another negative aspect.
2. The injected  $H^-$  beam should be matched to the machine in 6-D phase space. We need to limit the injected  $dp/p$ , and to stabilize the position of the beam at the foil in  $x-x'$  and  $y-y'$  phase space.
3. We need to choose an aperture large enough to contain the tails of the beam to the 99.9% level. Collimation schemes have to effectively restrict losses to the 100 nA level locally. Mainly, we are looking to absorb protons scattered out of the normal acceptance by large-angle scatters in the stripping foil.
4. Effective  $H^0$  and  $H^-$  dumps should be provided to remove partially stripped or unstripped particles.
5. Efforts should be made to reduce the number of foil traversals for circulating protons. These include beam bumping, transverse painting,  $x-y$  mixing by means of skew quadrupoles, etc. The foil should be positioned at a beam waist with small  $\beta^*$ .
6. The machines should have long straight sections for injection, extraction and rf cavities.
7. We need to maintain a clean kicker gap for lossless extraction.
8. The maximum transverse space-charge tune shift  $-dQ_y$  should not exceed 0.15. This requirement stipulates the beam core emittance.
9. With regard to coherent instabilities, we should endeavor to reduce the peak currents seen in the PSR, as well as maintain a significant  $dp/p$  width; this may be difficult to achieve with conventional rf systems. We really need to make a smooth vacuum chamber with gradual transitions.
10. Sextupole magnets should be included for chromaticity control, but their use should not reduce the ring admittance to below 1000 mm-mr.

The machine requirements have been met in a first order design which is the subject of the remainder of this report. The design layout is shown



in Fig. 1. The shape is that of a near racetrack. The four bend sections are  $90^\circ$  bend achromats. The two short straight sections each contain fast extraction systems. The rf cavity is located in a dispersion free zone. The long straight section containing the injection area includes a special injection chicane, the stripping foil, an  $H^-/H^0$  dump, two orbit bumpers, and two halo collimators. All of these are discussed below.

### 1.6 GeV Compressor

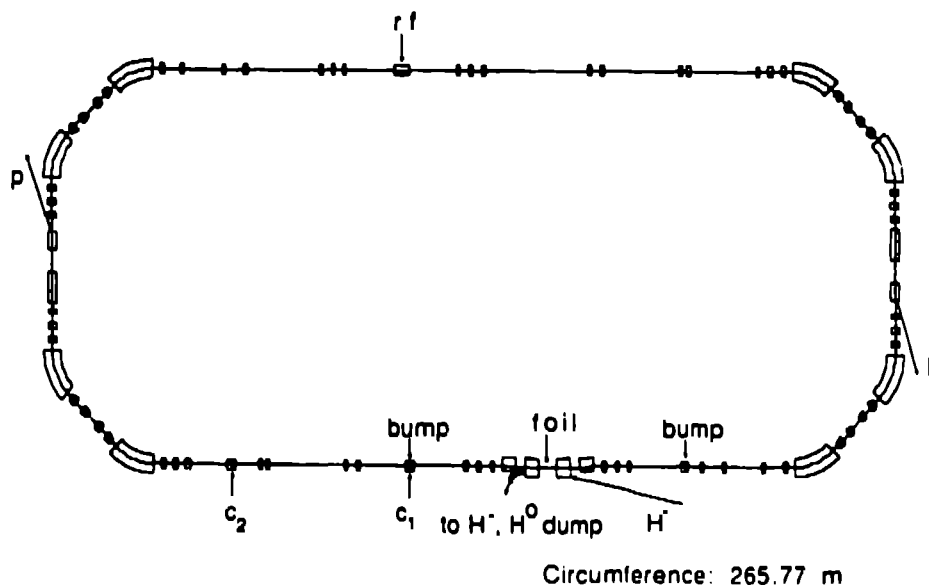


Fig. 1. Plan view layout of the new compressor rings.

Table I lists the parameters for the designed machines. The revolution frequency is 1.048 MHz, so the revolution time is 954 nsec. The pulses from the two rings will be extracted sequentially and sent in box-car fashion to the experimental areas. Allowing for a kicker gap of about 150 nsec, we would expect a final delivered pulse length of 1750 nsec ( $800 + 150 + 800$ ).

In Section 2, I discuss the lattice design. In Section 3, I explain the mechanics of beam transfers. Collimation is briefly discussed in Section 4. The rf system is treated in Section 5. The subject of coherent instabilities is treated in Section 6. Concluding remarks are given in Section 7.

**Table I. Machine Parameters**

Kinetic Energy	1.6 GeV
Average Current Delivered	1.2 mA
Repetition Rate	48 Hz
	(24 to produce spallation neutrons)
	(24 to produce neutrinos)
Circumference	265.77 m
Protons per Pulse	$1.5 \times 10^{14}$
Number of Rings/Superperiods	2/2
Circulating Current/Ring	12.6 A
Revolution Frequency	1.048 MHz
Number of Turns Injected	1048
Betatron Tunes $Q_x, Q_y$	5.23, 4.23
Chromaticity $Q'_x, Q'_y$	-7.32, -6.76
Transition Gamma $\gamma_t$	8.19

## 2. Lattice Design

The machine lattice functions across half the machine are depicted in Fig. 2(a); the maximum dispersion is 5.1 m in the center of an achromat. The  $\beta^*$  is 3.0 m at the stripping foil location. The beam halfwidths are shown in Fig. 2(b). These sizes were calculated using the expressions

$$x = \sqrt{\beta_x \epsilon_x} + \left| \eta_x \frac{dp}{p} \right| \quad \text{and} \quad y = \sqrt{\beta_y \epsilon_y} \quad (2.1) \text{ and } (2.2)$$

with  $\epsilon_x = \epsilon_y = 100$  mm-mr and  $dp/p = 40.003$ . These values were obtained from a study of the injection process. The maximum vertical beam size in the dipoles is of order 135 mm. The betatron tunes for the whole machine are  $Q_x = 5.23$  and  $Q_y = 4.23$ . The uncorrected chromaticities  $dQ_x/dp/p = -7.32$  and  $dQ_y/dp/p = -6.76$ . The transition gamma  $\gamma_t = 8.19$  so  $\eta = \gamma_t^2 - \gamma^2 = 0.1217$ .

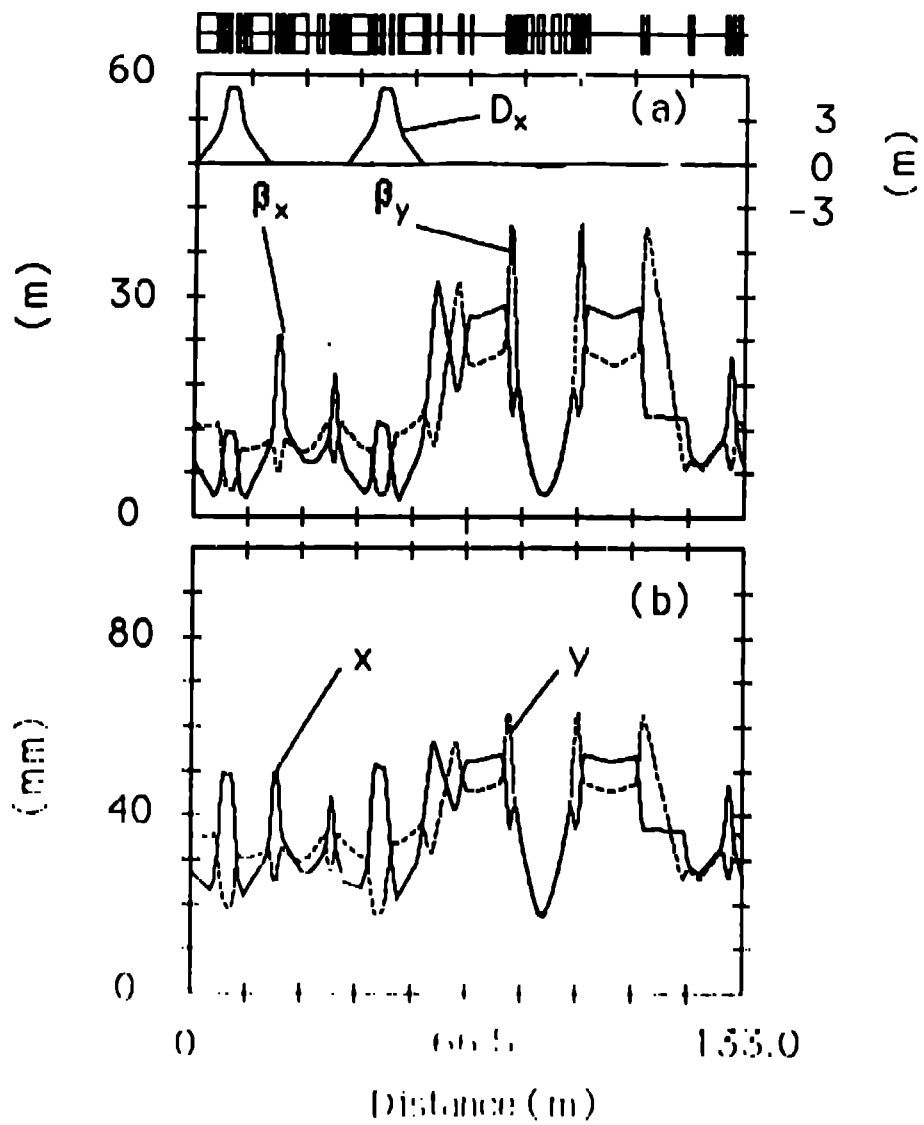


Fig. 2. (a) Machine lattice functions for 1 superperiod, (b) half beamwidths calculated using Eqs (2.1) and (2.2). The emittances  $\epsilon_x$  and  $\epsilon_y$  are both 100 nm-mr and  $dp/p = 0.003$ .

### 3. Beam Transfers

#### A. $H^-$ Injection

The ring injection takes place via the process  $H^- \rightarrow H^+$  in a  $250\text{-}\mu\text{g}/\text{cm}^2$  carbon stripping foil. A plan view of the injection region is shown in Fig. 3; the four dipoles in the center translate the proton beam 171.5 mm to beam left of center at the stripping foil location (call this the center). The two fast orbit bumpers are separated by  $180^\circ$  in horizontal betatron phase—they serve to further displace the translated proton beam at the foil. The bump starts out at 20 mm left of center and reduces to 10 mm during the 1-msec injection period (this time corresponds to 1050 turns). After the injection the bumps are rapidly reduced to zero. Referring to Fig. 3, the  $H^-$  are injected into the second dipole and are nominally placed at 25 mm beam left of center, and on axis vertically.

#### COMPRESSOR INJECTION REGION

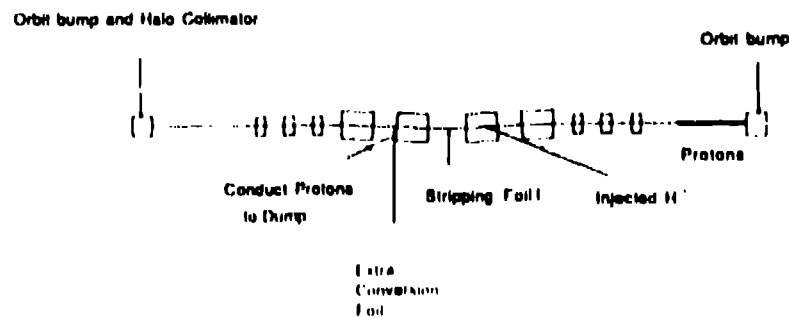
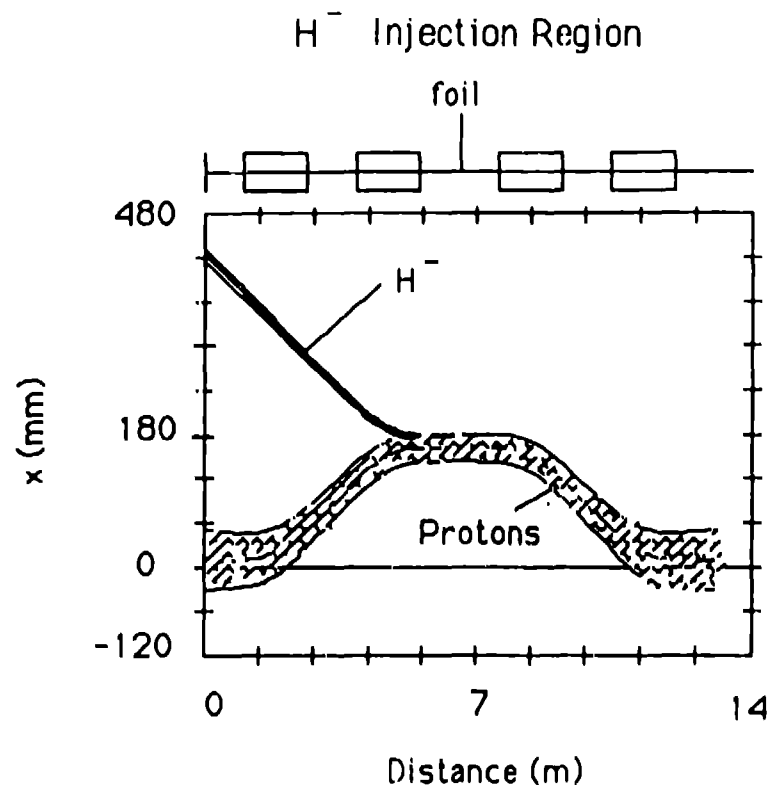


Fig. 3. Plan view of the  $H^-$  injection region.

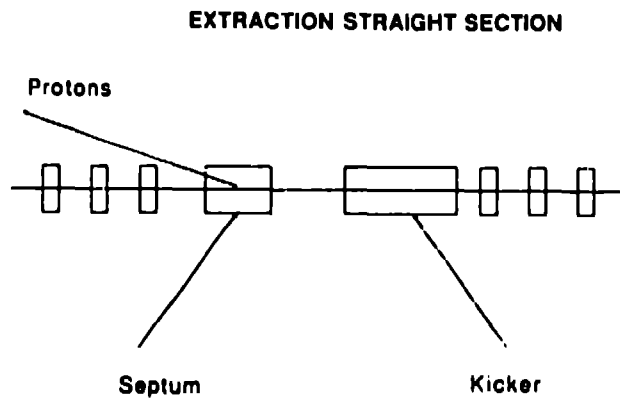
Figure 4 shows a closeup plan view of the circulating proton and injected  $H^-$  beams in the region of the four dipole chicane. Unstripped  $H^-$  or partially stripped  $H^0$  will exit the third dipole displaced to the outside of the proton beam; they will pass through another stripping foil, so as to convert to protons, and then be conducted away to a dump.



**Fig. 4.** Circulating proton and injected  $H^-$  beam envelopes within the four-dipole injection chicane. The proton beam geometric emittance is 100 mm·mr. The  $H^-$  injected emittance is of order 2-3 mm·mr.

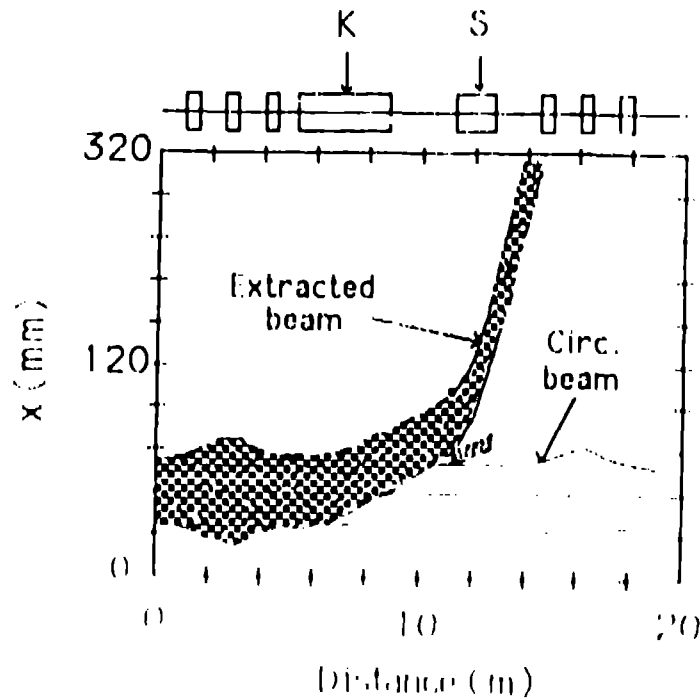
### **B. Fast Extraction**

Beam is extracted from each ring in a single turn and sent in box-car fashion to the experimental targets. Timewise, first one ring is filled in 1 msec and the second ring is filled 1/120 sec later. They are fast extracted together (separated by one revolution time). These processes are repeated 48 times per sec. A plan view layout of the extraction section is shown in Fig. 5. A 3.5 m ferrite kicker displaces the protons into the field region of a 1.5 m d.c. septum magnet from which they are conducted to the appropriate experimental area. Referring to Fig. 1, beam is extracted on alternate pulses from the two extraction sections and sent to the respective experimental targets at 24 Hz.



**Fig. 5.** Plan view of extraction straight section.

The horizontal beam envelopes in the extraction straight section are shown in Fig. 6; both the circulating and extraction envelopes are shown for an emittance of 100 mm-mr.



**Fig. 6.** Circulating and extracted proton beam envelopes in the extraction section. The emittance is 100 mm-mr.

#### 4. Collimation

The injection foil is positioned offset to the outside of the machine to reduce the number of repeated proton traversals. These traversals cause the rms transverse emittance to grow by an amount  $\beta^* \theta^2 f N(t)/2$  where  $\beta^*$  is the beta function at the foil,  $\theta$  is the rms scattering angle for a single traversal, and  $f N(t)$  is the number of foil traversals in  $N$  turns up to time  $t$ . To minimize the emittance growth we designed for  $\beta^* = 3.0$  m at the foil and we try to reduce the probability for a traversal ( $f$ ) by locating the foil edge close to the injected  $H^-$  beam spot. In fact, rms emittance growth due to foil scattering is only a few percent.

Of more concern are the large angle scatters due to nuclear or single coulomb scattering in the thin stripping foil. The largest angle we can reasonably expect to contain is about 2 mr. The probability for even larger scatters is  $\sim 7 \times 10^{-6}$ . If we roughly take 25 traversals for the average proton, then we would expect for 600  $\mu A$

$$\text{loss} = 600 \times 10^{-6} \times 25 \times 7 \times 10^{-6} = 105 \text{ nA} \quad (4.1)$$

This loss would activate each machine downstream of the foil. We plan to quickly absorb these large angle scatters in the downstream collimators  $C_1$  and  $C_2$  (see Fig. 1). The collimators are strategically placed  $90^\circ$  and  $180^\circ$  in betatron phase downstream of the stripping foil, respectively. Some adjustment to the actual design would be necessary since an orbit bump magnet is coincident with  $C_1$ .

#### 5. Rf System

The function of the rf system is to (i) maintain a longitudinal gap in the beam for lossless extraction and (ii) to produce enough relative momentum spread to keep the circulating protons coherently stable. The average circulating current is 12.6 amperes in each ring at full intensity. With a fundamental rf system, bunching will occur and the peak currents can be expected to rise to over 40 amperes; this will surely result in coherent instability and beam loss. For these rings I suggest use of the rf waveform shown in Fig. 7. The rf voltage is composed of the fundamental plus four harmonics

$$V(\phi) = V_0 \sum_{i=1}^5 V_i \sin(i\phi) \quad (5.1)$$

with the indicated values for  $V_i$ . The voltages on the end act like repulsive barriers to the beam, hence the name barrier bucket. This waveform should maintain a gap in the beam. However, little or no increase in the  $dp/p$  occurs. We obtain larger  $dp/p$  values by just sweeping the energy of the injected beam in the last linac module. This sweeping is done sinusoidally with two oscillations over the 1 msec injection period.

A simulation has been performed in order to demonstrate the viability of the method. Beam was injected uniformly in rf phase  $\phi$  for  $|\phi| \leq 2.4$  radians—this corresponds to populating  $\sim 146$  microbunches of the 192 possible. The  $dp/p$  were generated in a Gaussian fashion with  $\sigma_p/p = 0.05\%$ . During injection, the central value of the  $dp/p$  varied sinusoidally with turn number  $t$  as  $0.002 \sin(2\pi t/525)$  (in absolute units). The rf voltage of the fundamental  $V_0 + V_1 = 3.5$  kV, so the peak voltage of the waveform shown in Fig. 7 was 16.9 kV. The projections of  $\phi$  and  $dp/p$  are given in Figs. 8(a) and 8(b), respectively. The gap is maintained in Fig. 8 and the rms  $\phi$  width is unchanged from the injected value. The FWHM of the  $dp/p$  distribution is of order 0.5%.

The required rf voltages are relatively modest at the fundamental and its four higher harmonics. Perhaps two cavities will be required. The design can be similar to the PSR cavity with its very low R/Q, so beam loading should not be a problem. The effects of longitudinal space charge will be to decrease the action of the rf cavity, i.e., to fill in the extraction gap. Increased rf voltage is necessary to compensate this effect.

## 6. Beam Stability

### A. Space-Charge Tune Shift

The space-charge tune shift is given by

$$|\Delta Q_y| = G_y \frac{2.4 \text{ mm}}{t N} \frac{\text{m}}{10^{13}} \frac{N}{B\beta\gamma^2} \frac{E_y}{B\beta\gamma^2} \quad (6.1)$$

where  $G_y$  is a form factor depending upon the  $x$   $y$  spatial distribution,  $t_N$  is the normalized vertical emittance which contains 87% of the beam, and  $N$  is the number of circulating protons. The remaining term is approximated by

$$\frac{E_y}{B\beta\gamma^2} \sim \frac{1.02}{B\beta\gamma^2} + 0.045J \quad (6.2)$$

where  $B$  is the bunching factor,  $J = pe/F$ , and  $\gamma = E/moc^2$ .



## Harmonic 3 Barrier Bucket

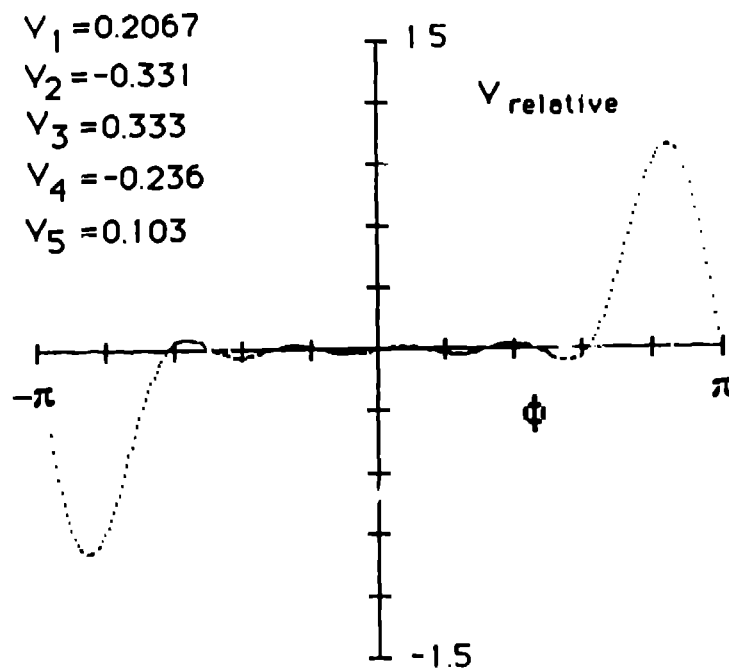


Fig. 7. Proposed rf waveform. The voltage is given by Eq. (5.1).

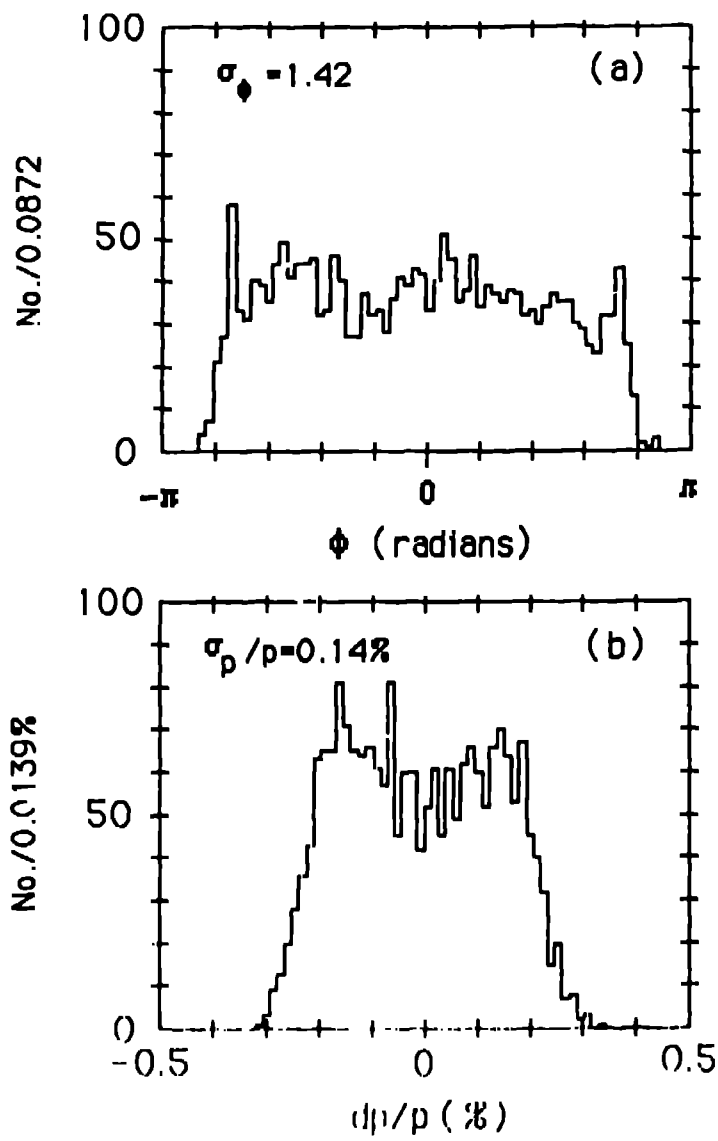


Fig. 8. Rf simulation results for 1050 turns of injection.

We pessimistically take  $G_v = 2$  corresponding to a 2D Gaussian distribution. Next,  $\epsilon_N$  is given by  $\epsilon_v \beta \gamma$  and we use  $\epsilon_v = 40$  mm-mr as determined in the injection simulations. I assume  $N = 7.5 \times 10^{13}$  and a bunching factor  $B = 0.65$ . With these choices the space-charge tune shift is computed to be  $|\Delta Q_v| = 0.098$ .

### B. Coherent Stability

The major coupling impedances are imaginary and due to space charge. They are

$$\frac{Z_\ell}{n} = \frac{i}{2} \frac{Z_0}{\beta \gamma^2} \left( 1 + 2 \ell n \frac{b}{a} \right) \quad (6.3)$$

where  $Z_0$  is the impedance of free space,  $Z_0 = 377$  ohms, and  $b/a$  is the ratio of beam pipe to beam radius  $b/a \sim 2.67$ . We obtain  $Z_\ell/n = i82\Omega$ . The transverse

$$Z_\perp = \frac{iRZ_0}{\beta^2 \gamma^2} \left( \frac{1}{a^2} - \frac{1}{b^2} \right) = i2.4 \times 10^6 \Omega/m \quad (6.4)$$

I chose  $a = 0.03$  m and  $b = 0.08$  m. The average circulating current  $I = 12.6$  amperes and the peak  $\hat{I} = 19.4$  amperes for the rf system contemplated.

The test for longitudinal stability

$$\left( \frac{dp}{p} \right) \geq \left[ \frac{\hat{I}}{\beta^2 |\eta| E} \left| \frac{Z_\ell}{n} \right| \right]^{1/2} \quad (6.5)$$

where  $\eta = \gamma_t^{-2} - \gamma^{-2} = -0.1218$ .

I find  $(dp/p)_{FWHM} \geq 0.24\%$ . This is easily satisfied by our beam with  $(dp/p)_{FWHM} \sim 0.5\%$  so the beam will be longitudinally stable.

The test for transverse stability

$$|Z_\perp| \leq 4 \frac{\beta E}{i} \frac{Q_v}{R} \left[ (n - Q_v) \eta + \frac{dQ_v}{dp/p} \right] \left( \frac{dp}{p} \right)_{FWHM} \quad (6.6)$$

results in

$$|Z_\perp| \leq 0.2395 \times 10^6 [(n - 4.23) \times 0.12 + 6.75]$$

If we use  $|Z_{\perp}| = 2.4 \times 10^6 \Omega/\text{m}$ , then we find the machine is stable for  $n > 31$  or frequencies  $f > 32.5$  MHz. Below this frequency the machine is unstable with a growth rate given by

$$\frac{1}{\tau} = \frac{Ic}{4\pi Q_y E} (Re Z_{\perp}) = 2.8 \times 10^{-2} Re(Z_{\perp}) \text{ sec}^{-1} .$$

For  $\tau > 500 \mu\text{sec}$  we need  $Re(Z_{\perp}) \leq 71 \text{ k}\Omega/\text{m}$ . This requirement may be difficult to meet. However, the beam can be stabilized by simply increasing the chromaticity  $dQ_y/(dp/p)$  to  $-10$  from its nominal value of  $-6.75$ .

## 7. Conclusion

These high-intensity machines do look feasible. If constructed, they would supply 12 times more beam power for producing spallation neutrons than the PSR design. A number of subjects still need to be addressed: collimator calculation, tracking, optimization, and a cost estimate.

## Reference

1. R. J. Macek, D. H. Fitzgerald, R. L. Hutson, M. A. Plum, and H. P. Thiessen, Los Alamos National Laboratory Report LA-UR-88-1682 (1988).

## Some neutronic calculations for KENS-II

*Y. Kiyanagi*

Department of Nuclear Engineering, Faculty of Engineering  
Hokkaido Univ. Sapporo 060  
JAPAN

*M. Arai and N. Watanabe*

National Laboratory for High Energy Physics  
1-1 Oho, Tsukuba-shi, Ibaraki 305  
JAPAN

### Introduction

Proton energies of the intense spallation neutron sources currently in operation or designed are in the range  $E_p \leq 1.1$  GeV. Optimization studies of the target station have so far been performed for these proton energies.

The KENS-II project has been included in the Japanese Hadron Facility Project where we have to share the proton accelerator, a so-called "First Ring", with Meson Arena for nuclear physics and  $\mu$ SR experiments. The possible highest proton energy for this accelerator is 2 GeV, which is the highest among the world's spallation neutron sources. We, therefore, performed some neutronic calculations with 2 GeV protons in order to have a good knowledge of the neutronic characteristics and the optimal parameters of the target station for KENS-II.

### Target model and calculation codes

First we considered cylindrical targets and then rectangular parallelepiped targets. The target was a uniform mixture of target metal with coolant and cladding<sup>[1]</sup>, which was similar to the model target used in the optimization study of ISIS<sup>[2]</sup>.

Source neutrons below 15 MeV produced in a target were calculated using the NMTC/JAERI code<sup>[3]</sup>. Leakage neutrons from a bare target and slow neutrons emitted from a moderator were calculated using the TOWTRAN-II<sup>[4]</sup> and MORSE-DD<sup>[5]</sup> codes, respectively, coupled with the NMTC/JAERI code.

### Number of source neutrons

Figure 1 shows the number of source neutrons below 15 MeV produced in the target of various materials as a function of proton energy. Here, the length and the radius are fixed at 32 and 5 cm, respectively. The proton-beam profile was assumed to be cylindrical, 2.35 cm in radius, for simplicity. The results do not include the neutron multiplication by low energy nuclear reactions.

We chose tungsten as a reference material for the non-fissile target because of its

relatively high neutron yield and the practicality. In the present study, we performed calculations only on two target materials U(uranium) and W(tungsten).

The number of source neutrons below 15 MeV produced in the target is shown in Fig. 2 as a function of target length. The number is saturated at about 16, 28, 43 and 50 cm for the proton energies 0.5, 0.8, 1.5 and 2 GeV, respectively.

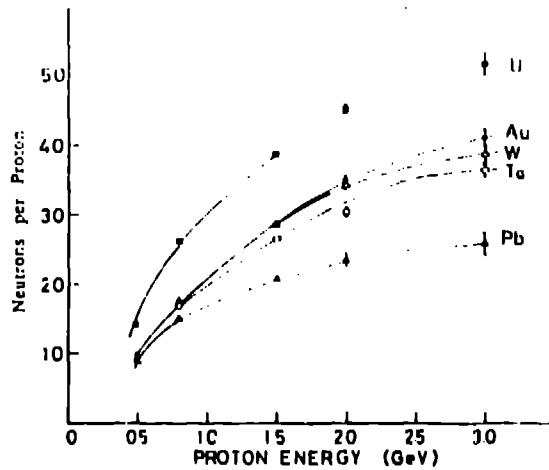


Fig. 1 Number of neutrons below 15 MeV produced in various targets per proton as a function of proton energy. Lines are guides for eye.

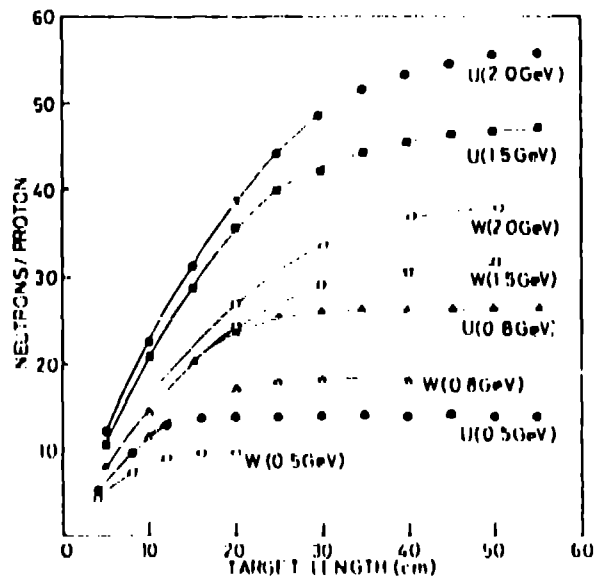


Fig. 2 Number of neutrons below 15 MeV produced in target per proton at various energies as a function of target length. Lines are guides for eye.

### Leakage neutrons

The number of leakage neutrons from the cylindrical surface of the bare target is shown in Fig. 3 as a function of target radius. The target lengths used in this calculation were 16, 30, 44, 55 cm for 0.5, 0.8, 1.5, 2 GeV, respectively, which gave the saturated neutron yield as shown in Fig. 2.

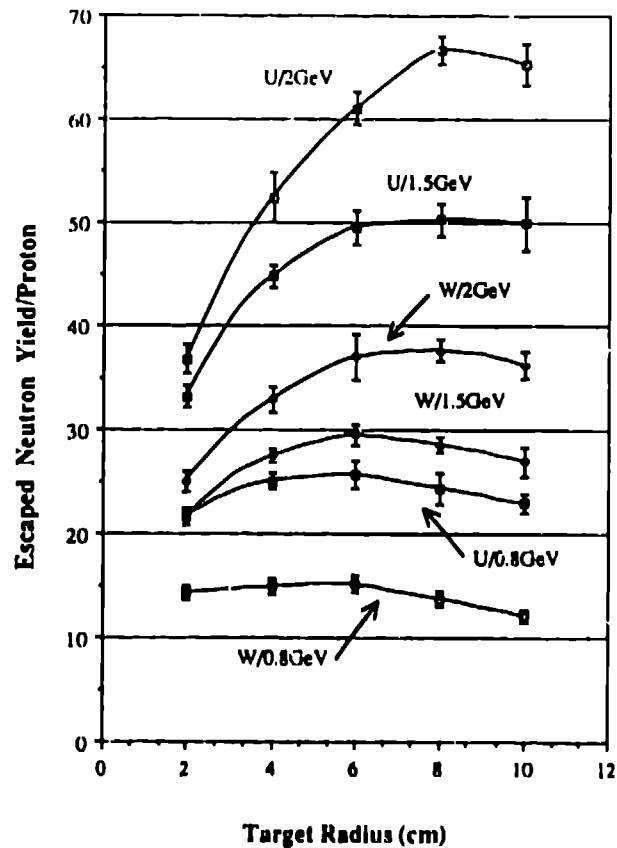


Fig. 3 Number of leakage neutrons from cylindrical surface of a target per 2 GeV proton as a function of target radius.

The number of leakage neutrons increases with increasing radius due to the neutron multiplication by low energy nuclear reactions such as  $(n, 2n)$ ,  $(n, f)$ , etc. The relative gain of a U-target to a W-target is larger for the number of leakage neutrons than for source neutrons. The reason is that uranium has lower threshold energies for such reactions than tungsten. The number of leakage neutrons from the cylindrical surface decreases at a larger radius, because the leakage from the end surfaces becomes significant.

The number of leakage high energy neutrons above 15 MeV from the U-target is plotted in Fig. 4 as a function of target radius for various proton energies. The

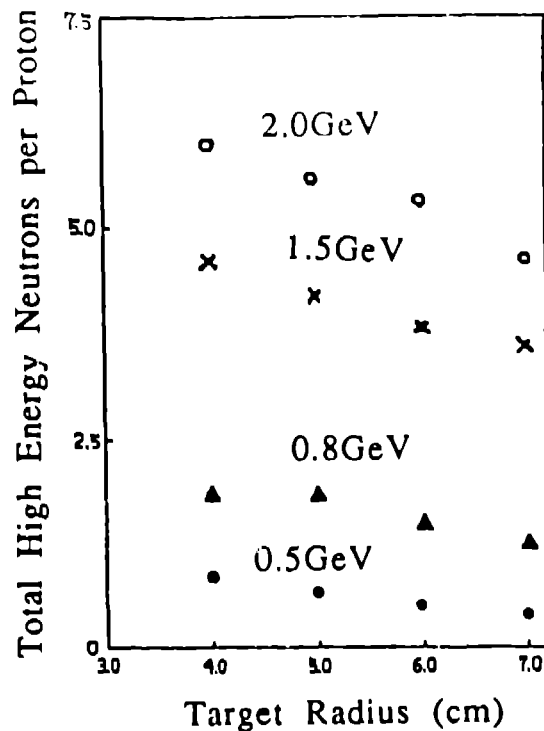


Fig. 4 Number of leakage high-energy neutrons ( $E_n > 15$  MeV) per proton as a function of target radius for various proton energies.

intensities decrease with increasing target radius. This is simply explained by the attenuation length of the target material for high energy neutrons. The number increases almost proportionally to the proton energy taking into account the attenuation and the leakage from the end face.

Leakage neutron spectra from the cylindrical surface of the U-target for 2 GeV protons are shown in Fig. 5. The peak value increases and the peak energy decreases with increasing radius. The softening of the spectra at the higher energy region is due to the inelastic scattering with target nuclei, while that at the lower energy region is mainly due to the neutron moderation by the coolant  $D_2O$  in the target. The energy spectra of high energy neutrons above 15 MeV did not show a large difference between U and W.

#### Slow neutrons

A model of the target-moderator-reflector assembly is shown in Fig. 6, where two reference moderators are positioned above the target for simplicity. The reference moderator is rectangular parallelepiped ( $10 \times 10 \times 5$  cm<sup>3</sup>) of  $H_2O$  with a  $B_4C$  decoupler of cutoff energy 20 eV. The size of proton beam entrance was fixed at 10 cm in diameter in the calculation.



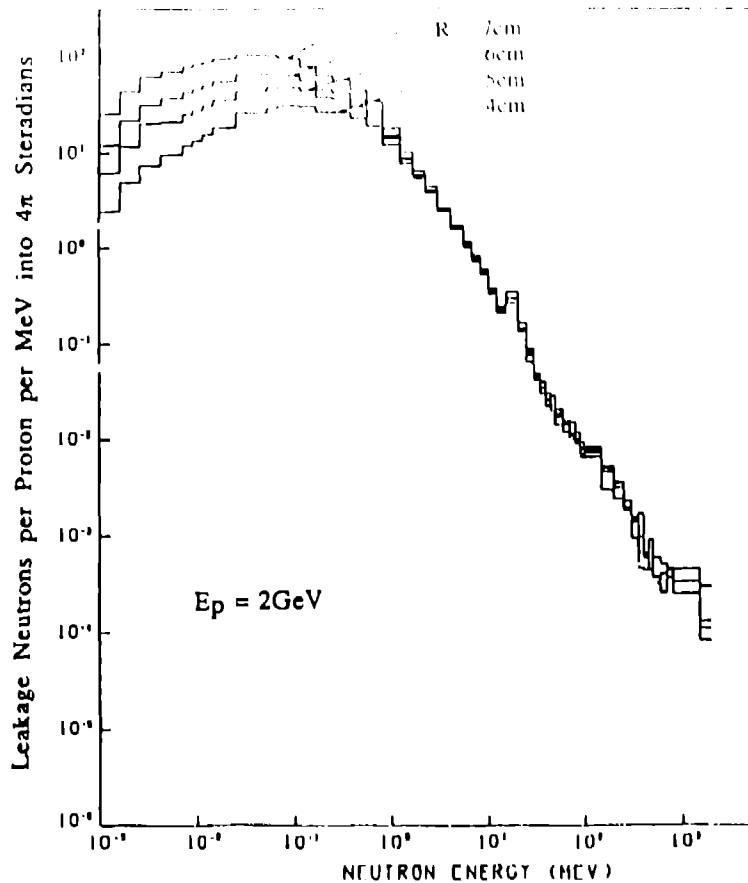


Fig. 5 Leakage neutron spectra from the cylindrical surface of a target for various target radii.

The radius is one of the most important design parameters of the target, because the coupling efficiency between the target and moderator decreases with increasing target radius. Figure 7 shows the target-radius dependence of the slow neutron intensities from the moderators for two different proton-beam sizes, 1.25 and 2.35 cm in radius. In the calculation the front face of the first moderator is aligned to the target face as shown in Fig. 6. It turned out that the optimal target radius which gives the maximum intensity is about 5 cm for both targets for the proton-beam size of 2.35 cm in radius. Present results with 2 GeV protons did not show a significant difference to those by Atchison with 0.8 GeV protons. The ratio between the maximum intensities of U- and W-targets is about 1.5, which is more or less smaller than the case for the lower proton energies. The optimal radius shifts toward smaller values for smaller proton-beam sizes. There exists appreciable gain with a smaller proton-beam size for U but not for W. This unexpected result could be attributed to the fixed size of the proton beam entrance.

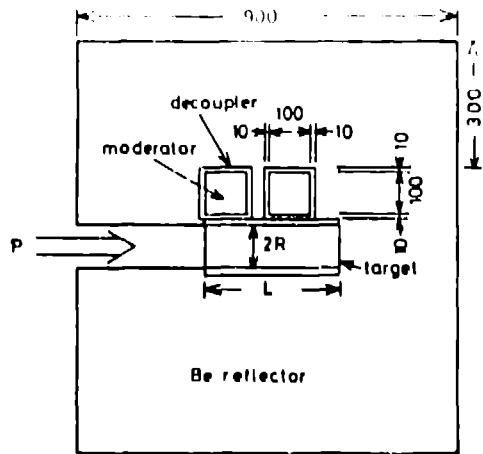


Fig. 6 Model of target-moderator-reflector assembly used for calculation.

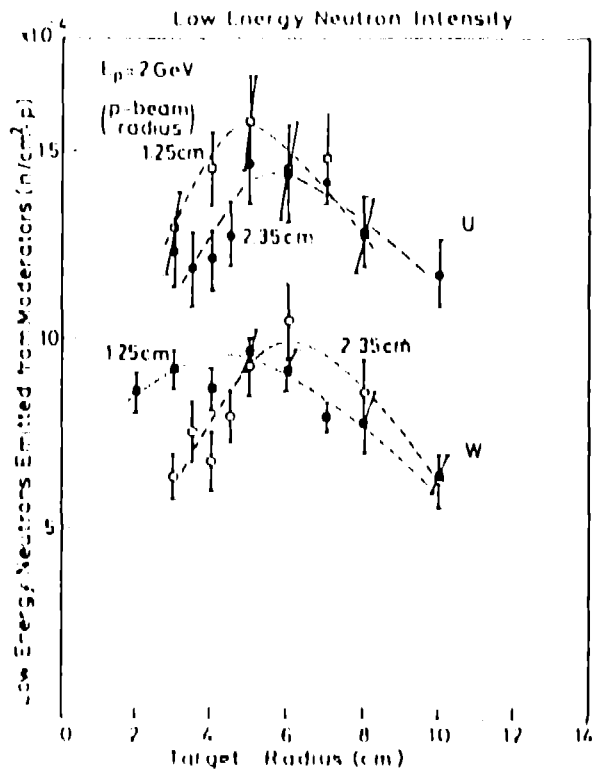


Fig. 7 Slow neutron ( $E_n < 0.9$  eV) intensities per 2 GeV proton obtained from two moderators with U- and W-target as a function of target radius for two different proton-beam sizes. Lines are guides for eye.

The axial position of moderators on the target is another important parameter to be optimized. Figure 8 shows slow neutron intensities from two moderators as a function of axial moderator position for two different proton energies. The target-moderator configuration is shown in the inset of Fig. 8. Here the parameters to be optimized are  $x$  and  $d$ . However, the separation,  $d$ , between the two moderators is fixed at 5 cm from a practical point of view. The sum of the intensities from the two moderators are also shown in the figure. A maximum appears at  $x=0$  cm for 2 GeV protons and at  $x=-4$  cm for 0.8 GeV protons. The difference reflects the axial source neutron distribution in the target shown in Fig. 9 in which we see broader features with less increase in the maximum intensity for higher proton energies. The slow neutron intensity at the maximum point for 2 GeV protons is about twice that for 0.8 GeV protons, so that the gain factor of the intensity per energy is 0.8 for 2 GeV protons against 0.8 GeV.

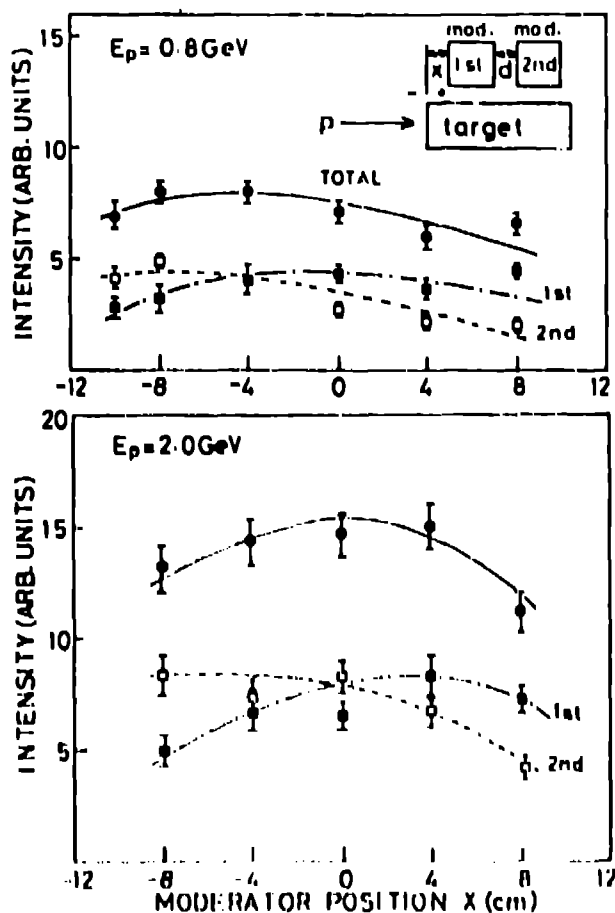


Fig. 8 Slow neutron ( $E_n < 0.9 \text{ eV}$ ) intensities per proton obtained from two moderators as a function of axial moderator position on the target. Lines are guides for eye.

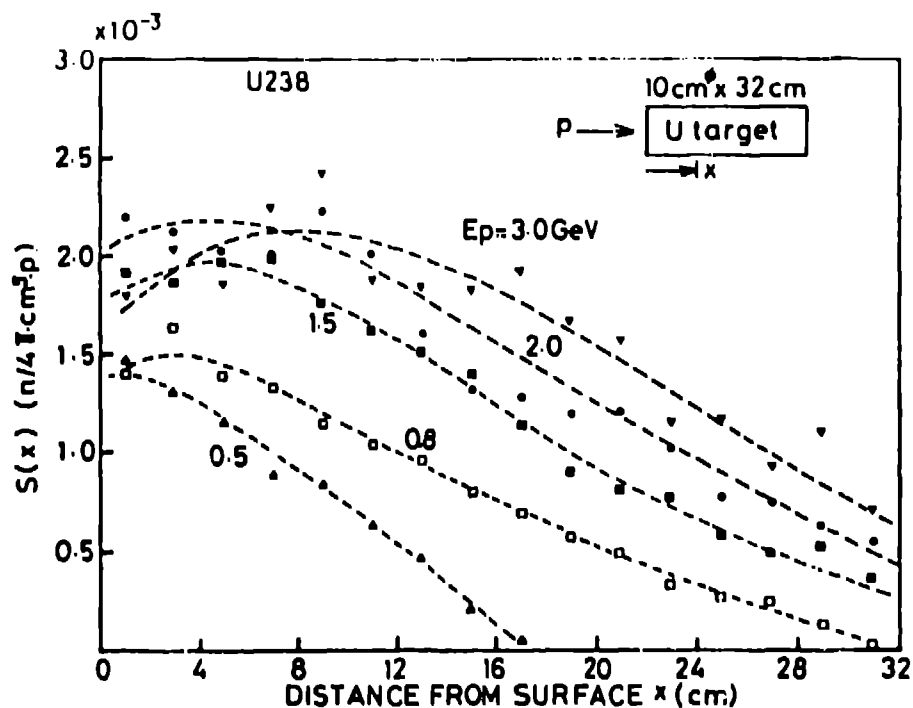


Fig. 9 Axial distributions of sub 15 MeV neutrons in target. Broken lines are guides for eye.

### Rectangular target

Next, we consider rectangular parallelepiped targets. We calculated the target width dependence on the slow neutron intensity. The dimension of the target is shown in the inset of Fig. 10, where the target height is fixed at 10 cm. The sum of the slow neutron intensities obtained from the two moderators with such a target is shown in Fig. 10. The gain of neutron intensity by increasing the lateral dimension of the target is about 10% for U but there is no gain for W. The reason is that reflected neutrons cause additional fission in the U-target but not in the W-target.

### Conclusion

The fraction of slow neutron intensity versus the proton energy becomes 0.8 for 2 GeV compared to that for 0.8 GeV, and this is higher than 0.67 calculated for source neutrons. The uranium target has a higher neutron productivity, 1.5 times that of the tungsten target, even for 2 GeV protons. The target radius and the moderator axial position have definite optimal values for 2 GeV protons in spite of the broader distribution of the source neutrons in target, and these are essentially similar to the results for 0.8 GeV protons<sup>(2)</sup>. The broad distribution with a little increase in the

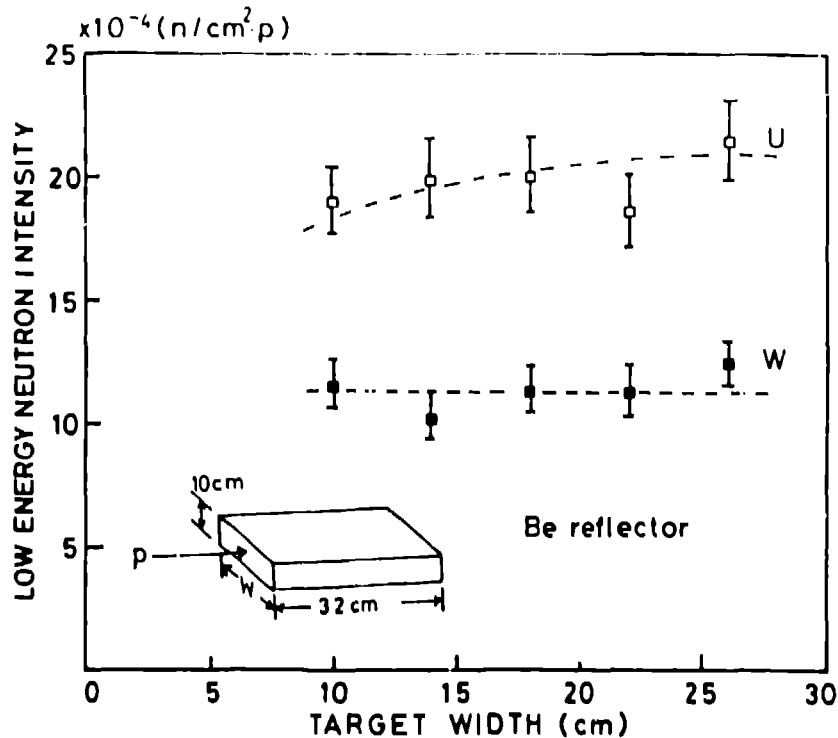


Fig. 10 Slow neutron ( $E_n < 0.9$  eV) intensities per 2 GeV proton obtained with U- and W-rectangular-parallelepiped-target as a function of target width. Broken lines are guides for eye.

maximum luminosity of source neutrons for 2 GeV protons could make it easier to remove the heat load from the target than the case for the same beam power with lower energy and higher proton current. Therefore, we could conclude that the 2 GeV protons for KENS-II do not have significant difficulties in producing slow neutrons, and that non-fissile material has higher advantages to produce neutrons for higher proton energies. Detailed neutronic calculations are now under way to design a neutron target station for KENS-II.

We acknowledge Dr. Y. Nakahara and Dr. T. Nishida for their helpful support in NMTC calculations and the stimulating discussions.



## References

1. M. Arai, et al., KENS REPORT-VI (1985/86), KEK Progress Report 86-2, 263
2. F. Atchison, RL-81-006 (1981)
3. Y. Nakahara and T. Tsutsui, JAERI-M 82-198 (1982)
4. K.D. Lathrop and F.W. Brinkley, LA-4848-MS (1973)
5. M. Nakagawa and T. Mori, JAERI-M 84-126 (1984)



## A consideration of cold neutron source for KENS-II

*N. Watanabe*

National Laboratory for High Energy Physics  
1-1 Oho, Tsukuba-shi, Ibaraki-ken, 305  
JAPAN

**ABSTRACT:** The importance of a coupled cold moderator for small angle neutron scattering experiments with pulsed neutrons is discussed in connection with a cold neutron source for KENS-II.

### Introduction

All the cold neutron sources presently in operation at pulsed spallation neutron facilities are decoupled moderators for relatively short pulse uses. Small angle scattering (SANS) of polarized and unpolarized cold neutrons is one of the most important fields of research using cold neutrons—not only in steady sources, but also in pulsed ones. However, it is believed that such experiments with a pulsed neutron source are not as favorable as with a high flux reactor. In these experiments the pulse width from such moderators is short enough for the required wavelength resolution, but the time-averaged intensity of cold neutrons is not adequate compared with that from a high flux reactor.

Table 1 compares some important parameters of cold neutron sources at the spallation neutron facilities with those at the ILL. Time-averaged cold neutron fluxes from the existing pulsed spallation neutron sources are more than two orders of magnitude smaller than that from the ILL, and therefore it seems to be difficult for those sources to compete with experiments at a high flux reactor in such fields, even though we take into account a gain factor (10–20 as discussed later) in pulsed sources, which comes from time structure. As a measure of the efficiency of a cold neutron source, here we introduce the conversion efficiency, which is defined as time-averaged  $4\pi$ -equivalent cold neutron flux on a moderator surface per fast neutron emitted from a neutron generating target or a reactor core. It may be obvious from the table that the conversion efficiency of a decoupled cold moderator in a large spallation neutron source as ISIS is much smaller than that of the ILL, while that of a small source as KENS-I is higher than that of a high flux reactor. The higher efficiency in KENS-I is due to the use of solid methane as moderator material and a larger coupling efficiency between target and moderator, which is only possible in a smaller system.

As far as neutronics is concerned, it was already proved that solid methane is the best moderator material for a pulsed cold neutron source due to higher hydrogen density and superior low energy modes compared to liquid hydrogen (Inoue et al., 1983).

**Table 1.** Comparison of world's cold-neutron-source efficiency

Neutron source	Type	Power	Fast neutron yield (n/s)	Cold source	Maxwellian integral flux	Conversion efficiency	Remarks
ILL	Reactor	58 MW	$1.8 \times 10^{18}$ **	Liq. D <sub>2</sub> in D <sub>2</sub> O reflector	$5.4 \times 10^{13}$	$3 \times 10^{-4}$	Achieved
KENS-I	Pulsed spallation	500 MeV 3 $\mu$ A U-target	$3 \times 10^{14}$	Solid CH <sub>4</sub> decoupled to Be reflector	$1.4 \times 10^{11}$	$4.8 \times 10^{-4}$	Achieved
ISIS	Pulsed spallation	800 MeV 200 $\mu$ A U-target	$3.5 \times 10^{16}$	Liq. H <sub>2</sub> decoupled to Be reflector	$2.1 \times 10^{12}$	$6 \times 10^{-5}$	Calc. value present Ip = 100 $\mu$ A
SNS Mock up	Quasi-continuous spallation	1.1 GeV 8 mA	$6.87 \times 10^{17}$	Liq. H <sub>2</sub> coupled to premoderator in C reflector	$3.1 \times 10^{14}$	$5 \times 10^{-4}$	SIN Exp. E <sub>1</sub> = 80 K (?)
KENS-II	Pulsed spallation	1 GeV 200 mA W-target	$2.5 \times 10^{16}$	?	$1.25 \times 10^{13}$	if same as KENS-I	Relative merit is close to ILL in D17-like exp.

\*for simplicity we calculated (Maxwellian integral/n<sub>f</sub>) instead of (cold neutrons/n<sub>f</sub>)

\*\*assuming one useful neutron per fission

This moderator, however, cannot be used at intense spallation neutron sources because it suffers from serious radiation damage (a so-called "burp" phenomena). ISIS has proved that liquid methane is still useful even at a beam current, 100  $\mu$ A of 800 MeV protons. This moderator, however, is not for providing higher flux of cold neutrons but just narrow pulses of thermal and epithermal neutrons.

There is no doubt that liquid hydrogen is at the present time the only proved material for a cold moderator which can be used as an intense cold neutron source, but the conversion efficiency of a decoupled liquid hydrogen moderator is too low. Kiyonagi, et al., studied various decoupled liquid hydrogen moderators and compared those with a reference decoupled solid methane moderator (5 cm thick) (Kiyonagi, et al., 1986). The conversion efficiency was increased up to 50% of that of the reference moderator by increasing the thickness of liquid hydrogen to 15 cm, but still not enough.

It is strongly desired that SANS experiments in KENS-II, which may not be as favorable as epithermal neutron scattering, must be a close second to D 17 at the ILL, Grenoble, even if we cannot catch up to them. This requires that the conversion efficiency in KENS-II must be, at least, as large as that of the present KENS-I, or hopefully much better, since the total number of fast neutrons expected from KENS-II is the same order of magnitude of ISIS. A composite moderator, which consists of the mixture of solid methane and liquid hydrogen, has been proposed but it is still in the stage of idea. A coupled moderator, especially a heterogeneous moderator that consists of a relatively small (or thin) liquid hydrogen moderator and a premoderator at room temperature, will be the shortest and most promising way to obtain higher efficiency.



### Coupled moderator

A coupled moderator has the following advantages compared to a decoupled moderator:

- (i) higher time-averaged flux of cold neutrons;
- (ii) lower energy deposition in the moderator (lower power density as well as lower total power);
- (iii) consequently, lower cost for cryogenic system;
- (iv) no need of super critical hydrogen (less severe safety regulation and higher safety factor);
- (v) lower leakage of fast and high-energy neutrons from neutron beam tube due to larger distance between target and moderator; consequently, lower cost for shielding around neutron beam lines and spectrometers;
- (vi) better signal to background ratio.

Longer pulse width from such a moderator is still short enough for SANS experiments but gives poor energy resolution in some classes of spectroscopy as those with LAM-80 at KENS-I' and IRIS at ISIS, where the resolution is directly determined by the pulse width. This is only one disadvantage of a coupled moderator. On the other hand, in other classes of high-resolution experiments, the longer pulse width becomes an advantage. For example in an inverted geometry back-scattering spectrometer with a pulse-shaping chopper, the resolution is determined by chopper pulse width, but the dynamic range of energy transfer covered by a spectrometer becomes wider proportionally to the pulse width of source neutrons. Another example is a direct-geometry Doppler instrument where the longer pulse width but higher time-averaged flux gives higher luminosity at sample position for a given energy resolution.

Kley proposed a heterogeneous cold moderator consisting of  $ZrH_2$  or  $H_2O$  at room temperature and of liquid parahydrogen at 20 K as a cold neutron source of a repetitive fast pulsed reactor SORA (Kley, 1971). Bauer, et al., performed measurements on such moderators as a part of an experimental program for optimizing the cold moderator for SNQ, the German spallation source, and showed that coupled moderators of liquid hydrogen (both normal and para) with  $H_2O$ -premoderator in a graphite reflector provide fairly large efficiency as shown in Table I (Bauer, et al., 1985). The value is about 10% lower than that of liquid hydrogen in a  $D_2O$  reflector, but the peak flux is higher than the latter.

Their results encouraged our developing program on a coupled moderator for KENS-II. However, they found a serious problem, that the effective neutron temperatures from those coupled moderators are unexpectedly high,  $T_N \sim 80K$ . We cannot understand the reason why, but it seems to be a fatal disadvantage to this kind of moderator if it is true because the gain factor relative to a decoupled moderator becomes lower at longer wavelength. They suggested that experiments on a coupled liquid deuterium moderator in a large  $D_2O$  moderator-reflector will give a larger gain factor at longer wavelength region.

### Preliminary experiments on coupled moderator

We have performed preliminary experiments on a coupled moderator. The results are reported in a separate contribution in this workshop (Watanabe, et al., 1988). Our results are very encouraging and summarized as follows:

- (i) Effective neutron temperature  $T_N$  is reasonably low and almost the same as those of a bare liquid hydrogen moderator and of a decoupled one in a graphite reflector. The results are essentially different from those by Bauer, et al.
- (ii) Gain factor of the coupled moderator increases at lower wavelength.
- (iii) Gain factors of coupled liquid hydrogen moderators, especially with polyethylene premoderator, are significantly (more than 5 times) higher than a decoupled one.
- (iv) Pulse widths in full width at half maximum from coupled moderators are not so broad compared to those from a decoupled one; about two times. The values are by only 1.5 times as long as those of the present solid methane decoupled moderator at KENS-I'.
- (v) Consequently, the peak height of the neutron pulses is significantly higher than that from a decoupled one.

In the present preliminary experiment, the fast neutron source was not a spallation one but an electron-induced photo-neutron source, and the top parts of the premoderator and the graphite reflector were missing due to the use of a relatively large cryostat that was not optimized for this purpose. Therefore, the estimation of the absolute conversion efficiency of the present coupled moderator is difficult, but we can discuss the relative gain. The relative gain factor of the present coupled liquid-hydrogen moderator with premoderator to the 5-cm-thick decoupled liquid-hydrogen moderator was more than five. On the other hand, the previous experiment (Kiyonagi, et al., 1986) showed that the relative gain factor of a 5-cm-thick decoupled liquid-hydrogen moderator to a reference decoupled moderator of 5-cm-thick solid methane at 20 K was about one third. This suggests that the gain factor of the present coupled liquid-hydrogen moderator with premoderator is superior to that of the reference solid methane, i.e., there may be a possibility that we can realize higher conversion efficiency than that of the present KENS-I', even taking into account a lower coupling efficiency between target and moderator in a larger system of KENS-II.

### Relative merit for SANS

Here we discuss the relative merit of a pulsed cold neutron source to a high flux reactor reactor in SANS experiments. The intensity  $I$  of a neutron beam at a sample position is proportional to the phase space density (Maler-Leibnitz, 1966), and for a Maxwellian distribution given by

$$I \propto \frac{\phi k_T}{2\pi k_T^3} \exp \left\{ -(k_x/k_T)^2 \right\} \Delta k_x,$$

with  $k_T = \sqrt{2mk_B T_N} / \hbar$ .

where  $\phi$  is the time-averaged neutron flux in the Maxwellian at the moderator,  $m$  the neutron mass,  $k_z$  the  $z$  component (beam direction) of the momentum of interest,  $k_B$  the Boltzman constant,  $T_N$  the neutron effective temperature.

Although  $T_N$  in a pulsed cold neutron source is different from that in a high flux reactor, we assume for simplicity that the  $T_N$ 's for both sources are the same. This assumption is not so bad when we compare the measured energy spectrum in our preliminary experiment on a coupled cold moderator for KENS-II (preceding section) with that of the ILL cold neutron source. In a reactor experiment, the data acquisition rate is proportional to  $I$  at a fixed  $k$ , while in a pulsed experiment it is proportional to the integral of  $I$  over the useful band width  $\Delta\lambda$  of incoming neutrons. The non-overlapping useful band width in angstroms is, as well known, given by

$$\Delta\lambda = 3.96 \times 10^3 / (fL),$$

where  $f$  is the repetition rate,  $L$  the flight path length between source and detector in meters. If we assume that we can realize a conversion efficiency in KENS-II as high as that in the present KENS-I, we have a time-averaged cold neutron flux of  $\phi = 1.25 \times 10^{13}$  n/cm<sup>2</sup>.sec as listed in Table I, which is about a factor of 40 smaller than that of the ILL high flux reactor.

On the other hand, in a pulsed source we have an extra gain that comes from time structure (useful band width). Here we consider a D17-like experiment at the ILL or a SANS-like experiment at KENS (a D11-like experiment with a pulsed source seems to be difficult). We concluded that the total flight path length of 13 m or hopefully 10 m will be possible, which gives the useful band width 6 Å or 7.9 Å for  $f = 50$  s<sup>-1</sup>. The gain is given by

$$\text{Gain} = \left( \int_{\lambda_{\min}}^{\lambda_{\max}} d\lambda/\lambda \right) / (\delta\lambda/\lambda)_{\text{reactor}}.$$

The denominator is the wavelength resolution in a reactor experiment, which is about 0.1.

If we assume that neutrons in the wavelength region between 1 and 7 Å (corresponds to  $\Delta\lambda = 6$  Å) or 1 and 8.9 (corresponds to  $\Delta\lambda = 7.9$  Å) are useful, we have

$$\begin{aligned} \text{Gain} &= \ln(7/1)/0.1 = 19.5 \\ &\text{or } \ln(8.9/1)/0.1 \sim 22. \end{aligned}$$

If we assume that neutrons only in a longer wavelength region, for example, between 4 and 10 Å or 4 Å and 11.9 Å, are useful, we have a gain of 9.2 or 10.9. Thus the gain from pulse structure is 10-20. This means that the relative merit of KENS-II to the ILL in a D17-like experiment is 1/2 or 1/4, assuming that time-averaged  $4\pi$ -equivalent flux of KENS-II is about a factor of 1/40 smaller than that of the ILL.

Since our preliminary experiment on a coupled moderator has given indication of higher conversion efficiency than the present KENS-I, a D17-like experiment with KENS-II is expected to be a close second to that with D17 at the ILL. It may be

well recognized that there exists another merit in a pulsed neutron experiment—much wider momentum range simultaneously covered by larger  $\Delta\lambda$ .

Relative merit of a coupled cold moderator in an application other than SANS will be discussed elsewhere.

### Moderator configuration

The total number of useful cold neutrons that can be extracted from one cold moderator or total number of cold neutron beam lines (direct beam holes and neutron guide tubes) that can view one cold moderator will be another important figure of merit of a cold neutron source. The maximum angular opening of one cold neutron moderator in a target-moderator-reflector assembly will be limited to a certain value, typically about 0.5 radian, because a much larger opening removes a significant part of the reflector and, consequently, sacrifices the beam intensity. The total number of

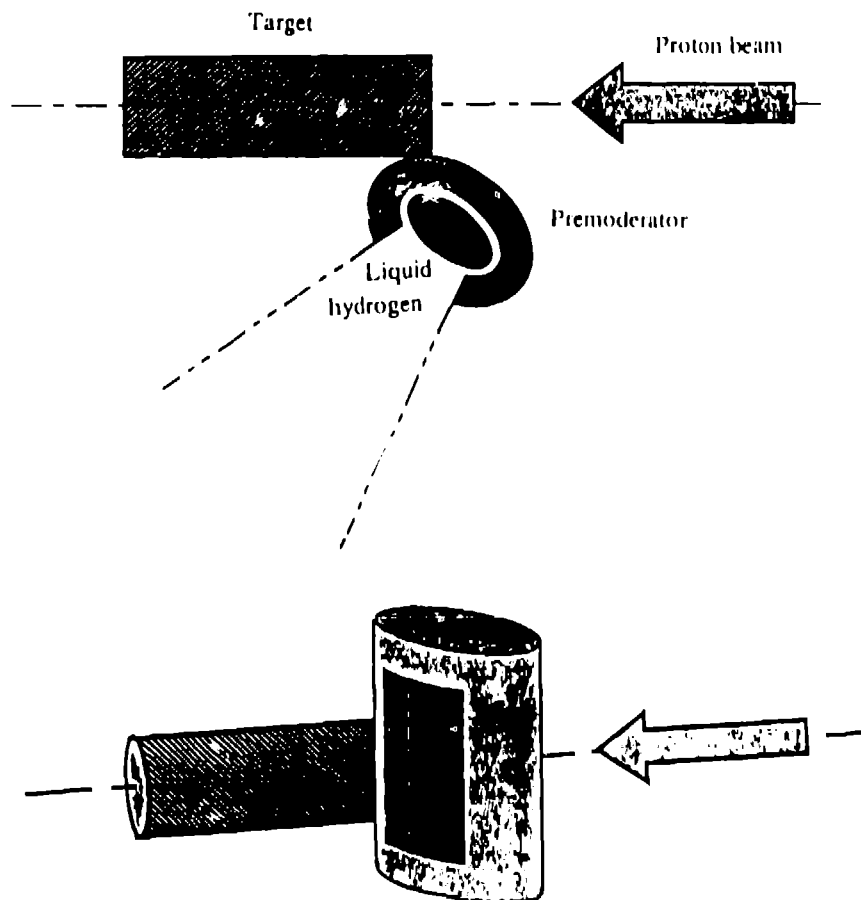


Fig. 1 A modified slab geometry for KENS-II cold neutron source.

neutron guide tubes accessible within this angle is, therefore, limited to about 10, assuming the distance between the moderator and the beginning of the guides to be about 1.5 m and the inner (outer) width of the guide about 5 cm (7.5 cm). This number is to be compared with that in a high flux reactor, where the number of guides extracted from a cold moderator is typically 5, but ultimately increased by about 3 times in the experimental hall. The growth in number is possible only in the case that the height of the moderator view-surface as well as the height of the guides at the inlet is as high as those in the high flux reactor at the ILL (about 15 cm). In pulsed spallation facilities the height is limited to about 5 cm because the cold moderators are coupled to the target in the wing geometry where the spatial distribution of cold neutrons has a peak at about 3 cm from the target-side end with rapid exponential decrease towards the opposite end.

A slab geometry in target moderator configuration will be a possible way to increase the bright zone on the view surface of the moderator. Generally, the slab geometry is susceptible to background fast neutrons and brings an extremely high dose equivalent rate around a neutron beam line. In order to improve this shortcoming, a modified slab geometry as illustrated in Fig. 1 shall be studied further. In this geometry no beam tube within the opening angle of about 30° views the target directly and a bright area about 10 cm wide by 15 cm high may be realized. Such a configuration will increase the capability for cold neutron usage in a pulsed spallation neutron facility.

We are thinking to adopt decoupled moderators for short pulse uses as usual which may be a liquid methane moderator and light water moderator(s). An optimal target-moderator-reflector configuration including a coupled moderator as shown in Fig.1 is under consideration.

#### References

- Bauer G., Conrad, H., Fischer, W., Grunhagen, K. and Spitzer, H., 1985, Proc. ICANS-VIII, RAL-85-110, p. 344  
Kiyonagi, Y., Inoue, K., Watanabe, N. and Iwasa, H., 1986, KENS Report-VI, KEK Progress Report 86-2, p. 270  
Kley, W., 1971, Proc. the Joint Meeting on Pulsed Neutrons and Their Utilization, EUR 4954e, p. 379  
Maier-Leibnitz, H., 1966, Nukleonik 8, p. 6;  
Watanabe, N., Kiyonagi, Y., Inoue, K., Furusaka, M., Ikeda, S., Arai, M. and Iwasa, H., 1988, to be published in these proceedings.

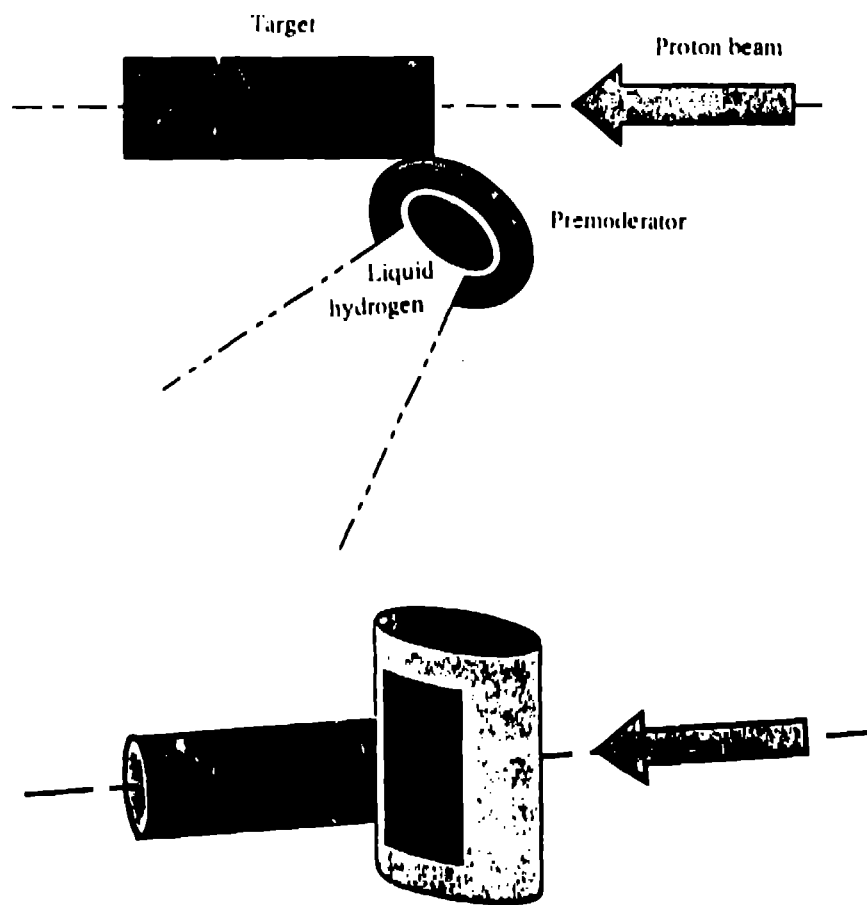


Fig. 1 A modified slab geometry for KENS-II cold neutron source.

## Calculation of the spallation product distribution in the evaporation process

*T. Nishida, I. Kanno, Y. Nakahara, and H. Takada*  
Japan Atomic Energy Research Institute  
Tokai-mura, Ibaraki-ken  
JAPAN

**ABSTRACT:** Some investigations are performed for the calculational model of nuclear spallation reaction in the evaporation process. A new version of a spallation reaction simulation code NUCLEUS has been developed by incorporating the newly revised Uno & Yamada's mass formula and extending the counting region of produced nuclei. The differences between the new and original mass formulas are shown in the comparisons of mass excess values. The distributions of spallation products of a uranium target nucleus bombarded by energy (0.38 - 2.9 GeV) protons have been calculated with the new and original versions of NUCLEUS. In the fission component Uno & Yamada's mass formula reproduces the measured data obtained from thin foil experiments significantly better, especially in the neutron excess side, than the combination of the Cameron's mass formula and the mass table compiled by Wapstra, et al., in the original version of NUCLEUS. Discussions are also made on how the mass-yield distribution of products varies dependent on the level density parameter  $a$  characterizing the particle evaporation.

### Introduction

In the nuclear spallation reaction of a heavy nucleus bombarded by high-energy protons, almost all kinds of nuclides are produced due to the vehemence of the reaction. Although most of them will decay to stable nuclides in a short time, it is very important in the research of the transuranic waste transmutations that the accumulation of nuclides with long lifetime can be estimated as accurately as possible.

In the assessment of the feasibility of the idea of transmuting the transuranic wastes by using spallation reactions, it is necessary to show that the storage time of transuranic wastes can be significantly shortened from the practical point of view. It is very interesting and important, also, from the pure nuclear physics point of view to investigate the details of spallation reaction and the decay mechanism of a strongly excited nucleus.

In our previous Monte Carlo calculations performed by using the NUCLEUS code<sup>(1)</sup>, the spallation reactions of a uranium nucleus were studied for incident proton energies of 0.38, 1, 2, and 2.9 GeV<sup>(2)</sup>. It has been found that in the comparisons of charge-dispersion curves, the agreements are not satisfactory enough with the measurements reported by G. Friedlander, et al.,<sup>(3)</sup> in particular, for the neutron excess wings of the

curves<sup>(1)</sup>. The computational scheme employed in the NUCLEUS code is essentially the same as that of the NMTC/JAERI code<sup>(4)</sup>, except that NUCLEUS simulates only the intra-nuclear cascade and the competition between high-energy fission and particle evaporations. In both codes, the binding energies of particles emitted during the reaction are calculated with the combined use of the Cameron's mass formula and the mass table compiled by Wapstra, et al., in the same way as in the original NMTC code<sup>(5)</sup>. Uno and Yamada have developed a new mass formula by utilizing recent experimental mass data to predict masses of unknown nuclides far from stability with greater reliability<sup>(6)</sup>. In the nuclear spallation a lot of nuclides, which often appear far apart from stability, are produced. This fact suggests that the use of the new mass formula will improve the accuracy of our calculations.

A new version of NUCLEUS has been developed by incorporating the newly revised Uno & Yamada's mass formula. The mass formula dependence of spallation product distribution has been investigated by using both the original and new versions of NUCLEUS. In the calculations both with the original NUCLEUS and NMTC/JAERI, some product nuclides near the neutron or proton drip line are often lost in counting the Monte Carlo events because of dimensional restriction in the code and the repulsion criterion for the events outside the current nuclide chart. These restrictions are removed in the new version of NUCLEUS to avoid the counting loss of nuclides which are unknown as yet experimentally.

On the other hand the isotope distribution of reaction products is examined for the nuclear spallations of a TRU nucleus of  $^{237}\text{Np}$  with 500 MeV protons. It is also shown how the distribution and the number of emitted particles are affected by the variation of the level density parameter  $a$  characterizing the evaporation probability in a highly excited compound nucleus.

### Theoretical model of nuclear spallation reaction

A nucleus bombarded by a sufficiently energetic particle, such as a proton with the energy of hundreds to thousands MeV, undergoes a complicated destruction process, i.e., so-called spallation. For simulating the spallation reaction we use the two-step model, which consists of the intranuclear cascade and the subsequent competing decay by the high-energy fission or particle evaporation. When a high-energy particle is injected into a heavy nucleus, the intranuclear cascade of nucleons, pions and knocked-on particles are computed as the fast step of the nuclear reaction. In the present model a nucleus is assumed to be a sphere of a degenerated Fermi gas, in which the two-body collision model<sup>(7)</sup> gives a good approximation to the collision processes during the intranuclear cascade in the energy range higher than about 100 MeV. The characteristics of nuclear matter are determined by the distributions of nucleon density, momentum and potential energy. Fission production cross sections are calculated using the Isobar model<sup>(8)</sup>.

At the instant when the intranuclear cascade has ceased, the residual nucleus remains in the strongly excited state of the excitation energy as high as hundreds MeV. In the slow step this excited nucleus decays selecting the path to the particle evaporation or the nuclear fission as the subsequent process according to the fission probability based on the Bohr-Wheeler theory with the level density parameters<sup>(9)</sup> fitted to Il'inov's experimental data<sup>(10)</sup>. A semi-empirical combination of the Gaussian and folded-



Gaussian distributions is used to determine masses of fission fragments, and their charges are selected from the Pik-Pichak & Strutinski! distribution.<sup>(9, 11)</sup>

The evaporation is calculated for neutron, proton, deuteron, triton, helium-3 and alpha particle emitted from an excited residual nucleus or excited fission fragments, using the Weisskopf model, which is based on the statistical theory for a degenerate Fermi gas.

The evaporation probability  $P_x$  of a particle  $x$  with the kinetic energy  $\epsilon$  from the excited compound nucleus is given as

$$P_x = (2S_x + 1) m_x \epsilon \sigma_{cx}(\epsilon) \omega(E),$$

- $S_x$ : particle  $x$ 's spin
- $m_x$ : particle  $x$ 's mass,
- $\sigma_{cx}$ : inverse reaction cross section,
- $E$ : (excitation energy of compound nucleus)  $= \epsilon + Q_x$ ,  
 $Q_x$  = particle  $x$ 's binding energy,
- $\omega(E)$ : level density in a nucleus with energy  $E$ ,

where  $\omega(E)$  is formulated by Hurwitz and Bethe as the following:

$$\omega(E) = \omega_0 \exp(2\sqrt{a(E - \delta)}),$$

- $a$ : level density parameter,
- $\delta$ : pairing energy correction,
- $A$ : mass number of a compound nucleus.

The binding energy is given as the function of the mass excess, defined as  $M(A,Z) = M - A$ , where  $M$  and  $Z$  are the mass and the atomic numbers, respectively. If we define the mass number, atomic number and mass excess of the particle  $x$  as  $AEP(x)$ ,  $ZEP(x)$  and  $EXMASS(x)$ , the binding energy  $Q_x$ , is calculated by the following equation:

$$Q_x = M(A - AEP(x), Z - ZEP(x)) + EXMASS(x) - M(A, Z). \quad (1)$$

In the present work we adopted two different mass formulas, Cameron's<sup>(12)</sup> and Uno & Yamada's<sup>(13, 14)</sup>, to examine their effects in the Monte Carlo simulation of nuclear spallation reactions. The difference between Cameron's old and Uno & Yamada's new mass formulas is attributed to those methods used to fit shell energy terms to measured data for selected nuclei and to data themselves.

Similarly the spallation products of both residual nuclides and some particles from an actinide nucleus bombarded by high energetic protons are examined by evaluating the contribution of level density parameter  $a$  to the evaporation calculation. The value of  $a$  was determined to be  $A/10$  and  $A/20$ , in fitting the measured data by Dostrovsky, et al., Barashenkov, et al., and Chen, et al. In the simulation code NUCLEUS, the Le Conteur's equation is employed as follows:

$$a = \frac{A}{B} \left( 1 + y \frac{(A - 2Z)^2}{A^2} \right), \quad (2)$$

where B is 8 MeV and y 1.5. This equation gives  $A/7.7 \sim A/7.4$  to the value of  $a$  for the nuclides with the mass number more than 200.

### Results and discussions

It is generally known that the products yielded in the nuclear spallation reaction consist mainly of residual nuclei in the evaporation stage of nuclear reaction. In the computer simulation, the precision of the mass formula is crucial in getting good results. To make clear how important the mass formula is in predicting the spallation-product distribution, we have performed the calculations of evaporated particles, using two mass formulas, i.e., Cameron's and Uno & Yamada's, and compared the results with measured data (reported in Friedlander, et al.'s paper<sup>(3)</sup>) for the spallation of a uranium nucleus bombarded by protons from 0.38 to 2.9 GeV. In the integral kind of data, e.g., the number of emitted particles and the mass distribution of reaction products, there are no remarkable discrepancies between the results obtained with the use of the two mass formulas.

The numerical values of mass excesses of nuclides calculated by both mass formulas are plotted in Fig. 1 for isotopes of each element with even Z from 92 down to 30. As seen in Fig. 1(a) for  $Z = 92 \sim 86$ , these parabolic curves are in the positive side and in a good agreement with each other; whereas, for  $Z = 84 \sim 72$ , the old Cameron's formula gives values larger than Uno & Yamada's formula in the neutron deficient side, and the discrepancy turns out to be more than 8 MeV for a nuclide with  $Z = 82$ ,  $A = 183$ . In the range from  $Z = 70$  to  $Z = 52$ , where the mass excesses have deeply negative values as seen in Fig. 1(b), both curves are in better agreement than in the other ranges. Their maximum discrepancy is only less than 3 MeV for the neutron deficient nuclides apart from the stable nuclide line. In this case, the new formula has values larger than the old one. In the lighter mass range for  $Z = 50 \sim 30$ , the curves approach positive values again as Z decreases (see Fig. 1(c)). The new mass formula has larger values for almost all isotopes than the old, and their difference becomes larger than 9 MeV, especially at the edge of the neutron deficient side.

The distribution of produced nuclides on a neutron number versus proton number plane, the  $(N, Z)$  plane, gives us the clear image of their decay schemes. Figure 2 illustrates the region where the Monte Carlo events corresponding to spallation fragment productions are counted. The region between the fine lines with blackened circles is the counting region allowed in the NMTC code and adopted also in the old versions of NMTC/JAERI and NUCLEUS. Monte Carlo events that happen to be outside the region are discarded as unphysical events. Through our experiences in computing the spallation reaction of a heavy nucleus, such as a transuranic nuclide with high energy protons, we have noticed that the number of discarded events would not be so few as to be allowed, considering the real possibility of the existence of nuclides unregistered on the chart. So we have extended the  $(N, Z)$  region to eliminate count losses of the events. The bold lines represent the extended region incorporated

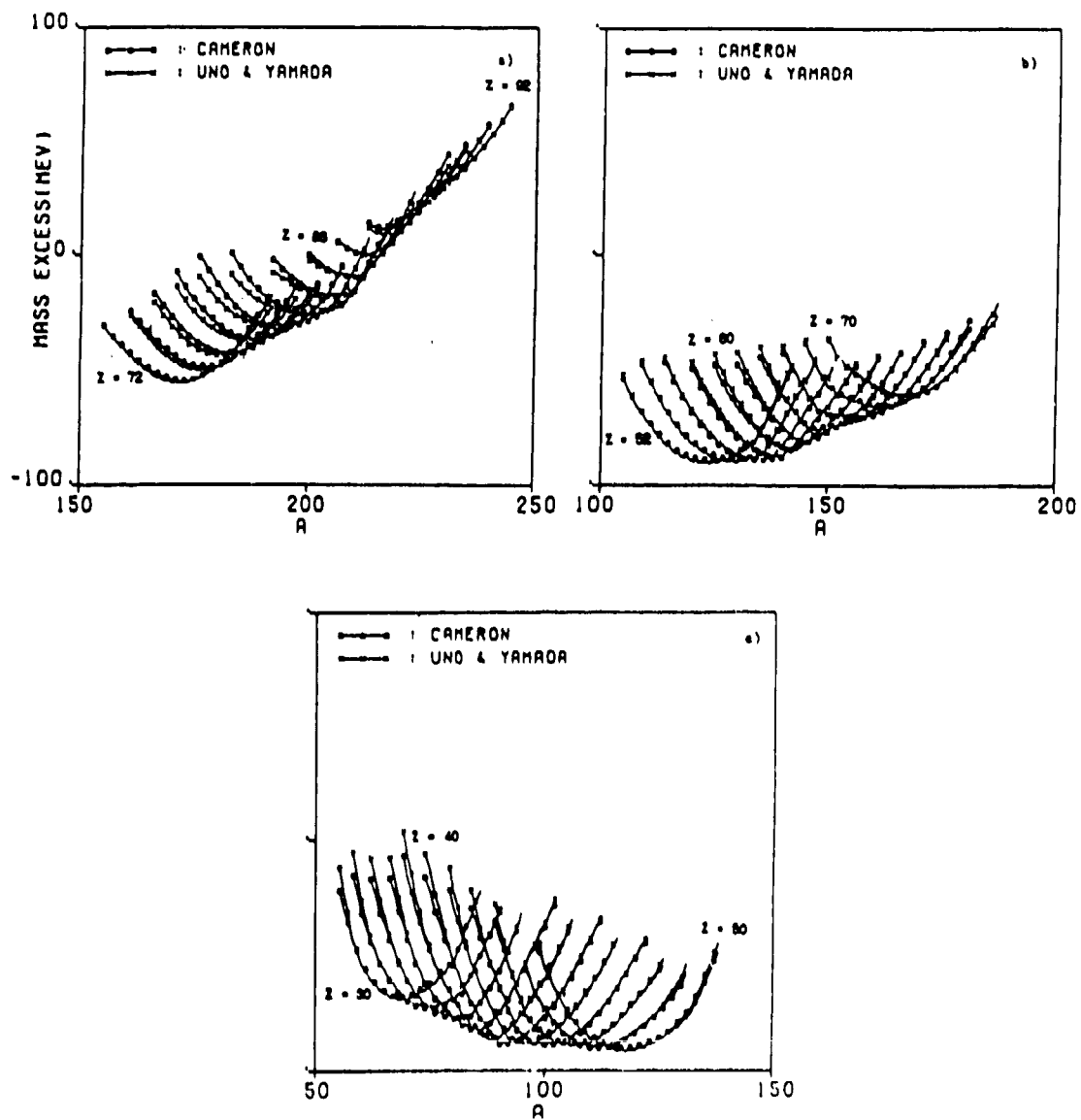


Fig. 1 Mass-excess distributions calculated by Cameron's and Uno & Yamada's mass formulas for elements with even Z: (a) 92 ~ 72, (b) 70 ~ 52, and (c) 50 ~ 30.

in the new version of the NUCLEUS code. These restricted and extended regions forming a band shape have widths of 31 and 61 nuclides in the N direction, respectively. The line with open squares represents the domain where nuclides were produced actually in the extended region in the spallation calculation of a uranium target nucleus for 1 GeV incident protons. As seen from Fig. 2, the domain of produced nuclides extends outside the old region. The nuclides on neutron deficient ( $N > 80$ ) and neutron excess extreme sides ( $75 > N > 45$ ) had been lost in the old calculations. The triangle  $\Delta$  denotes a stable nuclide. The line marked by cross (x) representing the boundary within which there exist nuclides listed in the current Chart of Nuclides<sup>(15)</sup> is depicted for reference. The straight lines in the figure will be explained later.

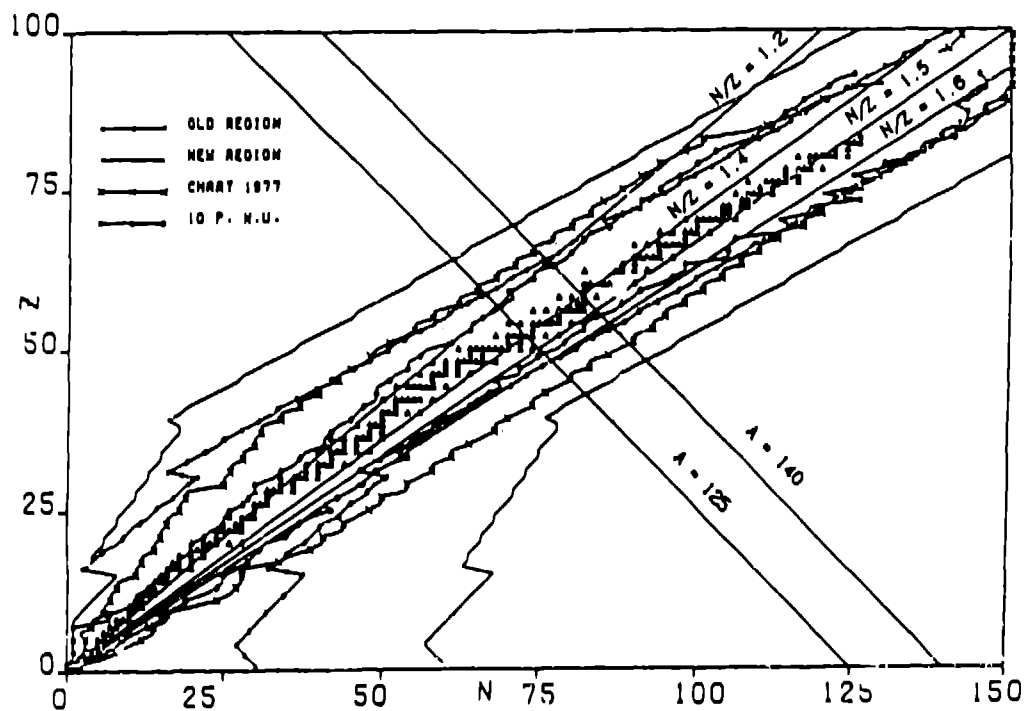
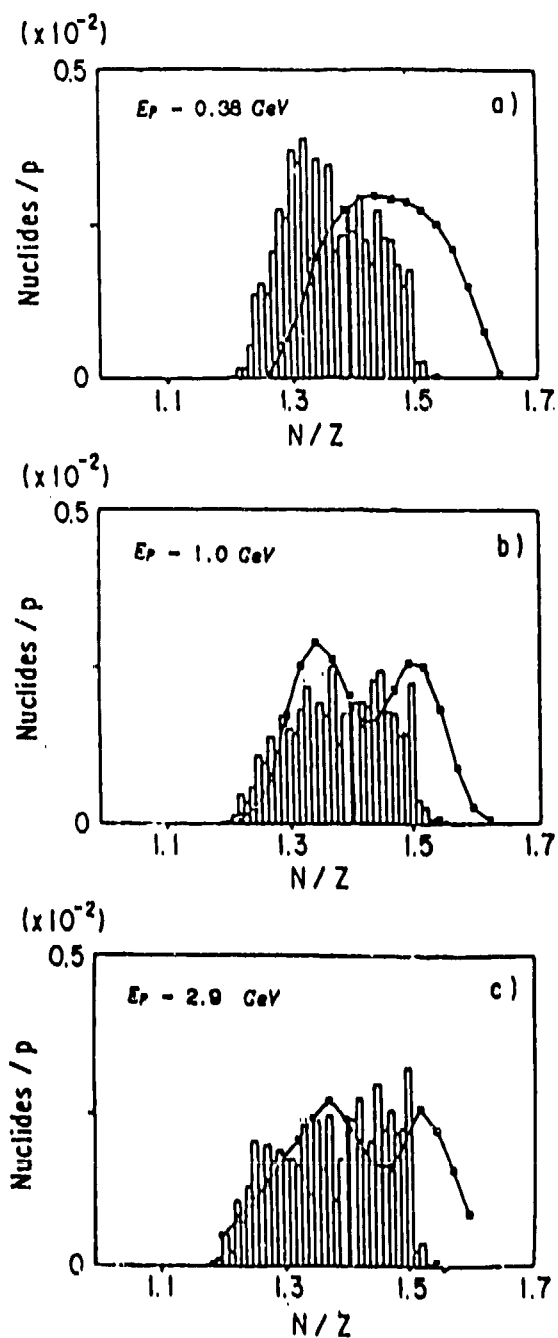


Fig. 2 Regions for spallation nuclides to be counted on the neutron number (N) versus the proton number (Z) plane.

The yields of spallation products for 1 GeV protons impinging on a uranium nucleus, calculated with the old mass formula and the restricted counting region and accumulated over the mass number range from 125 to 140, are plotted in Figs. 3(a), (b) and (c) to compare our simulation results with the measured data<sup>(3)</sup>. The lack of smoothness in the calculated histogram shows that the number of histories (50,000 protons) in the Monte Carlo calculation is not sufficiently large to obtain the fine distribution of product yields. The mean value of N/Z for stable nuclides in this mass range is about 1.4. A double-peaked distribution at energies above 1 GeV, corresponding to the neutron-excess and neutron-deficient nuclides, could not be



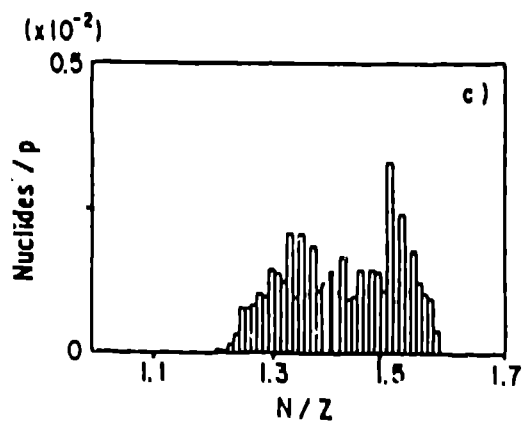
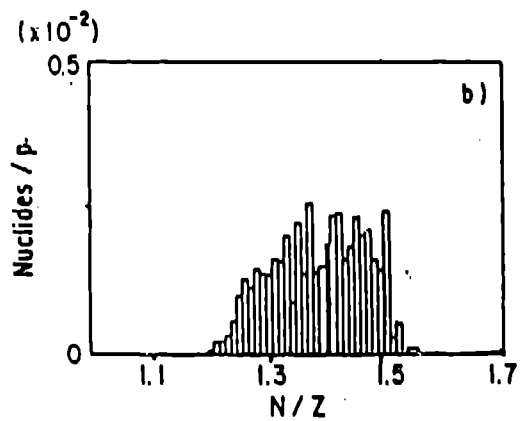
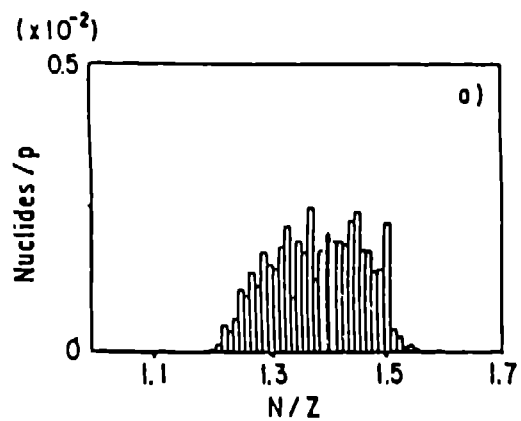
**Fig. 3** Spallation-product yields for  $A = 125 \sim 140$  versus  $N/Z$  for a uranium nucleus obtained by using the old version of NUCLEUS. The curves show the measured values<sup>[3]</sup> and the blackened square (a) 0.38 GeV, (b) 1 GeV, and (c) 2.9 GeV.

reproduced correctly by the calculations. However, the distributions on the side of lower  $N/Z$  values are in agreement with each other. Discrepancy is remarkable at the neutron-excess side ( $N/Z > 1.5$ ).

To see if the discrepancy can be improved by using the new mass formula, we performed the same calculations for three cases of (a) the old mass formula and nuclide region, (b) the old mass formula and the extended region, and (c) the new mass formula and the extended region. Prior to discussing the results shown in Fig. 4, let us examine Fig. 2 again. Two parallel lines drawn from the upper left side to the lower right side denote the mass number range of 125 ~ 140, used for getting cumulative yields. The straight lines drawn radially from the origin have each value of  $N/Z$  written in the figure. The minimum value of  $N/Z$ , below which spallation nuclides are scarcely produced, may be considered to be 1.2. The domain surrounded by the parallel lines and the two radial lines with  $N/Z$  values of 1.5 and 1.6 exists in the restricted region. Therefore, in the present calculation the reason for variation of yields of produced nuclei in this domain may be purely attributed to the selection of a mass formula. The computational results with the old mass formula (Figs. 4(a) and (b)) show the lack of some nuclides with the  $N/Z$  values larger than 1.5. The use of the new formula (Fig. 4(c)) has just resulted in redistributing the nuclides and produced the double-peaked distribution.

These spallation products with mass  $A = 125 \sim 140$  obtained by using the new mass formula are plotted also in Figs. 5(a), (b) and (c) for the proton energies of 0.38, 1.0 and 2.9 GeV to compare our simulation results with the measured data<sup>(3)</sup>. Both calculated and measured product distributions are in a good agreement in the whole range of  $N/Z$  from 1.2 to 1.6, except in the case of 0.38-GeV protons. A double-peaked distribution in the curve representing the measured data at energies above 1 GeV, corresponding to the neutron-excess and neutron deficient peaks, has been reproduced successfully by the present Monte Carlo calculation using the new mass formula. Quantitatively speaking, however, there are some discrepancies between our calculations and the measured data. The reasons of discrepancies may be attributed to both the experimental data processing and the computational methods. The portion of the experimental curve beyond the peak on the neutron-excess side does not show the measured data, but is the plot of values extrapolated by using the measured cumulative yields. The left tail of the distribution is also the extrapolation, except in the case of Fig. 5(a) where it is apparent the amount of neutron-deficient nuclides becomes relatively larger systematically in the calculation in comparison with the measurement, in spite of use of the new mass formula. This fact reminds us that it may be necessary to examine the consistency between the mass- and charge-distribution probabilities used in the Monte Carlo sampling of the fission fragments, because the former has been derived semi-empirically<sup>(9)</sup> and the latter is the theoretical one based on the statistical model of the fission.<sup>(11)</sup>

Figure 6 shows the isotope distribution of product yields, calculated with the same conditions as in the cases shown in Figs. 4(a), (b), and (c), for elements with even  $Z$  from 92 down to 84, close to the uranium nucleus bombarded by 2.9 GeV proton. As seen from these figures, a comparatively large amount of neutron-deficient nuclides are produced from the intranuclear cascade and evaporation processes. The peak for each element appears in the neutron-deficient side, far from the stable isotopes that exist in the right tail of each distribution, except for target uranium. Due



**Fig. 4** Spallation-product yields for  $A = 125 - 140$  versus  $N/Z$  for a uranium nucleus bombarded by 1 GeV protons. The computation was carried out for three cases of (a) the old mass formula and region, (b) the old mass formula and the extended region, and (c) the new mass formula and the extended region.

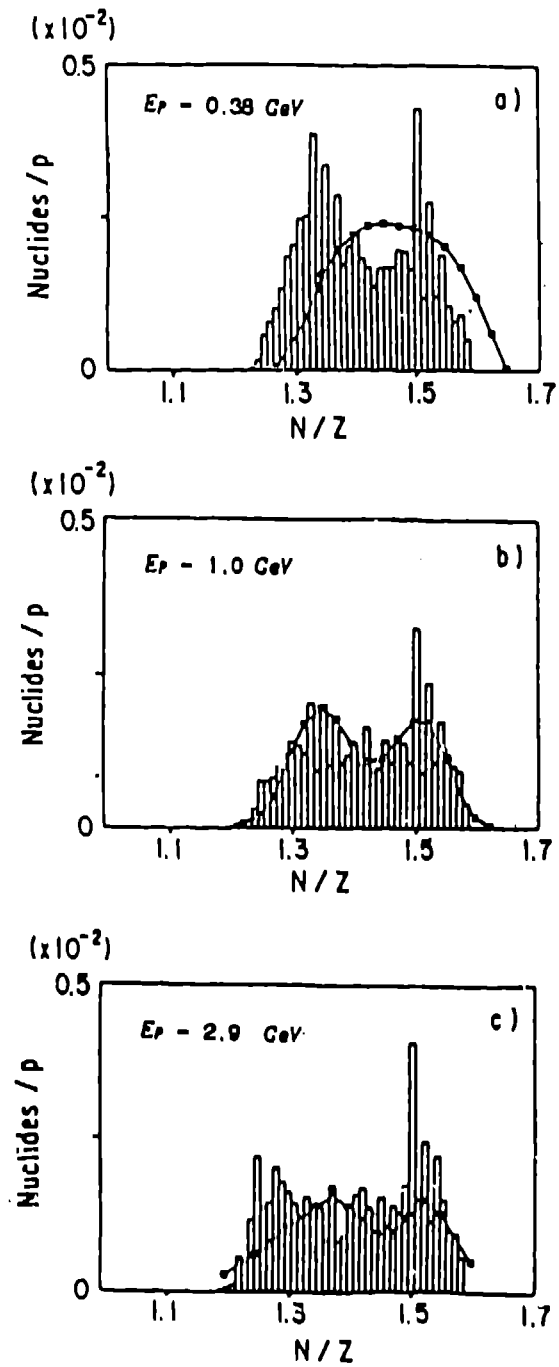
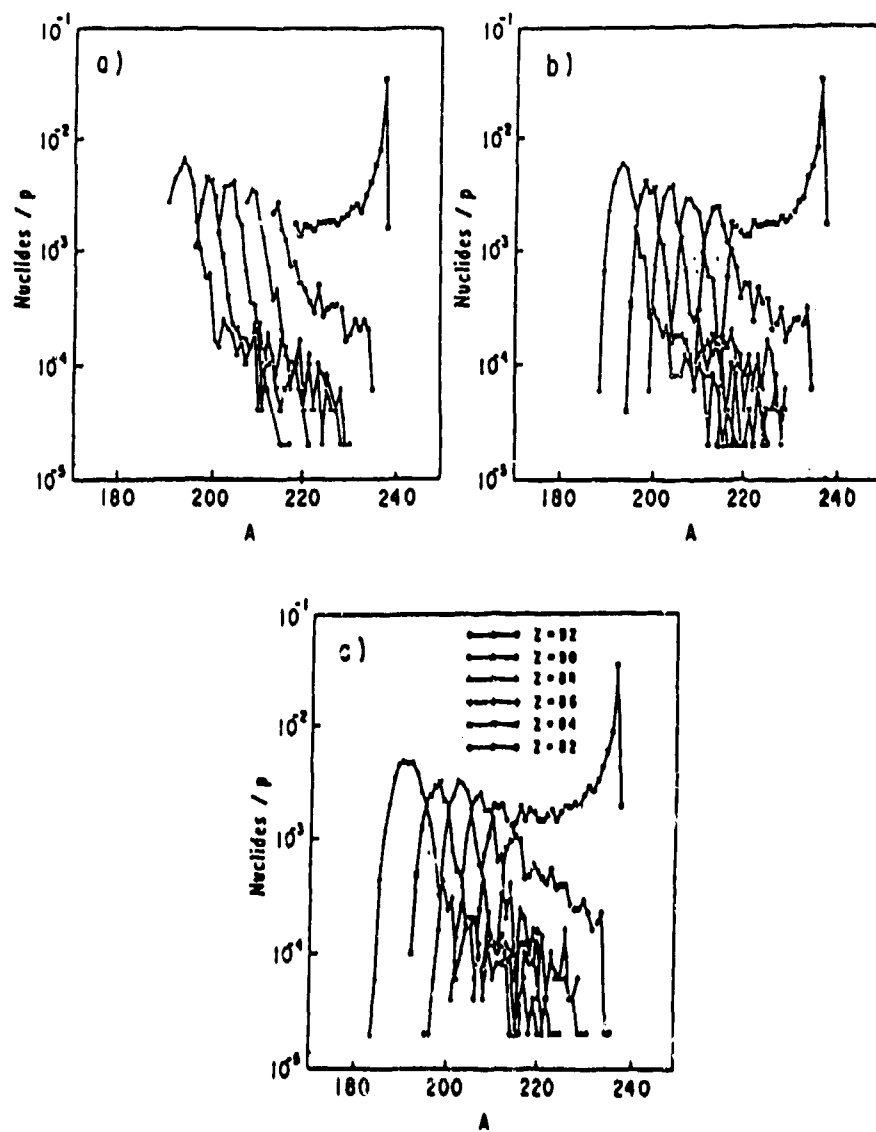


Fig. 5 Spallation-product yields for  $A = 125 - 140$  versus  $N/Z$  for a uranium nucleus obtained by using the new mass formula and the extended region (a) 0.38 GeV, (b) 1 GeV, and (c) 2.9 GeV.





**Fig. 6** Mass-yield distributions of products with even  $Z$  from 92 to 82 in the nuclear spallation reaction of a uranium nucleus with a 1 GeV proton for the same cases (a), (b), and (c) as in Fig. 4.

to their short half-lifetimes, most of them will change to stable nuclides in due time. As for uranium isotopes, there is a sharp peak at  $A = 237$  and it is higher by an order than other element peaks. In Fig. 6(a), the tail of a peak for each element is cut off in the neutron deficient side because of the artificial limitation in counting the corresponding Monte Carlo events. Then we find that for the case of (b), corresponding to the use of the old formula and the extended region, the count loss has just been recovered and the tail of peaks appears in the reasonable form. By the use of the new mass formula and the extended region, the corrected peaks have become wider than the ones in the case of (b), as seen in Fig. 6(c). As pointed out by Sato, et al.,<sup>[16]</sup> more unconfirmed kinds of nuclides outside the Chart of the Nuclides in our calculations can be considered reasonable and the region of counting the Monte Carlo events should not be restricted.

On the other hand, the spallation products of both residual nuclides and some particles from  $^{237}\text{Np}$  nucleus bombarded by protons of 500 MeV are examined by evaluating the contribution of level density parameter  $a$  to the evaporation calculation. The number of particles evaporated from the non-fission component of products is calculated for the parameter values between  $A/30$  and  $A/5$ . Table 1 summarizes ratios of the number of each particle for five parameter values to one calculated by the Le Contour's equation, where a figure in the parenthesis represents the number of evaporated particles. It is apparent that the yields of neutrons and protons decrease by  $\sim 30\%$  as  $a$  decreases to  $A/20 \sim A/30$ , but increase by 10% with  $a = A/5$ . For other particles, the inverse tendency is seen and their yields have wider tolerances than in cases of protons and neutrons. The number of total nucleons evaporated from an excited compound nucleus is almost the same in each case. In Fig. 7, the distributions of isotopes of the non-fission component are shown with odd atomic numbers  $Z = 93 \sim 83$  for  $a = A/30, A/20, A/10,$  and  $A/5$ . As seen from these figures, a lot of neutron-deficient isotopes are produced for each element, except the target element. When  $a$  decreases from  $A/5$  to  $A/30$ , the shape of neptunium distribution ( $Z = 93$ ) in the neutron-deficient side varies from a subsidiary peak to a steep slope. The tail of the protactinium ( $Z = 91$ ) peak in the neutron-excess side shrinks and the peak's width becomes wider. The height of the bismuth peak ( $Z = 83$ ) increases by about one order. Therefore, to calculate exactly the product yield of transmuted nuclei, it is necessary that the value of the level density parameter is reasonably fitted to measured data.

**Table 1** Ratios of particles emitted from a neptunium 237 nucleus bombarded by protons with 500 MeV in the non-fission component.

Level Density Para. $a$	$A/30$	$A/20$	$A/10$	Le Contour ( $A/7.7 - A/7.4$ )	$A/5$
Proton	0.70	0.71	0.89	1. (1.572)	1.12
Neutron	0.68	0.77	0.95	1. (7.412)	1.08
Deuteron	2.36	1.95	1.17	1. (0.233)	0.47
Triton	4.61	3.47	1.52	1. (0.085)	0.39
Helium 3	11.92	6.72	1.61	1. (0.0036)	0.17
Alpha	2.68	2.24	1.17	1. (0.121)	0.37
Nucleons/P	0.95	0.96	0.98	1. (10.200)	1.01

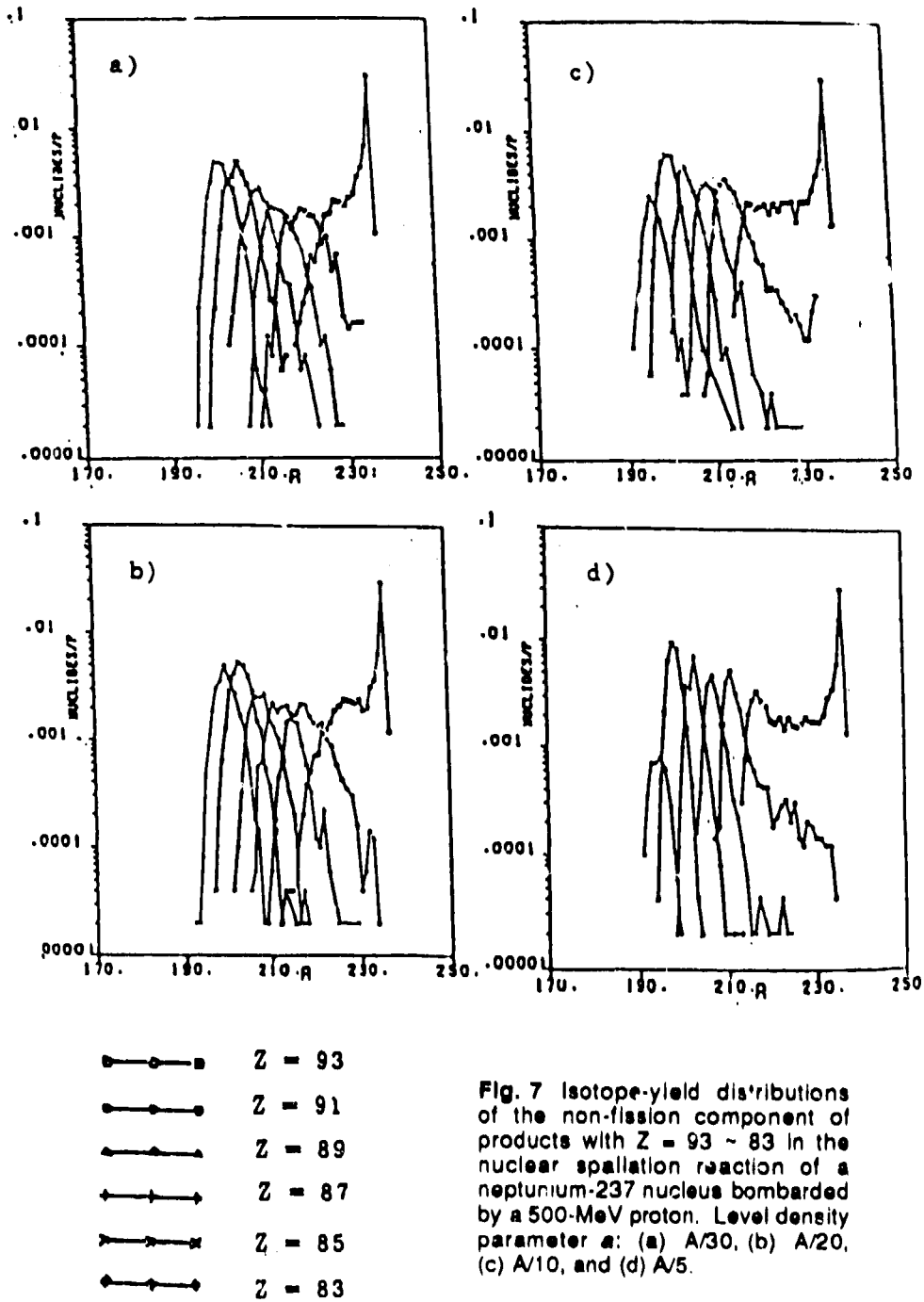


Fig. 7 Isotope-yield distributions of the non-fission component of products with  $Z = 93 \sim 83$  in the nuclear spallation reaction of a neptunium-237 nucleus bombarded by a 500-MeV proton. Level density parameter  $a$ : (a)  $A/30$ , (b)  $A/20$ , (c)  $A/10$ , and (d)  $A/5$ .

## Summary

To make evaluations of theoretical models for the nuclear spallation reaction, a simulation code has been modified and a new mass formula has been used to improve the precision in the Monte Carlo calculations. From the analyses of calculated results, we conclude as follows:








1. For nuclides with atomic numbers larger than 70, mass excesses calculated by Cameron's mass formula are greater than those by Uno & Yamada's formula; whereas, the reverse tendency is seen for numbers smaller than 70.
2. The results show that distributions of produced nuclei have natural patterns from a physical point of view when the artificial restrictions are removed in counting the nuclide production events.
3. The new mass formula can reproduce fairly well the experimental product yield distributions, especially in the neutron excess side.
4. It is found that the old mass formula gives lower estimation of the number of produced nuclei than the new one, especially in the nuclide region far from the stable nuclide line on the nuclear chart.
5. The reasonable estimation of the level density parameter is important to calculate the product yield of transmuted residual nuclides.

## Acknowledgements

The authors wish to express their hearty thanks to Dr. Y. Kaneko for his continued interest and encouragements, to Prof. M. Uno (Waseda Univ.) and Prof. H. Sato (Tokyo Univ.) for their helpful suggestions and offering us the use of the program of their new mass formula.

## References

1. Nishida, T., Nakahara, Y., and Tsutsui, T. 1986, "Development of a Nuclear Spallation Simulation Code and Calculations of Primary Spallation Product," JAERI-M 86-116 (In Japanese).
2. Nishida, T. and Nakahara, Y., 1987, "Analysis of Produced Nuclei and Emitted Neutrons in Nuclear Spallation Reaction," Kerntechnik 51, 193.
3. Friedlander, G., et al., 1963, Phys. Rev. 129, 1809.
4. Nakahara, Y. and Tsutsui, T., 1982, "NMTC/JAERI: A Simulation Code System for High Energy Nuclear Reactions and Nucleon-Meson Transport Processes," JAERI-M 82-198 (in Japanese).
5. Coleman, W. A., and Armstrong, T. W., 1970, "NMTC Monte Carlo Nucleon Meson Transport Code System," RSIC CCC-161.
6. Uno, M. and Yamada, M., 1975, Prog. Theor. Phys., 53, No. 4, 987.
7. Serber, R., 1947, Phys. Rev. 72, 1114.
8. Sternheimer, R. M., and Lindenbaum, S. J., Phys. Rev. 105, 1874 (1961); 109, 1723 (1958); 123, 333 (1961).
9. Nakahara, Y., 1983, J. Nucl. Sci. Technol. 20, 511.
10. Il'inov, A. S., et al., 1980, Sov. J. Nucl. Phys. 32, 166.
11. Pik-Pichak, G. A., and Strutinskii, V. M., 1964, "Physics of Nuclear Fission," Israel Program for Scientific Translation.

- 
- 
- 
- 
- 
- 
- 
12. Cameron, A. G. W., 1957, *Canada J. Phys.* **35**, 1021.  
13. Uno, M., and Yamada, M., 1981, "Atomic Mass Formula with Constant Shell Terms," *Prog. Theor. Phys.* **65**, No. 4, 1021.  
14. Ibid., 1982, "Atomic Mass Prediction from the Mass Formula with Empirical Shell Terms," JNS-NUMA-40.  
15. Yoshizawa, Y., Horiguchi, T., and Yamada, M., 1977, "Chart of the Nuclides," Japanese Nuclear Data Committee and Nuclear Data Center, JAERI.  
16. Sato, H. and Uno, M., 1981, *Butsuri* **39**, 892. (in Japanese).

## Preliminary optimization experiments of coupled liquid hydrogen moderator for KENS-II

*N. Watanabe, Y. Kiyonagi\*, K. Inoue\*, M. Furusaka, S. Ikeda, M. Arai, and H. Iwasa\**

National Laboratory for High Energy Physics  
1-1 Oho, Tsukuba-shi, Ibaraki-ken 305, JAPAN

\*Department of Nuclear Engineering, Faculty of Engineering  
Hokkaido University  
Sapporo 060 JAPAN

**ABSTRACT:** As a preliminary optimization experiment on the cold-neutron source for KENS-II, energy and time distributions of cold neutrons emanating from coupled liquid-hydrogen moderators with and without a premoderator in a graphite reflector were measured and compared with those from a decoupled liquid-hydrogen moderator. The results showed that the energy spectra from the coupled liquid-hydrogen moderators are almost the same as those from a decoupled one. Relative gain of the former to the latter is fairly high, more than 5, and further increases with increasing wavelength. The broadening of the neutron pulse width in coupled moderators at the cold-neutron region is not so significant and only 1.5 times compared to the solid methane moderator presently operated at KENS-I.

### Introduction

Development of a high-intensity cold neutron source is one of the most important R&D programs for KENS-II, the next generation pulsed neutron source in Japan. We are aiming at the realization of one order of magnitude higher beam intensity of time-averaged cold neutrons than ISIS with the nearly same proton beam intensity. The reason why we need it and a philosophy for the cold-neutron source in KENS-II are described in a separate contribution (Watanabe). As a first step of this program we decided to study coupled liquid-hydrogen moderators with a graphite reflector.

Bauer, et al., have already performed measurement of the effective multiplication factor  $k_{eff}$  of the system and reported a fairly large gain with a premoderator but an unexpected value of the effective multiplication factor. Higher gain is the most interesting feature of this kind of system, but higher  $T_N$  is a fatal disadvantage. Since we do not understand the reason why they observed such high  $T_N$ , we planned to perform careful measurements of energy spectra from these systems. In the present paper, we report the measured results on energy and time distributions from a liquid-hydrogen moderator with and without premoderators in a graphite reflector.

### Experiment

The electron linac at Hokkaido university was used as a neutron generator for the present optimization experiment. A target-moderator-reflector assembly is shown in

Fig. 1. The neutron generating target is a lead block of the dimensions shown in the figure. Energy and time-averaged electron beam current were 45 MeV and 60 nA, respectively, with a repetition rate of 47 Hz. The electron beam power was 27.5 W, which corresponds to the fast neutron production rate of  $6.9 \times 10^{10}$  n<sub>f</sub>/sec, assuming that the neutron yield from a non-fissionable heavy metal target is  $2.5 \times 10^{12}$  n<sub>f</sub>/sec/kW for this electron energy.

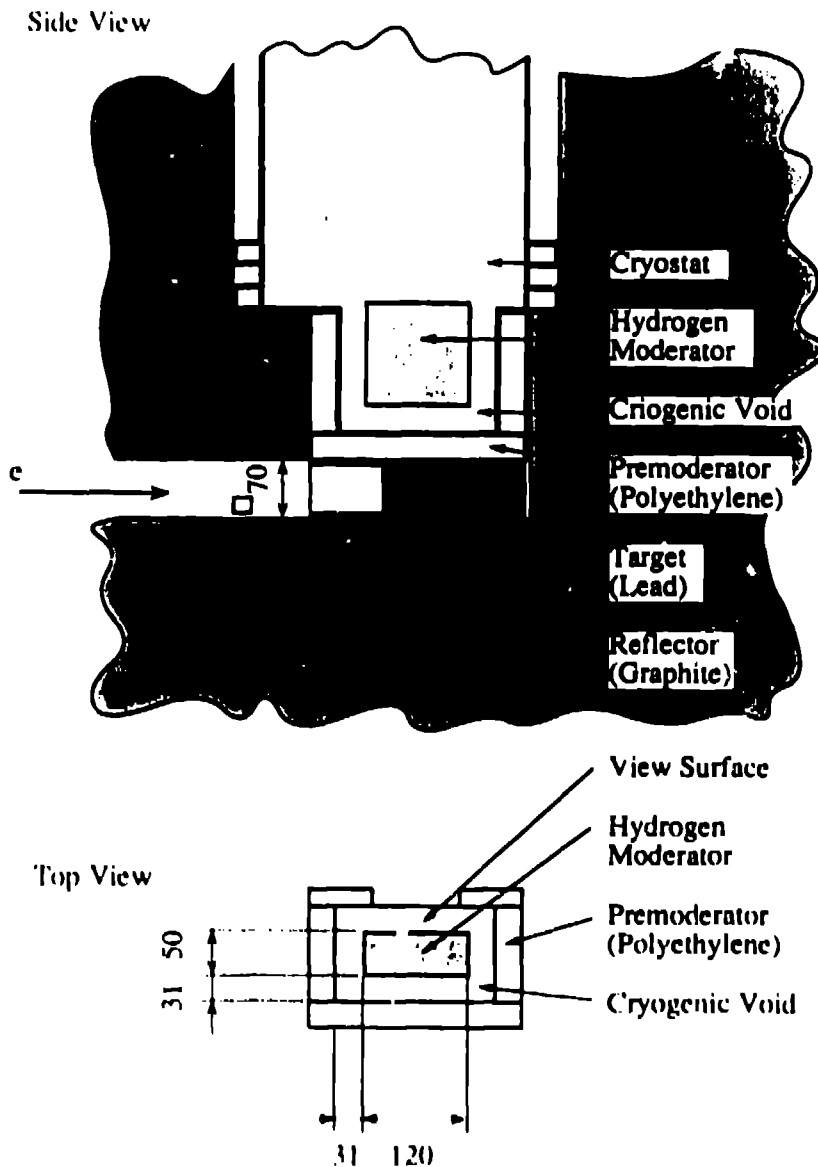


Fig. 1 Schematic representation of the target-moderator-reflector assembly used in the present experiment.

The cold moderator under study is liquid hydrogen, 12 cm wide x 12 cm high x 5 cm thick condensed in an aluminum container cooled by circulating low temperature helium. We initially performed measurements on a 5-cm-thick hydrogen moderator for convenience because it has already been shown that the gain factor of a coupled hydrogen moderator is not sensitive to the moderator thickness (Bauer, et al.) Polyethylene plates were used as the premoderator and the relative gain of the cold neutron beam intensity was measured as a function of the premoderator thickness. The target and the moderator were covered by a graphite reflector of the dimensions shown in Fig. 2, which has only two holes for the electron beam entrance and the neutron beam extraction. Figure 2 shows the layout of the experimental set-up. A helium-3 gas proportional counter of 1 inch in diameter and filled to 10 atoms. was used as a neutron detector. The detector was shielded by a sufficient amount of  $B_4C$  and borated resin. The detector was placed at about 6 m from the spectrum source for measurements of energy spectra by time-of-flight (TOF). In the case of the time distribution measurements, a crystal analyzer system shown in the figure was used. A mica crystal was used as analyzer crystal with Bragg angle  $2\theta_B = 160^\circ$  to obtain the required time resolution.

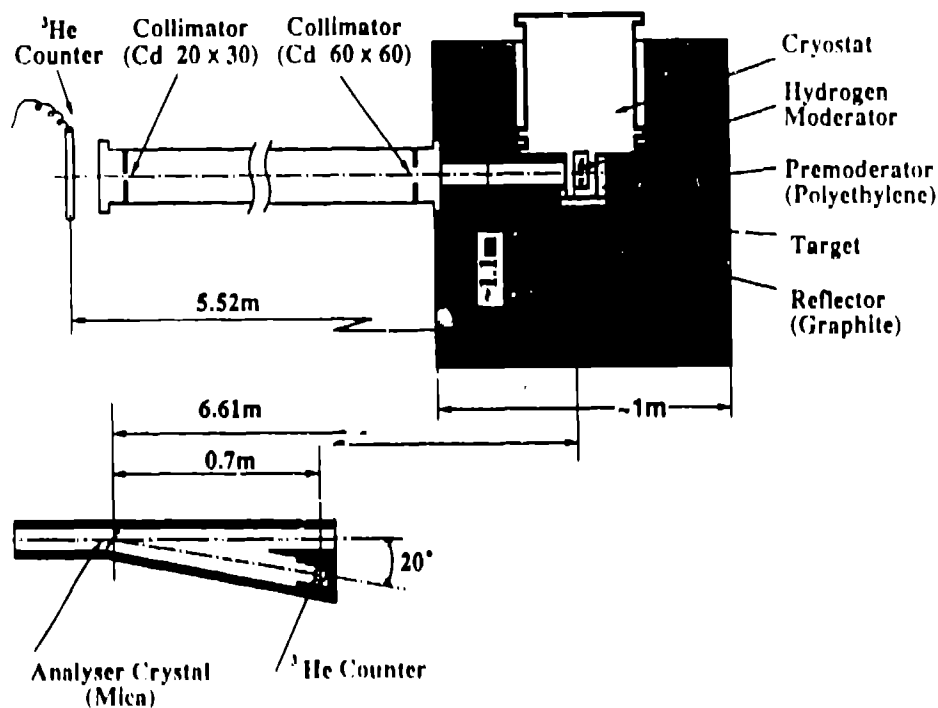


Fig. 2 Layout of the experimental set-up. The lower figure of the detecting system shows the crystal analyzer system used in the measurements of time distribution.



At the neutron beam exit of the target-moderator-reflector assembly, a beam slit made of cadmium with an opening of 60 mm x 60 mm was carefully positioned so the detector could view only the spectrum source. This is very important to obtain a correct  $T_N$  from a coupled moderator. Another cadmium slit with an opening of 20 mm x 30 mm was placed in front of the detector or the crystal analyzer system. Hydrogen gas was condensed in the moderator container cooled by a heat exchanger at the top of the moderator container. In the measuring time hydrogen was almost parahydrogen. The cryostat used in this preliminary experiment was not optimized for this purpose but was just an existing cryostat after the minimum modification. The cryostat, therefore, has a large volume above the moderator container and, consequently, removed considerable parts of the upper premoderator and the upper graphite reflector as shown in Fig. 2. Nevertheless, this system provided a fairly large gain factor as described later.

### Energy spectra

TOF spectra of neutrons from a cadmium-decoupled liquid-hydrogen moderator and various coupled ones in a graphite reflector, with and without premoderator, were measured. A bare liquid-hydrogen moderator was also measured for comparison. Measuring time was 2000 sec for each moderator. Figure 3 shows the energy spectra obtained from the TOF spectra after necessary corrections. The relative gain of the coupled moderators are considerably higher than either the bare moderator or the decoupled one.

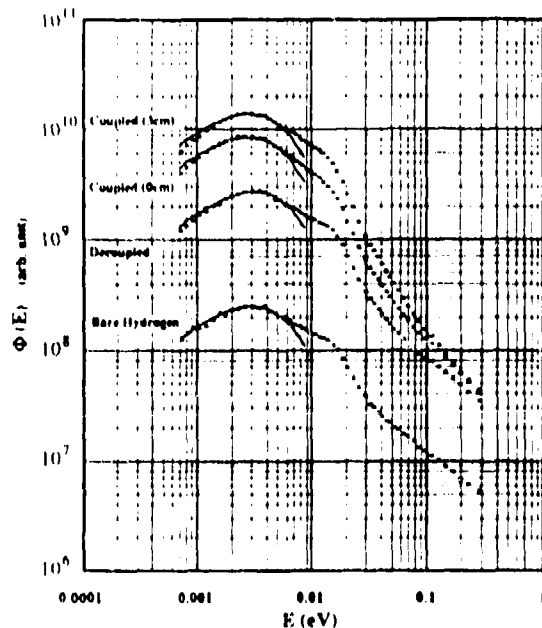


Fig. 3 Energy spectra from various moderators; from the top a coupled 5-cm-thick liquid hydrogen moderator with a 3-cm-thick polyethylene premoderator, a coupled one without premoderator and a decoupled one all in a graphite reflector, and a bare one. Solid curves show the Maxwell distributions fitted to the measured data below 5 meV.

It is well known that the energy spectrum from a liquid-hydrogen moderator is not expressed by a Maxwellian, but we fitted the spectra at lower energy region by Maxwellians as shown in Fig. 3 (solid curves). As obvious from the figure, the Maxwellian fits are not so bad if we restrict the energy range below 5 meV. The effective neutron temperatures  $T_N$  obtained by these fits are listed in Table 1.  $T_N$ 's of the coupled moderators with and without a premoderator are reasonably low and almost the same as that of the decoupled or the bare moderator. Present results are very much different from those by Bauer, et al. We confirmed  $T_N \sim 33\text{K}$ , while they reported a value of  $T_N \sim 80\text{K}$ . The present results show that the increase of the gain comes mainly from the coupling with reflector, and that the existence of the premoderator gives an additional gain that is not as large as the former.

**Table 1** Effective temperature of neutrons from various moderators.

Moderator	$T_N$ (K)*
Coupled (with polyethylene 3 cm thick)	33.2
Coupled (without premoderator)	32.8
Decoupled	36.5
Bare	34.8

\*accuracy of  $T_N$  is about  $\pm 1$  K

Next we studied the effect of the premoderator thickness on the relative gain. Here we define the relative gain as the ratio of the integrated cold-neutron-beam intensity below 5 meV from the coupled moderator to those from the decoupled one. Figure 4 shows the relative gain as functions of the bottom (between target and liquid hydrogen) and the side premoderator thickness. The relative gain increases with increasing bottom premoderator thickness and saturates at about 3 cm. The increase of the side premoderator thickness brings further increase of the relative gain, but it is rather modest and also saturates at about 3 cm as shown in the figures. The present results show that the optimal premoderator thickness is about 3 cm.

In Fig. 5 we plot the ratio of neutron beam intensity from the coupled moderator with the 3-cm-thick premoderator to that from the decoupled one as a function of neutron wavelength. The ratio increases slightly with neutron wavelength. This is also a benefit of the coupled moderator.

### Time distributions

We performed the measurement of neutron time distributions at various energies from the coupled moderator with the 3-cm-thick premoderator and from the decoupled moderator using the crystal analyzer system described in the preceding section. The results at selected energies are shown in Figs. 6 to 9 where the time distributions from both moderators are compared with each other. Solid curves show the enlarged profile from the decoupled moderator normalized at the pulse peak for direct comparison. The coupled moderator gives broader pulses than the decoupled one as expected, but the broadening is rather modest and the increase in the peak intensity is unexpectedly high. This means that the larger gain of the coupled moderator is not mainly due to the increase of the pulse width, but to the increase in the peak intensity. This feature is very much favorable for a pulsed cold-neutron source.

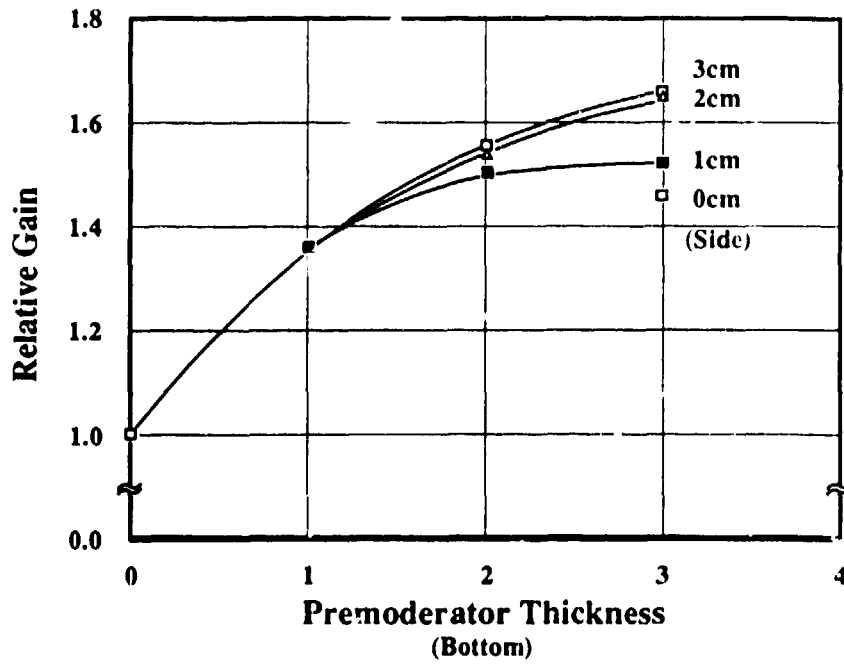


Fig. 4 Relative gain of coupled moderators below 5 meV as functions of bottom and side premoderator thickness.

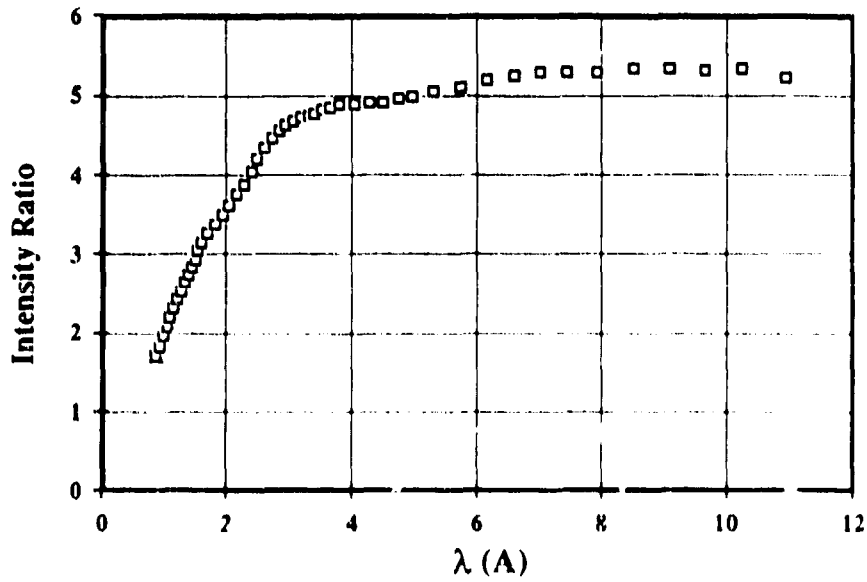


Fig. 5 Ratio of neutron beam intensity from the coupled moderator with a 3-cm-thick premoderator to that from decoupled one as a function of neutron wavelength.

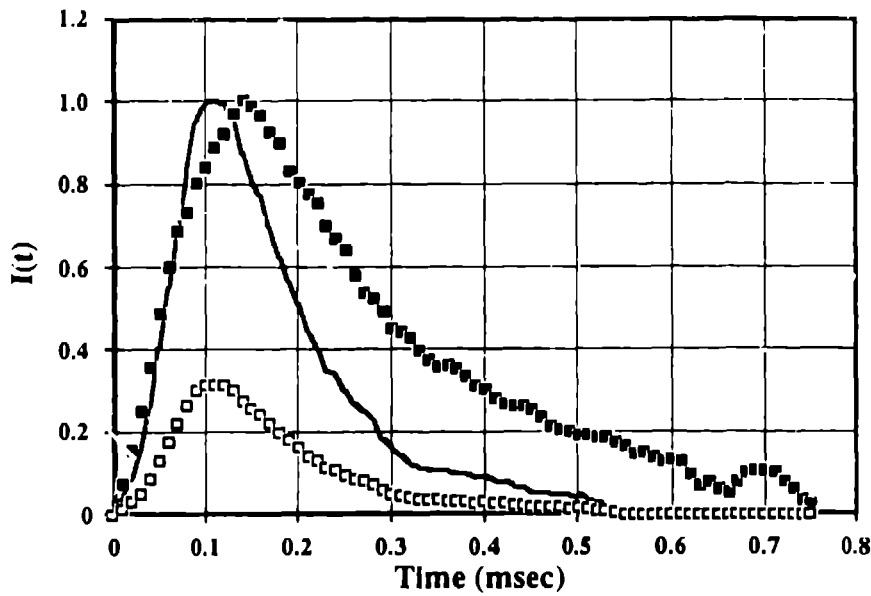


Fig. 6 Time distributions of 0.82 meV neutrons emanating from the coupled moderator (solid square) and the decoupled one (open square). Solid curve shows the latter normalized at pulse peak for direct comparison.

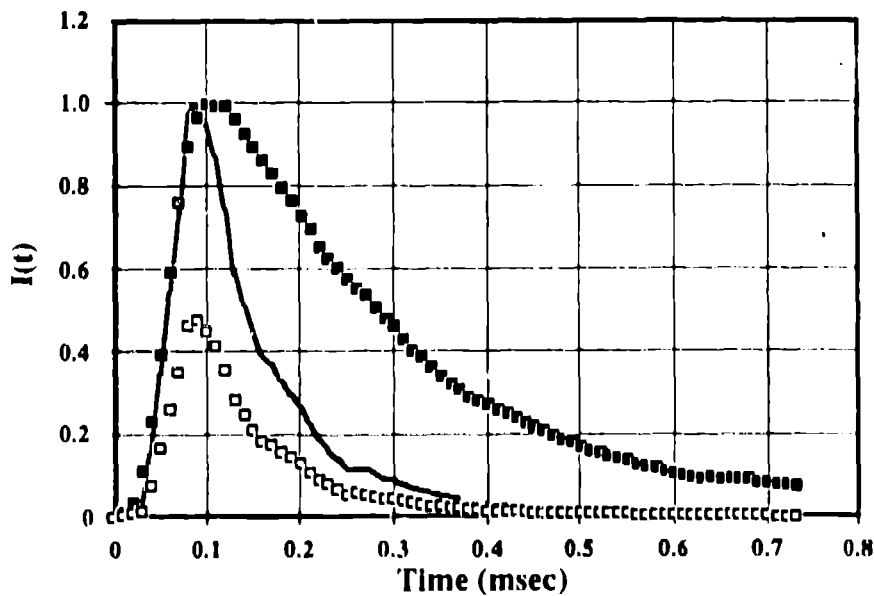


Fig. 7 Time distributions of 5.1 meV neutrons emanating from the coupled moderator (solid square) and the decoupled one (open square). Solid curve shows the latter normalized at pulse peak for direct comparison.

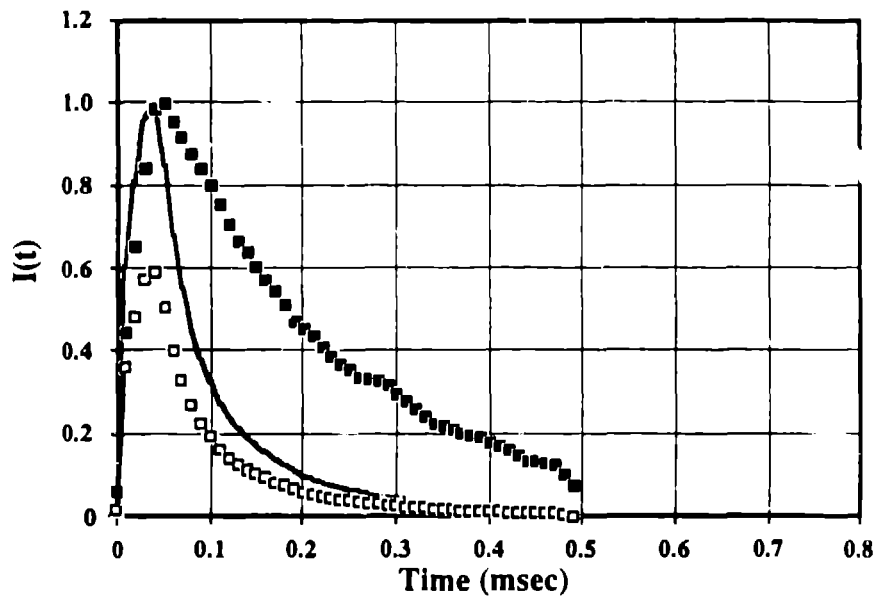


Fig. 8 Time distributions of 16.5 meV neutrons emanating from the coupled moderator (solid square) and the decoupled one (open square). Solid curve shows the latter normalized at pulse peak for direct comparison.

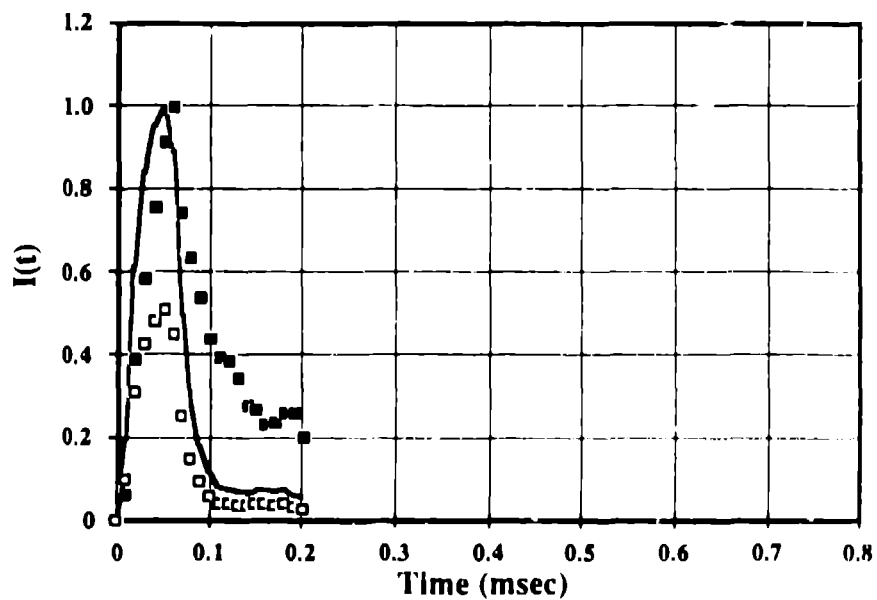


Fig. 9 Time distributions of 40.1 meV neutrons emanating from the coupled moderator (solid square) and the decoupled one (open square). Solid curve shows the latter normalized at pulse peak for direct comparison.

As obvious from the direct comparison with the data from the decoupled moderator (solid curves), the rising characteristics of the neutron pulses from the coupled moderator are almost the same as those from the decoupled one. This will be another important merit of this type of moderator. The present values, however, are considerably larger than those of the KENS solid methane moderator.

Neutron pulse widths, in full width at half maximum (FWHM), from these two moderators are plotted in Fig. 10 as a function of neutron wavelength. The corresponding values from the solid methane moderator at 20 K presently used at KENS are also shown by a solid curve for comparison. The pulse widths from the coupled moderator are about a factor of two broader than those from the decoupled one and only about a factor of 1.5 if we compared with those from the present KENS solid methane.

Figure 11 shows the semi-logarithmic plots of the time distributions displayed in Fig. 7. Reciprocal decay time  $\alpha$ 's at various wavelengths are obtained from these plots and shown in Fig. 12.

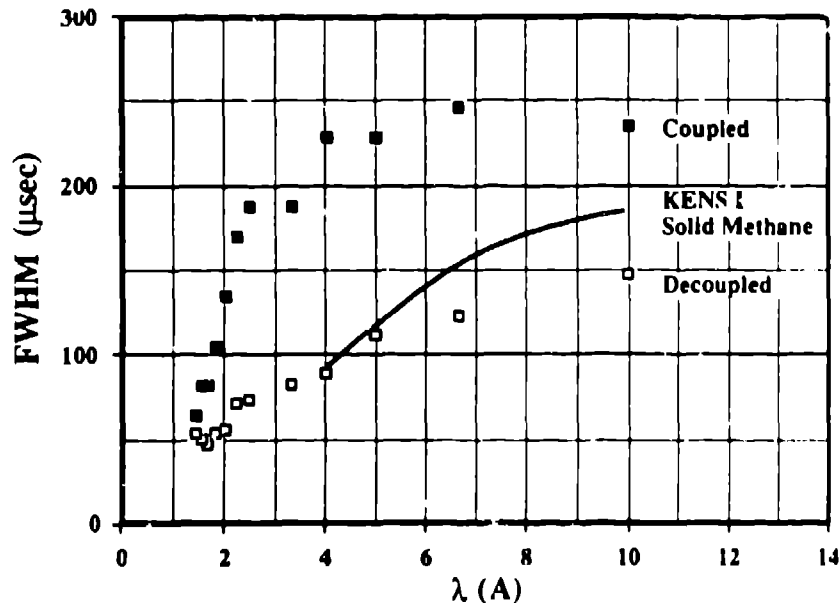


Fig. 10 Neutron pulse widths (FWHM) from the coupled (solid square) and decoupled (open square) moderators as a function of neutron wavelength. Solid curve shows the corresponding values of the present KENS solid methane at 20 K.

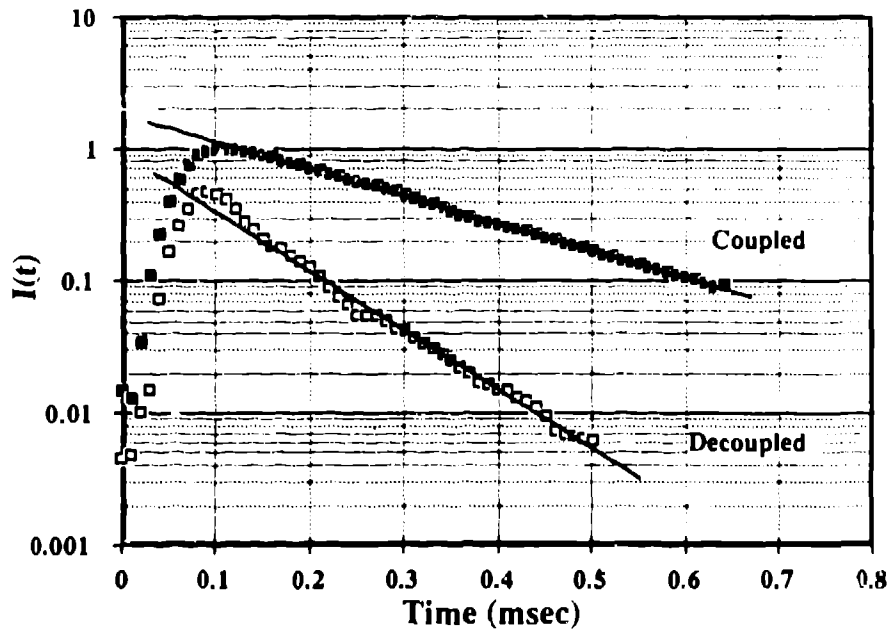


Fig. 11 Semi-logarithmic plots of the time distribution of 5.1 meV neutrons. Reciprocal decay time  $\alpha$ 's were determined from the straight line.

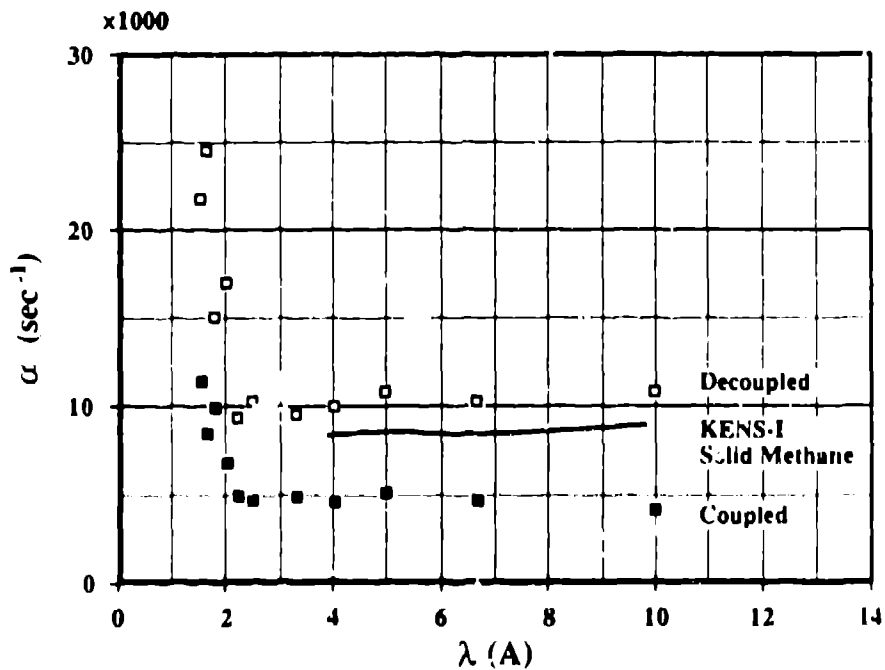




Fig. 12 Reciprocal decay time  $\alpha$ 's from the coupled and decoupled moderators as a function of neutron wavelength.



## Discussions and conclusions

In the present experiment on the preliminary optimization of coupled cold moderator, we confirmed a fairly large gain relative to the decoupled hydrogen moderator with a reasonably lower effective neutron temperature. The pulse characteristics of the coupled moderator turned out to be more encouraging than we expected; modest broadening in pulse width, higher peak intensity, and the same rising time as the decoupled one. The present experiment, however, is not absolute measurements but the relative ones. It is, therefore, difficult to argue about the absolute value of the conversion efficiency (cf. contribution by Watanabe). However, we estimated a rough value of the conversion efficiency achieved with the present coupled moderator, which is already better than the value in the present KENS solid methane moderator. Further optimization experiments with a dedicated cryostat are in progress.

## References

- Bauer, G., Conrad, H., Fischer, W., Grünhagen, K. and Spitzer, H., 1985, Proc. ICANS-VIII, RAL-85-110, p. 344.  
Watanabe, N., 1988, to be published in this proceedings.
- 
- 



## Measured neutron beam line shielding effectiveness of several iron/polyethylene configurations

*G. L. Legate*  
Los Alamos Neutron Scattering Center  
Los Alamos, New Mexico 87545 USA

*M. L. Howe and R. L. Mundis*  
Los Alamos Accelerator Health Protection Group  
Los Alamos, New Mexico 87545 USA

**ABSTRACT:** Neutron and gamma-ray leakage measurements were taken at various stages of shield construction for neutron flight path 5 (the Lash-up flight path) at LANSCE, to compare the relative effectiveness of several configurations. Dose equivalent rates were determined for three categories: "low-energy neutrons", below 20 MeV; "high-energy neutrons", above 20 MeV; and gamma rays, as measured by hand-held survey instruments. The low-energy neutrons were measured by activation of an indium foil in a paraffin-filled cadmium canister, sized to be generally insensitive above 20 MeV. High-energy neutrons were measured by (n,2n) production of Carbon 11 in a plastic scintillator with a 20-MeV threshold. Thermal neutrons were not measured at the shield-leakage test points. Room-scattered neutrons were observed by Albatross IV detector readings, which were taken beside the shield as a measure of variation of room background as the shield configuration changed.

A sketch of the final shield cross section is shown in Figure 1. For these tests, the walls were completed as shown, and the top was added in stages. Measurements were taken directly above the beam pipe at two and four feet from the LANSCE bulk shield. The four-foot data is more representative of shielding a beam pipe with neutron collimators, as opposed to data taken nearer the inefficient interface between the flight path shield and the bulk shield. We think that a strong component of high-energy neutrons impinges on the beam path collimators and nearby shielding because of lack of adequate high-energy collimation within the bulk shield. Thus, the source is strengthened by spallation and evaporation spectra within the flight-path shield.

The data tabulated in Table 1 are generally self explanatory. "P" refers to commercial high-density polyethylene, typically of specific gravity 0.94. "BP" refers to five-wt.-percent borated polyethylene of generic commercial varieties. One important indication of these data is the utility of efficient lamination and relative thicknesses of shield materials.

Although the data represent a small and perhaps specialized sample, one interesting finding is that the "plain" polyethylene reduces the neutron and total doses (in spite of the 2.2 MeV gammas) more than the borated polyethylene. This effect is not

unexpected for shields of this thickness, where a strong high-energy component occurs in the source; addition of the boron compounds displaces ~25% of the hydrogen in the polyethylene. The resulting effect is strongly source-dependent and may also be quite geometry-dependent, considering neutron buildup and reflection from opposite walls within the shielded cavity. Gary Russell has performed leakage calculations for a large number of shield configurations, reported elsewhere, which show the interplay of these effects.

#### ACKNOWLEDGEMENTS

This work was done with the scheduling support and encouragement of Dick Woods, A. Jerry Miller, and Roger Pynn, and with financial support of the U. S. Department of Energy, Office of Basic Energy Sciences. We acknowledge useful discussions with Gary Russell and typing support of Teri Cordova.

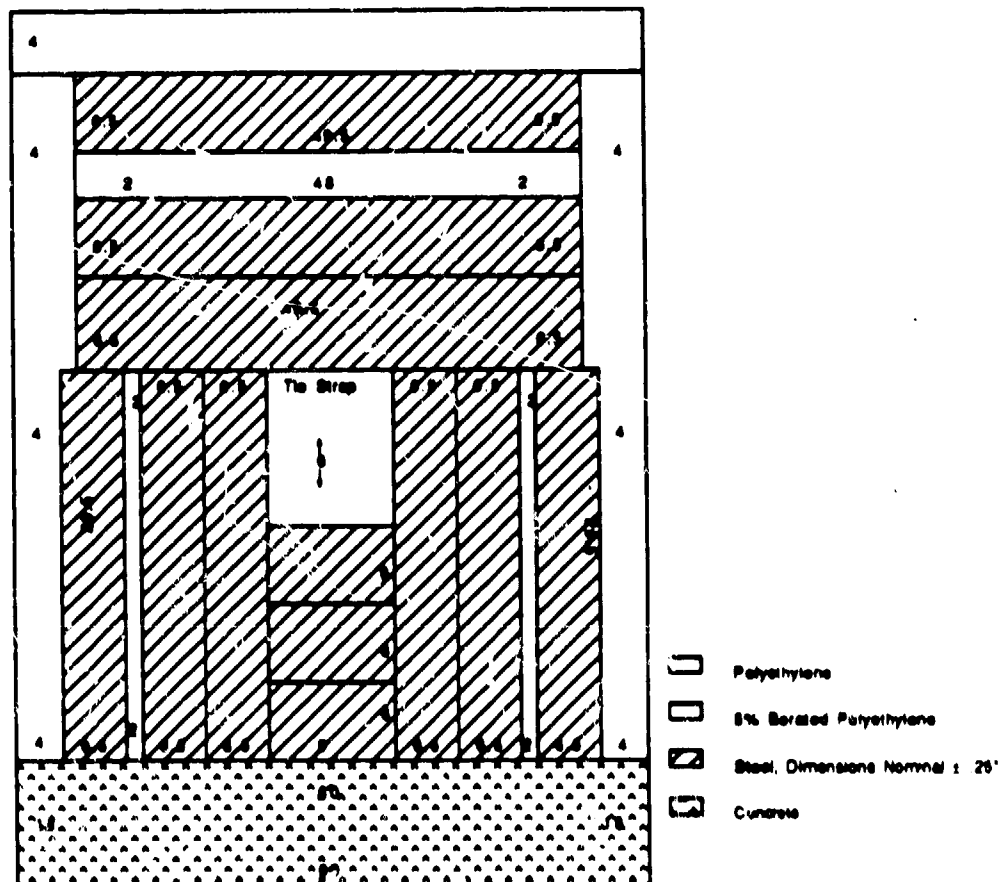


Fig. 1 Flight pr.th 5 shielding cross section schematic diagram.

Table I  
 FLIGHT PATH FIVE SHIELD TEST RESULTS, OCTOBER 25-31, 1987  
 mrem/hr

SHIELD CONFIGURATION INCHES	2 FT				4 FT				SIDE
	LEN	HEN	G	TOTAL	LEN	HEN	G	TOTAL	LEN
6Fe	1540	32	160	1730	1000	36	104	1140	23
6Fe,4BP	355	30	40	425	116	27	14	157	6.1
12Fe	1340	14	40	1400	787	10	25	822	20
12Fe,12BP	10	8	4	22	8	4	2	14	6.1
12Fe,2P,6Fe,4P	2.6	3.6	2.1	8.3	.9	1.2	1.1	3.2	0
12Fe,2P,6Fe	53	5.4	3.6	61	28	2	1.6	32	0.4
12Fe,2P,6Fe,4BP	4.7	3.4	1.6	9.7	3.2	1.8	0.6	5.6	1.4
Shutters Closed	0.6	6	0.4	7	0.6	6.4	0.4	7.4	3
Background									

HEN = High-energy neutrons, > 20 MeV, measured by carbon scintillator activation, using flux-to-dose rate conversion factor (5 n hr/mrem cm<sup>2</sup> s)

LEN = Low-energy neutrons, < 20 MeV, measured by moderated indium foil activation, using flux-to-dose rate conversion factor (7 n hr/mrem cm<sup>2</sup> s)

Thermal neutrons (< 3% of dose) not measured

Background (FP-4 and FP-5 shutters closed) subtracted from data

## Equivalent spherical-shield-neutron-dose calculations

G. J. Russell and H. Robinson  
Los Alamos Neutron Scattering Center  
Los Alamos, New Mexico 87545 U.S.A.

**ABSTRACT:** Neutron doses through 162-cm-thick spherical shields were calculated to be 1090 and 448 mrem/h for *regular* and *magnetite concrete*, respectively. These results bracket the measured data, for *reinforced regular concrete*, of ~600 mrem/h. The calculated fraction of the high-energy (> 20 MeV) dose component also bracketed the experimental data. The measured and calculated doses were for a graphite beam stop bombarded with 100 nA of 800-MeV protons.

### Introduction

Shielding issues were the highest priority concerns at the Los Alamos Neutron Scattering Center (LANSCE)<sup>(1)</sup> in FY-88. LANSCE uses 800-MeV protons from the Clinton P. Anderson Meson Physics Facility (LAMPF)<sup>(2)</sup> to produce neutrons for basic materials science and nuclear physics research. As can be seen in Fig. 1, the LANSCE target area has vertical proton insertion. LANSCE shielding concerns include: a) proton beam line shielding, b) target shielding, and c) neutron beam line, chopper, and beam-stop shielding. We launched both a computational endeavor<sup>(3)</sup> and an experimental effort<sup>(4)</sup> to better *understand* the complexities associated with adequately shielding a spallation neutron source.

Neutron-dose measurements were made<sup>(5)</sup> in the LANSCE experimental area below the proton beam line at a location downstream from where protons are extracted to the White Source experimental area (see Fig. 1). The 800-MeV proton beam impinged on a 50-cm-diam by 200-cm-long graphite beam stop. The proton current was 100 nA.

The shield under study was the reinforced regular concrete floor (152-cm-thick) of the proton beam line. Our previous experience had shown that the maximum dose (for this type of geometry) should be expected at about 60 degrees from the proton beam direction. Measurements were made at roughly 70 degrees (see Fig. 2).

The actual shield geometry was simplified for the calculations by assuming an equivalent spherical shield with a thickness of the 70-degree slant distance (162 cm) through the beam-channel floor. The high-energy (> 20 MeV) neutron-source term was chosen to be an isotropic point source located at the center of the spherical-shield cavity. The graphite beam stop per se was not mocked up in the Monte Carlo shielding calculations. The strength of the point source was taken to be  $4\pi$  times the neutrons per steradian in the angle bin 50-105 degrees leaking from the graphite beam stop (see Fig. 2).

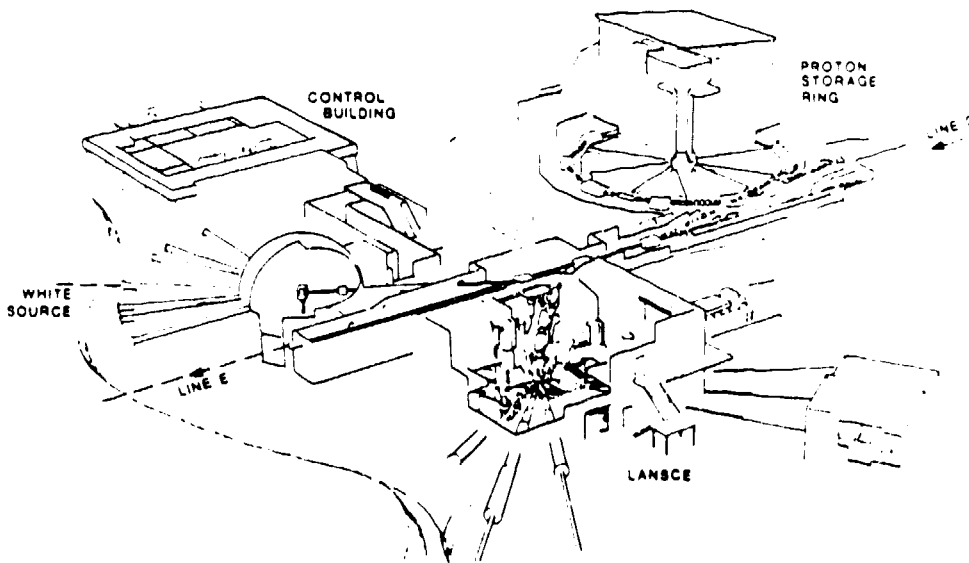


Fig. 1 General layout of the LANSCE/WNR complex. The Neutron Scattering Experimental Hall, completed in 1988, surrounds the present LANSCE experimental hall (shown in the foreground) and greatly enhances the overall LANSCE experimental area.

Primary low-energy ( $< 20$  MeV) neutrons produced in the graphite beam stop were ignored in the calculations. The high-energy neutrons and secondary low-energy neutrons produced by high-energy reactions in the shield were tracked to the detector location and converted to dose. The floor of the LANSCE experimental area was ignored in the computations. Air-filled regions were assumed to be both inside and outside the shield zone.

The computations were done with the Los Alamos Monte Carlo code package.<sup>(6)</sup>

## Results

The LANSCE beam-channel floor in the vicinity of the shield measurement is *reinforced regular concrete*. Since we did not know the iron content of this shield, we performed computations for both *regular* and *magnetite concrete*, hoping to bracket the effectiveness of the actual shield material. The results of the calculations, compared to experimental data, are shown in Table 1. Indeed, the experimental results are bracketed by our calculations. The magnetite concrete data is closer to the measured values, indicating the significance of the iron reinforcing bars used in the actual construction of the beam-channel floor. The effect of including the LANSCE experimental area floor in the computations would produce some low-energy albedo neutrons to add to the low energy dose component at the detector location.

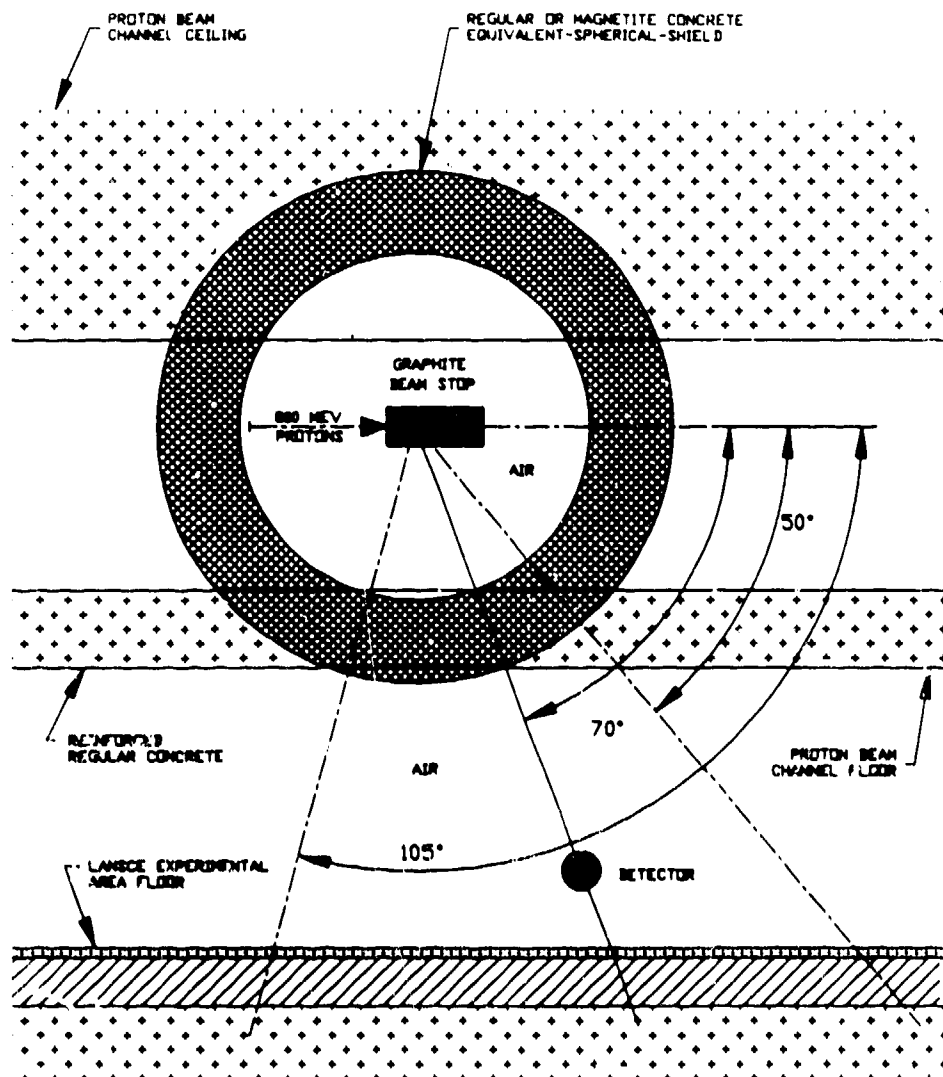


Fig. 2 A simplified schematic diagram of the LANSCE proton beam channel, showing the equivalent spherical shield for the beam channel floor. The location of the measurement, relative to the proton beam stop, is also illustrated. The graphite beam stop was replaced by a point isotropic source in the calculations.

Shield	mrem/hr		
	Hi-E E>20 MeV	Lo-E E<20 MeV	Total E<800 MeV
Magnetite Concrete (calc)	289	159	448
Reinforced Regular Concrete (exp)*			500-700
Regular Concrete (calc)	753	337	1090
	Dose E > 10 MeV		
Magnetite Concrete (calc)		69.4%	
Reinforced Regular Concrete (exp)*		70.0%	
Regular Concrete (calc)		74.0%	

\*M. Howe and R. Mundis (Ref. 5)

**Table 1** Neutron dose through various shields for 100 nA of 800 MeV protons on a graphite beam stop.

### Conclusions

Equivalent-spherical-shield calculations of a relatively complex proton-beam-stop/proton-beam-line shielding scenario yield results that agree with measured values. This lends confidence to employing simplified shield approximations to geometrically complicated problems.

### Acknowledgements

We appreciate useful discussions with Bill Wilson and Gail Legate and the continued support of Roger Pynn and Dick Woods for this work. We thank Teri Cordova for her typing help.

This work was performed under the auspices of the U. S. Department of Energy, Office of Basic Energy Sciences.

## References

1. G. J. Russell, et al., "The LANSCE Target System", ICANS-IX Proceedings of the 9th Meeting of the International Collaboration on Advanced Neutron Sources, Villigen, Switzerland, September 22-26, 1986, ISBN 3-907998-01-4, pp. 177-244 (April 1987).
2. M. S. Livingston, "LAMPF, A Nuclear Research Facility", Los Alamos National Laboratory Report, LA-6878-MS (1977).
3. G. J. Russell, "Shielding Concerns at a Spallation Source", these proceedings.
4. G. L. Legate, R. L. Mundis, and M. L. Howe, these proceedings
5. M. L. Howe and R. L. Mundis, "Neutron Spectrum Measurement, LANSCE/ER-1", these proceedings.
6. R. E. Prael, "High-Energy Particle Monte Carlo at Los Alamos", Monte Carlo Methods and Applications in Neutronics, Photonics, and Statistical Physics, eds., R. Alcouffe, R. Dautray, A. Forster, G. Ledanois, and B. Mercier, Springer-Verlag Publisher, Berlin/Heidelberg, 1985, pp. 196-206.



## Infinite slab-shield dose calculations

*G. J. Russell*  
Los Alamos Neutron Scattering Center  
Los Alamos, New Mexico 87545  
USA

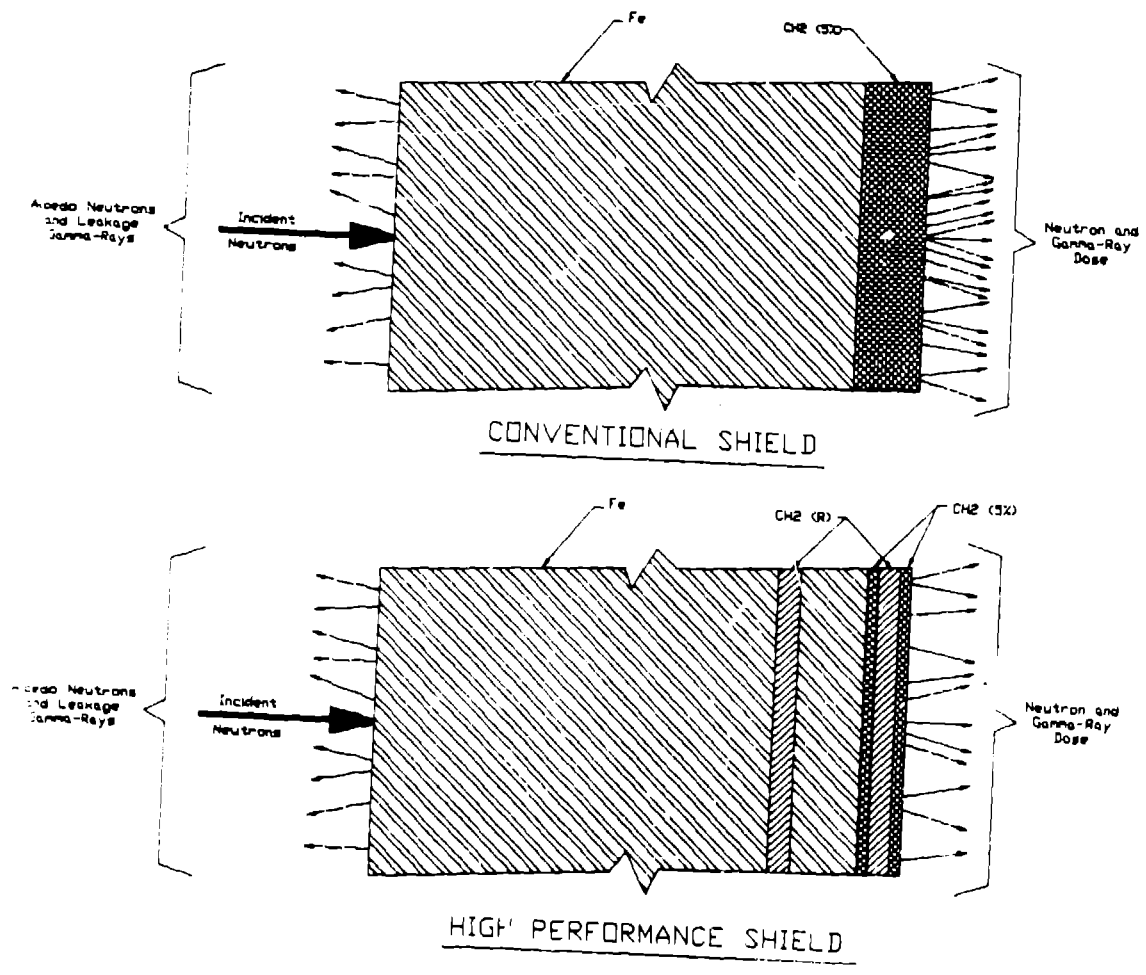
ABSTRACT: I calculated neutron and gamma-ray equivalent doses leaking through a variety of infinite (laminated) slab-shields. In the shield computations, I used, as the incident neutron spectrum, the leakage spectrum (< 20 MeV) calculated for the LANSCE tungsten production target at 90° to the target axis. The shield thickness was fixed at 60 cm. The results of the shield calculations show a minimum in the total leakage equivalent dose if the shield is 40-45 cm of iron followed by 20-15 cm of borated (5%B) polyethylene. *High-performance* shields can be attained by using multiple laminations. The calculated dose at the shield surface is very dependent on shield material.

### Introduction

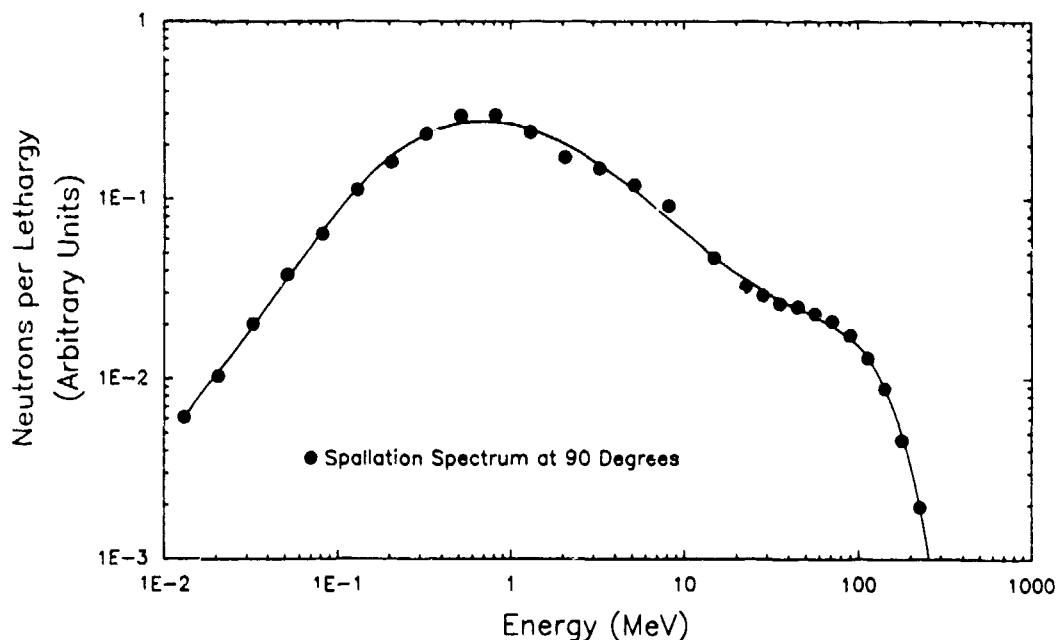
I performed a series of equivalent dose calculations for a variety of shield laminates bombarded by a neutron spectrum characteristic of the LANSCE tungsten production target. The computations were done using the Los Alamos Monte Carlo code MCNP<sup>(1)</sup>. I chose infinite slab geometry (see Fig. 1) to simplify problem execution and develop a "feel" for the issues involved. The incident spectrum was that calculated leaking below 20 MeV from the LANSCE 10-cm-diam tungsten target at 90° to the target axis<sup>(2)</sup> (see Fig. 2). A point source of mono-directional neutrons was assumed incident normal to the inner shield surface. I calculated neutron and gamma-ray surface-fluxes at the opposite (outer) shield surface and converted to equivalent dose using the flux-to-dose conversion factors in Ref 2. I also looked at albedo neutrons and leakage gamma rays at the inner shield surface.

I investigated a variety of shield materials. The overall shield thickness was fixed at 60 cm (a typical shield-size at LANSCE). The intent of this study was to analyze the sensitivity of the dose at the outer shield surface to variations in shield laminate composition. The primary motivation for the work was to recommend a shield configuration for the LANSCE FP-5 shield.<sup>(3)</sup>

In neutron beam line shield design, consideration must be given to neutron and gamma-rays at *both the inner and outer shield surfaces*. Inner-surface radiations can affect neutron instrument backgrounds; outer-surface radiations may contribute to instrument backgrounds, but are definitely a biological dose concern.



**Fig. 1.** Infinite slab-shield mockup showing conventional and high-performance shield configurations.

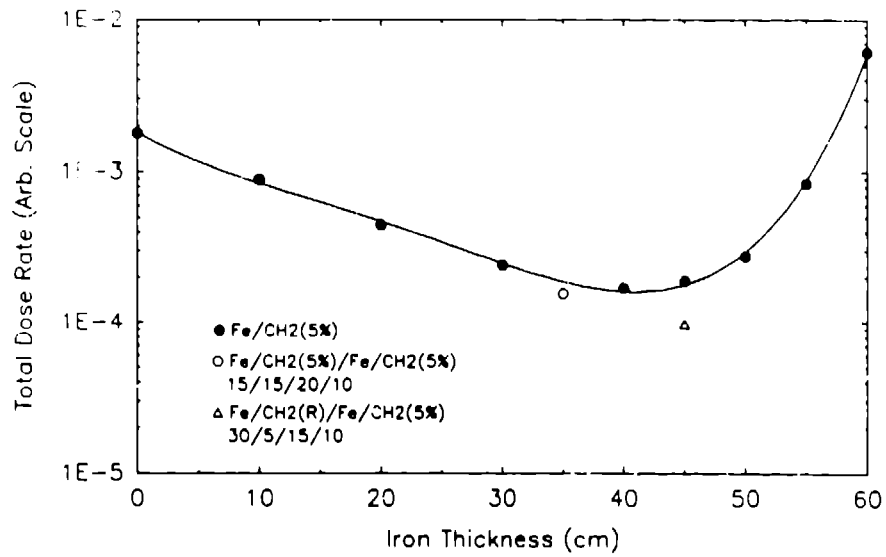


**Fig. 2.** Calculated neutron leakage (at 90°) from the 10-cm-diam LANSCE tungsten production target bombarded by 800-MeV protons. The neutron spectrum below 20 MeV was used in the shield studies.

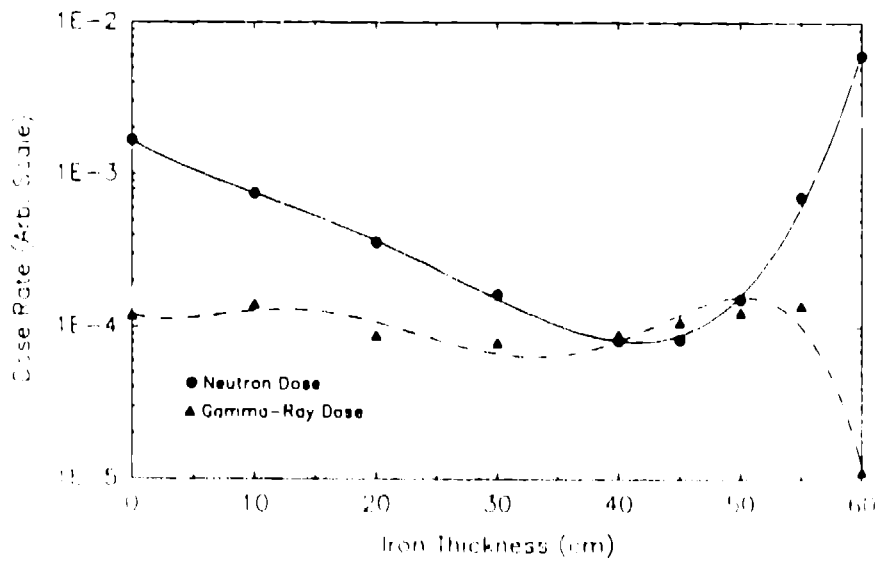
## Results

A summary of the shields studied are given in Tables I and II. The "conventional" method of constructing neutron beam line shielding at spallation sources is to have an inner iron zone followed by a borated outer region of wax or polyethylene.<sup>[4]</sup> We mocked up this conventional shield and varied the iron thickness from 0 cm (an all polyethylene shield) to 60 cm (an all iron shield). The results are shown in Fig. 3. There is a minimum in the total equivalent dose curve for a laminate shield of 40-45 cm of iron followed by 20-15 cm of polyethylene (5%B). I also studied other shield laminates. The results for two of these laminates are also shown in Fig. 3; *significant gains can be achieved by multiple (> 2) laminations*. No attempt was made to find the "optimum" laminate.

In Fig. 4, I show the neutron and gamma-ray equivalent dose components for the conventional shield configuration as a function of iron thickness. The neutron and gamma-ray dose components are equal at ~40 cm of iron. Except for the iron thickness range of ~35-50 cm, the total dose is dominated by the neutron dose. In the region of iron thickness where the gamma-ray dose component is significant, multiple laminates can be used to reduce the gamma-ray dose component (see Table I). For the all-iron shield, the total dose is nearly entirely due to neutrons; presumably, "windows" in the iron cross section are important in this context.



**Fig. 3.** Calculated total equivalent dose rates at the outer surface of infinite slab-shield laminates. The curve is drawn as a guide-to-the-eye.



**Fig. 4.** Calculated neutron and gamma-ray equivalent dose rate components at the outer surface of infinite slab-shield laminates. The curves are drawn as guides-to-the-eye.

Table I. Calculated Doses at the Outer Shield Surface			
Shield Configuration	Neutron Dose (Arb. Units)	Gamma-Ray Dose (Arb. Units)	Total Dose (Arb. Units)
(Reference) Fe/CH2(R)/Fe/CH2(5%)/CH2(R)/CH2(5%) 30/5/15/2.5/5/2.5 cm % of Total	6.49E-05 70.7	2.69E-05 29.3	9.18E-05
Fe/CH2(R)/Fe/CH2(R)/Pb/CH2(7%) 30/5/15/5/2.5/2.5 cm % of Total	8.31E-05 88.5	1.08E-05 11.5	9.39E-05
Fe/CH2(R)/Fe/CH2(5%) 30/5/15/10 cm % of Total	7.49E-05 76.3	2.33E-05 23.7	9.82E-05
Fe/CH2(R)/Fe/CH2(R) 30/5/15/10 cm % of Total	6.09E-05 55.9	4.80E-05 44.1	1.09E-04
Fe/CH2(5%)/Fe/CH2(5%) 15/15/20/10 cm % of Total	1.44E-04 92.2	1.22E-05 7.8	1.56E-04
Fe/CH2(5%) 40/20 cm % of Total	8.12E-05 47.8	8.88E-05 52.2	1.70E-04
Fe/CH2(5%) 45/15 cm % of Total	8.27E-05 43.4	1.08E-04 56.6	1.91E-04
Fe/CH2(5%) 30/30 cm % of Total	1.63E-04 67.3	7.90E-05 32.7	2.42E-04
Fe/CH2(5%) 50/10 cm % of Total	1.51E-04 54.9	1.25E-04 45.1	2.76E-04
Fe/CH2(5%) 20/40 cm % of Total	3.57E-04 80.2	8.80E-05 19.8	4.45E-04
Pb/CH2(5%) 45/15 cm % of Total	5.87E-04 83.7	1.14E-04 16.3	7.02E-04
Fe/CH2(5%) 55/5 cm % of Total	7.05E-04 83.6	1.38E-04 16.4	8.43E-04
Fe/CH2(5%) 10/50 cm % of Total	7.50E-04 84.2	1.41E-04 15.8	8.91E-04
CH2(5%) 60 cm % of Total	1.67E-03 93.3	1.19E-04 6.7	1.79E-03
Regular Concrete 60 cm % of Total	5.05E-03 95.7	2.26E-04 4.3	5.28E-03
Fe 60 cm % of Total	6.08E-03 99.8	1.12E-05 0.2	6.10E-03

Table II. Calculated Relative Shield Performance			
Shield Configuration	Neutron Dose	Gamma-Ray Dose	Total Dose
(Reference) Fe/CH <sub>2</sub> (R)/Fe/CH <sub>2</sub> (5%)/CH <sub>2</sub> (R)/CH <sub>2</sub> (5%) 30/5/15/2.5/5/2.5 cm	1.00	1.00	1.00
Fe/CH <sub>2</sub> (R)/Fe/CH <sub>2</sub> (R)/Pb/CH <sub>2</sub> (7%) 30/5/15/5/2.5/2.5 cm	1.28	0.40	1.02
Fe/CH <sub>2</sub> (R)/Fe/CH <sub>2</sub> (5%) 30/5/15/10 cm	1.15	0.87	1.07
Fe/CH <sub>2</sub> (R)/Fe/CH <sub>2</sub> (R) 30/5/15/10 cm	0.94	1.78	1.19
Fe/CH <sub>2</sub> (5%)/Fe/CH <sub>2</sub> (5%) 15/15/20/10 cm	2.21	0.45	1.70
Fe/CH <sub>2</sub> (5%) 40/20 cm	1.25	3.30	1.85
Fe/CH <sub>2</sub> (5%) 45/15 cm	1.27	4.01	2.07
Fe/CH <sub>2</sub> (5%) 30/30 cm	2.51	2.94	2.63
Fe/CH <sub>2</sub> (5%) 50/10 cm	2.33	4.63	3.01
Fe/CH <sub>2</sub> (5%) 20/40 cm	5.50	3.27	4.84
Pb/CH <sub>2</sub> (5%) 45/15 cm	9.04	4.26	7.64
Fe/CH <sub>2</sub> (5%) 55/5 cm	10.9	5.14	9.18
Fe/CH <sub>2</sub> (5%) 10/50 cm	11.6	5.24	9.70
CH <sub>2</sub> (5%) 60 cm	25.7	4.43	19.5
Regular Concrete 60 cm	77.9	8.47	57.5
Fe 60 cm	93.7	0.42	66.4

In Table I, you can see the dramatic increase in dose for lead/polyethylene and regular concrete shields compared to an iron/polyethylene shield. There may be some benefit in sublamination of the outer polyethylene zone. This is particularly true if minimizing neutron dose is more important than decreasing gamma-ray dose.

Note in Table II that regular polyethylene at the outer surface of a conventional shield is more effective (by ~22%) than borated polyethylene in reducing neutron dose at the outer shield surface. However, the gamma-ray dose and escaping gamma-ray energy are higher for regular polyethylene.

### Conclusions

In general, gamma-ray equivalent dose is not explicitly considered in the context of neutron beam line shielding at spallation neutron sources.<sup>(4)</sup> *It is important to contemplate the total (neutron plus gamma ray) equivalent dose in neutron beam line shield design.* For a conventional shield laminate of iron followed by borated (5%) polyethylene, I have shown that the minimum total equivalent dose is achieved when the lamination is 40-45 cm of iron followed by 20-15 cm of polyethylene. This is for an overall shield thickness of 60 cm, and for an incident neutron spectrum (< 20 MeV) characteristic of the LANSCE tungsten production target at 90° to the target axis.

I have shown that multiple laminates significantly improve shield performance, producing *high-performance shields*. No attempt was made to find the "optimum" laminate. The calculations indicate that (for dose considerations at the outer shield surface) caution should be exercised in using regular concrete and lead in neutron beam line shield applications.

No attention was explicitly given here to the importance of albedo neutrons and gamma-rays at the inner shield surface. These latter radiations are important in neutron beam line shield design because they can affect instrument backgrounds. For infinite slab-geometry, the magnitude of these albedo neutrons can be significant. For example, calculated neutron albedo currents at the inner shield surface are about 0.18, 0.56, 0.78, and 0.91 n/n for the polyethylene, regular concrete, iron, and lead shields, respectively.

For thicker shields, multiple laminations should provide high-performance shields. This work is essentially a "progress report" of what has been done to date. Considerable work needs to be done to explain all the effects found. I am studying shield laminates in spherical geometry for neutron beam line, chopper, and beam stop applications. In these deliberations, albedo neutrons can significantly affect total equivalent doses at the outer shield surface. For a fixed shield thickness, improvements in shield performance by factors of two or more (vis-à-vis high-performance shields) can have significant economic consequences.

We have evidence that shield performance is quite sensitive to the incident neutron spectrum; there appears to be significant shield performance enhancements for softer incident neutron spectra.

### **Acknowledgements**

I acknowledge the continued support of Roger Pynn and Dick Woods for this work, and for useful discussions with Gail Legate and Harold Robinson. I thank Teri Cordova for her typing help.

This work was performed under the auspices of the U. S. Department of Energy, Office of Basic Energy Sciences.

### **References**

1. J. F. Briesmeister, ed., "MCNP - A General Monte Carlo Code for Neutron and Photon Transport", Los Alamos National Laboratory report LA-7396-M, Rev. 2 (September 1986).
2. G. J. Russell, H. Robinson, C. L. Legate, "Shielding Concerns at a Spallation Source", in these proceedings.
3. G. L. Legate, M. L. Howe, and R. L. Mundis, "Measured Neutron Beam Line Shielding Effectiveness of Several Iron/Polyethylene Configurations", in these proceedings.
4. A. D. Taylor, T. A. Broome, and D. J. Picton, "Neutron Beam Shielding at ISIS", ICANS-IX, Proceedings of the 9th Meeting of the International Collaboration on Advanced Neutron Sources, F. Atchison and W. Fischer eds., Villigen, Switzerland, September 22-26, 1986, ISBN 3-907998-01-4, pp. 519-533 (July 1987).



## Workshop summary on computational techniques and shielding

*F. Atchison*  
Paul Scherrer Institute  
CH-5232 Villigen PSI  
SWITZERLAND

The target station workshop session on Thursday afternoon was in two parts: the first part was entitled "Computational Techniques and Shielding" and the second, which was chaired by Tim Broome, "Practical Concerns". As things turned out, a strict distinction between the two parts was not maintained and I am going to report about the first part which, by the end of the allotted time, had made the transition to practical concerns. Although the full text of the contributions should be included elsewhere in these proceedings, the summaries, as made at the Friday morning session, have been retained in this written version.

Before getting to the actual work discussed, I would like to make a couple of comments about the role of the calculator in source design. Calculations contributed in different ways at four principal stages of the project:

1. To sell a project to your management.
2. To allow the management to sell the project for funding.

I will skip over these.

3. To allow detailed design:

At this stage, the detailed calculations start. By their very nature these are principally theoretical, although they can be backed-up with results from other (running) facilities or an experimental program. There would seem to be three main goals:

- 3a. To produce the best system possible. This is principally neutronic optimization but carries with it the study of the other major concerns: heating, damage, activation, and radiation safety.
- 3b. To give/justify particular dimensions in the system. This is where the actual work lies: design engineers want exact numbers; normally the best we can do (not necessarily being engineers) is to say things like "make it as small as possible", or "as thin as possible."
- 3c. To restrain the design engineers. This is rather obvious and mainly involves neutronic considerations, e.g., trying to divert the engineers from neutronically bad materials.

#### 4. To improve an existing system.

Stage 4 calculations are rather different. Normally you have an operational source and real problems to solve (i.e., something has been measured that is unsatisfactory and must be fixed). The huge advantage is that the calculations can be backed up with measurements (compared to those at stage 3, where the measurements will be made after the calculations).

We started the session with an unscheduled but welcome "one-foil" presentation (Fig. 1) from Bruce Brown, to record the successful completion of mounting the IPNS Booster-target. This needs no summary!

The first presentation "*Design for a New PSR and LAMPF*" was given by Eugene Colton and described the motivation and design for a second generation proton storage ring at LAMPF.

The motivation comes from what he called the "Bauer" report and is to use the full potential of an upgraded LAMPF for production of spallation neutrons and neutrinos. The basis of the design is a pair of compressor rings for 1.6-GeV protons with an average current of 1.2 mA and a repetition frequency of 48 Hz. This will require that the present linac be upgraded by the addition of another 800 MeV of acceleration and the current from the ion-source be increased by a factor of two. The neutron and neutrino facilities are to have separate target stations, and each will receive alternate pulses (i.e., each facility will operate at 24 Hz). The aim is to provide pulses of length  $< 2 \mu\text{s}$  each containing  $1.5 \times 10^{14}$  protons. A major design goal is to keep losses very low ( $< 100 \text{ nA}$ ) so that "hands-on" maintenance can be done. In operation, the two rings are to be filled with  $7.5 \times 10^{13}$  protons, which are fast-extracted in a single turn to either one of the transfer lines. The two pulses are sent in box-car fashion to the source target(s) to give a 1.7- $\mu\text{s}$ -long pulse consisting of two 750-ns lumps of protons separated by 200 ns. The machine looks feasible on the basis that  $4 \times 10^{13}$  protons per pulse have been stored in the PSR and other basic ideas put forward in the design have been tested. There do remain many open questions and specific details; in particular, to achieve the low beam-losses required.

The second presentation "*Some Neutronic Calculations for KENS-II*" was by Masatoshi Arai and concerned the neutronic optimization of KENS-II. This work is typical of stage 3 calculations (see above) and also typifies the lot of the calculator, namely the huge amount of effort that has to be put in to settle comparatively few parameters. He presented the results of a calculational "tour-de-force" to allow selection of target material and dimensions and positions for the moderators: these calculations were based on use of moderated neutron intensity (i.e., usable flux) as figure-of-merit. He also studied the effect of different beam energies when the total beam power (product of beam energy and current) is kept constant. Summarizing, his results show that the increased incident energy (0.8 to 2 GeV) does give increased moderator flux, but when the reduced current (for equal power) is taken into account, the best flux is obtained with 0.8 GeV, i.e., beam current dominates.

The last four presentations:

*"Neutron Beam-Line Shield Calculations"*  
*"LANSCE Neutron Beam-Line FP-1 and FP-5 Shield Designs"*  
*"Bulk Shield/Neutron Instrument Shield Interface"*  
*"LANSCE Neutron Beam-Line Dose Measurements"*

were taken together and led by Gary Russell: these gave a good mixture of presentation and discussion. The main theme was how to shield the instrument-flight-path section outside the bulk shield at LANSCE (a good example of a stage 4 calculation). There are two simultaneous considerations: (i) external dose rate plus background at other instruments; and (ii) reflection back from the shielding to the flight path causing background problems at the instrument whose flight-path is being shielded. Gary presented the results of a wide survey for the performance of various laminated shields. Many of the results of the calculations have been confirmed by measurements.

We talked about the bulk-shield/instrument-flight-path interface. We came to the conclusion that this needs a lot of care, in particular the design of the outer layer of the bulk-shield should include recesses to allow stepping-in to join with the flight-path shield so that streaming paths are eliminated.

Noburu Watanabe pointed out the rather large size difference between beam-catchers at ISIS, IPNS, and LANSCE. I don't think we actually resolved the issue. One point that came out of the discussion was that the sizes are not necessarily only based on neutronic considerations. When you, for instance, have iron blacks in stock with rather larger dimensions than you really need, you use them (they are in some sense "free"): hence, part of the answer of the size-difference question comes from practical concerns.

Bruce —

The baby is in her  
cradle, resting peacefully.

Al Knox  
Gus Schulz  
Jack Reynolds

Fig. 1

⊕

## On the use of acceptance diagrams to calculate the performance of multiple-section straight-sided neutron guide systems

*J. R. D. Copley*  
University of Maryland  
College Park, Maryland  
and  
National Institute of Standards and Technology  
Gaithersburg, Maryland  
USA

⊕

**ABSTRACT:** We describe a method to calculate the performance of multiple section systems of straight-sided guides and collimators. The approach is based on the concept of acceptance diagrams, previously described by J. M. Carpenter and D. F. R. Mildner [Nucl. Instrum. Meth. **196**, 341 (1982)], which display the transverse spatial and angular coordinates of the neutrons in the system. For a given section of guide the construction of the exit diagram, from the entrance diagram, is shown to be accomplished using a shear transformation followed by translational and rotational operations applied to polygons representing respectively even and odd numbers of reflections within the section. The reflected neutron polygons are then truncated leaving only the neutrons that never strike a surface at an angle greater than the critical angle for total reflection.

⊕

### I. Introduction

In this paper we shall present a brief description of a generalization of the method of acceptance diagrams<sup>(1)</sup> which is used to study the behavior of neutron guide systems. The method may be applied to a wide variety of problems, including a parallel guide placed at a distance from a finite source<sup>(1)</sup>, parallel<sup>(1)</sup>, and converging<sup>(2)</sup> guides fed by an isotropic neutron source, and a converging guide following a long section of parallel guide<sup>(3)</sup>. Multiple-section systems may be handled, and angular and lateral displacements between sections are readily included. Open sections, which are equivalent to enclosed sections with non-reflecting walls, are simply treated as guide sections with zero critical angle for total reflection. The method is limited to one transverse dimension and to guides with straight sides, and the reflectivity of any given reflecting surface is assumed to be constant (not necessarily 100%) up to the critical angle. The source need not be uniformly illuminated, though calculations of intensity at the exit of the system are simplified if the source illumination is constant.

⊕

## II. Formulation

### IIa. Notation

The notation used to describe a typical guide section, and to characterize the trajectories of neutrons within the section, is illustrated in Fig. 1. The entrance and exit half-widths are  $W$  and  $W'$ , the length is  $L$ , and the critical angle is  $\theta$ : if  $\theta$  is zero we shall describe the section as a collimator. The neutron enters with spatial and angular coordinates  $y$  and  $\beta$ , and in the absence of any obstacle it strikes the exit plane ( $x = L$ ) with coordinates  $y^*$  and  $\beta^*$ , where (in the small angle approximation)

$$y^* = y + L\beta, \text{ and} \quad (1a)$$

$$\beta^* = \beta. \quad (1b)$$

If the neutron reaches the exit plane, either without encountering the walls of the guide or else by reflection, it crosses with coordinates  $y'$  and  $\beta'$ .

The neutrons at a given stage within a system may be represented by an "acceptance diagram" which displays their transverse spatial and angular coordinates. A typical diagram consists of one or more polygons such that all points internal to each polygon represent accepted neutron.

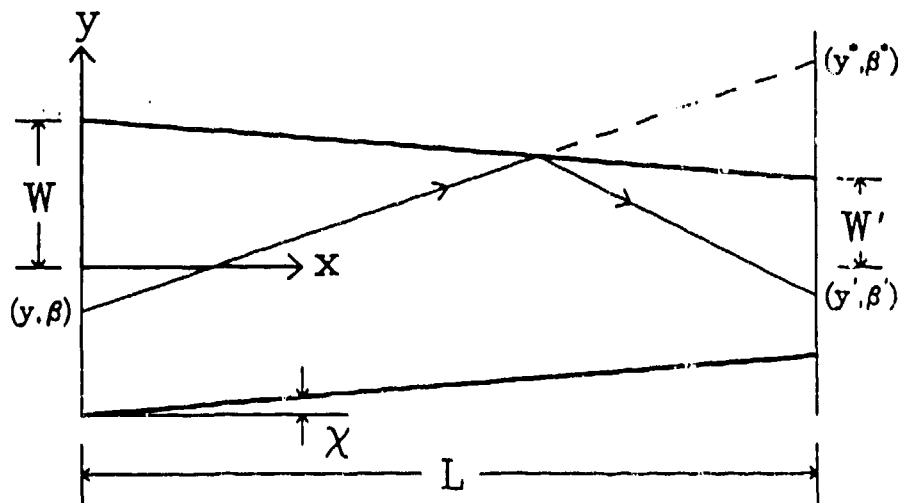


Fig. 1 A typical section of a multiple section guide system. Angles are measured with respect to the positive  $x$  axis. In this example the taper angle  $\chi$  is positive, and the trajectory of the neutron is such that  $\beta > 0$ ,  $\beta' < 0$ , and  $k = 1$ .

## 11b. The exit acceptance diagram

Let us assume for the moment that all angles of reflection are permitted, and derive expressions for  $y'$  and  $\beta'$  in terms of  $y^*$  and  $\beta^*$ . As a first step we need to define and determine the reflection index  $k$ . The magnitude of  $k$  is the number of reflections suffered by the neutron, and its sign is the sign of the  $y$ -coordinate at the first reflection. For neutrons which reach the exit without reflection, the reflection index is zero. In Fig. 2 we show a converging guide together with some of its multiple images, shown as bold solid and dashed lines respectively. Three possible neutron trajectories are shown, and we see that in general  $k$  is the integer  $\kappa$  which satisfies the inequality

$$(2\kappa - 1) W' \leq y^* \leq (2\kappa + 1) W' . \quad (2)$$

For neutrons with  $k = 0$  it is clear that  $y' = y^*$  and  $\beta' = \beta^*$ , since no reflection occurs. If  $k = 1$ ,  $y' + y^* = 2W'$ , and  $\beta' + \beta^* = -2\chi$ , where the taper angle  $\chi$  (see Fig. 1) is given by

$$\chi = (W - W')/L. \quad (3)$$

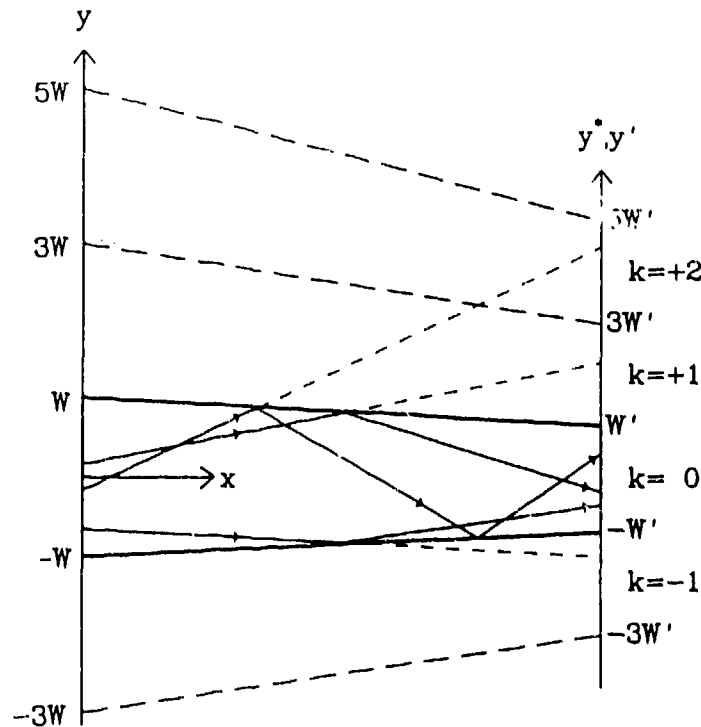


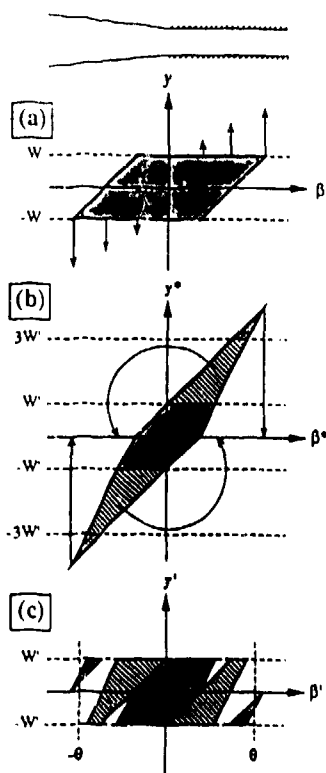
Fig. 2 A converging guide and some of its images, shown as bold solid and dashed lines respectively. The trajectories of three neutrons are shown; in each case the dashed lines indicate trajectories in the absence of the guide.

Thus, for  $k = 1$ ,  $y' = -y^* + 2W'$  and  $\beta' = -\beta^* - 2\chi$ . For  $k = 2$  we find that  $y' = y^* - 4W'$  and  $\beta' = \beta^* + 4\chi$ . In general we obtain (cf Reference 2)

$$y' = y^* - 2kW'; \beta' = \beta^* + 2k\chi \text{ for even } k, \quad (4)$$

$$y' = -y^* + 2kW'; \beta' = -\beta^* - 2k\chi \text{ for odd } k, \quad (5)$$

We are now in a position to construct the exit acceptance diagram for a single section of guide, given the entrance acceptance diagram and assuming that all angles of reflection are allowed. The first step, illustrated in Fig. 3, is the shear transformation represented by Eqs. (1). Lines at  $y^* = \pm(2\kappa - 1)W'$  (where  $\kappa$  is an integer) are then added to the image acceptance diagram, Fig. 3(b), in order to classify neutrons according to their reflection index. The exit acceptance diagram is formed by taking the polygons for each value of  $k$  and applying the appropriate transformation, Eqs. (4) or (5): for even  $k$  the polygon is translated by addition of the vector  $(-2kW', 2k\chi)$  whereas for odd  $k$  it is rotated through  $180^\circ$  about the point  $(kW', -k\chi)$ .



**Fig. 3** Acceptance diagrams for a parallel section of guide following a converging collimator. The collimator and guide have the same length  $L$ , and the collimator's entrance width is two times its exit width. The critical angle of the guide is  $2.75\chi$ , where  $\chi$  is the taper angle of the collimator. The entrance diagram, (a), is a simple parallelogram. The image coordinate diagram, (b), is obtained by the shear transformation, Eqs. (1), and the exit diagram, (c), is obtained by a series of translational and rotational operations, Eqs. (4) and (5). The critical angle restriction, Eq. (6a), removes small portions from the polygons with  $k = \pm 2$ . The effect of the critical angle restriction is also evident in diagrams (a) and (b): the bold outlines were obtained by back-transformation of the accepted regions in diagram (c). Note that diagrams (a) and (c) are essentially identical to the acceptance diagrams in Fig. 6 of Reference 1.

### IIc. Critical angle conditions

If the section under consideration is a collimator, the only neutrons which reach the exit, are those with  $k = 0$ .

If the section is a converging guide, all neutrons with  $k = 0$  reach the exit, and the additional neutrons (with nonzero  $k$ ) which reach the exit are those that satisfy the critical angle condition on the final reflection<sup>[2,3]</sup>

$$|\beta'| \leq \theta + \chi . \quad (6a)$$

This condition is applied to the exit diagram (excluding portions representing neutrons which reached the exit plane without reflection) after the transformations described by Eqs. (4) and (5) have been applied: it may or may not truncate polygons in the diagram.

If the section is a diverging guide, all neutrons with  $k = 0$  reach the exit, and the additional neutrons which reach the exit are those that satisfy the following condition on the first reflection:

$$|\beta| \leq \theta - \chi . \quad (6b)$$

In this case the condition is applied to all parts of the image coordinate diagram with  $|y^*| > W'$  (i.e., to all parts which represent reflected neutrons), before performing the transformations described by Eqs. (4) and (5): note that  $\beta^* = \beta$ .

In the case of a parallel guide conditions (6a) and (6b) are equivalent, since  $|\beta| = |\beta'|$  and  $\chi = 0$ . An example of the application of condition 6(a) to a parallel guide section is illustrated in Fig. 3(c).

A second example of the procedure described in the previous paragraphs is shown in Fig. 4. The only difference between the arrangements shown in Figs. 3 and 4 is that in the latter case the guide converges to one half its original width.

### II d. Additional sections

Having determined the acceptance diagram at the exit of a given section we may proceed to the next section, assuming there is one. If the axis of the new section is aligned with the axis of the preceding section, the entrance diagram for the new section is identical to the exit diagram of the preceding section: an exception occurs if the new section is narrower than the preceding section. Angular and lateral misalignments of a section with respect to the preceding section may be readily handled by coordinate displacements. In the case of a spatial (sideways) displacement  $v_i$  between sections  $i$  and  $i+1$ , the new and old  $y$  coordinates are related as follows:

$$y_{i+1} = y_i' - v_i . \quad (7)$$



whereas an angular displacement between successive sections,  $\eta_i$ , results in a change in the  $\beta$  coordinates in analogous fashion:

$$\beta_{i+1} = \beta_i' \cdot \eta_i \quad (8)$$

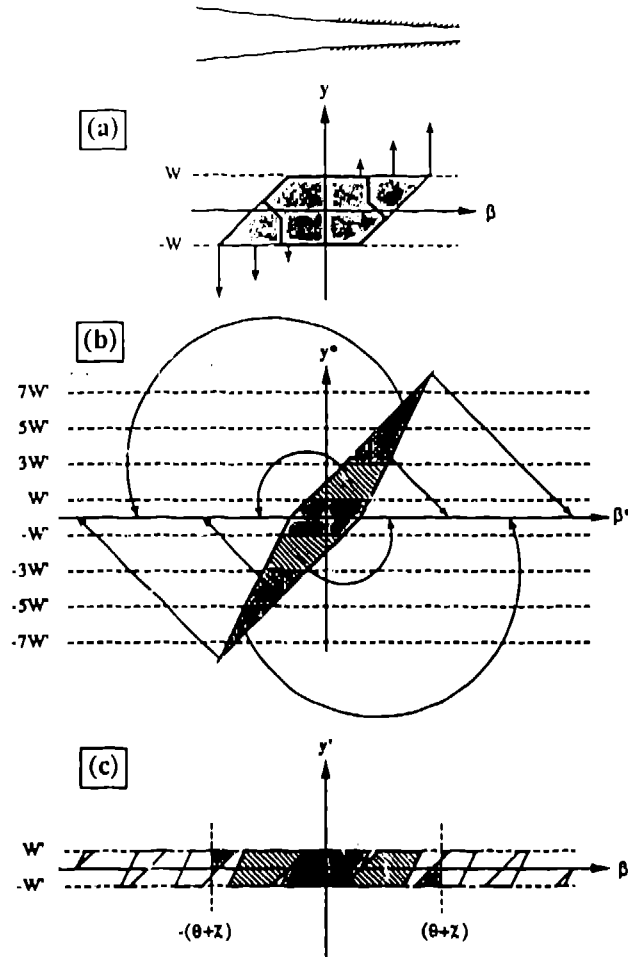


Fig. 4 Acceptance diagrams for a system similar to the system depicted in Fig. 3, except that the guide converges so that its exit width is one-half its entrance width. Its critical angle is the same as that of the guide shown in Fig. 3. Diagrams (b) and (c) were obtained as described in the caption to Fig. 3. In this case the critical angle restriction, Eq. (6a), removes all neutrons with  $|k| > 2$  and most of the neutrons with  $|k| = 2$ . The bold outlines in diagrams (a) and (b) were obtained by back-transformation of the accepted regions in diagram (c).

## IIe. The first section

The first section of a guide system is very often illuminated with neutrons traveling in all directions. In such cases the construction of the exit diagram for the first section differs somewhat from the procedure outline above, because the entrance diagram is bounded by the lines  $y = \pm W$ , but unbounded in  $\beta$ .

In the case of a converging section, the shear transformation, Eqs. (1), is performed first, followed by the transformations described by Eqs. (4) and (5). The only polygons which need be considered are those with  $|k| \leq k_{\max}$ , where  $k_{\max}$  is the integer  $\kappa$  which satisfies the inequality

$$2(\kappa - 1)W < L\theta \leq 2\kappa W. \quad (9a)$$

The result is one or more adjacent parallelograms, and some or all of the parallelograms representing reflected neutrons are then truncated according to the condition on the final reflection, eq. (6a).

In the case of a diverging section the shear transformation is again applied first, but polygons in the image coordinate diagram (outside the lines  $|y^*| = W'$ ) are then truncated using the condition on the first reflection, Eq. (6b). The exit diagram transformations, Eqs. (4) and (5), are then performed. The only polygons which potentially contribute to the exit diagram are those with  $|k| \leq k_{\max}$ , where  $k_{\max}$  is the integer  $\kappa$  which satisfies the inequality

$$2(\kappa - 1)W' < L\theta \leq 2\kappa W'. \quad (9b)$$

## III. Intensity calculations

The relative intensities of neutrons at different planes within a guide system may be calculated using the relevant acceptance diagrams, as long as the reflectivity of the reflecting surfaces is constant for angles less than the critical angle. If the source illumination is uniform, the intensity at a given position is proportional to the sum of the areas of the polygons in the acceptance diagram. Thus the fraction of neutrons which reach the exit of the guide shown in Fig. 3, obtained from the ratio of the hatched areas in diagrams (c) and (a), is 0.992, whereas the same quantity for the guide shown in Fig. 4 is only 0.680, assuming the entrance to the guide is uniformly illuminated in both cases. In the absence of uniform illumination, the best method to determine which of the neutrons in the entrance diagram were able to reach the exit is to back-transform the accepted areas in the exit diagram, as illustrated in Figs. 3 and 4. Relative intensities may then be determined by integrating the source illumination  $I(y, \beta)$  over appropriate regions in the entrance acceptance diagram.<sup>(4)</sup>

## III. Discussion

We have described a method to construct acceptance diagrams for systems of straight-sided guides and collimators. Relatively complicated arrangements can be treated in this way, and portions of complete systems may also be studied, since the

illumination of the entrance to the first section need not be constant. The method may in principle be extended<sup>(4)</sup> to include situations where the critical angles of the two sides of a guide section are different, and to account for the neutrons which are transmitted by non-absorbing guide surfaces. It may be too that additional spectrometer components, such as filters and monochromators, can be treated using this type of approach. The alternative Monte Carlo method is more appropriate in situations where guide elements are continuously curved, and where surfaces do not have constant reflectivity.

### **Acknowledgements**

It is a pleasure to thank my colleagues Ted Prince, Ian Anderson, and Craig Stone for helpful discussions. I also thank Craig Stone for assistance in creating the figures.

### **References**

1. J. M. Carpenter and D. F. R. Mildner, 1982, Nucl. Instrum. Meth. 196, 341.
2. D. F. R. Mildner, 1982, Nucl. Instrum. Meth. 200, 167.
3. I. S. Anderson, 1988, in Proceedings of 32nd Annual International Technical Symposium on Optical & Optoelectronic Applied Science and Engineering, San Diego, CA, 14-19 August 1988, paper 983-13.
4. J. R. D. Copley, paper in preparation.

# Neutron beam handling by inelastic interaction with time-dependent magnetic fields

*L. Niel, G. Badurek, H. Rauch, J. Summhammer, H. Weinfurter*  
Atominsitut der Österreichischen Universitäten, Scüttelstr  
115, A-1020  
Wien  
AUSTRIA

**ABSTRACT:** Two different methods of energy transfer to neutrons by time-dependent magnetic fields are experimentally demonstrated. The first method involves a change of the neutrons potential energy during the passage through the field region. The second method involves a change of the neutrons potential energy during the passage through the field region. The second method involves a spin-flip in an external magnetic field by an rf-flipping device. All experiments were performed on high-resolution perfect crystal spectrometers. Applications of these methods for active monochromatization and beam handling are discussed.

## Introduction

One of the most important objectives of neutron optics is to increase the percentage of neutrons in a beam which are in a distinct space, time or velocity interval. Most devices which are used today are passive in the sense that they select particles with the desired properties. Compared with the optics of charged particles and atoms, where effective cooling systems have been invented<sup>(1,2)</sup>, the handling of neutron beam is more difficult due to the weak interacting potentials. Therefore, active devices that involve inelastic action on the neutrons are still a challenging problem.

Among the active neutron optical components that can change the energy of thermal and cold neutrons are special moderators<sup>(3)</sup>, different techniques for the production of ultracold neutrons<sup>(4,5,6,7)</sup> and fast moving crystals<sup>(8)</sup>. Another class of active neutron optical components makes use of the interaction of the neutrons magnetic moment with time-dependent magnetic fields<sup>(9)</sup>. Here methods with spinflip<sup>(10,11)</sup> and without<sup>(12,13)</sup> can be distinguished.

## Energy change without spinflip

When a neutron moves in a homogeneous magnetic field whose strength varies in time, the potential energy of the particle changes as

$$\frac{dU}{dt} = \pm \mu \frac{dB}{dt}, \quad (1)$$

where  $\mu = 0.966 \times 10^{-26} \text{ JT}^{-1}$  is the neutrons magnetic moment, and the sign depends on the spin orientation compared with the field vector. This effect can be used for the acceleration and deceleration of neutrons and has been demonstrated recently<sup>[13]</sup>. The experimental arrangement (Fig. 1) consists of two aligned C-shaped electromagnets which produce a field varying sinusoidally in time. The frequency of the oscillation is matched to the time of flight through a magnet, in the sense that this time corresponds to one-half (modus A) or one-fourth period (mode B). The phase difference between the two field regions was:

$$\Delta\phi = \frac{l\pi}{4(1+d)}; \quad (2)$$

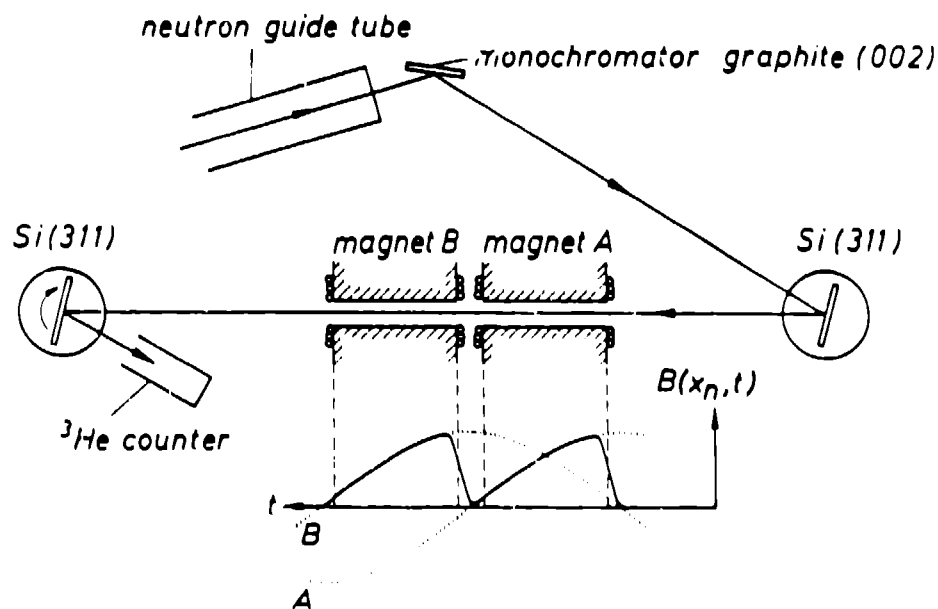


Fig. 1 Outline of the experimental set-up. Neutrons passing through the air gap of the two electromagnets experience two consecutive energy changes. The field amplitudes of the magnets (dotted lines) and the field amplitude at the location of one selected particle (solid line) are shown.

( $l = 105 \text{ mm}$  is the length of one magnet and  $d = 25 \text{ mm}$  is the distance between them) in mode A and twice this value in mode B. The field amplitude in this experiment was limited due to material constraints to  $0.4 \text{ T}$ . The measurements were performed at a wavelength of  $3.23 \text{ \AA}$  at the High Resolution Double Crystal Spectrometer (instrument S21) of the ILL, Grenoble. The counting of the particles was accomplished in eight time channels corresponding to different phases of the oscillating fields.

It was found that for those time channels where the neutron had to pass a field-inverting region between the magnets, the beam was partially depolarized (31%),

whereas for measurements where no field inversion between the magnets happens (only in mode A), all particles experienced a full change of energy. The results are shown in Fig. 2. Although the fields were too weak to generate a double-peaked curve, the data are in full agreement with the expected values and demonstrate clearly the predicted effect with an energy transfer  $\Delta E = \pm 2\mu B_{\max} = \pm 58.4$  meV.

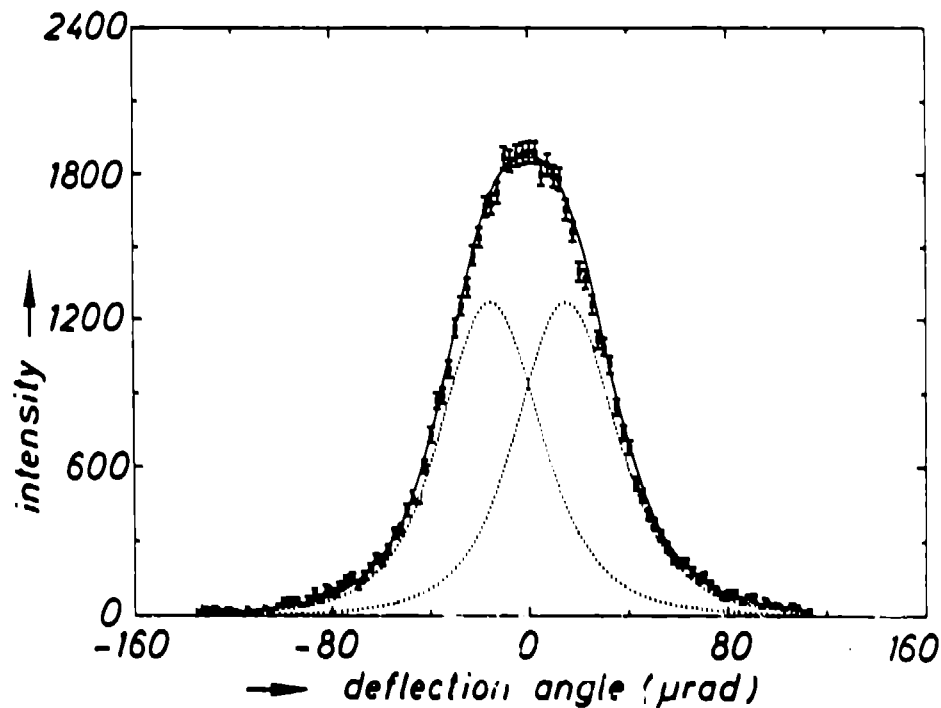


Fig. 2 Rocking curve of channel 5, mode A (maximum energy shift without depolarization). The dotted lines correspond to the two spin states.

### Energy change with spinflip

Another method of changing the energy of the neutron by time-dependent magnetic fields consists in the inelastic action of an rf-flipper, as it was predicted almost two decades ago<sup>(14)</sup> and verified later on by using a backscattering spectrometer<sup>(10)</sup>. For the flipping action two conditions have to be fulfilled: (i) the "frequency resonance" condition

$$2\mu B_0 = \hbar\omega ; \quad (3)$$

and (ii) the "amplitude resonance" condition

$$B_1 = \frac{\pi \hbar \nu_n}{\mu} ; \quad (4)$$

Here  $B_0$  is the static and  $B_1 \ll B_0$  the oscillating field,  $v_n$  the neutron velocity and  $l$  the length of the field region. If a gradient is applied to the static field, the amplitude resonance condition can be relaxed. This makes possible a broadband action of the flipper in the energy range of cold neutrons.

The inelastic action of such a gradient flipper has been demonstrated in an experiment at a perfect crystal spectrometer of the DIDO reactor of the KFA Jülich (Fig. 3). The results are shown in Fig. 4. The peaks corresponding to the two spin states can be separated. The measured energy transfer,  $\Delta E = 0.240(5) \mu\text{eV}$ , corresponds well to the calculated value  $\Delta E = h\nu = 0.243 \mu\text{eV}$  for  $\nu = 58.97 \text{ MHz}$  ( $B_0 = 2.022 \text{ T}$ ). In another experiment with polarization analysis, the flipping efficiency has been compared with theory<sup>[15]</sup> and the agreement has been confirmed. By a careful shaping of the magnetic fields, the wavelength dependence of the flipper action for the energy shift can be optimized<sup>[16]</sup>.

### Applications

There are many proposals for various beam handling systems that make use of the energy change demonstrated in the experiments described above. For example, systems for dynamical spin polarization<sup>[17]</sup> and for the storage of neutrons in a total reflecting ring or in a crystal resonator have been considered<sup>[11]</sup>.

Probably the most challenging application of inelastically acting devices are active monochromators that selectively accelerate and decelerate neutrons and, therefore, increase the flux in a distinct energy interval. Due to Liouville's theorem, this can only be done with pulsed sources. Clearly the energy changes obtained so far with active neutron optical devices based on interaction with time-dependent magnetic fields are not yet in the order of magnitude that can be useful for most neutron scattering experiments. For this purpose multistage systems have to be constructed, which are not only expensive, but also include the problem of depolarization. A monochromator using the energy shift of rf-flippers has been described<sup>[18]</sup>. Comparable to this is a multistage system based on magnets as described in the first experiment. This would be analogous to the accelerator design of Widerøe with the electric dipole fields replaced by magnetic quadrupole fields<sup>[13]</sup>.

Up to now we have considered only magnetic fields where the region of the accelerating gradient is fixed in space. This is not the case in the traveling wave monochromator<sup>[12]</sup>. A schematic drawing of such a system is shown in Fig. 5. For this system no small-scale version can be constructed. Therefore, we present some results of computer simulations.

A comparison of the intensity gain which can be achieved with different types of potentials is shown in Fig. 6. The various types of potentials considered in this comparison are (the primed variables refer to the moving potential frame):

- a) An oscillator potential with constant width  $2w$ ,

$$V(x) = \frac{1}{2} \mu B_{\text{max}} \left( \frac{x'}{w} \right)^2, \quad (5)$$

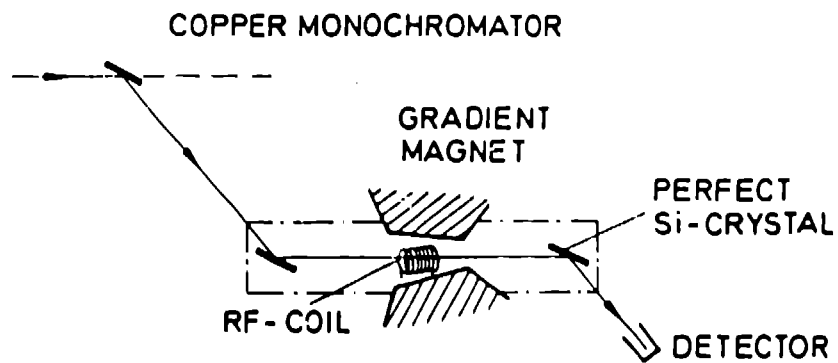


Fig. 3 Sketch of the experimental set up of the spinflip experiment.

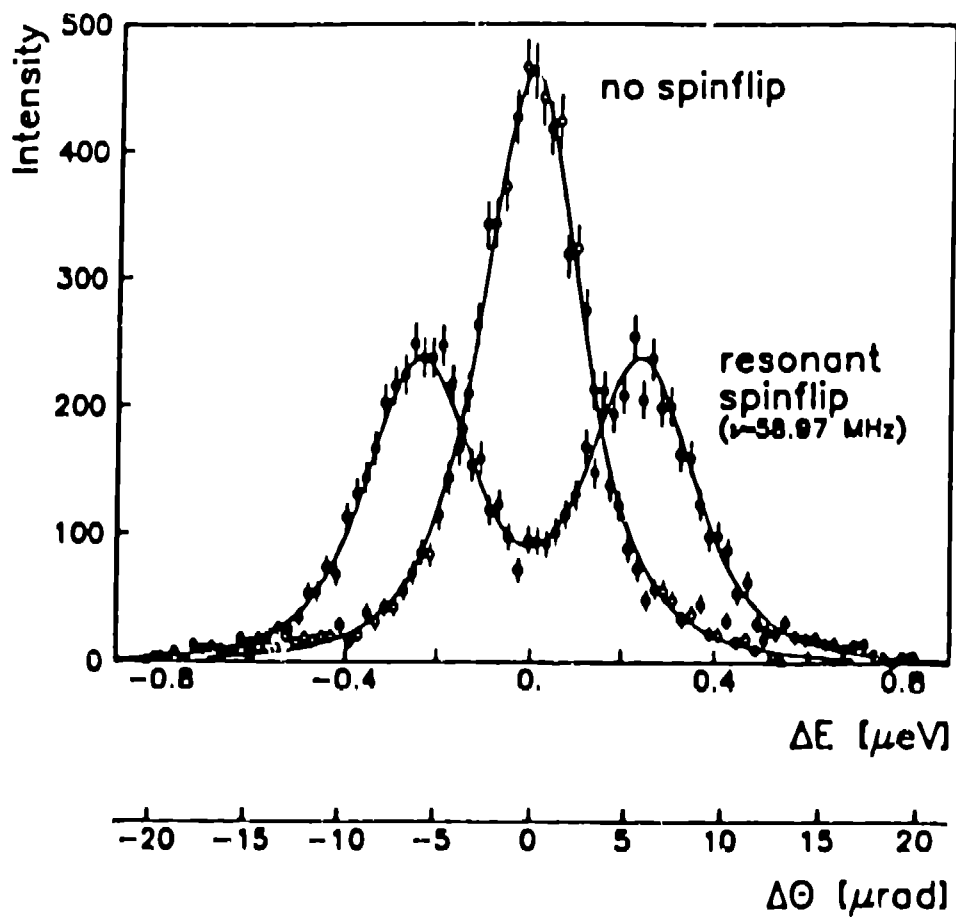


Fig. 4 Splitting of the rocking curve due to the inelastic action of the rf-flipper.



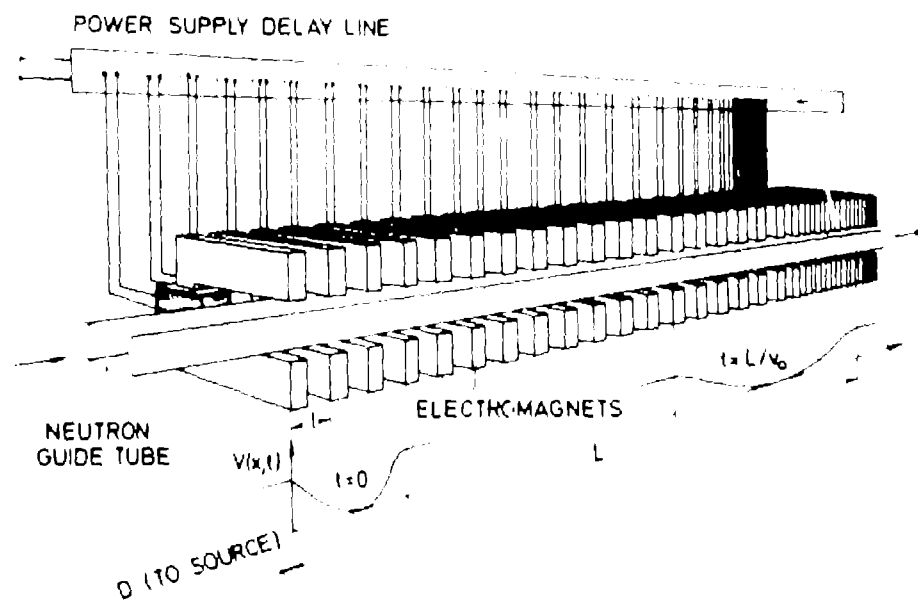


Fig. 5 Proposed scheme of a travelling wave monochromator.

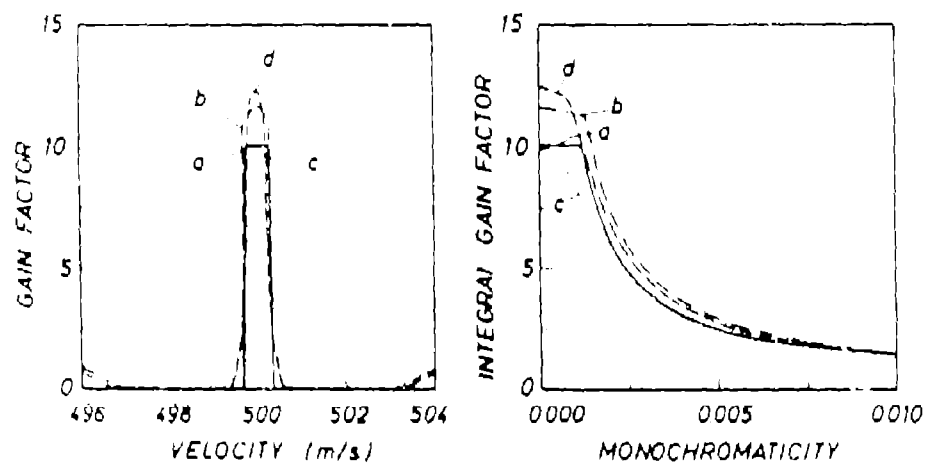


Fig. 6 Comparison of the expected gain factors and integral gain factors for traveling wave monochromators with different kinds of magnetic potentials. For details of the shaping of the potentials, see text. Common parameters: distance-source monochromator  $D = 10$  m, length of monochromator  $L = 20$  m, mean neutron velocity  $v_0 = 500$  m/s, pulse length  $\tau = 50 \mu\text{s}$ , magnetic field amplitude  $B_{\text{max}} = 1$  T.

In this case the phase space evolution of the particle trajectories is a simple rotation. Therefore, the analytical treatment of the problem is facilitated.

- b) An expanding oscillator potential with width  $2w(t)$ . A given neutron with velocity  $v'_{\max}$  that was emitted in the center of the pulse remains on the edge of the potential, which is the point of highest force. This allows, in principle, arbitrarily wide velocity intervals to be monochromatized.
- c) A sinusoidal potential with constant width. This is the type of potential that is the easiest to produce from the technological point of view.
- d) An expanding potential with trapezoidal form.

$$V(x', t) = \begin{cases} -\mu B_{\max} & |x'| \leq a(t) \\ -\mu B_{\max} \frac{b(t) - |x'|}{b(t) - a(t)} & a(t) < |x'| \leq b(t) \\ 0 & b(t) < |x'| \end{cases} \quad (6)$$

Three conditions determine the time evolution of the distances  $a$  and  $b$ :  $a(0) = 0$ ;  $b(t)$  has to fulfill the same condition as  $w(t)$  in case b); and a particle that was emitted in the middle of a pulse reaches  $a(t)$  when its velocity is  $v' = 0$ .

In general the gain factors  $g$  are not constant over the velocity interval  $\Delta v$ . Therefore, we define the integral gain factor  $g_I$ :

$$g_I(\Delta v) = \frac{1}{\Delta v} \int_{-\frac{\Delta v}{2}}^{\frac{\Delta v}{2}} g(v') dv' \quad (7)$$

For very monochromatic beams ( $\Delta E/E < 0.1\%$ ), an expanding trapezoidal potential is best. From the point of feasibility, sinusoidal and oscillator potentials have to be preferred.

Most of the systems for beam handling described in this paper are competing with instruments based on moving crystal and mirrors. The advantage of magnetic devices is the absence of any moving parts; the main disadvantage is the high power consumption. A lot of technological problems have to be solved before a large-scale active monochromator for thermal or cold neutrons can be realized. For very cold and ultracold neutrons, the design parameters are much easier to fulfill.

### Acknowledgements

Work supported by the Austrian *Fonds zur Förderung der wissenschaftlichen Forschung* (project S42/02).

## References

1. F. T. Cole, and F. E. Mills, 1981, *Ann. Rev. Nucl. Part. Sci.* **31**, 295.
2. St. Chu, J. E. Bjorkholm, A. Ashkin, and A. Cable, 1986, *Phys. Rev. Lett.* **57**, 314.
3. F. Atchison, and W. Fischer (ed.), 1987, *Proc. of ICANS-IX, SIN*.
4. R. Golub, and J. M. Pendlebury, 1979, *Rep. Prog. Phys.* **42**, 439.
5. T. O. Brun, J. M. Carpenter, V. E. Crohn, G. R. Ringo, J. W. Cronin, T. W. Dombek, J. W. Lynn, and S. A. Werner, 1980, *Phys. Lett.* **A 75**, 223.
6. A. Steyerl, H. Nage!, F. X. Schreiber, K. A. Steinhäuser, R. Gähler, W. Gläser, P. Ageron, J. M. Astruc, W. Drexel, R. Gervais, and W. Mampe, 1986, *Phys. Lett.* **A 116**, 347.
7. M. Utsuro, T. Ebisawa, K. Okomura, S. Shirahama, and Y. Kawabata, 1988, *Nucl. Instr. Meth. A* **270**, 456.
8. R. Scherm, and H. Stiller (ed.), 1984, *Proc. of the "Workshop on Neutron Scattering Instrumentation for SNQ", Jül-1984*.
9. H. Rauch, in ref. 3, P. 125.
10. B. Alefeld, G. Badurek, and H. Rauch, 1981, *Z. Phys.* **B 41**, 231.
11. H. Weinfurter, G. Badurek, H. Rauch, and D. Schwahn, 1988, *Z. Phys.* **B 72**, 195.
12. J. Summhammer, L. Niel, and H. Rauch, 1986, *Z. Phys.* **B 62**, 269.
13. L. Niel and H. Rauch, *Z. Phys. B* (in print).
14. G. M. Drabkin and R. A. Zhitnikov, 1960, *Sov. Phys. JETP* **11**, 231.
15. H. Weinfurter and G. Badurek, submitted to *Nucl. Instr. Meth. A*.
16. H. Weinfurter, G. Badurek and H. Rauch, *Proc. of the International Conference on Neutron Scattering, July 12 - 15, 1988, Grenoble (to appear in Physica B)*.
17. G. Badurek, H. Rauch, and A. Zeilinger, 1980., *Z. Phys.* **B 38**, 303.
18. H. Rauch, 1983, *Physica B+C* **120**, 71.

## SINQ guide concept

*I. Anderson and F. Atchison*  
Paul Scherrer Institute  
CH-5232 Villigen  
SWITZERLAND

### Introduction

In this paper we describe the present concept for the layout of the neutron guides at SINQ. The characteristics of the source will make it particularly competitive in the cold neutron region <sup>(1)</sup> through the inclusion of a liquid D<sub>2</sub> source, which is described in <sup>(2)</sup>. However, concomittant with the cold neutron production, there will be high energy neutrons ( $E > 15$  MeV) emitted from the source, which significantly influence many of the design parameters and, in particular, the required shielding. The guide system, although based on the demands for the foreseen instrumentation, has been designed to be as flexible as possible to allow reasonable future development, while taking into account the particular background problems arising from the high-energy neutrons.

### General requirements and aims

A clear aim for any general layout is to provide the maximum useful neutron flux over the wavelength range required by the instruments, while at the same time ensuring a minimum background. Thus, our concept for the SINQ guides, although not dependent on, does allow for the possibility of supermirror coatings for the guides outside the main shielding, with a critical angle of reflection  $m$  times that of natural nickel, giving a factor  $m^2$  increase in effective flux. Because these supermirrors constitute an essential part of the system, there is an active program within the institute to develop them. A survey of planned and possible future instruments to be accommodated in the guide hall has indicated a demand for wavelengths in the range 2 - 12 Angstroms and a variation of beam sizes. The guide system has thus been designed according to the following principles:

- The transmission is to be optimized for wavelengths in the range 2 - 12 Angstroms.
- In order to allow the implementation of focusing methods, the nominal guide size has been set at 120 mm high and 50 mm wide.
- The first sections of the guides will be curved to avoid direct line of sight for the fast and (more importantly) high-energy neutrons. For this curvature to be effective, good shielding must be mounted close to the guides to provide tight collimation, and all instruments should be placed at least 5 m after the line of sight.
- The guides outside the main shielding may have supermirror coatings with  $m = 1.5$ , giving a flux increase of 125% with respect to natural nickel. If high-reflectivity supermirror coatings cannot be made routinely at the time of

guide fabrication,  $^{58}\text{Ni}$  ( $m = 1.2$ ) will be used with a corresponding flux gain of 40% over natural nickel.

Figure 1 shows a general layout of the SINQ target and guide halls on which schematic drawings of some proposed spectrometers have been included to illustrate the probable beam positions. Referring then to Fig. 1, the guide system can be subdivided into four distinct parts: the in-shield sections, the shutter section, the blockhouse section and the guides in the guide hall proper.

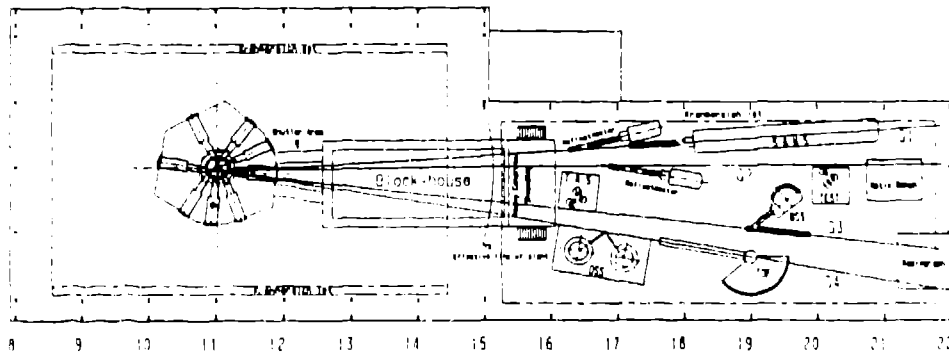


Fig. 1 Neutron guide layout.

### In-shield section

Four straight guides, with angles of  $\pm 4$  and  $\pm 6$  degrees with respect to the plug axis, will view the cold source from a distance of 1.5 m and continue 4.5 m to the outside of the main shielding where they will be directly coupled to the shutter sections. These guides will be fabricated from either non-boron glass or polished nickel plates with a surface coating of  $^{58}\text{Ni}$  and will be slightly converging away from the source to fully illuminate the following sections of guide having supermirror surfaces. The design of the insert will allow installation of a further central guide if required in the future.

### Shutter section

The shutter will be situated on the outside of the main shielding and will provide a means of replacing a 1 m evacuated guide section by a beam blocker. The details of this shutter have not yet been defined.

### Blockhouse section

After the shutter the guides are mounted in a shielding blockhouse, where they will be curved and tightly shielded to remove direct transmission of high-energy neutrons. In addition (referring to Fig. 1) guides G1 and G2, and similarly guides G3 and G4, will be curved in opposite directions such that the main shielding against direct flight neutrons will be situated between each pair of guides.

The combination of the requirements of a short characteristic wavelength,  $\lambda^*$ , together with a large guide width,  $w = 5$  cm, leads to an excessively long line-of-sight length,  $L_s$ , for all realistic values of  $m$ . This problem may be overcome by using curved guides that are divided vertically into subguides by means of thin glass plates similarly coated with supermirror, allowing the radius of curvature to be decreased.

Table 2 shows the line-of-sight lengths obtained and the radii of curvature ( $R$ ) required for different characteristic wavelengths as a function of the parameter  $m$  and the subguide width  $a$ . However, assuming that the center glass plates are transparent to high-energy neutrons, the effective line of sight,  $L_e$ , will be determined by the total guide width,  $w$ , and the effectiveness of the adjacent shielding. The estimated values of  $L_e$  (for  $w = 5$  cm) are also given in Table 2.

**Table 2**

		$\lambda^* = 2 \text{ \AA}$				
		m				
a (cm)		1	1.2	1.5	2	2.5
5	$L_s$ (m)	59	49	39	29	23
	$R$ (km)	8.7	6.0	3.8	2.2	1.4
	$L_e$ (m)	59	49	39	29	23
2.5	$L_s$ (m)	29	24.5	19.6	14.7	11.8
	$R$ (km)	4.3	3	1.9	1.1	0.7
	$L_e$ (m)	42	35	27.5	20.5	16.3
1.67	$L_s$ (m)	19.6	16	13.1	9.8	7.8
	$R$ (km)	2.9	2	1.3	0.7	0.5
	$L_e$ (m)	34	28	22.5	16.7	13.3
		$\lambda^* = 1.5 \text{ \AA}$				
		m				
a (cm)		1	1.2	1.5	2	2.5
5	$L_s$ (m)	78.5	65	52.3	39.2	31.4
	$R$ (km)	15.4	10.7	6.8	3.8	2.5
	$L_e$ (m)	78.5	65	52.3	39.2	31.4
2.5	$L_s$ (m)	39	32.7	26.1	19.6	15.7
	$R$ (km)	7.7	5.3	3.4	1.9	1.2
	$L_e$ (m)	55.4	46	37	27.7	22.2
1.67	$L_s$ (m)	26.1	21.8	17.4	13.1	10.5
	$R$ (km)	5.1	4.3	2.3	1.3	0.82
	$L_e$ (m)	45.3	37.5	30.2	22.6	18.1

Thus, in keeping with the design goals, each of the guides in the blockhouse will be constructed as two subguides (i.e., with one central glass plate) having a radius of curvature of 1.9 km. The effective line of sight for the present system (including the initial straight sections) is shown in Fig. 1 and falls within the blockhouse.

The use of supermirror coatings ( $m = 1.5$ ) in the curved sections is essential to ensure the characteristic wavelength of 2 Å, even though some instruments may not make use of the increased beam divergence. The effect of replacing the supermirror by  $^{58}\text{Ni}$  ( $m = 1.2$ ), or eventually natural nickel ( $m = 1$ ) for the SANS and the reflectometer, would be to increase the characteristic wavelength to 2.5 or 3 Å respectively, in addition to reducing the total flux.

The theoretical fluxes, based on the calculations of [2] with a  $10^{14}$  incident flux on a  $\text{D}_2$  source with a 10 cm re-entrant hole and taking into account the transmission of the curved guides (reflectivity = 100%), are shown in Fig. 2 for  $m = 1.5$ .

It is clear that the center channel will leave a hole in the illuminated phase space of the following open guide and that this hole will be transmitted, albeit transformed in shape, down the guide. We are at present performing calculations to investigate both the effect of this gap in illumination on the instruments, in particular those with crystal monochromators, and the possible optimum sitings along the guides to reduce adverse effects.

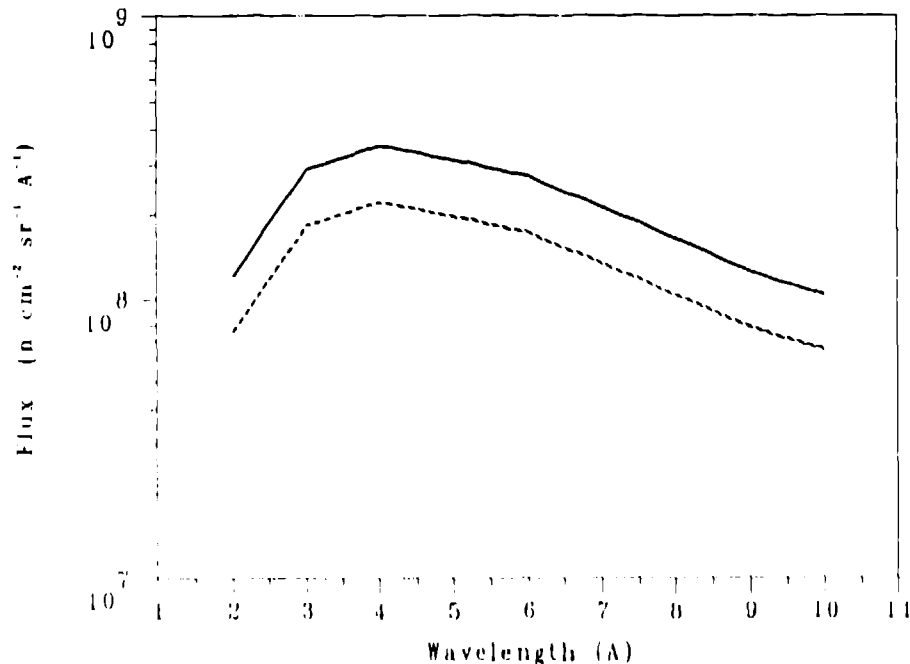


Fig. 2 The solid line shows the theoretical flux in the guides as described in the text. The dashed line represents the expected flux allowing for 10% absorption in the cold source structure and a realistic guide transmission of 70%.

### Guide-hall sections

After passing through the end wall of the blockhouse, the guides will be continued straight as single open guides, i.e., without a central reflector, through another 5 m of heavy concrete shielding before exiting into the guide hall. At present it is intended to continue guides G3 and G4 with the full size (120 x 50 mm<sup>2</sup>) for instruments that can make use of focusing techniques. It is possible that the final residual beams from one of these guides could be used for neutron radiography. Guides G1 and G2, however, may be split for an optimum disposition of instruments.

**Guide G1.** This guide will be split horizontally to provide two individual beams of cross-section 50 x 50 mm<sup>2</sup>; the top beam for a SANS instrument and the lower for another instrument, ideally, a reflectometer. Since both these instruments, in principle, cannot use large beam divergences, all or part of this guide could be made with a natural nickel coating. However, a reflectometer, which is intended to be used for surface diffraction, would require short wavelengths so that an alternative position has been foreseen on guide G2.

**Guide G2.** This guide will be similarly divided into two beams, the lower of which may be reserved for a reflectometer. The top half will continue in a guide of cross section 50 x 50 mm<sup>2</sup> to a neutron optic bench<sup>[3]</sup> situated in a special vibration free area at the end of the guide hall. The present design of this optic bench requires a beam 20 mm wide so that a third beam of cross section 50 x 30 mm<sup>2</sup> may be extracted from the guide either for another instrument or for test purposes.

**Instruments.** Of the instruments shown in Fig. 1, it is planned to have three operational in the guide hall as soon as neutrons are available. These are the SANS, Optic bench, and Time-of-flight spectrometers. Further instruments will be built depending on demand and the availability of funding. Hence, it will only be necessary to install three of the four guides for the initial source operation.

### Acknowledgements

We wish to thank Mr. P. Sinha for invaluable help in production of Fig. 1.

### References

1. F. Atchison, W. E. Fischer, M. Pepin, Y. Takeda, C. Tschaler, and A. Furrer, 1986, *Physica* **136B**, 97.
2. F. Atchison, W. Bucher, A. Hoehli, I. Horvath, and L. Nordstroem, this conference.
3. H. Rauch, SINQ Internal Report SINQ/897/RHW-801.



# Neutron beam compressors for pulse width reduction

*R. E. Lechner*  
Hahn-Meitner-Institut Berlin  
Glienicke Strasse 100  
D-1000 Berlin 39  
FEDERAL REPUBLIC OF GERMANY

**ABSTRACT:** In the context of intensity and resolution optimization of a neutron time-of-flight spectrometer several methods of beam width reduction at the chopper are considered aiming at a reduction of the neutron pulse width at minimum loss of intensity. The most advantageous technique discussed uses a "double-trumpet" arrangement in which the chopper is placed in between converging and diverging neutron guide sections.

## Introduction

It is one of the main tasks in optimizing a neutron spectrometer to strive for maximum intensity at any, and in particular at the best possible, resolution. For this reason every neutron optical device used in the spectrometer should have the highest possible transmission. In the present paper we shall consider part of this optimization problem with regard to a cold-neutron time-of-flight spectrometer for inelastic scattering experiments. (We are referring here to the multi-disk chopper spectrometer under construction at HMI Berlin, which is an improved version of the INS instrument (Douchin et al., 1973) at ILL in Grenoble). The primary part of such an instrument essentially consists of several choppers.

One of the choppers is intended to create or tailor a pulsed neutron beam. Another one is used for the monochromatization of the latter. In addition to these two principal choppers, further choppers are needed for tail-cutting and for overlap prevention. However, these do not necessarily affect the spectrometer resolution. The present discussion will therefore be restricted to the two principal choppers.

Since the transmission of every chopper enters into the final intensity, we have chosen to use very thin disk choppers with open windows (transmission = 1) produced by cutting slits into the disk edges. These disks run in narrow slots (transmission better than 0.99) cut perpendicularly to the beam into the neutron guide. The energy resolution at the detector of a system of two single choppers is given as (Lechner, 1985):

$$\Delta E = g_0 (\tau_1^2 g_1^2 + \tau_2^2 g_2^2)^{1/2} \quad (1)$$

if flight path length uncertainties are neglected,  $\Delta E$  is governed by the chopper pulse widths in time,  $\tau_1$  and  $\tau_2$ . Highest resolution (corresponding to minimum values of  $\tau_1$  and  $\tau_2$ ) is obtained at maximum chopper speed at the limit of mechanical

resistance of the disk material. An immediate improvement of the energy resolution by a factor of 2 is achieved, if one replaces each single chopper disk by a pair of identical, but counter-rotating disks (Hautecler et al., 1985) mounted at a small distance from each other and running at the same velocity. Formula (1) applies again, with  $\tau_1$  and  $\tau_2$  now being the effective chopper pulse widths of the first and the second pair, respectively. In the following, the term chopper will be used for such pairs of counter-rotating disks. Once the flight-path lengths (implicitly contained in the wavelength-dependent factors  $g_0$ ,  $g_1$  and  $g_2$ ) are fixed, a further improvement of resolution for a given neutron wavelength  $\lambda$  is then possible only by a reduction of the widths of chopper windows and beam, in order to further reduce the neutron pulse widths. As concerns intensity and resolution optimization it is generally advantageous to have  $\tau_2 < \tau_1$ , especially if the secondary flight path (sample to detector) is shorter than the primary flight path (distance between the two choppers). This also applies when one is interested in good resolution in neutron energy gain scattering. In the following we shall therefore consider possibilities of a reduction of  $\tau_2$ .

### Neutron beam bottlenecks

Beam width reduction corresponds to the construction of some kind of a "bottleneck" in the neutron guide. Figure 1 (schematically) shows several different ways of reducing the beam width (in the horizontal plane) in order to fit it to reduced-width chopper windows. A reduction factor of 2 has been chosen as an example:

- (a) normal neutron guide (parallel walls) with original width; a pair of counter-rotating disks, each of them spinning with a (tangential) velocity  $v$ , is placed at its end; effective pulse width:  $\tau_2$ .
- (b) the guide width has a step before the chopper; this method of guide width reduction was used in the case of IN5 at ILL; effective pulse width:  $\tau_2/2$ .
- (c) a comb-like mask is used in front of the chopper with chopper windows matched to the mask. The widths of the two windows add up to half of the guide width. This corresponds to the simplest case of the multiple-slit chopper concept (Copley, 1988). I am using this example for the purpose of comparison, assuming that the two counter-rotating disks are spinning at velocity  $v/2$ , in order to obtain the same pulse width as in case b) i.e.,  $\tau_2/2$ .
- (d) a converging neutron guide section, placed at the end of a normal (parallel-walled) guide, reduces its width just before the chopper and thus leads to a pulse width of  $\tau_2/2$  for a chopper velocity  $v$ .

We should like to choose the solution corresponding to a minimum loss in intensity at a given improvement in resolution. In order to make this choice let us now compare the intensities for each of these different cases.

The intensity  $I$  of an experiment is governed by the number of neutrons leaving the second chopper per unit of time. This is proportional

- (i) to the "duty cycle",  $\tau_1/P$ , i.e., to the fraction of time for which chopper 1 is open,
- (ii) to the incident neutron flux per unit of energy integrated over the beam

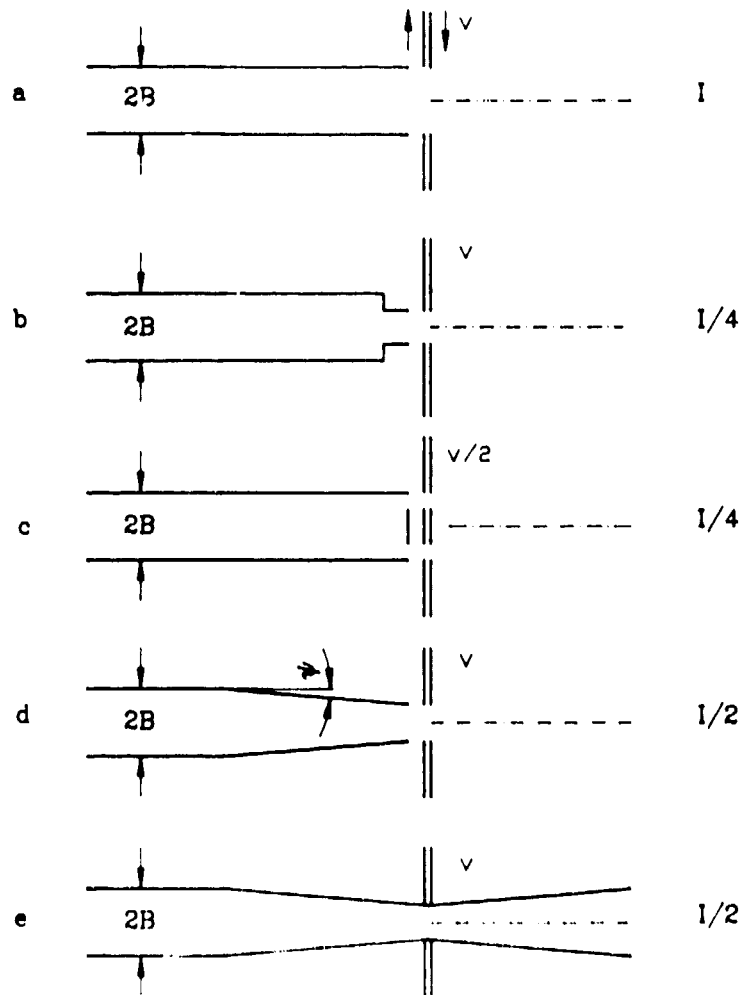


Fig. 1 Schematic drawing of a chopper consisting of a pair of counter-rotating identical disks placed at the end of a neutron guide. (a) mirror-coated guide with parallel walls, width  $2B$ , chopper velocity  $v$ . (b) to (d) three different ways of producing a bottleneck in the neutron beam, reducing the total beam width by a factor of 2 in order to decrease the chopper pulse width: (b) guide width reduced by a step to the value  $B$  before its exit; chopper velocity  $v$ . (c) the guide exit is reduced to two slits of width  $B/2$  each, using a mask; the chopper windows are matched to this mask, chopper velocity  $v/2$ . (d) a guide width reduction to the value  $B$  is achieved using a supermirror-coated converging guide section before the chopper; chopper velocity  $v$ . (e) as in case (d) the neutron guide has a converging section just before the chopper; however, in addition, a diverging neutron guide section is added just after the chopper in order to focus on the sample position guide section is entirely supermirror coated.

cross-section  $A$ ,  $A \, d\phi/dE_0$ , and  
 (iii) to the energy band width,  $\Delta E_0$ , selected during the chopper burst time  $\tau_2$ :

$$I \propto (\tau_1/P) A (d\phi/dE_0) \Delta E_0 \quad (2)$$

It is obvious that for the chopper velocities given above the energy band width factor is equally reduced in the cases b), c) and d) as compared to a) of Fig. 1, whereas the flux factor is affected only in cases b) and c). Thus, for the same improvement in resolution, the intensity  $I$  of case a) is reduced to  $1/4$  in b) and c), but only to  $1/2$  in case d). This is assuming that a converging guide section can be made with a transmission of 1, which is true to a good approximation (see below). We note that the result of case d) would also be obtained with a normal guide (case a), if it was possible to double the chopper speed. Furthermore, it should be noted that a pulse width reduction by another factor of 2 is possible in case c) if the maximum chopper velocity  $v$  is used. This leads to a pulse width of  $\tau_2/4$  and reduces the intensity by another factor of 2 (thus giving  $1/8$ ). Precisely the same result (within the present approximations), i.e., pulse width  $\tau_2/4$  and intensity  $1/8$ , is also obtained in case d) if the horizontal dimensions of the parallel and converging guide sections as well as that of the chopper window are reduced by a factor of 2. The latter case has the advantage of an intensity spatially concentrated within a single slit rather than in two.

#### Transmission of CGS and double-trumpet

Let us now consider the transmission of a converging guide section (CGS). Transmission and "gain factors" for such neutron guide elements have been calculated by several authors (Anderson, 1988; Mezei, 1988; Rossbach et al., 1988). We have also made such calculations (with a Monte Carlo program written by F. Mezei). Anderson has given analytical results. In the following I shall use his notation and consider the CGS of Fig. 1d as an example which, in one dimension, reduces the beam width from  $2B$  to  $2b$ , with a real space reduction factor  $\beta = B/b = 2$ . If the straight guide has a mirror coating with a critical angle  $\gamma_c$ , the CGS must be supermirror-coated with maximum reflection angle  $\gamma_{co}$ , in order to achieve high transmission. In our example we may choose a critical angle ratio of  $m = \gamma_{co}/\gamma_c = 2$ . Reflectivities of both neutron guide mirror and supermirror surfaces can be made close to 1 for reflection angles  $\alpha < \gamma_c$ . In the supermirror region,  $\gamma_c < \alpha < \gamma_{co}$ , average values of about 0.8 can be achieved. For simplicity we shall assume here that the reflectivities are equal to 1 in both cases. Under these assumptions the transmission of the CGS shows periodic oscillations with maxima equal to 1 at values of  $k = \Psi/\gamma_c = 1, 1/3, 1/5, 1/7$ , etc. These maxima correspond to transmission of all neutrons which enter the CGS. If, for instance, the CGS inclination angle  $\Psi$  (Fig. 1) is chosen equal to  $\gamma_c$  (at  $\lambda = 2 \text{ \AA}$ ) the transmission maxima are obtained at wavelength values of  $\lambda = 2(2N-1)\text{\AA}$ ,  $N = 1, 2, 3, \dots$ . The locations of the maxima can obviously be adapted to the experiment requirements by varying the above-mentioned CGS parameters.

We have thus shown that case d) of Fig. 1 is superior to b) and c) as regards neutron intensity just after the chopper for the given improvement in energy

resolution. The use of more realistic reflectivity values would not change this qualitative result. However, it is a serious disadvantage of the simple CGS arrangement, that the sample to be studied in the experiment usually can not be placed very close to the last chopper. Because of shielding, sample environment and scattering angle requirements, a distance of at least 1 m is typical. At such distances the increase in flux density achieved by a CGS at the location of the chopper window, is lost due to the corresponding increase in divergence (cf. Liouville's theorem). This problem can easily be solved considering that we do not need to conserve the narrow beam width, once the neutron pulse has passed the chopper. It is quite evident that the addition of a supermirror-coated diverging guide section (DGS) just after the chopper will not only allow for a certain increase in beam width but also reduce the beam divergence. Thus, the beam will be focussed at distances from the chopper window which are convenient for applications. Such a CGS-DGS "double-trumpet" arrangement is shown in Fig. 1e for the symmetric case (equal inclination angles  $\Psi$  and equal lengths). It is seen by inspection that every neutron passing through the CGS will also be transmitted by the DGS. Therefore, the transmission of this double-trumpet is 1 if that of the CGS is 1. We note that the double-trumpet does not have to be symmetric. For instance the double-trumpet of the HMI time-of-flight spectrometer for reasons of space requirements will have a truncated DGS. This leads to different focussing properties at an equally high transmission. We may conclude that the double-trumpet arrangement described above is a good solution for the bottleneck problem initially stated. It is evident that the same method could be used for further improvements of the energy resolution with a minimum loss of intensity if the maximum supermirror reflection angle  $\gamma_{\infty}$  could be increased beyond presently possible values. Detailed results of calculations of double-trumpet transmissions and focussed intensity distributions will be published elsewhere. Finally it should be mentioned that the multiple-slit chopper concept (Copley, 1988) in principle also permits still higher resolution if the number of slits per chopper is increased; however, this would require the use of a larger number of disks.

#### **Acknowledgements**

The author should like to thank I. S. Anderson, J. R. D. Copley and E. Mezei for interesting discussions.

## References

- Anderson, I. S., 1988, in "Thin Film Neutron Optical Devices", Proc. SPIE 983, to be published.
- Copley, J. R. D., 1988, Nucl. Instr. & Methods **A273**, 67-76.
- Douchin, F., Lechner, R. E., and Scherm, R., 1973. unpublished.
- Hautecler, S., Legrand, E., Vansteelandt, L., D'Hooghe, P., Seeger, A., Schalt, W., 1985, in "Neutron Scattering in the 'Nineties", IAEA Vienna, 211-215.
- Lechner, R. E., 1985, in "Neutron Scattering in the 'Nineties", IAEA Vienna, 401-407.
- Mezei, F., 1988, in "Thin Film Neutron Optical Devices", Proc. SPIE 983, to be published.
- Rossbach, M., Scharpf, O., Kaiser, W., Graf, W., Schirmer, A., Faber, W., Duppich, J., and Zeisler, R., 1988, Nucl. Instr. & Meth. **B35**, 181-190.

## Summary of the recent conference on thin-film neutron optical devices

*C. F. Majkrzak*  
National Institute of Standards and Technology  
Gaithersburg, Maryland 20899  
USA

**ABSTRACT:** The proceedings of the conference of the International Society for Optical Engineering on Thin-Film Neutron Optical Devices: Mirrors, Supermirrors, Multilayer Monochromators, Polarizers and Beam Guides, which was held in San Diego, California in August, 1988, are summarized here.

### Introduction

Substantial efforts have been made in recent years in the development of reflecting guide tubes for cold neutrons and of multilayered thin-film structures for use as neutron monochromators and polarizers. With new cold-neutron facilities presently under construction and next-generation reactor and pulsed sources currently being planned, it was considered timely to hold a conference specifically on the important applications of thin films and multilayers as neutron optical devices. A two-day conference was consequently organized by the International Society for Optical Engineering (SPIE) as part of its 32nd Annual International Technical Symposium. A synopsis of the proceedings of this conference<sup>(1)</sup>, which are relevant to the present workshop, follows.

### Supermirrors

The subject of the first of four sessions was the theoretical design, fabrication, and actual performance of both polarizing and non-polarizing supermirrors and was chaired by Feri Mezei. To begin, Gian Felcher of Argonne National Laboratory gave a general introduction on the principles of neutron reflectivity for magnetic and nonmagnetic materials. The formalism to calculate the reflectivity from a sample composed of stacked flat layers and, inversely, to calculate the stacking from reflectivity measurements was described. Feri Mezei next spoke about very high reflectivity supermirrors and their applications involving multiple reflections and transmission geometries. In particular, the design and characteristics of several novel devices such as polarizing cavities, beam compressors, and splitters were discussed. For example, the polarizing cavity, which utilizes polarizing supermirror coatings on transparent single crystal Si substrates within an ordinary Ni guide but inclined at the proper angle, can be used to polarize the entire flux transported by a guide with high efficiency over a relatively broad wavelength range. Roger Pynn then reviewed the widespread use of mirrors and supermirrors at the Institut Laue-Langevin in beam handling or transport through guides as well as in specific instrumental applications such as polarization analyzers. In the following paper by John Hayter and Herb

Mook, a new method of designing supermirrors based on a consideration of the contribution of each bilayer to the extinction in a given stack of bilayers was presented, including the derivation and solution of the discrete set of equations governing the selection of layer thicknesses. Anand Saxena then talked about the fabrication of non-polarizing singlespacing multilayer monochromators in the 60 to 200 Å range with reflectivities greater than 95% and compared the calculated and observed diffraction profiles from which it could be concluded that the multilayers had a significant degree of imperfection. The last paper of the session was by John Keem, et al., on an investigation of the microstructure of vapor deposited Ni-Ti multilayers and supermirrors using neutron and x-ray diffraction in addition to transmission electron microscopy. The measured neutron reflectivities of supermirrors were less than predicted. The study showed very convincing evidence of the formation of cusps in the Ni layers. This important finding strongly suggests that the reduction in reflectivity is due primarily to layer roughness.

### **Neutron guides**

The topic of the second session, chaired by Tasso Springer, was neutron guides. The first paper, by Ebisaiva, et al., described both conventional Ni-coated guides and a Ni-Ti supermirror guide tube installed at the Kyoto University Research Reactor in Japan. A detailed comparison of the actual performance of the two types of guides was given. Next, Francois Samuel gave a detailed description of the construction and installation of neutron guide networks at a number of European neutron scattering facilities. A thorough analysis of losses within a guide due to less than perfect Ni film reflectivity, spatial and angular misalignments, and gaps was presented. The third paper of the session, by Alefeld, et al., described the new neutron guide laboratory at the KFA, Jülich, FRG, and its special beam-forming devices. The measured neutron fluxes in the  $^{58}\text{Ni}$  guides were given along with a technical layout of the guide system, which supplies 10 instruments with cold neutrons from the hydrogen cold source. In addition, the design and performance of a neutron-guide junction at the entrance of the guide network, a multislit-bender with a radius of curvature of 57 m, and conical-focusing neutron guides coated with supermirror were discussed. The last two papers of the session were concerned with the calculation and measurement of the performance of converging neutron guides. Ian Anderson spoke first and gave a simple analytic approach to determine the flux gain that may be achieved in such a system as a function of the ratio of the entrance and exit widths, which also determines the wavelength dependence. The second paper, by Copley, et al., discussed the spatial and angular distributions of a beam emerging from a converging guide, which are generally nonuniform and wavelength-dependent. Analytic and numerical methods of calculation were considered and the results of selected Monte Carlo numerical calculations were presented. Measurements on a scaled-down version of a converging guide system were reported and found to compare well with calculation. It was found that flux gains as high as a factor of four (in two dimensions) using supermirror converging sections at the end of an ordinary guide are possible.

### **Other devices and applications**

Session 3 of the conference consisted of six presentations on other device applications. Albert Steyerl began with a report on the novel guides and mirrors for





cold and ultracold neutrons, which were used for the new intense turbine source of very slow neutrons at the High-Flux Reactor of the Institut Laue-Langevin, Grenoble. Neutron mirrors are essential components for Doppler-shifting turbines and high-resolution ultracold neutron spectrometers. The instrumentation for neutron microscopy that makes use of imaging mirrors was described as well as the results of detailed investigations of specular and nonspecular components in mirror reflection from glass and metal-coated glass mirrors. These results were compared with the characteristics of zero-order diffraction from a planar-ruled diffraction grating. A paper by Utsuro, et al., then described the ultracold neutron facility at the Kyoto University Reactor in Japan, including the characteristics and performance of the curved Ni mirror guide, supermirror turbine, and gravity spectrometer. The paper by Alefeld, et al., then considered the possibilities for focusing neutrons with curved mirrors. It was concluded from intensity calculations and experimental intensity profiles that focusing small-angle neutron scattering instruments with high-quality neutron mirrors will be superior to conventional pinhole instruments for high-scattering vector resolution  $\Delta Q \leq 10^{-3} \text{ \AA}^{-1}$ . Interesting experiments with a neutron "lens" and a microbender made up of multilayered thin film microguides were also discussed. A paper by Majkrzak, et al., then presented several applications of supermirrors and multilayers planned for the new Cold Neutron Project at the National Institute of Standards and Technology. Included in this presentation were descriptions of a novel polarized triple-axis spectrometer using a combination of supermirror polarizers and Drabkin resonance spin-flippers as monochromator and analyser, a neutron reflectometer, and a focusing mirror for a small-angle scattering spectrometer. Tasaki, et al., were the authors of a following paper on an interesting idea for a polarizing monochromator consisting of two multilayers in series. This combination serves not only as monochromator and polarizer, but collimator and beam bender as well. The final paper of the session was by DiNardo, et al., and dealt with the actual fabrication of polarizing multilayers by sputtering, in particular for the Fe-Si system, and compared observed reflectivities with predicted values.

### **Multilayer monochromators for X-rays and neutrons**

The conference on neutron optics concluded in a joint session with another symposium conference on X-ray multilayers.<sup>[2]</sup> Andreas Freund opened the session with a talk on the common and dissimilar aspects of beam-defining devices for x-rays and neutrons. Besides the intrinsic interaction properties of the two radiations with matter, the importance of the properties of the sources (e.g., neutron reactor or pulsed source and x-ray synchrotron) for the design of beam optics was discussed. Josef Feldhaus next gave an overview of soft x-ray monochromators for synchrotron radiation showing examples typical of various energy ranges and applications. A review of the theory of multilayer neutron monochromators was given by Varley Sears, in which both the kinematical and dynamical treatments were discussed. Two additional papers were presented, one by Smith, et al., on a W-C multilayer monochromator for x-rays and the other by Evans, et al., on the neutron reflectivity of Ni-Si multilayers.

### **Conclusion**

The quality of the papers presented and the exchange of information that occurred between people attending the x-ray and neutron conferences contributed significantly,



I believe, to the success of the meeting. It is hoped that a similar conference will be held in the future.

### **References**

1. SPIE Proceedings Vol. 983, "Thin-Film Neutron Optical Devices: Mirrors, Supermirrors, Multilayer Monochromators, Polarizers and Beam Guides", C. F. Majkrzak and A. M. Saxena, Eds. (SPIE, Bellingham, WA, in press).
2. SPIE Proceedings Vol. 984, "X-ray Multilayers for Diffractometers, Monochromators, and Spectrometers", Finn E. Christensen et al., Eds. (SPIE, Bellingham, WA, in press).



## Workshop summary on beam handling

*C. F. Majkrzak*  
National Institute of Standards and Technology  
Gaithersburg, Maryland 20899  
USA

In this particular session, five short talks were given with an appropriate amount of time between talks for informal discussion. To begin, John Copley described a method to calculate the properties of multiple-section systems of straight-sided guides based on the idea of acceptance diagrams. This two-dimensional geometrical representation of the spatial and angular coordinates of the neutrons in the system may be applied to a variety of practical design problems. In a related talk, Ruep Lechner discussed the effect of a guide "bottleneck" to spatially compress the beam at the position of a rotating disc chopper in order to improve the time resolution in a time-of-flight spectrometer application. Laurenz Niel next talked about two distinct methods of neutron energy transfer via time-dependent magnetic fields. In one method, energy is exchanged with neutron spin flip, and in the other, without. The results of experimental demonstrations of both techniques were reported. C. F. Majkrzak then summarized the proceedings of the International Society of Optical Engineering's recent Conference on Neutron Optical Devices. Twenty-four talks were presented at this conference on mirrors, supermirrors, multilayer monochromators, beam guides, and other applications of relevance to the current workshop session. Finally, Kent Crawford presented the results of work on Soller collimators for small angle scattering application.

The discussions following each of these talks served to clarify certain points as well as stimulate further thought on the subject.

## Neutron spectrum measurement, LANSCE/ER-1

*M. L. Howe and R. L. Mundis*  
Health Safety Environment Division  
Los Alamos National Laboratory  
Los Alamos, New Mexico 87545  
USA

**ABSTRACT:** Neutron spectral measurements were made in LANSCE Experimental Room 1 during an intentional spill of 100 nA on a carbon block in the beam channel. The relative response of two neutron dosimetry badges and a neutron survey meter were investigated. The resultant neutron spectrum had a strong high-energy component containing 25% of the flux density and 70% of the neutron dose equivalent. The dosimetry badges and the survey meter underresponded by 80, 20 and 50%, respectively. Due to their individual energy responses, a simple sum of the two dosimeter results gives a total dose equivalent, which is close enough to the unfolded spectrum value to be used for personnel dosimetry records.

### Introduction

On July 22, 1987 an experiment was run to measure the neutron energy spectrum in the LANSCE Experiment Room 1 (ER-1) with the proton beam being stopped in the carbon beam block in Line D directly downstream of the IR bender. The purpose of this measurement was to determine the neutron-energy spectrum and dose rate found in ER-1 under the conditions of beam spill, and determine the relative sensitivities of the Albatross-IV neutron survey instrument, the LANL TLD dosimeter badge that is worn by TA-53 personnel, and the NTA-type nuclear-track-emulsion dosimetry badge that formerly was used at the Lab for personnel neutron dosimetry.

### Detectors

The detectors used to determine the energy spectrum included a set of six polyethylene moderator spheres (5.08- to 30.48-cm diameter) with TLD 600 and TLD 700 LiF detectors in the center, an unmoderated set of TLD detectors, a cadmium covered set of unmoderated TLD detectors, a plastic scintillator C(n,2n) threshold activation detector, and a large bismuth fission counter. Each of these ten detectors has a unique sensitivity for neutron detection as a function of neutron energy. Computer codes are used to unfold the neutron-energy spectrum that matches input data from the ten detectors. The unfolding codes yield a spectrum that covers the energy range from 0.01 eV to 400 MeV. The upper limit is determined by the limits on the known response functions of the detectors. The C(n,2n) reaction has an energy threshold of 20 MeV, and the bismuth fission counter has a 50-MeV threshold energy. In addition, an Albatross-IV and two personnel dosimeter badges on a polyethylene phantom were placed next to the detector array. Two other sets of dosimeter badges were placed on phantoms in other locations in ER-1.

## Measurements

The array of detectors was set up in ER-1 at the location (#2) indicated in Fig. 1 at an elevation of ~1 m above the floor. The location of the carbon beam block in Line D (above) is also indicated on Fig. 1. The detectors were at an angle of ~70 degrees relative to the incident proton beam. The floor of the Line-D beam tunnel is 1.5 m of ordinary concrete at this location. The locations of other sets of dosimeters is also shown on Fig. 1 (#1 and #3). The proton beam was directed onto the carbon block from 2140 to 2245 hours with a down time of eight minutes at about the half-way point of the run. The proton beam current was determined to be steady at ~100 nA, based on several methods of estimation.

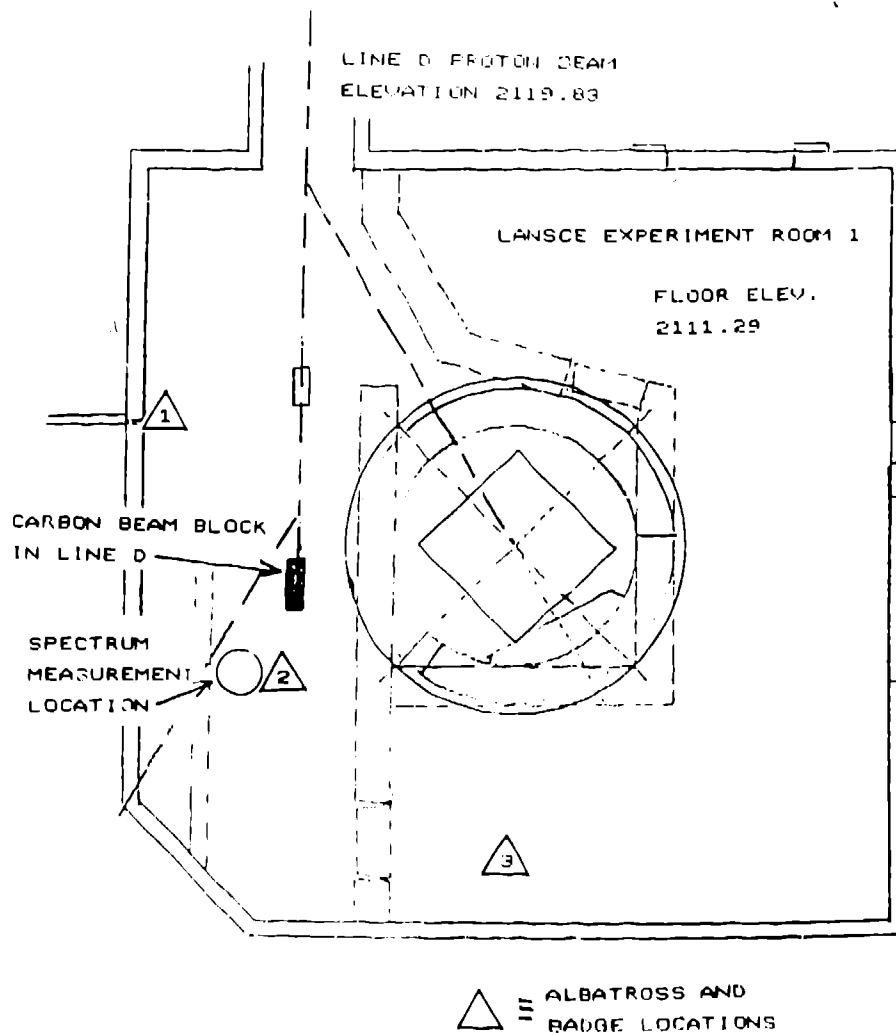


Fig. 1 Locations of neutron measurements in LANSCE/ER-1 relative to location of carbon block in Line D (above).

## Results

The neutron spectrum determined from the unfolding codes is shown in Fig. 2. The codes show good general agreement up to about 60 MeV. There is poorer agreement in the number of neutrons present above that energy. The neutron-radiation field parameters resulting from the spectrum unfolding codes are summarized on the figure. The important quantity is the computed dose equivalent rate of 610 mrem/h. The dose equivalent distribution in neutron energy indicates that 70% of the neutron dose is due to neutrons of energy greater than 10 MeV, although this region includes only about 25% of the total flux density.

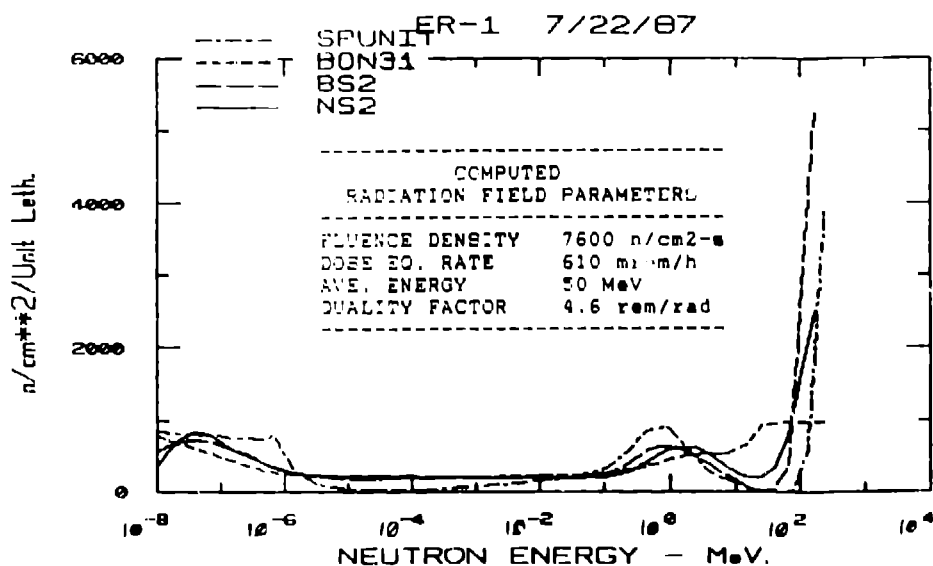


Fig. 2 Unfolded-neutron-energy spectrum (four unfolding codes) in LANSCE/ER-1.

Table 1 summarizes the results from each of the detectors used at the location of the spectrum measurement.

Table 1

Detector/Systems Used	DE Rate mrem/hr	Flux Density n/cm²s
Spectrum Unfolding (Ave.)	610	7600
Albatross (Location #2)	300	n/a
Carbon Scintillator	340	1700
Bismuth Fission Counter	420	2100
TLD Personnel Badge	100	n/a
NTA Track Film	480	n/a

The TLD Personnel Badge and the NTA Track Film were interpreted as if they were ordinary badges being worn by personnel, with the calibrations based on Cf-252 and Pu/Be neutrons, respectively.

The TLD and NTA dosimeters on phantoms at the other two locations in ER-1 indicated the dose results compared to the Albatross readings as shown in Table 2.

**Table 2**

Location	Dose (mrem)		
	TLD	NTA	Albatross
1	23	16	44
4	11	64	56

The Albatross readings are "eyeball" type averages of the remote readouts during the course of the measurement. Again, the TLD and NTA data were interpreted with the normal dosimetry calibrations.

### Conclusions

The following observations and conclusions can be made from these comparison data:

- The Albatross underestimates the true dose rate by ~50% for the measured neutron spectrum. This is not unexpected because the response of the Albatross falls off severely above 20-MeV neutron energy.
- The sum of the Albatross plus the plastic scintillator result gives good agreement with the total dose from the unfolded spectrum. This good agreement may be fortuitous, but it does look reassuring that everything is consistent.
- The TLD badge underresponds by a factor of six in the neutron spectrum at Location 2. This is because the sensitivity of the albedo-type dosimeter falls off very badly for neutrons of energy above 1 MeV.
- The NTA film at Location 2 also underresponds, but only by about 20%. (The NTA film has an effective threshold of ~1 MeV.) The sum of the TLD and NTA is 580 mrem, which is very close to the results from the spectrum-unfolding results. This, again, may be fortuitous, but it is consistent with the ranges of sensitivities of the two types of dosimeters.
- The TLD badges at the other two locations (1 and 4) also underestimated the dose compared to the Albatross to about the same degree as Location 2. What we don't know is how much the Albatross is underestimating at Locations 1 and 4.

Based on the above results and conclusions, personnel who had access and reason to work in ER-1 during the 1988 LAMPF running period were assigned both a TLD and an NTA badge. Interpretations for any positive results were based on the same calibrations as used in Table 1. The sum of these two numbers was used for an individual's total neutron-dose equivalent. For neutron spectra similar to those measured at location #2, this estimated value of dose equivalent should be within ±30% of the true value.

## The ISIS target halo monitors

A. Carne  
Rutherford-Appleton Laboratory  
Chilton, Nr Didcot, Oxon  
UNITED KINGDOM

### First halo monitor

The first ISIS target halo monitor was installed in July 1985 and was located some 360 mm in front of the input beam window of the target. It was provided because there was concern with the size and alignment of the extracted proton beam impacting the target. Size was important because of the unknown effects of energy depositions at the outer radius of the uranium disc (45 mm), on the circumferential uranium-zircaloy intermetallic bond, and on the zircaloy cup-to-stainless-steel picture frame compression fit. Alignment was important because of asymmetry effects on neutronic coupling, risk of increased charged-particle escapes (especially towards the lower, liquid-methane moderator), and of asymmetric energy deposition across the zircaloy and stainless-steel picture frame.

For an expected proton beam spot on target of parabolic intensity distribution of base 70 mm, the halo monitor diameter was 80 mm. Of the possible electrical or mechanical devices considered, a simple passive system was chosen of an annulus of metal (stainless steel) intercepting the beam halo. The annulus was thermally isolated and used reactor-grade thermocouples to measure the temperatures. The annulus was made into four quadrants to give some directivity, and each quadrant carried two thermocouples. Figure 1 is a drawing of the halo monitor, resting in its support frame. Though half the thermocouples were intended to act as spares, in practice all eight thermocouples were monitored and the resulting display gave a very graphic indication of the transmission of the beam through the aperture. In action the halo monitor was rather sluggish, with slow temperature rise and fall times and with a slow scanning speed (about 30 seconds per scan).

### New halo monitor

A new halo monitor was built and installed in March 1988 to overcome the limitations of the first one. Figure 2 gives a back view of the new device, where the thermocouples were mounted on eight smaller stainless-steel fingers (octants): four, at N, E, S, W have an inner diameter of 75 mm and the other four at 85 mm diameter. The resulting display (in color) thus gives a better indication of alignment and a first order indication of intensity distribution. A new scanner, based on a dedicated PC, is to be implemented to reduce the total scan time to four seconds. Figure 3 shows the halo-monitor display in a normal operating state with a 100- $\mu$ A proton beam. The circles based on the center cross indicate alignment and uniformity of distribution. Alarm states are shown by a change of color (from green to blue) of any thermocouple or pair of thermocouples. If a temperature difference across a



diameter exceeds  $15^\circ$ , the beam is ramped off; if a single thermocouple temperature exceeds  $90^\circ$ , the beam is tripped off. In either event, a message is displayed to this effect.

### **Target diagnostic plate**

In the initial construction of the Target Station, the target center was located well within a sphere of radius 1/2 mm and the center line lay within a cylinder of 1/2 mm radius. For reasons indicated in paragraph 1 above, the proton-beam alignment tolerance on target was sought at  $\pm 2$  mm. After several years operation the alignment of the target relative to the EBP or the neutron beams is no longer known to any great accuracy. Indeed surveys carried out in 1986 and 1987 showed the target to have "sunk" by between 5 and 10 mm! A resurvey is now difficult because access is limited for mechanical reasons and radiation safety. Yet, as the intensity and reliability of ISIS increase, the need to know the target alignment becomes more important.

Starting with target number 5 we propose to install a proton-beam monitor within the target itself, which will be used together with the external monitor (2 above) to define the target alignment. The system is dynamic, i.e., it gives the information all the time the proton beam is on. The present plate number 15 (of the 23 target plates) will be replaced by a solid zircaloy plate containing 8 thermocouples, as can be seen in Fig. 4. The thermocouples will be mounted in a similar format to the external halo monitor. From Ref. 1 it can be seen that despite the high energy cascade process, the beam still retains its parabolic distribution, at least as far as plate 15 (160 mm into the target), but its base has broadened from 70 to 76 mm diameter. Accordingly, the thermocouples will be located at 19-mm radius and 27-mm radius, corresponding to 0.75 and 0.5 time peak intensity, respectively. Energy density will be less than for uranium, so the expected peak temperature in the plate will be  $203^\circ$  C, rather than  $216^\circ$  C for uranium, at full intensity. There will be a penalty of less than 2-3% in sub-15 MeV neutron escapes; however, since the plate is situated between the two moderators (as can be seen in Fig. 5), the coupled effect should be less.

The opportunity is also being taken to change the distribution of thermocouples in the target: from alternate plates to 1 through 14, 15, 17, 18, 19, and 21. The new target may well be brought into operation in 1989.

### **Reference**

1. Atchison, F., 1981, "A Theoretical Study of a Target Reflector and Moderator Assembly for SNS", RL-81-006.

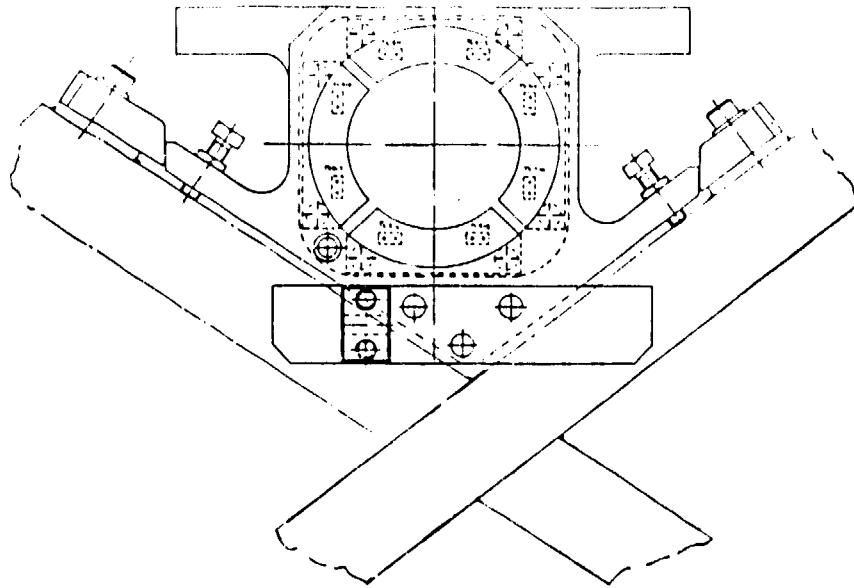


Fig. 1 Original quadrant halo monitor, front view.

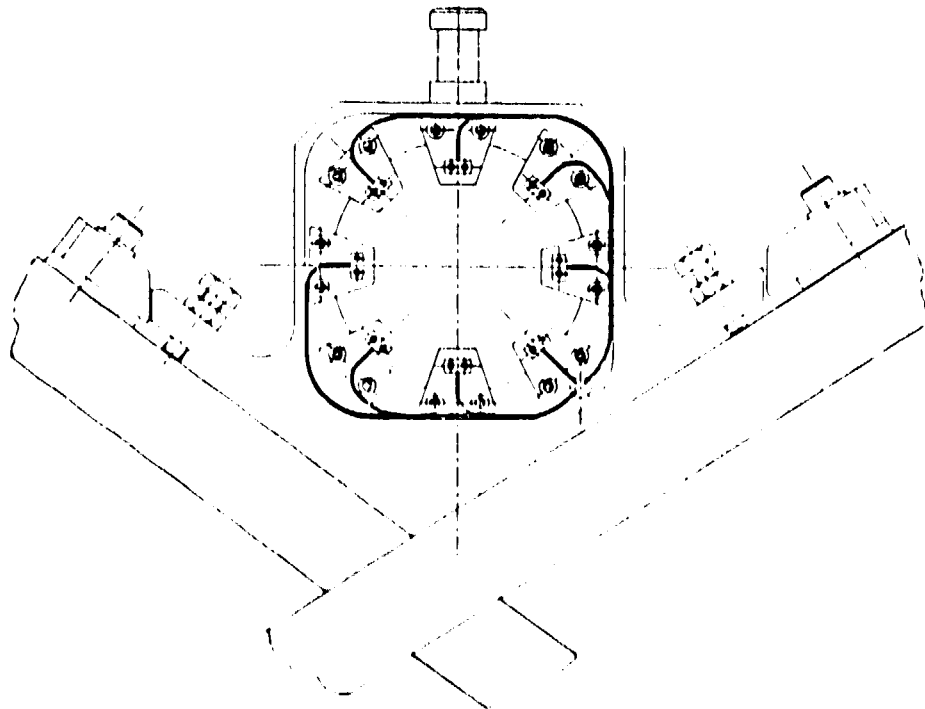


Fig. 2 New octant halo monitor, rear view.

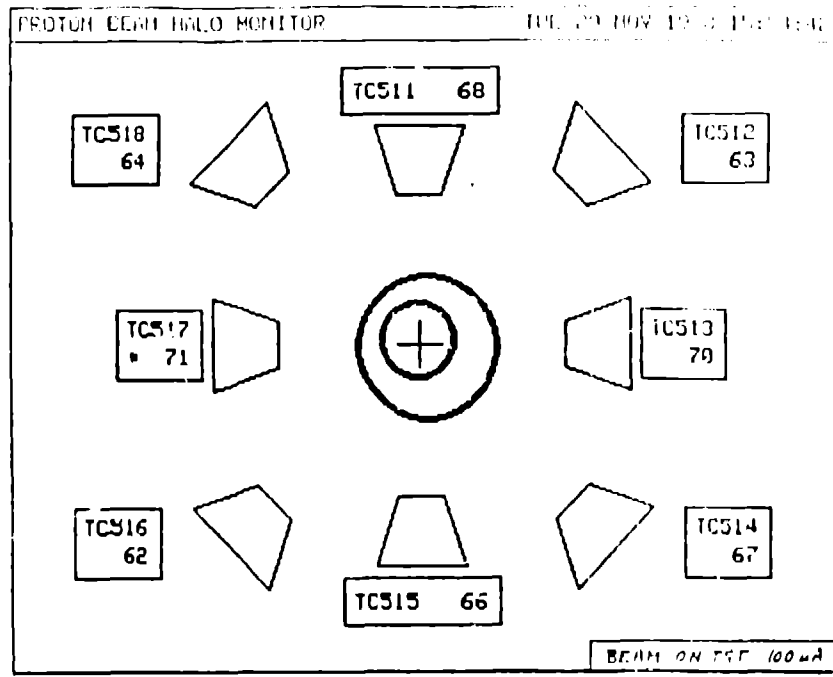


Fig. 3 Halo monitor display.

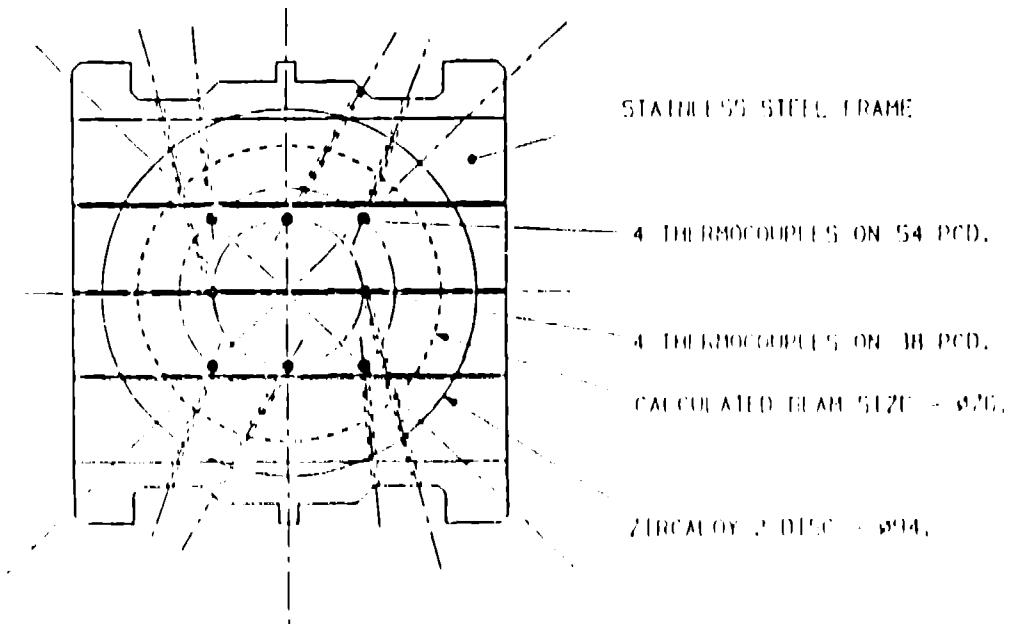


Fig. 4 Target (internal) diagnostic plate.



## Summary of the Los Alamos Spallation Radiation Effects Facility at LAMPF (LASREF)

*W. Sommer*  
Los Alamos National Laboratory  
Los Alamos, New Mexico 87545  
USA

### Facility

The following components and procedures are in place and have been demonstrated to be operationally reliable. We have also made progress in characterizing the neutron environment, through both calculation and activation foil measurements.

- Three proton irradiation ports, each with a usable volume of 150 cm<sup>3</sup>. Total permissible mass density in the beam is 10-20 gm/cm<sup>2</sup>, subject to occasional scheduling constraints.
- Proton flux in the beam center of 2 to 4 x 10<sup>14</sup> protons/cm<sup>2</sup>s.
- Proton irradiation capsules capable of controlled operation at elevated temperature.
- Twelve neutron irradiation ports, each with an irradiation volume bounded by dimensions of 10 x 20 x 40 cm.
- Neutron flux of 2-6 x 10<sup>13</sup> neutrons/cm<sup>2</sup>s (at 3 of the 12 ports) determined both by measurement and Monte Carlo calculations. The energy distribution resembles a fission spectrum with the addition of substantial numbers of neutron in the 10-100 MeV range, i. e., a high-energy tail.
- Neutron irradiation capsules/furnaces that have operated up to temperatures of 650°C. Samples experience an inert gas atmosphere.
- Closed-loop water and helium heating/cooling systems.
- On-line continuous data acquisition and experiment control.
- Remote handling of radioactive samples. Experiment changes have been made in 6 h during a scheduled LAMPF maintenance day.
- Field-Ion-Microscopy laboratory has been used successfully to explore atomic-resolution details of depleted zones.



### **Irradiation experiments performed**

- Five independent proton irradiations containing about 30 different materials/alloys.
- Four independent neutron irradiations containing about 50 different materials/devices.
- Seven approved LAMPF experiments over the last three years. Includes ceramics and graphites sponsored by KFA Julich for the European fusion community.

### **Active experiments/spokespersons/sponsors**

Experiment #769 "Proton Irradiation Effects on Candidate Materials for the German Spallation Neutron Source"

- W. Lohmann, KFA Julich, FRG
- W. Sommer, Los Alamos

Experiment #936 "Additional Measurements of the Radiation Environment at the Los Alamos Spallation Radiation Effects Facility at LAMPF"

- D. Davidson, Iowa State University
- M. Wechsler, Iowa State University

Experiment #943 "Microstructural Evolution and Mechanical Property Changes in 316 Stainless Steel, Al, and Mo under Irradiation with Different Displacement/Helium Production Rates and Ratios"

- J. Yu, Institute of Atomic Energy, Peoples Republic of China
- M. Borden, New Mexico Institute of Mining and Technology
- W. Sommer, Los Alamos

Experiment #929 "Crack Growth in 800-MeV Proton and Neutron Irradiated Alloy 718"

- R. Brown, Los Alamos

Experiment #952 "Radiation Damage in Magnetically Soft Crystalline and Amorphous Alloys"

- J. Cost, Los Alamos
- R. Brown, Los Alamos

Experiment #986 "Spallation Neutron Irradiation of Non-Oxide Ceramics for First-Wall Fusion Reactor Application"

- B. Thiele, KFA Julich
- J. Linke, KFA, Julich

Experiment #987 "Fast Neutron Irradiation Screening Test of Polycrystalline Graphites under First-Wall Fusion Conditions"

- W. Delle, KFA Julich
- B. Thiele, KFA Julich



Experiment #1014 "Proton, Spallation Neutron, and Fission Neutron Irradiation of Copper"

- A. Horsewell, RISO National Laboratory, Denmark
- W. Sommer, Los Alamos

Letter of Intent—"Measurement of Point Defect Concentrations in Metals During 800-MeV Proton Bombardment"

- M. Eltrup, A. Horsewell, and B. Singh, RISO National Laboratory, Denmark
- W. Sommer, Los Alamos
- S. Lin, Peoples' Republic of China

Letter of Intent—"Resistivity Measurements on Alumina"

- F. Clinard, Los Alamos

Letter of Intent—"Effects of Temperature, Neutron Spectrum, Size, and Composition on the Neutron-Induced Embrittlement of Nuclear Pressure Vessel Steels"

- A. Kumar, University of Missouri-Rolla
- F. Garner, Battelle Pacific Northwest Laboratories
- M. Hamilton, Battelle Pacific Northwest Laboratories
- G. Lucas, University of California-Santa Barbara

**Major results**

- Measured neutron flux and spectra are in good agreement with previous Monte Carlo calculations.
- Field-Ion-Microscopy of irradiated W shows detail of a depleted zone and suggests dynamic transport of atoms.
- Precipitation hardened alloys of Al-Mg-Si and cold-worked alloys of Al-Mg lose their strength to the annealed level at a low dose of  $3 \times 10^{20}$  protons/cm<sup>2</sup> and at a temperature <100 °C. In the Al-Mg-Si alloy, the Mg<sub>2</sub>Si precipitates dissolved and in the Al-Mg alloy, the dislocation structure was greatly altered. This material is a candidate for beamline windows and high conductivity/low activation applications for pulsed neutron sources in Germany, England, and the US.
- Irradiation of electrical components essential for *in-situ* stress-strain, fatigue, and creep measurements showed them to be sufficiently reliable when properly shielded.
- Measurement of gas production (He) in several materials irradiated with protons allows refinement of codes currently used to predict radiation damage parameters.

**Future plans/possibilities**

- *In-situ* measurement of mechanical properties of irradiated materials. Testing machines developed and built by KFA Julich are now available at LAMPF.

Since the KFA spallation neutron facility project has been canceled, we will need a dedicated team to bring this equipment into use.

- Measurement of microstructural evolution in Cu, Mo, and Al under varying ratios of gas production/atomic displacement. Irradiations are now underway using the LAMPF proton beam, the LAMPF neutron flux, and the Danish DR-3 fission reactor. This experiment tests a recent theory based on non-equilibrium thermodynamics and kinetics developed by Jinnan Yu (visiting scientist from the PRC) during his stay at Los Alamos.
- Measurement of point defect generation and transport using resistivity measurements, positron annihilation technique, field-ion-microscopy, and internal friction measurements. Resistivity measurements will begin at liquid He temperature; we expect to have a cryogenic facility.
- Development of a high-Z target for eventual use at LANSCE. Samples of U and U alloys have been irradiated and await analysis.
- Rutherford/ISIS advanced target development.
- LAMPF Advanced Hadron Facility target cell development.
- Investigations of properties of superconducting materials under radiation for the Superconducting Super Collider project.
- Increased involvement with universities/graduate students.

#### **Active collaborators**

- RISO National Laboratory, Denmark
  - A. Horsewell
  - M. Eltup
  - B. Singh
- KFA—Julich, West Germany
  - W. Lohmann
  - B. Thiele
- SIN/EIR, Switzerland
  - W. Green
  - M. Victoria
- Atomic Energy Commission, Peoples Republic of China
  - J. Yu
  - S. Lin
- Iowa State University
  - M. Wechsler
- New Mexico Institute of Mining and Technology
  - O. Inal
  - M. Borjen
- Battelle Pacific Northwest Laboratories
  - F. Garner



- Los Alamos National Laboratory
  - R. Brown
  - J. Cost
  - G. Russell
  - G. Legate
  - F. Clinard
- University of Missouri-Rolla
  - A. Kumar

### **Program Advisory Committee (PAC)**

LAMPF utilizes peer review of research proposals to determine the scientific merit and feasibility for each proposed experiment. A Materials Science Subcommittee of the PAC is in place. Present members of the PAC are:

Frank Garner, Battelle Pacific Northwest Laboratories, Chairman  
Ken Russell, Massachusetts Institute of Technology  
James Stubbins, University of Illinois  
Arvind Kumar, University of Missouri

### **Theoretical/computational**

L.N. Kinetyk, W.F. Sommer, J. Weertman, and W.F. Green, "An Analytic Comparison of the Effect of Steady State and Cyclic Pulsed Radiation on Void Growth and Swelling," *J. Nucl. Mater.* **85** and **86**, pp. 553-557 (1979).

L.N. Kinetyk, W.F. Sommer, and J. Weertman, "The Effect of Cyclic Pulsed Temperature on Void Growth in Metals During Irradiation," *J. Nucl. Mater.* **103** and **104**, pp. 1409-1414 (1981).

L.N. Kinetyk, J. Weertman, W.V. Green, D.M. Parkin, and W.F. Sommer, "Void Growth and Swelling for Cyclic Pulsed Radiation," *J. Nucl. Mater.* **98**, pp. 190-205 (1981).

Wechsler, M.S., Davidson, D.R., Greenwood, L.R., and Sommer, W.F., "Calculation of Displacement and Helium Production at the Clinton P. Anderson Meson Physics Facility (LAMPF) Irradiation Facility," Effects of Radiation on Materials: Twelfth International Symposium, ASTM STP 870, F.A. Garner and J.S. Perrin, Eds., American Society for Testing and Materials, Philadelphia, PA (1985), pp. 1189-1198.

J. Yu, W.F. Sommer, and J.N. Bradbury, "Microstructural Evolution under Particle (Neutron and Proton) Irradiation: Nonequilibrium Statistics Theory for Bubble Nucleation and Growth," LA-UR 85-2851 Rev., presented at the Second International Conference on Fusion Reactor Materials, Chicago, IL, April 13-17, 1986. To be published in J. Nucl. Mater.

J. Yu, W.F. Sommer, and J.N. Bradbury, "Interstitial Dislocation Loop Nucleation and Growth and Swelling Produced by High Energy Cascades," LA-UR 85-3011, presented at the Thirteenth International Symposium on Effects of Radiation on Materials, Seattle, WA, June 23-25, 1986. To be published in the Proceedings.

#### **Facility characterization/description**

W.F. Sommer, L.N. Kinetyk, W.V. Green, and R. Damjanovich, "Use of the LAMPF Accelerator as a Fusion Materials-Radiation Effects Facility," J. Nucl. Mater. 103 and 104, pp. 1583-1588 (1981).

K.E. Christensen, G.A. Bennett, and W.F. Sommer, "An In-Situ Mechanical-Radiation Effects Test Capsule for Simulating Fusion Materials Environments," J. Nucl. Mater. 103 and 104, pp. 1517-1521 (1981).

R.D. Brown and D.L. Grisham, "Design and Operation Water-Cooled Pyrolytic Graphite Targets at LAMPF," 1981 Particle Accelerator Conference, Accelerator Engineering and Technology, Washington, DC., March 11-13, 1981, IEEE Transactions on Nuclear Science, Vol. NS-28, 2940 (1981), Los Alamos National Laboratory Report LA-UR 81-955 (1981).

R.D. Brown and D.L. Grisham, "Graphite Targets at LAMPF," Particle Accelerator Conference, March 21-23, 1983, IEEE Transactions on Nuclear Science, Vol. NS-30, 2801 (1983), Los Alamos National Laboratory Report LA-UR 83-956 (1983).

L. Aznew, D. Grisham, R.J. Macek, W.F. Sommer, and R.D. Werbeck, "Design Features and Performance of the LAMPF High Intensity Beam Area," presented at

the ICANS VII meeting, Chalk River, Ontario, CANADA, Sept. 12-16, 1983. To be published in the Proceedings.

D.R. Davidson, R.C. Little, W.F. Sommer, J.N. Bradbury, and R.E. Prael, "Characterization of the Radiation Environment at a New Proposed Irradiation Facility at LAMPF," J. Nucl. Mater. 122 123, pp. 989-994 (1984).

M.S. Wechsler and W.F. Sommer, "The Radiation Damage Facility at the LAMPF A-6 Target Station," J. Nucl. Mater. 122 123, pp. 1078-1084 (1984).

Davidson, D.R., Greenwood, L.R., Reedy, R.C., and Sommer, W.F., "Measured Radiation Environment at the Clinton P. Anderson Meson Physics Facility (LAMPF) Irradiation Facility, Effects of Radiation on Materials: Twelfth International Symposium, ASTM STP 870, F.A. Garner and J.S. Perrin, Eds., American Society for Testing and Materials, Philadelphia, PA, 1985, pp. 1199-1208.

D.R. Davidson, W.F. Sommer, I.K. Taylor, R.D. Brown, and L. Martinez, "'Rabbit' System for Activation Foil Irradiations at the Los Alamos Spallation Radiation Effects Facility at LAMPF," LA-UR 85-3630 Rev., presented at the Second International Conference on Fusion Reactor Materials, Chicago, IL, April 13-17, 1986. Not to be published.

W.F. Sommer, W. Lohmann, I.K. Taylor, and R.M. Chavez, "Operating Experience at the Los Alamos Spallation Radiation Effects Facility at LAMPF," LA-UR 85-3917, presented at the Thirteenth International Symposium on Effects of Radiation on Materials, Seattle, WA, June 23-25, 1986. To be published in the Proceedings.

D.L. Grisham, J.E. Lambert, and W.F. Sommer, "Major Facility Overhauls at LAMPF," IEEE Transactions on Nuclear Science, NS-32(5), 3095-3097, (1985). Los Alamos National Laboratory document LA-UR 85-1736 (1985).

W. Lohmann and W.F. Sommer, "Materials Problems Relevant to a Pulsed High Power Spallation Target," Rutherford Report, ISIS/PGT/15, November 1986.

## Experiments

H. Jang, J. Moteff, L. Levinson, R.D. Brown, and W.V. Green, "Defect Formation in 800-MeV Proton Irradiated Aluminum," Los Alamos National Laboratory Report LA-8127-MS, November 1979.

R.D. Brown, W.F. Sommer, and W.V. Green, "Irradiation Damage in Metals Produced by 800-MeV Protons," Los Alamos Scientific Laboratory Report LA-7939-MS (July 1979).

O.T. Inal and W.F. Sommer, "800-MeV Proton Damage in Tungsten and Molybdenum, A Field-Ion Microscope Observation," J. Nucl. Mater. **98**, pp. 94-99 (1981).

J.R. Cost and W.F. Sommer, "Response of Metallic Glasses,  $\text{Fe}_{40}\text{Ni}_{40}\text{P}_{14}\text{B}_6$  and  $\text{Fe}_{80}\text{B}_{20}$  to Irradiation with 800-MeV Protons," J. Nucl. Mater. **103** and **104**, pp. 773-778 (1982).

W.F. Sommer, D.S. Phillips, W.V. Green, L.W. Hobbs, and C.A. Wert, "Proton Irradiation Damage in Cyclically-Stressed Aluminum," J. Nucl. Mater. **114**, pp. 267-276 (1983).

D.J. Farnum, W.F. Sommer, and O.T. Inal, "A Study of Defects Produced in Tungsten by 800-MeV Protons Using Field Ion Microscopy," J. Nucl. Mater. **122** and **123**, 998-1001 (1984).

R.D. Brown, J.R. Cost, and J.T. Stanley, "Effects of Neutron Irradiation on Magnetic Permeability of Amorphous and Crystalline Magnetic Alloys," Conference on Magnetism and Magnetic Materials, Pittsburgh, PA, November 8-11, 1983, published in J. Appl. Phys. **55**, 1754 (1984), Los Alamos National Laboratory Report LA-UR 83-2718 (1983).

R.D. Brown and J.R. Cost, "Mechanical Properties of 800-MeV Proton-Irradiated

Metals," Effects of Radiation on Materials, Eleventh Conference, ASM STP 782 H. R. Brager and J.S. Perrin, Eds., American Society for Testing and Materials, pp. 917-926, 1982, Los Alamos National Laboratory Report LA-UR 82-672 (1982).

R.D. Brown, J.R. Cost, and J.T. Stanley, "Irradiation-Induced Decay of Magnetic Permeability of Metglas 2605S-3 and Mumetal," published in *J. Nucl. Mater.*, **131**, 57 (1985), Los Alamos National Laboratory Report LA-UR 84-875 (1984).

D.R. Davidson, W.F. Sommer, and M.S. Wechsler, "Additional Measurements of the Radiation Environment at the Los Alamos Spallation Radiation Effects Facility at LAMPF," LA-UR 85-3502 Rev., presented at the Thirteenth International Symposium on Effects of Radiation on Materials held at Seattle, WA, June 23-25, 1986. To be published in the Proceedings.

D.J. Farnum, W.F. Sommer, O.T. Inal, and J. Yu, "Quantitative Study, by Field Ion Microscopy, of Radiation Damage in Tungsten after Neutron and Proton Irradiation," LA-UR 85-3918, presented at the Thirteenth International Symposium on Effects of Radiation on Materials, Seattle, WA, June 23-25, 1986. To be published in the Proceedings.

W. Lohmann, A. Ribbens, W.F. Sommer, and B. Singh, "Microstructure and Mechanical Properties of 800-MeV Proton Irradiated Commercial Aluminum Alloys," LA-UR 85-2296, presented at the RISO National Laboratory Workshop on The Relation Between Mechanical Properties and Microstructure Under Fusion Irradiation Conditions, June 27-July 2, 1985. To be published in *Rad. Effects*.

B.N. Singh, W. Lohmann, A. Ribbens, and W.F. Sommer, "Microstructural Changes in Commercial Aluminum Alloys after Proton Irradiation," LA-UR 85-4074, presented at the Thirteenth International Symposium on Effects of Radiation on Materials, Seattle, WA, June 23-25, 1986. To be published in the Proceedings.

B.N. Singh, W.F. Sommer, and W. Lohmann, "Transport and Accumulation of He-

limum Produced During 800-MeV Proton Irradiation of Aluminum and Aluminum Alloys," LA-UR 85-3403, presented at the Second International Conference on Fusion Reactor Materials, Chicago, IL, April 1983. To be published in the J. Nucl. Mater.

D.J. Farnum, W.F. Sommer, O.T. Inal, and J. Yu, "Field Ion Microscopy Study of Depleted Zones in Tungsten after Proton Irradiation," LA-UR 85-3916 Rev., presented at the Second International Conference on Fusion Reactor Materials, Chicago, IL, April 13-17, 1986. Not to be published.

K.O. Jensen, M. Eldrup, B.N. Singh, A. Horsewell, M. Victoria, and W.F. Sommer, "Characterization of Vacancy and Vacancy-Gas Agglomerates in Aluminum Irradiated with Medium-Energy Protons by Positron Annihilation," presented at the International Conference on Vacancies and Interstitials in Metals and Alloys, Berlin, FRG, September 14-19, 1986.

## Workshop summary on practical concerns


*T. A. Broome*  
Rutherford-Appleton Laboratory  
Chilton, Oxon  
UNITED KINGDOM

The purpose of this session was to provide an opportunity to discuss topics of practical concern in the operation and design of spallation sources. There were five presentations: each addressing a different subject.


Mike Howe (LANL) described, in detail, measurements of dose rates in Experimental Room 1 at LANSCE. The basic difficulty of high dose rates in ER1 when beam is lost in the adjacent proton channel had been mentioned in a previous session at the meeting. This presentation described the detailed investigations to quantify the problem and, thus, enable a practical solution to be developed in providing safe access to the area.

This was, in essence, a shielding experiment that had our two main features of general interest. The health-physics aspects establishes two things: the scale of the hazard in sufficient detail to enable decisions to be made on the control of access to the area; and dosimetry that provides safe working conditions. Standard personal dosimeters were exposed during the experiment to assess how effectively they measured the dose. The neutron spectrum was found to have a very large component of high-energy neutrons and, as a result, the TLD badges, which are insensitive in the high-energy regime, gave a poor measurement of the dose. For this reason a second type of badge using NTA film, which has a better high energy response, is used in addition to the TLD badge when personnel enter ER1. The second feature concerns the measurements themselves, both the techniques and the results. The source was well known—100 mA of 800-MeV protons incident on a copper beam stop—and the shield is a 5-ft.-thick concrete wall. The neutron spectrum, and dose rate, were measured using a variety of detectors and unfolding codes. The experimental data were in good agreement with shielding calculations.


The measurement of dose rates in a pulsed fast neutron field has always been a technical challenge. Mike Howe described a new instrument that has been developed from the "Albatross" detector. The principle of operation is unchanged. Polyethylene is used to moderate the neutrons. A Geiger tube wrapped in silver foil detects the gammas from both thermal neutron capture in silver and the external radiation field. A second Geiger tube wrapped in tin foil detects just the external gammas. Subtracting the two gives the neutron field. The main development has been in the electronics to give a faster response, which allows the instrument to be used in a trip system. It is now fully developed, commercially available, and is a significant advance in dosimetry for pulsed sources.




Recent ISIS target failures, discussed elsewhere at this conference, have highlighted the need to have accurate alignment of a high-intensity beam on a target. The very high prompt radiation levels limit the possible beam-position detectors that can be placed near a target. Alan Carne (RAL) described the approach used at ISIS to monitor the position of the beam as it enters the target. Eight thermocouples are mounted on thermally isolated stainless-steel plates and are positioned symmetrically around the theoretical beam axis, four on a circle of diameter 75 mm and four on a diameter of 85 mm in the tails of the beam. Beam misalignment is then detected as a temperature difference between opposite thermocouples. These data can then be used in graphic displays, to generate warning messages to the operations staff and, if required, trip the accelerator. The principle is to be developed further in future targets by installing a similar arrangement of thermocouples in a special plate about halfway along the target. It is hoped that the external beam-halo monitor and the new internal diagnostic plate will provide a substantial improvement in beam-position monitoring and control, which is vital to improve the lifetime of the targets. It was clear from the discussion that followed the problem of monitoring a high-intensity proton beam near a target is one of common interest and one that presents a serious, and continuing, technical challenge.





Radiation damage is a concern of great importance to high-power spallation sources, particularly for the design of targets and proton-beam windows. Very little information is available to quantify the damage processes in the radiation field around a spallation target, and extrapolation from reactor experiments is subject to quite basic uncertainties. Irradiation testing on crucial components will become an increasing part of the design process. Walt Sommer (LANL) described the irradiation test facilities at the LAMPF beam stop. The LAMPF proton current of 0.8 mA at an energy of 800 MeV makes this facility ideally suited for studies of spallation sources. In fact, experiments were carried out for the SINQ project and are planned to study proton-beam window design for the SINQ facility. Both proton and neutron irradiations can be performed, and there is great flexibility in the physical arrangement and environment of the irradiation samples. Irradiations at elevated temperatures (650°C in the proton capsule and 850°C in the neutron capsule) can be accommodated. A tensile test rig is available that is capable of simulating cyclic stress problems. The general arrangement of the irradiation volumes allows the user great freedom to design equipment to provide special sample conditions. This is an excellent international user facility with peer review for experiments. The use of the protons is parasitic, which eases scheduling problems and reduces the cost of an experiment. Users are responsible for any new experimental equipment required for the sample environment.



The use of equipment at cryogenic temperatures is a common feature of neutron scattering facilities. This includes the sample environments as well as the cold moderators operated or planned at all sources. Moderators present particular problems in that, as well the cryogenic temperatures of the sources (< 100 K), the moderator fluids are also potentially explosive. This combination imposes severe constraints on the designer to ensure the systems are safe to install, commission, operate, and maintain. That the moderators themselves also become radioactive adds further to the design problems. Ken Williamson (LANL) reviewed the safety aspects of designing and operating cryogenic systems. The basic considerations underpinning the design of cryogenic systems and the principal hazards were discussed in detail. Some of the









common causes of operational problems were discussed such as inadequate pressure relief and insufficient attention to cool-down stresses. There was a discussion of the administrative and technical systems at the different laboratories for dealing with operational safety matters, which also have an important influence on design.

The topics and the discussion at this session were concerned with quite basic practical problems of operating and designing spallation sources. ICANS presents a unique forum for such discussions and I believe all those present found the session most useful and informative.



## Summaries and future projections

*P. A. Egelstaff*  
Physics Department  
University of Guelph  
Ontario  
CANADA

### PART A: A SUMMARY OF THE PLENARY SESSIONS

#### Overviews



The overview session is best assessed by comparing such sessions from successive ICANS meetings. In this way it can be seen that while all sources are still experiencing teething troubles, they all are making substantial progress. Also, we might say that this meeting has celebrated the maturing of ISIS. It is approaching 100  $\mu$ A and long periods of steady running on ~10 instruments. We could take the combination of these three items as the measure of a mature modern installation.

The emphasis at both ISIS and LANSCE is now on reliability and uniform operation. This is also an indication of maturity because it shows that the early phase of just getting the source to work is over. At IPNS, the new topic is the booster target. We look forward to news of its operating characteristics. When the design performance is achieved, IPNS will be able to continue to be competitive with the other two sources. KENS works at a lower current and fewer days than the other sources, but it continues to produce good results in cases where some resolution can be sacrificed to increase intensity. Because of the steep relationship between intensity and resolution, they can do this successfully.

In reviewing the progress announced during the first session, a "hardened reactor user" was overheard to say that pulsed sources have now proved that they are here to stay.

#### Current Problems

The second session was devoted really to current problems. These included problems with several types of targets and moderators and with the performance of storage rings and of shields. It was possible during this session to pick up an unduly pessimistic view of the progress being made with pulsed sources. This session involved a frank debate over the technical problems that have prevented the full realization of the optimistic predictions of earlier years. A reasonable conclusion would be that the problems discussed are being resolved slowly and, therefore, those predictions were justified—albeit over a longer time scale. Alternatively, we can say that we are




learning how to design targets and moderators, how to operate accelerators and storage rings, and how to shield sources and experiments in the necessary depth and detail required to meet the initial specifications. Probably the depth required had not been appreciated or had not been fully funded, and consequently the necessary work had to be extended over many years. However, papers in this session revealed that reasonable solutions are possible and in many cases in hand, so that at the next ICANS meeting we can expect fewer problems to be reported.

### **Moderators and New Instruments**

The fertility of this field is (perhaps) demonstrated most aptly by the vivid discussion of new moderators, new instruments and new techniques in data handling and data reduction. New kinds of experiments were debated in a similar way also. While experience shows that not all these ideas will survive the test of time, there seems to be no doubt that a number of them will do so. Consequently, we can expect that future ICANS meetings will see the successful outcome of many of the proposals discussed this week, and the benefits that accrue to a field as fertile as this one. Of course, they will be optimized in different ways for each of the various scientific fields.



### **Future Sources**



No less than six future sources were discussed at this meeting. They may be divided into reactors (Maple and Advanced Neutron Source), C. W. accelerator (PSI Source), time-structured (Advanced Spallation Source), and pulsed accelerators (Aspun and KENS II). This discussion also demonstrates the fertility of the field and the benefits to be expected in the long run. In each case, the technical situation, operating characteristics, and funding were described clearly and frankly. The attainable flux levels and operating characteristics for the next decade are, thus, reasonably clear. Over the foreseeable future reactor fluxes will lie in the  $10^{14}$ - $10^{16}$  n/cm<sup>2</sup>/sec range, with the lower end being regarded as a worthwhile lower limit for useful experiments and available in many places. For pulsed sources an output of  $10^{15}$  to  $10^{16}$  protons per second is probably the maximum that can be expected in the foreseeable future. The emphasis by the users at this meeting on reliable scheduled operation from the accelerators is likely to dominate technical improvements over the next few years. Thus, the need for consolidation rather than brighter sources may delay further development of some of these ideas. Nevertheless, the idea that existing sources could be upgraded over the next decade, so that they might exploit some of the ideas discussed for new sources is a good idea which will be found on the agenda of future meetings.

### **The Scientific Programs**

An exciting scientific program for pulse neutron sources was described at this meeting. However, an ICANS meeting is not the proper forum at which to judge it.



quality. Rather, the various elements of this program will be rated on their merit by each discipline over the next few years at meetings devoted to research in each discipline.

## **PART B: PROSPECTS FOR THE FUTURE**

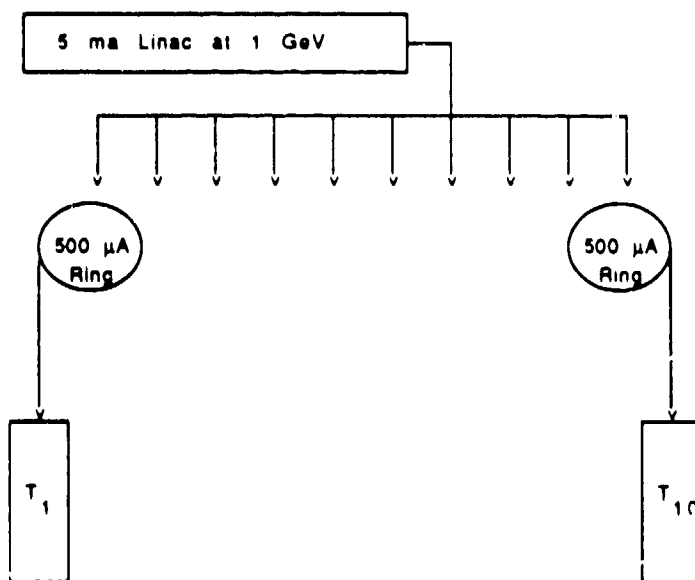
Some short-ranged projections have been given in the summary above, and so this section will be devoted to longer-ranged speculations that might provoke a fertile discussion.

The kinds and numbers of instruments at reactors are large, but they have taken about 30 years to develop and are still developing. This sets the relevant time scale. We might imagine that for pulsed accelerators, this process has gone about one-third as far as for reactors. Consequently, in about 15-20 years time, we might expect each accelerator source to have 30-40 instruments (maybe on more than one target), and that they will, in many cases, be complementary to the reactor instruments. In parallel with this gradual development, there will be an expansion in users: at present the users are fewer on the accelerators, but in 15-20 years we may expect them to equal or exceed the number at a large reactor. It is notable also that as this process of instrumental development takes place, the instrument scientists and users age in years. That is, new institutions attract young people and we see today that the accelerators have youth on their side compared to the staff at reactors. However, this difference is likely to disappear on the same time scale.

Accelerators are capable of supplying three types of sources—pulsed, time-structured and C. W. The proper roles for each are not yet clear, but will probably depend on the quality of the instruments developed for each type of source. Time-structured sources may, in particular, spawn new instruments. If this is so, the above 15-20 year time scale will apply to this source differentiation, also.

Another possibility is the multipurpose accelerator source. Several speakers pointed out that they would like to increase pulse length at the expense of resolution. This is easily accomplished through using large, high-temperature moderators. If the pulse repetition frequency is high and this type of moderator is taken to an extreme, it would overlap the structure of a time-structured source. Further, if several targets with different setups were used on one source, the distinction between these two different classes of sources may not be important. Moreover, the ideal pulse repetition frequency may vary from experiment to experiment or instrument to instrument, from 0.1 Hz giant pulses to 100 Hz normal pulses. Thus, giving the experimentalist some control over both pulse length and frequency may become an important future requirement. While it is not easy, at present, for the designer to meet these varied requirements, there is an important respect in which an accelerator source differs from a reactor source, which should be exploited. This is multiplexing. One can imagine a high-current accelerator feeding several storage

rings, each of which services a different class of users. Thus, in 20 years, we may see a cluster of storage rings and associated sources surrounding a high current accelerator. In this event, the number of users could greatly exceed those at the typical reactor. Figure 1 shows such an assembly, using a 5 ma linac feeding 10 storage rings each accepting 500  $\mu\text{A}$ . The larger the installation, the larger will be the number of users and the more user friendly will both the organization and the instruments need to be. Thus, user friendliness becomes an important goal of management, while management friendliness or administrator friendliness will be of lesser importance



Each experimental class has optimized facilities, due to multiple targets,  $T_1 \dots T_{10}$

**Fig. 1** A high Power Accelerator could run many sources of different kinds.

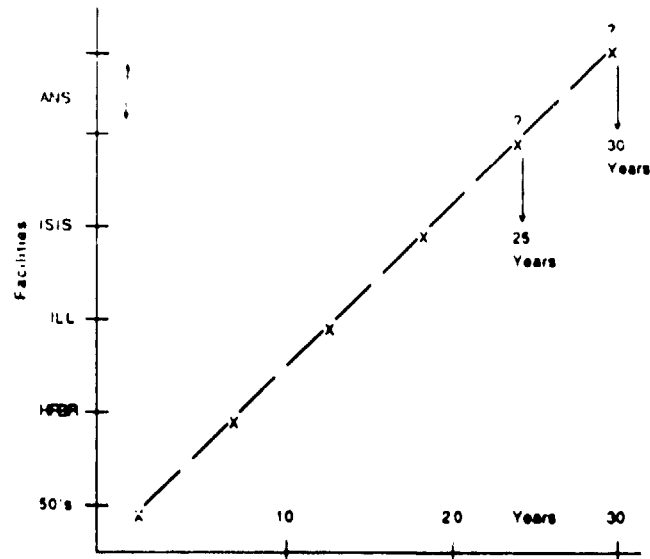
Many of today's instruments are designed to have a high productivity, and sometimes they have been criticized for putting productivity ahead of the scientific method. In the early days of the three-axis spectrometer and the constant-Q method, Bert Brockhouse praised this instrument for discarding most of the neutrons in both the incident and scattered beams. "It gives me only the points I want," he said "on a point-by-point basis at a human speed." Then he continued, "For this reason, when my first experiment is concluded, I have had time to interpret it, and have planned the next experiment!" As neutron sources proliferate and are used on a daily basis, we shall probably see a return to this notion of operating experiments at a "human speed", and thinking more deeply about the scientific method while they are in progress.

Because neutrons have so many useful properties and could be used by scientists in so many disciplines, there is need for a wide variety of sources and a variety of geographical locations. We may compare the availability of neutrons to photons (i.e., light- or x-rays). The difference lies in the absence of laboratory or local sources in the neutron case, compared to their ready availability in the case of photons. Neutron scattering will not develop unless this gap is closed. During the next 20 years, more attempts to close this gap will be made. On one hand, we can expect multiplexed accelerators offering a broad spectrum of options to an immense number of users, and on the other hand, we may expect inexpensive  $10^{14}$  n/cm<sup>2</sup> s reactors (e.g., the Maple) to become much more widespread. It is unlikely that the potential of neutron scattering in condensed-matter research will ever be realized unless the availability of medium-class sources proliferates in such ways. Thus, it is perhaps of greatest importance that designers regard cheapness, reliability and simplicity of operation as the primary goals for sources in this class.

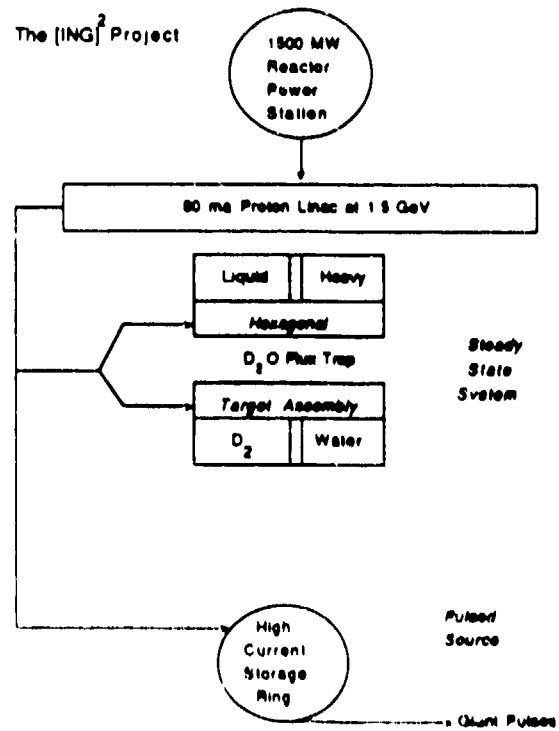
Some interesting predictions may be made by time projections of past experience. For example, the role of boosters on pulsed sources is changing. The Harwell electron linac booster (about 25 years ago) had a gain of 10, while the IPNS booster on a brighter source has a gain of 3. There are no plans for boosters on brighter sources. The reason seems to be that as the source brightness is increased, the instrument performance may be improved and the penalties of using a booster become more serious. To compensate for the defects, the booster gain is reduced; therefore, one can predict that boosters will disappear in about 10 years.

Another prediction in this class can be made by plotting the time-from-conception to regular use for each decade's high flux sources. This is shown in Fig. 2 for the most advanced source in four different periods (the time includes funding delays and other difficulties). It can be seen that the time scale increases uniformly, and if extrapolated for the case of the ANS, this graph predicts about 25-30 years. This is about twice the minimum time scale given by the designers. Thus, if the project was conceived during the late 70's, this argument would predict regular use in the early years of the next century. Such a time scale is close to the length of a research scientist's career and, hence, is likely to be unacceptable. If major projects are to be built successfully, this problem needs to be solved: it is, of course, a problem common to several fields.

Finally, there has been some speculation at this meeting on the ultimate source. My version of this is shown in Fig. 3, the (ING)<sup>2</sup>. An international group is likely to develop it, and (ING)<sup>2</sup> would provide the ultimate in C.W. sources for cold neutrons, thermal neutrons, and flux traps as well as the ultimate in pulsed sources, particularly in the field of giant pulses. It is also the ultimate in speculations.



**Fig. 2** Time from conception to regular use.



**Fig. 3** Inter-National Group for an Intense Neutron Generator.